# Tissue Mechanics

Stephen C. Cowin
Stephen B. Doty

# Tissue Mechanics

Springer

Stephen C. Cowin
New York Center for Biomedical
Engineering
The City College of The City University
of New York
Convent Avenue at 138th Street,
New York, NY 10031
scowin@earthlink.net

Stephen B. Doty
Hospital for Special Surgery
535 East 70th Street
New York, NY 10021
dotys@hss.edu

Library of Congress Control Number: 2006932976

ISBN-10: 0-387-36825-6
ISBN-13: 978-0-387-36825-2

Printed on acid-free paper.

©2007 Springer Science+Business Media, LLC
All rights reserved. This work may not be translated or copied in whole or in part without the written permission of the publisher (Springer Science+Business Media, LLC, 233 Spring Street, New York, NY 10013, USA), except for brief excerpts in connection with reviews or scholarly analysis. Use in connection with any form of information storage and retrieval, electronic adaptation, computer software, or by similar or dissimilar methodology now known or hereafter developed is forbidden.
The use in this publication of trade names, trademarks, service marks and similar terms, even if they are not identified as such, is not to be taken as an expression of opinion as to whether or not they are subject to proprietary rights.

9 8 7 6 5 4 3 2 1

springer.com

*The efforts of SCC in the preparation of this text are dedicated to his grandchildren.*

# FOREWORD

I was delighted when I learned in the fall of 2005 that Steve Cowin was working on a textbook in biomechanics. Steve and I were in the same department at Tulane University in the 1970s, and under his influence I learned the beauty and power of continuum mechanics as a means to better understand the musculoskeletal system. When I began teaching courses in biomechanics during that decade, it was natural to teach the material from a continuum mechanics perspective. Over the years I have used a variety of continuum mechanics texts, but, for the most part, I have had to find the biomedical examples I used directly from the research literature.

I have now had a chance to review a draft of *Tissue Mechanics* by Cowin and Doty, and it exceeds my high expectations. The material includes a rigorous and comprehensive introduction to continuum mechanics oriented toward biomechanics. Indeed, all of the foundation topics for continuum models of biological materials are covered. This material is illustrated through applications to the hard and soft tissues of the human body. Steve Cowin is now one of the leading researchers in the mechanics of bone, so one would expect the chapters on bone tissue and bone tissue adaptation to be of a very high order. But the presentation on collagen and cartilage mechanics is also excellent. Their presentation of finite deformation mechanics and its application to tendons and ligaments is one of the most accessible in the literature. The text is enhanced by a dedicated website, http://tissue-mechanics.com, which promises to continue to add to the text's richness.

I presently teach a two-course sequence in continuum biomechanics to advanced undergraduates and graduate students at New Jersey Institute of Technology. I look forward to using *Tissue Mechanics* as the main text for the course.

Cowin and Doty have performed a valuable service for the biomechanics community. For those of us who teach biomechanics, they have prepared the text that many of us have been looking for. But the principal beneficiaries of their efforts will be those who learn from this text with the aid of an instructor or on their own. As I did, thirty years ago, they will begin to appreciate the beauty and power of continuum mechanics as a way to better understand the biological world.

I wholeheartedly recommend this text to the biomechanics community.

*William C. Van Buskirk, PhD*
Distinguished Professor of Biomedical & Mechanical Engineering
Foundation Professor of Biomechanical Engineering
New Jersey Institute of Technology
Newark, New Jersey 07102

# PREFACE

The objective of this book is to describe the methods of formulating continuum models for biological tissues. The text is structured in a stepwise hierarchical fashion such that only the mechanics necessary for the development of a topic is presented before the topic. The text begins with two chapters that are introductory. The first chapter describes the structure of tissues and reviews some of the facilitating unresolved problems of tissue formation by active and passive biological processes. The second chapter describes the spectrum of mechanical modeling of biological tissue structures, how one does it, and why it is done. Chapters 3 through 7 describe the development of linear anisotropic continuum mechanics models: a development of basic continuum kinematics is presented in Chapter 3, the continuum formulations of conservation laws is recounted in Chapter 4, the process of modeling material symmetry is explained in Chapter 5, the steps in the formulation of constitutive equations are enumerated in Chapter 6, and four linear continuum theories — flow-through rigid porous media, elasticity, viscous fluid theory, and viscoelasticity — are described in Chapter 7. These four continuum models are combined in different ways and applied at the microstructural level in Chapters 8 and 9, chapters in which the process of modeling material microstructure and poroelasticity, respectively, are explained. In Chapter 10 collagen is employed as a model protein to describe how proteins are manufactured and how collagen performs similar basic functions in many tissues akin to those of steel in a machine or a tall building. Chapters 11 and 12 describe bone tissue and the adaptation of bone tissue to mechanical stimulus, respectively. In Chapter 13 the theory for modeling of electrical effects in tissues is developed. The mechanics of various cartilage structures are recounted in Chapter 14. The material of Chapter 15 represents a return to mechanics; modeling of the kinematics and mechanics of large deformations is described in this chapter. In Chapter 16 these results are employed in the development of tendon and ligament mechanics.

The presentations in the text differ from the customary presentations of these topics in many aspects, two of which are worth pointing out. First, all continuum models are developed for the anisotropic cases rather than the isotropic cases because most tissues are anisotropic in their material properties. Second, a slightly unconventional tensor-matrix notation is employed in this presentation. Its objective is to represent fourth-rank tensors as matrices that are composed of tensor components, something that the classical Voigt matrix notation for the anisotropic elasticity tensor does not achieve. In the notation employed here second- and fourth-rank tensors in three dimensions are represented as vectors and second-rank tensors, respectively, in six dimensions. Transformations in the six-dimensional space, corresponding to three-dimensional transformations, are six-by-six matrix multiplications that are easily entered and quickly computed with symbolic algebra software (Maple, Mathematica, MacSyma, and MatLab). In particular, the three-dimensional fourth-rank elasticity tensor is represented as a second-rank tensor in a space of six dimensions. This notation is described in the appendix on matrices and tensors.

The material in this text is covered in two courses by the first author. The first course is Continuum Mechanics and the second Cell and Tissue Mechanics. The Continuum Mechanics course regularly draws students from Chemical, Civil, and Mechanical Engineering as well as

Biomedical Engineering. The material in the Continuum Mechanics course, in the order covered, is Appendix A, some of the middle of Chapter 2, then Chapters 3 through 9. The Continuum Mechanics course is a prerequisite for the Cell and Tissue Mechanics course. In Cell and Tissue Mechanics the material covered includes Chapter 1, all of Chapter 2, and Chapters 10 through 16. One of the significant requirements of the Cell and Tissue Mechanics course is that the student prepare a term paper and, during the semester, make a poster and then a PowerPoint presentation on the topic of the term paper. The term papers are required to have an emphasis on some aspect of tissue morphogenesis, molecular self-assembly, supramolecular assembly, and the growth and remodeling of a particular tissue.

We would very much appreciate readers communicating with the authors on revisions to this book. In particular any corrections, comments, suggestions of material to be included (or excluded), and suggested problems with solutions for use as either examples or problems at the end of sections would be appreciated. Please email these materials to scowin@earthlink.net. We will maintain a record of corrections, suggested additions, and suggested (HW) problems with solutions. These materials, as well as other supplemental text material, will be available from a website designed for that purpose, http://tissue-mechanics.com. In particular, there are PowerPoint presentations of the material from each chapter on the website. We plan to develop additional chapters on various tissues and post them there.

A problem solutions manual is available from Springer for instructors using this text in a course.

Many people have been very helpful in the preparation of this text. Encouragement over the many years of preparation from Bill Van Buskirk, Michael Sacks, Jay Humphrey, Yi-Xian Qin, and Massimiliano Fraldi has been appreciated. The contributions from the students who took the courses in which the content of the book was contained in handouts presented have been most helpful; specifically, the contributions of Charles DaSalla, Jennifer Madeo, Mano Pahakis, Yuliya Vengrenyuk, and Liyun Wang stand out. Some of our colleagues have generously given their time to critique various chapters; in this regard we very much appreciate the efforts of Susannah Fritton, Weiyong Gu, Jacques Huyghe, Yi-Xian Qin, Agnès Rémond, Michael Sacks, Fred Silver, Yuliya Vengrenyuk, and Jeff Weiss. Monte Mehrabadi has made substantial indirect contributions to the text through his 35-year collaboration between one of us (SCC). Adam Curtis, Van Mow, Jean-Paul Revel, Jeff Weiss, and the late Art Winfree all contributed materials that were made into figures and we thank them. Finally, a special thanks to Tim Oliver, who configured the text submitted to Springer into the final product that you see, making the equations and, in particular, the figures more attractive in the process.

# CONTENTS

**Foreword** ..... v

**Preface** ..... vii

## 1: The Structure of Tissues

1.1. Introduction 1
1.2. The Adaptation of Tissues in the Species and in the Individual ..... 2
1.3. Tissue Types ..... 7
1.4. The Structure and Function of Cells ..... 9
1.5. The Hierarchical Structure of Tissues ..... 19
1.6. Plans for the Structure of a Tissue ..... 21
1.7. Structural Materials for the Tissue ..... 28
1.8. Assembly of the Tissue Structure ..... 29
1.9. References ..... 38

## 2: Mechanical Modeling of Biological Structures

2.1. Introduction ..... 41
2.2. Models and the Real Physical World ..... 43
2.3. Guidelines for Modeling Biological Tissues and Solving Biomechanics Problems ..... 45
2.4. The Types of Models Used in Biomechanics ..... 46
2.5. The Particle Model ..... 47
2.6. The Rigid Object Model ..... 50
2.7. The Deformable Continuum Model ..... 55
2.8. Lumped Parameter Models ..... 58
2.9. Statistical Models ..... 74
2.10. Cellular Automata ..... 77
2.11. The Limits of Reductionism ..... 84
2.12. References ..... 85
2A. Laplace Transform Refresher ..... 86
2B. Direction Integration of First-Order Differential Equations ..... 90
2C. Electrical Analogs of the Spring and Dashpot Models ..... 91

## 3: Basic Continuum Kinematics

3.1. The Deformable Material Model, the Continuum ..... 95
3.2. Rates of Change and the Spatial Representation of Motion ..... 104
3.3. Infinitesimal Motions ..... 110
3.4. The Strain Conditions of Compatibility ..... 116

## 4: Continuum Formulations of Conservation Laws


4.1. The Conservation Principles ... 119
4.2. The Conservation of Mass ... 120
4.3. The State of Stress at a Point ... 122
4.4. The Stress Equations of Motion ... 129
4.5. The Conservation of Energy ... 134
4.6. References ... 138


## 5: Modeling Material Symmetry


5.1. Introduction ... 139
5.2. The Representative Volume Element (RVE) ... 140
5.3. Crystalline Materials and Textured Materials ... 142
5.4. Planes of Mirror Symmetry ... 147
5.5. Characterization of Material Symmetries by Planes of Symmetry ... 150
5.6. The Forms of the Symmetric Three-Dimensional Linear Transformation A ... 154
5.7. The Forms of the Symmetric Six-Dimensional Linear Transformation $\hat{\mathbf{C}}$ ... 158
5.8. Curvilinear Anisotropy ... 162
5.9. Symmetries that Permit Chirality ... 163
5.10. Relevant Literature ... 166


## 6: Formulation of Constitutive Equations


6.1. Guidelines for the Formulation of Constitutive Equations ... 170
6.2. Constitutive Ideas ... 170
6.3. Localization ... 172
6.4. Invariance under Rigid Object Motions ... 173
6.5. Determinism ... 174
6.6. Linearization ... 175
6.7. Coordinate Invariance ... 175
6.8. Homogeneous versus Inhomogeneous Constitutive Models ... 176
6.9. Restrictions Due to Material Symmetry ... 176
6.10. The Symmetry of the Material Coefficient Tensors ... 178
6.11. Restrictions on the Coefficients Representing Material Properties ... 182
6.12. Summary of Results ... 183
6.13. Relevant Literature ... 184


## 7: Four Linear Continuum Theories


7.1. Formation of Continuum Theories ... 185
7.2. The Theory of Fluid Flow through Rigid Porous Media ... 186
7.3. The Theory of Elastic Solids ... 191
7.4. The Theory of Viscous Fluids ... 207
7.5. The Theory of Viscoelastic Materials ... 212
7.6. Relevant Literature ... 223

## 8: Modeling Material Microstructure


8.1. Introduction ..... 225
8.2. The Representative Volume Element (RVE) ..... 226
8.3. Effective Material Parameters ..... 228
8.4. Effective Elastic Constants ..... 231
8.5. Effective Permeability ..... 236
8.6. Structural Gradients ..... 237
8.7. Tensorial Representations of Microstructure ..... 239
8.8. Relevant Literature ..... 244


## 9: Poroelasticity


9.1. Poroelastic Materials ..... 247
9.2. The Stress–Strain–Pore Pressure Constitutive Relation ..... 249
9.3. The Fluid Content–Stress–Pore Pressure Constitutive Relation ..... 252
9.4. Darcy's Law ..... 254
9.5. Matrix Material and Pore Fluid Incompressibility Constraints ..... 254
9.6. The Undrained Elastic Coefficients ..... 257
9.7. Expressions of Mass and Momentum Conservation ..... 259
9.8. The Basic Equations of Poroelasticity ..... 260
9.9. The Basic Equations of Incompressible Poroelasticity ..... 261
9.10. Some Example Isotropic Poroelastic Problems ..... 262
9.11. An Example: The Unconfined Compression of an Anisotropic Disk ..... 270
9.12. Relevant Literature ..... 286


## 10: Collagen


10.1. Introduction ..... 289
10.2. The Extracellular Matrix (ECM) ..... 291
10.3. The Amino Acid Composition Sequence ..... 295
10.4. The Procollagen and Collagen Molecules ..... 297
10.5. Experimental and Theoretical Deduction of Collagen Structure ..... 305
10.6. The Axial Young's Modulus of a Collagen Molecule ..... 307
10.7. The Many Types and Classes of Collagens ..... 310
10.8. Collagen Structural Hierarchy ..... 312
10.9. Supramolecular Assembly ..... 321
10.10. Assembly of a Tendon ..... 324
10.11. References ..... 338


## 11: Bone Tissue


11.1. Introduction ..... 341
11.2. The Types of Bone Tissue ..... 342
11.3. Bone Interfaces, Porosities and Fluids or Gels ..... 347
11.4. Bone Cells ..... 353
11.5. The Elastic Symmetry of Cortical Bone ..... 356

11.6. The Poroelastic Model for Cortical Bone ..... 358
11.7. Electrokinetic Effects in Bone ..... 362
11.8. Cortical Bone Strength ..... 368
11.9. Cancellous Bone Architecture ..... 372
11.10. The Elastic Properties of Cancellous Bone ..... 374
11.11. The Literature of Bone Mechanics ..... 381

## 12: Bone Tissue Adaptation

12.1. Introduction ..... 385
12.2. Four Animal Experiments ..... 386
12.3. Representation of the Stimulus to Bone Remodeling ..... 389
12.4. A Phenomenological Theory of Surface Adaptation ..... 392
12.5. Estimating Remodeling Parameters ..... 395
12.6. Prediction of the Surface Adaptation Due to the Bending of Bone ..... 399
12.7. Summary of Surface Remodeling Results ..... 404
12.8. A One-Dimensional Phenomenological Internal Bone Strain Adaptation Model ..... 407
12.9. Three-Dimensional Phenomenological Bone Strain Adaptation Theories ..... 415
12.10. Possible Cellular Mechanisms for Bone Tissue Adaptation ..... 418
12.11. The Literature of Bone Tissue Adaptation ..... 421

## 13: Modeling Poroelastic and Electrical Effects in Soft Tissues

13.1. Introduction ..... 425
13.2. Kinematics of Mixtures ..... 427
13.3. The Conservation Laws for Mixtures ..... 430
13.4. A Statement of Irreversibility in Mixture Processes ..... 433
13.5. Donnan Equilibrium and Osmotic Pressure ..... 440
13.6. Continuum Model for a Charged Porous Medium: Constitutive Equations ..... 448
13.7. Linear Irreversible Thermodynamics and the Four-Constituent Mixture ..... 453
13.8. Modeling Swelling and Compression Experiments on the Intervertebral Disc ..... 458
13.9. Relevant Literature ..... 466

## 14: Cartilage

14.1. Introduction ..... 471
14.2. Hyaline Cartilage ..... 473
14.3. Elastic Cartilage ..... 474
14.4. Fibrocartilage ..... 474
14.5. The Perichondrium ..... 476
14.6. Common Properties of the Three Tissues: Intervertebral Disc, Articular Cartilage, and the Meniscus ..... 476
14.7. The Intervertebral Disc (IVD) ..... 479

14.8. Articular Cartilage ..... 482
14.9. Lubrication in Synovial Joints ..... 485
14.10. The Mechanical Modeling of Articular Cartilage Behavior ..... 492
14.11. Menisci ..... 499
14.12. Relevant Literature ..... 503

## 15: Kinematics and Mechanics of Large Deformations

15.1. Large Deformations ..... 507
15.2. Large Homogeneous Deformations ..... 508
15.3. Polar Decomposition of the Deformation Gradients ..... 515
15.4. The Strain Measures for Large Deformations ..... 519
15.5. Measures of Volume and Surface Change in Large Deformations ..... 526
15.6. Stress Measures ..... 528
15.7. Finite Deformation Elasticity ..... 531
15.8. The Isotropic Finite Deformation Stress–Strain Relation ..... 531
15.9. Finite Deformation Hyperelasticity ..... 534
15.10. Incompressible Elasticity ..... 536
15.11. Fung's Exponential Strain Energy Function ..... 537
15.12. Strain Energy Functions for Tissues ..... 547
15.13. Fung's Quasi-Linear Viscoelasticity (QLV) ..... 552
15.14. Relevant Literature ..... 555

## 16: Tendon and Ligament

16.1. Introduction ..... 559
16.2. The Constituents of Tendons and Ligaments ..... 561
16.3. The Cells and Cell Systems of the Tendon ..... 563
16.4. The Arrangement of Collagen Fibers in Tendons and Ligaments ..... 564
16.5. The Lubrication System in Tendons ..... 566
16.6. The Mechanical Properties of Tendons and Ligaments ..... 567
16.7. Constitutive Equations for Tendons and Ligaments ..... 575
16.8. Interstitial Fluid Flow ..... 587
16.9. The Insertions of Tendons and Ligaments ..... 588
16.10. Structural Adaptation ..... 590
16.11. References ..... 591

## Appendix: Matrices and Tensors

A.1. Introduction and Rationale ..... 595
A.2. Definition of Square, Column, and Row Matrices ..... 595
A.3. The Types and Algebra of Square Matrices ..... 596
A.4. The Algebra of *N*-Tuples ..... 602
A.5. Linear Transformations ..... 603
A.6. Vector Spaces ..... 609
A.7. Second-Order Tensors ..... 615
A.8. The Moment of Inertia Tensor ..... 621

A.9. The Alternator and Vector Cross-Products ..... 630
A.10. Connection to Mohr's Circles ..... 637
A.11. Special Vectors and Tensors in Six Dimensions ..... 639
A.12. The Gradient Operator and the Divergence Theorem ..... 645
A.13. Tensor Components in Cylindrical Coordinates ..... 649

**Credit Lines** ..... 653

**Index** ..... 669

# 1

# THE STRUCTURE OF TISSUES

The theme of this chapter is summarized by a paragraph from Trelstad and Silver (1981): "The processes of morphogenesis, growth, repair, adaptation and aging are all reflected in tissues by the processes of either changing the ratio of their constituents or the properties of their constituents. The capacity of cells in tissues to produce composite extracellular matrices that assemble into multiple diverse forms reflects a successful stratagem of multicellular organisms to segregate cells into functional units of tissues and organs able to contend with the forces of gravity and work in unison to transmit the forces necessary for movement. The shape and size of higher organisms are defined by spaces, partitions, and unique forms of the matrix. In the embryo, the extracellular matrix is the scaffolding that helps determine tissue patterns, and in the adult it serves to stabilize these same patterns. The mineralized matrices of the bones and teeth are stiff, hard structures, whereas the nonmineralized cartilages are flexible and compressible and serve as joint cushions during compression and translation of joints. The ropelike organization of tendons and ligaments provides them with the capacity to withstand large forces without stretching more than a few percent of their length, making movement possible. Elastic blood vessels transiently store pulse pressures generated by the heart and thus ensure a relatively continuous flow of blood. The stretchable, tough, and tight-fitting skin is a collagenous shield that serves to keep undesired materials out and desired materials in, whereas its counterpart covering the eye, the cornea, is a transparent lattice of collagen fibrils serving both barrier and optical functions."

## 1.1. INTRODUCTION

Tissues are composite materials whose constituents, and therefore structure, are continually changing due to growth and response to the tissue environment, including the mechanical environment. The objective of this chapter is to briefly describe the nature of the composite components of a tissue, the cellular processes that produce these constituents, the assembly of the constituents into a hierarchical structure, and the behavior of the tissue composite structure in the adaptation to its mechanical environment.

A tissue's mechanical environment is the history of mechanical loading experienced by the tissue in some reference time period, like a day. Physiologists use the term *homeostasis* to describe the maintenance of stable steady states in tissue and organs. Sometimes the word "equilibrium" is used in connection with homeostasis, but "equilibrium" in mechanics means rest (or moving with constant velocity), and physiologists intend to convey the notion of a number of active, continuous biological processes whose objective is to maintain the tissue and

organs in a functional state. The state is not a static "equilibrium" state but rather a state in which the net effect of the continuously ongoing biological processes is to maintain the functional state, which may not appear to change with time. A living tissue is always in the process of renewal and remodeling that does not cease until the cells of the tissue cease to function. The process of renewal and remodeling need not produce a net observable change in the tissue, but it often does. Sometimes these changes can be observed on the outside of a body, for example, a callus on the hands from a month of digging ditches with a shovel and a pick or at the fingertips from a period of playing a guitar. Changes are often imposed on a body to enhance the perceived beauty of the body as in the old practices of binding women's feet to keep them small or stacking bands around necks to elongate them. Another example is the healing of the piercing operation associated with the creation of a passage through living cartilage for the support of jewelry.

The beginnings of structural form (morphogenesis) are not easy to observe in animals, but are easily observed in plants; one has only to view the development of a plant from a seedling placed in soil against a transparent glass surface. Internal changes are usually not observable on the outside of the body. Tennis fans do not notice that the tennis stars have bones in their upper playing arm that are 30% greater in cross-sectional area than the bones in their nonplaying arm. Further, the deterioration in most of the structures of the human body that may begin in youth does not become apparent until much later in life. These changes occur in the cells of the tissue, the cellular process of the tissue, the tissue constituents made by the cells, and thus in the gross behavior of the tissue. Although all the principles upon which tissues may be viewed as continually changing composite materials are not yet firmly established, an effort is made in this chapter to draw together a picture of what has been established to date and to fill in the gaps with the current state of thought.

## 1.2. THE ADAPTATION OF TISSUES IN THE SPECIES AND IN THE INDIVIDUAL

Most animal bodies can be placed in one of two categories: radiata and bilateria (radiata have radial or spherical external symmetry and bilateria have bilateral external symmetry). The tissues of the radiata have only two major layers, whereas the bilateria have three. Bilateral external symmetry is an evolutionary development linked with an increasing capability of active locomotion. There are similarities in the general shape of the human body and the bodies of the other vertebrates that are a consequence of the earth's gravity field and the need of the organism to transport itself. A notable similarity is the left-to-right or bilateral external symmetry of the bodies of these creatures. There is a plane of mirror symmetry defined by the direction of gravity in an erect posture of the creature, the *superior-inferior* (*cranial-caudal*) direction (Figure 1.1), and the direction of customary locomotion, *the posterior-anterior* (*dorsal-ventral*) direction. This plane of mirror symmetry is called the *sagittal* plane. The two planes perpendicular to the sagittal plane are called the *coronal* plane and the *transverse* plane, and neither of these planes is a plane of mirror symmetry for man or animals. The transverse plane is not a plane of symmetry because the effect of gravity makes any symmetry in the superior-inferior (cranial-caudal) direction impractical; our lower limbs provide us with locomotion and our ankles must carry more force than our necks. As the size of an animal increases, the limbs tend to become thicker and the structure of the skeleton increases in order to sustain the additional weight; bones make up some 8% of the body of the mouse, 13 or 14% of the dog, and 17 or 18% of the human body (D'Arcy Thompson, 1942). Similarly there is lack of external symmetry in the posterior-anterior (dorsal-ventral) direction because it is necessary to see where one is going rather than where one has been.

Organisms that live in water are less influenced by gravity. There is little difference in the skeletal proportions between the porpoise and the whale. Marine creatures have greater external symmetry in the superior-inferior direction. A very interesting exception to the superior-

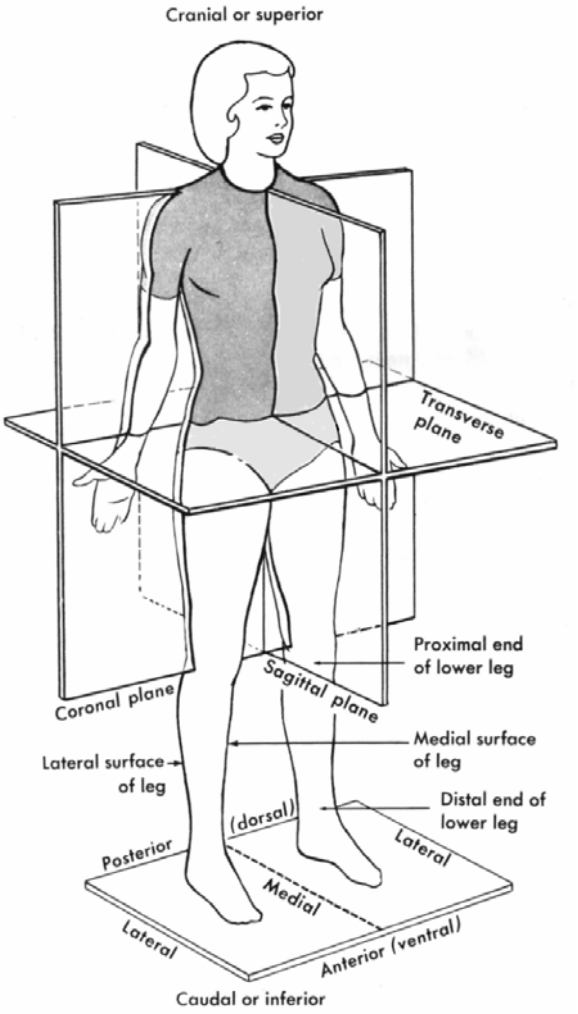



**Figure 1.1**. Anterior view of a human figure demonstrating the meaning of terms used in describing the body. Reprinted with permission from Anthony and Kolthoff (1975).

inferior external symmetry in marine creatures is the one-sided flatfish, such as sole and plaice. They are hatched with the usual external superior-inferior external symmetry of marine creatures with one eye on each side of their bodies, but as they grow a bar of cartilage above one eye dissolves and the eye slides over to the other side of the body, twisting the entire skull to the other side in the process; thus initial symmetries are not necessarily preserved in development (McManus, 2002).

The form of very small organisms is almost independent of gravity. Protozoa are animal-like, unicellular creatures from which multicellular animals arose. Amoebas, ciliates, and flagellates are protozoa. The locomotion of ciliate protozoa is by rhythmic movement of their cilia. This characteristic locomotion ability is associated with the axial external symmetry of the ciliate protozoa illustrated in Figure 1.2. Many small organisms have a spherical shape because the dominant force system to which they are subjected is the tension in the closed membrane that separates them from their fluid environment. The membrane tension is created by a

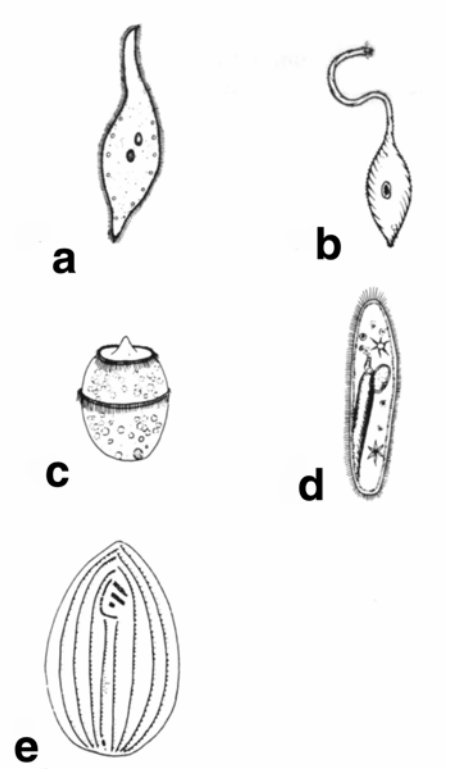



**Figure 1.2**. Ciliate protozoa. The cilia of these protozoa produce a rhythmical motion. Reprinted with permission from Goodwin (1989).

pressure difference between the inside and outside of the membrane, the greater pressure being necessarily internal. This is called a "turgor" pressure or just "turgor." Recall from above that animals with radial or spherical external symmetry are called radiates. Protozoa with spherical external symmetry are shown in Figure 1.3.

Internal symmetry does not follow from external symmetry in animals. In the human the heart is usually on the left side along with the stomach and spleen, and the liver is usually on the right side. In approximately 0.012% of the population this placement of organs is reversed: the heart, stomach and spleen are on the right and the liver is on the left side, a situation called *situs inversus* (McManus, 2002). Humans and animals with *situs inversus* lead normal lives, except for a syndrome that includes sinusitis, bronchiectasis, and infertility in the male but not the female. These three conditions are linked by a malfunction of the molecular motor associated with the cellular cilia, the cilia that move the sperm and clear the lungs of congestion and move the fluid-containing signaling molecules that normally place the heart on the right side during embryonic development. The human brain also functions asymmetrically, although it appears to have symmetrical left and right lobes. Not only does the left side of the brain control the right side of the body and vice versa, but certain brain functions are specific to particular lobes. The seat of language, for example, is in the left frontal lobe; damage to the left frontal lobe can cause a loss of language (aphemia).

A reference mentioned above was to the the famous book *On Growth and Form* (originally published in 1917) by D'Arcy Wentworth Thompson (1860–1948), a Greek scholar, naturalist and mathematician. D'Arcy Thompson held the Chair of Natural History in St.

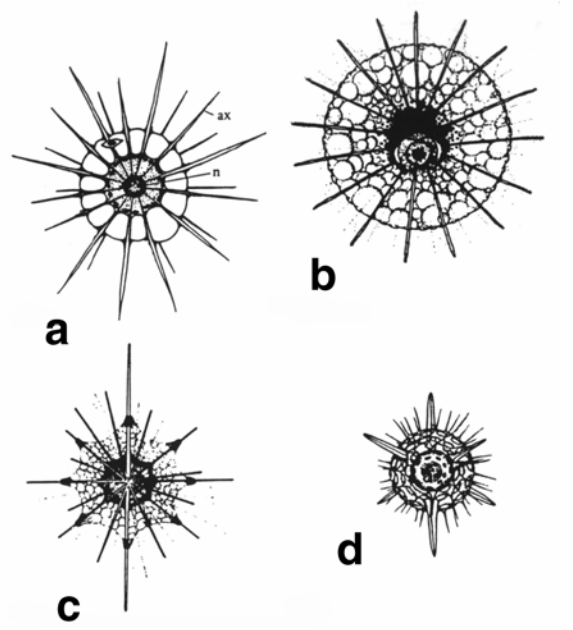



**Figure 1.3**. Protozoa with spherical symmetry. Protozoa are a large group of single-celled, usually microscopic, eukaryotic organisms, such as amoebas, ciliates, flagellates, and sporozoans. These are all typical forms of Heliozoa (a) and Radiolarians (b,c,d). Reprinted with permission from Goodwin (1989).

Andrews for 64 years. In the book he argues that all science and learning are one, and that many biological phenomena are illuminated by mathematical considerations. It is safe to suggest that most of the people interested in the present subject have read and enjoyed *On Growth and Form*, allowing for the fact that some of the material it contains is now out of date. It is the first major work to advocate and develop mathematical models for biological phenomena.

**Exercise 1.1**

**Problem**: In this chapter there may be many words whose definitions may not be familiar to the reader. Only simple definitions of anatomical and physiological terms will be included in the text. It is advised that the reader keep supplemental reference material at hand. At the minimum a dictionary is needed, but a medical dictionary as well as texts on anatomy and physiology would be helpful, as would a dictionary of etymology. Science takes customary words and gives them additional meanings. Thus the “transcription” process that occurs in a biological cell is different from the transcription of a radio or TV broadcast, and the “translation” process that occurs in a biological cell is different from the translation of a work from one language to another. There are two meanings of the word "cell" employed in science. One meaning stems from the early terminology for monastic rooms, then prison rooms. The other meaning is from biology, the biological cell. This ambiguousness developed because Robert Hooke examined cork under an early microscope and observed microscopical pores, over a billion of these tiny box shaped pores in a cubic inch of cork. Because they looked like the walled compartments of a honeycomb or the cells in a monastery, Hooke called them cells, the name they still bear (Inwood, 2002). However, when the walls of the cells or pores are included with the pore, Hooke had actually observed a biological cell of cork, which was formerly the living bark of a tree. That Hooke’s “cells” had this biological significance was not

understood until after Hooke's death. Thus the cells in cellular automata are like rooms and the cells in the human body are biological cells and cellular automata models of biological cell behavior is a phase that uses the two meanings of "cell." In the paragraph above locate unfamiliar words and look up their definitions, for example cranial, caudal, dorsal and ventral. In section 1.4 look up the words *transcription* and *translation*. Seek out the meanings of words that are unfamiliar, or familiar words that are used in unfamiliar ways.

**Solution**: Thus, for example, consulting a dictionary one finds that *cranial* is an adjective suggesting a relation to the skull or cranium. *Caudal* is an adjective referring to the tail or hind parts, posterior. *Dorsal* is an adjective referring the back or upper surface of an animal. *Ventral* is an adjective suggesting a nearness to the abdomen.

These observations illustrate one of the themes of this book — that the functional form of biological structures is strongly influenced by the force systems to which the structures are subjected. As other examples, consider the following body substructures: the tendon, ligament and muscle that carry tension; articular cartilage, bone, and teeth that are subjected to repeated compressive impact loads; membranes (cells, mesentery, skin) that protect one environment from another and cylinders (long bones, intestine, blood vessels) that are designed for structural support or the transport of fluids.

Another theme of this book is that these biological structures can adapt, or remodel, their structure, in the individual (epigenetically) as well as in the species (genetically), to accommodate a changed mechanical load environment. Numerous studies of biological systems in the last century and a half have demonstrated that slow evolutionary engineering over a period of millions of years has refined the properties of the biological structures, including mechanical properties. The results of this process are recorded in the genes. However, the biological structures of an individual may also accommodate to a changed mechanical load environment, as illustrated by the bodies of weightlifters or bodybuilders. In general, the form of a biological structure is due to both genetic and epigenetic information, but the contribution by each towards the final form is not known. Fortunately, with the present rate of decoding human genetic information, a great deal more will be understood in a decade.

The key genetic factor that lies at the base of structural adaptation is likely the sensitivity of cells of the biological structure to physical forces. Certain basic features of the full organism are recorded in the genes, but during embryonic development and during early growth the structure of the organism is modified or molded by the mechanical environment of the womb and the growth of the individual after birth. For example, the skin forming the soles of the feet is already thickened in the human fetus, but our common experience shows that walking barefoot or wearing poorly fitting footwear will contribute to the thickness and distribution of this tissue on the foot bottom. As an example of how precise the development driven by the genes may be, consider the case of the small worm *Caenorhabditis elegans*. It has been shown that of the 1090 cells formed during the development of the main body of an individual worm 131 always die (Coen, 1999). The programmed cell deaths are not random, but involve exactly the same cells in every individual. Programmed cell death is called "apoptosis" to distinguish it from cell death by other causes, which is called "necrosis." Apoptosis is an intracellular controlled process that fragments the cell nucleus while keeping the cell membrane intact.

Another example of extreme preciseness of genetic information is the source of Huntington's disease, the disease that felled the folksinger Woody Guthrie ("This Land is Your Land"). The source of the disease is a gene on chromosome 4; little is known about the general function of this gene. But we do know precisely how and why and where it can go wrong and what the consequences are for the body with the defective gene. The gene contains the amino-acid sequence C (Cysteine) A (Alanine) G (Glycine) (see Chapter 10), repeated over and over again: CAG, CAG, CAG, CAG ... The repetition may continue from six to more than a hundred times. Normally there are about ten to fifteen repeats. If CAG is repeated thirty-five times or fewer, there will not be a problem. "The age at which the madness will appear depends strictly and implacably on the number of repetitions of the CAG in one place in one gene. If

you have thirty-nine, you have a ninety-percent probability of dementia by the age of seventy-five and will on average get the first symptoms at sixty-six; if forty, on average you will succumb at fifty-nine; if forty-one, at fifty-four; if forty-two, at thirty-seven; and so on until those who have fifty repetitions of CAG will lose their minds at roughly twenty-seven years of age" (Ridley, 1999, p. 56). These two examples of extreme precision of the genes are the exception rather than the rule. Generally multiple genes often control a single structure or function. Genetic control may not always be so precise, or if they are so precise the effects of the precision are masked by the requirements of other genes.

As an illustration of the accommodation of the biological structures of the body to a changed mechanical load environment, consider the data on the response to weightlessness. Almost 1000 people have accumulated almost 70 person-years of spaceflight. The direct and indirect effects of weightlessness are numerous. The removal of gravity means that the limbs no longer have weight, and muscles are no longer required to maintain posture. The stretch sensors in the musculoskeletal system then receive a signal different from the one they receive on Earth. They no longer have to maintain the normal musculoskeletal structure of the body against gravity, and the system begins to diminish its capacity. Bone mass is lost from key parts of the skeleton at a rate of about 1% per month and some muscles atrophy rapidly. The vestibular system in the inner ear, the system that allows us to control our balance and equilibrium, automatically compensates for gravity, and some adaptation of this system is necessary when there is no gravity. A researcher studying the effect of microgravity on the vestibular system has indicated that we are not able to predict whether, after a yearlong trip from Earth, an astronaut would be able to stand up on Mars (Young, 1993). Much of the body is fluid and therefore the body in microgravity (keep in mind that the body is adapted for life in Earth's gravity field) experiences a fluid shift to the head and away from the feet in microgravity. The fluid shift initiates a number of interacting renal, hormonal, and mechanical effects that regulate fluid and electrolyte levels (White, 1998). The kidney filtration rate, for example, is increased by 20%. And the skull may actually gain bone rather than lose it because of the increased fluid pressure within the skull due to the caudal shift of fluids in microgravity.

The detruser, the smooth muscle of the bladder wall, provides an example of tissue adaptation to mechanical loading, and this example illustrates that all adaptations are not beneficial to the organism. The detruser undergoes hypertrophy and collagen deposition due to bladder outlet obstruction. When the outlet orifice of the bladder, the urethral orifice, is blocked, the load on this muscle increases. This blockage occurs, for example, in men due to prostate cancer. The decrease in urine outlet flow increases the lumen pressure and puts excess tension on the tissue of the bladder wall, and increased demand on the detruser. This requires that the detruser contract against a greater force to empty the bladder. The tissue wall thickens or hypertrophies, taking urine space from the lumen. The bladder capacity is lowered due to the increased stiffness of its wall caused by collagen deposition. This effect is similar to the counterproductive adaptations of arteries due to high blood pressure (hypertension).

## 1.3. TISSUE TYPES

A tissue is a collection of cells, and extracellular matrices, that perform specialized functions. The extracellular matrix consists of fibers (e.g., the proteins collagen and elastin) and a ground substance consisting of proteoglycans. Proteins are complex organic macromolecules that contain carbon, hydrogen, oxygen, nitrogen, and usually sulfur, and are composed of one or more chains of amino acids. Proteins are fundamental components of all living cells and include many substances, such as enzymes, hormones, and antibodies that are necessary for the proper functioning of an organism. Proteins are manufactured by the cells for many applications, including tissue construction. Animal tissues are classified into four main groups: connective, epithelial, muscle, and nerve. A short description of each of these tissue types is given below.

*Connective tissue* "connects" the body organs and tissues; it holds organs in place and provides the structure that gives the body a shape. Compared with other types of tissue, connective tissue has relatively few cells and much intercellular substance (material outside the cells). Connective tissues include cartilage, tendons, ligaments, the matrix of bone, and the adipose (fatty) tissues as well as skin, blood, and lymph. Blood and lymph are special connective tissues where the extracellular matrix is the fluid component. Skin is an example of dense connective tissue, but its outer layer, the epithelial layer, is obviously an epithelial tissue. Thin fibrous connective tissue is found to bind blood vessels and forms a basal membrane to support cells of the tissue of the liver and of muscle. Connective tissues are composed of various types of cells and extracellular matrix. The fibers of the extracellular matrix consist of insoluble high-molecular-weight polymers of the proteins collagen or elastin. The fibers may be either loosely woven or densely packed in either an ordered or disordered arrangement. In dense irregular connective tissue the fibers are closely interwoven in a random way, as in skin, whereas in dense regular connective tissue the fibers are arranged in parallel bundles, as in tendons. The relative abundance of the various tissue constituents varies greatly from one region of the body to another, depending upon the local structural requirements.

*Epithelium* consists of sheets of cells that line the inner and outer surfaces of the body and have a secretory as well as a protective function. Epithelial tissues include the cellular lining of the lungs, stomach, intestines, and blood vessels as well as the "skin" that covers the skin, the epithelial layer of skin. (The word "skin" has many meanings and is used here in two ways that should not be confused: first in the sense of tissue, and second in the sense of "skin," the outer covering.) In contrast to connective tissues, which may contain a great deal of extracellular matrix between each cell, the cells of epithelium are tightly packed with little extracellular substance between them, although they are usually supported on a basal membrane which contains components of the extracellular matrix. One of the main properties of epithelial tissues is a stable apico-basal (outside–inside) polarity, which is expressed not only in morphological, but also in electrophysiological and transport properties. The ionic channels are mostly located within the apical (outside) membrane domain while pumps are in the basolateral one (inside). This is of importance morphomechanically because this property provides a certain amount of turgor pressure in the subepithelial cavities and hence epithelial stretching. The epithelial cells are bound together by junctions to form an integrated net that gives the cell sheet mechanical strength and makes it impermeable to passive diffusion of small molecules. The junctions are important in mechanically holding the epithelial sheet together to form a protective layer and thus shield the body from injury and infection. One of the most remarkable properties of embryonic epithelial sheets is that cell rearrangement and replacement may occur without compromising the mechanical integrity and chemical barrier function. Extracellular structures also play a strengthening role. There are many kinds of epithelia. The stratified scaly tissue found in the skin and the linings of the esophagus and vagina is composed of thin layers of flat, scale-like cells that form rapidly above the blood capillaries and are pushed toward the tissue surface, where they die and flake off. Epithelial cells also produce hair, fingernails, and toenails and in other animals can give rise to feathers and hooves.

*Muscle cells* consume body fuel (e.g., sugars and fats) to create a force by contracting and thus do mechanical work. They are the body's motors or engines. There are three main types of muscle tissues: striated, smooth, and cardiac. Striated muscles attach to bone, which then forms a lever arm to do work. This muscle group is also called skeletal or voluntary muscle and consists of large multinucleated cells. Smooth, or involuntary muscle, is found in the internal organs and around larger blood vessels and consists of sheets of cells. Smooth muscle is present in the digestive tract, bladder, arteries, and veins and is activated by the autonomic nervous system. Cardiac muscles perform the pumping action of the heart. Cardiac muscle is characterized by the fact that the muscle cells are often branched. Cardiac tissue is unique in that there are junctional complexes used to help the cells physically adhere to each other and other junctions used to transmit electrical impulses through the muscle to create rhythmic contractions.

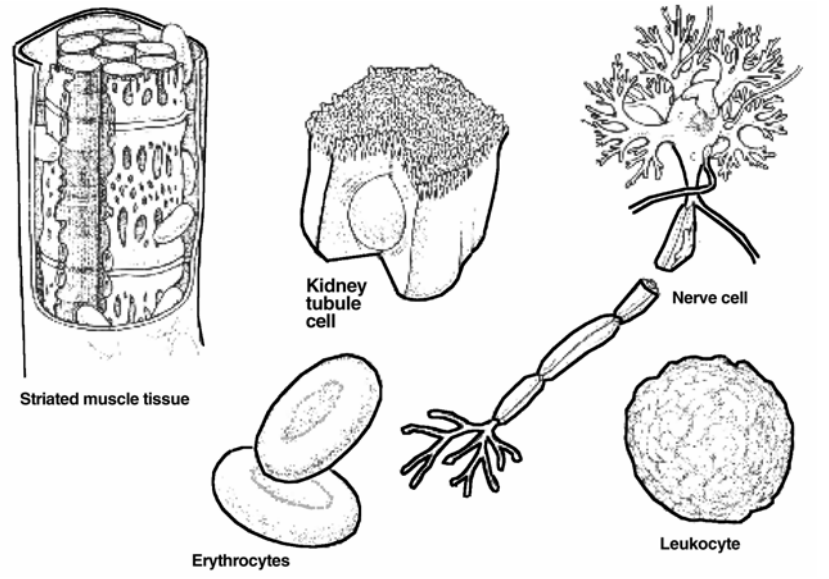



**Figure 1.4**. Various cell types. Scanned and modified with permission from p. 2 of de Duve (1984).

*Nerve cells*, or neurons, are specialized to transfer information from one part of the body to another. The brain and spinal cord are tissues composed of neuronal networks. Each neuron consists of a cell body or soma with branching processes called dendrites and one much longer fiber called the axon (Figure 1.4). The dendrites connect one neuron to another, and the axon transmits impulses. A synapse is a specialized neuronal junction where neurons connect with each other or with muscle cells. Electrical and chemical signals are passed from neuron to neuron or from neuron to muscle through the synapse.

**Problems**

1.3.1. Charles Darwin was the first to propose a successful explanation of evolutionary processes. Explain Darwin's theory.
1.3.2. What did Gregor Mendel discover through years of experiments with plants, chiefly garden peas?
1.3.3. What notable discovery did James Watson and Francis Crick make in 1953?
1.3.4. What is cartilage?
1.3.5. What is a tendon?
1.3.6. What is a ligament?
1.3.7. What are aponeuroses?
1.3.8. What is lymph?
1.3.9. Explain the difference between a lysosome (Figure 1.5) and a liposome (Figure 1.6).

## 1.4. THE STRUCTURE AND FUNCTION OF CELLS

Cells within or lining the surface of tissues control the structure of the tissue by manufacturing most of the tissue constituents, maintaining the tissue and adapting the tissue structure to changed environments, including mechanical load environments. The general structure of ani-

mal and plant cells is similar in that both types have a nucleus and are therefore classified as eukaryotes (prokaryotes have no nucleus); attention is restricted here to the types of cells in the human body, of which there are over 200. There are trillions of cells in the human body; they all originate from a single fertilized egg. During embryonic development, cellular differentiation gives rise to a wide variety of specialized cell types such as nerve, muscle, bone, fat, epithelial, and blood cells. The lifetimes of the specialized cells vary a great deal. Neutrophils live about a day, intestinal epithelial cells live about 3 days, red blood cells about 90 days, and neurons live as long as 90 years.

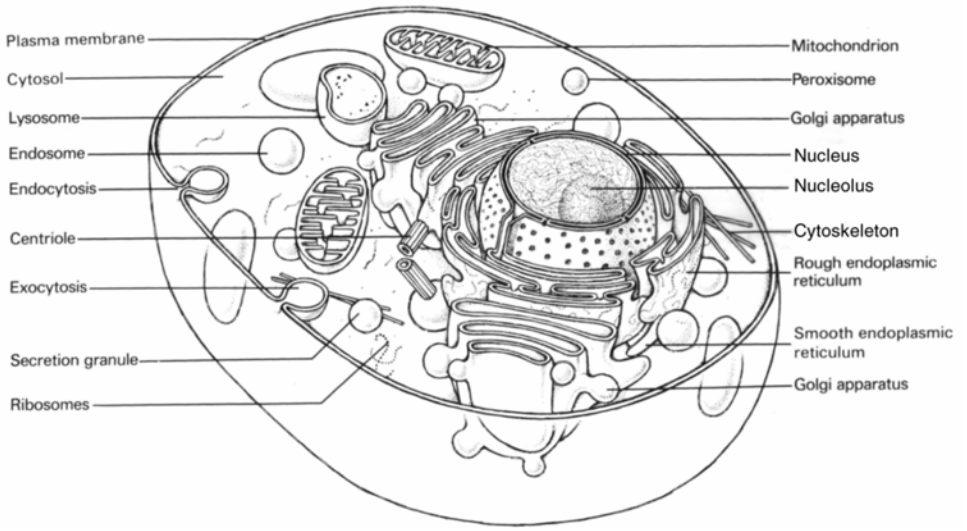



**Figure 1.5**. Map of a generic cell. Scanned with permission from p. 19 of de Duve (1984).

In this section the main parts of a cell are identified and their function indicated. The number of functions that a cell performs is really quite amazing given its small size — generally 10 to 100 microns in humans. In some ways the functioning of a cell can be compared with the functioning of a factory, a factory that makes the proteins that include the materials that make the tissue. In fact, the cell is a factory, and it is much more than a factory, but the analogy will help in understanding the functions of some of the cell's structures. The boundary between the cell and the outside world is the cell membrane (Figures 1.5 and 1.6). These are the walls of the factory. Within the confines of the cell membranes there are a number of differentiated structures called organelles in which many biochemical functions are carried out, such as protein and lipid fabrication and chemical energy storage and generation. These are subdivisions of the factory. This presentation of the structure of a typical animal cell is diagrammed in Figure 1.5. The structures or functions listed on the left- and right-hand sides of Figure 1.5 are described below starting with the top item on the left-hand side and continuing down the left-hand side before moving down the right-hand side. Because of the interconnections of structures and definitions, it is recommended to read the entire list to appreciate the cell activities (factory functions).

(a) Plasma membrane: the factory walls — The plasma membrane is the boundary of the cell and the site of the cell's interaction with its environment (Figure 1.6). To control and accomplish this interaction the plasma membrane contains specialized components involved in intercellular contacts and communication, hormonal response, and transport of both small and

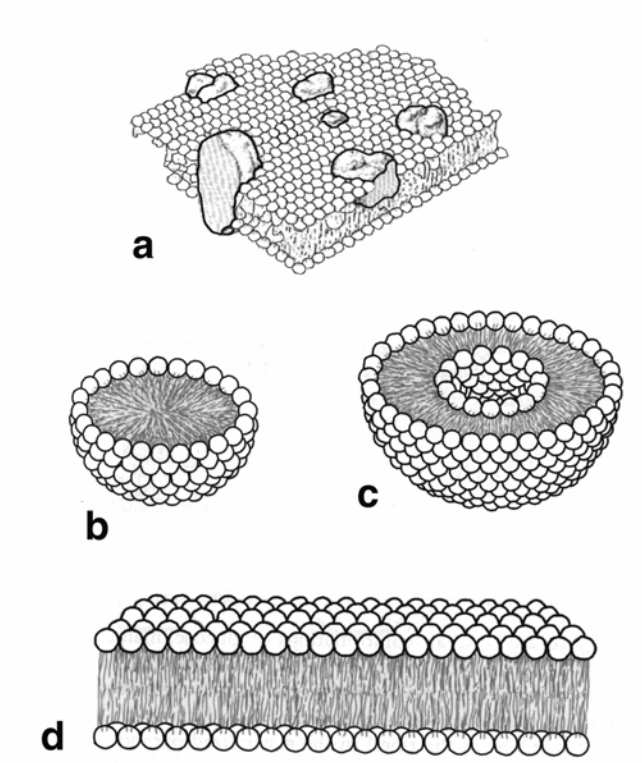



**Figure 1.6**. (a) The fluid mosaic model for the membrane structure. Phospholipid bilayer containing embedded proteins. Reprinted with permission from Gennis (1989). (b) Micelle. (c) Liposome. (d) Phospholipid bilayer sheet. (b), (c), and (d) adapted with permission from Darnell et al. (1990).

large molecules into and out of the cell. The cell membrane of a typical animal cell is 6 to 10 nm thick. Although the membrane is composed of two layers, under the electron microscope it appears to be composed of three layers, each approximately 2.5 nm thick. The reason that it appears to have three layers is the two layers that constitute the inner and outer layers of the membrane have a domain of overlap that appears to be a middle layer. The interior and exterior layers are composed of protein molecules. The "apparent" middle layer of the plasma membrane is a lipid bilayer composed of a double layer of phospholipid molecules. These phospholipids have a slight dipole, and orient themselves with the hydrophobic (nonpolar) end toward the inside of the membrane while the hydrophilic (polar) end orients itself toward the outside of the membrane. Phospholipids when placed into solution, will spontaneously form phospholipid bilayers (Figure 1.6d), sheets that are two molecules thick. The hydrophobic side chains of each layer minimize contact with water by aligning themselves together in the interior of the bilayer and forming the "apparent" middle layer. The phospholipid bilayers can form micelles (Figure 1.6b), which are spherical structures less than 20 nm in diameter, or liposomes (Figure 1.6c), whose function will be described below.

The lipid nature of this membrane is significant because it determines what type of materials may pass through the factory's walls. Many lipid-based materials will freely diffuse through the walls, as will most gases. However, polar, water-soluble materials as well as water

itself only enter at specific ports. The gates for special entry of lipid-insoluble materials, or large molecules, take the form of proteins that extend entirely through the lipid bilayer (Figure 1.6a). The current concept of the cell membrane, the fluid mosaic model, proposes that the transmembrane and surface proteins are not fixed, but float freely on the lipid bilayer. Adjacent to the lipid core is scaffolding of cytoskeletal proteins (e.g., actin), which supports the bilayer through specific sites of attachment along the inner surface of the membrane (see cytoskeleton below). The plasma membrane is itself divided into specialized regions in those cells that are simultaneously in contact with different environments. The membrane can form specialized structures such as the microvilli, which can greatly increase the effective surface area of the membrane and facilitate efficient transport. The membrane is very deformable and with low extension modulus, for example 0.1 to 1 kPa for the red blood cell (the modulus of soft rubber is 0.1 to 1 MPa). The lipid bilayer chemically isolates and regulates transport to and from the cell interior; the cytoskeletal network provides mechanical support and controls the ability of the cell to change shape and, in some cells, to move. Large deformations may be accompanied by great increases in surface area made possible by unwrinkling and unfolding the wrinkles and folds in the membrane, such as the formation of microvilli.

The cell has many transmembrane communication systems. These include ion channels with the exterior environment and gap junctions for intracellular communication. Gap junctions are pores that allow small molecules to pass through the plasma membranes of two adjacent cells. Cell surface receptors are located in the lipid membrane and have binding sites for other molecules on the cell membrane surface exposed to the external medium. The signaling molecules that bind can include hormones, cytokines, or second messengers, such as $Ca^{++}$ ions. Endocytosis and exocytosis are mechanisms for transport across the cell membrane; they are described below. There is also much communication and transport between the organelles of the cell's interior; these are also described below.

(b) Cytosol: There is not a good factory equivalent; the closest would be the air inside the factory. — The cytosol is the contents of the cell interior excluding the organelles and inclusions. The organelles bounded by a membrane include the endoplasmic reticulum, the Golgi apparatus, lysosomes, mitochondria, and the peroxisome. Other organelles, which are not bounded by a membrane, are the cytoskeleton, free ribosomes, and centriole. The cytosol is amorphous, contains proteins, salts and enzymes and is the gel-like material that surrounds the organelles and inclusions. The cytoplasm consists of the cytosol, and all the embedded organelles and inclusions.

(c) Lysosome: The factory incinerator or waste disposal — The lysosome is the membrane-bounded organelle responsible for macromolecular degradation, and contains a number of hydrolytic enzymes. Materials taken into the cell by endocytosis and phagocytosis, and which are to be degraded, are delivered via vesicles or vacuoles to the lysosome. Further, the breakdown involved in the normal turnover of cellular components is accomplished either within the lysosome or a phagosome (phagolysosome). The phagosome is an intracellular vacuole that contains phagocytized material to be degraded. The degradation is accomplished when lysosomal bodies fuse with the membrane of the phagosome and lysosomal enzymes are released into the phagosomal vacuole. Enzymes required for intracellular digestion are sequestered *within the matrix of* the lysosome. They are contained in this way to prevent *the enzymes* from attacking the cell itself (see Figure 1.7). Figure 1.8 illustrates the intracellular lysosomal system found in all cells.

**Exercise 1.2**

**Problem**: In this chapter there are a number of tissue illustrations that were obtained with microscopes. What is the difference between optical microscopes, transmission electron microscopes, and scanning electron microscopes in the method of magnification and in their ability to magnify?

**Solution**: Optical microscopes use visible light to create a magnified image of an object. The compound optical microscope employs two lenses mounted at opposite ends of a closed tube and can magnify an image more than 2000 times. With a good optical microscope the human eye can perceive no detail smaller than about half the wavelength of light. This puts the absolute limit of resolution of a microscope utilizing visible light at about a quarter of a micron. That means that a light microscope can tell us nothing about objects smaller that a quarter of a micron. The ultraviolet microscope, for example, uses the shorter wavelengths of the light spectrum's ultraviolet region to increase resolution. An electron microscope uses electrons rather than light to illuminate a specimen. Electrons are projected against the specimen and magnetic fields are used to create lenses that direct and focus the electrons. In a transmission electron microscope (TEM), the electron beam is directed onto the object to be magnified. The electrons that pass through the specimen form a magnified image of it; TEMs can magnify an object up to 1,000,000 times. The scanning electron microscope (SEM) functions by scanning the surface of an object with an electron beam and then collecting the secondary electrons released from the object. No electrons pass through the object because it is usually thicker than the samples used for TEM. Therefore, the resolution in SEM is greater than for light microscopy but less than that of TEM. However, SEMs can magnify objects 100,000 times or more and produce detailed three-dimensional images of an object's surface.

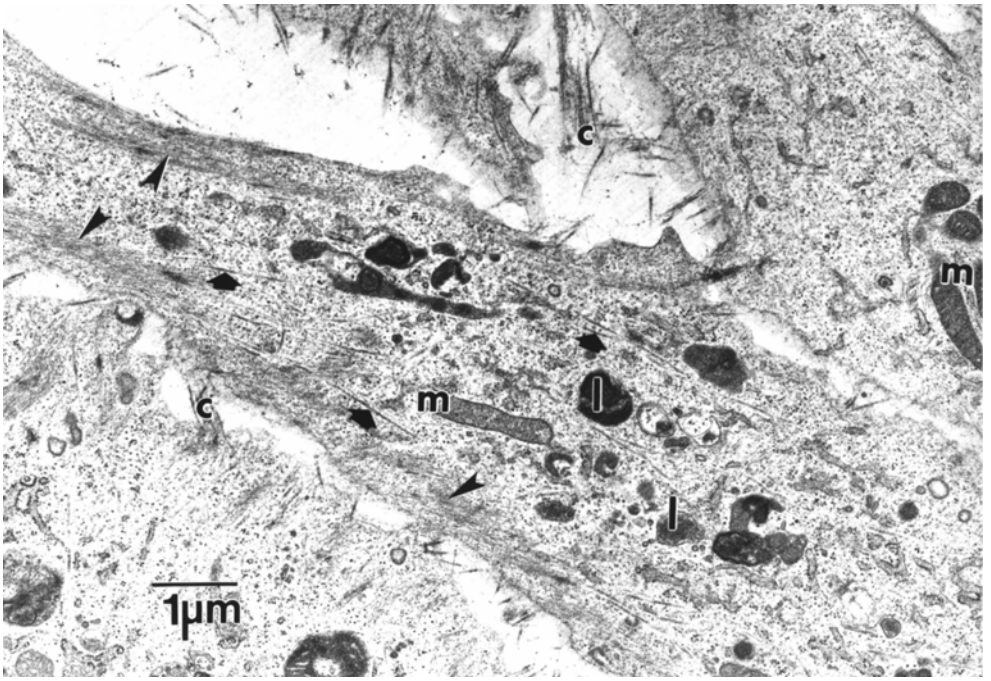



**Figure 1.7**. This electron micrograph illustrates how cytoplasmic extensions from a cell will contain numerous microtubules (solid arrows) and microfilaments (small arrowheads) that are used to propel or move the cell from place to place. There are some small collagen fibrils present (c) that are not part of the cytoskeleton since they are extracellular. Lysosomes (l) and mitochondria (m) are apparent in the cytoplasm. Magnification: 15,200X.

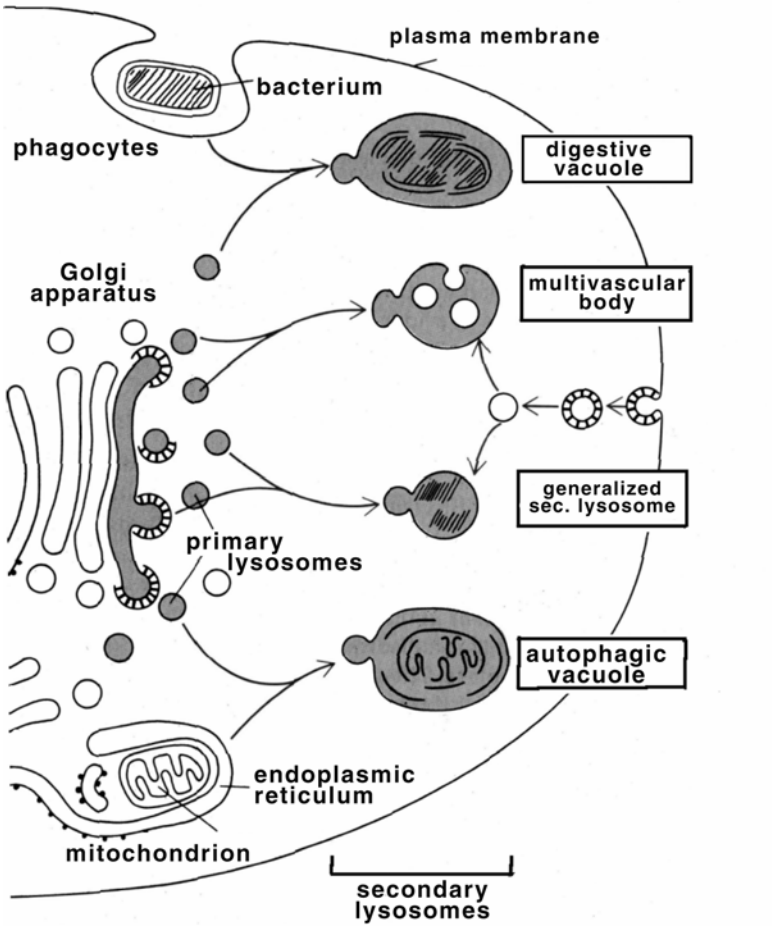



**Figure 1.8**. This diagram illustrates the intracellular lysosomal system found in all cells. The intracellular degradative enzymes are packaged in the Golgi system. Primary lysosomes containing these enzymes are formed from the Golgi membranes and are released into the cytoplasm. The primary lysosomes then fuse with cytoplasmic vacuoles, phagocytic vacuoles or large secondary lysosomes. The degradative enzymes are then released into the secondary lysosome or phagosome vacuole, and degradation occurs within these bodies, without damaging other cytoplasmic contents or organelles. Extracellular material can be transported into the cell through endocytosis and degraded using the same lysosomal process. Reprinted with permission from Alberts et al. (1983).

(d) Endosome: The factory internal division transfer system or mechanism — An endosome is a membrane-bounded vesicle used by the cell for transport in, for example, the processes of exocytosis and endocytosis. The vesicles form by budding off the cell membrane or the endoplasmic reticulum or Golgi membranes. See Figure 1.9.

(e) Endocytosis: The factory receiving department or mechanism — Endocytosis is a method for transport across the cell membrane from outside to inside, and a major source of new "supplies." The reverse process, exocytosis, is the main method of releasing "factory goods" made from the supplies. In the endocytic process portions of the external *cell* membrane invaginate and pinch off to form membrane-bounded cytoplasmic vesicles or liposomes (Figure 1.6c) containing substances that were present in the external medium or were adsorbed onto the cell surface. These endocytic vesicles may transport from one cell surface to another or from the cell surface to an internal organelle.

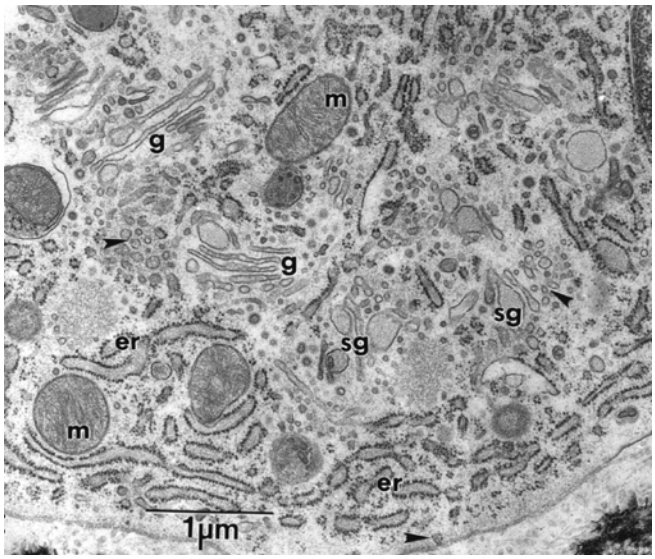



**Figure 1.9**. This is an electron micrograph of a small portion of the cytoplasm of a fibroblast. The Golgi saccules (g) are arranged in parallel layers and without any attached ribosomes. The rough endoplasmic reticulum (er) is also a sac-like arrangement, but ribosomes are present as small dark dots lining the membranes of this reticulum. Secretory granules (sg), which can be seen better in Figure 1.8, are budding off the ends of the Golgi saccules. Vesicles (arrowheads) are derived from the Golgi and the plasma membrane and carry material from structure to structure within the cytoplasm. Some mitochondria (m) are also present. Magnification: 33,800X.

(f) Centriole: Part of the whole factory replication mechanism — The two centrioles are principal structures in the centrosome. When the cell divides (undergoes mitosis) each pair of centrioles generates another pair and the twin pairs form the poles of the mitotic spindle. The centrosome is located near the nucleus and consists of the two centrioles, satellite bodies and differentiated cytoplasm.

(g) Exocytosis: The factory shipping department or mechanism — Exocytosis is a method for transport across the cell membrane from inside to outside. In this process membrane-bounded vesicles or liposomes (Figure 1.6c) inside the cell fuse with the plasma membrane and release their contents into the external medium.

(h) Secretion granules: The factory shipping containers — A secretion granule contains material synthesized by the cell and usually originates from the Golgi or endoplasmic reticulum. The secretory granules normally fuse with the external cell membrane to release material to the extracellular environment. If this material is defective due to an error in synthesis or if unneeded physiologically, the granule may deliver the material to the lysosome for degradation. See Figures 1.9 and 1.10.

(i) Ribosomes: The factory's main assembly division — The ribosomes are the centers of protein assembly and, therefore, the main executors of the genetic commands issued by the nucleus. The ribosome utilizes the amino acids available in the cytosol along with the messenger RNA to produce specific proteins. It is generally accepted that ribosomes attached to endoplasmic reticulum make protein to be exported from the cell, whereas ribosomes that are free in the cytosol make proteins to be used internally by the cell. See Figure 1.9.

(j) Mitochondrion: The factory's fuel manufacturing unit — The mitochondrion is the double membrane-bounded organelle that functions as the cell's manufacturer of fuel. The fuel is the high-energy phosphate compound adenosine triphosphate (ATP). The mitochondria combine oxygen with food molecules to make ATP. ATP is a fuel for many cellular functions, including muscle cell contraction. See Figures 1.7, 1.9, and 1.11.

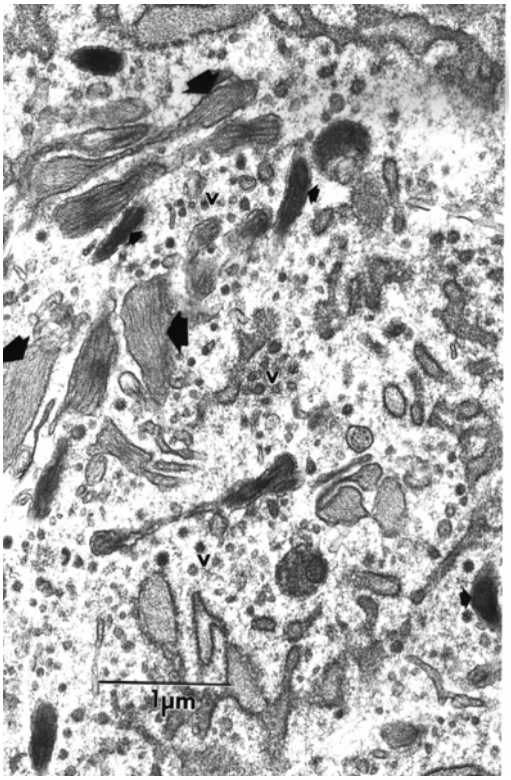



**Figure 1.10**. This electron micrograph demonstrates how the terminal portions of the Golgi saccules collect the fibrous protein (in this case, Type I procollagen, since this is an osteoblast cell), and condense it to form secretory granules which then move out to the cell membrane. Notice the variation in density of the protein in the Golgi saccules (large arrows) compared to the more dense content of the secretory granules (small arrow). Numerous small vesicles (v) are also present in this active region. Magnification: 39,000X.

**Exercise 1.3**

**Problem**: Using the information in Figure 1.11, estimate the length of a sarcomere.

**Solution**: Measure the lengths of both the scale mark of 1 μm and the distance *s*, the length of a sarcomere, extending between two Z lines in Figure 1.11. Dividing the first of the lengths into the second, one finds that the sarcomere is about 1.5 μm.

(k) Peroxisome: The factory's special type of waste disposal unit — The function of the peroxisome is to rid the body of toxic substances like hydrogen peroxide or other metabolites. It is a membrane-bounded organelle that breaks down small molecules, such as amino acids, xanthine and fatty acids. In the process the peroxisome generates and degrades dangerously reactive peroxides. The peroxisome is not found in all cells whereas the lysosome is always present.

(l) Golgi apparatus: The factory's finishing division for its product — The Golgi apparatus is the membrane-bounded organelle whose primary function is the post-translational modification of proteins synthesized initially in the endoplasmic reticulum and destined eventually for secretion or for incorporation in the plasma membrane or for delivery to the lysosome. Post-translational modifications include glycosylation, sulfation, fatty acid addition, and protein

folding or concentration. This organelle appears as a series of tubules and stacked, disk-shaped structures called cisternae. The Golgi membranes are devoid of ribosomes since no protein synthesis occurs in this organelle. The Golgi does increase in size as cellular activity increases and will be quite small in cells not actively synthesizing or secreting protein. See Figure 1.9.

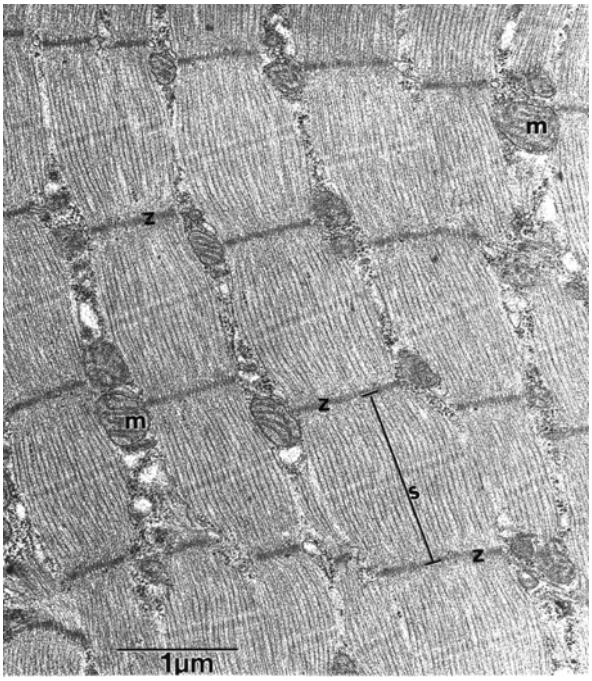



**Figure 1.11**. This electron micrograph shows the details of a skeletal muscle fiber. Mitochondria (m) are present and located between myofibrils. The darkest line is the Z band (z), and the functional unit, the sarcomere, extends between two Z lines. Within each sarcomere, actin filaments attach to each Z band, and myofilaments of myosin are placed between each actin filament. The muscle contraction is caused by the myosin and actin filaments slipping past one another. This mechanical activity requires utilization of ATP. Magnification: 33,800X.

(m) Nucleus: The factory's central planning office and records library — The nucleus is the membrane-bounded organelle that functions as the information-processing center of the cell. The main functions of the nucleus include maintenance of the genetic library and transcription. Transcription in biological cells is the process by which instructions are read from the information store and sent out to the cytoplasm for expression; that is to say, the instructions are "transcribed" to a messenger ribonucleic acid (RNA), denoted mRNA. It is by these mechanisms that genes exert their commanding influence over the cell. When a cell prepares to divide, the nucleus has to perform an additional duty, which consists of the complete and accurate duplication of the genetic library. The 23 pairs of chromosomes characteristic of human cells are located within the nucleus. DNA (deoxyribonucleic acid) within the chromosomes forms the genes that determine the characteristics of each cell as well as of the individual. Except during cell division, DNA and associated proteins are dispersed throughout the nucleus as thin strands about 4 to 5 nm in diameter. During division of the cell the DNA is compacted into dense chromosomes. In the nucleus DNA encodes the mRNA, which moves out of the

nucleus through the nuclear pores into the cytoplasm, where mRNA is template or blueprint for the "translation" into a specific protein. The information contained within nuclear DNA determines most of the chemical events that occur within the cell. See Figure 1.12.

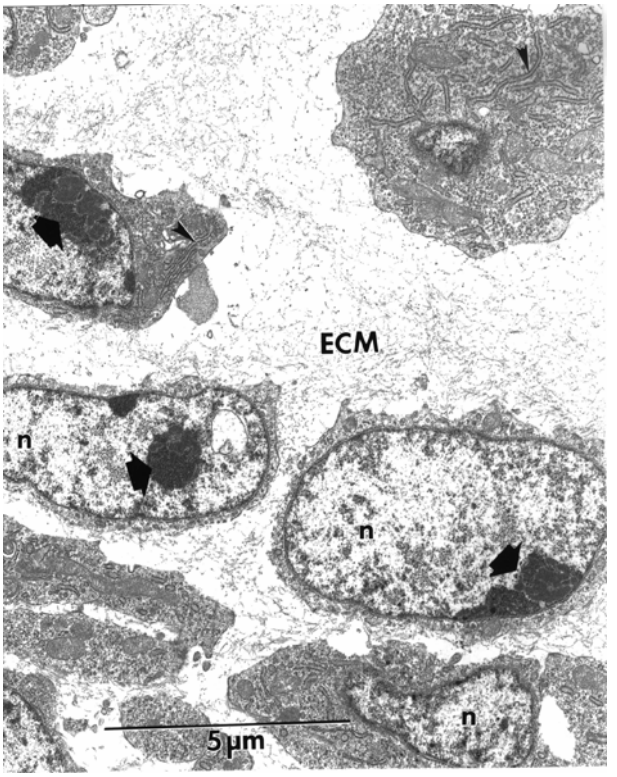



**Figure 1.12**. This electron micrograph illustrates the morphology of mesenchymal undifferentiated cells in the embryo, which will go on to develop into bone and cartilage cells. The nucleus (n) is very prominent in these cells because the cytoplasm is largely undifferentiated except for a small amount of rough endoplasmic reticulum (small arrowheads). A large nucleolus (large arrows) is evident in most nuclei. An extracellular matrix (ECM) usually consists of fibrous proteins and proteoglycans. Magnification: 13,000X.

(n) Nucleolus (nucleoli): Information processors in the factory's central planning office — Nucleoli are nuclear bodies within the nucleus and number from one to four per nucleus, depending on the cell. Within the nucleoli two major ribosomal subunits, each consisting of proteins and ribosomal RNA (rRNA), are separately assembled. The ribosomal subunits then move from the nucleus through the nuclear pores into the cytoplasm, where they join together along with the mRNA and function as sites of protein synthesis. See Figure 1.12.

(o) Cytoskeleton: The factory's building and building maintenance division — The cytoskeleton, located in the cytosol, consists of networks of protein filaments that give the cell its shape and provide a basis for its movements. In animal cells the cytoskeleton is often organized from an area near the nucleus that contains the cell's pair of centrioles. The main kinds of cytoskeletal filaments are microtubules (25-nm diameter), actin filaments (7-nm diameter), and intermediate filaments (10-nm diameter). Some cells are capable of changing their cytoskeleton structure within minutes by polymerization of actin filaments from stores of unpolymerized actin (Figures 1.7 and 1.11).

(p) Endoplasmic reticulum: Several divisions of the factory's production units — The endoplasmic reticulum is a double membrane-bounded organelle that is divided into rough-surfaced and smooth-surfaced parts depending on whether ribosomes are bound to its limiting membranes or not, respectively. The rough-surfaced endoplasmic reticulum collects and processes newly made protein for export, manufactured by ribosomes bound to its limiting membranes. These proteins are then either secreted, further modified by activity in the Golgi complex, internalized into lysosomes, or incorporated into the plasma membrane. The smooth-surfaced endoplasmic reticulum is a site for reactions involving sterol biosynthesis, detoxification reactions, and fatty acid desaturation (Figures 1.9 and 1.12).

**Problems**

1.4.1. What is an ion channel?
1.4.2. What are microvilli?
1.4.3. What is an organelle?
1.4.4. What is an amino acid?
1.4.5. What is an actin?
1.4.6. What are nucleotides?
1.4.7. What are the nucleotides that occur in DNA?
1.4.8. What are the nucleotides that occur in RNA?
1.4.9. What is the difference between the cellular processes called transcription and translation?
1.4.10. What is the difference between the cell classifications procaryote and eucaryote?
1.4.11. The polymorphonuclear leukocyte is a specialized white blood cell type that pursues invading microorganisms by following chemoattractants derived from the microorganisms' metabolism or from the invader's interaction with the complement cascade. This method of pursuit is an example of what ability of a cell?
1.4.12. The peroxisome and the lysosome are both membrane bound waste disposal organelles of the cell. What is the difference between their functions?
1.4.13. A recurring theme in the chapter is that cells mechanically communicate with their extracellular environment. This communication is bidirectional. One way that this is mediated is through proteins called integrins. Describe integrins and the role they play in this process.
1.4.14. What is the difference between a cell membrane and a nuclear membrane?

## 1.5. THE HIERARCHICAL STRUCTURE OF TISSUES

The structure of a tissue may be described at several levels, from the gross anatomy to the molecular organization. For example, in describing tendons, there are several levels of organization. Some authors identify six distinctive structural levels in a tendon (Baer et al., 1992). The first level is the collagen molecule, and the sixth level is the tendon itself. In between, in ascending order are the microfibrils, the fibrils, the fibers, and the fascicles. These six structural levels are illustrated in Figure 1.13. Although the hierarchy of structure in tissues represents the way the tissue is formed, the very efficient and effective performance of tissues is credited to the same hierarchy of structure, a hierarchy that extends over a large range of length scales.

The hierarchical architecture that collagen aggregates in the tendon provide is an example of a natural composite material designed for a specific mechanical function. All the connective tissues share this feature. As will be shown in a later chapter, even the cell membrane exhibits

properties that depend upon structures on many length scales. All the tissues and distinct tissue structures considered here share these properties. The National Materials Advisory Board of the U.S. National Research Council (Anonymous, 1994) characterized hierarchical materials systems in biology as follows: (1) by the recurrent use of molecular constituents (e.g., collagen), such that widely variable properties are obtained from apparently similar elementary units; (2) by the controlled orientation of structural elements (considered in the next section); (3) by the construction of durable interfaces; (4) by sensitivity to — and critical dependence on — the presence of water; (5) by properties that vary in response to performance requirements; (6) by fatigue resistance and resiliency; (7) by controlled and often complex shapes; and (8) by the capacity for self-repair.

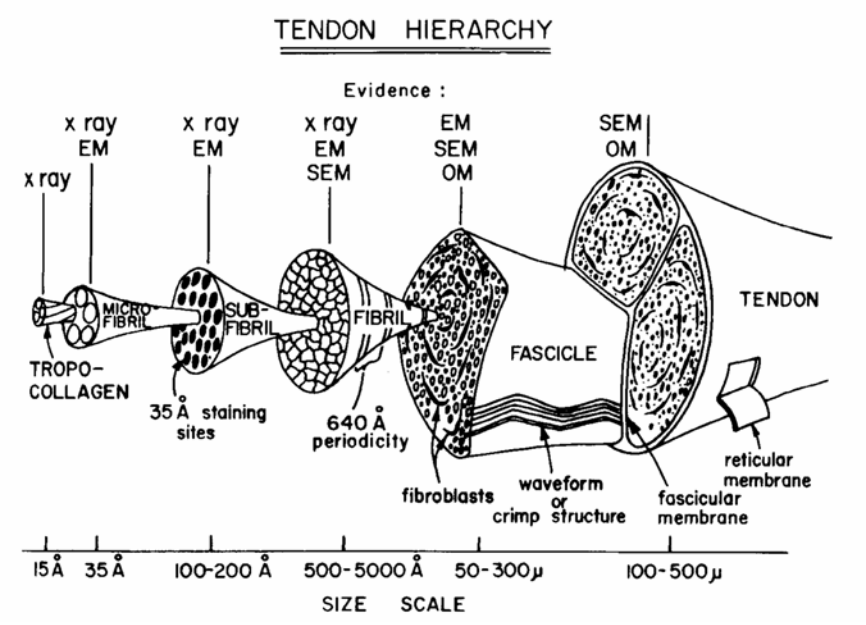



**Figure 1.13**. Hierarchical structure of a tendon. Modified with permission from Anonymous (1994).

The tissues of interest here are characterized by hierarchical structures in which organization is controlled on many discrete length scales, length scales that range from the molecular (nm) to the macroscopic (cm) (see Figure 1.13). These hierarchically structured tissues display properties that are affected by processes operating at all levels of the length-scale spectrum. Although the cells are actively producing only limited types of constituent materials, organisms have evolved an astonishing array of architectural strategies to realize a broad range of structure and function. Consider, for example, the widespread use of collagen in the many connective tissues in which it occurs and the many variations of collagen: collagen I, II, etc. Nature makes very different tissues out of collagen and similar macromolecular constituents, including some inorganic constituents. Tissues all have specific hierarchical composite structures with each tissue (e.g., tendon, intestine, cornea, bone) assembled to serve distinct, highly specific functions. Chapter 10 is devoted to a description of the structure of collagen.

## 1.6. PLANS FOR THE STRUCTURE OF A TISSUE

The structure of a tendon is an example of a distinctive and repeated tissue pattern found throughout the animal kingdom. Other examples of pattern formation include the structure of the five fingers of a hand arising from an amorphous shape at the end of an embryonic arm, the development of a fingerprint, or the development of a whole skeletal pattern. What are the mechanisms for these pattern formations? While the genes control much of the structure of a tissue, some development of tissue structure is an adaptive response of the tissue to the environment as well as the information from the genes. Many different epigenetic mechanisms have been proposed for the spontaneous development of patterns in living systems.

In this section the focus is on some of the different mechanisms that have been proposed for pattern- forming morphogenetic events. These include chemically reacting and diffusing systems, mechanical instabilities and different combinations of these mechanisms. Alan Turing, famous for creating, in 1936, the prototype plan for digital computers and, during World War II, for his effort in deciphering the German Enigma cipher, is also renowned for the chemical reaction mechanism hypothesis. In his 1952 paper entitled "The chemical basis of morphogenesis" he hypothesized that the diffusing patterns of reacting chemicals can form steady-state heterogeneous spatial patterns, and this phenomenon could be a biological mechanism of pattern formation (Turing, 1952). Turing introduced the term "morphogen" to describe the particular chemical substance that was the signal for structural change or development. In order to imagine a "Turing" reaction diffusion mechanism, recall the structure that appears in a cup of coffee after a heavy cream has been poured in the cup and the mixture in the cup has only been slightly stirred. One observes intertwined layers of the dark coffee and the white cream as distinct but starting to mix. Now imagine something that does not happen, namely that after the coffee moves into the space occupied by the cream and vice versa, it moves out again and then back again and then out again: alternatively advancing and retreating like opposing armies on a battlefield. Turing's model involves two chemicals — the activator and the retarder. The chemical reaction is driven forward by the activator, and, when the reaction has proceeded to a certain point, a sufficient amount of retarder builds up to drive the reaction the other way. The diffusing patterns of reacting chemicals envisioned by Turing are illustrated by the Belousov-Zhabotinskii or BZ reaction (Figure 1.14). Although the BZ reaction is characterized by an equation system similar to the one proposed by Turing, and although it is presented as an example of the Turing system, it is not a candidate for a reaction that occurs in morphogenesis. The reaction is striking in its oscillatory patterns and drew much attention in the 1970s. Belousov discovered the oscillations in ratios of concentrations of the catalyst in the oxidation of citric acid by bromate.

The development and application of the Turing system to biological and mathematical problems is summarized by Murray (1993). One particularly graphic use of the Turing system described by Murray is his own application of the reaction-diffusion equations to mammalian coat patterns (Figure 1.15). It is pattern applications of this kind that are thought to be the principal applications of the Turing system in biology. A Turing-related diffusion model to explain the development of skeletal pattern in the embryonic chick limb bud was presented in Newman and Frisch (1979). The pattern of development of the chick limb bud between 4 and 7 days of incubation is shown in Figure 1.16. The solid black regions represent definitive cartilage; striped areas represent early cartilage. The predicted pattern of limb development using the diffusion model of Newman and Frisch (1979) for the morphogen is shown in Figure 1.17. The solid black regions in this figure represent cartilage or precartilage condensation; the striped regions represent the distribution of the morphogen preceding chondrogenesis.

There is another set of models in which diffusion-like equations are combined with equations describing mechanical activity. The model of mesenchymal morphogenesis gives an example of this sort where an active stress exerted by cells is taken into account. The mesenchyme is part of the embryonic mesoderm, consisting of loosely packed, unspecialized cells set in a gelatinous ground substance consisting of proteoglycans, from which connective tissue,

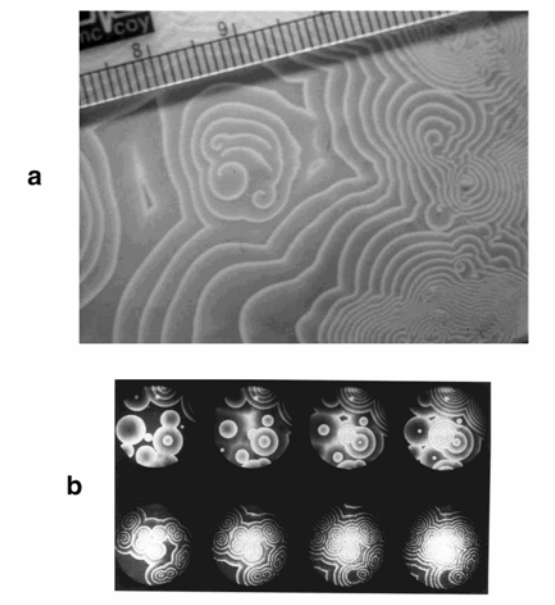



**Figure 1.14**. (a) The Belousov-Zhabotinskii or BZ reaction is an example of the diffusing patterns of reacting chemicals characterized by the Turing model. This figure is the image of this reaction at a particular time. The reaction proceeds in time in oscillating spirals. There are a number of websites that contain movies of BZ reactions. These movies give a better impression of the oscillatory character of the reaction than does this snapshot. This figure is the file liquidfire.gif downloaded from http://cochise.biosci.arizona.edu/~art/graphics/liquidfire.gif. Courtesy of Art Winfree. (b) Top row of four circular frames: target patterns (circular waves) generated by pacemaker nuclei in the Belousov-Zhabotinskii reaction. The photographs are about 1 minute apart. Second row of four circular frames: spiral waves, initiated by gently stirring the reagent. The spirals rotate with a period of about 2 minutes. Reprinted with permission from Murray (1993).

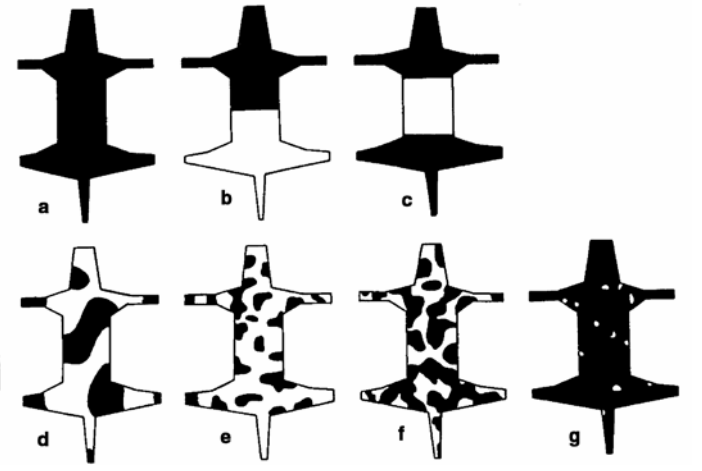



**Figure 1.15**. The patterns on the material surface of the epidermis formed by the reaction-diffusion mechanism. These results are model predictions, and the differences (a)–(g) are associated with a scale factor that is a measure of relative animal size. Reprinted with permission from Murray (1993).

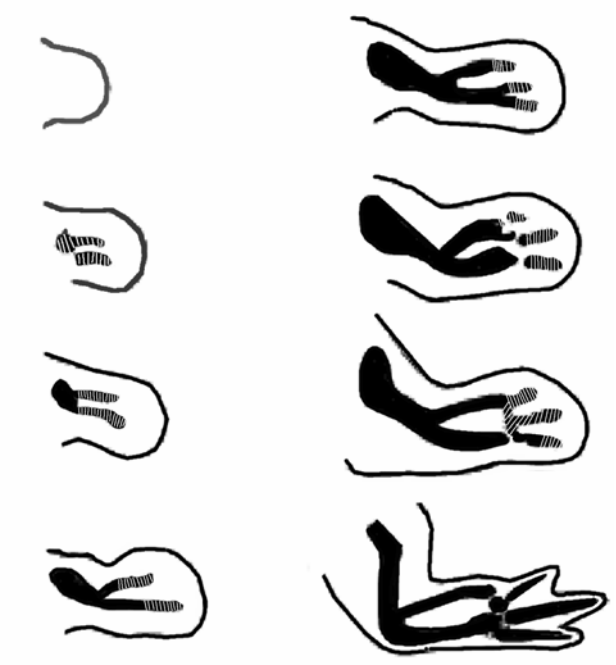


**Figure 1.16**. Development of the chick limb bud between days 4 and 7 of incubation. The solid black regions represent definitive cartilage; striated areas represent early cartilage. Reprinted with permission from Newman and Frisch (1979).

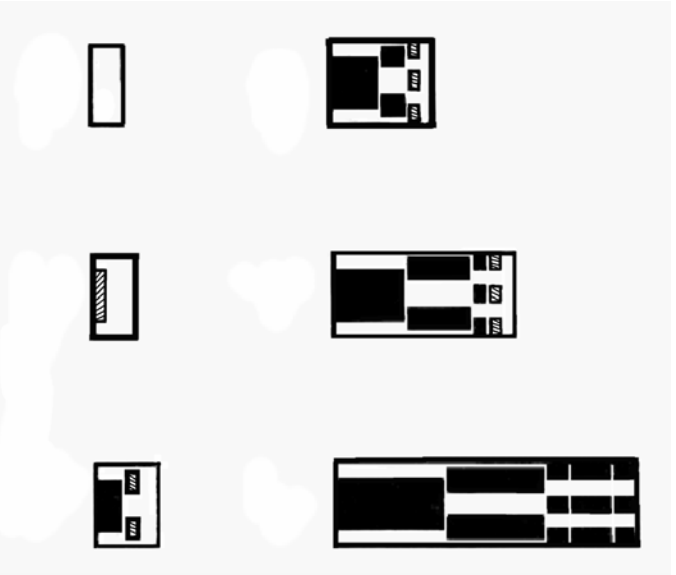


**Figure 1.17**. The predicted pattern of limb development using the Newman and Frisch (1979) diffusion model. The solid black regions represent cartilage or precartilage condensation; striated regions represent the distribution of the morphogen preceding chondrogenesis. Elongation of the domain is based on empirical measurements; it represents growth superposed on the diffusion in the domain. Reprinted with permission from Newman and Frisch (1979).

bone, cartilage, and the circulatory and lymphatic systems develop. The condensation of cartilaginous skeletal rudiments in the developing vertebrate limb was also modeled in Oster et al. (1983) with equations similar to those in Newman and Frisch (1979), but with a model that incorporated the cumulative effects of cell-generated forces (Harris et al., 1980) in place of the purely chemical diffusive mechanism used in Newman and Frisch (1979).

It is not clear how strong a role for the Turing model will be in explaining the development of biological structures. The work on the patterning of body segments of the fruit fly that was awarded a 1995 Nobel Prize did not involve the reaction and diffusion Turing mechanism in pattern formation, but rather a cascade of gene expression that began with a specific anatomical distribution of mRNA molecules and transcription activators already present in the egg (Keller, 2002).

A second mechanism for the morphogenetic event of pattern formation in tissue development is that cells somehow "sense" the tissue in which they reside and make use of this "positional information" to trigger further steps in development. This concept is due to developmental biologist Lewis Wolpert, who suggests that there is both a "weak" statement of the positional information mechanism and a "strong" statement (Wolpert, 1998; Keller, 2002). In the weak statement of the concept the operational mechanism of "positional information" is not specified. In this case a cell does something just by being in a certain tissue at a certain stage of its development — the cell knows where it is. In the "strong" statement of the positional information concept Wolpert suggests that the cell knows where it is because it can sense the concentration of some chemical or, to use Turing's term, morphogen. There is a gradient of the morphogen, and the cell "knows" from the concentration of the morphogen that it "measures" where it is located along the gradient.

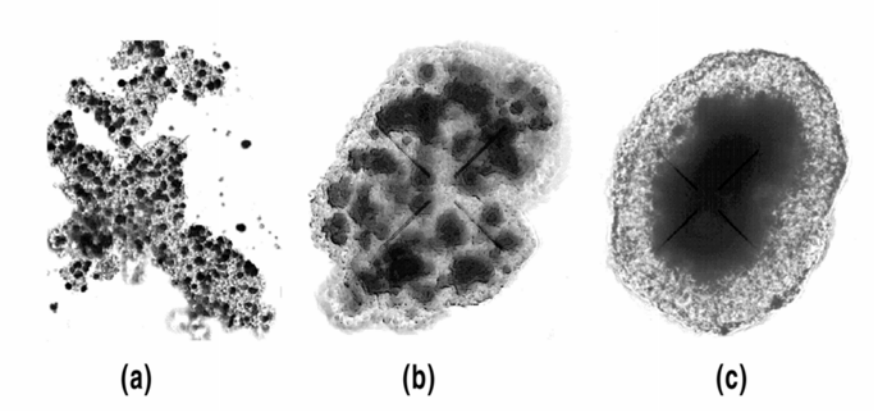



**Figure 1.18**. Experimental images from chicken embryo cells in culture: light cells are neural retinal cells, dark cells pigmented retinal cells. An initial random mixture of light and dark cells (a) forms dark clusters after about 10 hours (b), and eventually sorts to produce a dark cell core surrounded by light cells after around 72 hours. Reprinted with permission from Alber et al. (2003).

There are other suggested mechanisms that might classify as positional information mechanisms of the "weak" type. The idea underlying the differential adhesion hypothesis (Steinberg, 1962, 1964) is that combinations of different cell types behave as immiscible liquids (e.g., oil and water) because of surface tension, but with the cell-to-cell adhesion forces playing the role of molecule–molecule attraction forces. (An example of two miscible liquids is alcohol and water.) In immiscible liquids a liquid with a higher surface tension will form droplets enclosed by drops of another liquid with lower surface tension. In combinations of

different cell types cells with higher surface tension will band more tightly together, forcing the cells with lower surface tension to the outside. The last statement is the differential adhesion hypothesis. This sorting is illustrated in Figure 1.18, which shows experimental images from chicken embryo cells in culture. The light cells are neural retinal cells and the dark cells pigmented retinal cells. The initial situation, shown in the first panel, is random mixture of light and dark cells. The second panel shows the dark clusters formed at 10 hours, and the third panel shows the dark cell core surrounded by a light cell shell at 72 hours. It has been experimentally demonstrated (Beysens et al., 2000) that the mean size of the interconnected cellular domains, like those in panel (b) of Figure 1.18, increase linearly in time, consistent with the analogy between combinations of different cell types and immiscible fluids.

A mechanism other than surface tension-induced relative adhesiveness has been suggested to be consistent with the analogy between combinations of different cell types and immiscible fluids. Harris (1976) suggested that the observations that support the surface tension-induced relative adhesiveness mechanism are equally consistent with an explanation based on the cell's own contractility of its cytoskeletal structure. The idea is that the contraction of the surface layer of a cell induced by the contraction of the underlying cytoskeleton simulates surface tension since surface tension is due to the mutual attraction of subunits in a surface layer.

Mechanical instability, or buckling, is another mechanism that might classify as a positional information mechanism of the "weak" type. The first example of mechanical instability encountered in mechanics is the column in which only small deflections are considered. If the column is simply supported at both ends it will deflect from its straight shape into the shape of a half-sine wave when the compressive axial load acting on the column reaches a critical value called the critical load. There are other shapes that it will take as the compressive load is further increased. The other shapes are all of the form of $(N+1)$ half-sine waves where $N = 0$, 1, 2, 3, etc., and the value of $N$ increases with increasing load. Thus, mechanical load can cause an initially straight column, simply supported at both ends, to take the shape of $(N+1)$ half-sine waves, where $N$ depends upon the value of the compressive load. Realistic models for some biological pattern-forming processes are the large deflections of an (infinitely long) beam (or plate) on an elastic foundation under axial compression, which is like a column with lateral support from springs (Figure 1.19). The supporting springs are considered to be so close together that they can be treated as continuous elastic support. As the compressive axial load acting on this beam is increased it will deflect from its straight-line shape into the shape of $(N + 1)$ half-sine waves where $N = 0$, 1, 2, 3, etc., and where $N$ depends upon the value of the compressive load. This is just one example of many mechanical instability, or buckling, situations that might be used by developing organisms to generate patterns for their structure. This particular example gives rise to a one-dimensional pattern, whereas plates compressed in two directions will give rise to a great variety of two-dimensional patterns.

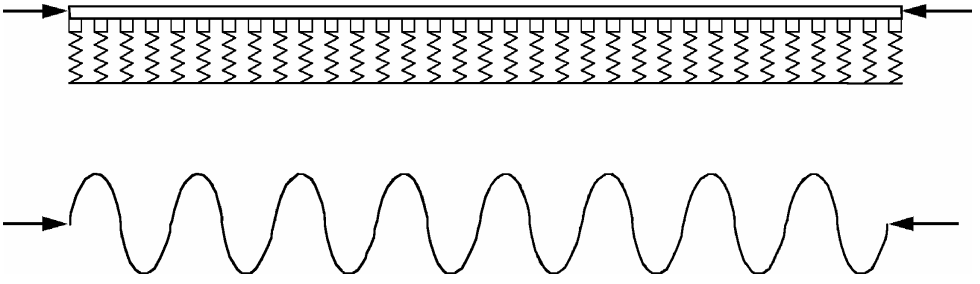


**Figure 1.19**. Beam on an elastic foundation. The beam is subjected to an axial compressive load and is supported by springs that are considered to be so close together that they can be treated as continuous elastic support. The lower sketch is the deflection curve of the beam. Large deflections are considered. Note the formation of pattern arising from a homogeneous field, in this case a sine-wave curve arising from a straight line.

A buckling model for the formation of fingerprints was suggested by Kuecken (2004). The ridge formations called fingerprints are influenced by different rates of formation at the discrete layers of the skin on the fingertips, called volar pads. Volar pads first appear in human embryos at about 6.5 weeks. A fingerprint pattern becomes established in volar pads at about the 10th to 16th week of pregnancy. The pattern emerges when a lower layer of the epidermis, the basal layer, becomes undulated (Figure 1.20). The pattern established by these undulations becomes visible on the skin surface in subsequent weeks of pregnancy. It is thought that an advantage of the ridge formations we call fingerprints is that they increase the friction between our fingers and a grasped object.

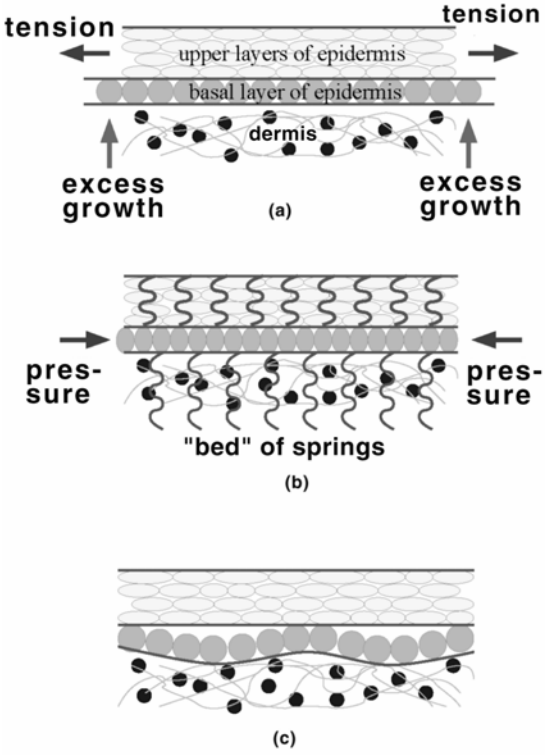



**Figure 1.20**. (a) A schematic of the Kuecken (2004) model of the surface skin layers of a finger. The basal layer is between the epidermis layer above and the dermis below. The key to the model is that the growth rate of the basal layer exceeds the growth rate of the layers above and below. (b) A compressive stress, parallel to the surface of the skin, develops in the basal layer due to the fact that its growth rate exceeds the growth rate of the layers above and below. In the subsequent buckling process, the dermis and the intermediate layer function as springs that give rise to forces that resist the buckling of the layer; they try to keep it in its place. (c) After the critical buckling stress is reached, the basal layer buckles. The buckled pattern is sinusoidal. Reprinted with permission from Kuecken (2004).

Human skin has multiple layers, including the outermost epidermis and the inner dermis. The outer and inner layers are separated by the less stiff basal layer, which is composed of cells that constantly divide. Human fingerprint patterns are created because less stiff basal skin grows faster than surface skin, which then buckles, forming ridges. The model of Kuecken (2004), which employed the theory of elastic shells, is illustrated in Figure 1.20. Figure 1.20a shows that the basal layer is between the upper epidermis layer above and the dermis below. The key to the model is that the growth rate of the less stiff basal layer exceeds the growth rate

of the stiffer layers above and below. Figure 1.20b indicates the compressive stress, parallel to the surface of the skin, which develops in the softer basal layer due to the fact that its growth rate exceeds the growth rate of the stiffer layers above and below. In the subsequent buckling process, the dermis and the upper epidermis layer function as stiff springs that give rise to forces that resist the buckling of the basal layer. They act to constrain the basal layer in its place. Figure 1.20c shows the buckled sinusoidal pattern that occurs after the critical buckling stress has been reached. Such expansion is resisted at the major flexion creases of the finger and at the furrow under the front of the fingernail. After the buckling occurs there is a second mechanism, a change in fingertip geometry at the time of pattern generation that provides a different source of growth stress. The combination of the two processes predicts the correct sequence of pattern spread over the fingertip. It also explains the observation that fingerprint configurations are related to the fingertip geometry at the time of ridge formation.

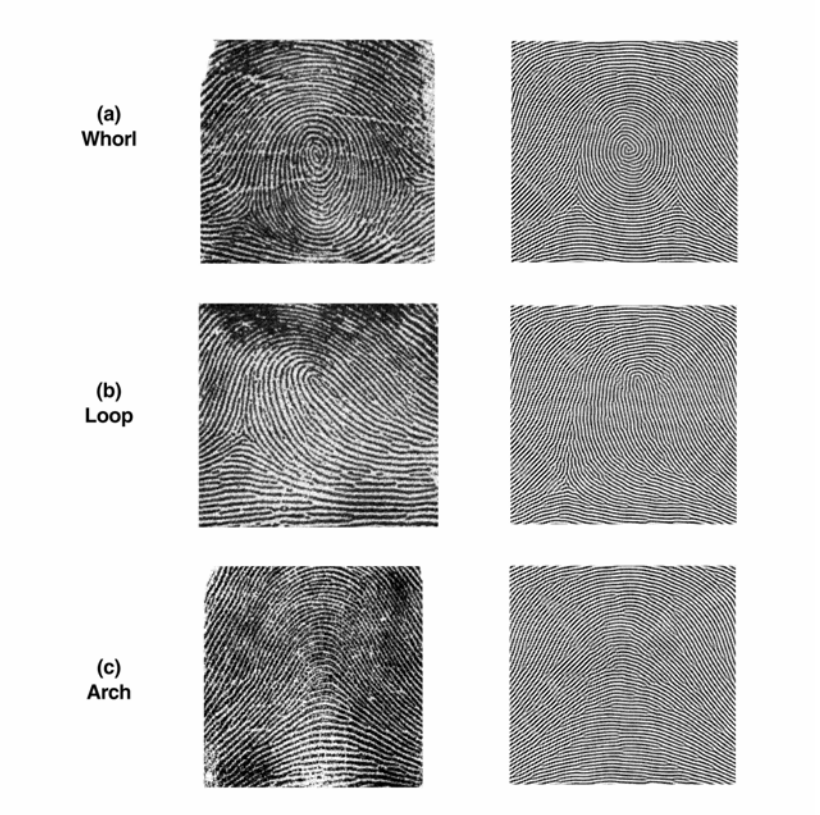



**Figure 1.21**. A typical real fingerprint is shown on the left and a fingerprint generated using the model of Kuecken (2004) is shown on the right for various typical fingerprint structures: (a) the whorl, (b) the loop, and (c) the arch. These patterns are some of the uncountable many that may be generated. They are shown by Kuecken (2004) to have the characteristic features used by fingerprint experts to classify fingerprints. Reprinted with permission from Kuecken (2004).

There are three basic patterns of fingerprints — known as arches, loops, and whorls — that form in response to the different directions of stress caused by shrinking of the volar pads (Figure 1.21). Other research on ridge formation has already shown that if a person has a high, rounded volar pad, they will end up with a whorl pattern. Kuecken's buckling model was able

to reproduce these large patterns, as well as the little intricacies that make an individual fingerprint unique.

These buckling mechanisms are favored by some over the morphogen approach of Turing for a number of reasons. First, mechanical instabilities can create physical structures directly, in one step, in contrast to the two or more steps that would be required with morphogens if positional information first had to be specified by morphogen gradients and then only secondarily implemented in physical form. Second, physical forces act at much longer range (and more quickly) than can diffusing chemicals. A difficulty with the morphogen approach is the identification of morphogens and the fact that quite different morphogen systems can produce the same pattern. Some argue that the mechanical activities of cells can themselves accomplish the morphogenetic functions usually attributed to the diffusion and reactions of chemical morphogens. Systems of cells may also accomplish this by exerting traction forces by which they can propel themselves and rearrange extracellular materials, in particular the fibrous protein collagen. Because the compression and alignment created by these cellular forces can, in turn, affect cell behavior, positive feedback cycles of several kinds arise, and these cycles are capable of spontaneously generating regular geometric patterns of cells and matrix.

Two possible models for self-organization of structure in developing biological systems have been considered above — the traditional activator–inhibitor models (chemical or not) based on systems of parabolic equations and mechanical instability models. There is another set of models in which diffusion-like equations are combined with equations describing mechanical activity. The model of mesenchymal morphogenesis gives an example of this sort where an active stress exerted by cells is taken into account.

The growth rate of a tissue depends upon its mechanical environment both when it is developing morphology and when it is simply increasing the size of existing morphological structures. The developmental growth of most structural tissues is enhanced by the use of those tissues and retarded by their disuse. Models of this type are special cases of some of the above models that deal with the formation of structure.

**Problem**

1.6.1. The early 19th century French scientist Jean Baptiste de Lamarck argued a theory of evolution now called Lamarckian. What is that theory?

## 1.7. STRUCTURAL MATERIALS FOR THE TISSUE

The production of the structural materials for a tissue is fairly well understood. Cell and molecular biologists have documented the manufacture of most of the tissue constituents by cells within or near the tissue. The cells not only manufacture these tissue constituents but also maintain the tissue and adapt the tissue structure to changed environments, including mechanical load environments. The general structure of animal and plant cells is similar; attention is restricted here to the types of cells in the human body, of which there are more than 200. Cellular differentiation gives rise to a wide variety of specialized cell types such as nerve, muscle, bone, fat, epithelial, and blood cells

The manufacture of proteins begins with the process of "transcription" in the nucleus of a cell (Figure 1.5). In this process a long mRNA (m for messenger) segment is formed in a pattern determined by the nucleotide sequence found in a DNA segment. The mRNA contains the information required to sequence the amino acids in a protein. The mRNA passes out of the nucleus and into the cytoplasm of the cell. Protein synthesis requires transfer RNA (tRNA) and ribosomal RNA (rRNA) in addition to mRNA, and it occurs at a ribosome on the rough endoplasmic reticulum (for proteins to be exported) or on free ribosomes within the cytoplasm (for proteins to be used within the cell). In the case of collagen the process of "translation" is the

synthesis of polypeptide α chains at the ribosome using the information contained in the mRNA molecules. The flattened sacks of the endoplasmic reticulum are called the cisternae; it is here that the alpha chains are released from the ribosome and form the triple helix of collagen. The helical structure (the pro-collagen) travels from the cisternae of the endoplasmic reticulum to the Golgi apparatus where the pro-collagen is packaged and condensed into a dense membrane-bounded granule. The cytoskeletal system moves these granules to the cell membrane, where there is fusion between the external membrane of the cell and the granule, so that the granule contents are released to the extracellular space. At this point, the terminal portions of the procollagen are enzymatically removed and the collagen molecules align themselves to form a collagen fibril. This last step is an extracellular event but occurs at the cell surface of the collagen producing cells (e.g., the fibroblasts or osteoblasts).

The cells do not make all the structural materials. Some, such as water and minerals, are delivered to the tissue from the vascular system. The mineral apatite combines with the collagen in bone to form a hard, stiff composite that is very different from the collagen itself in mechanical properties. The collagen–apatite system of bone is not the only model of mechanical stiffening and strengthening in nature. It is a scheme widely employed in living systems in which mechanical integrity is required. Different minerals are employed. While vertebrate bone and teeth are mineralized with calcium phosphates, certain invertebrate structures such as shells of clams and coral are mineralized with calcium carbonates. Even though the exoskeleton of insects and crustaceans can be purely organic (chitin, etc.), in many larger species such as crabs and lobsters, it is encrusted with calcium carbonates. Finally, the supporting structure of many plants often contains amorphous silicon oxide (silica) in addition to cellulose. Some sponges secrete silicon oxide spicules and others make spicules with calcium carbonates.

## 1.8. ASSEMBLY OF THE TISSUE STRUCTURE

It is of great interest to understand how a tissue develops from an amorphous form having no structure and orientation, to the structure that we know it to be, say, the mature tendon. Although this topic is of great interest, we are a long way from a complete knowledge of these processes. In this section a subset of the few understood aspects of these developmental processes are described as well as a few of the hypotheses that have been made to try to fill in the gaps. In biology the word “morphogenesis” is used to refer either to (i) the structural changes observed in tissues as an embryo develops or to (ii) the underlying mechanisms responsible for the structural changes. Both the underlying mechanisms for the structural changes and the changes in structure are of interest here. The unanswered scientific question is the relationship between the information stored in the genome and the resulting tissue structure. It is assumed that tissue structure is the result of specific interactions between the cells and their environment in a sequence leading to a structural phenotype. Once the phenotype has been established, there is further interaction with the genome for regeneration, repair and possible further development.

The unanswered scientific question concerning morphogenesis can be divided into the questions of what initiates a morphogenetic event, what is the morphogenetic process for building the tissue, and what stops the morphogenetic process when it is complete? Concerning initiation of the process, there are known examples in which the initiator is a molecule produced by another tissue. It is possible that the cells have an internal clock that initiates their activity. It is also possible that the trigger is some event in the physical environment of the cell, such as mechanical instability. These three suggestions are not exhaustive of the possibilities, which also include combinations of mentioned possibilities occurring.

The remainder of this section deals with some of these unanswered questions. It is divided into four subsections that deal with self-assembly at the molecular level, developmental embryology, assembly by cellular activity, and supramolecular assembly.

## Self-Assembly at the Molecular Level

The proteins that cells produce are configured before or after they leave the cell to adopt a shape appropriate for their assimilation into a tissue. It has been established that cells of one type (say, fibroblasts) that occur in different tissues are aware of the tissue of which they are a part. The term "molecular self-assembly" is employed to describe the assembly of large, highly ordered structures from substantial numbers of protein molecules. Molecular self-assembly of proteins is one of the better-understood aspects of tissue development. Protein subunits fit together like children's agglomeration toys in which similar pieces are fitted together (Figure 1.22); the fit is likely to be electrostatic as well as conformational. A classic example of self-assembly is the DNA double helix. Self-assembly occurs when two preexisting complementary DNA chains form a double helix (Figure 1.23). The folding of a single protein chain is an example of an assembly process that must occur along a certain narrowly constrained kinematic path if the result of the folding is to be useful to the resulting tissue. The spontaneous folding of a peptide is molecular self-assembly. When a template is used in the formation of a structure, it is called template assembly. Template assembly occurs when the DNA double helix is formed by polymerization of one chain upon another.

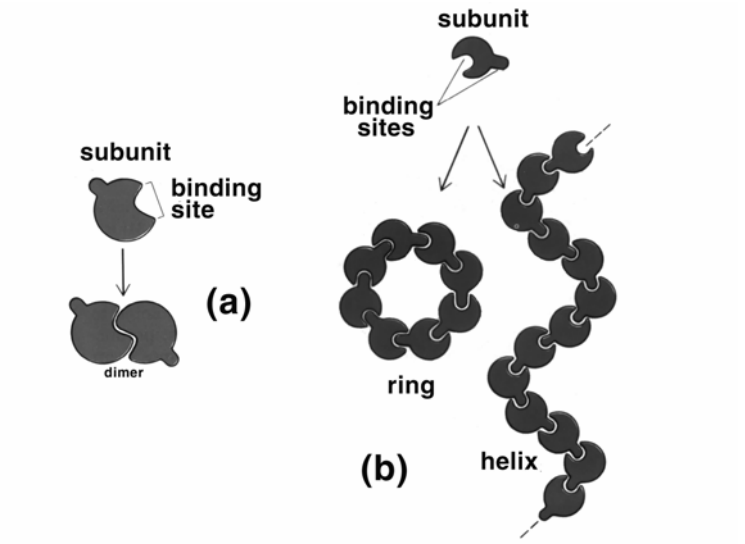



**Figure 1.22**. Self-assembly in proteins. (a) Cartoon of the formation of a dimer from a single type of protein subunit. (b) Rings or helices can form from a single type of protein subunit that interacts with itself repeatedly. Reprinted with permission from Alberts et al. (1983).

## Developmental Embryology

The British embryologist C.H. Waddington used the analogy of a railway-switching yard to describe the progressive assignment of embryonic cells in the development of an animal. Just as boxcars can be shunted into different sidings by throwing switches one way or the other, a series of genetic switches control whether a given cell turns on the set of genes appropriate for being a skin cell, or those appropriate for being a nerve cell, etc. (Figure 1.24). The development of an individual from a single cell involves many processes that have not yet been modeled. One mechanical model for the morphogenetic folding of embryonic epithelia based on hypothesized mechanical properties of the cellular cytoskeleton has drawn much interest

(Odell et al., 1981). While there are some caveats with the model, it is one of the first examples of a model considering self-organization and deformation as a united process. The model consisted of an epithelium whose cells are joined at their apices by circumferential junctions. Attached at each of these apical junctions are circumferential arrays of microfilament bundles assembled into a “purse string” or “noose” around the apex of the cell (Figure 1.25). Odell et al. assumed that, if the purse string circumference were increased by a small amount, there would be an elastic reaction to restore the original purse string circumference. However, if the purse string circumference were increased beyond a certain threshold, an active contraction would be initiated which "draws the purse-string" or “tightens the noose” and reduces the apical circumference of the cell to a new, shorter, resting length (Figure 1.26). This is a stretch-contraction model. In one model, a sheet of cells in the form of a spherical surface was considered. If one cell on the surface experienced a contraction of sufficient magnitude, it would stretch the apical circumferences of neighboring cells and, if their threshold were exceeded, cause them "to fire" and contract. The result is a propagating contraction wave that causes a deep pocket to form within the no-longer-perfect spherical surface. The resulting shape is that

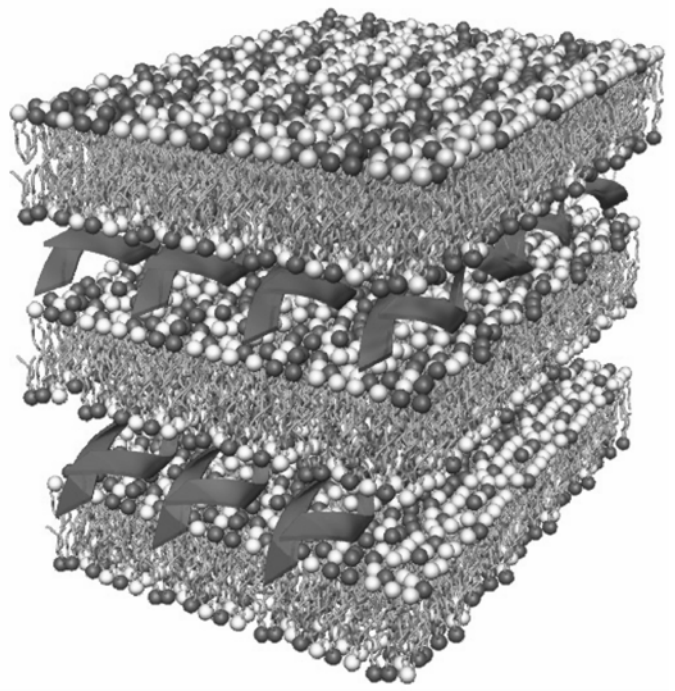


**Figure 1.23**. Illustration of natural and human-induced self-assembly. Diagram of a DNA–membrane complex, a material formed by mixing negatively charged DNA molecules with positively charged artificial versions of the membranes that form the protective coverings of cells. The DNA is an example of natural self-assembly and the entire complex is an example of human-induced self-assembly. These complexes, which are presently used as delivery vehicles in gene therapy, have a highly organized internal structure, which gives them many potential technological applications. The dark ribbons in this “double decker sandwich” represent the DNA double helices, which form a one-dimensional lattice between a double-layer sheet of the membrane. The small dark and light gray spheres represent the hydrophilic ("water-loving") ends of the charged and neutral molecules that respectively make up the membrane. The mesh between the layers of small spheres representing the hydrophilic ends are chains (two to each sphere) that represent the hydrophobic ("water-fearing") hydrocarbon "tails" in the molecules. These materials are molecularly aligned at mesoscopic length-scales (microns). The spaces between the DNA molecules can be tuned from 2.5 to 6.0 nm. This illustration is the file dna_memb.jpg from the web site (email physnews@aip.org) www.aip.org/physnews/graphics/html/dna_memb.htm.

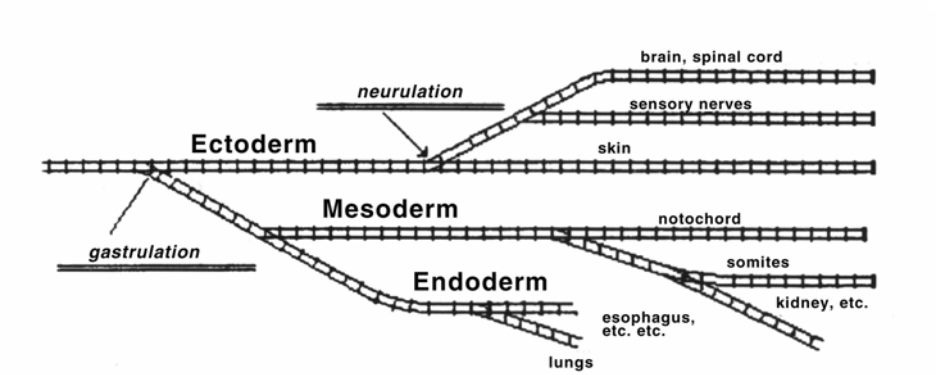



**Figure 1.24**. The Waddington switching yard. The British embryologist C.H. Waddington liked the analogy of a railway switching yard for describing the progressive assignment of embryonic cells. Just as boxcars can be shunted into different eventual sidings by throwing switches one way or the other, a series of genetic switches control whether a given cell turns on the set of genes appropriate for being a skin cell, or those appropriate for being a nerve cell, etc. Notice how often these epigenetic switch points correspond to physical rearrangements of cells. Gastrulation and neurulation are both good examples. Reprinted with permission from Harris (1994).

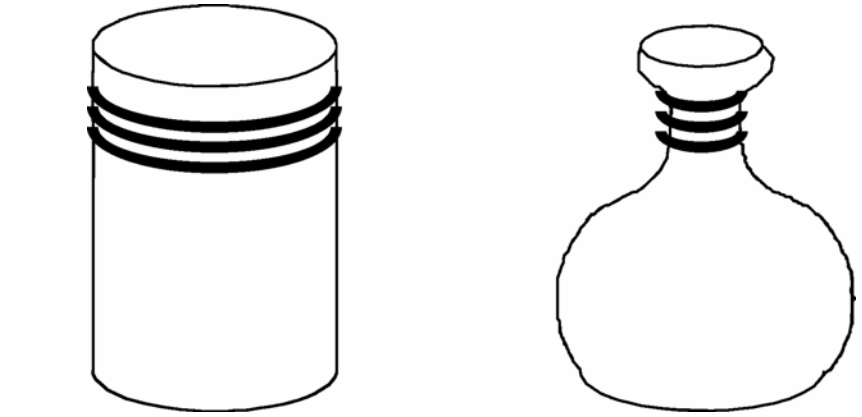


**Figure 1.25**. Actin belt tightening. The barrel-shaped cell (left), a member of a sheet of cells, has circumferential arrays of microfilament bundles assembled into a "purse string" or "noose" around the apex of the cell. The contraction of this "purse string" distorts the barrel shape as shown (right).

of a spherical gas-filled ball that has been “punched in” in one direction when its internal gas pressure is low (Figure 1.27). This model provides a possible explanation for the blastula-to-gastrula transition in embryonic development (Figure 1.27) of, say, a sea urchin (Figure 1.28). The blastula is a sheet of cells in the form of a spherical surface, and the gastrula has the shape of the “spherical gas-filled ball that has been ‘punched in’ in one direction.” The blastula-to-gastrula embryonic transition is actually one associated with the primitive development of a stomach cavity.

The interest in this model stems from the fact that embryonic transitions might be explained in terms of local mechanical events rather than in terms of genetic information. Odell et al. (1981) were the first to suggest a model of the passive–active stress feedback. However, the hypothecated stretching-contraction must stop functioning at some point in order for the gastrulation process to proceed. It is unclear what factors arrest the hypothecated mechanism.

The hypothecated stretching-contraction model has not yet had any definite experimental support in gastrula tissues. It has been supported, however, in experiments with the cytoplasmic strands of a slime mold, *physarum* (Belousov, 1998). Whether such a stretching-contraction takes place during gastrulation in metazoan embryos is still unclear..

The embryology of tendon formation is not well studied. Initially, one finds "patches" of mesenchymal unspecialized cells set in a gelatinous ground substance of proteoglycans. Similar areas of packed undifferentiated cells appear in the early stages of the development of most connective tissues, for example, bone, cartilage, and the circulatory and lymphatic systems. The signal for such cellular packing or condensation of cells is unknown. The forming tissue converts itself into the one-dimensional structure, a tendon precursor, but is forming simultaneously with embryonic bone and muscle. We speculate that fibroblasts, aligned by tractional forces, lay down bundles of aligned collagen fibrils that associate to form fine tendons.

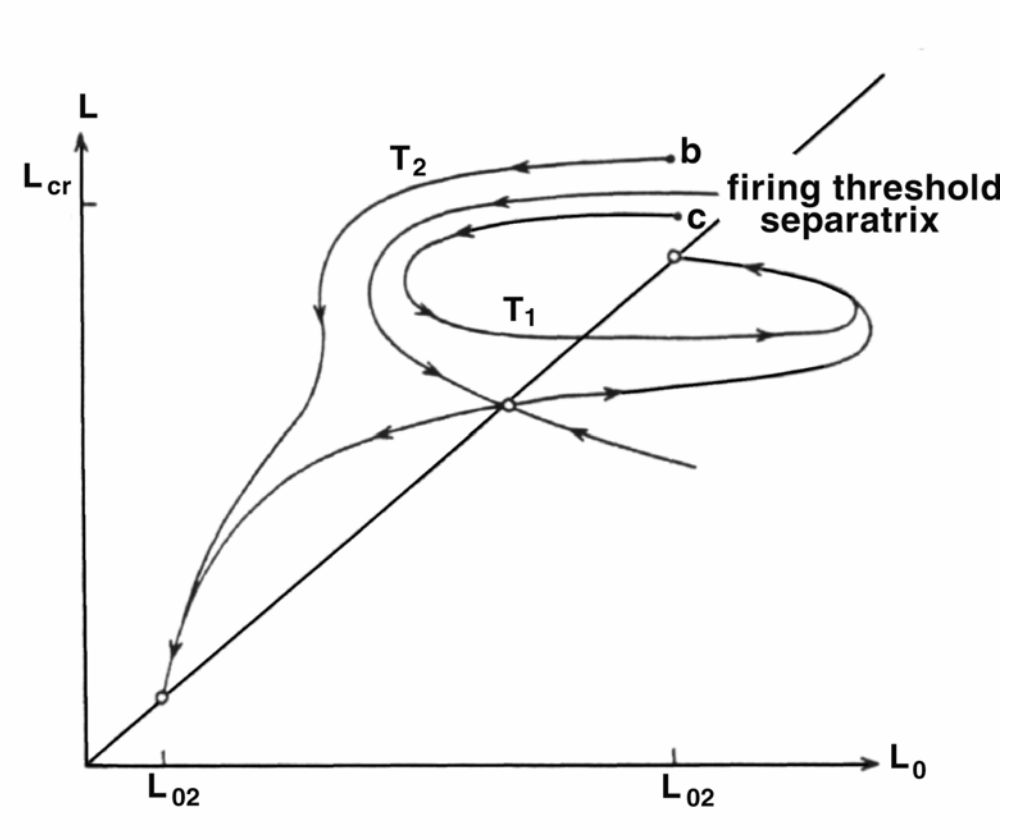



**Figure 1.26**. Mechanical model of actin belt: The vertical axis (L) represents the actual instantaneous length of the cell's apical bundle. The horizontal axis ($L_0$) represents the equilibrium (rest) length of the bundle, i.e., the length it would assume in the absence of stretching forces. The apical bundle is stress free only when the actual length equals the equilibrium length: $L = L_0$. In the simplest case, it is assumed that the apical bundle has only two stable equilibrium lengths: long ($L_{01}$) and short ($L_{02}$). Here stable means that following a small displacement in the actual length (L), the system returns to the same equilibrium point. For example, a dilation of the fiber bundle length from $L_{01}$ to a point *a* returns to $L_{01}$ along trajectory $T_1$. Separating the two stable equilibria is a "firing threshold." A dilation from $L_{01}$ to a point *b* that exceeds the firing threshold will not return to $L_{01}$, but will contract along trajectory $T_2$ to the shorter equilibrium length $L_{02}$. Reprinted with permission from Odell et al. (1981).

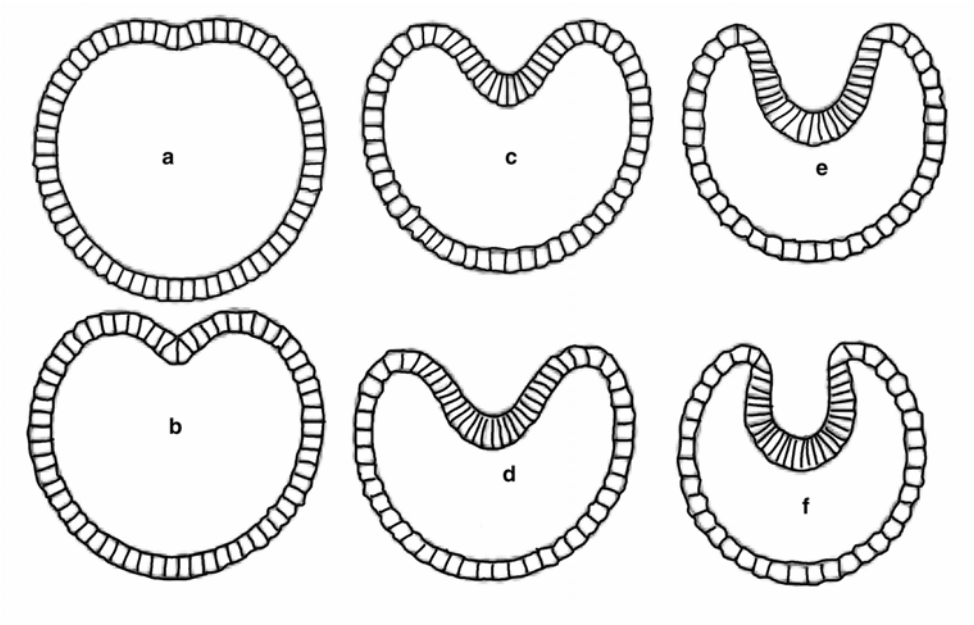



**Figure 1.27**. Odell gastrula: computer simulation of gastrulation in the sea urchin. The frames (ordered, a, b, c, ..., f), were extracted from a computer-generated film obtained by solving the model's equations. Reprinted with permission from Odell et al. (1981).

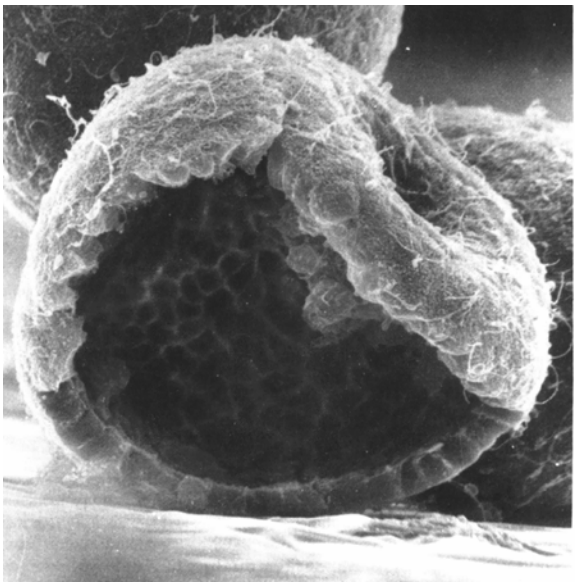


**Figure 1.28**. The blastula-to-gastrula transition. Gastrulation in the sea urchin egg. Courtesy of Jean-Paul Revel.

### Assembly by Cellular Activity

It is convenient to think of steps in the morphogenetic process for building a tissue as being caused by tissue-created forces that are self-equilibrated, that is to say, that the tissue itself is both the activator or creator of the force as well as the reactor or recipient of the force. These morphogenetic forces may involve both the cells and the extracellular matrix and can lead to the rearranging, moving, enlarging, folding, condensing, and shaping of tissue. The cell machinery used in generating morphogenetic forces includes cell division, cell sensitivity to stretch, voltage, and contact with other chemicals, the cell adhesion molecules, and the cytoskeletal ability for microfilament assembly. Cells contain actin and myosin, variant forms of the same proteins that are the key proteins for the development of force in muscle. These proteins are used in the development of microfilaments, which can be used by the cell to resist deformation, change cell shape, influence cell movement, or develop an external force. A number of actions that cells can accomplish are listed below. It is probable that these cell actions can contribute significantly to tissue assembly.

*Cell adhesion*: Cells adhere to surfaces by forces that are three to four orders of magnitude larger than their own weight. The cells can control this adhesion, and some cells can detach from a surface at their own signal. Cells have been observed moving towards more adhesive surfaces. Cell adhesions serve as anchoring points between cells and between the cell cytoskeleton and its extracellular matrix to ensure appropriate integrity and strength of the cell network and its connection to the extracellular matrix. The cytoskeleton consists of dynamic filamentous structures, of which there are three major filament types: actin filaments, intermediate filaments, and microtubules. There are various types of cell adhesions, namely desmosomes, hemidesmosomes, adherens junctions, tight junctions, gap junctions, and focal adhesions. The adhesive structures are connected to intermediate filaments (desmosomes and hemidesmosomes) or actin filaments (adherens junctions, tight junctions and focal adhesions), Figure 1.29. Association with the cytoskeleton is necessary for stable cell–cell and cell–matrix adhesion and for the integration of cell–cell contacts with changes in morphology that are characteristic of fibroblasts.

*Cell muscle*: A graphic demonstration of the tension field created by the fibroblasts was presented by Harris et al. (1980). Fibroblasts were placed on a thin sheet of silicone rubber to which they adhered tightly. The contraction and wrinkling of the rubber substrate began within a few minutes of cell placement on the silicone rubber (see Figure 1.30). In another experiment Harris et al. (1981) showed how cell systems can create a line of tension, lines extending many times the length of one cell, to orient collagen fibers. Two groups of chicken heart fibroblasts were planted about 1–2 cm apart on a thick gel of reprecipitated collagen. When the growing cells spread and clustered, they created a field of tension between the two explants. The resulting tensile stress stretched the collagen fibers into alignment (see Figure 1.30).

*Cell locomotion*: A cell is capable of self-propelled movement using different systems to propel itself at speeds measured in microns per hour. It can use its adhesion capability and its ability to form (polymerize) and dissolve (depolymerize) microfilaments as a means of locomotion (Figure 1.31). It has been suggested that cells might organize the energy from Brownian motion as motors for different activities including propulsion.

*Cell chemotaxis*: Cells are attracted to certain chemicals and repulsed by others. They can follow gradients in concentration of a chemical.

*Cell contact guidance*: Cells are known to be guided by manmade straight edges and by long fibers; this is called contact guidance (Figure 1.32).

*Cell sensors*: Cells have many sensors and different cells have different sensors. Cells are sensitive to stretch, voltage, and contact with chemicals. For example, hair cells in the ear can pick up very low-energy mechanical signals.

It appears reasonable that these cell capabilities can be modeled and simulations using these models might be able to demonstrate the possibility of cells accomplishing certain steps in tissue assembly.

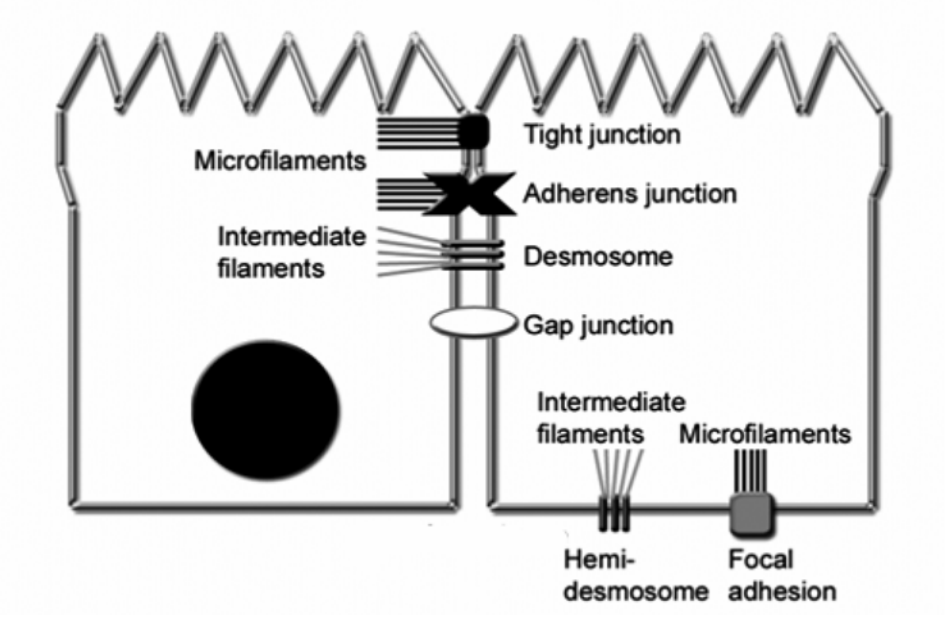



**Figure 1.29**. An illustration of cell adhesions. Two cells, left and right, resting on an extracellular matrix. The cell-to-cell adhesions are illustrated between the cells and the cell-to-matrix adhesions are illustrated on the bottom right. Types of cell adhesions include desmosomes, hemidesmosomes, adherens junctions, tight junctions, gap junctions, and focal adhesions. The adhesive structures are connected to intermediate filaments (desmosomes and hemidesmosomes) or actin filaments (adherens junctions, tight junctions, and focal adhesions). Modified with permission from http://herkules.oulu.fi/isbn9514271106/html/x369.html.

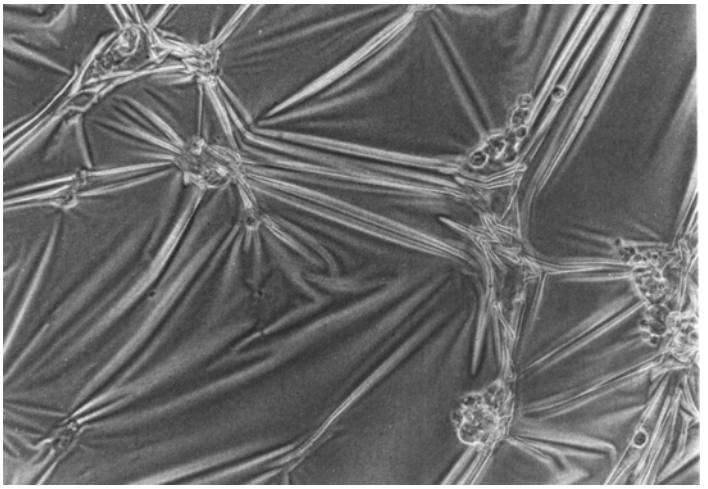


**Figure 1.30**. Mesenchymal cells on an elastic substratum. The strong tractions generated deform the substratum and create compression and tension wrinkles. The tension wrinkles can extend several hundreds of cell diameters. This demonstrates how cell systems can create a line of tension to orient collagen fibers. The cells create a field of tension between the two cell groups. The collagen fibers aligned with the resulting tensile stress. Photograph by A.K. Harris. Reprinted with permission from Murray (1993).

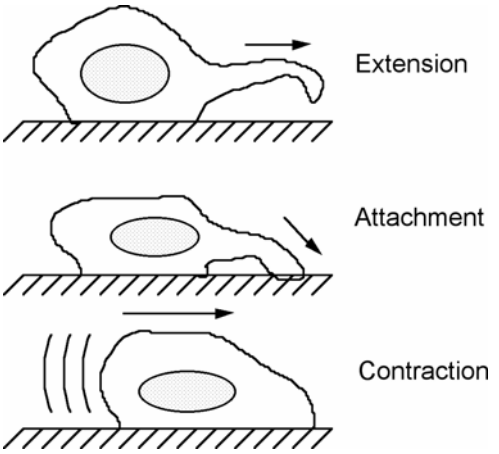



**Figure 1.31**. Cell Locomotion. The three principal stages in cell crawling: extension of the exploratory probe, attachment to the surface, and movement of the rear portion of cell forward. (Top) Extension of the exploratory probe. This entails the assembly of actin filaments. Free actin molecules move into the region of the advancing portion of the cell. (Middle) Attachment to the surface. Contact of the cell with a solid surface induces actin filaments to collect in that region. In cultured fibroblasts the membrane protein integrin, which has binding sites for several components of the extracellular matrix, accumulates at focal contacts. Rapidly locomoting cells form smaller, less permanent adhesions. (Bottom) Movement of the rear portion of the cell forward. Away from the exploratory probe of the cell, and especially in its tail region, the cortical network of actin contracts through the action of myosin. This has two important consequences. First, the contraction generates a polarized flow of cortical actin and a pulling of the cell as a whole toward points of anchorage. Second, it squeezes the cytoplasm, producing a hydrostatic pressure that drives cytoplasmic constituents to the front of the cell.

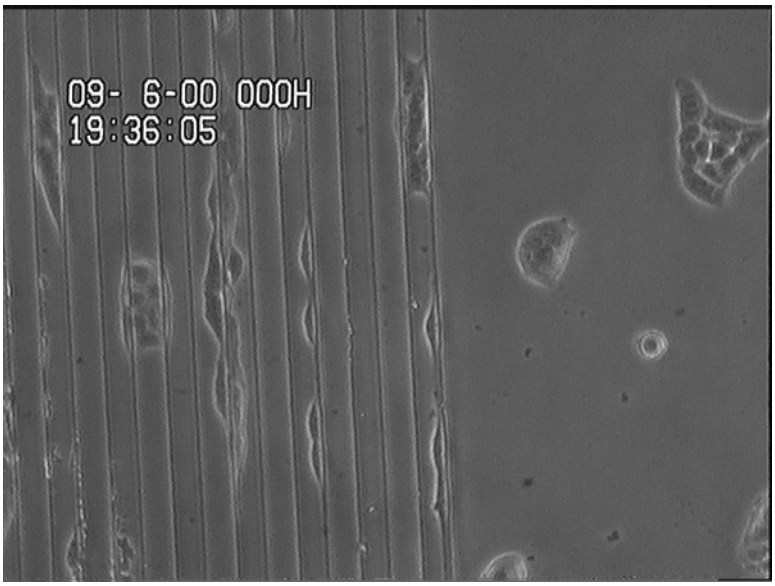



**Figure 1.32**. Cell contact guidance. Phase contrast microscope views of the same cell type on a flat surface (right) and on a surface with 10-micron wide and 5-micron deep grooves (left). The surface the cells are growing on is silica, but a similar result would be obtained with many other materials. The cells are epitenon cells. The epitenon is the connective tissue on the outside of the tendon. Courtesy of Adam Curtis.

### Supramolecular Assembly

The question of supramolecular assembly is not on the same firm ground as molecular self-assembly; however, the ideas involved are ones of deep engineering interest and have a great deal of future potential. The idea is equivalent to self-assembly at a higher structural level. The question of supermolecular assembly will be considered in Chapter 10.

## 1.9. REFERENCES


Alber MS, Kiskowski MA, Glazier JA, Jiang Y. 2002. On cellular automaton approaches to modeling biological cells. In *Mathematical systems theory in biology, communication, and finance, IMA*, Vol 142, ed. J Rosenthal, DS Gilliam. New York: Springer-Verlag.

Alberts B, Bray D, Lewis J, Raff M, Roberts K, Watson JD. 1983. *Molecular Biology of the Cell*, New York: Garland.

Anonymous. 1994. *Hierarchical structures in biology as a guide for new materials technology.* Committee on Synthetic Hierarchical Structures, National Materials Advisory Board, National Research Council, NMAB-464, Washington, DC: National Academy Press.

Anthony CR, Kolthoff N. 1975. *Textbook of anatomy and physiology*, 9th ed. St. Louis: Mosby.

Baer E, Hiltner A, Morgan R. 1992. Biological and synthetic hierarchical composites. *Physics Today.* October, pp. 60-67.

Belousov LV. 1998. *The dynamic architecture of the development of organisms*. Dordrecht: Kluwer Academic Publishers.

Beysens DA, Forgacs G, Glazier JA. 2000. Cell sorting is analogous to phase ordering in fluids. *Proc Natl Acad Sci USA* **97**:137–145.

Blauvelt CB, Nelson FRT. 1985. *A manual of orthopaedic terminology*. St. Louis: Mosby.

Coen E. 1999. *The art of genes: how organisms make themselves*. Oxford: Oxford UP.

D'Arcy Thompson W. 1942. *On growth and form*. Cambridge: Cambridge UP.

Darnell J, Lodish H, Baltimore D. 1990. *Molecular cell biology*. New York: Scientific American.

de Duve CA. 1984. *A guided tour of the living cell*. New York: Scientific American.

Fessenden RJ, Fessenden JS. 1979. *Organic chemistry*. Boston: Willard Grant Press.

Gennis RB. 1989. *Biomembranes*. New York: Springer.

Gilbert SF. 2000. *Developmental biology,* 6th ed. Sunderland, MA: Sinaur.

Goodwin BC. 1989. Unicellular morphogenesis. In *Cell Shape*, ed. WD Stein, F Bronner, pp. 365-91. New York: Academic Press.

Harris AK. 1976. Is cell sorting caused by differences on the work of intercellular adhesion? A critique of the Steinberg hypothesis, *J Theor Biol* **61**:267–285.

Harris AK. 1994. Multicellular mechanics in the creation of anatomical structures. In *Biomechanics of active movement and division of cells*, pp. 87–129, ed. N Akkas. Berlin: Springer-Verlag.

Harris AK, Wild P, Stopak D. 1980. Silicone rubber substrata: a new wrinkle in the study of cell locomotion. *Science* **208***:*177–179.

Harris AK, Stopak D, Wild P. 1981. Fibroblast traction as a mechanism for collagen morphogenesis. *Nature* **290***:*249–251.

Inwood S. 2002. *The forgotten genius; the biography of Robert Hooke 1635-1703*. San Francisco: MacAdam/Cage.

Keller EF. 2002. *Making sense of life*. Cambridge, MA: Harvard UP.

Koivunen J. 2003. NF1 tumor suppressor in epidermal differentiation and growth—implications for wound epithelialization and psoriasis. *Acta Universitatis Ouluensis, Medica*, D746.

Kuecken M. 2004. *On the formation of fingerprints*. PhD thesis. University of Arizona.

McManus C. 2002. *Right hand left hand*. Cambridge: Harvard UP.

Murray JD. 1993. *Mathematical biology*. New York: Springer Verlag.

Newman SA, Frisch HL. 1979. Dynamics of skeletal pattern formation in developing chick limb. *Science* **205**:662–668.

Odell GM, Oster GF, Alberch P, Burnside B. 1981. The mechanical basis of morphogenesis, I: epithelial folding and invagination. *Dev Biol* **85**:446–462.

Oster GF, Murray JD, Harris AK. 1983. Mechanical aspects of mesenchymal morphogenesis. *J Embryol Exp Morphol* **78**:83–125.

Radler JO, Koltover I. 1997. Structure of DNA-cationic liposome complexes: DNA intercalation in multilamellar membranes in distin. *Science* **275**:810-814.

Ridley M. 1999. *Genome*. New York: Harper Collins.

Steinberg M. 1962. Mechanism of tissue reconstruction by dissociated cells, II: time-course of events. *Science* **137**:762–763.

Steinberg M. 1964. *Cell membranes in development*. Academic Press.

Trelstad RL, Silver FH. 1981. Matrix Assembly, In *Cell biology of the extracellular matrix,* ed. ED Hay, pp. 179-216, New York: Plenum Press.

Turing AM. 1952. The chemical basis of morphogenesis. *Phil Trans Roy Soc London* **B237***:*37–72.

White RJ. 1998. Weightlessness and the human body. *Sci Am* September.

Wolpert L et al. 1998. *Principles of development*. Oxford: Oxford UP.

Young LR. 1993. Space and the vestibular system: what has been learned? [guest editorial] *J Vestib Res* **3**:203–206.

# 10

# COLLAGEN

The theme of this chapter is well summarized by a quote from Woodhead-Galloway (1980). "Indeed, many of the most interesting problems in Biology are provided by our attempts to comprehend the ways in which form is created, 'understanding what we can see in terms of what we cannot' as Francis Crick has remarked."

## 10.1. INTRODUCTION

The human body is about 60% water, with starch, sugar, some minerals and protein making up the rest. Proteins are the critical ingredient that integrate with familiar substances like water, starch, sugar, and mineral to form tissue. Proteins are macromolecules that contain carbon, hydrogen, oxygen, nitrogen, and sulfur and are composed of chains of amino acids. Fibrous proteins meet the structural and mechanical requirements of a wide range of biological systems, including hair, horn, nails, muscle, epidermis, cytoskeletal elements, and connective tissue. Fimbrin, keratin, and collagen are all fibrous proteins. Keratin is the main component of hair, skin, fingernails, and toenails, as well as hooves, scales, feathers, and horns. Collagen is the fibrous protein that is the focus of this chapter. Actually there are at least twenty types of collagen known and distinguished by roman numbers; only a subset of these collagens are fibrous — types I, II, III, V, and XI. It is interesting to note that, while most proteins are involved in cellular functioning, collagen, which is synthesized within cells, is secreted and performs its structural role in the extracellular matrices of skeletal and other connective tissues. Collagen is selected as the example of a fibrous protein to describe in detail for a number of reasons, but mainly because collagen accounts for roughly a third of total body protein and occurs in almost all tissues: about 40% is found in skin, 10 to 20% in bone and teeth, and 7 to 8% in blood vessels. Tendon contains the highest percentage of collagen content, but collagen is also found in cartilage, ligaments, internal organs, muscles, intervertebral discs, basement membranes, and the eye. Collagen provides strength and confers form while allowing flexibility and movement; it is the major structural component of tissues, carrying tension in soft tissues and providing a platform for mineralization in hard tissues that are subjected to compression.

The objective of this chapter is to describe the structure of collagen, from the formation of the procollagen molecule to incorporation of collagen fibers and fascicles into tissue structures, such as tendon or cornea. The pattern of the chapter generally follows the hierarchical structure

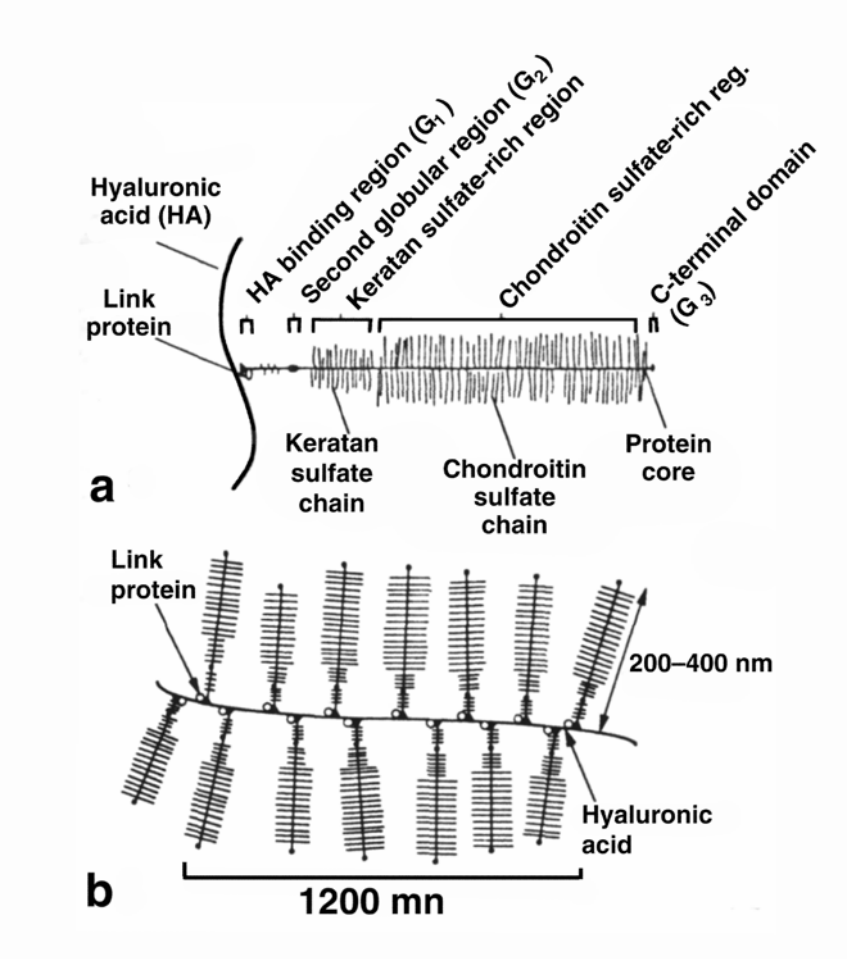



**Figure 10.1**. The organization of (a) a proteoglycan monomer; and (b) a proteoglycan aggregate formed by many proteoglycan monomers binding to a hyaluronate monofilament chain. Keratan sulfate (KS) and chondroitin sulfate (CS) are different types of glycosaminoglycans (GAGs). Reprinted with permission from Mow et al. (1992).

of collagen from molecule up to tissue. First, in the following section, there is a brief description of extracellular matrices because that is the environment in which collagen performs its function. Then, starting at a low level of the structural tree, the amino acid composition sequence of collagen is reviewed. There are then three sections relating to the collagen molecule, first a section on the formation of procollagen and collagen molecules, then one on the history of the deduction of the structure of the collagen molecule, and, finally, one on determination of the axial Young's modulus of the collagen molecule. Two sections, one that describes the many types of collagens and the other that reviews the hierarchical structures from the collagen molecule, follow these three sections. The final two sections describe supramolecular assembly and the assembly of a tendon.

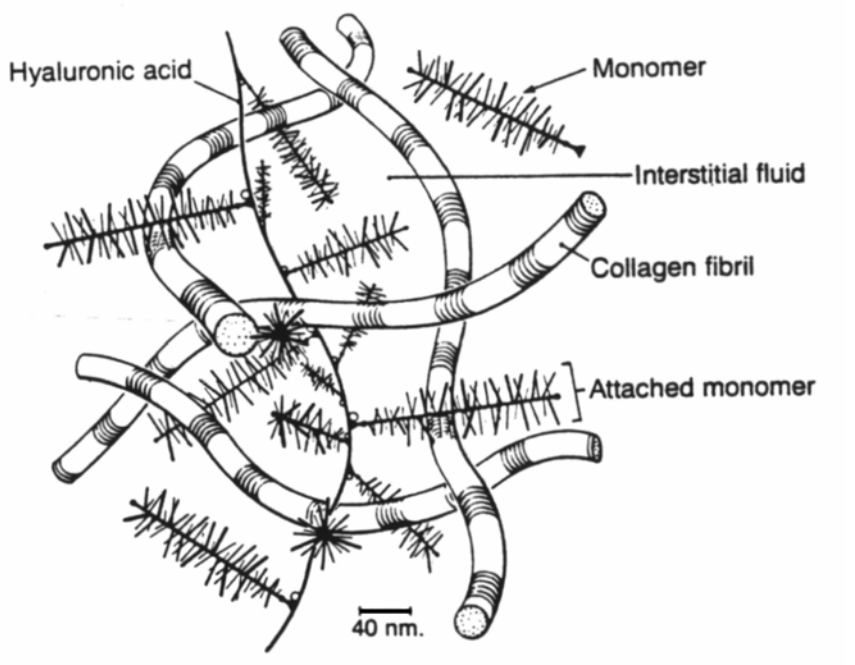



**Figure 10.2**. The collagen network interacting with the proteoglycan network in the extracellular matrix in cartilage. Reprinted with permission from Mow et al. (1992).

## 10.2. THE EXTRACELLULAR MATRIX (ECM)

Collagen is found in the extracellular matrix (ECM); it is one of the principal ingredients of the ECM. The ECM is defined as all the material of the tissue except the cells. In a dense connective tissue, such as tendon, ligament, or bone, the majority of tissue consists of ECM. The ECM consists of a network or mesh of interfibrillar matrix material containing proteoglycans (Figure 10.1) and glycosaminoglycans. Proteoglycans are glycoproteins that have a very high polysaccharide content and carry many negative charges (that is to say, they are polyanionic). Polysaccharides are polymers of more than about ten monosaccharide residues linked in branched or unbranched chains. A monosaccharide is a simple sugar (like sucrose or fructose) that does not hydrolyze to give other sugars — the simplest group of carbohydrates. In cartilage the proteoglycans are connected with and surround collagen fibrils (Figure 10.2). When their negative charge is not neutralized, the polysaccharide chains repel one another. Small amounts of proteoglycans in a solution can distend their chains and occupy large domains due to the distributed charge. The representation of a proteoglycan in Figure 10.1 does not represent its configuration in vivo; this image of its shape was obtained in vitro when the protein was spread out on a flat surface. In vivo a proteoglycan can extend its three-dimensional domain when its multiple arms are distended from each other due to the negative charges. If the charges are all neutralized with positive charges, then the proteoglycan will collapse into a smaller domain. Proteoglycans regulate the amount of water in the tissue using their ability to extend and collapse their charge-laden multiple arms. Much of our knowledge of the larger proteoglycans is derived from studies of articular cartilage (Figure 10.2), where proteoglycans

can dominate the mechanical behavior. There are a variety of proteoglycans of different size and structure. Only minor amounts of smaller proteoglycans are present in bone, tendons, and ligaments, but they play critical roles in these tissues. The arteries and veins in an umbilical cord (Figure 10.3) are embedded in a mass of ECM composed largely of glycoproteins and proteoglycans (Figure 10.4).

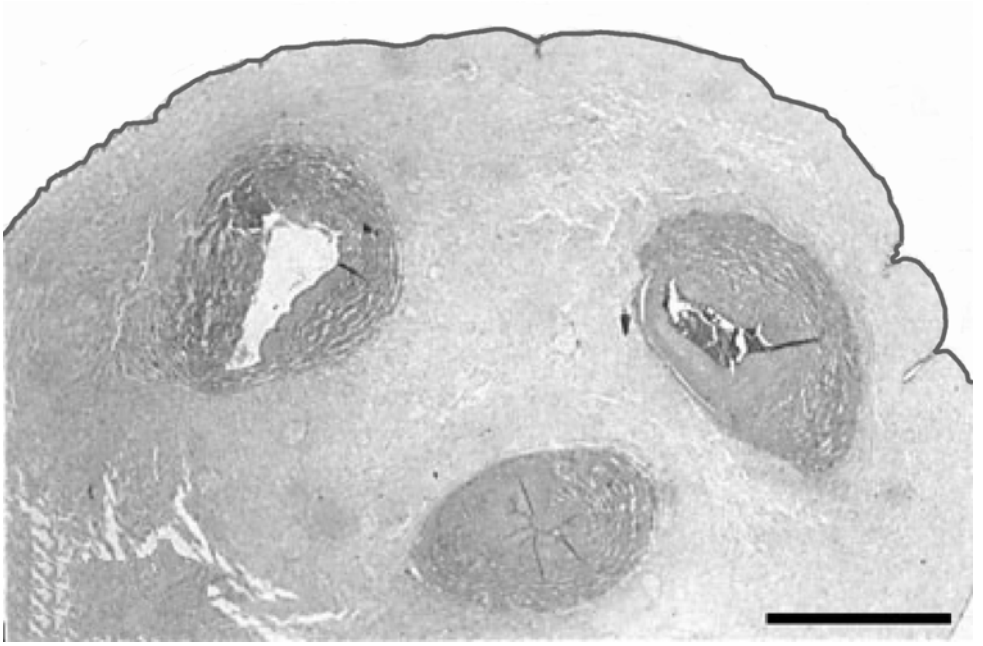


**Figure 10.3**. Umbilical cord. The two arteries and one vein (upper left) of the umbilical cord are surrounded by a large amount of connective tissue. Bar = 1 mm. Reprinted with permission from the Jay Doc HistoWeb, Milton Wolf and Marc Scarbrough, Department of Anatomy and Cell Biology University of Kansas Medical Center. http://www.kumc.edu/instruction/medicine/anatomy/histoweb/ct/Histoct.htm.

Elastin is an important non-collagenous fibrous protein in connective tissues. It is a composite of amorphous and structured regions, a protein of polypeptide chains covalently crosslinked to form an elastic material much like rubber; hence the name. The elasticity is due to the ability of individual protein molecules to uncoil reversibly whenever a stretching force is applied (Figure 10.5). Like collagen, elastin is secreted into the extracellular space, where it enables tissues like arteries (Figure 10.6) and lungs to deform and stretch without damage. It is present in the walls of blood vessels and in very small amounts, if at all, in most tendons and ligaments. It is the dominant tissue component in the few ligaments (ligamentum nuchae and ligamenta flava) associated with holding the head, neck, and upper torso erect where the ligament is under constant tension in an effort to maintain posture. As might be expected, the mechanical properties of these ligaments are quite different from those of other ligaments.

The structure of a ligament is very similar to that of a tendon; the differences will be described in a later chapter. Functionally, the ligaments are attachments between two bones, whereas tendons attach muscle to bone. In general the components of tendons and ligaments, with the exception of the elastic ligaments, consist of type I collagen with small amounts of proteoglycans and glycoproteins.

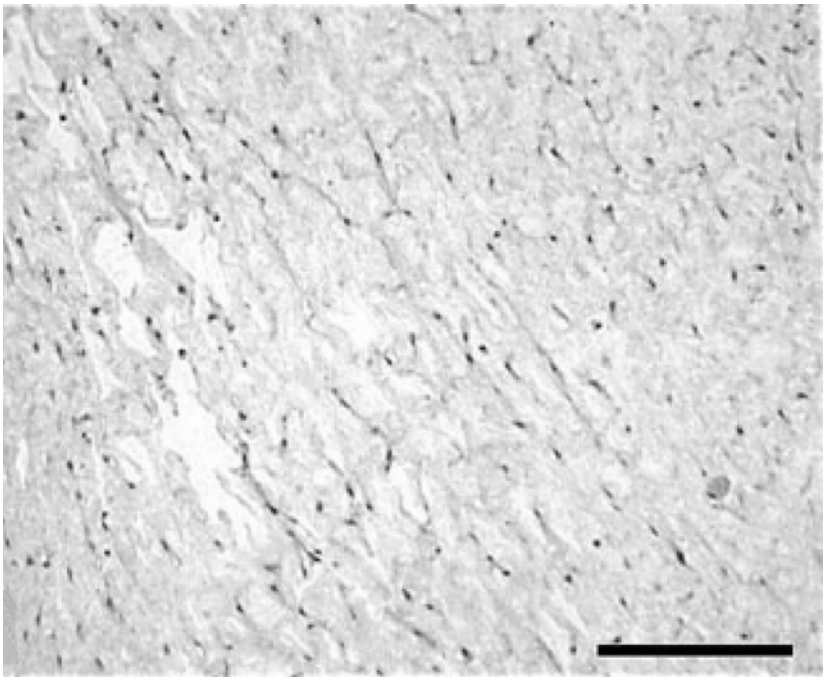


**Figure 10.4**. Umbilical cord. A closer look shows the preponderance of ECM (largely glycoproteins and proteoglycans) and relatively few cells. Bar = 100 μm. Reprinted with permission from the Jay Doc HistoWeb, Milton Wolf and Marc Scarbrough, Department of Anatomy and Cell Biology University of Kansas Medical Center. http://www.kumc.edu/instruction/medicine/anatomy/histoweb/ct/Histoct.htm.

Three connective tissue types — bone, articular cartilage, and tendon or ligament — along with the cell types that manufacture or build the associated ECM, osteoblasts for bone, chondroblasts for cartilage, and fibroblasts for tendon, ligament, and other tissues, are illustrated in Figure 10.7. Each of these cell types has a common precursor in the embryonic, stellate (star-shaped), mesenchyme cells (Figure 10.7). The mesenchyme is embryonic tissue of the mesoderm, or the middle of the three germ layers, the layer that gives rise to the musculoskeletal, blood, vascular, urinogenital systems, the connective tissues (including that of dermis), and contributes to some glands. It consists of loosely packed, unspecialized cells set in a gelatinous ECM. At an early stage in development the mesenchyme cells break away from the mesoderm and, in a predetermined pattern, distribute themselves throughout the embryo. This is the way in which the pattern of connective tissues is established throughout the animal body. The cells generally secrete the materials of the ECM, but the cells do not make all the structural materials. Some, such as water and minerals, are delivered to the tissue from the vascular system. The mineral apatite combines with the collagen in bone to form a hard, stiff composite that is very different from the collagen itself in mechanical properties.

**Problems**

10.2.1. What is the etymology of the word *collagen*?

10.2.2. What well-known substance is obtained by boiling collagen?

10.2.3 In the past old horses were sent to glue factories rather than to slaughterhouses. What was done with the old horses in the glue factory?

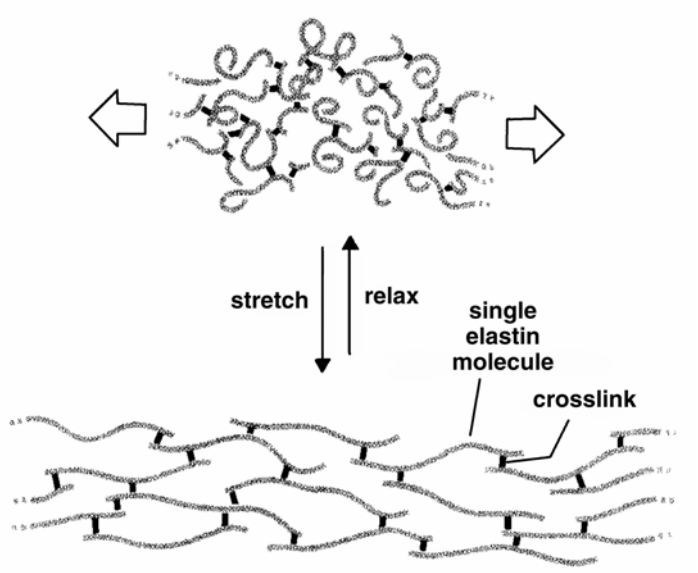



**Figure 10.5**. Elastin is composed of flexible polypeptides that are crosslinked together to create a rubbery matrix, with each molecule uncoiling into a more extended conformation when the matrix is stretched. The striking contrast between the physical properties of elastin and collagen is due to their very different amino acid sequences. Reprinted from Alberts et al. (1983).

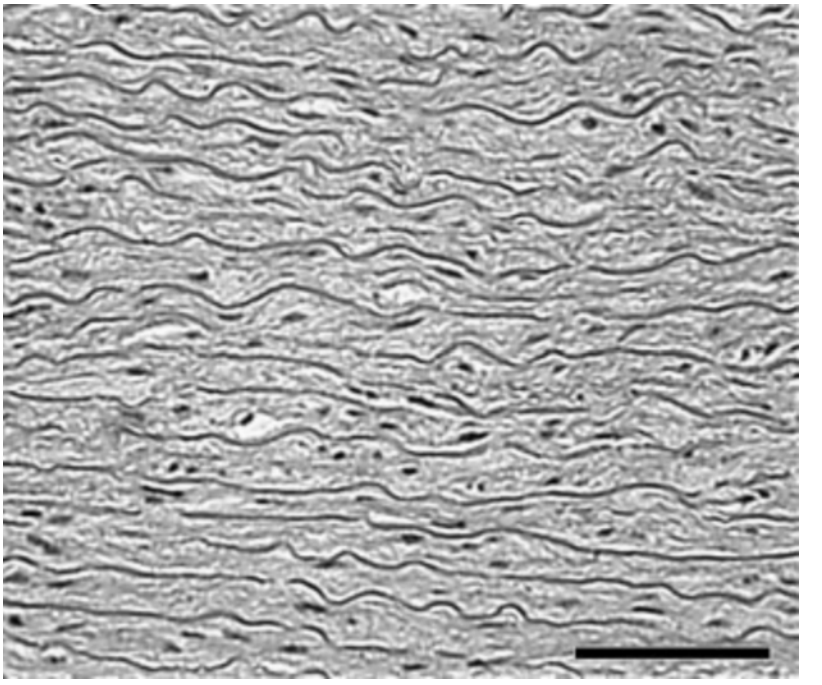


**Figure 10.6**. Sheets of elastic fibers, called elastic lamellae, from the aorta. Bar = 100 μm. Reprinted with permission from the Jay Doc HistoWeb, Milton Wolf and Marc Scarbrough, Department of Anatomy and Cell Biology University of Kansas Medical Center. http://www.kumc.edu/instruction/medicine/anatomy/histoweb/ct/Histoct.htm.

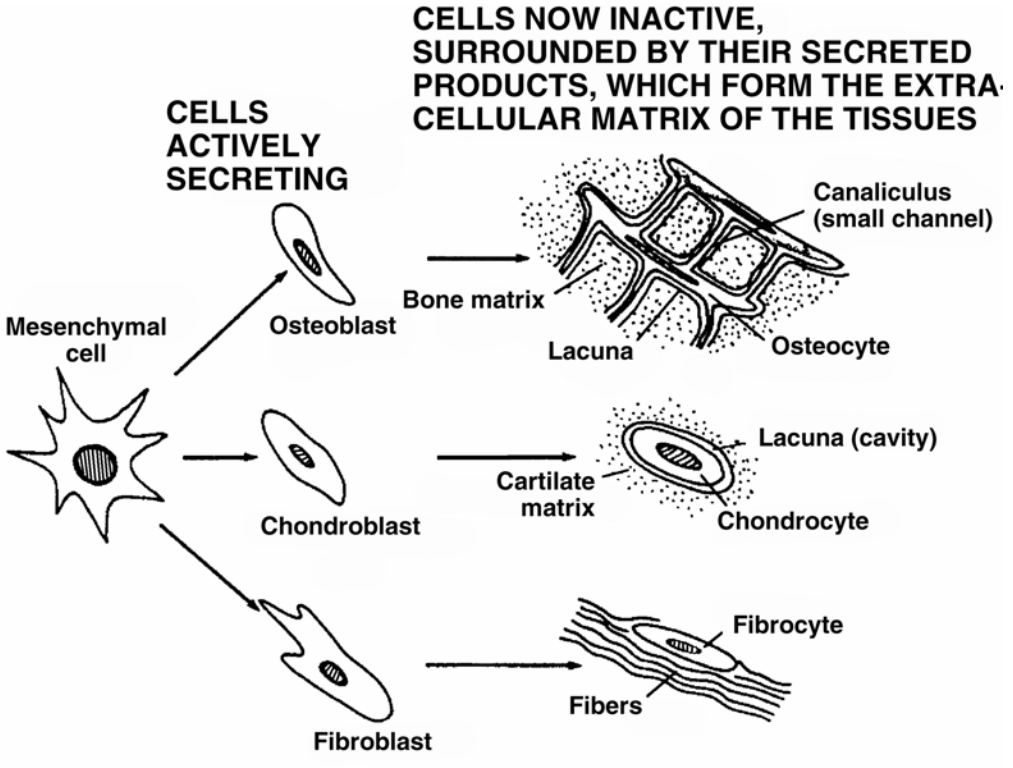



**Figure 10.7**. Diagram showing some of the sorts of connective tissue cells deriving from the embryonic, stellate (star-shaped), mesenchyme cells. At an early stage in development the mesenchymal cells break away from the mesoderm and scatter among the three germ layers of the embryo — the origin of the ubiquity of the distribution of the connective tissues. Reprinted with permission from Woodhead-Galloway (1980).

## 10.3. THE AMINO ACID COMPOSITION SEQUENCE

The term *amino* refers to the chemical group $–NH_2$, an organic molecule formally derived by the removal of a hydrogen atom from ammonia ($NH_3$). An *amino acid* is any organic acid containing one or more amino substituents. With one exception, each amino acid contains an *amino group* ($–NH_2$) and an acidic *carboxyl group* (–COOH). The exception, proline, has an imino group (–NH–) rather than an amino group; proline, at 22%, is the second most abundant acid (after glycine at 33%) in collagen. *Amino acid residues* are the amino acids less the atoms that have been removed during the formation of peptide bonds. A *peptide* is any compound containing two or more amino acid residues joined by a *peptide bond*, that is to say, a bond formed between the amino group ($–NH_2$) of one amino acid and the carboxyl group (–COOH) of another. A *protein* is a linear polymer of amino acid residues linked by peptide bonds in a specific sequence. The primary structure of peptides and proteins refers to the linear number and order of the amino acids present. The convention for designation of the order of amino acids is that the amino group or N-terminal end is to the left and the carboxyl group or C-terminal end is to the right. The orientation from N to C, illustrated in Figure 10.8, is thus a primary structural feature of peptides and proteins.

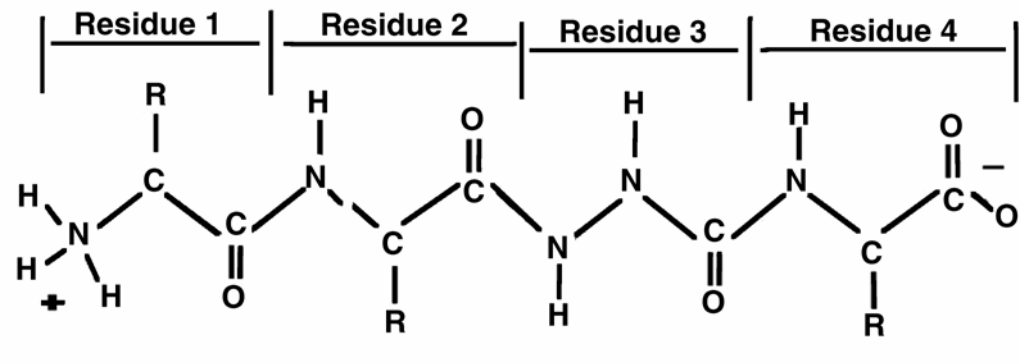



**Figure 10.8**. Illustration of the peptide orientation by the direction from the N terminal (amino) to the C terminal (carboxyl). The orientation from N to C is a primary structural feature of peptides and proteins. This illustration is of a short peptide, glycyl-alanyl-tyrosyl-glycine, called a tetrapeptide because it has four residues. Short peptides are often given a general name according to how many residues (amino acids) are linked together. Reprinted from Wampler (1996) http://bmbiris.bmb.uga.edu/wampler/tutorial/prot1.html.

**Table 10.1**. The Amino Acids

| Amino acid | Abbreviation | Abbreviated abbreviation | Human bone | Rat skin |
|---|---|---|---|---|
| Glycine | Gly | G | 31.9 | 32.7 |
| Proline | Pro | P | 12.3 | 11.7 |
| Aspartic acid | Asp | D | 4.7 | 4.7 |
| Glutamic acid | Glu | E | 7.2 | 7.4 |
| Asparagine | Asn | N | 3.7 | 5.1 |
| Glutamine | Gln | Q | 3.7 | 5.1 |
| Arginine | Arg | R | 4.7 | 4.9 |
| Histidine | His | H | 0.6 | 0.5 |
| Lysine | Lys | K | 2.8 | 2.9 |
| Alanine | Ala | A | 11.4 | 10.6 |
| Phenylalanine | Phe | F | 1.4 | 1.3 |
| Leucine | Leu | L | 2.5 | 2.5 |
| Isoleucine | Ile | I | 1.3 | 1.0 |
| Valine | Val | V | 2.4 | 2.2 |
| Methionine | Met | M | 0.5 | 0.6 |
| Serine | Ser | S | 3.6 | 4.1 |
| Threonine | Thr | T | 1.8 | 2.0 |
| Tyrosine | Tyr | Y | 0.5 | 0.3 |
| Cysteine | Cys | C | – | – |
| Tryptophan | Trp | W | – | – |
| *Hydroxyproline | Hyp | – | 10.0 | 10.0 |
| *Hydroxylysine | Hyl | – | 0.4 | 0.6 |
| Unspecified | X | X | – | – |

The first column is the name of the amino acid; the second and third are name abbreviations. The twenty common amino acids are listed without asterisks. Columns four and five are the percentages of each amino acid in human bone and rat skin.

Extracellular matrices are synthesized from the cells situated within them, for example, fibroblasts and osteoblasts, and numerous epithelial cells make particular types of collagen (Figure 10.7) for their respective tissues. The process of reading the formula for a protein from the cell's own library of genetic instructions and the cell's subsequent manufacture of the protein are described in the next section. In the manufacture of the polypeptide chain, any combination of 20 different common amino acids (Table 10.1) may be incorporated, according to the genetic instructions of the cell. The amino acid residues may be modified subsequently so that the chains may contain a much wider variety of residues, amounting to nearly 200. The primary structure of the peptide is the order of the specific amino acid residues; for example, part of a collagen sequence is Gly–Ala–Hyp–Gly–Pro–Hyp–Gly–Ala–Hyp–Gly–Ala–Hyp–Gly–Pro–Val–Gly–Pro–Ala–Gly–Lys–Ser–Gly–Asp–Arg–Gly–Glu–Thr–Gly–Pro–Ala–Gly, where the standard three-letter abbreviations for the amino acids (listed in Table 10.1) have been employed. A collagen may be recognized by its amino acid composition, i.e., the relative frequencies of the different amino acid residues. Complete analyses have been performed on collagens from many sources, and there are two main features that are always present (Woodhead-Galloway, 1980). One is the occurrence of glycine as a third of all residues. There is some small variation, which may occur in the non-helical ends. Second is the appearance of the imino acids: proline (Pro) and its chemical derivative hydroxyproline (Hyp). The latter is not in fact a naturally occurring free amino acid but is formed from proline, the chemical change taking place after the protein is synthesized. The process is called hydroxylation (Figures 10.9 and 10.10) and it adds one or more hydroxyl groups (–OH). Hydroxyproline is found only rarely in other proteins, but it comprises about 10% of all amino acids in collagen while a further 10% are unconverted proline. By analogy with hydroxyproline, there is also a derivative of lysine, hydroxylysine. Table 10.1 gives the amino acid compositions of two different collagens to show their similarity. In general the composition of mammalian collagens shows little variability, as the two data sets reported in Table 10.1 reflect.

## 10.4. THE PROCOLLAGEN AND COLLAGEN MOLECULES

The type I collagen molecule consists of three (polypeptide) $\alpha$ chains of about 1000 amino acid residues each (Figure 10.15, Table 10.2). It is a right-handed superhelix composed of the three $\alpha$ chains. Two of the $\alpha$ chains are identical, but the third one is slightly different with respect to its amino acid sequence (i.e., two alpha 1 and one alpha 2 chains). This molecule is the only fiber-forming collagen not having three identical chains and is rod-like: about 300-nm long and 1.5 nm in diameter.

The prefix *super* is used because each of the three $\alpha$ chains is itself wound into a left-handed helix with three amino acids in each turn of the helix. Thus, right-handed super-helix means a helix of a structure that is itself a left-handed helix (Table 10.2; Figure 10.17).

The formation of collagen follows the general manufacturing process of proteins before being specialized as collagen. The manufacture of proteins begins with the process of "transcription" in the nucleus of a cell (Figures 1.5 and 10.9). In this process a long mRNA (m for messenger) segment is formed in a pattern determined by the nucleotide sequence found in a DNA segment. The mRNA contains the information required to sequence the amino acids in a protein. The mRNA passes out of the nucleus and into the cytoplasm of the cell. Protein synthesis requires transfer RNA (tRNA) and ribosomal RNA (rRNA) in addition to mRNA, and it occurs at a ribosome on the rough endoplasmic reticulum.

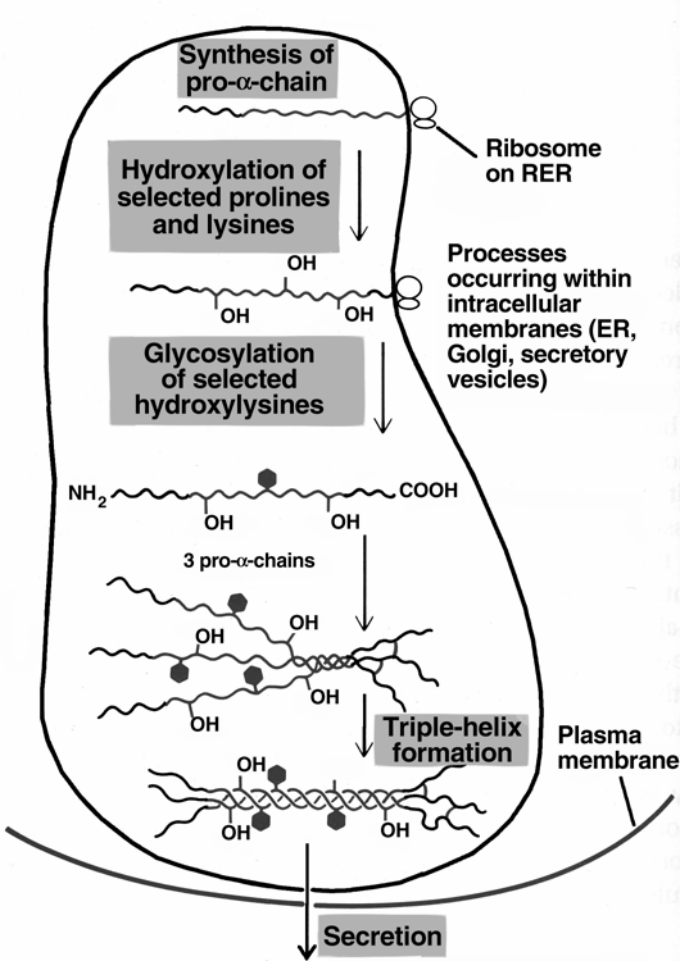



**Figure 10.9**. Flow diagram to show the "life" of a collagen molecule from synthesis to export from the cell. Note that the exported or secreted pre-tropocollagen molecule at the bottom of this figure is identical to the same structure at the top of Figure 10.16. In Figure 10.16, the illustration of the life cycle of the collagen molecule is completed. Reprinted from Alberts et al. (1983).

The process of "translation" is the synthesis of polypeptide α chains at the ribosome using the information contained in the mRNA molecules. The process of hydroxylation and glycosylation then occur, followed by the rough assembly of the α chain (Figure 10.10). (Glycosylation is the substitution of one or more glycosyl groups.) The flattened sacks of the endoplasmic reticulum are called the cisternae (Figure 1.5); it is here that the α chains are released from the ribosome and form the triple helix of collagen (Figure 10.11).

The helical structure (procollagen, Figure 10.12) travels from the cisterna of the endoplasmic reticulum to the Golgi apparatus, where the procollagen is packaged and condensed into a dense membrane-bound granule (Figure 10.13). The cytoskeletal system moves these granules to the cell membrane, where there is fusion between the external membrane of the cell

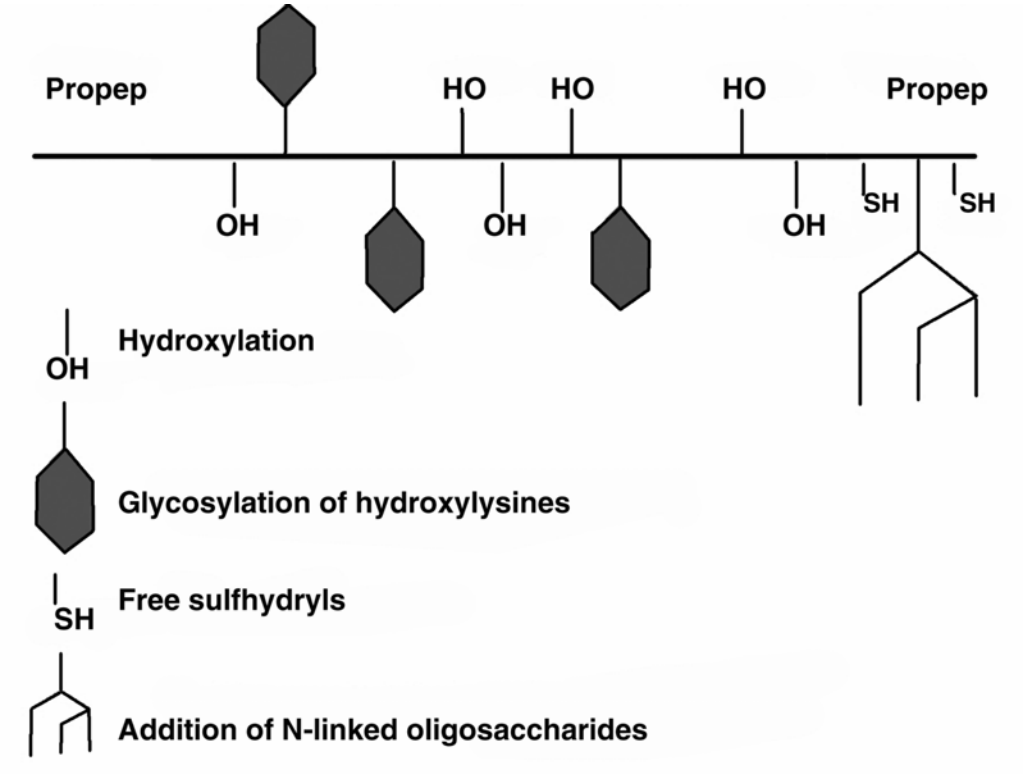



**Figure 10.10**. Posttranslational modifications.

**Table 10.2**. Structural Parameters of the Collagen Triple Helix*

| | Collagen triple helix |
|---|---|
| Sequence repair | $(Gly–X–Y)_n$ |
| Helix parameters | |
| Handedness | Left-handed |
| Residues per helix turn, $n$ | 3.33 |
| Rise/residue, $d$ (nm) | 0.286 |
| Helix radius, (nm) | 0.15 |
| Superhelix parameters | |
| Handedness | Right-handed |
| Supercoil radius, $R_0$ (nm) | 0.28 |
| Supercoil pitch (nm) | 8.55 |
| Mean mass-per-length ratio $(nm)^{-1}$ | 1000 |

*Reprinted with permission from Beck and Brodsky (1998).

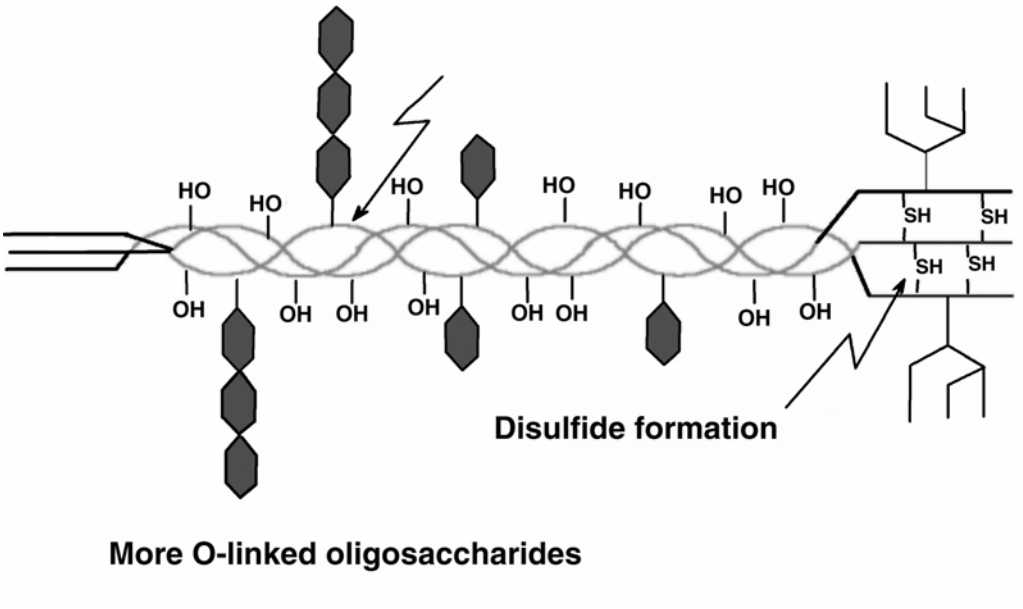



**Figure 10.11**. Formation of the collagen helix.

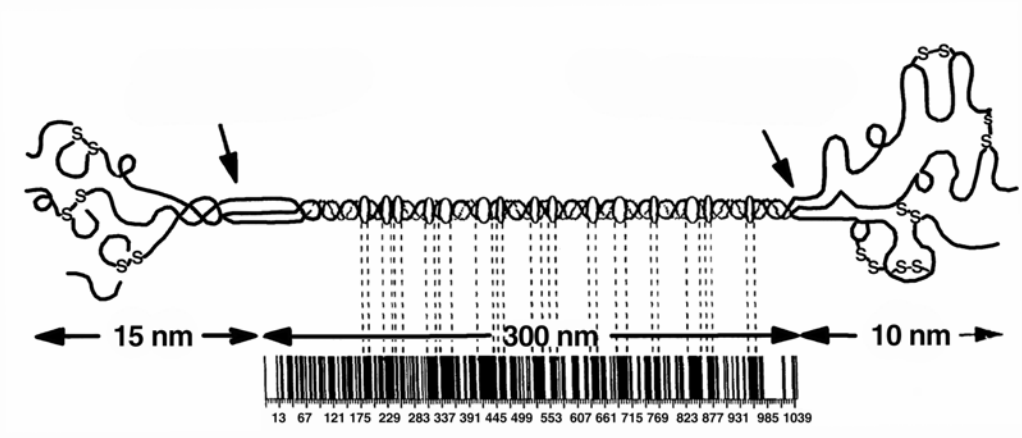



**Figure 10.12**. Procollagen type I molecule. The left end is the amino N end and the right end is carboxylic C end. The bar code at the bottom: dark bands are flexible regions, light bands are stiff regions. Reprinted with permission from Silver et al. (2003).

and the granule, so that the granule contents are released into the extracellular space (Figures 10.9 and 10.14). At this point, the terminal portions of the procollagen are enzymatically removed and the collagen molecules align themselves to form a collagen fibril. This last step is an extracellular event but occurs at the cell surface of collagen-producing cells (e.g., the fibroblasts or osteoblasts). This is illustrated in Figure 10.9, and the extracellular life cycle of a collagen molecule is shown in Figure 10.16.

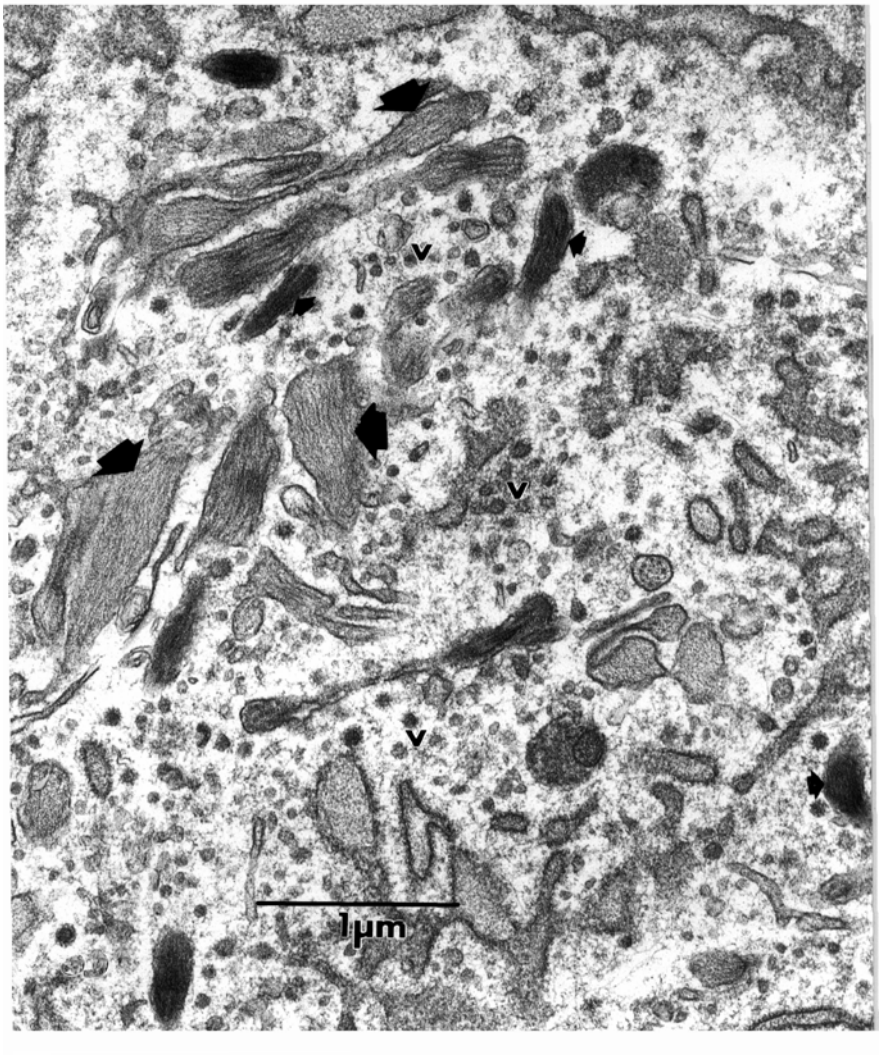



**Figure 10.13**. This electron micrograph demonstrates how the terminal portions of the Golgi saccules collect the fibrous protein (in this case, type I procollagen, since this is an osteoblast cell), and condense it to form secretory granules that then move out to the cell membrane. Notice the variation in density of the protein in the Golgi saccules (large arrows) compared to the more dense content of the secretory granule (small arrow). Numerous small vesicles (v) are also present in this active region. Magnification: 39,000X.

The structure of collagen is described as a "coiled-coil" because it is a coil that is itself composed of coils. Thus, the result is the right-handed superhelix that is a coiled coil with a pitch of approximately 30 amino acid residues or 8.55 nm. The reversal of twist at the next higher structural level is a technique used in the manufacture of rope and cable — it makes for a tighter structure that produces greater tensile strength.

The three amino acids that make up most of the chain include: glycine (33%), proline and hydroxyproline (10–12% each) (Table 10.1). Every third amino acid in each $\alpha$ chain is glycine, and this repetitive sequence is essential for proper formation of the triple helix. The small size of this amino acid allows tight helical packing of the collagen molecule. Glycine enhances

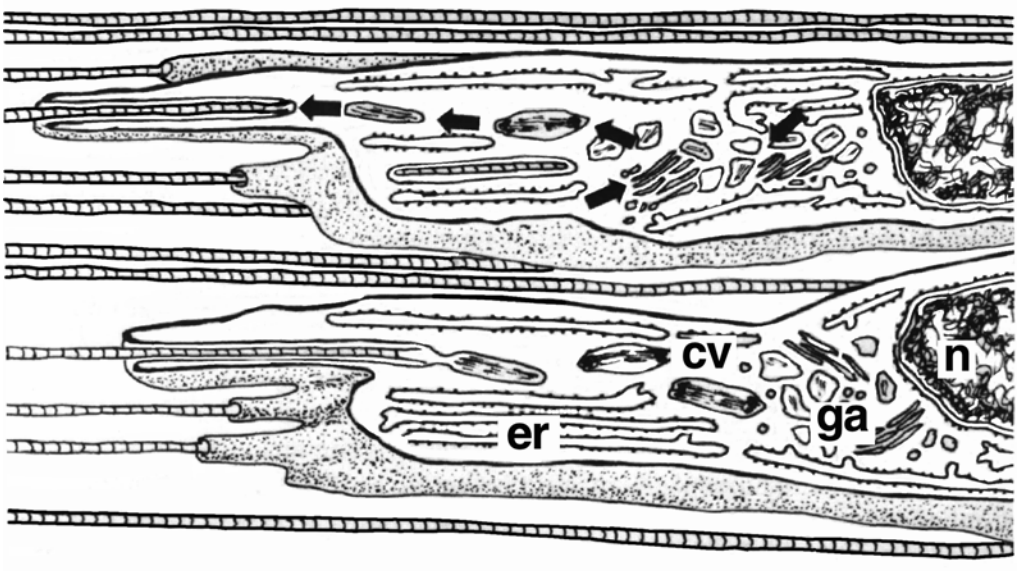



**Figure 10.14**. Probable secretory route of the collagen from the fibroblast. Following synthesis on the endoplasmic reticulum (er), the procollagen is transported to the Golgi apparatus (ga), where the procollagen is packaged and aggregation begins to occur. These aggregates are then moved to the cell surface in condensation vacuoles (co) and discharged into the extracellular space. Reprinted with permission from Trelstad and Silver 1983).

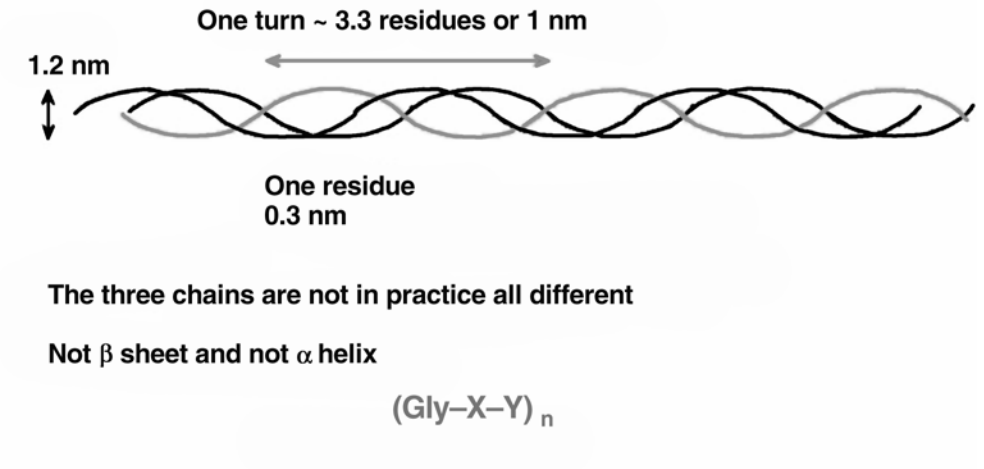



**Figure 10.15**. The collagen triple helix.

the stability of the molecule by forming hydrogen bonds among the three chains of the superhelix. Hydroxyproline and proline form hydrogen bonds, or hydrogen-bonded water bridges, within each chain. The intra- and interchain bonding, or crosslinking, between specific groups on the chains is essential to the stability of the molecule.

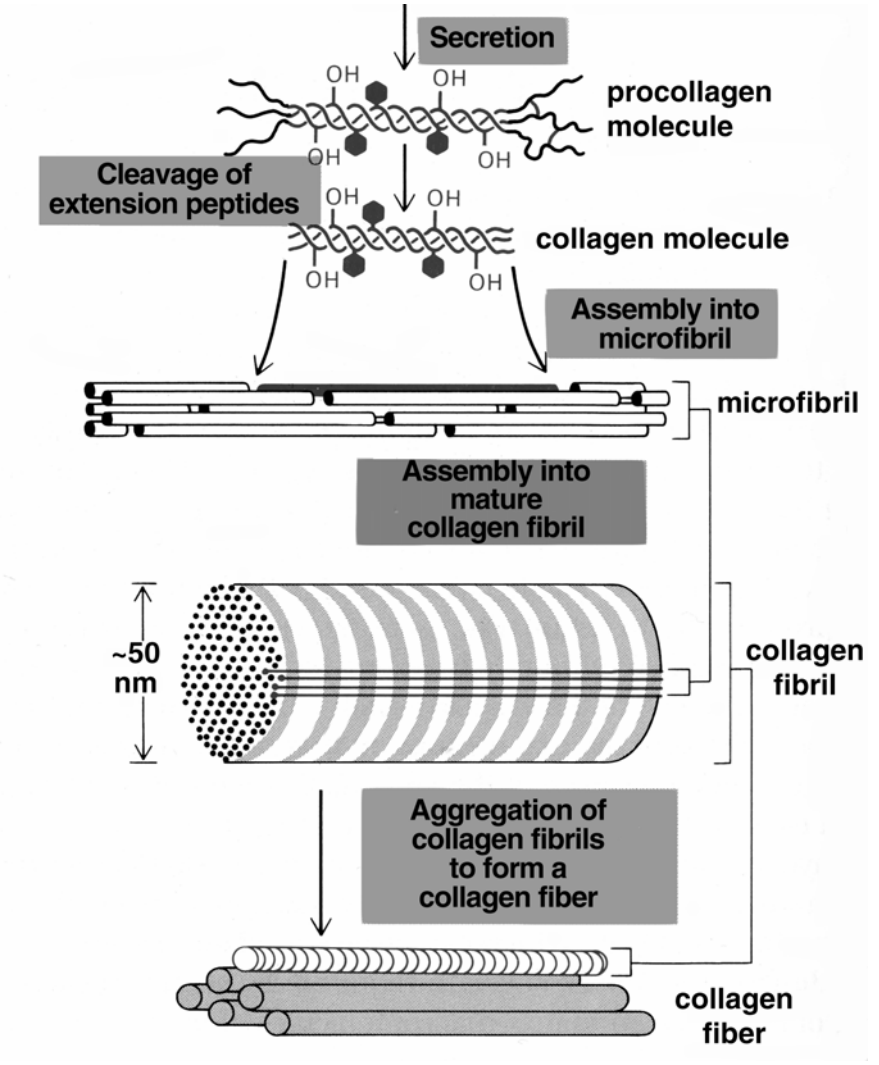



**Figure 10.16**. Flow diagram to show the "life" of a collagen molecule beginning with export from the cell through fiber formation. This is a continuation of Figure 10.9, which illustrates the production of collagen within the cell. Note that the exported or secreted pre-tropocollagen molecule at the top of this figure is identical to the structure at the bottom of Figure 10.9. Reprinted from Alberts et al. (1983).

**Problems**

10.4.1. Recall that cells secrete procollagen molecules that are then transformed to collagen molecules in the extracellular space. Procollagen differs chemically from collagen in having extra amino acids at the N-terminal of its peptide chains. Once outside the cell these extra amino acids are cleaved off and hence the collagen molecules self-assemble into fibrils. Give a physiological reason for the importance of forming procollagen inside the cell.

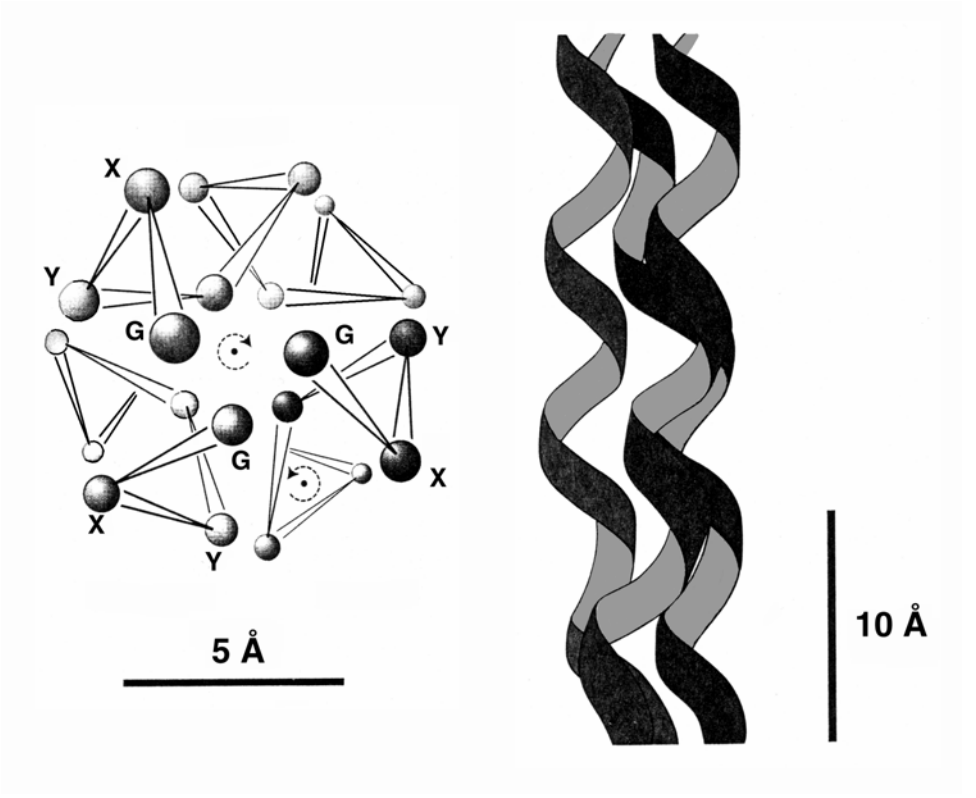



**Figure 10.17**. Cross-section (left) and longitudinal section (right) of a collagen triple-helix. Note that 10 Å = 1 nm. The cross-section is of the triple helix found in the crystal structure of a collagenous peptide. The scheme illustrates the more solvent exposed character of residues in position X of the Gly–X–Y triplet when compared to position Y. The longitudinal section highlights the extended character of the triple helix, with a helix rise of 0.86 nm per triplet. The segment shown for the triple helix represents 3 x 11 residues (0.286 nm x 3 = 0.86 nm). Reprinted with permission from Beck et al. (1998).

10.4.2. In order for a cell to increase its protein synthesis the nucleus has to respond to some cellular signal (e.g., hormonal or receptor stimulation). Describe how this response leads to new protein synthesis.

10.4.3. What is a chemical bond?

10.4.4. How is a covalent bond formed? What is the energy of a covalent bond in kilocalories per mole (kcal/mol)?

10.4.5. How is a hydrogen bond formed? What is the energy of a hydrogen bond in kilocalories per mole (kcal/mol)?

10.4.6. How is an ionic bond formed? What is the energy of an ionic bond in kilocalories per mole (kcal/mol)?

10.4.7. How is a Van der Waals bond formed? What is the energy of a Van der Waals bond in kilocalories per mole (kcal/mol)?

10.4.8. Order the following bonds from the one with the greatest breaking resistance to the one with the least: covalent, hydrogen, ionic, Van der Waals.

10.4.9. How does collagen change as it ages?
10.4.10. In order for connective tissues to show birefringence in polarized light, what must they must contain?
10.4.11. Why is glycine such an important amino acid in collagen?
10.4.12. At what stage in the formation of a collagen molecule is hydroxylation involved?
10.4.13. What type of collagen molecule does not have three identical $\alpha$ chains?

## 10.5. EXPERIMENTAL AND THEORETICAL DEDUCTION OF COLLAGEN STRUCTURE

The shape and size of collagen molecules have been explored and explained over the last seventy years of the 20th century by a combination of experiment, theory, and inspired guessing. The structure of collagen was first experimentally studied using x-ray diffraction. X-rays are electromagnetic waves of short wavelength, typically on the order of 0.1 nm, approximately the diameter of an atom or the distance between the centers of adjoining atoms in a molecule. If a collagen-containing tissue matrix, say tendon, is irradiated with a narrow beam of such x-rays and a photographic plate is exposed to the rays that have been scattered by the tissue, then a highly characteristic diffraction pattern is found on development of the plate. Very regular materials, such as crystals, produce patterns that may be easier to interpret, but the technique can be used with tissues like muscle, hair, and those containing collagen in which there is more disorder. The pattern can be used to decipher the structure of the original tissue. In 1938, V. T. Astbury reported that he could distinguish between the proteins of different tissues by just this method, and he revealed, for example, that patterns from muscle and hair were very similar to each other, but very different from the patterns produced by tendons. Astbury was the first to recognize the essential simplicity of fibrous proteins and their paradigmatic role in protein structure. Later it became apparent that patterns similar to those obtained from tendon were also produced by many species and many tissue types. For example, an x-ray diffraction pattern (Figure 10.18) of an unstretched kangaroo tail tendon contains the characteristic collagen pattern; note the strong 0.286-nm reflection on the meridian in Figure 10.18. This intense arc on the meridian of the pattern arises from a strong period of 0.286 nm in the tissue; the period represents the distance along the chain of amino acids from one residue to the next. This particular feature is characteristic of any diffraction pattern for a collagen. This spacing changes if the protein is held in a strained configuration during the process of x-ray diffraction pattern formation. This feature was used to measure the strain in a determination of the elastic Young's modulus of the collagen molecule, as will be explained in the following section, 10.6.

Tools in addition to x-ray diffraction are used for the investigation of collagen structure. The powers of magnification and resolution of electron microscopes far exceed those of the best optical microscopes. The investigation of protein structure is also accomplished with high-resolution nuclear magnetic resonance (NMR) spectroscopy. Structural problems in biochemistry and molecular biology are being studied with this tool; these include both the regulation of gene expression with aspects of both protein–nucleic acid interaction and protein–protein interaction. The aim is to understand these biomolecular recognition processes in terms of detailed three-dimensional structures and dynamics.

The early x-ray diffraction patterns were poor, and considerable thought was needed to infer structure from these images. The problem of inference of structure is the source of the quote that opened this chapter. Pauling, Crick, Ramachandran, and others, all exceptional men for their other contributions, then deciphered the poor diffraction patterns yielded by collagen. Linus Carl Pauling (1901–1994) was the 1954 Nobel Laureate in chemistry for his research

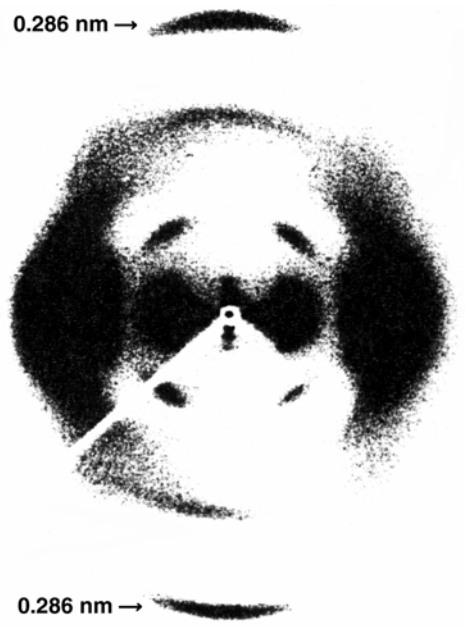



**Figure 10.18**. X-ray diffraction pattern of an unstretched kangaroo tail tendon showing the characteristic collagen pattern with a strong 0.286-nm reflection on the meridian. Reprinted with permission from Cohen (1998).

into the nature of the chemical bond and its application to elucidation of the structure of complex substances. Francis Harry Compton Crick (1916–2004) was the 1962 Nobel Laureate in medicine for the discovery (with James Dewey Watson and Maurice Hugh Frederick Wilkins) of the molecular structure of deoxyribonucleic acid (DNA). G. N. Ramachandran (1922–2001) is the creator of the Ramachandran diagram. The model produced by these investigators was the α-helical coiled coil and the collagen triple-helical coiled coil — both characterized by different local sequence periodicities. Longer-range sequence periodicities present in diverse fibrous proteins, such as collagen, tropomyosin, paramyosin, and myosin, were then shown to account for the characteristic axial repeats observed in filaments of these proteins.

The helical structures that serve as models for protein structures are considered to be secondary structural features. Recall from §10.3 and Figure 10.7 that the primary structural feature of peptides and proteins is the positive orientation from the N-terminal end to the carboxyl or C-terminal end. With this orientation in the direction of the sequence of amino acid residues along the chain, the helical structures that serve as models for protein structures are classified as right- or left-handed (Figure 10.19). The N-to-C direction is indicated by an arrowhead on the coil in Figure 10.19. The collagen triple helix contains elements of the two basic supercoiled multistranded protein structural motifs; it contains three left-handed helices and a right-handed superhelix (Figure 10.17). The coiled coil (or supercoil or superhelix) can be envisaged as resulting if a twisted three-strand wire were coiled by wrapping it around a finger.

These helical structures were originally characterized in fibrous proteins, but they were later found in a number of other proteins containing rod-shaped domains. Both structures were originally solved by fiber diffraction; crystallographic studies on small proteins and peptide models have confirmed the structure and provided molecular details. The differences in the

molecular conformations of these two motifs and the interactions stabilizing these conformations will be considered here. The molecular structures of both motifs constrain the amino acid sequence to recognizable patterns, requiring the $(Gly–X–Y)_n$ repeating sequence for the collagen triple helix.

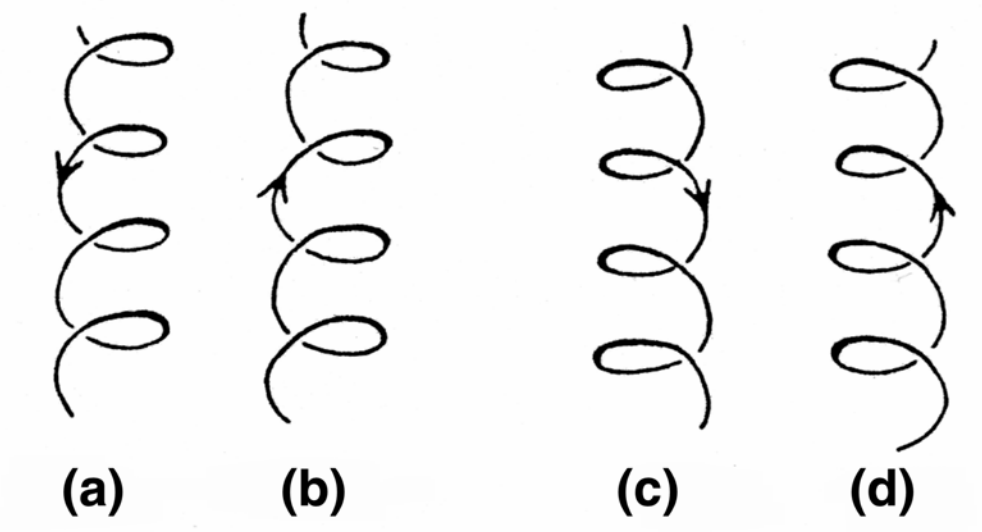



**Figure 10.19**. (a,b) Right-handed helices; (c,d) left-handed helices. The arrow symbolizes the direction of the sequence of atoms in the polypeptide chain. Reprinted with permission from Crick (1953).

Figure 10.17 shows the cross-sectional and axial view of the collagen triple helix. The parameters of the collagen triple-helix peptide determined in detail by x-ray crystallography were very similar to those modeled on the basis of fiber diffraction data and show extended left-handed individual helices supercoiled in a right-handed manner (Table 10.2). The experimental setup for fiber diffraction is rather simple — the orientated fiber is placed in a collimated x-ray beam at right angles to the beam and the "fiber diffraction pattern" is recorded on a film placed a few cm away from the fiber. The triple-helix conformation must always consist of three polypeptide chains, and these chains are parallel and staggered by one residue with respect to each other. However, modeling suggests that it is possible to fold back one chain into a triple helix, with one antiparallel chain, and such a conformation has been observed. The triple helix serves as a model for secondary structure in proteins.

## 10.6. THE AXIAL YOUNG'S MODULUS OF A COLLAGEN MOLECULE

There have been at least six efforts to experimentally estimate or determine the axial Young's modulus of a collagen molecule over the last thirty years. These studies have used collagen from different collagen-containing tissues and they have employed different experimental techniques. The measurements of Young's modulus have produced values from about 3 to 9 GPa (Table 10.3). This range of moduli at the low end corresponds to the Young's modulus of teflon and at the upper end, the modulus of wood, fairly rigid for an organic molecule.

**Table 10.3**. Measurements of Young's Modulus for Healthy and Pathological Collagen Molecules from Various Tissues by Various Methods

| Tissue from which the collagen was obtained | State | Nature of the test procedure | Young's modulus (GPa) | Source |
|---|---|---|---|---|
| Bovine Achilles tendon | Solid state in 0.15 M NaCl solution | Static X-ray diffraction | 2.9 ± 0.1 | Sasaki & Odajima (1996a) |
| Rat tail tendon NaCl solution | Solid state in 0.15 M | Brillouin scattering | 9.0 | Harley et al. (1977) |
| Rat tail tendon NaCl solution | Solid state in 0.15 M | Brillouin scattering | 5.1 | Cusack & Miller (1979) |
| Lathyritic rat skin | Acetate/NaCl/glycerol solution | Dynamic measurement of persistence length | 4.1 | Nestler et al. (1983) |
| Dermatosparaxic calf skin | 0.05 M acetic acid glycerol solution | Static measurement of persistence length | 5.1–3.0 | Hofmann et al. (1984) |

Lathyrism and dermatosparaxis are both pathologies that lead to defective collagen, so the values found for the persistence length (and consequently Young's modulus) may be quite different from the one of normal collagen. Lathyrism results from inhibition of lysyl oxidase, an important enzyme involved in crosslink formation and thus maturation of collagen. "Dermatosparaxis is a heritable disorder of the connective tissue observed in the calf and is related to the presence in the dermis of a form of procollagen, rather than collagen, forming the fibrous support of the skin. This alteration results from the lack of activity of procollagen peptidase, an enzyme required for the final processing of procollagen in collagen. Skin in dermatosparaxis displays abnormal mechanical properties. Procollagen forms poorly structured fibers loosely packed in sheets and dispersed within an excess of glycosaminoglycans. This disturbed architectural organization is responsible for the hyperextensibility and poor elasticity of the dermatosparactic dermis. Skin fragility is related to the impaired mechanical properties of the procollagen polymers. Rupture occurs in the mid-dermis in a location where the connective tissue is devoid of adnexae and elastic fibers." The material on dermatosparaxis is from the abstract of Pierard and Lapiere (1976).

Most recently, Sasaki and Odajima (1996a) determined a stress–strain curve for a collagen molecule and estimated Young's modulus of a molecule along the molecular axis using x-ray diffractometry. Recall from the previous section that the structure of collagen was first experimentally studied using x-ray diffraction, following a 1938 suggestion of V. T. Astbury. Cowan et al. (1955) measured the microscopic strain of molecules and fibrils in tendon collagen (type I collagen) as a response to macroscopic loading by means of the x-ray diffraction technique. However, they were not able to estimate the modulus of molecules and fibrils because the arrangement of collagen molecules in the collagen fibril was unknown at that time. Sasaki and Odajima (1996a) carried out the measurement suggested by the work of Cowan et al. (1955). These authors used x-ray diffractometry on bovine Achilles tendon in order to measure strain in the collagen molecule along the molecular axis as a response to a macroscopically applied force. Recall from Figure 10.18 that the x-ray diffraction pattern of unstretched collagen contains a strong 0.286-nm reflection on the meridian that arises from a period of 0.286 nm in the

tissue. The period represents the distance along the chain of amino acids from one residue to the next. As suggested by Cowan et al. (1955), Sasaki and Odajima (1996a) observed the change in the period of 0.286 nm due to the straining of collagen specimens; the strain was determined by the change in the 0.286-nm period divided by the period. From a knowledge of the applied force and the geometry of the collagen structure the stress–strain curve was then determined.

The stress–strain curve of the collagen molecule determined by Sasaki and Odajima (1996a) was almost linear. The x-ray diffraction technique of Sasaki and Odajima (1996a) is described as "static" because the collagen test sample was held in a fixed position when the test was conducted. The Young's modulus of the molecule was determined to be slightly smaller than when determined by dynamic mechanical methods (Table 10.3), methods in which the loading of the collagen test sample varied during the test. The difference between the static and dynamic test methods is thought to be significant because it is thought that the collagen molecule may behave in a viscoelastic manner. It has been suggested that this viscoelasticity could be related to the hydrogen bond network in the collagen molecule. Earlier, Harley et al. (1977) had suggested that the Young's modulus value of collagen preliminarily estimated from the results obtained by Cowan et al. (1955) was small compared with those obtained by dynamic methods. Thus, the difference in Young's modulus in Table 10.3 may be attributed partly to the measuring methods and differences in the origins and preservations of the tissue. This discussion suggests that the collagen molecule itself has a viscoelastic response to applied loading, in particular that the effective Young's modulus of a molecule increases with strain rate. Sasaki and Odajima (1996a) review the suggestion that the collagen molecule viscoelasticity may be related to the hydrogen bond network in the collagen molecule, the breaking and rebuilding of the bonds.

Nestler et al. (1983) and Hofmann et al. (1984) measured the persistence length to infer the Young's modulus, as the two quantities are proportional. The persistence length is a measure of the stiffness of a polymer molecule. It characterizes the length scale for which the chain can be thought to be rigid (see Figures 2.28 and 2.29 for illustrations of a model polymeric chain). The persistence length determines the step size that is appropriate to model the chain as a series of freely jointed links. Nestler et al. (1983) determined the persistence length from viscoelastic measurements of a dilute solution of collagen and obtained a persistence length of 170 nm. Hofmann et al. obtained the value of 57 nm by static observations.

Cusack and Miller (1979) and Harley et al. (1977) measured Young's modulus of the collagen molecule by Brillouin scattering. Brillouin scattering is the scattering of light waves caused by thermally driven density fluctuations. It may cause frequency shifts of several gigahertz at room temperature. Harley et al. (1977) suggested that Brillouin scattering measures the effective modulus of the triple-helical collagen molecule. Cusack and Miller (1979) demonstrated that Brillouin measurements probe the intermolecular forces.

It is possible to attribute the differences in the values of Young's moduli in Table 10.3 to several factors. First, there is the difference in the properties of the collagen from different tissues, some of which were not "normal" tissues. Second, there is the difference between the "static" and "dynamic" experimental methods that might be related to the viscoelasticity of the tissue and to the breaking and forming of bonds. In spite of these considerations, measurements of Young's modulus of collagen have produced values (3–9 GPa; see Table 10.3) that are not too greatly varied given the difficulty of the problem.

It has been suggested that collagen molecules are joined end to end before their incorporation in the next-level structure (Trelstad and Silver, 1981). Sasaki and Odajima (1996b) evaluated three models of molecular elongation and rearrangement of the collagen fibril and concluded that a fibril is composed of collagen molecules mechanically connected serially to each

other. Trelstad and Silver (1981) suggest that this end-to-end connection occurs by the equivalent of a biological welding process accomplished in invaginations of collagen-producing fibroblasts.

## 10.7. THE MANY TYPES AND CLASSES OF COLLAGENS

The suppliers of steel products to the building construction and manufacturing communities offer a variety of structural steel products that can include I beams, wide-flange beams, channels, plates, rods, angles, tubing, pipes, and specialty fittings to attach these components to one another. This diversity in products made of steel is analogous to the various types of collagen made by the various collagen-producing cells. Some collagens are fibrous, some are sheets, some are globular; about 20 types of collagen have been identified to date. Collagen is defined by its chemistry and is subdivided into types depending on slight variations in chemical content. It is also divided into classes depending upon its function in a tissue. In the following paragraphs the collagen family is broken down into classes. The breakdown is taken from Gilbert (1998).

Class 1 collagens include types I to III, V, and XI. All of these collagen types are fiber forming, all are of approximately the same length, and all have a lengthy uninterrupted collagenous domain with three $\alpha$ chains in the form of a triple helix. Each of these types is synthesized as a procollagen molecule. Several types of $\alpha$ chains are found in the different types of class I collagen. All of these types aggregate into staggered arrays, first into microfibrils of five collagen molecules that then aggregate into fibers. Type I is the major collagen found in skin, tendon, bone, dentin, meniscus, and annulus fibrosus. Mutations in collagen I produce osteogenesis imperfecta, a highly variable condition (depending on the place of the mutation) characterized by deformed bones, short stature, and abnormalities of teeth. Type II is a collagen specific for cartilage and vitreous humor. Mutations in collagen II can cause abnormalities of skeletal development and eye structure. Type III is a collagen frequently found with type I in skin, muscles, heart, synovium, and blood vessels. Type V is a collagen found in fetal tissue, placenta, and interstitial tissue and is co-distributed with type I. This collagen appears to be necessary for extracellular matrix assembly in connective tissues. Mice in which this gene has been knocked out have spinal deformities and poor skin and eye development. Type XI is a collagen found in cartilage and is co-distributed with type I.

Class 2 collagens include types IX, XII, and XIV, and they are the class of fibril-associated collagens with interrupted triple helices. Type IX is a collagen found in cartilage and the vitreous humor. This collagen is also a proteoglycan, combining with chondroitin sulfate and dermatan sulfate. Type XII is a collagen found in embryonic skin and tendons. Based on its position in dense connective tissues, this collagen is thought to crosslink fibrils and resist shear forces on skin and tendons. Type XIV is a collagen found in fetal skin and tendons.

Class 3 collagens include only one type, type VI. The class is one of fibril-associated collagens forming beaded filaments. Type VI is the collagen found in most interstitial tissues, blood vessels and muscle. It may be important in heart development and has been implicated in cell migration.

Class 4 collagens include types IV, VII, and X and are collagens that form sheets. Type IV is the major component of basement membranes, the membrane that forms a tough surface that supports the skin and many organs; it is also found in all basal laminae. Figure 10.20 depicts a cartoon of the contents of a basement membrane illustrating how type IV collagen forms the structural basis of this membrane. Type IV collagen has a globular head at one end and an extra tail at the other. Type VIII is a collagen found in endothelial cells and Descement's mem-

brane (of the cornea). Type X is a collagen found in the cartilage growth plate; it makes an appearance in hypertrophic cartilage cells prior to mineralization at the base of the growth plate. Class 5 collagens include only one type, type VII. This is the class of collagens that form anchoring fibrils. Type VII collagen is found in epithelia. Class 6 collagens are "other" collagens. A current member of this class is type XVII, a collagen found in squamous epithelial cells of the skin. The functions of collagens XIII, XVIII, XVI, XV. and XIX are unknown.

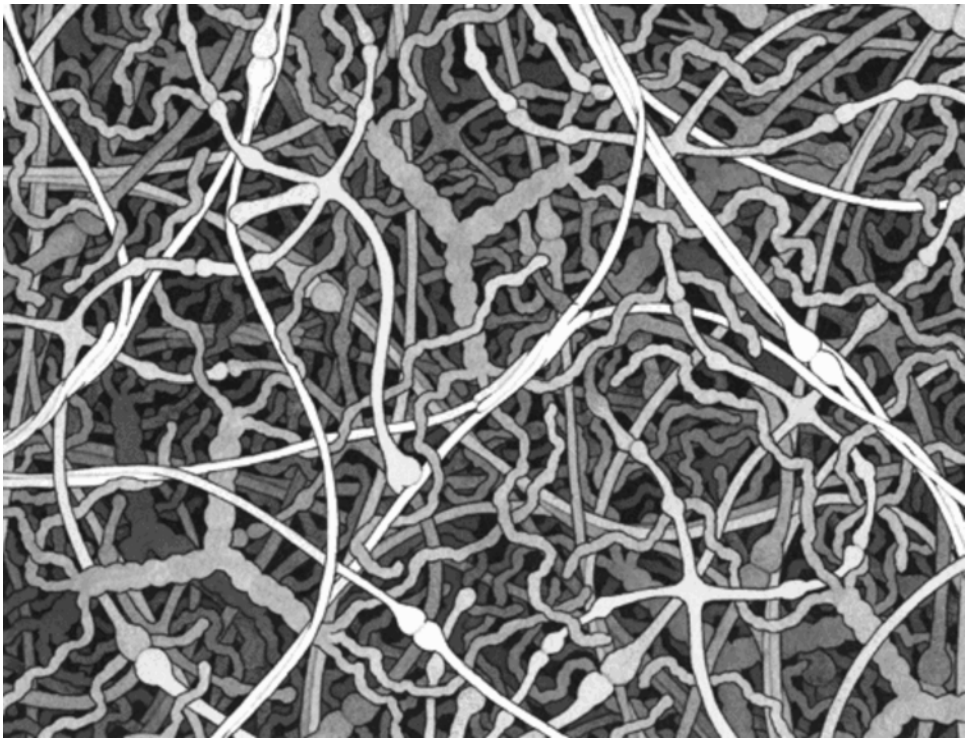


**Figure 10.20**. This illustration depicts a basement membrane, which forms a tough surface that supports the skin and many organs. Type IV collagen forms the structural basis of this membrane. Type IV collagen has a globular head at one end and an extra tail at the other. The heads bind strongly together, head-to-head, and four collagen molecules associate together through their tails, forming an X-shaped complex. Using these two types of interactions, type IV collagen forms an extended network, shown here as the structures in the lightest shade of gray. Other molecules, like the cross-shaped laminin and long, snaky proteoglycans, fill in the spaces, forming a dense sheet. Illustration by David S. Goodsell, the Scripps Research Institute, with permission.

The organization of fibrous collagen in a tissue may be visualized using polarized light. Many connective tissues are birefringent, that is, they have two refractive indices when examined under polarizing optics, owing to the ordered arrangement of their constituent macromolecules. Highly oriented structures allow light to pass in one plane of polarization more rapidly than light in a perpendicular plane, and comparisons of the slow and fast waves reveal details of the organization of the object. Practically, the slow and fast waves are detected by differences in light intensity and/or color and in black-and-white photomicrographs obviously only as levels of light intensity. The observed intensity of any birefringent object is dependent on the geometric relationship between the plane of the incident polarized light and the object itself. Accordingly, the birefringence pattern of an oriented material in a polarizing microscope changes with changes in positioning of the specimen. In bone, for example, the collagen fibrils

are organized into layers within which all fibrils course in the same direction. Adjacent layers of fibrils are ordered in different directions, thereby causing a change in the relative birefringence of the layers (Figure 10.21). This alternating pattern of fibril orientation provides increased strength for bony tissues, and the orientation of the fibrils is thought to be related to the stresses to which the bone is subjected. Collagen fibrils of cartilage are less oriented than those of bone, whereas the collagen fibrils of ligaments are highly ordered (Figure 10.21). Skin is also comprised of interlacing bundles of collagen fibrils, but in a less structured pattern than those of bone (Figures 10.20 and 10.21) since the forces on skin are much more random than forces on bone.

The different patterns of type I collagen-rich tissues are apparent from a comparison of skin, intervertebral disc, and tendon (Figure 10.22). In skin the collagen fibrils form a wickerwork of interlacing bundles, whereas in the annulus fibers of the intervertebral disc they are present in broad sheets in which the orientations of the collagen fibrils in adjacent sheets are in different directions (Figure 10.22). In tendons there is an unusual periodic change in the polarization pattern of the bundles of collagen, which has been explained by a planar crimp of the collagen fibrils along the tendon axis (Figure 10.22). This pattern allows for extension of tendinous structures without actual extension of the collagen fibril, thereby serving to absorb impact tensile loads without generating large amounts of heat, an important biomechanical function of tendons.

The collagen molecule is the basic structural element of many tissues. In §10.10 the use of collagen molecule to form the structure of tendon will be described.

**Problem**

10.7.1. What is the "vitreous humor?"

## 10.8. COLLAGEN STRUCTURAL HIERARCHY

There are six distinctive structural levels in a tendon (Baer et al., 1992). The first level is the collagen molecule described in §10.4; the sixth level is the tendon itself. In between, in ascending order are the microfibrils, the fibrils, the fibers, and the fascicles. These six structural levels are illustrated in Figures 1.12 and 10.27 and discussed below in ascending order.

Five collagen molecules are in vivo wound together into a left-handed super-superhelix by electrostatic forces to form a microfibril (Figure 10.23a). Recall that a superhelix is a helix of a structure that is itself a helix of opposite handedness, and thus a super-superhelix is a helix of a structure with opposite handedness that is itself a helix of a structure with the original handedness. There are discrete gaps between the ends of the collagen molecules as shown in Figures 10.23a,b and 10.24. These figures show a high degree of order in the collagen molecules in the axial direction of a microfibril. On electron microradiographs collagen fibrils have a distinctive cross-striation with an apparent periodicity of 67 nm (Figures 10.24–10.26). This period of dimension length is denoted by the letter D and is used as a primary reference scale in describing structural levels. The true period is 5 D (Woodhead-Galloway, 1980). The helical length of a collagen molecule is 4.4 D or approximately 291 nm, and the discrete gaps are 0.66 D or approximately 44 nm (some references give this as 35 nm) between two consecutive collagen molecules in a strand. At a gap there are only four collagen molecules in the strand, and the molecules tend to kink to fill the space uniformly as illustrated in Figure 10.23c. The actual gap is 0.6 D. In bone these gaps are the sites of nucleation for crystals of hydroxyapatite (the mineral component of bone tissue) to be deposited. The diameter of the microfibril is about 3.5

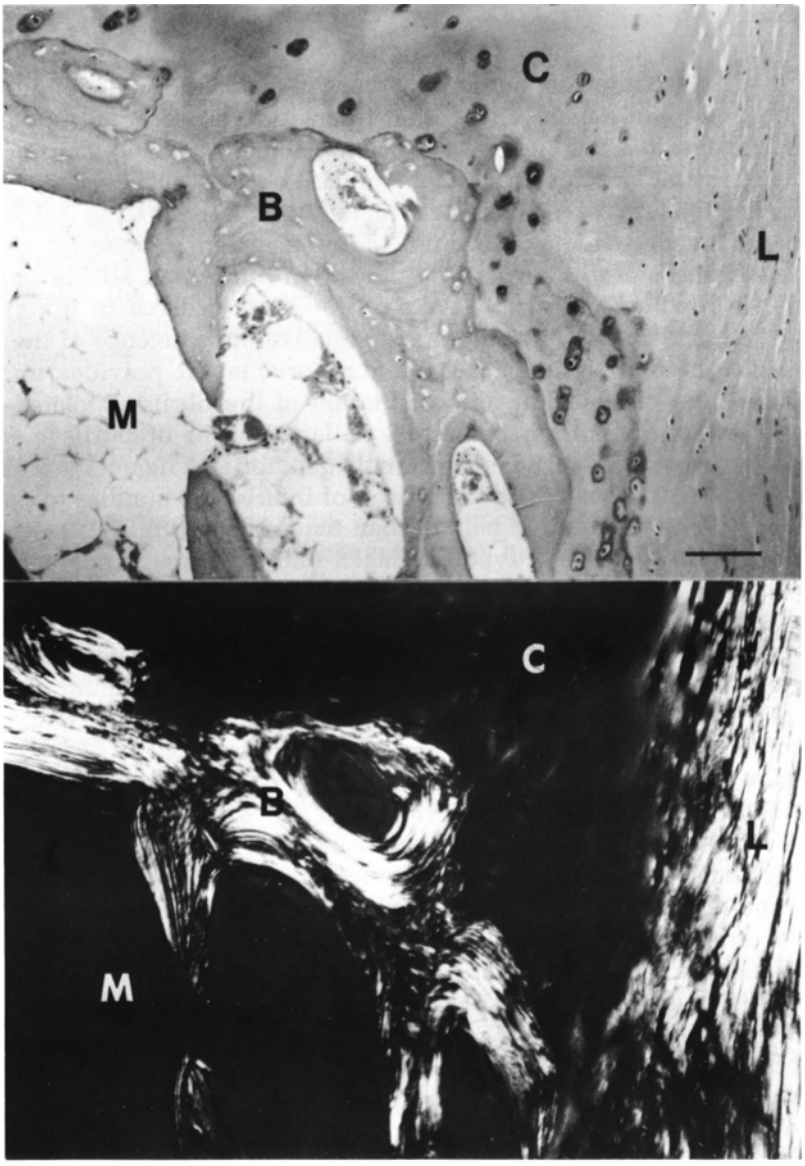



**Figure 10.21**. The upper micrograph is from the edge of a finger joint and illustrates cartilage (C), bone (B), bone marrow (M), and ligament (L). The differences in the underlying organization of the matrices of these tissues are not readily apparent in standard microscopic preparations, but if the same specimen is viewed between crossed polarizers, as illustrated in the lower micrograph, marked differences in the organization of the matrices in the cartilage, bone, and ligament are obvious. The ligament consists of bundles of collagen fibrils whose axes are generally in one direction, imparting to it strong birefringence. The cartilage, by contrast, contains few oriented fibrils and thus little birefringence; accordingly, this region of the section appears dark in the lower micrograph. The bone reveals a layered structure organized in sheets in both flat and circular configurations in which some regions appear very bright and others not. Simply turning the specimen in the microscope indicates that the dark areas in the bone are so only because of their angle with respect to the incident polarized light. On the other hand, the cartilage, being relatively non-birefringent, is dark at all sample positions. Both 112X, bar = 100 μm. Reprinted with permission from Trelstad and Hayashi (1979).



**Figure 10.22**. Light micrographs from skin (top), annulus fibers from the intervertebral disc (middle), and tendon (bottom) viewed in a polarizing microscope at the same magnification. Each tissue illustrates a difference in the orientation of the component fibrils, their width, and their geometric distribution. The skin type I collagen fibrils are organized into a wickerwork or cable-like structure. The type I collagen fibrils in the intervertebral disc (middle) are organized as sheets within which the collagen fibrils all course in the same direction (arrows) and between which there is a shift in orientation. The type I collagen fibrils in the tendon (bottom) are oriented in a general sense along one axis, but the fibril contains a regular crimp such that the birefringence alternates. The crimp is best explained by the collagen fibrils being distributed in a standing planar wave. All ×380, bar = 25 μm. Reprinted with permission from Trelstad and Silver (1981).

to 4 nm and its length is unknown. The microfibril is held together mainly by hydrophobic interactions and has very low mechanical strength by itself. The strength and stability during maturation of the microfibrils are achieved by the development of intermolecular crosslinks.

Microfibrils are wound together to make a fibril in a right-handed super-super-superhelix with a pitch of about 1090 nm. The resulting fibrils have a diameter of 30–150 nm and show

on electron micrographs the cross-striation with the apparent periodicity D characteristic of the fiber-forming collagens (Figures 10.24 and 10.25). In rat tail tendons, fibrils range in diameter from about 40 nm to perhaps 300 nm, with a few lying outside these limits. It is not known how fibril size is controlled; one possibility is that the amount of sugar in the collagen controls fibril diameters — the more sugar, the smaller the diameter. (Recall that collagen is a glycoprotein, i.e., a protein with associated sugars). The strength of fibrils is due, in part, to crosslinks that form between collagen molecules. These crosslinks are also associated with aggregation at the fibril level. However, all of the mechanisms holding fibrils together are not known.

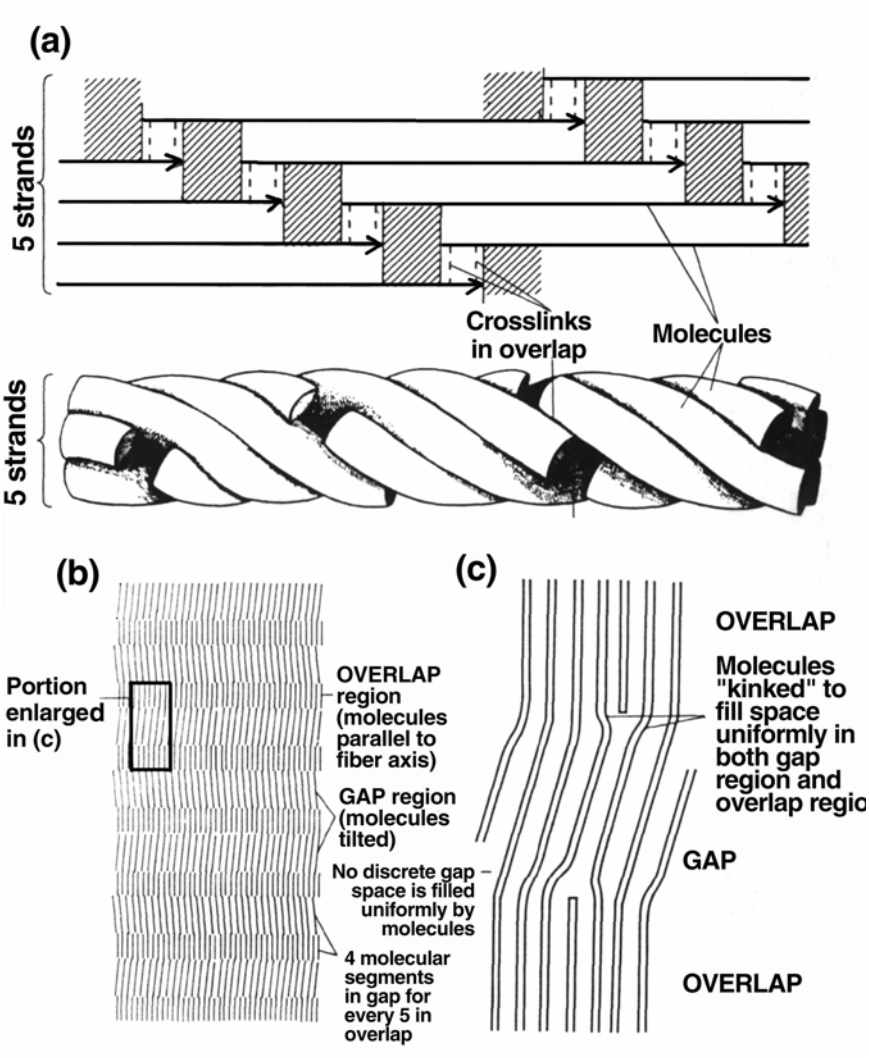



**Figure 10.23**. (a) Illustration of the five-stranded microfibril model (b). Schematic sketch of the liquid-crystal model. (c) Small part of (b) greatly enlarged, to show that the molecules are really continuous but kinked at the gap-overlap junction. It also demonstrates the reason for the difference in density between gap and overlap regions. Compare this drawing with that of Figure 10.24. Reprinted with permission from Woodhead-Galloway (1980).

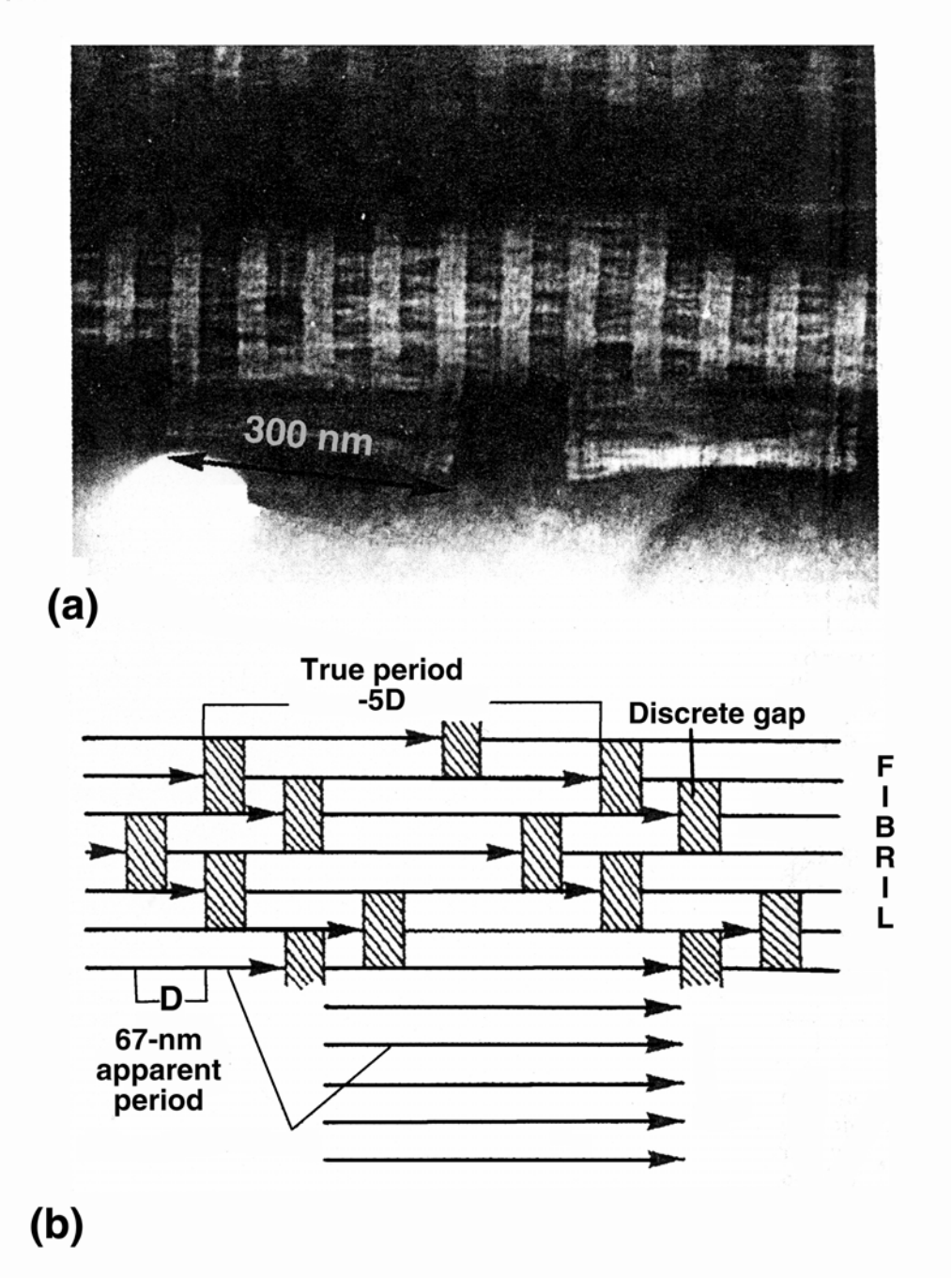



**Figure 10.24**. (a) Collagen molecules grown on native fibrils. A molecule can be seen to run through four gaps and five overlap regions. Thus the molecular length (*L*) is approximately equal to 4.4D. (b) Diagram of the composite structure of (a) showing the relationships among the molecules. Any two molecules are related by an axial displacement of an integral multiple of D, the apparent axial period. Modified with permission from Woodhead-Galloway (1980).

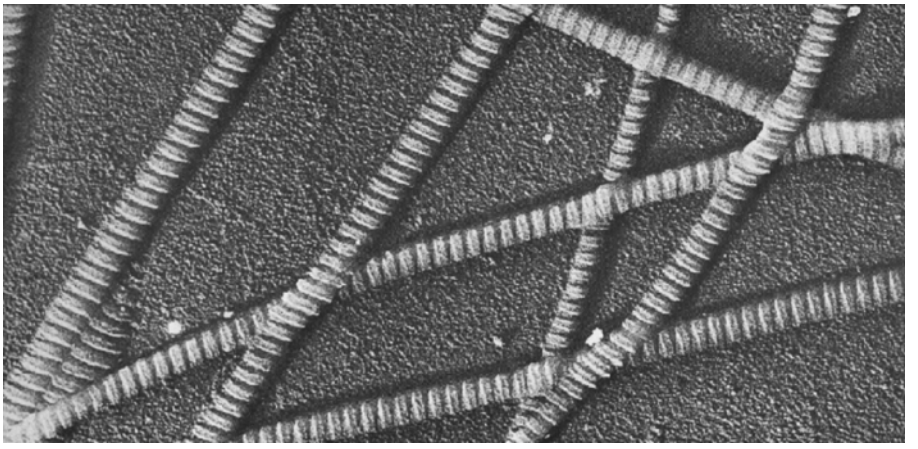


**Figure 10.25**. Collagen fibrils. Note the characteristic "railroad track" appearance of these fibrils.

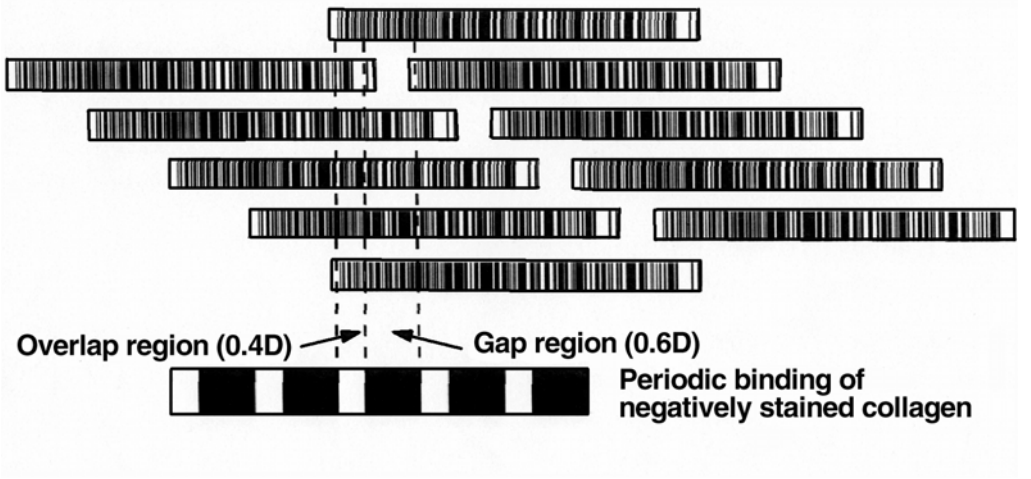



**Figure 10.26**. Diagram of quarter stagger packing pattern of type I collagen molecules in tendon. Neighboring collagen molecules, represented by a series of light and dark bands as shown in Figure 10.13, are shown staggered with respect to their nearest neighbors. In tendon, collagen molecules are staggered by a distance D after they are self-assembled into fibrils in tissues. When collagen is stained negatively and then viewed in the electron microscope, a series of light and dark bands are observed across the axis of the fibril which result from the stain penetrating only the hole region and not the molecule (light-dark repeat shown at bottom of figure). The distance D in tendon is 67 nm and is made up of a hole region of about 0.6D and an overlap region of about 0.4D. The D period is the characteristic fingerprint of fibrous collagen. When collagen is stained with heavy metals and viewed in the electron microscope, the D period is observed from either the light-dark repeat (negative staining pattern) seen or by the repeat of 12 bands (bands b2 through c1 at top of figure) by positive staining. In positive staining the stain penetrates into the molecule. The positive staining pattern arises when the stains bind directly to the charged amino acid residues on the molecule. Note that proteoglycans are observed bound to the d and e bands in the positive staining pattern. Reprinted with permission from Silver et al. (2003).

The hierarchical structure of the tendon is shown in Figure 10.27, the transverse cross-section is shown in Figures 10.28 and 10.29, and the longitudinal cross-section is shown in Figure 10.30. In the transverse cross-section, note the fine lines that separate fiber bundles and the numerous fibroblast nuclei. In the longitudinal cross-section, note the wavy fibroblasts that

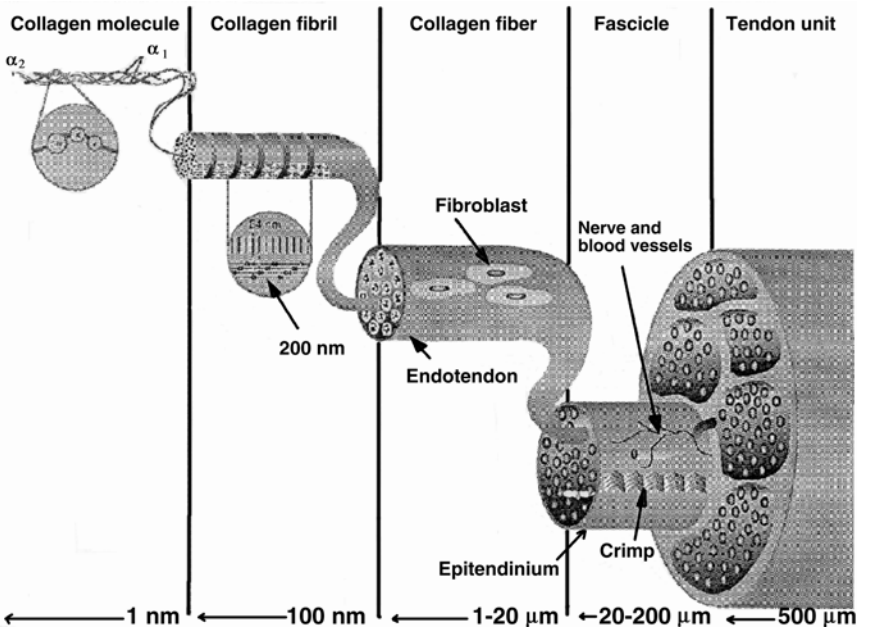



**Figure 10.27**. Hierarchical structure of the tendon. Diagram illustrating the relationship between collagen molecules, fibrils, fibers, fascicles, and tendon units. Although the diagram does not show fibril subunits, collagen fibrils appear to be self-assembled from intermediates that may be integrated within the fibril. Reprinted with permission from Silver et al. (2003).

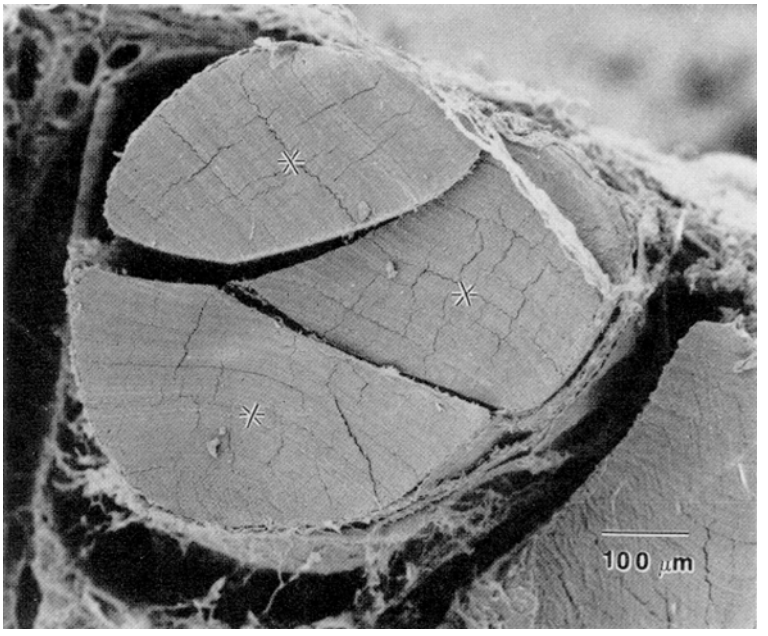



**Figure 10.28**. Scanning electron micrograph of rat tail tendon showing fascicle units (asterisk) that make up the tendon. Reprinted with permission from Freeman and Seehra (2003).

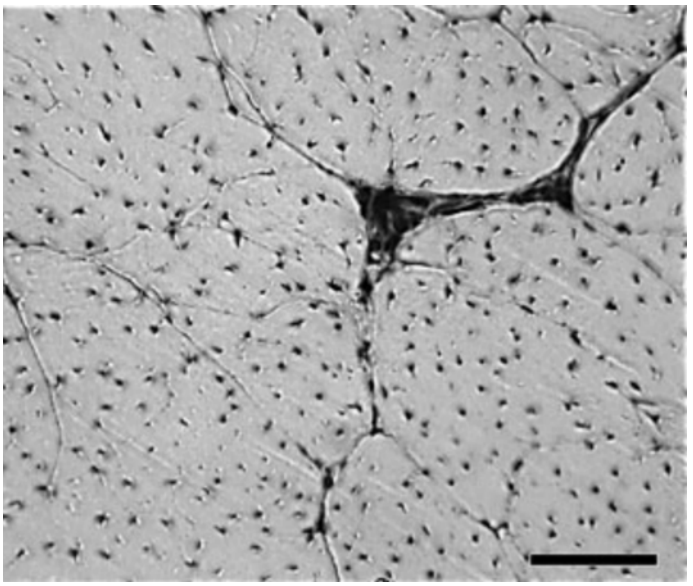


**Figure 10.29**. Tendon cross-section; collagen fibers make up the lighter background. The fine lines separate fiber bundles; numerous fibroblast nuclei can be seen. Bar = 50 μm. Reprinted with permission from the Jay Doc HistoWeb, Milton Wolf and Marc Scarbrough, Department of Anatomy and Cell Biology University of Kansas Medical Center. http://www.kumc.edu/instruction/medicine/anatomy/histoweb/ct/Histoct.htm.

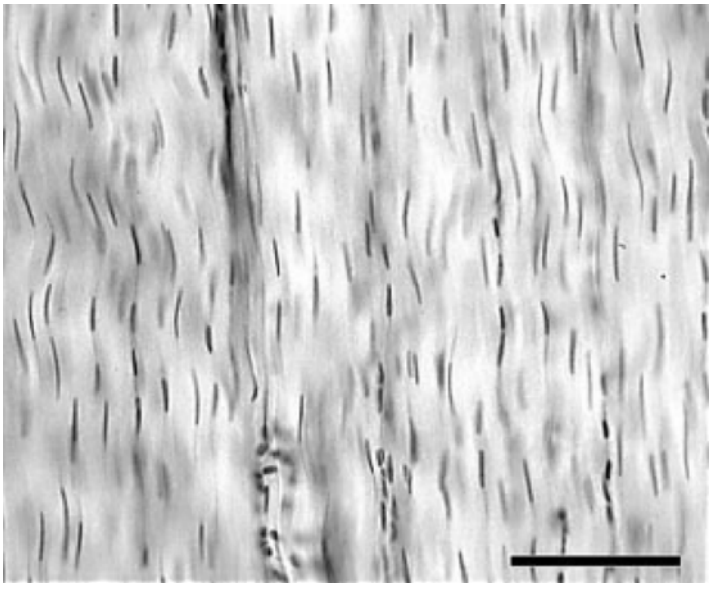


**Figure 10.30**. Tendon, longitudinal cross-section, showing wavy fibroblasts run along the tendon. Recall that the collagen and elastic fibers of the tendon are extracellular. Bar = 100 μm. Reprinted with permission from the Jay Doc HistoWeb, Milton Wolf and Marc Scarbrough, Department of Anatomy and Cell Biology University of Kansas Medical Center. http://www.kumc.edu/instruction/medicine/anatomy/histoweb/ct/Histoct.htm.

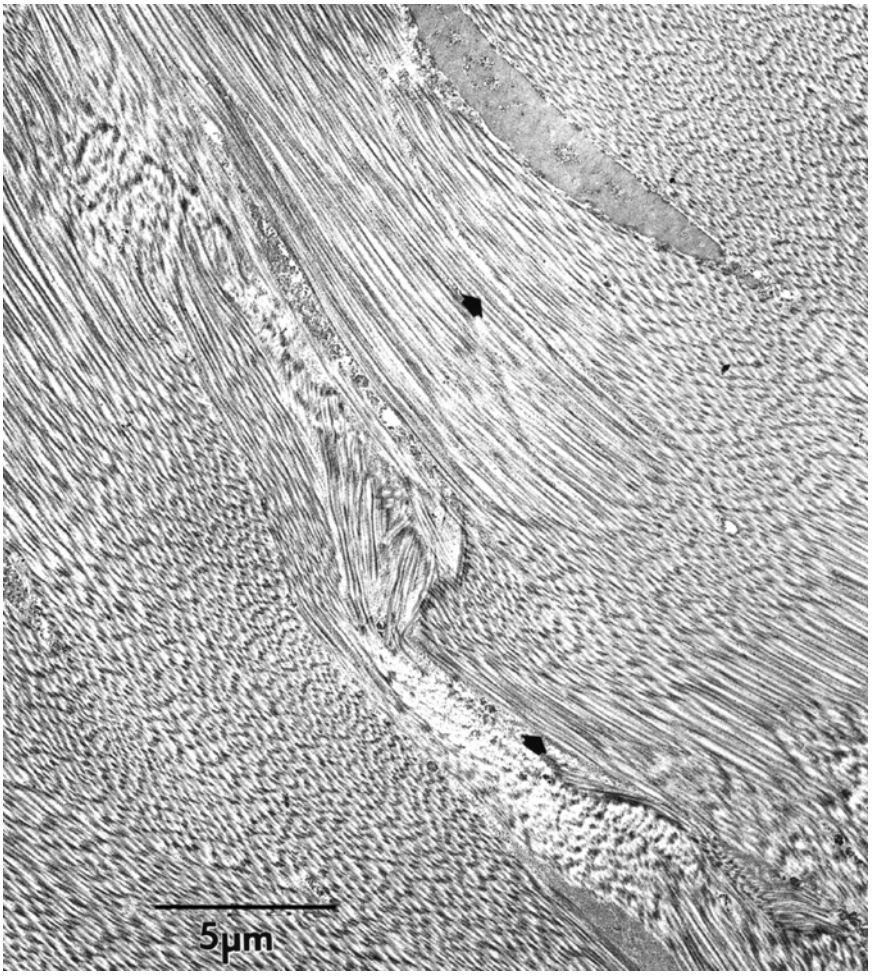



**Figure 10.31**. This electron micrograph demonstrates the orientation of collagen fibrils within a tendon. It often happens that the fibrils form in a "wavy" pattern so that in thin sections such as this the fibrils come into and out of the plane of section even though their general orientation is longitudinal to the long axis of the tissue. The striated pattern of individual fibrils (arrows) can be seen in the most longitudinal fibrils. Magnification: 7,800X.

run along the tendon. This wavy pattern is also illustrated in Figure 10.31, where the fibrils are seen to form in a "wavy" pattern, so that in thin sections such as this the fibrils come into and out of the plane of section even though their general orientation is longitudinal to the long axis of the tissue.

The fiber is composed of fibrils packed tightly together and is the smallest unit seen in light microscopy, having a diameter of 1–10 μm. Fascicles are composed of fibers. The fibers are assembled into primary and secondary bundles or fascicles and then into a tendon or ligament. On these hierarchical levels there is an undulating waviness or crimping (Figures 10.23 and 10.31) in the structure. The shape of this periodic form is sometimes described as sinusoidal and sometimes as zigzags. This undulation does not occur in bone collagen that is often subjected to compressive forces, but it occurs in tissues that are subjected to tensile forces such as the tendon, vertebrate skin, and heart pericardium. A very interesting feature of the organi-

zation of the subunits in tendons and ligaments is that there is no lateral coupling between fascicles. Fascicles can slide freely past each other, which is convenient from a mechanical point of view.

On fascicles and other higher-level structures in this hierarchy there are membranes or sheaths covering the structure (Figure 1.12). There is the composition of a textile or fabric to these sheaths, but not that of a woven fabric. The fiber arrangement is that of orthogonal crossings, and the fibers increase in dimension with the increase in the size of the structure the sheath surrounds.

## 10.9. SUPRAMOLECULAR ASSEMBLY

The question of supramolecular assembly is not on the same firm ground as molecular self-assembly; however, the ideas involved are ones of deep engineering interest and have a great deal of future potential. The idea is equivalent to self-assembly at a higher structural level. The concept is a useful working hypothesis for individual stages in the construction of supramolecular structures. For connective tissue a plausible but unproven analogy for supramolecular assembly is the liquid crystal analog. The term “liquid crystal” should initially strike one as an oxymoron; a crystal is a well-ordered solid characterized by regular stacking in a three-dimensional lattice with strong attractive forces holding it together, and a liquid has little obvious structure as it takes the shape of its container and changes shape with the changing shape of the container it occupies. A liquid crystal is a mesomorphic state (intermediate form) between a crystal and a liquid. Some organic materials do not show a single transition from solid to crystal but have a series of intermediate transitions involving new phases including the liquid crystal phase. In their defined range of temperature and concentration, liquid crystals are rodlike molecules oriented in one, two, or three dimensions. Their orientation is sometimes controllable by electromagnetic fields, and this has led to one liquid crystal (methoxybenzylidenebutylaniline) being used extensively in liquid crystal displays (LCDs).

Liquid crystals are classified as smectic, nematic, or cholesteric. Rods that lie parallel to one another in layers of equal thickness (Figure 10.32) characterize smectic liquid crystals. Smectic liquid crystals have the highest degree of order. Nematic liquid crystals are also characterized by rods that lie parallel to one another, but the layered structure of the smectic does not exist (Figure 10.32) and the nematic have the lowest degree of order. The ordering is purely orientational and the distribution of the rods in the direction of the rod axis is random. Cholesteric liquid crystals lie parallel to one another in each plane, but each plane is rotated by a constant angle from the next plane of crystals (Figures 10.33 and 10.34). The cholesteric is a chiral form of the nematic phase, chiral describing a structural characteristic of a molecule that prevents it from being superposed upon its mirror image.

The philosopher Goethe considered the problem of organization of structure in plants and animals, and he endorsed the idea of an analogy between the structure of a tissue and crystal growth, an idea afoot in his century and the previous one. When liquid crystals were discovered in 1888, they quickly became strong candidates for the mechanism by which nature forms living structures from homogeneous multi-chemical soups. This is because liquid crystals display a “striking form of self-organization in which directional order appears spontaneously in a homogeneous liquid, not incrementally, as in the growth of the familiar crystals layer by layer at the surface, but simultaneously throughout a substantial volume” (Mackay, 1999).

The terms "biological analogs of liquid crystals" and "pseudomorphoses" are used to describe those biological systems that appear to obey liquid crystalline geometries but have lost their liquid character. Generally these materials have a microstructure characterized by long

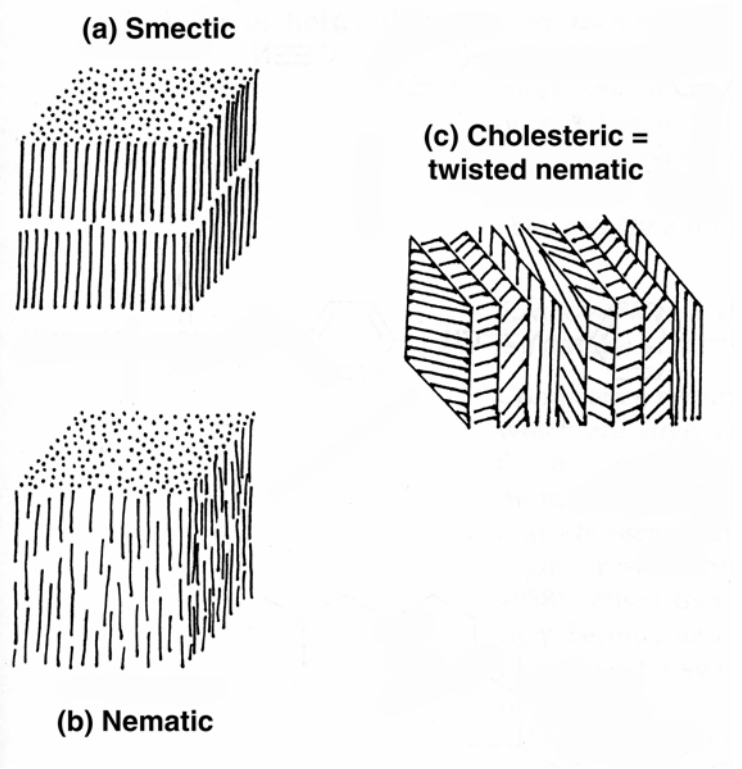



**Figure 10.32**. Structure of liquid crystals made of rod-like structures such as molecules, microfibrils, or fibrils. Smectic liquid crystals are characterized by rods that lie parallel to one another in layers of equal thickness; they diffuse freely within the layers but not between the layers. Nematic liquid crystals are also characterized by rods that lie parallel to one another, but the layered structure of the smectic does not exist. The ordering is purely orientational and the distribution of the rods in the direction of the rod axis is random. Cholesteric liquid crystals lie parallel to one another in each plane, but each plane is rotated by a constant angle from the next plane of crystals. Redrawn with permission from Neville (1993).

thin rods, such as the fibrils in collagen; microstructures of this type generally show birefringence in polarized light. It is possible that the formation mechanisms that occur in collagenous tissues, the mechanisms that form microfibrils and fibrils from collagen molecules, have analogs in the self-organizational processes that occur in liquid crystals. Other examples of birefringent biological materials that can be genuine liquids are biological membranes and certain gland secretions. Non-fluid analogues are cell walls and skeletal structures of plants and animals. The fibrillar material is aligned in a way geometrically similar to the arrangement of molecules in cholesteric liquid crystals; however, the length of the polymer, its crystallization, and the presence of crosslinks destroy the liquid character that must exist following the initial secretion of the organic components by the cells. The state of a forming or re-forming tissue is called here the *morphosis state*, and it is thought to have the characteristics of both a solid and a fluid state, enough fluidity for a structure to self-assemble and enough solidity to maintain the load-carrying capacity of the structure that is reforming. A morphosis state of a tissue is thought to exist during morphogenesis and during the process of tissue remodeling. In the case of bone, a morphosis state probably exists at some time during the formation of a secondary osteon and during the process of tooth movement.

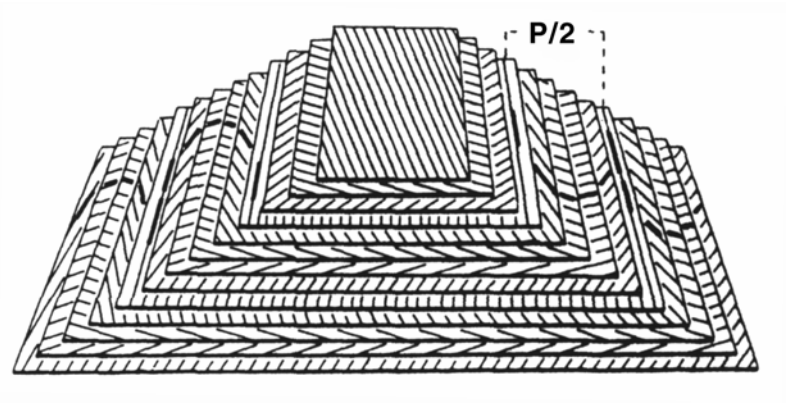



**Figure 10.33**. The twisted plywood model. The long axes of the molecules in each layer are rotated by a discrete angle from the long axes of the molecules in the layer above and in the layer below. Superposed series of nested arcs are visible on the sides of the stepped pyramid due to regular variations in the directions of the long axes of the molecules. Reprinted with permission from Giraud-Guille (1996).

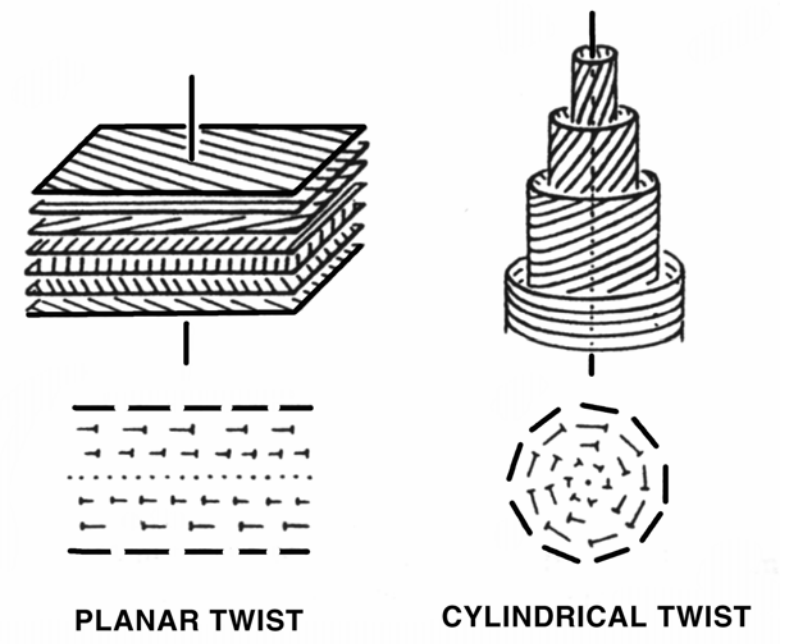



**Figure 10.34**. (a) In a planar twist, equidistant straight lines are drawn on horizontal planes, and the direction of the lines rotates regularly from plane to plane. (a') In the conventional notation for a cholesteric geometry applied to a planar twist, lines represent molecules longitudinal to the drawing plane and dots represent molecules perpendicular to it; molecules in oblique position are represented by nails whose points are directed toward the observer. (b) In a cylindrical twist, equidistant helices are drawn on a series of coaxial cylinders, and the angle of the helices rotates regularly from one cylinder to the next. (b') Conventional representation of a cholesteric geometry applied to a cylindrical twist. Reprinted with permission from Giraud-Guille (1996).

The "twisted plywood model" shown in Figure 10.33 is a model of the organization of molecules in a cholesteric structure. This model explains how typical series of arcing patterns observed in sections of cells and tissues result not from authentic curved filaments but originate from the successive molecular orientations found in the twisted plywood arrangement. The model is constructed as follows. The molecular directions are represented by parallel and equidistant straight lines on a series of rectangles, with the orientation of the lines rotating from one rectangle to the next by a small and constant angle. A periodicity is visible wherein each 180º rotation of the molecular directions corresponds to the half-cholesteric pitch $P/2$. The rotation is chosen to be left-handed, as has been found in most biological twisted materials studied so far (sugars are right-handed). A cholesteric axis is defined by the left-hand rule, the closed fist of the left hand indicating the progressive direction of twist and the extended thumb of the left hand pointing in the positive direction of the cholesteric axis. Directly visible on the oblique sides of the pyramid are what appear to be superposed series of parallel nested arcs. The concavities of the arcs are reversed on opposite sides of the model. In biological systems this particular geometry has often been described as a twisted plywood, but other terms, mentioned below, are also employed.

Two major types of twists are found in liquid crystals and their biological analogs, and are defined by the disposition of the fibrillar elements either in parallel planes (planar twist) or coaxial cylinders (cylindrical twist) (Figure 10.34). The coaxial cylinders or cylindrical twist are also described as helicoidal, a term that will be employed here. Collagen in the secondary osteons of bone tissue is observed to be in a helicoidal pattern. The developments of typical liquid crystal patterns have been associated with flowing liquid crystals. The assembly of collagen molecules in typical liquid crystalline phases in highly concentrated solutions after sonication for several weeks has been reported (Giraud-Guille, 1992, 1996). In this work it was shown that intact 300-nm long collagen molecules form cholesteric liquid crystalline domains. Sonication does not alter the triple-helical structure of the collagen fragments.

The origin of the cholesteric twist is thought to be a geometric effect. Under sonication or Brownian motion, in the morphosis state, the spontaneous alignment of elongated molecules at high concentration originates mainly from steric constraints involving the spatial configuration of the molecules. The rod-shaped molecules do not interpenetrate, and the excluded volume is reduced when the molecules lie parallel; consider a stack of forks. At high concentrations geometric factors associated with the chirality of the molecules govern the change in orientation between layers. A constant characteristic of biological polymers forming cholesteric liquid crystals is that they consist of layered helicoids. The contact between the layered helicoidal domains of assemblies of asymmetric molecules determines the orientation of one layer to its neighbor. To minimize steric hindrance, helical polymers are first aligned in layers, thus gaining maximum space. Each layer creates parallel and equidistant grooves, oblique to the helical axis, where a second layer of molecules can be deposited (Figure 10.35). This oblique packing generates a twisted plywood system over successive layers.

## 10.10. ASSEMBLY OF A TENDON

The purpose of this section is to describe what is both known and conjectured about the mechanisms used to form a tendon from collagen molecules in vivo. Recall that a tendon connects a muscle end to bone. It is clear from the fact that animals generally mature in repeatable fashion that a tendon must grow in length so as to maintain its connection to both bone and muscle during the maturation process. It must also grow in cross-sectional area so that it can transmit increasingly greater forces between muscle and bone during the maturation process.

In previous sections the production of the collagen molecule by the cell has been described (§10.4), how the structure of the collagen molecule was deduced (§10.5), as well as the structural hierarchy of the collagen fibrils (§10.8) and tendon (§1.5). In the previous section one proposal for the supramolecular assembly of collagen was described. In this section both in vivo and in vitro supramolecular assembly are described, starting with in vivo supramolecular assembly. The material that follows is a summary taken from Silver et al. (2003), where original citations for the work described are given.

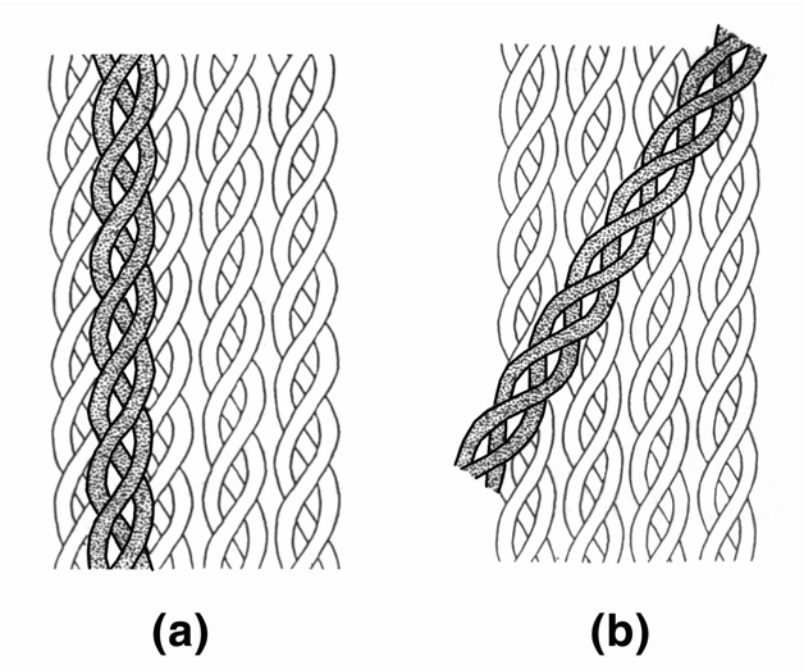



**Figure 10.35**. Possible relation between molecular conformation and angular rotation in collagen helicoids suggested by Neville. Collagen chains entwine to form triple helices (see Figure 1.12). If these pack in a sheet with a stagger (out of register), they create a system of lined-up grooves. The next sheet of triple helices may then adopt either of two possible stable positions. These are (a) in parallel with the initial layer in the grooves between triple helices or (b) in the grooves lying at an angle across the initial layer. The position shown in panel b could give the angular rotation required to generate a helicoid. The sense of twist changes from triple helix to helicoid, because the different levels in the hierarchy then pack together in a more stable manner. Reprinted with permission from Neville (1993).

In vivo supramolecular assembly can be accomplished using only the properties of the proteins, as will be described in the paragraph, and with the supervision and aid of the fibroblast, as will be described in subsequent paragraphs. The fundamental structural element in tendon is type I collagen in the form of fibrils. Recall the structure of the procollagen molecule (Figures 10.8 and 10.12) and the convention for the designation of the order of amino acids is that the amino group or N-terminal end is to the left and the carboxyl group or C-terminal end is to the right. This orientation from N to C, illustrated in Figures 10.8 and 10.12, is a primary structural feature of significance in the assembly of procollagen/collagen molecules into crosslinked fibrils. The presence of amino- (N) and carboxylic-terminal (C) extensions on the collagen molecule have been shown to limit self-assembly of procollagen to about 5 mole-

cules. Removal of the N- and C-propeptides by specific proteinases occurs prior to final fibril assembly. The C-propeptides are essential for both initiation of procollagen molecular assembly from the constituent chains and lateral assembly of procollagen molecules. There is a relationship between the attachment of N-propeptides to fibrils and the diameter of the fibrils. Studies suggest that fibrils to which the N-propeptides remain attached are limited to diameters in the range 20–30 nm, but when the N-propeptide is cleaved the fibril diameters appear to increase. This observation suggests that the N-propeptide is associated with initiation of fibrillogenesis. There are other studies that suggest that the presence of the N-propeptide on the fibril surfaces prevents tight packing of the collagen fibrils and results in fragility. Partial cleavage of the N-propeptide allows the N-propeptide to become incorporated within the body of the fibrils. This finding led to the proposal that the type 1 procollagen N-propeptides facilitate the fusion of small diameter fibrils.

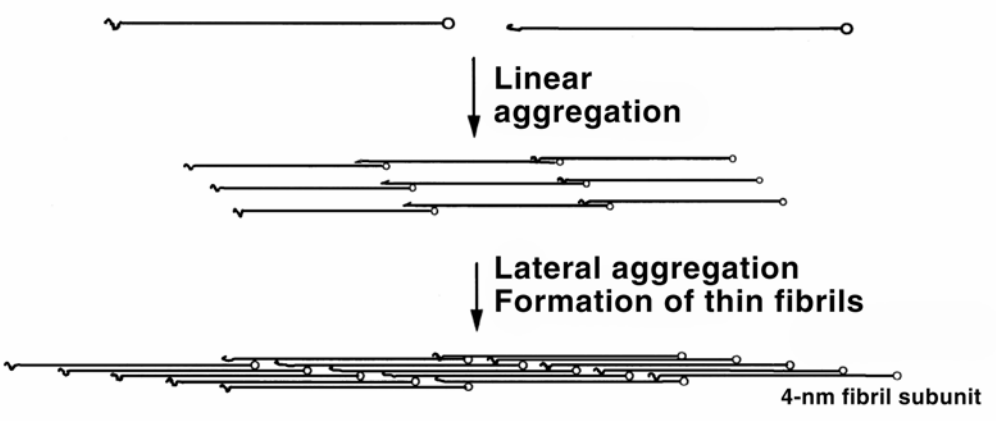



**Figure 10.36**. Diagram showing role of N- and C-propeptides in collagen self-assembly. The procollagen molecule is represented by a straight line with bent (N-propeptide) and circular (C-propeptide) regions. Initial linear and lateral aggregation is promoted by the presence of both N- and C-propeptides. In the presence of both propeptides, lateral assembly is limited and fibrils are narrow. Removal of the N-propeptide results in lateral assembly of narrow fibrils; removal of C-propeptide results in additional lateral growth of fibrils. As indicated in the diagram, the presence of N- and C- propeptides physically interferes with fibril formation. Reprinted with permission from Silver et al. (2003).

The C-propeptide of fibril-forming collagens appears to regulate later steps in the assembly of procollagen into fibrils; it is removed from small-diameter fibrils during growth, possibly during fibril fusion. The C-propeptide has been observed in fibrils with diameters between 30 and 100 nm, suggesting that it is involved in initiation and lateral growth of fibrils (Figures 10.36 and 10.37).

The studies of this process to be described in this and later paragraphs were done on developing chick embryos. The day-by-day development of a hatching chick is shown in Figure 10.38. Procollagen and the intermediates pN-collagen (containing the N-propeptide) and pC-collagen (containing the C-propeptide) are present in developing chick tendon up to 18 days embryonic. Collagen oligomers isolated from developing chick tendons include 4D staggered dimers of collagen molecules, suggesting that this is a preferred molecular interaction for initiation of collagen fibrillogenesis in vivo. About 50% of the fibrils formed in 18-day-old chick embryos are bipolar (molecules run in both directions along the axis of the tendon), while the

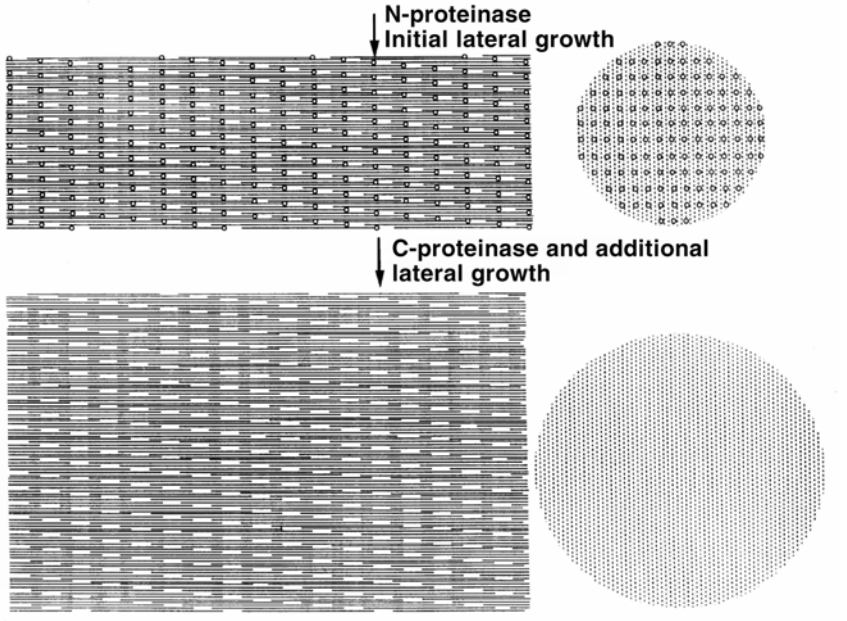



**Figure 10.37**. Continuation of the diagram showing role of N- and C-propeptides in collagen self-assembly. Reprinted with permission from Silver et al. (2003).

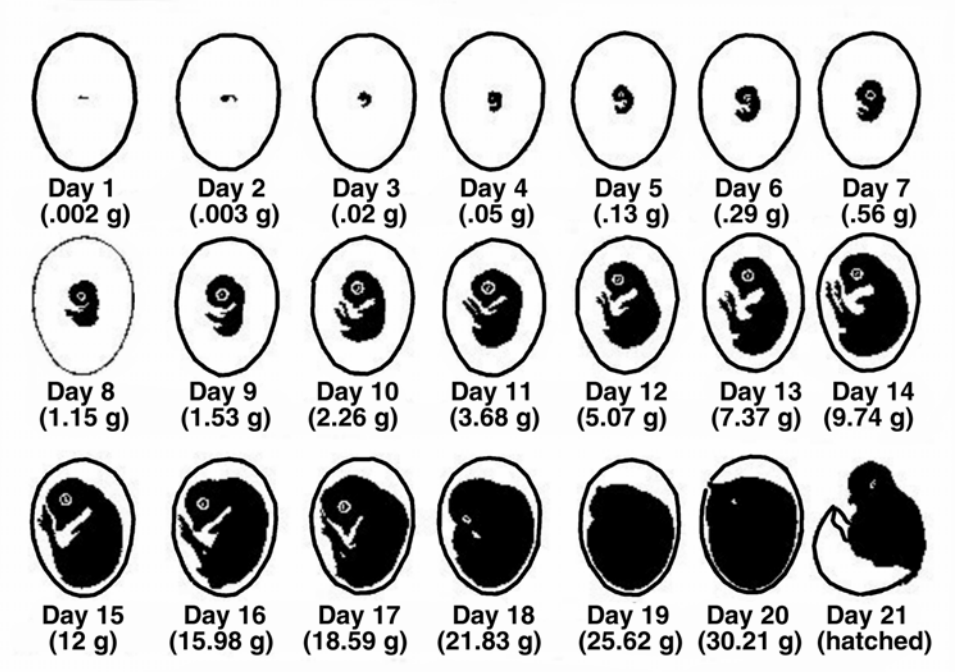



**Figure 10.38**. The day-by-day embryonic development of a hatching chick.

other half are unipolar. Analysis of the staining pattern of fibrils reveals the axial zone of molecular polarity to be highly localized.

During chick tendon development the structure and mechanical properties of tendon change rapidly. The morphology of embryonic development of collagen fibrils in chick tendon has been studied and characterized extensively. Two levels of structural organization of the collagen fibrils seem to occur during development of chick hind limb extensor tendons. Along the axis of the tendon, cytoplasmic processes of one or more axial tendon fibroblasts are observed to direct formation of groups of short collagen fibrils that appear to connect cells together (Figures 10.39 and 10.40). Groups of axial tendon cells are encircled by a second type of fibroblast, a type that forms bundles of collagen fibers. This type of cell encircles groups of collagen fibrils with a sheath that separates fascicles. Initially, axial tendon cells appear at both ends of growing fibrils (Figure 10.39). Once the fibrils begin to elongate they are then packed closely side to side (Figure 10.41). Later a planar crimp is introduced into collagen fibrils, perhaps by the contraction of cells at the ends of the fibrils or by shear stresses introduced by tendon cells between layers of collagen fibrils (Figure 10.42). Results of modeling studies suggest that the molecule and fibril have many points of flexibility where crimp could develop.

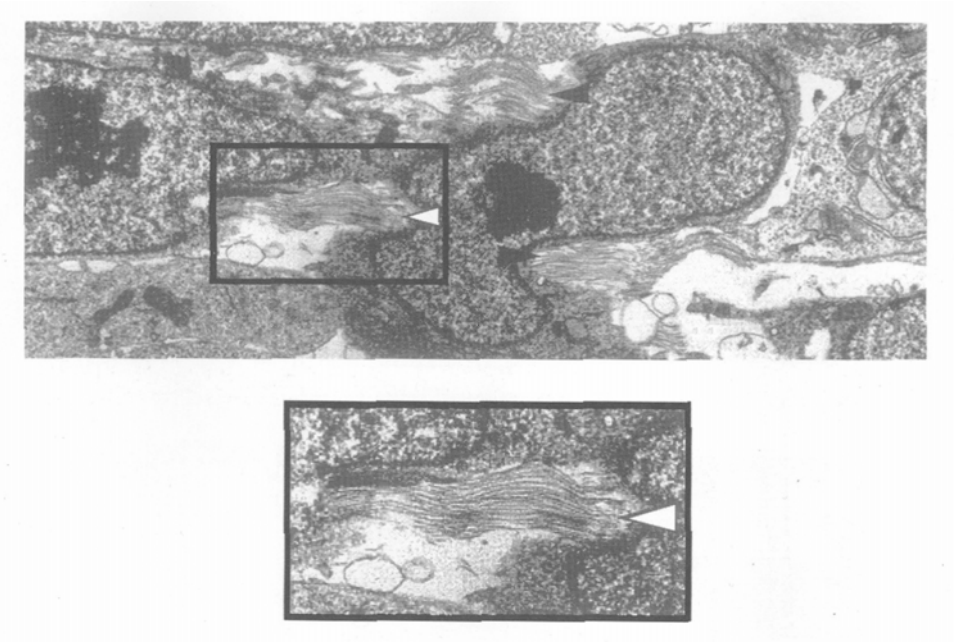


**Figure 10.39**. Directed cellular self-assembly of axial collagen fibrils during chick tendon development. Transmission electron micrograph showing collagen fibrils (see arrow in box) from a 7-day-old chick leg extensor tendon that appear to be connecting two fibroblasts during tendon development. Inset shows a high-magnification view of the collagen fibrils that originate from invaginations in the cell membranes on either side of the fibril. The collagen fibrils shown are about 50 nm in diameter. Reprinted with permission from Silver et al. (2003).

In cross-section, collagen fibers are made up of individual fibrils that appear to be released from invaginations in the cell membrane (Figures 10.14, 10.43, 10.44. and 10.45). Additional collagen diameter growth appears to occur by addition of materials that appear to originate

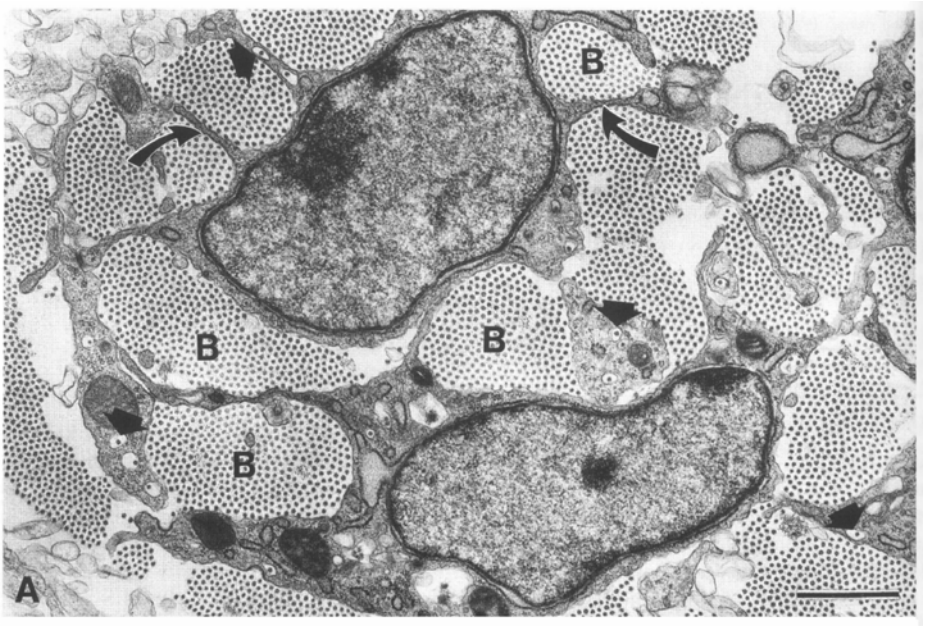



**Figure 10.40**. Fibroblast between the fibers. Tendon, longitudinal cross-section, showing wavy fibroblasts run along the tendon. Recall that the collagen and elastic fibers of the tendon are extracellular. Bar = 100 μm. TEM, 14-d chick embryo: (A) fibril-forming channels (B) bundle-forming compartments. Compartmentalization of the extracellular matrix during tendon development. Transmission electron micrographs illustrating the complexity of the fibroblast surface and the partitioning of the extracellular space with formation of extracellular compartments in tendon A section cut perpendicular to the tendon axis in a 14-d chick embryo (panel A) shows the fibril-forming channels (arrowhead), the bundle forming spaces (B), and the macro aggregate-forming spaces that form as cytoplasmic processes separating bundle-forming compartments retract (curved arrows) and bundles coalesce to form macro aggregates. Bar = 1 m. Reprinted with permission from Birk and Zycband (1994).

inside the Golgi apparatus. Later during lateral growth, these invaginations in the cell membrane disappear, causing lateral fusion of fibrils (Figure 10.46). Macroscopically this results in increases in fibril diameter and length (Figure 10.47).

Collagen fibrils are assembled from fibril ''segments'' in developing chick tendon (Figure 10.48). During development, fibril segments are assembled in extracytoplasmic channels defined by the fibroblast. In 14-day-old chick embryos, tendon fibril segments are deposited as units 10–30 mm in length. These segments can be isolated from tendon and studied by electron microscopy. Fibrils from 12-day-old chick embryos grow in length at constant diameter, and end-to-end fusion requires the C-terminal end of a unipolar fibril. By 18 days, embryonic fibril growth occurs at both fibril ends and is associated with increased diameter. Since fibril segments at 18 days cannot be isolated from developing tendon, it is likely that fibril fusion and crosslinking occur simultaneously.

Fibril segments appear to be intermediates in the formation of mature fibrils and range in length from 7 to 15 mm in 14-day-old embryonic tendon. Between 14 and 17 days the bundles begin to branch and undergo rotation over several micrometers, and the segments increase in length up to 106 mm. A rapid increase in length and diameter is seen between days 16 and 17 and is consistent with the rapid increase in tendon ultimate tensile strength. Although the fibril packing density of collagen does not change prior to and just after birth, the mean collagen

fibril width increases and the cell volume fraction decreases. This is believed to be associated with growth by fibril fusion.

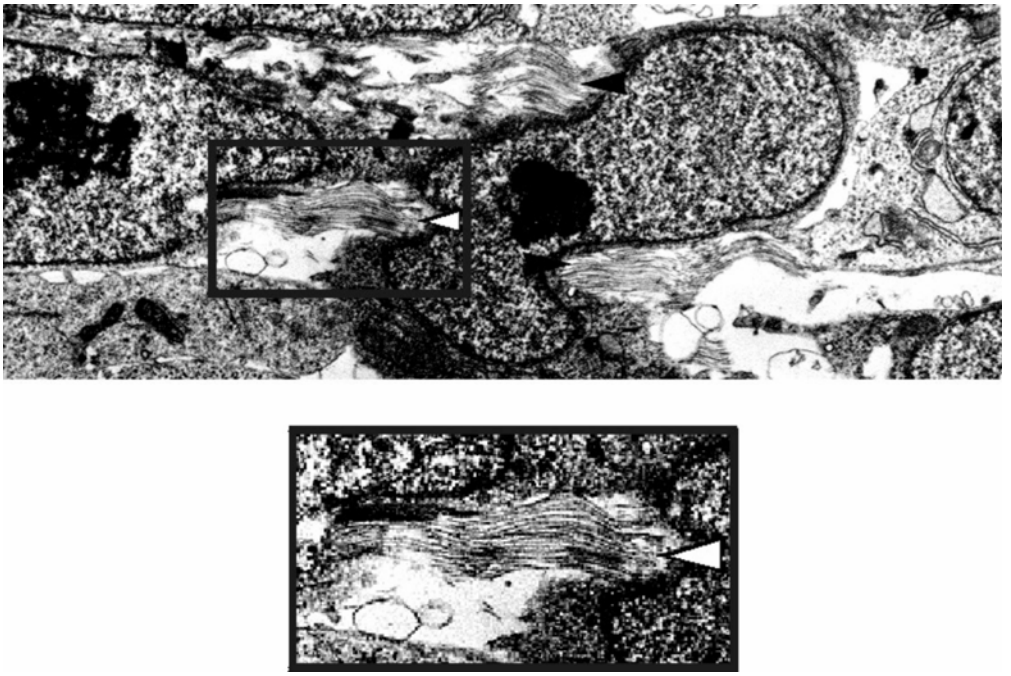


**Figure 10.41**. Lateral condensation of axial collagen fibrils and alignment of tendon fibroblasts. Transmission electron micrograph showing collagen fibrils from a 10-day-old chick leg extensor tendon. Note that the fibrils (see arrow) and fibroblasts appear to be more highly aligned and densely packed compared to the same structures at day 7. Fibrils shown have diameters of about 50 nm. Inset shows a high-magnification view of the relationship between the collagen fibrils and the cell surfaces on either side. Reprinted with permission from Silver et al. (2003).

In mature tendon, collagen fibril bundles (fibers) have diameters between 1 and 300 mm, and fibrils have diameters from 20 to over 280 nm (Figures 10.27 and 10.28). The presence of a crimp pattern in the collagen fibers has been established for rat tail tendon, as well as for patellar tendon and anterior cruciate ligament; the specific geometry of the pattern, however, differs from tissue to tissue. It is not clear that the crimp morphology of tendon is actually present in tendons that are under normal resting muscular forces.

Tendon contains a variety of proteoglycans, including decorin as well as hyaluronan, a high-molecular-weight polysaccharide. Other small leucine-rich proteoglycans like decorin include biglycan, fibromodulin, lumican, epiphycan, and keratocan. Proteoglycans are seen as filaments regularly attached to collagen fibrils in electron micrographs of stained tendons (Figure 10.49). Animal models employing genetic mutations lacking decorin demonstrate collagen fibrils with irregular diameters and decreased skin strength. Downregulation of decorin has been shown to lead to development of collagen fibrils with larger diameters and higher ultimate tensile strengths in ligament scar. These observations suggest that PGs such as decorin and other glycoproteins found in the extracellular matrix are required for normal collagen fibrillogenesis.

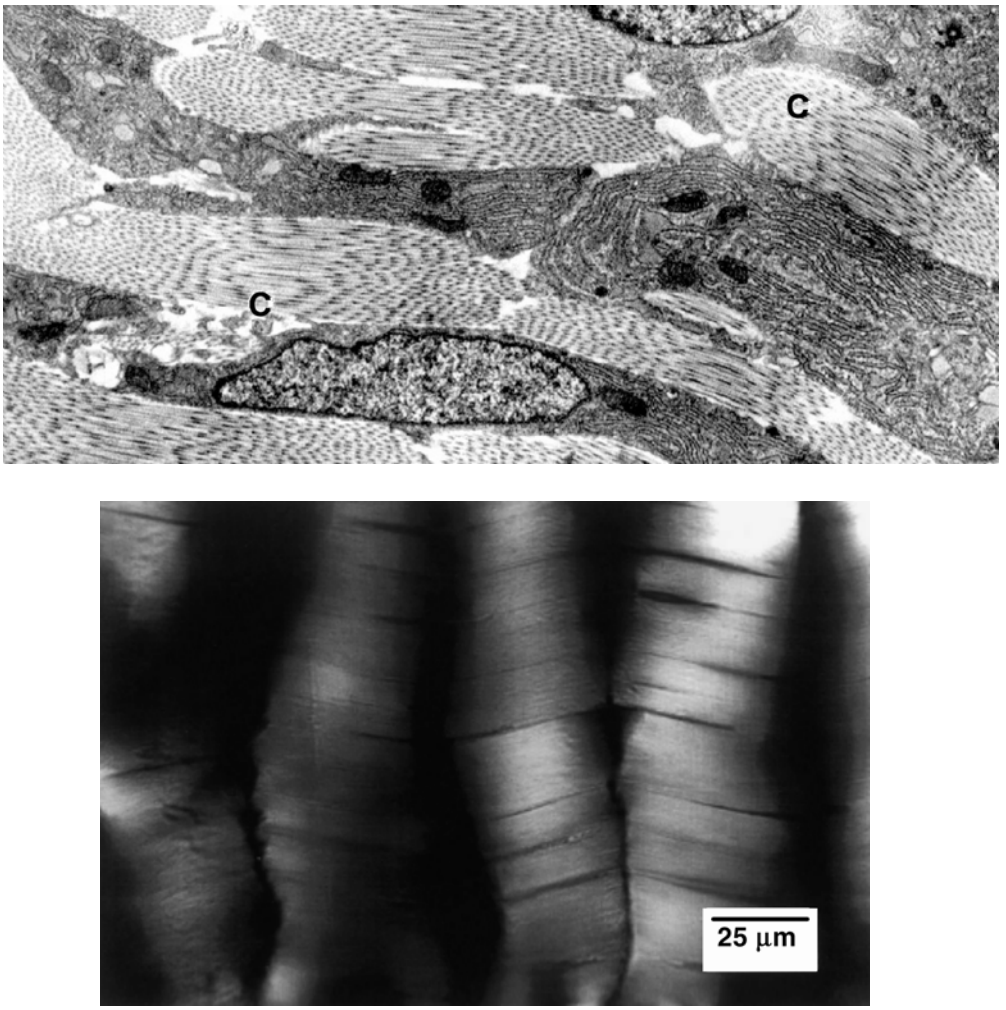



**Figure 10.42**. Formation of crimp in axial collagen fibrils during development of chick extensor tendon. (Top) Transmission electron micrograph showing collagen fibrils (C) from a 17-day-old chick leg extensor tendon. Note that the fibrils appear to be going in and out of the plane of section, consistent with formation of a crimped planar zigzag pattern. Fibrils shown have diameters of about 100 nm. (Bottom) Polarized light micrograph illustrating the crimp pattern seen in a rabbit Achilles tendon. Reprinted with permission from Silver et al. (2003).

Observations of in vitro supramolecular assembly also shed light on the in vivo process. Approximately 50 years ago it was first observed that purified collagen molecules in solution in vitro would spontaneously self-assemble to form rigid gels at neutral pH at room temperature to form fibrils that appeared to be identical to those seen in vivo. Collagen molecules and aggregates of molecules were observed to spontaneously self-assemble forming fibrils that had the characteristic 67-nm repeat distance when viewed in the electron microscope. Early electron microscopic studies suggested that linear growth of fibrils appeared to occur by addition of groups of collagen molecules to form a subfibril; lateral growth occurred by entwining these subfibrils.

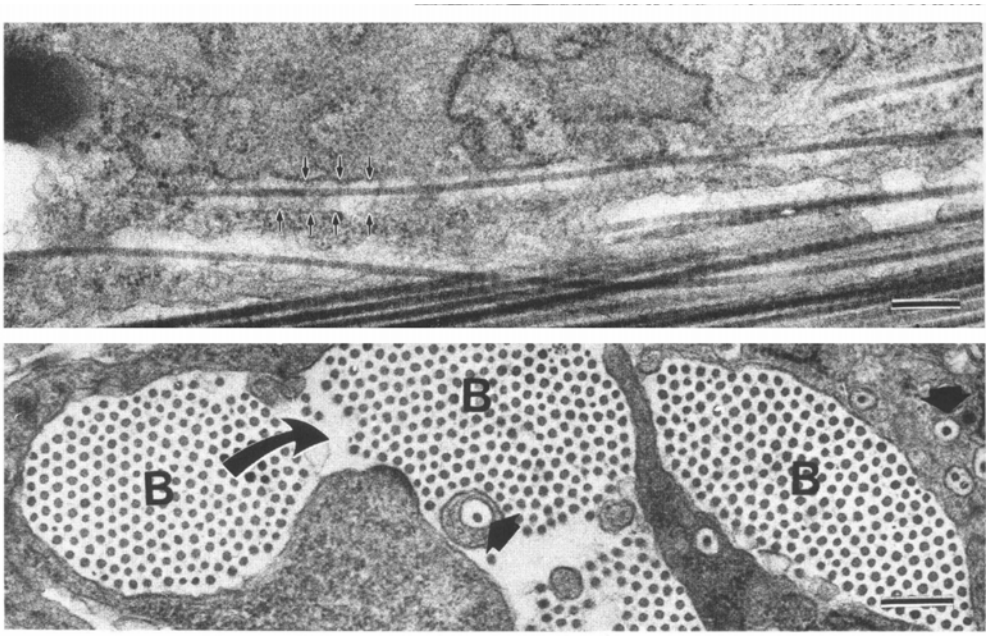



**Figure 10.43**. The upper panel is a TEM of a transverse section cut parallel to the axes of 14-d chick embryo tendon and illustrates a narrow cytoplasmic channel. This channel has periodic indentations (small arrows) of the plasma membrane, indicative of its formation from elongate secretory vacuoles, and contains a collagen fibril. In the lower panel, cross-sections of fibril formation channels are illustrated (arrowheads) in a TEM. The sections were 200–250 nm thick, and the bars are 500 nm. Adapted with permission from Birk and Zycband (1994).

There are several observations that help us understand the process of self-assembly. The first suggests that under typical solution conditions used for preparing soluble collagen, i.e., low pH and low salt content, collagen molecules are in equilibrium with larger aggregates. The aggregate in equilibrium with single molecules has been estimated to be between 1.5 and 5 million, or between about 5 and 17 molecules. As noted above, propeptides appear to limit association, thereby limiting the size of the aggregate in equilibrium with single molecules to only 5 molecules.

Data suggest that self-assembly of type I collagen leads to formation of characteristic units that range in length from 4D staggered dimers (about 570 nm) to aggregates that are about 700 nm long. This corresponds to between two and three collagen molecules long. Taken together these values of length and width suggest that aggregates formed during the initial phases of self-assembly contain 5–17 molecules and are 2–3 collagen molecules long. Estimates of the diameter of the first aggregates formed are initially 1–2 nm and then 2–6 nm. These observations are consistent with previously published models that state that self-assembly involves an initial linear step that is followed by both linear and lateral growth steps that occur simultaneously; reported results are also consistent with the formation of a unit that contains about 5 molecules packed laterally and is two or three collagen molecules long, as diagrammed in Figures 10.50 and 10.51. These units appear to grow laterally by fusion since autocorrelation of diameter distributions of self-assembled type I collagen fibrils shows a periodicity of about 4 nm.

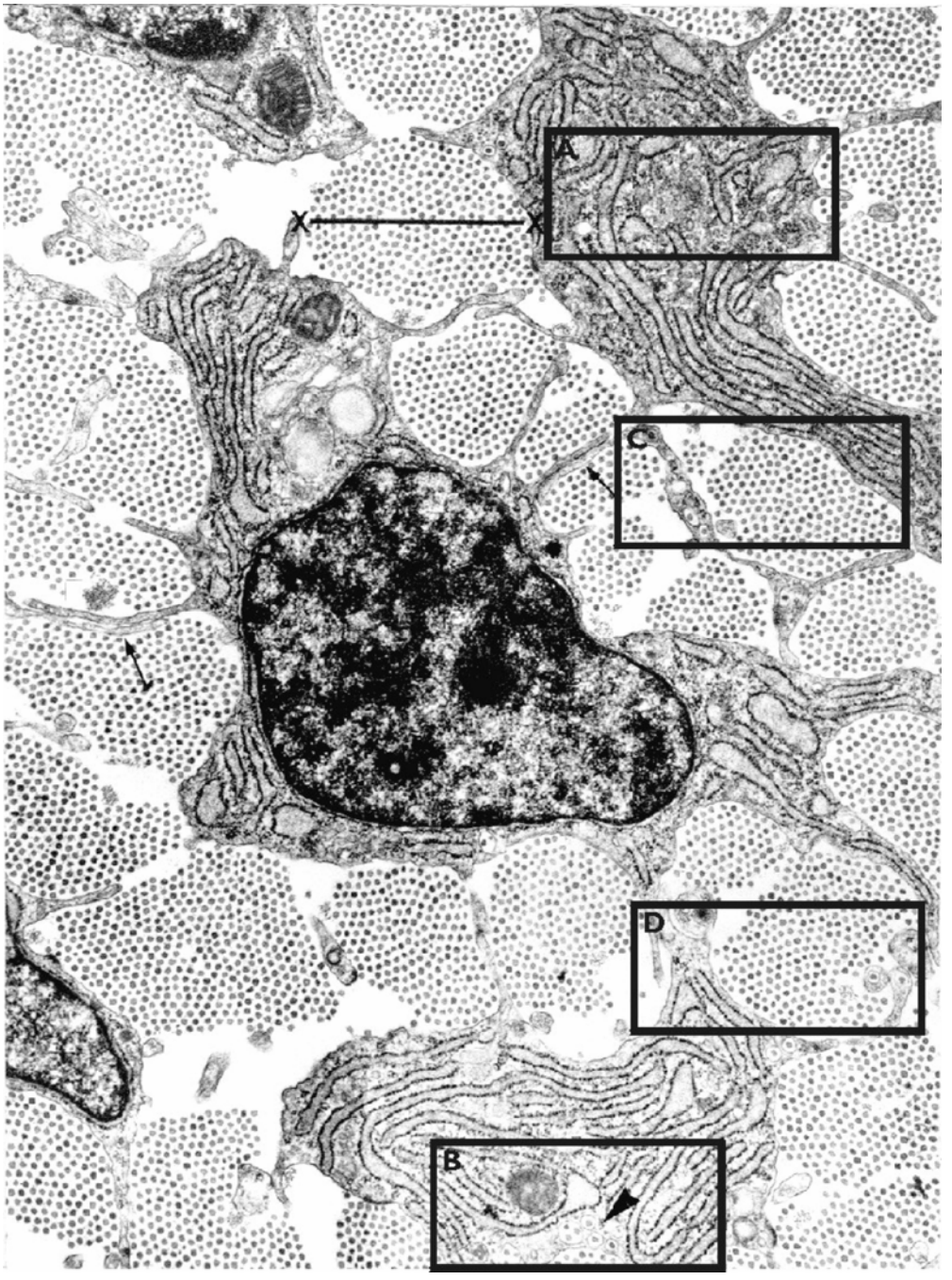



**Figure 10.44**. Micrographs: addition of axial collagen fibrils within invaginations in the cell membrane to a growing fibril. (Top) Transmission electron micrograph showing collagen fibril formation in invaginations within the cell membrane of a 14-day-old embryo. The arrows are placed in areas of the micrograph where collagen fibrils appear to be in the extracellular matrix and are in close proximity to the cell membrane. The collagen fibril bundle (fiber) diameter marked by the two Xs is 2 μm. Reprinted with permission from Silver et al. (2003).

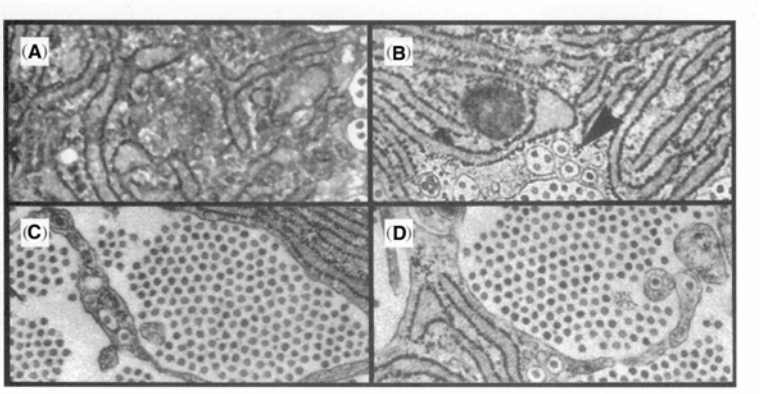



**Figure 10.45**. High-magnification view of insets shown in Figure 10.44. Addition of axial collagen fibrils within invaginations in the cell membrane to a growing fibril. A, B, C, and D show the close relationship between cytoplasmic endoplasmic reticulum and collagen fibrils that appear to be in the extracellular matrix. The middle insets (C,D) show areas where collagen fibrils are within cellular membranes that appear to bud off and add to a growing fibril. (Bottom) High-magnification view of insets shown in top micrograph. Reprinted with permission from Silver et al. (2003).

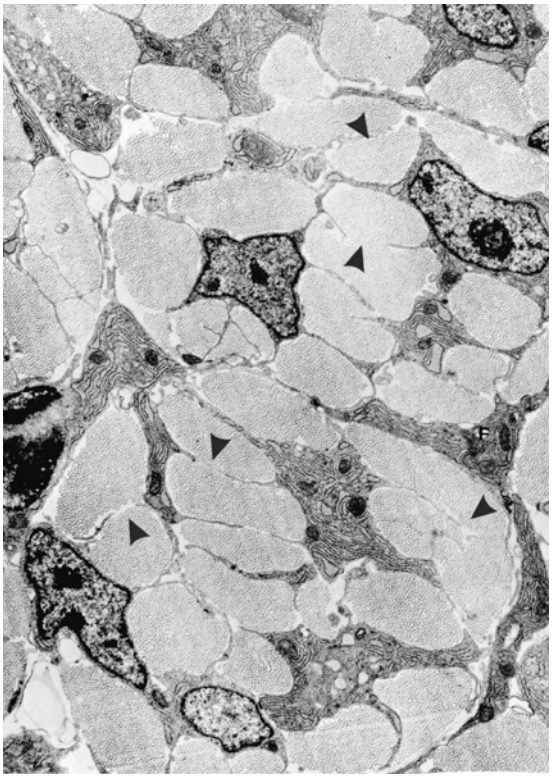


**Figure 10.46**. Lateral fusion of collagen fibrils during fascicle development of chick extensor tendon. Transmission electron micrograph showing the lateral fusion of collagen fibrils at day 17 of chick embryogenesis. Note that the demarcation between collagen fibrils (arrows) is less clear compared to the cross-section shown at day 14 (Figure 8). Several fibrils appear to be in the process of fusion generating fibrils with irregular cross-sections. The fibril bundle (fiber) diameter is still about 2 μm before fusion, similar to that observed on day 14. Reprinted with permission from Silver et al. (2003).

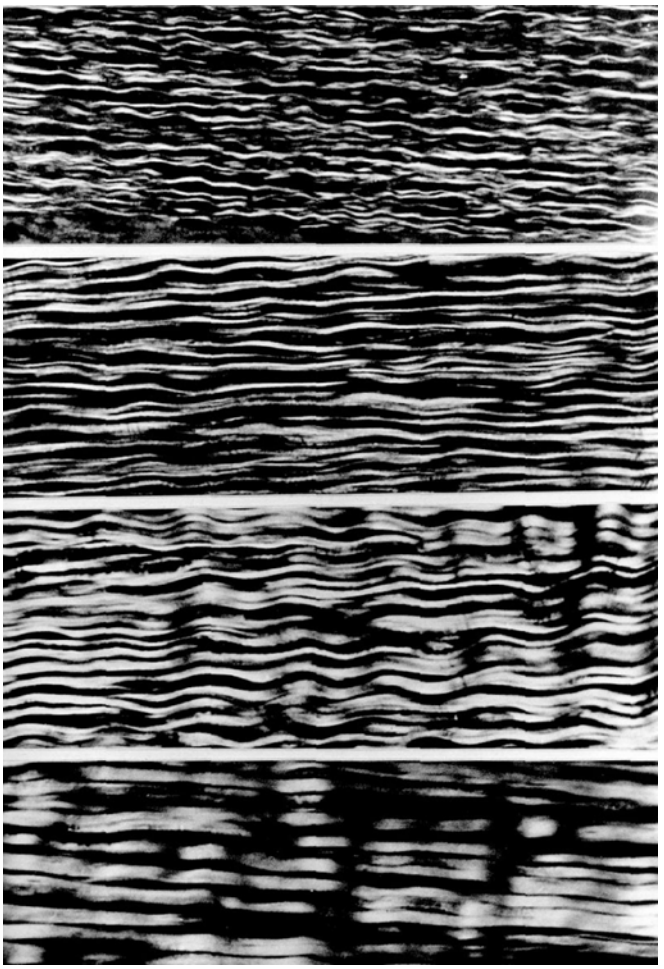


**Figure 10.47**. Polarized light micrograph of developing chick extensor tendon. This micrograph illustrates how the diameter and apparent length of collagen fibers increase from day 10 (top) through days 14 and 17 and after 1 day of hatching (bottom). Reprinted with permission from Silver et al. (2003).

From studies it has been concluded that the amino-terminal non-helical end is involved in formation of the initial thin fibrillar unit while the carboxy-terminal non-helical end is involved in lateral fusion of thin fibrillar units. These conclusions parallel the conclusions made based on self-assembly of procollagen (see Figures 10.36–10.37, 10.50–10.51), suggesting the effects of the propeptides and the non-helical telopeptides on type I collagen self-assembly appear to be similar.

One of the drawbacks to studying self-assembly using type I collagen is that the fibrils that form are narrow (20–40 nm in diameter) and are not circular. Narrow diameters are likely caused by reactions that occur during self-assembly that favor linear as opposed to lateral growth. Factors such as glycine that block lysine-derived aldehydes during fibrillogenesis increase the width of collagen fibrils. Changes in ionic strength lead to changes in fibril diameter, suggesting that lateral growth also involves electrostatic interactions. The nonuniformity

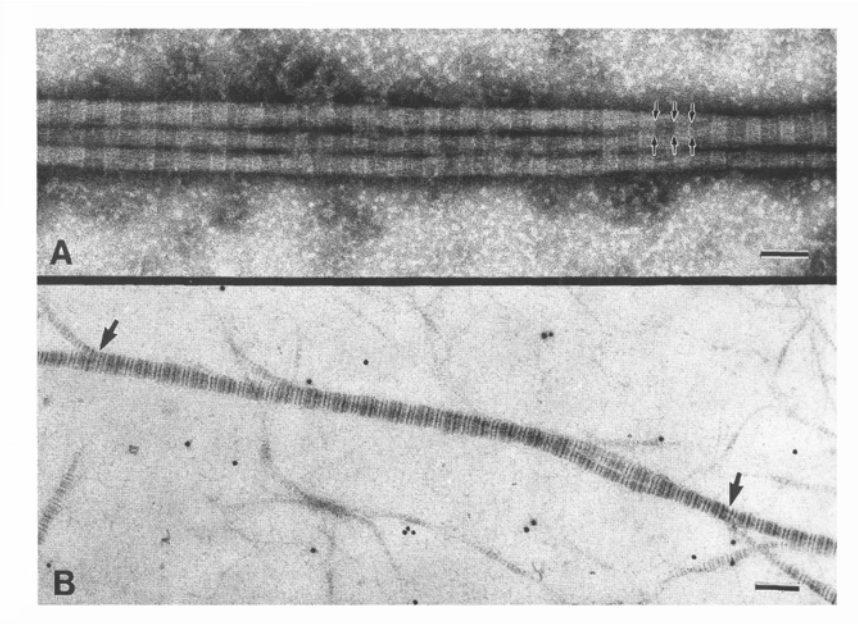



**Figure 10.48**. Collagen fibrils grow by lateral associations of fibril segments. Transmission electron microscopy of fibrils from extracted (A) and cryosectioned (B) tendons illustrating lateral association of fibril segments. The extensive lateral association/fusion of fibril segments would produce fibrils of increasing length and larger diameter. Bar = 100 nm. Reprinted with permission from Birk and Zycband (1994).

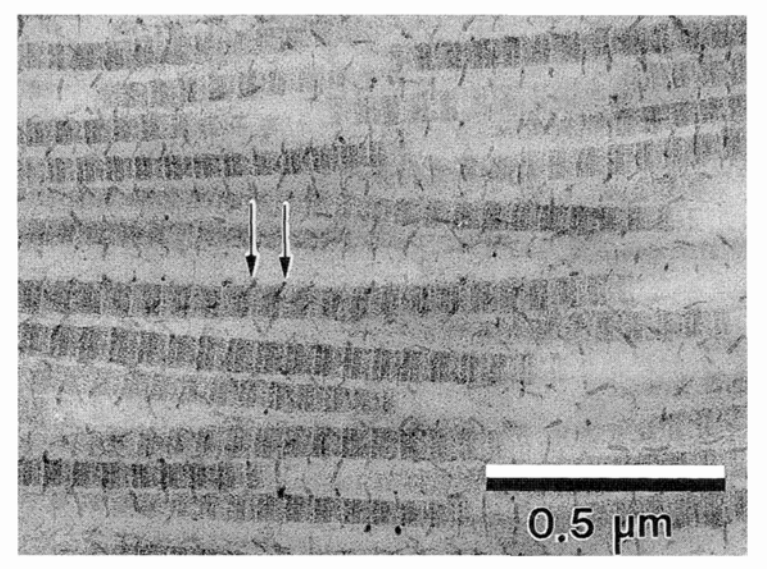



**Figure 10.49**. Relationship between proteoglycans and collagen fibrils in tendon. Transmission electron micrograph showing positive staining pattern of type I collagen fibrils from rabbit Achilles tendon stained with quinolinic blue showing proteoglycan filaments (arrows) attached to collagen fibrils. Reprinted with permission from Silver et al. (2003).

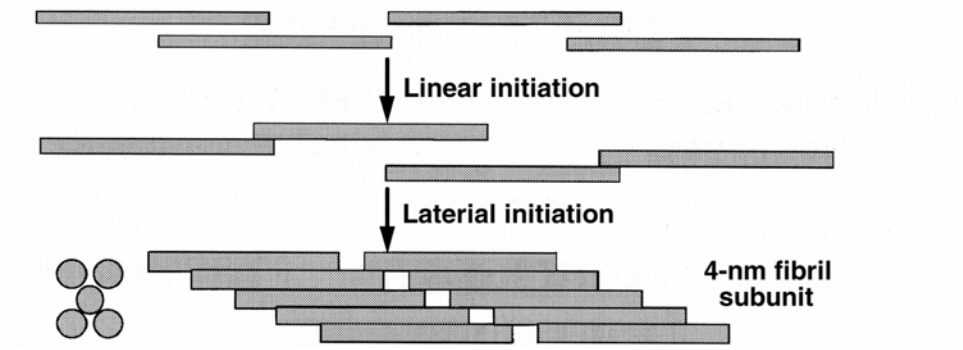



**Figure 10.50**. Model for type I collagen self-assembly. The mechanism for self-assembly of purified type I collagen molecules involves initial linear and lateral growth steps resulting in the formation of 4-D staggered dimers and a fibril subunit with a diameter of about 4 nm. Once the fibril subunit is formed, fibril growth occurs by lateral and longitudinal fusion of 4 nm wide subunits. The rate of linear and lateral growth of fibrillar subunits depends on the solution conditions. Removal of the non-helical ends promotes lateral growth while cross-linking promotes linear growth. Reprinted with permission from Silver et al. (2003).

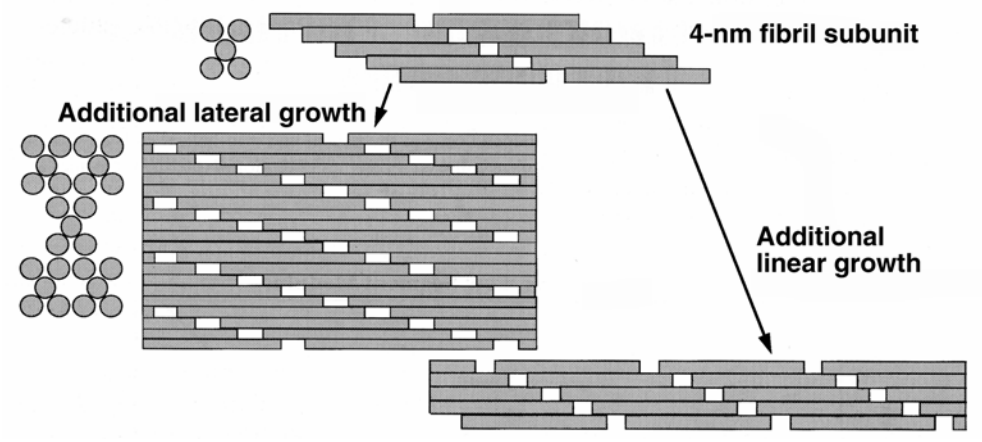



**Figure 10.51**. Continuation of model for type I collagen self-assembly. Reprinted with permission from Silver et al. (2003).

and small diameters seen in collagen fibrils self-assembled from collagen molecules suggest that other factors must play a role in controlling fibril fusion and diameter.

A model of collagen self-assembly was developed using selective cleavage of the procollagen I molecule. Solubility studies indicate that procollagen and pC-collagen (collagen containing the C propeptide) are both more soluble in solution than pN-collagen (collagen containing the N propeptide) and collagen. Assembly of pN-collagen leads to wide D-periodic sheet-like structures while pC-collagen assembles to form tape- and sheet-like structures. Incubation of pC-collagen I with C-proteinase processes the pC-collagen to collagen, and the collagen assembles into fibrils. Microscopy of the fibrils suggests that they are tightly packed and circular in outline. The average fibril diameter at 29 Celsius is about 650 nm while at 37 Celsius the average diameter is about 150 nm. These diameters are about a factor of ten larger than the diameters of fibrils formed from collagen. These observations suggest that addition of propep-

tides allows for formation of large-diameter fibrils, perhaps by promoting lateral over linear growth. For fibrils self-assembled from procollagen solutions, growth initially occurs at the pointed tip of the fibril; however, later growth occurs at both the pointed and blunt tips

## 10.11. REFERENCES


Alberts B, Bray D, Lewis J, Raff M, Roberts K, Watson JD. 1983. *Molecular biology of the cell*. New York: Garland.

Anonymous. 1994. *Hierarchical structures in biology as a guide for new materials technology*. Committee on Synthetic Hierarchical Structures, National Materials Advisory Board, National Research Council, NMAB-464. Washington DC: National Academy Press.

Baer EA, Hiltner A, Morgan R. 1992. Biological and synthetic hierarchical composites. *Physics Today*, October, pp. 60–67.

Beck K, Brodsky B. 1998. Supercoiled protein motifs: the collagen triple-helix and the α-helical coiled coil. *J Struct Biol* **122**:17–29.

Birk DE, Zycband EJ. 1994. Assembly of the tendon extracellular matrix during development. *J Anat* **184**:457–463.

Cohen C. 1998. Why fibrous proteins are romantic. *J Struct Biol* **122**:3–16.

Cowan PM, North ACT, Randall JT. 1955. x-ray diffraction studies of collagen fibers. *Symp Soc Exp Biol* **9**:115–126.

Crick FHC. 1953. The packing of α-helices: simple coiled coils. *Acta Crystallogr* **6**:689–697.

Cusack S, Miller A. 1979. Determination of the elastic constants of collagen by Brillouin light scattering. *J Mol Biol* **135**:39–51.

Darnell J, Lodish H, Baltimore D. 1990. *Molecular cell biology*. New York: Scientific American.

de Gennes PG, Prost J. 1993. *The physics of liquid crystals*. Oxford: Clarendon.

Fessenden RJ, Fessenden JS. 1979. *Organic chemistry*. Boston: Willard Grant Press.

Gilbert S. 1998. Virtual Library of Developmental Biology. http://zygote.swarthmore.edu/index.html; see http://zygote.swarthmore.edu/cell6.html.

Giraud-Guille MM. 1992. Liquid crystallinity in condensed type I collagen solutions: a clue to the packing of collagen in extracellular matrices. *J Mol Biol* **224**:861–873.

Giraud-Guille MM. 1996. Twisted liquid crystalline supramolecular arrangements in morphogenesis. *Int Rev Cytol* **166**:59–101.

Harley R, James D, Miller A, White JW. 1977. Phonons and the elastic moduli of collagen and muscle. *Nature* **267**:285–287.

Hofmann H, Voss T, Kuhn K, Engel J. 1984. Localization of flexible sites in thread-like molecules from electron micrographs — comparison of interstitial, basement membrane and intima collagen. *J Mol Biol* **172**:325–343.

Koivunen J. 2003. NF1 tumor suppressor in epidermal differentiation and growth: implications for wound epithelialization and psoriasis, *Acta Universitatis Ouluensis, Medica*, D746.

Mackay AL. 1999. Crystal souls (a translation of E Haeckel, 1917. *Kristallseelen — studien für das anorganische Leben*, Alfred Kroner Verlag, Leibzig). *FORMA* **14**:1–146.

Mow V, Ratcliffe A, Poole AR. 1992. Cartilage and diarthrodial joints as paradigms for hierarchical materials and structures. *Biomaterials* **13**:67–97.

Nestler FHM, Hvidt S, Ferry JD. 1983. Flexibility of collagen determined from dilute solution viscoelastic measurements. *Biopolymers* **22**:1747–1758.

Neville AC. 1993. *Biology of fibrous composites*. Cambridge: Cambridge UP.

Nordin M, Frankel VH. 1989. *Basic biomechanics of the musculoskeletal system*, 2nd ed., Philadelphia: Lea & Febiger.

Pierard GE, Lapiere M. 1976. Skin in dermatosparaxis: dermal microarchitecture and biomechanical properties. *J Invest Dermatol* **66**:2–7.

Radler JO, Koltover I. 1997. Structure of DNA–cationic liposome complexes: DNA intercalation in multilamellar membranes in distin. *Science* **275**:810-814.

Rudall KM. 1956. Protein ribbons and sheets. In *Lectures on the scientific basis of medicine*, pp 217–230. London: Athlone Press.

Sasaki N, Odajima S. 1996a. Stress–strain curve and Young's modulus of a collagen molecule as determined by the x-ray diffraction technique. *J Biomech* **29**:655–659.

Sasaki N, Odajima S. 1996b. Elongation mechanism of collagen fibrils and force–strain relations of tendon at each level of structural hierarchy. *J Biomech* **29**:1131–1136.

Silver FH, Freeman JW, Seehra GP. 2003. Collagen self-assembly and the development of tendon mechanical properties. *J Biomech* **36**:1529–1554.

Smith AD, ed. 2000. *Dictionary of biochemistry and molecular biology.* Oxford: Oxford UP.

Trelstad RL. 1984. *The role of extracellular matrix in development*. New York: Alan R. Liss.

Trelstad RL, Hayashi K. 1979. Tendon fibrillogenesis: intracellular collagen subassemblies and cell surface charges associated with fibril growth. *Dev Biol* **7**: 228–242

Trelstad RL, Silver FH. 1981. Matrix assembly. In *Cell biology of the extracellular matrix*, pp. 179–216. Ed ED Hay. New York: Plenum.

Viidik A. 1990. Structure and function of normal and healing tendons and ligaments. In *Proceedings of a symposium on biomechanics of diarthrodial joints*, 1st World Congress on Biomechanics. Ed VC Mow, A Radcliffe, SL-Y Woo. Berlin: Springer.

Woodhead-Galloway J. 1980. *Collagen: the anatomy of a protein*. Studies in Biology no. 117. London: Arnold.

# 11

# BONE TISSUE

"During the daily activities of life the bones of the skeleton, individually and collectively, are subjected to a variety of force systems. The response of the bones to these systems is a function, to a large extent, of the mechanical properties of the bones. Of course, the type, magnitude, direction, and point of application of the force as well as whether or not it is applied slowly, rapidly, repetitively, or for a long duration must also be considered. Additional variables include whether the bone is living or dead, embalmed or fresh, and the age, sex, race, and species of animal from which the bone is obtained. The specific bone and part of the bone being studied as well as its microscopic structure influence its mechanical properties as do the amount of moisture in it and the temperature at which the mechanical properties are determined." (F. Gaynor Evans, 1973, preface)

## 11.1. INTRODUCTION

Bone is a remarkable and extremely complex connective tissue. It has at least two major functions. First, it is the material from which the skeleton is made, and the skeleton provides mechanical support and protection for the organism. The bone tissue of the skeleton is continually changing to adapt its form and structure to this task. From the birth to the death of the organism it modifies its structure by laying down new bone tissue and resorbing old. A second function of bone is to store the minerals, particularly $Ca^{++}$, needed to maintain a mineral homeostasis in the body by regulating the concentrations of the key blood electrolytes including $Ca^{++}$, $H^{+}$, and $HPO_4^{-}$.

Bone differs from the other connective tissues because of its greater stiffness and strength. These properties stem from its being a composite material formed by the deposition of a mineral, apatite or hydroxyapatite, in a frame of collagen. The stiffness of bone is the key to understanding why it differs so greatly from other tissues. Bone is unique in that, while other connective tissues grow interstitially, bone grows only by the addition of tissue on a cell-laden surface. Bone does not retain its scar tissue like other tissues do, and long bones have a very complicated mechanism for growing longer.

After the next two sections, in which the gross- and micro-anatomy of a long bone is briefly described, there is a short description of the five types of cells associated with bone tissue. This is followed by four sections on cortical bone (elastic symmetry, poroelastic model, electrokinetic effects, and strength) and two sections on cancellous bone (architecture and elastic properties). The last four sections concern the structural adaptations that occur in living bone tissue to accommodate changes during the environmental loading the whole bone is subjected to. The final section concerns the relevant literature.

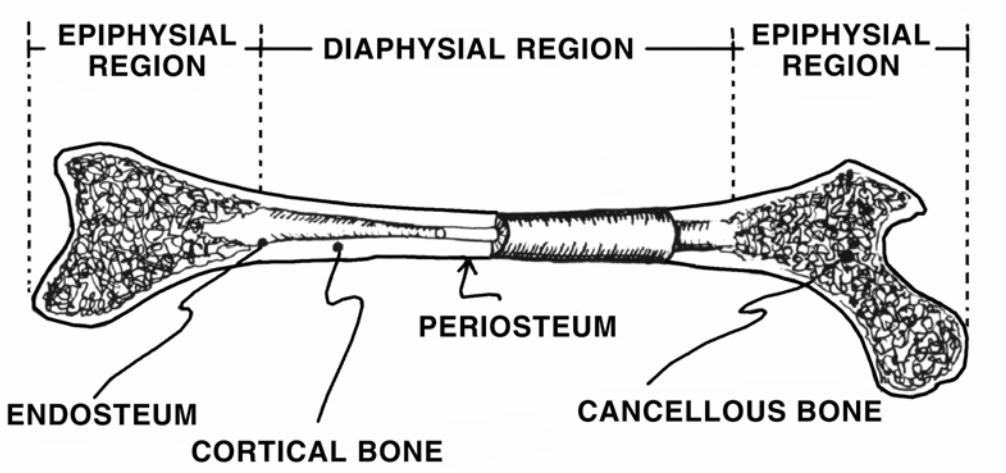



**Figure 11.1**. Longitudinal section of the femur illustrating cancellous and cortical bone types. Reprinted with permission from Cowin (1981).

## 11.2. THE TYPES OF BONE TISSUE

At the macroscopic level there are two major forms of bone tissue, called *compact* or *cortical* bone and *cancellous* or *trabecular* bone. The location of these bone types in a femur is illustrated in Figure 11.1. Cortical or compact bone is a dense material with a specific gravity of almost two in humans and a little over two in cattle (see Figure 11.2). It forms most of the outer shell of a whole bone, a shell of variable thickness. The external surface of bone is smooth and is called the periosteal surface or periosteum. The periosteum is a specialized membrane, a layered and highly vascularized structure, covering most of the external surface of a bone. It consists of an outer dense layer of collagenous fibers and fibroblasts. This relatively impermeable fiber stocking is attached to the exterior surface of bone and is always under tension. The longitudinal central tubular passage in a long bone (illustrated but not labeled in Figure 11.1) is called the medullary canal. The surface of this canal is called the endosteal surface or the endosteum. The endosteum is mainly a cell layer; it does not contain the extensive collagenous structure of the periosteum. The diaphysial region of a long bone is the midshaft and the epiphysial regions are the ends of the bone. The flared regions in between are called the metaphysial regions.

Each of the bone tissue types described above is mineralized. As noted, the mineralization is orderly except in the case of woven bone. Deposition of the mineral in the collagen template is illustrated in Figure 11.3. The spaces in the hierarchical structure of collagen that are designed to receive the mineral are illustrated in Figures 10.23 and 10.24. The mineral is apatite or hydroxyapatite ($[Ca_{10}(PO)_4](OH)_2$) or some amorphous or approximate form of hydroxyapatite. The simultaneously occurring interactive growth of collagen, apatite, and bone tissue is illustrated in Figure 11.4.

Each of the bone tissue types is described below: cancellous bone and the three types of cortical bone — lamellar, osteonal (Haversian), and woven.

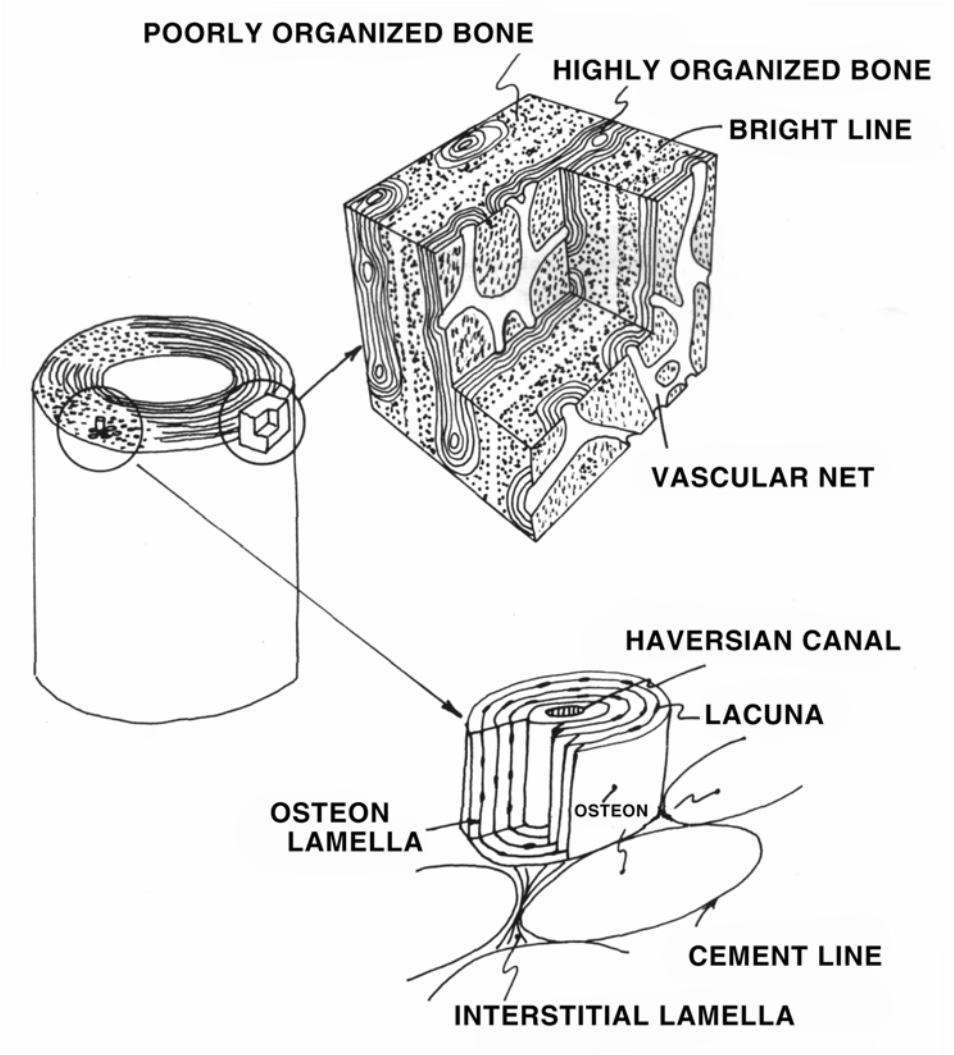



**Figure 11.2**. Typical bone structure in the diaphysis of the femur. Two types of cortical bone are illustrated: lamellar and osteonal. Reprinted with permission from Cowin (1981).

## Cancellous Bone

Cancellous bone generally exists only within the confines of the cortical bone coverings. Cancellous bone is also called trabecular bone because it is composed of short struts of bone material called trabeculae (from the Latin for "little beam"). The connected trabeculae give cancellous bone a spongy appearance, and it is often called spongy bone (Figure 11.5). There are seldom blood vessels within the trabeculae, but there are vessels immediately adjacent to the tissue and they weave in and out of the large spaces between the individual trabeculae. Cancellous bone has a vast surface area as would be suggested by its spongy appearance. This is illustrated by the human pelvis, which has an average volume of 40 $cm^3$ and an average periosteal surface area of 80 $cm^2$, but the average surface area of its trabecular bone is 1600 $cm^2$.

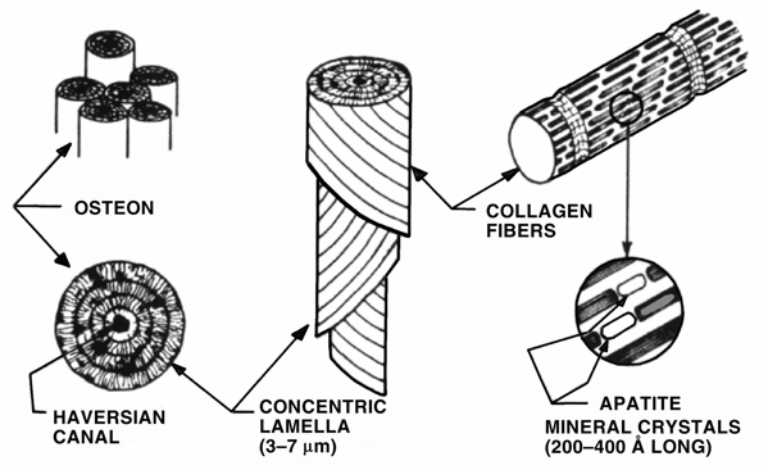



**Figure 11.3**. The detailed structure of an osteon. Reprinted with permission from Cowin et al. (1987).

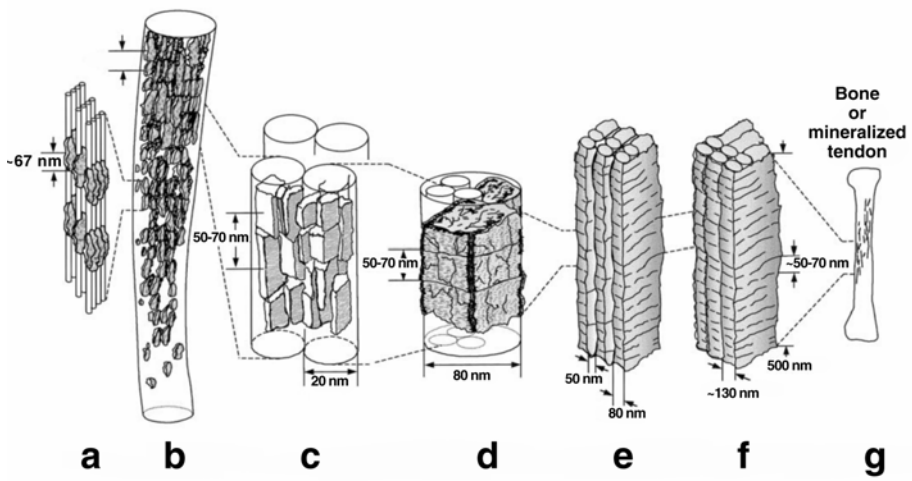



**Figure 11.4**. A schematic diagram of the organization and interaction of collagen and mineral at different structural levels of hierarchy for a calcified vertebrate tissue. (a) Based on the current model of collagen assembly and the manner of its association with mineral, crystal platelets nucleate in collagen channels or gaps created by periodic (≈67 nm) hole and overlap zones. (b) Crystal platelets grow in length along their crystallographic *c*-axes and in width through the channel or gap spaces. (c) As collagen macromolecules grow as well to microfibrils and fibrils (≈20 nm in diameter), crystals fuse into larger and thicker plates in which their periodic deposition (≈50–70 nm) and parallel nature are still maintained. At this stage, interfibrillar plates may be developing. (d) Crystal plates grow larger in all dimensions at the level of collagen fibers (≈80 nm and greater in diameter). (e) Fibers next associate to create a series of parallel plate aggregates that may vary in length, width, and thickness. Some of the aggregates may represent the interfibrillar plates formed earlier. The typical thickness of the aggregates is ≈80 nm and a frequent size along their length is ≈500 nm. Individual plate aggregates are initially separated by ≈50 nm (e), but this space gradually disappears as mineral deposition proceeds in the tissue and aggregates would grow to thicknesses of ≈130 nm. (f) Edges of plate aggregates still maintain ≈50- to 70-nm periodicity, indicative of the basic collagen structure underlying mineral formation. (g) Ultimately the plate aggregates become lamellar in shape and constitute a portion of bone or mineralized tendon. Independent of the mineralization associated with the hole and overlap zones, there is surface mineralization of the collagen structures in b–f. This aspect of mineral formation is not depicted in b–d. Reprinted with permission from Siperko and Landis (2001).

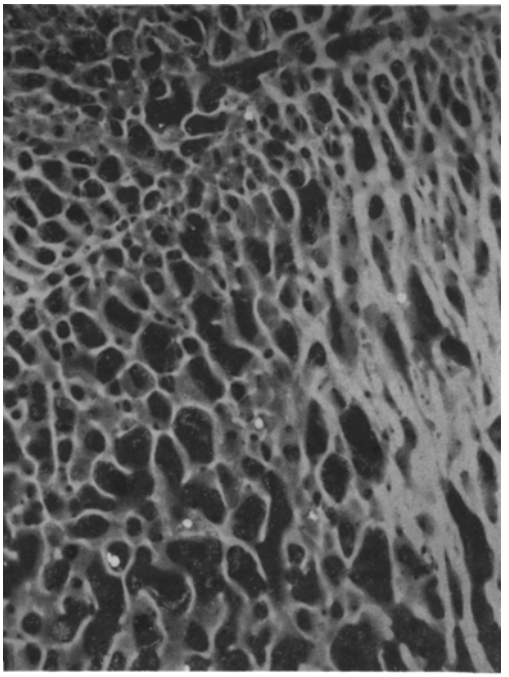


**Figure 11.5**. The porous structure of cancellous bone tissue. Reprinted with permission from Cowin and Mehrabadi (1989).

### Lamellar Bone

Lamellar bone consists of a number of concentrically arranged laminae when it occurs in the mid-shaft of a long bone, as illustrated in Figures 11.2 and 11.6. The thickness of the laminae is about 200 μm. Between each lamina there is a net-like system of blood vessels that is essentially two dimensional, with an occasional large radial vessel through a lamina connecting two of the tangential two-dimensional nets. Each lamina is divided into the three zones shown in Figure 11.2. The first zone, which extends from the surface of the blood network to about a third of the way across the lamina, is of highly organized bone, which is dense. The second zone, which also extends for about one-third the distance, is a poorly organized tissue. This zone is interrupted in the middle by a line that, in ordinary light, appears to be bright. This line, called the bright line, is the boundary between the two blood supply networks bounding the lamina. The lamina is symmetric about the bright line, and there is another half-layer of poorly organized bone, followed by a full layer of highly organized bone before the next blood network is reached (Currey, 1960).

### Osteonal Bone

Osteonal bone is illustrated in Figures 11.2 and 11.3. It consists of quasi-cylindrical elements called *osteons* or Haversian systems. These bone microstructures were originally named after Clopton Havers (1650–1702), an English physician and anatomist. However, they were first identified by Antonie van Leeuwenhoek (1632–1723), a Dutch maker of microscopes who

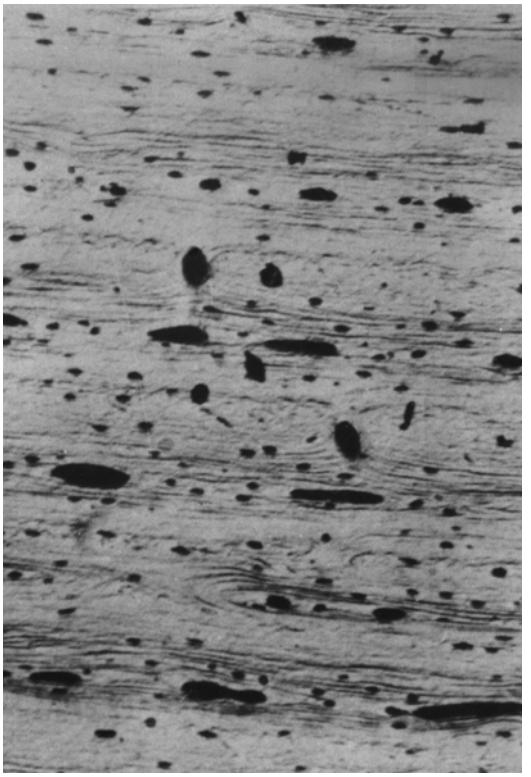


**Figure 11.6**. The lamellar structure of cortical bone tissue. Reprinted with permission from Cowin and Mehrabadi (1989).

made pioneering discoveries at the microscopic scale. Contemporary preference is to avoid eponyms and call the structures osteons rather than Haversian systems. There are two kinds of osteons — primary and secondary. Primary osteons are the structures around blood vessels that are formed when the bone is initially formed. Secondary osteons are osteons formed after the tissue is mineralized by a process in which bone cells first excavate a tubular path through the hard tissue, then deposit the osteon layer by layer. Secondary osteons are the osteons of primary interest because important human adult bones (e.g., leg and arm bones) consist mainly of secondary osteons. Because the secondary osteons are the osteons of primary interest, the prefix secondary is usually dropped when referring to them. The prefix primary is not dropped when referring to primary osteons. This is one of the rare cases when the secondary is more important than the primary.

Osteons are typically about 200 μm in diameter, the same thickness as the laminae in lamellar bone, and about 1–2 cm long. The thickness is the same because the blood supply for the osteon is a central lumen containing a blood vessel, and thus every point in the osteon is no more than about 100 μm from the blood supply, as is the case with lamellar bone. Osteonal bone is organized to accommodate small arteries, arterioles, capillaries, and venules of the microcirculation. While the blood vessels in the osteonal canal transport blood generally along the long axis of a long bone, it is the Volkmann canals that contain the blood vessels that

transport blood generally perpendicular to the long axis of a long bone. These canals were named after the German physiologist Alfred Wilhelm Volkmann (1800–1877), who discovered them. A Volkmann canal connects different osteonal canals, generally intersecting the osteonal canals at right angles. In the discussion of the "twisted plywood model" of supramolecular tissue structure in Chapter 10, it was noted that the collagen in osteons is observed to be in a helicoidal pattern (Figure 10.34b).

### Woven Bone

Woven bone is found typically in both cortical and cancellous bone of young growing animals and in adults after a bone injury. During normal maturation woven bone is gradually replaced by lamellar bone, so that in man, for example, there is normally no woven bone present after the age of 14–16 years. An additional distinguishing feature of woven bone is the relationship of mineral to collagen. In lamellar and osteonal bone these elements are present in fixed ratios, and it seems virtually impossible for lamellar bone to become hypermineralized. The ratio of mineral to collagen in woven bone varies enormously, and hyper-mineralization is often observed. Woven bone appears to bear the same relationship to lamellar bone as temporary scaffolding bears to a completed structure.

### Similarities and Conversions of Bone Types

The osteons of osteonal bone and the laminae of lamellar bone appear to be just different geometric configurations of the same material. It was indicated above that in both geometric configurations no point in the tissue is more than about 100 μm away from the blood supply. Both osteonal and lamellar bone occur simultaneously in the long bones of mature animals. In very young animals the long bones are composed of woven bone with a few primary osteons. With maturation the woven bone is converted to lamellar bone and, at maturity, there is a partial conversion to osteonal bone. The conversion from lamellar to osteonal bone is somewhat of a biological enigma. Osteonal bone is known to have a less efficient local circulation system and to have less mechanical strength compared to lamellar bone, yet the percentage of osteonal bone generally increases with age.

## 11.3. BONE INTERFACES, POROSITIES AND FLUIDS OR GELS

There are three levels of bone porosity within cortical bone and within the trabeculae of cancellous bone, all containing a fluid or gel; these are, from the one with the largest to the one with the smallest pores, vascular porosity, lacunar-canalicular porosity, and collagen-apatite porosity. In addition, there is a porosity of the "spongy" bone that consists of pores external to the trabeculae in trabecular bone. There are two interfaces between the three levels of bone porosity within cortical bone and within the trabeculae of cancellous bone. There is an additional interface, called the cement line, which forms the outside boundary of an osteon. The purpose of this section is to describe these interfaces, porosities, and the fluids or gels within them. A sketch of a partial cross-section of an osteon (Figure 11.7) shows some of the small-scale features of bone. It was noted above that osteons are cylindrical structures about 100 μm in radius. They make an angle of 5–15° with the long axis of a bone and trace a generally helical path. They contain at their center an osteonal canal (Haversian canal). This canal contains blood vessel(s), a nerve, and some space occupied by bone fluid. The walls of the osteonal canals are covered with cells, and behind the cells are the entrances to the canaliculi. The canaliculi are passageways that run between an array of roughly disk-shaped cavities called lacunae, which contain bone cells (osteocytes), or from the lacunae to the osteonal canal (Figure

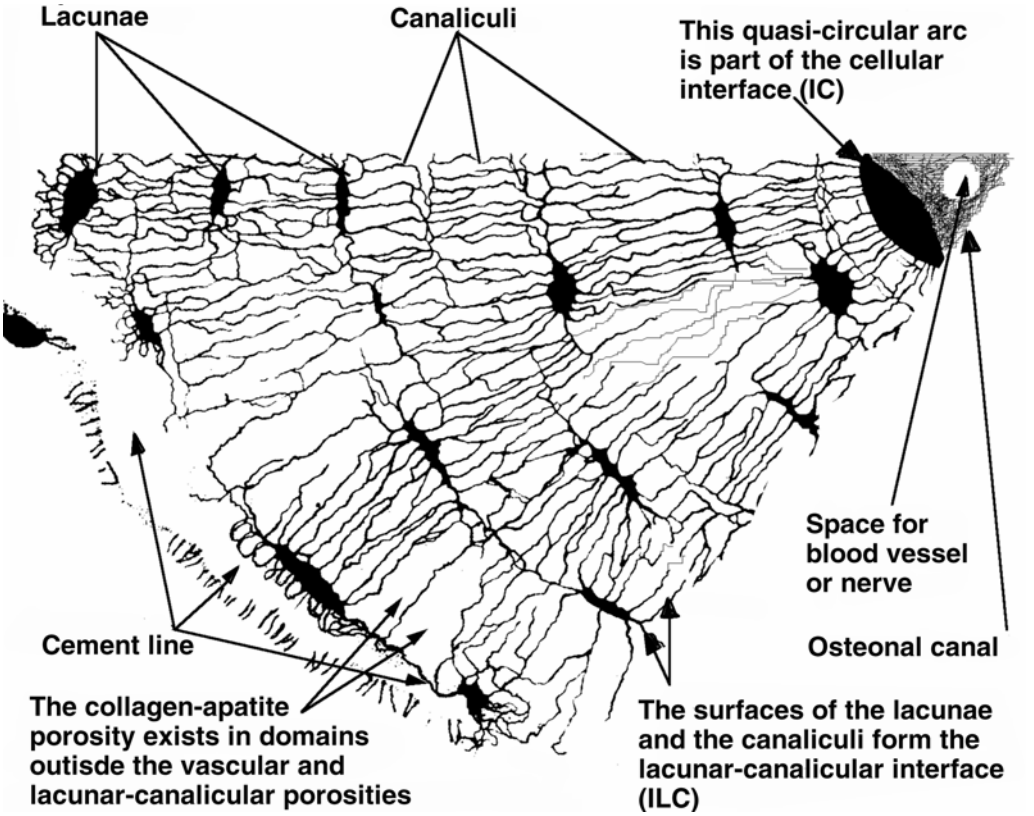



**Figure 11.7**. A pie-shaped section of an osteon. The osteonal canal is on the upper right, the cement line to the left. The osteonal canal is part of the vascular porosity (PV); the lacunae and the canaliculi are part of the lacunar-canalicular porosity (PLC), and the material in the space that is neither PV or PLC contains the collagen-apatite porosity (PCA). The three interfaces, the cement line, the cellular interface (IC), and the lacunar-canalicular interface are each indicated. The radius of an osteon is usually about 100 μm, and the long axis of a lacuna is about 15 μm. Using this information, it should be possible to establish the approximate scale of the printed version of this illustration. Reprinted with permission from Cowin (1999).

11.7). The three-dimensional region between adjacent osteons is called the cement line. The bone interfaces are described below — the periosteum, the cellular interface (IC) (which includes the endosteum), the interface consisting of the walls of the lacunae and the canaliculi (ILC), and the cement lines. The porosities, also described in greater detail below, include vascular porosity (PV), lacunar-canalicular porosity (PLC), collagen-apatite porosity (PCA), and the porosity of the inter-trabecular space (PIT). These acronyms have been selected so that the first letter indicates the structure, interface (I) or porosity (P), and the subsequent letters in the acronym indicate which interface or which porosity. The fluids or gels are bone marrow, fat, blood. and bone fluid.

The interfaces are structures of varying thickness and permeability between the relevant fluid compartments and structures in bone.

### IC — The cellular interface, including the endosteum

All the surfaces of the tubular cavities of bone that contain the vasculature, the osteonal canals, and the Volkmann canals, as well as the endosteum and the inner layer of the periosteum, form a single cellular interface. This interface, a small part of which is illustrated in Figure 11.7, is a continuous confluent layer of bone-lining cells, one side of which faces the vascular space and the other side of which faces the mineralized matrix. The region interior to this interface was called the "milieu intérieur" by the French physiologist Claude Bernard (1813–1878). There is transport of bone fluids through the interface. During each cycle of bone loading due to the animal's activity, the fluid on the vascular side of the interface will mix briefly with the fluid on the mineralized matrix side of the interface. As a first approximation it appears reasonable to assume that the hydraulic resistance of this interface is much less than the hydraulic resistance of lacunar-canalicular porosity, which is on the bone side of the interface.

### ILC — The interface consisting of the walls of the lacunae and the canaliculi

The interface consisting of the walls of the lacunae and the canaliculi — the ILC — divides these spaces from the mineralized tissue (Figure 11.7). All the ILC is topologically contained within the IC. It could be considered as part of the IC, but it is considered as distinct here because it is necessary to distinguish between vascular porosity (PV) and lacunar-canalicular porosity (PLC) and their boundaries for mechanical and physiological reasons. The evidence suggests that the ILC is relatively impermeable. There is a caveat to the conclusion that the ILC is relatively impermeable: it does not hold for very young bones. The ILC and the associated bone porosities change rapidly after birth, being quite porous at birth and subsequently reducing their porosities as the bone tissue becomes fully mineralized.

An important physiological consideration concerning the IC and the ILC arises from the fact that bone serves as a reservoir for calcium and phosphorus, and these mineral reserves should be connected to the circulation. Clearly, these minerals must cross the IC, but must they cross the ILC? That is to say, can the necessary minerals be supplied by the bone-lining cells from the bone matrix they are situated upon, or must the bone cells between the IC and ILC (the osteocytes) be involved in this process? It is possible that sufficient mineral can be supplied by the bone-lining cells, consistent with the suggestions above that the ILC is relatively impermeable and that the IC offers relatively small hydraulic resistance. It is also possible that the interface permeability of the ILC might be changed by physiological demands.

### Cement Lines

Cement lines appear as the boundary of osteons (Figures 11.2 and 11.7). They represent the limit of the new tissue, a front where the bone removal activity associated with construction of a new osteon has ceased and bone deposition activity associated with the new osteon begins. It was thought at one time that canaliculi do not cross the cement lines, but evidence that they do is now well established. The number density per unit area of the canaliculi crossing cement lines has not been established, nor has the anatomical distribution of their crossing been investigated.

There are at least four identifiable levels of porosities in bone.

### PV — The Vascular Porosity

All the quasi-cylindrical passageways in the bone matrix — the osteonal canals and the Volkmann canals — are called the vascular porosity (PV). The PV contains the vasculature (blood vessels), nerves and, in the space not occupied by blood vessels and nerves, bone fluid. The characteristic lineal dimension associated with this space is the radius of the Volkmann and osteonal lumens (order = 20 μm); by this criterion, this porosity is the largest bone fluid porosity. The values of the porosity and the permeability of the PV are given in Table 11.1a. The boundaries of this porosity are the IC.

**Table 11.1**. Measurements of the Porosity and Permeability for the Two Levels of Bone Porosity of Interest

a. Vascular porosity (PV)

| Reference | Porosity $\phi$ | Reference | Permeability $k$ ($m^2$) |
|---|---|---|---|
| Frost, 1962 | 0.06 | Rouhana et al., 1981 | $3.0 \times 10^{-13}$ |
| Morris et al., 1982 | 0.015 | Li et al., 1987 | $5.0 \times 10^{-15}$ |
| Schaffler & Burr, 1988 | 0.04 | Zhang et al., 1998 | $6.35 \times 10^{-13}$ |
| Zhang et al. 1998 | 0.04 | Smit et al., 2002 | |

b. Lacunar-Canalicular Porosity (PLC)

| Reference | Porosity $\phi$ | Reference | Permeability $k$ ($m^2$) |
|---|---|---|---|
| Frost, 1960 | 0.023 | Zhang et al., 1998 | $1.47 \times 10^{-20}$ |
| Morris et al., 1982 | 0.042 | | |
| Baylink & Wergedal, 1971 | 0.035 | | |
| Zhang et al. 1998 | 0.05 | | |

The values from Zhang et al. (1998) are estimates based on the data from the literature and calculations.

Bone fluid freely exchanges with the vascular fluids because of the high permeability of the thin endothelium, the absence of a smooth-muscle layer, and the sparse basement membrane layer of the capillary walls. The bone fluid pressure in the PV cannot generally exceed the local blood pressure, as the vessels would collapse. Thus, the pressure of the bone fluids is probably similar to the blood pressure in bone, on the order of 40 to 60 mm Hg, which is low compared to the bone fluid pressures in the lower characteristic lineal dimension lacunar-canalicular porosity (PLC), described below.

### PLC — The Lacunar-Canalicular Porosity

All the space in the lacunae and the canaliculi is called the lacunar-canalicular porosity (PLC). The characteristic lineal dimension associated with this space is the radius of the canaliculus (order = 0.1 μm). The values of the porosity and the permeability of the PLC are given in Table 11.1b. Since the bone fluid porosity with the largest lineal dimension, the PV, is always at a low pressure, the middle characteristic lineal dimension porosity — the PLC — appears to be the most important porosity for consideration of mechanical and mechanosensory effects in bone. The bone fluid in the PLC can sustain higher pressures for longer times due to mechanical loading. Thus, the PV functions as a low-pressure reservoir that interchanges bone fluid

with the PLC. This interchange is facilitated by the fact that the lineal dimension associated with the PV is two orders of magnitude larger than that associated with the PLC, and the PV is typically at blood pressure, which is low in bone.

The PLC is the porosity associated with slower relaxation of excess pore pressure due to mechanical loading. It is also the porosity associated with osteocytes; the osteocyte is the prime candidate for the mechanosensory cell in bone. It has been suggested that the region between the cell membrane of the osteocyte (and the osteocytic process) on one hand and the walls of the canaliculi and lacunae on the other, is filled with the cell glycocalyx (also called the surface matrix or capsule). The contents of this PLC, the combination of the glycocalyx and the bone fluid, is thought to function as a gel.

### PCA — The Collagen-Apatite Porosity

The porosity associated with the spaces between the collagen and the crystallites of the mineral apatite (order = 10-nm radius) is called the collagen–apatite porosity (PCA). This porosity is within the ILC and is the lowest characteristic lineal dimension porosity. The movement of the bone fluid in the collagen–apatite porosity is negligible because most of the bone water in that porosity is bound by interaction with the ionic crystal. This portion of the bone water is considered to be part of the collagen–apatite structure.

### PIT — The Porosity of the Inter-Trabecular Space

The bone porosity with the largest, but quite variable, characteristic lineal dimension (up to 1 mm) is associated with cancellous bone; it is referred to here as the inter-trabecular porosity (PIT) of cancellous bone. It is the porosity external to, and surrounding, the trabeculae. The IC on the surface of trabeculae divides the PIT and the mineralized matrix in the trabeculae. This porosity is well connected to the medullary cavity and may contain marrow, fat, and blood vessels. The characteristic lineal dimension of the PIT varies with anatomical location; it is smaller near the load-bearing surfaces and increases to its greatest magnitude as the medullary canal is approached.

Each of the porosities contains fluids or gels. Each of these fluids is briefly discussed below.

### Blood Supply

The circulation of blood in a long bone is a model for the circulation in any bone. The main supply of blood comes through the nutrient arteries, which pass directly through the cortex of cortical bone and into the medullary canal before dividing into smaller vessels. About two-thirds of the blood supply comes through the nutrient arteries with most of the rest being supplied by the periosteal arteries. The influx vasculature and collateral circulation in bone has a great deal of redundancy, as does the circulation in other tissues. The medullary canal forms an inner compartment with variations of intravascular hydrostatic pressure from 16 mm Hg in the diaphysis to 27 mm Hg in the metaphysis of the human tibia. Outside the bone, the pressure drops to 19 mm Hg in the nutrient vein, from an inflow nutrient artery value of 123 ± 15 mm Hg. High medullary canal pressures could result from contraction of muscles supplying vasculature to the periosteum or from increased compartment pressures outside the bone. The general relationships of influx and efflux vasculature within a bone section are illustrated in Figure 11.8. More than one nutrient artery/vein may perforate the diaphysis of the long bone. After branching in the medullary canal, there is a division into two main networks: the marrow sinu-

soids and vessels radially penetrating the endosteum. In the medullary canal, branches from the nutrient artery form sinusoidal vessel networks that associate intimately with hematopoietic tissue before emptying into the central sinus.

Endosteal and periosteal vessels predominantly follow a longitudinal path within osteonal (Haversian) canals parallel with the long bone axis. Radial connections are maintained through side branches following Volkmann's canals, as shown in Figure 11.8. Generally, an osteonal (Haversian) canal is 25 to 75 μm wide and contains one or two vessels.

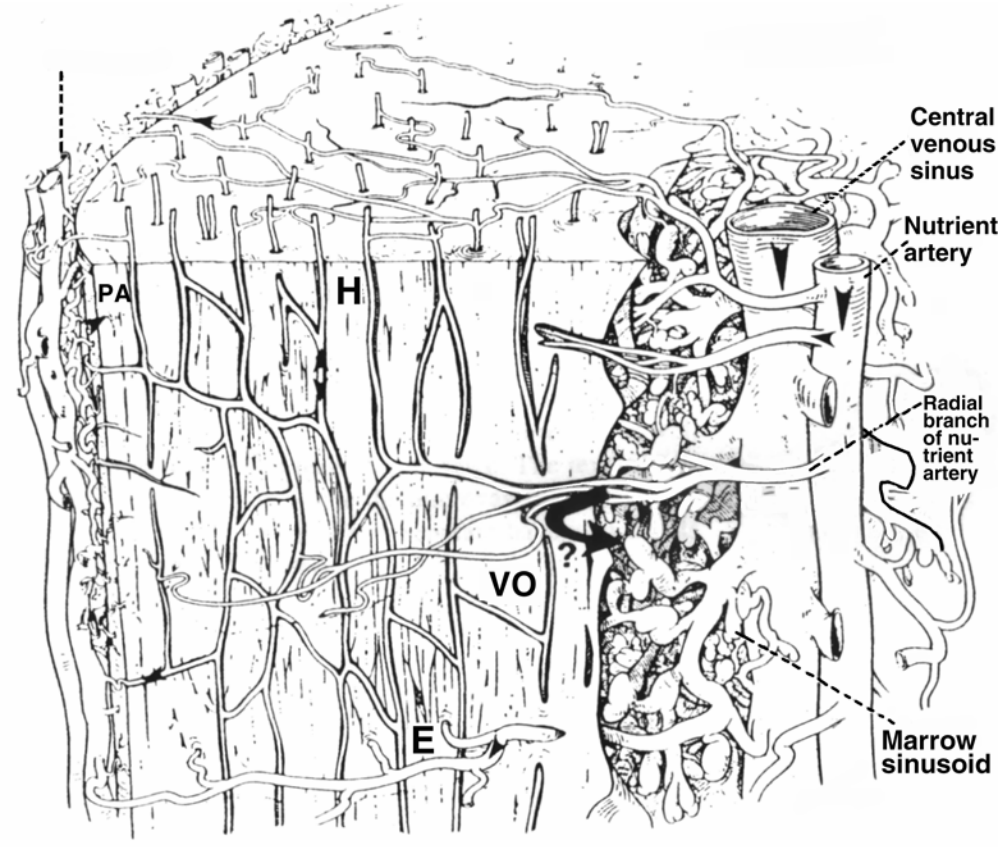



**Figure 11.8**. Three-dimensional view of a cortical bone wedge in a representative diaphysis. Vessels in osteonal (Haversian) canals (H) may flow in either direction and can reverse, as indicated by oppositely directed arrowheads. Nutrient artery branches may split into endosteal (small arrow, furthest right) and medullary (next small arrow to left) branches in a parallel arrangement, or endosteal vessels may loop through sinusoids in a serial arrangement (largest arrow with "T"). Vessels in Volkmann's canals (VO) may be arteriolar or venular. Vessels emptying sinusoids and Haversian canals supply emissary veins (E). Periosteal arteries (PA) provide blood from attached soft tissue. Pressure gradient is from right to left, but may reverse, and with it flow, as a result of trauma. Reprinted with permission from Williams et al. (1984).

## Bone Fluid

The vascular porosity contains blood vessels — small arteries, arterioles, capillaries, and venules of the microcirculation — through which blood flows. In the region exterior to the

blood vessels the vascular porosity contains bone fluid. Nutrients from the blood pass through the blood vessel walls into the bone fluid and are transported to the cells through the lacunar-canalicular porosity (PLC). The PLC contains bone fluid and cellular proteins, the exact composition of which is unknown. It is thought that the combination of bone fluid and proteins in the PLC probably functions as a gel.

### Bone Marrow and Fat

The fluid or gel contents of the porosity of the intertrabecular space (PIT) are bone marrow and fat, mostly bone marrow in youth and mostly fat in old age. It is in the bone marrow that red blood cells are formed and in old age it is only the sternum that houses this production. The reports of the viscosity of the PIT fluid contents are widely scattered due to the widely varied nature of the fluid or gel that is found in this space. These fluid materials have a viscosity one to two orders of magnitude larger than the viscosity of the bone fluid in the PV or PLC.

### Problems

11.3.1. Find the foramen (hole) for the nutrient artery to enter a chicken limb bone. Note the slant of the foramen with respect to the cortical tissue through which it passes. Place a straight pin in the foramen. Is the exposed part of the straight pin inclined toward the nearest joint or away from the nearest joint? Please attempt an explanation for this orientation based on whether this is a good design for a chicken or not.

11.3.2. List the similarities and the differences in the microstructure of cancellous and cortical bone.

## 11.4. BONE CELLS

The description of the five kinds of bone cells found in the growing and adult skeleton will be organized on the basis of the anatomical sites associated with these cells. The osteocytes are housed in the lacunae illustrated in Figure 11.7. The other four cell types — the osteoprogenitor cells, the osteoblasts, the bone-lining cells, and the osteoclasts — are all located upon the cellular interface (IC), which includes all the surfaces of the tubular cavities of bone that contain the vasculature, the osteonal canals, and the Volkmann canals, as well as the endosteum and the inner layer of the periosteum (Figure 11.7).

***Osteoprogenitor Cells.*** There are two types of osteoprogenitor cells: one type (preosteoblasts) gives rise to the bone-building osteoblasts and the other (preosteoclasts) gives rise to bone-resorbing osteoclasts. The suffix *–blast* is from the Greek for bud, and the suffix *–clast* is from the Greek *klastos*, broken, or *klan*, to break. Osteoprogenitor cells are commonly found near the IC. The osteoprogenitor cells of osteoclasts (precursor of osteoclasts, preosteoclasts) are believed to be mononuclear phagocytes of hematopoietic stem cell origin.

***Osteoblasts.*** Osteoblasts are bone-forming cells. They synthesize and secrete unmineralized collagenous bone matrix, the osteoid. Osteoblasts also appear to participate in the calcification of bone, and they seem to regulate the flux of calcium and phosphate in and out of bone.

***Osteoclasts.*** Osteoclasts are multinucleated giant cells responsible for the resorption of bone. These cells have diameters that range from 20 to over 100 μm and may contain from 2 to 50 nuclei. Actively resorbing osteoclasts are usually found on the IC near resorption pits (Howship's lacunae).

***Bone-Lining Cells.*** Most of the IC is covered with bone-lining cells. The cells are very flat (0.1 μm thick) and elongated. They have spindle-shaped nuclei. Bone-lining cells are believed to be derived from osteoblasts and/or osteoblast precursors that have ceased their activity or differentiation and flattened out on bone surfaces. The fate of bone-lining cells is an enigma. They can return to stem cells or preosteoblast pool and/or meet their demise.

***Osteocytes.*** The osteocytes are the bone cells with special location. They are housed in the lacunae of the mineralized matrix, as illustrated in Figure 11.7. Osteocytes derive from osteoblasts. As a bone surface grows outward certain osteoblasts are selected to become osteocytes. These osteoblasts stay behind as the mineralization front advances and, consequently, they become encased in the mineralized matrix. These new osteocytes maintain their gap junction contact with their previous neighboring cells (bone-lining cells or osteoblasts) in the IC by the extrusion of cellular processes. Since this process happens each time an osteoblast undergoes a change of phenotype and becomes an osteocyte, each osteocyte, enclosed within its mineralized lacuna, has several (perhaps as many as 80) cytoplasmic processes. These processes are approximately 15 μm long and are arrayed three dimensionally in a manner that permits them to interconnect with similar processes of up to 12 neighboring cells. These processes lie within canaliculi (Figure 11.7).

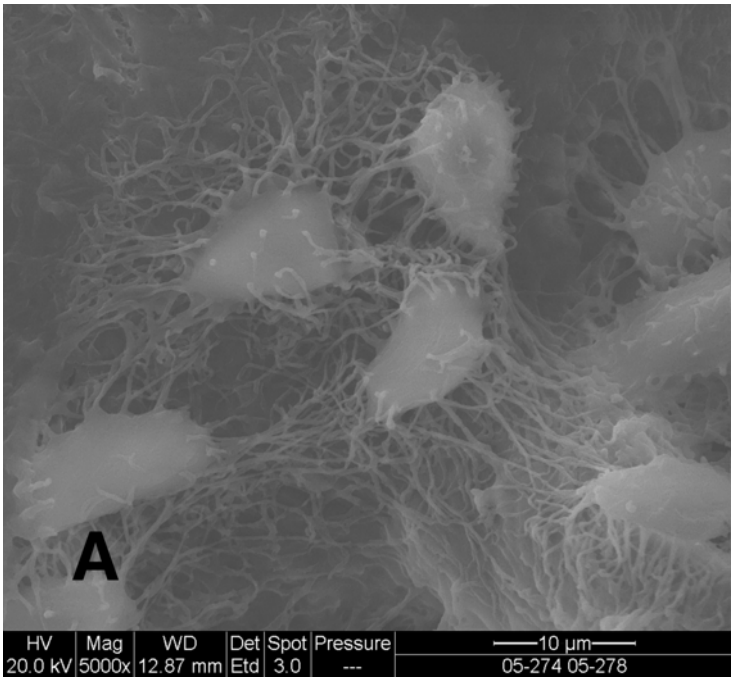



**Figure 11.9**. (a) Scanning electron micrograph (SEM) of the connected cellular network shows mouse osteocytes and their touching cell processes that form a connected cellular network. The line is 10 μm. SEM by Stephen D. Doty. (b) (opposite) This SEM of the connected lacunar-canalicular networks shows the replicas of lacunae and caniculi in situ in mandibular bone from a young subject, aged 22 years. The inset shows enlarged lacunae identified by a rectangle. This micrograph illustrates the interconnectivity of the space containing the connected cellular network. Reprinted with permission from Atkinson and Hallsworth (1983).

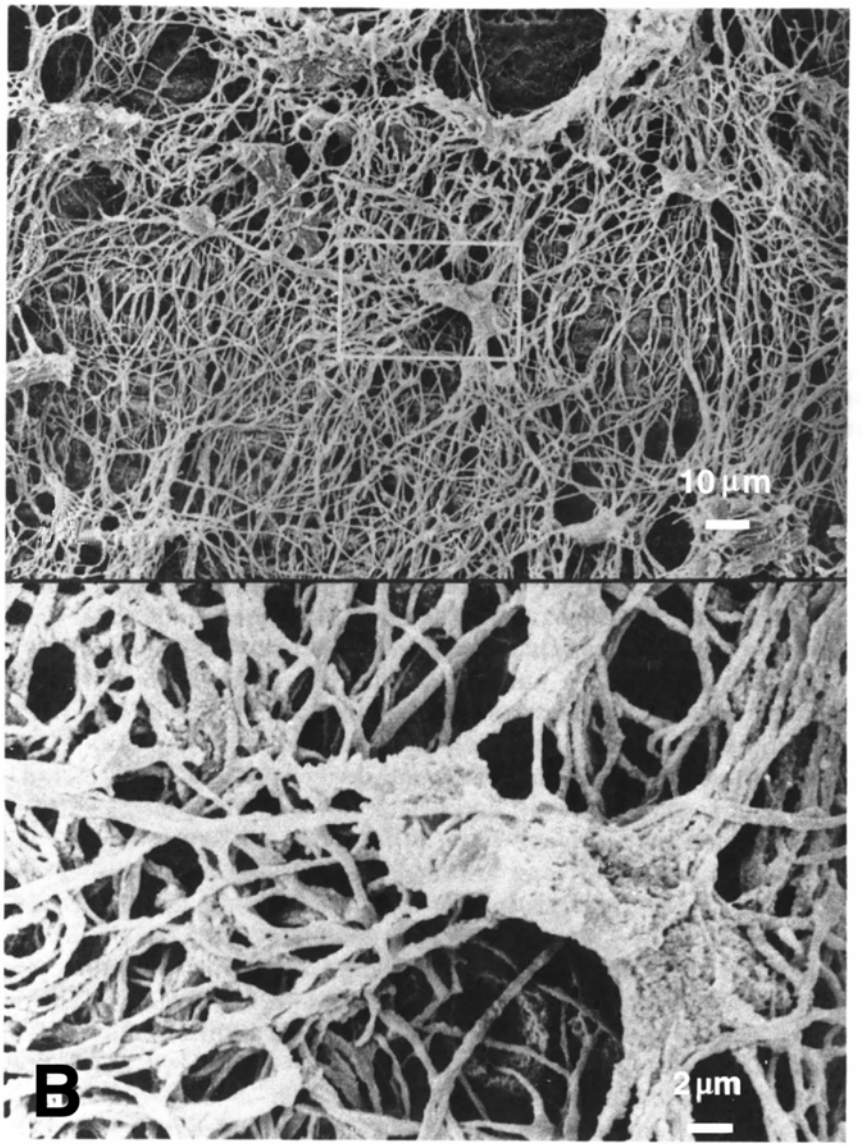



**Figure 11.9**, cont'd.

***Connected Cellular Network.*** The osteoblasts and osteocytes (i.e., all bone cells except the osteoclast lineage) are extensively interconnected by the cell processes of the osteocytes, forming a connected cellular network (Figure 11.9a). The interconnectivity of the connected cellular network is graphically illustrated by Figure 11.9b, which is a scanning electron micrograph showing the replicas of lacunae and canaliculi in situ in mandibular bone from a young subject aged 22 years. The inset shows enlarged lacunae identified by a rectangle. Gap junctions connect superficial osteocytes to periosteal and endosteal osteoblasts. All osteoblasts are similarly interconnected laterally on the IC; perpendicular to the IC, gap junctions connect

periosteal osteoblasts with preosteoblastic cells, and these, in turn, are similarly interconnected. Effectively, each connected cellular network is a true syncytium. In compact bone, canaliculi cross the cement lines that form the outer boundary of osteons. Thus, extensive communication exists between osteons and interstitial regions.

## 11.5. THE ELASTIC SYMMETRY OF CORTICAL BONE

A visual inspection of cortical bone tissue suggests that, like a tree, it has shape-intrinsic orthotropic elastic symmetry. The degree of textured anisotropy of bone tissue also varies with anatomic site (and from individual to individual); thus, some cortical bone tissue might be transversely isotropic, or even isotropic. The process for visual identification of the symmetry of cortical bone tissue parallels that described for plant and animal tissue in Chapter 5. As noted above, cortical bone tissue can be lamellar or osteonal (Haversian). If it is lamellar, then the suggestions of orthotropic symmetry are easy to see. The laminated structure of cortical bone tissue is illustrated in Figure 11.6. These laminates correspond to growth rings in trees or the layers in plant stem structure and in similar animal structures. If the cortical tissue is osteonal and the osteons have hexagonal packing, or totally random packing, then a transversely isotropic elastic symmetry is suggested. However, if the packing is neither hexagonal nor totally random, orthotropy is suggested.

Recalling that the selection of a reference coordinate system is of considerable significance for an anisotropic symmetry, a grain coordinate system is selected as described in Chapter 5. In colloquial speech, by the “grain of the wood” we mean the direction along the long axis of the wood fibers, fibers that are generally coincident with the long axis of the tree trunk. Here we define “bone grain” as a set of three orthogonal, ordered directions, the first one of which coincides with the local "colloquial" bone grain direction, which is locally the stiffest direction; the second and third directions are directions orthogonal to each other in the plane perpendicular to the "colloquial" grain direction and also represent directions of extrema in stiffness in the local region of the bone. These directions are the directions tangential and perpendicular to the circumferential lamellae in Figure 11.2. The existence of these three perpendicular planes of mirror symmetry, and no others, means that bone has orthotropic material symmetry. We refer to the symmetry coordinate system for an orthotropic material as the "grain" coordinate system. In the grain coordinate system the strain–stress relations may be written in the form of (7.27).

These drained technical elastic constants consist of three Young's moduli, $E_1$, $E_2$, and $E_3$, three shear moduli, $G_{23}$, $G_{13}$, and $G_{12}$, and six Poisson's ratios, $\nu_{12}$, $\nu_{13}$, $\nu_{21}$, $\nu_{23}$, $\nu_{31}$, and $\nu_{32}$ (only three of which are independent). The Young's moduli are denoted by $E_i$, $i = 1, 2, 3$, the shear moduli by $G_{ij}$, and Poisson's ratios by $\nu_{ij}$ where $i, j = 1, 2, 3$, and $i$ is not equal to $j$. Although this is a total of twelve symbols, there are only nine distinct technical elastic constants because of the three relationships (7.28): $\nu_{23}/E_2 = \nu_{32}/E_3$, $\nu_{13}/E_1 = \nu_{31}/E_3$, and $\nu_{12}/E_1 = \nu_{21}/E_2$. In the special case of transverse isotropy, the nine independent elastic constants reduce to five. If $x_3$ is the axis parallel to the long axis of the bone, the elastic constants of eq. (7.27) reduce to those for a transversely isotropic material, $E_1 = E_2$, $\nu_{12} = \nu_{21}$, $\nu_{32} = \nu_{31} = \nu_{13} = \nu_{23}$, $G_{23} = G_{31}$, and $2G_{12} = E_1/(1 + \nu_{12})$. In the case of isotropy all the subscripts on the drained technical elastic constants may be dropped and $2G = E/(1 + \nu)$, so there are only two distinct drained isotropic technical elastic constants.

There are a number of reports of the measurement of the orthotropic (ORTH) or transversely isotropic (TI) drained elastic constants of human cortical bone. The technical constants measured by various investigators are given in Table 11.2. In making their measurements some

**Table 11.2**. Drained Technical Constants for Human Cortical Bone

| | Investigators | | | |
|---|---|---|---|---|
| | Reilly, Burstein, & Frankel (1974) | Yoon & Katz (1976) | Knets & Malmeisters (1977) | Ashman, Cowin, Van Buskirk, & Rice (1984) |
| Bone | Femur | Femur | Tibia | Femur |
| Symmetry | TI | TI | ORTH | ORTH |
| Method | M | U | M | U |
| $E_1$ (GPa) | 11.5 | 18.8 | 6.91 | 12.0 |
| $E_2$ (GPa) | 11.5 | 18.8 | 8.51 | 13.4 |
| $E_2$ (GPa) | 17.0 | 27.4 | 18.4 | 20.0 |
| $G_{12}$ (GPa) | 3.6a | 7.17 | 2.41 | 4.53 |
| $G_{13}$ (GPa) | 3.3 | 8.71 | 3.56 | 5.61 |
| $G_{23}$ (GPa) | 3.3 | 8.71 | 4.91 | 6.23 |
| $\nu_{12}$ | 0.58 | 0.312 | 0.49 | 0.376 |
| $\nu_{13}$ | 0.31[a] | 0.193 | 0.12 | 0.222 |
| $\nu_{13}$ | 0.31[a] | 0.193 | 0.14 | 0.235 |
| $\nu_{21}$ | 0.58 | 0.312 | 0.62 | 0.422 |
| $\nu_{31}$ | 0.46 | 0.281 | 0.32 | 0.371 |
| $\nu_{32}$ | 0.46 | 0.281 | 0.31 | 0.350 |

Please note that the 3 direction is coincident with the long axis of the bone; the 1 and 2 directions are radial and circumferential, respectively. Method U is ultrasound and method M standard mechanical testing. Superscript *a* indicates a quantity not measured.

investigations assumed cortical bone to be transversely isotropic (TI) and others assumed it to be an orthotropic (ORTH) material. The different methods of measurement, ultrasonic and mechanical, of the elastic constants are indicated in Table 11.2. When ultrasound is employed, various velocities are measured from which the elastic coefficients are determined. The technical constants are then found by matrix inversion. Are the drained elastic properties of cortical bone better represented as transversely isotropic (TI) or as orthotropic (ORTH)? In one study of the elastic properties of the human tibia the following statistically significant inequalities were noted: $E_3 > E_2 > E_1$, $G_{23} > G_{13} > G_{12}$, and $\nu_{21} > \nu_{12} > \nu_{31} > \nu_{23} > \nu_{13}$. An examination of the results in Table 11.2 reveals that, in general, these inequalities are borne out. This suggests that the usual assumption of TI for bone is not sufficiently general. The choice of material symmetry for an elastic model of bone depends to a large extent on the intended application of the elastic model by the investigator. An example indicates that the stress analysis of a human femur is adequately served with a transversely isotropic elastic model. The data presented in Table 11.2 indicate that the percentage difference between the elastic constants obtained using the assumption of ORTH and those obtained using the assumption of TI are quite small and are unlikely to have a significant effect on the stress analysis of a bone. Thus, if the intended use of the elastic constants is for stress analysis of a particular bone, the assumption of the greater symmetry of TI can be easily justified. When one is considering the physiological behavior of bone tissue as a composite material, the difference in the assumption of ORTH or TI might be significant. As an example, consider the suggestion that the elastic symmetry of

bone may be linked to the circulation of blood in the bone. Although there is little difference in the constants determined using the assumptions of ORTH and TI, the difference is always consistent in that the stiffness in the circumferential direction is always greater than the stiffness in the radial direction. If bone were transversely isotropic, these two elastic constants would be the same. As noted above, blood normally flows from the medullary canal to the periosteum, that is, in an outward radial direction. This suggests that the lower stiffness in the radial direction is associated with the greater permeability in that direction. There is a significantly smaller need for blood flow in the circumferential direction, so the permeability is less and the stiffness higher. Thus, there appears to be at least one physiological reason for the cortical tissue of long bones to be orthotropic rather than transversely isotropic.

The variation in the elastic properties of whole bones with anatomical site has been measured. Variations on the order of 25% for the nine independent orthotropic elastic constants in six zones around the circumference of the mid-diaphysis of the human tibia have been reported. The anterior half of the tibia has been found to be more stiff than the posterior region and it has been observed that the anterior portion of the tibia is subjected to large tensile stresses. Variations of about half that along the length and around the circumference for both human and canine bone have also been reported. It is noteworthy that human femoral bone was found to be most stiff in the mid-shaft region and in the lateral and medial quadrants and to observe that the bending stress in the femur is greatest in precisely those regions with the greatest stiffness.

## 11.6. THE POROELASTIC MODEL FOR CORTICAL BONE

A poroelastic model is employed for cortical bone tissue in order to describe the mechanical properties of bone tissue in a way that acknowledges the detailed bone microstructure described above. For example, the fluid-filled porosities of bone may affect the elastic response of bone to applied loading by sustaining pressures for different time periods. In Chapter 9 it was noted that there are three sets of elastic constants of interest in a poroelastic medium — the drained, the undrained, and matrix elastic constants. In the drained case the fluid pressure in the pores is zero; this is achieved by draining all the pores before the test or doing the test so slowly that the pores drain from a negligible fluid pressure. In the undrained case the pores that permit fluid to exit the test specimen are sealed; thus, pressure will build in the specimen when it is loaded by other forces, but the pressure cannot cause the fluid to move out of the specimen. The matrix elastic constants are the elastic constants of the material containing no pores. The representative volume element (RVE) for cortical bone may be taken as a small cube that is large enough compared to the size of the largest pores so that it may be treated as homogeneous, and at the same time small enough, compared to the scale of the macroscopic phenomena in which we are interested, so that it may be considered as infinitesimal in the mathematical treatment. In this section we consider the drained elastic properties of cortical bone tissue.

The drained elastic response of bone to applied loading is altered by sustaining pressures in the fluids, which could last for different time periods depending upon the particular porosity under consideration. In the collagen–apatite porosity (PCA) the fluid is bound to the structure and does not move under physiological conditions; there is a bone fluid pressure, but its effect is incorporated in the drained elastic constants. In the porosity of the inter-trabecular space (PIT), due to the fact that this is a porosity with very large pores, the fluid (bone marrow and fat) pressure relaxes faster than any physiological loading rise time and so is not considered to have an effect on the physiological elastic stress–strain behavior. However, for the vascular porosity (PV) and the lacunar-canalicular porosity (PLC), the question of significant pore fluid

pressure becomes less clear cut than it was for the PCA and the PIT. Defining an impact load as an impulse stress history with a short (but finite) stress rise time and a short descent time, impact loads can be characterized by their time duration. For football players, impact time duration ranges from 1 to 150 ms, with most lasting 2 ms (Reid and Reid, 1984). For car accidents, the impact time is also on the order of several to tens of milliseconds. Macaulay (1987) has summarized the injury thresholds of the human body under impact loading, and noted that impact duration times were usually larger than 1 ms. Thus, even under accidental impact loading, the stress rise time never approaches the PV relaxation time of 1.36 μs given in Table 11.3. However, since the pore fluid pressure relaxation time for the PLC is about 4.9 ms (also from Table 11.3), the effect of pore fluid pressure in this porosity is attainable under impact loading. These arguments build a case for consideration of the effect of pore fluid pressure on the physiological elastic stress–strain relation only in the case of loadings with rapid rise times. The need to include the effects of pore fluid pressure in the physiological elastic stress–strain relation also stems, however, from the fact that mechanical loading causes gradients in the volumetric elastic strains within the tissue, and these gradients in the volumetric elastic strains give rise to pore fluid pressure gradients that cause the pore fluid to flow. It has been suggested that the flow of the pore fluid is related to the mechanosensation of bone, to the mineralization of bone, and to nutrition of the osteocytes. This suggestion will be explored later in this chapter, as these are the more significant reasons for the inclusion of pore fluid pressure in the physiological elastic stress–strain relation for cortical bone.

**Table 11.3**. Summary of Poroelastic Constants Related to the Pore Water Pressure Relaxation Times for the two Porosities of Interest, the PV, and the PLC

| Porosity level | $v_0$ | $k$ | μ | $L$ | $c$ | $\tau_R$ |
|---|---|---|---|---|---|---|
| PV | 0.04 | $6.36 \times 10^{-13}$ m$^2$ | $10^{-3}$ Pa s | 1 cm | 18.4 m$^2$/s | 1.36 μs |
| PLC | 0.05 | $1.47 \times 10^{-20}$ m$^2$ | $10^{-3}$ Pa s | 100 μm | $5.1 \times 10^{-7}$ m$^2$/s | 4.9 ms |

Here $v_0$ is the porosity, $k$ is the specific permeability, μ is the fluid viscosity, $L$ is the characteristic length associated with this porosity (in the case of the lacunar-canalicular it is the radius of an osteon, 100 μm, and in the case of the PV it is the bone cortical thickness, which would be on the order of 1 cm in a large animal, but smaller in a smaller animal), $c$ is the pore fluid pressure diffusion coefficient, and $\tau_R$ is the characteristic relaxation time of the pore fluid pressure in that porosity. Reprinted with permission from Zhang et al. (1998).

In order to apply poroelastic theory to bone, the values of the parameters appearing in the theory must be known from measurement or estimated from the drained constants in the previous section. The values of all the anisotropic parameters have not yet been measured or estimated, but the values for all the isotropic parameters have. These values for the PV and PLC of bone will be summarized here along with, for comparison, those for fluid-saturated porous rocks. The bulk modulus $K^f$ for salt water is 2.3 Gpa, and it is assumed that bone fluid has this bulk modulus. Estimates of the values of the porosity and the permeability associated with the two distinct porosities of bone of interest, the PV and PLC, are given in Table 11.1a,b. The permeability associated with the PV and PLC is dominated by vascular permeability. A summary of calculated (as opposed to measured) poroelastic constants related to the pore water pressure relaxation times for the two porosities of interest, the PV and PLC, is given in Table 11.3. Of particular interest is the large difference in magnitude between the values of parame-

ters associated with the two porosities. The three orders of magnitude difference in the relaxation times of these two porosities, 1.36 μs for the PV and 4.9 ms for the PLC, indicates that a pressure peak in the PV will relax 1000 times faster than a pressure peak in the PLC. The difference in the relaxation times reflects the difference in the specific permeabilities of these two porosities, or equivalently, the difference in pore fluid pressure diffusion coefficient $c$ of these two porosities, as shown in Table 11.3.

**Table 11.4**. Summary of Poroelastic Constants for the PLC and for Various Rocks

| Property (units, if any) | Bone (PLC) | Marble | Granites | Sandstones |
|---|---|---|---|---|
| $G$ (GPa) — shear modulus | 5.5 | 24 | 15–19 | 4.2–13 |
| $\nu^d$ — drained Poisson ratio | 0.32 | 0.25 | 0.25–0.27 | 0.12–0.20 |
| $\nu^u$ — undrained Poisson ratio | 0.33 | 0.27 | 0.30–0.34 | 0.28–0.33 |
| $K^d$ (GPa) — drained bulk modulus | 12 | 40 | 25–35 | 4.6–13 |
| $K^u$ (GPa) — undrained bulk modulus | 13 | 44 | 41–42 | 1.3–30 |
| $B$ — compressibility coefficient | 0.40 | 0.51 | 0.58–0.85 | 0.50–0.88 |
| $K^m$ (GPa) — bulk modulus of the matrix | 14 | 50 | 45 | 31–42 |
| $\alpha$ — effective stress coefficient | 0.14 | 0.19 | 0.27–0.47 | 0.65–0.85 |
| $\phi$ — porosity | 0.05 | 0.02 | 0.01–0.02 | 0.02–0.26 |
| $c$ ($m^2\ s^{-1}$) x $10^6$ — pore fluid pressure diffusion coefficient | 0.51 | 13 | 7.0–22 | 5400–1.6 x $10^6$ |
| $k$ ($m^2$) x $10^{20}$ — specific permeability | 0.22–1.5 | 10 | 10–40 | 20000–8.0 x $10^7$ |

The data on granites are the range for two granites, and the data on sandstones indicate the range for six sandstones. The data are from Detournay and Cheng (1993) and Zhang et al. (1998), where the details on the specific rock data are given.

The isotropic elastic constants of the bone tissue matrix material are $K^m$ = 13.92 GPa for the bulk modulus and $G^m$ = 5.50 GPa for the shear modulus. These values were estimated by bounding the effective isotropic elastic constants of an anisotropic elastic material. These effective isotropic elastic moduli are equivalent to a Young's modulus of $E^m$ = 14.58 GPa and a Poisson's ratio of $\nu^m$ = 0.325. These and the other parameters associated with cortical bone are listed in Table 11.4 along with the values of the same parameters for certain porous rocks. It is interesting to compare the parameter values for the PLC of bone tissue with the parameter values for fluid-saturated porous rocks. The elastic properties of bone and fluid-saturated porous rocks are quite similar. The pore-related fluid diffusivities of the PLC of bone tissue are close to those of granite and marble, as may be seen from Table 11.4. Sandstones are much too porous to be compared with the PLC of bone. Although the material properties associated with the PLC of bone and those associated with fluid-saturated porous granite and marble are similar, significant differences in the responses of these materials can be expected because the characteristic lengths associated with the boundary-value problems for the two different porous materials differ by four to seven orders of magnitude. The characteristic length associated with a bone boundary-value problem is on the order of the radius of an osteon, 100 μm, or the bone cortical thickness, 1 cm, while that associated with porous rocks could range up to kilometers.

It is important to note the large difference between bulk modulus $K^m$ of the bone tissue matrix material (14 GPa) and bulk modulus $K^f$ of bone water (2.3 GPa); the solid bone matrix has a bulk modulus six times that of water. This leads to a Skempton compressibility coefficient, $S$,

defined by (9.40), of 0.40 and to considerable pressure differences between the solid bone matrix and the bone pore fluid. In the case of soft tissues the bulk moduli of the soft tissue matrix and the pore water are almost the same and compressibility coefficient $B$ is about 1. Recall that $S$ has a range from 0 to 1. Thus, for soft tissues the incompressibility assumptions of the fluid and solid constituents are a reasonable approximation and $S = 1$. However, for bone, the incompressibility assumption is inconsistent with the large differences in compressibility of the constituents and, if made, could lead to large errors in the determination of the bone fluid pressures.

The small strain, compressible poroelastic model is an appropriate model for the study of bone fluid movement and bone fluid pressures for the following reasons:

1. Infinitesimal strain theory is appropriate for bone. Since the normal, physiological strain that bone experiences seldom ranges above 0.4%, infinitesimal strain theory is adequate.
2. Although bone has four levels of porosity, only two of them, the PV and the PLC, are considered to be significant with respect to bone fluid movement. These two porosities have considerably different properties, particularly pore fluid pressure relaxation times. Poroelastic models can be constructed for each of these porosities and for the interaction of the bone fluid in these porosities (Tables 11.1a,b and 11.3).
3. Based on existing evidence, it is reasonable to conclude that the ILC is relatively impermeable and that the IC has a small hydraulic resistance compared to that in the PLC. Thus, on the ILC border between the PV and PLC, we need make no assumption of a barrier to fluid flow.
4. The incompressibility assumption of the fluid and solid phases, reasonable for soft tissues, is inappropriate for mineralized bone because the bulk modulus of the bone matrix is six times that of the pore fluid. The incompressibility assumption may be acceptable for embryonic or immature bone because the bulk modulus difference is not so great as it is in maturing and mature bone. It has not been incorporated in the presentation above.

These considerations suggest the use of a two-porosity poroelastic model for bone fluid; such models have been employed before in geomechanics. The suggested two-porosity model would consider the bone fluid pressure in the PV to be normally equal to the blood pressure, and the bone fluid pressure in the PLC would be determined by the poroelastic equations using the values of parameters given above. If the domain of the poroelastic boundary-value problem were taken to be the domain bounded by the IC, then the single porosity poroelastic model associated with the PLC could be employed, along with boundary conditions that set the bone fluid pressure equal to the blood pressure on the boundary. Using the two-porosity model, Zhang et al. (1998) estimated the maximum pore fluid pressures due to uniaxial compression for both the PV and PLC of live cortical bone. Neglecting inertial effects, they estimated that the peak pore water pressure would be 19% of the applied axial stress in the PV and 12% of the applied axial stress in the PLC for step loading. The two-porosity model also predicts a slight hydraulic stiffening of the bulk modulus due to longer draining time of the PLC. The undrained bulk modulus is 6% higher than the drained bulk modulus in this case. One should keep in mind, however, that the convected transport of bone fluid due to whole bone mechanical loading is thought to be important for bone mineralization, osteocyte nutrition, and the bone mechanosensory system. Thus, the whole bone mechanical loading is thought to have a major influence on bone fluid motion, but bone fluid is thought to have only a small effect on the resistance of the whole bone to mechanical loading.

**Problems**

11.6.1. Calculate spring constant $k_2$ of a specimen of human cortical bone that is a 7 mm cube. The direction of interest for the spring constant is the $x_2$ axis, and the other two edges are parallel to the other two cortical grain directions. Use the orthotropic elastic constant values determined by ultrasonic methods.

11.6.2. Calculate torsional spring constant $w_{23}$ of a specimen of human cortical bone that is 4 mm long and 1 mm in diameter. The long direction is parallel to the $x_1$ axis. Use the orthotropic elastic constant values determined by ultrasonic methods.

## 11.7. ELECTROKINETIC EFFECTS IN BONE

Electrodes placed on two different bone surfaces will measure a difference in voltage when wet bones are deformed quasi-statically or dynamically. These voltages are called strain-generated potentials (SGPs). SGPs in wet bone are now recognized as dominantly electrokinetic phenomena explained by an extension of poroelasticity to include the effects of charges convected by the bone fluid flow. From an experimental viewpoint SGPs are a significant technique for investigation of the poroelastic behavior of bone. The mechanism for the creation of SGPs is illustrated in Figure 11.10. The extracellular bone matrix is negatively charged due to negative fixed charges on carbohydrates and proteins. Thus, a fluid electrolyte bounded by the extracellular matrix, or a fiber in a bone fluid channel, will have a diffuse double layer of

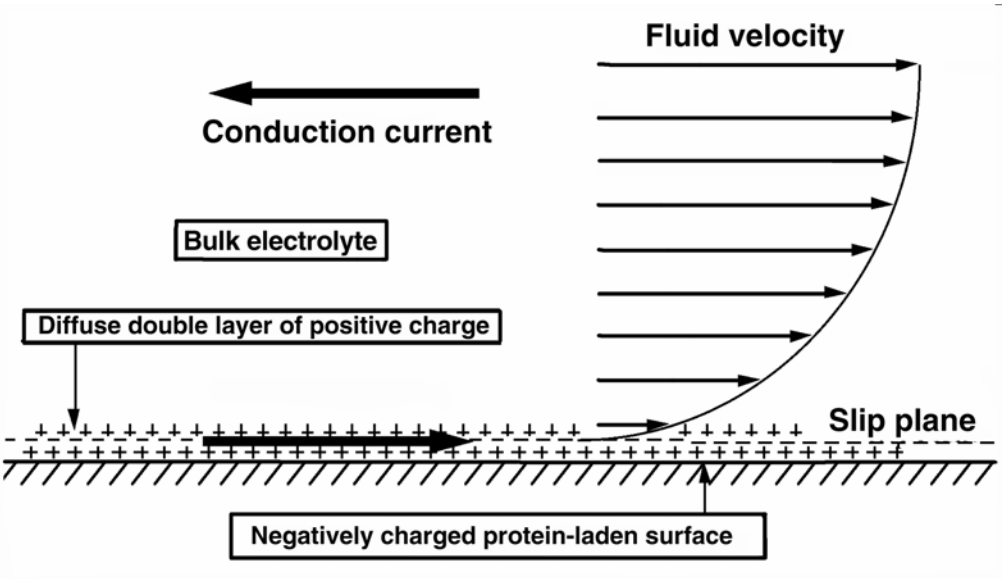



**Figure 11.10**. Strain-generated potentials (SGPs) in bone fluid channels. The source of SGPs stems from the fact that the extracellular bone matrix is negatively charged due to negative fixed charges on carbohydrates and proteins; thus, a fluid electrolyte bounded by the extracellular matrix will have a diffuse double layer of positive charges (see also Figure 11.11). When the fluid moves, the excess positive charge is convected, thereby developing streaming currents and streaming potentials. A conduction current is thought to balance the convection current. The bulk electrolyte is neutral with respect to charge. The fluid motion is caused by the pore fluid pressure gradients induced by the deformation of the extracellular matrix due to whole bone mechanical loading.

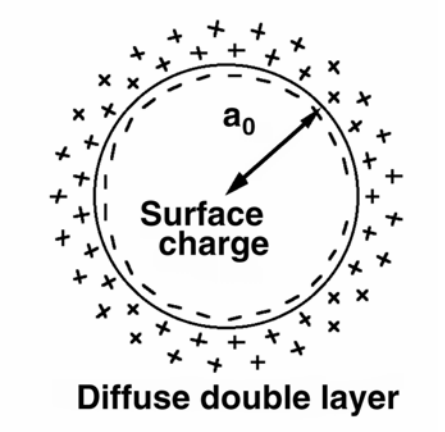



**Figure 11.11**. The diffusive double layer around a cylindrical structure such as a fiber or a strand of a protein.

positive charges (see Figure 11.11). When the fluid moves, the excess positive charge is convected, thereby developing streaming currents and streaming potentials. The fluid motion is caused by the pore fluid pressure gradients induced by the deformation of the extracellular matrix due to whole bone mechanical loading, and thus the SGPs are poroelastically driven. The extension of poroelasticity to include a theory for strain-generated potentials is due to Pollack and coworkers. The extension begins with fluid movement in the bone channels convecting the charge accumulated in the diffuse double layer of positive charges. The charge distribution in the channel is determined from the linear Poisson-Boltzmann equation. The electrical potential attenuates exponentially with distance into the fluid, perpendicular to the charged surface, divided by $\lambda$, where $\lambda$ is the Debye length characterizing the diffuse double layer. The typical $\lambda$ for normal physiological saline is 1 nm or less, and hence the decay of the potential with respect to distance from the surface is very rapid. The solution of the Poisson-Boltzmann equation yields the electrical potential as a function of the distance from the surface; this is illustrated in Figure 11.12. The diffuse region of the potential is described in terms of the Debye length, which decreases with increasing ion concentration. The material between the surface and the slip plane is material not involved in the flow; only at the slip plane does the material flow. The value of the potential at the slip plane is called the zeta potential. At the lowest ion concentration, $C_1$, a negative zeta potential exists at the intersection of the slip plane and the electric potential of the double layer. As the fluid ion concentration is increased, the Debye length decreases and the zeta potential also decreases. In the presence of adsorbed charged layers (as illustrated in Figure 11.12), it is possible for the zeta potential to change sign with increasing ion concentration if the ion adsorption density also increases with concentration. Such sign reversals in zeta potentials have been reported in minerals similar to calcium hydroxyapatite.

The total streaming current vector per unit area, **j**, passing through all the channels of a material due to the pore pressure-driven axial flow can be obtained by multiplying the charge density by the local velocity field in the channel and integrating this result over the cross-section of the channel. Total streaming current vector **j** is a flux vector similar to fluid mass flow rate vector **q**. Linear irreversible thermodynamics provides a structure for relating these fluxes. For small departures from equilibrium in isotropic materials total streaming current

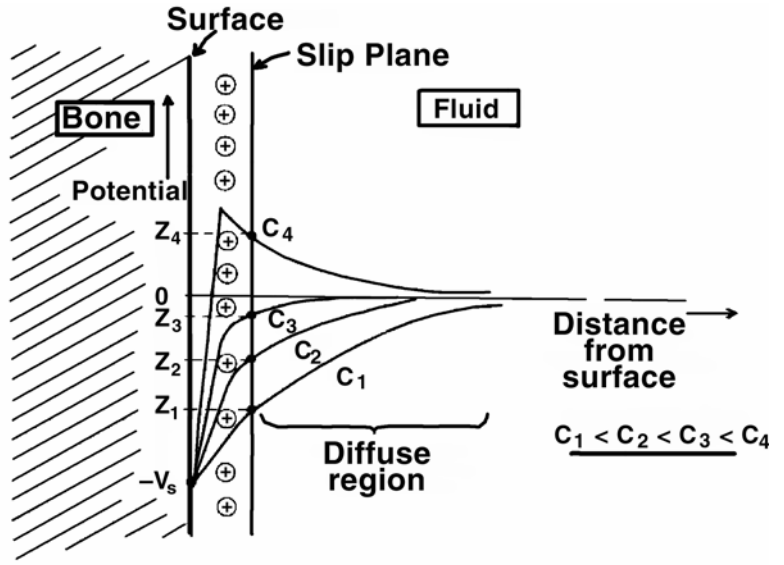



**Figure 11.12**. Plot of potential vs. distance for various concentrations of ions, $C_1$, $C_2$, $C_3$, and $C_4$ in the presence of an adsorbed layer of ions whose density increases with concentration. The surface potential is $-V_s$, and the zeta potentials decrease in amplitude with increasing concentration and change sign, from negative to positive, at sufficiently high concentration, $C_4$. Reprinted with permission from Pollack et al. (1984).

vector **j** and fluid mass flow rate vector **q** are related to the gradients of pressure $p$ and voltage $V$ by

$$\mathbf{q} = -(k/\mu)\,\nabla p + c_x\,\nabla V \quad \text{and} \quad \mathbf{j} = c_x\,\nabla p - \Omega\,\nabla V, \tag{11.1}$$

where coefficients $k/\mu$, $c_x$, and $\Omega$ are material properties. These equations state that total streaming current vector **j** and fluid mass flow rate vector **q** are linearly dependent upon the voltage gradient, $\nabla V$, as well as the pressure gradient, $\nabla p$. When $\nabla V = 0$ the first equation of (11.1) reduces to Darcy's law (9.20) (i.e., $\mathbf{q} = -(k/\mu)\,\nabla p$). When $\nabla p = 0$ the second equation of (11.1) reduces to Ohm's law in its field version ($\mathbf{j} = -\Omega\,\nabla V$). The two cross-flux coefficients, $c_x$, are equal in the two equations of (11.1) by the Onsager reciprocity theorem. The significant and useful connection between pressure and voltage arises from the recognition that the convective and conductive currents are equal and opposite (Figure 11.10), so that there is no net current flow, $\mathbf{j} = 0$; thus, from the second of (11.1):

$$\nabla p = (\Omega / c_x)\,\nabla V. \tag{11.2}$$

Integration of this result yields the fact that the pressure must be proportional to the voltage:

$$\mathrm{p} = (\Omega / \mathrm{c_x})\,V + \text{a function of time.} \tag{11.3}$$

This means that when a potential difference in bone is measured in connection with an electrokinetic event the potential difference is proportional to a pore pressure difference between the same two points used to measure the potential difference. Since electrodes are much smaller than pore pressure probes, this theory provides a useful tool for probing the poroelastic response of bone.

**Example 11.7.1**

How does the voltage potential in the consolidation problem of Example 9.10.2 vary if the porous medium is drained? Recall that in Example 9.10.2 a layer of poroelastic material resting on a stiff impermeable base is subjected to constant surface loading $T_{33} = -P(t) = -p_o h(t)$. The layer, illustrated in Figure 9.1, is in the $x_1$, $x_2$ plane and the $x_3$ positive coordinate direction is downward. The conditions for the drainage of the layer are described in Example 9.10.1. Determine the formula for the voltage potential, $V(x_3, t)$, associated with the consolidation process.

**Solution**: Since, from (11.3), the voltage is directly proportional to pressure,

$$V(x_3,t) = \frac{c_x}{\Omega}\{p(x_3,t) - f(t)\},$$

it follows from the pressure solution in Example 9.10.2 that

$$V(x_3,t) = \frac{c_x}{\Omega}\ \frac{(\nu^u - \nu)}{(1-2\nu)\alpha(1-\nu^u)} p_o h(t) + p^*(x_3,t) - f(t)\quad ,$$

where $p^*$ is given by

$$p^* = p_o \frac{(\nu^u - \nu)}{(1-2\nu)\alpha(1-\nu^u)} \left\{ \sum_{m=0}^{\infty} \frac{4}{(1+2m)\pi} \sin\left( \frac{(1+2m)\pi x_3}{2L} \right) e^{-\frac{(1+2m)^2\pi^2 ct}{4L^2}} \right\}.$$

As a demonstration of the effectiveness of this theory and of using experimental SGP measurements as a tool for exploring bone microstructure and permeability, the computational two-porosity poroelastic model constructed by Wang et al. (1999) to illustrate an SGP effect noted in the experiments of Starkebaum et al. (1979) is described. Starkebaum et al. (1979) subjected a small bone specimen to 1-Hz oscillatory bending and measured the voltage distribution as one microelectrode was moved across a surface of exposed bone osteonal microstructure, while viewing through a microscope (see Figure 11.13). Starkebaum et al. (1979) showed that the value of the potential rose steeply from the osteonal lumen to a peak at the cement line and then descended to the lumen of the next osteon on the compression side of the specimen in bending (see Figure 11.14). The potential profile is thus a cusp. It was found that local voltage gradients surrounding the osteonal canal were as much as thirty times the voltage gradient across the entire bone specimen. The steep cusps in the potential difference were observed around osteonal canals, with the cusps opening upward or downward depending upon whether the osteon was currently experiencing the tension or the compression phase of the bending. Due to the proportionality between the pore pressure gradient and the SGP gradient, eq. (11.2), this means that both the variation in pore pressure and the SGP on the scale of the radius of an osteon is much greater than the variation of these fields on the specimen scale. It also illustrates the effectiveness of the microelectrode SGP measurements in documenting the local pore microstructure of bone.

In the two-porosity model of Wang et al. (1999) the osteons were arranged periodically with six adjacent osteons across the specimen thickness. (Figure 11.15 is a schematic illustration of the model). In Figure 11.15 the PV is represented by the osteonal lumens (Haversian canals) and all the other domain of the specimen is assumed to have only the PLC. The pressure in the PV is taken to be the blood pressure that is much less than the pore pressure and is assumed to be zero; the pore pressure in the PLC is evaluated using poroelasticity theory. In

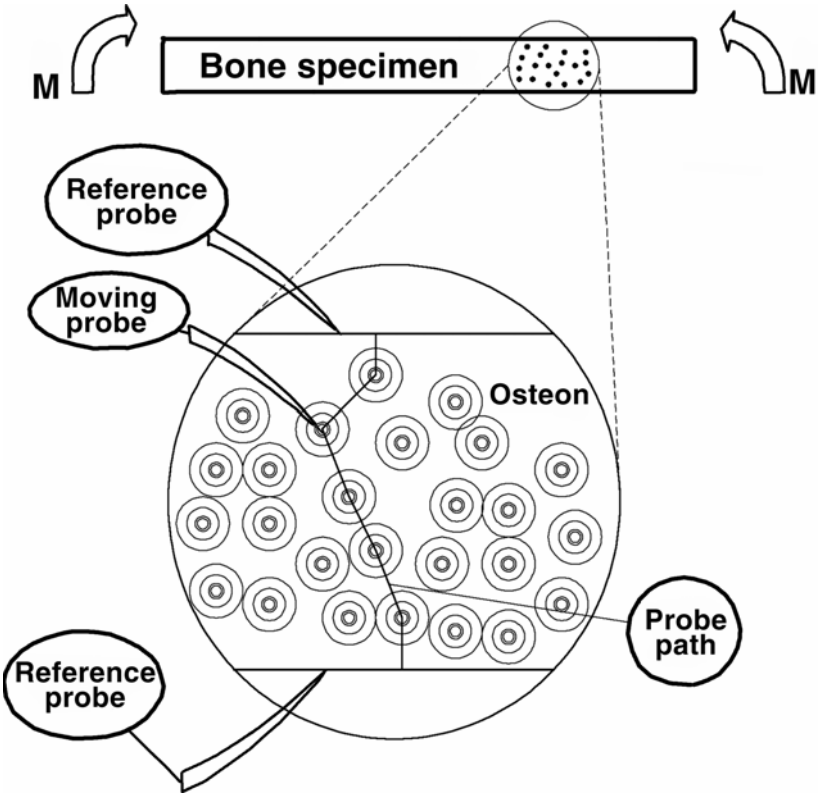



**Figure 11.13**. Cartoon of the experiment of Starkebaum et al. 1979. At the top is a plate-shaped cortical bone specimen subjected to 1-Hz oscillatory bending. A section of the thin specimen is enlarged to show the view through the microscope. Note the exposed bone osteonal microstructure. Reference voltage microprobes are placed at either surface and a moving microprobe is manipulated under the microscope. The voltage distribution is measured as the moving microelectrode traces the indicated path across the surface as the bone specimen is bent back and forth with the 1-Hz oscillatory bending. Reprinted with permission from Wang et al. (1999).

this model the test microelectrode is envisioned as moving from one side of the idealized specimen in Figure 11.15 to the other, imitating the experiment illustrated in Figures 11.12 or 11.13. The voltage difference measured as this test line is traversed is illustrated schematically in Figure 11.16. The voltage difference vanishes when the osteonal lumen is reached, giving very inhomogeneous profiles of the local pressure or voltage distribution in each osteon. These results are qualitatively consistent with the measured osteonal SGP spatial profiles reported in Starkebaum et al. (1979) and illustrated in Figure 11.14. The model of Wang et al. (1999) demonstrates that the consideration of the two porosities is necessary to obtain correct local bone fluid flow patterns. Wang et al. (1999) also considered the variation of these results as a function of the frequency of the applied bending loading when the permeability of the cement line and the size of the osteonal lumen are varied. Two relaxation systems are found within a two-porosity bone specimen: one associated with the PV, through which the pore pressure relaxes when the loading frequency is lower than 20 Hz, and one associated with the PLC, through which the pore pressure cannot relax when the loading frequency is higher than 1 Hz (if no flow is permitted across the external boundaries). This suggests that the PV is the dominant relaxation system for bone fluid flow during mechanical loading.

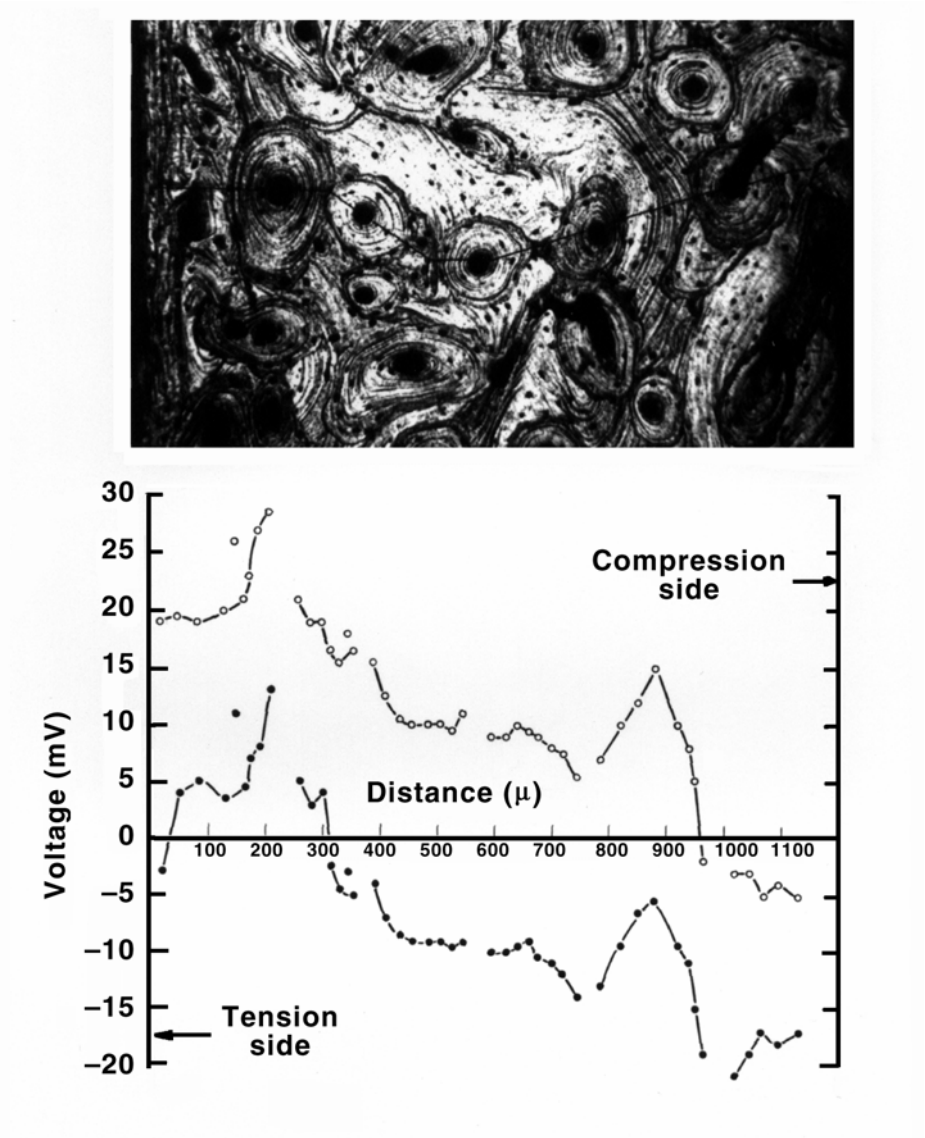



**Figure 11.14**. Experimental results of Starkebaum et al. 1979. At the top is a poor reproduction of the bone specimen in which, if one studies carefully, one can see straight lines indicating the path of the microprobe across the specimen. At the bottom is a plot of the voltage measurement as a function of the distance along the path across the specimen. Note that the value of the potential rises steeply from the osteonal lumen to a peak at the cement line and then descends to the lumen of the next osteon on the tension side of the specimen in bending. The potential profile is thus a cusp. The steep cusps in the potential difference were observed around osteonal canals, with the cusps opening upward or downward depending on whether the osteon was currently experiencing the tension or the compression phase of the bending. Reprinted with permission from Starkebaum et al. (1979).

Poroelasticity and electrokinetics can be used to explain strain-generated potentials in wet bone. It is noted that strain-generated potentials can be used as an effective tool in the experimental study of local bone fluid flow, and that the knowledge of this technique will contribute

to the answers of a number of questions concerning bone mineralization, osteocyte nutrition, and the bone mechanosensory system.

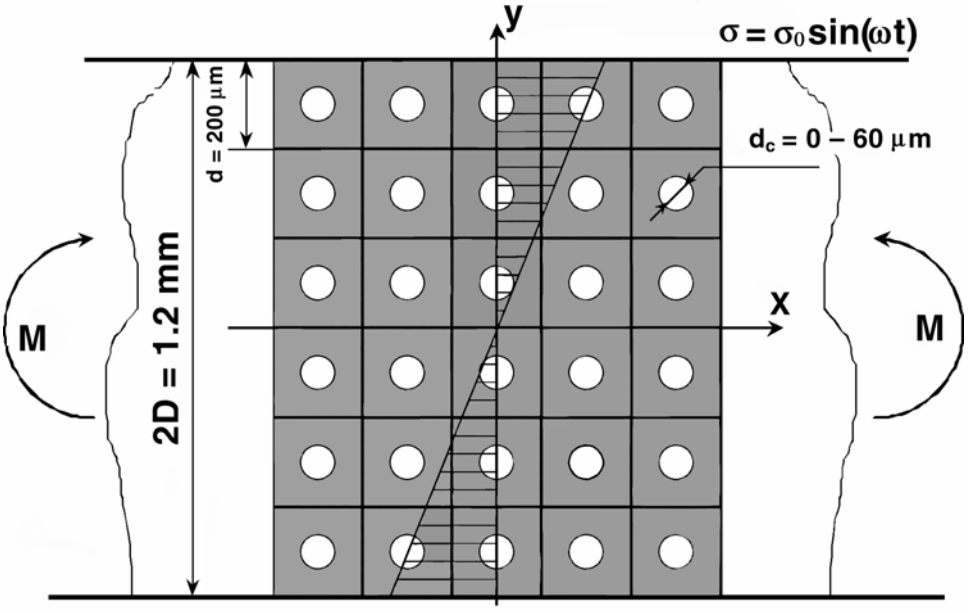



**Figure 11.15**. The two-porosity model of Wang et al. 1999. The osteons are arranged periodically with six adjacent osteons across the specimen thickness. The PV is represented by the osteonal lumens (the circles), and all the other domain of the specimen (the gray area outside the circles) is assumed to have only the PLC. Reprinted with permission from Wang et al. (1999).

The anatomical site in bone tissue that contains the fluid source of the experimentally observed SGPs is not currrently agreed upon, but Cowin et al. (1995) argued that it should be the PLC. Salzstein and Pollack (1987) concluded that the site of SGP creation was the PCA, because small pores of approximately 16-nm radius were consistent with their experimental data if a poroelastic-electrokinetic model with unobstructed and connected circular pores was assumed.

## 11.8. CORTICAL BONE STRENGTH

Strength is usually the first of the mechanical properties of a material to be determined; bone is no exception. However, the results of the numerous strength tests are varied for a number of reasons. First, a variety of specimens prepared in different ways — wet, dry, embalmed — have been used for testing. Second, the strength of a bone is heterogeneous and varies with anatomical site. For example, the strength in the axial direction is maximum at the mid-diaphysis of a long bone and decreases toward the ends of the bone, while the strength in the radial and circumferential directions shows a reversed dependence upon position. Third, it has been shown that the strength of bone decreases with age of the individual. Fourth, strength varies with bone type — cancellous, lamellar, or osteonal. For example, there is a strong negative correlation between the number of osteons and tensile strength, with the tensile strength of

totally osteonal bone about 30% less than that of lamellar bone. This result is attributed to the combined effect of decreased bone mass due to secondary osteons having a larger central canal and a lower degree of calcification.

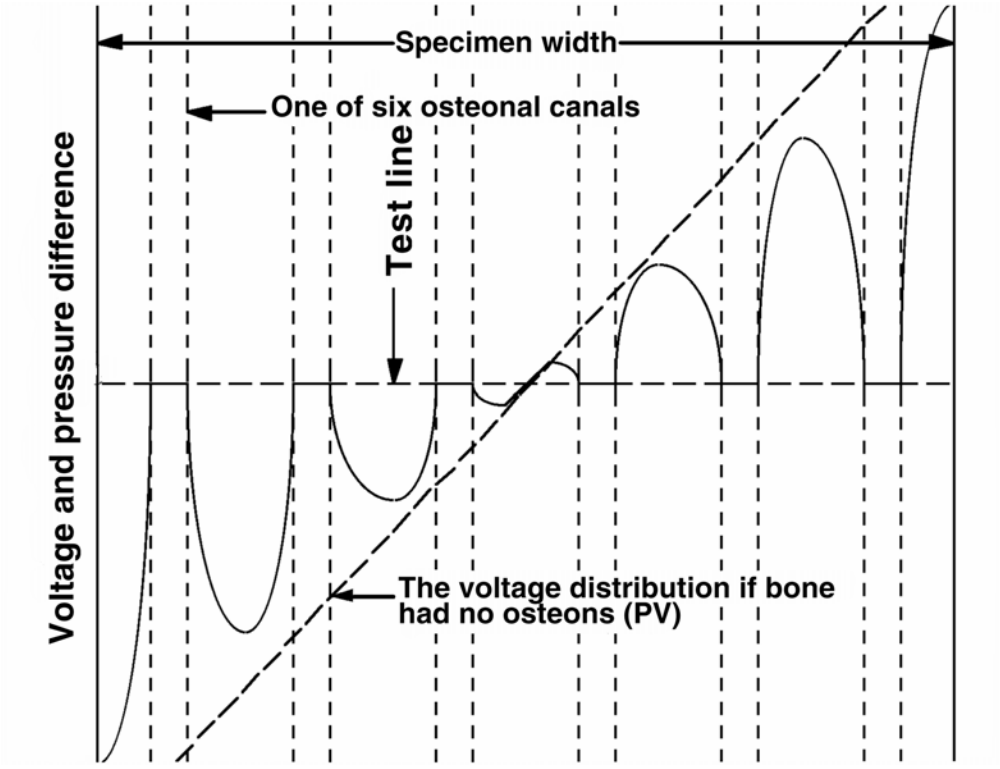



**Figure 11.16**. Schematic illustration of the results of the Wang et al. (1999) model for pressure/SGP generated by bending of osteonal bone. The curves are voltage or pressure difference due to the low pore fluid pressure in the osteonal canals. In this model the test microelectrode is envisioned as moving along the test line of Figure 11.13 or 11.14 or model 11.15 from one side of the specimen to the other. The voltage difference measure as this test line is traversed is illustrated above. The voltage difference vanishes when the osteonal lumen is crossed, giving a very inhomogeneous structure to the local pressure or voltage distribution in each osteon. If the osteons were removed, the voltage distribution would be a straight line in the central portion of the cross-section and would decrease in slope as each of the boundaries is approached. The straight line portion is shown as a longer dashed line above; its curved approach to the boundary is not illustrated. Reprinted with permission from Cowin (1999).

Although Galileo Galilei (1564–1642) mentions bones in his consideration of mechanical properties of materials and tissues, without a doubt Guillaume Wertheim (1815–1861) did the first significant mechanical testing of bone and other tissues. Wertheim was born in Vienna, educated there as a physician, and later studied mathematics and physics in Berlin (Bell, 1973). In Paris in (1846–47) he measured the elastic moduli and strength not only of bone, but also of tendons, nerves, arteries, veins, and muscle (Wertheim, 1847). His published values for these

properties appear in standard reference texts up until about a hundred years after his death, which occurred after he leaped from the tower of the cathedral of St. Gathein in Tours when in a deranged state. Evans (1973) summarizes the literature on the mechanical properties of bone up to 1970, including the work of Wertheim. The majority of the work on bone in that period occurs after 1950. Careful measures of the anisotropic elasticity and strength of bone did not appear in the literature again until 1974.

**Table 11.5**. Yield Stress, Ultimate Stress, and Ultimate Strain for Human Bone Tissue

| Type of yield stress (angle with long axis) | Yield stress (MPa) | Ultimate stress (MPa) | Ultimate strain or rotation |
|---|---|---|---|
| Tensile (0°) | 115 (11.2) [202] | 133 (14.1) [202] | .0293 (.0094) [202] |
| Compressive (0°) | 182 (14.4) [19] | 195 (19.6) [114] | .0220 (.0057) [114] |
| Tensile (30°) | | 100 (11.4) [23] | .0198 (.0083) [23] |
| Compressive (30°) | | 173 (13.8) [5] | .0280 (.0052) [5] |
| Tensile (60°) | | 61 (12.2) [19] | .0069 (.0022) [19] |
| Compressive (60°) | | 133 (15.0) [7] | .0311 (.0010) [7] |
| Tensile (90°) | | 51 (11.1) [31] | .0072 (.0016) [31] |
| Compressive (90°) | 121 (9.2) [3] | 133 (16.7) [13] | .0462 (.0260) [13] |
| Shear | 54 (5.2) [19] | 69 (4.4) [31] | .3299 (.0890) [19] |

This table represents a summary and condensation of data in Reilly and Burstein (1975) and Cezayirlioglu et al. (1985). In the yield stress column and the ultimate stress column, the first number is the yield or ultimate stress in MPa. The number in parentheses is the standard deviation, and the number in square brackets the number of specimens. In the last column, the first number is the ultimate strain or the ultimate rotation (in radians), the number in parentheses is the standard deviation, and the number in square brackets is the number of specimens. Reprinted with permission from Cowin et al. (1987).

In that year Reilly and Burstein (1974, 1975) reported the results of experiments to determine the ultimate strength and elastic moduli of cortical bone. Similar data were reported a decade later by Cezayirlioglu et al. (1985), and these combined data are summarized in Table 11.5 for human tissue and in Table 11.6 for bovine tissue. Since Reilly and Burstein and Cezayirlioglu et al. assumed that bone was transversely isotropic (TI), all directions making a fixed angle with the axial direction were assumed to be equivalent. Thus, they determined the tensile strengths at angles of 0, 30, 60, and 90° with the axial direction of the long bone. The 0° direction is the axial direction and the 90° direction any direction in the plane perpendicular to the axial direction. They also determined the axial shear strengths for each of the bone types given in Tables 11.5 and 11.6. An extensive table with other bone strength data is given in Cowin (1989) (Table 6, Chap. 6).

Bone tissues appear to be optimized in different ways depending upon their particular function. In an interesting comparison of tissue types, the mechanical properties of three types of bone were compared in a way that illustrated the optimization of various extremes (Currey, 1979). The bone types were deer's antler, cow's femur, and fin whale's tympanic bulla, a bone of the ear. The results of this comparison are summarized in Table 11.7. The functions of deer's antler, which in the red deer is found in males only, are for display and fighting. From

**Table 11.6**. Yield Stress, Ultimate Stress, and Ultimate Strain for Bovine Bone Tissue

| Type of yield stress (angle with long axis) | Yield stress (MPa) | Ultimate stress (MPa) | Ultimate strain or rotation |
|---|---|---|---|
| Tensile (0°) | 141 (17.1) [58] | 156 (23.5) [66] | .0324 (.0161) [66] |
| Compressive (0°) | 196 (18.5) [25] | 237 (38.6) [49] | .0253 (.0096) [49] |
| Tensile (30°) | – | 109 (9.0) [21] | .0118 (.0025) [21] |
| Compressive (30°) | – | 190 (12.6) [14] | .0250 (.0038) [14] |
| Tensile (60°) | – | 60 (9.8) [12] | .0075 (.0019) [12] |
| Compressive (60°) | – | 148 (2.6) [2] | .0320 (.0006) [2] |
| Tensile (90°) | – | 50 (12.5) [52] | .0067 (.0024) [52] |
| Compressive (90°) | 150 (30.7) [22] | 178 (31.1) [26] | .0517 (.0199) [26] |
| Shear | 57 (8.4) [21] | 73 (9.6) [49] | .3910 (.0908) [21] |

This table represents a summary and condensation of data in Reilly and Burstein (1975) and Cezayirlioglu et al. (1985). In the yield stress column and the ultimate stress column, the first number is the yield or ultimate stress in MPa. The number in parentheses is the standard deviation and the number in square brackets the number of specimens. In the last column the first number is the ultimate strain or the ultimate rotation (in radians), the number in parentheses is the standard deviation, and the number in square brackets is the number of specimens. Reprinted with permission from Cowin et al. (1987).

**Table 11.7**. Some Mechanical Properties of Different Bone Types

| | Antler | Femur | Bulla |
|---|---|---|---|
| Work of fracture ($Jm^{-2}$) | 6168 (5, 552)<br>100% | 1710 (13, 207)<br>28% | 200 (3, 8)<br>3.2% |
| Bending strength (MPa) | 179.4 (7, 6.6)<br>73% | 246.7 (6, 11.6)<br>100% | 33.0 (3, 6.6)<br>13% |
| Modulus of elasticity (GPa) | 7.4 (7, 0.34)<br>24% | 13.5 (6, 0.95)<br>43% | 31.3 (10, 0.97)<br>100% |
| Mineral content (% weight remaining) | 59.3 (5, 0.49)<br>69% | 66.7 (25, 0.17)<br>77% | 86.4 (2, 0.05)<br>100% |
| Density ($10^3$ kg $m^{-3}$) | 1.86<br>75% | 2.06<br>83% | 2.47<br>100% |

This table gives the value (sample size, standard error). In each row the values are expressed as a percentage of the highest value. Adapted with permission from Currey (1979).

Table 11.7 it is seen that deer's antler has the largest work to fracture of the three bone types tested. It has good impact resistance, but low modulus and rather low bending strength. The function of cow's femur is structural and, from Table 11.7, it is seen to have the largest bending strength, but no real property extreme. The tympanic bulla of the whale is isolated from the rest of the skull by a gas-filled foam; it performs no structural function. To perform its auditory

function its acoustic impedance, $\sqrt{\rho E}$, should be as high as possible so as to reduce the sound energy reaching the middle ear by any route other than through the chain of middle ear ossicles. From Table 11.7 it can be seen that both the density and modulus of elasticity of the tympanic bulla are the largest of the three bone types tested.

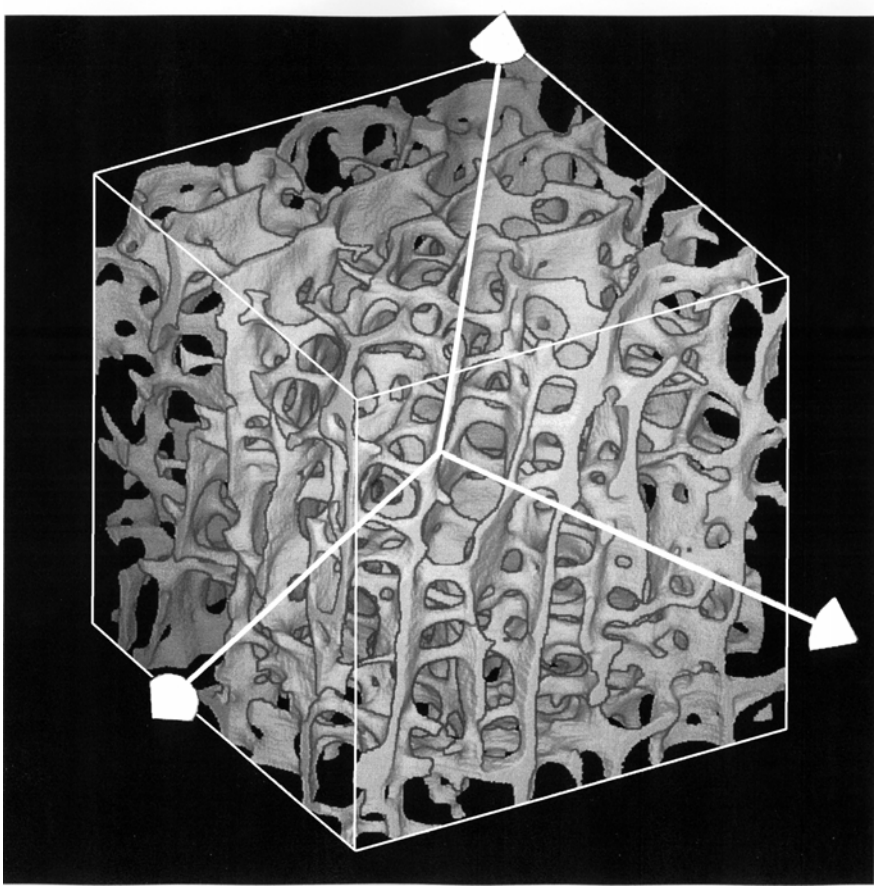


**Figure 11.17**. An illustration of the trabecular grain. By trabecular grain we mean a set of three ordered orthogonal directions, the first of which lies along the local predominant trabecular direction, which is locally the stiffest direction; the second and third directions are directions orthogonal to each other in the plane perpendicular to the first direction and represent directions of extrema in stiffness in the local region of the cancellous bone. The specimen is a 7-mm cube. Reprinted with permission from Yang et al. (1999).

## 11.9. CANCELLOUS BONE ARCHITECTURE

The emphasis shifts here from cortical bone to cancellous bone. Cancellous bone architecture, illustrated in Figures 11.5 and 11.17, has been difficult to characterize quantitatively. The concern in this presentation is primarily with those characteristics of the cancellous bone architec-

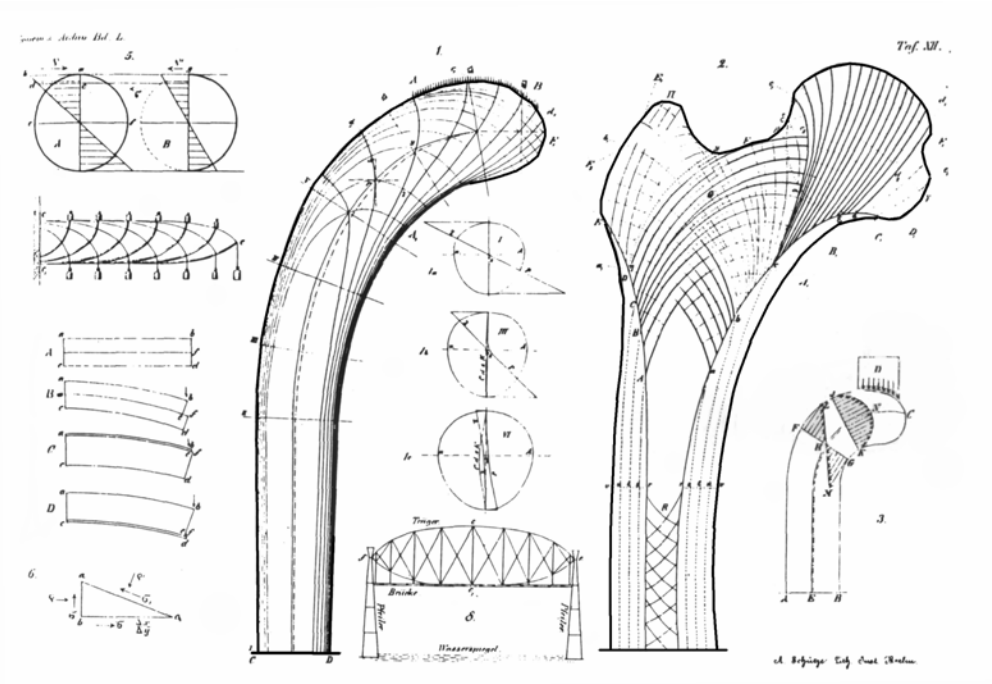


**Figure 11.18**. On the left is the Culmann crane with the principal stress trajectories indicated. On the right is Meyer's sketch of the trabecular architecture in a section through the proximal end of the human femur. Both the femur and Culmann's crane are loaded transversely at their cantilevered ends, as illustrated in the small drawing at the lower far right. Reprinted with permission from Wolff (1870).

ture that determine the elastic constants of cancellous bone, namely, the solid volume fraction and the trabecular grain. In this section the considerations of §8.7 on the tensorial measures of microstructure are specialized to cancellous bone, particularly the concept of fabric. A number of quantitative stereological procedures have been used to measure cancellous bone architecture. The most important of these parameters of architecture is solid volume fraction $\phi$ , which is equal to the solid bone volume (BV) per unit total volume (TV). The notation for solid volume fraction $\phi$ widely employed in bone histology is BV/TV, thus, $\phi$ and BV/TV stand for the same quantity. The second important quantitative stereological parameter is the orientation of the trabecular grain coordinate system. By trabecular grain we mean a set of three ordered orthogonal directions, the first one of which lies along the local predominant trabecular direction, which is locally the stiffest direction; the second and third directions are orthogonal to each other in the plane perpendicular to the first direction and represent directions of extrema in stiffness in the local region of the cancellous bone, see Figure 11.17. We know that these directions are orthogonal because it has been shown that cancellous bone has orthotropic elastic symmetry, that is to say, three perpendicular planes (or, alternatively, axes) of mirror or reflective symmetry exist in each local region of the bone tissue. This symmetry and its representation using the fabric tensor is described in §8.7.

In regions of bones loaded consistently with large forces, say the proximal femur where it contacts the pelvis and the calcaneous (heel bone) where it is near the point of contact of the foot with the ground, there are two apparently orthogonal sets of trabeculae. Sketches of these orthogonal sets in the proximal femur by Meyer (1867) are shown as part of Figure 11.18. (The entire Figure 11.18 will be discussed in Chapter 12.) The trabecular grain in the plane of the

illustration coincides with the orthogonal nets in the proximal femur sketched by Meyer. The distinctive structural anisotropy of cancellous bone tissue recorded by Meyer (1867) appears to have been overlooked in the literature of quantitative bone stereology before the work of Whitehouse (1974) and Whitehouse and Dyson (1974). Whitehouse and Dyson measured the mean intercept length, $L$, in cancellous bone tissue as a function of direction on polished plane sections. This work was described in Chapter 8. The mean intercept length tensor is a good measure of the structural anisotropy in cancellous bone tissue (Whitehouse, 1974; Harrigan and Mann, 1984; Turner et al., 1990; Odgaard, 1997; Odgaard et al., 1997), and it is employed in representation of the elastic constants for that tissue.

## 11.10. THE ELASTIC PROPERTIES OF CANCELLOUS BONE

The elastic properties of cancellous bone considered here are the drained elastic properties. The drained elastic constants are the only set that need be considered because the pore pressure in the bone marrow and fat in the PIT is always very low because of the large permeability associated with the PIT. Any pressure generated in the PIT can dissipate as quickly as the load is applied, with the exception of loads that are continually rising at a rapid rate for a period sufficiently long to destroy the animal or person. Thus, while all considerations of poroelasticity described in §§11.6 and 11.7 for cortical bone may also be applied to cancellous bone, the values of the parameters associated with permeability in the PIT make any mechanical effect or physiological effect associated with the pore pressure unlikely.

Cancellous bone is not only anisotropic, but also very inhomogeneous due to the significant variation in the solid volume fraction, $\phi$, that occurs in any whole bone. The identification of the type of elastic symmetry is complicated by the inhomogeneity of the material, which makes the analysis of the elastic constant measurement data difficult. A solution to this problem in which identification of the type of elastic symmetry and analysis of the inhomogeneity are separated and analyzed independently will be described here. The method consists of averaging eigenbases, that is to say, the bases composed of the orthogonal sets of eigenvectors of different measurements of the elasticity tensor, in order to construct an average eigenbasis for the entire data set. This is possible because the eigenbases, composed of eigenvectors, are independent of solid volume fraction $\phi$ while the eigenvalues are not. The eigenvalues of all the specimen anisotropic elastic coefficient matrices can then be transformed to the average eigenvector basis and regressed against the solid volume fraction $\phi$. This method treats the individual measurement as a measurement of a tensor instead of as a collection of individual elastic constant or matrix element measurements, recognizing that the measurements by different authors will reflect the systematic invariant tensorial properties of a material, like eigenvectors and eigenvalues. This method for averaging different measurements of the anisotropic elastic constants for a specific material has advantages over the traditional method of averaging the individual matrix components of the elasticity or compliance matrices. Averaging invariants removes the effect of the reference coordinate system in the measurements, while the traditional method of averaging the components may induce errors due to the various reference coordinate systems and may distort the nature of the symmetry. This averaging process explicitly retains the orthonormality of the eigenvector basis (Cowin and Yang, 1997).

An interesting result that emerges from analysis of this type is a method for dealing with inhomogeneous anisotropic elastic materials. In the case of porous inhomogeneous isotropic materials, for example, it is customary to regress the Young's modulus against the solid volume fraction and obtain expressions for Young's modulus $E$ as a function of solid volume fraction $\phi$; for example, $E = (\text{constant})\,\phi^n$. The method of data analysis employed here extends this

empirical method to anisotropic materials. This method of analysis also identifies the type of elastic symmetry possessed by the material. No a priori assumption as to type of elastic symmetry is made. The type of symmetry is identified from the character of the eigenvectors that are calculated. For example, in the analysis described here it was shown that human cancellous bone has orthotropic elastic symmetry at the 95% confidence level (Yang et al., 1999).

The results for cancellous bone presented here are based upon an analysis of a database consisting of 141 human cancellous bone specimens. This database, reported by van Rietbergen et al. (1996, 1999) and Kabel et al. (1999), is superior to previous databases because the authors provide the entire set of anisotropic elastic constants without an a priori assumption of a particular material symmetry and without an assumption of the direction in which the maximum Young's modulus occurs. This database is unique in many different ways, the most important of which is the large number of specimens and its method of construction, but also because it is not based entirely on measurements of real specimens. The database of elastic constants of 141 human cancellous bone specimens employed here was constructed by imaging real specimens, then computationally determining their elastic constants. This cyberspace method of construction appears to be more accurate than the conventional mechanical testing procedures for evaluating the elastic constants of human cancellous bone. The determination of the elastic constants of cancellous bone by conventional mechanical test procedures is very difficult. The basic problem is that, due to the size of the human body, it is difficult to obtain specimens of cancellous bone that are more than 5-mm cubes. The logical way to test small cubes such as these is compression testing. However, compression testing is highly inaccurate for cancellous bone because of (1) the frictional end effects of the platens, (2) the near impossibility of identifying, a priori, the trabecular grain in a bone specimen and thus cut a specimen in the grain directions, (3) the stiffening effect of the platens on the bone near the platens, and (4) the unpredictable inhomogeneity of the specimen. These and other difficulties in the mechanical testing of cancellous bone are described in Keaveny et al. (1997).

Construction of the database of elastic constants of 141 human cancellous bone specimens employed here was a major advance because it provided a relatively inexpensive method of determining the full set of anisotropic elastic constants for a small specimen of cancellous bone by a combination of imaging the specimen (Odgaard et al., 1997; Kabel et al., 1999) and subsequently evaluating the effective elastic constants using computational techniques based on the finite-element (FE) method (van Rietbergen et al., 1996, 1998; Hollister et al., 1991). A sequence of loadings was applied to the FE models of the specimen and the responses determined (van Rietbergen et al., 1996, 1998). The sequence of loadings was sufficient in number to determine all 21 elastic constants. Thus, no material symmetry assumptions were made in determination of the constants.

In this method the actual matrix material of the trabeculae comprising the bone specimen is assumed to have axial Young's modulus $E_t$. The value of $E_t$ may be fixed from a knowledge of the axial Young's modulus for the tissue, or from the shear modulus about some axis, or by measuring tissue modulus $E_t$ itself. For purposes of numerical calculation $E_t$ was taken to be 1 GPa (van Rietbergen et al., 1996, 1998; Odgaard et al., 1997; Kabel et al., 1999). However, since these are linear FE models, the FE results can be scaled for any other modulus by multiplying the results with the new value of $E_t$ (in GPa). Tissue modulus $E_t$ thus is a scale factor that magnifies or reduces all the elastic constants. The inverse of the tissue modulus, $1/E_t$, multiplies each component in the elastic compliance matrix. The cancellous bone elastic constant results are presented here as multiples of $E_t$ (cf., e.g., Table 11.8). Once the image of the specimen was in the computer and a finite-element mesh was generated, a sequence of loadings was applied to the specimen and the responses determined. Quantitative stereological programs were used to determine solid volume fraction $\phi$ for each specimen.

**Table 11.8**. Results of the Linear Log-Log Regression of the Eigenvalue Invariants vs. Volume Fraction $\phi$

| | Cancellous human bone | | | | | |
|---|---|---|---|---|---|---|
| Eigenvalue | $\Lambda_1$ | $\Lambda_2$ | $\Lambda_3$ | $\Lambda_4$ | $\Lambda_5$ | $\Lambda_6$ |
| MPa | $1460E_t\phi^{1.717}$ | $871E_t\phi^{1.895}$ | $493E_t\phi^{1.923}$ | $533E_t\phi^{2.038}$ | $633E_t\phi^{1.972}$ | $973E_t\phi^{1.984}$ |
| $R^2$ | 0.911 | 0.905 | 0.868 | 0.879 | 0.902 | 0.889 |

Reprinted with permission from Yang et al. (1999).

The data on the elastic constants of cancellous human bone and their volume fractions were analyzed in five steps (Yang et al., 1999). First, the eigenvalues and eigenvectors associated with the six-by-six matrix of elastic constant data were determined for each specimen. Second, an average of 141 eigenbases was determined. Third, observing that the elements in the average eigenvector basis associated with other than orthotropic symmetry were near zero, the eigenvector basis was statistically tested for its closeness to orthotropic symmetry. It was found that the set of 141 specimens had orthotropic symmetry at the 95% confidence level. Fourth, the data for each specimen were referred to the common average eigenvector basis. The transformation law for second-rank Cartesian tensors was employed to transform the elasticity tensor from its original coordinate system, which reflected no symmetry to the common average eigenvector basis where it reflected orthotropic symmetry except for a few small deviations. The elastic constants that were associated with other than elastic orthotropic symmetry were near zero and were neglected. The error associated with the neglect of these near-zero terms was less than 3.5% of the largest eigenvalue for the sixth specimen (shown in Figure 11.17) and the maximum error was 4.4% for specimen 36. This result demonstrated that the common average eigenvector basis was indeed common and almost independent of volume fraction $\phi$. Fifth, the six compositionally dependent invariants were regressed against their volume fractions employing linear log-log relationships (Hodgskinson and Currey, 1990a). The results of this analysis for cancellous bone, the dependence of the eigenvalues upon the solid volume fraction, are shown in Table 11.8. In Table 11.8, under each of the eigenvalues, are the squared correlation coefficients $(R^2)$ for the correlation of that eigenvalue with the corresponding set of eigenvalues of the original data. A plot of the data on the first eigenvalue vs. solid volume fraction is presented in Figure 11.19. Then, using the spectral representation of the matrix of elastic coefficients in terms of its eigenvalues and eigenvectors, where the eigenvalues are compositionally dependent and the eigenvectors are not, the strain–stress relations were constructed. These relations reflect the explicit dependence upon solid volume fraction $\phi$. For the cancellous human bone the strain–stress relations are given by

$$E_{11} = (1/E_t)[(1/(1240\phi^{1.8}))\, T_{11} - (1/(7056\phi^{2.048}))\, T_{22} - (1/(3929\phi^{1.991}))\, T_{33}],$$

$$E_{22} = (1/E_t)[(-1/(7056\phi^{2.048}))\, T_{11} + (1/(885\phi^{1.886}))\, T_{22} - (1/(3456\phi^{1.972}))\, T_{33}],$$

$$E_{33} = (1/E_t)[(-1/(3929\phi^{1.991}))\, T_{11} - (1/(3456\phi^{1.972}))\, T_{22} + (1/(528.8\phi^{1.919}))\, T_{33}],$$

$$E_{23} = T_{23}/(533.25E_t\phi^{2.038}),\ \ E_{13} = T_{13}/(633.34E_t\phi^{1.972}),$$

$$E_{12} = T_{12}/(972.63E_t\phi^{1.984}), \tag{11.5}$$

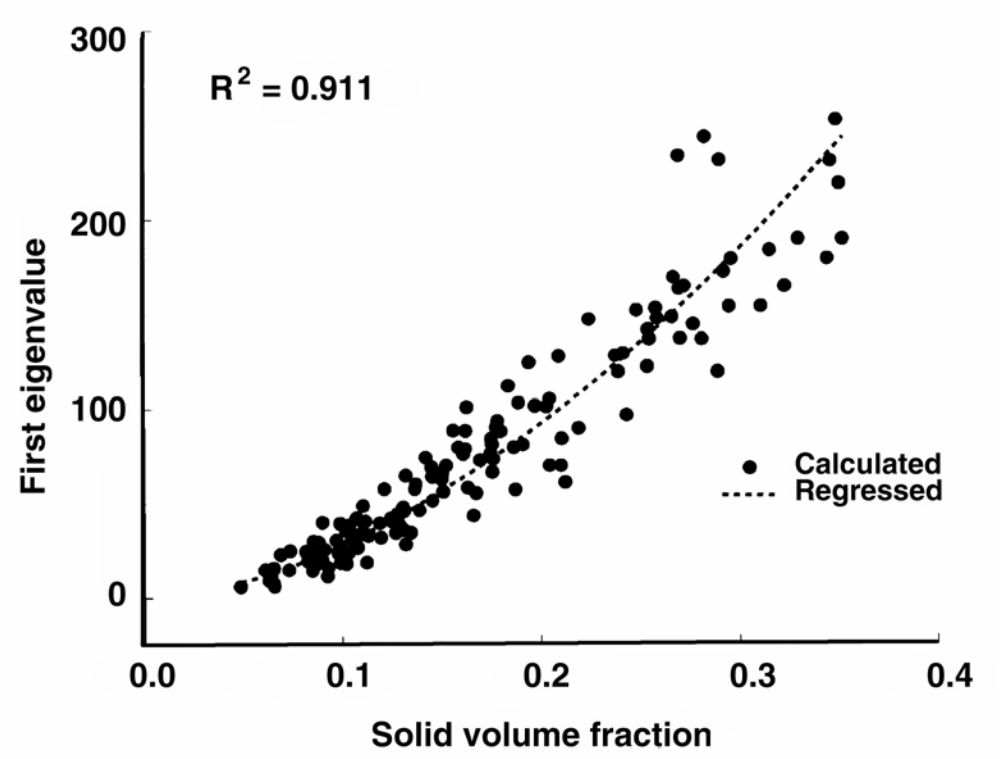



**Figure 11.19**. A plot of the data on the first eigenvalue for human cancellous bone against the solid volume fraction. The vertical scale is dimensionless because the value of the first eigenvalue is divided by $E_t$. The horizontal scale (solid volume fraction) is also dimensionless. Reprinted with permission from Yang et al. (1999).

where $E_t$ has the dimension of stress and the other numbers multiplying all $\phi$'*s* raised to a power are dimensionless. The squared correlation coefficients *($R^2$)* for the orthotropic elastic coefficients are as follows: for $1/E_1$, $R^2 = 0.934$; for $1/E_2$, $R^2 = 0.917$; for $1/E_3$, $R^2 = 0.868$; for $1/(2G_{23})$, $R^2 = 0.870$; for $1/(2G_{13})$, $R^2 = 0.887$; for $1/(2G_{12})$, $R^2 = 0.876$; for $-\nu_{12}/E_1$, $R^2 = 0.740$; for $-\nu_{13}/E_1$, $R^2 = 0.841$; and for $\nu_{21}/E_2$, $R^2 = 0.666$.

Representation (11.5) of the elastic coefficients for human bone is quite interesting and contains revealing insights. The Young's modulus of human cancellous bone of the average representation (11.5), plotted as a function of direction at volume fraction $\phi = 0.35$, is shown in Figure 11.20. This three-dimensional closed, peanut shell-shaped surface reflects the three orthogonal planes of mirror symmetry associated with orthotropy. For an isotropic material the surface shown in Figure 11.20 would be a sphere. As the solid volume fraction of cancellous bone changes, the overall average shape of the surface in Figure 11.20 stays the same, but the intercept values of the surface with the three principal directions increase or decrease with the volume fraction; that is to say the plot in Figure 11.20 is simply enlarged or reduced. It is interesting to note that the anisotropy ratios ($E_1/E_2$, $E_1/E_3$, and $E_2/E_3$) calculated from (11.5) are mildly decreasing with increasing volume fraction, and thus the more dense material is associated with less pronounced anisotropy.

The data on human cancellous bone were from six anatomical sites. The results of the analysis of the data were grouped only on the basis of six anatomical sites (vertebral, calcane-

ous, proximal tibia, distal femur, proximal femur, and proximal humerus). For most of the specimens and most of the sites, the shape of the plot of Young's modulus as a function of direction is similar to that for the average representation (11.5) shown in Figure 11.20, although the values of the intercepts along the axes may change. The site that produces the plot of Young's modulus as a function of direction that is most different from that illustrated in Figure 11.20 is the distal femur. The plot of the average Young's modulus from all individuals as a function of direction for the cancellous bone from the distal femur is shown in Figure 11.21. Note that the shape of the surface representing the directional dependence of the Young's modulus in Figure 11.21 is only slightly different from average representation (11.5) shown in Figure 11.20, and that both surfaces have three-dimensional peanut shell shapes. The difference between these figures, a broadening of the mid cross-section in one direction in Figure 11.21, reflects a difference in the directional dependence of the average Young's modulus in the cancellous bone of the distal femur from the anatomically averaged directional dependence of the Young's modulus of human cancellous bone model represented by (11.5). The purpose of this illustration is to show that these differences in shape exist, but they appear to be minor.

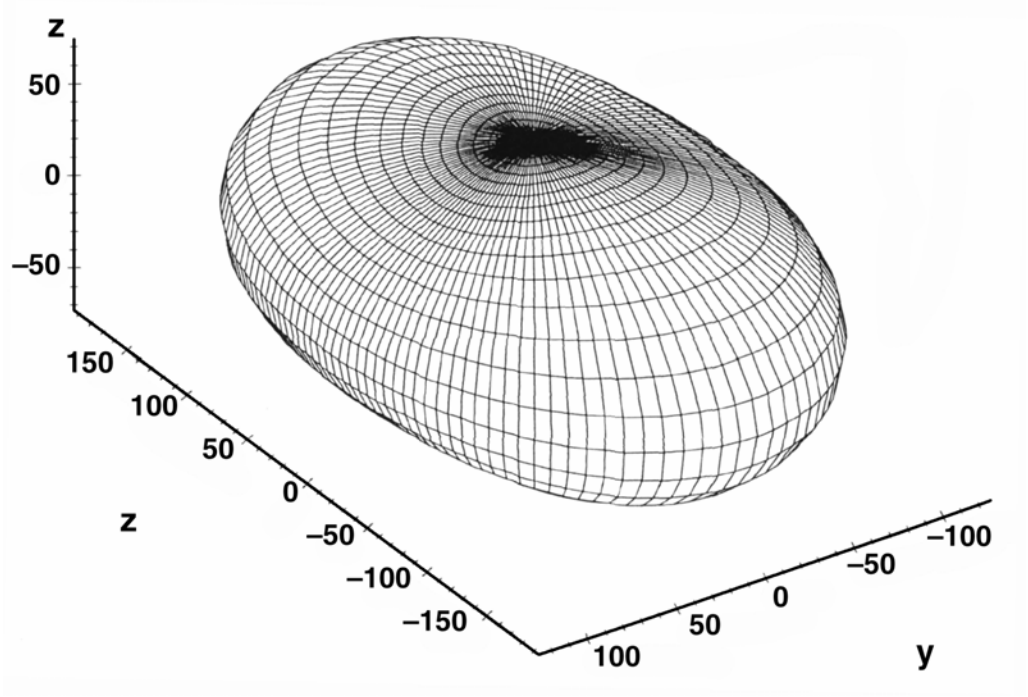



**Figure 11.20**. Young's modulus of human cancellous bone of the 141 specimen average representation (3) plotted as a function of direction at the highest volume fraction measured, $\phi = 0.35$. The scales of the axes are dimensionless because the value of Young's modulus is divided by $E_s$. Reprinted with permission from Yang et al. (1999).

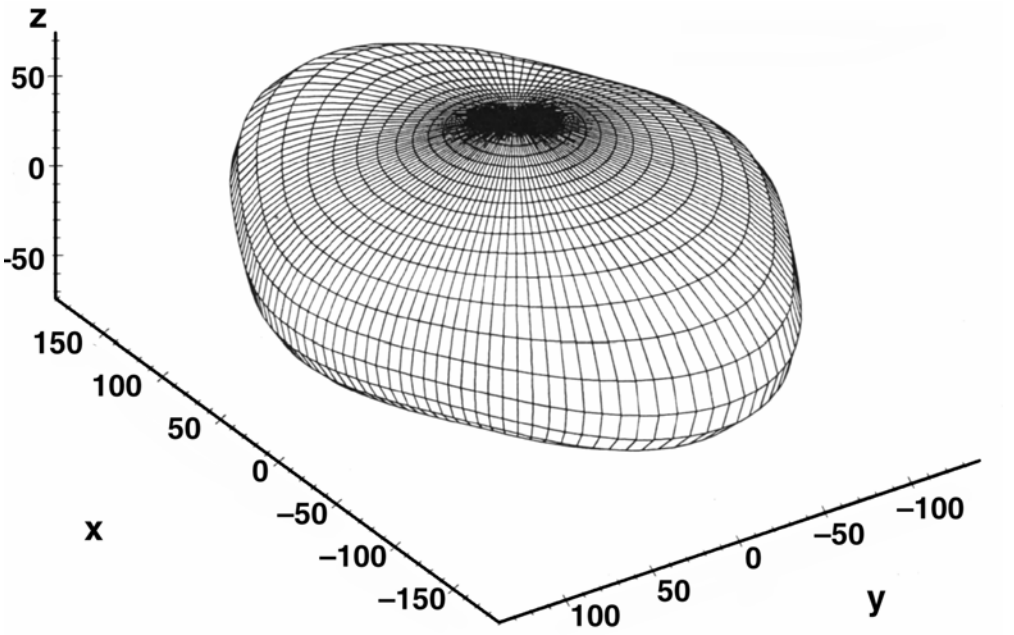



**Figure 11.21**. Young's modulus of human cancellous bone from the distal femur based on an average of 20 specimens plotted as a function of direction at the highest volume fraction measured, $\phi = 0.35$. The tissue from this region shows the largest deviation from the 141 specimen average shape given by Figure 11.22. The scales of the axes are dimensionless because the value of Young's modulus is divided by $E_t$. Reprinted with permission from Yang et al. (1999).

The plot of the 141 specimen average Poisson's ratios against volume fraction for human cancellous bone is shown in Figure 11.22. Note that, in general, the values of these Poisson's ratios are all greater than zero and less than one-half, the customary range of Poisson's ratios for isotropic materials (note that $\nu_{13}$ is larger than 0.5 for very low volume fractions). The permitted value range for orthotropic materials is much larger than that for isotropic materials. Note that, for human bone, there is a consistent trend of decreasing Poisson's ratio as an increasing function of volume fraction. While anisotropy is reflected in Poisson's ratios, it is not exaggerated, as the values of the Poisson's ratios all stay in the range of those for isotropic materials.

The data set on the cancellous bone is high-quality data in that it contains all 21 elastic constants and the solid volume fraction for 141 specimens. The results concerning these data are strong because of the large number of specimens; the central limit theorem states that the difference between the true mean and the estimated mean depends inversely upon the number of specimens. Thus, the true mean and the estimated mean approach each other as the number of specimens increases. The superiority of this model for representing the compositional dependence of the elastic constants is established by comparing it with the results obtained using other models. In the case of porous materials the customary model is to assume elastic isotropy and to regress the Young's modulus against the solid volume fraction and obtain expressions for Young's modulus $E$ as a function of solid volume fraction $\phi$; for example, $E$ = (constant) $\phi^n$. This is done for cancellous bone and other materials, particularly sintered materials. For

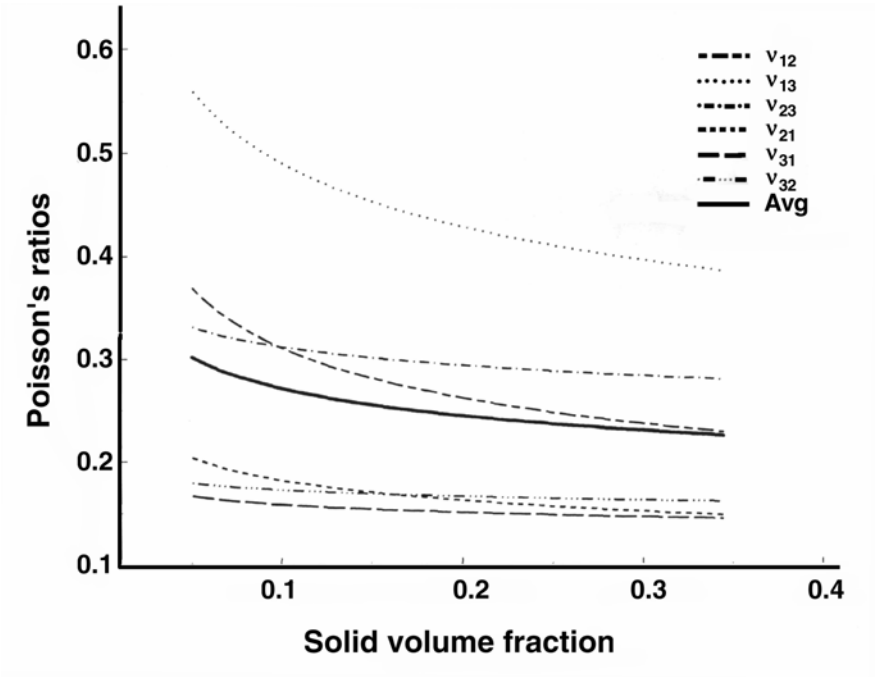



**Figure 11.22**. Plot of the 141 specimen average Poisson's ratios against volume fraction for human cancellous bone. The various Poisson's ratios are identified on the basis of their value at a volume fraction of 0.05. From the top: $\nu_{13}$, $\nu_{12}$, $\nu_{23}$, and the average of all six Poisson's ratios: $\nu_{21}$, $\nu_{32}$, and $\nu_{31}$. The vertical scale (Poisson's ratio) is dimensionless, as is the horizontal scale (solid volume fraction). Reprinted with permission from Yang et al. (1999).

cancellous bone, when the traditional model is employed (Rice et al., 1988; Cowin, 1989; Hodgskinson and Currey, 1990 a,b) the squared correlation coefficients $(R^2)$ are in the range of 0.4 to 0.70; with the present model the squared correlation coefficient is 0.934 for the largest Young's modulus, about one-third higher. However, the reader should keep in mind that the squared correlation coefficients reported were not obtained directly from experimental data as were the earlier ones. This reminder is not meant to imply that the method employed to obtain the elastic constants reported in van Rietbergen et al. (1996 & 1998) and Kabel et al. (1999) is any less accurate, only different. In fact, the data reported by van Rietbergen et al. (1996, 1998) and Kabel et al. (1999) are superior to previous data because they provide the entire set of anisotropic elastic constants without an a priori assumption of a particular material symmetry and without an assumption of the direction in which the maximum Young's modulus occurs. The databases employed by Rice et al. (1988) (see also Cowin, 1989) consisted generally of uniaxial compression tests of small cubes of cancellous bone in which only Young's modulus was reported. In these studies the direction of the maximum Young's modulus was assumed or estimated.

**Problems**

11.10.1. Calculate, as a function of volume fraction $\phi$ and tissue modulus $E_s$, spring constant $k_3$ of a specimen of cancellous bone that is a cube with dimension $L$. The direction of in-

terest for the spring constant is the $x_3$ axis and the other two edges are parallel to the other two cortical grain directions.

11.10.2. Calculate, as a function of volume fraction $\phi$ and the tissue modulus $E_t$, torsional spring constant $w_{23}$ of a specimen of human cancellous bone that is of radius $R$ and is $10R$ long. The long direction is parallel to the $x_1$ axis.

11.10.3. Are the values of the three Young's moduli — $E_1$, $E_2$, and $E_3$ — and the three shear moduli — $G_{23}$, $G_{13}$, and $G_{12}$ — positive for all values of volume fraction $\phi$? Why is it important that these moduli all be positive?

## 11.11. THE LITERATURE OF BONE MECHANICS

The books that deal with bone mechanics include Currey (1984, 2002), Martin Burr and Sharkey (1998), and the edited volumes by Cowin (1989, 2001). The principal journals for bone mechanics are the *Journal of Biomechanics*, the *International Journal of Biomechanics and Modeling in Mechanobiology*, and the American Society of Mechanical Engineers' *Journal of Biomechanical Engineering*. There are journals in which bone mechanics-related material appears, including *Bone*, the *Annals of Biomedical Engineering*, the *Journal of Bone and Joint Surgery*, and the *Journal of Orthopaedic Research*.

### References


Ashman RB, Cowin SC, Van Buskirk WC, Rice JC. 1984. A continuous wave technique for the measurement of the elastic properties of cortical bone. *J Biomech* **17**:349–361.

Atkinson PJ, Hallsworth AS. 1983. The changing structure of aging human mandibular bone. *Gerodontology* **2**:57–66.

Baylink D, Wergedal J. 1971. Bone formation and resorption by osteocytes. In *Cellular mechanisms for calcium transfer and homeostasis*, ed. G Nichols Jr, pp. 257–289. New York: Academic Press.

Bell JF. 1973. The experimental methods of solid mechanics. In *Handbuch der physik*, Vol. Via/1, ed. C Truesdell, pp. 1–813. Berlin: Springer-Verlag.

Brooks M, Revell W. 1998. *Blood supply of bone*. London: Springer.

Brown TD, Pedersen DR, Gray ML, Brand RA, Rubin CT. 1990. Toward an identification of mechanical parameters initiating periosteal remodeling: a combined experimental and analytic approach. *J Biomech* **23**:893–905.

Cezayirlioglu H, Bahniuk E, Davy DT, Heiple KG. 1985. Anisotropic behavior of bone under combined axial force and torque. *J Biomech* **18**:61–72.

Cormack DM. 1987. *Ham's histology*, 9th ed. Chapter 12. Philadelphia: Lippincott.

Cowin SC. 1981. Mechanical properties of bones. In *Mechanics of structured media*, ed. APS Selvadurai, pp. 151–184. Philadelphia: Elsevier.

Cowin SC. 1985. The relationship between the elasticity tensor and the fabric tensor. *Mech Mater* **4**:137–147.

Cowin SC. 1989. *Bone mechanics*. Boca Raton, FL: CRC Press.

Cowin SC. 1999. Bone poroelasticity. *J Biomech* **32**:218–238.

Currey JD. 2002. *Bones*. Princeton: Princeton UP.

Cowin SC, ed. 2001. *Bone mechanics handbook*. Boca Raton, FL: CRC Press (ISBN/ISSN: 0849391172).

Cowin SC. 2003. Adaptive elasticity: A review and critique of a bone tissue adaptation model. *Eng Trans* **51**:1–79.

Cowin SC, Hegedus DH. 1976. Bone remodeling, I: theory of adaptive elasticity. *J Biomech* **6**:313–326.

Cowin SC, Mehrabadi MM. 1989. Identification of the elastic symmetry of bone and other materials. *J Biomech* **22**:503–515.

Cowin SC, Moss ML. 2000. Mechanosensory mechanisms in bone. In *Textbook of tissue engineering*, 2nd ed., ed. R Lanza, R Langer, W Chick, pp. 723–738. San Diego: Academic Press.

Cowin SC, Van Buskirk WC, Ashman RB. 1987. The properties of bone. In *Handbook of bioengineering*, ed. R Skalak, S Chien, pp. 2.1–2.27. New York: McGraw-Hill.

Cowin SC, Weinbaum S, Yu Zeng. 1995. A case for bone canaliculi as the anatomical site of strain-generated potentials. *J Biomech* **28**:1281–1296.

Cowin SC, Yang G. 1997. Averaging anisotropic elastic constant data. *J Elast* **46**:151–180.

Currey JD. 1960. Differences in the blood supply of bone of different histological type. *Q J Microsc Sci* **101**:351–370.

Currey JD. 1979. Changes in the impact energy absorption of bone with age. *J Biomech* **12**:459–470.

Currey JD. 1984. *The mechanical adaptation of bones*. Princeton: Princeton UP.

Currey JD. 2002. *Bones*. Princeton: Princeton UP.

De Groot SR, Mazur P. 1969. *Non-equilibrium thermodynamics*. Amsterdam: North Holland.

Detournay E, Cheng H-DA. 1993. Fundamentals of poroelasticity. In *Comprehensive rock engineering: principles, practice and projects*. ed. JA Hudson, pp. 113–171. Oxford: Pergamon.

Evans FG. 1973. *Mechanical properties of bone*. Springfield, IL: Charles C. Thomas.

Frost HM. 1960. Measurement of osteocytes per unit volume and volume components of osteocytes and canaliculae [sic] in man. *Henry Ford Hosp Med Bull* **8**:208–211.

Frost HM. 1962. Specific surface and specific volume of normal human lamellar bone. *Henry Ford Hosp Med Bull* **10**:35–41.

Frost HM. 1964. *The laws of bone structure*. Springfield, IL: Charles C. Thomas.

Frost HM. 1969. Tetracycline-based histological analysis of bone remodeling. *Calcif Tissue Res* **3**:211–237.

Harrigan T, Mann RW. 1984. Characterization of microstructural anisotropy in orthotropic materials using a second rank tensor. *J Mater Sci* **19**:761–767.

Hegedus DH, Cowin SC. 1976. Bone remodeling, II: small strain adaptive elasticity. *J Elast* **6**:337–352.

Hodgskinson R, Currey JD. 1990a. Effects of structural variation on Young's modulus of non-human cancellous bone. *J Eng Med, Proc. Inst Mech Eng* **204**:43–52.

Hodgskinson R, Currey JD. 1990b. The effect of variation in the structure on Young's modulus of cancellous bone: a comparison of human and non-human material. *J Eng Med, Proc Inst Mech Eng* **204**:115–121.

Hollister SJ, Fyhrie DP, Jepsen KJ, Goldstein SA. 1991. Application of homogenization theory to the study of trabecular bone mechanics. *J Biomech* **24**:825–839.

Jaworski ZFG, Liskova-Kiar M, Uhthoff HK. 1980. Effect of long-term immobilization on the pattern of bone loss in older dogs. *J Bone Joint Surg* **62B**:104–111.

Jee WSS. 1983. The skeletal tissues. In *Cell and tissue biology*, 6th ed., ed. L. Weiss, pp. 200–255. Baltimore: Urban and Schwartzenberg.

Kabel J, van Rietbergen B, Dalstra M, Odgaard A, Huiskes R. 1999. The role of an effective isotropic tissue modulus in the elastic properties of cancellous bone. Submitted to *J Biomech* **32**:673–680.

Keaveny TM, Pinilla TP, Crawford RP, Kopperdahl DL, Lou A. 1997. Systematic and random errors in the testing of trabecular bone. *J Orthop Res* **15**:101–110.

Knets I, Malmeister A. 1977. *Deformability and strength of human compact bone tissue: mechanics of Biological Solids*. Sofia: Bulgarian Academy of Sciences.

Lanyon LE, Goodship AE, Pye CJ, MacFie JH. 1982. Mechanically adaptive bone remodeling. *J Biomech* **15**:141–154.

Li G, Bronk JT, An KN, Kelly PJ. 1987. Permeability of cortical bone of canine tibiae. *Microcirc Res* **34**:302–311.

Macaulay MA. 1987. *Introduction to impact engineering*, pp. 201–30. London: Chapman and Hall.

Martin RB, Burr DB. 1989. *Structure, function and adaptation of compact bone*. New York: Raven Press.

Martin RB, Burr DB, Sharkey NA. 1998. *Skeletal tissue mechanics*. New York: Springer.

Morris MA, Lopez-Curato JA, Hughes SPF, An KN, Bassingthwaighte JB, et al. 1982. Fluid spaces in canine bone and marrow. *Microvasc Res* **23**:188–200.

Meyer GH. 1867. Die architectur der spongiosa. *Arch Anat Physiol Wiss Med, Reich DuBois-Reymon Arch* **34**:615–628.

Odgaard A. 1997. Three-dimensional methods for quantification of cancellous bone architecture. *Bone* **20**:315–328.

Odgaard A, Kabel J, van Rietbergen B, Dalstra M, Huiskes R. 1997. Fabric and elastic principal directions of cancellous bone are closely related. *J Biomech* **30**:487–495.

Pollack SR, Salzstein R, Pienkowski D. 1984. The electric double layer in bone and its influence on stress-generated potentials. *Calcif Tissue Int* **36**:S77–S81.

Reid SE, Reid SE Jr. 1984. *Head and neck injuries in sports*, p. 54. Springfield, IL: Charles C. Thomas.

Reilly DT, Burstein AH, Frankel VH. 1974. The elastic modulus for bone. *J Biomech* **7**:271–281.

Reilly DT, Burstein AH. 1975. The elastic and ultimate properties of compact bone tissue. *J Biomech* **8**:393–405.

Rice JC, Cowin SC, Bowman JA. 1988. On the dependence of the elasticity and the strength of cancellous bone on apparent density. *J Biomech* **22**:155–168.

Rice JR, Cleary MP. 1976. Some basic stress diffusion solutions for fluid-saturated elastic porous media with compressible constituents. *Rev Geophys Space Phys* **14**:227–241.

Rouhana SW, Johnson MW, Chakkalakal DR, Harper RA, Katz JL. 1981. Permeability of compact bone. *Joint ASME–ASCE Conf Biomech Symp* **43**:169–172.

Salzstein RA, Pollack SR. 1987. Electromechanical potentials in cortical bone, II: experimental analysis. *J Biomech* **20**:271–280.

Salzstein RA, Pollack SR, Mak AFT, Petrov N. 1987. Electromechanical potentials in cortical bone, I: a continuum approach. *J Biomech* **20**:261–270.

Schaffler MB, Burr DB. 1988. Stiffness of compact bone: effects of porosity and density. *J Biomech* **21**.13–16.

Siperko LM, Landis WJ. 2001. Aspects of mineral structure in normally calcifying avian tendon. *J Struct Biol* **135**:313–320.

Smit TH, Huyghe JM, Cowin SC. 2002. Estimation of the poroelastic parameters of bone. *J Biomech* **35**:829–836.

Starkebaum W, Pollack SR, Korostoff E. 1979. Microelectrode studies of stress-generated potentials in four-point bending of bone. *J Biomed Mater Res* **13**:729–751.

Turner CH, Cowin SC, Rho JY, Ashman RB, Rice JC. 1990. The fabric dependence of the orthotropic elastic properties of cancellous bone. *J Biomech* **23**:549–561.

Uhthoff HK, Jaworski ZFG. 1978. Bone loss in response to long-term immobilization. *J Bone Joint Surg* **60-B**:420–429.

Van Leeuwenhoeck A. 1678. Microscopical observations on the structure of teeth and other bones. *Phil Trans Roy Soc* **12**:1002–1003.

Van Rietbergen B, Odgaard A, Kabel J, Huiskes R. 1996. Direct mechanical assessment of elastic symmetries and properties of trabecular bone architecture. *J Biomech* **29**:1653–1657.

Van Rietbergen B, Odgaard A, Kabel J, Huiskes R. 1998. Relationships between bone morphology and bone elastic properties can be accurately quantified using high-resolution computer reconstructions. *J Orthop Res* **16**:23–28.

Wang L, Fritton SP, Cowin SC, Weinbaum S. 1999. Fluid pressure relaxation depends upon osteonal microstructure: modeling of an oscillatory bending experiment. *J Biomech* **32**:663–672.

Weinbaum S, Cowin SC, Zeng Yu. 1991. A model for the fluid shear stress excitation of membrane ion channels in osteocytic processes due to bone strain. *1991 advances in bioengineering*, pp. 317–20, ed. R Vanderby. New York: American Society of Mechanical Engineers.

Wertheim G. 1847. Mémorie sur l'elasticité et la cohésion des principaux tissues du corps humain. *Annals de chemie et de physique* (3rd ser) **21**:385–414.

Weinbaum S, Cowin SC, Zeng Yu. 1994. A model for the excitation of osteocytes by mechanical loading-induced bone fluid shear stresses. *J Biomech* **27**:339–360.

Whitehouse WJ. 1974. The quantitative morphology of anisotropic trabecular bone. *J Microsc* **101**:153–168.

Whitehouse WJ, Dyson ED. 1974. Scanning electron microscope studies of trabecular bone in the proximal end of the human femur. *J Anat* **118**:417–444.

Williams EA, Fitzgerald RHJ, Kelly PJ. 1984. Microcirculation in bone. In *The physiology and pharmacology of the microcirculation*, ed. NA Mortillaro. New York: Academic Press.

Wolff J. 1870. Uber der innere Architektur der Knochen und ihre Bedeutung fur die Frage vom Knochenwachstum. *Arch Path Anat Physiol Med, Virchovs Arch* **50**:389–453.

Wolff J. 1892. *Das gesetz der transformation der knochen*. Berlin: Hirschwald.

Wolff J. 1986. *The law of bone remodelling*. Berlin: Springer.

Woo SLY, Kuei SC, Dillon WA, Amiel D, White FC, et al. 1981. The effect of prolonged physical training on the properties of long bone — a study of Wolff's Law. *J Bone Joint Surg* **63-A**:780–787.

Yang G, Kabel J, van Rietbergen B, Odgaard A, Huiskes R, et al. 1999. The anisotropic Hooke's law for cancellous bone and wood. *J Elast* **53**:125–146.

Yoon HS, Katz JL. 1976. Ultrasonic wave propagation in human cortical bone, II: measurements of elastic properties and micro-hardness. *J Biomech* **9**:459–470.

Zhang D, Cowin SC, Weinbaum S. 1997. Electrical signal transmission and gap junction regulation in bone cell network: a cable model for an osteon. *Ann Biomed Eng* **25**:357–374.

Zhang D, Weinbaum S, Cowin SC. 1998. Estimates of the peak pressures in the bone pore water. *J Biomech Eng* **120**:697–703.

# 12

# BONE TISSUE ADAPTATION

> "A perceptive man, who watches living bone grow or adapt to disease, must realize that he is seeing an exquisitely controlled directionality and metering of the cell behavior responsible for the form, size, and location in space of bone. Similar control of directionality is shown by other human tissues, by all other vertebrate and most nonvertebrate animal tissues and by most botanical tissues." (Harold Frost, 1964, preface)

## 12.1. INTRODUCTION

Functional adaptation is the term used to describe the ability of organisms to increase their capacity to accomplish their function upon increased demand and to decrease their capacity with lessened demand. Living bone is continually undergoing processes of growth, reinforcement, and resorption that are collectively termed "strain adaptation." The strain adaptation processes in living bone are the mechanisms by which the bone adapts its overall structure to changes in its load environment. An example of bone strain adaptation was mentioned at the beginning of Chapter 1 when it was noted that professional tennis players have bones in their upper playing arm that are 30% greater in cross-sectional area than the bones in their nonplaying arm. The time scale of the strain adaptation processes is on the order of months or years. Changes in lifestyle that change the loading environment, for example, taking up jogging, have strain adaptation times on the order of many months. Bone strain adaptation associated with trauma has a shorter strain adaptation time — on the order of weeks in humans. The time scales of these strain adaptation processes should be distinguished from developments in bone due to growth, which have a time scale on the order of decades in humans, and developments due to Darwinian natural selection (adaptive evolution) that have a time scale of many lifetimes.

A distinction is made between *surface* and *internal* strain adaptation (Frost, 1964). Surface strain adaptation refers to resorption or deposition of the bone material on the external surface of the bone. Actually, all bone strain adaptation is surface adaptation, that is to say, that all deposition and resorption of bone occurs on a surface, the IC. Recall from the previous chapter that the IC includes the endosteum, the inner layer of the periosteum, all the surfaces of the tubular cavities of bone that contain the vasculature, and the external surface of the trabeculae. Internal strain adaptation refers to resorption or reinforcement of the bone tissue internally by changing the bulk density of the tissue, but this is actually accomplished by surface strain ad-

aptation. Internal strain adaptation is the average over an RVE of the surface strain adaptation that is occurring within the volume. In cancellous bone the trabeculae become more or less numerous and their thickness can vary. In cortical bone internal strain adaptation occurs by changes in the diameter of the lumen of the osteons and by the total replacement of osteons.

Understanding and predicting the strain-controlled adaptation properties of living bone are particularly important for proper design of prosthetic devices that contact bone tissue. These devices include fracture fixation plates, surgical screws, and artificial joints. A prosthesis places a stress on adjacent bone tissue, and if this stress is different from the stress that the bone tissue is accustomed to, the bone will remodel. It is possible that the remodeled bone tissue will be weaker in some sense and lead to failure of the surgical procedure. It has been suggested that femoral resorption could be the predominant factor in implant stem fracture of a total hip replacement.

The objective of a theory of tissue adaptation is to provide numerical models or the basis for boundary problems that will predict the adaptive behavior of the tissue under altered environmental load. The types of problems to which these theories are applied include strain adaptation around bone implants and modeling of the type of experiments on the adaptation of bone tissue to its strain environment described in §§2.4–12.9. The word "phenomenological" is employed to describe these theories because each makes a hypothesis in the form of a constitutive equation concerning the stimulus of the bone structural adaptation. These theories do not attempt to explain the cellular mechanisms by which the bone senses the mechanical loading and begins to deposit or resorb tissue. A cellular level physiological or mechanistic understanding of the bone tissue mechanosensory system will provide insight into the following three important clinical problems: (a) how to maintain the long-term stability of bone implants, (b) the physiological mechanism underlying osteoporosis, and (c) how to maintain bone in long-duration spaceflights and long-term bed rest. These cellular mechanisms are only partially understood, and some current understanding will be sketched in §12.10.

## 12.2. FOUR ANIMAL EXPERIMENTS

Four animal experiments are discussed here in order to illustrate functional adaptation. In the first two experiments the mechanical load on the animal bone is reduced and in the second two it is increased. The first of these experiments involved disuse atrophy in young beagles (Uhthoff and Jaworski, 1978). In this study one forelimb of 1-year-old beagles was immobilized in a plaster cast for different time periods, from 2 to 40 weeks. The contralateral forelimb was used as a control. Following sacrifice, the metacarpal bones were examined for evidence of surface and internal strain adaptation. The results showed significant bone resorption at the periosteal surface, but little net movement of the endosteal surface, and little net internal strain adaptation. Figure 12.1a shows the cross-section of a metacarpal bone from the contralateral control limb of one of the experimental animals, and Figure 12.1b shows the cross-section of a metacarpal bone from one experimental limb following 40 weeks of immobilization. The second comparison experiment is one that repeated the study described above but used 8-year-old beagles (Jaworski et al., 1980). In contrast to the results with young beagles, the study with older animals showed little net strain adaptation on the periosteal surface but significant bone resorption on the endosteal surface. Again, there was little net internal strain adaptation. Figure 12.2a shows the cross-section of a metacarpal bone from the contralateral control limb of one of the experimental animals, and Figure 12.2b shows the cross-section of a metacarpal bone from an experimental limb following 40 weeks of immobilization.

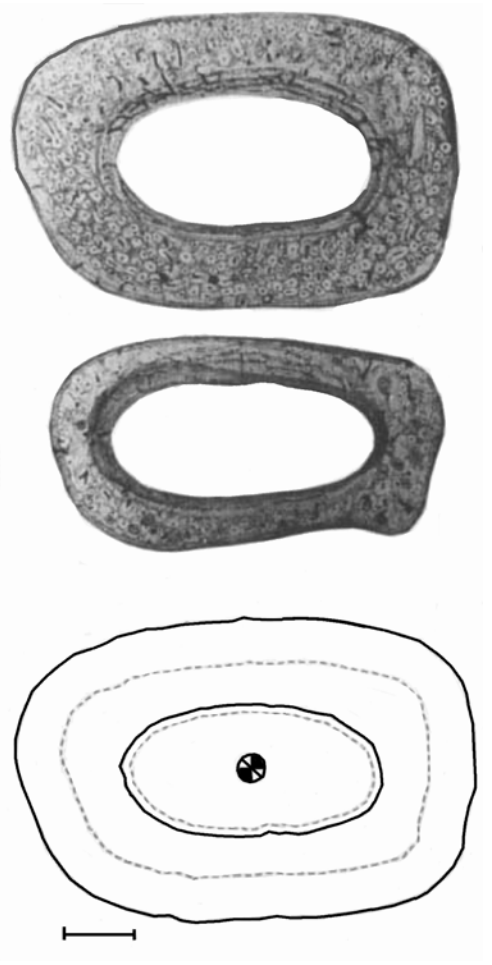


**Figure 12.1**. The young beagle experiment (Uhthoff and Jaworski, 1978). Each illustration represents the cross-section of a metacarpal. (a) (top) The contralateral control metacarpal at 40 weeks. (b) (middle) The experimental metacarpal at 40 weeks, showing marked periosteal resorption and slight endosteal deposition. (c) (bottom) The calculated remodeling. The solid lines represent the surfaces of the control bone, (a, top) above, and the dashed lines represent the predicted geometry at 40 weeks using the constants shown in Table 12.1. The indicated length is 1 mm.

The experiments associated with increased loading of bones are more varied. The third animal experiment showed that increased exercise activity in young and small pigs could result in net bone deposition on both the endosteal and periosteal bone surfaces of the femora (Woo et al., 1981). The exercise program consisted of forced jogging for 1 hour every day, and for 30 additional minutes every other day, over a period of a year. Figure 12.3a shows the cross-section of the femur from one pig in the control group, and Figure 12.3b is the cross-section of a femur from one of the exercised animals. Notice that the periosteal surface appears to have increased slightly in size, and there is also significant new bone deposition on the endosteal surface. The fourth experiment was an ulnar osteotomy (Lanyon et al., 1982). This study was conducted with the objective of measuring the change in bone strain while inducing a functional adaptation to hyperphysiological stress states. Mature sheep were subjected

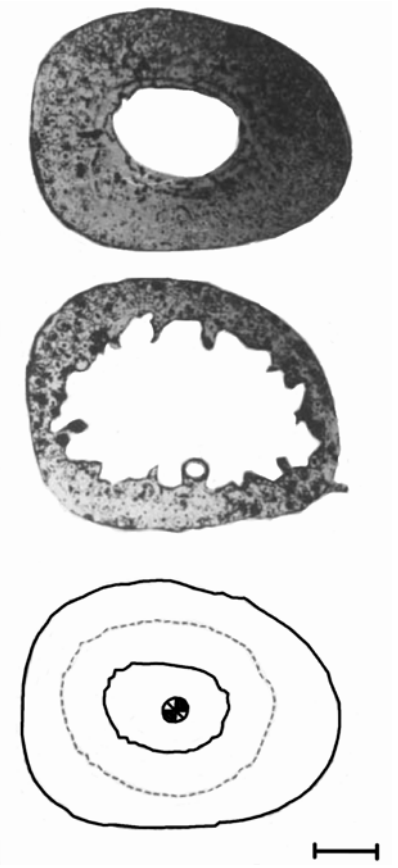


**Figure 12.2**. The old beagle experiment (Jaworski et al., 1980). Each illustration represents the cross-section of a metacarpal. (a) (top) The contralateral control metacarpal at 40 weeks. (b) (middle) The experimental metacarpal at 40 weeks, showing marked endosteal resorption. (c) (bottom) The calculated remodeling. The solid lines represent the surfaces of the control bone, (a, top) above, and the dashed lines represent the predicted geometry at 40 weeks using the constants shown in Table 12.1. The indicated length is 1 mm.

to an ulnar osteotomy (removal of a section of the ulnar diaphysis) on their right limb, and the left forelimb was used as a control. The strain in the radii was monitored by means of in vivo strain gauging at the cranial and caudal periosteal surfaces. Figure 12.4a is a photograph of the cross-section of the intact ulna and radius from the left control limb. Figure 12.4b shows the radius from the right experimental limb 1 year after removal of the ulna. Immediately following surgery to remove the ovine ulna, there was, on average, an 8% increase in compressive strain on the side facing the missing ulna (caudal side), and, on average, a 20% increase in tensile strain on the opposite (cranial) side. One year later, the compressive strain on the face of the radii facing the removed ulna was 10% less than the strain on the control radius. On the opposite side of the radius, the measured tensile strain was 19% less than the opposite control radii. Thus, although most of the bone deposition occurred on the compressive side of the radius that faced the missing ulna, both tensile and compressive strains were reduced to below that recorded on the control radii.



**Figure 12.3**. The exercised young swine experiment (Woo et al., 1981). Each illustration represents the cross-section of a femur. (a) (top) A femur from the control group. (b) (middle) The femur of an experimentally exercised animal after 1 year showing both endosteal and periosteal bone deposition. (c) (bottom) The calculated remodeling. The solid lines represent the surfaces of the control bone, (a, top) above, and the dashed lines represent the predicted geometry at 1 year using the constants shown in Table 12.1. The indicated length is 1 mm.

## 12.3. REPRESENTATION OF THE STIMULUS TO BONE REMODELING

The theories of bone strain adaptation considered here are all conceptually based on the poroelastic model for bone tissue described in Chapter 9. The bone matrix, that is to say, the solid extracellular material and the bone cells, is modeled as a solid structure with interconnected pores, a porous anisotropic linear elastic solid. The extracellular fluid and blood are modeled as a single fluid. Thus, the basic model of bone is as saturated porous, anisotropic linear elastic solid perfused with a fluid, a poroelastic model. However, the bone strain adaptation poroelastic model is chemically reacting. The bone cells control and mediate the chemical reactions



**Figure 12.4**. The ulnar ostectomy experiment with mature sheep (Lanyon et al., 1982). Each illustration represents the bone cross-sections in the sheep forelimb. (a) (top) The contralateral control limb at 1 year showing the radius with the intact ulna. (b) (middle) The experimental radius at 1 year, showing marked asymmetric periosteal deposition. (c) (bottom) The calculated remodeling. The solid lines represent the surfaces of the control bone, (a, top) above, and the dashed lines represent the predicted geometry at 9 months using the constants shown in Table 12.1. The indicated length is 1 mm.

that convert body fluids into solid porous bone matrix and vice versa. As a result of the chemical reactions, mass, momentum, energy, and entropy are transferred to or from the solid porous bone matrix. The rates of these chemical reactions depend on strain and are very slow. It can be estimated, from studies using tetracycline labeling (Frost, 1969), that the characteristic time for these reactions is on the order of months. The characteristic time of the chemical reaction is several orders of magnitude greater than the characteristic time associated with complete perfusion of the blood plasma in the bone; hence, any excess heat generated by the chemical reactions is quickly dissipated. Characteristic times are a significant aspect of the modeling of the strain adaptation process, and additional characteristic times should enter modeling considerations. Let $T_A$ denote the time that biological processes take to complete significant growth (or

strain adaptation) associated with a mechanical loading, and let $T_L$ denote the characteristic period of mechanical loading. Rough estimates of these numbers are 2 weeks (but up to months) and 1 second, respectively; thus, $T_L/T_A$ is a small number, on the order $10^{-6}$ or smaller. Because $T_A$ is so large compared to $T_L$, inertia effects are neglected in analysis of the remodeling process. In order to keep the loading and adaptation time scales separate, let $t$ denote time on the loading time scale and $T$ denote time on the adaptation time scale.

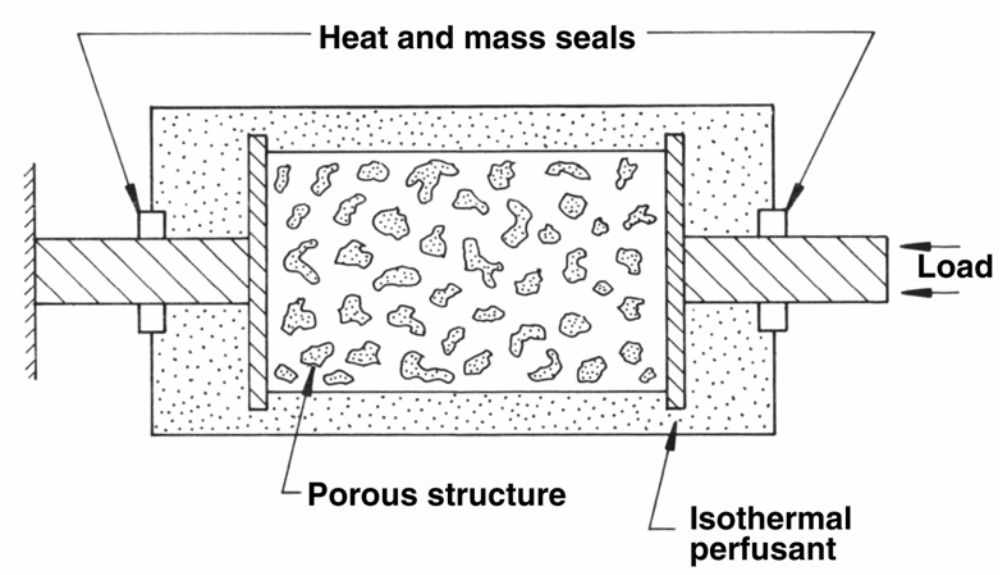



**Figure 12.5**. Schematic illustration of the idealized model for bone stress adaptation. The fact that living bone is encased in a living organism is reflected in the model by setting the elastic porous solid in a bath of the perfusant. The mechanical load is applied directly to the porous structure across the walls of the perfusant bath as illustrated. The system consisting of the elastic porous solid and its perfusant bath is considered to be closed with respect to mass, heat energy, and entropy transfer, but open with respect to momentum transfer from loading. The system consisting of only the elastic porous solid without its entrained perfusant is open with respect to momentum transfer as well as mass, energy, and entropy transfer. The bone matrix is taken as the control system since the changes in the mechanical properties of the bone matrix alone determine the changes in the mechanical properties of the whole bone. Reprinted with permission from Cowin and Hegedus (1976).

The "phenomenological" bone strain adaptation theories are based on the postulate that there exists a causal relationship between the rate of deposition or resorption of the bone matrix at any point and a stimulus, generally a measure of the mechanical loading (strain, strain rate, strain energy, stress, fatigue microdamage) at that point in the bone matrix. A schematic diagram of this model is shown in Figure 12.5. The fact that living bone is encased in a living organism is reflected in the model by setting the elastic porous solid in a bath of the perfusant. The mechanical load is applied directly to the porous structure across the walls of the perfusant bath as illustrated. The system consisting of the elastic porous solid and its perfusant bath is considered to be closed with respect to mass, heat energy, and entropy transfer, but open with respect to momentum transfer from loading. The system consisting of only the elastic porous solid without its entrained perfusant is open with respect to momentum transfer as well as mass, energy, and entropy transfer. The bone matrix is taken as the control system since

changes in the mechanical properties of the bone matrix alone determine the changes in the mechanical properties of the whole bone.

The critical feature in these models is the constitutive equation (hypothesis) that specifies the relationship between the rate of deposition or resorption of the bone matrix at any point and a measure of the mechanical loading history at that point in the bone matrix. The measure of the mechanical loading history (strain, strain rate, strain energy, stress, fatigue microdamage) at a point that is the true biological stimulus, although much discussed and written about, is not precisely known. A variety of mechanical loading stimuli associated with ambulation (at a frequency of one to two Hz) have been considered for bone strain adaptation. The majority have followed Wolff (1892; translated into English 1986) in suggesting that some aspect of mechanical loading of bone is the stimulus. The mechanical stimuli suggested include strain, stress, strain energy, strain rate, and fatigue microdamage. In some cases the time-averaged values of these quantities are suggested as the mechanical stimulus, and in others the amplitudes of the oscillatory components and/or peak values of these quantities are the candidates for the mechanical stimulus. Two dozen possible stimuli were compared in a combined experimental and analytical approach (Brown et al., 1990). The data supported strain energy density, longitudinal shear stress, and tensile principal stress or strain as stimuli; no stimulus that could be described as rate dependent, nor any related to cracks and microdamage, were among the two dozen possible stimuli considered in the study. The case for strain rate as a bone adaptation stimulus has been building over the last quarter century (see Cowin and Moss, 2000, for a review of the literature). Animal studies have suggested the importance of strain rate, and experiments have quantified the importance of strain rate over strain as a strain adaptation stimulus. Skeletal muscle contraction is a typical bone-loading event and has been implicated as a stimulus. Frequency is one of the critical parameters of the muscle stimulus and it serves to differentiate this stimulus from the direct mechanical loads of ambulation, which occur at a frequency of 1–2 Hz. The frequency of contracting muscle in tetanus is from 15 Hz to a maximum of 50–60 Hz in mammalian muscle. The case for fatigue microdamage as a bone adaptation stimulus is an old suggestion that has been given renewed impetus by the recent discovery of microcracking in bone using histological staining techniques. In the models considered here the strain is denoted by $\varepsilon$ and considered to be a function of both time scales, $t$ and $T$; thus, $\varepsilon = \varepsilon(t, T)$. The as-yet-undiscovered operation of extracting from the strain history the portion that actually influences bone adaptation is denoted by $\mathcal{S}\{\varepsilon(t,T)\}$, and the result of this operation by $\bar{\varepsilon}(T)$, thus

$$\mathcal{S}\{\varepsilon(t,T)\} = \bar{\varepsilon}(T) . \tag{12.1}$$

Thus, $\bar{\varepsilon}(T)$ represents the stimulus that induces bone strain adaptation, although we are not sure exactly what aspects of the strain history of the bone tissue it represents.

## 12.4. A PHENOMENOLOGICAL THEORY OF SURFACE ADAPTATION

The objective of this section, and of §12.8, is to present the two prototype analytical models for the strain adaptation process, namely, the phenomenological theories of surface bone strain adaptation and internal bone strain adaptation, respectively. The common background and assumptions underlying the theories of surface and internal bone strain adaptation have been described in the previous section. There are two important distinctions between the two theories, one of RVE length scale and one of location of the chemical reactions. The surface strain adaptation theory is more accurate because all changes in bone structure occur on the IC and a small RVE length scale may be used. The internal strain adaptation theory has a much larger

length scale RVE; this larger RVE represents an average over the internal IC of bone and treats the structural adaptation on the IC as changes in the solid volume fraction. The second distinction between the two theories is made upon the locations at which the chemical reactions occur and the way in which mass is added or removed from the solid porous bone matrix. In the theory of surface strain adaptation the chemical reactions occur only on the IC of the bone, and mass is added or removed from the bone by changing the external shape of the whole bone or internal bone structure, such as the width of an osteonal lumen. During surface strain adaptation the region interior to the IC of the bone remains at constant bulk density. In the theory of internal strain adaptation the chemical reactions occur everywhere within the solid porous bone matrix, and mass is added by changing the bulk density of the bone matrix and without changing the exterior dimensions of the bone. In both cases, the rate and direction of the chemical reaction at a point are determined by the stimulus at the point. It is important to note that these two theories are neither contradictory nor incompatible.

The theories of surface strain adaptation acknowledge the observed fact that external changes in bone shape are induced by changes in the loading environment of the bone. This type of theory postulates a causal relationship between the rate of surface deposition or resorption and the stimulus at the surface of the bone. The bone is considered to be an open system with regard to mass transport, and the mass of the bone will vary as the external shape of the bone varies. The assumption is made in the theories of surface strain adaptation that bone can be modeled as a linear elastic object whose free surfaces move according to an additional specific constitutive relation (Cowin and Van Buskirk, 1979). The additional constitutive relation for the movement of the free surface is the result of a postulate that the rate of surface deposition or resorption is proportional to the change in the stimulus at the surface from a reference value of the stimulus. Let $S$ denote the stimulus and $S_R$ denote the reference value of the stimulus. The stimulus is a function of the loading time scale $t$, and thus $S(t)$. The influential part of the stimulus is determined from the stimulus by operation $\mathcal{S}\{S(t)\} = \overline{S}(T)$, a notation introduced in eq. (12.1). At the reference value of the stimulus, $\overline{S}_R$, there is no movement of the surface. In order to express the constitutive equation for the surface movement in equation form, some notation is introduced. Let $Q$ denote a surface point on the linear elastic object representing the bone tissue and let $\mathbf{n}$ denote an outward unit normal vector of the tangent plane to the surface of the object at $Q$ (Figure 12.6). Let $U$ denote the speed of the adapting surface normal to the surface on adaptation time scale $T$, that is to say, $U$ is the velocity of the surface in the $\mathbf{n}$ direction. The velocity of the surface in any direction in the tangent plane is zero because the surface is not moving tangentially with respect to the object. The hypothesis for surface strain adaptation is that the speed of strain adaptation surface $U$ is proportional to stimulus difference $\overline{S} - \overline{S}_R$; thus,

$$U(Q,T) = C(Q)[\overline{S}(T) - \overline{S}_R] \tag{12.2}$$

where $C(Q)$ is the surface strain adaptation rate function that is completely contracted with stimulus difference $\overline{S} - \overline{S}_R$. Surface strain adaptation rate function $C(Q)$ has a tensorial order that is the same as the tensorial order of stimulus $\overline{S}$, so that when the two are completely contracted with each other, the result is a scalar. Thus, if $\overline{S}$ is a second-order tensor, as it would be in the case of strain, strain rate, stress, and fatigue microdamage, $C(Q)$ is also a second-order tensor. On the other hand, if $\overline{S}$ is a scalar such as the strain energy, then $C(Q)$ is also a scalar. When a definite stimulus and a specific form of surface strain adaptation rate function $C(Q)$ have been selected, the material parameters that characterize the function are called surface strain adaptation coefficients. The surface strain adaptation rate coefficients and the reference values of stimulus are phenomenological coefficients of the bone surface and must be deter-

mined by experiment. If it is assumed here that surface strain adaptation rate function $C$ is not site specific, that is to say, independent of the position of surface point $Q$ on any specified surface of the IC, then $Q$ is eliminated from the right-hand side of (12.2). Experimental data suggest that $C$ may have different values on different IC surfaces, such as the endosteum and periosteum.

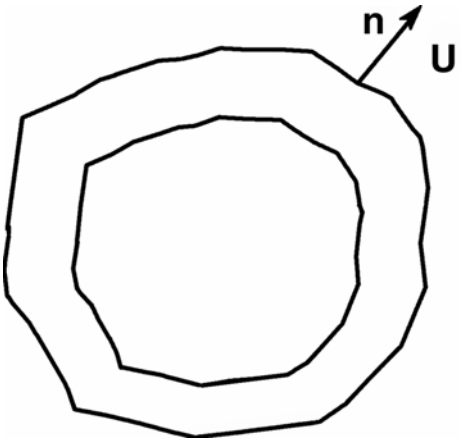



**Figure 12.6**. Cross-section of an animal long bone. Unit vector **n** denotes an outward unit normal vector of the tangent plane to the surface of the long bone. **U** is the speed of the surface in the **n** direction.

Equation (12.2) gives the normal velocity of the surface at point $Q$ as a function of the existing stimulus value at $Q$. If the stimulus value at $Q$, $\overline{S}(Q,T)$, is equal to reference stimulus value $\overline{S}_R$, then the velocity of the surface is zero and no adaptation occurs at that surface point. If the right-hand side of (12.2) is positive, the surface will be growing by deposition of material. If, on the other hand, the right hand side of (12.2) is negative, the surface will be resorbing. Equation (12.2) by itself does not constitute the complete theory. The theory is completed by assuming that bone is a linearly elastic material. Thus, the complete theory is a modification of linear elasticity in which the external surfaces of the object move according to the rule prescribed by equation (12.2). A boundary-value problem will be formulated in the same manner as a boundary-value problem in linear elastostatics, but it will be necessary to specify the boundary conditions for a specific time period. As the object evolves to a new shape, the stimulus value and the stress and strain states will be varying quasistatically. At any instant the object will behave exactly as an elastic object, but moving boundaries will cause local stimulus, stress, and strain to redistribute themselves slowly with time.

**Problem**

12.4.1. If history of stress $T_{zz}(Q,t)$ that a bone tissue experiences at point $Q$ is the sum of many sinusoidal stresses at different amplitudes, $A_{zz}^{(i)}(Q)$ and different frequencies, $\omega_i$, then $T_{zz}(Q,t)$ has the following representation:

$$T_{zz}(Q,t) = P_{zz}^{(o)}(Q) + \sum_{i=1}^{N} A_{zz}^{(i)}(Q)\sin\omega_i t$$

and the stimulus is defined as operation (12.4), should $\mathbf{T}$, $\dot{\mathbf{T}}$, or $\ddot{\mathbf{T}}$ be averaged to provide a stimulus that increases with increasing frequency, consistent with experimental observations? Please provide a rationale for your conclusion.

## 12.5. ESTIMATING REMODELING PARAMETERS

The methods of determining quantitative estimates of both the stress state responsible for inducing the surface remodeling response as well as the remodeling equilibrium stress state will now be described for the animal experiments summarized in §12.2. For three of the experiments little quantitative data are provided to accurately determine the mechanical loading history estimates on the normal bone or on the abnormally loaded bone (Uhthoff and Jaworski, 1978; Jaworski et al., 1980; Woo et al., 1981). In addition, strain gauge data provided by Lanyon et al. (1982) for the sheep osteotomy study did not provide sufficient information to uniquely determine either the points of application or the magnitudes of the loading forces. Consequently, only the very approximate and crude mechanical loading history estimates described below were employed. The ideal experimental information for use with a remodeling theory based on describing and predicting the mechanical objectives of bone remodeling would include sufficient information to accurately determine the loading history on both the experimental and control bones, the geometry of both bones, the material distribution in the bones, and the time course of the remodeling process. The analysis of these surface remodeling animal experiments may presently only be accomplished by making ad-hoc estimates of the mechanical loading history for each animal experiment. The ad-hoc methods of estimating the mechanical loading history are described in Cowin et al. (1985) and are repeated below. These ad-hoc methods produce only gross estimates of the mechanical loading history. They were used because there were little or no recorded data on the mechanical loading history during these animal experiments. Despite the simplicity of the model and the lack of data that would be required to uniquely define the load environments, the remodeling constants for each of these animal experiments are of approximately the same magnitude. This similarity, despite differences in loading environment, animal species, and age, gives reason to be optimistic about the applicability of the surface remodeling theory as a tool for prediction of in vivo bone remodeling.

### Immobilization Experiments

In order to determine the magnitudes of the centric load and changes in the magnitude of the centric loading during the immobilization experiments, some assumptions are necessary since no load or strain data were obtained during these experiments. These assumptions concern the magnitude of the time-averaged physiological loads on the forelimbs. For the immobilization studies (Uhthoff and Jaworski, 1978; Jaworski et al., 1980), the convention that two-thirds of body weight is distributed over the upper torso of a canine was used (Van Cochran, 1982). Assuming that the load on the upper portion of the body is distributed equally between the left and right sides, one third of the entire body weight is therefore carried by each forelimb. The bone under study in these experiments is the third metacarpal of the right forelimb. Assuming that the load on the limb is distributed equally among the four metacarpals in the canine, then the load on the third metacarpal would equal one twelfth of total body weight. The mean body weight of the young beagles was 10 kg, while the mean body weight of the older beagles was 13.5 kg. Using these assumptions concerning the time-averaged load on the metacarpals and

the cross-sectional areas of the control metacarpals, the equilibrium stresses were calculated to be –0.43 MPa for the younger beagles, and –0.73 MPa for the older beagles.

After immobilization, the bones were subjected to hypophysiological loads that resulted in bone resorption. The loads on the metacarpals following immobilization were assumed to be significantly reduced but not zero due to the assumptions that some muscle forces were still present, and that casting did not totally prevent use of the limb. Therefore, the change in loading magnitude was assumed to have decreased in proportion to the loss of cross-sectional bone area by means of resorption. The time-averaged load following immobilization was thus 45% of the time-averaged load for the control bone in the young beagle, and 51% of the time-averaged load on the control bone for the old beagle.

Some error may be associated with this scheme if, during the course of the immobilization experiments, the load experienced by the bones was significantly closer to zero than we have assumed for computational purposes. It could be that the experimental bones have reached some genetically determined minimum bone mass (Lanyon, 1984a). Experimental measurements of the bone strain would be required to accurately determine the actual loads due to the immobilization created by plaster casting.

### Exercise Experiments

The exercise experiments of Woo et al. (1981) led to increased loads on the femora and to hypertrophy of that bone. The centric load magnitude and the change in centric loading magnitudes were calculated by assuming that a third of the body weight is distributed equally across the two hind legs, so that the normal time-averaged physiological load on each femur was calculated to be one-sixth of the body weight. From the mean body weight of the exercised swine (66 kg) and from calculated cross-sectional areas of the control femora, the equilibrium stress was calculated to be –0.49 MPa.

The exercise program consisted of forced jogging that was an average of 1.25 h of running each day for 1 yr. Since the loads used in this study are time averaged, the hyperphysiological load was averaged over a 24-h period. It was assumed that for 22.75 h of each day, the load on the femur was one sixth body weight, while for the remaining 1.25 h the load was the hyperphysiological load due to exercise. Using the concept of a dynamic load factor to relate the strains due to dynamic loads to the strains that would be caused by a static load of the same magnitude, the dynamic load was assumed to be twice the static load (Van Cochran, 1982). When a four-legged animal breaks stride, the forelimbs are on the ground, followed by the hind limbs on the ground. Thus, the total dynamic load is equally distributed on the two femora. The time-averaged hyperphysiological load due to the exercise was calculated to be

$$P_{avg} = (1/24)[t_s P_s, + t_d P_d] \tag{12.3}$$

where, $t_s$ = length of time of static load application per day (h); $t_d$ = length of time of dynamic load application per day (h); $P_s$ = magnitude of average static load; $P_d$ = magnitude of average dynamic load.

The time-averaged load calculated in this manner was –141.5 N, and the initial hyperphysiological stress for the experimental bone cross-section considered was thus –0.64 MPa. This represents a time-averaged increase in stress of 31% when compared with the control group.

### Ulnar Osteotomy

Before the ulna is removed, the radius and the ulna are assumed to be loaded by an axial compressive load, $-P$. In our, now rejected, preliminary analysis the compressive axial load was assumed to act through the centroid of the original combined areas. As described subsequently, the experimental strain gauge data show that there must be an original eccentricity of the axial load due to the distribution of tensile and compressive strains in the control radius. This eccentric loading gives rise to a remodeling equilibrium stress that varies linearly across the cross-sections of the two forelimb bones. The situation before the ulna is removed is illustrated in Figure 12.10.

The ulnar ostectomy is then modeled by removal of the ulna from between the platens, as shown in Figure 12.11. The platens are assumed to be constrained to move vertically, allowing no rotation. Therefore, a further eccentricity is added to the initial eccentric axial load now carried entirely by the radius. The effect of this additional eccentricity is an additional bending moment applied to the radius due to the moment arm created by the distance between the current point of load application and the point of initial load application. The magnitude of the time-averaged load is assumed to be constant.

In addition to the experimental strain gauge data reported, several assumptions were required to find the magnitude of the time-averaged load, the change in the average load, as well as the point of load application. The method of determining these time-averaged loads is described below.

### Ovine Ulnar Ostectomy

A schematic of the ovine ulnaectomy accomplished by Lanyon et al. (1982) is shown in Figure 12.7. In the lower right panel of Figure 12.7 the remodeling induced by the ulnaectomy is indicated by the shaded area. The initial assumption of a compressive axial load acting through the centroid of the original combined areas was checked by comparing the calculated strains with the peak strains measured by Lanyon et al. (1982) on the cranial and caudal surfaces and found to be inadequate. The strain data showed that the radius must sustain significant bending loads while remaining in remodeling equilibrium because tensile strains were measured on the cranial side while compressive strains were measured on the caudal side of the radius. Since the data from only two strain gauges were reported, one on the caudal surface and one on the cranial surface — the approximate locations are represented by the arrows on Figure 12.8 — the point of load application could not be uniquely established from the published data (the results from the two experimental radii that had three gauges around the circumference of the bone were not published). Therefore, in order to place a limit on the possible locations of the point of application of the resultant load, a line was constructed connecting the centroids of the radius and the ulna, and it was hypothesized that the point of load application would lie on this line.

The point of load application was then repositioned along this centroidal line (Figure 12.9) until the strains calculated were close to the peak strains measured by Lanyon et al. (1982). Since sufficient data were not provided to accurately determine either the magnitude of the peak loading corresponding to the peak strains measured or the point of application of the resultant force, various loading magnitudes were tested as well. It was found that relocation of the point of load application, represented by an X on Figure 12.8, along the line joining the centroids of the radius and ulna, resulted in a linear variation of the strains calculated at cranial and caudal surfaces. The final location chosen shown on Figures 12.8 and 12.9 gave calculated strains close to the peak strains measured with the loading magnitude set equal to 3.5 times

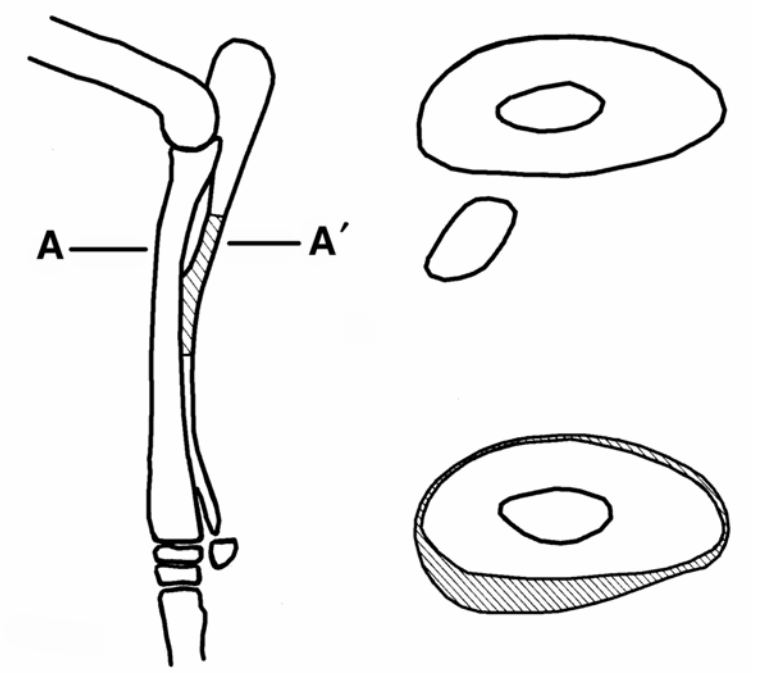



**Figure 12.7**. A schematic diagram of the bone tissue removed in the ulnar ostectomy experiment with mature sheep (Lanyon et al., 1982). Above right: the contralateral control limb at 1 year showing the radius with the intact ulna. Below right: the experimental radius at 1 year, showing the calculated remodeling.

body weight. Further confidence in this choice for the position of the eccentric axial load comes from the lateral view of the longitudinal geometry of a sheep forelimb (Lanyon et al., 1982). A line drawn from the middle of the upper joint to the middle of the lower forelimb provides a rough estimation of the line of action of the force due to the weight of the animal. Since there is a gradual curvature of the shaft of the radius at the level where the gauges were attached, the line places the load just outside the periosteum of the radius on the caudal side. This position corresponds closely to the position found by moving the load along the centroidal line and comparing calculated strain with experimentally measured strain.

Using the point of load application as indicated on Figure 12.8 with a magnitude of 3.5 times body weight gave calculated values for strain, at the point on the caudal surface corresponding to a strain gauge location of –1182 microstrain, as compared to a measured strain of –1172 ± 14 microstrain. Strain calculated at the point on the cranial surface was 419 compared to a measured strain of 635 ± 5 microstrain. The loading of 3.5 times body weight was the minimum loading that could generate tensile strains on the cranial surface close to those measured by Lanyon et al. (1982). Since for humans (normally with two-legged stance) Seireg and Arvikar (1975) report peak reaction forces of 7.1 times body weight in the knee, the value of 3.5 times body weight for sheep (normally four-legged stance) did not seem unreasonable. A further assumption required to find the remodeling equilibrium stresses on the radius was that, although the magnitude of the load associated with the remodeling equilibrium stresses would be less than the load associated with the peak strains described above, the point of load application of the two loads would be the same. The load magnitude associated with the remodeling equilibrium stress level was a time-averaged estimate of the dynamic loads, based on strains measured on the radius.

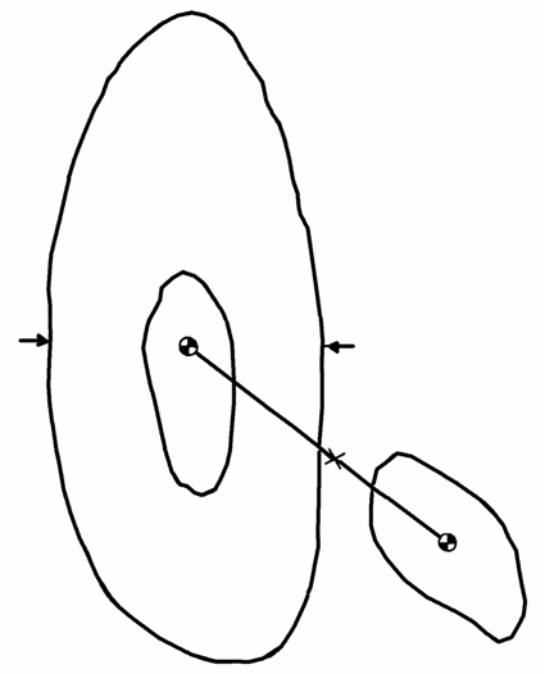


**Figure 12.8**. Cross-section of intact ovine forelimb. Line connects centroids of the radius and ulna, and the point of application of the resultant load is represented by the X. Arrows indicate location of strain calculations corresponding to the location of experimentally applied strain gauges.

Lanyon et al. (1982) published plots of the measured principal strains and directions for three gait cycles of normal sheep. The compressive strain on the caudal cortex fluctuates from nearly 0 to a peak value of –1172 microstrain. The area between the compressive strain curve and the time axis was approximated giving a time-averaged strain level of approximately 0.4 times the peak value. The previously discussed loading analysis for finding the peak loading gave 3.5 times body weight, or –1375 N, to provide calculated peak caudal strains near the experimentally measured –1172 microstrain. Hence, a constant force of –550 N provides the time-averaged strain for one gait cycle. During an hour of steady walking, the forelimb experienced approximately 3500 loading cycles, and during the other 23 hours each day the limb experienced a total of 950 loading cycles when casual limb movements are taken into account (Lanyon et al., 1982). It follows that during the 23 hours of relative inactivity the forelimb experienced (950/3500) hours of effective walking. Thus, the limb was estimated to have experienced 1.27 hours of loading at –550 N, and 22.73 hours with no load, giving a time-averaged load over one day of –29.1 N.

## 12.6. PREDICTION OF THE SURFACE ADAPTATION DUE TO THE BENDING OF BONE

In this section the conceptual formulation of the surface-remodeling problem in long bones subjected to eccentric axial loads is described. Observe again the schematic of the ovine ulnaectomy accomplished by Lanyon et al. (1982) shown in Figure 12.7. The mechanics problem with centric axial loads is a special case of the eccentric loading mechanics problem. The

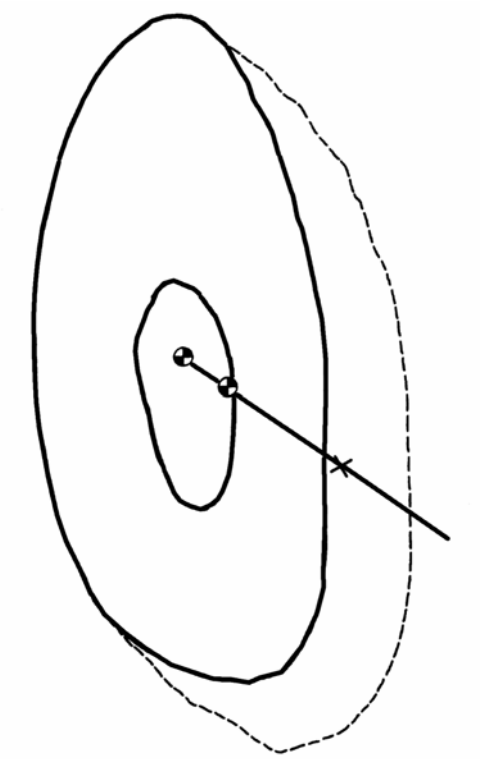


**Figure 12.9**. Cross-section of intact ovine forelimb after ulnaectomy. Line connects the centroid of the radius and the point of application of the resultant load, represented by the X. The dashed line represents the calculated remodeling at 1 year.

midsection of the long bone is modeled as a right cylinder with an initial cross-section coincident with the control cross-section in each of the four animal experiments described above. As an example, Figure 12.10 shows a model of the midsection of the control ovine radius and ulna using this prescription. The control cross-section is moved along an axis perpendicular to the cross-section to generate the pair of right cylinders illustrated. Similar right cylinders are generated for the other four animal experiments considered. The axial loading that is assumed to act on the model of the midsection of the long bone is different for each of the animal experiments considered. Figure 12.11 shows an axial load applied to platens that transmit the load to the right cylinder representing the bone. If the axial load, $-P$, in Figure 12.10 acts through the combined centroid of the two bones, indicated by a solid dot, the load is said to be centric. Otherwise, the load is eccentric. The loading changes induced by the immobilization and exercise experiments are modeled by changing the magnitude of the centric axial load, but assuming that it remains centric. The load change in ulnar ostectomy studies are modeled by the removal of the ulna from the model shown in Figure 12.10. The resulting model situation is illustrated in Figure 12.11. The same load, $-P$, continues to be applied, but only the radius remains to carry it and the loading eccentricity relative to the remaining bone has been increased. In the special case of centric loading, the point of application of the load remains at the centroid and the magnitude of the time-averaged load changes.

This completes the description of the general and qualitative methods of determining the altered stress state that induce surface remodeling shape changes. The phenomenological

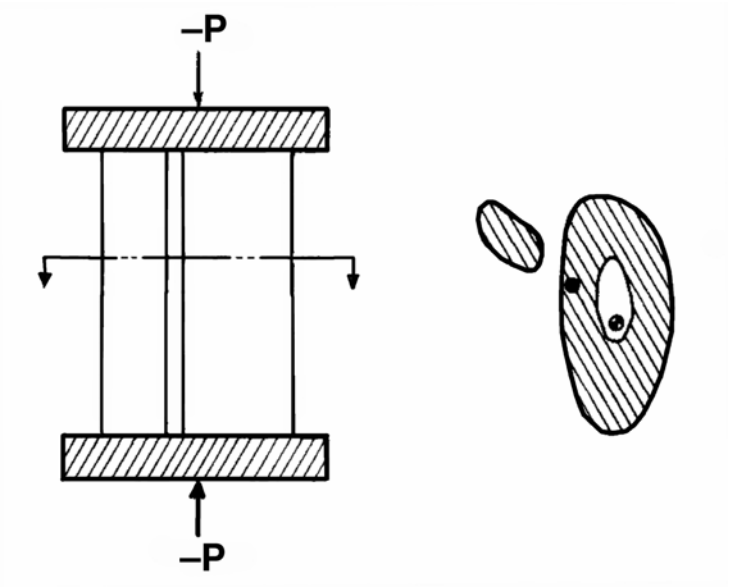



**Figure 12.10**. Model of axial loading. This figure shows an axial load applied via platens to the two right cylinders representing the limb bones. If the axial load, **–P**, acts through the combined centroid of the two bones, indicated by a solid dot, the load is said to be centric. Otherwise, the load is eccentric.

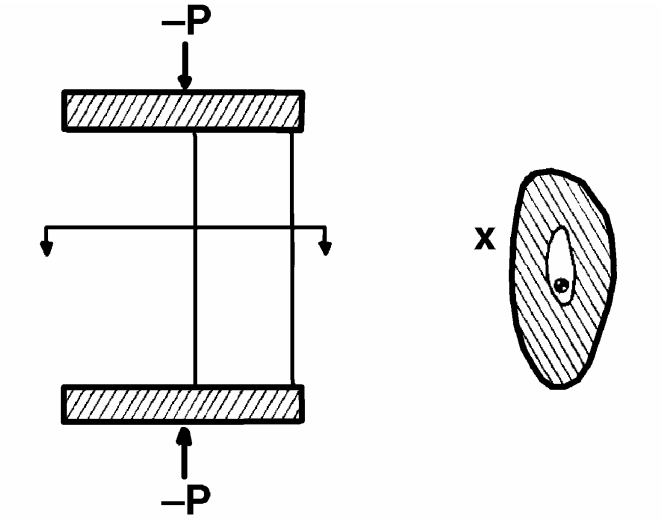



**Figure 12.11**. Model of axial loading. The load change in ulnar ostectomy studies is modeled by the removal of the ulna from the model shown in Figure 12.10. The same load, **–P**, continues to be applied, but only the radius remains to carry the load. Since the point of application of the load is no longer the centroid, the loading is eccentric relative to the remaining bone, the radius.

theory of surface remodeling described in §12.4 will now be combined with the elementary theory of beams to develop a computational formulation to predict the surface movement in the models of the four animal experiments described in §12.2 using the parameters estimated

in §12.5. We consider the right cylinder representing the midsection of a long bone to be subjected to only axial loads and therefore only axial stresses. The $z$-coordinate direction is selected to coincide with the axial direction, and therefore the only nonzero component of the stress tensor is $T_{zz}$. In this analysis stimulus $\overline{S}$ is assumed to be the average over period $P$ of axial stress $T_{zz}$ in the bar model of the bone:

$$\overline{S} \Rightarrow \overline{T}_{zz}(Q,T) = \frac{1}{P}\int_{T-P}^{T} T_{zz}(Q,t)dt\,. \tag{12.4}$$

Since the stimulus is taken as the component of a second-order tensor, remodeling rate constant $C(Q)$ must also be a component of a second-order tensor, and it is denoted here as $B_{zz}$. It then follows from eq. (12.2) that with selections $C(Q) \Rightarrow B_{zz}(Q)$ and $\overline{S} \Rightarrow \overline{T}_{zz}(Q,T)$, surface speed $U$ is given by

$$U(Q,T) = B_{zz}(Q)\left[\overline{T}_{zz}(Q,T) - \overline{T}^{o}_{zz}(Q,T)\right]. \tag{12.5}$$

This formula relates the remodeling speed at $Q$, $U(Q,T)$, to the difference between the actual stress at point $Q$, $\overline{T}_{zz}(Q,T)$, and the remodeling equilibrium stress at that point, $\overline{T}^{o}_{zz}(Q,T)$, by single-surface remodeling stress rate coefficient $B_{zz}(Q)$.

In the following, the bending and axial components of stress $T_{zz}(Q)$ are calculated using beam theory. Example 7.3.1 in Chapter 7 illustrated how the linear theory of elasticity could be applied to a long rectangular bar made of an orthotropic elastic material to determine the formula that relates axial stress $T_{zz}$ in the bar to applied moment in the case of pure bending. The coordinate system used was Cartesian and $x_3$ lay along the long axis of the bar, with the $x_1$ and $x_2$ coordinates lying in the plane of the cross-section and the applied bending moment about the $x_1$ axis. The axial stress component was denoted by $T_{33}$, the applied bending moment component by $M_1$, the area moment of inertia about the $x_1$ axis by $I_{11}$, and the relation obtained between the three quantities was $T_{33} = M_1 x_2 / I_{11}$. This formula appears in all elementary mechanics of material books in the case of a beam made of an isotropic material. In the present situation the beam is of bone, and bone may be considered to have orthotropic material symmetry, as discussed in Chapter 11. However, the beam is subjected to a force and a couple rather than just to a couple, so the force system is a little bit more complicated than that in Example 7.3.1. Axial stress $T_{zz}(Q)$ for the bone beam is shown in eq. (12.5) and is complicated only because the geometry of the beam is changing due to remodeling. To keep track of the changing geometry a global coordinate system $(x, y)$, shown in Figure 12.12, is employed. The coordinates of the centroid are given by $(x_c, y_c)$, and the centroid is the origin of the centroidal coordinate system $(\overline{x}, \overline{y})$ with axes parallel to the global coordinate axes. The point of load application is given in global coordinates by $(x_p, y_p)$. The general case is that of a beam loaded in unsymmetrical bending with an axial load. The analysis of this situation is discussed, for example, by Timoshenko (1955). The axial stress is calculated by the formula

$$T_{zz} = -\frac{P}{A} - \frac{P(x_p - x_c)[I_{\overline{xy}}(y - y_c) - I_{\overline{xx}}(x - x_c)]}{I_{\overline{xx}}I_{\overline{yy}} - I_{\overline{xy}}I_{\overline{xy}}} -$$

$$\frac{P(y_p - y_c)[I_{\overline{xy}}(x - x_c) - I_{\overline{yy}}(y - y_c)]}{I_{\overline{xx}}I_{\overline{yy}} - I_{\overline{xy}}I_{\overline{xy}}}, \tag{12.6}$$

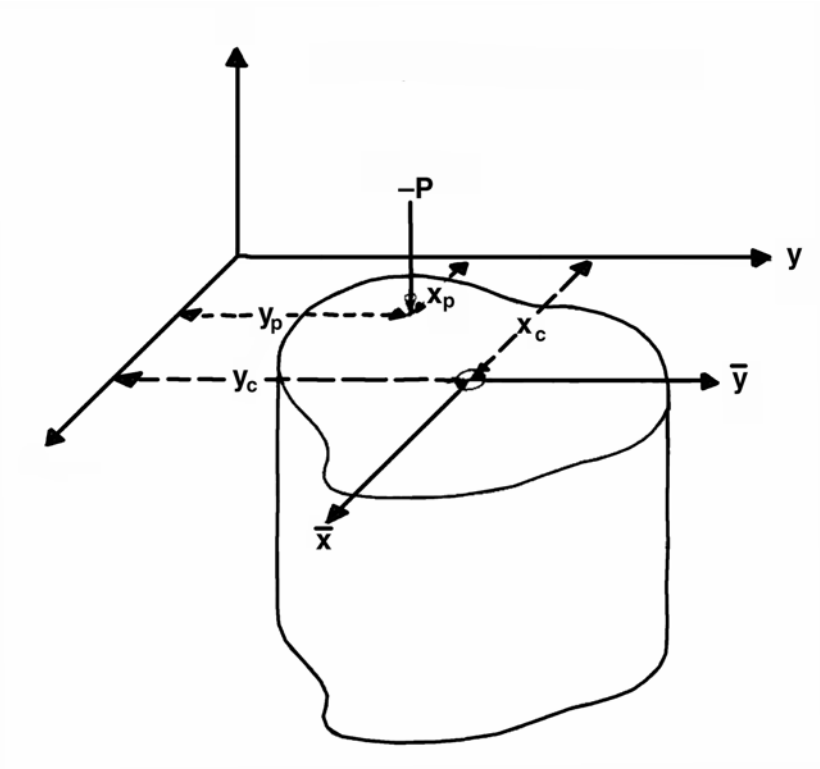



**Figure 12.12**. Cross-sectional bone model. The global coordinate system is the $(x,y)$ system. The coordinates of the centroid are given by $(x_c,y_c)$, and the centroid is the origin of the centroidal coordinate system $(\bar{x},\bar{y})$ with axes parallel to the global coordinate axes. The point of load application is given in the global coordinates by $(x_p,y_p)$. The general case is that of a beam loaded in unsymmetrical bending with an axial load.

where $T_{zz}$ is the magnitude of the axial stress (acting in the global $z$-direction) at the point defined by global coordinates $(x, y)$, $P$ is the magnitude of the axial load which acts in the $z$-direction, $A$ is the total cross-sectional area of bone in the $x$–$y$ plane, $(x_p, y_p)$ are the global coordinates of the point of load application, $(x_c, y_c)$ are the global coordinates of the centroid of bone lying in the $x$–$y$ plane, $I_{\bar{x}\bar{x}}$ is the area moment of inertia of the cross-sectional area with respect to the centroidal $\bar{x}$ axis, $I_{\bar{y}\bar{y}}$ is the area moment of inertia of the cross-sectional area with respect to the centroidal $\bar{y}$ axis, and $I_{\bar{x}\bar{y}}$ is the area product of inertia of the cross-sectional area with respect to the centroidal $\bar{x}$ and $\bar{y}$ axes. The calculation of surface movement is accomplished by using the cross-section shape of the unadapted contralateral bone as an initial cross-section shape and loading the bone-beam model with that axial load determined in §12.5. From these data initial stress $T_{zz}$ may be calculated using (12.5). With the accumulated information, speed of surface movement $U$ may be calculated using (12.4). The movement of the bone surfaces in increment of time $\Delta T$ may be determined from the knowledge of $U$ at all points on the surface of the bone. Thus, it is possible to calculate the cross-sectional shape of the bone at time $T + \Delta T$, given the shape of the cross-section at time $T$. This process is then continued in iterative fashion until the surface movement ceases and strain remodeling equilibrium is achieved. The only material parameter involved in the problem will be the surface remodeling stress rate coefficient, $B_{zz}(Q)$. This is the only constant to be determined from

each of the four animal experiments, but it is assumed to be different for deposition and for resorption.

**Problems**

12.6.1. Simplify formula (12.6) to the case when force $P$ is applied at the centroid of the cross-section.

12.6.2. Simplify formula (12.6) to the case when the centroidal coordinate system is one determined by the principal axes of the area moment of inertia tensor. The area moment of inertia tensor is developed in §A.8; particularly see the material preceding Examples A.8.3 and A.8.4.

12.6.3. Consider the surface remodeling of a solid circular cylinder of bone under an axial loading applied at the centroid of the circular cross-section. There are no solid circular cylinders of bone, but it provides a simple geometry in which to illustrate a strain adaptation calculation. Let the initial time adaptation equilibrium be an axial load $P_o$ at a cylinder radius of $b_o$. A changed axial load, $P$, is applied at time $t = 0$. Let the long-time adaptation equilibrium cylinder radius be denoted $b_\infty$. Use eq. (12.5) with $\bar{T}_{zz}(Q,T) = P/A$ and $\bar{T}^o_{zz}(Q,T) = P_o/A_o$. Find an implicit solution for $b(t)$ and an expression for $b_\infty$.

## 12.7. SUMMARY OF SURFACE REMODELING RESULTS

The results of the computations described consist of the computed remodeling coefficients for each of the four animal experiments considered above, and the corresponding calculated shape of the remodeled cross-section obtained for each of the experiments. The coefficients determined are given in Table 12.1. The calculated remodeled cross-sections using the theory of surface remodeling (12.4) with the constants contained in Table 12.1 are shown in Figures 12.1c, 12.2c, 12.3c, and 12.4c. In one case the remodeled cross-section was calculated at 2 years to see how much it differed from the 1-year prediction (Figure 12.13).

For each of the four cross-sections there is good qualitative agreement between the experimentally remodeled shape, shown in Figures 12.1b, 12.2b, 12.3b, and 12.4b middle, and the calculated shape, shown in the corresponding "c" panels of those figures. This qualitative agreement prompts two observations: first, the surface remodeling theory is an approximately adequate tool for describing the remodeled bone geometry found from the in vivo experiments considered here, and, second, coupled with the initial geometry and the loading conditions, the remodeling rate constants reported in Table 12.1 are adequate for approximate qualitative predictions for each of the remodeled geometries.

The values for the remodeling equilibrium stress, $T^0$, are listed in Table 12.1. $T^0$ is a different constant for each of the three centric loading experiments, but it varies with position on the bone cross-section for the eccentric loading experiment, the ulnar ostectomy. In the case of the ulnar ostectomy, the extreme values are listed in Table 12.1 for both the endosteal and periosteal surfaces. Also listed is the calculated experimental "severity ratio," defined as the ratio of the time-averaged stress calculated at the start of the experiment, $T$, and the calculated time-averaged remodeling equilibrium stress, $T^0$. A negative number for this ratio means that a point on the surface of the bone with a remodeling equilibrium stress that is normally compressive (tensile) is being experimentally loaded so that the point is now in tension (compression). For each of the first three experiments in Table 12.1, both the remodeling equilibrium stress and the stress at the start of the experimental period were compressive. The ulnar ostectomy experiment with mature sheep shows that a portion of the periosteal bone (cranial surface) has a

tensile remodeling equilibrium stress, while the remaining bone has a compressive remodeling equilibrium stress. The magnitude of the time-averaged stresses increased as a result of the ulnar ostectomy, but the sign of the maximum and minimum stresses listed in the table was unchanged. In contrast with the sheep study, the results of the ulnar ostectomy on young swine show that the entire radius has compressive remodeling equilibrium stresses. However, as a result of the ulnar ostectomy, portions of bone on both the endosteal and periosteal surfaces were subjected to tensile loads, giving negative numbers for two of the severity ratios listed. The severity ratios for the ostectomy studies are significantly higher than those for the immobilization and exercise experiments.

**Table 12.1**. Summary of Measured Data and Calculated Results

| Type of study | Experimental animal | Reference | $T_0$ (MPa) | $T/T_0$ | $B_{zz}$ (mm/day GPa) | $U_{avg}$ (μm/day) | $U_{init}$ (μm/day) | Remarks |
|---|---|---|---|---|---|---|---|---|
| Immobilization | Young beagles | Uthoff & Jaworski (1978) | –0.43 | 0.45 | +5.6 (E)<br>–22.2 (P) | +0.4 (E)<br>–2.2 (P) | +1.3 (E)<br>–5.2 (P) | Simultaneous deposition & resorption |
| Immobilization | Old beagles | Jaworski et al. (1980) | –0.73 | 0.51 | –15.3 (E)<br>0.0 (P) | –2.6 (E)<br>0.0 (P) | –5.4 (E)<br>0.0 (P) | Endosteal resorption only |
| Exercise | Young swine | Woo et al. (1981) | –0.49 | 1.31 | –20.4 (E)<br>–15.3 (P) | +1.7 (E)<br>+1.2 (P) | +3.1 (E)<br>+2.3 (P) | Endosteal & periosteal deposition |
| Ulnar ostectomy | Mature sheep | Lanyon et al. (1982) | –0.05E<br>–0.27E<br>+0.17P<br>–0.48P | 0.0<br>2.2<br>4.1<br>2.5 | 0.0 ET<br>0.0 EC<br>+5.6 PT<br>–36.0 PC | 0.0<br>0.0<br>+1.1<br>+8.8 | 0.0<br>0.0<br>+2.9<br>+25.9 | Periosteal deposition only. Different rate constants for tension & compression |

Note that E denotes Endosteal Surface, P denotes Periosteal Surface, T denotes Tension, and C denotes Compression.

The remodeling rate constants, $B_{zz}(\mathbf{P})$, reported in Table 12.1 are in units of mm/day $GPa^{-1}$. Thus, the initial surface velocity, $U$, in eq. (12.4) can be found by multiplying the difference between the actual value of stress at a particular point and the equilibrium stress for that point by the remodeling rate constant, $B_{zz}(\mathbf{P})$. The surface velocity found in this manner, $U_{init}$, is thus the *initial* surface velocity and, as the bone adapts, the observed surface velocity will decrease toward zero. The experimentally determined maximum *average* surface velocity, $U_{avg}$, is estimated by measuring the maximum depth of the bone deposited or resorbed on the surface and dividing by the remodeling time period. The maximum initial velocities as well as the maximum average surface velocities are reported in Table 12.1. As would be expected, the maximum average surface velocity measured from the photographs of the remodeled bone cross-sections are smaller than the calculated initial velocity. Equality of the two velocity measures would have implied that the remodeled cross-section had not yet approached the equilibrium configuration since the initial velocity has remained constant.

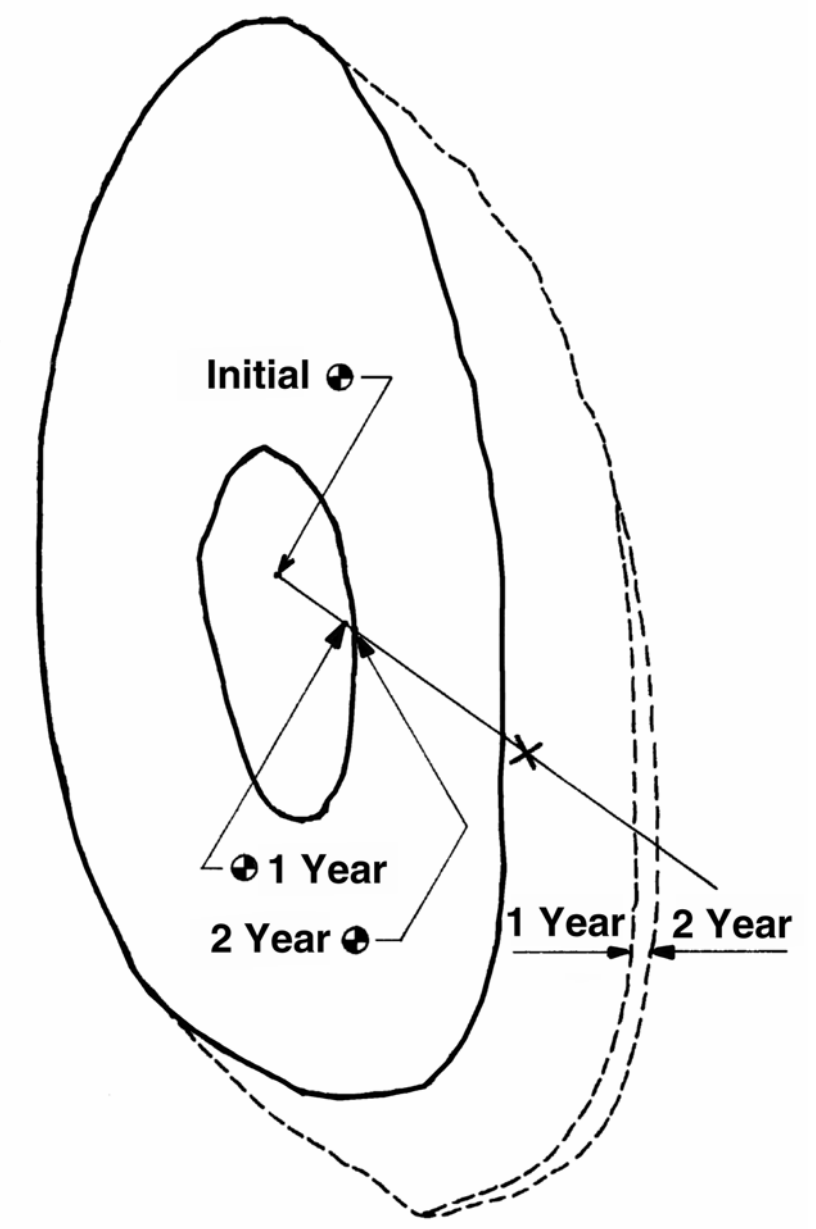



**Figure 12.13**. Cross-section of intact ovine forelimb after the ulnaectomy. The line connects the centroid of the radius and the point of application of the resultant load, represented by the X. The dashed lines represent the calculated remodeling at 1 and 2 years.

The sign convention used in Table 12.1 is as follows. If new bone is deposited on an external surface, then the velocity, $U$, is considered to be positive, while negative surface velocity implies that bone on the external surface is resorbed. If the difference between the actual stress and the remodeling equilibrium stress, $(T - T^0)$, is positive, then positive $B_{zz}$ leads to bone

deposition and $B_{zz}$ negative leads to bone resorption. On the other hand, if the difference between the stresses is negative, then $B_{zz}$ positive leads to bone resorption and $B_{zz}$ negative leads to bone deposition.

The calculated surface remodeling represented in the bottom panels of Figures 12.1–12.4 all show geometries that have evolved to a shape that is close to the experimental geometry at the time listed with each figure. The evolution of the calculated remodeled geometry is almost complete since, at the time shown, the axial stress is almost equal to the remodeling equilibrium stress, $T^o$. The change in the periosteal surface position and the radius centroid in the time between the predicted geometry at 9 months, shown in the bottom panel of Figure 12.4, and the predicted geometry at 1 yr (not shown) from that value is small. This indicates that the functional adaptation response was almost complete at the end of the 9-month period used in the calculations. This computational result is also in qualitative agreement with the experimental results that showed tetracycline labeling at the end of the 6-month experimental group, but an absence of labeling on the 12-month group (Lanyon et al., 1982).

The remodeling rate constants have values that are all of the same order of magnitude, although we are comparing experiments with several independent variables. Among these are the animal species, age, severity of experiment in terms of change from the normal strain environment, and the degree of data extrapolation necessary for the calculations reported here. The factor that governs the relative activity of the endosteal and periosteal surfaces seems to be animal age and not the experimental methodology used to induce the net remodeling response.

## 12.8. A ONE-DIMENSIONAL PHENOMENOLOGICAL INTERNAL BONE STRAIN ADAPTATION MODEL

In this section a one-dimensional phenomenological bone strain adaptation model is described and its basic predictions mathematically explored. The adaptation of bone to environmental loads is a fundamentally nonlinear process because the properties of the bone are changing as the loading of the bone changes. The changing load and changing bone properties interact, and the interaction is the source of the nonlinearity. This nonlinearity characterizes all tissue adaptation processes and therefore all models of tissue adaptation processes. It is thus a property of the one-dimensional phenomenological bone strain adaptation model described in this section. However, the nonlinearity is so simple in this model that it may be transformed into a linear differential equation, solved, and then the solution may be transformed back to the solution of the nonlinear problem. This is the advantage of this simple model, and it is used here to demonstrate the type of results that may be expected in the interaction between environmental loading and changing tissue properties.

The one-dimensional model considered in this section is a hollow circular cylinder subjected to an axial compressive load (Figure 12.5). The bulk density, $\rho$, of the porous material of the cylinder is written as the product of $\gamma$ and $\nu$, $\rho = \gamma\nu$, where $\gamma$ is the density of the material that composes the matrix structure and $\nu$ is the solid volume fraction of that material. Both $\gamma$ and $\nu$ can be considered as field variables. Let $\xi$ denote the value of the solid volume fraction in an unstrained reference state. The density, $\gamma$, of the material composing the matrix is assumed to be constant; hence, the conservation of mass will give the equation governing $\xi$. It is assumed that there exists a unique zero-strain reference state for all values of $\xi$. Thus, $\xi$ may change without changing the reference state for strain on adaptation time scale $T$, but not on loading time scale $t$. One might imagine a block of porous elastic material with the four points, the vertices of a tetrahedron, marked on the block for the purpose of measuring the strain. When the porosity changes on the adaptation time scale, material is added to or taken away

from the pores, but if the material is unstrained it remains so and the distances between the four vertices marked on the block do not change. Thus, $\xi$ can change while the zero-strain reference state remains the same. The change in volume fraction, *e,* from reference volume fraction $\xi_0$ is denoted by *e*:

$$e = \xi - \xi_o. \tag{12.7}$$

Since the structure of the tissue only changes on the adaptation time scale, *e* is a function of *T*. The rate of change of the geometric parameter on the tissue adaptation time scale, *de/dT*, is the rate of change of the solid volume fraction of the cylinder. The strain adaptation of the tissue occurs to the internal pore structure, either increasing or decreasing the porosity of the bone. The model considered in this section only admits a linear relationship between the axial stress and axial strain; transverse stress and strains are neglected. From Hooke's law the axial normal stress is related to the axial normal strain by

$$\sigma(t,T) = E_{\text{eff}}(T)\varepsilon(t,T)\,, \tag{12.8}$$

where $E_{\text{eff}}(T)$ is the effective Young's modulus, represented by

$$E_{\text{eff}}(T) = E_o + E_1 e(T)\,. \tag{12.9}$$

This expression for $E_{\text{eff}}(T)$ reflects the fact that Young's modulus changes as the solid volume fraction changes; $E_{\text{eff}}(T)$ increases (decreases) as the solid volume fraction increases (decreases). If the change in solid volume fraction is small, the change in $E_{\text{eff}}(T)$ is small and linear model (12.9) is appropriate.

The application of the $\mathcal{S}\{\bullet\}$ operation, (12.1)–(12.8), is used to define influential stress $\overline{\sigma}(T)$ associated with influential strain $\overline{\varepsilon}(T)$:

$$\overline{\sigma}(T) = E_{\text{eff}}(T)\overline{\varepsilon}(T)\,. \tag{12.10}$$

The constitutive assumption for the time rate of change of the change in solid volume fraction, *de/dT*, is that it depends upon the instantaneous values of the change in solid volume fraction and of influential strain $\overline{\varepsilon}(T)$:

$$\frac{de}{dT} = f(e(T), \overline{\varepsilon}(T))\,, \tag{12.11}$$

but the requirement of linearity in influential strain $\overline{\varepsilon}(T)$, due to the fact that the strain is small and its squares are negligible, permits the reduction of (12.11) to

$$\frac{de}{dT} = c(e(T)) + a(e(T))\overline{\varepsilon}(T)\,. \tag{12.12}$$

This representation is still too general to be useful, and a further assumption about the dependence of the representation upon *e(T)* must be made. If it is assumed that the change in solid volume fraction, *e*, is as small as the strain, then the right-hand side of (12.12) reduces to $c_o + c_1 e + a_o \overline{\varepsilon}$, where $c_0$, $c_1$ $a_0$ are constants. This assumption is too strong, as the resulting equation and system are then linear. In order to maintain a nonlinear system, and hence the possibility of adaptation, a term involving product $e\overline{\varepsilon}$ must be retained. This can be done if it is assumed that only terms greater than the square of *e* are negligible; then (12.12) reduces to

$$\frac{de}{dT} = c_o + c_1 e + c_2 e^2 + a_o \bar{\varepsilon} + a_1 e \bar{\varepsilon} \,. \tag{12.13}$$

This form of the constitutive equation for the time rate of change of the change in solid volume fraction, *de/dT*, maintains the nonlinear character of the original equation.

The basic system of equations for this model consists of expression (12.9) for effective Young's modulus $E_{\text{eff}}(T) = E_0 + E_1 e(T)$, Hooke's law in form (12.10), $\bar{\sigma}(T) = E_{\text{eff}}(T)\bar{\varepsilon}(T)$, and formula (12.13) for the time rate of change of the change in solid volume fraction, *de/dT*. The initial condition for this differential equation is that

$$e(0) = 0 \,. \tag{12.14}$$

If it is assumed that $\bar{\varepsilon}(T)$ is known, then these equations may be solved for $e(T)$ and $\bar{\sigma}(T)$, in that order. Alternatively, if it is assumed that $\bar{\sigma}(T)$ is known, then these equations may be solved for $e(T)$ and $\bar{\varepsilon}(T)$, in that order. This is accomplished by using the inverse of (12.9), computed in a manner consistent with the approximation made to obtain (12.13):

$$\frac{1}{E_{\text{eff}}} = \frac{1}{E_0}\left(1 - \frac{E_1}{E_0} e + \frac{E_1^2}{E_0^2} e^2\right), \tag{12.15}$$

and Hooke's law in form $\bar{\sigma}(T) = E_{\text{eff}}(T)\bar{\varepsilon}(T)$ (12.10) to eliminate $\bar{\varepsilon}(T)$ from (12.13) in favor of $\bar{\sigma}(T)$, and thus

$$\frac{de}{dT} = c_o + c_1 e + c_2 e^2 + b_0 \bar{\sigma} + b_1 e \bar{\sigma} \,, \tag{12.16}$$

where

$$b_0 = \frac{a_0}{E_0}, \; b_1 = \frac{a_1}{E_0} - \frac{a_0}{E_0}\frac{E_1}{E_0} \,. \tag{12.17}$$

Expressions (12.13) and (12.16) for $de/dT$ must vanish in remodeling equilibrium (RE) due to the definition of remodeling equilibrium. Consider a system initially in RE from which $e(T)$ is measured. The RE is characterized by RE strain, $\bar{\varepsilon}_{0RE}$, and RE stress, $\bar{\sigma}_{0RE}$ and by both $e(T)$ and $de/dT$ vanishing; therefore, from (12.13) it follows that $c_0 + a_0\bar{\varepsilon}_{0RE}$, and from (12.16), $c_0 + b_0\bar{\sigma}_{0RE}$. Thus, we set $c_0 = -a_0\bar{\varepsilon}_{0RE}$ in (12.13) and $c_0 = -b_0\bar{\sigma}_{0RE}$ in (12.16), with these results:

$$\frac{de}{dT} = c_1 e + c_2 e^2 + a_0(\bar{\varepsilon} - \bar{\varepsilon}_{0RE}) + a_1 e \bar{\varepsilon} \,. \tag{12.18}$$

$$\frac{de}{dT} = c_1 e + c_2 e^2 + b_0(\bar{\sigma} - \bar{\sigma}_{0RE}) + b_1 e \bar{\sigma} \,. \tag{12.19}$$

First-order nonlinear differential equations (12.18) or (12.19) are known as Riccati differential equations. Differential equations of this type may be transformed from first-order nonlinear differential equations to second-order linear differential equations with variable coefficients. In this particular case the transformation introduces function *q(T)*, which is related to *e(T)* by

$$e = -\frac{1}{c_2 q}\frac{dq}{dT} = -\frac{\dot{q}}{c_2 q}. \tag{12.20}$$

When this transformation is employed in differential equation (12.19) and in its initial condition (12.14), one obtains the following linear second-order differential equation with variable coefficients:

$$\ddot{q} - (c_1 + b_1\bar{\sigma})\dot{q} + b_0(\bar{\sigma} - \bar{\sigma}_{0RE})c_2 q = 0, \tag{12.21}$$

and its associated initial condition,

$$\dot{q}(0) = 0 \quad \text{at} \quad T = 0. \tag{12.22}$$

Steady stress (strain) is the phrase used to describe the situation in which the stress (strain) at $T = 0$ is changed to a new specified value and held constant in time thereafter. For both the steady-stress and steady-strain situations, differential equations (12.13) and (12.16) take the form

$$\dot{e} = a(e^2 - 2be + c), \; e(0) = e_0, \tag{12.23}$$

where, in the case of a steady influential stress $\bar{\sigma}_{\infty RE}$, which, as the notation indicates, will be the final RE stress.

$$a = c_2, \;\; b = -\frac{1}{2c_2}(c_1 + b_1\bar{\sigma}_{\infty RE}), \;\; c = \frac{b_0}{c_2}(\bar{\sigma}_{0RE} - \bar{\sigma}_{\infty RE}), \tag{12.24}$$

and where $a$, $b$, and $c$ are independent of time. In formulating (12.23) it has been assumed that $c_2$ is not equal to zero. The solution to the problem when $c_2$ is zero is very simple, relatively uninteresting, and not recorded here. Using the transformation for Riccati differential equations, the solution to differential equation (12.23) is straightforward. Using transformation (12.20), (12.23) can be reduced to a linear differential equation of second order with constant coefficients:

$$\ddot{q} + 2ab\dot{q} + a^2 cq = 0. \tag{12.25}$$

The solution to (12.25) is obtained in the obvious straightforward method and then substituted back into (12.20) twice, and solution *e(T)* is obtained. This solution is expressed in terms of the solutions to quadratic equation $e^2 - 2be + c = 0$, which are denoted by $e_1$ and $e_2$,

$$e_1, e_2 = b \pm \sqrt{b^2 - c}, \tag{12.26}$$

and where the convention $e_1 \geq e_2$ is employed when $e_1$ and $e_2$ are real and distinct. The solutions to eq. (12.23) are as follows:

$$e = \frac{e_1 e_2 (e^{-a(e_1 - e_2)T} - 1)}{e_2 e^{-a(e_1 - e_2)T} - e_1} \tag{12.27}$$

for $e_1$ and $e_2$ real and $e_1 > e_2$;

$$e = \frac{a e_1^2 T}{1 + a e_1 T} \tag{12.28}$$

for $e_1$ and $e_2$ real and $e_1 = e_2$; and

$$e = b + \sqrt{(c - b^2)} \tan\left\{ aT\sqrt{(c - b^2)} + \tan^{-1} \frac{\sqrt{(c - b^2)}}{b} \right\} \tag{12.29}$$

for $e_1$ and $e_2$ complex conjugate. An inspection of these solutions shows that in certain cases $e$ can become infinite within finite time. Specifically, for $a > 0$, $e$ tends to $+\infty$ as

$$T \to \frac{1}{a(e_1 - e_2)} \ln \frac{e_2}{e_1} \tag{12.30}$$

for $e_1$ and $e_2$ real and $e_0 > e_1 > e_2$;

$$T \to \frac{1}{a(e_1 - e_2)} \tag{12.31}$$

for $e_1$ and $e_2$ real and $e_0 > e_1 = e_2$; and

$$T \to \frac{1}{a\sqrt{(c - b^2)}} \left( \frac{\pi}{2} - \tan^{-1} \frac{\sqrt{(c - b^2)}}{b} \right) \tag{12.32}$$

for $e_1$ and $e_2$ complex conjugate. Also, for $a < 0$, $e$ tends to $-\infty$ as $T$ tends to the value given by (12.30) for $e_1$ and $e_2$ real and $e_1 > e_2 > e_o$; as $T$ tends to the negative of the value given by (12.31) for $e_1$ and $e_2$ real and $e_1 = e_2 > e_o$; as

$$T \to \frac{-1}{a\sqrt{(c - b^2)}} \left( \frac{\pi}{2} + \tan^{-1} \frac{\sqrt{(c - b^2)}}{b} \right) \tag{12.33}$$

for $e_1$ and $e_2$ complex conjugate. Inspection of the solutions (12.27)–(12.29) also shows that $e$ tends to certain finite values in infinite time under certain conditions. Specifically, $e \to e_2$ as $T \to \infty$ for $a > 0$, $e_1 \geq 0$ and $e_1$ and $e_2$ real. Also $e \to e_1$ as $T \to \infty$ for $a < 0$, $0 \geq e_2$ and $e_1$ and $e_2$ real.

Some insight into the behavior of these solutions to remodeling rate equation (12.23) can be obtained by considering their representation in the phase plane. In Figure 12.14 the solution to remodeling rate equation (12.23) is plotted in the case when $e_1$ and $e_2$ are real and unequal for both $a > 0$ and $a < 0$. In this case the remodeling equation is a parabola in $\dot{e}$ and $e$ that crosses the $e$ axis at two points and opens up or down depending on the sign of $a$. These parabolas are sketched in Figure 12.14. The arrowheads on the parabolas indicate the direction in which a solution will evolve in positive time for a given value of $e$. Thus, for example, the fact that $e \to e_2$ in infinite time for $e_1$ and $e_2$ real, $a > 0$ and $e_1 \geq 0$ is indicated by the arrowheads on the parabola to the left and the right of $e_2$ being directed towards $e_2$. That the arrowheads to the right of $e_1$ are oppositely directed is consistent with the fact that $e \to \infty$ in finite time for $e_1$ and $e_2$ real, $a > 0$ and $e_o > e_1$. A completely analogous description holds for the case $a < 0$ shown in Figure 12.14. When $e_1$ and $e_2$ are complex conjugates, the parabola described by remodeling rate equation (12.23) does not cross the $e$ axis. This situation is illustrated in Figure 12.15. The fact that all solutions of (12.23) tend to $\pm\infty$ for $e_1$ and $e_2$ complex conjugate is indicated by the unidirectionality of the arrowheads. When $e_1$ and $e_2$ are real and equal, the parabola described by (12.23) is tangent to the $e$ axis at point $e = e_1 = e_2$. This situation would be illustrated by

parabolas exactly like those in Figure 12.14, except that they would be tangent at their extremum points to the *e* axis.

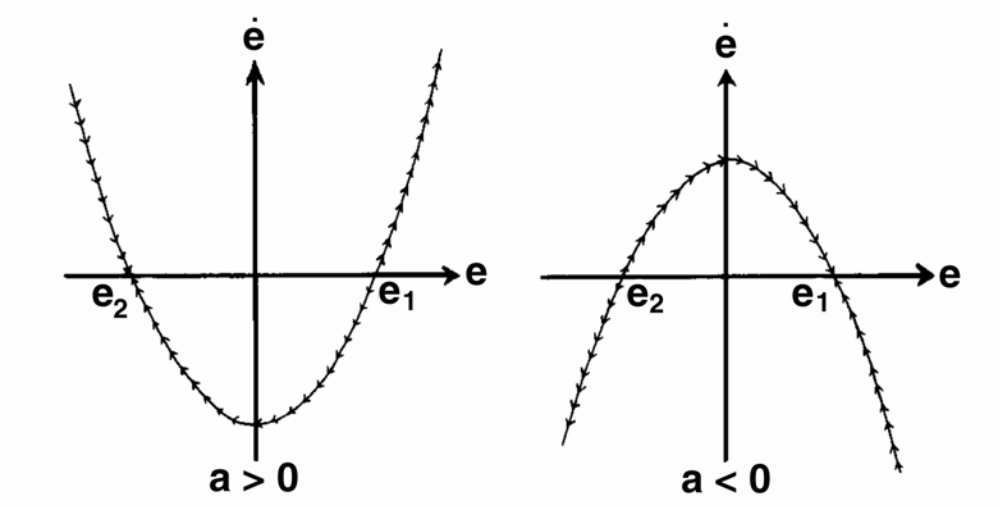



**Figure 12.14**. A phase plane plot of the solution to remodeling eq. (11.21) when $\mathbf{e}_1$ and $\mathbf{e}_2$ are real and unequal.

We have observed that there are two situations in which the solutions of remodeling equation (12.23) tend to finite values. In the first of these situations, $e \to e_2$ as $T \to \infty$ for $a > 0$, $e_1 \geq e_0$ and $e_1$ and $e_2$ real. In the second, $e \to e_1$ as $T \to \infty$ for $a < 0$, $0 \geq e_2$ and $e_1$ and $e_2$ real. An analysis of the Liapunov type for the stability of these solutions shows that in the first situation ($a > 0$) solution $e_1 = 0$ is unstable and all others are stable, while in the second situation ($a < 0$) solution $e_2 = 0$ is unstable while all other solutions are stable. The solutions that are stable are, in fact, asymptotically stable. The instability of solutions $e \to e_2$ as $T \to \infty$ for $a > 0$, $e_1 \geq 0$ and $e \to e_1$ as $T \to \infty$ for $a < 0$, $e_2 = 0$ can be inferred from Figure 12.14. In Figure 12.14 we see that these solutions correspond to the points where the system is started with an initial datum corresponding to the single point where the directionality of the arrowheads on the parabola reverse themselves. An arbitrarily small change in initial datum completely changes the response of the system. A simple mechanical analogy of this unstable situation is a sphere in unstable equilibrium on top of a second sphere.

It is now possible to state the conditions under which differential equation (12.23) yields stable solutions that tend to finite, physiologically possible values. The solution for $a > 0$ is $e \to e_2$ as $T \to \infty$ for $a > 0$ if $e_1$ and $e_2$ are real, $e_1 \geq 0$, $1 - \xi_{\text{o}} > e_2 > -\xi_{\text{o}}$ and $1 - \xi_{\text{o}} > 0 > -\xi_{\text{o}}$. The solution for $a < 0$ is $e \to e_1$ as $T \to \infty$ for $a > 0$ if $e_1$ and $e_2$ are real, $0 > e_2\ 1 - \xi_{\text{o}} > e_1 > -\xi_{\text{o}}$ and $1 - \xi_{\text{o}} > 0 > -\xi_{\text{o}}$. In terms of coefficients $a$, $b$ and $c$ occurring in eq. (12.23), these conditions are

$$a > 0,\ b^2 > c,\ \ b + \sqrt{(b^2 - c)} > e_o,\ \ 1 - \xi_{\text{o}} > b - \sqrt{(b^2 - c)} > -\xi_{\text{o}}, \tag{12.34}$$

or

$$a < 0,\ b^2 > c,\ \ e_o > b - \sqrt{(b^2 - c)},\ 1 - \xi_{\text{o}} > b + \sqrt{(b^2 - c)} > -\xi_{\text{o}}. \tag{12.35}$$

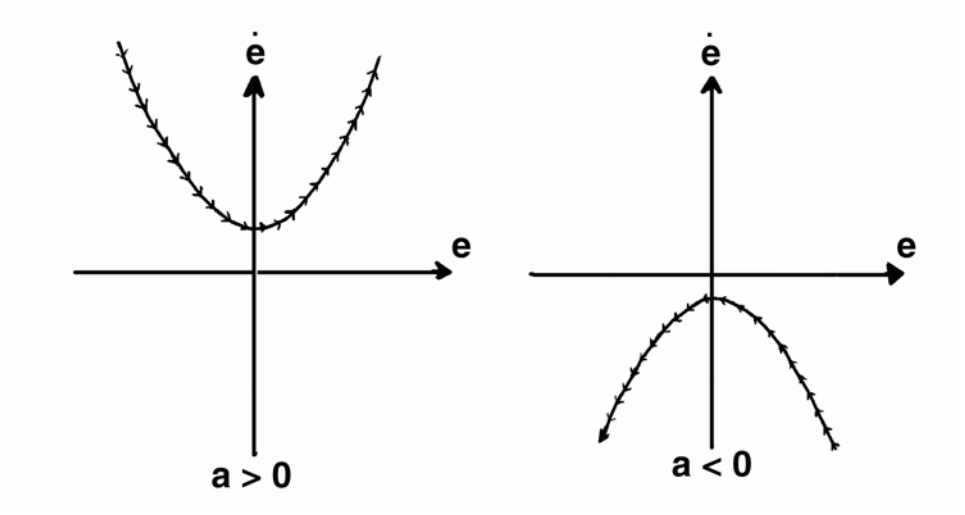



**Figure 12.15**. A phase plane plot of the solution to remodeling eq. (11.21) when $\mathbf{e}_1$ and $\mathbf{e}_2$ are complex conjugates.

Since coefficients *a, b,* and *c* are expressed by eqs. (12.24) in terms of the material properties and the applied steady strain or steady stress, conditions (12.34) and (12.35) can be rewritten in terms of these variables. Thus, for a specified material and a specified steady strain or steady stress, it can be determined whether the value of *e* will remain finite or tend to one of its pathological extremes.

The solution for $e(T)$ is now used to calculate $E_{\text{eff}}(T)$ and $\bar{\varepsilon}(T)$ using (12.9), $E_{\text{eff}}(T) = E_0 + E_1 e(T)$, and (12.10), $\bar{\sigma}(T) = E_{\text{eff}}(T)\bar{\varepsilon}(T)$, respectively; thus,

$$E_{\text{eff}}(T) = E_o + E_1 \frac{e_1 e_2 (e^{-a(e_1-e_2)T} - 1)}{e_1 e^{-a(e_1-e_2)T} - e_2}, \tag{12.36}$$

and

$$\bar{\varepsilon}(T) = \frac{\bar{\sigma}_{\infty \text{RE}} (e_1 e^{-a(e_1-e_2)T} - e_2)}{E_0 (e_1 e^{-a(e_1-e_2)T} - e_2) + E_1 e_1 e_2 (e^{-a(e_1-e_2)T} - 1)}, \tag{12.37}$$

where solution (12.23) for *e(T),* the case $e_1$ and $e_2$ real and $e_1 > e_2$ has been employed.

**Example 12.8.1**

Consider a hollow circular cylinder under RE stress $\bar{\sigma}_{\text{oRE}} = 5$ MPa for a long time, $T < 0$. The change in volume fraction *e* is zero, and *de/dT* = 0 since the cylinder is in RE. This means there is a particular steady-state stimulus associated with the steady influential stress, and the values of the elastic stiffness coefficients are steady. At $T = 0$ the axial applied compressive stress is increased to a new value, $\bar{\sigma}_{\infty \text{RE}} = 6$ MPa, and held at the new value for all $T > 0$. Calculate and plot the evolution in time of *de/dT, e(T), $E_{eff}(T)$,* and $\bar{\varepsilon}(T)$ for $T \geq 0$, assuming that

the parameters have the following values: $E_o$ = 16 GPa, $E_1 = 1.43E_o$ per unit of change in volume fraction, $c_1$ = 0.001/days, $b_o$ = 0.001/MPa-day, $b_1$ = –0.000666/MPa-day, and $c_2 = a = -(20 \text{ days})^{-1}$.

**Solution**: Using the values given above for $c_1$, $c_2$, $b_o$, and $b_1$, it follows that $b$ = - 0.05 and $c$ = –0.02, thus from (12.26) that $e_1$= 0.1 and $e_2$ = –0.2. Thus, from (12.27) the change in volume fraction *e(T)* is given by

$$e = \frac{(-0.02)(1-e^{-(0.015)T})}{0.2+0.1e^{-(0.015)T}},$$

and it follows that *de/dT* is

$$\frac{de}{dT} = \frac{(0.00009)e^{(0.015)T})}{(0.2+0.1e^{-(0.015)T})^2}.$$

From (12.36) one may calculate effective Young's modulus $E_{\text{eff}}(T)$, and thus

$$E_{\text{eff}}(T) = 16\{1+1.43\frac{(-0.02)(1-e^{-(0.015)T})}{0.2+0.1e^{-(0.015)T}}\},$$

and it follows from (12.37) that the strain history is given by

$$\bar{\varepsilon}(T) = \frac{0.0012+0.006e^{-(0.015)T}}{3.6576+1.424e^{-(0.015)T}}.$$

The plots of $\bar{\varepsilon}(T)$, *de/dT*, *e(T),* and *E(T)* against $T$ are shown in Figures 12.16a–d, respectively. These curves represent the bone adaptation process. When the stress stimulus is stepped or jumped from $\bar{\sigma}_{\text{oRE}} = 5$ MPa to $\bar{\sigma}_{\infty\text{RE}} = 6$ MPa at $T$ = 0, strain $\bar{\varepsilon}(T)$ also jumps to a nonzero value from a value of zero, as shown at the left of plot (a). Since there are jumps in the stress and the strain, the time rate of change of *e(T), de/dT*, also jumps as shown at the left of plot (b) and by eqs. (12.18) and (12.19). Since *de/dT* is nonzero for $T > 0$, $e$ will change with time and $e$ increases as a result of the increased stimulus, as shown in (c). Since $e$ is increasing for $T > 0$, Young's modulus will increase as indicated by solution (12.36) and as shown in (d). It follows that if the influential stress is constant and the elastic coefficients are increasing, then influential strain $\bar{\varepsilon}(T)$ must decrease in time, as indicated by (12.37) and plot (a). Since the stimulus is decreasing in time, it follows that rate *de/dT* will decrease (plot b) and that $e$ will continue to increase (plot c), but more and more slowly. Thus, for very large times, *de/dT* will tend to zero (plot b) and the object will evolve to a new value of *e(T)* (plot c). The strain adaptation of the cylinder is then complete.

**Problem**

12.8.1. This problem is the same as the one considered in Example 12.8.1, but the value of $c_1$ is changed to $c_1$ = 0.004/days, from its value of $c_1$ = 0.001/days in Example 12.8.1 Consider a hollow circular cylinder under RE stress $\bar{\sigma}_{oRE} = 5$ MPa for a long time, $T < 0$. Geometric parameter $e$ is zero and *de/dT* = 0 since the cylinder is in RE. This means there is a particular steady-state stimulus associated with the steady influential stress, and the values of the elastic stiffness coefficients are steady. At $T$ = 0 the axial applied compressive stress is increased to a new value, $\bar{\sigma}_{\infty RE} = 6$ MPa and held at the new value for all $T > 0$. Calculate and plot the evo-

lution in time of *de/dT, e(T), $E_{eff}(T)$*, and $\bar{\varepsilon}(T)$, assuming that the parameters have the following values: $E_o$ = 16 GPa, $E_1 = 1.43E_o$ per unit of change in volume fraction, $c_1$= 0.004/days, $b_o$ = 0.001/MPa-day, $b_1$ = -0.000666/MPa-day, and $c_2$ = a = -(20 days)$^{-1}$.

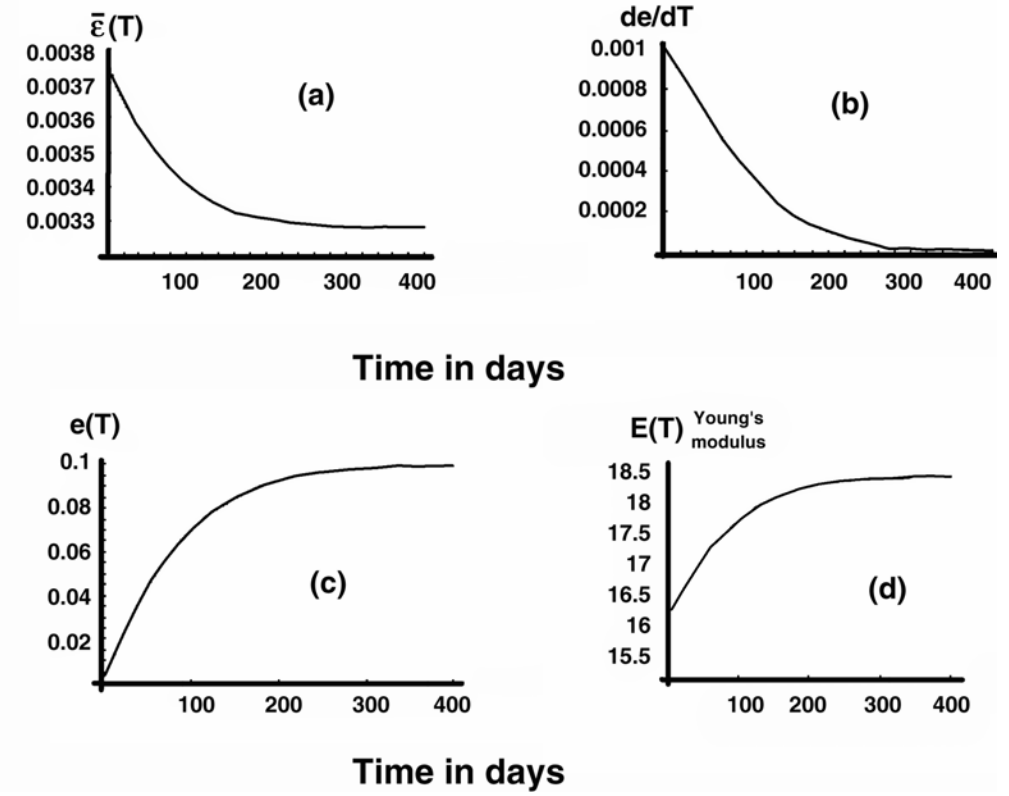



**Figure 12.16**. (a) Plot of the compressive strain, $\bar{\varepsilon}(T)$, against *T* for Example 12.8.1. (b) Plot of *de/dT* against *T* for Example 12.8.1. (c) Plot of *e*(*T*) against *T* for Example 12.8.1. (d) Plot of Young's modulus *E*(*T*) against *T* for Example 12.8.1.

## 12.9. THREE-DIMENSIONAL PHENOMENOLOGICAL BONE STRAIN ADAPTATION THEORIES

The small strain theories of internal strain adaptation (Cowin and Hegedus, 1976; Hegedus and Cowin, 1976; Cowin and Nachlinger, 1978; see Cowin, 2003, for a critique of these models) are also a modification of the theory of the equilibrium of elastic solids described in Chapter 7. The key adaptation variable is the change in volume fraction from a reference volume fraction, *e(T),* introduced by eq. (12.7), which appeared at the beginning of the previous section. The additional constitutive relation for the change in volume fraction, *e*, is the result of a postulate that rate of change of *e* is a function of point *Q* and the change in the stimulus at the point from a reference value of the stimulus, and thus

$$de/dT = f(Q, T, \bar{S}(T) - \bar{S}_R), \tag{12.38}$$

where $f$ is the internal strain adaptation rate function, which depends, in general, upon point $Q$ and adaptation time scale $T$. The internal strain adaptation rate function, $f$, is scalar-valued and stimulus $\overline{S}(T)$ has a tensorial order appropriate to its character: second-order tensors for strain, strain rate, stress and fatigue microdamage, and a scalar for strain energy. When a definite stimulus and a specific form of internal strain adaptation rate function $f$ have been selected, the material parameters that characterize the function are called internal strain adaptation rate coefficients. The internal strain adaptation rate coefficients and the reference values of the stimulus are phenomenological coefficients of the bone surface and must be determined by experiment. If it is assumed here that internal strain adaptation rate function $f$ is not site specific, that is to say, independent of the position of surface point $Q$, then $Q$ is eliminated from the right-hand side of (12.38). If the stimulus value at $Q$, $\overline{S}(T,Q)$, is equal to reference stimulus value $\overline{S}_R$, then the rate of change of $e$ is zero and no adaptation occurs at point $Q$. If the right-hand side of (12.38) is positive, the solid volume fraction will increase. If, on the other hand, the right-hand side of (12.38) is negative, the solid volume fraction will decrease. Equation (12.38) by itself does not constitute the complete theory. The theory is completed by other equations of elasticity theory and by assuming that bone is a linearly elastic material with a modified Hooke's law (Chapter 7):

$$\hat{\mathbf{T}}(\mathbf{x},t,T) = \xi_o \hat{\mathbf{C}}^o \cdot \hat{\mathbf{E}}(\mathbf{x},t) + e(\mathbf{x},T)\hat{\mathbf{C}}^1 \cdot \hat{\mathbf{E}}(\mathbf{x},t)\,, \tag{12.39}$$

where constant elasticity tensor $\hat{\mathbf{C}}$ in stress–strain relations (5.33H), $\hat{\mathbf{T}} = \hat{\mathbf{C}} \cdot \hat{\mathbf{E}}$, has been replaced by the slowly time-varying elasticity tensor, $\hat{\mathbf{C}}(\mathbf{x},T) = \xi_o \hat{\mathbf{C}}^o + e(\mathbf{x},T)\hat{\mathbf{C}}^1$, which varies with time because it depends upon change in volume fraction $e(\mathbf{x}, T)$. A boundary-value problem will be formulated in adaptive elasticity theory in the same manner as a boundary-value problem in linear elastostatics, but it will be necessary to specify the boundary conditions for a specific time period on the adaptation time scale. As the object evolves to a new solid volume fraction, $e(\mathbf{x}, T)$ on adaptation time scale $T$, the stimulus value and the stress and strain states will be varying quasistatically on loading time scale t. At any instant the object will behave exactly as an elastic object, but the changing solid volume fraction will cause local stimulus, stress, and strain to redistribute themselves slowly with time, on time scale $T$. The theory of internal strain adaptation acknowledges the orthopedic principle that prolonged straining of a bone tends to make the bone stiffer and denser while prolonged bed rest or inactivity will tend to make the bone less stiff and less dense.

As an example of the predictions of this theory, consider an inhomogeneous, adaptive elastic material object that is in mechanical and remodeling equilibrium for time $T < 0$. By mechanical and remodeling equilibrium it is meant that there exists steady stress $\hat{\mathbf{T}}^o(\mathbf{x})$, steady strain $\hat{\mathbf{E}}^o(\mathbf{x})$, and steady volume fraction $e_o(\mathbf{x})$ that satisfy the conditions for remodeling equilibrium. In order to illustrate the devolution of this inhomogeneous object into a homogeneous one, the inhomogeneous object, which is in mechanical and remodeling equilibrium for $T < 0$, is subjected to a homogeneous steady stress state for $T > 0$. Specifically, at $T = 0$ stress field $\hat{\mathbf{T}}^o(\mathbf{x})$ is changed to steady homogeneous field $\hat{\mathbf{T}}^*$. Since the action-at-a-distance force is zero and the stress is homogeneous, the equation of equilibrium ((4.37) in case $\ddot{\mathbf{x}} = 0$) is satisfied identically. The strain tensor for $T > 0$ can be determined by inversion of (12.39), and thus

$$\hat{\mathbf{E}}(\mathbf{x},T) = \hat{\mathbf{S}}^o \cdot \hat{\mathbf{T}}^* - \hat{\mathbf{S}}^o \cdot \hat{\mathbf{C}}^1 \cdot \hat{\mathbf{S}}^o \cdot \hat{\mathbf{T}}^* e(\mathbf{x},T)\,, \tag{12.40}$$

where constant compliance tensor $\hat{\mathbf{S}}$ in strain–stress relations (5.12H), $\hat{\mathbf{E}} = \hat{\mathbf{S}} \cdot \hat{\mathbf{T}}$, has been replaced by slowly time-varying compliance tensor $\hat{\mathbf{S}}(\mathbf{x},T) = \hat{\mathbf{S}}^o - \hat{\mathbf{S}}^o \cdot \hat{\mathbf{C}}^1 \cdot \hat{\mathbf{S}}^o e(\mathbf{x},T)$ that varies

with time because it depends upon change in volume fraction $e(T)$. Representation (12.40) for the strain tensor is then substituted into the 3D tensorial form of remodeling rate eq. (12.28):

$$\dot{e}(e,\hat{\mathbf{E}}) = c_1 e + c_2 e^2 + \hat{\mathbf{A}}^{\mathrm{o}} \cdot (\hat{\mathbf{E}} - \hat{\mathbf{E}}_{\mathrm{oRE}}) + e\hat{\mathbf{A}}^{1} \cdot \hat{\mathbf{E}}\,,$$

which may be rewritten in the form of 1D remodeling rate equation (12.23) with a position dependence, and thus the differential equation governing the evolution of $e(\mathbf{x}, T)$ is

$$\dot{e}(\mathbf{x},T) = a(e^2(\mathbf{x},T) - 2be(\mathbf{x},T) + c)\,,\ e(\mathbf{x},0) = e_{\mathrm{o}}(\mathbf{x}), \tag{12.41}$$

where $a = c_2$ and $b$ and c are constants now defined by

$$b = -\frac{1}{2c_2}\left(c_1 + \hat{\mathbf{A}}^{1} \cdot \hat{\mathbf{S}}^{\mathrm{o}} \cdot \hat{\mathbf{T}}^{*}(\mathbf{x}) - \hat{\mathbf{A}}^{\mathrm{o}} \cdot \hat{\mathbf{S}}^{\mathrm{o}} \cdot \hat{\mathbf{c}}^{1} \cdot \hat{\mathbf{S}}^{0} \cdot \hat{\mathbf{T}}^{*}(\mathbf{x})\right) \text{ and}$$

$$c = \frac{1}{c_2}(c_o + \hat{\mathbf{A}}^{\mathrm{o}} \cdot \hat{\mathbf{S}}^{\mathrm{o}} \cdot \hat{\mathbf{T}}^{*}(\mathbf{x}))\,.$$

The initial condition indicated as the second part of (12.41) requires that the inhomogeneity at time $T = 0$ be that associated with the mechanical and remodeling equilibrium state that existed for $T < 0$. The solution to differential equation (12.41) is the same as solution (12.27) to differential equation (12.23) except that the initial condition, $e(\mathbf{x}, 0) = e_{\mathrm{o}}(\mathbf{x})$, rather than $e(0) = 0$ is employed. As was the case with solution (12.27) to differential equation (12.23), the solution to differential equation (12.41) is stable only if $e_1$ and $e_2$ are real and distinct and, under those conditions on $e_1$ and $e_2$, $e(\mathbf{x}, t)$ is given by

$$e(\mathbf{x},t) = \frac{e_1(e_{\mathrm{o}}(\mathbf{x}) - e_2) + (e_1 - e_{\mathrm{o}}(\mathbf{x}))e_2 e^{-a(e_1 - e_2)t}}{(e_{\mathrm{o}}(\mathbf{x}) - e_2) + (e_1 - e_{\mathrm{o}}(\mathbf{x}))e^{-a(e_1 - e_2)t}}\,. \tag{12.42}$$

In the special case of a cylinder in which the inhomogeneity only lies along the axis of the cylinder, then $\mathbf{x}$ in (12.42) may be replaced by $x_3$, the coordinate axis along the axis of the cylinder. If the initial inhomogeneity is sinusoidal in form,

$$e_{\mathrm{o}}(x_3) = 0.1 \sin\frac{\pi x_3}{L}\,, \tag{12.43}$$

where the cylinder is of length $4L$, and appropriate choices are made for the other coefficients, Firoozbakhsh and Cowin (1980), then

$$e(x_3,T) = \frac{(0.129)(4.4 - \sin\frac{\pi x_3}{L}) + (0.44)(\sin\frac{\pi x_3}{L} - 1.29)e_2 e^{-T/\tau}}{(4.4 - \sin\frac{\pi x_3}{L}) + (\sin\frac{\pi x_3}{L} - 1.29)e^{-T/\tau}}\,, \tag{12.44}$$

where $\tau = 147$ days. This result is plotted in Figure 12.17 for various values of time.

When a metallic pin is fitted into the medullary canal of a long bone as part of a prosthetic device, the bone in the vicinity of the pin will remodel and alter its local structure. A mathematical analysis of the internal bone remodeling induced by a medullary pin according to the theory developed above was given in Cowin and Van Buskirk (1978). The problem is illustrated in Figure 12.18. This analysis shows that the force fitting of a medullary pin will neces-

sarily induce one of three following situations: (a) a reduction in stiffness of the bone surrounding the pin, and therefore, a loosening of the pin, (b) osteoporosis, a pathological bone structure of low porosity, or (c) osteopetrosis, a pathological bone structure of too high porosity. Although (c) is highly unlikely, it is mathematically possible at the present state of this predictive science. The results of this analysis show that the grip of the bone on the medullary pin will, most likely, loosen over time.

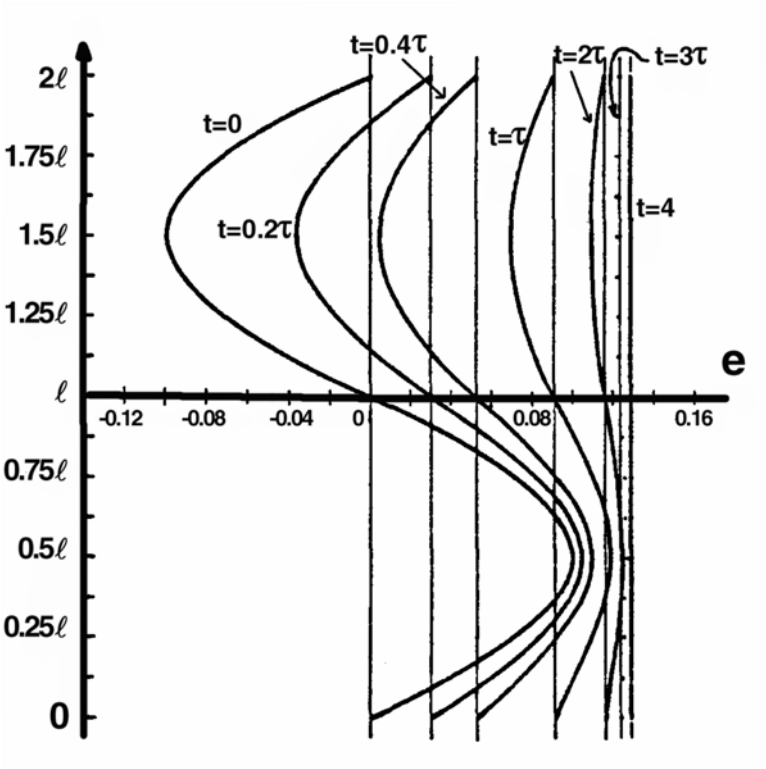



**Figure 12.17**. Devolution of the initial inhomogeneity. A graphical representation of the solution $e(x_3,T)$ given by eq. (12.44).

## 12.10. POSSIBLE CELLULAR MECHANISMS FOR BONE TISSUE ADAPTATION

Progress is being made in understanding the cell mechanisms that accomplish absorption and deposition of bone tissue. The physiological mechanism by which the mechanical loading applied to bone is sensed by the tissue and the mechanism by which the sensed signal is transmitted to the cells on the IC that accomplish surface deposition, removal, and maintenance have not been identified. The purpose of this section is to review some of the background research on these mechanosensory mechanisms and to outline candidates for the mechanosensory system.

Bone cells, like many other cell types, respond to alterations in their external environment. It is believed that the mechanosensing processes of an osteocyte enable it to sense the presence

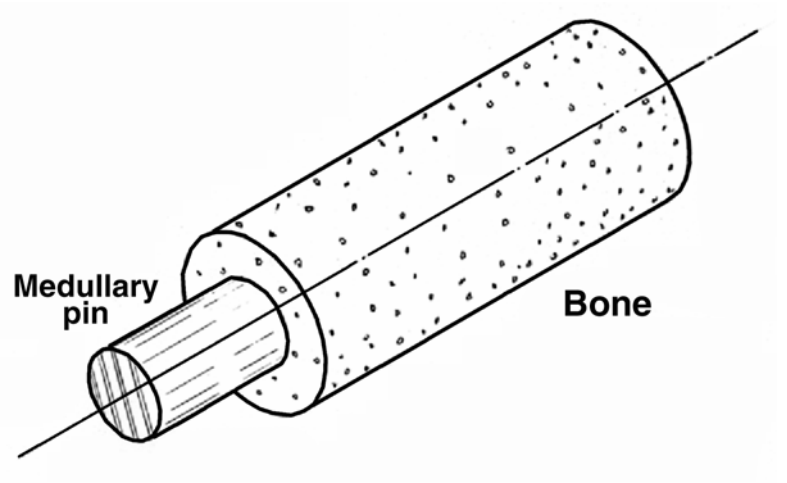



**Figure 12.18**. A bone with a medullary pin inserted in its medullary canal.

of, and to respond to, extrinsic physical loadings. Tissue sensibility is a property of a connected set of cells, and it is accomplished by the intracellular processes of mechanoreception and mechanotransduction. *Mechanoreception* is the term used to describe the process that transmits the informational content of an extracellular mechanical stimulus to a receptor cell. *Mechanotransduction* is the term used to describe the process that transforms the mechanical stimuli content into an *intra*-cellular signal. The term *mechanosensory* is employed to mean both mechanoreception and mechanotransduction. Additional processes of *inter*-cellular transmission of transduced signals are required at tissue, organ, and organismal structural levels.

Recall that the osteoblasts on the IC and the osteocytes buried in the bone matrix are extensively interconnected by the cell processes of the osteocytes forming a connected cellular network (CCN). The interconnectivity of the CCN is graphically illustrated by Figure 11.8, which is a scanning electron micrograph showing the replicas of lacunae and canaliculi in situ in mandibular bone from a young subject aged 22 years. The touching cell processes of two neighboring bone cells contain gap junctions; recall that a gap junction is a channel connecting two cells. Gap junctions connect nearby osteocytes to osteoblasts on the IC. All osteoblasts are similarly interconnected laterally to other osteoblasts on the IC and to osteocytes perpendicular to the IC. The CCN represents the hard wiring of bone tissue.

The *stimulus* for bone remodeling is defined as that particular aspect of the bone's stress or strain history that is employed by the bone to sense its mechanical load environment and to signal for the deposition, maintenance, or resorption of bone tissue. The bone tissue domain or region over which the stimulus is felt is called the *sensor* domain. When an appropriate stimulus parameter exceeds or falls below threshold values, loaded tissues respond by the triad of bone adaptation processes: deposition, resorption, and maintenance. The CCN is the site of intracellular stimulus reception, signal transduction, and intercellular signal transmission. It is thought that stimulus reception occurs in the osteocyte, and that the CCN transduces and transmits the signal to the IC. The osteoblasts on the IC alone directly regulate bone deposition and maintenance, and indirectly regulate osteoclastic resorption.

The true biological stimulus, although much discussed, is not precisely known. As mentioned in §12.2, a variety of mechanical loading stimuli associated with ambulation (at a frequency of 1–2 Hz) have been considered for bone strain adaptation. Most believe that some aspect of the mechanical loading of bone is the stimulus. In the preceding section it was noted that the mechanical stimuli suggested include strain, stress, strain energy, strain rate, or fatigue microdamage. The osteocyte has been suggested as the stimulus sensor, the receptor of the stimulus signal; histologic and physiologic data are consistent with this suggestion. The placement and distribution of osteocytes in the CCN three-dimensional array is architecturally well suited to sense deformation of the mineralized tissue encasing them. The osteocytes in the CCN are potential mechanoreceptors by virtue of their networked organization. Osteocytic mechanotransduction may involve a number of different processes or cellular systems. These processes include stretch- and voltage-activated ion channels, cyto-matrix sensation–transduction processes, cyto-sensation by fluid shear stresses, cyto-sensation by streaming potentials, and exogenous electric field strength.

A complete model for the mechanism by which the osteocytes housed in the lacunae of mechanically loaded bone sense the load applied to the bone by the detection of dynamic strains has been developed (Weinbaum et al., 1994). In the complete model, poroelasticity is used to convert the mechanical loads applied to a whole bone to fluid motion in the PLC. The osteocytes in the PLC are stimulated by relatively small fluid shear stresses acting on the membranes of their osteocytic processes. It has been established that osteocytes are stimulated by small fluid shear stresses, those on the order of 0.5 Pa. In this complete model the sensitivity of strain detection is a function of frequency; in the physiological frequency range (1–30 Hz), associated with either locomotion (1–2 Hz) or maintenance of posture (15–30 Hz), the fluid shear stress is nearly proportional to the product of frequency and strain. Thus, if bone cells respond to strains on the order of 0.1% at frequencies of 1–2 Hz, they will also respond to strains on the order of 0.01% at frequencies of 20 Hz. The fluid shear stresses would also strain the macromolecular mechanical connections between the cell and the extracellular bone matrix as well as the connections of the cell membrane to the nuclear membrane. Thus, fluid shear stress is also potentially capable of transmitting information from the surface of the cell to the nuclear membrane, where it might effectively regulate genomic functions.

In order to transmit a signal over the CCN one osteocyte must be able to signal a neighboring osteocyte that will then pass the signal on until it reaches an osteoblast on the IC. There are a variety of chemical and electrical cell-to-cell communication methods. The passage of chemical signals, such as $Ca^{2+}$, from cell to cell appears to occur at a rate that would be too slow to respond to the approximately 30-Hz signal associated with muscle firing. We focus here on a cable model for the electrical cell-to-cell communication in an osteon (Zhang et al., 1997). The spatial distribution of intracellular electric potential and current from the cement line to the lumen of an osteon was estimated as the frequency of the loading and conductance of the gap junction were altered. In this cable model the intracellular potential and current are driven by the mechanically induced strain-generated streaming potentials (SGPs) produced by the cyclic mechanical loading of bone. The model pursues a physiological approach in which the micro-anatomical dimensions of the connexon pores, osteocytic processes, and the distribution of cellular membrane area and capacitance are used to quantitatively estimate the leakage of current through the osteoblast membrane, the time delay in signal transmission along the cable, and the relative resistance of the osteocytic processes and the connexons in their open and closed states. The model predicts that the cable demonstrates a strong resonant response when the cable coupling length approaches the osteonal radius. The cable theory also predicts that the characteristic diffusion time for the spread of current along the membrane of the osteocytic processes is of the same order as the PLC pore pressure relaxation time. This coincidence

of characteristic times produced a spectral resonance in the cable at 30 Hz. These two resonances lead to a large amplification of the intracellular potential and current in the osteoblasts on the IC; this current could serve as the initiating signal for osteoblasts to conduct strain adaptation. This resonance might also explain why live bone appears to be selectively responsive to mechanical loading in a specific frequency range (15–60 Hz), as has been experimentally demonstrated for several species.

It is probable that electrical and mechanical transductive processes are neither exhaustive nor mutually exclusive. While utilizing differing intermediate membrane mechanisms and/or processes, they share a common final pathway, i.e., both mechanical and electrical transductions result in transplasma membrane ionic flow(s), creating a signal(s) capable of intercellular transmission to neighboring bone cells via gap junctions. These signals are inputs to a CCN, whose outputs regulate the bone adaptational processes.

The primacy of electrical signals is suggested here, because, while bone cell transduction may also produce small biochemical molecules that can pass through gap junctions, the time course of mechanosensory processes is believed to be too rapid for involvement of secondary messengers. As we noted above, the passage of chemical signals, such as $Ca^{2+}$, from cell to cell appears to occur at a rate that would be too slow to respond to the approximately 30-Hz signal associated with muscle firing.

## 12.11. THE LITERATURE OF BONE TISSUE ADAPTATION

In an 1867 paper entitled "Die Architektur der Spongiosa," Swiss anatomist G. H. Meyer presented a line drawing of the cancellous or "spongy" bone structure he had observed in the proximal end of the human femur. An important Swiss structural engineer of the period, C. Culmann, was struck by the similarity between Meyer's sketches of the cancellous bone in a frontal section of the proximal femur and the principal stress trajectories in a crane-like curved bar he was then in the process of designing. A sketch of the trabecular architecture of the type Meyer published is shown in Figure 11.18 along with a sketch of Culmann's crane; these are the *Culmann and Meyer drawings*. There are colorful versions of the origin of the Culmann and Meyer drawings. Some suggest (Jansen, 1920) that the origin of these drawings is a discussion that occurred at a meeting of the "naturforschende Gesellschaft," a society interested in understanding nature, in Zurich, held in the late summer 1866. In attendance were Meyer and Culmann, who was Professor of Engineering Science (Ingenieurwissenschaft) at the newly created Eidgenoessischen Polytechnikum (ETH) in Zurich. Professor Culmann was a leading structural engineer, and his book on graphical statics (Culmann, 1866), then current, standard procedure for structural stress analysis, appeared that year. (The finite-element method is the standard procedure for structural stress analysis today.) Meyer made a presentation that displayed preparations and his drawings of the cancellous architecture seen in frontal section of the proximal end of the human femur. Culmann observed that the form of the trabeculae in the proximal femur closely resemble the form of the stress trajectories of a homogeneous and continuous elastic object of the same shape as the bone and loaded in the same way. He made that observation based on his experience with a crane design that was similar in shape to the frontal section of a human femur. Figure 11.18, taken from Wolff (1870), illustrates the relationship between trabecular architecture and the stress trajectories of Culmann's crane. The Culmann and Meyer drawings are considered by many to be the origin of what is perceived to be Wolff's law (Jansen, 1920; D'arcy Thompson, 1942; Murray, 1936; Dibbets, 1992). Dibbets (1992) points out that Roux (1885a) put the Culmann and Meyer drawings in the modern context of

structural adaptation. This observation of Dibbets (1992) is consistent with those of other writers (Koch, 1917; Keith, 1918; Murray, 1936; Roesler, 1987; Brand and Claes, 1989).

There is no mention of J. Wolff being a party to the creation of the Culmann and Meyer drawings, although he came on the scene very shortly thereafter and interacted with Culmann (Wolff, 1870); he published his book on the subject 22 years later (Wolff, 1892; English translation, 1986). The reports sustaining the validity of "Wolff's law of trabecular architecture" are generally visual comparisons of the trabecular architecture in a bone with the carefully selected static stress trajectories of a loaded homogeneous, isotropic elastic object of similar shape, the prototype of this argument being the Culmann and Meyer drawings (Figure 11.18). The critical rejection of Wolff's trajectorial hypothesis by numerous students of the subject is reviewed by Cowin (2001). While "Wolff's law of trabecular architecture" does not stand up to scrutiny, references to Wolff's law in the literature are reasonable, but a bit imprecise. They are reasonable because they generally refer to Roux's (1885a) concept of functional adaptation of osseous tissue, an aspect of Wolff's law that is founded in biological thought and experiment, and with which Wolff did not fully agree (Dibbets, 1992).

After the contributions of Culmann, Meyer, Wolff and Roux in the late 1800s and Koch and Murray in the first half of the 1900s, the sustained contribution of Harold Frost (Frost, 1964; and hundreds of later papers and books) beginning in the 1960s and continuing for over 40 years was a major factor in developing research in this area. In the 1970s and 1980s there were a number of whole animal experiments (for example, those reviewed in §12.2); see Goodship and Cunningham (2001) for a wider survey of these experiments. The animal experiments motivated the phenomenological strain adaptation models described in §§12.3–12.9. These models were more numerous than those mentioned in §§12.3–12.9, and wider surveys of these models are given by Hart (2001). Also not described here are the extensive efforts at computational models for bone adaptation; these are also reviewed by Hart (2001).

In the 1990s the emphasis of research switched to study of mechanosensation in bone, that is to say, efforts to determine the cellular mechanisms involved in sensing mechanical loading on a bone and signaling other cells to deposit or resorb tissue. This work, up to the end of the 20th century, is described by Burger (2001) and Cowin and Moss (2001); the devices that have been developed to mechanically load bone cells are described in Brown (2001). Mechanosensation in bone is a very active area of research today because the basic questions concerning mechanical sensation by cells and signaling among bone cells have not yet been answered (Cowin et al., 1991).

The currently available books that deal with bone adaptation mechanics include Currey (1984, 2002), Martin and Burr (1989), Martin, Burr, and Sharkey (1998), and the edited volumes by Cowin (1989, 2001). The principal journals for bone mechanics are the *Journal of Biomechanics,* the *International Journal of Biomechanics and Modeling in Mechanobiology,* and the American Society of Mechanical Engineers' *Journal of Biomechanical Engineering*. There are journals in which bone mechanics-related material occurs; these include the journal *Bone*, the *Annals of Biomedical Engineering*, the *Journal of Bone and Joint Surgery*, and the *Journal of Orthopaedic Research*.

## References

Brand R, Claes L. 1989. Review of the English translation of the book *The Law of Bone Remodelling* by J. Wolff. *J Biomech* **22**:185–187.

Brown TD. 2001. Devices and techniques for in vitro mechanical stimulation of bone cells. Chapter 27 in *Bone mechanics handbook*, ed. SC Cowin. Boca Raton, FL: CRC Press.

Brown TD, Pedersen DR, Gray ML, Brand RA, et al. 1990. Toward an identification of mechanical parameters initiating periosteal remodeling: a combined experimental and analytic approach. *J Biomech* **23**:893–905.

Burger EH. 2001. Experiments on cell mechanosensitivity: bone cells as mechanical engineers. Chapter 28 in *Bone mechanics handbook*, ed. SC Cowin. Boca Raton, FL: CRC Press.

Cowin SC. 1981. Mechanical properties of bones. In *Mechanics of Structured Media*, ed. APS Selvadurai, pp. 151–184. Philadelphia: Elsevier.

Cowin SC, ed. 1989. *Bone mechanics*. Boca Raton, FL: CRC Press.

Cowin SC, ed. 2001. *Bone mechanics handbook*. Boca Raton, FL: CRC Press (ISBN/ISSN: 0849391172).

Cowin SC. 2003. Adaptive elasticity: a review and critique of a bone tissue adaptation model. *Eng Trans* **51**:1–79.

Cowin SC, Hegedus DH. 1976. Bone remodeling, I: theory of adaptive elasticity. *J Biomech* **6**:313–326.

Cowin SC, Mehrabadi MM. 1989. Identification of the elastic symmetry of bone and other materials. *J Biomech* **22**:503–515.

Cowin SC, Moss ML. 2000. Mechanosensory mechanisms in bone. In *Textbook of tissue engineering*, 2nd ed., ed. R Lanza, R Langer, W Chick, pp. 723–738. San Diego: Academic Press.

Cowin SC, Moss ML. 2001. Mechanosensory mechanisms in bone. *Bone mechanics handbook*, ed. SC Cowin. Boca Raton, FL: CRC Press.

Cowin SC, Nachlinger RR. 1978. Bone remodeling, III: uniqueness and stability in adaptive elasticity theory. *J Elast* **8**:285–295.

Cowin SC, Van Buskirk WC. 1979. Surface bone remodeling induced by a medullary pin. *J Biomech* **12**:269–276.

Cowin SC, Hart RT, Balser JR, Kohn DH. 1985. Functional adaptation in long bones: establishing in vivo values for surface remodeling rate coefficients. *J Biomech* **18**:665–684.

Cowin SC, Moss-Salentijn L, Moss ML. 1991. Candidates for the mechanosensory system in bone. *J Biomech Eng* **113**:191–197.

Culmann K. 1866. *Die graphische statik*. Zurich: Verlag von Meyer & Zeller.

Currey JD. 1960. Differences in the blood supply of bone of different histological type. *Q J Microsc Sci* **101**:351–370.

Currey JD. 1979. Changes in the impact energy absorption of bone with age. *J Biomech* **12**:459–470.

Currey JD. 1984. *The mechanical adaptation of bones*. Princeton: Princeton UP.

Currey JD. 2002. *Bones*. Princeton: Princeton UP.

D'arcy Thompson W. 1942. *On growth and form*. Cambridge: Cambridge UP.

Dibbets JMH. 1992. One century of Wolff's law. In *Bone biodynamics in orthodontic and orthopaedic treatment*, ed. DS Carlson, SA Goldstein, pp. 1–13 (Craniofacial Growth Series, Vol 27). Ann Arbor: U Michigan P.

Firoozbakhsh K, Cowin SC. 1980. Devolution of inhomogeneities in bone structure: predictions of adaptive elasticity theory. *J Biomech Eng* **102**:287–293.

Frost HM. 1964. *The laws of bone structure*. Springfield, IL: Charles C. Thomas.

Frost HM. 1969. Tetracycline-based histological analysis of bone remodeling. *Calcif Tissue Res* **3**:211–237.

Goodship AE, Cunningham JL. 2001. Pathophysiology of functional adaptation of bone in remodelling and repair in vivo. Chapter 26 in *Bone mechanics handbook*, ed. SC Cowin. Boca Raton, FL: CRC Press.

Hart RT. 2001. Bone modeling and remodeling. Chapter 31 in *Bone mechanics handbook*, ed. SC Cowin. Boca Raton, FL: CRC Press.

Hegedus DH, Cowin SC. 1976. Bone remodeling, II: small strain adaptive elasticity. *J Elast* **6**:337–352.

Jansen M. 1920. *On bone formation — its relation to tension and pressure*. London: Longmans, Green & Co.

Jaworski ZFG, Liskova-Kiar M, Uhthoff HK. 1980. Effect of long-term immobilization an the pattern of bone loss in older dogs. *J Bone Joint Surg* **62B**:104–111.

Keith A. 1918. Hunterian lecture on Wolff's law of bone transformation. *Lancet* **16**:250–252.

Koch JC. 1917. Laws of bone architecture. *Am J Anat* **21**:177–298.

Lanyon LE. 1984. Functional strain as a determinant for bone remodeling. *Calcif Tissue Int* **36**:S56–S61.

Lanyon LE, Goodship AE, Pye CJ, MacFie JH. 1982. Mechanically adaptive bone remodeling. *J Biomech* **15**:141–154.

Martin RB, Burr DB. 1989. *Structure, function and adaptation of compact bone*. New York: Raven Press.

Martin RB, Burr DB, Sharkey NA. 1998. *Skeletal tissue mechanics*. New York: Springer.

Murray PDF. 1936. *Bones — a study of the development and structure of the vertebrate skeleton*. Cambridge: Cambridge UP.

Roesler H. 1987. The history of some fundamental concepts in bone biomechanics. *J Biomech* **20**:1025–1034.

Roux W. 1885. Beitrage zur morphologie der funktionellen anpassung. *Arch Anat Physiol Anat Abt*, pp. 120–185.

Seireg A, Arvikar RJ. 1975. The prediction of muscular load sharing and joint forces in the lower extremities during walking. *J Biomech* **8**:89–102.

Timoshenko S. 1955. *Strength of materials*, 3rd ed., Vol. 1, Chapter 8. New York: Van Nostrand.

Uhthoff HK, Jaworski ZFG. 1978. Bone loss in response to long term immobilization. *J Bone Joint Surg* **60-B**:420–429.

Van Cochran C. 1982. *Primer of orthopaedic biomechanics*. New York: Churchill Livingstone.

Weinbaum S, Cowin SC, Zeng Yu. 1994. A model for the excitation of osteocytes by mechanical loading-induced bone fluid shear stresses. *J Biomech* **27**:339–360.

Wolff J. 1870. Uber der innere architektur der knochen und ihre bedeutung fur die frage vom knochenwachstum. *Arch Path Anat Physiol Med, Virchovs Arch* **50**:389–453.

Wolff J. 1892. *Das gesetz der transformation der knochen*. Berlin: Hirschwald.

Wolff J. 1986. *The law of bone remodelling*. Berlin: Springer.

Woo SLY, Kuei SC, Dillon WA, Amiel D, White FC, et al. 1981. The effect of prolonged physical training on the properties of long bone-a study of Wolff's Law. *J Bone Joint Surg* **63-A**:780–787.

Zhang D, Cowin SC, Weinbaum S. 1997. Electrical signal transmission and gap junction regulation in bone cell network: a cable model for an osteon. *Ann Biomed Eng* **25**:357–374.

# 13

# MODELING POROELASTIC AND ELECTRICAL EFFECTS IN SOFT TISSUES

"The earth is a living body. Its soul is its ability to grow. This soul, which also provides the earth with its bodily warmth, is located in the inner fires of the earth, which emerge at several places as baths, sulfur mines or volcanoes. Its flesh is the soil, its bones are the strata of rock, its cartilage is the tufa [rock composed of volcanic detritus, fused together by heat], its blood is the underground streams, the reservoir of blood around its heart is the ocean. The systole and diastole of the blood in the arteries and veins appear on the earth as the rising and sinking of the oceans." (*The Codex Leicester*, Leonardo da Vinci)

## 13.1. INTRODUCTION

The modeling of interstitial fluid flow in tissues whose fluid and matrix constituents include cations and anions and which may be assumed to be incompressible is the subject of this chapter. Modeling of interstitial fluid flow in tissues whose components are compressible was dealt with in Chapter 9 on poroelasticity. In Chapter 9 it was shown how the incompressible case may be approached from the compressible, thus demonstrating that it is possible to treat the compressible and incompressible cases jointly, but it is easier to address them separately because the interaction of interstitial fluid flow and solid matrix in these two tissue types is significantly different.

Pursuing the analogy of the earth as a living body suggested in the quote from Leonardo da Vinci above, the porous medium behavior of hard tissues is similar to the behavior of saturated porous rocks, marble and granite, while the porous medium behavior of soft tissues is similar to the behavior of saturated soils, the sort of geological deposits one might call "swampy soils." Although both are saturated porous media, their detailed modeling and physical behavior are quite different. The term "unsaturated porous media" generally refers to cases when the matrix pores are filled with a fluid and a gas as, for example, the soil near the roots of a plant may contain water, air, and soil solids. In the case of hard tissues and saturated porous rocks, the fact that the bulk stiffness of the matrix material is large compared to the bulk stiffness of water means that (1) they do not exhibit swelling, (2) only a fraction of the hydrostatic stress in the matrix material is transferred to the pore fluid, and (3) the strain levels in many practical problems of interest are small. In the case of soft tissues and the saturated porous

soils, (1) the strains can be large (however, only small strains are considered in this chapter), (2) they exhibit swelling, and (3) the bulk stiffness of the matrix material is about the same as the bulk stiffness of water, which means that almost all of the hydrostatic stress in the matrix material is transferred to the pore fluid. The effective Skempton parameter defined by eq. (9.8) is a measure of the fraction of the hydrostatic stress in the matrix material that is transferred to the pore fluid. For soft tissues and saturated soils the Skempton parameter approaches 1, indicating that almost 100% of the hydrostatic stress in the matrix material is transferred to the pore fluid. As a consequence of this fact that the response to volumetric deformation of the fluid and the solid matrix in soft tissue is much stiffer than the deviatoric response, it is reasonable to assume that the soft tissues and the contained fluid phase are incompressible. Thus, soft tissues are "hard" with respect to hydrostatic deformations and soft with respect to shearing or deviatoric deformations. This fact is the justification for the assumption of incompressibility of both the matrix material and the pore fluid made in the development of porous media models for soft tissues. The assumption of incompressibility is not correct for marble, granite, and hard tissue. For marble and granite the Skempton parameter is between 0.5 and 0.6, and for the lacunar canalicular porosity of bone it is between 0.4 and 0.5. This means that only about 50% of the hydrostatic stress in the matrix material is transferred to the pore fluid in these materials with a stiff bulk modulus.

Swelling occurs in many of the biological soft tissues of interest and in many biological processes of interest. One source of swelling is an effect of electric charges, where the electric charges fixed to the porous solid component are balanced by corresponding charges in the fluid. Swelling is just one of the many electrical effects that occur in biological tissues. Electromechanical phenomena observed in many biological tissues include mechano-electrochemical coupling phenomena such as streaming potentials and currents, osmosis, and electroosmosis (see Table 13.1). In this chapter a continuum porous media model for the passive transport of electrolytes in charged porous soft tissues, and for ion exchange in membranes, will be described. The continuum mixture model is suitable for a description of the mechano-electro-chemical behaviors associated with deformation and fluid flow in charged-hydrated biologic tissues because it provides a flexible and general basis that permits the development of a unified viewpoint for many diverse and perhaps simultaneously occurring phenomena. In several important ways the mixture model of saturated porous media is more general than the Biot (1941, 1972) model of poroelasticity described in Chapter 9; Bowen (1980, 1982) recovered the model of Biot (1941) from the mixture theory approach. The most important way in which the mixture model is more general than the Biot poroelastic model is that the mixture model admits the possibility of following many constituents, particularly the charged constituents of interest here, the anions and the cations, as well as the solid and fluid solvent components in the Biot model. A brief history of the modern development of mixture theory and its application to physiology and cell biology is contained in the final section of this chapter.

The definition of a material mixture employed in science is a material with two or more ingredients, the particles of which are separable, independent, and uncompounded with each other. If the distinct phases of a mixture retain their identity, the mixture is said to be immiscible; if they lose their identity, the mixture is said to be miscible. Tissues are mixtures of numerous distinct proteins, water, various ions and solutes. The theory of immiscible mixtures is employed to model the interaction of electrical and mechanical effects in tissues. In this chapter the theory of mixtures is described briefly; it is then employed to construct a multiconstituent mixture for use in tissue models. The constituents include a solid, a fluid, anions, cations, and solutes. A brief summary of results from electrochemistry concerning osmotic pressure and Donnan equilibrium is included.

**Table 13.1**. Direct and Couple Flow Phenomena Induced by Pressure, Chemical Potential, Electrical Potential, and Temperature Gradients in Charged Porous Media

| Driving ⇒ mechanism flux ⇓ | Pressure gradient | Chemical potential gradient | Electrical potential gradient | Temperature gradient |
|---|---|---|---|---|
| Fluid | Filtration (Darcy's law) | Osmosis | Electro-osmosis | Thermal osmosis |
| Solute | Ultra-filtration | Diffusion (Fick's law) | Electro-phoresis | Thermal diffusion |
| Current | Streaming current | Diffusion current | Electrical conduction (Ohm's law) | Thermal electricity |
| Heat | Isothermal heat transfer | Dufour effect | Peltier effect | Thermal conduction (Fourier law) |

Modified with permission from Huyghe and Janssen (1999).

This presentation of the theory of mixtures is restricted to the situation in which all the mixture constituents are incompressible, immiscible, non-reacting (no chemical reactions), and all are at the same temperature, $\theta$. It is assumed that terms proportional to the square of diffusion velocities will be negligible. Bowen (1976, see p. 27) considers the case where they are not negligible. It is also assumed that the stress tensor associated with each constituent is symmetric and that there are no action-at-a-distance couples, as there would be, for example, if the material contained electric dipoles and was subjected to an electrical field. The restrictions associated with each of these assumptions may be removed; they are imposed to restrict this presentation to an economical path for the development of a tissue-appropriate model for normal physiological phenomena.

## 13.2. KINEMATICS OF MIXTURES

In the theory of mixtures each place $\mathbf{x}$ in a fixed spatial frame of reference might be occupied by several different particles, one for each constituent $\mathbf{X}_{(a)}$, $a = 1, 2, \ldots, N$, of the mixture. This representation is a direct generalization of the single constituent continuum considered in Chapter 3; thus, material description of motion (3.2) is generalized to a description that recognizes all the constituents of the mixture:

$$\mathbf{x} = \boldsymbol{\chi}(\mathbf{X}_{(a)}, \mathrm{t}) \text{ for all } \mathbf{X}_{(a)} \subset O_{(a)}(0). \tag{13.1}$$

The inverse of motion (13.1) is then, in analogy with the relationship between (3.2) and (3.15), given by

$$\mathbf{X}_{(a)} = \boldsymbol{\chi}_{(a)}^{-1}(\mathbf{x}, t) \text{ for all } \mathbf{X}_{(a)} \subset O_{(a)}(0). \tag{13.2}$$

Similar generalizations to multicomponent mixtures of the formulas for the deformation gradient and its inverse, (3.13) and (3.14), are straightforward. The deformation gradient tensor for the $a$th constituent $\mathbf{F}_{(a)}$ is defined by

$$\mathbf{F}_{(a)} = [\nabla_{(a)} \otimes \boldsymbol{\chi}(\mathbf{X}_{(a)}, \mathrm{t})]^{\mathrm{T}} \text{ for all } \mathbf{X}_{(a)} \subset O_{(a)}(0), \tag{13.3}$$

and inverse deformation gradient tensor $\mathbf{F}_{(a)}^{-1}$ is, from (13.2), defined by

$$\mathbf{F}_{(a)}^{-1} = [\nabla \otimes \boldsymbol{\chi}_{(a)}^{-1}(\mathbf{x}, t)]^{\mathrm{T}} \text{ for all } \mathbf{x} \subset O_{(a)}(t). \tag{13.4}$$

The determinant of the tensor of deformation gradient for the $a$th constituent, $J_{(a)}$, is the Jacobian of the transformation from $\mathbf{x}$ to $\mathbf{X}_{(a)}$, and thus

$$J_{(a)} \equiv \text{Det } \mathbf{F}_{(a)} = 1/\text{Det } \mathbf{F}_{(a)}^{-1}, \tag{13.5}$$

where it is required that

$$0 < J_{(a)} < \infty, \tag{13.6}$$

so that a finite continuum volume always remains a finite continuum volume.

The velocity, $\mathbf{v}_{(a)}$, and acceleration, $D^{(a)}v_{(a)}/Dt$, of a particle of the $a$th constituent, $\mathbf{X}_{(a)}$, are defined by formulas that are generalizations of definitions (3.24) for velocity $\mathbf{v}$ and acceleration $D\mathbf{v}/Dt$ in a single-component continuum:

$$\mathbf{v}_{(a)} = \frac{D^a \mathbf{x}_{(a)}}{Dt} = \left.\frac{\partial \chi_{(a)}(\mathbf{X}_{(a)}, t)}{\partial t}\right|_{\mathbf{X}_{(a)}\text{fixed}}, \tag{13.7}$$

$$\frac{D^a \mathbf{v}_{(a)}}{Dt} = \left.\frac{\partial^2 \chi_{(a)}(\mathbf{X}_{(a)}, t)}{\partial t^2}\right|_{\mathbf{X}_{(a)}\text{fixed}}, \tag{13.8}$$

where $\mathbf{X}_{(a)}$ is held fixed because it is the velocity or acceleration of particle $\mathbf{X}_{(a)}$ that is being determined. The *spatial description of motion* of particle $\mathbf{X}_{(a)}$ (as opposed to the *material description of motion* of particle $\mathbf{X}_{(a)}$ represented by (13.1)) is obtained by substituting (13.2) into expressions (13.7) for the velocity; and thus,

$$\mathbf{v}_{(a)} = \frac{D^a}{Dt} \chi_{(a)}(\mathbf{X}_{(a)}, t)$$

becomes

$$\mathbf{v}_{(a)} = \frac{D^a}{Dt} \chi_{(a)}(\chi_{(a)}^{-1}(\mathbf{x}, t), t) = \mathbf{v}_{(a)}(\mathbf{x}, t), \tag{13.9}$$

which is a generalization of (3.26). The *material time derivative* of the $a$th constituent is the time derivative following material particle $\mathbf{X}_{(a)}$; it is denoted by $D^a/Dt$ and is defined as the partial derivative with respect to time with $\mathbf{X}_{(a)}$ held constant. If $\Gamma(\mathbf{x}, t)$ represents a function of $\mathbf{x}$ and $t$, the material time derivative of the $a$th constituent is given by

$$\frac{D^a \Gamma}{Dt} = \left.\frac{\partial \Gamma(\chi_{(a)}(\mathbf{X}_{(a)}, t), t)}{\partial t}\right|_{\mathbf{X}_{(a)}\text{fixed}}. \tag{13.10}$$

This definition is simply a generalization of (13.7) to arbitrary function $\Gamma(\mathbf{x}, t)$. It then follows from (3.29) that

$$\frac{D^a \Gamma}{Dt} = \frac{\partial \Gamma(\mathbf{x}, t)}{\partial t} + \mathbf{v}_{(a)} \cdot \nabla[\Gamma(\mathbf{x}, t)]. \tag{13.11}$$

The modeler may select one component of the mixture as special because, from the viewpoint of the modeler, that constituent serves as a key reference relative to which the movement of all the other constituents may be referred. This constituent of the mixture is denoted by *s*. The motion of the selected constituent is, from (13.1), given by $\mathbf{x} = \boldsymbol{\chi}(\mathbf{X}_s, t)$ for all $\mathbf{X}_s \subset O_s(0)$. The material time derivative following the selected constituent is given by (13.11) with label *a* replaced by label *s*. A relationship between the time derivative following selected constituent *s* and the time derivative following generic constituent *a* is obtained by subtracting the two formulas for the time derivatives:

$$\frac{D^a\Gamma}{Dt} = \frac{D^s\Gamma}{Dt} + (\mathbf{v}_{(a)} - \mathbf{v}_{(s)}) \cdot \nabla[\Gamma(\mathbf{x},t)] \,. \tag{13.12}$$

The tensor of velocity gradients for the *a*th constituent, $\mathbf{L}_{(a)}$, is formed by taking the spatial gradient of the velocity field for the *a*th constituent, $\mathbf{v}_{(a)} = \mathbf{v}_{(a)}(\mathbf{x},t)$, and thus

$$\mathbf{L}_{(a)} = \nabla \otimes \mathbf{v}_{(a)} \,. \tag{13.13}$$

Please note that this definition is completely analogous to the definition of the tensor of velocity gradients for a single-constituent material, $\mathbf{L}$, given by (3.31). Using the chain rule it is easy to show that $\mathbf{L}_{(a)}$ also has this representation:

$$\mathbf{L}_{(a)} = \frac{D^a\mathbf{F}_{(a)}}{Dt}\mathbf{F}_{(a)}^{-1} \,. \tag{13.14}$$

If $\rho_{(a)}$ denotes the density of the *a*th constituent, then the density of the mixture may be defined by

$$\rho(\boldsymbol{x},\, \mathrm{t}) = \sum_{a=1}^{N} \rho_{(a)}(\mathbf{x},t) \,. \tag{13.15}$$

Physically, $\rho_{(a)}$ represents the mass of the *a*th constituent per unit volume of the mixture. The true material density for the *a*th constituent is denoted by $\gamma_{(a)}$ and represents the mass of the *a*th constituent per unit volume of the *a*th constituent. Quantity $\rho_{(a)}$ is sometimes called the bulk density as opposed to the *true material density,* $\gamma_{(a)}$. The *volume fraction* of the *a*th constituent, $\phi_{(a)}$, that is to say, the volume of the *a*th constituent per unit volume of mixture, is defined by

$$\phi_{(a)}(\mathbf{x},t) = \frac{\rho_{(a)}(\mathbf{x},t)}{\gamma_{(a)}(\mathbf{x},t)} \,, \tag{13.16}$$

and it is assumed that the sum of all volume fractions divided by the total volume is equal to 1:

$$\sum_{a=1}^{N} \phi_{(a)}(\mathbf{x},t) = 1 \,. \tag{13.17}$$

If the *a*th constituent is incompressible, then $\gamma_{(a)}$ is a constant. Observe from (13.16) that bulk density $\rho_{(a)}$ need not be constant even if the *a*th constituent is incompressible since volume fraction $\phi_{(a)}$ may change. The mixture is only incompressible when all $\gamma_{(a)}$, $a = 1, 2, \ldots, N$, are incompressible. If less than *N* constituents are incompressible, (13.17) is a constraining relationship between the densities. Note that mixture density $\rho$ given by (13.15) may be variable

even when all the constituents are incompressible, that is to say, all $\gamma_{(a)}$ are constant, because volume fraction (13.16) of the constituents present at point **x** is variable.

## 13.3. THE CONSERVATION LAWS FOR MIXTURES

In this section equations are postulated for the balance of mass, momentum, and energy for each constituent and then the necessary and sufficient conditions are obtained so that the usual global balance of mass, momentum, and energy for the entire mixture is satisfied. In order to postulate equations for the balance of mass, momentum, and energy for each constituent $\mathbf{X}_{(a)}$, $a = 1, 2, \ldots, N$, each constituent of the mixture is assigned density $\rho_{(a)}$, action-at-a-distance force density $\mathbf{d}_{(a)}$, partial stress $\mathbf{T}_{(a)}$, partial internal energy density $\varepsilon_{(a)}$, a partial heat flux, and partial heat supply density $r_{(a)}$.

The local statement of mass conservation for a single-constituent continuum,

$$\frac{\partial \rho}{\partial t} + \nabla \cdot (\rho \mathbf{v}) = 0 , \tag{4.6 repeated}$$

may be written for each constituent $a = 1, 2, \ldots, N$ as

$$\frac{\partial \rho_{(a)}}{\partial t} + \nabla \cdot (\rho_{(a)} \mathbf{v}_{(a)}) = 0 . \tag{13.18}$$

The constituent form of mass balance (13.18) summed over all the constituents produces continuum statement (4.6) if definitions (13.15) for the density of the continuum mixture and mean mixture velocity **v**,

$$\mathbf{v} = \frac{1}{\rho} \sum_{a=1}^{N} \rho_{(a)} \mathbf{v}_{(a)} , \tag{13.19}$$

are employed. The conservation of momentum for a single-constituent continuum,

$$\rho \dot{\mathbf{v}} = \nabla \cdot \mathbf{T} + \rho \mathbf{d} , \tag{4.29 repeated}$$

may be written as

$$\rho_{(a)} \frac{D^{(a)} \mathbf{v}_{(a)}}{Dt} = \nabla \cdot \mathbf{T}_{(a)} + \rho_{(a)} \mathbf{d}_{(a)} + \check{\mathbf{p}}_{(a)} , \tag{13.20}$$

where $\mathbf{T}_{(a)}$ is the partial stress, $\mathbf{d}_{(a)}$ is the action-at-a-distance force density, and $\varepsilon_{(a)}$ is the momentum supply associated with constituent $a$. Momentum supply $\varepsilon_{(a)}$ is the only term that is not directly associated with a term in (4.29); it represents the transfer of momentum from the other constituents to constituent $a$. In this presentation it is assumed that all partial stress tensors $\mathbf{T}_{(a)}$ are symmetric. The assumption is consistent with the mixture theory applications that are to be considered here, but it is an assumption that may be avoided if necessary (Bowen 1976, 1980). The conservation of energy for constituent $a$ is a similar generalization of the single-constituent continuum result (4.52):

$$\rho \dot{\varepsilon} = \mathbf{T} : \mathbf{D} - \nabla \cdot \mathbf{q} + \rho r , \tag{4.52 repeated}$$

and thus

$$\rho_{(a)} \frac{D^a \varepsilon_{(a)}}{Dt} = \mathbf{T}_{(a)} : \mathbf{D}_{(a)} - \nabla \cdot \mathbf{q}_{(a)} + \rho_{(a)} r_{(a)} + \breve{\varepsilon}_{(a)} , \tag{13.21}$$

where $\varepsilon_{(a)}$ is the partial internal energy density, $\mathbf{q}_{(a)}$ is the partial heat flux vector, $r_{(a)}$ is the heat supply density, $\breve{\varepsilon}_{(a)}$ is the energy supply, and $\mathbf{D}_{(a)} = (1/2)\,(\mathbf{L}_{(a)} + (\mathbf{L}_{(a)})^{\mathrm{T}})$ by the extension of (3.32) to each constituent. The energy supply, $\breve{\varepsilon}_{(a)}$, is the only term that is not directly associated with a term in the single-constituent continuum form of energy conservation (4.52); it represents the transfer of energy from the other constituents to constituent *a*.

The summation of the forms of balance of mass (13.18), balance of momentum (13.20), and balance of energy (13.21) for each constituent over all the constituents is required to produce again the single-constituent continuum forms of balance of mass (4.6), balance of momentum (4.29), and balance of energy (4.52), respectively. In the case when the summation is over the density-weighted time derivatives of specific quantities following the generic constituent as, for example, on the left-hand side of (13.21), the result is difficult to interpret. Thus, a formula relating the time derivative of the selected component to the sum of the density-weighted time derivatives has been developed. Let the constituent-specific quantity per unit mass be denoted by $\varpi_{(a)}$ and its density-weighted sum by $\rho\varpi$; thus,

$$\varpi = \frac{1}{\rho} \sum_{a=1}^{N} \rho_{(a)} \varpi_{(a)} . \tag{13.22}$$

The desired formula relating the sum of the density-weighted, constituent-specific time derivatives to the time derivative following the selected component is written as

$$\sum_{a=1}^{N} \rho_{(a)} \frac{D^a \varpi_{(a)}}{Dt} = \rho \frac{D^s \varpi}{Dt} - \varpi \nabla \cdot [\rho(\mathbf{v} - \mathbf{v}_{(s)})] + \sum_{a=1}^{N} (\nabla \cdot [\varpi_{(a)} \rho_{(a)} \mathbf{u}_{(a)}]) , \tag{13.23}$$

where $\mathbf{u}_{(a)}$ is the diffusion velocity relative to the selected component:

$$\mathbf{u}_{(a)} = \mathbf{v}_{(a)} - \mathbf{v}_{(s)} . \tag{13.24}$$

Note that, from (13.24), (13.19), and (13.15), the following relationship is easily obtained:

$$\rho(\mathbf{v} - \mathbf{v}_{(s)}) = \sum_{a=1}^{N} \rho_{(a)} \mathbf{u}_{(a)} = \sum_{b=1}^{N-s} \rho_{(b)} \mathbf{u}_{(b)} , \tag{13.25}$$

where the last equality follows from the fact that, from (13.24), $\mathbf{u}_{(s)}$ must be zero. Please recall that, in the development of this chapter, terms of order of diffusion velocity $\mathbf{u}_{(b)}$ squared are to be neglected. The derivation of (13.23) involves expressions for time derivatives (13.11) and (13.12), constituent specific mass balance (13.18), and the definition of density-weighted sum $\rho\varpi$ in terms of the constituent-specific quantity per unit mass, denoted by $\varpi_{(a)}$, (13.22). When result (13.25) is incorporated into (13.23), it takes the form

$$\sum_{a=1}^{N} \rho_{(a)} \frac{D^a \varpi_{(a)}}{Dt} = \rho \frac{D^s \varpi}{Dt} + \sum_{b=1}^{N-s} \{\nabla \cdot [\varpi_{(b)} \rho_{(b)} \mathbf{u}_{(b)}] - \varpi \nabla \cdot [\rho_{(b)} \mathbf{u}_{(b)}]\} . \tag{13.26}$$

Note that (13.25) reduces to

$$\sum_{a=1}^{N} \rho_{(a)} \frac{D^a \varpi_{(a)}}{Dt} = \rho \frac{D\varpi}{Dt} + \sum_{a=1}^{N} (\nabla \cdot [\varpi_{(a)} \rho_{(a)} \mathbf{u}_{(a)}]) \tag{13.27}$$

when $\mathbf{v}_{(s)} = \mathbf{v}$ and to

$$\sum_{a=1}^{N} \rho_{(a)} \frac{D^a \varpi}{Dt} = \rho \frac{D^s \varpi}{Dt} + \rho(\mathbf{v} - \mathbf{v}_{(s)}) \cdot \nabla \varpi = \rho \frac{D\varpi}{Dt} \tag{13.28}$$

when $\varpi_{(a)}$ is assumed not to have a dependence upon index $a$. Application of formula (13.26) relating the sum of the density-weighted, constituent-specific time derivatives to the time derivative following the selected component to the special case of velocity $\mathbf{v}_{(a)}$ yields the following representation:

$$\sum_{a=1}^{N} \rho_{(a)} \frac{D^a \mathbf{v}_{(a)}}{Dt} = \rho \frac{D^s \mathbf{v}_{(s)}}{Dt} + \rho \frac{D^s (\mathbf{v} - \mathbf{v}_{(s)})}{Dt} + \nabla \cdot [\rho(\mathbf{v} - \mathbf{v}_{(s)}) \otimes \mathbf{v}_{(s)}] \tag{13.29}$$

where terms of order of diffusion velocity $\mathbf{u}_{(b)}$ squared have been neglected. Note that the term $(\mathbf{v} - \mathbf{v}_{(s)})$, occurring frequently in (13.29) is, from (13.25), equal to

$$\frac{1}{\rho} \sum_{b=1}^{N-s} \rho_{(b)} \mathbf{u}_{(b)} \, .$$

In the special case when the velocity of the selected component is equal to the mean velocity of the mixture, $\mathbf{v}_{(s)} = \mathbf{v}$, where $\mathbf{v}$ is given by (13.19), then

$$\sum_{a=1}^{N} \rho_{(a)} \frac{D^a v_{(a)}}{Dt} = \rho \frac{Dv}{Dt} \, . \tag{13.30}$$

With results (13.26) and (13.29) in hand it is now possible to return to the development of the sums of the constituent-specific balance equations. Recall that it is required that summation of the forms of balance of mass (13.18), balance of momentum (13.20) and balance of energy (13.21) for each constituent over all the constituents is required to produce again the single-constituent continuum forms of balance of mass (4.6), balance of momentum (4.29), and balance of energy (4.52), respectively. Summation of the component-specific form of conservation of linear momentum (13.20), employing representation (13.29) for the sum of the density-weighted, component-specific time derivatives of the component-specific velocities, one obtains a result that is similar to the single-component form (4.29):

$$\rho \frac{D^s \mathbf{v}_{(s)}}{Dt} + \rho \frac{\partial (\mathbf{v} - \mathbf{v}_{(s)})}{\partial t} - (\mathbf{v} - \mathbf{v}_{(s)}) \nabla \cdot \{\rho(\mathbf{v} - \mathbf{v}_{(s)})\} +$$
$$\rho \nabla \cdot \{\mathbf{v}_{(s)} \otimes (\mathbf{v} - \mathbf{v}_{(s)})\} = \nabla \cdot \mathbf{T} + \rho \mathbf{d} \tag{13.31}$$

or

$$\rho \frac{D\mathbf{v}}{Dt} = \nabla \cdot \mathbf{T} + \rho \mathbf{d} \, , \tag{13.32}$$

if $\mathbf{v}_{(s)} = \mathbf{v}$. In either the case when $\mathbf{v}_{(s)} = \mathbf{v}$ or the case when $\mathbf{v}_{(s)} \neq \mathbf{v}$, total stress $\mathbf{T}$ is defined by

$$\mathbf{T} = \sum_{a=1}^{N} \mathbf{T}_{(a)} \, , \tag{13.33}$$

where terms of order of diffusion velocity $\mathbf{u}_{(b)}$ squared have been neglected, and the sum of the action-at-a-distance forces denoted by

$$\mathbf{d} = \frac{1}{\rho}\sum_{a=1}^{N}(\rho_{(a)}\mathbf{d}_{(a)})\,, \tag{13.34}$$

and constituent momentum supply $\breve{\mathbf{p}}_{(a)}$ is restricted by the following condition:

$$\sum_{a=1}^{N}\breve{\mathbf{p}}_{(a)} = 0\,. \tag{13.35}$$

If the velocity of the selected component is equal to the mean velocity of the mixture, $\mathbf{v}_{(s)} = \mathbf{v}$, results (13.31)–(13.35) will coincide with the results that appear in Bowen (1967, 1976, 1980, 1982).

The summation of balance of energy (13.21) for each constituent over all the constituents, employing formula (13.23) with $\varpi_{(a)}$ replaced by $\varepsilon_{(a)}$, yields

$$\rho\frac{D^s\varepsilon}{Dt} = \rho r + \sum_{a=1}^{N}\{\mathbf{T}_{(a)} : \mathbf{D}_{(a)} - \mathbf{v}_{(a)}\cdot\breve{\mathbf{p}}_{(a)} - \nabla\cdot[\mathbf{q}_{(a)} + \varepsilon_{(a)}\rho_{(a)}\mathbf{u}_{(a)}]\}\,, \tag{13.36}$$

where $\varepsilon$ is the specific internal energy density for the mixture, and $r$ is the heat supply density for the mixture, given by

$$\varepsilon = \frac{1}{\rho}\sum_{a=1}^{N}\rho_{(a)}\varepsilon_{(a)}\,,\quad r = \frac{1}{\rho}\sum_{a=1}^{N}\rho_{(a)}r_{(a)}\,, \tag{13.37}$$

and where energy supply $\breve{\varepsilon}_{(a)}$ is restricted by the following condition:

$$\sum_{a=1}^{N}\{\breve{\varepsilon}_{(a)} + \mathbf{v}_{(a)}\cdot\breve{\mathbf{p}}_{(a)} + \varepsilon\nabla\cdot[\rho_{(a)}\mathbf{u}_{(a)}]\} = 0\,. \tag{13.38}$$

The key results of this section are the statements of the conservation of mass, momentum, and energy for each constituent and the summation of these component forms to yield statements of these conservation principles for the mixture. Kinematic identities (13.23) and (13.29) form the other important result; its derivation is a suggested problem below.

**Problems**

13.3.1. Show that the constituent form of mass balance (13.18) summed over all the constituents will produce continuum statement (4.6).

13.3.2. Derive the formula relating the sum of the density-weighted, constituent-specific time derivatives to the time derivative following the selected component, (13.23). In the course of this derivation you will likely employ (13.11), (13.12), and (13.22).

13.3.3. Derive formula (13.29) from (13.23) by setting $\varpi_{(a)}$ equal to $\mathbf{v}_{(a)}$.

## 13.4. A STATEMENT OF IRREVERSIBILITY IN MIXTURE PROCESSES

Thus far in the development of the subjects of this book it has not been necessary to formulate a specific equation restricting the direction of development or evolution of material processes.

In Chapter 7, where the linear continuum theories of heat conduction, elastic solids, viscous fluids, and viscoelastic materials were developed, direct physical arguments about irreversible processes could be made. These arguments influenced only the signs of material coefficients and stemmed from intuitively acceptable statements like "heat only flows from hot to cold." The further development of the mixture theories cannot proceed without such a formal algebraic statement of the irreversibility principle.

Many physical quantities can be considered as influencing the specific internal energy density, $\varepsilon$, of a material object. (Recall that specific internal energy density $\varepsilon$ was introduced in the section on the conservation of energy, §4.5). These include, for example, the specific volume, the components of a tensor measuring deformation of strain, the densities or the concentrations of the constituents of the mixture, and so on. In the mixtures of interest here the set of parameters characterizing the thermodynamic substate of particle $\mathbf{X}$ of the mixture, which actually represents an RVE, will be infinitesimal strain tensor $\mathbf{E}$ given by (3.52) and each of the densities of the constituents, $\rho_{(a)}$. Notation $\{\mathbf{E},\rho_{(a)}\}$ is introduced for these parameters. Set of parameters $\{\mathbf{E},\rho_{(a)}\}$ is said to characterize the thermodynamic substate of particle $\mathbf{X}$ in an object (i.e., a thermodynamic system).

Knowledge of thermodynamic substate $\{\mathbf{E},\rho_{(a)}\}$ does not, however, completely characterize the thermodynamic properties of a thermodynamic system because it does not describe the relationship between two substates. Given two thermodynamic substates, $\{\mathbf{E},\rho_{(a)}\}$ and $\{\mathbf{E}^*,\rho_{(a)}^*\}$, the knowledge is not sufficient to specify whether transition $\{\mathbf{E},\rho_{(a)}\} \rightarrow \{\mathbf{E}^*,\rho_{(a)}^*\}$ is possible or not. This ordering of thermodynamic substates is accomplished by introduction of entropy; the steps of this introduction we develop in the following paragraph.

Transition $\{\mathbf{E},\rho_{(a)}\} \rightarrow \{\mathbf{E}^*,\rho_{(a)}^*\}$ between thermodynamic substates is simply an ordered pair — $\{\mathbf{E},\rho_{(a)}\}$, $\{\mathbf{E}^*,\rho_{(a)}^*\}$ — of thermodynamic substates. If transitions $\{\mathbf{E},\rho_{(a)}\} \rightarrow \{\mathbf{E}^*,\rho_{(a)}^*\}$ and $\{\mathbf{E}^*,\rho_{(a)}^*\} \rightarrow \{\mathbf{E},\rho_{(a)}\}$ are both possible, the transition is said to be *reversible*. If transition $\{\mathbf{E},\rho_{(a)}\} \rightarrow \{\mathbf{E}^*,\rho_{(a)}^*\}$ is possible, but $\{\mathbf{E}^*,\rho_{(a)}^*\} \rightarrow \{\mathbf{E},\rho_{(a)}\}$ is not, then the transition is said to be *irreversible*. The directionality of transitions may be expressed in the following axiom of ordering: given two thermodynamic substates $\{\mathbf{E},\rho_{(a)}\}$ and $\{\mathbf{E}^*,\rho_{(a)}^*\}$, it is possible to decide whether transition $\{\mathbf{E},\rho_{(a)}\} \rightarrow \{\mathbf{E}^*,\rho_{(a)}^*\}$ is possible or not.

The existence of an ordering of substates is analogous to the existence of the "greater than" relation ">" for real numbers. For example, given two distinct real numbers $a$ and $a^*$, we have either $a > a^*$, $a^* > a$, or $a = a^*$, while no such ordering holds for, say, the complex numbers. This permits construction of a homeomorphism between the ordering of thermodynamic states and the ordering of real numbers. This is done by introducing real-valued function $\eta$ that assigns a real number to each thermodynamic substate, $\eta = \eta(\mathbf{E},\rho_{(a)})$, in such a way that $\eta(\mathbf{E}^*, \rho_{(a)}^*) > \eta(\mathbf{E}, \rho_{(a)})$ if transition $\{\mathbf{E},\rho_{(a)}\} \rightarrow \{\mathbf{E}^*,\rho_{(a)}^*\}$ is irreversible. The substates are thereby ordered and labeled by means of the real-valued function of the substate, $\eta$. In any particular physical situation such a function is empirically determinable, and if $\eta$ is one such function, then so is $f(\eta)$, where $f$ is a monotonically increasing function of its argument. Assuming a particular function $\eta$ to have been chosen, it is called the empirical entropy of the thermodynamic system.

The thermodynamic state of particle $\mathbf{X}$ in an object is completely specified by the thermodynamic substate, $\{\mathbf{E},\rho_{(a)}\}$, and entropy $\eta$ of the (RVE associated with the) particle. The basic assumption of thermodynamics is that the thermodynamic state completely determines (specific) internal energy $\varepsilon$ independent of time, place, motion, and stress, and thus $\varepsilon = \varepsilon(\eta, \mathbf{E}, \rho_{(a)}, \mathbf{X})$. Choice of the exact functional form of $\varepsilon$ defines different thermodynamic substances. If $\mathbf{X}$ does not appear in the form of $\varepsilon$ chosen, the substance is said to be thermodynamically simple.

In order to develop a rationale for a differential equation in entropy production $\eta$, time rate of change of internal energy $\varepsilon$ in conservation of energy (4.52) is expressed in two different ways:

$$\rho \frac{D^s \varepsilon}{Dt} = P_E + Q_E = P_I + Q_I, \tag{13.39}$$

where $P_E$ and $Q_E$ denote the contribution of the external mechanical and non-mechanical power, and $P_I$ and $Q_I$ denote the division into internal mechanical and non-mechanical power, respectively. The external quantities are defined, using (4.52), by

$$P_E = \mathbf{T}:\mathbf{D}, \quad Q_E = \rho r - \nabla \cdot \mathbf{h}, \tag{13.40}$$

where $\mathbf{h}$ is the heat flux vector. The internal mechanical power is represented by the power generated by the time rate of change of internal parameters $\{\mathbf{E}, \rho_{(a)}\}$ contracted with the corresponding internal force systems to form scalar quantities with the dimension of energy. The internal non-mechanical power is represented by the product of the time rate of change of the specific entropy with the density and temperature $\theta$, and thus

$$Q_I = \rho\theta \frac{D^s \eta}{Dt}. \tag{13.41}$$

From (13.39) and (13.41) it follows that

$$\rho\theta \frac{D^s \eta}{Dt} = P_E - P_I + Q_E; \tag{13.42}$$

thus, the production of specific entropy is the difference between the external and internal mechanical work plus the external non-mechanical power.

Let $N$ denote the entropy of an entire object and let $\eta$ denote the entropy per unit mass or specific entropy at particle $\mathbf{X}$ of the object; thus,

$$N = \int_O \rho\eta dv. \tag{13.43}$$

The time rate of change of $N$ and $\eta$ are related by

$$\frac{D^s N}{Dt} = \int_O \rho \frac{D^s \eta}{Dt} dv, \tag{13.44}$$

which follows from (4.8). Total entropy production $D^S N / Dt$ is written as the sum of external production $D^S N_{(e)} / Dt$ and internal production $D^S N_{(i)} / Dt$; thus,

$$\frac{D^s N}{Dt} = \frac{D^s N_{(i)}}{Dt} + \frac{D^s N_{(e)}}{Dt}. \tag{13.45}$$

The external entropy production, $D^S N_{(e)} / Dt$, is associated with the total flux of non-mechanical power, divided by absolute temperature $\theta$, and thus

$$\frac{D^s N_{(e)}}{Dt} = -\bigcirc_{\partial O} \frac{\mathbf{h} \cdot \mathbf{n}}{\theta} da + \int_O \frac{\rho r}{\theta} dv, \tag{13.46}$$

and internal entropy production $D^S N_{(i)}/Dt$ is simply related to similar specific internal entropy production quantity $D^s\sigma/Dt$:

$$\frac{D^S N_{(i)}}{Dt} = \int_O \rho \frac{D^s \sigma}{Dt} dv\,, \tag{13.47}$$

where $\sigma$ is the specific internal entropy. From experiment and experience it is known that, at constant temperature, the excess of external power over internal power, $(P_E - P_I)$, must be greater than zero; that is to say, at constant temperature one cannot recover from an object more power than was supplied to the object. It is also a fact of experience and experiment that heat flows from the hotter to the colder parts of an object and not in the reverse way. In equation form we note this last assertion by

$$\mathbf{q}\cdot\nabla\theta \geq 0 \text{ for } P_E - P_I = 0, \tag{13.48}$$

while the former assertion is summarized in the statement that $(P_E - P_I) \geq 0$.

Guided by these results, it is postulated that the internal entropy production is always greater than or equal to zero, $D^S\eta/Dt \geq 0$. This postulate is a form of the second law of thermodynamics: the postulate of irreversibility. The second law applied to an object occupying volume $O$ may be stated as $D^S N_{(i)}/Dt = D^S N/Dt - D^S N_{(e)}/Dt \geq 0$. In terms of $D^S N/Dt$, $D^S N_{(e)}/Dt$, and $D^S N_{(i)}/Dt$, the following terminology is customary: an equilibrium state is defined by $D^S N/Dt = 0$, a reversible process is characterized by $D^S N_{(i)}/Dt = 0$, an irreversible process is characterized by $D^S N_{(i)}/Dt > 0$; $D^S N/Dt = D^S N_{(i)}/Dt$ characterizes an adiabatic process, and only in the case of an adiabatically insulated system does the second law of thermodynamics in the form $D^S N/Dt \geq 0$ apply. It should be noted that, in general, the various entropies might satisfy the three inequalities: $D^S N/Dt > 0$, $D^S N_{(i)}/Dt > 0$, and $D^S N_{(e)}/Dt < 0$.

In terms of the specific or continuum variables, the second law of thermodynamics, $D^S N_{(i)}/Dt = D^S N/Dt - D^S N_{(e)}/Dt \geq 0$ may be written as

$$\int_O \rho \frac{D^s \eta}{Dt} dv + \oint_{\partial O} \frac{\mathbf{h}\cdot\mathbf{n}}{\theta} da - \int_O \frac{\rho r}{\theta} dv \geq 0 \tag{13.49}$$

using (13.44) and (13.46). In order to convert integral equation (13.49) to a field or point equation, divergence theorem (A183) is employed as well as the argument that was used to convert integral eq. (4.4) to field eq. (4.5). Recall that this was an argument employed four times in Chapter 4. Applying these arguments to (13.49) it follows that

$$\rho \frac{D^s \eta}{Dt} + \nabla\cdot\left(\frac{\mathbf{h}}{\theta}\right) - \frac{\rho r}{\theta} \geq 0\,. \tag{13.50}$$

Integral equations such as (4.4) and (13.49) are global statements because they apply to an entire object. However, results (4.5) and (13.50) are local, point-wise conditions valid at the typical point (place) in the object. Thus, transitions (4.4)→(4.5) and (13.49)→(13.50) are from the global to the local or from the object to the point (or particle) in the object.

On the molecular level, each macroscopic substate $\{\mathbf{E},\rho_{(a)}\}$ corresponds to a large set of molecular states. In other words, the relationship between the molecular states and the macroscopic states is injective; they are in one-to-one correspondence. If we attribute an equal probability to each molecular state, the probability that one thermodynamic state, $\{\mathbf{E},\rho_{(a)}\}$, is different from another thermodynamic state, $\{\mathbf{E}^*,\rho_{(a)}^*\}$, can be calculated from the number of

molecular states to which it corresponds. In statistical physics, the concept of entropy is defined as the logarithm of the number of molecular states that correspond to that particular molecular state (multiplied by Boltzmann's constant). The entropy thereby provides a measure of the relative probability of different macrostates. The second law, stating that entropy moves toward increasing entropy, simply states that the system has a natural tendency to evolve from less probable states towards more probable states. In this sense one can interpret the second law as being almost a tautology.

Returning to the continuum model note that, in terms of internal energy $\varepsilon(\eta, \mathbf{E}, \rho_{(a)}, \mathbf{X})$, the temperature, stress, and electrochemical (or chemical) potential may be defined as the derivatives of $\varepsilon(\eta, \mathbf{E}, \rho_{(a)}, \mathbf{X})$ with respect to entropy, strain, and volume fraction, respectively:

$$\theta = \left(\frac{\partial \varepsilon}{\partial \eta}\right)_{\mathbf{E},\rho_{(a)}}, \quad \mathbf{T} = \left(\frac{\partial \varepsilon}{\partial \mathbf{E}}\right)_{\eta,\rho_{(a)}}, \quad \mu_{(a)} = \left(\frac{\partial \varepsilon}{\partial \rho_{(a)}}\right)_{\mathbf{E},\eta}. \tag{13.51}$$

The time derivative of internal energy $\varepsilon$ may then be expressed as follows:

$$\frac{D^s \varepsilon}{Dt} = \theta \frac{D^s \eta}{Dt} + \mathbf{T} : \mathbf{D} + \sum_{a=1}^{N} \mu_{(a)} \frac{D^s \rho_{(a)}}{Dt}. \tag{13.52}$$

The Helmholz free energy is defined by

$$\psi(\theta, \mathbf{E}, \rho_{(a)}, \mathbf{X}) = \varepsilon(\eta, \mathbf{E}, \rho_{(a)}, \mathbf{X}) - \eta\theta, \tag{13.53}$$

and the derivatives of free energy $\psi$ with respect to temperature, strain, and volume fraction yield the entropy, stress, and electrochemical (or chemical) potential, respectively:

$$\eta = -\left(\frac{\partial \psi}{\partial \theta}\right)_{\mathbf{E},\rho_{(a)}}, \quad \mathbf{T} = \left(\frac{\partial \psi}{\partial \mathbf{E}}\right)_{\theta,\rho_{(a)}}, \quad \mu_{(a)} = \left(\frac{\partial \psi}{\partial \rho_{(a)}}\right)_{\mathbf{E},\theta}. \tag{13.54}$$

The time derivative of free energy $\psi$ may then be expressed as follows:

$$\frac{D^s \psi}{Dt} = \eta \frac{D^s \theta}{Dt} + \mathbf{T} : \mathbf{D} + \sum_{a=1}^{N} \mu_{(a)} \frac{D^s \rho_{(a)}}{Dt}. \tag{13.55}$$

It is assumed that each constituent of the mixture has the regular properties of a thermodynamic substance, so that the Helmholz free energy of each constituent, $\psi_{(a)}$, is related to temperature $\theta$ and constituent specific internal energy $\varepsilon_{(a)}$ and entropy $\eta_{(a)}$ by the component specific form of (13.53):

$$\psi_{(a)} = \varepsilon_{(a)} - \theta\eta_{(a)}, \tag{13.56}$$

where

$$\psi = \frac{1}{\rho} \sum_{a=1}^{N} \rho_{(a)} \psi_{(a)}. \tag{13.57}$$

Either the condition $D^s N_{(i)} / Dt = D^s N / Dt - D^s N_{(e)} / Dt \geq 0$ or integral (13.49) or field eq. (13.50) is called the Clausius Duhem inequality for internal entropy production. They are equivalent statements of the second law of thermodynamics. In order to generalize the inequal-

ity (13.50) to a mixture, three substitutions into (13.50) are made. First $\eta$ in (13.50) is replaced by the density-weighted average of constituent-specific internal entropy $\eta_{(a)}$, and thus

$$\eta = \frac{1}{\rho}\sum_{a=1}^{N}\rho_{(a)}\eta_{(a)}\,, \tag{13.58}$$

and, second, a similar replacement, the second of (13.37) is made for $\rho r$. Third, formula (13.26) for the density-weighted sum of all the time derivatives of $\varpi_{(a)}$ following all the constituents is related to the time derivative after the selected constituent is applied to the density-weighted average of the constituent-specific internal entropy $\eta_{(a)}$:

$$\sum_{a=1}^{N}\rho_{(a)}\frac{D^a\eta_{(a)}}{Dt} = \rho\frac{D^s\eta}{Dt} + \sum_{b=1}^{N-s}\{\nabla\cdot[\eta_{(b)}\rho_{(b)}\mathbf{u}_{(b)}] - \eta\nabla\cdot[\rho_{(b)}\mathbf{u}_{(b)}]\}\,. \tag{13.59}$$

The entropy inequality for a mixture may now be formulated using the entropy inequality for single-component continuum (13.50) as the guide. Term $\rho(D^s\eta/Dt)$ in (13.50) is eliminated using (13.59). Heat supply density $r$ in (13.50) is replaced by that for the mixture given by the second of (13.37), and thus the entropy inequality for a mixture takes the form

$$\sum_{a=1}^{N}\rho_{(a)}\frac{D^a\eta_{(a)}}{Dt} + \nabla\cdot\left[\sum_{a=1}^{N}\frac{\mathbf{h}_{(a)}}{\theta} - \rho_{(a)}\eta_{(a)}\mathbf{u}_{(a)}\right] + \sum_{a=1}^{N}\eta\nabla\cdot[\rho_{(b)}\mathbf{u}_{(b)}] - \frac{1}{\theta}\sum_{a=1}^{N}\rho_{(a)}r_{(a)} \geq 0\,. \tag{13.60}$$

It is important to note that, while there were forms of each of the conservation principles for each of the constituents — (13.18), (13.20), (13.21) — that were summed over to obtain statements of those principles that applied to the mixture as whole — (4.6), (4.29), (4.52) — respectively, it was not assumed that there were constituent specific forms of entropy inequality (13.60). The literature is somewhat divided on the use of constituent specific forms of the entropy inequality (Bowen, 1976, §1.7). The conservative position is to assume only the mixture level inequality. Thus, the entropy inequality employed here only makes a statement for the entire mixture, not for any particular constituent.

The remainder of this section presents the development of an alternate form of entropy inequality (13.60). First, product $\rho_{(a)}r_{(a)}$ is eliminated between (13.21) and (13.60), and then, second, the result is multiplied by $\theta$; third, it is assumed that the constituent-specific flux vectors, $\mathbf{h}_{(a)}$ and $\mathbf{q}_{(a)}$, are related by

$$\mathbf{h}_{(a)} = \mathbf{q}_{(a)} + \rho_{(a)}\theta\eta_{(a)}\mathbf{u}_{(a)}\,, \tag{13.61}$$

and thus

$$\sum_{a=1}^{N}\rho_{(a)}\left(\theta\frac{D^a\eta_{(a)}}{Dt} - \frac{D^a\varepsilon_{(a)}}{Dt}\right) + \theta\nabla\cdot\left[\sum_{a=1}^{N}\left(\frac{\mathbf{q}_{(a)}}{\theta}\right)\right] + \sum_{a=1}^{N}\theta\eta\nabla\cdot[\rho_{(b)}\mathbf{u}_{(b)}] + \sum_{a=1}^{N}\mathbf{T}_{(a)} : \mathbf{D}_{(a)} - \nabla\cdot\mathbf{q}_{(a)} + \breve{\varepsilon}_{(a)} \geq 0\,. \tag{13.62}$$

Then, using (13.38), (13.56), and

$$\mathbf{q} = \sum_{a=1}^{N} \mathbf{q}_{(a)} \,, \tag{13.63}$$

(expression (13.63) for the heat flux is an approximation that neglects several terms associated with difussion velocities; this point is discussed on p. 27 of Bowen, 1976), it follows that

$$-\rho\eta \frac{D^s\theta}{Dt} - \frac{1}{\theta}\mathbf{q}\cdot\nabla\theta + \sum_{a=1}^{N} \theta\eta\nabla\cdot[\rho_{(b)}\mathbf{u}_{(b)}] +$$

$$\sum_{a=1}^{N}\left[\mathbf{T}_{(a)} : \mathbf{D}_{(a)} - \mathbf{v}_{(a)}\cdot\breve{\mathbf{p}}_{(a)} - \rho_{(a)}\frac{D^a\psi_{(a)}}{Dt}\right] \geq 0 \,. \tag{13.64}$$

The expression relating the terms in (13.64) containing the time derivatives of the specific free energy density for the mixture, $\psi_{(a)}$, is replaced by

$$\sum_{a=1}^{N} \rho_{(a)} \frac{D^a\psi_{(a)}}{Dt} = \rho\frac{D^s\psi}{Dt} + \sum_{b=1}^{N-s}\{\nabla\cdot[\psi_{(b)}\rho_{(b)}\mathbf{u}_{(b)}] - \psi\nabla\cdot[\rho_{(b)}\mathbf{u}_{(b)}]\} \,, \tag{13.65}$$

a result that was obtained by substituting $\psi_{(a)}$ for $\varpi_{(a)}$ in (13.23); thus, (13.64) becomes

$$-\rho\frac{D^s\psi}{Dt} - \rho\eta\frac{D^s\theta}{Dt} - \frac{1}{\theta}\mathbf{q}\cdot\nabla\theta + \sum_{a=1}^{N}\varepsilon\nabla\cdot[\rho_{(b)}\mathbf{u}_{(b)}] +$$

$$\sum_{a=1}^{N}[\mathbf{T}_{(a)} : \mathbf{D}_{(a)} - \mathbf{v}_{(a)}\cdot\breve{\mathbf{p}}_{(a)} - \nabla\cdot[\psi_{(b)}\rho_{(b)}\mathbf{u}_{(b)}]] \geq 0 \,, \tag{13.66}$$

where use has been made of (13.53) in setting $\psi + \eta\theta = \varepsilon$.

Entropy inequality (13.66) will now be restricted to the case of accelerationless processes. Neglecting both the acceleration and the action-at-a-distance forces, the balance of momentum for continuum (4.29) reduces to $\nabla\cdot\mathbf{T} = 0$, and the balance of momentum for each constituent of continuum (13.20) reduces to $\breve{\mathbf{p}}_{(a)} = -\nabla\cdot\mathbf{T}_{(a)}$. Thus, we now have the following representations for the divergence of the total stress and divergence of the constituent specific partial stress:

$$\nabla\cdot\mathbf{T} = 0 \,, \quad \nabla\cdot\mathbf{T}_{(a)} = -\breve{\mathbf{p}}_{(a)} \,. \tag{13.67}$$

An algebraic development will now be used to obtain an alternate representation for the first two terms of the sum in (13.66). This manipulation begins with the identity that follows easily from (13.67) and the separation of the selected constituent stress related components from the other stress-related components;

$$\sum_{a=1}^{N}[\mathbf{T}_{(a)} : \mathbf{D}_{(a)} - \mathbf{v}_{(a)}\cdot\breve{\mathbf{p}}_{(a)}] = \sum_{a=1}^{N}[\mathbf{T}_{(a)} : \mathbf{D}_{(a)} + \mathbf{v}_{(a)}\cdot\nabla\mathbf{T}_{(a)}] =$$

$$\mathbf{T}_{(s)} : \mathbf{D}_{(s)} + \mathbf{v}_{(s)}\cdot\nabla\mathbf{T}_{(s)} + \sum_{b=1}^{N-s}[\mathbf{T}_{(b)} : \mathbf{D}_{(b)} + \mathbf{v}_{(b)}\cdot\nabla\mathbf{T}_{(b)}] \,. \tag{13.68}$$

Observing from (13.33) that the selected components of stress $\mathbf{T}_{(s)}$ may be expressed in terms of the remaining components and the total stress.

$$\mathbf{T}_{(s)} = \mathbf{T} - \sum_{b=1}^{N-s} \mathbf{T}_{(b)} \,, \tag{13.69}$$

then the first two terms of the sum in (13.66) have an alternate representation:

$$\sum_{a=1}^{N} [\mathbf{T}_{(a)} : \mathbf{D}_{(a)} - \mathbf{v}_{(a)} \cdot \breve{\mathbf{p}}_{(a)}] =$$

$$\mathbf{T} : \mathbf{D}_{(s)} + \sum_{b=1}^{N-s} [\mathbf{T}_{(b)} : [\nabla \otimes \mathbf{u}_{(b)}] + \mathbf{u}_{(b)} \cdot \nabla \mathbf{T}_{(b)} \tag{13.70}$$

where (13.68) has been employed. Substitution of (13.70) into (13.66) yields this inequality:

$$-\rho \frac{D^s \psi}{Dt} - \rho\eta \frac{D^s \theta}{Dt} - \frac{1}{\theta} \mathbf{q} \cdot \nabla\theta + \sum_{a=1}^{N} \varepsilon \nabla \cdot [\rho_{(b)} \mathbf{u}_{(b)}] + \mathbf{T} : \mathbf{D}_{(s)} +$$

$$\sum_{b=1}^{N-s} [\mathbf{T}_{(b)} : [\nabla \otimes \mathbf{u}_{(b)}] + \mathbf{u}_{(b)} \cdot \nabla \mathbf{T}_{(b)} - \nabla \cdot [\psi_{(b)} \rho_{(b)} \mathbf{u}_{(b)}]] \geq 0 \,. \tag{13.71}$$

Inequality (13.71) for accelerationless processes in the absence of action-at-a-distance forces will be applied, after further specializing it for a charged porous medium, in the section after next.

## 13.5. DONNAN EQUILIBRIUM AND OSMOTIC PRESSURE

Biological tissues are almost electrically neutral because they contain about equal numbers of positive (cation) and negative (anion) charges. Tissues are said to be electrically charged when their non-fluid phases are electrically charged. The other component of the tissue, the pore or interstitial fluid, contains mobile ions ($Na^+$, $Ca^{++}$, $H^+$, $K^+$, $Cl^-$, $SO_3^{--}$, $HPO_4^{--}$) in sufficient number to balance the charges in the non-fluid phase. Thus, the overall biological tissue is electroneutral under normal, physiological conditions. The relative motion of the charged fluid in the tissue to its charged solid phase is the source of the electromechanical phenomena observed in numerous biological tissues. These include mechano-electro-chemical coupling phenomena such as ion-induced swelling, streaming potentials and currents, osmosis, and electroosmosis (see Table 13.1). These phenomena often play important roles in physiological processes. The mechano-electro-chemical coupling behavior of biological tissues arises from the numerous fixed charges on the ubiquitous macromolecules (e.g., proteoglycans) in the extracellular matrix of tissues. Analysis of the transport of electrolyte solutions within biological tissues under mechanical, osmotic, or electrical loading provides a framework for understanding many aspects of cell and tissue physiology.

In order to model these effects we let $c^{(fc)}$ denote the fixed charge density per unit mixture volume, taken positive for positive charges and negative for negative charges, and let $c^+$ and $c^-$ denote the cationic and anionic concentrations per unit mixture volume (in moles/m$^3$), respectively. The electroneutrality condition characteristic of most tissues is then written as

$$\pm c^{(fc)} + \sum_{b=1}^{N-c} z^{(b)} c^{(b)} = 0\,, \tag{13.72}$$

where $z^{(b)}$ are the valences, the + sign is taken for positively charged tissues and the – sign for negatively charged tissues, and $c^{+}$ and $c^{-}$ are included in the sum. Recall that a valence is a positive or negative integer used to represent the combining capacity of an atom or radical determined by the number of electrons that it will lose, add, or share when it reacts with other atoms. The most common valences of the elements are those that can be determined from the Periodic Table, but the situation is generally more complicated. Since the fixed charges are fixed to the solid constituent, the requirement that they be fixed in time is referred to the initial configuration and the result has the form of (13.18) with $\rho_{(a)}$ replaced by $c^{(fc)}$ and $\mathbf{v}_{(a)}$ set equal to $\mathbf{v}_{(s)}$, and thus

$$\frac{\partial c^{(fc)}}{\partial t} + \nabla\cdot(c^{(fc)}\mathbf{v}_{(s)}) = 0\,, \tag{13.73}$$

and, from (13.72),

$$\sum_{b=1}^{N-c} z^{(b)} \left\{ \frac{\partial c^{(b)}}{\partial t} + \nabla\cdot(c^{(b)}\mathbf{v}_{(s)}) \right\} = 0\,. \tag{13.74}$$

The volume fraction per $\phi_{(b)}$ is related to the current molar concentration (moles per unit mixture volume), $c^{(b)}$, by

$$\phi_{(b)} = \bar{V}^{(b)} c^{(b)}\,, \tag{13.75}$$

where $\bar{V}^{(b)}$ is the partial molar volume of the solvent or solute constituent phase $b$. Combining (13.74) and (13.75), it follows that

$$\sum_{b=1}^{N-s} \frac{z^{(b)}}{\bar{V}^{(b)}} \nabla\cdot(\phi_{(b)}\mathbf{u}_{(b)}) = 0\,, \tag{13.76}$$

where (13.18) was again employed, this time with $\rho_{(a)}$ replaced by $\phi_{(a)}$, since matrix density $\gamma_{(a)}$ is a constant due to the incompressibility assumption. This form of the statement of the electroneutrality condition will be used in the development in the next section of the constitutive equations for a continuum porous media model of the passive transport of electrolytes in charged porous soft tissues.

When a charged porous medium is in contact with a monovalent salt solution, the diffusion of salt ions and flow of fluid take place between the medium and the salt solution until equilibrium is reached. The passage of a pure solvent from a solution of lesser to one of greater solute concentration when the two solutions are separated by a membrane that selectively prevents the passage of solute molecules, but is permeable to the solvent, is called osmosis. A diagram (Figure 13.1) to be used in the analysis of this phenomenon is a system composed of two solutions separated by a semipermeable membrane (or an equivalent structure) that is impermeable to at least one of the species. The impermeable species may be some colloidal particle. In any gel, in an ion-exchange membrane containing charged groups fixed to its matrix, or in a substance, such as articular cartilage or clay, ionized into very large and small ions, the equilibria that exist will be of the Donnan type. We note that a biological structure that may be identified as a semipermeable membrane may actually be a more diverse structure. In articular

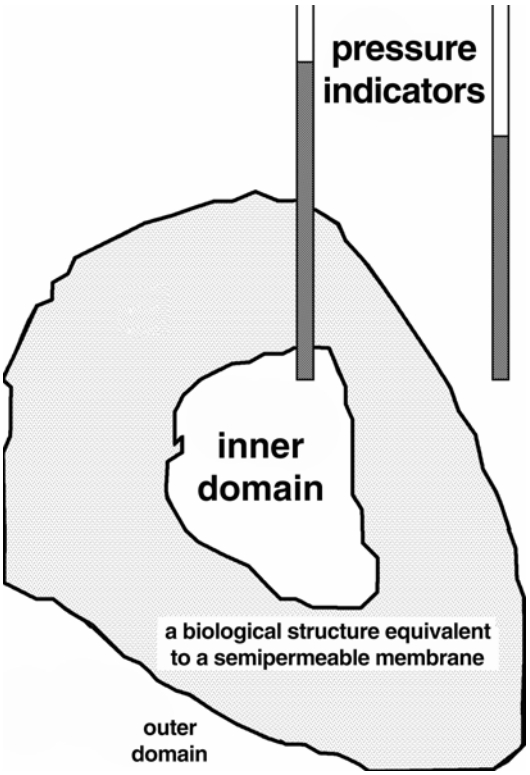



**Figure 13.1**. Sketch of a model of a Donnan equilibrium situation. The usual diagram associated with the analysis of osmotic phenomena consists of two solutions separated by a semipermeable membrane that is impermeable to at least one of the charged species. One solution is termed the outer solution and the other the inner solution. The additional height of the fluid in the inner chamber over that in the outer chamber is the osmotic pressure. The presence of a semipermeable membrane is not essential; any gel, in an ion-exchange membrane containing charged groups fixed to its matrix, or in a substance, such as a soft tissue, will exhibit the same phenomena.

cartilage the semipermeable membrane is analogous to the stiff collagen network that surrounds and traps the large negatively charged proteoglycans within the tissue; the exact structure of a semipermeable membrane is not essential. The chemical potentials of the anions, cations and solvent in the inside domain of Figure 13.1 are indicated by $\mu_{(+)}^{(i)}$, $\mu_{(-)}^{(i)}$ and $\mu_{(f)}^{(i)}$ and those in the outside domain by $\mu_{(+)}^{(0)}$, $\mu_{(-)}^{(0)}$, and $\mu_{(f)}^{(0)}$, respectively. When a system such as the one described above is in a state of equilibrium with respect to the flux of solvent and solutes, the equilibrium is called Donnan equilibrium. In terms of the chemical potentials in the inside and outside domains, the Donnan equilibrium is characterized by

$$\mu_{(+)}^{(i)} = \mu_{(+)}^{(0)}, \quad \mu_{(-)}^{(i)} = \mu_{(-)}^{(0)}, \quad \mu_{(f)}^{(i)} = \mu_{(f)}^{(0)}. \tag{13.77}$$

Three important features are involved in Donnan equilibrium: (1) unequal distribution of ions; (2) osmotic pressure; and (3) potential difference between the two phases (Lakshminarayanaiah, 1984). In the paragraphs that follow, formulas associated with each of these features are derived.

Representations of the chemical potentials used in electrochemistry are recorded here, but space does not allow a detailed development of these results (for references, see §13.10, Relevant Literature). In electrochemistry the chemical potential for a typical solute is given by

$$\mu_{(a)} = \mu_{(a)}^{\text{ref}} + \frac{1}{\bar{V}^{(a)}}(R\theta \ln a_{(a)} + z_{(a)}F\xi)\,, \tag{13.78}$$

where $\mu_{(a)}^{\text{ref}}$ are the reference values of the chemical potential, $\bar{V}^{(a)}$ the partial molar volume, $a_{(a)}$ the activities, $z_{(a)}$ the valence of constituent $a$, $\theta$ the absolute temperature, $R$ the universal gas constant, $F$ Faraday's constant, and $\xi$ the electrical potential. For the solvent the chemical potential is given by

$$\mu_{(a)} = \mu_{(a)}^{\text{ref}} + p + \frac{R\theta}{\bar{V}^{(a)}} \ln a_{(a)}\,, \tag{13.79}$$

where $p$ is the fluid pressure. Activities $a_{(a)}$ are related to molar concentrations $c_{(a)}$ (i.e., moles/m$^3$) by the following formula:

$$a_{(a)} = f_{(a)} c_{(a)}\,, \tag{13.80}$$

where $f_{(a)}$ is a correction factor called the activity coefficient.

In the case of a four-component mixture — solid, solvent, anions and cations — these formulas specialize to the following (Huyghe and Janssen, 1997):

$$\mu_{(+)} = \mu_{(+)}^{\text{ref}} + \frac{1}{\bar{V}^{(+)}}(R\theta \ln a_{(+)} + F\xi)\,, \tag{13.81}$$

$$\mu_{(-)} = \mu_{(-)}^{\text{ref}} + \frac{1}{\bar{V}^{(-)}}(R\theta \ln a_{(-)} - F\xi)\,, \tag{13.82}$$

$$\mu_{(f)} = \mu_{(f)}^{\text{ref}} + p + \frac{R\theta}{\bar{V}^{(f)}} \ln a_{(f)}\,. \tag{13.83}$$

Employing (13.81) and (13.82), the combination of the first two of equations (13.77) leads to

$$a_{(-)}^{(i)} a_{(+)}^{(i)} = a_{(-)}^{(0)} a_{(+)}^{(0)} \tag{13.84}$$

and

$$\xi^{(i)} - \xi^{(0)} = \frac{R\theta}{2F} \ln \frac{a_{(-)}^{(i)} a_{(+)}^{(0)}}{a_{(+)}^{(i)} a_{(-)}^{(0)}}\,. \tag{13.85}$$

In the case of a four-component mixture the electroneutrality conditions are

$$c_{(-)}^{(i)} = c_{(+)}^{(i)} + c^{(fc)}, \quad c_{(-)}^{(0)} = c_{(+)}^{(0)} = c^{(0)}\,. \tag{13.86}$$

Combining (13.85) with (13.80), it follows from the second electroneutrality condition above that

$$c_{(-)}^{(i)} c_{(+)}^{(i)} = f^2 (c^0)^2\,, \quad \text{where} \quad f^2 = \frac{f_{(-)}^{(0)} f_{(+)}^{(0)}}{f_{(-)}^{(i)} f_{(+)}^{(i)}}\,; \tag{13.87}$$

thus, from the first of (13.86) and (13.87) it follows that

$$c_{(+)}^{(i)}(c_{(+)}^{(i)} + c^{(fc)}) = f^2(c^0)^2 . \tag{13.88}$$

This is the expression originally obtained by Donnan (1924) for the equilibrium ion concentration within such a semipermeable chamber of a charged macromolecule. The Donnan equilibrium concentration of the ions in the inner domain, $c_{(+)}^{(i)}$ and $c_{(-)}^{(i)}$, is calculated from the first of (13.86) and (13.88), and thus

$$2c_{(+)}^{(i)} = c^{(fc)} + \sqrt{(c^{(fc)})^2 + 4f^2(c^0)^2} , \tag{13.89}$$

$$2c_{(-)}^{(i)} = -c^{(fc)} + \sqrt{(c^{(fc)})^2 + 4f^2(c^0)^2} . \tag{13.90}$$

These results show that the cationic concentration jumps to a higher value and the anionic concentration to a lower value when entering the inner domain. These concentration jumps are responsible for the attraction of water into the porous medium during swelling and for the associated osmotic pressure, $p_{os}$.; the effect of this imbalance creates an osmotic swelling pressure whose magnitude is determined by the concentration difference across the semipermeable membrane. Using eq. (13.83) one can derive the van't Hoff relation for osmotic pressure $p_{os}$ from the third and last of equations (13.77):

$$p_{\text{os}} = p_{(i)} - p_{(0)} = R\theta[\Phi_{(f)}^{(i)}(c_{(+)}^{(i)} + c_{(-)}^{(i)}) - 2\Phi_{(f)}^{(0)}c^{(0)}], \tag{13.91}$$

where (13.86) has been employed and where $\Phi_{(b)}^{(i)}$ and $\Phi_{(b)}^{(o)}$ are the inner and outer osmotic coefficients defined by

$$\Phi_{(b)}^{(i)} = \frac{\partial \ln a_{(b)}^{(i)}}{\partial \ln m_{(b)}^{(i)}} , \quad \Phi_{(b)}^{(0)} = \frac{\partial \ln a_{(b)}^{(0)}}{\partial \ln m_{(b)}^{(0)}} , \quad b = f, +, -, \tag{13.92}$$

and where $m_{(f)}^{(i)}$ and $m_{(f)}^{(0)}$ are the molar fractions of the fluid in the inner and outer solutions,

$$m_{(b)}^{(i)} = \frac{c_{(b)}^{(i)}}{c_{(f)}^{(i)} + c_{(+)}^{(i)} + c_{(-)}^{(i)}} , \quad m_{(b)}^{(0)} = \frac{c_{(b)}^{(0)}}{c_{(f)}^{(0)} + c_{(+)}^{(0)} + c_{(-)}^{(0)}} , \quad b = f, +, -. \tag{13.93}$$

It may be clear from the above considerations that physical phenomena occurring in charged porous media are a combination of mechanical and electrical effects.

In the case when the activity coefficients are all equal to one, $f_{(a)} = 1$; then from (13.80), $a_{(a)} = c_{(a)}$, and it may be shown that

$$\frac{\partial \ln c_{(f)}^{(i)}}{\partial \ln m_{(f)}^{(i)}} = 1 \quad \text{and} \quad \frac{\partial \ln c_{(f)}^{(0)}}{\partial \ln m_{(f)}^{(0)}} = 1 , \tag{13.94}$$

and it follows from (13.91) that

$$p_{\text{os}} = p_{(i)} - p_{(0)} = RT[(c_{(+)}^{(i)} + c_{(-)}^{(i)}) - 2c^{(0)}]. \tag{13.95}$$

An alternate expression is obtained for sum $(c_{(+)}^{(i)} + c_{(-)}^{(i)})$ by adding (13.89) and (13.90) together, and thus

$$p_{\text{os}} = p_{(i)} - p_{(0)} = RT\left[\sqrt{(c^{(fc)})^2 + 4f^2(c^0)^2} - 2c^0\right]. \tag{13.96}$$

In the case when the right-hand side of this equation is multiplied by a correction factor (to account for non-ideal materials), the resulting equation with $c^{(fc)}$ = (0.24 x $10^3$) mol/$m^3$ is employed to represent the experimentally measured relation between osmotic pressure and external salt (NaCl) concentration (Figure 13.2). The triangles in Figure 13.2 represent experimentally measured osmotic pressure datapoints in a synthetic material of ionized polymer chains subjected to an external salt concentration that is controlled by the experimenter. The curve based on (13.96) represents the experimentally measured relation between osmotic pressure and external salt (NaCl) concentration very well, as Figure 13.2 shows.

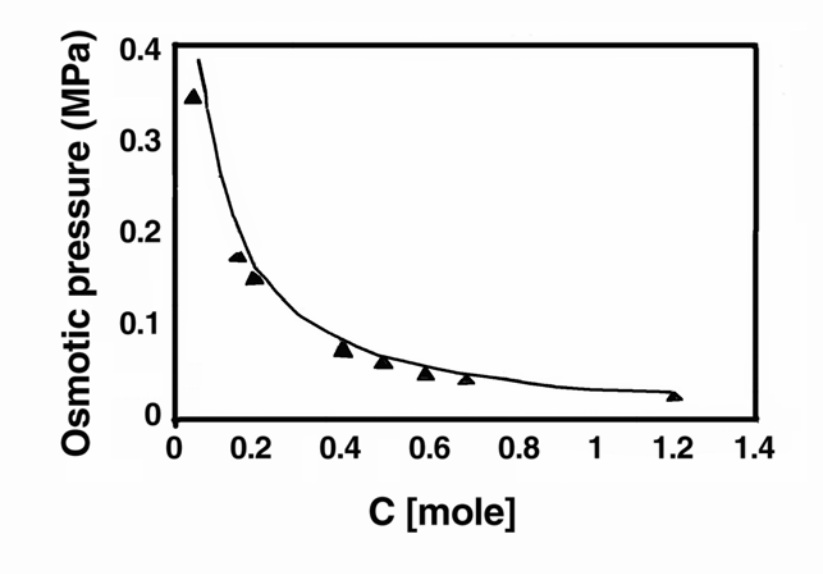



**Figure 13.2**. The triangles represent experimentally measured osmotic pressure data points in a synthetic material of ionized polymer chains subjected to an external salt concentration that is controlled by the experimenter. The curve in the plot is of a slightly modified eq. (13.96) in which the right-hand side of this equation is multiplied by a correction factor of 0.93 (to account for non-ideal materials), and $c^{(fc)}$ is taken to be (0.24 x $10^3$) mol/$m^3$. The curve represents the experimentally measured relation between osmotic pressure and external salt (NaCl) concentration very well. Reprinted with permission from Huyghe and Bovendeerd (2003).

The examples below will be applications of formula (13.96) for the osmotic pressure, and in these applications manipulation of units is necessary. Universal gas constant $R$ has the value of 8.315 (Pa-$m^3$)/( ºK mole), where ºK stands for degrees Kelvin, and a mole is the number of gram molecular weights (gMW). For example, NaCl has a gMW of 58.5, obtained by adding the gMW of Na, 23, to the gMW of Cl, 35.5. A molar solution (dimension M) is a solution that contains 1 mole of solute in each liter of solution, thus 1M = 1 gMW of solute per liter solution. A liter of solution is 1000 cubic centimeters or ($10^{-3}$) $m^3$, thus 1M = 1 gMW ($10^3$) $m^{-3}$ = 1 mole ($10^3$) $m^{-3}$, and $R$ may also be expressed as $R$ = 8315 (Pa)/( ºK-M).

**Example 13.5.1**

A piece of soft hydrated biological tissue has a fixed charge concentration of 0.1 M and the following set of drained elastic constants: $E_1$ = 120 kPa, $E_2$ = 134 kPa, $E_3$ = 200 kPa, $G_{12}$ = 47 kPa, $G_{13}$ = 55 kPa, $G_{23}$ = 70 kPa, $\nu_{12}$ = 0.376, $\nu_{13}$ = 0.222, $\nu_{23}$ = 0.235, $\nu_{21}$ = 0.422, $\nu_{31}$ = 0.371, and $\nu_{32}$ = 0.350. This example is adapted from Huyghe and Bovendeerd (2003). These values are measured for an equilibrium with a 0.2 M NaCl solution at a temperature of 300°K. The tissue sample is then put into a 0.15-M NaCl solution. Employing the four-component mixture of a fluid, solid, anions, and cations with activity coefficients equal to 1 as a model, determine the three principal strains induced in the sample in its final state relative to its initial state.

**Solution**: The formula (13.96) for $p_{os}$ with $f = 1$ applies to both the before and after situations, and thus

$$p_{\text{before}} = 8315(300)\left[\sqrt{(0.1)^2 + 4(0.2\text{M})^2} - 0.4\text{M}\right] = 0.0307 \text{ MPa} \quad \text{and}$$

$$p_{\text{after}} = 8315(300)\left[\sqrt{(0.1)^2 + 4(0.15\text{M})^2} - 0.3\text{M}\right] = 0.0405 \text{ MPa} .$$

It follows that $p_{os} = p_{\text{after}} - p_{\text{before}} = 0.01$ MPa. The strains are calculated using (7.27) and setting $T_{11} = T_{22} = T_{33} = p_{os}$, and thus,

$$E_{11} = \left(\frac{1}{E_1} - \frac{\nu_{21}}{E_2} - \frac{\nu_{31}}{E_3}\right) p_{os}, \quad E_{22} = \left(\frac{1}{E_2} - \frac{\nu_{12}}{E_1} - \frac{\nu_{32}}{E_3}\right) p_{os}, \quad E_{33} = \left(\frac{1}{E_3} - \frac{\nu_{23}}{E_2} - \frac{\nu_{13}}{E_1}\right) p_{os} .$$

Substituting the values of the elastic constants and $p_{os} = 0.01$ MPa into these equations, it follows that $E_{11} = 0.033$, $E_{22} = 0.026$, and $E_{33} = 0.014$. Note that these strains are the consequence of chemical loading only; there are no stresses applied to the surfaces of the tissue specimen. The specimen has swollen.

**Example 13.5.2**

If the Darcy experiment described in §2.8 and illustrated by Figure 2.17 is performed on a tissue specimen rather than a sand layer, how do fixed charges on the tissue specimen and a charged electrolyte modify the analysis of the experiment? This example is adapted from Huyghe and Bovendeerd (2003). Recall that in a Darcy-type experiment the fluid pressure decreases linearly from pressure $p_0$ at the top of the layer to a pressure of 0 at the bottom of the layer. If the layer has thickness $L$, this pressure distribution is $p(x_3) = p_0(x_3 - L)/L$, where $x_3$ is the Cartesian axis pointing downward through the layer. In the linear analysis of the Darcy experiment, the poroelastic medium is assumed to be orthotropic with incompressible constituents, and thus effective stress $\hat{\mathbf{T}}^{\text{eff}}$ is given by (9.30), $\hat{\mathbf{T}}^{\text{eff}} = \hat{\mathbf{T}} + \hat{\mathbf{U}}p$, and Hooke's law is of the form of (9.7), $\hat{\mathbf{E}} = \hat{\mathbf{S}}^{\text{d}} \cdot \hat{\mathbf{T}}^{\text{eff}}$. In this special one-dimensional case of the Darcy experiment, the only nonzero component of the stress is the 33 component; thus, these equations reduce to $T_{33}^{\text{eff}} = T_{33} + p$ and $E_{33} = \partial u_3 / \partial x_3 = T_{33}^{\text{eff}} / E_3^d$, respectively, where we have used strain-displacement relations (3.49) to relate the strain to displacement component $u_3$. In the steady-state situation considered, the medium is accelerationless and the action-at-a-distance forces are assumed to be 0, and thus the equilibrium condition is that the divergence of the total stress be zero, $\nabla \cdot \hat{\mathbf{T}} = 0$, which in this case requires that $\partial / \partial x_3 (T_{33}^{\text{eff}} - p) = 0$. Since $T_{33}^{\text{eff}} - p$ = constant, it follows that $T_{33}^{\text{eff}} = -p_0 x_3 / L$. A plot of the pressure distribution across the layer is shown in Figure 13.3 immediately to the right of the tissue specimen layer and the fluid reservoir providing its pressure head. Placing this expression for $T_{33}^{\text{eff}}$ into $\partial u_3 / \partial x_3 = T_{33}^{\text{eff}} / E_3^d$ and

integrating using boundary condition $u(L) = 0$, it follows that $u_3(x_3) = -(p_0 / 2LE_3^d)(x_3^2 - L^2)$. Please repeat this analysis for the case when there is a fixed charge in the poroelastic medium and the perfusing fluid is an electrolyte.

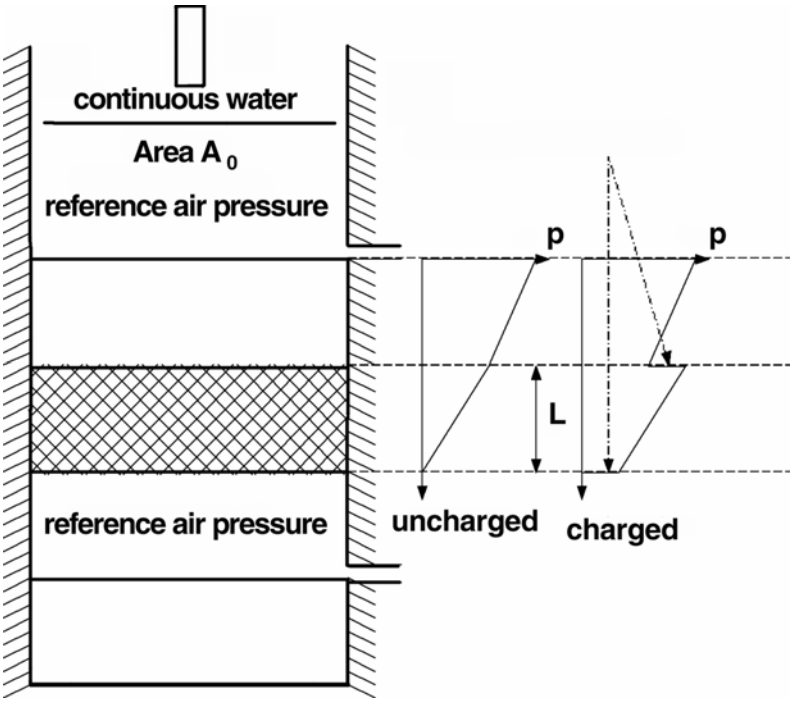



**Figure 13.3**. Illustration for Example 13.6.3. The figure is a modification of Figure 2.17, which illustrated the original Darcy experiment in which a sand layer was subjected to a constant pressure gradient to measure its permeability. The modification is that the sand layer is replaced by a tissue specimen layer and two situations are considered: one in which the tissue layer and perfusant fluid are uncharged, and the other in which the tissue specimen has a fixed charge and the perfusant fluid is a charged electrolyte. The difference is shown in the pressure-versus-distance diagrams to the right of the tissue specimen layer and the fluid reservoir providing its pressure head. While the pressure gradient is constant and equal in both cases, there is a pressure jump entering and leaving the tissue specimen due to the osmotic pressure established by the electrical charges.

**Solution:** In the one-dimensional steady-state condition under consideration in an orthotropic poroelastic medium with incompressible constituents, it follows from (9.54) that $\partial^2 p / \partial x_2^2 = 0$. It follows that the pressure again has a linear distribution across the tissue specimen. At the top of the layer the pressure is $p_0 + p_{os}$, and at the bottom it is just $p_{os}$, and thus

$$p(x_3) = \frac{p_0(x_3 - L)}{L} + p_{os},$$

where from (13.96), $p_{os} = p_{(i)} - p_{(0)} = RT\left[\sqrt{(c^{(fc)})^2 + 4f^2(c^0)^2} - 2c^0\right]$. Since $T_{33}^{\text{eff}} - p$ is also a constant in this situation, it follows that $T_{33}^{\text{eff}} = -(p_0 x_3 / L) + p_{os}$. Again placing this expression for $T_{33}^{\text{eff}}$ into $\partial u_3 / \partial x_3 = T_{33}^{\text{eff}} / E_3^d$ and integrating using boundary condition $u(L) = 0$, it follows that $u_3(x_3) = p_{os}(x_3 - L) - (p_0 / 2LE_3^d)(x_3^2 - L^2)$. Figure 13.3 is a modification of Figure 2.17, which illustrated the original Darcy experiment in which a sand layer was subjected to a constant pressure gradient to measure its permeability. The modification is that a tissue

specimen layer replaces the sand layer and the difference between the uncharged and charged situations is shown in the pressure-versus-distance diagrams to the right of the tissue specimen layer and the fluid reservoir providing its pressure head. While the pressure gradient is constant and equal in both cases, there is a pressure jump entering and leaving the tissue specimen due to the osmotic pressure established by the electrical charges.

**Problems**

13.5.1. List the valences for each of the following pore or interstitial fluid mobile ions: $Na^+$, $Ca^{++}$, $H^+$, $K^+$, $Cl^-$, $SO_3^{2-}$, $HPO_4^{2-}$.

13.5.2. Derive results (13.84) and (13.85) from (13.77), (13.81), and (13.82).

13.5.3. A physiological solution is a solution with a concentration of 0.15-M NaCl. What is the osmotic pressure in a physiological solution at body temperature, 310°K? This problem is taken from Huyghe and Bovendeerd (2003).

## 13.6. CONTINUUM MODEL FOR A CHARGED POROUS MEDIUM: CONSTITUTIVE EQUATIONS

In this section the conservation principles of mass, linear momentum, and energy and the entropy inequality are first specialized to the development of a continuum mixture model of a fluid-saturated porous medium containing charged porous solid and $N - 1$ other species, including an ionic pore fluid, anions, cations, and neutral solutes. Then the constitutive equations for the charged porous medium are developed following these same steps outlined in Chapter 6 and employed in Chapter 7 in the development of the four linear continuum theories considered, but here placing a greater emphasis on the use of the entropy inequality to restrict the constitutive assumptions. This presentation is close to that of Huyghe and Janssen (1997, 1999) and follows in the spirit of the work of Lai et al. (1991, 1998, 2000) and Gu et al. (1993, 1998, 1999).

The porous solid is taken to be the selected constituent in the mixture, hence the "$s$" subscript or superscript notation now means solid as well as "selected". The porous solid constituent is special because it contains all the other constituents and limits their behavior. From the viewpoint of the modeler it serves as a structure relative to which the movement of all the other constituents may be referenced. It is therefore singled out for special consideration in models of the charged porous medium.

Since the true density of each constituent, $\gamma_{(a)}$, is assumed to be constant, the local statement of mass conservation for a single constituent continuum, (13.18), is written for each constituent $a = 1, 2, \ldots, N$ in terms of the local volume fractions, $\phi_{(a)}$, as

$$\frac{\partial \phi_{(a)}}{\partial t} + \nabla \cdot (\phi_{(a)} \mathbf{v}_{(a)}) = 0 \,. \tag{13.97}$$

Since the solid constituent is treated as special, restriction (13.17) is rewritten as

$$\phi_s(\mathbf{x},t) + \sum_{b=1}^{N-s} \phi_{(b)}(\mathbf{x},t) = 1 \,, \tag{13.98}$$

where summation index $b$ runs over all the constituents except $s$. Summing all constituent mass conservation equations (13.97), and employing (13.17), it follows that

$$\nabla \cdot \left( \sum_{a=1}^{N} \phi_{(a)} \mathbf{v}_{(a)} \right) = 0 \,. \tag{13.99}$$

Multiplying (13.17) by $\mathbf{v}_s$ and subsequently taking the divergence of the result, it follows that

$$\nabla\cdot\mathbf{v}_s-\nabla\cdot\left(\sum_{a=1}^{N}\phi_{(a)}\mathbf{v}_{(s)}\right)=0\,; \tag{13.100}$$

the sum of (13.99) and (13.100) yields

$$\nabla\cdot\mathbf{v}_s+\nabla\cdot\left(\sum_{a=1}^{N}\phi_{(a)}\mathbf{u}_{(a)}\right)=0\,, \tag{13.101a}$$

where the definition of the diffusion velocity, (13.24), or $\mathbf{u}_{(a)}=\mathbf{v}_{(a)}-\mathbf{v}_{(s)}$, has been employed. However, since $\mathbf{u}_{(s)}=0$, it follows that (13.101a) is equivalent to

$$\nabla\cdot\mathbf{v}_s+\nabla\cdot\left(\sum_{b=1}^{N-s}\phi_{(b)}\mathbf{u}_{(b)}\right)=0\,. \tag{13.101b}$$

It is required that this entropy inequality (13.71) hold for all states of the mixture complying with the balance laws, and the incompressibility and electroneutrality conditions, and that it hold for all states of the mixture. The implementation in inequality (13.71) of the constraints of electroneutrality and incompressibility is accomplished by introducing two Lagrange multipliers, $\lambda$ for electroneutrality and $p$ for incompressibility (for this use of Lagrange multipliers, see Example 7.4.1 concerning pressure as a Lagrange multiplier in incompressible fluids; for another method of imposing the incompressibility constraint in poroelasticity, see Chapter 9). Lagrange multiplier $p$ for incompressibility is introduced by multiplying the following form of (13.101),

$$\nabla\cdot\mathbf{v}_s+\left(\sum_{b=1}^{N-s}\phi_{(b)}\nabla\cdot\mathbf{u}_{(b)}+\mathbf{u}_{(b)}\nabla\cdot\phi_{(b)}\right)=0\,, \tag{13.102}$$

by $p$ and adding the result to (13.71). Lagrange multiplier $\lambda$ for electroneutrality is introduced by multiplying result (13.76) by $\lambda$ and adding the result to (13.71); thus, by these two additions (13.71) becomes

$$\begin{aligned}&-\rho\frac{D^s\psi}{Dt}-\rho\eta\frac{D^s\theta}{Dt}-\frac{1}{\theta}\mathbf{q}\cdot\nabla\theta+\sum_{a=1}^{N}\varepsilon\nabla\cdot[\rho_{(b)}\mathbf{u}_{(b)}]+\mathbf{T}^{\text{eff}}:\mathbf{D}_{(s)}+\\&\sum_{b=1}^{N-s}\left\{\left[\mathbf{T}_{(b)}+\phi_{(b)}\left(p+\lambda\frac{z^{(b)}}{\bar{V}^{(b)}}\right)\mathbf{1}+\rho_{(b)}\psi_{(b)}\mathbf{1}\right]:[\nabla\otimes\mathbf{u}_{(b)}]\right\}+\\&\sum_{b=1}^{N-s}\left\{\mathbf{u}_{(b)}\cdot\left[\nabla\cdot\mathbf{T}_{(b)}+\left(p+\lambda\frac{z^{(b)}}{\bar{V}^{(b)}}\right)\nabla\phi_{(b)}-\nabla\rho_{(b)}\psi_{(b)}\right]\right\}\geq 0\,,\end{aligned} \tag{13.103}$$

where the effective stress has been introduced:

$$\mathbf{T}^{\text{eff}}=\mathbf{T}+p\mathbf{1}\,. \tag{13.104}$$

The development of four, relatively simple constitutive relations was described in Chapter 7. The process of developing constitutive relations was described in Chapter 6. The steps in this process consisted of the constitutive idea and the restrictions associated with the notions of localization, invariance under rigid object motions, determinism, coordinate invariance, and material symmetry. In that development, restrictions on the coefficients representing material

properties were developed without recourse to the second law of thermodynamics; ad-hoc arguments equivalent to those obtainable from the second law were employed. The present development proceeds by making constitutive assumptions that are consistent with the restrictions of localization, invariance under rigid object motions, determinism, and coordinate invariance by assuming a general form for their functional dependence on localized tensorial variables that are invariant under rigid object motions, and that have no dependence upon time except for the present time. Then the entropy inequality is employed to restrict the constitutive assumptions. This is a straightforward process that often appears complex due to the notation for the many factors that must be accounted for in a mixture. To ease the reader into this method, a simpler example is first presented.

**Example 13.6.1**

Restrict the functional dependence of free energy $\psi$, entropy $\eta$, and heat flux vector $\mathbf{q}$ in a rigid isotropic heat conductor using the entropy inequality and arguments concerning the functional dependence of these three functions.

**Solution**: Democratic but elementary constitutive assumptions are made for free energy $\psi$, entropy $\eta$, and heat flux $\mathbf{q}$. The independent variables for these three functions are assumed to be the same for all three quantities; they are temperature $\theta$ and temperature gradient $\nabla\theta$, and thus, $\psi = \psi(\theta, \nabla\theta)$, $\eta = \eta(\theta, \nabla\theta)$, and $\mathbf{q} = \mathbf{q}(\theta, \nabla\theta)$. The time rate of change of the free energy, $\psi = \psi(\theta, \nabla\theta)$, is determined using the chain rule,

$$\frac{D^s\psi}{Dt} = \frac{\partial\psi}{\partial\theta}\frac{D^s\theta}{Dt} + \frac{\partial\psi}{\partial\nabla\theta}\cdot\frac{D^s\nabla\theta}{Dt},$$

and constitutive assumptions $\psi = \psi(\theta, \nabla\theta)$, $\eta = \eta(\theta, \nabla\theta)$, and $\mathbf{q} = \mathbf{q}(\theta, \nabla\theta)$ are then substituted into entropy inequality (13.103), and one obtains the following inequality:

$$-\rho\left(\eta + \frac{\partial\psi}{\partial\theta}\right)\frac{D^s\theta}{Dt} - \frac{1}{\theta}\mathbf{q}\cdot\nabla\theta - \rho\frac{\partial\psi}{\partial\nabla\theta}\frac{D^s\nabla\theta}{Dt} \geq 0.$$

The argument originated by Coleman and Noll (1963) is that this inequality must be true for all possible physical processes and the functional dependence upon the independent variables, in this case $\{\theta, \nabla\theta\}$, must be restricted so that is the case. In view of this set of independent variables, the last summand of the inequality above is linear in the time derivative of temperature gradient $D^s\nabla\theta/Dt$. This time derivative is not contained in the set of independent variables $\{\theta, \nabla\theta\}$, and it does not appear elsewhere in the inequality, and thus it may be varied when the set of independent variables at a point is held fixed. In order that it not be varied in a way that the inequality is violated, it is necessary that coefficient $\partial\psi/\partial\nabla\theta$ of $D^s\nabla\theta/Dt$ must vanish. However, if $\partial\psi/\partial\nabla\theta = 0$, it follows that the function dependence of $\psi = \psi(\theta, \nabla\theta)$ is reduced to $\psi = \psi(\theta)$. With the reduced dependence, $\psi = \psi(\theta)$, the inequality above reduces to

$$-\rho\left(\eta + \frac{\partial\psi}{\partial\theta}\right)\frac{D^s\theta}{Dt} - \frac{1}{\theta}\mathbf{q}\cdot\nabla\theta \geq 0.$$

The argument made above is now repeated to show that the term involving the time derivative of the temperature, $D^s\theta/Dt$, must vanish; thus, one concludes that $\eta = -\partial\psi/\partial\theta$. When restrictions $\partial\psi/\partial\nabla\theta = 0$ and $\eta = -\partial\psi/\partial\theta$ are substituted back into the form of the entropy

inequality above, it reduces to $-(1/\theta)\mathbf{q}\cdot\nabla\theta \geq 0$. In the case when the isotropic form of the Fourier law of heat conduction gives the heat flux, $\mathbf{q} = -k\nabla\theta$, the inequality reduces to $(k/\theta)\nabla\theta\cdot\nabla\theta \geq 0$, and it requires only that $k$ be positive, since the temperature is positive as a consequence of its definition.

Finally, note that the argument involving $D^s\nabla\theta/Dt$ was performed first, then the argument involving $D^s\theta/Dt$. This ordering of the arguments is required because $D^s\theta/Dt$ depends on $\nabla\theta$,

$$\frac{D^s\theta}{Dt} = \frac{\partial\theta(\mathbf{x},t)}{\partial t} + \mathbf{v}_{(s)}\cdot\nabla[\theta(\mathbf{x},t)]\,,$$

a result that is a special case of (13.11).

The method of this example will next be applied to the mixture of interest. Constitutive assumptions will now be made for free energy $\psi$, entropy $\eta$, effective stress $\mathbf{T}^{\text{eff}}$, each constituent specific free energy $\psi_{(b)}$, each constituent specific partial stress $\mathbf{T}_{(b)}$, and heat flux $\mathbf{q}$. The independent variables included in the constitutive assumptions are localized small strain tensor $\mathbf{E}$, temperature $\theta$, temperature gradient $\nabla\theta$, constituent densities $\rho_{(b)}$, and diffusion velocities $\mathbf{u}_{(b)}$. These functional dependencies are expressed as equations in the following forms:

$$\psi = \psi(\mathbf{E},\theta,\nabla\theta,\phi_{(b)},\mathbf{u}_{(b)})\,,\quad \eta = \eta(\mathbf{E},\theta,\nabla\theta,\phi_{(b)},\mathbf{u}_{(b)})\,,$$

$$\mathbf{T}^{\text{eff}} = \mathbf{T}^{\text{eff}}(\mathbf{E},\theta,\nabla\theta,\phi_{(b)},\mathbf{u}_{(b)})\,,\quad \psi_{(c)} = \psi_{(c)}(\mathbf{E},\theta,\nabla\theta,\phi_{(b)},\mathbf{u}_{(b)})\,,$$

$$\mathbf{T}_{(c)} = \mathbf{T}_{(c)}(\mathbf{E},\theta,\nabla\theta,\phi_{(b)},\mathbf{u}_{(b)})\,,\ \mathbf{q} = \mathbf{q}(\mathbf{E},\theta,\nabla\theta,\phi_{(b)},\mathbf{u}_{(b)})\,. \tag{13.105}$$

These constitutive assumptions are now substituted into entropy inequality (13.103); in the case of free energy $\psi$, the chain rule is applied, and thus

$$\frac{D^s\psi}{Dt} = \frac{\partial\psi}{\partial\theta}\frac{D^s\theta}{Dt} + \frac{\partial\psi}{\partial\mathbf{E}}:\frac{D^s\mathbf{E}}{Dt} + \frac{\partial\psi}{\partial\phi_{(a)}}\frac{D^s\phi_{(a)}}{Dt} +$$

$$\frac{\partial\psi}{\partial\mathbf{u}_{(a)}}\cdot\frac{D^s\mathbf{u}_{(a)}}{Dt} + \frac{\partial\psi}{\partial\nabla\theta}\cdot\frac{D^s\nabla\theta}{Dt}\,; \tag{13.106}$$

thus,

$$-\rho\left(\eta + \frac{\partial\psi}{\partial\theta}\right)\frac{D^s\theta}{Dt} - \frac{1}{\theta}\mathbf{q}\cdot\nabla\theta + \left(\mathbf{T}^{\text{eff}} - \rho\frac{\partial\psi}{\partial\mathbf{E}}\right):\mathbf{D}_{(s)} - \rho\frac{\partial\psi}{\partial\nabla\theta}\cdot\frac{D^s\nabla\theta}{Dt} +$$

$$-\sum_{a=1}^{N}\rho\frac{\partial\psi}{\partial\mathbf{u}_{(b)}}\cdot\frac{D^s\mathbf{u}_{(b)}}{Dt}\Big) + \sum_{b=1}^{N-s}\{[\mathbf{T}_{(b)} + \phi_{(b)}\mu_{(b)}\mathbf{1} - \rho_{(b)}\psi_{(b)}\mathbf{1}]:[\nabla\otimes\mathbf{u}_{(b)}]\} +$$

$$\sum_{b=1}^{N-s}\{[\nabla\cdot\mathbf{T}_{(b)} + \mu_{(b)}\nabla\phi_{(b)} - \nabla\rho_{(b)}\psi_{(b)}]\cdot\mathbf{u}_{(b)}\} \geq 0\,, \tag{13.107}$$

where $\mu_{(b)}$ are the electrochemical potentials of the constituents other than the porous solid:

$$\mu_{(b)} = \rho \frac{\partial \psi}{\partial \phi_{(b)}} + \gamma_{(b)} \varepsilon + p + \lambda \frac{z^{(b)}}{V^{(b)}}. \tag{13.108}$$

Lagrange multiplier $p$ can be interpreted as the fluid pressure and $\lambda$ as the electrical potential of the medium multiplied by the constant of Faraday, $F$, as may be seen by comparing this result with the classical equations for the chemical potential (13.78) developed in electrochemistry. We now employ the Coleman and Noll (1963) argument described in the example above, namely, that assumed constitutive dependencies (13.105) must be restricted so that inequality (13.107) is true for any value of the final set of independent variables. In view of this set of independent variables, the last summand of (13.107) is linear in the time derivative of the diffusion velocity, $D^s \mathbf{u}_{(b)} / Dt$. This time derivative is not contained in the set of independent variables, $(\mathbf{E}, \theta, \nabla\theta, \phi_{(b)}, \mathbf{u}_{(b)})$ $\psi = \psi(\mathbf{E}, \theta, \nabla\theta, \phi_{(b)}, \mathbf{u}_{(b)})$, and it does not appear elsewhere in the inequality, and thus it may be varied when the set of independent variables at a point is held fixed. It follows that coefficient $\partial\psi / \partial \mathbf{u}_{(a)}$ of $D^s \mathbf{u}_{(b)} / Dt$ must vanish, and thus the functional dependence of $\psi = \psi(\mathbf{E}, \theta, \nabla\theta, \phi_{(b)}, \mathbf{u}_{(b)})$ is reduced to $\psi = \psi(\mathbf{E}, \theta, \nabla\theta, \phi_{(b)})$. Repeating the same argument, coefficient $\partial\psi / \partial\nabla\theta$ of $D^s \nabla\theta / Dt$ must vanish, and thus the functional dependence of $\psi = \psi(\mathbf{E}, \theta, \nabla\theta, \phi_{(b)})$ is reduced to $\psi = \psi(\mathbf{E}, \theta, \phi_{(b)})$. In view of the reduced dependence of $\psi = \psi(\mathbf{E}, \theta, \phi_{(b)})$, a repetition of the previous argument for this reduced set of independent variables is applied to the coefficient of the first summand of (13.107) involving the time derivative of the temperature, $D^s\theta / Dt$, and so the coefficient of the third summand is linear in solid rate of deformation tensor $\mathbf{D}_{(s)}$; thus ,

$$\eta = -\frac{\partial \psi}{\partial \theta} \text{ and } \mathbf{T}^{\text{eff}} = \rho \frac{\partial \psi}{\partial \mathbf{E}}. \tag{13.109}$$

This result shows that the entropy and effective stress of a charged porous medium can be derived from a regular strain energy function, $\psi = \psi(\mathbf{E}, \theta, \phi_{(b)})$, which physically has the same meaning as in single phase or multiphasic media, but which can depend on both strain and solute concentrations in the medium. Concerning the summands within the summation signs in (13.107), there is one summand linear in the gradient of diffusion velocity $\nabla \otimes \mathbf{u}_{(b)}$, and this term appears nowhere else in the reduced inequality. In order to satisfy this restriction, the following equation for the partial stress is implied:

$$\mathbf{T}_{(b)} = \phi_{(b)} (\gamma_{(b)} \psi_{(b)} - \mu_{(b)}) \mathbf{1}; \tag{13.110}$$

thus, the partial stress of the fluid and the solutes are all seen to be scalars.

When the reduced functional dependence of the free energy to $\psi = \psi(\mathbf{E}, \theta, \phi_{(b)})$ and the three restrictions, (13.109) and (13.110), obtained from inequality (13.108) are substituted back into (13.108), it reduces to the following:

$$-\frac{1}{\theta} \mathbf{q} \cdot \nabla\theta - \sum_{b=1}^{N-s} \phi_{(b)} \mathbf{u}_{(b)} \cdot \nabla \mu_{(b)} \} \geq 0. \tag{13.111}$$

Note that the functional dependence of the terms in (13.111) is not uniform. In particular, note that $\mu_{(b)}$ in (13.111) depends only upon $(\mathbf{E}, \theta, \phi_{(b)})$, the independent variables of the free energy, while $\mathbf{q}$ depends upon $(\mathbf{E}, \theta, \nabla\theta, \phi_{(b)}, \mathbf{u}_{(b)})$ by assumption (13.105). In the case when the anisotropic form of the Fourier law of heat conduction gives the heat flux, $\mathbf{q} = -\mathbf{K} \cdot \nabla\theta$, the inequality reduces to $(1/\theta) \nabla\theta \cdot \mathbf{K} \cdot \nabla\theta \geq 0$, and it requires only that $\mathbf{K}$ be positive definite, since

the temperature is positive as a consequence of its definition. The entropy inequality then reduces to the following:

$$-\sum_{b=1}^{N-s}[\mathbf{u}_{(b)}\cdot(\phi_{(b)}\nabla\mu_{(b)})]\geq 0\,. \tag{13.112}$$

Developments beyond this point could include the specification of constitutive equations for the gradients of the chemical potentials, $\phi_{(b)}\nabla\mu_{(b)}$, as is done in the following section. Inequality (13.112) may then be used to restrict the coefficients in these constitutive relationships.

**Problem**

13.6.1. Derive the statement of mass balance for the entire mixture, (13.101), by summing (13.97) over all constituents and employing (13.98).

## 13.7. LINEAR IRREVERSIBLE THERMODYNAMICS AND THE FOUR CONSTITUENT MIXTURE

In this section the results of the previous section are specialized to the case of four constituents — the fluid, anionic, and cationic constituents as well as the selected solid porous component — and an assumption of linearity is employed. This linearity assumption simplifies representation of the inequality and permits connection of the preceding results with the methods of irreversible thermodynamics. Specifically, it is assumed that the typical summand in (13.112), $\phi_{(b)}\nabla\mu_{(b)}$, has a linear dependence on each of the three diffusion velocities — $\mathbf{u}_{(f)}$, $\mathbf{u}_{(+)}$, and $\mathbf{u}_{(-)}$ — thus,

$$\phi_{(b)}\nabla\mu_{(b)}=-\mathbf{B}^{(bf)}\cdot\mathbf{u}_{(f)}-\mathbf{B}^{(b+)}\cdot\mathbf{u}_{(+)}-\mathbf{B}^{(b-)}\cdot\mathbf{u}_{(-)}\,, \tag{13.113a}$$

or, for each component,

$$\begin{aligned}
\phi_{(f)}\nabla\mu_{(f)}&=-\mathbf{B}^{(ff)}\cdot\mathbf{u}_{(f)}-\mathbf{B}^{(f+)}\cdot\mathbf{u}_{(+)}-\mathbf{B}^{(f-)}\cdot\mathbf{u}_{(-)}\,,\\
\phi_{(+)}\nabla\mu_{(+)}&=-\mathbf{B}^{(+f)}\cdot\mathbf{u}_{(f)}-\mathbf{B}^{(++)}\cdot\mathbf{u}_{(+)}-\mathbf{B}^{(+-)}\cdot\mathbf{u}_{(-)}\,,\\
\phi_{(-)}\nabla\mu_{(-)}&=-\mathbf{B}^{(-f)}\cdot\mathbf{u}_{(f)}-\mathbf{B}^{(-+)}\cdot\mathbf{u}_{(+)}-\mathbf{B}^{(--)}\cdot\mathbf{u}_{(-)}\,,
\end{aligned} \tag{13.113b}$$

where the various $\mathbf{B}$ tensors represent the frictional resistance between the specified binary constituents and are therefore assumed to be symmetric, $\mathbf{B}^{(ab)}=\mathbf{B}^{(ba)}$, where $a$ and $b$ are $f$, –, or +. In the case of the prospective tissue applications it is reasonable to make the following assumptions relating the various $\mathbf{B}$ tensors:

$$\mathbf{B}^{(+f)}=-\mathbf{B}^{(++)}\,,\quad \mathbf{B}^{(-f)}=-\mathbf{B}^{(--)}\,,\quad \mathbf{B}^{(+-)}=0\,. \tag{13.114}$$

The first (second) of these equalities indicates that the frictional resistance between the fluid and the cations (anions) is equal to the negative of the frictional resistance between the cations (anions) themselves. This assumption is based on the repulsive nature of like charges, while the third expression in (13.114) is based on the attractive nature of opposite charges. These assumptions are reasonable if the frictional interactions between cation and anion, as well as

between ion and solid phases are negligible. Placing assumptions (13.114) in (13.113), (13.113) reduces to the following:

$$\begin{aligned}
\phi_{(f)}\nabla\mu_{(f)} &= -\mathbf{B}^{(ff)}\cdot\mathbf{u}_{(f)} + \mathbf{B}^{(++)}\cdot\mathbf{u}_{(+)} + \mathbf{B}^{(--)}\cdot\mathbf{u}_{(-)}, \\
\phi_{(+)}\nabla\mu_{(+)} &= -\mathbf{B}^{(++)}\cdot(\mathbf{u}_{(+)} - \mathbf{u}_{(f)}), \\
\phi_{(-)}\nabla\mu_{(-)} &= -\mathbf{B}^{(--)}\cdot(\mathbf{u}_{(-)} - \mathbf{u}_{(f)}).
\end{aligned} \tag{13.115}$$

Solving the last two of these three equations for $\mathbf{u}_{(+)}$ and $\mathbf{u}_{(-)}$, respectively, and then substituting the two results into the first of (13.115) yields an expression that contains only one diffusion velocity, $\mathbf{u}_{(f)}$. Solving the resulting expression for $\mathbf{u}_{(f)}$, subsequent multiplication of the result by $\phi_{(f)}$ leads to a representation of the volume flux of fluid in terms of the gradients of the chemical potentials:

$$\phi_{(f)}\mathbf{u}_{(f)} = -\mathbf{K}_f\cdot[\phi_{(f)}\nabla\mu_{(f)} + \phi_{(+)}\nabla\mu_{(+)} + \phi_{(-)}\nabla\mu_{(-)}] \tag{13.116}$$

where

$$\mathbf{K}_f = \phi_{(f)}^2(\mathbf{B}^{(ff)} - \mathbf{B}^{(++)} - \mathbf{B}^{(++)})^{-1}. \tag{13.117}$$

Set of equations (13.115) may then also be solved for fluxes $\phi_{(+)}\mathbf{u}_{(+)}$ and $\phi_{(-)}\mathbf{u}_{(-)}$:

$$\begin{aligned}
\phi_{(+)}\mathbf{u}_{(+)} &= -\frac{\phi_{(+)}}{\phi_{(f)}}\mathbf{K}_f\cdot[\phi_{(f)}\nabla\mu_{(f)} + \phi_{(+)}\{\mathbf{1} + \phi_{(f)}(\mathbf{K}_f\mathbf{B}^{(++)})^{-1}\}\nabla\mu_{(+)} + \phi_{(-)}\nabla\mu_{(-)}], \\
\phi_{(-)}\mathbf{u}_{(-)} &= -\frac{\phi_{(-)}}{\phi_{(f)}}\mathbf{K}_f\cdot[\phi_{(f)}\nabla\mu_{(f)} + \phi_{(+)}\nabla\mu_{(+)} + \phi_{(-)}\{\mathbf{1} + \phi_{(f)}(\mathbf{K}_f\mathbf{B}^{(--)})^{-1}\}\nabla\mu_{(-)}].
\end{aligned} \tag{13.118}$$

Results (13.116) and (13.118) representing the fluxes of the fluid and the charges in the porous medium are easily recast in the form of equations in the so-called "irreversible thermodynamic" (De Groot and Mazur, 1962) or "thermodynamics of the steady state" (Denbigh, 1951). Let **j** represent a 3-tuple of the three flux vectors in (13.116) and (13.118):

$$\mathbf{j} = [\phi_{(f)}\mathbf{u}_{(f)}, \phi_{(+)}\mathbf{u}_{(+)}, \phi_{(-)}\mathbf{u}_{(-)}]^T, \tag{13.119}$$

and let **f** represent a 3-tuple of the three chemical potential gradients ("forces") in (13.116) and (13.118):

$$\mathbf{f} = [\nabla\mu_{(f)}, \nabla\mu_{(+)}, \nabla\mu_{(-)}]^T; \tag{13.120}$$

then the three equations, (13.116) and (13.118), may be concisely expressed as a matrix equation:

$$\mathbf{j} = \mathbf{L}\cdot\mathbf{f}, \tag{13.121}$$

where **L** is a matrix of matrices representing a linear transformation defined by

$$\begin{bmatrix} \mathbf{L}^{(ff)} & \mathbf{L}^{(f+)} & \mathbf{L}^{(f-)} \\ \mathbf{L}^{(+f)} & \mathbf{L}^{(++)} & \mathbf{L}^{(+-)} \\ \mathbf{L}^{(-f)} & \mathbf{L}^{(-+)} & \mathbf{L}^{(--)} \end{bmatrix} = \tag{13.122}$$

$$\begin{bmatrix} \phi_{(f)}\mathbf{K}_f & \phi_{(+)}\mathbf{K}_f & \phi_{(-)}\mathbf{K}_f \\ \phi_{(+)}\mathbf{K}_f & \phi_{(+)}^2\{\frac{1}{\phi_{(f)}}\mathbf{K}_f + (\mathbf{B}^{(++)})^{-1}\} & \frac{\phi_{(+)}\phi_{(-)}}{\phi_{(f)}}\mathbf{K}_f \\ \phi_{(-)}\mathbf{K}_f & \frac{\phi_{(+)}\phi_{(-)}}{\phi_{(f)}}\mathbf{K}_f & \phi_{(-)}^2\{\frac{1}{\phi_{(f)}}\mathbf{K}_f + (\mathbf{B}^{(--)})^{-1}\} \end{bmatrix}.$$

**L** is, by (13.121), a linear transformation that transforms the chemical potential gradients (i.e., the "forces") **f** into fluxes **j**. In linear algebra matrices are included in an algebraic structure called a ring. An algebraic ring permits matrices whose entries are matrices themselves, such as **L** as well as column matrices **j** and **f** introduced above. The first important conclusion from (13.122) is that matrix **L** is symmetric:

$$\mathbf{L} = \mathbf{L}^T . \tag{13.123}$$

The symmetry of this matrix is not always true when other systems of forces and fluxes are considered. Result (13.123) is usually called an "Onsager relation," although the proof that Onsager gave was for a restricted class of thermodynamic systems and many investigators choose to prove, or try to prove, that it is true for the system they are considering.

The second important conclusion from (13.122) is that the second law in the form (13.112) requires that $\mathbf{f}\cdot\mathbf{L}\cdot\mathbf{f} \geq \mathbf{0}$, and, furthermore, that the sum of the quadratic forms based on each submatrix **L** is also positive definite, and thus

$$-\sum_{b=1}^{N-s}\{\phi_{(b)}\mathbf{u}_{(b)}\cdot\nabla\mu_{(b)}\} = \mathbf{f}\cdot\mathbf{L}\cdot\mathbf{f} = \tag{13.124}$$

$$\nabla\mu_{(f)}\cdot\mathbf{L}^{(ff)}\cdot\nabla\mu_{(f)} + \nabla\mu_{(+)}\cdot\mathbf{L}^{(++)}\cdot\nabla\mu_{(+)} + \nabla\mu_{(-)}\cdot\mathbf{L}^{(--)}\cdot\nabla\mu_{(-)} +$$

$$2\nabla\mu_{(f)}\cdot\mathbf{L}^{(f+)}\cdot\nabla\mu_{(+)} + 2\nabla\mu_{(+)}\cdot\mathbf{L}^{(+-)}\cdot\nabla\mu_{(-)} + 2\nabla\mu_{(f)}\cdot\mathbf{L}^{(f-)}\cdot\nabla\mu_{(-)} \geq 0 ,$$

where the symmetry of **L** has been employed to reduce the number of summands in this equation from 9 to 6. This result requires that **L** and each of its principal component matrices, namely $\mathbf{L}^{(ff)}$, $\mathbf{L}^{(++)}$, $\mathbf{L}^{(--)}$,

$$\begin{bmatrix} \mathbf{L}^{(ff)} & \mathbf{L}^{(f+)} \\ \mathbf{L}^{(f+)} & \mathbf{L}^{(++)} \end{bmatrix}, \begin{bmatrix} \mathbf{L}^{(++)} & \mathbf{L}^{(+-)} \\ \mathbf{L}^{(+-)} & \mathbf{L}^{(--)} \end{bmatrix}, \text{ and } \begin{bmatrix} \mathbf{L}^{(ff)} & \mathbf{L}^{(f-)} \\ \mathbf{L}^{(f-)} & \mathbf{L}^{(--)} \end{bmatrix},$$

be positive definite.

A detailed component form of representation (13.121) is obtained by considering each flux as the sum of three fluxes, one stemming from each of the three driving forces (chemical potential gradients). To obtain the representation, each flux is parsed as follows:

$$\mathbf{j}=\begin{bmatrix}\phi_{(f)}\mathbf{u}_{(f)}\\ \phi_{(+)}\mathbf{u}_{(+)}\\ \phi_{(-)}\mathbf{u}_{(-)}\end{bmatrix}=\begin{bmatrix}\mathbf{j}^{(ff)}+\mathbf{j}^{(f+)}+\mathbf{j}^{(f-)}\\ \mathbf{j}^{(+f)}+\mathbf{j}^{(++)}+\mathbf{j}^{(--)}\\ \mathbf{j}^{(-f)}+\mathbf{j}^{(-+)}+\mathbf{j}^{(--)}\end{bmatrix}, \tag{13.125}$$

and it is then possible to obtain expressions for the nine component fluxes, the three along the diagonal:

$$\mathbf{j}^{(ff)}=-\mathbf{L}^{(ff)}\cdot\nabla\mu_{(f)},\ \ \mathbf{j}^{(++)}=-\mathbf{L}^{(++)}\cdot\nabla\mu_{(+)},\ \mathbf{j}^{(--)}=-\mathbf{L}^{(--)}\cdot\nabla\mu_{(-)} \tag{13.126}$$

and the other six:

$$\mathbf{j}^{(f+)}=-\mathbf{L}^{(f+)}\cdot\nabla\mu_{(+)},\ \ \mathbf{j}^{(f-)}=-\mathbf{L}^{(f-)}\cdot\nabla\mu_{(-)},\ \ \mathbf{j}^{(+-)}=-\mathbf{L}^{(+-)}\cdot\nabla\mu_{(-)}\ ,$$

$$\mathbf{j}^{(+f)}=-\mathbf{L}^{(+f)}\cdot\nabla\mu_{(f)},\ \ \mathbf{j}^{(-f)}=-\mathbf{L}^{(-f)}\cdot\nabla\mu_{(f)},\ \ \mathbf{j}^{(-+)}=-\mathbf{L}^{(-+)}\cdot\nabla\mu_{(+)}. \tag{13.127}$$

The first of (13.126) is a form of Darcy's law and the second two equations in (13.126) are examples of Fick's law; they represent the diffusion of the two charge types by the gradients in the associated chemical potential. The second two equations in (13.126) may be recast in more familiar form by introduction of the diffusion tensors for each of the ions:

$$\mathbf{D}^{(+)}=R\theta c^{(+)}\left\{\frac{1}{\phi_{(f)}}\mathbf{K}_f+(\mathbf{B}^{(++)})^{-1}\right\},$$

$$\mathbf{D}^{(-)}=R\theta c^{(-)}\left\{\frac{1}{\phi_{(f)}}\mathbf{K}_f+(\mathbf{B}^{(--)})^{-1}\right\}; \tag{13.128}$$

and thus from (13.121) and the last two equations of (13.126), Fick's law for the anions and cations may be written in these forms:

$$\mathbf{j}^{(++)}=\frac{(\bar{V}^{(+)})^2c^{(+)}}{R\theta}\mathbf{D}^{(+)}\cdot\nabla\mu^{(+)},\ \ \mathbf{j}^{(--)}=\frac{(\bar{V}^{(-)})^2c^{(-)}}{R\theta}\mathbf{D}^{(-)}\cdot\nabla\mu^{(-)}. \tag{13.129}$$

The six equations of (13.127) represent the cross-fluxes, that is to say, they are the flux components that are being driven by chemical potentials ("forces") other than the one with which they are associated. For example, the first of these is an expression for the flux of the fluid (solvent) that is being driven by the gradient in the chemical potential for the cations; the fourth of these equations, (13.127), is an expression for the reverse effect, namely, the flux of the cations that is being driven by the gradient in the chemical potential for the fluid (solvent). The fact that the two coefficients $\mathbf{L}^{(f+)}$ and $\mathbf{L}^{(+f)}$ relating the fluxes and the gradients of the chemical potentials in these two cases are equal, $\mathbf{L}^{(f+)}=\mathbf{L}^{(+f)}$, is a consequence of the symmetry of $\mathbf{L}$, (13.123). The symmetry of $\mathbf{L}$ also implies two other equalities in set of equations (13.127), namely, $\mathbf{L}^{(f-)}=\mathbf{L}^{(-f)}$ and $\mathbf{L}^{(-+)}=\mathbf{L}^{(+-)}$. Relations of this type are often called "Onsager relations," as noted above. This finishes the excursion into the notation of the irre-

versible thermodynamics or thermodynamics of the steady state; the alternative presentation is often helpful in understanding the material.

Equations (13.128) and (13.129) define the diffusivity of ions in porous media. However, these definitions do not separate the effects of convection from those of diffusion. In (13.129) both $\mathbf{j}^{(++)}$ and $\mathbf{j}^{(--)}$ could include convective flux as well as diffusive flux. The fact that the convective flux is not represented is a consequence of defining the diffusivity by the absence of "other driving forces" (e.g., the gradients of chemical potential for other species). This procedure does not guarantee that convection is absent, and consequently diffusivities (13.128) are explicit functions of $\mathbf{K}_f$. This observation is made in Gu et al. (1998). The alternative they suggest (their eq. (39)) is that the diffusivity can be defined as that when the convection effect is absent (instead of when other driving forces are absent). In the present situation the revised definitions for the diffusion tensors for each of the ions would be as follows:

$$\mathbf{D}^{(+)} = R\theta c^{(+)}(\mathbf{B}^{(++)})^{-1}\,,\ \mathbf{D}^{(-)} = R\theta c^{(-)}(\mathbf{B}^{(--)})^{-1}\,. \tag{13.130}$$

Alternate expressions for the fluxes will be developed in this paragraph using some approximations explained below. Using the special cases of (13.108) given by (13.81), (13.82), and (13.83), (13.116) takes the form

$$\phi_{(f)}\mathbf{u}_{(f)} = -\mathbf{K}_f \cdot [\nabla p + R\theta\{\frac{1}{\bar{V}^{(f)}}\nabla \ln a_{(f)} +$$

$$\frac{\phi_{(+)}}{\bar{V}^{(+)}}\nabla \ln a_{(+)} + \frac{\phi_{(-)}}{\bar{V}^{(-)}}\nabla \ln a_{(-)} + (\frac{\phi_{(+)}}{\bar{V}^{(+)}} - \frac{\phi_{(-)}}{\bar{V}^{(-)}})F\nabla\xi)\}\big]\,. \tag{13.131}$$

Alternatively, using (13.75) and (13.86), the representation of the volume flux of fluid may be written as

$$\phi_{(f)}\mathbf{u}_{(f)} = -\mathbf{K}_f \cdot [\nabla p - Fc^{(fc)}\nabla\xi +$$

$$R\theta\{\nabla \ln a_{(f)} + c^{(+)}\nabla \ln a_{(+)} + c^{(-)}\nabla \ln a_{(-)}\}\big]\,. \tag{13.132}$$

Alternative expressions for each of the three terms in (13.132) that are multiplied by $R\theta$ will now be developed. In these developments the gradients of $c^{(i)}_{(f)}$ are neglected and use is made of the fact that the volume fractions of the anionic and cationic constituents are much less than that of the fluid, so that where these three constituents are considered together, the combination is basically the fluid component. First,

$$R\theta\nabla \ln a_{(f)} = -R\theta\Phi^{(i)}_{(f)}m^{(i)}_{(f)}(\nabla c^{(i)}_{(+)} + \nabla c^{(i)}_{(-)})\,, \tag{13.133}$$

where $\Phi^{(i)}_{(f)}$ is the inner osmotic coefficient defined by (13.92), and where the molar fraction of the fluid in the inner solution, $m^{(i)}_{(f)}$, is given by (13.93). Observing from (13.91) that the gradient of osmotic pressure has representation

$$\nabla p_{os} = R\theta\Phi^{(i)}_{(f)}(\nabla c^{(i)}_{(+)} + \nabla c^{(i)}_{(-)})\,, \tag{13.134}$$

where the outer domain components have been assumed to be homogeneous, it follows that (13.133) may be rewritten as

$$R\theta\nabla \ln a_{(f)} = -m^{(i)}_{(f)}\nabla p_{os}\,, \tag{13.135}$$

but since the molar fractions of anionic and cationic constituents are much less than that of the fluid, the molar fraction of the fluid in the inner solution is almost one, $m^{(i)}_{(f)} \cong 1$, and thus

$$R\theta\nabla \ln a_{(f)} = -\nabla p_{os}\,. \tag{13.136}$$

An alternate expression for the second and third terms in (13.132) multiplied by RT is developed next, but the RT is dropped in the development:

$$c^{(+)}\nabla \ln a_{(+)} + c^{(-)}\nabla \ln a_{(-)} = \Phi^{(i)}_{(+)}(\nabla c^{(i)}_{(+)} - m^{(i)}_{(+)}\nabla c^{(i)}_{(-)}) + \Phi^{(i)}_{(-)}(\nabla c^{(i)}_{(-)} - m^{(i)}_{(-)}\nabla c^{(i)}_{(+)})\,, \tag{13.137}$$

but since the molar fractions of the anions and the cations in the inner domain are negligible, it follows that $m^{(i)}_{(+)} \cong 0$ and $m^{(i)}_{(-)} \cong 0$, and thus

$$c^{(+)}\nabla \ln a_{(+)} + c^{(-)}\nabla \ln a_{(-)} = \Phi^{(i)}_{(+)}\nabla c^{(i)}_{(+)} + \Phi^{(i)}_{(-)}\nabla c^{(i)}_{(-)}\,. \tag{13.138}$$

Using alternative representations (13.136) and (13.138) in (13.119), the volume flux of fluid may be written as

$$\phi_{(f)}\mathbf{u}_{(f)} = -\mathbf{K}_f \cdot [\nabla(p - p_{os}) - Fc^{(fc)}\nabla\xi + R\theta\{\Phi^{(i)}_{(+)}\nabla c^{(i)}_{(+)} + \Phi^{(i)}_{(-)}\nabla c^{(i)}_{(-)}\}]\,. \tag{13.139}$$

This result shows that the flow of the fluid is caused by (a) the gradients of the difference between the fluid pressure and the osmotic pressure, (b) the gradients in anion and cation charge concentrations, and (c) the gradient of the electrical field. Compare this result with (13.116), which expresses the flow of the fluid as a consequence of the gradients of the chemical potentials of the fluid, the cations, and the anions. Result (13.139) is significant in that it makes explicit that the electrical field may also drive the fluid flow. Equations (13.116) and (13.139) are equivalent, but the emphasis of the represented information is different. Equation (13.139) follows from (13.116) by the use of other relationships and the specified approximations.

## 13.8. MODELING SWELLING AND COMPRESSION EXPERIMENTS ON THE INTERVERTEBRAL DISC

An intervertebral disc consists of a gelatinous center, the nucleus pulposus, surrounded by several concentrically arranged anisotropic lamellae, the annulus fibrosus (Figure 13.4). Each lamella is a network embedded in a hydrated proteoglycan gel. The orientations of these collagen fiber networks are different for each successive lamella. In Chapter 10 it was noted that collagen is a rod-like protein molecule built of long polypeptide chains. Also in Chapter 10 it was noted that proteoglycans are large molecules consisting of many glycosaminoglycans linked to core proteins. These glycosaminoglycans are, in turn, made up of long chains of polysaccharides. Owing to the physiological pH and the ionic strength of the interstitial fluid, the carboxyl and sulfate groups of the polysaccharides are ionized. The proteoglycans are capable of retaining water up to 50-fold their own weight due to this ionization. The ionization is the source of fixed charge density in the lamellae of the intervertebral disc.

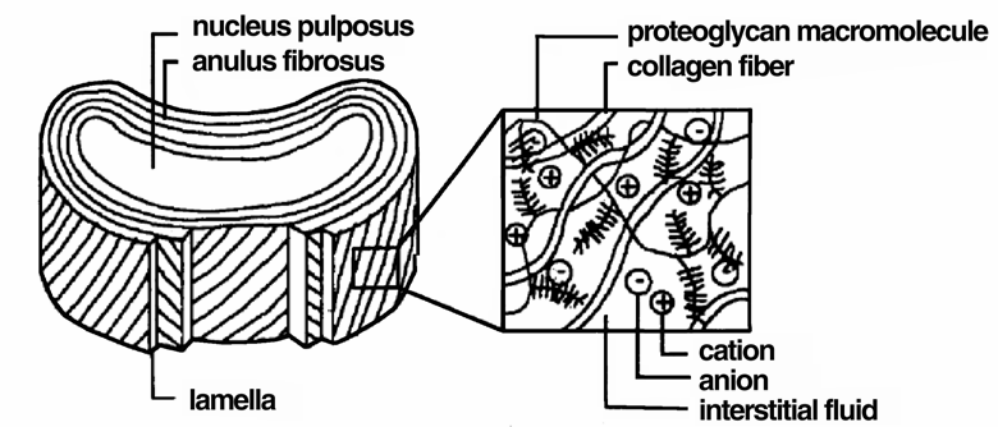



**Figure 13.4**. Schematic view of an intervertebral disc in which a part of the disc is removed to show the lamellar structure. Reprinted with permission from Frijns et al. (1997).

The intervertebral disc tissue, like other biological tissue, exhibits swelling or shrinking behavior. This behavior depends on the external salt concentration. A specimen of the nucleus pulposus can increase to 200% of its original volume in pure water. Even in a physiological salt solution the tissue swells substantially. Not only the geometry but also the composition of the tissue is changed in the process of swelling.

The experiment described in this section was reported by Frijns et al. (1997). Cylindrical specimens were made from the annulus fibrosus of the intervertebral disc at the L6–L7 level of large dogs. The axial direction of the specimen was transverse to the lamellae, in the ventrolateral direction. The diameter of these cylindrical specimens was 4 mm and the height about 1 mm. The experiments were performed at room temperature in the testing chamber shown in Figure 13.5. During the experiment the specimen was constrained in a fixed diameter, impermeable confining ring; hence the term "confined compression" is used to describe the experiment. The very precisely fitting tissue specimen was placed in the cylindrical chamber, open at one end to a porous filter, which allows a saturated specimen to drain or fluid to be delivered to the specimen, and at the other end to a piston controlled by a load cell. The resistance to flow in the filter is much smaller than the resistance to flow in the specimen. The piston may be used to squeeze the specimen against the porous filter. A linear variable displacement transducer measured the piston displacements during the experiment; these measurements were recorded every 8 s. The experimenter controls the salt concentration in the fluid flowing through the filter and a stepwise change in the salt concentration is considered to be a chemical load applied to the specimen. At the bottom of the specimen was a porous glass filter through which the controlled volume of salt solution flowed (Figure 13.5). The permeability of the glass filter was selected to be much larger than the sample permeability in order to ensure well-defined boundary conditions along the filter–sample interface. An insulating silicon oil film was used at the bottom of the test apparatus (Figure 13.5) to ensure that there was no electrical current through the sample.

The experiment was conducted in four periods, each lasting 6 hours, as illustrated by the sample height vs. time data in Figure 13.6. The four periods were a conditioning period, a swelling period, a consolidation period, and a control period. In the swelling and consolidation

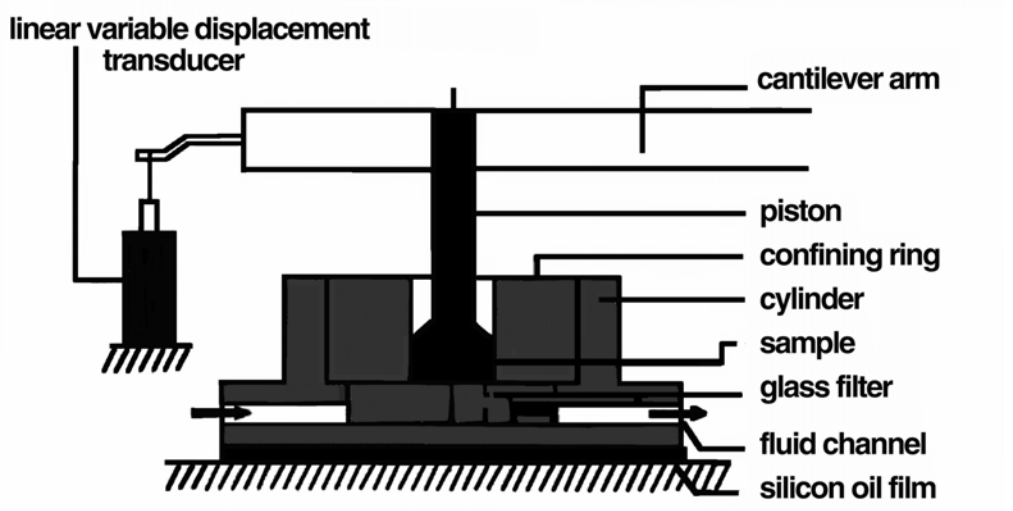



**Figure 13.5**. Schematic representation of the testing chamber. Reprinted with permission from Frijns et al. (1997).

periods different boundary conditions were prescribed, but in the conditioning period and the control period the boundary conditions were the same. In the conditioning period (a), the specimen reached equilibrium under constant chemical and mechanical load conditions, specifically a salt concentration of 0.469 ± 0.026 M. A period of six hours was allowed for the specimen to come to equilibrium under these load conditions and, at final equilibrium, the piston pressure was 0.078 MPa. In the chemical loading period (b) the concentration of the ionic solution was decreased from 0.469 ± 0.026 to 0.159 ± 0.014 M and the piston pressure held fixed at 0.078 MPa. This chemical loading under constant piston pressure led to swelling of the specimen, a combination of osmotic, diffusion, and convective effects. The concentration gradient between specimen and filter caused an outflow of ions from the specimen and an influx of water into the specimen. The outflow of ions was limited because the specimen had to remain electrically neutral and therefore a permanent inflow of fluid occurred and the tissue swelled. As noted in an earlier section, this swelling is caused by electrostatic effects and is *Donnan osmosis*. At the end of this chemical loading period the tissue specimen was an equilibrium balance between the applied piston pressure of 0.078 MPa and the swelling pressure in the fluid, that swelling pressure being related to osmotic and electrical effects associated with a salt concentration of 0.159 ± 0.014 M. In the mechanical loading period (c) the piston pressure was increased incrementally from 0.078 to 0.195 MPa while the salt concentration was held constant at 0.159 ± 0.014 M. Under these loading conditions the fluid and solid phases were effectively incompressible and the specimen behaved like a Terzaghi consolidation model element (Figure 2.18c) in that the increased load was at first carried by the liquid component only. However, the pressure gradient between the pore fluid in the specimen and the pore fluid in the filter drove fluid from the specimen and the outflow of fluid results in a shrinking of the specimen. Deformation of the specimen increased the stress carried by the porous matrix material, effectively gradually transferring the load caused by the piston from the pore fluid to the porous matrix material. At the end of this period the force carried by the porous matrix material exactly balanced the force applied to the piston and the pore fluid pressure equaled the

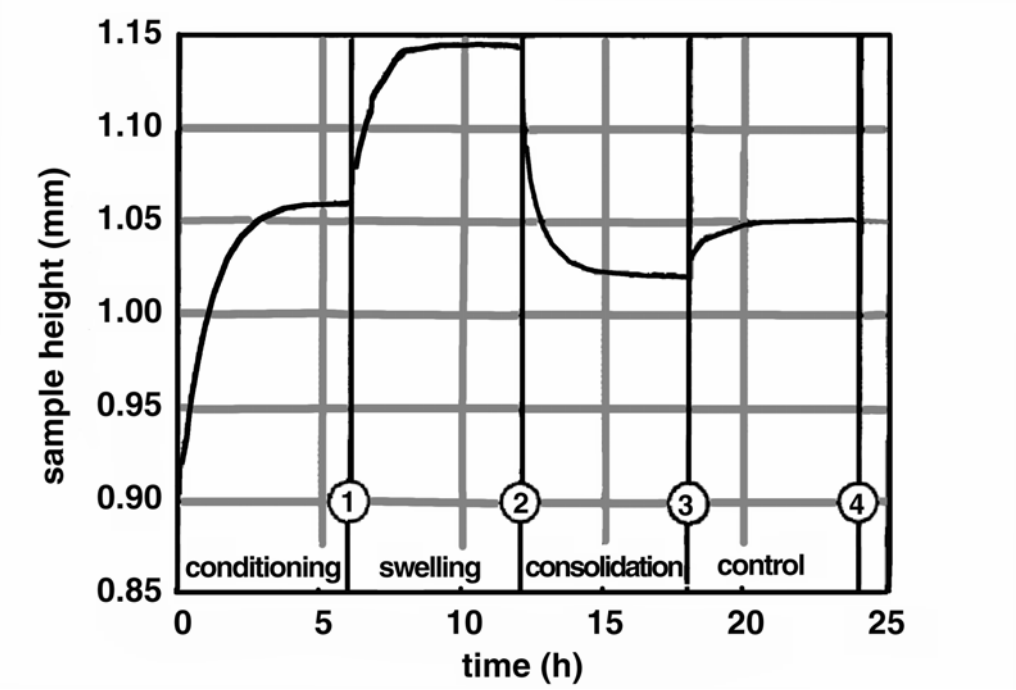



**Figure 13.6**. Results of a confined swelling and compression experiment. Reprinted with permission from Frijns et al. (1997).

pressure in the pore fluid of the filter. In the unloading period (d) the constant chemical and mechanical load conditions of phase (a) were reestablished. The sample height at the end of the control period was 2% lower than the sample height at the end of the conditioning period (Figure 13.6), although the same boundary conditions were applied. Frijns et al. (1997) suggest that this is probably caused by fixed charges that leached out during the experiment, due to damage inside the sample. The fixed charge density was measured after the experiment was completed by using a radioactively labeled NaCl solution. Porosity $\phi^f$ was also determined afterwards by measuring the sample weight before and after water was removed by freeze-drying.

Only the swelling and the consolidation periods were considered in the numerical simulations of the experiment accomplished by Frijns et al. (1997). The conditioning period was not considered because the starting conditions were unknown. In modeling this experiment the axis of the specimen, chamber, and piston (Figure 13.7) was taken as the $x_3$ direction. Axial diffusion coefficients $D_{33}^{+}$ and $D_{33}^{-}$, components of the diffusion tensors defined by (13.129), permeability coefficient $k_3$ and drained elastic Young's modulus in the axial direction $E_3^d$ were assumed to be constant. The initial conditions are given by the Donnan equilibrium, (13.89) and (13.90), respectively, and the osmotic pressure by (13.91). The electrical potential is described by

$$\xi^{(i)} = \frac{R\theta}{F} \ln \frac{a_{(+)}^{(o)}}{a_{(+)}^{(i)}} + \xi^{(o)}, \tag{13.139}$$

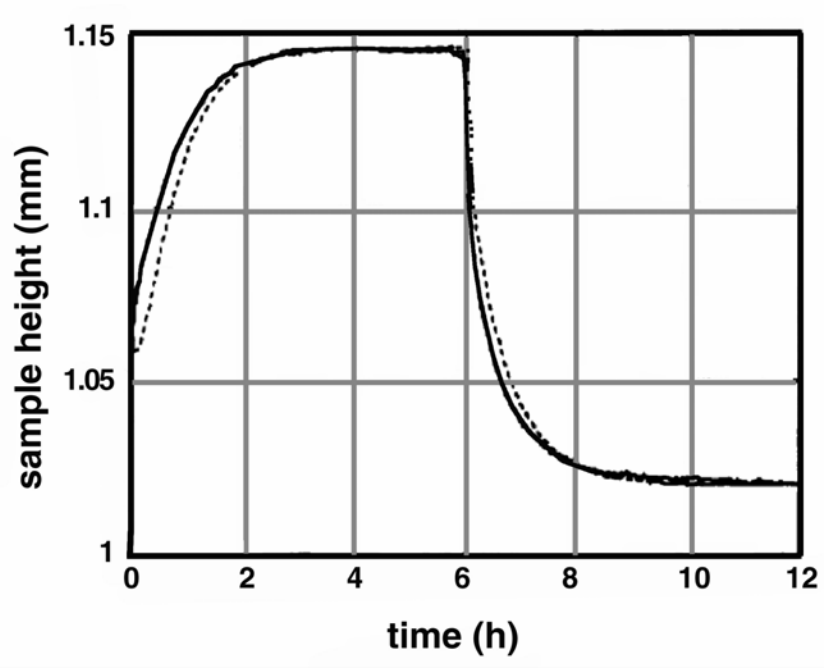



**Figure 13.7**. The swelling and consolidation periods of the experiment whose history is plotted in Figure 13.6. The solid line represents the experimental data, while the dashed line represents results computed from the model. Reprinted with permission from Frijns et al. (1997).

which follows from (13.85), with $a_{(-)}^{(o)} = a_{(+)}^{(o)}$ and $a_{(-)}^{(i)} = a_{(+)}^{(i)}$ (the number of cations and anions are equal for NaCl; the valence of Na is +1, that of Cl is –1), and where $\xi^{(0)}$ is the electrical potential in the glass filter, which was chosen to be zero and the ratio of the activity coefficients was set equal to one. The boundary conditions on top of the sample are

$$T_{33}^{\text{eff}} - p = P \ , \ u_3^f = 0 \ , \ j_3^{(++)} = 0 \ , \ j_3^{(--)} = 0 \ , \tag{13.140}$$

where $P$ is the external mechanical load and the boundary conditions at the side of the glass filter are

$$p - p_{\text{os}} = -2R\theta\Phi_{(f)}^{(0)} c^{(0)} \ , \ u_3 = 0 \ , \ \mu_{(+)} = \frac{R\theta}{\bar{V}^{(+)}} \ln a_{(+)}^{(0)} \ ,$$

$$\mu_{(-)} = \frac{R\theta}{\bar{V}^{(-)}} \ln a_{(-)}^{(0)} . \tag{13.141}$$

A one-dimensional finite-element formulation is used to solve the resulting nonlinear equations. The computed data and the experimental data are both plotted in Figure 13.7 for the chemical loading or swelling (six-hour) period and the mechanical loading or consolidation (six-hour) period. The fit of the experimental data to the theory provided the values for four parameters assumed to be constant. Axial diffusion coefficients $D_{33}^{+}$ and $D_{33}^{-}$ were determined to be from 4.5 to 5.4 x $10^{-10}$ $m^2/s$ and from 7.0 to 8.5 x $10^{-10}$ $m^2/s$, respectively. The values

given in the literature for these diffusion coefficients are 4.8 x $10^{-10}$ and 7.8 x $10^{-10}$ $m^2$/s, respectively. Permeability coefficient $k_3$ was determined to be between 1.5 and 4.0 x $10^{-16}$ $m^4$/N-s, while the values given in the literature for this permeability coefficient range from 2.2 to 4.0 x $10^{-16}$ $m^4$/N-s. The drained elastic Young's modulus in the axial direction, $E_3^d$, was determined to be between 0.75 and 1.08 Mpa, while the values given in the literature for this modulus range between 0.36 and 0.96 MPa. The fit of the experimental data is reasonable, as illustrated by Figure 13.7

This analysis of this experiment showed that a four-constituent mixture model with physically realistic diffusion coefficients could be used to fit the data of the confined compression experiments. The electrical potential, which was included in the four-constituent mixture model, causes a slower fluid outflow in the beginning of the swelling period. The micromechanical phenomenon that causes this slowing down is the friction between water and the counter ions that are electrostatically linked to the fixed charges. This is illustrated by eq. (13.139) with the osmotic coefficients set equal to one:

$$\phi_{(f)}\mathbf{u}_{(f)} = -\mathbf{K}_f \cdot [\nabla(p - p_{oz}) - Fc^{(fc)}\nabla\xi + RT\{\nabla c_{(+)}^{(i)} + \nabla c_{(-)}^{(i)}\}] \qquad . (13.142)$$

This equation shows that the gradient of the electrical potential as well as the gradients of the pore fluid and osmotic pressure and the gradients in the cation and anion concentrations influence the fluid flux. Note that the electrical potential gradient is a drag on the fluid flux. At the beginning of the swelling period, the electrical potential gradient is high (Figure 13.8). In this figure a negative sample height means that these points are in the glass filter and not in the sample. From the simulation illustrated in Figure 13.8 and eq. (13.142) it is clear that the potential gradient contributes negatively to the fluid flow. So, this phenomenon should not be neglected if precision is desired.

**Example 13.8.1**

This example is an analysis of a swelling and consolidation experiment adapted from Huyghe and Bovendeerd (2003). The experimental setup is shown in Figure 13.9a. A very precisely fitting tissue specimen is placed in a cylindrical container open at one end to a porous filter, which allows a saturated specimen to drain or fluid to be delivered to the specimen, and at the other end to a piston controlled by a load cell. The resistance to flow in the filter is much smaller than the resistance to flow in the specimen. The piston may be used to squeeze the specimen against the porous filter. The experimenter controls the salt concentration in the fluid flowing through the filter, and a stepwise change in the salt concentration is considered to be a chemical load applied to the specimen. The response of the tissue to both the chemical and mechanical load is measured in terms of variation of the height of the specimen. The experiment is conducted in four phases, illustrated in Figure 13.9b. It begins with a conditioning phase (a), during which the specimen reaches equilibrium under constant chemical and mechanical load conditions, specifically a salt concentration of 0.6 M and a piston pressure of 0.08 MPa. It takes 4 hours for the specimen to come to equilibrium under these load conditions, and at the final equilibrium the specimen height is 1.12 mm. In the chemical loading phase (b) the concentration of the ionic solution is decreased from 0.6 to 0.2 M and the piston pressure is held fixed at 0.08 MPa. This chemical loading under constant piston pressure leads to swelling of the specimen, a combination of osmotic, diffusion, and convective effects. The concentration gradient between specimen and filter causes an outflow of ions from the specimen and an influx of water into the specimen. The outflow of ions is limited because the

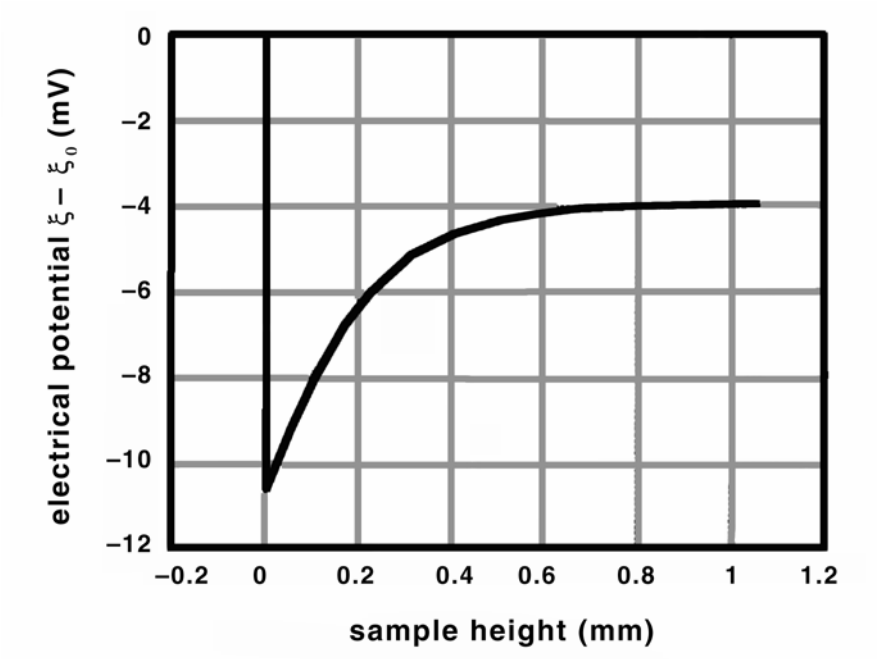



**Figure 13.8**. Electrical potential at the beginning of the swelling period ($t$ = 50 s) relative to the potential of the electrolyte solutions in the glass filter. Reprinted with permission from Frijns et al. (1997).

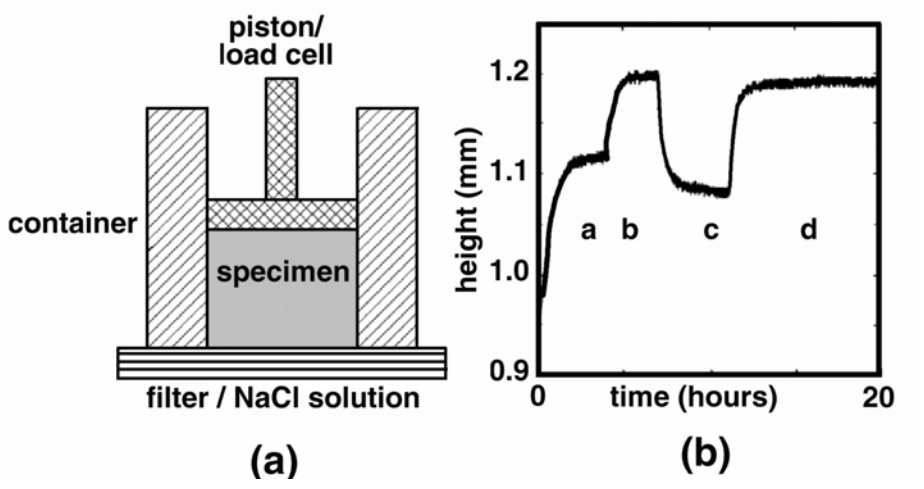



**Figure 13.9**. (a) The experimental system for the swelling and consolidation experiment. (b) A curve giving the measured variation of the height of the specimen through the four phases (a–d) of the experiment described in the text. Reprinted with permission from Huyghe and Bovendeerd (2003).

specimen has to remain electrically neutral, and therefore a permanent inflow of fluid occurs and the tissue swells (*Donnan osmosis*). At the end of this chemical loading phase the tissue specimen is in equilibrium balance between the applied piston pressure of 0.08 MPa and the swelling pressure in the fluid related to osmotic and electrical effects associated with a salt

concentration of 0.2 M. It takes 3 hours for the specimen to come to equilibrium under these load conditions, and at the final equilibrium the specimen height is 1.20 mm. In the mechanical loading phase (c) the piston pressure is increased incrementally from 0.08 to 0.2 MPa while the salt concentration is held constant at 0.2 M. Under these loading conditions the fluid and solid phases are effectively incompressible and the specimen behaves like a Terzaghi consolidation model element (Figure 2.18c) and the increased load is at first carried by the liquid component only. However, the pressure gradient between the pore fluid in the specimen and the pore fluid in the filter drives fluid from the specimen and the outflow of fluid results in shrinking of the specimen. The deformation of the specimen increases the stress carried by the porous matrix material, effectively gradually transferring the load exerted by the piston from the pore fluid to the porous matrix material. At the end of this period the force carried by the porous matrix material exactly balances the force applied to the piston and the pore fluid pressure equals the pressure in the pore fluid of the filter. It takes 4 more hours for the specimen to come to equilibrium under these load conditions, and at the final equilibrium the specimen height is 1.08 mm. In the unloading phase (d) the constant chemical and mechanical load conditions of phase (a) are reestablished.

Using the data from the end of the chemical and mechanical loading phases, B and C, determine drained elastic modulus $K^d$, permeability $\kappa$, intrinsic permeability $k$, and the fixed charge density of the tissue specimen.

**Solution**: During the mechanical loading phase the specimen height changes from 1.20 to 1.08 mm, a decrease of 0.12 mm, while, due to the confining cylindrical walls, there are no strains in the two perpendicular directions; thus, the total volumetric strain is 0.12/1.2 or –0.1. The stress in the specimen is changed from 0.08 to 0.2 MPa, an increase of 0.12 MPa. Drained bulk modulus $K^d$ is the pressure increase of 0.12 MPa divided by the total volumetric specimen strain, –0.1, and thus $K^d$ = 0.12 MPa/0.1 = 1.2 MPa. Recall from Chapter 2 that Darcy experimentally determined permeability $\kappa$ by dividing the volume flow rate by the pore fluid pressure gradient applied across a specimen of known thickness. This worked because in Darcy's experiment the volume flow rate and the pressure gradient were constant; that is not the case in the present situation so a different but appropriate method is sought here for calculating the permeability. To that end, note that the formula for the pore pressure (9.54) in the case of compressible constituents reduces to

$$\frac{1}{K^d}\frac{\partial p}{\partial t} - \kappa\frac{\partial^2 p}{\partial z^2} = -\frac{1-2\nu}{E}\frac{tr\mathbf{T}}{\partial t}$$

in an isotropic porous medium. Recall that permeability $k$, which has the dimension of length squared, is related to intrinsic permeability $\kappa$ by $k = \kappa\mu$. Since the stress is held constant for 4 hours during the mechanical loading phase, the right-hand side of the equation above is zero, and thus $\partial p/\partial t = \kappa K^d(\partial^2 p/\partial z^2)$.

A formula for calculating $\kappa$ is obtained from this result by replacing $\partial p/\partial t$ by $\Delta p/\Delta t$ and $\partial^2 p/\partial z^2$ by $\Delta p/(\Delta z)^2$, and thus $\kappa = K^d(\Delta z)^2/\Delta t$. Using $\Delta z$ = 1.2 mm and $\Delta t$ = 3 hours, it follows that $\kappa$ = 1.11 x $10^{-16}$ $m^2$/Pa-s since $K^d$ is given above as 1.2 MPa. Since the viscosity of water at 20°C is 0.001 Pa-s, it follows from $k = \kappa\mu$ that $k$ = 1.11 x $10^{-19}$ $m^2$. Osmotic pressure $p_{os}$ is equal to the change in swelling pressure during the chemical loading phase, $p_{os} = p_{after} - p_{before}$. Thus, $p_{os}$ is given by $K^d$ times the volumetric strain ({0.08 mm/1.2 mm} = 0.0714) or 85,700 Pa. Expression (13.96) with $f$ = 1 applies to both the before and after situations, and thus

$$p_{\text{after}} = RT\left[\sqrt{(c^{(fc)})^2 + 4(0.2\text{M})^2} - 0.4\text{M}\right] \text{ and}$$

$$p_{\text{before}} = RT\left[\sqrt{(c^{(fc)})^2 + 4(0.6\text{M})^2} - 1.2\text{M}\right].$$

Osmotic pressure $p_{\text{os}} = p_{\text{after}} - p_{\text{before}}$ will now be calculated using these two formulas, subsequently dividing through by RT. Noting,

$$\frac{p_{\text{os}}}{RT} = \frac{85{,}700\ \text{Pa}}{(8315)(300)\ \text{Pa/M}} = 0.034\ \text{M},$$

and thus

$$-0.766\ \text{M} = \sqrt{(c^{(fc)})^2 + 4(0.2\ \text{M})^2} - \sqrt{(c^{(fc)})^2 + 4(0.6\ \text{M})^2}\ .$$

The solution of this equation shows that the fixed change density, $c^{(fc)}$, is 0.21 M.

## 13.9. RELEVANT LITERATURE

The theory of mixtures is based on diffusion models and stems from a fluid mechanics and thermodynamics tradition, and goes back to the century before last. Fick (1855) and Stefan (1871) suggested (Truesdell and Toupin 1960, §§158 and 295) that each place in a fixed spatial frame of reference might be occupied by several different particles, one for each constituent of the mixture. Truesdell (1959) assigned to each constituent of a mixture in motion a density, an action-at-a-distance force density, a partial stress, a partial internal energy density, a partial heat flux, and a partial heat supply density. Truesdell postulated equations of balance of mass, momentum, and energy for each constituent and derived the necessary and sufficient conditions that the balance of mass, momentum, and energy for the mixture be satisfied. Bowen (1967) summarized the formative years of this subject. A readable history of the subject and its applications in the period 1957–75 is given by Atkin and Craine (1976a,b); de Bore (1996, 2000) has presented more up-to-date histories. Of key importance in the development of the mixture theories is the application by Bowen (1967, 1976, 1980, 1982) of a thermodynamically based analytical approach developed by Coleman and Noll (1963) to restrict the form of constitutive equations. At that time (1966–67) the thermodynamically based Coleman and Noll approach was very new. In his history of the development of theories for porous media, de Boer (2000) credits Goodman and Cowin (1972) with the first use of the decomposition of bulk density into a volume fraction and a true or material density (13.16). The introductory material in this chapter is taken from Bowen (1976, 1980, 1982). An advance in the universal importance of the application of these theories equal to the contribution of Truesdell (1959) and Bowen (1976, 1980, 1980) was the extension by Lai et al. (1991) to electrical effects in biological tissues. This advance is illustrated in the theory for the swelling and deformation behavior of articular cartilage by Lai et al. (1991) and Gu et al. (1993). There are many other applications of the mixture theory approach to the flow through porous media in biomechanics other than bone, for example, skin (Oomens et al., 1987), the swelling of soft tissue (Lanir, 1987), pressure sores (Mak et al., 1994), intervertebral discs (Frijns, et al., 1997), and blood perfusion of contracting skeletal muscle (Vankan et al., 1996; 1997a).

From the present perspective, the next significant contribution to the development of the theory of mixtures was its application to biological tissues in the work of Huyghe and his coworkers (Huyghe and Janssen, 1997; 1999). These investigators showed that the four-component-mixture (fluid, solid, cation, anion) theory provided a realistic model for many phenomena observed in biological tissues. Another innovation in the development of the four-

component-mixture theory by Huyghe and his coworkers was the use of a Lagrangian approach. This work is similar in sprit to the Eulerian approach of Gu et al. (1997, 1999) and Lai et al. (1998).

This developing electro-chemo-mechanical mixture theory appears to have an expanding future. Theoretical explanations based on the theory for electro-chemo-mechanical phenomena that were previously explained by ad-hoc local models are being presented now with some regularity. For example, the Hodgkin-Huxley model of membrane depolarization, the basis for our understanding of nerve electrical activity, was modeled with the theory by Gu et al. (1998, 1999) and the process of cell swelling was modeled with the theory by Ateshian et al. (2005).

Bowen (1982) showed that it was possible to recover the Biot constitutive equations (Chapter 9) from the mixture theory approach. In particular, Bowen derived equations (his (9.23) and (9.24)) that have the same form as eqs. (7) and (8) of Rice and Cleary (1976); these equations are the isotropic versions of eqs. (9.1) and (9.7) in Chapter 9. The governing equations of the small strain, incompressible poroelastic formulation of Mow et al. (1980) based on the mixture theory approach, the "biphasic theory," coincide with the governing equations of the effective medium formulation, as shown by Mow and Lai (1980, note, p. 291) and recapitulated in the present Chapter 9.

In the development of this material, representations of the chemical potentials used in electrochemistry are needed, but space does not allow a detailed development of these results. The details of the development of these chemical potential representations and related results are given in a number of standard reference works. The reference works used in the preparation of this chapter include the following portions of the following books: Chapter IV, section on "Osmotic Pressure and Membrane Equilibrium," in Alexander and Johnson (1949); Chapter 3, §VI on "Donnan Equilibrium," in Lakshminarayanaiah (1984); Chapter 1, section on "Donnan Equilibrium," in Friedman (1986); §6.3 on "The Lipid Bilayer Membrane has Three Basic Functions," in Evans and Wennerström (1999), §9.3.1, on "Osmotic Pressure," in Truskey et al. (2004).

## References


Alexander AE, Johnson P. 1949. *Colloidal science*. Oxford: OUP.

Ateshian GA, Likhitpanichkulk M, Hung CT. 2005. A mixture theory analysis for passive transport in osmotic loading of cells. *J Biomech*. In press. Available at http://www.columbia.edu/~ga29/pdf/AteshianJBinPress.pdf.

Atkin RJ, Craine RE. 1976a. Continuum theories of mixtures: basic theory and historical development. *Q J Mech Appl Math* **29**:209–244.

Atkin RJ, Craine RE. 1976b. Continuum theories of mixtures: applications. *J Inst Math Appl* **17**:153–207.

Biot MA. 1935. Le problème de la consolidation des matières argileuses sous une charge. *Ann Soc Sci Bruxelles* **B55**:110–113.

Biot MA. 1941. General theory of three-dimensional consolidation. *J Appl Phys* **12**:155–164.

Biot MA. 1956a. Theory of propagation of elastic waves in a fluid-saturated porous solid, I: low frequency range. *J Acoust Soc Am* **28**:168–178.

Biot MA. 1956b. Theory of propagation of elastic waves in a fluid-saturated porous solid, II: higher frequency range. *J Acoust Soc Am* **28**:179–191.

Biot MA. 1962. Generalized theory of acoustic propagation in porous dissipative media. *J Acoust Soc Am* **34**:1254–1264.

Biot MA. 1972. Theory of finite deformation of porous solids. *Indiana Univ Math J* **21**:597–620.

Biot MA. 1982. Generalized Lagrangian equations of non-linear reaction-diffusion. *Chem Phys* **66**:11–26.

Biot MA, Willis DG. 1957. The elastic coefficients of the theory of consolidation. *J Appl Mech* **24**:594–601.

Bowen RM. 1967. Toward a thermodynamics and mechanics of mixtures. *Arch Rat Mech Anal* **24**:370–403.

Bowen RM. 1976. Theory of mixtures. In *Continuum physics*, Vol 3: *Mixtures and EM field theories*, ed. AC Eringen, pp. 1–127. New York: Academic Press.

Bowen RM. 1980. Incompressible porous media models by use of the theory of mixtures. *Int J Eng Sci* **18**:1129–1148.

Bowen RM. 1982. Compressible porous media models by use of the theory of mixtures. *Int J Eng Sci* **20**:697–735.

Burridge R, Keller JB. 1981. Poroelasticity equations derived from microstructure. *J Acoust Soc Am* **70**:1140–1146.

Carroll MM. 1979. An effective stress–strain law for anisotropic elastic deformation. *J Geophys Res* **84**:7510–7512.

Coelho D, Shapiro M, Thovert JF, Adler PM. 1996. Electroosmotic phenomena in porous media. *J Colloid Interface Sci* **181**:169–190.

Coleman BD, Noll W. 1963. The thermodynamics of elastic materials with heat conduction. *Arch Rat Mech Anal* **13**:167–178.

Coussy O. 1995. *Mechanics of porous continua*. New York: Wiley.

De Boer R. 1996. Highlights in the historical development of the porous media theory: toward a consistent macroscopic theory. *Appl Mech Rev* **49**:201–262.

De Boer R. 2000. *Theory of porous media: highlights in the historical development and current state*. Berlin: Springer-Verlag.

De Groot SR, Mazur P. 1969. *Non-equilibrium thermodynamics*. Amsterdam: North Holland.

Denbigh KG. 1951. *The thermodynamics of the steady state*. London: Methuen.

Donnan FG. 1924. The theory of membrane equilibria. *Chem Rev* **1**:73–90.

Evans DF, Wennerström H. 1999. *The colloidal domain*, 2nd ed. New York: Wiley-VCH.

Fick A. 1855. Über diffusion. *Ann Phys* **94**:59–86.

Friedman MH. 1986. *Principles and models of biological transport*. Berlin: Springer-Verlag.

Frijns AJH, Huyghe JM, Janssen JD. 1997. A validation of the quadriphasic mixture theory for intervertebral disc tissue. *Int J Eng Sci* **35**:1419–1429.

Goodman MA, Cowin SC. 1972. A continuum theory for granular materials. *Arch Rat Mech Anal* **44**:249–266.

Gu WY, Lai WM, Mow VC. 1993. Transport of fluid and ions through a porous-permeable charged-hydrated tissue, and streaming potential data on normal bovine articular cartilage. *J Biomech* **26**:709–723.

Gu WY, Lai WM, Mow VC. 1997. A triphasic analysis of negative osomotic flows through charged hydrated soft tissues. *J Biomech* **30**:71–78.

Gu WY, Lai WM, Mow VC. 1998. A mixture theory for charged-hydrated soft tissues containing multi-electrolytes: passive transport and swelling behaviors. *J Biomech Eng* **120**:169–180.

Gu WY, Lai WM, Mow, VC. 1999. Transport of multi-electrolytes in charged hydrated soft tissues. *Transport Porous Media* **34**:143–157.

Huyghe JM. 2004. Private communication.

Huyghe JM, Bovendeerd PHM. 2003. *Biological Mixtures*. Lecture notes for course 4A650, Technische Universiteit Eindhoven.

Huyghe JM, Janssen JD. 1997. Quadriphasic mechanics of swelling incompressible porous media. *Int J Eng Sci* **35**:793–802.

Huyghe JM, Janssen JD. 1999. Thermo-chemo-electro-mechanical formulation of saturated charged porous media. *Transp Porous Media* **34**:120–141.

Huyghe JM, Oomens CW, van Campen DH, Heethaar RM. 1989. Low Reynolds number steady state flow through a branching network of rigid vessels. *Biorheology* **26**:55–71.

Huyghe JM, van Campen DH. 1995a. Finite deformation theory of hierarchically arranged porous solids, I: balance of mass and momentum. *Int J Eng Sci* **33**:1861–1871.

Huyghe JM, van Campen DH. 1995b. Finite deformation theory of hierarchically arranged porous solids, II: constitutive behavior. *Int J Eng Sci* **33**:1873–1886.

Lai WM, Gu WY, Mow VC. 1998. On the conditional equivalence of chemical loading and mechanical loading on articular cartilage. *J Biomech* **31**:1181–1185.

Lai WM, Hou JS, Mow VC. 1991. A triphasic theory for the swelling and deformation behaviors of articular cartilage. *J Biomech Eng* **113**:245–258.

Lai WM, Mow VC, Sun DD, Ateshian GA. 2000. On the electric potentials inside a charged soft hydrated biological tissue: streaming potential versus diffusion potential. *J Biomech Eng* **122**:336–346.

Lakshminarayanaiah N. 1984. *Equations of membrane biophysics*. Orlando: Academic Press.

Lanir Y. 1987. Biorheology and fluid flux in swelling tissues, I: Bicomponent theory for small deformations, including concentration effects. *Biorheology* **24**:173–187.

Mow VC, Lai WL. 1980. Recent developments in synovial joint mechanics. *SIAM Rev* **22**:275–317.

Mow VC, Kuei SC, Lai WL, Armstrong C. 1980. Biphasic creep and stress relaxation of articular cartilage in compression: theory and experiments. *J Biomech Eng* **102**:73–84.

Mow VC, Wang CC, Hung CT. 1999. The extracellular matrix, interstitial fluid and ions as a mechanical signal transducer in articular cartilage. *Osteoarth Cart* **7**:41–58.

Müller I. 1968. A thermodynamic theory of mixtures. *Arch Rat Mech Anal* **28**:1–39.

Müller I. 1985. *Thermodynamics*. Boston: Pitman.

Oomens CWJ, van Campen DH, Gorrtenboer HJ. 1987. A mixture approach to the mechanics of skin. *J Biomech* **20**:887–885.

Rice JR, Cleary MP. 1976. Some basic stress diffusion solutions for fluid-saturated elastic porous media with compressible constituents. *Rev Geophys Space Phys* **14**:227–241.

Skempton AW. 1954. The pore pressure coefficients A and B. *Géotechnique* **4**:143–147.

Slattery JC. 1967. Flow of viscoelastic fluids through porous media. *AIChE J* **13**:1066–1071.

Stefan J. 1871. Über das gleichgewicht und bewegung, insbesondere die diffusion von gasmengen. *Sitzgesber Akad Wiss Wein* **632**:63–124.

Thompson M, Willis JR. 1991. A reformation of the equations of anisotropic poroelasticity. *J Appl Mech* **58**:612–616.

Truesdell CA. 1957. Sulle basi della termomeccania. *Rend Lincei* **22**:33–38, 1158–166.

Truesdell CA, Toupin RA. 1960. The classical field theories. In *Handbuch der physik*, ed. S Flugge, pp. 226–859. Berlin: Springer-Verlag.

Truskey GA, Yuan F, Katz DF. 2004. *Transport phenomena in biological systems*. Upper Saddle River, NJ: Prentice-Hall.

Vankan WJ, Huyghe JM, Janssen JD, Huson A. 1996. Poroelasticity of saturated solids with an application to blood perfusion. *Int J Eng Sci* **34**:1019–1031.

Vankan WJ, Huyghe JM, Janssen TJD, Huson A, Hacking WJG, Schreiner W. 1997a. Finite element analysis of blood flow through biological tissue. *Int J Eng Sci* **35**:375–385.

Vankan WJ, Huyghe JM, Drost MR, Janssen JD, Huson A. 1997b. A finite element model for hierarchical porous media. *Int J Num Meths Eng* **40**:1019–1031.

Whitaker S. 1967. Diffusion and dispersion in porous media. *AIChE J* **13**:420–427.

# 14

# CARTILAGE

"… After a half a century of research on diarthroidal joint lubrication, the enigma still remains, namely, how can fluid film lubrication be achieved in a diarthroidal joint to provide (such) extraordinary low coefficients of friction?" (From Mow et al., 1992)

## 14.1. INTRODUCTION

The major connective tissues of the musculoskeletal system include bones, tendons, ligaments, articular cartilage, menisci, and intervertebral discs. The main purpose of these tissues is to connect the muscles and bones of the body together, forming levers and joints of the machine that is the animal body. These connective tissues provide structural stability for the musculoskeletal system and constrain the motion of joints when required. A brief description of three cartilaginous tissues — articular cartilage, the meniscus, and the intervertebral disc — is given in this chapter. Tendons and ligaments, non-cartilaginous tissues constructed mainly of collagen, are considered in the chapter after next.

Cartilage is a specialized, fibrous, dense connective tissue. It contains no blood vessels, and nutrients must be diffused or convected through its ECM (extracellular matrix). It is found in the joints, the rib cage, the ear, nose, and throat, and between intervertebral discs. Cartilage plays an important role in the growth and development mechanisms of the organism by forming most of the temporary skeleton in the embryo that is used as the pattern for the development of the adult skeleton. Different types of cartilage occur, the most important of which are hyaline cartilage, elastic cartilage, and fibrocartilage. Hyaline cartilage is most prominently found in diarthroidal joints covering long bones (Figure 14.1), and it forms the growth plate by which long bones grow during childhood. Elastic cartilage exists in the epiglottis and eustachian tube. Fibrocartilage is present in three major locations in the body — the intervertebral discs of the spine, as a covering of the mandibular condyle in the temporomandibular joint, and in the meniscus of the knee. It also exists temporarily at bone fracture sites.

Of the three joint types in the human body, two have significant cartilage in their construction and the third has fibrous collagen. The joint types are classified as either fibrous, cartilaginous, or synovial. Fibrous joints, which often interdigitate like the connections of the pieces of a jigsaw puzzle, connect bones very tightly and allow no relative movement of the pieces. The bones of the skull and pelvis are held together by fibrous joints, as are the union of the spinous processes and vertebrae. The fiber is usually fibrous collagen. In cartilaginous joints the bones

are attached by cartilage. These joints allow for only a little movement, such as in the spine or ribs. In this chapter some of the properties and mechanical function of the intervertebral disc will be described. Synovial joints are fully articulated and allow for much more movement than cartilaginous joints. Synovial fluid bathes the contact surfaces of the joint; it helps lubricate and protect the bones and is contained within bursa sacks. In this chapter the structure and mechanical behavior of hyaline cartilage in diarthroidal joints, typically called articular cartilage, will be described. Articular cartilage is a major component of a diarthroidal or synovial joint like the knee, elbow, or ankle. The word *diarthroidal* means relating to diarthrosis, or movable articulations. A diarthroidal joint is the same as a synovial joint. A synovial joint consists of opposing bony surfaces that are covered with a layer of cartilage, a joint cavity containing synovial fluid and lined with synovial membrane, and it is reinforced by a fibrous capsule and ligaments (Figure 14.1). Most of the cartilage in synovial joints is hyaline cartilage, the notable exception being the temporomandibular joint, a synovial joint in which fibrocartilage covers the bone ends.

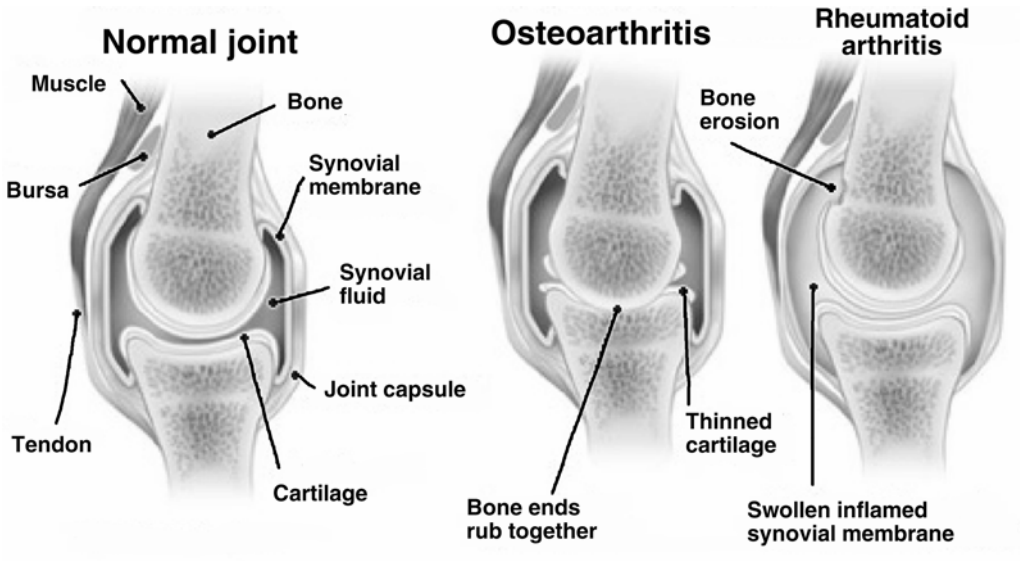



**Figure 14.1**. A normal diarthroidal joint is shown on the left. Diarthroidal joints with the two predominant types of arthritis are shown at the center and on the right. Notice the loss of articular cartilage in the osteoarthritis joint. Reprinted with permission from http://www.medicinenet.com/osteoarthritis/page2.htm.

The principal cell type of cartilage is the chondrocyte, a cell type found only in cartilage. Chondrocytes are responsible for the secretion and maintenance of the cartilage ECM, and they are housed in lacunar cavities similar to those of the osteocytes in bone tissue.

There are diseases that can affect the cartilage. Chondrodystrophies are a group of diseases characterized by a disturbance of growth and subsequent ossification of cartilage. Some common diseases affecting/involving the cartilage include arthritis, achondroplasia, costochondritis, and herniated disc. Two types of arthritis are identified (Figure 14.1) — osteoarthritis and rheumatoid arthritis — and the exact cause of each is not known. In osteoarthritis the cartilage breaks down in response to physical stress (wear and tear), the ends of the bones thicken, and the joint may lose its normal shape. The ends of the two bones in the joint may begin to

rub together, causing pain if the cartilage separator between the two bones completely breaks down. Rheumatoid arthritis is an autoimmune disease in which the body's natural immune system does not operate as it should; it attacks healthy joint tissue, initiating a process of inflammation and joint damage. Achondroplasia is caused by the reduced proliferation of chondrocytes in the epiphyseal plate of long bones, resulting in a form of dwarfism. Costochondritis is inflammation of cartilage in the ribs that causes chest pain, and a herniated disc is an intervertebral disc rupture of the cartilage ring, causing the tissue to herniate into the spinal canal. On the plus side, the cartilage matrix acts as a barrier preventing the entry of lymphocytes or diffusion of immunoglobins across its domain. This property allows for transplantation of cartilage from one individual to another without fear of tissue rejection.

## 14.2. HYALINE CARTILAGE

Hyaline is the most abundant type of cartilage; it is a semitransparent, opalescent cartilage with a blue tint. The name *hyaline* is derived from the Greek *hyalos*, meaning glass. This refers to the translucent matrix or ground substance (Figure 14.2). Type II collagen makes up 40% of the dry weight of hyaline cartilage; the collagen is arranged in cross-striated fibers, 15–45 nm in diameter, that do not assemble into large bundles. Hyaline cartilage forms most of the fetal skeleton and is found in the trachea, larynx, and diarthroidal joint surfaces of the adult.

At an early period in fetal development the greater part of the skeleton is cartilaginous. This cartilage is called temporary because it later becomes calcified cartilage which, in time, is

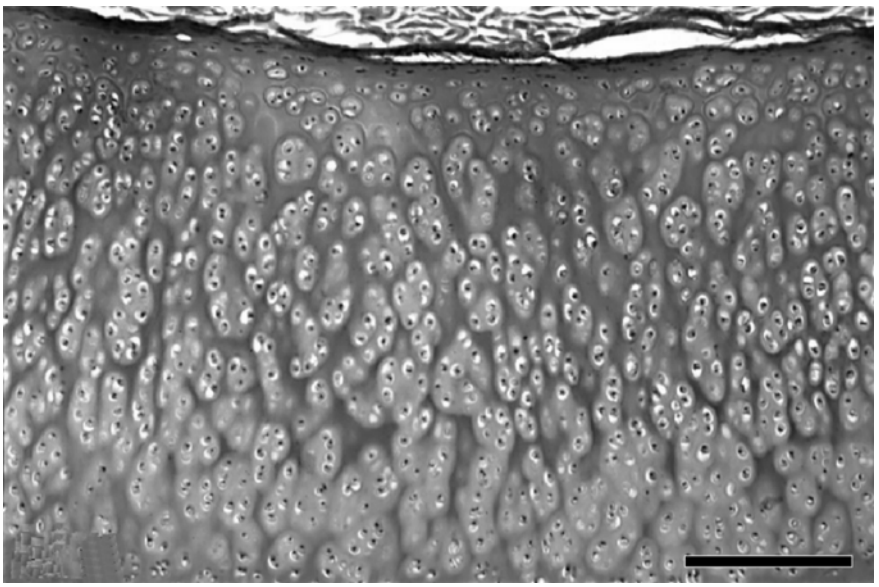


**Figure 14.2**. Hyaline cartilage is distinguished by its homogenous matrix surrounding the small nests of chrondrocytes. The tissue in the upper portion of the illustration is the perichondrium. Bar = 250 μm. Reprinted with permission from the JayDoc Histoweb http://www.kumc.edu/instruction/medicine/anatomy/histoweb/ index.htm.

replaced by bone. The use of the word "temporary" then distinguishes this cartilage from permanent cartilage, which remains unossified during its existence. Recall that the bone of the fetus is formed in two ways — *intramembranous* ossification forms flat bones of the face and skull, and *endochondral* ossification forms most of the other bones in the body. In endochondral ossification hyaline cartilage "patterns" or "models" the initial shape of various skeletal parts that first form in the embryo. In addition to serving as a center of ossification or bone growth, hyaline cartilage forms the growth plate by which long bones grow during childhood. The development of the chick limb bud between 4 and 7 days of incubation is illustrated in Figure 1.17. In this figure the solid black regions represent definitive cartilage; striped areas represent early cartilage. At 4.5 days the chick limb buds become irreversibly committed to one of several developmental pathways, leading to different types of limb tissue: the cells will express themselves as cartilage, bone, or connective tissue (Caplan, 1984). Most of the skeletal system is derived from mesoderm tissue. Chondrification is the process in which cartilage is formed from condensed mesenchyme tissue; the mesenchymal cells differentiate into chondrocytes and the chondrocytes begin secreting the proteins that form the matrix.

## 14.3. ELASTIC CARTILAGE

Elastic cartilage is histologically, and embryonically, closely related to hyaline cartilage, but the two tissues have vastly different mechanical and biochemical properties. Elastic cartilage is structurally similar to hyaline cartilage except that it contains, in addition to Type II collagen fibers, a dense network of branching and anastomosing elastin fibers (Figure 14.3). Type II collagen fibers are composed predominantly of chondroitin sulfates and hyaluronic acid, with lesser amounts of keratin sulfate and herparin sulfate. Glycoproteins, the glue that holds the matrix together, include link proteins, fibronectin, chondronectin, and tissue fluid. At the core of the elastic cartilage mass, the network is at its densest. Elastic cartilage, also called yellow cartilage, is found in the pinna of the ear and several tubes, such as the walls of the auditory and eustachian canals and larynx. The function of the elastic cartilage is to keep the tubes permanently open. Elastic cartilage is similar to hyaline cartilage but contains bundles of elastin scattered throughout the matrix. This provides a tissue that is stiff yet elastic. The front of the rib cage is elastic cartilage. This enables the cage to expand with the lungs.

Elastic cartilage develops from a primitive type of connective tissue, consisting of fibroblasts and wavy bundles of fibrils that are neither elastin nor collagen. Fibroblasts secrete elastin in the fetus and the fiber bundles branch, and are crosslinked, creating a gel-like consistency. The fibroblasts are transformed into chondroblasts. As with hyaline cartilage, the fetal tissue chondrocytes differentiate from the chondroblasts at the center of the forming tissue, secreting matrix material, which then separates the individual cells from each other. During embryonic development, mesenchymal cells retract their cytoplasmic extensions and assume the rounded shape of chondroblasts. As they become tightly packed, the increased cell-to-cell contact stimulates cartilage differentiation, progressing from the center outwards to the periphery of the fetal tissue.

## 14.4. FIBROCARTILAGE

Fibrocartilage, as its name implies, is a type of cartilage arranged in a fibrous matrix that is similar to fibrous connective tissues (Figure 14.4). The resident chondrocytes are usually arranged in short rows of 3 or 4 and are separated by dense bundles of collagenous fibers. Fibrocartilage, also called white cartilage, is a specialized type of cartilage found in areas requiring

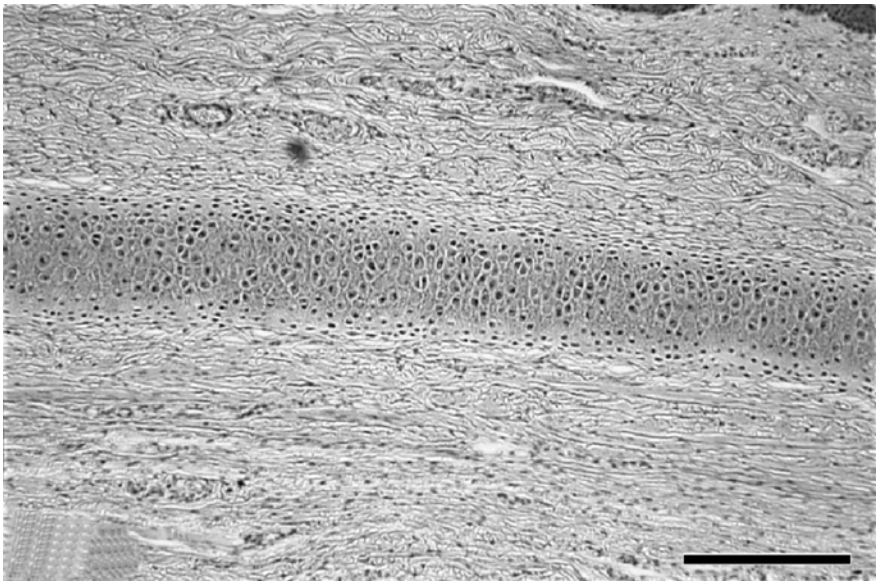


**Figure 14.3**. Elastic cartilage is the slightly darker strip of tissue in this image. Bar = 250 μm. Reprinted with permission from the JayDoc Histoweb: http://www.kumc.edu/instruction/medicine/anatomy/histoweb/index.htm.

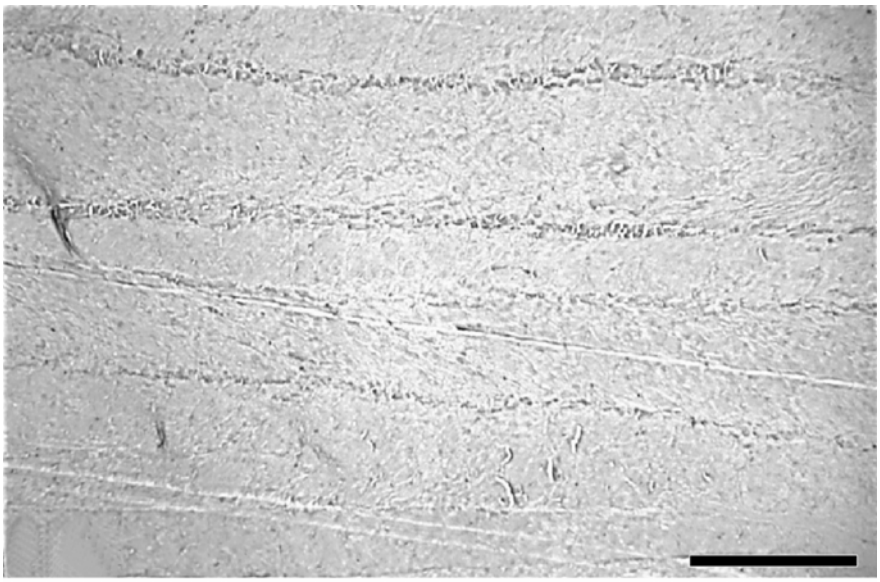


**Figure 14.4**. Fibrocartilage often displays a herringbone pattern. Bar = 250 microns. From the JayDoc Histoweb http://www.kumc.edu/instruction/medicine/anatomy/histoweb/index.htm.

tough support or great tensile strength, such as between intervertebral discs, the pubic and other symphyses, and at sites connecting tendons or ligaments to bones. There is rarely any clear line of demarcation between fibrocartilage and the neighboring hyaline cartilage or connective tissue. The fibrocartilage found in intervertebral discs contains more collagen compared to hyaline cartilage. When hyaline cartilage on joint surfaces is damaged, it is often replaced with fibrocartilage, though it remains a poorer substitute.

## 14.5. THE PERICHONDRIUM

The tissue in the upper portion of Figure 14.2 is the perichondrium, a membrane of fibrous connective tissue that closely surrounds hyaline and elastic cartilage, except at the articular surfaces; fibrocartilage lacks a perichondrium. The perichondrium has two distinct layers: an outer fibrous layer and an inner chondrogenic layer. The fibrous layer contains fibroblasts that can produce collagen fibers, while the inner layer contains undifferentiated or chondrogenic cells capable of forming chondrocytes. The perichondrium also nourishes the avascular cartilage.

Two types of growth can occur in cartilage: appositional and interstitial. Appositional growth results in an increase of the diameter or thickness of the cartilage by addition of cells and matrix to preexisting surfaces. Interstitial growth results in increased cartilage mass and occurs by proliferation of cells within the tissue. Chondrocytes undergo mitosis within their lacunae but remain imprisoned in the matrix, which results in clusters of cells called isogenous groups. Growth from the perichondrium is appositional growth. Cartilage growth occurs from the perichondrium like bone growth occurs similarly from the periosteum and endosteum. If cartilage is transformed to bone, the perichondrium becomes the periosteum.

## 14.6. COMMON PROPERTIES OF THE THREE TISSUES: INTERVERTEBRAL DISC, ARTICULAR CARTILAGE AND THE MENISCUS

The intervertebral disc, articular cartilage, and the menisci are compositionally and structurally unique. Macromolecules that provide the mechanical properties of each of these tissues, namely water, collagen, and proteoglycans are similar, however. The amounts of collagen, proteoglycan, and water in articular cartilage, meniscus, and intervertebral disc are listed in Table 14.1. All three tissues are saturated poroelastic materials (Chapter 9) with a fixed charged density, an internal electrolyte solution, and the resulting charge-induced osmotic pressure (Chapter 13). The solid or matrix phase represents 20–30% of the tissue by wet weight. However, in the solid phase, the collagen type and fibrillar network are quite different in each tissue, and the distribution of the proteoglycan component is distinct for each of these three tissues. The inorganic salts dissolved in the interstitial water phase yield the ions that are required to balance the electric charges exhibited by the proteoglycans. Like any saturated poroelastic material, mechanical loading creates pressure gradients in the pore water. The movement of this pore water is essential for their function and nutrition.

Type I collagen is the major collagen of meniscus, and type II is the primary collagen of articular cartilage. Intervertebral discs contain both fibrocartilage and layers of collagen, so that significant amounts of both type I and II collagen are present, their relative concentrations depending upon location within the tissue. The quantitatively minor collagens may also make important contributions to the structure of the matrix. For example, type IX collagen, a short non-fibrillar collagen, which contains a glycosaminoglycan chain and is therefore also consid-

ered a proteoglycan, binds covalently to type II collagen fibrils and may help link fibrils together or bind fibrils to other matrix molecules. (Collagen types are discussed in Chapter 10.)

**Table 14.1**. Approximate Composition of Articular Cartilage, Meniscus, and Intervertebral Disc

| Tissue | Collagen (% dry weight) | Proteoglycan (% dry weight) | Water (% dry weight) |
|---|---|---|---|
| Articular cartilage | 50–75 | 15–30 | 58–78 |
| Meniscus | 75–80 | 2–6 | ≈70 |
| Intervertebral disc: nucleus pulposus | 15–25 | ≈50 | 70–90 |
| Intervertebral disc: annulus fibrosus | 50–70 | 10–20 | 60–70 |
| Tendon | ≈23–30 | ≈7 | ≈70 |
| Ligament | ≈23 | ≈7 | ≈70 |

Reprinted with permission from Mow et al. (1990).

In articular cartilage, proteoglycans constitute the second largest portion of the solid phase, accounting for 5–10% of wet weight. The proteoglycans of the cartilage matrix consist mainly of the large aggregating type and large non-aggregating proteoglycans, with distinct small proteoglycans also being present. Proteoglycans of cartilage contribute significantly to the compressive and swelling properties of these tissues. It is believed that the large, high-molecular-weight proteoglycan monomers contribute most significantly to these properties. These large proteoglycan monomers consist of an extended protein core with several distinct regions: an N-terminal region with two globular domains, a keratan sulfate-rich domain, a longer chondroitin sulfate-rich domain that may also contain some interspersed keratan sulfate and neutral oligosaccharide chains, and a C-terminal globular domain (Chapter 10).

The size, structural rigidity, and complex molecular conformations of normal proteoglycan aggregates make important contributions to the behavior of articular cartilage. The large size of proteoglycans will arrest or minimize diffusion or pore fluid convective transport of molecules through the extracellular matrix due to steric exclusion or intermolecular frictional effects.

As a class of chemicals, glycosaminoglycans (GAGs) are present in most forms of connective tissue. They are found in skin, bone, cartilage, tendon, heart valves, arterial walls, synovial fluid, and the aqueous humour of the eye. Chemically, they are long chains of polysaccharides, each chain consisting of a repeated sequence of two molecules called the repeating unit. These repeating units consist of a sugar molecule and a sugar molecule with an amine attached, and the nomenclature "glycosaminoglycan" is designed to reflect the sequence sugar–amine–sugar in their structure.

Water is the most abundant component of articular cartilage, meniscus, and intervertebral disc, comprising from 65 to 85% of the weight of the tissue. In the tissues, the proteoglycan solution domain contains approximately 70% of the water and the collagen intrafibrillar space contains the remaining 30%. Although water makes up 65–80% of these tissues, the effective

pore size within these tissues has been estimated from hydraulic permeation experiments to range from 30 to 65 Å. Inorganic ions such as sodium, calcium, chloride, and potassium are the common ions dissolved in the tissue water. These ions balance the fixed charges on the proteoglycans and generate significant osmotic swelling pressure (Chapter 13).

The interactions between the solid phase components, collagen, proteoglycans, glycoproteins, and other non-collagenous proteins, produce a strong, cohesive, porous, and permeable solid matrix capable of sustaining large loads for long periods. The size and complex organization of these tissues are also known to promote proteoglycan–proteoglycan networking and proteoglycan–collagen interactions. Pure proteoglycan solutions exhibit proteoglycan networks at concentrations similar to those found in situ; these networks are capable of storing energy elastically. This networking capacity of proteoglycans undoubtedly will contribute to their functional role in cartilage by maintaining and adding to the stiffness and strength of the extracellular matrix.

The charge and hydroxyl groups that are a part of proteoglycans render them soluble in solution and are able to entrain up to 50 times their weight in water. This expanded conformational state results mainly from three factors. First, to maintain electroneutrality, osmotically active counterions (e.g., $Na^+$) enter the molecular domain, resulting in an osmotic swelling pressure. Second, the negative charges on the glycosaminoglycan chains exert electrostatic repulsive forces on one another. Third, a highly solvated, extended molecule is entropically favored since it maximizes the number of possible conformational states of the molecule. Their surrounding tissue matrix dramatically alters the conformation and interactions of the proteoglycan molecules. In articular cartilage, for example, the normally water-soluble proteoglycan molecules are prevented by the collagen mesh from passing into solution; they are restrained to less than 20% of their free solution volume. Such conformational changes concentrate the neutralizing cations that give rise to a significant increase of the osmotic swelling effect (Chapter 13) and bring the fixed negative charges into closer proximity, thereby increasing the electrostatic repulsive forces. The magnitude of the osmotic pressure in articular cartilage has been measured to approach 0.35 MPa and is dependent upon the negative charge density of the proteoglycans. These internal swelling forces are balanced by tension in the surrounding collagenous network. As a result, connective tissues rich in proteoglycan possess high water content, but low hydraulic permeabilities and high compressive stiffness. The local proteoglycan units and aggregates are convoluted to form complex, three-dimensional molecules, like large and small tangles of cotton wool (Figure 14.5). Since these molecules have the property of attracting and retaining water, the water-absorbing properties are similar to those of a ball of cotton wool (Bogduk, 1997).

Collagen–collagen interactions consist of inter- and intramolecular crosslinks between collagen molecules. These crosslinks interlock the molecules and increase the tensile strength and stiffness of articular cartilage. Collagen–proteoglycan interactions involve mechanical entanglement, electrostatic bonds, and excluded volume effects. Physical entanglement is felt to be assisted by the complexing of proteoglycan monomers to form large multimolecular aggregates. Proteoglycan networking also helps to immobilize the proteoglycans in the collagen meshwork. Proteoglycan–collagen interactions are thought to also play significant roles in regulating collagen fibril formation, size, and spacing. For example, type XI collagen, a minor fibrillar collagen, may be involved in controlling the diameter of type II fibrils. Consequently, structural interactions not only have strong influences on the mechanical properties of a given tissue but also have important implications in terms of its assembly and organization (see Chapter 10).

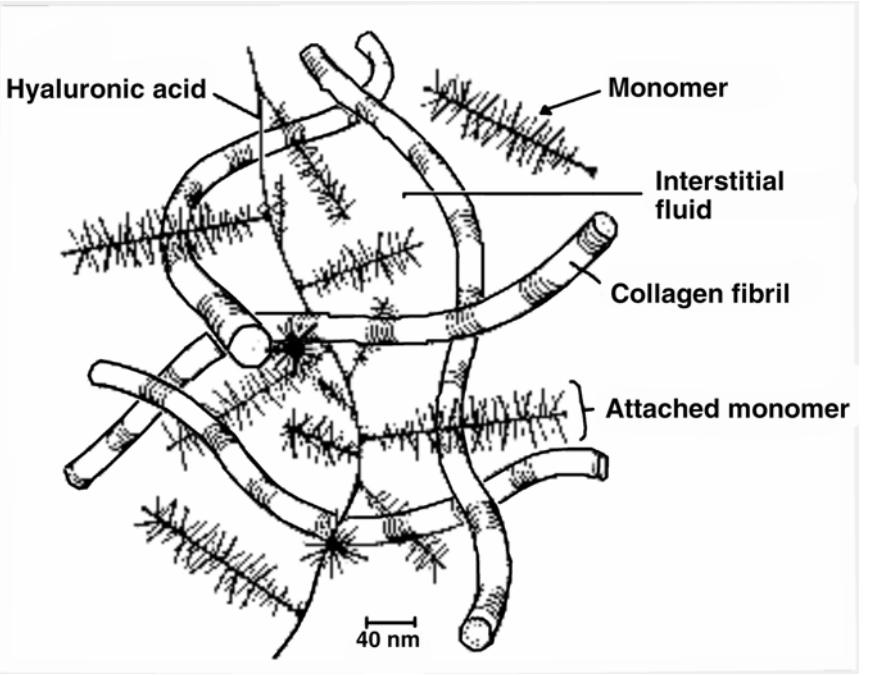



**Figure 14.5**. Collagen network interacting with proteoglycan network in the extracellular matrix. Reprinted with permission from Mow et al. (1992).

## 4.7. THE INTERVERTEBRAL DISC (IVD)

The intervertebral discs are located between the vertebral bodies (Figure 14.5) and serve as both a shock absorber and a hinge to allow movement of the spine by bending compliance. The intervertebral joints of the spine are not diarthroidal joints, as they are fibrocartilaginous and their compliance is by bending rather than articulation (Figure 14.6). The overall structure of the IVD consists of the thick annulus fibrosus on the outside of the disc and the nucleus pulposus that is in the center of the disc (Figure 14.7; see also Figure 13.4). Although the nucleus pulposus is quite distinct in the center of the disc, and the annulus fibrosus is distinct at its periphery, there is no clear boundary between the nucleus and the annulus within the disc; the peripheral parts of the nucleus pulposus merge with the deeper parts of the annulus fibrosus. A third component of the intervertebral disc comprises two layers of cartilage that cover the top and bottom aspects of each disc. Each is called a vertebral endplate (Figure 14.7). The vertebral endplates separate the disc from the adjacent vertebral bodies, and it is debatable whether the endplates are strictly components of the disc or whether they actually belong to the respective vertebral bodies. The interpretation employed here is that the endplates are components of the intervertebral disc. Normally there are no blood vessels in the disc and no nerves in the disc. The body's weight is carried on the spine with the vertebral body above pressing down on the disc with an oscillation occurring during each step while walking. With each oscillation the nucleus pulposus, which is normally soft, squishes down and out against the annulus fibrosus on the sides. The pressure is then transferred to the annulus fibrosus, which bulges out slightly with each step, and then rebounds to an uncompressed state like a spring. The experiment described in §13.8 on the modeling of a swelling and compression experiment on the

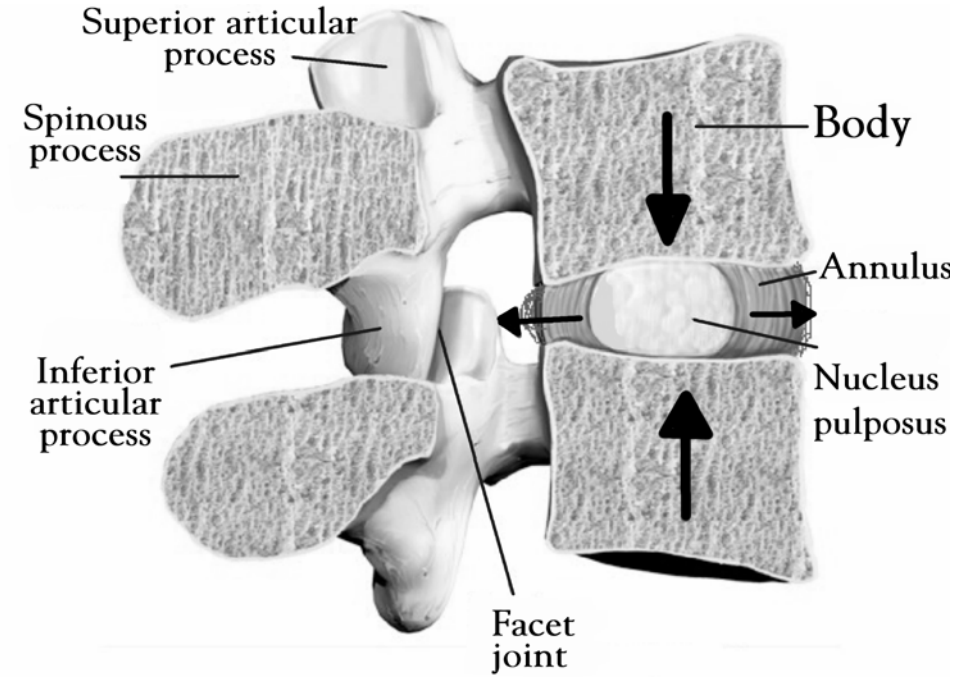



**Figure 14.6**. Axial loading of the spine and the intervertebral disk. http://www.apmsurgery.com/images/Spinal_Forces.bmp.

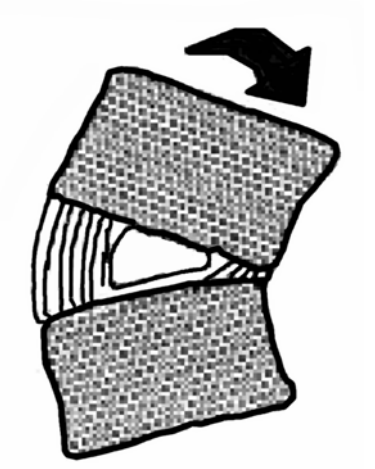


**Figure 14.7**. Bending compliance of the IVD. Reprinted with permission from Panagiotacopulos et al. (1977).

intervertebral disc employed cylindrical specimens that were made from the annulus fibrosus of the intervertebral disc at the L6–L7 level of large dogs.

The nucleus pulposus is composed of a semi-fluid or gelatinous material and is located in the ovoid central region of the center of the disc. It has the consistency of toothpaste in the healthy intervertebral discs of young adults (Bogduk, 1997). Embryologically, the nucleus pulposus is a remnant of the notochord. Histologically, it consists of a few cartilage cells and some irregularly arranged collagen fibers, dispersed in a medium of semi-fluid ground substance. The nucleus pulposus deforms under vertical compressive spinal loading, but its near water-like character and the high bulk modulus of water (2.3 GPa) mean that it will deform laterally rather than compress its volume and thus transmit pressure laterally as well as in reaction to the vertical compressive spinal loading. A suitable analogy is a balloon filled with water. Compression of the balloon deforms it; pressure in the balloon rises and stretches the walls of the balloon in all directions.

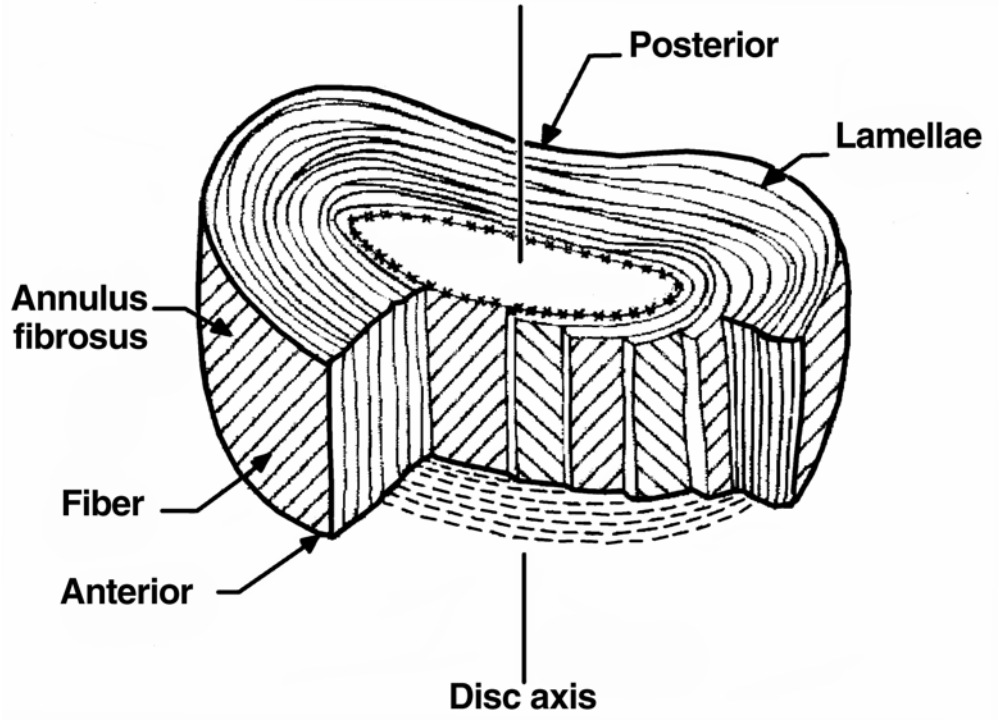



**Figure 14.8**. Some of the prominant structures of the IVD. Reprinted with permission from Panagiotacopulos et al. (1977).

The annulus fibrosus is composed of a fibrocartilaginous material that is arranged in an onion-like structure consisting of a concentric system of 11 to 20 layers or lamellae (from the Latin *lamella*, meaning "little leaf"), as illustrated in Figure 14.8. These lamellae may be separated for mechanical testing (Figure 14.9). The lamellae are thick in the anterior and lateral

portions of the annulus, thicker towards the center of the disc, but posteriorly they are finer and more tightly packed. Consequently, the posterior portion of the annulus fibrosus is thinner than the rest of the annulus. Within each lamella, the collagen fibers lie parallel to one another, the orientation of all the fibers in any given lamella being ±65–70° from the vertical, as may be seen in Figure 14.7. Each vertebral endplate is a layer of cartilage about 0.6–1 mm thick that covers the transverse surface of the vertebral body. The two endplates of each disc cover the nucleus pulposus in its entirety, but peripherally they fail to cover the entire extent of the annulus fibrosus. Histologically, the endplate consists of both hyaline cartilage and fibrocartilage. Hyaline cartilage occurs toward the vertebral body and is most evident in neonatal and young discs. Fibrocartilage occurs towards the nucleus pulposus, and in older discs the endplates are virtually entirely fibrocartilage. The fibrocartilage is formed by the insertion into the endplate of collagen fibers of the annulus fibrosus.

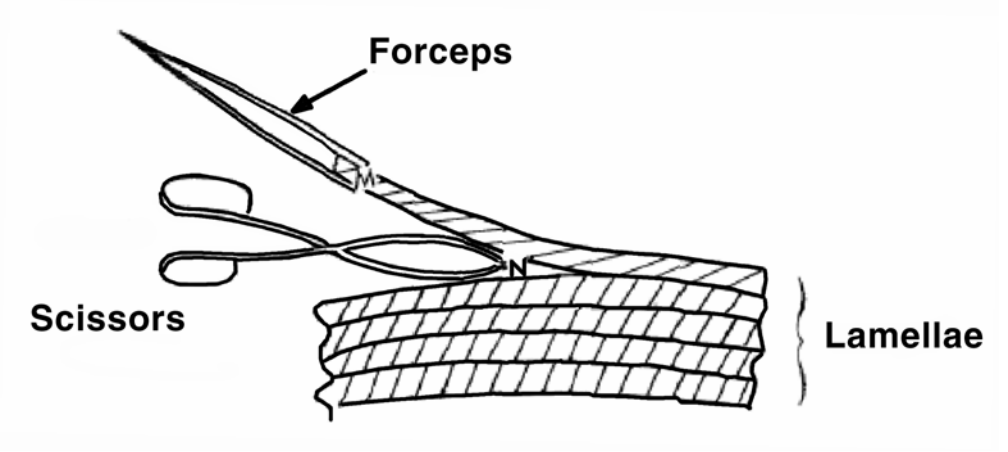



**Figure 14.9**. The peeling of a lamella from an annulus fibrosus. Reprinted with permission from Panagiotacopulos et (1977).

## 14.8. ARTICULAR CARTILAGE

*Articular cartilage* is the thin layer of hyaline cartilage (0.5–5 mm thick) covering the articular surfaces of the bones participating in a synovial joint. It is also called arthroidal, diarthroidal, or investing cartilage. Physiologically, it is virtually an isolated tissue, devoid of blood vessels, lymph channels, and nerves. Furthermore, its cellular density is less than that of any other tissue. It has an extremely low coefficient of friction, as it serves to provide smooth motion at joints. It also functions as a shock absorber. It is a soft tissue made up of a proteoglycan matrix reinforced with collagen. It is highly hydrated, 60 to 85% water, and the water exists in pores 2 to 6 nm. Permeability is low, from $10^{-14}$ to $10^{-15}$ $m^4$ /N-s, and the intrinsic permeability is from $10^{-15}$ to $10^{-16}$ $m^2$ assuming the viscosity of the fluid to be that of water, $\mu = 0.1$ N-s/$m^2$.

Chondrocytes, the sparsely distributed cells in articular cartilage, account for less than 10% of the tissue's volume. Despite their sparse distribution, chondrocytes manufacture, secrete, and maintain the organic component of the extracellular compartment, the matrix. The

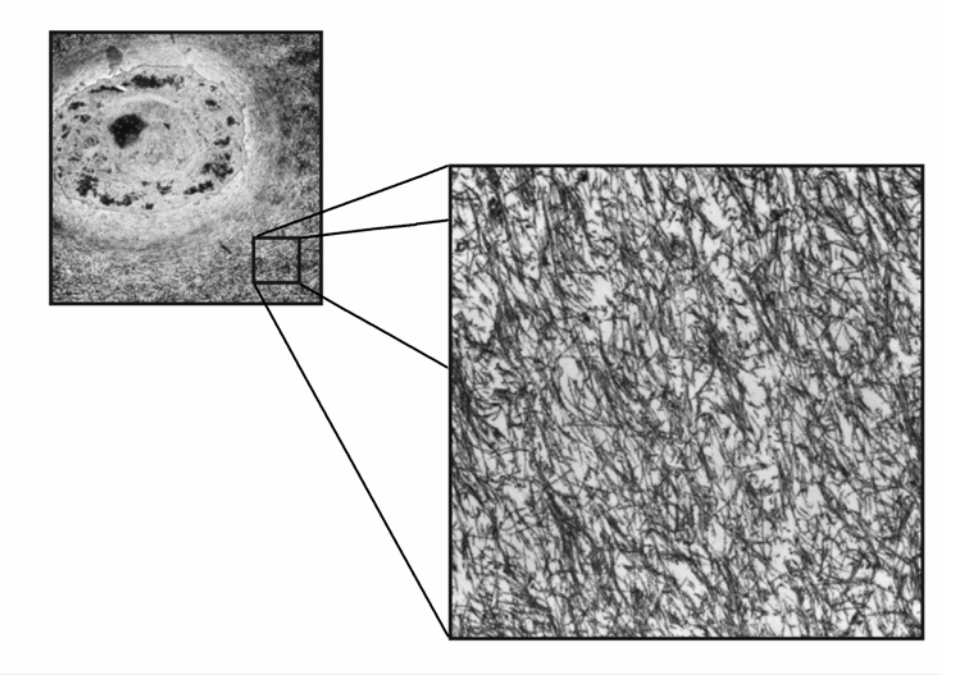


**Figure 14.10**. The chondrocyte and extracellular matrix of articular cartilage showing the underlying collagen fibril meshwork (transmission electron microscopy). Reprinted with permission from Eyre (2002).

ECM immediately surrounding the chondrocytes is referred to as the territorial or pericellular matrix and is easily distinguished from the interstitial matrix (Figure 14.10); it is surrounded by a capsule. It is suggested that the chondrocyte, its pericellular matrix, and capsule together constitute the "chondron," a primary functional and metabolic unit of cartilage that functions to protect the integrity of the chondrocyte and its pericellular microenvironment during compressive loading (Poole et al., 1987, 1988). The matrix is composed of a dense network of fine collagen (type II) fibrils enmeshed in a concentrated solution of proteoglycans (PGs). The collagen content of cartilage tissue ranges from 10 to 30% by net weight and the PG content from 3 to 10% by wet weight; the remaining 60 to 87% is water, inorganic salts, and small amounts of other matrix proteins, glycoproteins, and lipids. Collagen fibrils and PGs are the structural components supporting the internal mechanical stresses that result from loads being applied to the joint cartilage; it is these structural components, together with water, that determine the biomechanical behavior of this tissue.

The collagen in articular cartilage is inhomogeneously distributed, giving the tissue a layered character. A zonal arrangement for the collagen network is shown schematically in Figure 14.11. The organization at this level can actually be divided into the four zones described in the paragraphs below; the surface, middle, deep, and tidemark zones. The tidemark zone is the interface between articular cartilage and the calcified cartilage beneath. The amount of collagen decreases in each zone moving closer to the bone, dropping to 68% in the middle zone. This inhomogeneity of fiber orientation is mirrored by zonal variations in collagen content, which is highest at the surface and then remains relatively constant throughout the deeper zones. This layering inhomogeneity appears to function in a manner to distribute the stresses more uniformly across the loaded regions of the joint tissue.

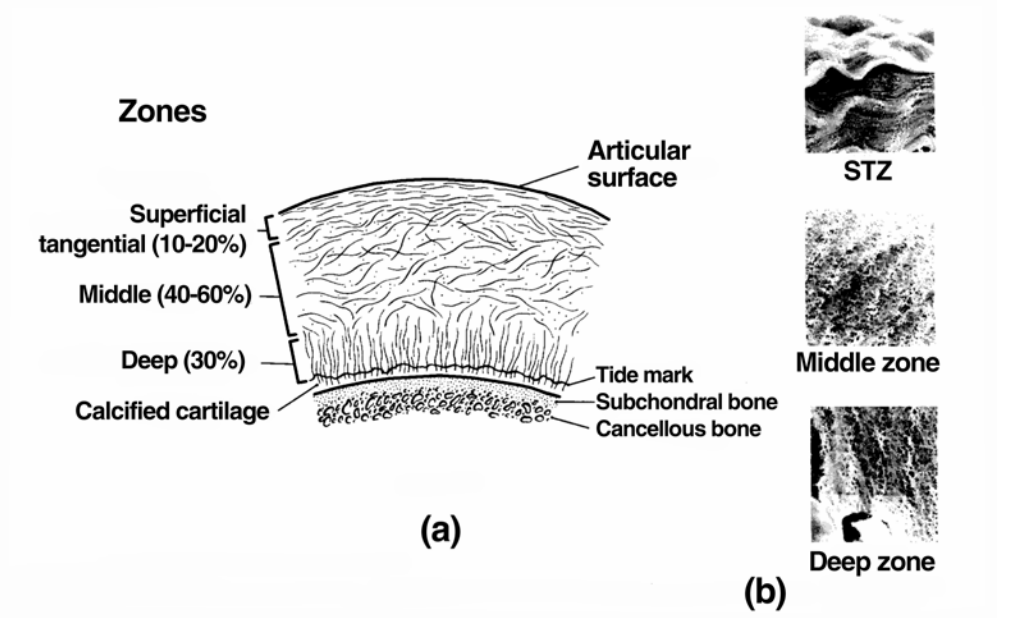



**Figure 14.11**. The zones contain different collagen organization as well as different amounts of proteoglycans. The superficial or tangential zone contains the highest collagen content: about 85% by dry weight. The amount of collagen decreases in each zone moving closer to the tidemark, dropping to 68% in the middle zone. Reprinted with permission from Mow et al. (1992).

The surface or superficial tangential zone, which represents 10–20% of the total thickness and contains the highest collagen content (about 85% by dry weight), is composed of sheets of fine, densely packed fibers randomly arranged in planes parallel to the articular surface. The collagen fibrils are oriented parallel to the joint surface, indicating that a primary function of this zone may be to resist shear stresses. The anisotropy of the articular cartilage surface structure is related to the collagen fiber arrangements in the planes parallel to the articular surface. This structure is made visible by piercing the articular surface with a small awl with a circular cross-section and viewing the subsequent deformation of the circular surface hole into a hole with an elliptical cross-section. The set of many such deformed holes are called *split lines*, and they reveal the underlying collagenous structure (Figure 14.12). The origin of the pattern is related to the directional variation of the tensile stiffness and strength characteristics of articular cartilage. An illustration of a circle being deformed into an ellipse in a homogenous deformation (Chapters 3 and 15) is given in Figure 15.4. The split lines are often used as part of a material-fixed reference coordinate system for the tissue (see §14.10). Variations in collagen fiber crosslink density, as well as variations in collagen and PG interactions, also contribute to articular cartilage anisotropy.

In the middle zone, which represents about 40–60% of the total thickness, the randomly oriented and homogeneously dispersed fibers are farther apart. In the deep zone, which represents about 30% of the total thickness, the fibers come together, forming larger, radially oriented fiber bundles. Below the deep zone is the "tidemark" zone, where the fiber bundles of the deep zone cross the interface between articular cartilage and the calcified cartilage, to enter the calcified cartilage and form an interlocking system that anchors the cartilage to the underlying bone.

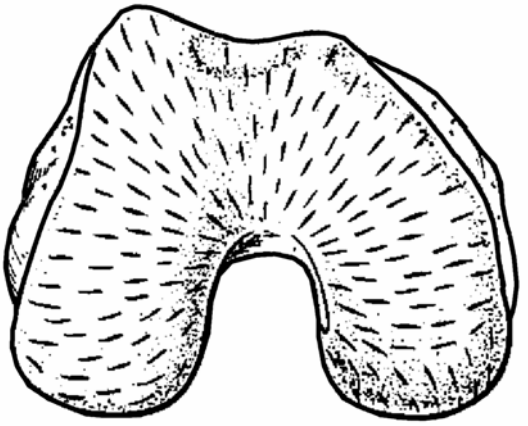


**Figure 14.12**. The split line pattern on the surface of a human femoral condyle. Reprinted with permission from Hultkrantz (1898).

## 14.9. LUBRICATION IN SYNOVIAL JOINTS

A great diversity of mechanical loading is experienced by a synovial joint in the human lower limbs, and yet under normal circumstances the cartilage surface sustains little wear. Consider the different force levels experienced by the human hip or knee joints when the associated human is sleeping, sitting, standing, walking, running, broad jumping, and tackling or being tackled in football or rugby. Light loads are sustained during high-speed motions such as the swing phase of walking or running and impact loads of large magnitude and short duration during such activities as jumping or at the heel strike of walking. Sophisticated lubrication processes are suggested by the fact that these activities cause little wear on the cartilage of the joint. As part of, or coupled with, these sophisticated lubrication processes are bearing load-driven convected transport processes that move fluid out of the articular cartilage and cause the articular cartilage to imbibe fresh synovial fluid containing nutrients for the cells resident in the cartilage. A schematic representation of this fluid exudation and subsequent imbibing due to passage of a bearing loading over the articular cartilage surface is shown in Figure 14.13. As with bone, it is likely that convection of nutrients due to mechanical loading of the tissue is the more likely primary mechanism for nourishment of the resident cells than diffusion, a mechanism suggested in the older literature.

The coefficient of friction of animal bearings is extraordinarily low, permitting human bearings to endure for human lifetimes that extend 8 or 9 decades. The majority of measurements of the coefficient of friction of articular cartilage report its value to be from 0.002 to 0.04. For comparison, the coefficient of friction of steel on steel is 0.6 and that of ice on ice at 0°C is from 0.01 to 0.1, so the coefficient of friction of articular cartilage is less than the coefficient of friction of ice on ice. The quote at the beginning of this chapter expresses the fact that the mechanism that makes the low coefficient of friction for articular cartilage possible is still unknown, despite more than a half century of research on the topic.

Different types of lubrication are described in the paragraphs that follow. There are two main types of lubrication that are thought to occur in articular cartilage — fluid film lubrica-

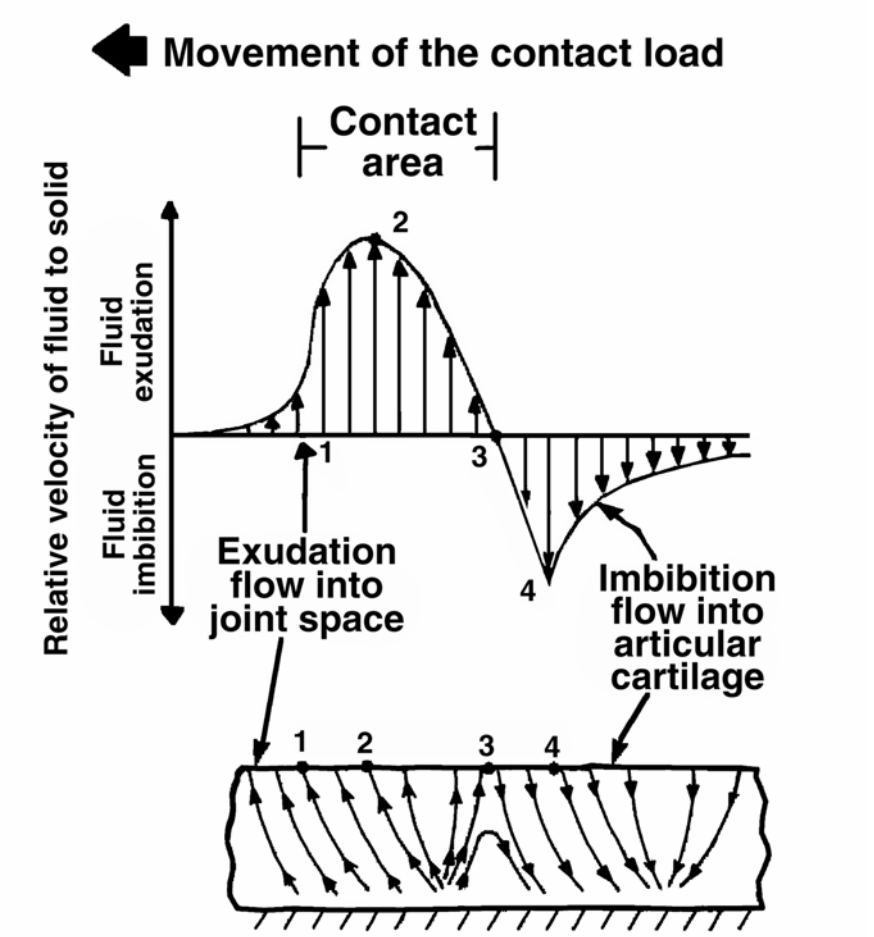



**Figure 14.13**. Fluid exchanges between the fluid in the articular cartilage and synovial fluid. Between points 1 and 3 the contact load fluid is driven from the articular cartilage and reabsorbed at the trailing edge of the contact load, between points 3 and 4. Adapted with permission from Mow et al. (1989).

tion and boundary lubrication. Both these types of lubrication are thought to occur in articular cartilage in order to deal with the diverse mechanical loading that the tissue experiences. Other types of lubrication are also described below, as they are possible in articular cartilage or helpful in understanding lubrication mechanisms in general.

In *fluid film lubrication* a thin film separates two bearing surfaces that are sliding relative to each other and there is no surface-to-surface contact. The pressure created in fluid film by the relative motion balances the load transverse to the bearing surfaces. The term "fluid film lubrication" includes slider, squeeze file, and elastohydrodynamic lubrication. These modes of lubrication require generally high relative sliding speeds between two solid surfaces to create a lubricant film with significant load-bearing capacity. Two modes of fluid film lubrication in machinery with rigid bearing surfaces are illustrated in Figure 14.14; the fluid film thickness associated with these bearings is usually less than 20 μm. In slider or hydrodynamic lubrication a lifting pressure is generated in the wedge of fluid as the bearing motion transports the fluid into the gap between the surfaces (the left panel of Figure 14.14). In squeeze film lubrica-

tion the bearing surfaces move toward each other and in the gap between the two surfaces the pressure is generated by pushing the fluid lubricant out of the gap (the right panel of Figure 14.14). For both slider and squeeze film lubrication the magnitude of the bearing pressure generated depends upon the fluid viscosity.

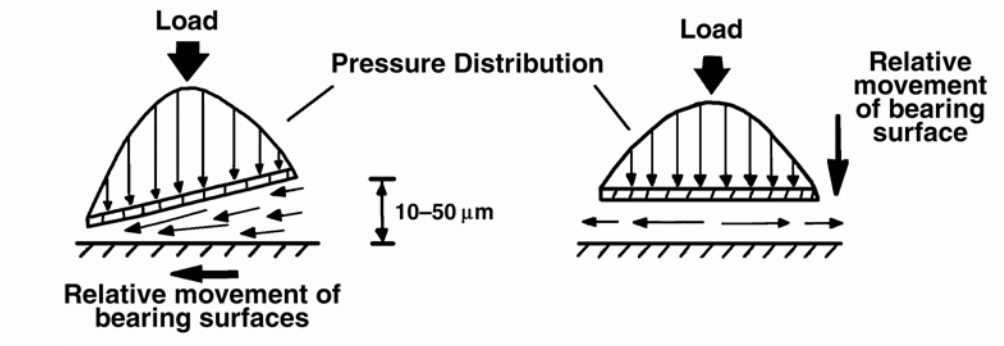



**Figure 14.14**. The panel on the left illustrates sliding or hydrodynamic lubrication in which non-parallel rigid surfaces move relative to each other and thereby form a wedge of fluid between the surfaces. A lifting pressure between the surfaces, proportional to the viscosity of the fluid, is generated. The panel on the right illustrates squeeze-film lubrication in which parallel rigid surfaces are moved together, squeezing the fluid film from between the surfaces. Again a lifting pressure between the surfaces, a lifting pressure that is proportional to the viscosity of the fluid, is generated. Adapted with permission from Mow et al. (1989).

*Elastohydrodynamic lubrication* occurs when the bearing material is not rigid but relatively soft, like articular cartilage. Sliding and squeeze film lubrication are shown in the left and right panels of Figure 14.15, respectively, in the case of rigid bearings. In the case of soft bearings, sliding and squeeze film elastohydrodynamic lubrication are shown in the left and right panels of Figure 14.16, respectively; note the deformation of the bearing material indicated by the bearing shape change in both panels of Figure 14.16. Bearing deformation and interface friction are considered to be the mechanisms of energy dissipation in articular cartilage. The load-bearing capacity of deformable bearings is increased over equivalent rigid bearings because the deformations tend to increase the surface area, beneficially altering film geometry. Due to increasing bearing contact area, the lubricant is retained longer between the bearing surfaces, generating a longer-lasting lubricant film. It is thought that both the sliding and squeeze type elastohydrodynamic fluid films play important roles in joint lubrication. Mow et al. (1989) considered the various types of joint lubrication that occur during human walking. During the swing phase, when loads on the joint are minimal, a substantial layer of synovial fluid film is probably maintained. After the first peak force, at heel strike, a supply of fluid lubricant is forced from the articular cartilage. During the high load of the stance phase, a squeeze film is created and the thickness of the fluid film will begin to decease. It is possible that a fresh supply of fluid film is generated at toe-off, thereby providing lubricant during the next swing phase. "Toe-off" is the second peak force during the walking cycle; it occurs just before the toe leaves the ground, when the joint is swinging in the opposite direction.

By contrast, there is no fluid film in *boundary lubrication*, the term used to describe the situation in which the lubricant or bearing material is between surfaces moving at low relative speeds and transmitting high loads (e.g., oil lubricants of machine gears). In articular cartilage,

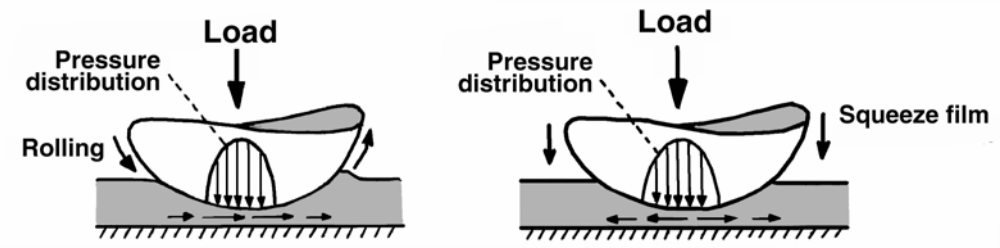



**Figure 14.15**. In fluid film lubrication, rigid bearings create high pressures. Sliding or hydrodynamic lubrication is illustrated on the left. Squeeze-film lubrication is illustrated on the right. Adapted with permission from Mow et al. (1989).

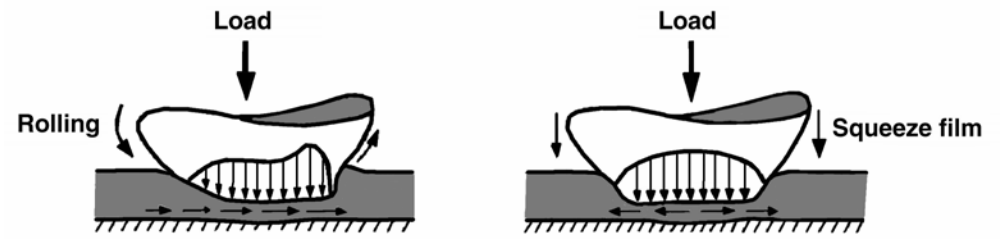



**Figure 14.16**. In elastohydrodynamic fluid film lubrication, deformable bearings create lower pressures than rigid bearings. Elastohydrodynamic lubrication for a slider bearing is illustrated on the left; note the plowing effect to the right of the upper bearing surface due to the unidirectional or sliding motion. Elastosqueeze-film lubrication is illustrated on the right. Adapted with permission from Mow et al. (1989).

boundary lubrication is considered to involve a single monolayer of lubricant molecules adsorbed on each bearing surface. This prevents direct, surface-to-surface contact and eliminates most surface wear. Boundary lubrication is fairly independent of the physical properties of either the lubricant (e.g., its viscosity) or the bearing material (e.g., its stiffness), but instead depends almost entirely on the chemical properties of the lubricant. In synovial joints the glycoprotein *lubricin* is a major component of synovial fluid and is responsible for boundary lubrication. Lubricin is adsorbed as a macromolecule monolayer to each articulating surface (Figure 14.17). These two layers, ranging in combined thickness from 1 to 100 nm, are able to carry loads and appear to be effective in reducing friction. Rhee et al. (2005) created lubricin-mutant mice. Lubricin is a product of the gene proteoglycan 4, which also encodes the related gene products that include *superficial zone protein*. Superficial zone protein is expressed by superficial zone chondrocytes at the cartilage surface but not by intermediate or deep zone chondrocytes. Following Rhee et al. (2005), the term "lubricin" is also used when referring to the protein products expressed by cells within articulating joints. The mice lacking lubricin were viable and fertile, and in the newborn period their joints appeared normal. As the mice aged, Rhee et al. (2005) observed abnormal protein deposits on the cartilage surface and disappearance of underlying superficial zone chondrocytes. In addition to cartilage surface changes and subsequent cartilage deterioration, intimal cells in the synovium surrounding the joint space became hyperplastic, which further contributed to joint failure. The investigators noted that tendon and tendon sheath involvement was present in the ankle joints of the lubricin-mutant mice; morphologic changes and abnormal calcification of these structures were also

observed. They concluded that lubricin has multiple functions in articulating joints and tendons that include protection of surfaces and control of synovial cell growth. In any bearing the effective mode of lubrication depends on the applied loads and the relative velocity of bearing surfaces. Adsorption of lubricin to articular surfaces seems to be most important under severe loading conditions, when contact surfaces are moving at high relative speeds.

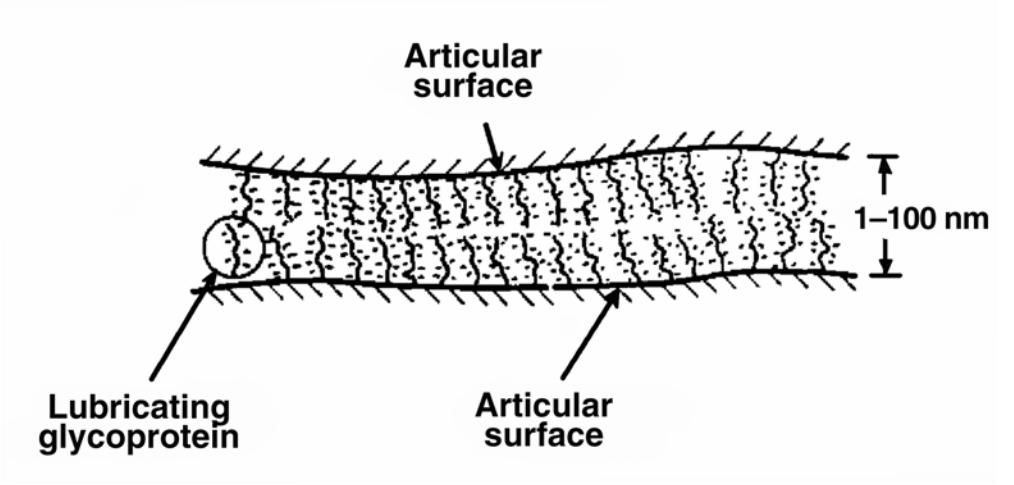



**Figure 14.17**. Boundary lubrication of articular cartilage; the load is carried by a monolayer of the lubricating protein lubricin. This protein is adsorbed onto the two opposing surfaces in the joint. Reprinted with permission from Mow et al. (1989).

*Boosted lubrication* is another mechanism by which the articular cartilage surfaces might be protected during joint articulation. In this lubrication mechanism the solvent component of the synovial fluid actually passes into the articular cartilage during squeeze film action, leaving a residue of hyaluronan molecules in the fluid film. A fluid with an increasing concentration of larger particles will become more viscous than the carrier fluid (the usual synovial fluid). Furthermore, this viscosity will increase as the two articular surfaces approach each other because the hyaluronan molecules in the synovial fluid will find it more difficult to escape from the gap between the surfaces because they are larger than the other particles (Figure 14.18). The smaller particles, the water and small solute molecules, can still escape with ease into the articular cartilage through the cartilage surface and laterally into the joint space at the periphery of the joint. Under extreme loading conditions, such as during an extended period of standing following impact, the fluid film may be eliminated, allowing surface-to-surface contact. The surfaces, however, will probably still be protected, either by a thin layer of ultrafiltered synovial fluid gel or by the adsorbed lubricin monolayer.

Synovial fluid is described as a non-Newtonian fluid because its viscosity $\mu$ is not a constant as it is in the constitutive equation for a Newtonian fluid (6.326N), but depends upon the rate of deformation (or rate of strain or rate of shearing) and also because synovial fluid exhibits a normal stress effect perpendicular to the shear direction. The viscosity of synovial fluid decreases with increasing strain rate, a phenomenon referred to as shear thinning. Normal synovial fluid is a clear to yellow, highly viscous fluid composed primarily of serum, which is similar to blood plasma except there are fewer proteins. Long chains of hyaluronic acid give

synovial fluid its non-Newtonian character. The viscosity of hyaluronic acid samples plotted against shear rate is shown in Figure 14.19. The higher-molecular-weight hyaluronic acid samples showed significant shear thinning effects; however, the 0.75-M molecular weight fluid displayed nearly Newtonian behavior. The rheological properties of high-molecular-weight hyaluronic acid solutions are representative of synovial fluid from healthy joints (Conrad, 2001). The viscoelastic properties of synovial fluid are illustrated in Figure 14.20 by plots of the loss and storage moduli, $G''$ and $G'$, respectively (Chapter 7). At low frequencies the loss modulus is much larger than the storage modulus ($G'' >> G'$) and the fluid behavior is largely viscous. As the frequency increases, both moduli increase in magnitude. For frequencies greater than 2 rad/s the storage modulus exceeds the loss modulus and elastic behavior dominates. This is consistent with the shear thinning behavior mentioned above. Frequencies associated with walking (3 rad/s) and running (15.7 rad/s) lie in a range where elastic forces dominate. With age, both the storage and loss moduli decrease and $G''$ contributes more significantly at all frequencies (Truskey et al., 2004).

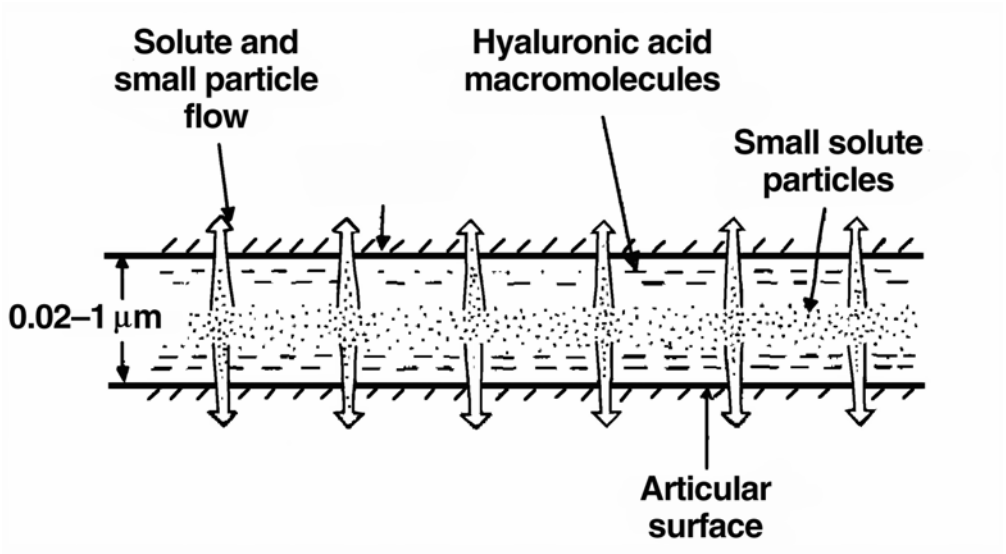



**Figure 14.18**. This figure illustrates the ultrafiltration of synovial fluid into a more viscous gel. As the bounding articular surfaces come together the small solute molecules migrate into the articular cartilage, leaving the larger HA molecules in the domain between the surfaces. By this mechanism the concentration of these macromolecules in the domain between the surfaces increases, effectively increasing the viscosity of the remaining fluid. This type of lubrication is called boosted lubrication. Reprinted with permission from Mow et al. (1989).

Diarthroidal joints appear to experience several lubrication processes, fluid film lubrication and boundary lubrication with lubricin, and different combinations of the two processes. Boundary-lubricated surfaces typically have a coefficient of friction one or two orders of magnitude greater than those of surfaces lubricated by a fluid film. As noted above, intact synovial joints have an extremely low coefficient of friction, approximately 0.02, suggesting that synovial joints are lubricated, at least in part, by the fluid film mechanism. It is quite possible that synovial joints use the mechanism that will most effectively provide lubrication under current loading conditions. Unresolved, though, is the manner in which synovial joints generate the fluid lubricant film.

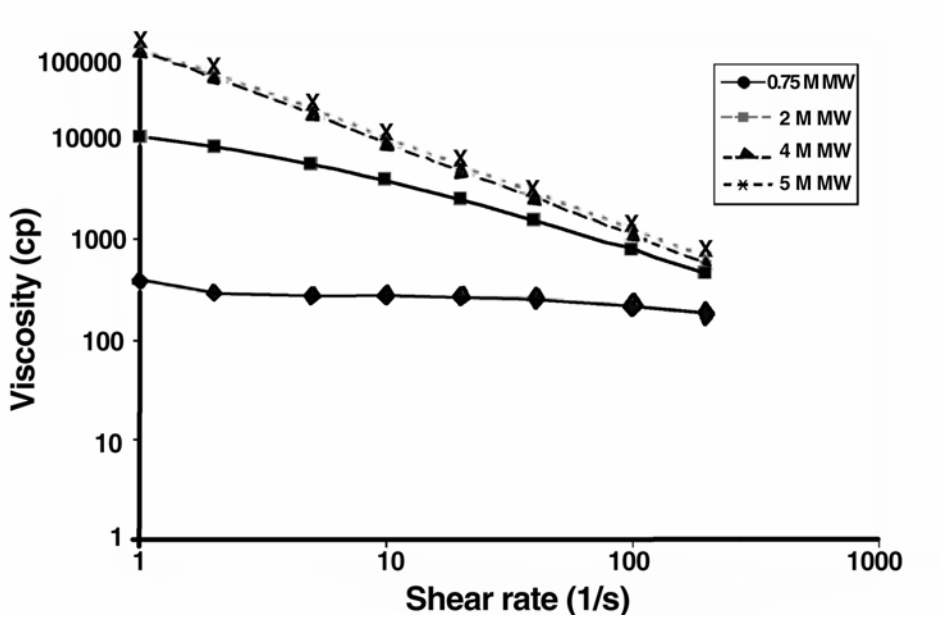



**Figure 14.19**. Viscosity plotted against shear rate for non-Newtonian hyaluronic acid samples tested on the cone-plate viscometer (log–log plot). High-molecular-weight (HMW) hyaluronic acid samples showed significant shear thinning effects; however, the 0.75 M HMW fluid displayed nearly newtonian behavior. It is expected that the rheological properties of HMW hyaluronic acid solutions are representative of synovial fluid from healthy joints. Reprinted with permission from Conrad (2001).

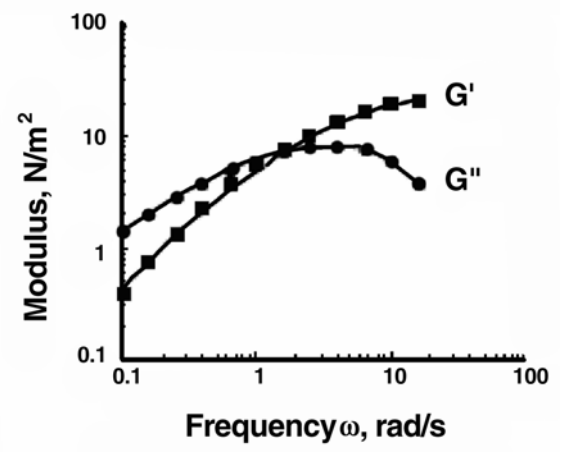



**Figure 14.20**. Storage and loss moduli for human synovial fluid. Reprinted with permission from Balazs and Gibbs (1970).

Articular cartilage, like all surfaces, is not perfectly smooth; asperities project from the surface. In synovial joints, then, situations may occur wherein the fluid film thickness is of the same order as the mean articular surface asperity. At such times boundary lubrication between the asperities may come into play. If so, a mixed mode of lubrication is operating, with the

joint surface load sustained both by the fluid film pressure in areas of no contact and by the boundary lubricant lubricin in the areas of asperity contact. In mixed lubrication it is probable that most of the friction (which is still extremely low) is generated in the boundary-lubricated areas while most of the load is carried by the fluid film.

## 14.10. THE MECHANICAL MODELING OF ARTICULAR CARTILAGE BEHAVIOR

The mechanical modeling of articular cartilage behavior is a still -developing research topic. The use of linear continuum models began in the early 1980s with the use of poroelastic models in which fluid and matrix constituents were constrained to be incompressible (the biphasic theory) and continue to be applied today to model some aspects of articular cartilage behavior. These models of articular cartilage assumed that the collagen–proteoglycan matrix was an intrinsically incompressible, porous-permeable solid matrix and that the interstitial fluid was an incompressible fluid. This particular model is developed in Chapter 9 in the general case of the theory in which incompressibility of constituents is not assumed, so that it could be applied to hard as well as soft tissues. Also in Chapter 9, the solution to the experimentally important problem of unconfined compression of a poroelastic cylinder (with both compressible and incompressible constituents) was presented. This model has been able to describe the response of articular cartilage in confined compression creep, stress-relaxation, and dynamic loading (Mow et al., 1980; Lee et al., 1981; Soltz and Ateshian, 1998, 2000b).

The second phase of development of linear models for articular cartilage was initiated when it was realized that it is necessary to account for the fact that the negatively charged proteoglycans in articular cartilage produce an osmotic pressure that swells the tissue and contributes to its compressive stiffness (Chapter 13). Proteoglycans are also responsible for various electromechanical effects such as streaming potentials and currents and reduced tissue permeability. To model these effects the poroelastic model was extended using the theory of mixtures to include cations and anions as constituents of the fluid and solid matrix material. Lai et al. (1991) proposed such a mixture theory (called the triphasic theory) as an extension of the poroelastic model with incompressible constituents (biphasic) theory, where proteoglycans are modeled as a negative charge density fixed to the solid matrix and monovalent ions in the interstitial fluid modeled as additional fluid phases. This model was later extended to incorporate two bivalent ions by Huyghe and Janssen (1997) and multiple polyvalent ions by Gu et al. (1998). A simple version of this theory is described in Chapter 13. Thus, these useful models of articular cartilage behavior are described elsewhere in the text, and only the limitations of these theories due to the assumptions of linearity upon which they are based will be discussed here.

Linear models have significant advantages because solution of problems is generally straightforward and often easy. However, the assumptions of small strains and constitutive linearity in the linear poroelasticity theories restrict their application to a limited range of articular cartilage behavior. The restriction to small strains is often referred to as the geometric linearity assumption to distinguish it from the linear relation between stress and strain (Hooke's law) that is referred to as constitutive linearity. Both assumptions are made in linear poroelastic theory and both are not satisfied in certain ranges of articular cartilage behavior. Recall that the criterion for infinitesimal deformations or small strains is that the square of the components of displacement gradient tensor (3.37) must be small compared to their own values. The movement of the boundary of an object in a boundary-value problem formulated in linear elasticity or linear poroelasticity is a term proportional to the square of the components

of displacement gradient tensor (3.37), which are neglected. This means that the movement of a boundary of an object in a boundary-value problem in these linear theories is negligible in infinitesimal deformations. In particular, the movement of the boundaries of pores is negligible, although the volumetric strain of the pore volume is not. For this reason, in linear poroelasticity, the volume of the pores can change even though the permeability must be a constant. In the remainder of this section, some of the properties of articular cartilage that deviate from the features of a linear poroelastic model are recounted.

There are a number of phenomena that contribute to the observed nonlinear character of articular cartilage. While these nonlinearities are a disadvantage from the viewpoint of the modeler trying to make a model of the functioning of the tissue, most modelers believe that it is precisely these nonlinearities of the tissue that endow it with its extraordinary beneficial properties in accomplishing tissue function. A prime source of nonlinearity is the anatomical variation of material properties, the inhomogeneous character of articular cartilage described in §14.7. Another contributor is the fact that these tissues experience large deformations in the physiologically normal range of their functioning. Large deformations introduce geometric nonlinearities and are characterized by nonlinear stress–strain relations. The stress–strain relation of articular cartilage is not even linear at small strain due to a tension–compression nonlinearity, as will be described below. The permeability of articular cartilage in the physiologically normal range is not a constant; it depends on the applied compressive strain.

It has been experimentally demonstrated that the permeability of articular cartilage is highly dependent upon the compressive strain and pore pressure that the tissue is experiencing. Plots of experimental measurements of articular cartilage permeability against the applied compressive strain confining the specimen for various applied pressure differences are shown in Figure 14.21. The data indicate that the permeability decreases as an exponential function of both increasing applied compressive strain and/or increasing applied pressure. In the absence of a pore pressure, the strain is the determining variable for cartilage permeability, and the intrinsic strain-dependent permeability relationship may only be defined in the limit of zero pore pressure. An exponential constitutive law for the intrinsic isotropic strain-dependent permeability function has been used to describe this behavior (Lai and Mow, 1980):

$$\hat{\mathbf{K}} = \frac{k}{\mu}\hat{\mathbf{U}}\,,\; k = k_o e^{M\mathrm{tr}\mathbf{E}} \tag{14.1}$$

where the trace of the strain tensor, tr**E**, is a measure of the volume change per unit volume of the solid matrix, and $k_o$ and $M$ are two intrinsic material properties. The dimensions of the intrinisic permeability tensor $\hat{\mathbf{K}}$ are $m^2$, $k_0$ has the units of permeability, N-s/$m^4$ (see Figure 14.21), $\mu$ has the dimensions of N-s/$m^2$, and $M$ is dimensionless, with values that range from 2 to 20. In order to account for the strain dependence of permeability (14.1), a slight modification in the development of the equation governing pore pressure in poroelasticity must be accomplished. The equation governing the pore pressure in incompressible poroelasticity (9.53) is changed in that operator $\hat{\mathbf{O}}$ is also applied to the permeability as well as the pore pressure; thus, (9.53) is replaced by

$$\frac{\partial p}{\partial t} - \frac{K^d_{R\mathrm{eff}}}{\mu}\hat{\mathbf{O}}\cdot(\hat{\mathbf{K}}p) = -K^d_{R\mathrm{eff}}(\hat{\mathbf{U}}\cdot\hat{\mathbf{S}}^{\mathrm{d}}\cdot\frac{\partial\hat{\mathbf{T}}}{\partial t})\,. \tag{14.2}$$

When expression (14.1) for permeability is placed in (14.2) and the result expanded by differentiating by parts, the following result is obtained:

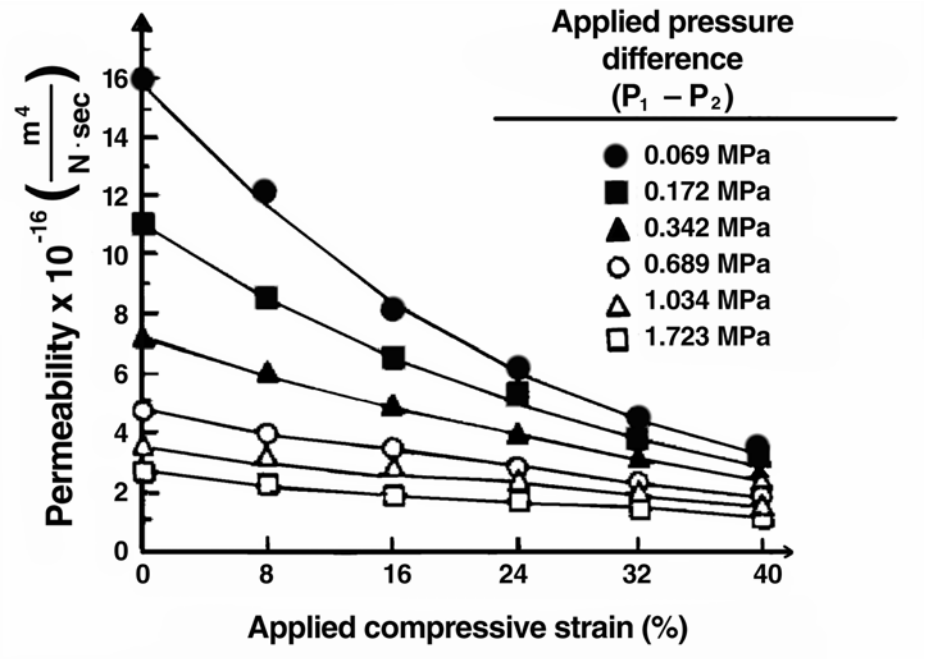



**Figure 14.21**. Plot of experimental measurements of articular cartilage permeability against the applied compressive strain confining the specimen for various applied pressure differences ($P_1 - P_2$). The data indicate that the permeability decreased as an exponential function of both increasing applied compressive strain and increasing applied pressure. Reprinted with permission from Mow et al. (1989).

$$\frac{\partial p}{\partial t} - \frac{K^d_{Reff}}{\mu} k \nabla^2 p - \frac{K^d_{Reff}}{\mu} Mkp \nabla^2 \mathrm{tr}\mathbf{E} -$$

$$\frac{K^d_{Reff}}{\mu} 2Mk \nabla p \cdot \nabla \mathrm{tr}\mathbf{E} - \frac{K^d_{Reff}}{\mu} M^2 kp \nabla \mathrm{tr}\mathbf{E} \cdot \nabla \mathrm{tr}\mathbf{E} = -K^d_{Reff} (\hat{\mathbf{U}} \cdot \hat{\mathbf{S}}^{\mathrm{d}} \cdot \frac{\partial \hat{\mathbf{T}}}{\partial t}), \qquad (14.3)$$

since $\hat{\mathbf{O}} \cdot \hat{\mathbf{U}} = \nabla \cdot \nabla = \nabla^2$. Three extra nonlinear terms now appear in the differential equation; these terms render the equation nonlinear and thus more difficult to solve. These are the terms proportional to $\nabla^2 \mathrm{tr}\mathbf{E}$, $\nabla p \cdot \nabla \mathrm{tr}\mathbf{E}$, and $\nabla \mathrm{tr}\mathbf{E} \cdot \nabla \mathrm{tr}\mathbf{E}$; all were created by the dependence of the permeability on the strain; these terms vanish in the special case where the trace of the strain tensor, tr**E**, is independent of position, $\nabla \mathrm{tr}\mathbf{E} = 0$ everywhere in the domain of the problem.

The nonlinearity of the stress–strain relationship in articular cartilage is illustrated in the plot on the left in Figure 14.22. In the panel on the right in Figure 14.22 the suggested bilinearity of the stress–strain relation at zero strain is shown. Note that this figure suggests that there is a jump in the slope of the relationship at the origin, consistent with a step discontinuity between the linear elastic modulus of articular cartilage in the transition between tension and in compression. This tension–compression bilinearity of the drained matrix was incorporated into the poroelastic model with incompressible constituents (the biphasic model), and the model has been able to describe the response of cartilage in unconfined compression as well (Soulhat et al., 1999; Soltz and Ateshian, 2000a).

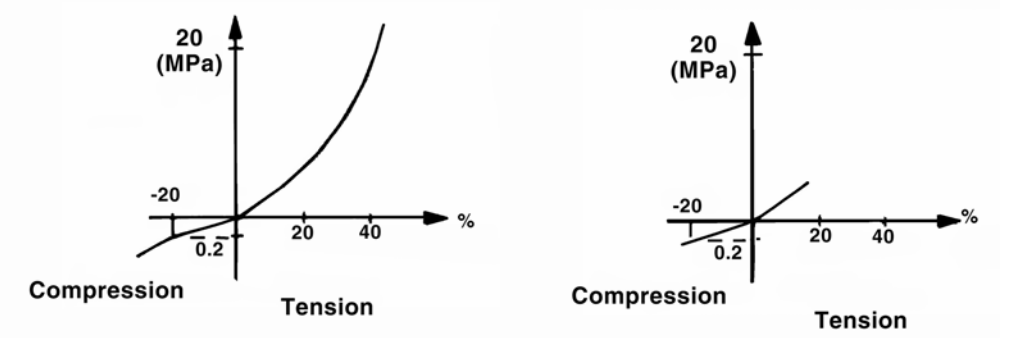



**Figure 14.22**. The nonlinearity of the stress–strain relationship in articular cartilage is illustrated in the plot on the left by the curved nature of the relationship compared with a linear relationship. The suggested bilinearity of the stress–strain relation at zero strain is illustrated on the right. There appears to be a jump in the slope of the relationship at the origin, suggesting that the linear elastic modulus of articular cartilage in tension is not equal to the modulus in compression. Adapted with permission from Mow et al. (1992).

An experimental study (Chahine et al., 2004) reported a series of unconfined compression experimental protocols in the presence of osmotic swelling. In this study the anisotropy of the tissue in both tension and compression was determined in experiments conducted along each of three mutually perpendicular loading directions, parallel to the split-line (the 1-direction), perpendicular to the split-line (the 2-direction) and along the depth direction (the 3-direction). Measurements in the 3-direction, perpendicular to the articular surface, make it possible to account for tissue inhomogeneity between the surface and deep layers. Tensile moduli were found to be strain dependent while compressive moduli were nearly constant. The peak tensile (+) Young's moduli in 0.15-M NaCl were $E_1^{(+)} = 3{:}1 \pm 2.3$, $E_2^{(+)} = 1{:}3 \pm 0{:}3$, $E_3^{\text{surface}(+)} = 0{:}65 \pm 0.29$, and $E_3^{\text{deep}(+)} = 2{:}1 \pm 1{:}2$, all in MPa. The corresponding compressive (–) Young's moduli were $E_1^{(-)} = 0.23 \pm 0.07$, $E_2^{(-)} = 0.22 \pm 0.07$, $E_3^{\text{surface}(-)} = 0.18 \pm 0.07$, and $E_3^{\text{deep}(-)} = 0.35 \pm 0.11$, all in MPa. The peak tensile Poisson's ratios were $\nu_{12}^{(+)} = 0.22 \pm 0.06$; $\nu_{21}^{(+)} = 0.13 \pm 0.07$; $\nu_{31}^{\text{surface}(+)} = 0.10 \pm 0.03$, and $\nu_{31}^{\text{deep}(+)} = 0.20 \pm 0.05$, while the compressive Poisson's ratios were $\nu_{12}^{(-)} = 0.027 \pm 0.012$; $\nu_{21}^{(-)} = 0.017 \pm 0.007$; $\nu_{31}^{\text{surface}(-)} = 0.034 \pm 0.009$, and $\nu_{31}^{\text{deep}(-)} = 0.065 \pm 0.024$ . Similar measurements were also performed at 0.015 and 2-M NaCl, and those measurements demonstrated strong variations in these elastic parameters with variations of ionic strength.

The experimental results reported by Chahine et al. (2004), combined with an analytical model, indicate that there is a smooth transition in the stress–strain and modulus–strain responses in the transition between the tensile and compressive regimes, as opposed to the bilinear relation with a jump in the slope plotted in the right panel of Figure 14.22. The experimental results also showed that cartilage exhibits orthotropic symmetry within the framework of tension–compression nonlinearity. The strain-softening behavior of cartilage, that is to say, the initial decrease in Young's moduli with increasing compressive strain, can be interpreted in the context of osmotic swelling and tension–compression nonlinearity. A two-part mechanical analysis of nonlinear strain-dependent response by Ateshian (Ateshian et al., 2003, 2004) showed that the elastic modulus was actually continuous and the point of discontinuity could be replaced by a smooth curve with a small radius of curvature that transitioned between the compression and tension moduli (Figure 14.23). In this discussion the summary of the simplified analysis in the appendix to Chahine et al. (2004) is followed closely.

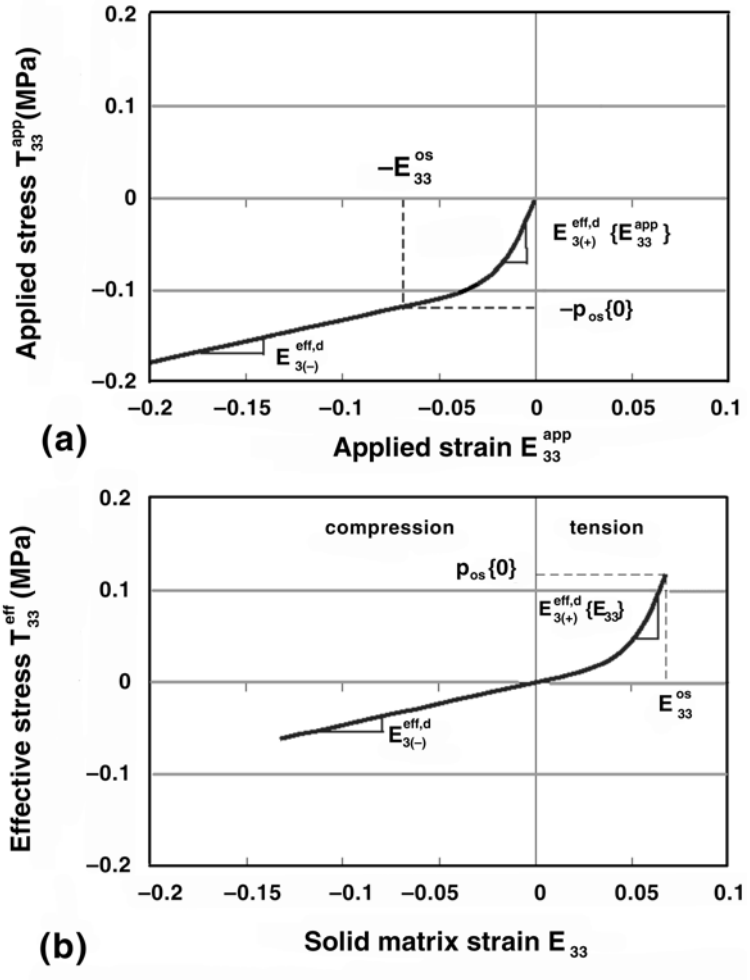



**Figure 14.23**. These plots show that the supposedly bilinear stress–strain relation is actually a smooth function with a small domain of high curvature between two different linear regions. (a) Plot of $T_{33}(E_{33}^{app})$ versus $E_{33}^{app}$ based on (14.12). (b) Plot of $T_{33}(E_{33}) + p_{os}(0) \approx T_{33}^{eff}(E_{33})$ versus $E_{33}$ based on (14.11).

First, a point about unconfined compression, as in the example that is the content of §9.11, and confined compression, as in the Darcy experiment described in §2.8 and illustrated by Figure 2.17 (see also Example 13.5.2). In *unconfined compression,* lateral expansion is permitted and the only stress is a normal stress applied in one selected direction. If the selected direction is taken as the 3-direction, only $T_{33}$ is nonzero. The strains are determined from strain–stress relation (9.7), $\hat{\mathbf{E}} = \hat{\mathbf{S}}^{\mathrm{d}} \cdot \hat{\mathbf{T}}^{\mathrm{eff}}$, and it is found that the only nonzero strains are created by $T_{33}^{\mathrm{eff}}$ and determined by the orthotropic form of (9.7): $E_{11} = -\nu_{31}(T_{33}^{\mathrm{eff}} / E_3^d)$, $E_{22} = -\nu_{32}(T_{33}^{\mathrm{eff}} / E_3^d)$, and $E_{33} = (T_{33}^{\mathrm{eff}} / E_3^d)$. In *confined compression,* lateral expansion is not permitted and the only strain is a normal strain applied in one selected direction. If the selected direction is taken as the 3-direction, only $E_{33}$ is nonzero. The associated stresses are determined from the inverse of strain–stress relation (9.7), $\hat{\mathbf{T}}^{\mathrm{eff}} = \hat{\mathbf{C}}^{\mathrm{d}} \cdot \hat{\mathbf{E}}$, and it is found that the only non-

zero stresses created by $E_{33}$ and determined by the orthotropic form of $\hat{\mathbf{T}}^{\text{eff}} = \hat{\mathbf{C}}^{\text{d}} \cdot \hat{\mathbf{E}}$ are $T_{11}^{\text{eff}} = \hat{C}_{13}^{\text{d}} E_{33}$, $T_{22}^{\text{eff}} = \hat{C}_{23}^{\text{d}} E_{33}$, and $T_{33}^{\text{eff}} = \hat{C}_{33}^{\text{d}} E_{33}$, where $\hat{C}_{33}^{\text{d}}$ is related to the drained compliance elastic constants by

$$\hat{C}_{33}^{\text{d}} = \frac{E_3^d (1 - \nu_{12}^d \nu_{21}^d)}{1 - \nu_{12}^d \nu_{21}^d - \nu_{23}^d \nu_{31}^d - \nu_{23}^d \nu_{32}^d - \nu_{13}^d \nu_{31}^d - \nu_{21}^d \nu_{32}^d \nu_{13}^d}.$$

The normal stresses in the 1- and 2-directions are necessary to maintain the zero strain in those directions. In the analysis that follows, only equilibrium states are considered, that is to say, the movement of fluid in and out of the tissue model is not considered and only the no-flow equilibrium states that occur after fluid movement has stopped are considered in the analysis.

To be consistent with the example that is the content of §9.11, the direction of unconfined compression is taken to be the 3-direction in the descriptive prose that occupies the remainder of this section. However, as noted, Chahine et al. (2004) tested specimens in the 1-, 2-, and 3-directions, and we have selected the 3-direction for this presentation of a one-dimensional analysis to be consistent with §9.11, with the understanding that the reader may substitute 1 or 2 for 3 and obtain the appropriate result for that test direction. The purpose of the analytical development in the appendix of Chahine et al. (2004) was to demonstrate the close connection between the theory (Ateshian et al., 2003, 2004) that the experiment reported in Chahine et al. (2004) as well as to show the combined effects of tension–compression nonlinearity and osmotic swelling, and to explain how the free-swelling strain can be determined from the transition from a nonlinear to a linear regime in the stress–strain response.

Only equilibrium conditions are considered in the current analysis, in analogy to the experiments described above. In this case the total axial normal stress in cartilage, which is also the applied stress, is given by

$$T_{33} = -p_{\text{os}} + T_{33}^{\text{eff}} \tag{14.4}$$

where $p_{\text{os}}$ is the osmotic pressure in the interstitial fluid and $T_{33}^{\text{eff}}$ is the effective axial normal stress resulting from axial normal strain in the matrix. The solid matrix strain is denoted by $E_{33}$ and the drained Young's modulus by $E^d$. However, $E^d$ is now considered to be strain dependent, and thus $T_{33}^{\text{eff}} = E^d(E_{33}) E_{33}$. In addition, since the osmotic pressure is a function of proteoglycan fixed-charge density and since this fixed-charge density is a function of the solid matrix strain (Lai et al., 1991), it is assumed that $p_{\text{os}}$ is also a function of solid matrix strain $E_{33}$; thus, $p_{os} = p_{os}(E_{33})$, and it follows that (14.4) may be rewritten with these functional dependences made explicit:

$$T_{33}(E_{33}) = -p_{\text{os}}(E_{33}) + E^d(E_{33}) E_{33}. \tag{14.5}$$

The dependence of $p_{\text{os}}$ and $E^d$ on the ionic environment is implicit in this relation. When there is no applied stress on the tissue $T_{33}$, osmotic pressure $p_{\text{os}}$ will place the tissue in an initial state of tensile free-swelling solid matrix strain, $E_{33}^{\text{os}}$, given by the solution to the (generally nonlinear) equation

$$0 = -p_{\text{os}}(E_{33}^{\text{os}}) + E^d(E_{33}^{\text{os}}) E_{33}^{\text{os}}. \tag{14.6}$$

Recall that tensile free-swelling solid matrix strain tensor $\mathbf{E}^{\text{os}}$ was calculated for the example of free swelling of a piece of soft anisotropic hydrated biological tissue in Example 13.5.1.

Chahine et al. (2004) measured applied strain $E_{33}^{\text{app}}$ relative to this free-swelling configuration, where $E_{33}^{\text{app}}$ is defined by

$$E_{33}^{\text{app}} = E_{33} - E_{33}^{\text{os}}. \tag{14.7}$$

Applied strain $E_{33}^{\text{app}}$ is therefore equal to zero under free-swelling conditions when the solid matrix strain is equal to $E_{33}^{\text{os}}$. The measured effective drained modulus (the slope of the stress–strain curve) is obtained by taking the derivative of $T_{33}(E_{33})$ given by (14.5) with respect to $E_{33}$ (or equivalently $E_{33}^{\text{app}}$ since $dE_{33} = dE_{33}^{\text{app}}$) to yield

$$E^{\text{eff,d}}(E_{33}) = \frac{dT_{33}}{dE_{33}} = \frac{dT_{33}}{dE_{33}^{\text{app}}} = -\frac{dp_{\text{os}}}{dE_{33}} + E^{d}(E_{33}) + \frac{dE^{d}(E_{33})}{dE_{33}}. \tag{14.8}$$

It is important to note that the first term on the right-hand side of this equation, $(dp_{\text{os}}/dE_{33}) = (dp_{\text{os}}/dE_{33}^{\text{app}})$, a term which represents the rate of change of osmotic pressure with strain, is the contribution of fixed-charge density to cartilage stiffness (Ateshian et al., 2003a). Based on the experimental results of Chahine et al. (2004), $E^{\text{eff},d}(E_{33})$ is nearly constant in the range of compressive solid matrix strains, so that it is reasonable to assume that

$$\frac{dp_{\text{os}}}{dE_{33}} \approx \frac{dE^{d}(E_{33})}{dE_{33}} \approx 0 \text{ when } E_{33} < 0. \tag{14.9}$$

However, unlike $E^{d}(E_{33})$, which depends on the collagen matrix and increases rapidly with tensile strain, $dp_{\text{os}}/dE_{33}$ depends only on fixed-charge density and its strain dependence in tension should be no different than in compression (under small strains). Based on (14.9), it can be concluded that $dp_{\text{os}}/dE_{33}$ is approximately constant for both tensile and compressive strains in the range of small strains. Expanding $p_{\text{os}}(E_{33})$ in a Taylor series and retaining only the first-order terms, $p_{\text{os}}(E_{33}) = p_{\text{os}}(0) - (dp_{\text{os}}/dE_{33})E_{33}$. When this approximation is used in (14.5), one obtains

$$T_{33}(E_{33}) = -p_{\text{os}}(0) + \left[\frac{dp_{\text{os}}}{dE_{33}} + E^{d}(E_{33})\right]E_{33}. \tag{14.10}$$

This relationship implies that this study's experiments can only yield $(dp_{\text{os}}/dE_{33}) + E^{d}(E_{33})$ but not $dp_{\text{os}}/dE_{33}$ or $E^{d}(E_{33})$ on their own. In principle, however, $dp_{\text{os}}/dE_{33}$ may be obtained from the knowledge of the fixed-charge density. Based on their experimental data, Chahine et al. (2004) proposed the following constitutive relation:

$$\frac{dp_{\text{oz}}}{dE_{33}} + E_{3}^{d}(E_{33}) = E_{3(-)}^{\text{eff},d} \text{ for } E_{33} \le 0, \tag{14.11a}$$

$$\frac{dp_{\text{os}}}{dE_{33}} + E^{d}(E_{33}) = E_{3(-)}^{\text{eff},d} + D^{\text{eff},d}(E_{33})^{n-1} \text{ for } E_{33} \ge 0 \tag{14.11b}$$

or, equivalently,

$$T_{33}(E_{33}) = -p_{\text{os}}(0) + E_{3(-)}^{\text{eff},d}E_{33} \text{ for } E_{33} \le 0, \tag{14.12a}$$

$$T_{33}(E_{33}) = -p_{\text{os}}(0) + E_{3(-)}^{\text{eff},d}E_{33} + D^{\text{eff},d}(E_{33})^{n} \text{ for } E_{33} \ge 0, \tag{14.12b}$$

where $E^{\text{eff,d}}_{3(-)}$, $E^{\text{eff,d}}_{(-)}$, $D^{\text{eff,d}}$, and $n$ ($n \geq 2$) are material coefficients independent of strain, $E^{\text{eff,d}}_{3(-)}$ is the drained Young's modulus in compression. Alternatively, this relation can also be formulated in terms of $T_{33}(E^{\text{app}}_{33})$ versus $E^{\text{app}}_{33}$ using (14.7):

$$T_{33}(E^{\text{app}}_{33}) = E^{\text{eff},d}_{3(-)} E^{\text{app}}_{33} - D^{\text{eff},d}(E^{\text{os}}_{33})^n \text{ for } E^{\text{app}}_{33} \leq -E^{\text{os}}_{33}, \tag{14.13a}$$

and

$$T_{33}(E^{\text{app}}_{33}) = E^{\text{eff},d}_{3(-)} E^{\text{app}}_{33} + D^{\text{eff},d}[(E^{\text{app}}_{33} + E^{\text{os}}_{33})^n - (E^{\text{os}}_{33})^n], \tag{14.13b}$$

for $E^{\text{app}}_{33} \geq -E^{\text{os}}_{33}$, where it is recognized that since $T_{33}(E_{33}) = 0$ when $E^{\text{app}}_{33} = 0$ (no applied stress under free-swelling conditions), and

$$p_{\text{os}}(0) = E^{\text{eff},d}_{3(-)} E^{\text{os}}_{33} + D^{\text{eff},d}(E^{\text{os}}_{33})^n. \tag{14.14}$$

Clearly, both (14.11) and (14.12) are different representations of the same underlying phenomenon, namely, that the modulus of cartilage remains constant under compressive matrix strains but rises rapidly with tensile matrix strains. Both equations are plotted in Figure 14.23, with Figure 14.23a ($T_{33}(E^{\text{app}}_{33})$ vs. $E^{\text{app}}_{33}$) being representative of the experimental response. Figure 14.23b ($T_{33}(E_{33}) + p_{\text{os}}(0) \approx T^{\text{eff}}_{33}(E_{33})$ vs. $E_{33}$) provides a more conventional representation of the tension–compression nonlinearity of the solid matrix, showing a linear response when the true matrix strain is compressive and a nonlinear response when the true matrix strain is tensile. Values of $E^{\text{eff,d}}_{3(-)}$, $D^{\text{eff,d}}$, and $n$ are obtained from curve fitting the experimental stress–strain responses reported in Chahine et al. (2004). The source of the tensile matrix strain, whether from osmotic swelling or from an applied tensile traction, does not affect this one-dimensional analysis. The strain-dependent modulus is given by the slope of the stress–strain response:

$$\frac{dT_{33}(E^{\text{app}}_{33})}{dE^{\text{app}}_{33}} = E^{\text{eff},d}_{3(-)} \text{ for } E^{\text{app}}_{33} \leq -E^{\text{os}}_{33}, \tag{14.15a}$$

$$\frac{dT_{33}(E^{\text{app}}_{33})}{dE^{\text{app}}_{33}} = E^{\text{eff,d}}_{3(-)} + nD^{\text{eff,d}}(E^{\text{app}}_{33} + E^{\text{os}}_{33})^{n-1} \equiv E^{\text{eff,d}}_{3(+)}(E^{\text{app}}_{33}), \tag{14.15b}$$

for $E^{\text{app}}_{33} \geq -E^{\text{os}}_{33}$, and $n \geq 2$.

This constitutive model assumes that the transition from compression to tension ($E_{33} = 0$ or, equivalently, $E^{\text{app}}_{33} = -E^{\text{os}}_{33}$) occurs at the point where a nonlinear response is observed, and based on this assumption it is possible to identify the magnitude of the swelling strain, $E^{\text{os}}_{33}$, by increasing the applied compressive strain until the stress–strain response transitions from a nonlinear to a linear response. While it may seem paradoxical at first that the free-swelling strain is determined by compressing the tissue, representations (14.11) and (14.12) clarify the rationale for this approach.

## 14.11. MENISCI

The contact surface of the knee joint, where the rounded condyles of the femur pivot on the relatively flat tibial plateau, is so loosely constrained that it has been likened to the fit of a teacup into a saucer. This is because the relative size and curved spacing between the outside of the teacup and the upper curved surface of the saucer is spacious and not unlike the relation-

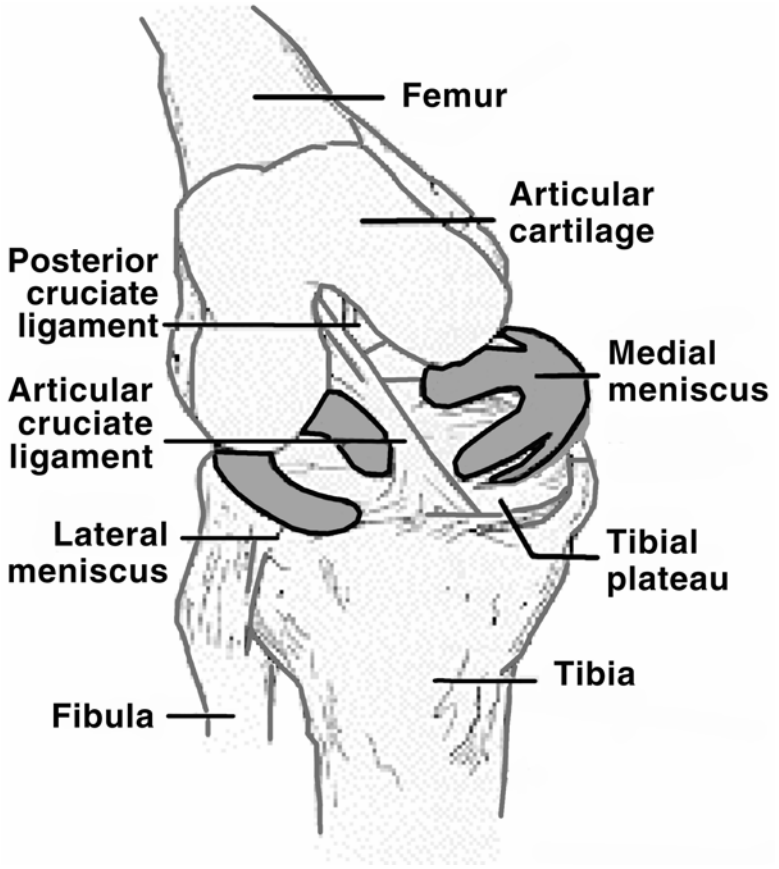



**Figure 14.24**. Exploded front view of the knee joint showing the menisci. Adapted with permission from http://www.stoneclinic.com/menca.htm.

ship of the exterior surface of the condyle and the upper surface of the tibia. The menisci, which are two crescent-shaped structures of fibrocartilage between the femur and tibia, occupy the space between the condyle (teacup) and the tibia (saucer), Figure 14.24. Their function is thought to be constraining the relative displacement of the condyle from the tibia in the tibial plateau plane and, like articular cartilage, to absorb some of the impact loading on the joint. The medial meniscus lies below the medial condyle and the lateral meniscus below the lateral condyle (Figure 14.24). From their insertions on the tibial plateau, the menisci wrap around the rounded surfaces of the condyles. The extracellular matrix of the menisci is reinforced by bundles of collagen fibers; the majority of these collagen fibers are aligned to increase strength in the circumferential direction (Figure 14.25), thus giving the meniscus transversely isotropic material properties. The strongest attachment of the menisci is at its horns, the beginning and endpoints of their crescent shape, where the collagen fibers of the menisci are inserted into and woven with the cortical bone of the tibia. These insertion points provide a strong restraining anchor for the hoop forces generated by the downward compression and the lateral motion of the femur. The outer periphery of the meniscus is attached to the inside of the synovial capsule (Arnoczky, 1992; Aspeden, 1985; Mow, 1992b).

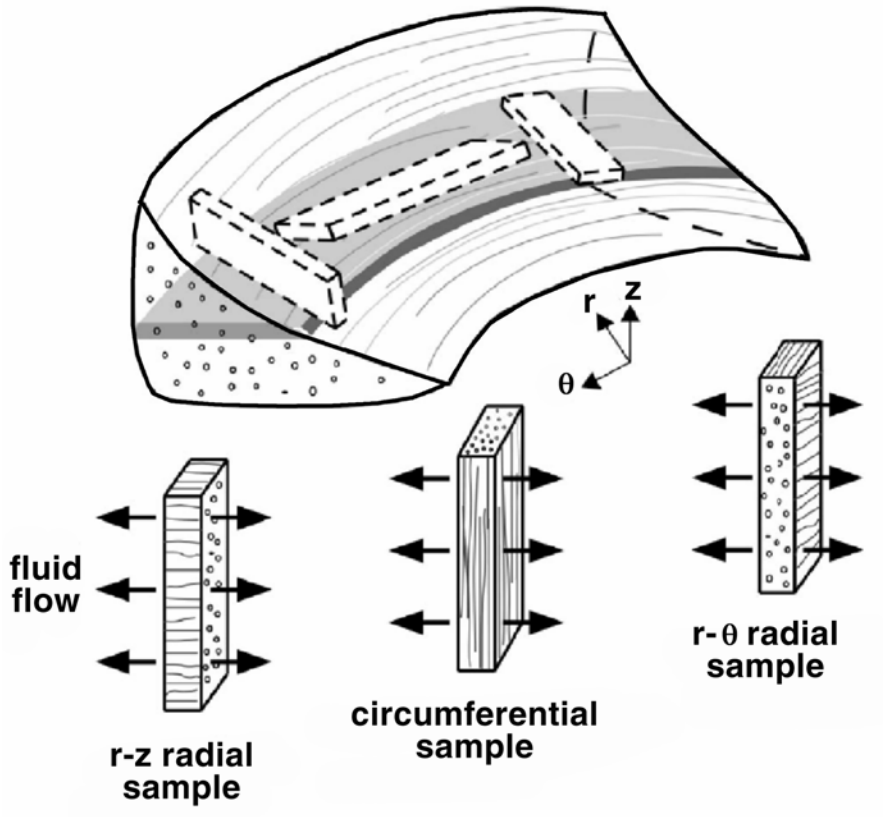



**Figure 14.25**. Schematic of meniscal sample orientations for tensile testing to determine the transversely isotropic elastic properties and permeability coefficients. The permeability coefficient in the direction of the collagen fibers, $\kappa_\theta$, was determined from radial samples in the $r$–$z$ plane, while the permeability coefficient in the transverse direction, $\kappa_r = \kappa_z$, was determined from both $r$—$\theta$ radial samples and circumferential samples. Reprinted with permission from LeRoux and Setton (2002).

At the beginning of the twentieth century the functions of the menisci were not well understood; for instance, some anatomists regarded the menisci as the useless remains of leg muscle, and surgeons often removed an injured meniscus in its entirety, due to its poor propensity to heal. It is now appreciated that the menisci contribute to load support and knee joint stability. Surgeons currently use minimally invasive orthoscopic techniques to repair a meniscus and are careful to leave as much of the tissue intact as possible. Many studies have shown that complete excision of the meniscus results in eventual degeneration of knee joint articular cartilage and osteoarthritis. This evidence has motivated a change in surgical procedure away from meniscectomy toward emphasizing the preservation of as much viable tissue as possible in an injured meniscus (Wyland et al.. 2002).

The meniscus is about 74% water by weight. The desiccated meniscus is approximately 75% collagen, 8–13% noncollagenous proteins, and 1% hexosamine. Type I collagen is 90% of the total collagen, with types II, III, V, and VI in the remaining 10%. Type II fibers are more

prominent in the surface layers. In the thin surface layer the collagen fibers are oriented randomly within the plane of that layer, as if to create a mesh layer that holds the interior together. Below the surface the majority of fibers are grouped in bundles with a predominantly circumferential orientation that follows the curved crescent shape of the meniscus and forms the structural framework of the tissue (Figure 14.25).

The menisci begin development in the fetus from intermediate layer mesenchymal tissue. By 8 weeks they are visible but consist mainly of fibroblast cells. With further development circumferentially aligned collagen fibrils begin to appear in the extracellular matrix of the meniscus. The increase in quantity and alignment of the collagen continues after birth. Joint motion is thought to encourage this alignment (Arnoczky, 1992). Blood vessels, initially present throughout the meniscus, begin to recede, and by adolescence they are present only in the outer 20–30% of the circumferential periphery. This leaves the central region of the meniscus without a blood supply; therefore, it must receive nutrition through either diffusion or fluid convection generated by the regular compression and relaxation of the joint generated during walking or other physical activities. Evidence suggests that, due to the densely fibrous nature of the extracellular matrix, the rate of diffusion is poor, so the mechanical pumping force is likely essential for nutrition.

Classification of cell types within the meniscus has been the subject of debate. Previously, because of the fibrous composition of the tissue, meniscal cells have been referred to as fibroblasts and fibrocytes. However, photomicrographs reveal that the cells near the surface of the meniscus are oval or fusiform in shape, resembling chondrocytes in the tangential zone of articular cartilage, while the cells deeper within the meniscus are rounded or polygonal in shape. The oval surface layer cells have short cell processes, little cytoplasm, and few organelles, but usually have a Golgi complex, while the deeper cells have a large rough endoplasmic reticulum, a large Golgi complex, and often contain lipid droplets and glycogen deposits. Elongated fibroblasts are seen where the meniscus attaches to the synovial joint capsule. This segregation of morphologically distinct cell types into different depths is similar to that of articular cartilage, as described earlier in this chapter. The term "fibrochondrocyte" has been used to describe the majority of cells in the meniscus. Meniscal cells also have a pericellular or boundary matrix around them similar to the chondron associated with chondrocytes. The main difference between the two tissue types is that meniscal fibrochondrocytes produce type I collagen while hyaline chondrocytes produce type II.

The predominantly circumferential orientation of collagen is consistent with the meniscus having to withstand compressive stresses. The weight of the femur is transmitted normal to the concave inner surface of the meniscus. This force has a horizontal component that creates a tensile hoop stress in the meniscus, stretching its collagen fibrils. The restoring elastic force in the stretched fibril then opposes this horizontal force of the femur. Unreacted, this horizontal force could be destabilizing to the animal.

The tensile behavior of meniscal tissue is similar across human, canine, bovine, and ovine species when allowance is made for the fact that the knees of humans articulate in the reverse directions from those of these animals (think of a cow walking). Meniscal tensile stress and strain curves show a toe region of low stiffness at small strains followed by a linear relationship at higher strains (Setton et al., 1999). To be consistent with the primarily circumferential orientation of the fibers in a meniscus, transversely isotropic material symmetry in a cylindrical coordinate system is employed. The fibers then lie along the circumferential or $\theta$ direction and the plane of isotropy is perpendicular to the $\theta$ direction in the $r, z$ plane. Tensile test specimens have been cut at different orientations from the meniscus to determine how its elastic properties varied with direction. Radial test specimens are cut from a radial slice of the meniscus, while circumferential test strips are cut from the longitudinal direction of the meniscus

(Figure 14.25). Specimens taken from the thin surface layer are isotropic, while specimens taken from the deeper zones are anisotropic, with the circumferential direction being much stronger than the radial. Table 14.2 contains a summary of the measured tensile mechanical properties of the human meniscus reported by LeRoux and Setton (2002). Note the almost seven-fold difference between Young's modulus in the θ direction and Young's modulus in the perpendicular plane.

**Table 14.2**. Transversely Isotropic Drained Elastic Constants and Permeabilility of the Canine Meniscus

| Tensile modulus | Poisson's ratios | Permeability |
|---|---|---|
| $E_\theta^d = 67.8$ MPa | $\nu_{\theta_r} = 2.13$ | $\kappa_\theta$ 9 x $10^{-18}$ $m^4$/N-s |
| $E_r^d = E_z^d = 11.2$ MPa | $\nu_{r\theta} = 1.5$ | $\kappa_r = \kappa_z \approx$ 10 x $10^{-18}$ $m^4$/N-s |
| | $\nu_{rz} = \nu_{rz} = 1.02$ | |

Reprinted with permission from LeRoux and Setton (2002).

The compressive behavior of the meniscus is dependent upon its poroelastic composition of roughly 75% fluid and 25% solid. When loaded, hydrostatic pressure will be generated within the meniscus as its relatively low permeability (Table 14.2) slows the rate of fluid flow out of the tissue. Scanning electron microscopy has revealed holes with a diameter of 10 μm on the surface of the meniscus. Light microscopy and staining with India ink have revealed that these holes open up into a series of canals that tunnel into the body of the meniscus (Adams and Hukins, 1992). The bulk of the load is initially supported by the fluid phase, distributing it evenly throughout the meniscus. As fluid flows out of the tissue, the meniscus deforms further, thus lowering the stress on the joint surface by increasing the contact area. As the load is removed, fluid flows back into the matrix, restoring the meniscus to its original shape. This diffusion of fluid into and out of the matrix is thought to provide nutrients to cells in the avascular regions of the menisci, and to aid in lubrication of the knee.

As with most tissues, the exact means by which mechanical loading causes the cell to alter the extracellular matrix structure is not yet known. It is known that regions subject to tensile forces are reinforced with collagen fibers in the direction of those tensile forces, and regions subject to compression contain more proteoglycans.

## 14.12. RELEVANT LITERATURE

In spite of the fact that articular cartilage, meniscus, and intervertebral disc are similar cartilaginous tissues, they are generally treated separately in the literature. The references most consulted in the preparation of this chapter are the review articles and volumes written or edited by Van Mow. His presentations generally place an emphasis on the mechanical as well as the biological and chemical and therefore fit very well with the philosophy of this text. Mow et al. (1989) and Mow et al. (1992a) were the principal references for articular cartilage, and Mow et al. (1992b) was the principal reference for the meniscus. The principal reference for the anatomy and histology of the intervertebral disc was Bogduk (1997) and for the mechanics of that tissue the work of LeRoux and Setton (2002). Chapter 8 of Mow et al. (1990) contains

some material comparing the three cartilaginous tissues of interest here and has been used in §14.6.

## References


Adams ME, Hukins DWL. 1992. The extracellular matrix of the meniscus. In *Knee meniscus: basic and clinical foundations*, ed. VC Mow, SP Arnoczky, DW Jackson, pp. 14–28. New York: Raven Press.

Ahmed AM. 1992. The load-bearing role of the knee menisci. In *Knee meniscus: basic and clinical foundations*, ed. VC Mow, SP Arnoczky, DW Jackson, pp. 59–73. New York: Raven Press.

Arnoczky SP. 1992. Gross and vascular anatomy of the meniscus and its role in meniscal healing, regeneration, and remodeling. In *Knee meniscus: basic and clinical foundations*, ed. VC Mow, SP Arnoczky, DW Jackson, pp. 1–14. New York: Raven Press.

Aspeden RM, Yarker YE, Hukins DWL. 1985. Collagen orientations in the meniscus of the knee joint. *J Anat* **140**:371–380.

Ateshian GA, Chahine NO, Basalo IM, Hung CT. 2004. The correspondence between equilibrium biphasic and triphasic material properties in mixture models of articular cartilage. *J Biomech* **37**:391–400.

Ateshian GA, Soltz MA, Mauck RL, Basalo IM, Hung CT, Lai WM. 2003. The role of osmotic pressure and tension-compression nonlinearity in the frictional response of articular cartilage. *Transp Porous Media* **50**:5–33.

Balazs F, Gibbs D. 1970. The rheological properties and biological function of hyaluronic acid. In *Chemistry and biology of the intercellular matrix*, ed. F Balazs, pp. 1241–1253. Academic Press.

Bogduk N. 1997. *Clinical anatomy of the lumbar spine and sacrum*, 3rd ed. New York: Churchill Livinstone.

Caplan AI. 1984. Cartilage. *Sci Am* **251**:84–94.

Chahine NO, Wang CC-B, Hung CT, Ateshian GA. 2004. Anisotropic strain-dependent material properties of bovine articular cartilage in the transitional range from tension to compression. *J Biomech* **37**:1251–1261.

Conrad BP. 2001. The effects of glucosamine and chondroitin on the viscosity of synovial fluid in patients with osteoarthritis. Masters of Engineering Thesis, University of Florida.

Eyre D. 2002. Articular cartilage and changes in arthritis: collagen of articular cartilage. *Arthr Res Ther* **4**:30–35.

Gu WY, Lai WM, Mow VC. 1998. A mixture theory for charged-hydrated soft tissues containing multielectrolytes: passive transport and swelling behaviors. *J Biomech Eng* **120**:169–180.

Hultkrantz J. 1898. Ueber die spaltrichtungen der gelenkknorpel. *Verh Anat Ges* **12**:248–256.

Huyghe JM, Janssen JD. 1997. Quadriphasic mechanics of swelling incompressible porous media. *Int J Eng Sci* **35**:793–802.

Lai WM, Hou JS, Mow VC. 1991. A triphasic theory for the swelling and deformation behaviors of articular cartilage. *J Biomech Eng* **113**:245–258.

Lee RC, Frank EH, Grodzinsky AJ, Roylance DK. 1981. Oscillatory compressional behavior of articular cartilage and its associated electromechanical properties. *J Biomech Eng* **103**:280–292.

LeRoux MA, Setton LA. 2002. Experimental and biphasic FEM determinations of the material properties and hydraulic permeability of the meniscus in tension. *J Biomech Eng* **124**:315–321.

Mow VC, Radcliffe A, Woo SL-Y, eds. 1990. *Biomechanics of diarthroidal joints*, Vols. 1 and 2. New York: Springer.

Mow VC, Radcliffe A, Poole, AR. 1992a. Cartilage and diarthroidal joints as paradigms for hierarchical materials. *Biomaterials* **13**:67–97.

Mow VC, Radcliffe A, Chern KY, Kelly MA. 1992b. Structure and function relationships of the menisci of the knee. In *Knee meniscus: basic and clinical foundations*, ed. VC Mow, SP Arnoczky, DW Jackson, pp. 37–57. New York: Raven Press.

Mow VC, Proctor CS, Kelly, MA. 1989. Biomechanics of articular cartilage. In *Basic biomechanics of the musculoskeletal system*, 2nd ed., ed. M Nordin, VH Frankel, pp. 31–58. Philadelphia: Lea & Febiger.

Panagiotacopulos ND, Bloch R, Knauss WG, Harvey P, Patzakis M. 1977. *Viscoelastic behavior of the human intervertebral disc under consideration of moisture migration*. Interim Progress Report, AFOSR Grant #77-3139, Cal Tech, June 27.

Poole CA, Flint MH, Beaumont BW. 1987. Chondrons in cartilage: ultrastructural analysis of the pericellular microenvironment in adult human articular cartilages. *J Orthop Res* **5**:509–522.

Poole CA, Ayad S, Schofield JR. 1988. Chondrons from articular cartilage, I: immunolocalization of type VI collagen in the pericellular capsule of isolated canine tibial chondrons. *J Cell Sci* **90**:635–643.

Rhee DK, Marcelino J, Baker M, Gong Y, Smits P, Lefebvre V, Jay GD, Stewart M, Wang H, Warman ML, Carpten JD. 2005. The secreted glycoprotein lubricin protects cartilage surfaces and inhibits synovial cell overgrowth. *J Clin Invest* **115**:622–631.

Setton LA, Guilak FG, Hsu EW, Vail TP. 1999. Biomechanical factors in tissue engineered meniscal repair. Clin Orthop Relat Res **367S**:S254–S272.

Soltz MA, Ateshian GA. 1998. Experimental verification and theoretical prediction of cartilage interstitial fluid pressurization at an impermeable contact interface in confined compression. *J Biomech* **31**:927–934.

Soltz MA, Ateshian GA. 2000a. A conewise linear elasticity mixture model for the analysis of tension-compression nonlinearity in articular cartilage. *J Biomech Eng* **122**:576–586.

Soltz MA, Ateshian GA. 2000b. Interstitial fluid pressurization during confined compression cyclical loading of articular cartilage. *Ann Biomed Eng* **28**:150–159.

Soulhat J, Buschmann MD, Shirazi-Adl A. 1999. A fibril network-reinforced biphasic model of cartilage in unconfined compression. *J Biomech Eng* **121**:340–347.

Truskey GA, Fan Y, Katz DF. 2004. *Transport prenomena in biological systems*. Englewood Cliffs, NJ: Prentice-Hall.

Wang CC-B, Chahinea NO, Hung CT, Ateshian GA. 2003. Optical determination of anisotropic material properties of bovine articular cartilage in compression. *J Biomech* **36**:339–353.

Wyland DJ, Guilak F, Elliott DM, Setton LA, Vail TP. 2002. Chondropathy after meniscal tear or partial meniscectomy in a canine model. *J Orthop Res* **20**:996–1002.

# 15

# KINEMATICS AND MECHANICS OF LARGE DEFORMATIONS

After noting that his approach to the development of the nonlinear stress–strain-history relationship in large deformations of living tissues "is theoretical, although in search for simplicity we shall be guided by experimental data," Y. C. Fung (1967) writes "One may ask what is the merit of the theoretical approach? The answer is threefold: (1) To facilitate data collection and data analysis. If an experimental curve can be characterized mathematically by a few parameters, then these parameters can be tabulated and used to correlate the mechanical property of the tissues with other physical and physiological parameters, such as age, sex, injury, temperature, chemical environment, etc. (2) To derive three-dimensional stress–strain-history law under finite deformation. Such a law is needed for the analysis of any practical boundary-value problems, but is not yet available. Since it is very difficult to experiment with biological materials in three-dimensional stress fields, it is natural to turn to theoretical formulation and then derive solutions to appropriate problems that can be tested experimentally. In other words, a theoretical study may be used to formulate critical experiments to validate the basic hypotheses. (3) To unify different types of experiments, such as the static (very slow) elasticity, dynamic elasticity (finite strain rate), stress relaxation under fixed strain, creep deformation under fixed stress, strain-cycle hysteresis, and cyclic stress fatigue. A correct theoretical formulation should bring out the unity among these experiments. Only the formulation that is consistent with all the experimental results can be accepted."

## 15.1. LARGE DEFORMATIONS

Large deformations are more difficult to model mathematically than either small deformations or fluid motions. The difficulty stems from the fact that, for analysis of large deformations, the knowledge associated with at least two different configurations must be maintained. In the case of fluid motions, only the knowledge of the present or instantaneous configuration is necessary, and, in the case of small deformations of solids, the difference between the initial reference configuration and the present configuration is a small higher-order quantity, and it is neglected. In fact, this neglect of higher-order terms between the two configurations is the definition of "small" deformations. These difficulties may be illustrated using the concept of stress in large deformations. For small deformations the only definition of stress employed is

force per unit of instantaneous cross-sectional area. This is adequate since there is a negligible difference between the area in the reference configuration and the area in the instantaneous configuration in the case of small deformations. In practice, in the case of small deformations, the stress is generally calculated approximately using the original cross-sectional area, even though the definition is for the instantaneous cross-sectional area. For large deformations, however, the cross-sectional area can change considerably. Consider a rubber band in its unstressed state and measure or visualize the cross-sectional area of the rubber band perpendicular to the long axis of the band, the long axis that forms the closed loop of the band. When the rubber band is stretched, note how the cross-sectional area decreases. When the band is stretched the force on the band is increased, and, since stress is defined as force per unit area and the area is decreasing, the increasing stress is due not only to the increasing force but also to the decreasing cross-sectional area of the rubber band. Each incremental increase in the force increases the stress, but it also reduces the cross-sectional area, thereby further increasing the stress.

This feature of the concept of stress at large deformations, the fact that its change is not only due to changing force but also to changing area, is a characteristic feature of large deformations, namely, that the analysis of large deformations requires nonlinear mathematics. Nonlinear mathematics is generally more difficult than linear.

A development of the kinematics of large deformations is presented in this chapter. It begins in the following section with homogenous deformations and continues with the polar decomposition theorem, strain tensors for large deformations, and formulas for the calculation of volume and area change. Using the formulas for area change, the appropriate definitions of stress for large deformations are then developed. These large deformation stress measures are incorporated in the stress equations of motion. Constitutive equations for both Cauchy elastic and hyperelastic materials capable of large deformations are then considered along with the special cases of isotropic material models and incompressible material models. The development of Fung's exponential strain energy function for tissues is described. The constitutive equations for Fung's nonlinear viscoelasticity (QLV) are also described. The chapter closes with a discussion of the development of strain energy functions for tissues and the relevant literature.

## 15.2. LARGE HOMOGENEOUS DEFORMATIONS

In this section the easily understood and easily illustrated large class of deformations called homogeneous deformations is described. It is most important for the modeler to understand homogeneous deformations because most mechanical testing of materials requires homogeneous deformations, and many finite deformation problems for this class of deformations are easily solved. *Homogeneous deformations* are deformations that are exactly the same for all particles, that is to say, all particles experience the same deformation, the same strain, and the same rotation. Recalling representation (3.2) for a motion, $\mathbf{x} = \boldsymbol{\chi}(\mathbf{X}, t)$, and the fact that the strain and rotation are derivatives of the motion with respect to $\mathbf{X}$, the motion must be linear in $\mathbf{X}$ so that the strain and rotation measures such as the deformation gradients will be constant. Thus, a homogeneous deformation is mathematically defined as a deformation that has a representation of the form

$$\mathbf{x} = \mathbf{L}(t)\cdot\mathbf{X}, \tag{15.1}$$

where $\mathbf{L}(t)$ is a tensor independent of $\mathbf{X}$. Recalling definition (3.13) of deformation gradient tensor $\mathbf{F}$, $\mathbf{F} = [\nabla_o \otimes \boldsymbol{\chi}(\mathbf{X}, t)]^T$, it follows that for a homogeneous deformation,

$$\mathbf{F} = \mathbf{L}. \tag{15.2}$$

Thus, as would be expected for the definition of a homogeneous deformation, the tensor of deformation gradients is independent of **X**. Lord Kelvin and P. G. Tait in their *Treatise on Natural Philosophy* extensively developed the geometrically interesting properties of homogeneous deformations. Their study of the effect of homogeneous deformations upon simple geometric figures is briefly reviewed here. Recall that a plane may be defined by its normal and specification of one point in the plane. Let **a** denote the vector normal to a plane and let $\mathbf{X}_0$ denote a point in the plane. Then all the other points in the plane are points **X** such that $\mathbf{a}\cdot(\mathbf{X} - \mathbf{X}_0) = 0$. This is so because condition $\mathbf{a}\cdot(\mathbf{X} - \mathbf{X}_0) = 0$ requires that vector $(\mathbf{X} - \mathbf{X}_0)$ be perpendicular to **a**, the normal to the plane. If we set $\mathbf{a}\cdot\mathbf{X}_0 = c$, a constant; then a material surface that forms a plane may be described in material coordinates by

$$\mathbf{a}\cdot\mathbf{X} = c. \tag{15.3}$$

Substituting the inverse of (15.2), $\mathbf{X} = \mathbf{L}^{-1}\,\mathbf{x}$, into (15.3) yields

$$\mathbf{a}^*\cdot\,\mathbf{x} = c, \tag{15.4}$$

where a new constant vector, **a*,** by $\mathbf{a}^* = \mathbf{a}\cdot\mathbf{L}^{-1}$ has been defined. Equation (15.3) is also the equation of a plane, a plane in the spatial coordinate system, thus permitting one to conclude that a plane material surface is deformed into a plane spatial surface by a homogeneous deformation. More simply stated, homogeneous deformations map planes into planes. Selecting different values for constant $c$ in (15.3) and (15.4), it may be concluded that parallel planes will deform into parallel planes since the normals to parallel planes have the same direction. Since the intersection of two planes is a straight line (Figure 15.1), it follows that parallel straight lines go into parallel straight lines, parallelograms go into parallelograms, and parallelepipeds deform into parallelepipeds. These results are illustrated in Figure 15.2.

**Problem 15.2.1**

Sketch the set of parallel lines given by the intersection of planes $\mathbf{a} = [2, 3, 0]^T$, with $c = 0$ and 5, and $X_{III} = 0$. These lines have representations $2X_I + 3X_{II} = 0$ and $2X_I + 3X_{II} = 5$, respectively. Sketch the set of parallel lines after subjecting them to homogeneous deformation

$$\mathbf{F} = \begin{bmatrix} \sqrt{3} & 1 & 0 \\ 0 & 2 & 0 \\ 0 & 0 & 1 \end{bmatrix}.$$

**Solution**: A sketch of the set of parallel lines given by $2X_I + 3X_{II} = 0$ and $2X_I + 3X_{II} = 5$ is shown in Figure 15.3a. The inverse of homogeneous deformation **F** is given by

$$\mathbf{F}^{-1} = \begin{bmatrix} \dfrac{1}{\sqrt{3}} & \dfrac{-1}{2\sqrt{3}} & 0 \\ 0 & \dfrac{1}{2} & 0 \\ 0 & 0 & 1 \end{bmatrix},$$

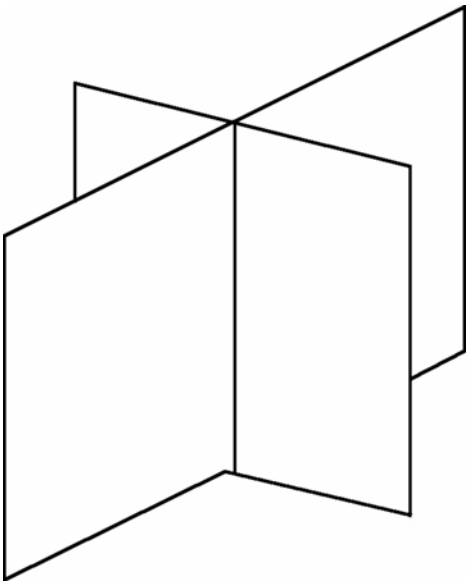


**Figure 15.1**. The intersection of two planes is a straight line.

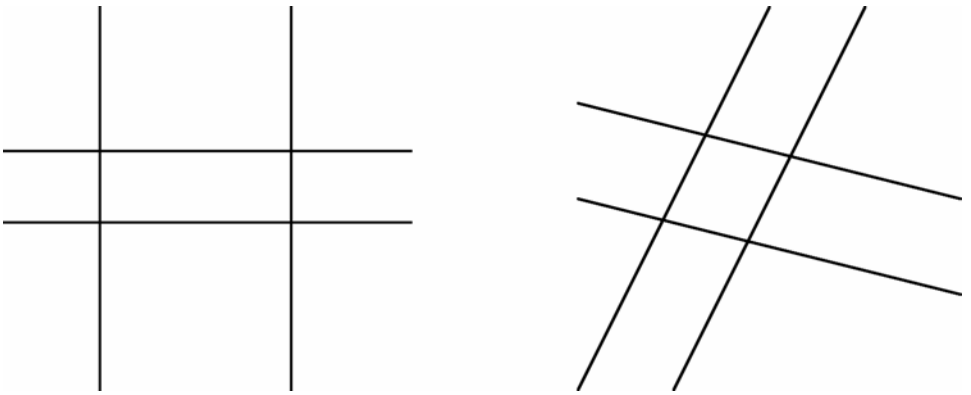


**Figure 15.2**. Illustration of sets of parallel lines deforming into sets of parallel lines and a parallelogram deforming into a parallelogram.

thus, $\mathbf{a}^* = \mathbf{a}\cdot\mathbf{L}^{-1} = [2/\sqrt{3},\ (3/2) - 1/\sqrt{3},\ 0]^T$. The set of deformed parallel lines is determined by the intersection of the planes, $\mathbf{a}^* = [2/\sqrt{3},\ (3/2) - 1/\sqrt{3},\ 0]^T$ with $c = 0$ and 5, and $x_3 = 0$. This set of parallel lines is given by $2x_1/\sqrt{3} + ((3/2) - 1/\sqrt{3})x_2 = 0$ and $2x_1/\sqrt{3} + ((3/2) - 1/\sqrt{3})x_2 = 5$ and is sketched in Figure 15.3b.

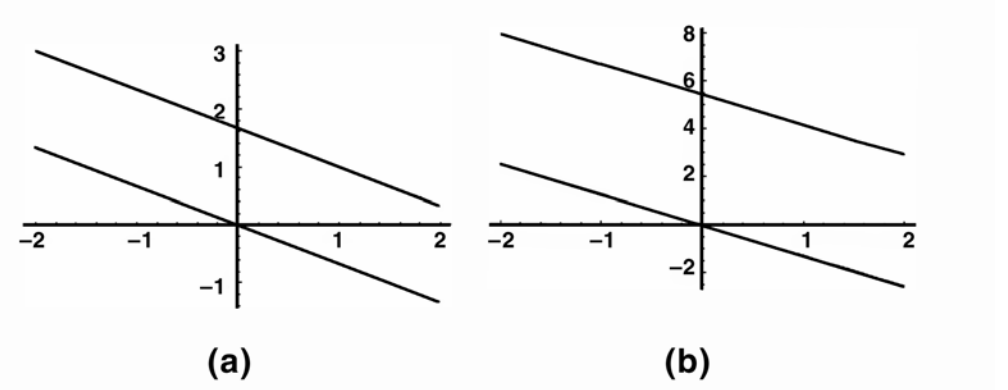



**Figure 15.3**. Illustration of Example 15.2.1: a set of parallel lines deforming into a set of parallel lines.

The effect of homogeneous deformations on ellipsoids is similar. Recall that the Cartesian equation for an ellipsoid is

$$\frac{X_{\mathrm{I}}^2}{a^2}+\frac{X_{\mathrm{II}}^2}{b^2}+\frac{X_{\mathrm{III}}^2}{c^2}=1\,, \tag{15.5}$$

where constants $a$, $b$, and $c$ represent the intersection points of the ellipsoid on the Cartesian coordinates axes. In material coordinates an ellipsoid has representation

$$\mathbf{X}\cdot\mathbf{A}\cdot\mathbf{X}=1, \tag{15.6}$$

where $\mathbf{A}$ is a constant second-rank tensor. To see that (15.5) and (15.6) are equivalent representations of an ellipsoid, let $\mathbf{A}$ be in its principal coordinate system and set $A_{11}=a^{-2}$, $A_{22}=b^{-2}$, $A_{33}=c^{-2}$. Substituting the inverse of (15.2), $\mathbf{X}=\mathbf{L}^{-1}\,\mathbf{x}$, into (15.6) yields

$$\mathbf{x}\cdot\mathbf{A}^{*}\cdot\mathbf{x}=1, \tag{15.7}$$

where a new constant second-rank tensor, $\mathbf{A}^{*}$, has been defined by the following transformation: $\mathbf{A}^{*}=(\mathbf{L}^{-1})^{\mathrm{T}}\cdot\mathbf{A}\cdot\mathbf{L}^{-1}$. Equation (15.7) is also the equation of an ellipsoid, an ellipsoid in the spatial coordinate system, thus permitting us to conclude that an ellipsoid in the material system is deformed into an ellipsoid in the spatial system by a homogeneous deformation. In particular, spheres will deform into ellipsoids and, in planar deformations, ellipses into ellipses (or circles into ellipses). This result is illustrated in the planar case where ellipses deform into ellipses or circles into ellipses in Figure 15.4.

**Problem 15.2.2**

Sketch the ellipse given by $X_{\mathrm{I}}^2/9+X_{\mathrm{II}}^2/4=1$, and then sketch the same ellipse after it is subjected to the homogeneous deformation of Example 15.2.1.

**Solution**: A sketch of the ellipse given by $X_{\mathrm{I}}^2/9+X_{\mathrm{II}}^2/4=1$ is shown in Figure 15.5a. Using the inverse of homogeneous deformation $\mathbf{F}$ determined in Example 15.2.1, tensor $\mathbf{A}$ representing ellipse $X_{\mathrm{I}}^2/9+X_{\mathrm{II}}^2/4$,

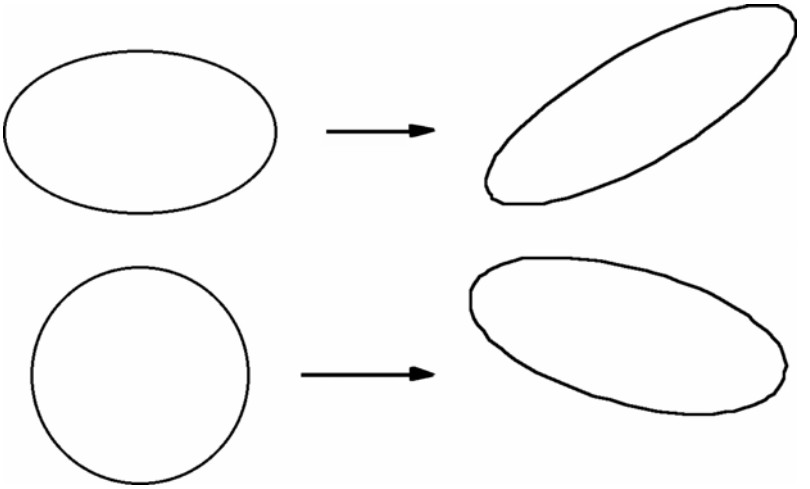


**Figure 15.4**. Illustration of an ellipse being deformed into an ellipse and of a circle being deformed into an ellipse.

$$\mathbf{A} = \begin{bmatrix} \frac{1}{9} & 0 & 0 \\ 0 & \frac{1}{4} & 0 \\ 0 & 0 & 0 \end{bmatrix},$$

is transformed into $\mathbf{A}^*$, $\mathbf{A}^* = (\mathbf{L}^{-1})^T \cdot \mathbf{A} \cdot \mathbf{L}^{-1}$,

$$\mathbf{A}^* = \frac{1}{54}\begin{bmatrix} 2 & -1 & 0 \\ -1 & \frac{31}{8} & 0 \\ 0 & 0 & 0 \end{bmatrix},$$

and the deformed ellipse is given by $\frac{1}{27}\left(x_1^2 + \frac{31}{16}x_2^2 - 2x_1x_2\right) = 1$. A sketch of the deformed ellipse is shown in Figure 15.5b.

The geometric results of this example give an intuitive insight into a number of tissue deformation situations. Consider the case when a circle is inscribed on a tissue and the tissue is then greatly deformed. Figure 15.6 illustrates the deformation of a circle with a ratio of principal axes of 1 to 1 through 10 steps to a ratio of principal axes of 1 to 19; this is the deformation of a circle inscribed on a surface subjected to a homogeneous deformation. At a ratio of principal axes of 1 to 19 the deformed circle looks more like a crack than an ellipse or the original

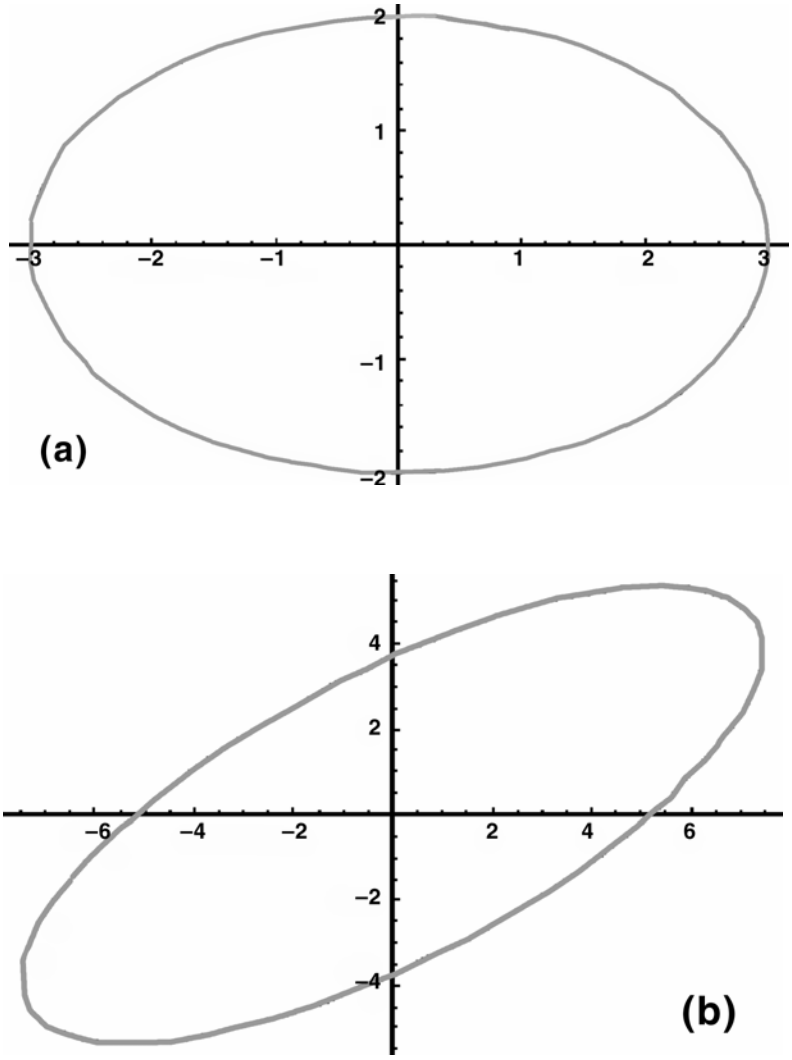



**Figure 15.5**. Illustration of Example 15.2.2: an ellipse deforming into an ellipse: (a) before deformation, (b) after deformation.

circle. It is not an exact analogy but one can, from this result, imagine what happens to the circular hole punched in a deformed tissue as not being greatly different. This gives one an intuitive understanding of how the split lines in Figure 14.12 occur after a punch is used to create a circular hole and how Langer lines can be created in the skin of a cadaver by the same method (Danielson, 1973; Danielson and Natarajan, 1975) (see Figure 15.7).

A most significant point concerning homogeneous deformation is that any deformation in a sufficiently small neighborhood of a point is a homogeneous deformation. This may be mathematically verified by expanding motion $\mathbf{x} = \boldsymbol{\chi}(\mathbf{X}, t)$ in a Taylor series in $\mathbf{X}$ about point $\mathbf{X}_o$ and retaining only the first order-term, which is the deformation gradient evaluated at $\mathbf{X}_o$. Thus, for a sufficiently small domain about point $\mathbf{X}_o$, the deformation gradient evaluated at $\mathbf{X}_o$

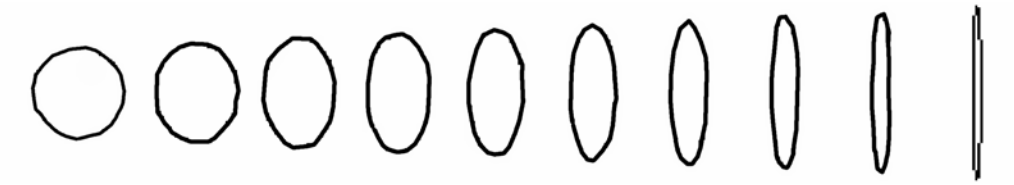


**Figure 15.6**. Illustration of a circle deforming into an ellipse by an increasingly unequal biaxial extension. The deformation deforms a principal axis ratio of 1 to 1 to one of 19 to 1.

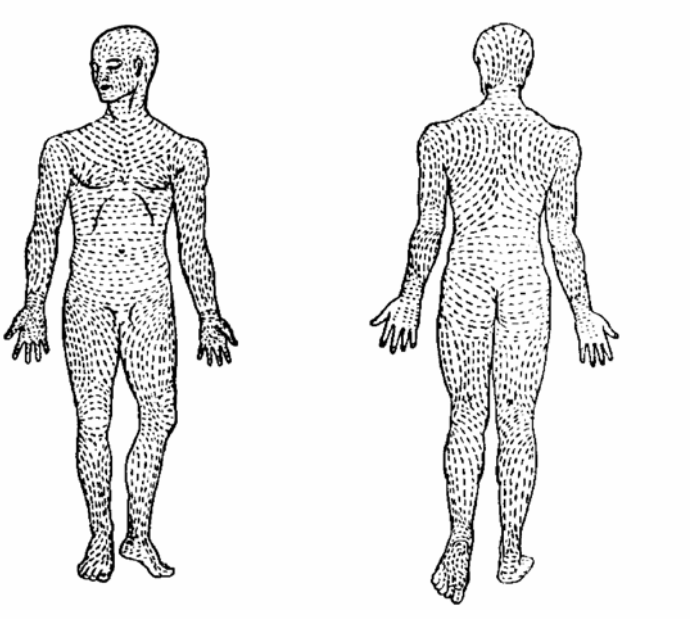


**Figure 15.7**. Langer lines on a cadaver. Reprinted with permission from Danielson (1973).

represents the deformation. Since this deformation gradient is independent of **X**, the deformation in this small domain is a homogeneous deformation. One easy way to illustrate the general truth of this mathematical result is to draw a small circle or parallelepiped on the skin with a washable ink, and then apply a deformation to the skin surface. Alternatively, the small circle can be drawn on a rubber eraser, and the eraser may be deformed to visualize the transition. The circle is easily seen to deform into an ellipse and must make an effort to obtain a non-elliptical shape. The same is true of parallelepipeds.

**Problems**

15.2.1. Sketch the set of parallel lines given by $\mathbf{a} = [-2, 1, 0]^T$ and $c = 0$ and 5, $-2X_I + X_{II} = 0$ and $-2X_I + X_{II} = 5$; then sketch the set of parallel lines after subjecting them to the homogeneous deformation of Example 15.2.1.

15.2.2. Sketch the ellipse given by $(X_I^2/16) + X_{II}^2 = 1$, and then sketch the same ellipse after it is subjected to the homogeneous deformation of Example 15.2.1.

15.2.3. Show that deformation $x_1 = (9/4)X_I$, $x_2 = X_{II}$, $x_1 = X_{II}$, carries ellipse $(X_I/4)^2 + (X_{II}/9)^2 = 1$ into circle $(x_1/9)^2 + (x_2/9)^2 = 1$, and that the inverse deformation carries circle $(X_I/4)^2 + (X_{II}/4)^2 = 1$ into ellipse $(x_1/9)^2 + (x_2/4)^2 = 1$. Provide a sketch of the undeformed and deformed ellipses and circles.

15.2.4 Why is it not possible for an ellipse to deform into a hyperbola?.

## 15.3. POLAR DECOMPOSITION OF THE DEFORMATION GRADIENTS

It can be shown that deformation gradient **F** can be algebraically decomposed in two ways into a pure deformation and a pure rotation. This decomposition is multiplicative and is written

$$\mathbf{F} = \mathbf{R}\cdot\mathbf{U} = \mathbf{V}\cdot\mathbf{R}, \tag{15.8}$$

where **R** is an orthogonal tensor ($\mathbf{R}^T\cdot\mathbf{R} = \mathbf{R}\cdot\mathbf{R}^T = \mathbf{1}$) representing the rotation and called the rotation tensor, and **U** and **V** are called the right and left stretch tensors, respectively. Both **U** and **V** represent the same pure deformation, but in different ways that will be demonstrated. The right and left stretch tensors, **U** and **V**, are related to **F** by

$$\mathbf{U} = \sqrt{\mathbf{F}^T\cdot\mathbf{F}}, \quad \mathbf{V} = \sqrt{\mathbf{F}\cdot\mathbf{F}^T}. \tag{15.9}$$

In order to define the square root of a tensor involved in (15.9), the tensor must be symmetric and positive definite. In that case the square root is constructed by transforming the tensor to its principal axes where the eigenvalues are all positive; then the square root of the tensor is the diagonalized tensor coincident with the principal axes but containing the square roots of the eigenvalues along the diagonal. To show that definitions (15.9) are reasonable it should be shown that tensors $\mathbf{U}^2$ and $\mathbf{V}^2$ are positive definite:

$$\mathbf{U}^2 = \mathbf{F}^T\cdot\mathbf{F}, \ \mathbf{V}^2 = \mathbf{F}\cdot\mathbf{F}^T. \tag{15.10}$$

The positive definite character of $\mathbf{U}^2$ may be seen by letting it operate on vector **a**, and then taking the scalar product with **a**; thus,

$$\mathbf{a}\cdot\mathbf{U}^2\cdot\mathbf{a} = \mathbf{a}\cdot\mathbf{F}^T\cdot\mathbf{F}\cdot\mathbf{a} = (\mathbf{F}\cdot\mathbf{a})\cdot(\mathbf{F}\cdot\mathbf{a}) \geq 0, \tag{15.11}$$

where the fact that $\mathbf{a}\cdot\mathbf{F}^T = (\mathbf{F}\cdot\mathbf{a})$ has been used. A similar proof will show the positive definite character of $\mathbf{V}^2$. The fact that tensor **R** is orthogonal follows from the definitions of **U** and/or **V**. From (15.8) **R** is given by $\mathbf{R} = \mathbf{F}\cdot\mathbf{U}^{-1}$ (or $\mathbf{R} = \mathbf{V}^{-1}\cdot\mathbf{F}$), and thus calculation of $\mathbf{R}^T\cdot\mathbf{R}$ (or $\mathbf{R}\cdot\mathbf{R}^T$) yields

$$\mathbf{R}^T\cdot\mathbf{R} = \mathbf{U}^{-1}\cdot\mathbf{F}^T\cdot\mathbf{F}\cdot\mathbf{U}^{-1} = \mathbf{U}^{-1}\cdot\mathbf{U}^2\cdot\mathbf{U}^{-1} = \mathbf{1},$$

where the fact that **U** and its inverse are symmetric and definition (15.10) have been employed. As an example of this decomposition, consider the **F** associated with a simple shearing deformation illustrated in Figure 15.8. The decomposition of this simple shearing deformation is shown in Figure 15.9.

**Problem 15.3.1**

Determine the polar decomposition of deformation gradient tensor

$$\mathbf{F} = \begin{bmatrix} \sqrt{3} & 1 & 0 \\ 0 & 2 & 0 \\ 0 & 0 & 1 \end{bmatrix}.$$

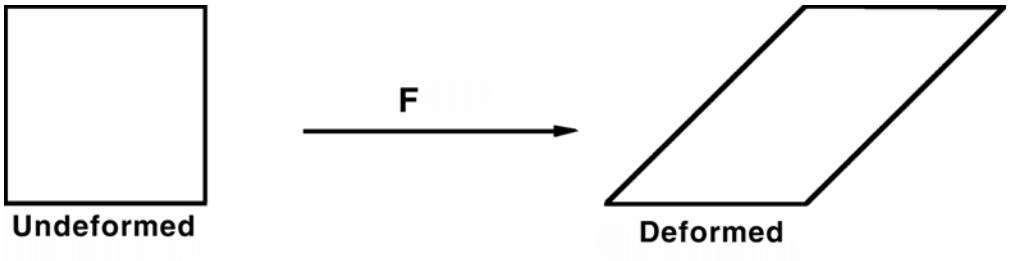



**Figure 15.8**. Deformation of a square by **F**.

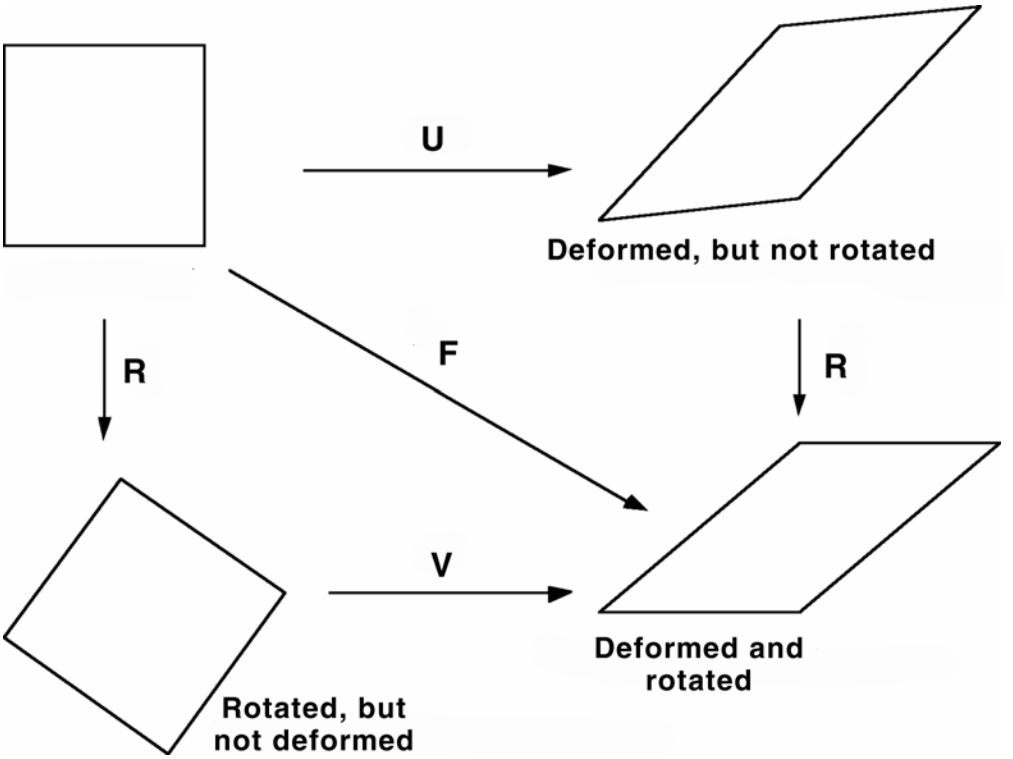



**Figure 15.9**. Deformation of a square by **F**, illustrating the polar decomposition of **F**.

**Solution**: The squares or the right and left stretch tensors are calculated directly from **F**; thus,

$$\mathbf{U}^2 = \mathbf{F}^T \cdot \mathbf{F} = \begin{bmatrix} 3 & \sqrt{3} & 0 \\ \sqrt{3} & 5 & 0 \\ 0 & 0 & 1 \end{bmatrix}, \quad \mathbf{V}^2 = \mathbf{F} \cdot \mathbf{F}^T = \begin{bmatrix} 4 & 2 & 0 \\ 2 & 4 & 0 \\ 0 & 0 & 1 \end{bmatrix}.$$

The square roots of these two tensors are constructed by transforming the tensor to its principal axes where the eigenvalues are all positive; then the square root of the tensor is the diagonalized tensor coincident with the principal axes but containing the square roots of the eigenvalues along the diagonal:

$$\mathbf{U}=\begin{bmatrix}\sqrt{3}A & \sqrt{3}B & 0\\ \sqrt{3}B & 2A+B & 0\\ 0 & 0 & 1\end{bmatrix},\quad \mathbf{V}=\begin{bmatrix}2A & 2B & 0\\ 2B & 2A & 0\\ 0 & 0 & 1\end{bmatrix},$$

where

$$A=\cos 15^{\circ}=\frac{\sqrt{3}+1}{2\sqrt{2}},\quad B=\sin 15^{\circ}=\frac{\sqrt{3}-1}{2\sqrt{2}}.$$

The fact that $\mathbf{U}$ and $\mathbf{V}$ given above are the square roots of $\mathbf{U}^2$ and $\mathbf{V}^2$, respectively, may be verified simply by squaring $\mathbf{U}$ and $\mathbf{V}$. The orthogonal tensor $\mathbf{R}$ may be computed in several ways:

$$\mathbf{R}=\mathbf{V}^{-1}\cdot\mathbf{F}=\mathbf{F}\cdot\mathbf{U}^{-1}=\begin{bmatrix}A & B & 0\\ -B & A & 0\\ 0 & 0 & 1\end{bmatrix}.$$

The polar right and left decompositions of the given deformation gradient tensor are then given by

$$\mathbf{F}=\mathbf{R}\cdot\mathbf{U}=\begin{bmatrix}A & B & 0\\ -B & A & 0\\ 0 & 0 & 1\end{bmatrix}\begin{bmatrix}\sqrt{3}A & \sqrt{3}B & 0\\ \sqrt{3}B & 2A+B & 0\\ 0 & 0 & 1\end{bmatrix}=\begin{bmatrix}\sqrt{3} & 1 & 0\\ 0 & 2 & 0\\ 0 & 0 & 1\end{bmatrix},$$

and

$$\mathbf{F}=\mathbf{V}\cdot\mathbf{R}=\begin{bmatrix}2A & 2B & 0\\ 2B & 2A & 0\\ 0 & 0 & 1\end{bmatrix}\begin{bmatrix}A & B & 0\\ -B & A & 0\\ 0 & 0 & 1\end{bmatrix}=\begin{bmatrix}\sqrt{3} & 1 & 0\\ 0 & 2 & 0\\ 0 & 0 & 1\end{bmatrix},$$

respectively.

**Problem 15.3.2**

Develop a geometric interpretation of deformation gradient tensor **F** of Problem 15.3.1 by considering it as representing homogeneous deformation **x** = **F**·**X** acting on a unit square with vertices (0, 0), (1, 0), (1, 1), (0, 1).

**Solution**: The scalar equations equivalent to homogeneous deformation **x** = **F**·**X,** where **F** is given in the statement of Example 15.3.1, are

$$x_{\mathrm{I}} = \sqrt{3}X_{\mathrm{I}} + X_{\mathrm{II}},\ \ x_2 = 2X_{\mathrm{II}},\ \ x_3 = X_{\mathrm{III}}.$$

This unit square is deformed by **F** into a parallelogram with corners at points (0, 0), (√3, 0), (1 + √3, 2), and (1, 2) as illustrated in Figure 15.10. Consider the left decomposition, **F** = **V**·**R**, first. In this decomposition rotation **R** is applied first, then left deformation or left stretch **V**. The effect of **R** on the unit square is a clockwise rotation of 15°; this is illustrated in Figure 15.11. Following this rotation of the unit square, there is a left stretch, **V,** that carries the rotated square into the deformed shape illustrated in Figure 15.9. The other decomposition choice, **F** = **R**·**U,** reverses the order of the deformation and the rotation. The deformation or right stretch **U** is first applied to the unit square and it deforms the square into the shape illustrated in Figure 15.12. The clockwise rotation of 15° is then applied, and it rotates the deformed shape illustrated in Figure 15.9 into its final position, illustrated in Figure 15.8.

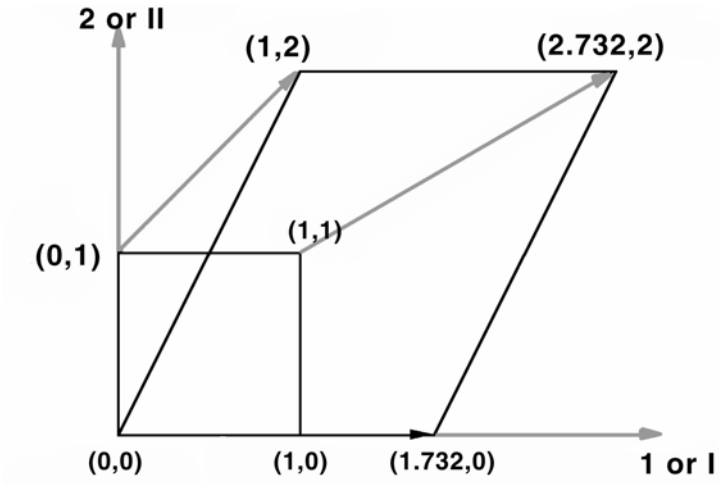



**Figure 15.10**. Deformation of a unit square by the **F** of Example 15.3.1.

**Problems**

15.3.1. Prove that **a**·**F**$^{\mathrm{T}}$ = **F**·**a**.

15.3.2. Find the square root of matrix

$$\mathbf{V}^2 = \begin{bmatrix} 4 & 1 & -1 \\ 1 & 6 & 0 \\ -1 & 0 & 2 \end{bmatrix}.$$

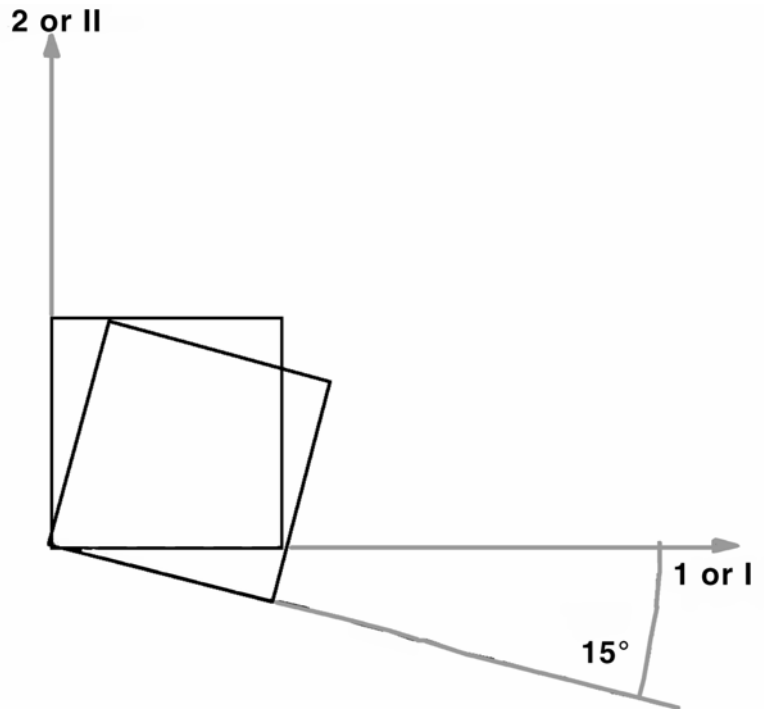



**Figure 15.11**. Deformation of a unit square by the **R** of Example 15.3.1.

15.3.3. Find the square root of matrix

$$\mathbf{A} = \begin{bmatrix} 31 & -5\sqrt{3} & 0 \\ -5\sqrt{3} & 21 & 0 \\ 0 & 0 & 4 \end{bmatrix}.$$

15.3.4. Find the polar decomposition of tensor

$$\mathbf{F} = \begin{bmatrix} 1 & \alpha & 0 \\ 0 & 1 & 0 \\ 0 & 0 & 1 \end{bmatrix}.$$

## 15.4. THE STRAIN MEASURES FOR LARGE DEFORMATIONS

The deformation gradient is the basic measure of local deformational and rotational motion. It maps a small region of the undeformed object into a small region of the deformed object. If the motion is a pure translation with no rotation, then $\mathbf{F} = \mathbf{1}$. If the motion is a rigid object rotation, then $\mathbf{F} = \mathbf{R}$, where $\mathbf{R}$ is an orthogonal matrix: $\mathbf{R}\cdot\mathbf{R}^{\mathrm{T}} = \mathbf{R}^{\mathrm{T}}\cdot\mathbf{R} = \mathbf{1}$.

The local state of deformation may be investigated by considering the deformation of an infinitesimal material filament denoted by $d\mathbf{X}$. In the instantaneous configuration the same

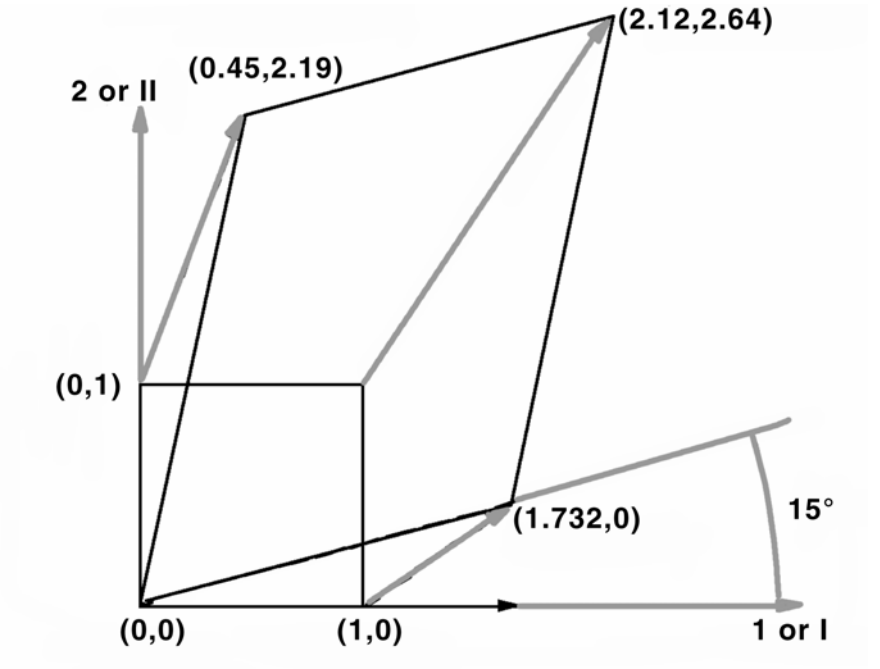



**Figure 15.12**. Deformation of a unit square by the **U** of Example 15.3.1.

material filament has a position represented by $d\mathbf{x}$. Recalling representation (3.2) for a motion, $\mathbf{x} = \boldsymbol{\chi}(\mathbf{X}, t)$, and representation (3.16) for $\mathbf{F}$, it is easy to see that $d\mathbf{x}$ and $d\mathbf{X}$ are related by $d\mathbf{x} = \mathbf{F}\cdot d\mathbf{X}$, or from the polar decomposition theorem, $d\mathbf{x} = \mathbf{R}\cdot\mathbf{U}\cdot d\mathbf{X} = \mathbf{V}\cdot\mathbf{R}\cdot d\mathbf{X}$. Thus, with a pure rotational motion for which $\mathbf{U} = \mathbf{V} = \mathbf{1}$**,** the length of $d\mathbf{X}$ will be preserved but its direction will be rotated. If the motion includes a deformational component, then the length of $d\mathbf{x}$ will be different from the length of $d\mathbf{X}$, in general. To calculate this change in length we denote the square of the final length by $ds^2 = d\mathbf{x}\cdot d\mathbf{x}$, and the square of the initial length by $dS^2 = d\mathbf{X}\cdot d\mathbf{X}$. The difference in the squares of these length changes is written $ds^2 - dS^2 = d\mathbf{x}\cdot d\mathbf{x} - d\mathbf{X}\cdot d\mathbf{X}$. This expression for $ds^2 - dS^2$ can be written entirely in terms of the material filament, $d\mathbf{X}$**,** or entirely in terms of its image, $d\mathbf{x}$**,** at time $t$. To accomplish both of these objectives we observe that, using $d\mathbf{x} = \mathbf{F}\cdot d\mathbf{X}$, $d\mathbf{x}\cdot d\mathbf{x}$ has representation

$$d\mathbf{x}\cdot d\mathbf{x} = (\mathbf{F}\cdot d\mathbf{X})\cdot(\mathbf{F}\cdot d\mathbf{X}) = d\mathbf{X}\cdot\mathbf{F}^{\mathrm{T}}\cdot\mathbf{F}\cdot d\mathbf{X}, \tag{15.12}$$

and that $d\mathbf{X} = \mathbf{F}^{-1}\cdot d\mathbf{x}$, and $d\mathbf{X}\cdot d\mathbf{X}$ has representation

$$d\mathbf{X}\cdot d\mathbf{X} = (\mathbf{F}^{-1}\cdot d\mathbf{x})\cdot(\mathbf{F}^{-1}\cdot d\mathbf{x}) = d\mathbf{x}\cdot(\mathbf{F}^{-1})^{\mathrm{T}}\cdot\mathbf{F}^{-1}d\mathbf{x}. \tag{15.13}$$

The two formulas may then be derived from expression $ds^2 - dS^2 = d\mathbf{x}\cdot d\mathbf{x} - d\mathbf{X}\cdot d\mathbf{X}$, one by substituting for $d\mathbf{x}\cdot d\mathbf{x}$ from (15.12) and the other by substituting for $d\mathbf{X}\cdot d\mathbf{X}$ from (15.13), and thus

$$ds^2 - dS^2 = d\mathbf{x}\cdot d\mathbf{x} - d\mathbf{X}\cdot d\mathbf{X} = \{\mathbf{F}^{\mathrm{T}}\cdot\mathbf{F} - \mathbf{1}\}\, d\mathbf{X}\cdot d\mathbf{X} = \{\mathbf{1} - (\mathbf{F}^{-1})^{\mathrm{T}}\cdot\mathbf{F}^{-1}\}\, d\mathbf{x}\cdot d\mathbf{x}. \tag{15.14}$$

Lagrangian or material strain tensor $\mathbf{E}$ and Eulerian or spatial strain tensor $\mathbf{e}$ are defined by

$$\mathbf{E} = (1/2)\{\mathbf{F}^{\mathrm{T}}\cdot\mathbf{F} - \mathbf{1}\}, \quad \mathbf{e} = (1/2)\{\mathbf{1} - (\mathbf{F}^{-1})^{\mathrm{T}}\cdot\mathbf{F}^{-1}\}. \tag{15.15}$$

In terms of the strain tensors, change $ds^2 - dS^2$ takes the form

$$ds^2 - dS^2 = 2d\mathbf{X}\cdot\mathbf{E}\cdot d\mathbf{X} = 2d\mathbf{x}\cdot\mathbf{e}\cdot d\mathbf{x}. \tag{15.16}$$

Clearly, if either of these strain tensors is zero, then so is the other, and there is no change in length for any material filament, $ds^2 = dS^2$.

Lagrangian strain tensor $\mathbf{E}$ and Eulerian strain tensor $\mathbf{e}$ are defined for large strains and represented in terms of the deformation gradient and its inverse in (15.15). A component representation of these two tensors in terms of displacement vector $\mathbf{u}$ will now be obtained. From (3.20) and Figure 3.4, $\mathbf{u}$ is given by $\mathbf{u} = \mathbf{x} - \mathbf{X} + \mathbf{c}$. If $\mathbf{u}$ is referred to the spatial coordinate system and the spatial gradient taken, or if $\mathbf{u}$ is referred to the material coordinate system and the material gradient taken (§3.2), then

$$[\nabla_o \otimes \mathbf{u}(\mathbf{X}, t)]^T = \mathbf{F}(\mathbf{X}, t) - \mathbf{1} \text{ and } [\nabla \otimes \mathbf{u}(\mathbf{x}, t)]^T = \mathbf{1} - \mathbf{F}^{-1}(\mathbf{x}, t). \quad \text{(3.23) repeated}$$

These equations are then solved for $\mathbf{F}$ and $\mathbf{F}^{-1}$; thus,

$$\mathbf{F}(\mathbf{X}, t) = \mathbf{1} + [\nabla_o \otimes \mathbf{u}(\mathbf{X}, t)]^T \quad \text{and} \quad \mathbf{F}^{-1}(\mathbf{x}, t) = \mathbf{1} - [\nabla \otimes \mathbf{u}(\mathbf{x}, t)]^T. \tag{15.17}$$

Lagrangian strain tensor $\mathbf{E}$ and Eulerian strain tensor $\mathbf{e}$ are related to the displacement gradients by substituting the two equations of (15.17) into the two equations of (15.15), and thus

$$\mathbf{E} = (1/2)\{ [\nabla_o \otimes \mathbf{u}(\mathbf{X}, t)]^T + [\nabla_o \otimes \mathbf{u}(\mathbf{X}, t)] + [\nabla_o \otimes \mathbf{u}(\mathbf{X}, t)][\nabla_o \otimes \mathbf{u}(\mathbf{X}, t)]^T \}, \tag{15.18}$$

$$\mathbf{e} = (1/2)\{ [\nabla \otimes \mathbf{u}(\mathbf{x}, t)]^T + [\nabla \otimes \mathbf{u}(\mathbf{x}, t)] - [\nabla \otimes \mathbf{u}(\mathbf{x}, t)][\nabla \otimes \mathbf{u}(\mathbf{x}, t)]^T \}. \tag{15.19}$$

The expanded component forms of (15.18) and (15.19) are given by

$$E_{\mathrm{I\,I}} = \frac{\partial u_{\mathrm{I}}}{\partial x_{\mathrm{I}}} + \frac{1}{2}\left[\left\{\frac{\partial u_{\mathrm{I}}}{\partial x_{\mathrm{I}}}\right\}^2 + \left\{\frac{\partial u_{\mathrm{II}}}{\partial x_{\mathrm{I}}}\right\}^2 + \left\{\frac{\partial u_{\mathrm{III}}}{\partial x_{\mathrm{I}}}\right\}^2\right],$$

$$E_{\mathrm{II\,II}} = \frac{\partial u_{\mathrm{II}}}{\partial x_{\mathrm{II}}} + \frac{1}{2}\left[\left\{\frac{\partial u_{\mathrm{I}}}{\partial x_{\mathrm{II}}}\right\}^2 + \left\{\frac{\partial u_{\mathrm{II}}}{\partial x_{\mathrm{II}}}\right\}^2 + \left\{\frac{\partial u_{\mathrm{III}}}{\partial x_{\mathrm{II}}}\right\}^2\right],$$

$$E_{\mathrm{III\,III}} = \frac{\partial u_{\mathrm{III}}}{\partial x_{\mathrm{III}}} + \frac{1}{2}\left[\left\{\frac{\partial u_{\mathrm{I}}}{\partial x_{\mathrm{III}}}\right\}^2 + \left\{\frac{\partial u_{\mathrm{II}}}{\partial x_{\mathrm{III}}}\right\}^2 + \left\{\frac{\partial u_{\mathrm{III}}}{\partial x_{\mathrm{III}}}\right\}^2\right],$$

$$E_{\mathrm{I\,II}} = \frac{1}{2}\left[\frac{\partial u_{\mathrm{I}}}{\partial x_{\mathrm{II}}} + \frac{\partial u_{\mathrm{II}}}{\partial x_{\mathrm{I}}} + \frac{\partial u_{\mathrm{I}}}{\partial x_{\mathrm{I}}}\frac{\partial u_{\mathrm{II}}}{\partial x_{\mathrm{I}}} + \frac{\partial u_{\mathrm{II}}}{\partial x_{\mathrm{I}}}\frac{\partial u_{\mathrm{II}}}{\partial x_{\mathrm{II}}} + \frac{\partial u_{\mathrm{III}}}{\partial x_{\mathrm{I}}}\frac{\partial u_{\mathrm{III}}}{\partial x_{\mathrm{II}}}\right], \tag{15.20}$$

$$E_{\mathrm{I\,III}} = \frac{1}{2}\left[\frac{\partial u_{\mathrm{I}}}{\partial x_{\mathrm{III}}} + \frac{\partial u_{\mathrm{III}}}{\partial x_{\mathrm{I}}} + \frac{\partial u_{\mathrm{I}}}{\partial x_{\mathrm{I}}}\frac{\partial u_{\mathrm{III}}}{\partial x_{\mathrm{I}}} + \frac{\partial u_{\mathrm{II}}}{\partial x_{\mathrm{I}}}\frac{\partial u_{\mathrm{II}}}{\partial x_{\mathrm{III}}} + \frac{\partial u_{\mathrm{III}}}{\partial x_{\mathrm{I}}}\frac{\partial u_{\mathrm{III}}}{\partial x_{\mathrm{III}}}\right],$$

$$E_{\mathrm{II\,III}} = \frac{1}{2}\left[\frac{\partial u_{\mathrm{II}}}{\partial x_{\mathrm{III}}} + \frac{\partial u_{\mathrm{III}}}{\partial x_{\mathrm{II}}} + \frac{\partial u_{\mathrm{I}}}{\partial x_{\mathrm{II}}}\frac{\partial u_{\mathrm{II}}}{\partial x_{\mathrm{III}}} + \frac{\partial u_{\mathrm{II}}}{\partial x_{\mathrm{III}}}\frac{\partial u_{\mathrm{II}}}{\partial x_{\mathrm{III}}} + \frac{\partial u_{\mathrm{III}}}{\partial x_{\mathrm{II}}}\frac{\partial u_{\mathrm{III}}}{\partial x_{\mathrm{III}}}\right],$$

and

$$e_{11} = \frac{\partial u_1}{\partial x_1} - \frac{1}{2}\left[\left\{\frac{\partial u_1}{\partial x_1}\right\}^2 + \left\{\frac{\partial u_2}{\partial x_1}\right\}^2 + \left\{\frac{\partial u_3}{\partial x_1}\right\}^2\right],$$

$$e_{22} = \frac{\partial u_2}{\partial x_2} - \frac{1}{2}\left[\left\{\frac{\partial u_1}{\partial x_2}\right\}^2 + \left\{\frac{\partial u_2}{\partial x_2}\right\}^2 + \left\{\frac{\partial u_3}{\partial x_2}\right\}^2\right],$$

$$e_{33} = \frac{\partial u_3}{\partial x_3} - \frac{1}{2}\left[\left\{\frac{\partial u_1}{\partial x_3}\right\}^2 + \left\{\frac{\partial u_2}{\partial x_3}\right\}^2 + \left\{\frac{\partial u_3}{\partial x_3}\right\}^2\right],$$

$$e_{12} = \frac{1}{2}\left[\frac{\partial u_1}{\partial x_2} + \frac{\partial u_2}{\partial x_1} - \frac{\partial u_1}{\partial x_1}\frac{\partial u_2}{\partial x_1} - \frac{\partial u_2}{\partial x_1}\frac{\partial u_2}{\partial x_2} - \frac{\partial u_3}{\partial x_1}\frac{\partial u_3}{\partial x_2}\right], \tag{15.21}$$

$$e_{13} = \frac{1}{2}\left[\frac{\partial u_1}{\partial x_3} + \frac{\partial u_3}{\partial x_1} - \frac{\partial u_1}{\partial x_1}\frac{\partial u_3}{\partial x_1} - \frac{\partial u_2}{\partial x_1}\frac{\partial u_2}{\partial x_3} - \frac{\partial u_3}{\partial x_1}\frac{\partial u_3}{\partial x_3}\right],$$

$$e_{23} = \frac{1}{2}\left[\frac{\partial u_2}{\partial x_3} + \frac{\partial u_3}{\partial x_2} - \frac{\partial u_1}{\partial x_2}\frac{\partial u_2}{\partial x_3} - \frac{\partial u_2}{\partial x_3}\frac{\partial u_2}{\partial x_3} - \frac{\partial u_3}{\partial x_2}\frac{\partial u_3}{\partial x_3}\right],$$

respectively. The products of the displacement gradients appear in eqs. (15.20) and (15.21) for strain tensor **E** and **e**. This is called geometrical nonlinearity to distinguish it from physical or constitutive nonlinearity (e.g. the relation between stress and strain), which will be considered later in this chapter. If the deformation of the object is so small that the square of the displacement gradients can be neglected, and thus the difference between the material and spatial coordinates, then both Lagrangian strain tensor **E** and Eulerian strain tensor **e** coincide with the infinitesimal strain tensor (3.44).

The geometrical interpretation of Lagrangian strain tensor **E** and Eulerian strain tensor **e** are algebraically straightforward but not very simple geometrically. If $\delta_I$ represents the change in length per unit length in the $X_I$ direction, then deformation gradient **F** and Lagrangian strain tensor **E** are given by

$$\mathbf{F} = \mathbf{1} + \delta_I \begin{bmatrix} 1 & 0 & 0 \\ 0 & 0 & 0 \\ 0 & 0 & 0 \end{bmatrix}, \quad \mathbf{E} = (1/2)\{\mathbf{F}^T \cdot \mathbf{F} - \mathbf{1}\} = \left(\delta_I + \frac{1}{2}\delta_I^2\right)\begin{bmatrix} 1 & 0 & 0 \\ 0 & 0 & 0 \\ 0 & 0 & 0 \end{bmatrix}; \tag{15.22}$$

thus, all the components of **E** are zero except for

$$E_{\mathrm{I\,I}} = \left(\delta_I + \frac{1}{2}\delta_I^2\right). \tag{15.23}$$

If $\delta_{II}$ represents the change in length per unit length in the $X_{II}$ direction, and $\sin\phi$ indicates a shear, then the deformation gradient is given by

$$\mathbf{F} = \begin{bmatrix} 1+\delta_I & (1+\delta_I)\sin\phi & 0 \\ 0 & 1+\delta_{II} & 0 \\ 0 & 0 & 1 \end{bmatrix}, \tag{15.24}$$

and Lagrangian strain tensor component $E_{\mathrm{I\,II}}$ is related to $\delta_I$, $\delta_{II}$, and to the change in right angle $\phi$ between the filaments lying in the I and II directions by

$$E_{\mathrm{I\,II}} = \left(\frac{1}{2}\right)(1+\delta_{\mathrm{I}})(1+\delta_{\mathrm{II}})\sin\phi\,. \tag{15.25}$$

Thus, unless extensions $\delta_{\mathrm{I}}$, $\delta_{\mathrm{I}}$, and $\phi$ are small, so that the square of each may be neglected, the traditional geometric interpretation for small strains,

$$E_{\mathrm{I\,I}} \approx \delta_{I}\,,\; E_{\mathrm{I\,II}} \approx \frac{\phi}{2}\,, \tag{15.26}$$

namely, that $E_{\mathrm{I\,I}}$ is the extension in the I direction and $E_{\mathrm{I\,II}}$ is one-half the change in an angle that was originally a right angle, is not accurate. Equations (15.23) and (15.24) representing $E_{\mathrm{I\,I}}$ and $E_{\mathrm{I\,II}}$ in terms of $\delta_{\mathrm{I}}$, $\delta_{\mathrm{II}}$, and $\phi$ show that the geometric interpretation of the finite strain tensors in terms of extensions and changes in right angles is possible, but is awkward and not very useful due to its nonlinear nature.

**Example 15.4.1**

Compute Lagrangian strain tensor **E** and Eulerian strain tensor **e** for the motion given by (3.12). Determine the range of values of $t$ for which these two strain measures coincide in this special motion.

**Solution**: The deformation gradient and inverse deformation gradient for the motion (3.12) are given in Example 3.1.1:

$$\mathbf{F} = \begin{bmatrix} 1+t & t & 0 \\ t & 1+t & 0 \\ 0 & 0 & 1 \end{bmatrix} \text{ and } \mathbf{F}^{-1} = \frac{1}{1+2t}\begin{bmatrix} 1+t & -t & 0 \\ -t & 1+t & 0 \\ 0 & 0 & 1+2t \end{bmatrix}.$$

These values for **F** and $\mathbf{F}^{-1}$ can then be substituted into (15.15) for Lagrangian strain tensor **E** and Eulerian strain tensor **e**; thus,

$$\mathbf{E} = t(1+t)\begin{bmatrix} 1 & 1 & 0 \\ 1 & 1 & 0 \\ 0 & 0 & 0 \end{bmatrix} \text{ and } \mathbf{e} = \frac{t(1+t)}{(1+2t)^2}\begin{bmatrix} 1 & 1 & 0 \\ 1 & 1 & 0 \\ 0 & 0 & 0 \end{bmatrix}.$$

These expressions are, of course, valid for large strains. If we restrict ourselves to small strains, then the two strain tensors must coincide. Since each component of **E** is proportional to $t + t^2$ and each component of **e** is proportional to

$$\frac{t(1+t)}{(1+2t)^2} = t - 3t^2 + 8t^3 - \ldots,$$

the two strain tensors coincide only if terms of order $t^2$ and higher are neglected. Thus, motion (3.12) is one of small strain only when all terms of order $t^2$ and higher are neglected.

There are several other strain measures used in the development and analysis of finite deformations. Two of the most widely used are the right and left Cauchy-Green tensors, **C** and **B**, respectively. These two tensors are simply the squares of the right and left stretch tensors, **U** and **V**:

$$\mathbf{C} = \mathbf{U}^2 = \mathbf{F}^{\mathrm{T}}\cdot\mathbf{F}, \quad \mathbf{B} = \mathbf{V}^2 = \mathbf{F}\cdot\mathbf{F}^{\mathrm{T}}. \tag{15.27}$$

It is also convenient to introduce the inverse of the left Cauchy-Green tensor, denoted by **c**,

$$\mathbf{c} = \mathbf{B}^{-1} = \mathbf{V}^{-2} = (\mathbf{F}\cdot\mathbf{F}^{\mathrm{T}})^{-1}. \tag{15.28}$$

Lagrangian strain tensor **E** and Eulerian strain tensor **e** are expressed in terms of **C** and **c** by the following formulas that follow from (15.15), and the definitions of **C** and **c** given as (15.27) and (15.28) above:

$$\mathbf{2E} = \mathbf{C} - \mathbf{1}, \quad \mathbf{2e} = \mathbf{1} - \mathbf{c}. \tag{15.29}$$

The eigenvalues of the various strain measures may be interpreted using the concept of *stretch*. The stretch, $\lambda_{(\mathbf{N})}$, in the fiber coincident with $d\mathbf{X}$ is defined by

$$\lambda_{(\mathbf{N})} = \sqrt{\frac{d\mathbf{x}\cdot d\mathbf{x}}{d\mathbf{X}\cdot d\mathbf{X}}}, \tag{15.30}$$

where **N** is a unit vector in the direction of $d\mathbf{X}$. The related concept of extension, $\delta_{(\mathbf{N})}$, is then defined in terms of stretch by

$$\delta_{(\mathbf{N})} = \lambda_{(\mathbf{N})} - 1. \tag{15.31}$$

As an illustration of homogeneous deformations, and of the relationship of the stretch concept to the various strain measures that have been introduced, the special case of *pure homogeneous deformation*s is considered. A pure homogeneous deformation is a deformation for which the rotation $\mathbf{R} = \mathbf{1}$ and the deformation gradient tensor becomes symmetric, $\mathbf{F} = \mathbf{U} = \mathbf{V}$. In its principal coordinate system the deformation gradients of a pure homogeneous deformation have representation

$$\mathbf{F} = \mathbf{U} = \mathbf{V} = \begin{bmatrix} \lambda_{\mathrm{I}} & 0 & 0 \\ 0 & \lambda_{\mathrm{II}} & 0 \\ 0 & 0 & \lambda_{\mathrm{III}} \end{bmatrix}, \tag{15.32}$$

where $\lambda_{\mathrm{I}}$, $\lambda_{\mathrm{II}}$, $\lambda_{\mathrm{III}}$ are the principal stretches. The principal stretches represent the effect of the deformation upon material filaments in the coordinate directions as they are the ratios of the final length of the filament to the initial length of the filament. In terms of the principal stretches, deformation tensors **C** and **c** have representations

$$\mathbf{C} = \begin{bmatrix} \lambda_{\mathrm{I}}^2 & 0 & 0 \\ 0 & \lambda_{\mathrm{II}}^2 & 0 \\ 0 & 0 & \lambda_{\mathrm{III}}^2 \end{bmatrix}, \quad \mathbf{c} = \begin{bmatrix} \lambda_{\mathrm{I}}^{-2} & 0 & 0 \\ 0 & \lambda_{\mathrm{II}}^{-2} & 0 \\ 0 & 0 & \lambda_{\mathrm{III}}^{-2} \end{bmatrix}, \tag{15.33}$$

and Lagrangian strain tensor **E** and Eulerian strain tensor **e**:

$$2\mathbf{E} = \begin{bmatrix} \lambda_{\mathrm{I}}^2 - 1 & 0 & 0 \\ 0 & \lambda_{\mathrm{II}}^2 - 1 & 0 \\ 0 & 0 & \lambda_{\mathrm{III}}^2 - 1 \end{bmatrix}, \quad 2\mathbf{e} = \begin{bmatrix} 1 - \lambda_{\mathrm{I}}^{-2} & 0 & 0 \\ 0 & 1 - \lambda_{\mathrm{II}}^{-2} & 0 \\ 0 & 0 & 1 - \lambda_{\mathrm{III}}^{-2} \end{bmatrix}. \tag{15.34}$$

Two special cases of pure homogeneous deformation are of particular interest. A *simple extension* is characterized by $\lambda_{\mathrm{I}} \neq \lambda_{\mathrm{II}} = \lambda_{\mathrm{III}}$ and is illustrated in Figure 15.13. A *uniform dilation* is characterized by $\lambda = \lambda_{\mathrm{I}} = \lambda_{\mathrm{II}} = \lambda_{\mathrm{III}}$ and is illustrated in Figure 15.14 In the case of uniform dilation, $\mathbf{F} = \mathbf{U} = \mathbf{V} = \lambda\mathbf{1}$, $\mathbf{C} = \lambda^2\mathbf{1}$, $\mathbf{c} = \lambda^{-2}\mathbf{1}$, $\mathbf{2E} = (\lambda^2 - 1)\mathbf{1}$, $2\mathbf{e} = (1 - \lambda^{-2})\mathbf{1}$.

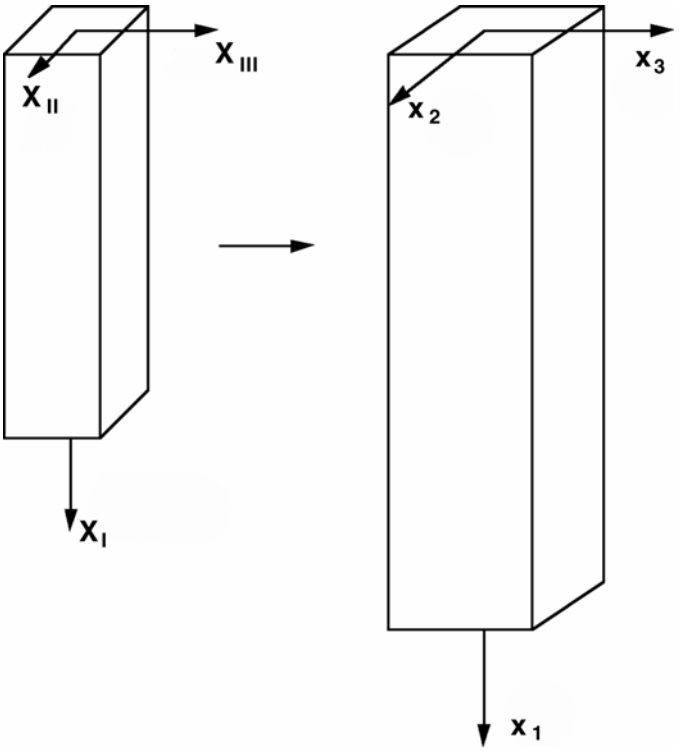



**Figure 15.13**. Illustration of a simple extension, a type of pure homogeneous deformation.

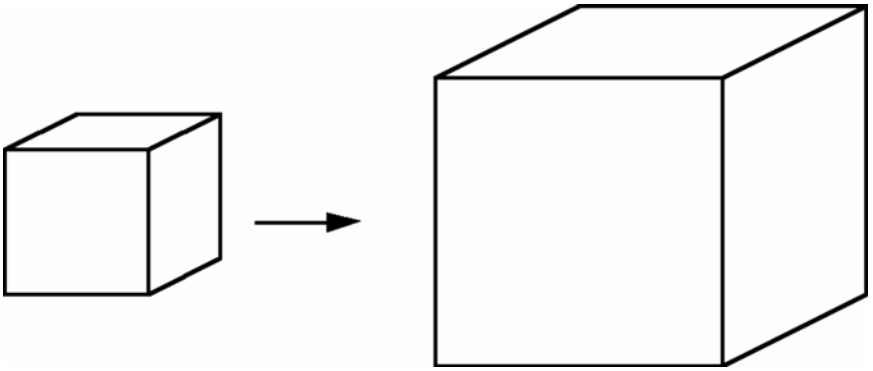


**Figure 15.14**. Illustration of a uniform dilation, a type of pure homogeneous deformation.

## Problems

15.4.1. For the six motions of form (3.10) given in Problem 3.1.1, namely, 3.1.1a–3.1.1f, compute Lagrangian strain tensor **E** and Eulerian strain tensor **e**, the right and left Cauchy-Green tensors, **C** and **B**, respectively, and the inverse of the right Cauchy-Green tensor. Dis-

cuss briefly the significance of each of the tensors computed. In particular, explain the form or value of the deformation strain tensors in terms of the motion.

15.4.2. Prove that, in the case of no deformation, the invariants of **C** and **c** satisfy the following relationships: $I_c = I_C = II_c = II_C = 3$, $III_c = III_C = 1$.

15.4.3. Show that Jacobian $J$ is related to $III_C$ by $J^2 = III_C$.

## 15.5. MEASURES OF VOLUME AND SURFACE CHANGE IN LARGE DEFORMATIONS

In this section we will consider volume and area measures of deformation. Consider volume deformation first. A material filament denoted by $d\mathbf{X}$ is mapped into its present position $d\mathbf{x}$ by deformation gradient $\mathbf{F}$, $d\mathbf{x} = \mathbf{F}\cdot d\mathbf{X}$. By considering the mapping of three non-planar $d\mathbf{X}$'s — $d\mathbf{X}(q)$, $d\mathbf{X}(r)$, and $d\mathbf{X}(s)$ — into their three-image $d\mathbf{x}$'s — $d\mathbf{x}(q)$, $d\mathbf{x}(r)$, and $d\mathbf{x}(s)$ — a representation of the volumetric deformation may be obtained. This algebra uses the triple scalar product to calculate the volume associated with the parallelepiped defined by three vectors coincident with the three edges of the parallelepiped that come together at one vertex. The element of volume, $dV$, in the undeformed configuration is given by $dV = d\mathbf{X}(q)\cdot(d\mathbf{X}(r) \times d\mathbf{X}(s))$, and in the deformed configuration by $dv = d\mathbf{x}(q)\cdot(d\mathbf{x}(r) \times d\mathbf{x}(s))$. Substituting $d\mathbf{x} = \mathbf{F}\cdot d\mathbf{X}$ into $dv = d\mathbf{x}(q)\cdot(d\mathbf{x}(r) \times d\mathbf{x}(s))$ three times, it follows that

$$dv = \{\mathbf{F}\cdot d\mathbf{X}(q)\}\cdot(\{\mathbf{F}\cdot d\mathbf{X}(r)\} \times \{\mathbf{F}\cdot d\mathbf{X}(s)\}), \tag{15.35}$$

which may be expanded and, using the fact that a determinant of a product of matrices is the product of the determinants, rewritten as

$$dv = JdV, \tag{15.36}$$

where $J = \text{Det}\,\mathbf{F}$ and $dV = d\mathbf{X}(q)\cdot(d\mathbf{X}(r) \times d\mathbf{X}(s))$ are both determinants. Thus, the element of volume, $dV$, in the undeformed configuration is deformed into volume $dv$ in the deformed configuration according to rule $dv = JdV$, where $J = \text{Det}\mathbf{F}$ is called the Jacobian of the deformation. In order that no region of positive finite volume be deformed into a region of zero or infinite volume, it is required that $0 < J < \infty$.

Consider now the question of the deformation of differential elements of area where similar formulas for area change can be constructed. Let $d\mathbf{A}$ be a differential vector representation of area in the material reference frame obtained by taking the cross product of two different material filaments $d\mathbf{X}$, $d\mathbf{A} = d\mathbf{X}(r) \times d\mathbf{X}(s)$. Similarly, let $d\mathbf{a}$ be a differential vector representation of area in the spatial reference frame, representing the deformed shape of the same material area, obtained by taking the cross product of deformed images $d\mathbf{x}$, $d\mathbf{a} = d\mathbf{x}(r) \times d\mathbf{x}(s)$ of material filaments $d\mathbf{X}(r)$ and $d\mathbf{X}(s)$. The relationship between $d\mathbf{a}$ and $d\mathbf{A}$ is constructed by twice substituting $d\mathbf{x} = \mathbf{F}\cdot d\mathbf{X}$ into $d\mathbf{a} = d\mathbf{x}(r) \times d\mathbf{x}(s)$:

$$d\mathbf{a} = \{\mathbf{F}\cdot d\mathbf{X}(r)\} \times \{\mathbf{F}\cdot d\mathbf{X}(s)\}. \tag{15.37}$$

Vector $d\mathbf{a}$ is then dotted with deformation gradient $\mathbf{F}$ from the left, and thus

$$d\mathbf{a}\cdot\mathbf{F} = \{\mathbf{F}\cdot d\mathbf{X}(r)\} \times \{\mathbf{F}\cdot d\mathbf{X}(s)\}\cdot\mathbf{F}. \tag{15.38}$$

The right-hand side of this equation may be expanded, as the one for volume was above, and, using the fact that a determinant of a product of matrices is the product of the determinants, rewritten as

$$d\mathbf{a}\cdot\mathbf{F} = J\,d\mathbf{A}. \tag{15.39}$$

On the other hand, the relationship between $d\mathbf{A}$ and $d\mathbf{a}$ is constructed by twice substituting $d\mathbf{X} = \mathbf{F}^{-1}\cdot d\mathbf{x}$ into $d\mathbf{A} = d\mathbf{X}(r) \times d\mathbf{X}(s)$:

$$d\mathbf{A} = \{\mathbf{F}^{-1}\cdot d\mathbf{x}(r)\} \times \{\mathbf{F}^{-1}\cdot d\mathbf{x}(s)\}. \tag{15.40}$$

Vector $d\mathbf{A}$ is then dotted with inverse deformation gradient $\mathbf{F}^{-1}$ from the left, and thus

$$d\mathbf{A}\cdot\mathbf{F}^{-1} = \{\mathbf{F}^{-1}\cdot d\mathbf{x}(r)\} \times \{\mathbf{F}^{-1}\cdot d\mathbf{x}(s)\}\cdot\mathbf{F}^{-1}. \tag{15.41}$$

The right-hand side of this equation may be expanded, as a similar one for $d\mathbf{a}$ was above, and, using the fact that a determinant of a product of matrices is the product of the determinants, rewritten as

$$d\mathbf{A}\cdot\mathbf{F}^{-1} = J^{-1}d\mathbf{a}. \tag{15.42}$$

These formulas relating $d\mathbf{A}$ and $d\mathbf{a}$ are called the *formulas of Nanson*. These formulas will be employed in relating the various definitions of stress associated with large deformations.

**Example 15.5.1**

Consider the plane area that forms the right-hand face of the unit cube illustrated in Figure 15.9. Use the formulas of Nanson to determine the magnitude and orientation of the deformed area as a result of the deformation specified in Problem 15.3.1.

**Solution**: The undeformed area is represented by $d\mathbf{A}^{T} = (1, 0, 0)$. The value of $J$ is $2\sqrt{3}$, and the tensor of inverse deformation gradients is given by

$$\mathbf{F}^{-1} = \begin{bmatrix} \dfrac{1}{\sqrt{3}} & \dfrac{-1}{2\sqrt{3}} & 0 \\ 0 & \dfrac{1}{2} & 0 \\ 0 & 0 & 1 \end{bmatrix}.$$

From (15.42) it follows that $d\mathbf{a} = Jd\mathbf{A}\cdot\mathbf{F}^{-1}$, and thus

$$d\mathbf{a} = 2\sqrt{3}\left\{[1 \quad 0 \quad 0]\begin{bmatrix} \dfrac{1}{\sqrt{3}} & \dfrac{-1}{2\sqrt{3}} & 0 \\ 0 & \dfrac{1}{2} & 0 \\ 0 & 0 & 1 \end{bmatrix}\right\} = \begin{bmatrix} 2 \\ -1 \\ 0 \end{bmatrix}.$$

The deformed representation of the plane area that forms the right-hand face of the unit cube illustrated in Figure 15.7 is shown as the right sloping right-hand face in Figure 15.8. From that figure it is seen that the face associated with this area is two units high and one unit wide, and that the unit normal to this face is indeed $(2/\sqrt{3}, -1/\sqrt{3}, 0)$.

**Problems**

15.5.1. Compute the volume of the parallelepiped whose three edges meeting at one vertex are characterized by vectors (1, 2, 3), (2, 3, 3), (–3, –2, –1).

15.5.2. Consider the plane area that forms the top face of the deformed parallelogram illustrated in Figure 15.8. Use the formulas of Nanson to determine the magnitude and orientation of the original area if the deformed area was a consequence of the deformation specified in Problem 15.3.1.

## 15.6. STRESS MEASURES

The stress equations of motion are the most useful form of Newton's second law in continuum mechanics. In §4.4 these field equations were shown to have the form

$$\rho\ddot{\mathbf{x}} = \nabla\cdot\mathbf{T} + \rho\mathbf{d}\,,\ \mathbf{T} = \mathbf{T}^T\,. \qquad \text{(4.37) repeated}$$

These equations involve the most common stress measure, Cauchy stress **T**, introduced in Chapter 4. It was not called the Cauchy stress in Chapter 4 because there was only one stress tensor under discussion there. The Cauchy stress is referred to the instantaneous or spatial coordinate system; it is measured relative to the instantaneous area. In mechanical testing the phrase "true stress" is used to denote a stress calculated using the instantaneous rather than the original cross-sectional area. Cauchy stress, which is sometimes called Eulerian stress, is therefore a "true stress."

There are three different stress measures used in the study of finite deformations of materials. The first is the Cauchy stress. The second stress measure is the first Piola-Kirchhoff stress tensor, which is sometimes called the Lagrangian stress tensor. This stress tensor is referred to the reference configuration. Consider an object in both its deformed and undeformed configurations. Since this is the same object in the two configurations, it must have the same total mass, $M$, in each configuration, and eq. (4.1) may be rewritten to express that fact:

$$M = \int_0 \rho_R(\mathbf{X})dV = \int_0 \rho(\mathbf{x},t)dv\,, \qquad (15.43)$$

where $\rho_R(\mathbf{X})$ is the density in the initial configuration and $\rho(\mathbf{x}, t)$ is the density in the instantaneous or deformed configuration; $dV$ is an element of volume in the initial configuration, and $dv$ is an element of volume in the final configuration. Substituting relationship (15.36) between $dv$ and $dV$, $dv = JdV$, into (15.43), it follows that

$$M = \int_0 \rho_R(\mathbf{X})dV = \int_0 \rho(\mathbf{x},t)JdV\,. \qquad (15.44)$$

Since this same result must hold for each and every part of the object, we conclude that the relationship between the two density fields is given by the simple formula

$$\rho_R = J\rho, \qquad (15.45)$$

which is an alternative statement of mass balance. The argument that is used to go from (15.44) to (15.45) is the same argument that was used to go from (4.4) to (4.5), and it was employed three more times in Chapter 4. In order to relate the stresses referred to the two different configurations, a similar procedure to the arguments leading to result $\rho_R = J\rho$ above is followed. Total force **f** acting on an object, or on any particular sub-part of the object, is considered. The total force is the same in both configurations; therefore, the product of the stress and a differential area element integrated over the object must be the same in both configurations. Thus,

$$\mathbf{f} = \int_{\partial 0} \mathbf{T}^{1PK}\cdot d\mathbf{A} = \int_{\partial 0} \mathbf{T}\cdot d\mathbf{a}\,, \qquad (15.46)$$

where $\mathbf{T}^{1PK}$ and $d\mathbf{A}$ are the stress tensor and differential area element in the initial configuration, and $\mathbf{T}$ and $d\mathbf{a}$ are the stress and differential area in the instantaneous or deformed configuration. $\mathbf{T}$ is the Cauchy stress, of course. When the relationship of Nanson between $d\mathbf{a}$ and $d\mathbf{A}$ given by (15.42) is substituted into (15.46), we find that

$$\mathbf{f} = \int_{\partial 0} \mathbf{T}^{1PK} \cdot d\mathbf{A} = \int_{\partial 0} J\mathbf{T} \cdot (\mathbf{F}^{-1})^T \cdot d\mathbf{A} \,. \tag{15.47}$$

Since this must hold for all parts of the object, the same argument as in the transitions from (15.44) → (15.45) and (4.4) → (4.5), it may be concluded that

$$\mathbf{T}^{1PK} = J\mathbf{T} \cdot (\mathbf{F}^{-1})^{\mathrm{T}}, \text{ or } \mathbf{T} = J^{-1}\mathbf{T}^{1PK} \cdot \mathbf{F}^{\mathrm{T}}. \tag{15.48}$$

$\mathbf{T}^{1PK}$ is called the *first Piola-Kirchhoff* or Lagrangian stress tensor. The relation of Cauchy involving the Cauchy stress tensor and the spatial reference frame, namely, that stress vector $\mathbf{t}_{(\mathbf{n})}$ acting on any plane whose normal is $\mathbf{n}$ is given by $\mathbf{t}_{(\mathbf{n})} = \mathbf{T} \cdot \mathbf{n}$, may be extended to the first Piola-Kirchhoff stress tensor, $\mathbf{T}^{1PK}$, and the material coordinate system; thus, $\mathbf{t}_{(\mathbf{N})} = \mathbf{T}^{1PK} \cdot \mathbf{N}$, where $\mathbf{N}$ is the unit normal vector to the plane in the material coordinate system. Using this result, the stress equations of motion may be rederived in the material coordinates and in terms of the first Piola-Kirchhoff stress tensor; thus,

$$\rho_R \ddot{\mathbf{x}} = \nabla_{\mathbf{o}} \cdot \mathbf{T}^{1PK} + \rho_R \mathbf{d} \,, \;\; \mathbf{T}^{1PK} \cdot \mathbf{F}^{\mathrm{T}} = \mathbf{F} \cdot (\mathbf{T}^{1PK})^{\mathrm{T}}; \tag{15.49}$$

where the density of the initial configuration, $\rho_R$, is used as the reference density and the divergence is now with respect to material rather than spatial coordinates. Recall from Chapter 4 that the gradient symbol, $\nabla_{\mathbf{o}}$, with a subscripted boldface $\mathbf{o}$, will indicate a gradient with respect to spatial coordinate system $\mathbf{X}$, rather than the usual gradient symbol $\nabla$, used to indicate a gradient with respect to spatial coordinate system $\mathbf{x}$. The second of (15.49) shows that the first Piola-Kirchhoff stress tensor is not symmetric like the Cauchy stress tensor. To see that this is the case, the second of (15.48) may be substituted twice in the second of (4.37) to verify.

In order to have a measure of stress referred to the initial configuration that is symmetric, the *second Piola-Kirchhoff* stress tensor is introduced; this is also called the Kirchhoff stress tensor. This new stress tensor is denoted by $\mathbf{T}^{2PK}$ and defined as follows:

$$\mathbf{T}^{2PK} \equiv \mathbf{F}^{-1} \cdot \mathbf{T}^{1PK} = J\mathbf{F}^{-1} \cdot \mathbf{T} \cdot (\mathbf{F}^{-1})^{\mathrm{T}}. \tag{15.50}$$

Substituting $\mathbf{T}^{1PK} = \mathbf{F} \cdot \mathbf{T}^{2PK}$ into (15.49), the equations of motion in terms of the second Piola-Kirchhoff stress tensor are obtained:

$$\rho_R \ddot{\mathbf{x}} = \nabla_{\mathbf{o}} \cdot (\mathbf{F} \cdot \mathbf{T}^{2PK}) + \rho_R \mathbf{d} \,, \;\; \mathbf{T}^{2PK} = (\mathbf{T}^{2PK})^{\mathrm{T}}. \tag{15.51}$$

This shows that the second Piola-Kirchhoff stress tensor, $\mathbf{T}^{2PK}$, is symmetric.

**Example 15.6.1**

A solid specimen capable of large deformations is extended by a force of magnitude $P$ in the $x_1$ or $X_1$ direction (these directions are coincident here). This uniaxial stress situation is illustrated in Figure 15.15. Determine the Cauchy and the first and second Piola-Kirchhoff stress tensors in this uniaxial situation. Construct the relationships between each of these tensors in this particular situation.

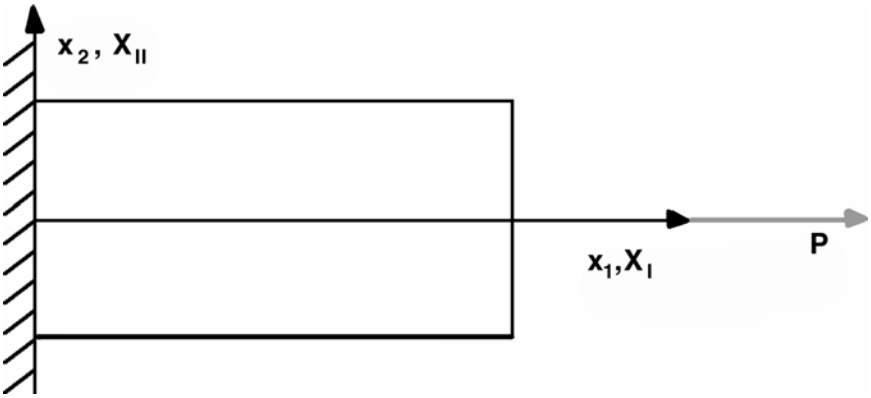



**Figure 15.15**. Illustration for a uniaxial stretching deformation due to a load **P**.

**Solution**: The principal axes of extension are obviously the direction of the applied load and the two perpendicular transverse directions. The deformation can be represented in terms of principal stretches $\lambda_I$, $\lambda_{II}$, and $\lambda_{III}$ by

$$x_1 = \lambda_I X_I,\ x_2 = \lambda_{II} X_{II},\ x_3 = \lambda_{III} X_{III},$$

and deformation gradients **F** by (15.32). It follows that Jacobian $J$ is given by $J = \lambda_I\lambda_{II}\lambda_{III}$. The area perpendicular to the $x_1$- or $X_I$-axis will change with the deformation. Using the formula of Nanson (15.42), it follows that

$$d\mathbf{a} = J(\mathbf{F}^{-1})^T \cdot d\mathbf{A} = \lambda_I\lambda_{II}\lambda_{III}\begin{bmatrix} \lambda_I^{-1} & 0 & 0 \\ 0 & \lambda_{II}^{-1} & 0 \\ 0 & 0 & \lambda_{III}^{-1} \end{bmatrix}\begin{bmatrix} dA_I \\ 0 \\ 0 \end{bmatrix},$$

or $da_1 = \lambda_{II}\lambda_{III}dA_I$, $da_2 = 0$, and $da_3 = 0$; thus, we can conclude that the relationship between instantaneous area A and initial area $A_0$ is $A = \lambda_{II}\lambda_{III}A_o$. The only nonzero Cauchy stress is $T_{11} = P/A = P/(\lambda_{II}\lambda_{III}A_0)$. From (15.48), the only nonzero component of the first Piola-Kirchhoff stress tensor is given by $T_{1I}^{1PK} = \lambda_{II}\lambda_{III}T_{11} = \lambda_{II}\lambda_{III}P/A = P/A_o$, and from (15.50) the only nonzero component of the second Piola-Kirchhoff stress tensor is given by

$$T_{1I}^{2PK} = (T_{1I}^{1PK})/\lambda_I = (\lambda_{II}\lambda_{III}T_{11})/\lambda_I = \lambda_{II}\lambda_{III}P/(\lambda_I A) = P/(\lambda_I A_o).$$

In the special case when the material is incompressible, $J = \lambda_I\lambda_{II}\lambda_{III} = 1$, and the cross-section transverse to the extension is symmetric: $\lambda_I = \lambda$, $\lambda_{II} = \lambda_{III} = 1/\sqrt{\lambda}$; then, $T_{1I}^{2PK} = (T_{1I}^{1PK})/\lambda = T_{11}/\lambda^2 = P/(\lambda^2 A) = P/(\lambda A_o)$.

**Problem**

15.6.1. Determine Cauchy stress $T_{11}$, first Piola-Kirchhoff stress $T_{1I}^{1PK}$, and second Piola-Kirchhoff stress $T_{1I}^{2PK}$ for a unit cube subjected to (a) a uniaxial extension and (b) a biaxial extension. The uniaxial extension is created by net force $P$ in the $x_1$ or $X_I$ direction, and the motion is described by $x_1 = (1 + t)\,X_I$, $x_2 = X_{II}$, $x_3 = X_{III}$. The biaxial extension is created by net force $P_1$ in the $x_1$ or $X_I$ direction and net force $P_2$ in the $x_2$ or $X_{II}$ direction. The motion in this

case is described by $x_1 = (1 + t)\, X_I$, $x_2 = (1 + 2t)\, X_{II}$, $x_3 = X_{III}$. Note that each face of the unit cube has an initial area $A_o$ that is unity, $A_o = 1$. Begin by illustrating these uniaxial and biaxial deformations. Evaluate the three stresses when $t = 0$, $t = 1$, and $t = 2$. Which stress measure is most realistic from a physical viewpoint?

## 15.7. FINITE DEFORMATION ELASTICITY

An elastic material is a material characterized by a constitutive equation, which specifies that stress is a function of strain only. It is also possible to represent an elastic material by a constitutive equation that specifies stress as a function of deformation gradients **F**, provided one keeps in mind that, due to invariance under rigid object rotations, the stress must be independent of the part of **F** that represents rotational motion. In terms of Cauchy stress **T** and deformation gradient **F**, the constitutive equation for an elastic material can be written $\mathbf{T} = \mathbf{g}(\mathbf{F})$. Invariance under rigid object rotations requires

$$\mathbf{g}(\mathbf{Q}\cdot\mathbf{F}) = \mathbf{Q}\cdot\mathbf{g}(\mathbf{F})\cdot\mathbf{Q}^{\mathrm{T}} \tag{15.52}$$

for all orthogonal tensors **Q**. If we take $\mathbf{Q} = \mathbf{R}^{\mathrm{T}}$, where **R** is the rigid object rotation and **U** the right stretch tensor, which are related to **F** by $\mathbf{F} = \mathbf{R}\cdot\mathbf{U}$ (eq. 15.8), it follows from (15.52) that $\mathbf{g}(\mathbf{R}^{\mathrm{T}}\cdot\mathbf{F}) = \mathbf{g}(\mathbf{U}) = \mathbf{R}^{\mathrm{T}}\cdot\mathbf{g}(\mathbf{F})\cdot\mathbf{R}$; thus, $\mathbf{T} = \mathbf{g}(\mathbf{F}) = \mathbf{R}\cdot\mathbf{g}(\mathbf{U})\cdot\mathbf{R}^{\mathrm{T}}$, or

$$\mathbf{T} = \mathbf{R}\cdot\mathbf{f}(\mathbf{C})\cdot\mathbf{R}^{\mathrm{T}}, \tag{15.53}$$

where $\mathbf{g}(\mathbf{U}) = \mathbf{f}(\mathbf{C}) = \mathbf{f}(\mathbf{U}^2)$ (since $\mathbf{C} = \mathbf{U}^2$ (eq. 15.27)). In terms of first Piola-Kirchhoff stress tensor $\mathbf{T}^{1PK}$, the constitutive equation for an elastic material is

$$\mathbf{T}^{1PK} = \mathbf{h}(\mathbf{F}), \tag{15.54}$$

or, due to the invariance of constitutive equations under rigid object rotations, $\mathbf{h}(\mathbf{Q}\cdot\mathbf{F}) = \mathbf{Q}\cdot\mathbf{h}(\mathbf{F})$, and taking $\mathbf{Q} = \mathbf{R}^{\mathrm{T}}$, $\mathbf{h}(\mathbf{U}) = \mathbf{R}^{\mathrm{T}}\cdot\mathbf{h}(\mathbf{F})$; thus, $\mathbf{h}(\mathbf{F}) = \mathbf{R}\cdot\mathbf{h}(\mathbf{U})$, and

$$\mathbf{T}^{1PK} = \mathbf{R}\cdot\mathbf{h}(\mathbf{U}). \tag{15.55}$$

In terms of second Piola-Kirchhoff stress tensor $\mathbf{T}^{2PK}$, the constitutive equation for an elastic material has the form

$$\mathbf{T}^{2PK} = \mathbf{t}(\mathbf{C}). \tag{15.56}$$

These constitutive equations are said to describe a material with Cauchy elasticity; that is to say, a material in which stress is a function of some measure of the strain or deformation.

## 15.8. THE ISOTROPIC FINITE DEFORMATION STRESS-STRAIN RELATION

While biological tissues are not, in general, isotropic, the assumption of isotropic symmetry of a material is sometimes an adequate model of tissues. Recall from Chapter 5 that, in the case of a stress strain relation, isotropy means that the response of stress to an applied strain is the same in any direction in the material. The mathematical statement of this notion is that the stress tensor, say $\mathbf{T}^{2PK}$, in (15.56) is an isotropic function of right Cauchy-Green tensor **C**. Thus, tensor-valued function $\mathbf{T}^{2PK} = \mathbf{t}(\mathbf{C})$, given by (15.56), satisfies relation

$$\mathbf{Q}\cdot\mathbf{T}^{2PK}\cdot\mathbf{Q}^{\mathrm{T}} = \mathbf{t}(\mathbf{Q}\cdot\mathbf{C}\cdot\mathbf{Q}^{\mathrm{T}}). \tag{15.57}$$

The isotropy requirement is a special case of (8.33). The development objective of this section is use isotropy requirement (15.57) to restrict the functional form of relationship (15.56). The first step in this development is to show that the principal axes of $\mathbf{T}^{2PK}$ must coincide with the principal axes of right Cauchy-Green tensor $\mathbf{C}$ if isotropy requirement (15.57) is satisfied.

To show that this is the case, let $\mathbf{c}$ denote an eigenvector of $\mathbf{C}$ corresponding to the eigenvalue, say, $\lambda_{\mathrm{I}}^2\, C$; thus, $\mathbf{C}\cdot\mathbf{c} = \lambda_{\mathrm{I}}^2\mathbf{c}$. Eigenvector $\mathbf{c}$ is used to construct reflective symmetry transformation $\mathbf{R}^{(\mathbf{c})}$ with the properties specified by (5.1) for vector $\mathbf{a}$. Replacing $\mathbf{a}$ in (5.2) by $\mathbf{c}$, it follows that

$$\mathbf{R}^{(\mathbf{c})} = \mathbf{1} - 2\mathbf{c}\otimes\mathbf{c} \quad (R_{ij}^{(\mathbf{c})} = \delta_{ij} - 2c_i c_j); \tag{15.58}$$

then, setting $\mathbf{Q} = \mathbf{R}^{(\mathbf{c})}$ in (15.57), it follows that

$$\mathbf{R}^{(\mathbf{c})}\cdot\mathbf{T}^{2PK}\cdot\mathbf{R}^{(\mathbf{c})T} = \mathbf{t}(\mathbf{R}^{(\mathbf{c})}\cdot\mathbf{C}\cdot\mathbf{R}^{(\mathbf{c})T}). \tag{15.59}$$

For symmetric second-order tensor $\mathbf{A}$ it is easy to show, using (15.58), that

$$\mathbf{R}^{(\mathbf{c})}\cdot\mathbf{A}\cdot\mathbf{R}^{(\mathbf{c})T} = \mathbf{A} - 2\mathbf{c}\otimes\mathbf{A}\cdot\mathbf{c} - 2\mathbf{A}\cdot\mathbf{c}\otimes\mathbf{c} + 4(\mathbf{c}\cdot\mathbf{A}\cdot\mathbf{c})\mathbf{c}\otimes\mathbf{c}, \tag{15.60}$$

and, in particular, when $\mathbf{A} = \mathbf{C}$, it follows from the fact that $\mathbf{c}$ is an eigenvector of $\mathbf{C}$ that

$$\mathbf{R}^{(\mathbf{c})}\cdot\mathbf{C}\cdot\mathbf{R}^{(\mathbf{c})T} = \mathbf{C}. \tag{15.61}$$

Substitution of (15.61) into (15.59) reduces (15.59) to

$$\mathbf{R}^{(\mathbf{c})}\cdot\mathbf{T}^{2PK}\cdot\mathbf{R}^{(\mathbf{c})T} = \mathbf{t}(\mathbf{C}). \tag{15.62}$$

Next, let $\mathbf{A} = \mathbf{t}(\mathbf{C})$ in identity (15.60); then it follows with a little algebra, and recalling that $\mathbf{R}^{(\mathbf{c})}\cdot\mathbf{c} = -\mathbf{c}$, that

$$\mathbf{t}(\mathbf{C})\cdot\mathbf{c} = (\mathbf{c}\cdot\mathbf{t}(\mathbf{C})\cdot\mathbf{c})\mathbf{c}. \tag{15.63}$$

Since $\mathbf{c}\cdot\mathbf{t}(\mathbf{C})\cdot\mathbf{c}$ is a scalar, this result shows that $\mathbf{c}$ is an eigenvector of $\mathbf{t}(\mathbf{C})$ as well as $\mathbf{C}$. It then follows that any eigenvector of $\mathbf{C}$ is also an eigenvector of $\mathbf{T}^{2PK} = \mathbf{t}(\mathbf{C})$. Since $\mathbf{C}$ and $\mathbf{T}^{2PK} = \mathbf{t}(\mathbf{C})$ have the same set of principal axes, then eigenvalues $(T_{11}^{2PK}, T_{22}^{2PK}, T_{33}^{2PK})$ of $\mathbf{T}^{2PK}$ are functions of eigenvalues $(\lambda_{\mathrm{I}}^2, \lambda_{\mathrm{II}}^2, \lambda_{\mathrm{III}}^2)$ of $\mathbf{C}$ given by (15.33), and thus

$$T_{11}^{2PK} = t_{11}(\lambda_{\mathrm{I}}^2, \lambda_{\mathrm{II}}^2, \lambda_{\mathrm{III}}^2), \quad T_{22}^{2PK} = t_{22}(\lambda_{\mathrm{I}}^2, \lambda_{\mathrm{II}}^2, \lambda_{\mathrm{III}}^2),$$
$$T_{33}^{2PK} = t_{33}(\lambda_{\mathrm{I}}^2, \lambda_{\mathrm{II}}^2, \lambda_{\mathrm{III}}^2). \tag{15.64}$$

In order to express more specific function forms of (15.64), recall that each eigenvalue $(\lambda_{\mathrm{I}}^2, \lambda_{\mathrm{II}}^2, \lambda_{\mathrm{III}}^2)$ of a matrix like $\mathbf{C}$ satisfies the same characteristic equation (A54), and thus

$$\lambda^6 - I_C\lambda^4 + II_C\lambda^2 - III_C = 0, \tag{15.65}$$

where

$$I_C = \mathrm{tr}\mathbf{C}, \quad II_C = \frac{1}{2}[(\mathrm{tr}\mathbf{C})^2 - \mathrm{tr}\mathbf{C}^2], \quad III_C = \mathrm{Det}\mathbf{C}. \tag{15.66}$$

If the expression for $T_{11}^{2PK} = t_{11}(\lambda_{\mathrm{I}}^2, \lambda_{\mathrm{II}}^2, \lambda_{\mathrm{III}}^2)$ were expanded in a power series in $\lambda_{\mathrm{I}}^2$, (15.65) above could be used to eliminate any term not proportional to 1, $\lambda_{\mathrm{I}}^2$, or $\lambda_{\mathrm{I}}^4$. With this motiva-

tion eigenvalues $(T_{11}^{2PK}, T_{22}^{2PK}, T_{33}^{2PK})$ of $\mathbf{T}^{2PK}$ are expressed as functions of eigenvalues $(\lambda_{\mathrm{I}}^2, \lambda_{\mathrm{II}}^2, \lambda_{\mathrm{III}}^2)$ of $\mathbf{C}$ as follows:

$$T_{11}^{2PK} = a_o + a_1\lambda_{\mathrm{I}}^2 + a_2\lambda_{\mathrm{I}}^4\,,\;\; T_{22}^{2PK} = a_0 + a_1\lambda_{\mathrm{II}}^2 + a_2\lambda_{\mathrm{III}}^4\,,$$

$$T_{33}^{2PK} = a_0 + a_1\lambda_{\mathrm{III}}^2 + a_2\lambda_{\mathrm{III}}^4\,. \tag{15.67}$$

This system of equations has a unique solution for three unknown functions $a_o$, $a_1$, and $a_2$. These functions are elementary symmetric functions of three eigenvalues $(\lambda_{\mathrm{I}}^2, \lambda_{\mathrm{II}}^2, \lambda_{\mathrm{III}}^2)$ or the three (isotropic) invariants of $\mathbf{C}$; thus,

$$a_0 = a_0(\lambda_{\mathrm{I}}^2, \lambda_{\mathrm{II}}^2, \lambda_{\mathrm{III}}^2) = a_0(I_C, II_C, III_C)\,,\;\; a_1 = a_1(\lambda_{\mathrm{I}}^2, \lambda_{\mathrm{II}}^2, \lambda_{\mathrm{III}}^2) = a_1(I_C, II_C, III_C)\,, \tag{15.68}$$

$$a_2 = a_2(\lambda_{\mathrm{I}}^2, \lambda_{\mathrm{II}}^2, \lambda_{\mathrm{III}}^2) = a_2(I_C, II_C, III_C)\,.$$

In the principal coordinate system it then follows that

$$\mathbf{T}^{2PK} = a_0\mathbf{1} + a_1\mathbf{C} + a_2\mathbf{C}^2\,, \tag{15.69}$$

an expression that is equivalent to (15.67) in the principal coordinate system of $\mathbf{C}$ (or $\mathbf{t}(\mathbf{C})$), but that also holds in any arbitrary coordinate system. A necessary and sufficient condition that constitutive relation (15.56), $\mathbf{T}^{2PK} = \mathbf{t}(\mathbf{C})$, satisfy material isotropy requirement (15.57), $\mathbf{Q}\cdot\mathbf{T}^{2PK}\cdot\mathbf{Q}^{\mathrm{T}} = \mathbf{t}(\mathbf{Q}\cdot\mathbf{C}\cdot\mathbf{Q}^{\mathrm{T}})$, is that $\mathbf{T}^{2PK} = \mathbf{t}(\mathbf{C})$ have a representation of form (15.69) with $a_o$, $a_1$, and $a_2$ given by (15.68).

Representation (15.69) of $\mathbf{T}^{2PK}$ as an isotropic function of $\mathbf{C}$ may also be expressed as an equivalent isotropic relationship between Cauchy stress $\mathbf{T}$ and left Cauchy-Green tensor $\mathbf{B}$. The algebraic manipulations that achieve this equivalence begin with recalling from (15.27) that $\mathbf{C} = \mathbf{F}^{\mathrm{T}}\cdot\mathbf{F}$, and thus (15.69) may be written in the form

$$\mathbf{T}^{2PK} = a_0\mathbf{1} + a_1\mathbf{F}^T\cdot\mathbf{F} + a_2\mathbf{F}^T\cdot\mathbf{F}\cdot\mathbf{F}^T\cdot\mathbf{F}\,, \tag{15.70}$$

then premultiplying by $(\mathbf{F}^T)^{-1}$ and post-multiplying by $\mathbf{F}^{-1}$; thus,

$$(\mathbf{F}^T)^{-1}\cdot\mathbf{T}^{2PK}\cdot\mathbf{F}^{-1} = a_0(\mathbf{F}^T)^{-1}\cdot\mathbf{F}^{-1} + a_1(\mathbf{F}^T)^{-1}\cdot\mathbf{F}^T\cdot\mathbf{F}\cdot\mathbf{F}^{-1} + ,$$

$$a_2(\mathbf{F}^T)^{-1}\cdot\mathbf{F}^T\cdot\mathbf{F}\cdot\mathbf{F}^T\cdot\mathbf{F}\cdot\mathbf{F}^{-1}\,. \tag{15.71}$$

This expression reduces to

$$\mathbf{T} = \frac{a_1}{J}\mathbf{1} + \frac{a_2}{J}\mathbf{B} + \frac{a_0}{J}\mathbf{B}^{-1}, \tag{15.72}$$

when one takes note of (15.27), (15.28), and the second of (15.51). This expression is rewritten in the form

$$\mathbf{T} = h_0\mathbf{1} + h_1\mathbf{B} + h_{-1}\mathbf{B}^{-1}\,, \tag{15.73}$$

when it is observed that $I_C = I_B$, $II_C = II_B$, and $III_C = III_B = J$, and the following notation is introduced:

$$h_o = h_0(I_C, II_C, III_C) = h_0(I_B, II_B, III_B) = \frac{a_1}{J}(I_C, II_C, III_C),$$

$$h_1 = h_1(I_C, II_C, III_C) = h_1(I_B, II_B, III_B) = \frac{a_0}{J}(I_C, II_C, III_C), \tag{15.74}$$

$$h_{-1} = h_{-1}(I_C, II_C, III_C) = h_{-1}(I_B, II_B, III_B) = \frac{a_2}{J}(I_C, II_C, III_C).$$

Problem 15.8.1. Setting **A** = **t**(**C**) in identity (15.60), verify formula (15.63), $\mathbf{t}(\mathbf{C})\cdot\mathbf{c} = (\mathbf{c}\cdot\mathbf{t}(\mathbf{C})\cdot\mathbf{c})\mathbf{c}$.

## 15.9. FINITE DEFORMATION HYPERELASTICITY

A *hyperelastic material* is an elastic material for which the stress is derivable from a scalar potential called a strain energy function. Thus, a hyperelastic material is automatically a Cauchy elastic material, but not the reverse. In the case of small deformation elasticity, a strain energy function always exists, and therefore the small deformation theory is hyperelastic. The strain energy per unit volume, *W*, is obtained from the specific strain energy, that is to say, the strain energy per unit mass, by multiplying it by $\rho_R$, where $\rho_R$ is the density function in the initial configuration. In terms of the Cauchy stress and the first and second Piola-Kirchhoff stress tensors. the definition of a hyperelastic material has the following forms:

$$\mathbf{T} = \frac{\rho}{\rho_R}\mathbf{F}\cdot\left(\frac{\partial W}{\partial \mathbf{F}}\right)^T, \quad \mathbf{T}^{1PK} = \frac{\partial W}{\partial \mathbf{F}}, \quad \mathbf{T}^{2PK} = \mathbf{F}^{-1}\cdot\left(\frac{\partial W}{\partial \mathbf{F}}\right). \tag{15.75}$$

On first encounter, the variety of forms for the constitutive relation for hyperelastic materials is bewildering. Not only are there three different stress measures, but there are many different strain measures — **C**, **c**, **F**, **E**, **e**, etc. Thus, for example, if we introduce right Cauchy-Green deformation tensor **C**, since $\mathbf{C} = \mathbf{U}^2 = \mathbf{F}\mathbf{F}^{\mathrm{T}}$, $\partial\mathbf{C}/\partial\mathbf{F} = 2\mathbf{F}$, and then

$$\frac{\partial W}{\partial \mathbf{F}} = 2\mathbf{F}\cdot\frac{\partial W}{\partial \mathbf{C}}, \tag{15.76}$$

and constitutive relations (15.57) take the form

$$\mathbf{T} = 2\frac{\rho}{\rho_R}\mathbf{F}\cdot\left(\frac{\partial W}{\partial \mathbf{C}}\right)^T\cdot\mathbf{F}^T, \quad \mathbf{T}^* = 2\mathbf{F}\cdot\frac{\partial W}{\partial \mathbf{C}}, \quad \mathbf{T}^{2PK} = 2\frac{\partial W}{\partial \mathbf{C}}. \tag{15.77}$$

Alternatively, these relations can be expressed in terms of Lagrangian strain tensor **E**, $2\mathbf{E} = \mathbf{C} - \mathbf{1}$, by (15.29), and thus

$$\frac{\partial W}{\partial \mathbf{C}} = \frac{\partial W}{\partial \mathbf{E}}:\frac{\partial \mathbf{E}}{\partial \mathbf{C}} = \frac{1}{2}\frac{\partial W}{\partial \mathbf{E}}, \tag{15.78}$$

and

$$\mathbf{T} = \frac{\rho}{\rho_R}\mathbf{F}\cdot\left(\frac{\partial W}{\partial \mathbf{E}}\right)^T \cdot \mathbf{F}^T, \quad \mathbf{T}^* = \mathbf{F}\cdot\frac{\partial W}{\partial \mathbf{E}}, \quad \mathbf{T}^{2PK} = \frac{\partial W}{\partial \mathbf{E}}, \tag{15.79}$$

for example.

In the special case of an isotropic hyperelastic material, the strain energy function, $W = W(\mathbf{C}) = W(\lambda_{\mathrm{I}}^2, \lambda_{\mathrm{II}}^2, \lambda_{\mathrm{III}}^2)$, depends upon $\mathbf{C}$ only through (isotropic) invariants $(I_C, II_C, III_C)$ of $\mathbf{C}$; thus,

$$W = W(I_C, II_C, III_C), \tag{15.80}$$

where $(I_C, II_C, III_C)$ are given by (15.66). Substituting this isotropic expression for the strain energy into (15.72) and making use of the following expressions for the derivatives of invariants $I_C$, $II_C$, and $III_C$ with respect to $\mathbf{C}$,

$$\frac{\partial I_{\mathbf{C}}}{\partial \mathbf{C}} = \mathbf{1}, \quad \frac{\partial II_{\mathbf{C}}}{\partial \mathbf{C}} = I_{\mathbf{C}}\mathbf{1} - \mathbf{C}, \quad \frac{\partial III_{\mathbf{C}}}{\partial \mathbf{C}} = III_{\mathbf{C}}\mathbf{C}^{-1}. \tag{15.81}$$

it follows that $\mathbf{T}^{2PK}$ has representation

$$\mathbf{T}^{2PK} = 2\left[\left\{\frac{\partial W}{\partial I_{\mathbf{C}}} + I_{\mathbf{C}}\frac{\partial W}{\partial II_{\mathbf{C}}}\right\}\mathbf{1} - \frac{\partial W}{\partial II_{\mathbf{C}}}\mathbf{C} + \frac{\partial W}{\partial III_{\mathbf{C}}}III_{\mathbf{C}}\mathbf{C}^{-1}\right]. \tag{15.82}$$

This constitutive relation may also be written in a form that contains $\mathbf{C}^2$ rather than $\mathbf{c}^{-1}$:

$$\mathbf{T}^{2PK} = 2\left[\left\{\frac{\partial W}{\partial I_{\mathbf{C}}} + I_{\mathbf{C}}\frac{\partial W}{\partial II_{\mathbf{C}}} + \frac{\partial W}{\partial III_{\mathbf{C}}}II_{\mathbf{C}}\right\}\mathbf{1} - , \right.$$

$$\left.\left\{\frac{\partial W}{\partial II_{\mathbf{C}}} + I_{\mathbf{C}}\frac{\partial W}{\partial III_{\mathbf{C}}}\right\}\mathbf{C} + \frac{\partial W}{\partial III_{\mathbf{C}}}\mathbf{C}^2\right] \tag{15.83}$$

by use of the Cayley Hamilton theorem, which states that a matrix satisfies its own characteristic equation, and thus $\mathbf{C}$ may replace $\lambda^2$ in (15.65): $\mathbf{C}^3 - I_c\mathbf{C}^2 + II_c\mathbf{C} - III_c = 0$. A term-by-term comparison of (15.78) with (15.69) shows that coefficients $a_o$, $a_1$, and $a_2$ in (15.69) are given in the case of hyperelasticity by

$$a_0 = 2\left\{\frac{\partial W}{\partial I_{\mathbf{c}}} + I_{\mathbf{c}}\frac{\partial W}{\partial II_{\mathbf{c}}} + \frac{\partial W}{\partial III_{\mathbf{c}}}II_{\mathbf{c}}\right\},$$

$$a_1 = -2\left\{\frac{\partial W}{\partial II_{\mathbf{c}}} + I_{\mathbf{c}}\frac{\partial W}{\partial III_{\mathbf{c}}}\right\}, \quad a_2 = 2\frac{\partial W}{\partial III_{\mathbf{C}}}. \tag{15.84}$$

Also, in the case of an isotropic hyperelastic material, coefficients $h_o$, $h_1$, and $h_2$ in the constitutive relation between Cauchy stress $\mathbf{T}$ and left Cauchy-Green tensor $\mathbf{B}$, (15.73), may be expressed in terms of the strain energy function by the following formulas:

$$h_0 = \frac{2}{J}\left\{II_{\mathbf{c}}\frac{\partial W}{\partial II_{\mathbf{c}}} + \frac{\partial W}{\partial III_{\mathbf{c}}}III_{\mathbf{c}}\right\}, \quad h_1 = \frac{2}{J}\frac{\partial W}{\partial I_{\mathbf{C}}}, \quad h_{-1} = -\frac{2}{J}III_{\mathbf{C}}\frac{\partial W}{\partial II_{\mathbf{C}}}. \tag{15.85}$$

## 15.10. INCOMPRESSIBLE ELASTICITY

The assumption of incompressibility is an idealization that means that no agency (stress, strain, electric field, temperature, etc.) can change the volume of the model of the material. Jacobian $J$ = Det $\mathbf{F}$ relates the element of volume, $dV$, in undeformed configuration to volume $dv$ in deformed configuration according to rule (15.36), $dv = JdV$. Jacobian $J$ is related to the principal stretches by $J = \lambda_I\lambda_{II}\lambda_{III}$. The requirement of incompressibility may then be expressed in algebraic forms related to the deformation — $J = 1$, $\lambda_I\lambda_{II}\lambda_{III} = 1$, $III_C = III_B = 1$, etc., and to algebraic forms related to the motion such as $\mathrm{tr}\mathbf{D} = \boldsymbol{\nabla}\cdot\mathbf{v} = 0$ (§7.4). The assumption of incompressibility requires that density $\rho$ be a constant. Pressure field $p$ in an incompressible material is a Lagrange multiplier (see Example 7.4.1) that serves the function of maintaining the incompressibility constraint, not a thermodynamic variable. Because the volume of the model material cannot change, $p$ does no work; it is a function of $\mathbf{x}$ and $t$, $p(\mathbf{x}, t)$, to be determined by solution of the system of differential equations and boundary/initial conditions.

Recall from §15.7 that the constitutive equation for an elastic material can be written $\mathbf{T} = \mathbf{g}(\mathbf{F})$ in terms of Cauchy stress $\mathbf{T}$ and deformation gradient $\mathbf{F}$ or as $\mathbf{T}^{1PK} = \mathbf{h}(\mathbf{F})$ (15.54) in terms of first Piola-Kirchhoff stress tensor $\mathbf{T}^{1PK}$ or as $\mathbf{T}^{2PK} = \mathbf{t}(\mathbf{C})$ (15.56) in terms of second Piola-Kirchhoff stress tensor $\mathbf{T}^{2PK}$ and right Cauchy-Green tensor $\mathbf{C}$. For incompressible elastic materials Cauchy stress tensor $\mathbf{T}$ must be replaced by $\mathbf{T} + p\mathbf{1}$, where $p$ is the constitutively indeterminate pressure described above and conveniently interpreted as a Lagrange multiplier. The response functions, say $\mathbf{g}(\mathbf{F})$ above, are defined only for deformations or motions that satisfy condition $J$ = Det $\mathbf{F}$ = 1. Thus, $\mathbf{T} = \mathbf{g}(\mathbf{F})$ is replaced by $\mathbf{T} + p\mathbf{1} = \mathbf{g}(\mathbf{F})$ when the assumption of incompressibility is made. Similarly, $\mathbf{T}^{1PK} = \mathbf{h}(\mathbf{F})$ given by (15.54) becomes

$$\mathbf{T}^{1PK} + p(\mathbf{F}^{-1})^{\mathrm{T}} = \mathbf{h}(\mathbf{F}), \tag{15.86}$$

and $\mathbf{T}^{2PK} = \mathbf{t}(\mathbf{C})$, (15.56), becomes

$$\mathbf{T}^{2PK} + p\mathbf{C}^{-1} = \mathbf{t}(\mathbf{C}), \tag{15.87}$$

where functions $\mathbf{h}(\mathbf{F})$ and $\mathbf{t}(\mathbf{C})$ are defined only for deformations or motions that satisfy incompressibility condition Det $\mathbf{F}$ = 1.

When an elastic model material is both isotropic and incompressible, there are further simplifications in the constitutive relations. For example, (15.69) and (15.73) are now written in simpler forms:

$$\mathbf{T}^{2PK} + p\mathbf{C}^{-1} = a_1\mathbf{C} + a_2\mathbf{C}^2, \tag{15.88}$$

and

$$\mathbf{T} + p\mathbf{1} = h_1\mathbf{B} + h_{-1}\mathbf{B}^{-1}, \tag{15.89}$$

where the functions of the isotropic invariants in these representations also simplify:

$$a_1 = a_1(I_C, II_C), \quad a_2 = a_2(I_C, II_C) \tag{15.90}$$

and

$$h_{-1} = h_{-1}(I_C, II_C) = h_{-1}(I_B, II_B),$$

$$h_{-1} = h_{-1}(I_C, II_C) = h_{-1}(I_B, II_B). \tag{15.91}$$

When an elastic model material is isotropic, incompressible, and hyperelastic, there are even further simplifications in the constitutive relations. In this case the strain energy per unit volume, $W$, depends only on $I_C = I_B$ and $II_C = II_B$, and (15.93) reduces to

$$\mathbf{T} = -p\mathbf{1} + h_1\mathbf{B} + h_{-1}\mathbf{B}^{-1}, \tag{15.92}$$

where

$$h_1 = 2\frac{\partial W}{\partial I_\mathbf{C}}, \quad h_{-1} = -2\frac{\partial W}{\partial II_\mathbf{C}}. \tag{15.93}$$

Even with all these restrictive assumptions (hyperelasticity, isotropy, and incompressibility), a complete solution of many interesting problems is not possible. Simpler models based on specialized assumptions but which retain the basic characteristics of the nonlinear elastic response have been proposed for polymeric materials and for biological tissues. An example that stems from research on the constitutive behavior of rubber is the *Mooney-Rivlin material* with the following constitutive equation (Mooney 1940; Rivlin and Saunders 1976):

$$\mathbf{T} = -p\mathbf{1} + \mu\left(\frac{1}{2} + \beta\right)\mathbf{B} - \mu\left(\frac{1}{2} - \beta\right)\mathbf{B}^{-1}, \tag{15.94}$$

where $\mu$ and $\beta$ are constants, which has the following strain energy function:

$$W = \frac{1}{2}\mu\left[\left(\frac{1}{2} + \beta\right)(I_B - 3) + \left(\frac{1}{2} - \beta\right)(II_B - 3)\right], \tag{15.95}$$

where inequalities $\mu > 0$ and $(1/2) \geq \beta \geq -(1/2)$ are imposed upon constants $\mu$ and $\beta$, so that strain energy $W$ is a positive semi-definite quantity. The special case of the Mooney-Rivlin material when $\beta = (1/2)$ is called *neo-Hookian* material:

$$\mathbf{T} = -p\mathbf{1} + \mu\mathbf{B}. \tag{15.96}$$

Employing the assumption of incompressibility in the development of a constitutive model for a soft biological tissue is quite easy to justify because soft tissues contain so much water that their effective bulk compressibility is that of water, 2.3 GPa. When one compares the shear or deviatoric moduli of a soft biological tissue with 2.3 GPa, these moduli are usually orders of magnitude less. Only in the case of hard tissues do the shear or deviatoric moduli approach and exceed (up to an order of magnitude) the effective bulk compressibility of water.

## 15.11. FUNG'S EXPONENTIAL STRAIN ENERGY FUNCTION

This section draws heavily from the work of Y. C. Fung (Fung, 1967; Lanir and Fung 1974a,b; Fung, 1993) in which it was shown that the elastic stress for the many specific soft tissues may be mathematically modeled as an exponential function of the extension ratio. This means that Young's modulus (or the tangential modulus because of the nonlinearity) varies exponentially with strain. Fung showed experimentally that Young's modulus is almost zero at small strain but increases exponentially as strain increases. As a consequence the strain energy in a tissue is an exponential function of most strain measures. Fung's contribution provided a philosophy (see the introductory quote in this chapter) for characterization of experimental stress–strain

curves by a mathematical expression that contains two or three parameters, and can be used for systematic study of the tissue under varied conditions. In this work it was shown that the most important parameter is the exponential index, defined as the slope of $dT^{1PK}/d\lambda$ vs. $T^{1PK}$ curve. The exponential index is designated by dimensionless symbol $a$, and the values of $a$ are a measure of the deviation of this slope from (linear) Hooke's law because the value of $a$ is zero for all materials that obey Hooke's law. As will be described below, Fung developed these data and the associated representations from experiments on the mesentery of the rabbit, and has shown that the model could apply to other tissues such as muscles and skin.

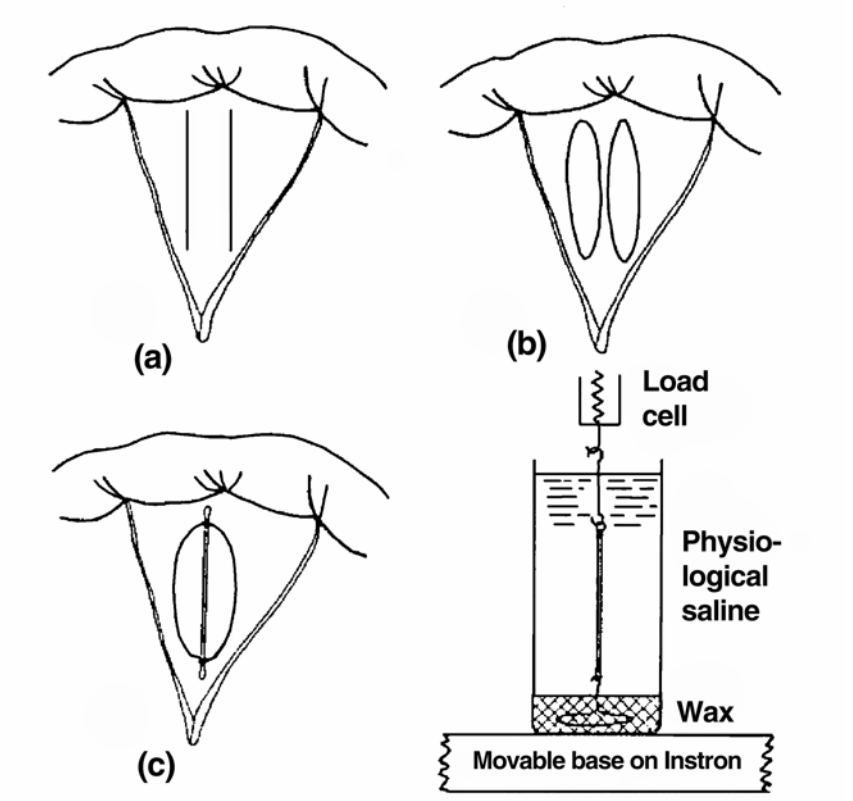



**Figure 15.16**. Sketch of the preparation of the mesentery specimen for the uniaxial tension test. Reprinted with permission from Fung (1967).

The rabbit mesentery test specimens were obtained by spreading the mesentery out flat on a platform in the natural dimensions defined by the surrounding intestines and large blood vessels, to which no restraint other than gravity and friction on the platform was imposed (Figure 15.16). It will become clear from what is to be described below that the mesentery membrane was actually highly stretched in this configuration. The tensile stress was not small (of the order of 101 dynes/cm), but owing to the comparative thinness of the tissue (0.06 cm), the resultant force (of order 6 g/cm) was not large enough to move the intestines and large blood vessels. An area of the membrane free from fat and large blood vessels was selected. A special

cutter that consisted of two parallel razor blades 1 cm apart was then dropped on this membrane, cutting two parallel slits 3.66 cm long. On lifting the cutter it was seen that the mesentery shrank immediately away from the cuts, leaving two large elliptical holes. The strip that remained between the elliptical holes was tied with fine silk threads at both ends and cut free. This cutting produced a further contraction in the size of the specimen. The size of the final specimen was much smaller than that defined by the spread-out intestine. Small hooks were attached to the specimen, and the specimen was mounted in the Instron testing machine (Figure 15.16). A questionable influence concerning specimen testing arose from the fine silk thread ties at the specimen ends that induced a localized residual stress. Due to the considerable length of the specimen, this end effect was assumed to be negligible.

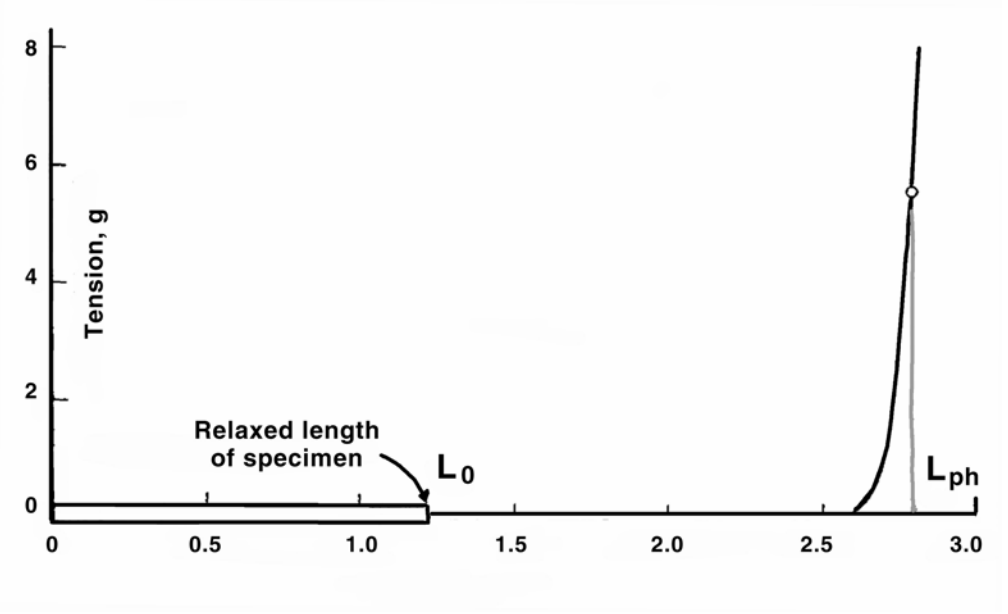



**Figure 15.17**. Load-deflection curve of a rabbit mesentery in tension. The ordinate shows the load in grams. The abscissa shows the deflection in centimeters. The state corresponding to the naturally spread-out mesentery is marked by the small circle. The point $L_0$ marks the relaxed length of the specimen. Reprinted with permission from Fung (1967).

A variety of load-deflection curves were obtained with the rabbit mesentery specimens. They are illustrated in Figures 15.17–15.21. The load-deflection curve of a specimen when the rate of strain imposed was 0.254 cm/mm is shown in Figure 15.17. Note that the specimen had rest length $L_0$ = 1.22 cm. When the specimen was stretched from $L_0$ to $L$ = 2.54 cm, the corresponding tension induced was very small; in fact it, was not readable in the chart illustrated in Figure 15.17. Extension beyond $L$ = 2.54 cm, however, induced a rapidly increasing tension. The load-deflection relationship is seen from Figure 15.17 to be nonlinear. A small circle in Figure 15.17 marks the state corresponding to the naturally spread-out mesentery, considered to be the normal physiological state. Measured length $L_{ph}$ of the specimen located this point before it was cut from the mesentery. It is seen that considerable tensile stress must have existed in the normal physiological state of the specimen.

Typical hysteresis curves of a mesentery specimen strained at a rate of ±0.254 cm/min are shown in Figure 15.18. The large loop shows the first complete cycle and indicates that

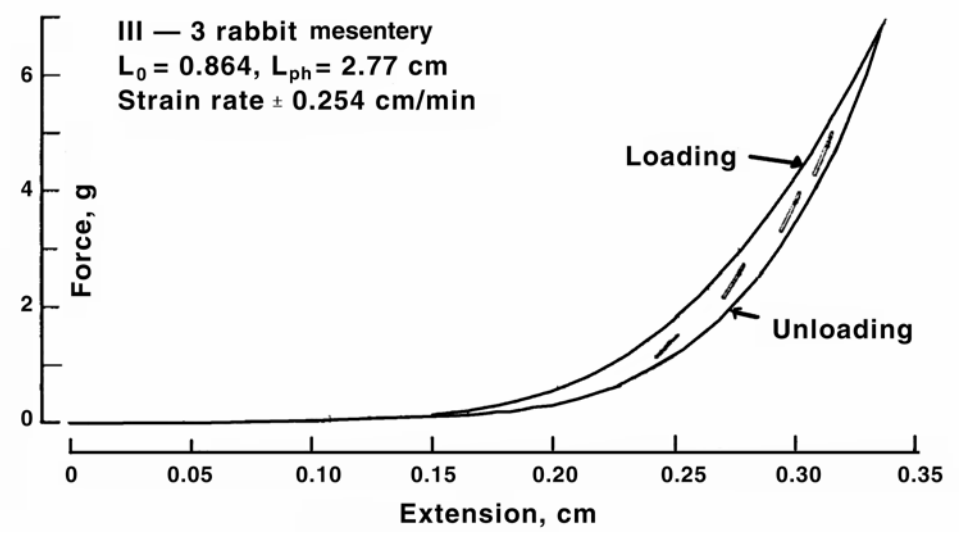



**Figure 15.18**. Hysteresis curves. Rabbit mesentery. Loading and unloading at a rate of 0.254 cm/mm. The large loop shows the first complete cycle. The specimen was then stressed to an intermediate point and cycles of small amplitude performed. Note the difference in slope of the small dynamic loops from the large one and from each other. Reprinted with permission from Fung (1967).

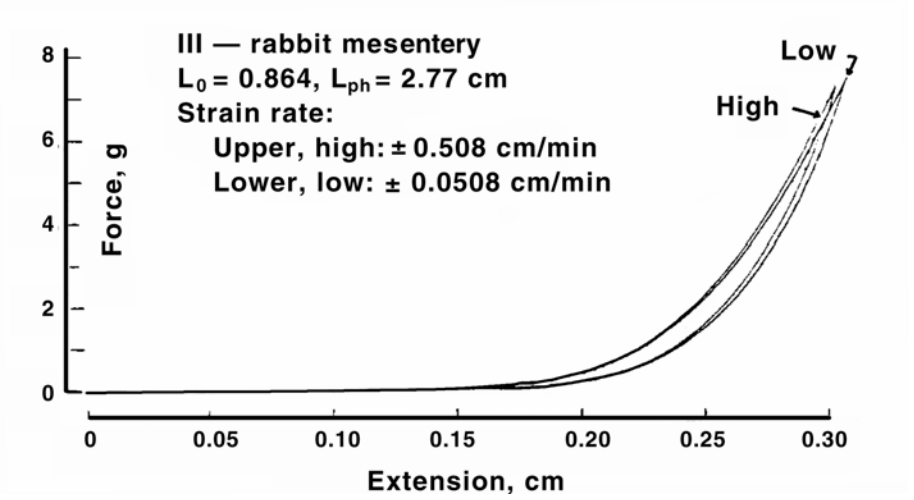



**Figure 15.19**. Hysteresis curves of rabbit mesentery obtained at different strain rates. The high rate was 10 times that of the low rate. Only a slight change in hysteresis curves was obtained. The investigator suggested that some of the small difference is due to fatigue, and some due to strain rate. Reprinted with permission from Fung (1967).

hysteresis existed, but that it was not very large. Restressing the specimen to an intermediate point and performing cycles of small-amplitude at the same strain rate obtained the small loops in Figure 15.18. Note the difference in slope of the small dynamic loops from the large one and from each other. The effect of strain rate on hysteresis is illustrated in Figure 15.19. The curve

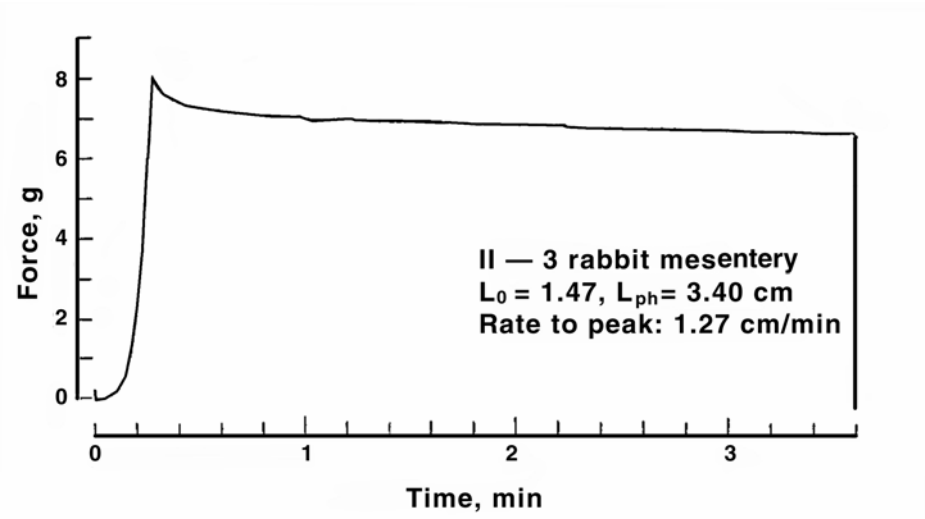



**Figure 15.20**. A relaxation curve for a rabbit mesentery subjected to ramp-strain loading followed by a constant strain loading. The specimen was stressed at a strain rate of 1.27 cm/mm to the peak, then the moving head of the testing machine was suddenly stopped so that the strain remained constant. The subsequent relaxation of stress is shown.

marked "high" was produced at a strain rate 10 times faster than that marked "low." It is seen that the hysteresis loops did not depend very much on the rate of strain.

A stress-relaxation curve is shown in Figure 15.20. The specimen was strained at a constant rate until tension $T_1$ was obtained. The length of the specimen was then held fixed; the change in tension over time is shown in Figure 15.20. Examination of a large number of such relaxation curves showed that the total amount of relaxation (i.e., $T_1 - T_\infty$) was roughly proportional to peak-applied load $T_1$. The load-deflection curve for a specimen strained up to failure is shown in Figure 15.21. The authors described the failure as rather gradual. The ultimate strain at failure was large. The specimen failed by tearing at some unpredictable points.

In the analysis of the data obtained from these experiments on the mesentery of the rabbit, Fung (1967) employed a continuum-based mathematical model of a right-angled parallelepiped of incompressible elastic material subjected to homogeneous deformation. Recall Example 15.6.1 in which a solid right-angled parallelepiped specimen capable of large deformations was extended by a force of magnitude $P$ in the $x_1$ direction (Figure 15.15). In the special case when the material is incompressible, $J = \lambda_I\lambda_{II}\lambda_{III} = 1$, and the cross-section transverse to the extension is symmetric, then $\lambda_I = \lambda$, $\lambda_{II} = \lambda_{III} = 1/\sqrt{\lambda}$. The before and after cross-sectional areas are related by $A = \lambda^2 A_0$. The Cauchy and first and second Piola-Kirchhoff stress tensors in this uniaxial situation are given by $T_{11} = P/A = \lambda P/A_0 = \lambda^2 T_{1I}^{2PK} = \lambda T_{1I}^{1PK}$. The most striking feature of the elasticity of a living tissue, as seen from Figure 15.17, is the very small stress in response to a fairly large strain. In Figure 15.17 an extension up to about 100% of the relaxed length yields only a small tension that was too small to be plotted. However, for $\lambda > 2$ the stress rises exponentially. The slope of the loading curve was computed from loading curves such as the one shown in Figure 15.18. The slope of the elastic tension deflection curve was then plotted against the corresponding stress, $T_{1I}^{1PK}$, in the specimen (Figure 15.22). This plot suggests that in first approximation to a mathematical representation of these experimental data the slope of the elastic tension deflection curve is proportional to the corresponding stress $T_{1I}^{1PK}$ in the specimen, and thus

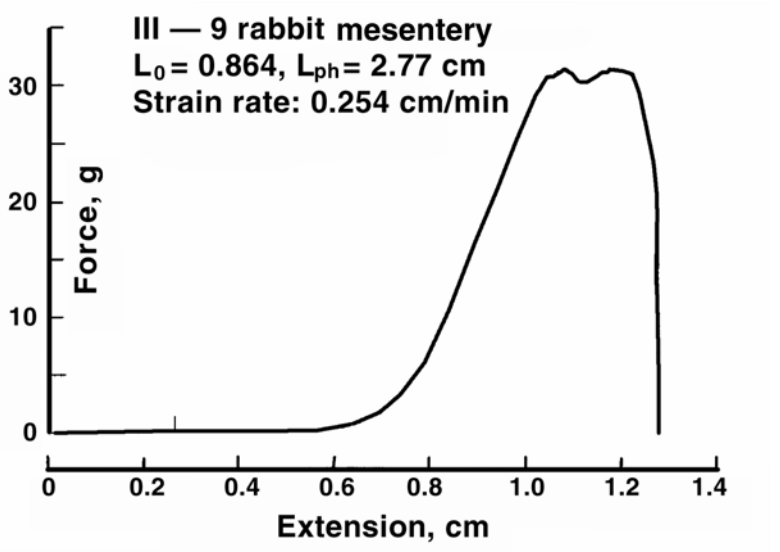



**Figure 15.21**. A load deformation curve of a rabbit mesentery specimen that was loaded to failure. Failure appeared to occur by gradual tearing. Reprinted with permission from Fung (1967).

$$\frac{dT_{1I}^{1PK}}{d\lambda} = aT_{1I}^{1PK}, \tag{15.97}$$

where exponential index $a$ is a constant of proportionality determined from figures similar to Figure 15.22. The stress–strain relation, $T_{1I}^{1PK} - \lambda$, is obtained from (15.97) by integration; thus,

$$T_{1I}^{1PK} = \frac{1}{c} e^{a\lambda}, \tag{15.98}$$

where $c$ is a constant of integration. The strain energy per unit volume of the deformed specimen is obtained by integrating the stress–stretch relation (15.98) from the initial length to the final length of the specimen at the end of the deformation and dividing by the initial volume, $A_0 L_0$, and thus

$$W(\lambda) = \frac{1}{A_0 L_0} \int_{L_0}^{L} T_{1I}^{1PK}(L) A_o dL = \frac{1}{c} \int_{1}^{\lambda} e^{a\lambda} d\lambda = \frac{1}{ca} [e^{a\lambda} - e^{a}]. \tag{15.99}$$

This result suggests that the strain energy per unit volume of the rabbit mesentery is an exponential function of the applied stretch. This result was later extended to suggest that the conclusion also applies to other tissues.

Although the insights gained from this experimental study have a wide impact on the modeling of constitutive equations for soft tissues, there is a limitation to the use of this data because the test loading did not correspond to a physiological loading of a mesentery. In a physiological loading the mesentery is under biaxial tension while in this experiment the

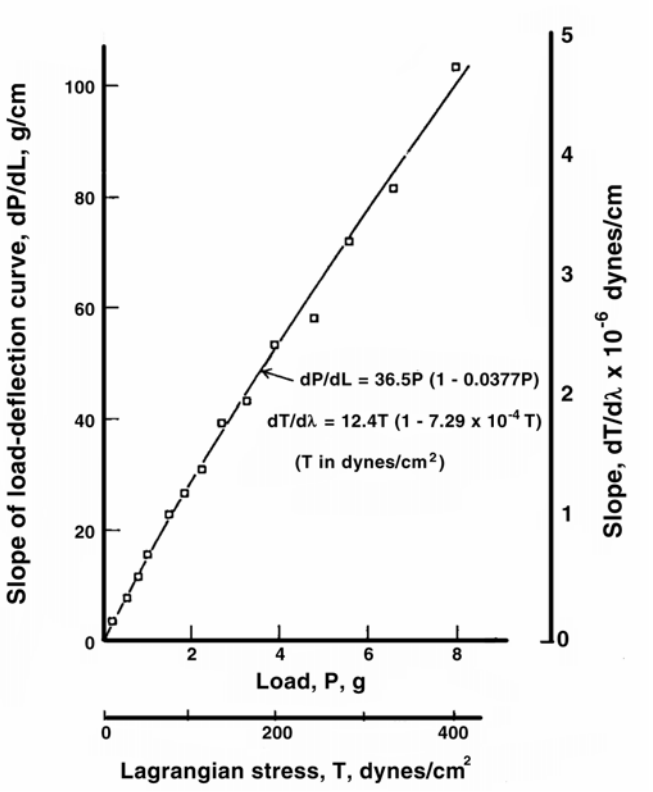



**Figure 15.22**. The tangential elastic modulus from hysteresis curves for one rabbit mesentery specimen. In this figure the symbol $T$ stands for the axial component of the first Piola-Kirchhoff stress $T^{1PK}$ tensor that is sometimes called the Lagrangian stress tensor. Young's modulus of the rabbit mesentery is plotted against the corresponding tension $T = T^{1PK}$. For this figure, $L_0 = 0.865$ cm, $A_0 = 0.0193$ cm$^2$, $\lambda_{ph} = 3.21$, $T = 51.8$ P (dynes/cm$^2$). Reprinted with permission from Fung (1967).

specimen was collapsed, and no tension was applied, in the directions perpendicular to the test direction. The experiments were one-dimensional experiments on a tissue that functions in vivo as a two-dimensional tissue. Therefore, the results were not physiological for the specific tissue examined because the experimental study did not control or measure the stress or strain in the direction perpendicular to the test direction. This concern was addressed in subsequent work by Lanir and Fung (1974a,b) in which a biaxial test device was employed. The biaxial-loading testing equipment has to be much more elaborate than the uniaxial one described above because of the need to control boundary conditions on four edges of a rectangular specimen. The edges must be allowed to expand freely. In the target region, the stress and strain states should be uniform so that data analysis can be done simply. The region from which the data is to be taken must be away from the outer edges in order to avoid the stress concentrations in the specimen mounting and the disturbing influence of the loading device. The strain should be measured optically to avoid mechanical disturbances. The method of testing a rectangular specimen of uniform thickness in biaxial loading is illustrated in Figure 15.23. A schematic view of the test device used to biaxially stretch the rectangular specimen is shown in Figure 15.24. The test specimen floated in a physiological saline solution and was hooked along its four edges by means of small staples. Each hook is connected by means of a

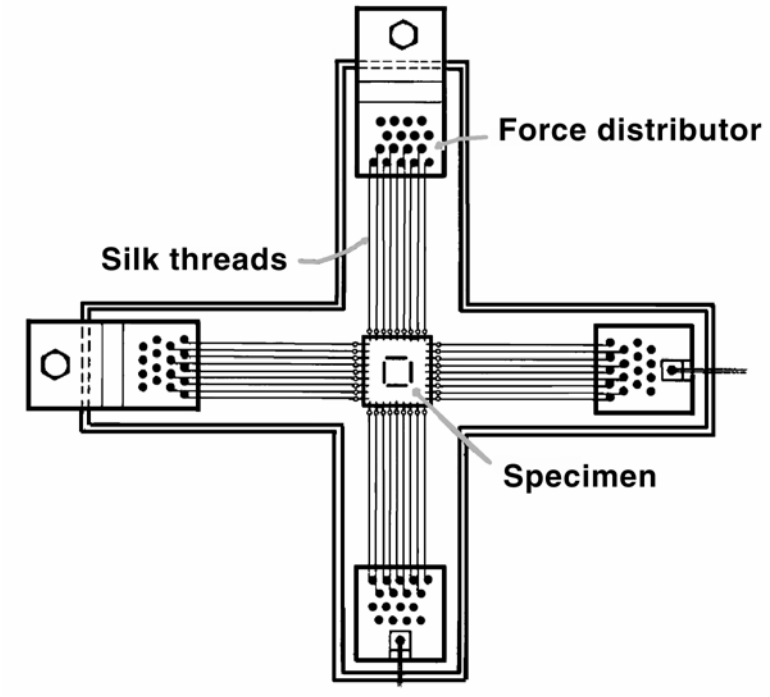



**Figure 15.23**. The specimen is represented by the square in the middle. The smaller square within the specimen square — the square without complete corners — represents inked lines on the specimen that are visible in the captured image of the specimen and used for the measurement of strain. The silk threads hooked to the specimen and also to the force distributor are adjustable to maintain a homogeneous deformation. The force distributors are represented by the four squares at the end of the silk threads. They contain the pins, represented by black dots in the force distributors, to which the silk threads are attached. Reprinted with permission from Lanir and Fung (1973a).

silk thread to a screw on one of the four force-distributing platforms (Figure 15.23). This setup allows individual adjustment of the tension of each thread to maintain a homogeneous deformation. The force-distributing platforms are bridged over the edges of the saline tray in an identical manner for both directions (Figure 15.24). One platform is rigidly mounted to the carriage of a sliding mechanism; the opposite platform is horizontally attached to a force transducer. Both the support and transducer are rigidly connected to the carriage of another sliding unit. A pulley system on this carriage allows the force distributor to be pulled by a constant weight on top of the force exerted by the transducer. The carriages of the opposite sliding units are displaced by means of an interconnected threaded drive shaft. The threads of the left and right sliding units are pulled by the drive shaft at an equal rate in opposite directions, so that the specimen can be stretched or contracted without changing its location. The stretching mechanism can stretch the tissue in two directions either independently or coordinated according to a prescribed program.

The loading strings are approximately parallel when the equipment is in operation. These strings are "tuned" (in the manner of piano tuning by turning a set of screws) at the beginning in such a way that the rectangular benchmarks made on a relaxed specimen in ink remain rectangular upon loading, without visible distortion. The dimensions of the specimen between the benchmarks are continuously measured and monitored by a video dimension analyzer (VDA),

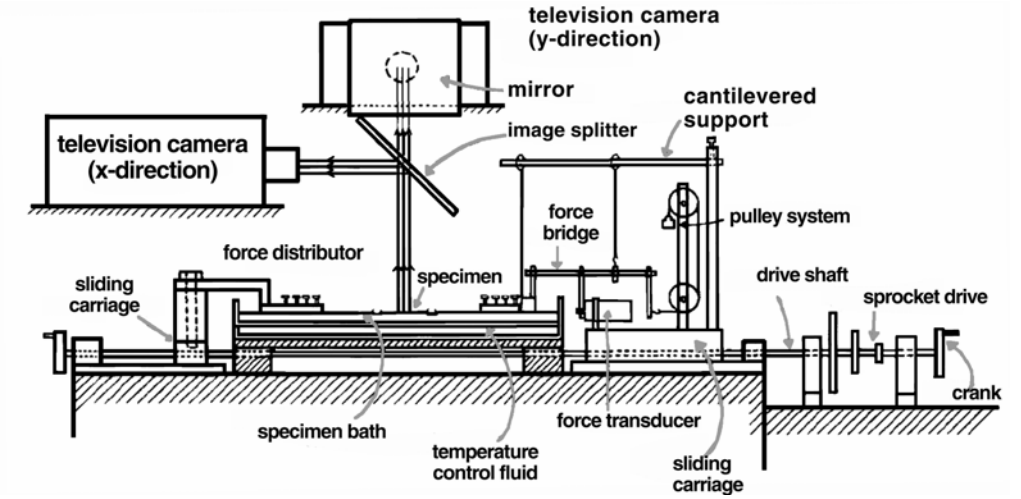



**Figure 15.24**. A schematic view of the biaxial testing device for planar soft tissues. This view shows the stretching mechanism in one direction and the optical system for measuring the deformation. Reprinted with permission from Lanir and Fung (1973a).

which measures the distance between the markers. The strain in the specimen can be measured in two perpendicular directions.

The data on rabbit skin obtained using this biaxial testing apparatus will be described below after a description of the extension of Fung's model of the exponential dependence of the strain energy upon strain measures. Before leaving the description of this biaxial test apparatus it is appropriate to note that it was subsequently improved and that it has been used to test other tissues. The improvements include computerization of the operation and recording and analysis of the data. Applications to the testing of lung tissue, with an additional method for thickness measurement, are presented in Vawter, Fung, and West (1978), Zeng et al. (1987), Yager et al. (1992), and Debes and Fung (1992).

In the years following his (1967) paper, Fung extended the constitutive model of the exponential dependence of the strain energy upon strain measures to two and three dimensions. A three-dimensional form that achieved some success is represented by the following strain energy function:

$$W(\hat{\mathbf{E}}) = \frac{1}{2}\hat{\mathbf{E}}\cdot\hat{\mathbf{A}}\cdot\hat{\mathbf{E}} + \frac{c}{2}e^{\hat{\mathbf{E}}\cdot\hat{\mathbf{C}}\cdot\hat{\mathbf{E}}} \tag{15.100}$$

where $\hat{\mathbf{A}}$ and $\hat{\mathbf{C}}$ are symmetric second-rank tensors in six dimensions, and $\hat{\mathbf{E}}$ is the three-dimensional strain tensor represented as a vector in six dimensions (recall §A.11 and (6.27H)). The stresses are calculated from the strain energy function using formula (15.79) in its form as a vector representation in six dimensions rather than its form as a second-order tensor in three dimensions, and thus

$$\hat{\mathbf{T}}^{2PK} = \frac{\partial W}{\partial \hat{\mathbf{E}}} = \hat{\mathbf{A}}\cdot\hat{\mathbf{E}} + c\hat{\mathbf{C}}\cdot\hat{\mathbf{E}}e^{\hat{\mathbf{E}}\cdot\hat{\mathbf{C}}\cdot\hat{\mathbf{E}}}\,. \tag{15.101}$$

This constitutive equation is algebraically a six-dimensional equation, but it represents a situation that is physically three dimensional. The fact that Lagrangian strain tensor $\mathbf{E}$ is used rather

than the principal stretches that appear in (15.100) is only a change in notation, as one can see from (15.34) that Lagrangian strain tensor $\mathbf{E}$ and the stretches are directly related to each other.

As many tissues such as the mesentery and skin are, effectively, two-dimensional structures, specialization of (15.100) and (15.101) to the planar case is important. In the case of a planar situation strain energy function (15.100) simplifies to

$$W^{(p)} = \frac{1}{2}\hat{\mathbf{E}}^{(p)} \cdot \hat{\mathbf{A}}^{(p)} \cdot \hat{\mathbf{E}}^{(p)} + \frac{c}{2} e^{\hat{\mathbf{E}}^{(p)} \cdot \hat{\mathbf{C}}^{(p)} \cdot \hat{\mathbf{E}}^{(p)}}, \tag{15.102}$$

where the $p$ superscripted in parentheses $(p)$ stands for planar — for example, planar strain energy function $W^{(p)}$. The planar components of six-dimensional strain vector $\hat{\mathbf{E}} = [E_{11}, E_{22}, E_{33}, \sqrt{2}E_{23}, \sqrt{2}E_{13}, \sqrt{2}E_{12}]^T = [\hat{E}_1, \hat{E}_2, \hat{E}_3, \hat{E}_4, \hat{E}_5, \hat{E}_6]^T$ are represented by a 3-vector matrix by removing the 3, 4, and 5 components, and so $\hat{\mathbf{E}}^{(p)}$ is given by

$$\hat{\mathbf{E}}^{(p)} = [E_{11}, E_{22}, \sqrt{2}E_{12}]^T. \tag{15.103}$$

In similar fashion, the expressions for second-rank tensors $\hat{\mathbf{A}}$ and $\hat{\mathbf{C}}$ in six-dimensional representations are reduced from the usual form of the 6-by-6 matrix for the matrix of a six-dimensional second-rank tensor, given in Table 5.4, to a 3-by-3 matrix representation by removing the 3, 4, and 5 rows and the 3, 4, and 5 columns of the 6-by-6 matrix. In the case of orthotropy, which is assumed in this mathematical modeling process, the vanishing of the 3-by-3 submatrices in the lower right-hand corner and the upper left-hand corner of the 6-by-6 matrix representing orthotropy (see Table 5.4) show that $\hat{\mathbf{A}}^{(p)}$ and $\hat{\mathbf{C}}^{(p)}$ are given by

$$\hat{\mathbf{A}}^{(p)} = \begin{bmatrix} \hat{A}_{11} & \hat{A}_{12} & 0 \\ \hat{A}_{12} & \hat{A}_{22} & 0 \\ 0 & 0 & \hat{A}_{66} \end{bmatrix}, \quad \hat{\mathbf{C}}^{(p)} = \begin{bmatrix} \hat{C}_{11} & \hat{C}_{12} & 0 \\ \hat{C}_{12} & \hat{C}_{22} & 0 \\ 0 & 0 & \hat{C}_{66} \end{bmatrix}. \tag{15.104}$$

The associated stresses are obtained from (15.102) by taking the derivative with respect to each of the associated strains; thus,

$$\hat{\mathbf{T}}^{2PK(p)} = \frac{\partial W}{\partial \hat{\mathbf{E}}^{(p)}} = \hat{\mathbf{A}}^{(p)} \cdot \hat{\mathbf{E}}^{(p)} + c\hat{\mathbf{C}}^{(p)} \cdot \hat{\mathbf{E}}^{(p)} e^{\hat{\mathbf{E}}^{(p)} \cdot \hat{\mathbf{C}}^{(p)} \cdot \hat{\mathbf{E}}^{(p)}}, \tag{15.105}$$

or, in component form,

$$T_{11}{}^{2PK(p)} = \hat{T}_1{}^{2PK(p)} = \frac{\partial W}{\partial \hat{E}_1{}^{(p)}} = \hat{A}_{11}\hat{E}_1 + \hat{A}_{12}\hat{E}_2 + c(\hat{C}_{11}\hat{E}_1 + \hat{C}_{12}\hat{E}_2) e^{\hat{\mathbf{E}}^{(p)} \cdot \hat{\mathbf{C}}^{(p)} \cdot \hat{\mathbf{E}}^{(p)}}$$

$$T_{22}{}^{2PK(p)} = \hat{T}_2{}^{2PK(p)} = \frac{\partial W}{\partial \hat{E}_2{}^{(p)}} = \hat{A}_{12}\hat{E}_1 + \hat{A}_{22}\hat{E}_2 + c(\hat{C}_{12}\hat{E}_1 + \hat{C}_{22}\hat{E}_2) e^{\hat{\mathbf{E}}^{(p)} \cdot \hat{\mathbf{C}}^{(p)} \cdot \hat{\mathbf{E}}^{(p)}}$$

$$\sqrt{2}T_{12}{}^{2PK(p)} = \hat{T}_6{}^{2PK(p)} = \frac{\partial W}{\partial \hat{E}_6{}^{(p)}} = \hat{A}_{66}\hat{E}_6 + c\hat{C}_{66}\hat{E}_6 e^{\hat{\mathbf{E}}^{(p)} \cdot \hat{\mathbf{C}}^{(p)} \cdot \hat{\mathbf{E}}^{(p)}}, \tag{15.106}$$

where

$$\hat{\mathbf{E}}^{(p)} \cdot \hat{\mathbf{C}}^{(p)} \cdot \hat{\mathbf{E}}^{(p)} = \hat{C}_{11}\hat{E}_1^2 + \hat{C}_{22}\hat{E}_2^2 + 2\hat{C}_{12}\hat{E}_1\hat{E}_2 + \hat{C}_{66}\hat{E}_6^2 =$$
$$\hat{C}_{11}E_{11}^2 + \hat{C}_{22}E_{22}^2 + 2\hat{C}_{12}E_{11}E_{22} + 2\hat{C}_{66}E_{12}^2. \tag{15.107}$$

The predictions of constitutive equations (15.106) were compared with the experimental data obtained by Lanir and Fung (1973b) and by Tong and Fung (1976). They began by noting that the derivatives of $\hat{T}_1^{2PK(p)}$ and $\hat{T}_2^{2PK(p)}$ with respect to strains $\hat{E}_1$ and $\hat{E}_2$ are given by

$$\frac{\partial \hat{T}_1^{2PK(p)}}{\partial \hat{E}_1^{(p)}} = \hat{A}_{11} + c\{\hat{C}_{11} + 2(\hat{C}_{11}\hat{E}_1 + \hat{C}_{12}\hat{E}_2)^2\} e^{\hat{\mathbf{E}}^{(p)}\cdot\hat{\mathbf{C}}^{(p)}\cdot\hat{\mathbf{E}}^{(p)}},$$

$$\frac{\partial \hat{T}_2^{2PK(p)}}{\partial \hat{E}_2^{(p)}} = \hat{A}_{22} + c\{\hat{C}_{22} + (\hat{C}_{12}\hat{E}_1 + \hat{C}_{22}\hat{E}_2)^2\} e^{\hat{\mathbf{E}}^{(p)}\cdot\hat{\mathbf{C}}^{(p)}\cdot\hat{\mathbf{E}}^{(p)}},$$

and

$$\frac{\partial \hat{T}_1^{2PK(p)}}{\partial \hat{E}_2^{(p)}} = \frac{\partial \hat{T}_2^{2PK(p)}}{\partial \hat{E}_1^{(p)}} = \hat{A}_{12} +$$

$$c\{\hat{C}_{12} + (\hat{C}_{11}\hat{E}_1 + \hat{C}_{12}\hat{E}_2)(\hat{C}_{12}\hat{E}_1 + \hat{C}_{22}\hat{E}_2)\} e^{\hat{\mathbf{E}}^{(p)}\cdot\hat{\mathbf{C}}^{(p)}\cdot\hat{\mathbf{E}}^{(p)}}. \tag{15.108}$$

The values of the matrices of constants $\hat{\mathbf{A}}^{(p)}$ and $\hat{\mathbf{C}}^{(p)}$ and scalar constant $c$ were determined by requiring that $\hat{T}_1^{2PK(p)}$ and $\hat{T}_2^{2PK(p)}$ and their derivatives measured experimentally are fit exactly by eqs. (15.106) and (15.108) at certain selected datapoints. The choice of these points, denoted by A, B, C, and D, is illustrated in Figure 15.25. This figure contains plots of the force-vs-stretch ratio curves in two perpendicular directions, and the resulting data illustrated the anisotropy of rabbit abdominal skin tissue. The curves with solid lines are for the case in which $E_{22} = \hat{E}_2$ is held constant at zero and force in the 1 or $x$ direction is varied, while the curves with dashed lines are for the case that $E_{11} = \hat{E}_1$ is held constant at zero and force in the 2 or $y$ direction is varied. A pair of points, labeled A and C in Figure 15.25, are located on the curves in a region where stresses change rapidly, whereas points B and D are located in a region in which the strains are relatively small. Matrix constants $\hat{\mathbf{A}}^{(p)}$ are determined essentially by experimental data at B and D, whereas matrix constants $\hat{\mathbf{C}}^{(p)}$ and scalar constant $c$ are determined essentially by the data at points A and C in Figure 15.25. The exact locations of points A, B, C, and D are not very important. The values of the constants change very little by choosing different (reasonable) points on any two sets of data curves. The value of constant $c$ determined is 0.779 Pa, and the matrices of constants $\hat{\mathbf{A}}^{(p)}$ and $\hat{\mathbf{C}}^{(p)}$ were found to be

$$\hat{\mathbf{A}}^{(p)} = \begin{bmatrix} 1020 & 254 & 0 \\ 254 & 1020 & 0 \\ 0 & 0 & \text{NM} \end{bmatrix} (\text{Pa}), \quad \hat{\mathbf{C}}^{(p)} = \begin{bmatrix} 3.59 & 0.578 & 0 \\ 0.578 & 12.7 & 0 \\ 0 & 0 & \text{NM} \end{bmatrix}, \tag{15.109}$$

where NM stands for the fact that these constants were not measured in the experiment. They were not measured because they are shear moduli, and it was assumed that the testing was conducted in the principal coordinate systems of stress and strain.

## 15.12. STRAIN ENERGY FUNCTIONS FOR TISSUES

In this section a representative selection of proposed strain energy functions for soft biological tissues is described. Certain general observations can be made about the development of

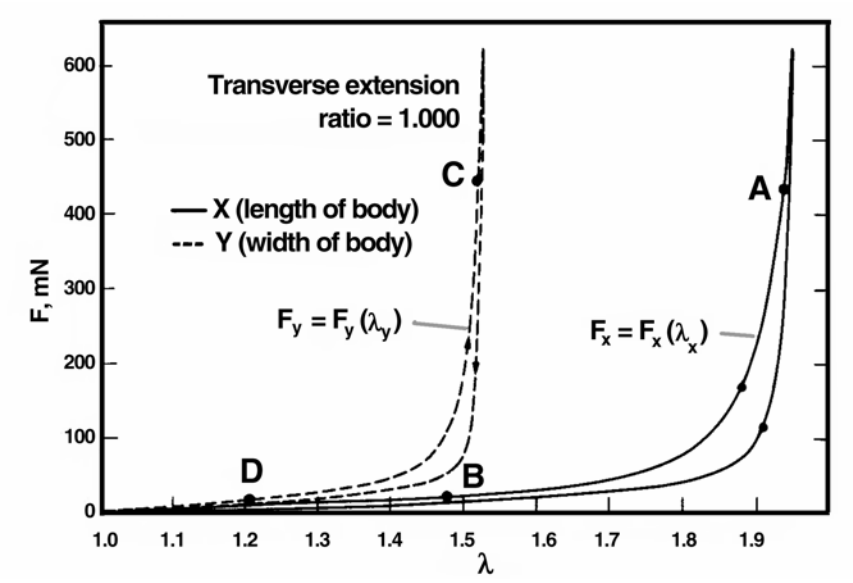



**Figure 15.25**. The force-vs.-stretch ratio curves in perpendicular directions illustrate the anisotropy of rabbit abdominal skin tissue. The curves with solid lines are for the case that $E_{22} = \hat{E}_2$ is held constant at 0 and force in the 1 or $x$ direction is varied while the curves with dashed lines are for the case that $E_{11} = \hat{E}_1$ is held constant at 0, and force in the 2 or $y$ direction is varied. The meaning of the points labeled A, B, C, and D in the figure is explained in the text. The $x$ or $x_1$ axis points in the direction from the head to the tail. Experimental results are from Lanir and Fung (1974b). Reprinted with permission from Tong and Fung (1976).

constitutive relations for soft tissues. First, most of the proposed constitutive relations are motivated directly by data on the underlying microstructure, and especially the orientations of a structurally important collagen that forms as undulated crosslinked fibers. As a corollary to the first observation, most contributions either report or rely on multiaxial mechanical data. Second, most of the proposals are for hyperelastic as opposed to Cauchy elastic materials, and hence there is a focus on strain energy functions from which the constitutive equations follow. Third, most of the proposed constitutive relations assume anisotropy of the issue, generally orthotropy or transverse isotropy. Fourth, many of the proposals assume that the soft tissue is incompressible.

Structurally motivated approaches to the development of constitutive equations for biological tissues have become the method of choice — these were championed early on by Lanir (1983) but now appear in many forms. In order for the microstructural constitutive theories to provide accurate predictions of overall tissue response, they should incorporate microstructural morphological data at the fiber and bulk tissue levels. There are demonstrations of the failure to do this in the biomechanics literature in that one soft tissue constitutive model that matches the data of one experimental investigation does not match the data of a second experimental investigation. The failure of the modeling match in the two situations is likely due to the non-incorporation of microstructural morphological data at the fiber and bulk tissue levels. Such data is likely to be unique for each specimen because of the adaptive capacity of living tissues.

Following the experimental study of Fung (1967), one of the earlier studies cited frequently is that of Veronda and Westmann (1970). Based on their results from uniaxial tests on

cat skin, Veronda and Westmann (1970) developed an elastic strain energy function for large deformations:

$$W_1 = C_1(e^{\beta(I_C-3)}-1)+C_2(II_C-3)+U(J) \tag{15.110}$$

where $C_1$, $C_2$, and $\beta$ are constants, $J = det\mathbf{F} = III_C = III_B$, and $U$ is a function defined so that $U(1) = 0$ when the material is incompressible, $J = 1$. Lanir (1983) used a strain energy approach to form a continuum model for fibrous connective tissue. The energy of deformation was assumed to arise from the tensile stretch in the collagen fibers, with the only contribution from the matrix being a simple hydrostatic pressure. The model described an incompressible composite of undulating collagen fibers embedded in a fluid matrix. The model also assumed that the collagen fibers buckle under a compressive load and the unfolding of the fibers during deformation squeezed the matrix, resulting in an internal hydrostatic pressure. The stress due to deformation was described by

$$\mathbf{T} = -p\mathbf{1}+\lambda\frac{\partial W}{\partial\lambda}\mathbf{a}\otimes\mathbf{a}, \tag{15.111}$$

where $\lambda$ is the collagen fiber stretch, $W$ is the strain energy contribution from the collagen fibers, $\mathbf{a}$ is a unit vector describing the local fiber direction, and $p$ is the hydrostatic pressure arising from the matrix. For a uniaxial tensile test along the fiber direction, the model reduces to one dimension, with the entire stress carried by the collagen fibers and $p = 0$.

A constitutive model for a transversely isotropic, hyperelastic soft tissue and a finite-element implementation that allows for fully incompressible material behavior was presented by Weiss et al. (1996). The tissue was represented as a fiber-reinforced composite with transversely isotropic material symmetry using a hyperelastic strain energy. The strain energy function was assumed to depend only upon deformation tensor $\mathbf{C}$ and unit vector $\mathbf{a}_o$, which was aligned with the local direction of the collagen fibers, and thus

$$W = W(\mathbf{C},\mathbf{a}_0)\,. \tag{15.112}$$

Using the fact that an isotropic function of tensor $\mathbf{C}$ and unit vector $\mathbf{a}_0$ may only depend upon the isotropic invariants of $\mathbf{C}$, $I_\mathbf{C}, II_\mathbf{C}, III_\mathbf{C}$, and the joint isotropic invariants of $\mathbf{C}$ and $\mathbf{a}_o$, $\mathbf{a}_o\cdot\mathbf{C}\cdot\mathbf{a}_o$ and $\mathbf{a}_o\cdot\mathbf{C}^2\cdot\mathbf{a}_o$, it follows that (15.112) above reduced to

$$W = W(I_\mathbf{C}, II_\mathbf{C}, III_\mathbf{C}, \mathbf{a}_o\cdot\mathbf{C}\cdot\mathbf{a}_o, \mathbf{a}_o\cdot\mathbf{C}^2\cdot\mathbf{a}_o)\,. \tag{15.113}$$

After noting that $\mathbf{a}_o\cdot\mathbf{C}\cdot\mathbf{a}_o = \lambda^2_{\text{fiber}}$, and the square of the stretch in the fiber direction,

$$\mathbf{a}_o\cdot\mathbf{C}\cdot\mathbf{a}_o = \lambda^2_{\text{fiber}}, \quad \mathbf{a}_o\cdot\mathbf{C}^2\cdot\mathbf{a}_o = \lambda^4_{\text{fiber}}, \tag{15.114}$$

and also recalling that $J^2 = III_\mathbf{C} = III_B$, Weiss et al. (1996) approximated (15.113) by

$$W = W(I_\mathbf{C}, II_\mathbf{C}, J, \lambda_{\text{fiber}})\,. \tag{15.115}$$

Weiss (1996, 2001, 2002) then assumed that the strain energy may be partitioned as follows:

$$W = W_1(I_\mathbf{C}, II_\mathbf{C}, J)+W_2(\lambda_{\text{fiber}})+W_3(I_\mathbf{C}, II_\mathbf{C}, J, \lambda_{\text{fiber}})\,, \tag{15.116}$$

where function $W_1$ represents the matrix strain energy, $W_2$ represents the fiber family strain energy, and $W_3$ represents the interaction between the matrix and the fibers. In this model fiber family strain energy $W_2$ satisfies conditions

$$\lambda_{\text{fiber}} \frac{\partial W_2}{\partial \lambda_{\text{fiber}}} = 0\,, \text{ for } \lambda_{\text{fiber}} < 1\,,$$

$$\lambda_{\text{fiber}} \frac{\partial W_2}{\partial \lambda_{\text{fiber}}} = C_3[e^{C_4(\lambda_{\text{fiber}}-1)} - 1], \text{ for } 1 < \lambda_{\text{fiber}} < \lambda^*_{\text{fiber}}, \text{ and} \tag{15.117}$$

$$\lambda_{\text{fiber}} \frac{\partial W_2}{\partial \lambda_{\text{fiber}}} = C_5 \lambda_{\text{fiber}} + C_6, \text{ for } \lambda \geq \lambda^*_{\text{fiber}},$$

where the fiber stress is exponentially stiffening up to a level of fiber stretch, $\lambda^*_{\text{fiber}}$, after which the fiber is straight and the stress–strain behavior is linear. To appreciate the significance of the modeling associated with the division of domains at level of fiber stretch $\lambda^*$, consider any one of the curves in Figures 15.17–15.19, 15.21, 15.25, or 15.26. Constant $C_4$ represents that rate of collagen fiber uncrimping, and $C_5$ is the modulus of straightened collagen. Constant $C_6$ is determined from the condition that the right-hand sides of the second and third equations in set (15.117) are equal at $\lambda = \lambda^*_{\text{fiber}}$:

$$C_5 \lambda^*_{\text{fiber}} + C_6 = C_3 \left[ e^{C_4(\lambda^*_{\text{fiber}}-1)} - 1 \right]. \tag{15.118}$$

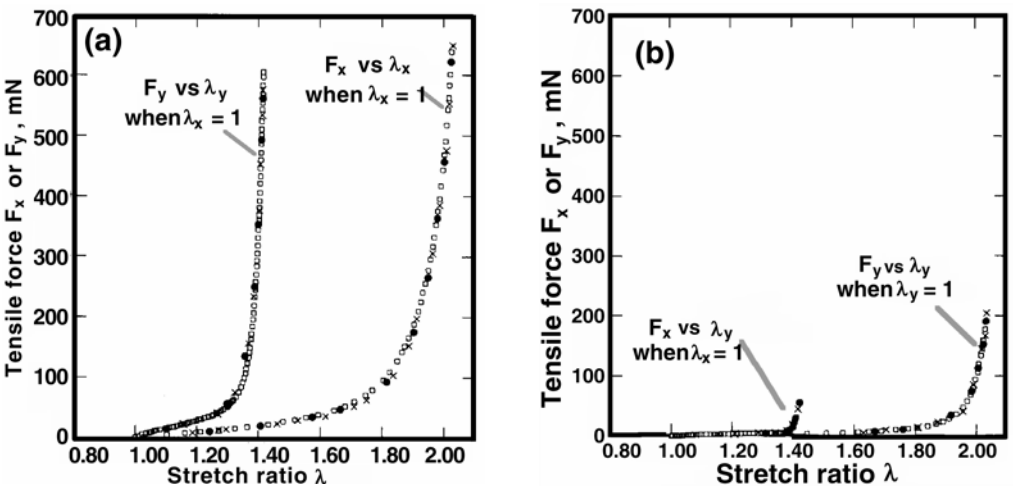



**Figure 15.26**. Plots of the experimental data and the theoretical curves based on the first two equations of (15.103) and (15.105). The tensile forces $F_x$, $F_y$ are given in milli-Newtons (mN). The stress $T_x^{1pk}$ is equal to $F_x$ divided by the cross-sectional area perpendicular to the $x$-axis, $A_x$. The squares indicate experimental data. The circles indicate model predictions from (15.103) and (15.105), with the numerical value of $\hat{\mathbf{A}}^{(p)}$ and $\hat{\mathbf{C}}^{(p)}$, and given by (15.106). Reprinted with permission from Tong and Fung (1976).

This model has been employed in analysis of several different sets of experimental data. In one study human fascia data were subjected to uniaxial tensile tests both parallel and transverse to the collagen fiber direction. This allowed determination of material parameters and evaluation of the model's ability to describe three-dimensional behavior. The model was then used to pre-

dict the results of an experimental strip biaxial test. In a separate study the model was successfully used to describe uniaxial tensile data from human medial collateral ligaments tested both parallel and transverse to the collagen fiber direction. This data, and the modeling thereof, will be considered in the next chapter.

Weiss et al. (1996) also present a strain energy formulation that separates volumetric and deviatoric components using a kinematics described by Flory (1961). A multiplicative decomposition of deformation gradient **F** into volumetric and deviatoric components is clearly defined:

$$\mathbf{F} = \text{vol}\mathbf{F} \cdot \text{dev}\mathbf{F} \,, \tag{15.119}$$

because both vol**F** and dev**F** may be constructed from **F**; thus,

$$\text{vol}\mathbf{F} \equiv J^{1/3}\mathbf{1} \tag{15.120}$$

and

$$\text{dev}\mathbf{F} = J^{-1/3}\mathbf{F} \,. \tag{15.121}$$

When the inverse, $\mathbf{F} = J^{1/3}\text{dev}\mathbf{F}$, of (15.121) is substituted into the definitions of deformation tensors **C** and **B** given by (15.27), one can easily obtain the relations between dev**C** and dev**B** on one hand, and **C** and **B** on the other:

$$\text{dev}\mathbf{C} = \text{dev}\mathbf{F}^T \cdot \text{dev}\mathbf{F} = J^{2/3}\mathbf{C} \,, \quad \text{dev}\mathbf{B} = \text{dev}\mathbf{F} \cdot \text{dev}\mathbf{F}^T = J^{2/3}\mathbf{B} \,. \tag{15.122}$$

The transversely isotropic form of strain energy function (15.116) with uncoupled deviatoric and dilatational behavior has the form

$$W = W_1(I_{\text{dev}\mathbf{C}}, II_{\text{dev}\mathbf{C}}, J) + W_2(\text{dev}\lambda_{\text{fiber}}) + W_3(I_{\text{dev}\mathbf{C}}, II_{\text{dev}\mathbf{C}}, J, \text{dev}\lambda_{\text{fiber}}) \,, \tag{15.123}$$

where $\mathbf{a}_0 \cdot \text{dev}\mathbf{C} \cdot \mathbf{a}_0 \equiv \text{dev}\lambda^2_{\text{fiber}}$.

The important problem of the formulation of strain energy functions for modeling of blood vessel deformation has been widely considered. There have been a number of strain energy proposals that modeled the vessels as two dimensional (by assuming uniform behavior across the thickness), homogeneous, and of uniform structure. A form of Fung's exponential strain energy function was specialized for arteries by Fung et al. (1979). A two-dimensional polynomial expression for the strain-energy function of canine thoracic aorta was proposed in an early paper of Vaishnav et al. (1973). Three polynomial expressions with 3, 7, or 12 material parameters were considered. Vaishnav et al. (1973) reported that the three-parameter model was too inaccurate for a serious investigation and that the twelve-parameter model does not have a significant advantage over the seven-parameter model. The seven-parameter model is written in the form

$$W(\hat{\mathbf{E}}) = c_1\hat{E}_1^2 + c_2\hat{E}_1\hat{E}_2 + c_3\hat{E}_2^2 + c_4\hat{E}_1^3 + c_5\hat{E}_1^2\hat{E}_2 + c_6\hat{E}_1\hat{E}_2^2 + c_7\hat{E}_2^3 \tag{15.124}$$

where $c_1$–$c_7$ are material parameters. These material parameters were fitted to experimental data from rabbit carotid arteries by Fung et al. (1979); $c_1$ = –24.385, $c_2$ = –3.589, $c_3$ = –1.982, $c_4$ = 46.334, $c_5$ = 32.321, $c_6$ = 3.743, and $c_7$ = 3.266 — each of which has units of kPa. A dif-

ferent two-dimensional strain energy function was proposed by Takamizawa and Hayashi (1987).

The successes and limitations of these two-dimensional strain energy formulations (Vaishnav et al., 1973; Fung et al., 1979; Takamizawa and Hayashi, 1987) and for blood vessels are discussed by Holzapfel et al. (2001). The authors point out that the strain-energy function should be convex to ensure physically meaningful and unambiguous mechanical behavior, and that the three two-dimensional strain energy functions mentioned above have a general lack of convexity. They show that strain-energy function (15.118) suggested by Vaishnav et al. (1973) is not convex for any set of material parameters. The strain-energy functions of Fung et al. (1979) and Takamizawa and Hayashi (1987) are not convex for all possible sets of material parameters, and restrictions on these parameters are therefore needed to ensure convexity and, therefore, to avoid material instabilities. The application of convexity arguments in the present context is described in the book of Ogden (1984) in Chapter 6 and in an appendix on convex functions. Holzapfel et al. (2001) propose a microstructural model that recognizes the layered structure of an artery; each layer is fiber reinforced.

## 15.13. FUNG'S QUASI-LINEAR VISCOELASTICITY (QLV)

While the theory of large-deformation elasticity developed in the middle years of the last century was a theoretical and experimental success for understanding the mechanical behavior of rubber and other polymeric materials, the general theories of nonlinear viscoelastic materials developed in the 1950s and 1960s were theoretically sound but generally required an impractical amount of experimental information to be useful in modeling nonlinear viscoelastic behavior. Thus, there is a general theory of nonlinear viscoelastic materials that was not covered in this work. In the present section a particular nonlinear viscoelastic model from special hypotheses introduced by Fung (1972) is described. As Fung (1993) stated, "Instead of developing a constitutive equation by gradual specialization of a general formulation, I shall go at once to a special hypothesis." This special development relies strongly on ideas from infinitesimal linear viscoelasticity as well as nonlinear elasticity. Fung's approach is a very creative use of a well-understood and well-developed theory, linear viscoelasticity, in a new and different way. He superposes a structure similar to that of linear viscoelasticity upon the elastic component of the stress in order to model nonlinear viscoelastic material behavior. When QLV theory is compared, using integral expression (7.46) for the stress in terms of strain history in linear viscoelasticity theory, one sees that strain history in linear viscoelasticity theory is replaced by elastic stress history in the QLV theory.

In this development we begin by recalling the idea of a stress relaxation test. In a stress relaxation test a constant strain is applied to an object and the resulting stress is determined as a function of time. This measured stress is generally a monotonically decreasing function of time. Consider a test situation in which a large step in the stretch (from $\lambda_I = 1$ to $\lambda_I = \lambda$) is applied to a specimen. First Piola-Kirchhoff stress tensor component $T_{1I}^{1PK}$ is used to denote the stress resulting from this step in stretch. Relaxation function $G(\lambda, t)$ is the history of the stress response; it is the stress history of $T_{1I}^{1PK}$ as a result of the step in stretch. Fung assumes that relaxation function $G(\lambda, t)$ is given by

$$G(\lambda,t) = \bar{G}(t)T^{1PK(e)}(\lambda)\,, \quad \bar{G}(0) = 1\,, \tag{15.125}$$

in which $\bar{G}(t)$, a normalized function of time, is called the *reduced relaxation function*, and $\mathbf{T}^{1PK(e)}(\lambda)$, a function of $\lambda$ only, is the elastic response of the material. The concepts of *reduced relaxation function* $\bar{G}(t)$ and elastic stress response $\mathbf{T}^{1PK(e)}(\lambda)$ will be used to develop a

formula for total stress $\mathbf{T}^{1PK}(t)$ resulting from arbitrary stretch history $\lambda(\tau)$, $-\infty < \tau \leq t$. The arguments employed to develop the expression for total stress $\mathbf{T}^{1PK}(t)$ parallel completely the arguments employed to develop the integral representation of linear viscoelasticity in terms of the creep function. Assuming then that the effects of an arbitrary stretch history, $\lambda(\tau)$, $-\infty < \tau \leq t$, are superimposable using reduced relaxation function $\bar{G}(t)$, the analogy with linear viscoelasticity leads to the following expression for total stress (compare eq. (7.45)):

$$\mathbf{T}^{1PK}(t) = \int_{-\infty}^{t} \bar{G}(t-s)\frac{\partial \mathbf{T}^{1PK(e)}}{\partial \lambda}\frac{\partial \lambda}{\partial s}ds = \int_{-\infty}^{t} \bar{G}(t-s)\frac{\partial \mathbf{T}^{1PK(e)}}{\partial s}ds . \tag{15.126}$$

Thus, the total stress at time $t$ is the sum of the contributions from the stretch history (or, equivalently, the elastic stress history) reduced by an amount determined by reduced stress relaxation function $\bar{G}(t-s)$ at a time delay of $t - s$. Function $\mathbf{T}^{1PK(e)}(\lambda)$ plays the role assumed by the strain in infinitesimal linear viscoelasticity; therefore, many of the concepts, methods, and results from linear viscoelasticity are directly transferable. For example, the inverse of (15.126) may be written as

$$\mathbf{T}^{1PK(e)}(\lambda) = \int_{-\infty}^{t} \bar{J}(t-s)\frac{\partial \mathbf{T}^{1PK}}{\partial s}ds , \tag{15.127}$$

where $\bar{J}(t-s)$ is the reduced creep function. If we let $\boldsymbol{f}(\lambda) = \mathbf{T}^{1PK(e)}(\lambda)$, so $\lambda = \mathbf{f}^{-1}(\mathbf{T}^{1PK(e)})$, then for a step change of tensile stress $\mathbf{T}^{1PK}$ at $t = 0$, the time history of the extension is

$$\lambda(t) = f^{-1}(\bar{J}(t)) . \tag{15.128}$$

The lower limits of integration in (15.126) and (15.127) are written as $-\infty$, to be taken from before the very beginning of the motion. However, if the motion starts at $t = 0$ and the stress and strain are zero for $t < 0$, then (15.126) can be written in the form

$$\mathbf{T}^{1PK}(t) = \mathbf{T}^{1PK(e)}(0^+)\bar{G}(t) + \int_{0}^{t} \bar{G}(t-s)\frac{\partial \mathbf{T}^{1PK(e)}}{\partial s}ds . \tag{15.129}$$

Integration of this equation by parts leads to

$$\mathbf{T}^{1PK}(t) = \mathbf{T}^{1PK(e)}(t)\bar{G}(0) + \int_{0}^{t} \mathbf{T}^{1PK(e)}(t-s)\frac{\partial \bar{G}(s)}{\partial s}ds =$$

$$\frac{\partial}{\partial t}\int_{0}^{t} \mathbf{T}^{1PK(e)}(t-s)\bar{G}(s)ds , \tag{15.130}$$

where it has been assumed that $\partial \mathbf{T}^{1PK(e)}/\partial s$ and $\partial \bar{G}/\partial s$ are continuous in $0 \leq t < \infty$. Since, by (15.126), $\bar{G}(0) = 1$, (15.130) becomes

$$\mathbf{T}^{1PK}(t) = \mathbf{T}^{1PK(e)}[\lambda(t)] + \int_{0}^{t} \mathbf{T}^{1PK(e)}[\lambda(t-s)]\frac{\partial \bar{G}(s)}{\partial s}ds . \tag{15.131}$$

This result shows that the total tensile stress at any time $t$, $\mathbf{T}^{1PK}(t)$, is equal to the instantaneous elastic stress response, $\mathbf{T}^{1PK(e)}[\lambda(t)]$, decreased by an amount depending on the past history,

because $\partial \bar{G}/\partial s$ is negative due to the fading memory hypothesis. Recall (7.48) and the discussion of the fading memory hypothesis from Chapter 7.

In linear viscoelasticity the relaxation function is often expressed as a sum of terms, each of which contains a relaxation time:

$$\bar{G}(t) = \bar{G}_\infty + \bar{G}_o \sum_{i=1}^{n} A_i e^{-t/\tau_i} . \tag{15.132}$$

Recall, for example, that for linear viscoelasticity characterized by the uniaxial constitutive relation

$$\hat{\mathbf{T}}(\mathbf{x}, t) = \int_{s=-\infty}^{s=t} \hat{\mathbf{G}}(t-s) \cdot \frac{D\hat{\mathbf{E}}}{Ds}(\mathbf{x}, s) ds , \qquad \text{(5.33V) repeated}$$

the stress relaxation function for a standard linear solid is given by

$$G(t) = G_\infty + G_\infty \left( \frac{\tau_r}{\tau_0} - 1 \right) e^{-t/\tau_0} , \quad G_\infty = G(\infty) , \quad G(0) = G_\infty \frac{\tau_r}{\tau_0} . \tag{15.133}$$

Fung illustrates the difficulty in determining $n$ and quantities $A_i$ and $\tau_i$ in a relaxation test and proposes an alternative to (15.132). He observes that the amount of energy dissipated in cyclical deformation of many soft tissues is, to a good approximation, independent of the rate at which the material is cycled, and he observes that this suggests there is a continuous rather than discrete distribution of relaxation times. For these materials (15.132) is replaced by

$$\bar{G}(t) = \bar{G}_\infty + \bar{G}_0 \int_0^\infty A(\tau) e^{-t/\tau} d\tau , \tag{15.134}$$

or, given in terms of logarithmic spectrum $H(\tau)$, by

$$\bar{G}(t) = \bar{G}_\infty + \bar{G}_0 \int_0^\infty H(\tau) e^{-t/\tau} d(\ln \tau) . \tag{15.135}$$

This last representation is useful because it has been observed that in some biological soft tissues the relaxation and creep are observed to take place roughly as linear functions of the logarithm of time over a wide range of times. It can be shown that box spectrum

$$H(\tau) = E_o, \text{ for } \tau_1 < \tau < \tau_2, \quad \text{and} \quad H(\tau) = 0 \quad \text{for} \quad \tau < \tau_1, \ \tau > \tau_2 \tag{15.136}$$

reproduces this relaxation and creep behavior and, in addition, renders the dissipation in cyclical elongations independent of the rate of cycling over a wide range of frequencies.

The QLV model works very well with a single load or elongation level and has been shown to describe tendon and ligament very well in the case of single load data (Haut and Little, 1972; Woo, 1982). The advantages and limitations of the use of single load or elongation level data in this general context were discussed by Pipkin and Rogers (1968). To comprehend this point recall how in §7.5 creep function $\hat{J}_{11}(s)$ was defined as the uniaxial strain versus time response of the uniaxially stressed specimen to the step increase in stress, $\hat{T}_1 = T_0 h(t)$, and then the creep function determined in this manner was used as the basis for determining the response to an arbitrary loading. The time history of the strain associated with each step in

stress, independent of stress magnitude, was predicted by the same $\hat{J}_{11}(s)$. In the following chapter the case of a ligament that does not follow this rule will be described.

**Problem**

15.12.1. Derive eq. (15.130) from (15.129) using integration by parts.

## 15.14. RELEVANT LITERATURE

The development of knowledge concerning the physiology and mechanical response of soft biological tissues requires the modeling of large deformation viscoelastic behavior. In the previous century the theory of finite deformation elasticity was developed by people interested in understanding the behavior of long-chain molecules like rubber. These developments in nonlinear continuum mechanics are described in many books, for example, Truesdell (1960), Truesdell and Toupin (1960), Green and Adkins (1960), Januzemis (1967), Treloar (1967), Truesdell and Noll (1965), and Ogden (1984). Aspects of the nonlinear continuum mechanics of biological tissues are contained in books of a more recent vintage: Holzapfel (2000), Humphrey (2002), Taber (2004), and three volumes by Fung, one of which is Fung (1993). The first investigators that experimentally evaluated the mechanical behavior of tissues walked in the footprints of the people that experimentally determined the mechanical behavior of rubber. For example, the testing of a skin specimen reported by Lanir and Fung (1974a,b) was parallel to the procedure pioneered by Rivlin and Saunders (1951) for rubber; a figure similar to Figure 15.23 appears in the Rivlin and Saunders paper. Not only was the experimental procedure taken from earlier papers on rubber, but so was the theory.

However biological tissues are not really elastic, although they have some elastic properties. Fung (1967) set the rationale for partitioning the purely elastic response from the viscoelastic response as follows: "It is evident from the curves shown in ... Figures 15.17–15.22 ... that the stress–strain relationship for the mesentery and the arteries is nonlinear, that the stress does not depend on the strain alone, but also on the strain history. Let the stress–strain relationship be separated into two parts: an elastic part and a history dependent part. The elastic part defines a unique stress-strain relationship, i.e., the 'elasticity' of the material. The history-dependent part is time dependent; it is related to the hysteresis, stress relaxation, creep, and other non conservative phenomena." Good references on viscoelasticity theory are Lockett (1972), Pipkin (1972), and Wineman and Rajagopal (2000). In the previous section of this chapter a particular nonlinear viscoelastic model from special hypotheses introduced by Fung was described.

The opening quote of this chapter, from Fung (1967), stated that a correct theoretical formulation of the nonlinear stress–strain history relationship in large deformations of living tissues should bring out the unity among experiments; experiments such as static (very slow) elasticity, dynamic elasticity (finite strain rate), stress relaxation under fixed strain, creep deformation under fixed stress, strain-cycle hysteresis, and cyclic stress fatigue. The more recent literature by the next generation of students has added to this viewpoint. The theoretical formulation of constitutive relations should be three dimensional (see, e.g., Holzapfel 2001; Weiss and Gardiner 2001), microstructural (see, e.g., Lanir l983; Holzapfel 2001) and the strain energy function should be convex (see, e.g., Holzapfel 2001; Weiss and Gardiner 2001).

## References


Cowin SC, Humphrey JH, eds. 2001. *Cardiovascular soft tissue mechanics*. New York: Kluwer. [This volume is a reprint of a special issue of the *Journal of Elasticity* **61**(1–3), 2001, on the topic of the "Finite Elastic Modeling of Soft Tissue Deformation."]

Danielson DA. 1973. Human skin as an elastic membrane. *J Biomech* **6**:539–546.

Danielson DA, Natarajan S. 1975. Tension field theory and the stress in stretched skin. *J Biomech* **8**:135–142.

Debes J, Fung YC. 1992. The effect of temperature on the biaxial mechanics of excised lung parenchyma of the dog. *J Appl Physiol* **73**:1171–1180.

Flory PJ. 1961. Thermodynamic relations for high elastic materials. *Trans Faraday Soc* **57**:829–838.

Fung YC. 1967. Elasticity of soft tissues in simple elongation. *Am J Physiol* **213**:1532–1544.

Fung YC. 1968. Biomechanics: its scope, history, and some problems of continuum mechanics in physiology. *Appl Mech Rev* **21**:1–20.

Fung YC. 1972. Stress–strain history of soft tissues in simple elongation. In *Biomechanics, its foundations and objectives*, ed. YC Fung, N Perrone, M, pp. 181–208. Englewood Cliffs, NJ: Prentice-Hall.

Fung YC. 1993. *Biomechanics — mechanical properties of living tissues*, 2nd ed. New York: Springer.

Fung YC, Fronek K, Patitucci P. 1979. Pseudoelasticity of arteries and the choice of its mathematical expression. *Am J Physiol* **237**:H620–H631.

Green AE, Adkins JE. 1960. *Large elastic deformations and non-linear continuum mechanics*. Oxford: Claredon.

Haut RC, Little RW. 1972. A constitutive equation for collagen fibers. *J Biomech* **5**:423–430.

Holzapfel GA. 2000. *Nonlinear solid mechanics*. New York: Wiley.

Holzapfel GA, Gasser TC, Ogden RW. 2001. A new constitutive framework for arterial wall mechanics and a comparative study of material models. *J Elast* **61**:1–48.

Humphrey JD. 2002. *Cardiovascular solid mechanics*. New York: Springer.

Januzemis, W. 1967. *Continuum mechanics*. New York: Macmillian.

Lanir Y. 1979a. A structural theory for the homogeneous biaxial stress–strain relationship in flat collagenous tissues. *J Biomech* **12**:423–436.

Lanir Y. l979b. The rheological behavior of the skin: experimental results and a structural model. *Biorheology* **16**:191–202.

Lanir Y. l983. Constitutive equations for fibrous connective tissues. *J Biomech* **16**:1–12.

Lanir Y, Fung YC. 1974a. Two-dimensional mechanical properties of rabbit skin, I: experimental system. *J Biomech* **7**:29–34.

Lanir Y, Fung YC. 1974b. Two-dimensional mechanical properties of rabbit skin, II: experimental results. *J Biomech* **7**:171–182.

Lockett FJ. 1972. *Nonlinear viscoelastic solids*. New York: Academic Press.

Mooney M. 1940. A theory of large elastic deformation. *J Appl Phys* **11**:582–592.

Ogden RW. 1984. *Non-linear elastic deformations*. Chichester: Ellis Horwood.

Pipkin AC. 1972. *Lectures on viscoelasticity theory*. New York: Springer.

Pipkin AC, Roger TG. 1968. A nonlinear integral representation for viscoelastic behavior. *J Mech Phys Solids* **16**:59–74.

Rivlin RS, Saunders DW. 1951. Large elastic deformations of isotropic materials, VII: experiments on the deformation of rubber. *Philos Trans Soc London A* **243**:251–288.

Rivlin RS, Saunders DW. 1976. The strain energy function for elastomers. *Trans Soc Rheol* **20**:545–557.

Taber LA. 2004. *Nonlinear theory of elasticity-applications in biomechanics*. London: World Scientific.

Takamizawa K, Hayashi K. 1987. Strain energy density function and uniform strain hypothesis for arterial mechanics. *J Biomech* **20**:7–17.

Thomson W (Lord Kelvin), Tait PG. 1867. *Treatise on natural philosophy*. Cambridge: Cambridge UP.

Tong P, Fung YC. 1976. The stress–strain relationship for the skin. *J Biomech* **9**:649–657.

Treloar LRG. 1967. *The physics of rubber elasticity*, 2nd ed. New York: Oxford UP.

Truesdell CA. 1960. *Principles of continuum mechanics*. Colloquium Lectures in Pure and Applied Science. Dallas: Socony Mobil Oil.

Truesdell CA, Noll W. 1965. The non-linear field theories of mechanics. In *Handbuch der physik*, ed. S Flugge, pp. 1–602. Berlin: Springer-Verlag.

Truesdell CA, Toupin RA. 1960. The classical field theories. In *Handbuch der physik*, ed. S Flugge, pp. 226–880. Berlin: Springer-Verlag.

Vaishnav RN, Young JT, Patel DJ. 1973. Distribution of stress and strain energy density through the wall thickness in a canine aortic segment. *Circ Res* **32**:577–583.

Vawter D, Fung YC, West JB. 1978. Elasticity of excised dog lung parenchyma. *J Appl Physiol* **45**:261–269.

Veronda DR, Westmann RA. 1970. Mechanical characterizations of skin — finite deformations. *J Biomech* **3**:111–124.

Weiss JA, Gardiner JC. 2001. Computational modeling of ligament mechanics. *Crit Rev Biomed Eng* **29**:1–70.

Weiss JA, Maker BN, Govindjee S. 1996. Finite element implementation of incompressible, transversely isotropic hyperelasticity. *Computer Methods Appl Mech Eng* **135**:107–128.

Weiss JA, Gardiner JC, Bonifasi-Lista C. 2002. Ligament material behavior is nonlinear, viscoelastic and rate-independent under shear loading. *J Biomech* **35**:943–950.

Wineman AS, Rajagopal KR. 2000. *Mechanical response of polymers*. Cambridge: Cambridge UP.

Woo SL. 1982. Mechanical properties of tendons and ligaments, I: quasi-static and nonlinear viscoelastic properties. *Biorheology* **19**:385–396.

Yager D, Feldman H, Fung YC. 1992. Microscopic vs. macroscopic deformation of the pulmonary alveolar duct. *J Appl Physiol* **72**:1348–1354.

Zeng YJ, Yager D, Fung YC. 1987. Measurement of the mechanical properties of the human lung tissue. *J Biomech Eng* **109**:169–174.

# 16

# TENDON AND LIGAMENT

"The three principal structures that closely surround, connect, and stabilize the joints of the skeletal system are the tendons, the ligaments, and the joint capsules. Although these structures are passive (i.e., they do not actively produce motion as do the muscles), each plays an essential role in joint motion." (From Carlstadt and Nordin, 1989)

## 16.1. INTRODUCTION

Tendons and ligaments, along with the joint capsules, connect the bones and muscles of joints and help guide the motion and maintain joint stability by a combination of bony geometry and tendon, ligament, and other soft tissue interactions. The function of the tendons is to attach muscle to bone and to transmit tensile loads from muscle to bone, thereby producing joint motion. The tendon also enables the muscle belly to be at a distance from the joint on which it acts without requiring an extended length of muscle between origin and insertion. The function of ligaments is to guide and restrict the motion of the joint. The tendons that originate at the end of the muscles in the arm and terminate in the digits are called the flexor digitorum superficialis tendons, and all four are illustrated in Figure 16.1. The ligaments that connect the femur, tibia, and fibula are illustrated in Figure 16.2. These include the anterior cruciate ligament (ACL), the posterior cruciate ligament (PCL), the medial collateral ligament (MCL), and the lateral collateral ligament (LCL).

The structure of the tendon was described in two different contexts earlier in this text, in Chapters 1 and 10. In Chapter 1 it was used as an example of a tissue with hierarchical structure (Figure 1.12), and in Chapter 10 on collagen, where molecular assembly collagen was considered, the tendon was used as an example of supramolecular collagen assembly (§10.10). Like Figure 1.12, Figure 10.27 is a cartoon of tendon hierarchical structure. Figures 10.30 and 10.39–10.41 show the tendon and its principal cells — fibroblasts (specialized elongated fibroblasts). These earlier descriptions and figures are relevant to the material in the present chapter.

A "direct tendon" is tendon that has a straight and direct course between its muscle connection and its bone connection. A "wraparound tendon" is any tendon that bends around a bony pulley or threads through a fibrous one between its muscle connection and its bone connection. Some ligaments are also wraparound or compress against bone (Benjamin and Ralphs, 1998). Wraparound tendons have surrounding structures that assist in their function. The canals or bony grooves through which these tendons glide are low-friction passages made low

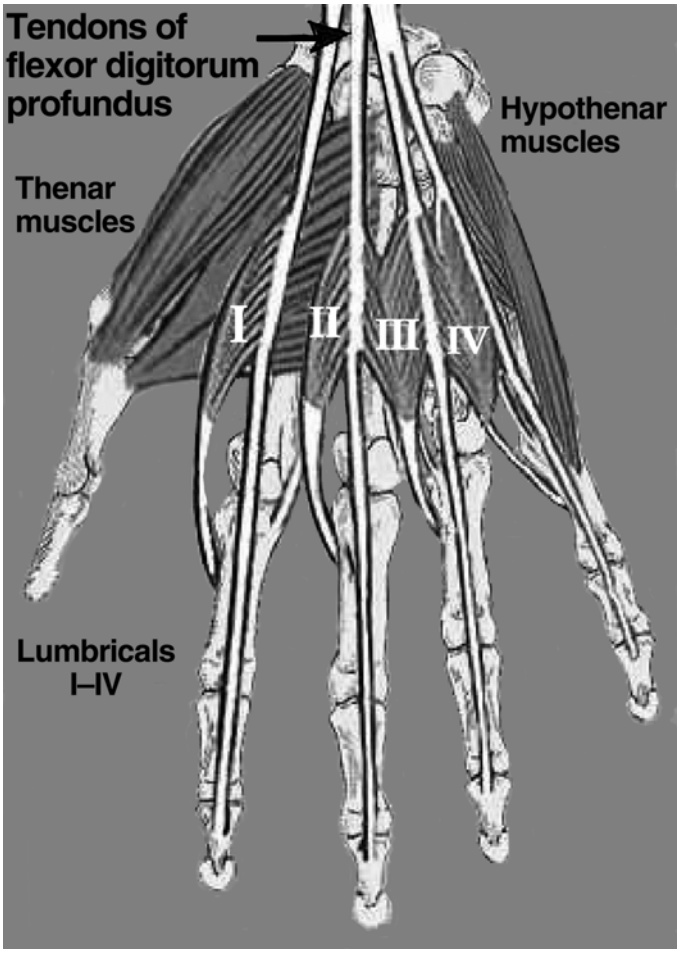



**Figure 16.1**. The tendons of the hand: the flexor digitorum superficialis tendons: I (index), II (middle), III (ring), and IV (small). Reprinted with permission from http://mywebpages.comcast.net/wnor/lesson5mus&tendonsofhand.htm.

friction by a fibrocartilaginous bottom and covered by fibrous sheaths called retinacula. Retinacula occur in the hands and feet.

The study of the structure and chemical composition of ligaments and tendons is made easier by the strong similarities between these tissues in humans and the corresponding ones in many animal species such as rats, rabbits, dogs, and monkeys. In this chapter there are a number of reports of implicit extrapolations of features in human ligaments and tendons made on the basis of results of studies on these features in various animal species.

The first section below describes the constituents of tendons and ligaments. The sections that follow this first section are on the cells and cell systems of tendons and ligaments, their arrangement of collagen fibers, and the lubrication of tendons. After those sections, there are sections on the mechanical properties of tendons (their elastic constants and strength values) and on the appropriate constitutive equations for these tissue structures. Interstitial fluid flow

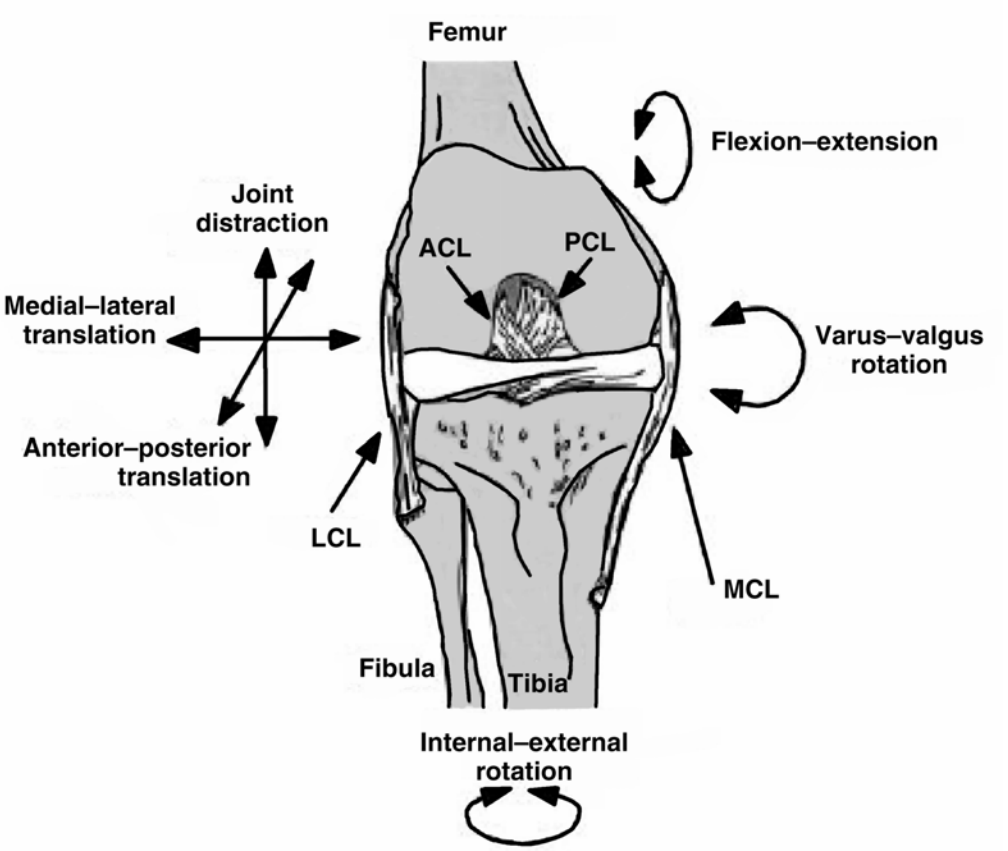



**Figure 16.2**. Anterior view of the knee joint. The femur, tibia, and fibula are connected by the anterior cruciate ligament (ACL), posterior cruciate ligament (PCL), medial collateral ligament (MCL), and lateral collateral ligament (LCL). The clinical rotations and translations are indicated. Reprinted with permission from Weiss and Gardiner (2001).

of tendons and ligaments is then described, followed by a section on the structural adaptations that occur (or do not occur) in tendons and ligaments.

## 16.2. THE CONSTITUENTS OF TENDONS AND LIGAMENTS

Tendons and ligaments are constituted mainly of fibers of fibrous type I collagen and are dense, often parallel-fibered, tissues. The collagen structure of a tendon is described in §10.10, where the tendon is employed as an example of supramolecular collagen assembly. Generally, tendons and ligaments consist of about 20% cellular material and about 80% extracellular material; the extracellular material is further subdivided into about 30% solids and 70% water. These extracellular solids are collagen, the ground substance, and a small amount of elastin (1 to 2% of dry weight). The collagen content is generally over 75% and is somewhat greater in tendons than in ligaments (Table 16.1); in tendons of the extremities the collagen may be up to 99% of dry weight.

**Table 16.1**. Table of Quantitative Measures of the Chemical Composition of Two Tendons (Achilles and Patellar) and Three Ligaments (Medial Collateral Ligament and the Anterior and Posterior Cruciate Ligaments)

| | Achilles tendon | Patellar tendon | Medial collateral ligament | Cruciate (anterior & posterior) ligaments |
|---|---|---|---|---|
| Total collagen (mg/g dry tissue) | 868.2 ± 10.2 | 867.2 ± 8.9 | 797.1 ± 11.1 | 802.6 ± 9.8 |
| % Type I collagen | > 95 | > 95 | 91 ± 2 | 88 ± 2 |
| % Type III collagen | < 5 | < 5 | 9 ± 2 | 12 ± 2 |
| Total DNA (mg DNA/mg dry tissue) | 1.74 ± 0.04 | 1.40 ± 0.05 | 2.56 ± 0.06 | 2.73 ± 0.05 |
| Total GAGs (mg hexosamine/g dry tissue) | 2.75 ± 0.20 | 3.92 ± 016 | 4.56 ± 0.26 | 9.89 ± 0.56 |
| Crosslink I | 0.15 ± 0.04 | 0.16 ± 0.06 | 1.86 ± 0.17 | 2.77 ± 0.73 |
| Crosslink II | 1.32 ± 0.06 | 1.47 ± 0.213 | 3.17 ± 0.37 | 4.64 ± 0.73 |

Crosslinks I and II are the measures DHLNL/HLNL and DHLNL+HLNL/HHMD, respectively, where DHLNL means dihydroxylysinonorleucine, HLNL means hydroxylysinonorleucine, and HHMD means histidinohydroxymerodesmosine. Adapted with permission from Amiel et al. (1984).

While elastin is scarcely present in tendons and extremity ligaments, in elastic ligaments such as the ligamentum flavum the proportion of elastic fibers is substantial — a 2-to-1 ratio of elastin to collagen fibers occurs in the ligamenta flava. The ligamentum flavum connects the laminae of the vertebrae and serves to protect the neural elements and the spinal cord and stabilize the spine so that excessive motion between the vertebral bodies does not occur. Together with the laminae, it forms the posterior wall of the spinal canal. Due to its high elastin content, the ligament stores and returns energy to the spine during body activities such as walking and running. The term "flavum" is used to describe the yellow appearance of this ligament in its natural state. In addition to its specialized role of protecting the spinal nerve roots from mechanical impingement, these ligaments prestress (preload) the motion segment (the functional unit of the spine), and provide some intrinsic stability to the spine (Nachemson and Evans, 1968).

The ground substance in ligaments and tendons consists of proteoglycans (PGs) (up to about 20% of the solids) along with structural glycoproteins, plasma proteins, and a variety of small molecules. The PG units are macromolecules composed of various sulfated polysaccharide chains (glycosaminoglycans) bonded to a core protein. Some ligament PGs occur as extremely high-molecular-weight PG aggregates like those found in the ground substance of articular cartilage. Other PGs, such as those with decorin or biglycan as their core protein, consist of only one or two relatively short GAG chains. Although the exact mechanical roles of PGs in ligaments and tendons are unknown, as they are in bone, it is likely that the large PG aggregates function similarly to those in articular cartilage, binding extracellular water to create a gel-like material extrafibrillar matrix. The smaller proteoglycans (decorin and bigylcan)

serve to modulate collagen fibril growth and may contribute to fibril–fibril mechanical integrity.

The differences between tendons and ligaments are not often discussed or considered because of their strong similarities. An exception to this is an interesting study of the differences by Amiel et al. (1984). In this study two rabbit tendons (Achilles tendon (AT) and patellar tendon (PT)) and three ligaments (medial collateral ligament (MCL), anterior cruciate ligament (ACL), and posterior cruciate ligament (PCL)) were compared morphologically and biochemically. There were clear visual differences between the excised tendons and ligaments, but it was difficult to discern one tendon from another or one ligament from another. Histological and chemical differences were demonstrated between tendons and ligaments, and smaller differences were found between individual ligaments (the collateral and the cruciate) and between two tendons (the Achilles and the patellar). These differences are tabulated in Table 16.1. Amiel et al. (1984) concluded that ligaments are more metabolically active than tendons because they have more plump cellular nuclei, higher DNA content, larger amounts of reducible crosslinks, and contain more type III collagen. They also contain slightly less total collagen than tendons and more glycosaminoglycans (GAGs).

The physical properties of collagen and of the tissues it composes are closely associated with the number and quality of the bonds within and between the collagen molecules (Chapter 10). During maturation (up to 20 years of age), the number and quality of crosslinks increases, resulting in increased tensile strength of the tendon and ligament. An increase in collagen fibril diameter is also observed. After maturation, as aging progresses, collagen reaches a plateau with respect to its mechanical properties, after which the tensile strength and stiffness of the tissue begin to decrease. The collagen content of tendons and ligaments also decreases during aging, contributing to a gradual decline in their mechanical properties (strength, stiffness, and ability to withstand deformation).

## 16.3. THE CELLS AND CELL SYSTEMS OF THE TENDON

Like other connective tissues, the tendon consists of relatively few cells and an abundant extracellular matrix. Fibroblasts and fibrocytes comprise about 90–95% of the cells and the other 5–10% include chondrocytes at the places where the tendon is subjected to compressive applied pressure, synovial cells of the tendon sheath on the tendon surface, and vascular cells such as capillary endothelial cells and smooth muscle cells of the arterioles in the endo- and epitenon (Kannus, 2000). The endotenon is a thin sheath of fibrillar connective tissue that covers each collagen fiber and also binds subfascicles to create a secondary fiber bundle or fascicle. Fascicles are bound together by the endotenon to form tertiary fiber bundles (diameters from 1 to 3 mm). The epitenon is a dense-layer fibrillar connective tissue that surrounds tertiary fiber bundles to form individual tendons. In the tendon, the elongated fibroblasts and fibrocytes are sometimes referred to as tenoblasts and tenocytes, respectively, but the exact difference between these respective cell types has not been documented.

***Fibroblasts:*** Fibroblasts manufacture the collagen and other proteins that have a function or form part of a tendon. They orient their elongated direction with fiber direction in the tendon and squeeze between fibers. Figure 10.30 shows a longitudinal cross-section of a tendon with wavy fibroblasts running along the tendon axis. The size of the tendon fibroblast varies, the length from 20 to 70 μm and their width from 8 to 20 μm. Numerous long and slender cytoplasmic processes extend into the extracellular matrix (Figure 10.40). Fibroblasts form desmosomal junctions, tight junctions, and gap junctions (§1.8 and Figure 1.30). Fibrocytes appear to age with the tissue. The newborn tendon has a very high cell-to-extracellular matrix

ratio, but in the young tendon there is a gradual decrease in the cell-to-extracellular matrix ratio and fibroblasts take on a more spindle-like shape. In the adult tendon the cell-to-extracellular matrix ratio further decreases and the cells become fibrocytes (see below) (Kannus, 2000).

***Fibrocytes:*** Fibroblasts transform into fibrocytes and become very elongated. They occasionally revert to fibroblasts (Kannus, 2000). In transverse sections fibrocytes appear to have a spider-like shape; their long cell processes maintain close contact with the cells and extracellular matrix components. It is thought that the number of fibrocytes in a tendon increases as the tendon ages, relative to the number of fibroblasts in the tendon, and that the longer cell processes are needed to maintain the connected cellular network (see below).

***Connected cellular network:*** Gap junctions on their bodies and on their cell processes extensively interconnect the fibroblasts and fibrocytes, forming a connected cellular network (CCN) similar to that in bone (Chapter 11) and likely similar to connected cell networks (CCNs) in many tissues. Gap junctions connect the fibroblasts, fibrocytes, and, perhaps, some of the other cell types. The gap junction connexins are 43 and 32, suggesting that there are two distinct communication networks (McNeilly et al., 1996). This connected cellular network is a syncytium that is thought to sense mechanical load and coordinate a response to it. The intimate relationship between cell processes and collagen fibril bundles illustrated in Figures 10.30 and 10.39–10.41 suggest not only that the cells are involved in the formation of tendon structure, but are also involved in load sensing and coordination of structural changes in response to the load sensed. As McNeilly et al. (1996) note, the intricate 3D network of cell processes associated with collagen bundles is an ideal arrangement for sensing tensile loads transmitted by the tendon — the cell processes must undergo deformation when tendons are stretched, or where they are bent around pulleys and compressed — for the digital flexor tendons, where they pass through the fibrous pulleys associated with the phalanges. Where tendons experience compression they express molecules more typical of cartilage, to form fibrocartilage (Benjamin and Ralphs, 1995). This fibrocartilaginous differentiation is most intense at the site of compression and becomes progressively less far away from the load as the fibrocartilage blends into pure tendon. There is therefore a graded and coordinated response of tendon cells to the mechanical load, just as happens with calcium transients in the in-vitro cell deformation experiments (Banes et al., 1995). If this in-vitro evidence relates to what happens in vivo, it might then be expected that frequent calcium transients pass between cells when the tendon is under load. Given the different characteristics of connexin 43 and connexin 32 junctions and their different distributions between tendons, it could be that the two different types of junction are responsible for sensing two different forms of loading. McNeilly et al. (1996) suggest that one may be important in detecting tensile loads and the other compressive loads. There is in-vitro evidence that connexin 43 expression is unregulated under conditions of intermittent tensile loading (Banes et al., 1995). The many processes and junctions associated with the cells of the epitenon might suggest that this outer layer (the first to encounter compressive or shear forces) coordinates the response of the internal tendon fibroblasts to load. A range of other molecules can pass through gap junctions, leading to the possibility of metabolic cooperation between cells.

## 16.4. THE ARRANGEMENT OF COLLAGEN FIBERS IN TENDONS AND LIGAMENTS

The broad, general description of the structure of tendons and ligaments is that the collagenous fibers composing the tendons have a parallel arrangement and that the collagenous

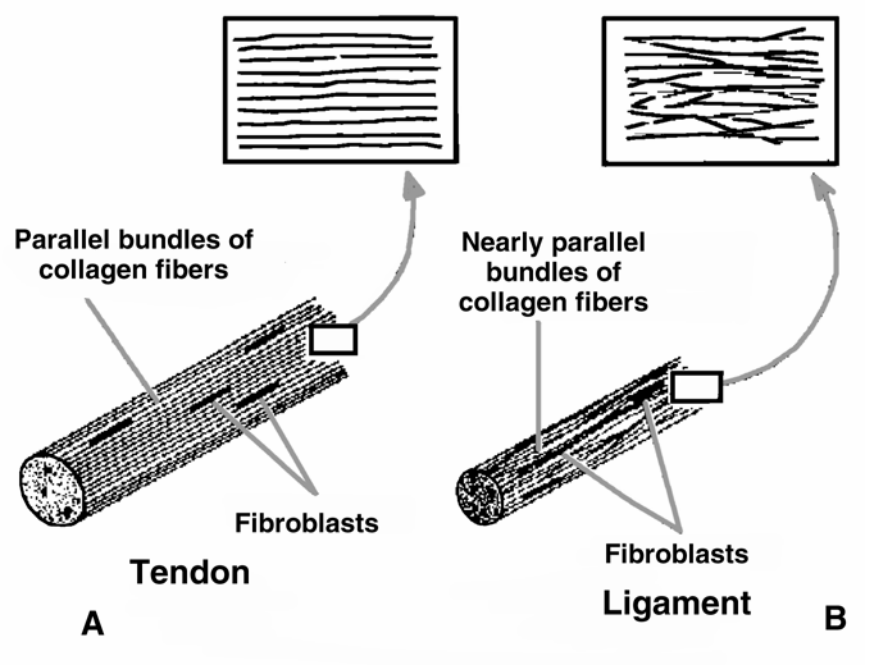



**Figure 16.3**. Comparison of tendon and ligament structure. Reprinted with permission from Nordin (1989).

fibers composing ligaments may not be completely parallel but are close to parallel with one another (Figure 16.3). This description of tendon structure is reasonable for tendons and ligaments that are subjected to frequent high uniaxial tensile loads, but loadings of many tendons and most ligaments are more diverse because they touch bone (or another soft tissue) at more than two distinct places. Leonardo da Vinci (1452–1519) illustrated the divergent spiral arrangement of fibers of the flexor digitorum superficialis tendon to encircle the tendon of the flexor digitorum profundus (Figure 16.1) (Kannus, 2000). It is now well documented, using TEM and SEM, that collagen fibrils may be oriented not only longitudinally, but also transversely, quasi-transversely, and quasi-longitudinally. They may cross each other in many ways and they may form spirals (Figure 16.4). However, it has not been shown that the collagen fibrils are woven like a fabric, or a bird's nest, by functioning as warp and weft fibers. A tendon is composed of many almost aligned fibrils that have lengths that far exceed their small diameters, similar to the structure of string cheese. The fibrils of the tendon are not perfectly aligned; some fibers wander about as they run their course in the tendon and interweave with the other fibers. They do *not*, however, form a woven pattern as people do with textiles or basketwork nor braid as one might do with long hair, although the definition of "woven" and "braided" are flexible enough at their extreme to include the structure of tendons.

A broad general description of the fiber structure of unstressed tendons is that they exhibit gentle planar sinusoidal waviness. In the past there has been some controversy about the undulations in the fiber structure, some suggesting that is was of a zigzag nature (Diamant et al., 1972) rather than sinusoidal and others, suggesting that it had a helical character. A review of this controversy is given by (Viidik, 1990), and it is believed that the evidence presently comes down on the side of the planar sinusoidal waviness in the collagen structure. The waviness in unstressed tendons is called the “crimp” of collagen, and it is highlighted when polarized light

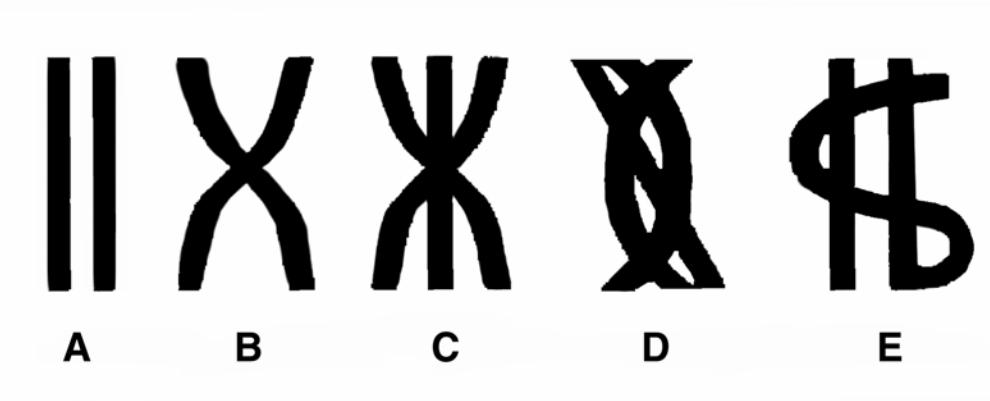



**Figure 16.4**. The types of collagen fiber crossing in tendons: (A) parallel fibers, (B) fibers in an X crossing, (C) fibers in an X crossing with straight fiber, (D) a plait with three fibers, and (E) a fiber wandering amongst parallel fibers. Reprinted with permission from Kannus (2000).

is directed at this tissue (Figure 16.5). An initial effect of a load as applied to a tendon is to straighten out this "crimp." In this "straightening out" process the tendon exhibits a smaller Young's modulus than it exhibits after the crimp is removed. This mechanism is described in greater detail in the following section.

## 16.5. THE LUBRICATION SYSTEM IN TENDONS

Tendons and ligaments are both surrounded by a loose areolar (tissue with a gel-like matrix) connective tissue. In ligaments this tissue is sometimes referred to as the *epiligament* or *fascia*, while in tendons it is referred to as the *paratenon*. More structured than the connective tissue surrounding the ligaments, the paratenon forms a sheath that protects the tendon and enhances gliding. In some tendons, such as the flexor tendons of the digits, the sheath runs the length of the tendons, and in others the sheath is found only at the point where the tendon bends in concert with a joint.

Wraparound tendons are subjected to particularly high friction forces at the wraparounds, that is to say, in the palm, in the digits, and at the level of the wrist joint. A parietal synovial layer is found just beneath the paratenon; this synovium-like membrane, called the *epitenon* and described in the previous section, surrounds several fiber bundles. The synovial fluid produced by the synovial cells of the epitenon facilitates gliding of the tendon. In locations where tendons are subjected to lower friction forces, they are surrounded by the paratenon only. On its outer surface the epitenon is contiguous with the paratenon and on its inner surface with the endotenon. Each fiber bundle in a tendon is surrounded and bound together by the endotenon, which continues at the musculotendinous junction into the perimysium.

The three terms describing anatomical structures of the tendon mentioned in the previous two paragraphs — the paratenon, the epitenon, and endotenon — all have "tenon" at the end of the word; one of the three descriptive modifiers — para- (by the side of), epi- (outside), and endo- (within) — at the start of the word. As indicated above, the paratenon is the tissue between a tendon and its sheath. The epitenon (also epitendinum) is the white fibrous synovial sheath around the outside of a tendon, and endotenon is the fibrous sheath around each collagen fiber in a tendon.

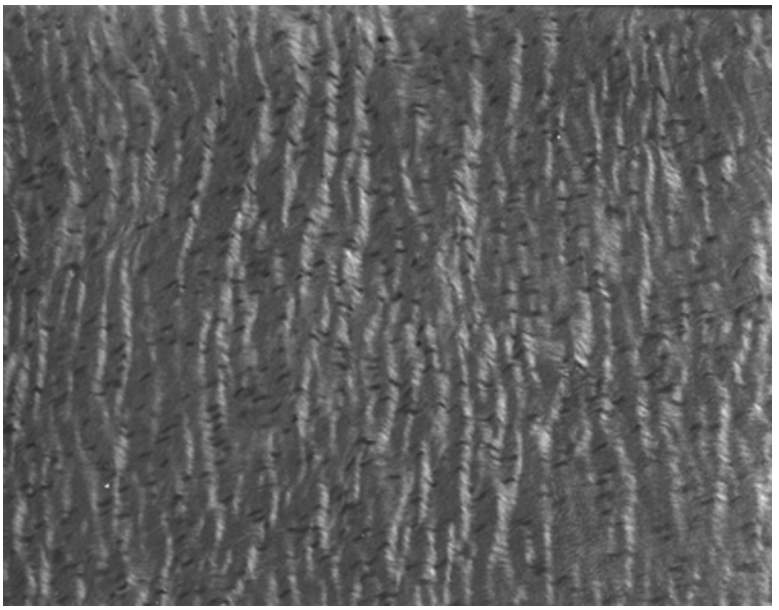


**Figure 16.5**. Histological cross-section of a New Zealand white rabbit achilles tendon showing the collagen crimp pattern. Reprinted with permission from Weiss and Gardiner (2001).

A hyaluronidase solution was shown to be the lubricant in the boundary lubrication mechanism between the human flexor digitorum profundus tendon and a pulley over which the tendon passes (Uchiyama et al., 1997). Recall from Chapter 14 that in synovial joints the glycoprotein *lubricin* is a major component of synovial fluid and is responsible for boundary lubrication. Rhee et al. (2005) noted tendon and tendon sheath involvement was present in the ankle joints of the lubricin-mutant mice; morphologic changes and abnormal calcification of these structures were observed. They concluded that lubricin has multiple functions in articulating joints and tendons that include the protection of surfaces and the control of synovial cell growth.

## 16.6. THE MECHANICAL PROPERTIES OF TENDONS AND LIGAMENTS

The mechanical properties of tendons and ligaments depend strongly upon the properties of the collagen fibers, but also on the arrangement and proportion of the constituents, particularly the collagen and the elastin.

***Stress–strain curves in the collagen fiber direction:*** Tensile tests of tendon or ligament tissue are usually performed along the collagen fiber axis as this axis is the predominant loading direction in vivo. The resulting tensile force-elongation curve of tendon or ligament tissue is nonlinear (Figures 16.6 and 16.7). With initial lengthening of the tissue, the curve is upwardly concave as the collagen crimp pattern is straightened. Small force levels are required to elongate the tissue initially in the toe region. As loading continues, the stiffness of the tissue increases and progressively greater force is required to produce equivalent amounts of elongation. This portion of the force-elongation curve is known as the "toe region" and typically extends to a strain of 2 to 3%, although there can be considerable inter-specimen variability. At

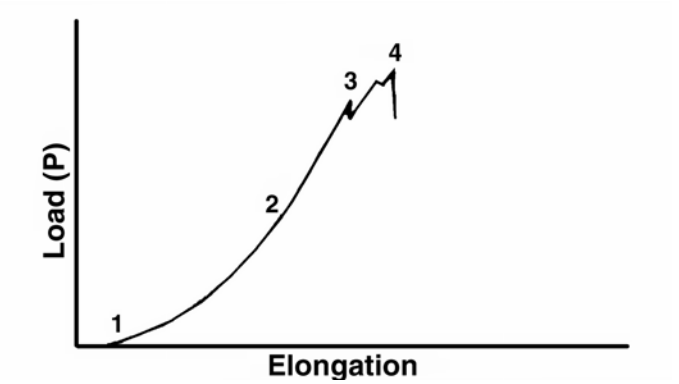



**Figure 16.6**. Load-elongation curve for rabbit tendon tested to failure in tension. The numbers indicate the four characteristic regions of the curve. (1) Primary, or "toe," region, in which the tissue elongated with a small increase in load as the wavy collagen fibers straightened out. (2) Secondary, or "linear," region, in which the fibers straightened out and the stiffness of the specimen increased rapidly. Deformation of the tissue began and had a more or less linear relationship with load. (3) End of the secondary region. The load value at this point is designated as **P**. Progressive failure of the collagen fibers took place after **P** was reached, and small force reductions (dips) occurred in the curve. (4) Maximum load, reflecting the ultimate tensile strength of the tissue. Complete failure occurred rapidly, and the specimen lost its ability to support loads. Adapted with permission from Carlstedt (1987).

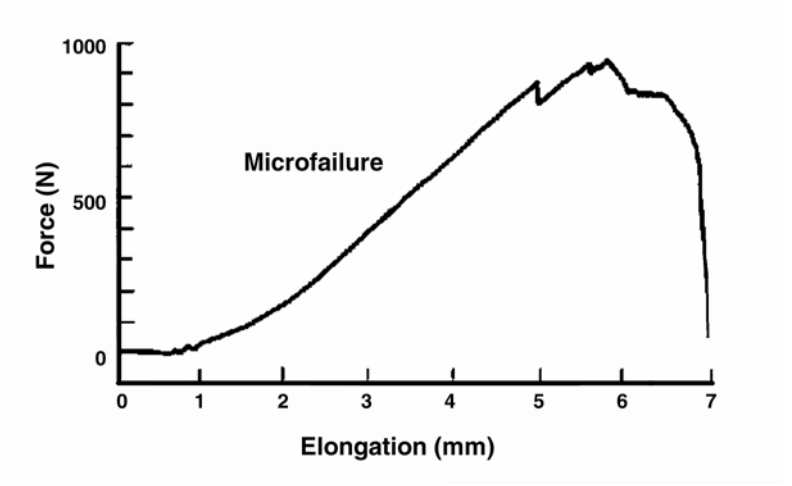



**Figure 16.7**. Progressive failure of the anterior cruciate ligament (ACL) from a cadaver knee tested in tension to failure at a physiologic strain rate (Noyes. 1977). The joint was displaced 7 mm before the ligament failed completely. The force-elongation curve generated during this experiment is correlated with various degrees of joint displacement recorded photographically.

the end of the toe region there is a gradual transition into the linear region of the force-elongation curve as the collagen is straightened. This portion of the curve is dominated by the material behavior of the straightened collagen. At the end of the linear region, small and irregular force reductions can sometimes be observed in the loading curves for both tendons and ligaments (Figures 16.6 and 16.7). These dips are caused by the early progressive or sequential

failure of a few greatly stretched fiber bundles. Beyond the linear region, widespread failure of fiber bundles occurs in a stochastic manner, the weaker links giving way first. With the attainment of maximum load, which when divided by the instantaneous cross-sectional area is the *ultimate tensile strength* of the specimen, complete failure occurs rapidly, and the load-supporting ability of the tendon or ligament is substantially reduced. The strain corresponding to the ultimate tensile strength is the ultimate strain. Under normal in-vivo physiologic conditions ligaments and tendons are subjected to a stress magnitude that is only about one-third the ultimate tensile strength.

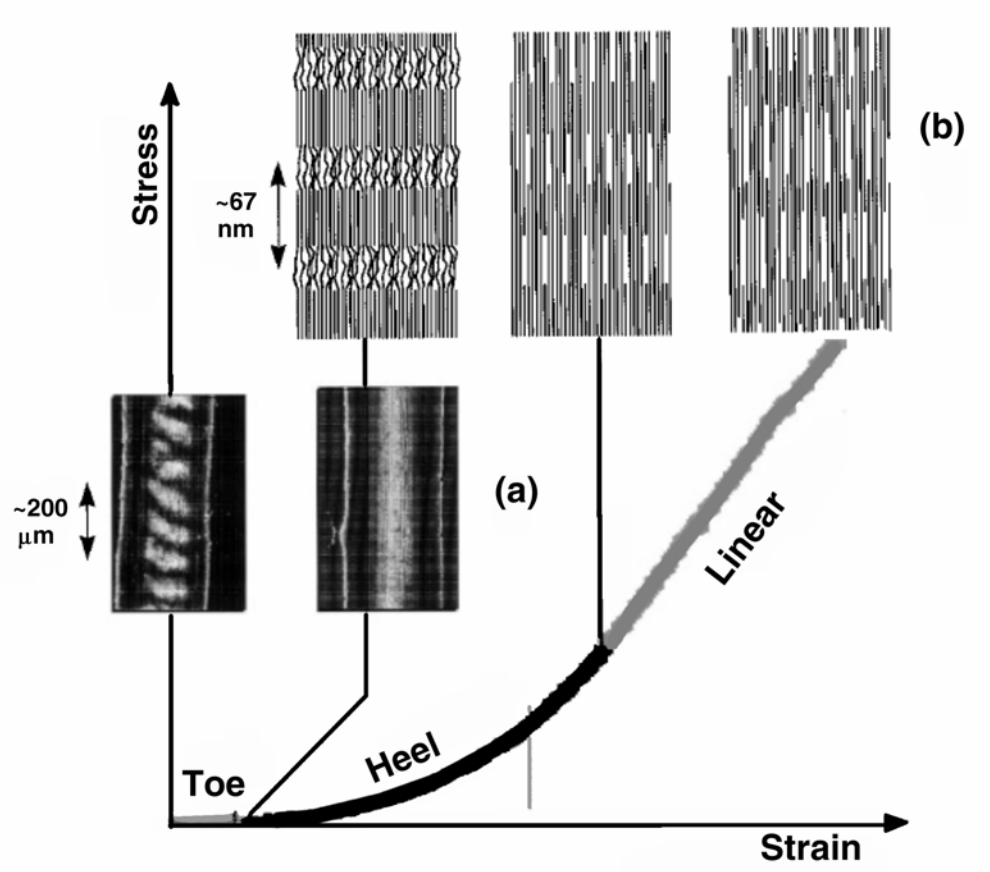



**Figure 16.8**. Typical stress–strain curve of a rat tail tendon detailed with illustrations of associated microstructural deformations. In the toe region, where the tendon can be extended with very little force, a macroscopic crimp of the fibrils with a typical period in the order of 100 µm is removed by increasing strain (Diamant et al., 1972). This can be visualized using polarized light (a). Further microstructural changes occur at the fibrillar level (b). The heel region of the stress–strain curve may correspond to a straightening of molecular kinks in the gap (Misof et al., 1997a) and the linear region to a gliding of molecules (Folkhart et al., 1986). Synchrotron diffraction data suggest that a disruption of the fibrillar structure starts with an increased fuzziness of the gap/overlap interface (see schematic picture, top right). Reprinted with permission from Fratzl et al. (1997).

Recent synchrotron x-ray scattering experiments have revealed drastic changes in the molecular packing of collagen fibrils in the rat-tail tendon under strain (Fratzl et al., 1997). While at low strains a straightening of molecular kinks seems to dominate, molecular gliding is ob-

served at large strains and leads to an increasingly irregular extension and, ultimately, to a disruption of the fibrillar structure. The mechanisms are summarized in Figure 16.8a, which shows the macroscopic effects occurring in the toe region of the stress–strain curve. Figure 16.8b shows mechanisms at the fibrillar level. A straightening of molecules occurs initially, and this process is followed by an increase of the gap region in the fibrils that is accompanied by a smearing of the gap/overlap interface. Important questions regarding these microstructural deformations remain unsolved — for example, the role of intermolecular crosslinking is still unclear. The molecular gliding described by Fratzl et al. (1997) implies a considerable force on the crosslinks. Preliminary data on the stress–strain curves of crosslink-deficient rat-tail tendons have shown that the tendons break at very small forces and, in particular, there is no linear region in the stress–strain curve. the tendons lacking crosslinks were observed to behave more like a viscous liquid than a solid fiber (Misof et al., 1997b). Almost nothing is known about the role of the intrafibrillar substance in terms of mechanical properties and, in particular, about its role in mechanically linking neighboring fibrils (Viidik, 1990; Fratzl et al., 1997). The data of Fratzl et al. (1997) suggest a considerable importance, since only 40% of the strain on the rat-tail tendon is actually transmitted to the fibrils.

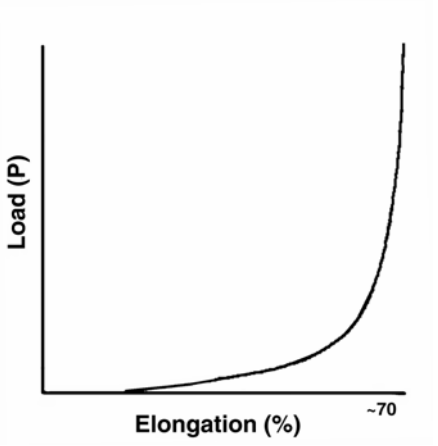



**Figure 16.9**. Load-elongation curve for a human ligamentum flavum (60 to 70% elastic fibers) tested in tension to failure. At 70% elongation the ligament exhibited a great increase in stiffness with additional loading and failed abruptly without further deformation. Adapted with permission from Nachemson and Evans (1968).

The variability of the compositional structure of individual tendons and ligaments is illustrated by comparing the force-elongation curve of the ligamentum flavum with its high proportion of elastic fibers (Figure 16.9) with the curve in Figure 16.7 for the anterior cruciate ligament (ACL) or the curve in Figure 16.10 for the medial cruciate ligament (MCL). In tensile testing of a human ligamentum flavum, elongation of the specimen reached 50% before stiffness increased appreciably. Beyond this point stiffness increased greatly with additional loading and the ligament failed abruptly with little further deformation (Nachemson and Evans, 1968). This tendon-to-tendon and ligament-to-ligament variability in also illustrated by the reported values of the material properties (Table 16.2). The variability in the medial cruciate ligament (MCL) is illustrated in Figure 16.10. The tangent modulus for ligamentous tissue ranges from 250 to over 1600 MPa, whereas the tensile strength ranges between 35 and 125 MPa. Ultimate strain has been reported to be between 12 and 18%. Aging results in a decline in the mechanical properties of tendons and ligaments, i.e., their strength, stiffness, and ability to withstand deformation.

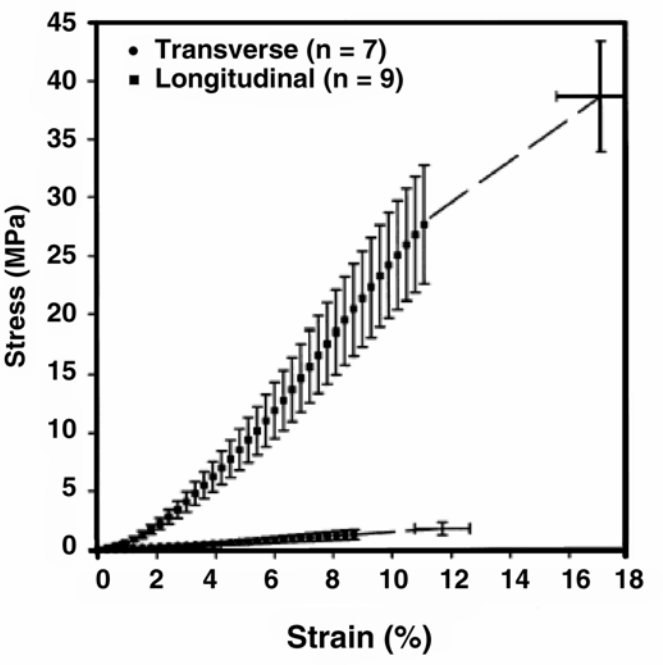



**Figure 16.10**. Stress–strain curves for human MCL tested parallel and transverse to the collagen fiber direction. The final point in each curve was the average failure point for the specimens. The error bars indicate the standard error for the average ultimate strain and tensile stress. The tangent modulus of the longitudinal curve was over an order of magnitude greater than the tangent modulus of the transverse curve. Reprinted with permission from Quapp and Weiss (1998).

***Viscoelastic properties:*** Tendons and ligaments have time- and history-dependent viscoelastic properties that arise from both the inherent viscoelasticity of the solid phase and the interaction of water with the ground substance matrix. Both creep and stress relaxation are observed and measured. The loading and unloading curves of ligaments under tension do not follow the same path. A hysteresis loop, similar to that observed by Fung (1967) (Figure 15.19) is typically observed during tensile testing of these tissues. The variation of ligament stress–strain behavior with strain rate is another indicator of the viscoelastic nature of the tissue. The material properties of rabbit MCLs were experimentally measured at five different strain rates (Table 16.3) by Woo et al. (1990). These data show that changes in strain rate of greater than four orders of magnitude had relatively small effects on the material properties of ligaments. Note that the tensile strength and ultimate strain increased slightly with increasing strain rate, but the tangent modulus went up and down in value, suggesting that it remained essentially unchanged, given the standard deviation in the data set.

Hingorani et al. (2004) showed that, for the rabbit MCL in the physiological loading range, the rates of stress relaxation and creep are dependent on strain and stress, respectively. This type of viscoelastic behavior has previously been observed in rat ligaments (Provenzano et al., 2001), and data from this study confirm similar stress- and strain-dependent nonlinear viscoelastic behavior in rabbit ligament. Hingorani et al. (2004) proposed a nonlinear viscoelastic model for this behavior that is described in §16.6 below.

**Table 16.2**. Material Properties of Human and Animal Ligaments and Tendons (Mean ± SEM)

| Specimen type | Source | Tangent modulus (MPa) | Tensile strength (MPa) | Ultimate strain (%) |
|---|---|---|---|---|
| Human MCL | Quapp & Weiss, 1998 | 332.2 ± 58.3 | 38.6 ± 4.8 | 17.1 ± 1.5 |
| Rabbit MCL | Woo et al., 1990 | 740 ± 90 | 77.7 ± 1.9 | 12.9 ± 1.2 |
| Human PCL (anterolateral bundle)* | Race & Amis, 1994 | 248 ± 119 | 35.9 ± 16.2 | 18.0 ± 5.3 |
| Rabbit ACL | Woo et al., 1986 | 516 ± 64 | 62.3 ± 5.2 | 12.5 ± 1.5 |
| Human ACL, LCL, PCL* | Butler et al., 1990 | 345.0 ± 22.4 | 36.4 ± 2.5 | 16.0 ± 0.8 |
| Human patellar tendon* | Butler et al., 1990 | 643.1 ± 53.0 | 68.5 ± 6.0 | 13.5 ± 0.7 |
| Goat patellar tendon** | Gibbons et al., 1991 | 1639.1 ± 435.9 | 126.8 ± 20.8 | 16.2 ± 3.9 |

These tests were performed using noncontact strain measurement techniques that isolated the ligament/tendon substance except those marked "*". The test marked "**" utilized an area micrometer technique that has been shown to underestimate cross-sectional area. Thus, the values for tangent modulus and tensile strength from this study are likely. The MEAN ± SEM rather than the MEAN ± SD is reported here. The standard deviation (SD) represents variation in the values of a variable, whereas the standard error of the mean (SEM) represents the spread that the mean of a sample of the values would have if sample taking continued. The SEM is a measure of the accuracy of the mean, and the SD is a measure of the variability of single observations. The two are related: SEM = SD/(square root of sample size). Reprinted with permission from Weiss and Gardiner (2001).

**Table 16.3**. Effects of Strain Rate on the Material Properties of Rabbit MCL (Mean ± SEM)

| Strain rate (mm/s) | Tangent modulus (MPa) | Tensile strength (MPa) | Ultimate strain (%) |
|---|---|---|---|
| 0.008 | 700 ± 70 | 75.2 ± 2.4 | 9.5 ± 0.5 |
| 0.1 | 840 ± 150 | 81.4 ± 7.4 | 10.0 ± 0.5 |
| 1.0 | 800 ± 60 | 85.7 ± 7.7 | 11.0 ± 0.5 |
| 10.0 | 910 ± 50 | 87.2 ± 6.0 | 11.5 ± 1.0 |
| 113.0 | 760 ± 160 | 106.7 ± 6.8 | 13.0 ± 1.0 |

These data indicate that large variations in strain rate have relatively small effects on ligament material properties. Reprinted with permission from Woo et al. (1991). The comment concerning the MEAN ± SEM and the MEAN ± SD in the caption to Table 16.2 also applies to here.

The mechanisms driving viscoelastic behavior in ligament are not yet completely understood. As discussed in §16.7 below on interstitial flow, there is growing evidence that fluid exudation is a source of viscoelastic behavior. In regard to creep behavior, Thornton et al. (1997) suggested that differences in stress relaxation and creep behavior are due to progressive recruitment of collagen fibers during creep and that this microstructural behavior is unlikely to

have as significant an effect on stress relaxation as on creep. Subsequent experiments strongly suggest that collagen fiber recruitment does in fact play a role in creep behavior (Thornton et al., 2001a,b, 2002). Hence, the progressive recruitment of collagen fibers could also explain the decrease in the rate of creep with increasing load (Hingorani et al., 2004). As larger loads are applied to the ligament, more fibers are recruited, leaving fewer fibers to be progressively recruited after initial loading and therefore decreasing the creep response.

***Anisotropy of the stress–strain relation***: Tendons and ligaments are highly anisotropic because of their strongly unidirectionally oriented fibrous structure. Collagen provides the primary resistance to tensile loading but offers negligible resistance to compression. Like strings, tendons and ligaments also offer little resistance to bending, as illustrated by the fact that they will fold under their own weight when held vertically from the bottom. Quapp and Weiss (1998) performed tensile tests on samples from human MCLs harvested both parallel and transverse to the collagen fiber direction. These data showed that the tensile strength, ultimate strain, and tangent modulus were significantly higher for tests oriented along the collagen direction. In addition, the toe region was absent from the stress–strain curves of transverse specimens (Figure 16.10). Chuong et al. (1991) experimentally investigated the anisotropy of the canine diaphragmatic central tendon. Tensile tests were performed on samples oriented parallel and transverse to the predominant fiber direction. The results showed significantly higher tangent modulus and tensile strength for the samples oriented parallel to the fiber direction. The ultimate strains were not significantly different between the two sample groups.

***Material inhomogeneities***: Material inhomogeneities are present within individual ligaments. These were surveyed by Weiss and Gardiner (2001) in their summary of ligament research, a publication that is drawn upon in this section and elsewhere in this chapter. Butler et al. (1992) compared the material properties between different bundles of the human ACL. The anteromedial bundle and anterolateral bundles were found to have significantly higher modulus, ultimate stress and strain energy density than the posterior bundle. The ultimate strain was not significantly different between the three bundles. A difference in the biochemical composition of ligaments has been studied in an effort to explain the observed material property inhomogeneities (Frank et al., 1988; Mommersteeg et al., 1994). Frank et al. (1988) studied the normal rabbit MCL and found different levels of water content, glycosaminoglycan content, and collagen concentration along the length of the ligament. Mommersteeg et al. (1994) showed that collagen density is nonuniformly distributed throughout human knee ligaments. The variations in collagen density measured by Mommersteeg et al. (1994) appeared to correspond with variations in modulus found throughout the ACL and PCL in separate studies by Butler et al. (1990, 1992). Material inhomogeneities are believed to be especially common near the insertion sites, although this has not been well quantified experimentally due to the difficulties in performing mechanical measurements in such a small region of tissue.

***Stress–strain curves for shear in the fiber direction***: The ligament response to shear loading under both quasi-static and rate-dependent loading conditions was investigated by Weiss et al. (2002). Rectangular specimens for shear testing were obtained from five human cadavers from the anterior region of the human MCL, just distal to the medial meniscus. Experimentally, the specimens were clamped on a material testing machine with the fiber direction oriented vertically (Figure 16.11A). They were then subjected to a finite strain simple shear deformation (Figure 16.11B) after being allowed to equilibrate in a stress-free configuration for 30 minutes before the testing sequence. A saw tooth displacement profile was applied at a shear strain rate of 1.3 %/s, with a shear strain amplitude of $\tan\theta = 0.4$ for 10 cycles; the angle $\theta$ is shown in Figure 16.11. This amplitude was chosen based on preliminary testing to determine the maximum shear strain that could be consistently applied without damage to the specimen, as indicated by a drop in load during application of shear strain. Global applied

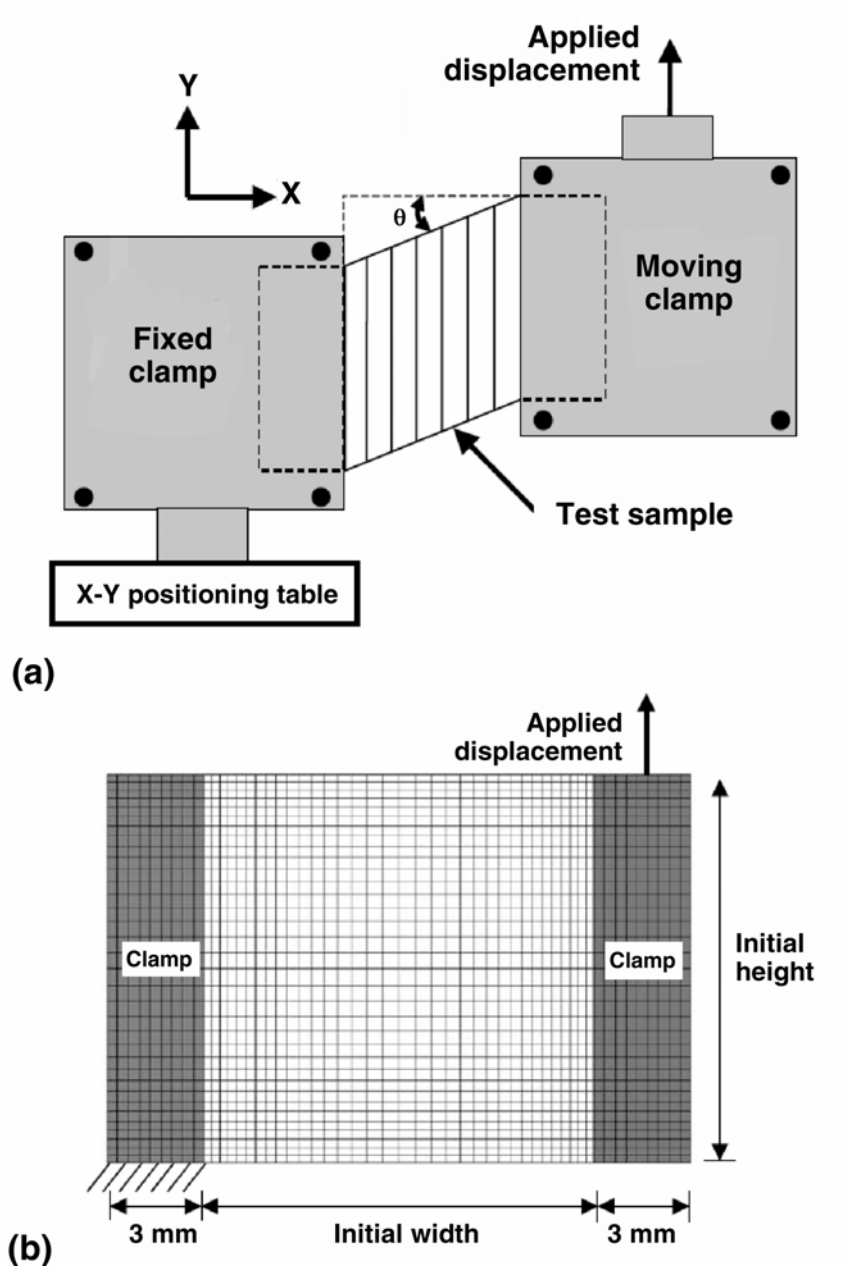



**Figure 16.11**. (A) Schematic of the test configuration. One of the clamps was mounted to an X–Y positioning table to facilitate alignment, while the other clamp was attached to a moving crosshead. The test sample was oriented so that the fibers were aligned with the vertical movement axis of the test machine. (B) FE mesh and boundary conditions used in the parameter optimization studies. Three millimeters of the specimen were simulated as clamped. The left clamped section was fixed on the surfaces, while the right clamped section was subjected to prescribed displacements corresponding to the experimentally measured crosshead displacement. Test specimen dimensions were assigned using specimen-specific experimental measurements for each simulation. Reprinted with permission from Weiss et al. (2002).

shear strain was computed using the specimen's initial dimensions and crosshead displacement measurements. The clamp reaction force and global applied shear strain from the loading portion of the 10th cycle were used for parameter estimation. Following cyclic testing and a subsequent 30-min recovery period, consecutive stress relaxation tests were performed at three different strain rates (1.3, 13, and 130 %/s) with a strain amplitude of tan θ = 0.4. For each strain rate, the specimen was allowed to stress relax for 30 minutes, followed by a 30-min recovery period. The relaxation time was based on preliminary testing that showed no measurable change in the force after 30 minutes. During three pilot tests, the stress relaxation test at a strain rate of 1.3 %/s was repeated and the response was unaffected by the intervening tests at 13 and 130 %/s, demonstrating that damage and preconditioning did not affect the results due to order of testing. An effective shear stress was defined as the clamp reaction force divided by the sample cross-sectional area. The peak and equilibrium effective shear stresses for the static stress relaxation tests were calculated from the data for each of the three strain rates.

These stress relaxation tests demonstrated that the tissue was highly viscoelastic in shear, with peak loads dropping over 40% during 30 min of stress relaxation. The stress relaxation response was unaffected by three decades of change in shear strain rate (1.3, 13, and 130 %/s). The experimentally measured clamp displacements and reaction forces from the simple shear tests were used with a nonlinear optimization strategy based around function evaluations from a finite-element program.

The mathematical modeling of these data is described in the following section.

## 16.7. CONSTITUTIVE EQUATIONS FOR TENDONS AND LIGAMENTS

In order to appropriately characterize the mechanical response, the theoretical formulation of constitutive relations for tendons and ligaments, as well as for other soft tissues, should be three dimensional as opposed to one dimensional (see, for example, Quapp and Weiss, 1998; Holzapfel, 2001; Weiss and Gardiner, 2001). The one-dimensional or uniaxial models for tendons and ligaments are described in Quapp and Weiss (1998) and Weiss and Gardiner (2001). Three-dimensional modeling of the MCL in axial deformation (Quapp and Weiss, 1998; Untaroiu et al., 2005) and in shearing deformation (Weiss et al., 2002) is described below.

***Axial loading***: The model for axial loading of the MCL employed by Quapp and Weiss (1998) was a three-dimensional, transversely isotropic, strain energy function (15.116) in the incompressible case with special forms for the functions $W_1$, representing the matrix strain energy, $W_2$, representing the fiber family strain energy, and $W_3$, representing the interaction between the matrix and the fibers. In this application, strain energy function $W_3$ was considered as representing a shear coupling between the matrix and the fibers, but since this testing and the modeling of the testing were uniaxial, this coupling term was taken as zero. With these assumptions strain energy function (15.116) reduces to

$$W = W_1(I_{\mathbf{C}}, II_{\mathbf{C}}) + W_2(\lambda_{\text{fiber}}) . \tag{16.1}$$

The first term, $W_1(I_{\mathbf{C}}, II_{\mathbf{C}})$, models the ground substance matrix and is made specific by assuming it is Mooney-Rivlin material, and from (15.95),

$$W_1 = \frac{C_1}{2}(I_C - 3) + \frac{C_2}{2}(II_C - 3) . \tag{16.2}$$

The second term, $W_2(\lambda_{\text{fiber}})$, specified by (15.117), is designed to capture the behavior of crimped collagen in tension and works only in the fiber direction defined in the model. Recall

that constant $C_4$ in (15.117) represents the rate of collagen fiber uncrimping and $C_5$ is the modulus of the straightened collagen. Constant $C_6$ is determined from condition (15.118) that the right-hand sides of the second and third equations in set (15.117) are equal at $\lambda = \lambda^*_{\text{fiber}}$.

The stress is determined from (16.1) using the last equation of (15.77) and formulas (15.81) for the derivatives of the isotropic invariants of $\mathbf{C}$ with respect to $\mathbf{C}$, and the formula for the derivative of $\lambda_{\text{fiber}}$ with respect to $\mathbf{C}$, which is obtained by taking the derivative of the first of (15.114), $\mathbf{a}_0 \cdot \mathbf{C} \cdot \mathbf{a}_0 = \lambda^2_{\text{fiber}}$, and thus

$$\frac{\partial \lambda_{\text{fiber}}}{\partial \mathbf{C}} = \frac{1}{2\lambda_{\text{fiber}}} \mathbf{a}_0 \otimes \mathbf{a}_0 \tag{16.3}$$

and

$$\mathbf{T}^{2PK} = 2\frac{\partial W}{\partial \mathbf{C}} = p\mathbf{C}^{-1} + 2\left\{\frac{\partial W_1}{\partial I_{\mathbf{C}}} + I_C\left(\frac{\partial W_1}{\partial II_{\mathbf{C}}}\right)\mathbf{1} - \frac{\partial W_1}{\partial II_{\mathbf{C}}}\mathbf{C}\right\} + \frac{1}{\lambda_{\text{fiber}}}\frac{\partial W_2}{\partial \lambda_{\text{fiber}}}\mathbf{a}_0 \otimes \mathbf{a}_0 . \tag{16.4}$$

The stress contribution obtained by taking the derivative of $W_2(\lambda_{\text{fiber}})$ with respect to the stretch, shown in (15.117), has an exponential function that describes the straightening of the fibers and a linear function once they are straightened past a critical stretch level, $\lambda^*_{\text{fiber}}$.

Quapp and Weiss (1998) obtained experimental data from nine specimens cut longitudinally from a human MCL (Figure 16.10) and seven specimens cut transversely (Figure 16.10). If the axial or longitudinal direction is taken to be $\mathbf{e}_1$ and the transverse direction $\mathbf{e}_2$, then expressions for the normal stress components in these directions are given by

$$T_{11}^{2PK} = pC_{11}^{-1} + 2\left\{\frac{\partial W_1}{\partial I_{\mathbf{C}}} + I_C\left(\frac{\partial W_1}{\partial II_{\mathbf{C}}}\right) - \frac{\partial W_1}{\partial II_{\mathbf{C}}}C_{11}\right\} + \frac{1}{\lambda_{\text{fiber}}}\frac{\partial W_2}{\partial \lambda_{\text{fiber}}} \tag{16.5}$$

and

$$T_{22}^{2PK} = pC_{22}^{-1} + 2\left\{\frac{\partial W_1}{\partial I_{\mathbf{C}}} + I_C\left(\frac{\partial W_1}{\partial II_{\mathbf{C}}}\right) - \frac{\partial W_1}{\partial II_{\mathbf{C}}}C_{22}\right\}. \tag{16.6}$$

Unknown material coefficients $C_1$– $C_6$ were evaluated from these data using an optimization process. Unfortunately, the values of $C_2$ appearing in (16.2) in Quapp and Weiss (1998) were not constrained to be positive; negative numbers for $C_2$ can produce non-physical behavior in compression (Weiss, 2005). This problem was not caused by an inadequacy in the Mooney-Rivlin material model for this aspect of the MCL response, but by a failure to properly constrain the optimization program that determined the $C_2$ fit (Weiss, 2005).

The problem of modeling MCL behavior considered in Quapp and Weiss (1998) was considered again in an experimental and modeling study reported by Untaroiu et al. (2005). The form of the strain energy function assumed was almost the same as in Quapp and Weiss (1998) (see (16.1) above), but rather than assuming fully incompressible behavior, the material was represented as slightly compressible using an additional term to represent the bulk response of the material as a function of volume ratio $J$:

$$W = W_1(I_{\text{dev}\mathbf{C}}, II_{\text{dev}\mathbf{C}}) + W_2(\text{dev}\lambda_{\text{fiber}}) + \frac{K_{\text{eff}}}{2}\{\ln J\}^2, \tag{16.7}$$

where $W_1$ and $W_2$ are as specified above, and $K_{\text{eff}}$ represents the effective bulk modulus of the material. This time a good fit was again reported, but the value of $C_2$ associated with the good fit was not reported.

***Shear loading:*** In their modeling of the MCL response to shear loading under both quasi-static and rate-dependent loading conditions, Weiss et al. (2002) used a slightly different constitutive model from the one described above. The particular constitutive model for the strain energy function used by Weiss et al. (2002) to represent their shear testing ligament data was (16.7). The expression for $W_2$ was the same as above, but the Mooney-Rivlin representation (16.2) for $W_2$ in (16.1) was replaced by strain energy (15.110). introduced by Veronda and Westmann (1970),

$$W_1 = C_1(e^{C_2((I_{\text{dev}\mathbf{C}})-3)} - 1) - \frac{C_1 C_2}{2}(II_{\text{dev}\mathbf{C}} - 3). \tag{16.8}$$

This strain energy is convex and exhibits physically reasonable behavior under tension, compression, and shear. Weiss et al. (1996) point out that this uncoupled deviatoric/dilatational constitutive formulation has numerical advantages for simulating nearly incompressible material behavior with the FE method. However, in this discussion of the Weiss et al. (2002) model, analysis of only the incompressible case will be considered and the dilatational strain energy term, $K_{\text{eff}}\{\ln J\}^2/2$, in (16.7) will be neglected. It was demonstrated by Gardiner and Weiss (2001) that the initial bulk modulus had very little effect on the predicted response of the ligament to finite shear because the deformation remained nearly isochoric regardless of the choice of $K_{\text{eff}}$ ; this observation was strengthened by the work of Weiss et al. (2002), which is not discussed here.

Recall that for a simple shear deformation (see Figure 15.8) the deformation gradient is given by

$$\mathbf{F} = \begin{bmatrix} 1 & \kappa & 0 \\ 0 & 1 & 0 \\ 0 & 0 & 1 \end{bmatrix}, \tag{16.9}$$

where the amount of shear is given by $\kappa = \tan\theta$, and where $\theta$ is the angle of rotation of the vertical lines in Figure 15.8. It then follows from (15.27) that the right and left Cauchy-Green tensors, $\mathbf{C}$ and $\mathbf{B}$, respectively are given by

$$\mathbf{C} = \begin{bmatrix} 1 & \kappa & 0 \\ \kappa & 1+\kappa^2 & 0 \\ 0 & 0 & 1 \end{bmatrix}, \quad \mathbf{B} = \begin{bmatrix} 1+\kappa^2 & \kappa & 0 \\ \kappa & 1 & 0 \\ 0 & 0 & 1 \end{bmatrix}, \tag{16.10}$$

and from (15.122) it follows that $\text{dev}\mathbf{C} = \mathbf{C}$ and $\text{dev}\mathbf{B} = \mathbf{B}$, and thus

$$I_{\mathbf{C}} = I_{\text{dev}\mathbf{C}} = I_{\mathbf{B}} = I_{\text{dev}\mathbf{B}} = II_{\mathbf{C}} = II_{\text{dev}\mathbf{C}} = II_{\mathbf{B}} = II_{\text{dev}\mathbf{B}} = 3+\kappa^2$$

$$III_{\mathbf{C}} = III_{\text{dev}\mathbf{C}} = III_{\mathbf{B}} = III_{\text{dev}\mathbf{B}} = 1. \tag{16.11}$$

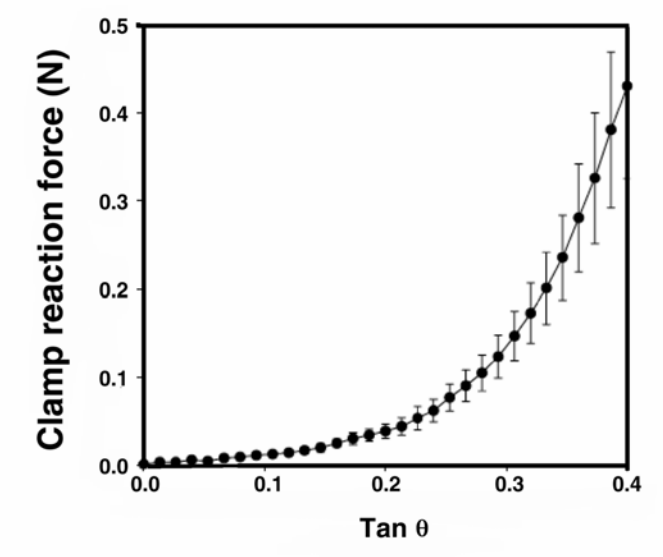



**Figure 16.12**. Experimentally determined clamp reaction force as a function of applied shear strain $q$ as measured in terms of clamp displacement. The response stiffened rapidly after a value of $\kappa = \tan\theta = 0.2$. Reprinted with permission from Weiss et al. (2002).

The experimental data on shear testing reported by Weiss et al. (2002) demonstrated stiffening behavior for the clamp force vs. clamp displacement (Figure 16.12). Using the forms for $W_1$ and $W_2$ specified above, Cauchy shear stress $T_{12}$ is equal to $T_{12}^{2PK}$ and may be expressed in terms of shear strain $\kappa = \tan\theta$ as

$$T_{12} = T_{12}^{2PK} = G(\kappa)\kappa\,, \tag{16.12}$$

where shear dependent shear modulus $G(\kappa)$ is given by

$$G(\kappa) = 2C_1C_2(2e^{C_2\kappa^2} - 1)\,. \tag{16.13}$$

This model provided a reasonable fit to the experimental load–displacement curves. The shear modulus $G(\kappa)$ of human MCL showed a significant increase with increasing shear strain, reaching a maximum of $1.72 \pm 0.49$ MPa. The results obtained suggested that viscoelasticity *in shear* does not likely result from fluid flow. Gradual loading of transversely oriented microstructural features such as intermolecular collagen crosslinks or collagen-proteoglycan cross–linking may be responsible for the stiffening response under shear loading.

Despite the large amount of shear strain, the resulting stresses were <1 MPa. The integrated overall effective shear stress–strain relationship was highly nonlinear (Figure 16. 12). A large amount of relaxation, regardless of the strain rate, was shown in the stress relaxation testing. There was no effect of strain rate on the peak stress or the ratio of the peak/equilibrium stress. For each sample, the load–displacement curve from the loading part of the stress relaxation test was nearly identical for all three strain rates.

The nonlinear optimization program was successful in minimizing the difference between experimental and FE force–displacement data for all specimens. The fit of the experimental

force–displacement data to that predicted by parameter optimization was excellent in all cases, as demonstrated by $R^2$ values that were always >0.995 (Table 16.4). The magnitude of $C_1$, which scales the matrix stress response, demonstrated considerable variation between samples (Table 16.4). This reflects the variation in force–displacement curves that were obtained during experiments. In contrast, coefficient $C_2$ that controls the rate of rise of exponential matrix stresses exhibited much less variation (Table 16.4). Thus, the general shape of the response curve was consistent between samples. Finally, note that this $C_2$ is the $C_2$ in Veronda and Westmann strain energy (16.8) and not the $C_2$ in Mooney-Rivlin strain energy (16.2).

**Table 16.4**. Optimized Material Coefficients for the Matrix Behavior of the MCL

| Sample# | $C_1$ (Pa) | $C_2$ | $R^2$ |
|---|---|---|---|
| 1 | 1059.7 | 11.08 | 0.999 |
| 2 | 300.5 | 9.23 | 0.997 |
| 3 | 1644.1 | 9.73 | 0.998 |
| 4 | 697.7 | 11.37 | 0.995 |
| 5 | 460.2 | 13.86 | 0.996 |
| Mean ± STD | 832.4 ± 536.2 | 11.05 ± 1.81 | |

The coefficient scaling the stress response, $C_1$, demonstrated significant variation between samples, while the coefficient controlling the rate of stiffening, $C_2$, exhibited a smaller deviation. There was little effect of the assumed bulk/shear ratio on the predicted material coefficients. Modified from Weiss et al. (2002).

***Viscoelasticity:*** In their experimental and theoretical study of axial deformation of the MCL that followed in the footsteps of the Quapp and Weiss (1998) study, Untaroiu et al. (2005) moved beyond Quapp and Weiss in that they considered tissue viscoelasticity. They modeled their axial viscoelasticity data with the quasi-linear viscoelasticity QLV model described in §15.13 (Fung 1972, 1993). Recall that the QLV model is a constitutive equation (15.126) for the time-dependent stress as a convolution of the elastic stress and a *reduced relaxation function* $\bar{G}(t)$ defined by (15.125). Following Puso and Weiss (1998), Untaroiu et al. (2005) represented the reduced relaxation function $\bar{G}(t)$ by a three-term Prony series in which the parameters are the spectral strength coefficients $S_i$ and material characteristics times $T_i$:

$$\bar{G}(t) = \sum_{i=1}^{3} S_i e^{-t/T_i} \ . \tag{16.14}$$

Use of the QLV model improved the correspondence between the data and the theory compared with the use of the simple hyperelastic model, as shown in Figure 16.13.

The model most commonly employed to describe ligament viscoelasticity is the QLV model. The QLV model works very well with a single load or elongation level and has been shown to describe tendon and ligament very well in the case of single-load data (Haut and Little, 1972; Woo, 1982; Untaroiu et al., 2005). The data reported by Hingorani et al. (2004) on the rabbit MCL was not well modeled by the QLV formulation due to nonlinearity in the data. In order to understand the nonlinearity that occurred recall how, in §7.5, creep function $\hat{J}_{11}(s)$ was defined as the uniaxial strain-versus-time response of the uniaxially stressed specimen to the step increase in stress, $\hat{T}_1 = T_o h(t)$, and how the creep function determined in that manner

was used as the basis for determining the response to an arbitrary loading in a superposition procedure. In this procedure the time history of the strain associated with each incremental step in stress (Figure 7.5) was determined by multiplying the stress increment by stress-independent creep function $\hat{J}_{11}(s)$. $\hat{J}_{11}(s)$ itself was not independent of the stress magnitude in the experimental study reported by Hingorani et al. (2004), so the authors employed a nonlinear model.

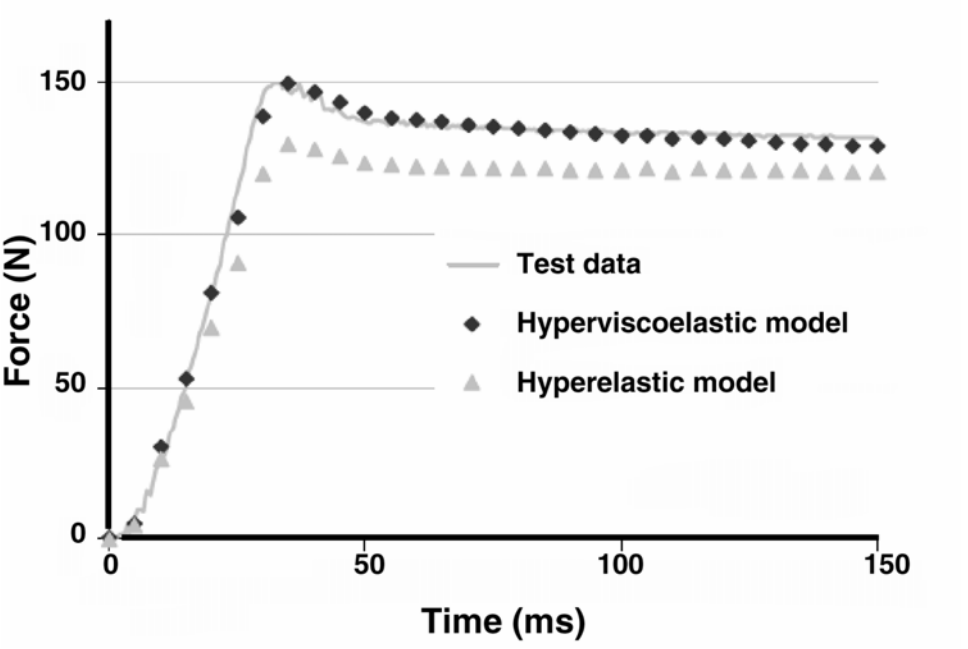



**Figure 16.13**. Dynamic axial tensile testing of the MCL: a comparison between test data and FE simulation results for the hyperelastic model and the QLV model. Reprinted with permission from Untaroiu et al. (2005).

This nonlinear model was obtained by recasting linear representation (7.44) for the uniaxial strain-versus-time response of the uniaxially stressed specimen as integral over the stress rate history and creep function $\hat{J}_{11}(s)$ by making the creep function stress level dependent, and thus

$$\hat{E}_1(t) = \int_0^t \hat{J}_{11}(t - t_i; \hat{T}_1) \frac{d\hat{T}_1}{ds} ds \,. \tag{16.15}$$

The physical significance of stress level-dependent creep function $\hat{J}_{11}(s; T_0)$ is the following: it is the uniaxial normal strain $\hat{E}_1(t)$ versus time response of a specimen subjected to a step increase in the normal stress in the same direction, $\hat{T}_1 = T_o h(t)$. Representation (16.15) reduces to (7.44) if $\hat{J}_{11}$ is not stress level dependent. Hingorani et al. (2004) assume that the form of the resulting nonseparable, stress level-dependent creep function is

$$\hat{J}_{11}(s;\hat{T}_1) = \frac{1}{E(\hat{T}_1)} t^{n(\hat{T}_1)}, \tag{16.16}$$

where $E(\hat{T}_1)$ is a function representing the initial elastic modulus, and exponent $n(\hat{T}_1)$ of $t$ is stress level dependent. Substitution of (16.16) into (16.15) yields the following representation of the strain response:

$$\hat{E}_1(\hat{T}_1, t) = \hat{E}_{1o} t^{n(\hat{T}_1)}, \tag{16.17}$$

where $\hat{E}_{10} = \hat{T}_1 / E(\hat{T}_1)$ is the initial strain — stress $\hat{T}_1$ divided by initial elastic modulus $E(\hat{T}_1)$. An analogous formulation exists for stress relaxation in which the relaxation function is dependent upon time and strain level; thus,

$$\hat{T}_1(t) = \int_{s=0}^{s=t} \hat{G}_{11}(t-s;\hat{E}_1) \frac{d\hat{E}_1}{ds} ds . \tag{16.18}$$

The physical significance of strain level-dependent relaxation function $\hat{G}_{11}(s;E_o)$ is the following: it is the uniaxial normal stress $\hat{T}_1(t)$ versus time response of a specimen subjected to a step increase in the normal strain in the same direction, $\hat{E}_1 = E_0 h(t)$. Representation (16.18) reduces to (7.46) if $\hat{G}_{11}$ is not strain level dependent. Hingorani et al. (2004) assume that the form of the resulting nonseparable relaxation function is

$$\hat{G}_{11}(s;\hat{E}_1) = E(\hat{E}_1) t^{n(\hat{E}_1)}, \tag{16.19}$$

where $E(\hat{E}_1)$ is a function representing the initial elastic modulus and exponent $n(\hat{E}_1)$ of $t$ is strain level dependent. Substitution of (16.19) into (16.18) yields the following representation of the stress response:

$$\hat{T}_1(\hat{E}_1, t) = \hat{T}_{10} t^{n(\hat{E}_1)}, \tag{16.20}$$

where $\hat{T}_{1o} = \hat{E}_1 E(\hat{E}_1)$ is the initial stress that is a product of initial elastic modulus $E(\hat{E}_1)$ and strain $\hat{E}_1$.

In order to decouple time-dependent (viscoelastic) and strain-dependent (nonlinear elastic) behavior so that the nonlinearity can be properly visualized in a stress–strain plot independent of viscoelasticity, an *isochronal* curve at time $t$ = 2.4 s was constructed (Figure 16.14). An *isochronal curve* is one generated from a set of points at a specific time, but at different strain levels within a set of relaxation curves. This particular isochronal curve (Figure 16.14) shows that these viscoelastic data are obtained from tests in which the elastic behavior is consistent with the typical strain-stiffening behavior previously reported for rabbit MCLs. All tissues tested by Hingorani et al. (2004) exhibited a definite nonlinear trend in both creep and stress relaxation rates with stress or strain, respectively. Both stress relaxation and creep rates changed by approximately an order of magnitude throughout the loading range examined. Statistical analyses reveal that the rate of stress relaxation is dependent upon strain magnitude, while creep was dependent on stress magnitude. Multiple tests at varying strain levels demonstrate that the rate of stress relaxation decreases in magnitude with increasing strain (Figure 16.15). The five types of data points, indicated by different geometric symbols in Figure 16.15, correspond to the following indicated strain levels and stress relaxation representations: circle, $\hat{E}_1$ = 0.81%, $\hat{T}_1 = 2.4488 t^{-0.2619}$, $R^2$ = 0.98; square, $\hat{E}_1$ = 0.87%; $\hat{T}_1 = 6.6249 t^{-0.1602}$, $R^2$ = 0.99;

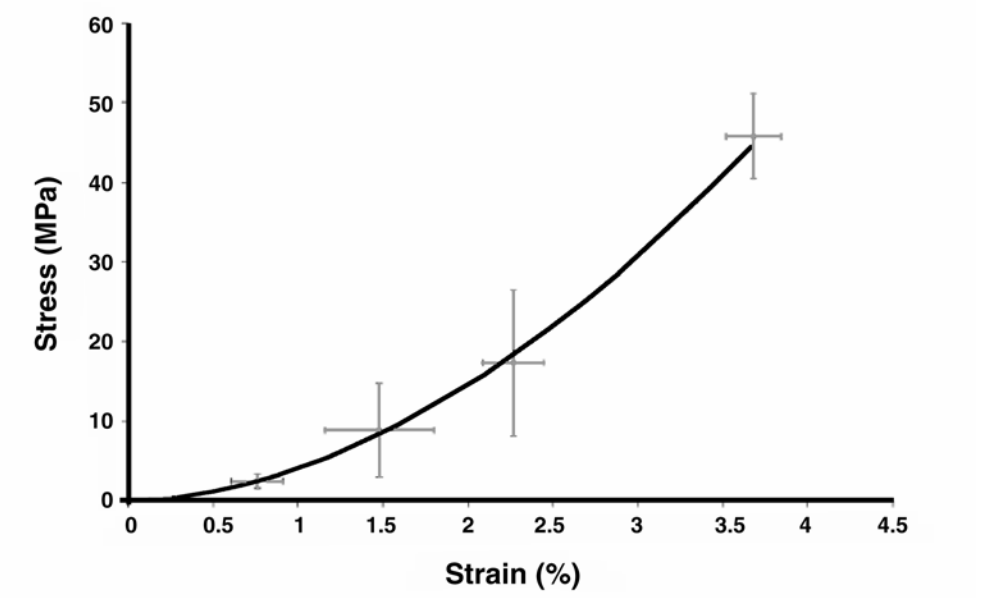



**Figure 16.14**. Isochronal curve at time 2.4 s obtained from stress relaxation tests performed on 15 MCLs: $\hat{T}_1 = 4.095\hat{E}_1^{1.835}$, $R^2 = 0.9984$. The graph shows the nonlinear strain-stiffening behavior found in ligaments. Error bars represent the standard deviation. Reprinted with permission from Hingorani et al. (2004).

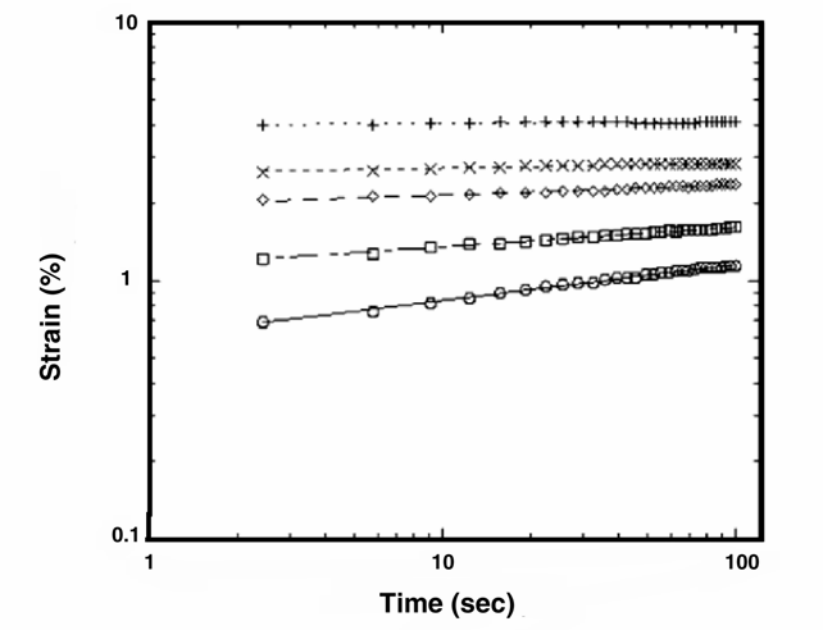



**Figure 16.15**. Creep at multiple levels of stress (log–log scale). The rate of creep decreases as the stress level is increased. Reprinted with permission from Hingorani et al. (2004).

diamond, $\hat{E}_1 = 1.24\%$, $\hat{T}_1 = 13.357t^{-0.1058}$, $R^2 = 0.996$; cross, $\hat{E}_1 = 1.96\%$, $\hat{T}_1 = 27.999t^{-0.0698}$, $R^2 = 0.99$; and plus sign, $\hat{E}_1 = 3.57\%$, $\hat{T}_1 = 41.978t^{-0.0582}$, $R^2 = 0.999$. Creep data at multiple levels of stress reveal that the rate of creep decreases with increasing stress (Figure 16.16). The five types of data points, indicated by different geometric symbols in Figure 16.16, correspond to the following indicated stress levels and creep representations: circle, $\hat{T}_1 = 2{:}98$ MPa; $\hat{E}_1 = 0.60681t^{0.13927}$; $R^2 = 0.99$; square, $\hat{T}_1 = 8{:}08$ MPa; $\hat{E}_1 = 1.1323t^{0.075519}$; $R^2 = 0.99$; diamond, $\hat{T}_1 = 15{:}85$ MPa; $\hat{E}_1 = 1.9495t^{0.039312}$; $R^2 = 0.99$; cross, $\hat{T}_1 = 34{:}89$ MPa; $\hat{E}_1 = 2.5907t^{0.019652}$; $R^2 = 0.96$; and plus sign, $\hat{T}_1 = 54{:}80$ MPa; $\hat{E}_1 = 3.9825t^{0.006287}$; $R^2 = 0.70$.

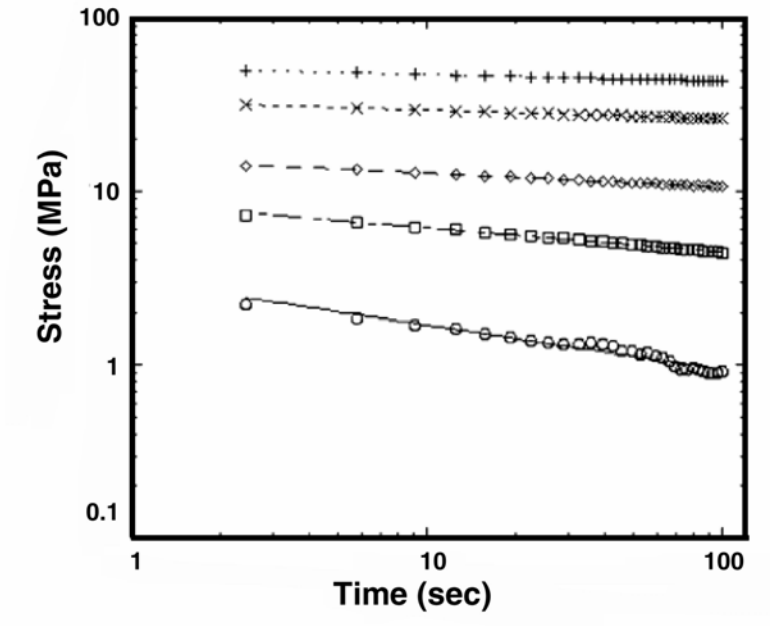



**Figure 16.16**. Stress relaxation at multiple levels of strain (log–log scale). The rate of relaxation decreases as the strain level is increased. Reprinted with permission from Hingorani et al. (2004).

Bonifasi-Lista et al. (2005) reported an experimental study of the linear viscoelastic behavior of the human medial collateral ligament (MCL). In these experiments small strains were superimposed upon a finitely deformed MCL specimen. The finitely deformed state was then taken as the zero reference state for the superimposed small deformations. These reference states for the small deformation were one of three fixed large homogeneous deformation states: 10, 20, and 30% strain. At each fixed large deformation, incremental stress relaxation testing was performed, followed by application of small sinusoidal strain oscillations at three different large strain levels. The test configurations included tensile experiments in the longitudinal and transverse directions of the MCL and shearing experiments along the fiber direction at each of the three fixed finite strain levels.

The peak and relaxed stress–strain curves (Figure 16.17) for the longitudinal, transverse, and shear tests demonstrate that the instantaneous and long-time stress–strain response of the tissue differs significantly between loading conditions of along-fiber stretch, cross-fiber

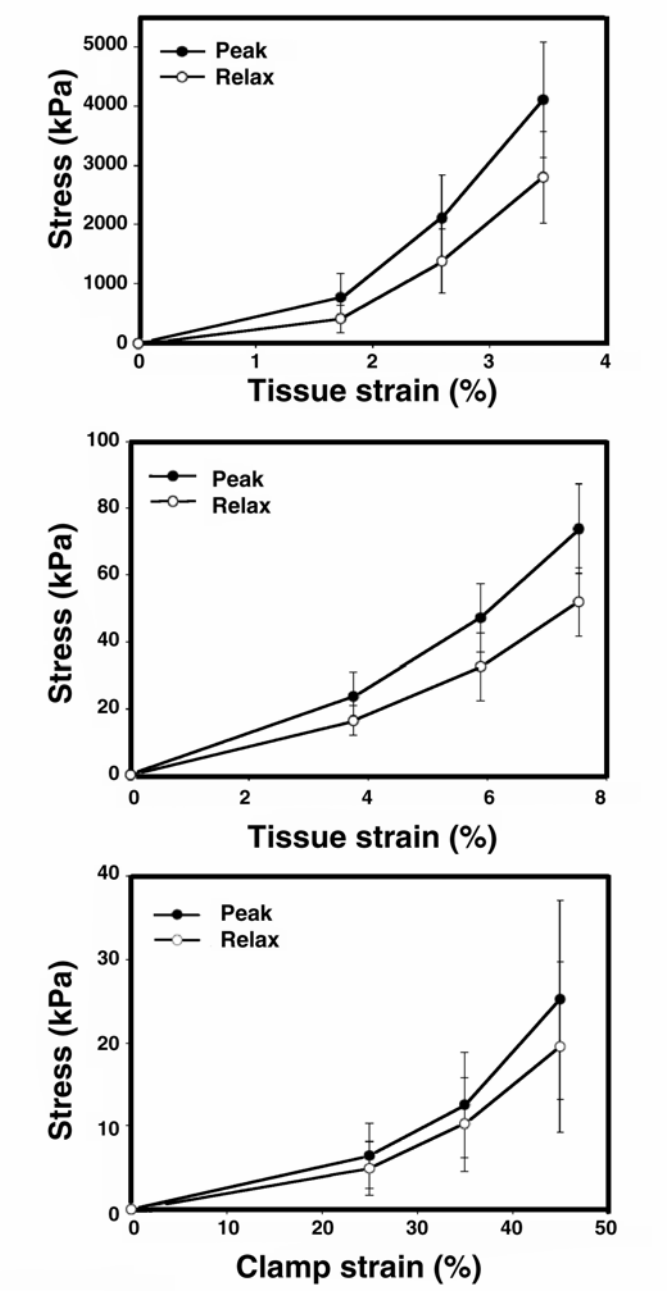



**Figure 16.17**. Peak and equilibrium stress vs. strain (mean ± standard deviation) are shown in these three panels for the incremental stress relaxation tests for the longitudinal (top), transverse (middle), and shear (bottom) tests. Data for the longitudinal and transverse tests are in terms of tissue strain, while data for the shear test are in terms of clamp strain. Note the different scales for the three plots. Reprinted with permission from Bonifasi-Lista et al. (2005).

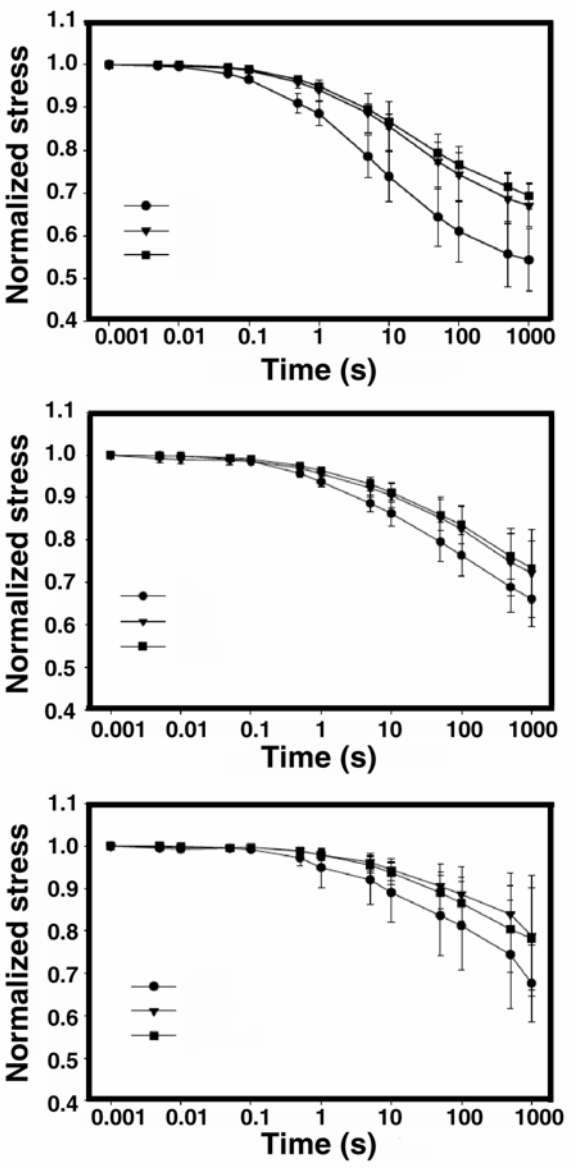



**Figure 16.18**. Reduced stress relaxation curves for longitudinal (top), transverse (middle), and shear tests (bottom). Legends indicate applied clamp-to-clamp strain. Mean ± standard deviation. Reprinted with permission from Bonifasi-Lista et al. (2005).

stretch, and along-fiber shear. The reduced relaxation curves appear to be characterized by two different slopes (Figure 16.18), suggesting at least two relaxation times, and possibly different viscoelastic dissipation mechanisms, for all three test types. Relaxation resulted in stresses that were 60–80% of the initial stress after 1000 s. Incremental stress relaxation proceeded faster at the lowest strain level for all three test types.

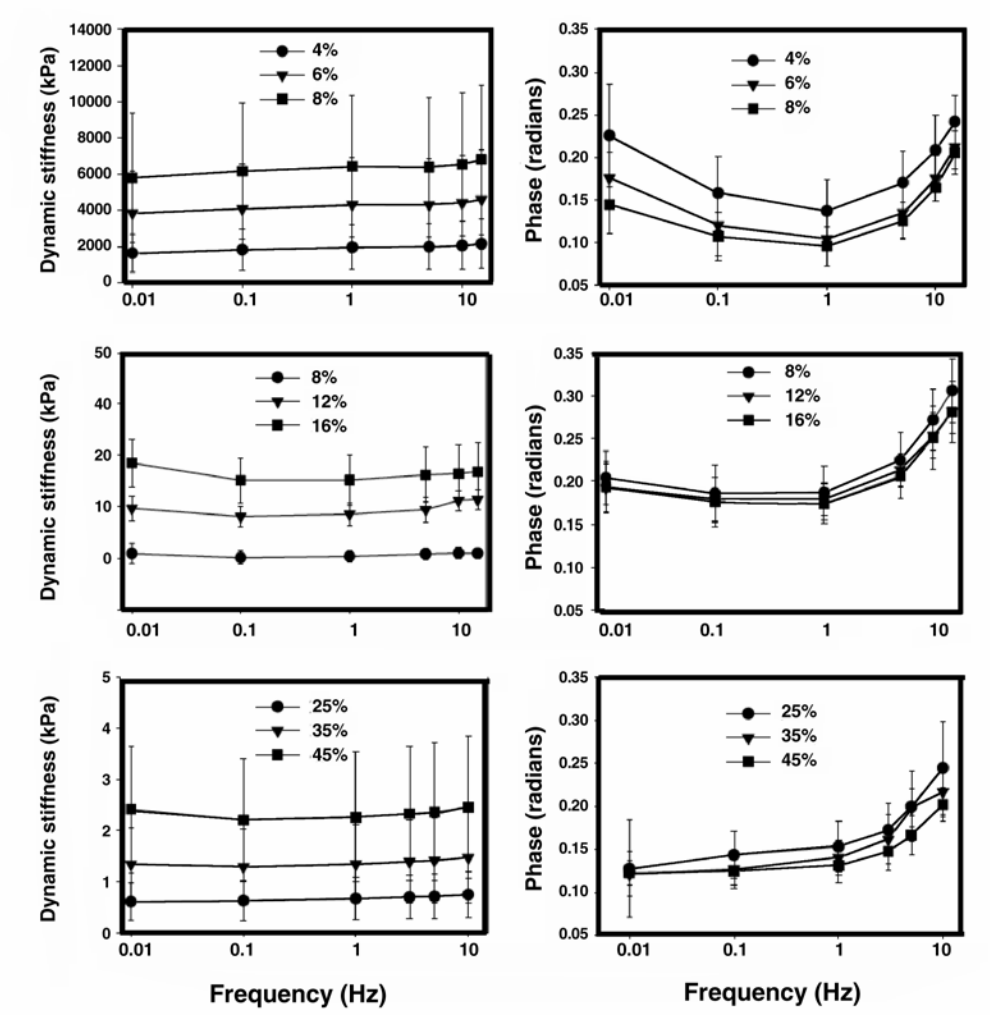



**Figure 16.19**. Dynamic stiffness (left column) and phase angle (right column) as a function of oscillation frequency and strain amplitude for longitudinal (top row), transverse (middle row), and shear (bottom row) test configurations. Legends indicate applied clamp-to-clamp strain. Dynamic stiffness for the longitudinal and transverse tests is presented in terms of measured tissue strain. Mean ± standard deviation. Reprinted with permission from Bonifasi-Lista et al. (2005).

In the cyclic loading experiments the dynamic stiffness varied greatly with test mode and equilibrium strain level (Figure 16.19). The dynamic stiffness exhibited a modest but significant increase with increasing frequency of the applied strain oscillations in the longitudinal and shear tests. The phase angle was unaffected by strain level (with the exception of the lowest strain level for longitudinal samples) but showed a significant increase with increasing strain oscillation frequency (Figure 16.19). There was a minimal effect of test type on the phase angle. The results suggest that the long-time relaxation behavior and the short-time dynamic energy dissipation of ligament may be governed by different viscoelastic mechanisms, yet these mechanisms may affect tissue viscoelasticity similarly under different loading configurations.

## 16.8. INTERSTITIAL FLUID FLOW

The mechanisms driving viscoelastic behavior in ligament are not yet completely understood. Provenzano et al. (2001) suggested that the decrease in relaxation rate with increasing strain could be the result of larger strains causing greater water loss (the wringing-out effect), which causes the tissue to be more elastic (less viscous) than tissues subjected to lower strains. Consistent with that hypothesis, Chimich et al. (1992) reported increased relaxation with increased hydration, and Hannafin and Arnoczky (1994) reported a decrease in tissue water content with cyclic loading, which probably drives fluid out of the ligament during loading. As noted above, the results obtained by Weiss et al. (2002) suggested that viscoelasticity *in shear* does not likely result from fluid flow, an observation that does not contradict the above statements because it has to do with shear rather that axial deformation. Further study of fluid content under varying levels of strain would add insight into the mechanism by which stress relaxation varies with strain.

From the discussion of poroelasticity in the case of incompressibility with constituent-specific constraints on both the matrix material and the pore fluid (§9.5), a point to be recalled here is that, despite the incompressiblity of both phases of the fluid-saturated porous solid, a net volume change of the poroelastic object was possible. It was possible because the pore water could be driven from the fluid-saturated porous solid and, under certain conditions, reimbibed under tension. In tissues this volume change may occur due to fluid exudation (Hannafin and Arnoczky, 1994) or as a result of the inherent compressibility of the solid phase. Because of the limited availability of experimental data describing interstitial fluid flow in ligaments and tendons, FE models have been used to gain a better understanding of the flow behavior. Chen et al. (1998) proposed a microstructural model to study interstitial flow parallel and transverse to the collagen fibril direction based on previously measured values for fibril diameter and water content. Results indicated that ligaments are likely to be much more permeable to flow in the longitudinal direction than in the transverse direction. Experimental data suggest that permeability transverse to the collagen fiber direction in ligaments is approximately an order of magnitude less than the permeability of cartilage. Weiss and Maakestad (2006) measured the permeability of human medial collateral ligament (MCL) in the direction transverse to the collagen fiber direction. These permeability experiments were performed on human MCL specimen when the specimen was pre-strained in finite extension deformations of 10, 20, and 30%. The apparent permeability of human MCL ranged from 0.40 ± 0.05 to 860 ± 0.77 x$10^{-16}$ $m^4$/Ns depending on pre-strain and pressure gradient. There was a significant decrease in apparent permeability with increasing compressive pre-strain and pressure gradient.

The results of Yin and Elliott (2004) provide quantitative evidence for fluid flow as a mechanism that contributes to tendon viscoelasticity. In order to evaluate the contribution of poroelastic effects to the observed viscoelasticity of tendon, Yin and Elliott (2004) determined the poroelastic properties of the mouse-tail tendon. Earlier Elliott et al. (2003) reported on the uniaxial tension testing of mouse-tail tendon fascicles from 3- to 8-week-old C57BL/6 mice. These average-tensile-incremental-stress-relaxation experiments were performed following the model described in Example 9.11.1 using ramp loading $\varepsilon(t) = \dot{\varepsilon}_o[th(t) - (t - t_o)h(t - t_o)]$. The coefficients in ramp loading were constant strain rate $\dot{\varepsilon}_0 = 0.005$/s and period of ramping $t_0 = 1$ s; the period of ramping is the period during which the applied strain rises linearly from 0 to $t_0\dot{\varepsilon}_0 = 0.005$. After time $t_0 = 1$ s, the value of $\varepsilon(t)$ is constant at $t_0\dot{\varepsilon}_0 = 0.005$. In the stress relaxation phase that follows, the strain was held constant for 600 s. The incremental stress–relaxation steps were repeated on a mouse-tail tendon specimen until failure.

The analysis of Yin and Elliott (2004) was based on the transversely isotropic poroelastic model with incompressible constituents (Chapter 9). The solution for this model in unconfined

uniaxial compression or tension was given by Cohen et al. (1998) and is contained as a special case of the solution given in Example 9.11.1. The use of this model fits the physical situation well. It appears that tendon has a much greater axial permeability than radial permeability — 2.5 times greater for rabbit Achilles tendon (Wellen et al., 2004, 2005). Therefore, the pore pressure created by ramp loading will equalize more quickly in the axial than the radial direction, creating a situation in which there is little axial variation in pore pressure or any other variable of interest. The variation of these quantities will be in the transverse plane, as is assumed in the solution given in Example 9.11.1; the temporal response to ramp loading in axial strain is the radial flow of water from the tendon and no axial flow. Yin and Elliott (2004) determined the poroelastic material properties from experimental data reported by Elliott et al. (2003) and described in the previous paragraph. The poroelastic parameters were evaluated as linear increments from specified levels of applied strain like infinitesimal deformations superimposed upon a fixed strain state. The strain level in the fixed strain state did not have an effect on the transverse drained modulus, $E_1^d$, fiber-aligned Poisson's ratio $\nu_{31}^d$, or transverse Poisson's ratio $\nu_{21}^d$. The average values for these parameters were $E_1^d$ = 0.0457 MPa, $\nu_{31}^d$ = 2.73 and $\nu_{21}^d$ = 0.96. However, parameters $E_3^d$ and $\mu^{-1}K_{rr}$ were to be dependent on the reference strain in the state from which they were measured (Figures 16.20, and 16.21). The relationship between fiber-aligned modulus $E_3^d$ and strain $\varepsilon$ was modeled with an exponential law. The exponential relationship fit the data; average $E_3^d$ was 20.7 MPa in the toe region ($\varepsilon$ = 0) and 86.1 MPa in the linear region ($\varepsilon$ = 0.05). (See Figure 16.6 for indications of the toe region and the linear region on a graphic.) The shape of the relationship between $\mu^{-1}K_{rr}$ and $\varepsilon$, where the apparent permeability decreased with applied strain (Figure 16.20), resembled the nonlinear permeability described in §14.10 for cartilage in confined compression. Equation (14.1) for nonlinear permeability in compression, $\mu^{-1}K_{rr} = k = k_o e^{M\tau r\mathbf{E}}$, predicted the permeability well in this case also. The average $\mu^{-1}K_{rr}$ was 5.5 x $10^{-18}$ $m^4$/N-s in the toe region ($\varepsilon$ = 0) and 0.32 x $10^{-18}$ $m^4$/N-s in the linear region ($\varepsilon$ = 0.05). If the viscosity of water is assumed to be $\mu$ = 0.1 N-s/$m^2$, then the average $K_{rr}$ was 5.5 x $10^{-19}$ $m^2$ in the toe region ($\varepsilon$ = 0) and 0.32 x $10^{-19}$ $m^2$ in the linear region ($\varepsilon$ = 0.05). Piecewise linearity was assumed for the solid matrix and permeability material properties. That is, each incremental strain step was assumed to be sufficiently small to permit assumptions of linear elasticity. The linear elastic properties of $E_3^d$ and $\mu^{-1}K_{rr}$, calculated independently at each strain increment, were shown to vary with strain and followed expected trends. The transversely isotropic material properties of the solid matrix were consistent with previously published tendon tissue and fascicle data. Fascicle permeability was similar to previously reported meniscus tissue permeability in tension. Table 14.2 contains a summary of the measured tensile mechanical properties of the human meniscus reported by LeRoux and Setton (2002). The similar permeabilities of both fascicle and tissue-level samples suggest that fluid flow from individual fascicles, not the packing of multiple fascicles together, may be the primary barrier to fluid flow in tendon, and thus the primary mechanism for viscoelasticity. In summary, an anisotropic poroelastic model, with incompressible constituents, of the mechanical behavior of a tendon under uniaxial tensile loading was developed. and fluid flow was quantitatively shown to be a mechanism of tendon viscoelasticity.

## 16.9. THE INSERTIONS OF TENDONS AND LIGAMENTS

In the introduction it was noted that a "direct tendon" is tendon that has a straight and direct course between its muscle connection and its bone connection. However, as Benjamin and Ralphs (1998) point out, the term "enthesis" is commonly used in rheumatology to denote the

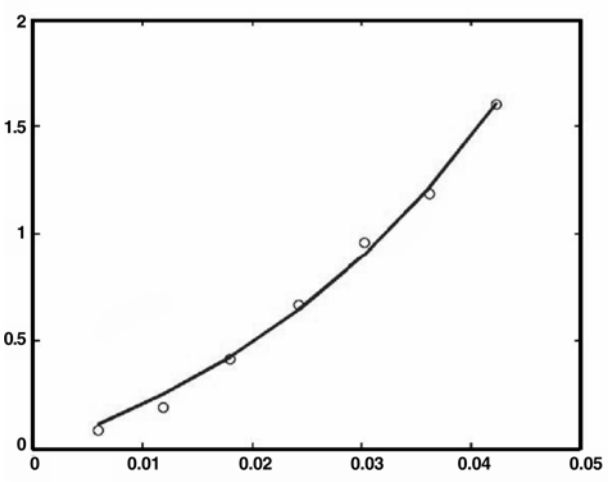



**Figure 16.20**. Values of axial ($x_3$) equilibrium stress calculated at each strain increment show an exponential dependence on strain. It follows that the derivative of stress with respect to strain (not shown) is the fiber-aligned drained elastic modulus, $E_3^d$, and also has an exponential dependence. Reprinted with permission from Yin and Elliott (2004).

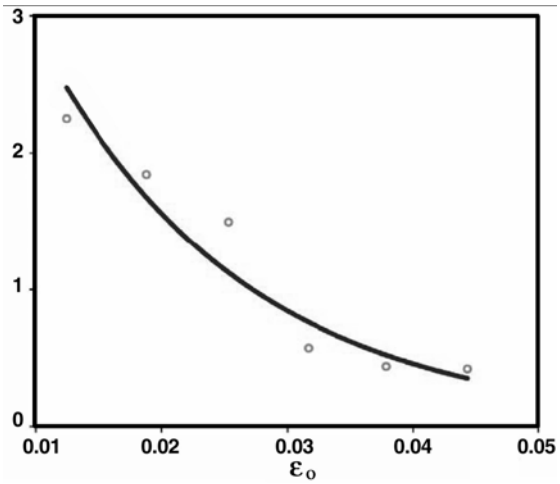



**Figure 16.21**. The permeability, $k$, has the previously observed exponential decrease with strain. Reprinted with permission from Yin and Elliott (2004).

junction between a tendon or ligament and a bone. It has long been known that there are two fundamentally different types of entheses according to the presence or absence of fibrocartilage at the attachment sites. Benjamin and Ralphs (1995) call the two types of entheses fibrocartilaginous and fibrous, but others have called them chondral and periosteal (Knese, 1979) or direct and indirect (Woo et al., 1988). Typically, tendons and ligaments that attach to the epiphyses of long bones or to the short bones of the tarsus or carpus have fibrocartilaginous entheses, whereas those that attach to metaphyses or diaphyses have purely fibrous insertions.

At the tendo-osseous junction, the collagen fibers of the endotenon continue into the bone as the perforating Sharpey fibers and become continuous with the periosteum and bone. The structure of the insertion into bone is similar in ligaments and tendons and consists of four zones; at the end of the tendon (zone 1), the collagen fibers intermesh with fibrocartilage (zone 2). This fibrocartilage gradually becomes mineralized fibrocartilage (zone 3) and then merges into cortical bone (zone 4) (Dolgo-Saburoff, 1929; Cooper and Misol, 1970). A line called the tidemark that lies at the outer limit of calcification separates the zones of calcified and uncalcified fibrocartilage from each other. This tidemark is straight, not crossed by blood vessels, and continuous, with a similar tidemark beneath adjacent articular cartilage.

The cells in the zone of uncalcified fibrocartilage are rounded or oval, and typically arranged in longitudinal rows separated by parallel collagen fibers. The fibrocartilage cells are isolated within the ECM, for, in contrast to the midsubstance of a tendon/ligament, they do not communicate with each other via gap junctions (Ralphs et al., 1998). Thus, enthesis fibrocartilage acts as a barrier to communication between the network of communicating osteocytes in the bone and the fibroblasts that communicate with each other in the tendon. The significance of this barrier and of the lack of vascular communication between tendon/ligament and bone is unclear and a very interesting piece of a puzzle.

Tendon and ligament failure at fibrocartilaginous entheses most often occurs both clinically and experimentally in the subchondral bone, suggesting that the bone itself is weaker than the transitional region between hard and soft tissues (Woo et al., 1988). Since tendons and ligaments narrow transversely as they stretch, the reduced cross-sectional area effectively increases the axial stress level. Knese & Biermann (1958) suggested that enthesis fibrocartilage might mitigate stress concentrations associated with tendon or ligament thinning under stress at the point where it enters the bone. This is consistent with the marked increase in cross-sectional area that many tendons and ligaments exhibit as they approach the bone. In a similar vein, it is also possible that fibrocartilage in wraparound tendons reduces the risk of tendon narrowing at its vulnerable points of contact with bone.

## 16.10. STRUCTURAL ADAPTATION

Like bone, ligament and tendon remodel in response to the mechanical demands placed upon them; they become stronger and stiffer when subjected to increased stress, and weaker and less stiff when the stress is reduced (Noyes, 1977; Tipton et al., 1970). Physical training has been found to increase the tensile strength of tendons (Tipton et al., 1967, 1970; Viidik, 1967, 1979) and of the ligament–bone interface (Tipton et al., 1967; Vüdik, 1968; Cabaud et al., 1980). Tipton and coworkers (1970) compared the strength and stiffness of medial collateral ligaments from dogs that were exercised strenuously for six weeks with the values for ligaments from a control group of animals. The ligaments of the exercised dogs were stronger and stiffer than those of the control dogs, and the collagen fiber bundles had larger diameters.

Immobilization has been found to decrease the tensile strength of ligaments (Noyes, 1977; Amiel et al., 1982). Noyes (1977) demonstrated a reduction in the mechanical properties of the bone–ligament–bone complex in knees of primates immobilized in body casts for eight weeks. When tested in tension to failure, the anterior cruciate ligaments from these animals showed a 39% decrease in maximum load to failure and a 32% decrease in energy stored to failure compared with ligaments from a control group of animals. The immobilized ligaments also displayed more elongation and were significantly less stiff than the control specimens.

Amiel and coworkers (1982) showed a similar decrease in the strength and stiffness of lateral collateral ligaments in rabbits immobilized for nine weeks. As the cross-sectional area of

the specimens did not change significantly, the degeneration of mechanical properties was attributed to changes in the ligament substance itself. The tissue metabolism was noted to increase, leading to proportionally more immature collagen with a decrease in the amount and quality of the crosslinks between collagen molecules.

In the experiments conducted by Noyes (1977), assessment of the effects of a reconditioning program initiated directly after the eight-week immobilization period demonstrated that considerable time was needed for the immobilized ligaments to regain their former strength and stiffness. After five months the reconditioned ligaments still showed considerably less stiffness and 20% less strength than did ligaments from control animals. At 12 months the reconditioned ligaments had strength and stiffness values comparable to those of control group ligaments.

## 16.11. REFERENCES


Amiel D, Woo SL-Y, Harwood FL, Akeson WH. 1982. The effect of immobilization on collagen turnover in connective tissue: a biochemical-biomechanical correlation. *Acta Orthop Scand* **53**:325–333.

Amiel D, Frank C, Harwood F, Fronek J, Akeson W. 1984. Tendon and ligaments: a morphological comparison. *J Orthop Res* **1**:257–265.

Banes AJ, Hu P, Xiao H, Sanderson MJ, Boitano S, Brigman B, et al. 1995. Tendon cells of the epitenon and internal tendon compartment communicate mechanical signals through gap junctions and respond differentially to mechanical load and growth factors. In *Repetitive motion disorders of the upper extremity*, ed. SL Gordon, SJ Blair, LJ Fine LJ, pp. 231–245. Rosemont, IL: American Academy of Orthopedic Surgeons.

Benjamin M, Ralphs JR. 1995. Functional and developmental anatomy of tendons and ligaments. In *Repetitive motion disorders of the upper extremity*, ed. SL Gordon, SJ Blair, LJ Fine LJ, pp. 185–203. Rosemont, IL: American Academy of Orthopedic Surgeons.

Benjamin M, Ralphs JR. 1998. Fibrocartilage in tendons and ligaments — an adaptation to compressive load. *J Anat* **193**:481–494.

Bonifasi-Lista C, Lake SP, Small MS, Weiss JA. 2005. Viscoelastic properties of the human medial collateral ligament under longitudinal, transverse and shear loading. *J Orthop Res* **23**:67–76.

Butler DL. 1995. *Material-structural correlations in ligaments and tendons*. Course notes ASE/EM 605, University of Cincinatti.

Butler DL, Sheh MY, Stouffer DC, Samaranayake VA, Levy MS. 1990. Surface strain variation in human patellar tendon and knee cruciate ligaments. *ASME J Biomech Eng* **112**:38–45.

Butler DL, Guan Y, Kay MD, Cummings JF, Feder SM, Levy MS. 1992. Location-dependent variations in the material properties of the anterior cruciate ligament. *J Biomech* **25**:511–518.

Cabaud HE, Chatty A, Gildengorin V, Feltman RJ. 1980. Exercise effects on the strength of the rat anterior cruciate ligament. *Am J Sports Med* **8**:79–87.

Carlstedt CA, Nordin M. 1989. Biomechanics of tendons and ligaments. In *Basic biomechanics of the musculoskeletal system*, 2nd ed., ed. M Nordin, VH Frankel. Philadelphia: Lea & Febiger.

Chimich D, Shrive N, Frank C, Marchuk L, Bray R. 1992. Water content alters viscoelastic behavior of the normal adolescent rabbit medial collateral ligament. *J Biomech* **25**:831–837.

Chen CT, Malkus DS, Vanderby R. 1998. A fiber matrix model for interstitial fluid flow and permeability in ligaments and tendons. *Biorheology* **35**:103–118.

Chuong CJ, Sacks MS, Johnson RL, Reynolds R. 1991. On the anisotropy of the canine diaphragmatic central tendon. *J Biomech* **24**:563–576.

Cohen, B, Lai, WM, Mow VC. 1998. A transversely isotropic biphasic model for unconfined compression of growth plate and chondroepiphysis. *J Biomech Eng* **120**:491–496.

Cooper RR, Misol S. 1970. Tendon and ligament insertion. A light and electron microscopic study. *J Bone Joint Surg* **52A**:1–20.

Diamant J, Keller A, Baer E, Litt M, Arridge RGC. 1972. Collagen: ultrastructure and its relation to mechanical properties as a function of aging. *Proc R Soc Lond B* **180**:293–315.

Dolgo-Saburoff B. 1929. Über ursprung und insertion der skeletmuskein. *Anat Anz* **68**:80–87.

Elliott DM, Robinson PS, Gimbel JA, Sarver JJ, et al. 2003. Effect of altered matrix proteins on quasilinear viscoelastic properties in transgenic mouse tail tendons. *Ann Biomed Eng* **31**:599–605.

Frank C, McDonald D, Lieber R, Sabiston P. 1988. Biochemical heterogeneity within the maturing rabbit medial collateral ligament. *Clin Orthop* **236**:279–285.

Fratzl P, Misof K, Zizak I, Rapp G, Amenitsch H, Bernstorff S. 1997. Fibrillar structure and mechanical properties of collagen. *J Struct Biol* **122**:119–22.

Fung YC. 1967. Elasticity of soft tissues in simple elongation. *Am J Physiol* **213**:1532–1544.

Fung YC. 1972. Stress–strain history of soft tissues in simple elongation. In *Biomechanics, its foundations and objectives*, ed. YC Fung, N Perrone, M Anliker, pp. 181–208. Englewood Cliffs, NJ: Prentice-Hall.

Fung YC. 1993. Biomechanics — mechanical properties of living tissues, 2nd ed., New York: Springer.

Gardner JC, Weiss JA. 2001. Simple shear testing of parallel-fibered planar soft tissues. *J Biomech Eng* **123**:170–175.

Hannafin JA, Arnoczky SP. 1994. Effect of cyclic and static tensile loading on water content and solute diffusion in canine flexor tendons: an in vitro study. *J Orthop Res* **12**:350–356.

Hansen KA, Weiss JA, Barton JK. 2002. Recruitment of tendon crimp with applied tensile strain. *J Biomech Eng* **124**:72–77.

Haut RC, Little RW. 1972. A constitutive equation for collagen fibers. *J Biomech* **5**:423–430.

Hingorani RV, Provenzano PP, Lakes RS, Escarcega A, Vanderby R. 2004. Nonlinear viscoelasticity in rabbit medial collateral ligament. *Ann Biomed Eng* **32**:306–312.

Holzapfel GA, Gasser TC, Ogden RW. 2001. A new constitutive framework for arterial wall mechanics and a comparative study of material models. *J Elast* **61**:1–48.

Jenkins JT. 1976. *Mechanical Properties of Tendon*. Unpublished MS.

Józsa L, Kannus P. 1997. *Human tendons: anatomy, physiology, and pathology*. Champaign, IL: Human Kinetics.

Kannus P. 2000. Structure of the tendon connective tissue. *Scand J Med Sci Sports* **10**:312–320.

Knese K-H, Biermann H. 1958. Die knockenbildung an sehnenund bandsätzen im bereich ursprunglich chondraler apophysen. *Z Zell Mikrosk Anat* **49**:142–187.

Knese K-H. 1979. Stützgewebe und skelettsystem. In *Handbuch der mikroskopischen anatomie des menschen il/s*, ed. W von Mellendorff, W Bargmann, pp. 1–938. Berlin: Springer.

LeRoux MA, Setton LA. 2002. Experimental and biphasic FEM determinations of the material properties and hydraulic permeability of the meniscus in tension. *J Biomech Eng* **124**:315–321.

McNeilly CM, Banes AJ, Benjamin M, Ralphs JR. 1996. Tendon cells in vivo form a three dimensional network of cell processes linked by gap junctions. *J Anat* **189**:593–600.

Misof K, Rapp G, Fratzl P. 1997a. A new molecular model for collagen based on synchrotron x-ray scattering evidence. *Biophys J* **72**:1376–1381.

Misof K, Rapp G, Landis WJ, Klaushofer K, Hulmes DJS, Fratzl P. 1997b. Mechanical properties of normal and defective collagen — implications for osteogenesis imperfecta, *Bone* **20**(Suppl. 4):11S.

Mommersteeg TJ, Blankevoort L, Kooloos JG, Hendriks JC, Kauer JM, Huiskes R. 1994. Nonuniform distribution of collagen density in human knee ligaments. *J Orthop Res* **12**:238–245.

Nachemson AL, Evans JH. 1968. Some mechanical properties of the third human interlaminar ligament (ligamentum favum). *J Biomech* **1**:211–216.

Nordin M, Frankel VH. 1989. *Basic biomechanics of the musculoskeletal system*, 2nd ed. Philadelphia: Lea & Febiger.

Noyes FR. 1977. Functional properties of knee ligaments and alterations induced by immobilization. *Clin Orthop* **123**:210–222.

Noyes FR, Torvik PJ, Hyde WB, De Lucas JL. 1974. Biomechanics of ligament failure, II: an analysis of immobilization, exercise and reconditioning effects in primates. *J Bone Joint Surg* **56A**:1406–1408.

Pipkin AC, Roger TG. 1968. A nonlinear integral representation for viscoelastic behavior. *J Mech Phys Solids* **16**:59–74.

Provenzano PP, Lakes RS, Keenan T, Vanderby R. 2001. Nonlinear ligament viscoelasticity. *Ann Biomed Eng* **29**:908–914.

Puso MA, Weiss JA. 1998. Finite-element implementation of anisotropic quasilinear viscoelasticity. *J Biomech Eng* **120**:62–70.

Quapp KM, Weiss JA. 1998. Material characterization of human medial collateral ligament. *J Biomech Eng* **120**:757–763.

Ralphs JR, Benjamin M, Waggett AD, Russell DC, Messner K, Gao J. 1998. Regional differences in cell shape and gap junction expression in rat Achilles tendon: relation to fibrocartilage differentiation. *J Anat* **193**:215–222.

Rhee DK, Marcelino J, Baker M, Gong Y, Smits P, Lefebvre V, Jay GD, Stewart M, Wang H, Warman ML, Carpten JD. 2005. The secreted glycoprotein lubricin protects cartilage surfaces and inhibits synovial cell overgrowth. *J Clin Invest* **115**:622–631.

Thornton GM, Oliynyk A, Frank CB, Shrive NG. 1997. Ligament creep cannot be predicted from stress relaxation at low stress: a biomechanical study of the rabbit medial collateral ligament. *J Orthop Res* **15**:652–656.

Thornton GM, Frank CB, Shrive NG. 2001a. Ligament creep behavior can be predicted from stress relaxation by incorporating fiber recruitment. *J Rheol* **45**:493–507.

Thornton GM, Shrive NG, Frank CB. 2001b. Altering ligament water content affects ligament pre-stress and creep behavior. *J Orthop Res* **19**:845–851.

Thornton GM, Shrive NG, Frank CB. 2002. Ligament creep recruits fibers at low stresses and can lead to modulus-reducing fiber damage at higher creep stresses: a study in rabbit medial collateral ligament model. *J Orthop Res* **20**:967–974.

Tipton CM, Schild RJ, Tomanek RJ. 1967. Influence of physical activity on the strength of knee ligaments in rats. *Am J Physiol* **212**:783–793.

Tipton CM, James SL, Mergner W, Tcheng T. 1970. Influence of exercise on strength of medial collateral ligaments of dogs. *Am J Physiol* **218**:894–905.

Uchiyama S, Amadio PC, Ishikawa JI, An KN. 1997. Boundary lubrication between the tendon and the pulley in the finger. *J Bone Joint Surg* **79**:213–218.

Untaroiu CK, Darvish J, Crandall J, Deng B, Wang JT. 2005. Characterization of the lower limb soft tissues in pedestrian finite element models. In *Proc. 19th International technical conference on the enhanced safety of vehicles conference*. Washington, DC: ESV.

Veronda DR, Westmann RA. 1970. Mechanical characterizations of skin — finite deformations. *J Biomech* **3**:111–124.

Viidik A. 1967. The effect of training on the tensile strength of isolated rabbit tendons. *Scand J Plast Reconstr Surg* **1**:141–150.

Viidik A. 1979. Biomechanical behavior of soft connective tissues. In *Progress in biomechanics*, ed. N Akkas, A Aan den Rijn, pp. 75–113. Oslo: Sijthoff and Nordhoff.

Viidik A. 1990. Structure and function of normal and healing tendons and ligaments. In *Biomechanics of diarthroidal joints*, Vol. 1, ed. VC Mow, A Radcliffe, SL-Y Woo, pp. 1–39. New York: Springer.

Weiss JA. 2005. Private communication.

Weiss JA, Gardiner JC. 2001, Computational modeling of ligament mechanics. *Crit Rev Biomed Eng* **29**:1–70.

Weiss JA, Maakestad BJ. 2006. Permeability of human medial collateral ligament in compression transverse to the collagen fiber direction. *J Biomech* **39**:276–283.

Weiss JA, Maker BN, Govindjee S. 1996. Finite element implementation of incompressible, transversely isotropic hyperelasticity. *Computer Methods Appl Mech Eng* **135**:107–128.

Weiss JA, Gardiner JC, Bonifasi-Lista C. 2002. Ligament material behavior is nonlinear, viscoelastic and rate-independent under shear loading. *J Biomech* **35**:943–950.

Wellen J, Helmer KG, Grigg P, Sotak CH. 2004. Application of porous-media theory to the investigation of water ADC changes in rabbit Achilles tendon caused by tensile loading. *J Magn Reson* **170**:49–55.

Wellen J, Helmer KG, Grigg P, Sotak CH. 2005. Spatial characterization of $T1$ and $T2$ relaxation times and the water apparent diffusion coefficient in rabbit Achilles tendon subjected to tensile loading. *Magn Reson Med* **53**:535–544.

Woo SL. 1982. Mechanical properties of tendons and ligaments, I: Quasi-static and nonlinear viscoelastic properties. *Biorheology* **19**:385–396.

Woo SL-Y, Maynard J, Butler D, Lyon R, Torzilli P, Akeson W., et al. 1988. Ligament, tendon, and joint capsule insertions to bone. In *Injury and repair of the musculoskeletal soft tissues*, ed. SL-Y Woo, JA Buckwalter, pp. 133–166. Park Ridge, IL: American Academy of Orthopaedic Surgeons.

Woo SL-Y, Peterson RH, Ohiand KJ, Sites TJ, Danto MI. 1990. The mechanical properties of the medial collateral ligament in skeletally mature rabbits: a biomechanical and histological study. *J Orthop Res* **8**:712–721.

Yin L, Elliott DM. 2004. A biphasic and transversely isotropic mechanical model for tendon: application to mouse tail fascicles in uniaxial tension. *J Biomech* **37**:907–916.

# 2

# MECHANICAL MODELING OF BIOLOGICAL STRUCTURES

The reader of this chapter may draw inspiration from the following quote from research biologist Albert Harris (Harris, 1994): "Systems of interacting forces and stimuli don't have to be very complicated before the unaided human intuition can no longer predict accurately what the net result should be. At this point computer simulations, or other mathematical models, become necessary. Without the aid of mechanicians, and others skilled in simulation and modeling, developmental biology will remain a prisoner of our inadequate and conflicting physical intuitions and metaphors." The theme of this chapter is summarized by a paragraph from the book entitled "How to Solve It" (Polya, 1945): "In order to translate a sentence from English into French two things are necessary. First, we must understand thoroughly the English sentence. Second, we must be familiar with the forms of expression peculiar to the French language. The situation is very similar when we attempt to express in mathematical symbols a condition proposed in words. First, we must understand thoroughly the condition. Second, we must be familiar with the forms of mathematical expression."

## 2.1. INTRODUCTION

From the beginning to the end of the 20th ccntury, the practice of medicine turned from an emphasis on the medical arts to an emphasis on the medical sciences and technology. The need for people trained both in the biological and physical sciences has increased because of this change in emphasis. The quantification and measurement of the relevant health variables has become a more important activity and the modeling and simulation of the physiological processes and healing strategies have become widespread activities in health related research. Early in the century it was argued by some that the biological and medical sciences would never be amenable to study with the type of mathematical models that had been so successful in the physical sciences for the previous two centuries. Few doubt the utility of mathematical modeling in the biological sciences today; note the quote from the work of Albert Harris above.

Typical models that have been employed in the mechanical analysis of biological tissues are described in this chapter. These are biomechanical models. Biomechanics is the application of classical mechanics to biological problems; thus, biomechanics is based on both classical mechanics and biology. There is an aspect of the application of conservation principles of me-

chanics (those of mass, momentum, angular momentum, energy, etc.) that is an artisan-like skill that requires some experience on the part of the modeler. Most engineering students acquire this skill when they learn to construct "free object diagrams" to apply Newton's laws to solid objects or to draw "control volumes" to apply the conservation principles of mechanics to fluids. These diagrams or volumes are selected to satisfy the criteria of the modeler, which are generally to define the problem by representing the unknown quantities and the known quantities in a way that the conservation principles can be applied to obtain equations representing the unknown quantities in terms of the known quantities. The construction of free object diagrams or control volumes is an artisan-like skill because there is not a unique way to construct them; the modeler must have insight into the problem. Infinitely many such physically correct diagrams can be drawn, but it is likely that only a few will yield the modeler the relationship between quantities that he or she sought. This creative aspect of the application of conservation principles of mechanics is prominent in biomechanics because of the great diversity of structures considered. These structures range in size from a portion of a molecule, through cell-level structures, to organs, and to the entire body.

Both free object diagrams and control volumes are drawings made to simplify the application of conservation principles to a particular physical situation. A conservation principle can often be written in the form of an accounting statement:

[The time rate of change of a quantity in a system] =
[the amount of the quantity coming into the system per unit time] –
[the amount of the quantity leaving the system per unit time] +
[the amount of the quantity produced within the system per unit time] –
[the amount of the quantity consumed within the system per unit time].

Thus the application of the conservation of mass (or momentum) of a fluid employs a drawing to balance the net flow or change in the quantity, much like a financial account for an organization is balanced.

Note that the word "body" used in modeling non-biological applications of Newton's laws, for example "free body diagrams" and "rigid body motion," is replaced in this work by the word "object"; thus, reference is made here to "free object diagrams" and "rigid object motions." The reason for this shift in terminology is to avoid the use of the same word for two different meanings in the same phrase, like a "free body diagram" of a body or a "rigid body motion" of a body.

In the section that follows, the relationship between models and the real physical world is discussed. There is then a section with guidelines for modeling biological tissues and solving biomechanics problems. A section on the types of models used in biomechanics is followed by seven sections that describe particle models, rigid object models, continuum models, lumped parameter models, electrical analogs of lumped parameter models, statistical models and cellular automata, respectively. The material in each of these sections is illustrated by applications to biomechanics problems.

The material in this chapter — which describes the various models, particle, rigid object, deformable continuum, lumped parameter, molecular and statistical, and cellular automata — may be viewed as a brief overview of biomechanics. Whole-body biomechanics, which includes occupational and sports biomechanics, generally employs the rigid object model, or linked rigid object models. Cell and tissue level biomechanics, as well as implant and injury biomechanics, generally employ deformable continuum models. Biological, as well as non-biological, molecules are modeled as ensembles whose behavior is statistically analyzed. Cellular automata already have significant applications in fluid flow analysis and developmental

biology. However, the modeler should view these model types as tools, and the task of the modeler is to select the proper tool for the problem at hand.

The content of this chapter is not material that can be learned by rote memorization. It is material that must be thought about and practiced in order to acquire a modeler's skill. In the next section the first problem in modeling, the concept of time, is considered, and then that of space.

## 2.2. MODELS AND THE REAL PHYSICAL WORLD

Models have been found to be the best tools for the analysis of physical problems, including the physical and mechanical problems associated with biological structures. The basic elements of these models are Euclidean or classical geometry and the concept of time. The concept of time is intuitive, while our mathematical model of time, the real line, that is to say, the line representing all real numbers, is abstract. The connection between the mathematical abstraction and our intuitive perception of time is a philosophical matter that should be accepted by the reader; this relationship is rigorously discussed in a classical book (Weyl, 1987) by the German-American mathematician Hermann Weyl (1883–1955) entitled "The Continuum." Once one has accepted the real line as a geometric model for time, the next step of accepting the real line as a geometric model for a one-dimensional structure (such as a string or a tendon) is not difficult. Real lines are used in forming one-, two-, and three-dimensional Cartesian reference coordinate systems for one-, two-, and three-dimensional Euclidean spaces. The real lines used as the reference Cartesian coordinate systems in two and three dimensions are mutually orthogonal.

In the initial stages of model construction for an object or a tissue, cell or molecule, it is necessary to project the object into Euclidean space (Figure 2.1). The portion of the three-dimensional Euclidean space that the object occupies is often an exact replica of the space in

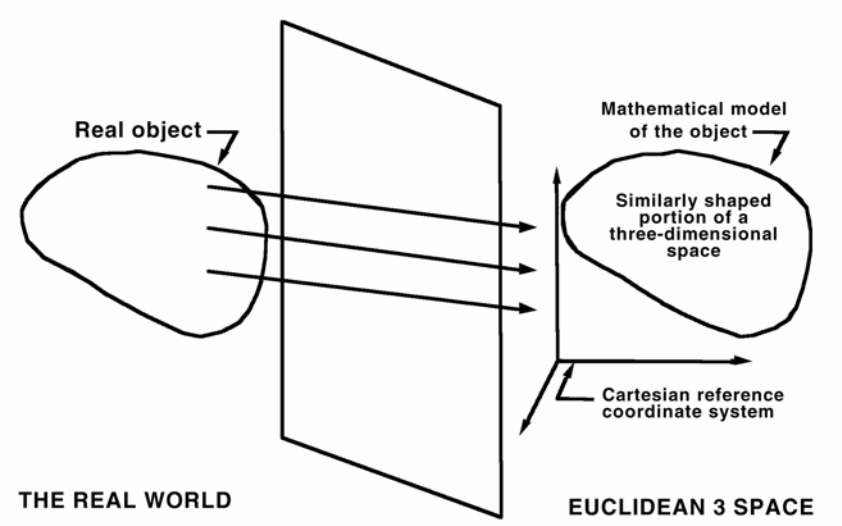



**Figure 2.1**. The Euclidean space model of a real object.

the real world occupied by the real object. However, the structure of the real object is not carried over into the model unless the modeler makes provision for it. For example, if the object is fibrous, the fibers are not represented in the model unless the modeler explicitly provides for their representation. The advantage of the model is that all the points in the real object now have Cartesian addresses. The triplet of Cartesian coordinates $(x_1, x_2, x_3)$ locates a point in the Euclidean space occupied by a particular point in the real object. This permits the measurement of distance between points in the object, and if the object moves or deforms the resulting motion can be quantitatively documented. The volume of the object and its centroid may be determined by use of the integral calculus. The greatest advantage, however, is the ability to define functions of physical interest in terms of the reference coordinate system. Thus, for example, the temperature distribution throughout the object can be specified by a function $\theta = \theta(x_1, x_2, x_3)$ defined for all of the Cartesian coordinates $(x_1, x_2, x_3)$ located within the object. If the function is smooth, then a derivative of the function can be taken and the temperature gradient is determined for all of the Cartesian coordinates $(x_1, x_2, x_3)$ located within the object. The point of these remarks is that the consequence of making a Euclidean space model of an object is that it permits the powerful computational machinery of classical geometry and the integral and differential calculus to be used to calculate quantities of physical or biological interest.

Since the representation of physical phenomena must be independent of the observer, it is necessary to express physical quantities in ways that are independent of coordinate systems. This is because different observers may select different coordinate systems. It therefore becomes a requirement that physical quantities be invariant of the coordinate system selected to express them. On the other hand, in order to work with these physical quantities, it is necessary to refer physical quantities to coordinate systems, as was done in Figure 2.1. The resolution of this conflict is to express physical quantities as tensors; vectors are tensors of order one and scalars are tensors of order zero. Thus, it is no surprise that in classical mechanics the essential concepts of force, velocity, and acceleration are all vectors; hence the mathematical language of classical mechanics is that of vectors. In the mechanics of deformable media the essential concepts of stress, strain, rate of deformation, etc., are all second-order tensors; thus, by analogy, one can expect to deal quite frequently with second-order tensors in this branch of mechanics. The reason for this widespread use of tensors is that they satisfy the requirement of invariance of a particular coordinate system on one hand and yet permit the use of coordinate systems. Thus a vector $\mathbf{u}$ represents a quantity that is independent of coordinate system, i.e. the displacement of a point on an object, yet it can be expressed relative to the three-dimensional Cartesian coordinate system with base vectors $\mathbf{e}_\alpha$, $\alpha$ = I, II, III, as $\mathbf{u} = u_{\mathrm{I}}\mathbf{e}_{\mathrm{I}} + u_{\mathrm{II}}\mathbf{e}_{\mathrm{II}} + u_{\mathrm{III}}\mathbf{e}_{\mathrm{III}}$, and also expressed relative to another three-dimensional Cartesian coordinate system with base vectors $\mathbf{e}_i$, $i$ = 1, 2, 3, by $\mathbf{u} = u_1\mathbf{e}_1 + u_2\mathbf{e}_2 + u_3\mathbf{e}_3$. The vector $\mathbf{u}$ and the two coordinate systems are illustrated in Figure 3.2. These two representations of the components of the vector $\mathbf{u}$ are different, and both are correct because a rule, based on the relationship between the two vector bases $\mathbf{e}_\alpha$, $\alpha$ = I, II, III, and $\mathbf{e}_i$, $i$ = 1, 2, 3, can be derived for calculating one set of components in terms of the other. Thus the vector $\mathbf{u}$ has a physical significance independent of any coordinate system, yet it may be expressed in component form relative to any coordinate system. The property of vectors is shared by all tensors. This is the reason that tensors, as well as vectors and scalars, play a leading role in modeling biomechanics phenomena.

## 2.3. GUIDELINES FOR MODELING BIOLOGICAL TISSUES AND SOLVING BIOMECHANICS PROBLEMS

A well-known guide to problem solving in the mathematical and physical sciences is the book by Polya (1945) entitled *How to Solve It*. George Polya (1887–1985) was a Hungarian-American mathematician. The book deals with problem solving in general and recommends four steps. The ***first*** step is to understand the problem. To accomplish this, the problem solver must study the problem carefully, understand the definitions employed, ascertain what is to be determined (the unknowns), what is known or given, and what the restrictions or conditions are upon the outcome. It is recommended that a diagram be drawn in the first step and that a notation be introduced. At least one free object diagram, or a balance diagram, of a physical quantity that is conserved (e.g., force, moment, mass, or energy) is usually most helpful. Be prepared to revise notation as the solution to the problem develops; the problem will appear simpler when the most efficient notation is introduced. The ***second*** step is to devise a plan to solve the problem, that is to say, to connect the known(s) or given(s) to the unknown(s). It is at this point that Polya recommends that you review your experience with problems to determine if you have ever seen a problem similar to the one that is now before you. If a plan of solution does not emerge in your mind, try to restate the problem. Reformulate the knowns, unknowns and the conditions or restrictions of the problem. The ***third*** step is to execute your plan of solution. Try to verify each step of your analysis or calculation. The ***fourth*** step is an examination of the solution obtained, a double check. Does the answer make sense? Can the result be verified in a different way? If the result is changed by a small amount, does the answer still make sense? Are the dimensions of the result correct?

When first analyzing quantitative problems in biomechanics, an analysis of the order of magnitude of the time and length scales involved is often most fruitful. Frequently this type of analysis either excludes the type of phenomenon under consideration or suggests that the type of phenomenon under consideration is not too far fetched. The length and time scales in biological problems can vary over many orders of magnitude due to the hierarchical structures and the diverse phenomena occurring on many different time scales. For example, the mechanical loading of a tissue may be on the time scale of seconds and the adaptation of tissue to its mechanical load environment on the time scale of weeks.

The solution to research problems in biomechanics is different from the solution of textbook problems in that the person doing the modeling must have an understanding of the basic biology of the problem, or a theory of the basic biology. It is advised that the modeler obtain knowledge of the problem by reading the relevant literature, which can be located by consulting the appropriate library databases, medical and engineering indices, and searching the web. The modeler should try to extract from the biology and the mechanics the variables that are most significant in the problem, then identify the conservation laws and constitutive models that relate the variables identified. The formal solution of the problem is then executed and the modeler has the task of interpreting the solution in terms of the model. The modeler must reverse the step illustrated in Figure 2.1 and interpret the model solution in terms of the real world. A fallacy that sometimes occurs in a modeler's thinking is that he or she begins to think of the model as the reality, rather than as a mental construct. It is thus important that in the modeling process the modeler passes both ways, from the real world to the model initially, then from the model to the real world in the end. If the modeler confuses the model with the reality, or vice versa, the modeling process may not be effective.

## 2.4. THE TYPES OF MODELS USED IN BIOMECHANICS

It is possible to divide the discipline of mechanics according to the predominant type of motion an object is considered to be undergoing. The three types of motion are translational, rotational, and deformational. In translational motion all the points of the moving object have the same velocity vector at any instant of time. A translational motion is illustrated in Figure 2.2a. In pure rotational motion the velocities of all the points of the moving object, at any instant, are proportional to the distance of the point from one single fixed axis. This situation is illustrated in Figure 2.2b in the special case, where the fixed axis is perpendicular to the plane of the page. A deformational motion (Figure 2.2c) is a motion in which some points on the same object move relative to one another. It can be shown that the motion of any object or material system can, at any time, be decomposed into the sum of three motions — a translational motion, a rotational motion, and a deformational motion. If there are many objects (e.g., molecules) and only average properties of the ensemble are sought by statistical methods, the model is said to be one of statistical mechanics.

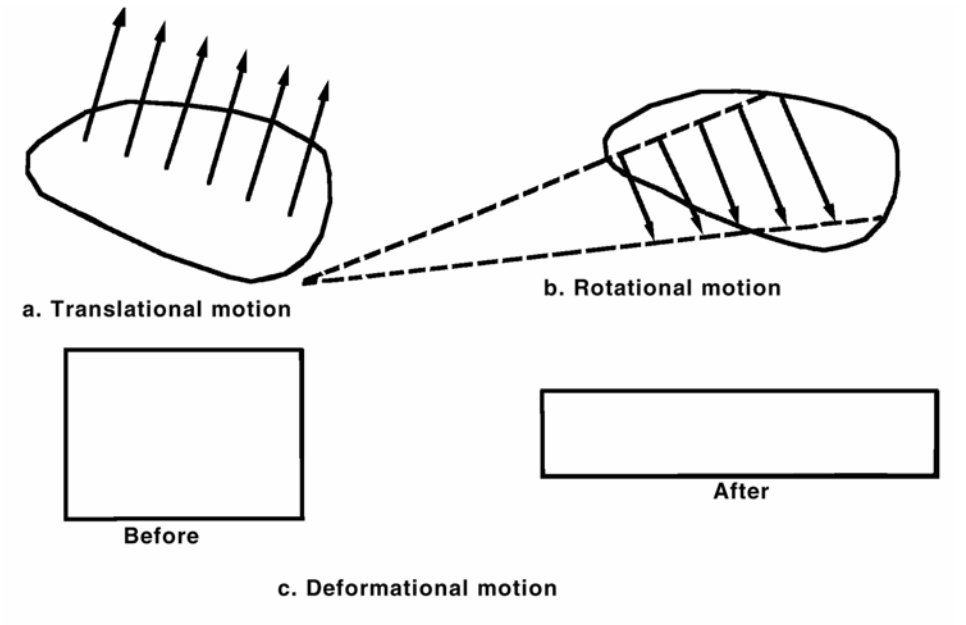



**Figure 2.2**. The three types of motion possible for an object.

These motions suggest three of the six types of models of objects used in mechanics: the particle model, the rigid object model, and the deformable continuum model. These models of objects are differentiated from one another on the basis of the type of motion modeled. The particle model only emulates the translational motion of the object, the rigid object model emulates both translational and rotational motion of the object, and the deformable continuum model emulates all three types of motion. The first two models — the particle model and the rigid object model — are described in mechanics books dealing with statics and dynamics of particles and rigid objects. The deformable continuum model is described in books dealing with the mechanics or strength of materials or in books on elasticity and fluid or continuum mechanics.

There is an important fourth category of model used in mechanics that overlaps the first three model types: the lumped parameter model, a very important model type in biomechanics. The particle model, rigid object model, deformable continuum model, and lumped parameter model are discussed in the next five sections.

The fifth and sixth categories of model used in representing the mechanics of biological tissue are the statistical models and cellular automata models. Cellular automata models are always digital models, and statistical models are often also digital. Various statistical models allow the molecules to have any of these motion types but consider the average properties of a large number of molecules. Statistical models will be found in books on statistical mechanics, the kinetic theory of gases, and the kinetic theory of rubber. Cellular automata models replace equations by the simple step-by-step procedures of computer programs. In these algorithms time and space are no longer considered as continuous but as digital steps. The continuum is replaced by a grid or lattice. A section is devoted to each of these model types in this chapter. The remaining chapters comprise an elaboration of the deformable continuum model for biological tissues.

## 2.5. THE PARTICLE MODEL

The particle model is the simplest model in the hierarchy of models in classical mechanics. This model of an object considers the entire mass of the object as located at the center of mass and only the translational motion of the mass center is modeled. Thus the image of the model shown in Euclidean space in Figure 2.1 shrinks to a mass point located at the mass center, as illustrated in Figure 2.3. Since the mass center is a point, the particle model is a point model;

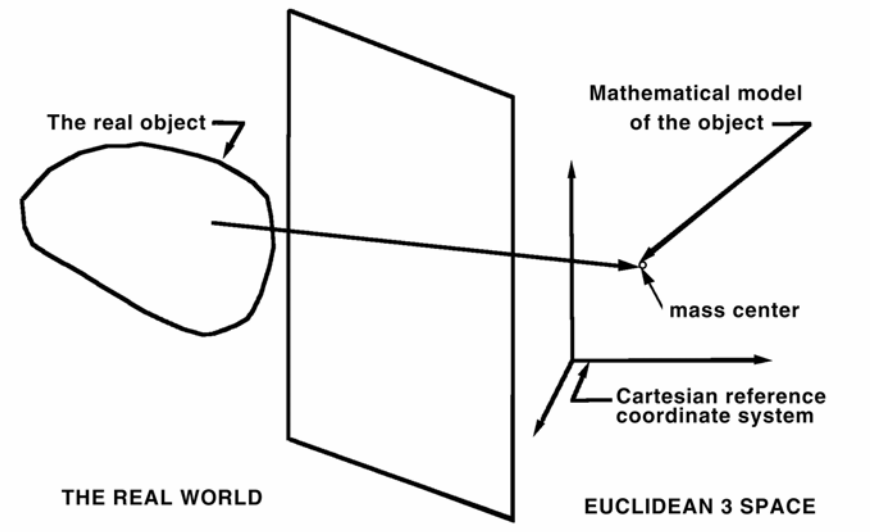



**Figure 2.3**. The particle model of a real object.

rotational motions and deformations of the object are neglected. The English natural philosopher Isaac Newton (1642–1727) created the particle model when he took the sun and planets to be particles and used his universal law of gravitation and his second law of motion to provide an analytical derivation of the three empirical laws of the German astrologer-astronomer Johannes Kepler (1571–1630). In particular, Newton's model showed that the planets move around the sun in elliptical orbits, a fact previously established by Kepler's observational data. Moments and rotational motions are not considered in the particle model; they are considered in the rigid object model.

The modeling structure described above may be employed as a framework for the statement of Newton's second law. This may be accomplished by letting the vector $\mathbf{p}$ denote the position of a typical point in the mathematical model of the object, $\mathbf{p} = x_1\mathbf{e}_1 + x_2\mathbf{e}_2 + x_3\mathbf{e}_3$, where $\mathbf{e}_1$, $\mathbf{e}_2$ and $\mathbf{e}_3$ are the Cartesian unit base vectors. The position vector to the mass center of the object is denoted by $\mathbf{p}_{(mc)} = x_{(mc)1}\mathbf{e}_1 + x_{(mc)2}\mathbf{e}_2 + x_{(mc)3}\mathbf{e}_3$. If the object is moving, then the location of the point of the object is changing in the Euclidean space and the Cartesian coordinates $x_1$, $x_2$, $x_3$ are all continuous, twice differentiable, functions of time, $x_1 = x_1(t)$, $x_2 = x_2(t)$, $x_3 = x_3(t)$, and it is therefore possible to compute the velocity of the mass center of the object, or of any point on the object, as well as its acceleration. The acceleration of the mass center is given by

$$\mathbf{a}_{mc} = (d^2x_{(mc)1}/dt^2)\,\mathbf{e}_1 + (d^2x_{(mc)2}/dt^2)\,\mathbf{e}_2 + (d^2x_{(mc)3}/dt^2)\,\mathbf{e}_3. \tag{2.1}$$

Denoting the total mass of the object by $m$ and the sum of the forces acting on the object by $\mathbf{F}$, a statement of the second law of Newton can then be written in the form

$$\mathbf{F} = m\,\mathbf{a}_{mc}. \tag{2.2}$$

As an illustration of the particle model in biomechanics, consider the question of determining the airborne trajectory of a ski jumper. In the air the ski jumper is acted upon by the attraction of gravity, the drag of the wind, and the momentum established in the downhill run before contact with the ground ceased (Figure 2.4). The ski jumper's trajectory is determined by solution of Newton's second law with these specified forces. The trajectory is obtained by an analysis that is completely equivalent to that of an artillery shell or a suborbital rocket. While the particle model is adequate for determining the trajectory of the skier, it is an inadequate model for transition of the skier's position from the crouch of the downhill run to the erect and forward leaning body posture adopted for flight, and inadequate to deal with the question of impact upon landing.

This traditional method of analysis of macroscopic force systems is also applied at the microscopic level. For example, one method of studying the response of cells to mechanical loading situations is to culture or grow the cells on a surface such as glass and subject the surface to fluid shear stresses, as illustrated in Figure 2.5a. Some of the forces that act on the cell in this flow situation are shown in Figure 2.5b. The forces that act on a cell include the weight of the cell, $W_{cell}$, the buoyant force on the cell due to its aqueous environment, $W_{buoyant}$, the adhesive force of the cell to its substrata, $F$, the fluid pressure on the cell, the shear force due to fluid flowing over the surface of the cell, forces due to electrical charge or magnetic fields, and self-generated forces by the cell. The same forces act on these cells in vivo, but the forces are illustrated in vitro because it is an easier situation to visualize and to draw. The weight of the cell, $W_{cell,}$ is about one pico-Newton. The cell is subjected to a buoyancy force as a consequence of its immersion in an aqueous environment. The buoyant force on the osteocyte is equal to the weight of the water it displaces, $W_{buoyant} = 0.9$ pN, nine-tenths of a pico-Newton. The processes of cell adhesion to substrata, as well as the influence of substratum surface properties on cell adhesion, have been studied in recent years by subjecting cells, in vitro, to

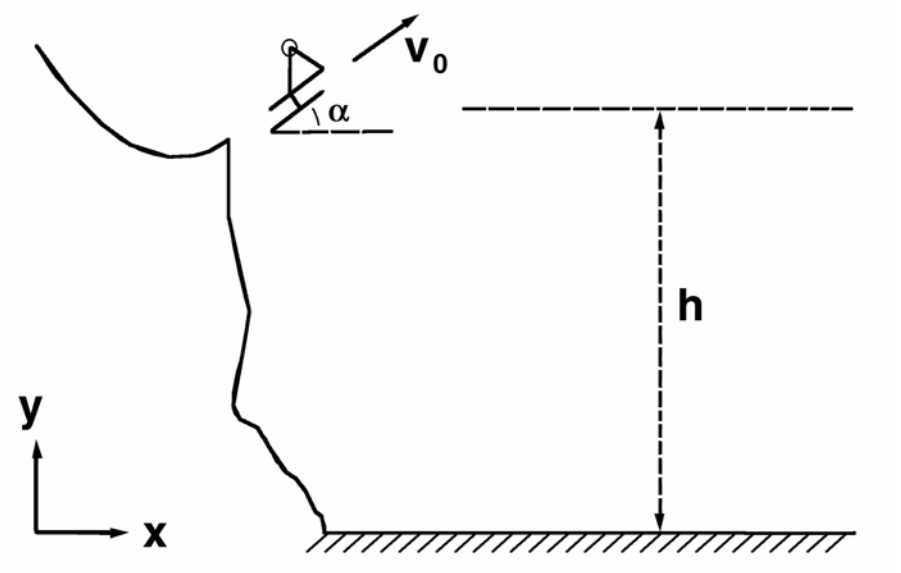



**Figure 2.4**. An illustration of the particle model in biomechanics, determining the airborne trajectory of a ski jumper. In the air the ski jumper is acted upon by the attraction of gravity, the drag of the wind, and the momentum established in the downhill run before contact with the ground ceased. The ski jumper's trajectory is determined by the solution of Newton's second law with these specified forces.

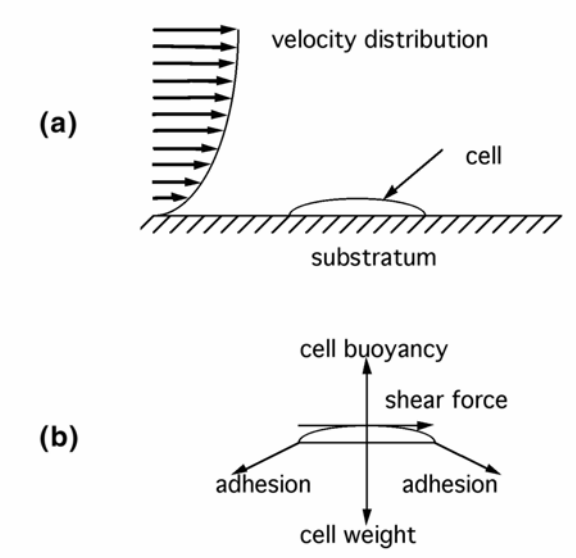



**Figure 2.5**. (a) A cell adherent to a substratum and subjected to a fluid shearing action. (b) An analysis of the forces on a cell of Fig. 2.5a, the cell adherent to a substratum and subjected to a fluid shearing action.

fluid shear stress. Adhesion of cells to solid substrata is influenced by several substratum surface properties including substratum wettability, surface roughness and surface charge. The force $F$ of adhesion for a single cell is the surface area $A$ that the cell presents to the flow times the shear stress when the cell is removed from the surface by the fluid shear stress. The shear stress at which cells capable of adhesion detach from a glass substratum is about 400 dynes/cm$^2$. Assuming an appropriate surface area, the adhesive force on the cell $F$ is about 6000 pN. Since $W_{\text{cell}} = 1$ pN, $F = 6000\ W_{\text{cell}}$. Thus, a cell can express adhesive forces that are three to four orders of magnitude larger than the cell weight. For man on the surface of the earth, the largest forces with which we must cope are generally those due to gravity, that is to say, the forces that manifest themselves in the weight of objects. It is quite a different story for the cell because the largest force system they experience is due to adhesion. The adhesive forces on a cell are three to four orders of magnitude larger than the gravitational forces on a cell. More importantly, cells control their adhesive forces; man does not control gravity.

**Problem**

2.5.1. A ski jumper leaves the ski jump with a velocity $v_o$ in a direction that is an angle $\alpha$ above the horizon (see Figure 2.4). The final point on the ski jump is an elevation $h$ above the valley floor. If the drag of the wind is neglected, show that the horizontal and vertical velocities, $v_x$ and $v_y$, respectively, of the skier as he reaches the flat valley floor are given by $v_x = v_o \cos\alpha$ and $v_y = -((v_o \sin\alpha)^2 + 2gh)^{1/2}$. Find the time, $t_{\text{touch}}$, at which the skier touches the valley floor as a function of $v_o$, $\alpha$, $h$, and $g$, the acceleration due to gravity.

## 2.6. THE RIGID OBJECT MODEL

The rigid object model differs from the particle model in that the rotational motion as well as the translational motion of the object is considered. Deformations are neglected; hence the adjective "rigid" modifying object. Thus, not only Newton's second law of motion is involved, but also Euler's equations (after their creator, the Swiss mathematician/engineer/physicist Léonard Euler, 1707–1783) for the rotational motion. Euler's equations are special forms of the conservation of angular momentum expressed in a reference coordinate system at the mass center of the rigid object (or at a fixed point of rotation of the object), fixed to the rigid object, and coincident with the principal axes of inertia. If $I_{11}$, $I_{22}$ and $I_{33}$ represent the principal moments of inertia (see §A.8), and $M_1$, $M_2$, and $M_3$ represent the sums of the moments about the three axes, then Euler's equations may be written in the form

$$\begin{aligned} M_1 &= I_{11}(d\omega_1/dt) + \omega_2\omega_3(I_{33} - I_{22}), \\ M_2 &= I_{22}(d\omega_2/dt) + \omega_3\omega_1(I_{11} - I_{33}), \\ M_3 &= I_{33}(d\omega_3/dt) + \omega_1\omega_2(I_{22} - I_{11}), \end{aligned} \tag{2.3}$$

where $\omega_1$, $\omega_2$, and $\omega_3$ are the components of the angular velocity about the respective coordinate axes. In the case when there is only one nonzero component of the angular velocity, $\omega_3$, and $\omega_1 = \omega_2 = 0$, then (2.3) reduces to

$$M_3 = I_{33}\alpha_3, \tag{2.4}$$

where $\alpha_3 = d\omega_3/dt$ is the angular acceleration. This is the one-dimensional form of the conservation of angular momentum, or of Euler's equations, a form that usually appears in basic mechanics texts.

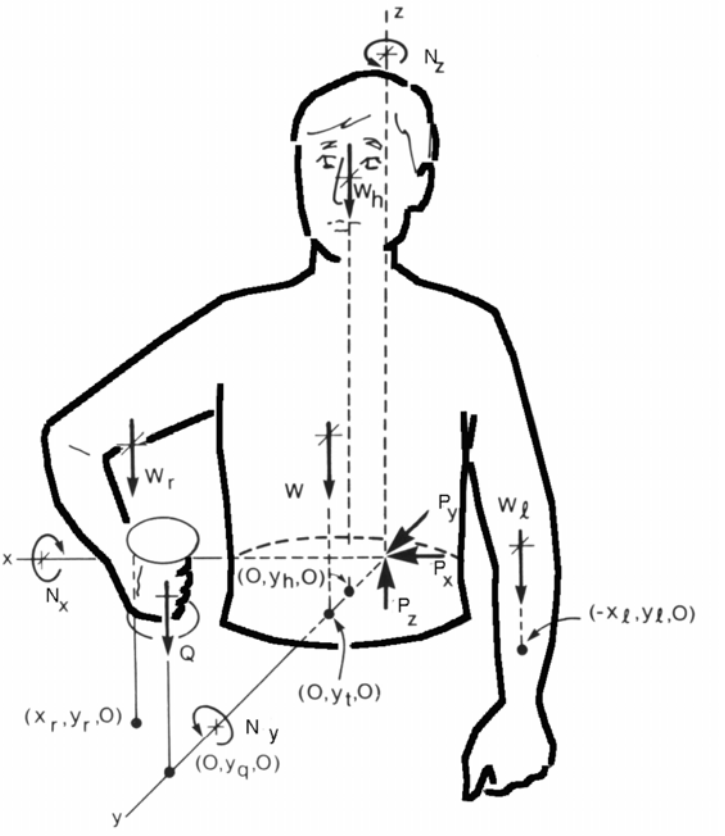



**Figure 2.6**. Spinal loading due to lifting an object. The unknowns are the three components of the force and moment acting at the lumbar spine — $P_x$, $P_y$ and $P_z$, and $N_x$, $N_y$ and $N_x$, respectively — and the knowns are the anatomical distances and the weights of the various body parts and the object the person is lifting — $W_h$, $W_l$, W, $W_r$, and Q. Reprinted with permission from Schultz and Andersson (1981).

For stationary objects, or objects moving with constant velocity, the conservation of linear and angular momentum reduce to the conditions that the sum of the forces and the sum of the moments must be zero. These conditions provide six equations in the case of a three-dimensional problem and three equations in the case of a two-dimensional problem. Free object diagrams for the analysis of the total force on the lumbar spine are shown in Figures 2.6 and 2.7. In Figure 2.6 the unknowns in the problem are the three components of the force and moment acting at the lumbar spine, $P_x$, $P_y$, and $P_z$, and $N_x$, $N_y$, and $N_z$, respectively, and the knowns are the anatomical distances and weights of the various body parts and the object the person is lifting, $W_h$, $W_l$, $W$, $W_r$, and $Q$. In Figure 2.7 the unknowns in the problem are the muscle forces and the knowns the three components of the force and moment acting at the lumbar spine, which were determined experimentally. Both free object diagrams and control volumes are drawings made to simplify the application of conservation principles to a particular physical situation. In the case of free object diagrams like Figures 2.6 and 2.7 for the analysis of the total force on the lumbar spine, two quantities are being balanced: linear and angular momentum. Since this analysis of the lumbar spine is static, the time rates of change of linear and angular momentum are zero and the general balance reduces to requirements that the sum of the forces and the sum of the moments be zero.

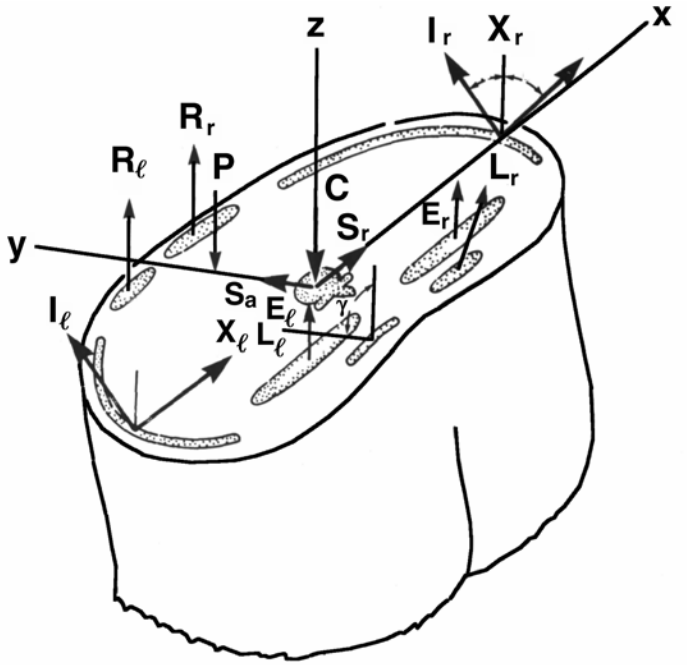



**Figure 2.7**. Spinal loading due to a work activity. Reprinted with permission from Schultz et al. (1982).

As a second illustration of the rigid object model in biomechanics, consider the analysis of a gymnast executing a giant circle on the rings (Figure 2.8a). A four-segment linked system of rigid objects is used here; the values of the masses and the moments of inertia of the four links are shown in Figure 2.8b. A prediction of this simulation model is shown in Figure 2.8c. In addition to application of the conservation of angular momentum, this model illustrates a general feature about models in general, namely, that they are selected by their creators to accomplish certain objectives, or to answer certain questions, and the same model might not be a good one to answer another question. In this case the creators (Sprigings et al., 1999) of this model are fine tuning a gymnastic movement by removing swing from a handstand on rings using a properly timed backward giant circle. Their model would not necessarily be a good model to analyze other movements, for example, the dismount of the gymnast from the rings.

If the rigid object restriction is relaxed a bit to allow the moment of inertia $I_{33}$ in (2.4) to vary, then the conservation of angular momentum about an axis may be written in this special case as

$$M_3 = d(I_{33}\omega_3)/dt. \tag{2.5}$$

This is the form of the conservation of angular momentum that is employed to explain why a figure skater spinning at one place on the surface of the ice can increase or decrease his or her angular velocity by extending the arms out from the torso or lowering the arms to the sides of the torso. If the skater is spinning, there is no moment about the axis that is the intersection of the sagittal and frontal or coronal planes; thus, $M_3 = 0$, and, from (2.5) above, the product $I_{33}\omega_3$ must be a constant. Since $I_{33}\omega_3$ = constant, when the skater extends (lowers) the arms, the moment of inertia of the skater increases (decreases) and the angular velocity of the spin must decrease (increase).

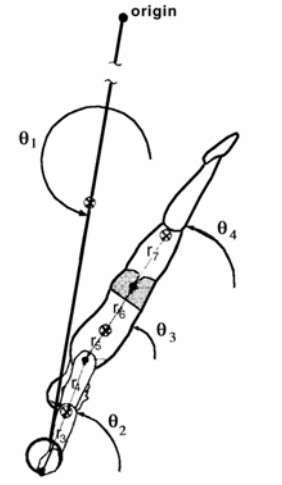



**Figure 2.8a**. Four-segment simulation model for the gymnastic movement of a backward giant circle on rings. Reprinted with permission from Sprigings et al. (1999).

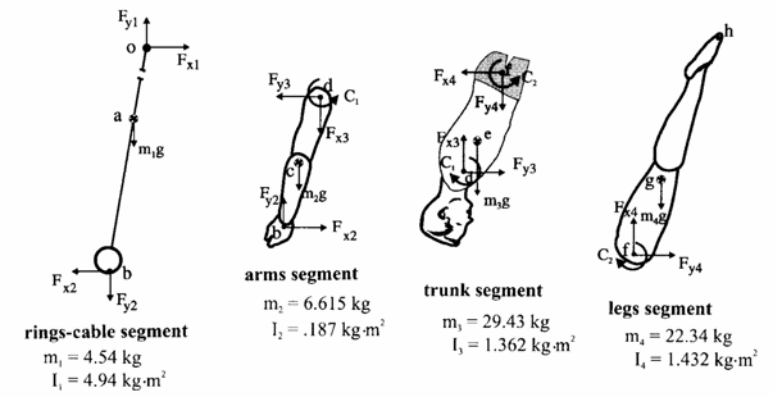



**Figure 2.8b**. Free-object diagrams for the four-segment simulation model. The moment of inertia values are with respect to the segment's center of mass. Reprinted with permission from Sprigings et al. (1999).

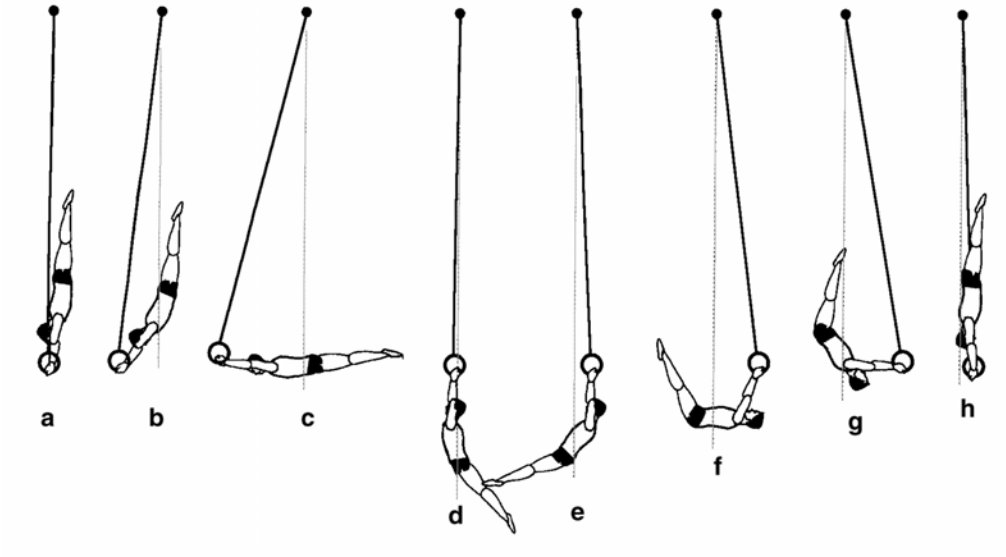



**Figure 2.8c**. Results of the four-segment simulation of the gymnastic movement of a backward giant circle on rings. Reprinted with permission from Sprigings et al. (1999).

**Problems**

2.6.1. The distance $m$ in Figure 2.9 is 6 cm, the distance E to H is 35.5 cm, and the distance E to CM is 17.2 cm. The weight held in the hand is 200 N, the weight of the forearm is 12.4 N, the weight of the hand is 3.4 N, and the weight of the upper arm is 21.3 N. What is the force in the biceps brachii? What is the value of the reactive force $R$ on the lower limb, due to the upper limb, at the elbow joint?

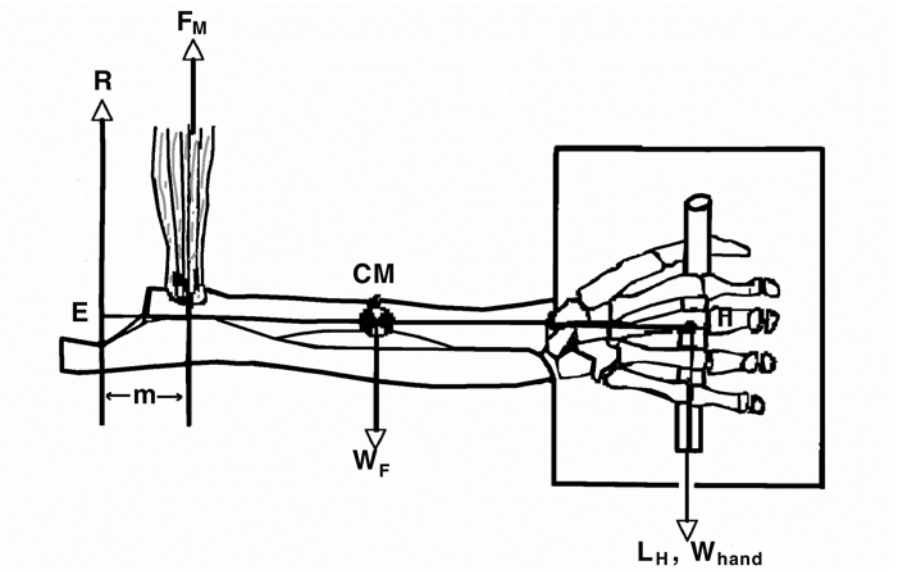



**Figure 2.9**. Illustration of forces acting on the forearm-hand. See Problem 2.4.1. Modified with permission from Chaffin and Andersson (1991).

2.6.2. Derive expressions for each of the three components of the forces and moments — $P_x$, $P_y$, $P_z$ and $N_x$, $N_y$, $N_z$, respectively — for the spinal loading (associated with lifting an object) illustrated in Figure 2.6.

2.6.3. Derive expressions for each of the three components of the forces and moments — $F_x$, $F_y$, $F_z$, and $M_x$, $M_y$, $M_z$, respectively — for the ice skater illustrated in Figure 2.10. The skater is balanced on one leg, which is aligned in the vertical direction, and his other three limbs are arranged to achieve this balance as he glides on the ice.

2.6.4. A diver rotates faster when her arms and legs are tucked tightly in, so that she is almost like a ball, rather than when the limbs are extended in the common diving posture like a straight bar. Consider a diver with a mass of 63 kg, an extended length of 2 meters, and a tucked length of 1 m. (a) Determine the factor by which her angular velocity in the tucked-in configuration exceeds her angular velocity in the extended configuration. It is reasonable to approximate the body in the two configurations as cylinders, and to assume that the centroid of the cylinder coincides with the center of mass of the diver. In the extended configuration the cylinder has a length of 2 m and an average radius of 0.1 m, while in the tucked configuration the cylinder will have a length of 1 m and an average radius of 0.1414 m. Recall that the mass moment of inertia of a cylinder about an axis perpendicular to its long axis and passing

through its mass center is $M(3r^2 + h^2)/12$, where $r$ is the radius of the cylinder and $h$ is the height of the cylinder. (b) What is the parameter that predominates in determining this ratio?

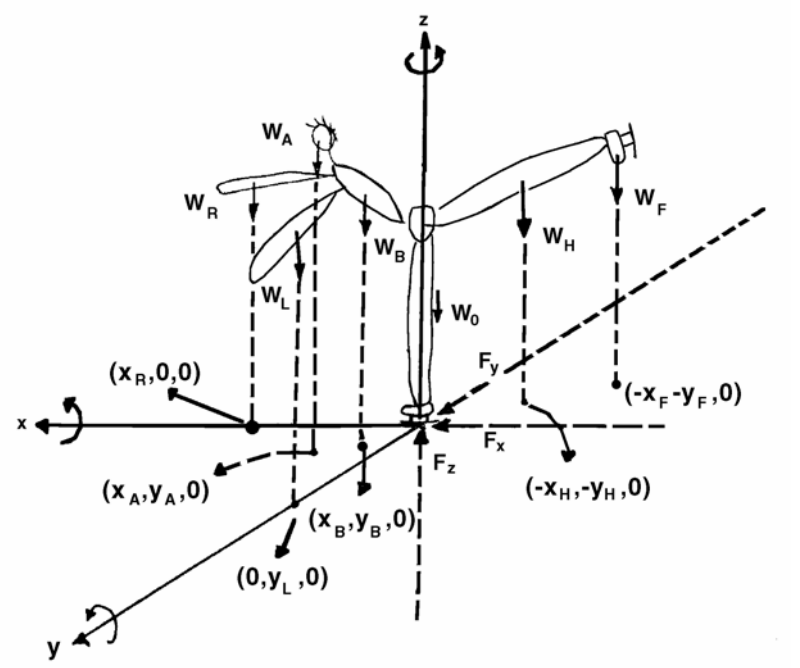



**Figure 2.10**. Illustration of an ice skater balanced on one leg, which is aligned in the vertical direction, and his other three limbs are arranged to achieve this balance as he glides on the ice. See Problem 2.6.3.

## 2.7. THE DEFORMABLE CONTINUUM MODEL

The deformable continuum model differs from the particle and rigid object models in that relative movement or motion is permitted between two points in the model. Examples of deformable continua include the elastic solid used, for example, in the analysis of beam bending and viscous fluid used in the model of flow though a pipe. The use of the word "continuum" in describing these models stems from the idea illustrated in Figure 2.1, namely, that the model is a domain of Cartesian space in the same shape of the object being modeled. It therefore has all the properties necessary to use the analytical machinery of the calculus. In particular, displacements, strains, velocities, and rates of deformation may be calculated. These developments will be presented in the next and subsequent chapters. The deformable continuum is the focus of this text because it is the primary class of models employed in the study of biological tissues and fluids at the macro scale, at the nanometer scale, and at scales in between.

The applications of continuum models to nanometer-scale biological structures and continuum models of fluid and solid behavior are both illustrated by a model of the contents of a canaliculus, a 0.2-μm diameter tunnel in solid bone matrix that contains a 0.1-μm diameter cell process of the cell, the osteocyte, which is encased in the solid bone. Three panels illustrating

the model of the canaliculus and its contents are contained in Figure 2.11. The left panel is a transverse circular cross-section of the model canaliculus that also cuts a transverse circular cross-section of the cell process located at the center of the canaliculus. The cell process contains internal protein structures, is enclosed by a cell membrane, and is maintained in its central position by protein fibers that run from the canalicular wall to the protein structures within the cell membrane. The protein structures in the interior of the cell process form an actin filament network comprised of actin filaments connected by fimbrin, which is, in turn, connected to the protein fibers in the annular region of the canaliculus by transmembrane proteins. Both the inside of the cell process and the annular region between the cell process membrane and canalicular wall contain fluids. The fluid in the annular region is flowing between the protein support fibers spaced at 40 nm and supporting glycosaminoglycans (GAGs) that have a spacing of 7 nm, as indicated in the central panel of Figure 2.11. The drag of the fluid flow on the protein fibers in the annular region causes the cell process to increase its diameter and to distend radially the actin filament network, as illustrated in the last panel of Figure 2.11. This deformation is thought to be part of a mechanosensory and cell signaling process.

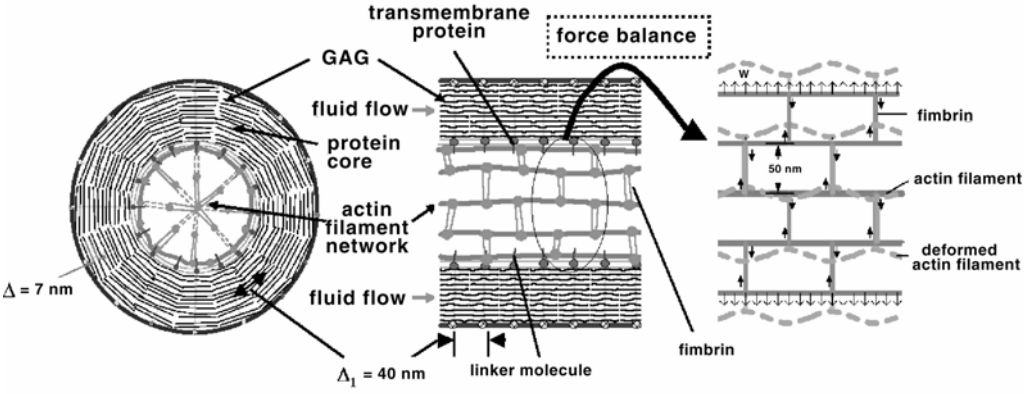



**Figure 2.11**. The left panel is an illustration of the transverse cross-section of a canaliculus showing the annular shape of the region between the cell process at the center and the canalicular wall at the boundary. The middle panel is a longitudinal cross-section showing the undeformed protein network and the fluid flow in the annular region. The right panel is again a longitudinal cross-section of the canaliculus and it shows the deformed protein network. Reprinted with permission from You et al. (2001).

The frame structure shown in all the panels of Figure 2.11 has the same geometry as the frame structures used in building construction and was analyzed using the same methods (You et al., 2001). The difference between the cell process and a building is that the structural elements in a building would have cross-sectional dimensions on the order of meters while in the cell process the cross-sectional dimensions of the structural elements are on the order of nanometers, a difference of eight to ten orders of magnitude. This analogy between the nanometer scale protein networks of subcellular structures and the frame structures of large buildings is also readily apparent in the nanometer-scale cell dendritic structure illustrated in Figure 2.12. This is an illustration of the protein network of a dendritic process, a microvillus, of a brush border cell of the small intestine. It is called a *border* cell because it is of the cell type that lines the small intestine, a *brush* border cell because the face of the cell facing the inside of the

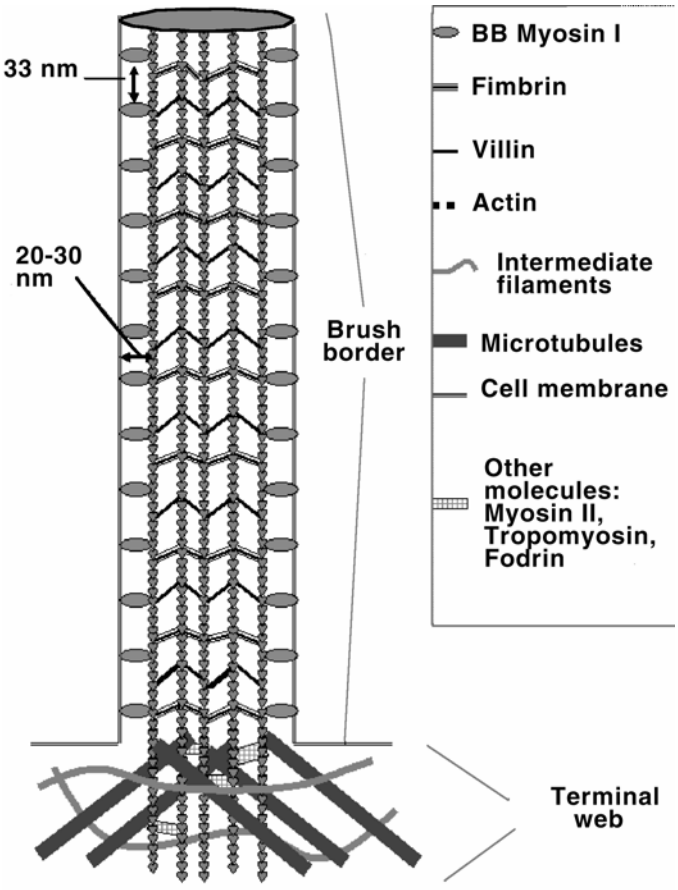



Figure **2.12**. An illustration of the protein network of a dendritic process, a microvillus, of a brush border cell of the small intestine. Compare the protein network of this dendritic process with the frame structure of a large building. They are similar except for a length scale difference of eight to ten orders of magnitude. Adapted with permission from Furukawa and Fechheimer (1997).

intestine looks like a brush due to the large number of uniform-height dendritic processes that look like cantilever beams sticking out from the flat surface of the brush border cell. Figure 2.12 is a cartoon of the structure of one of these dendritic processes. The similarities between the structure of one of these dendritic processes and a contemporary large building structure include the vertical columns of actin that are similar to vertical columns in a building; the transverse structural elements of fimbrin and villin are like the transverse structural elements in a building; the microtubules in the terminal web are like foundation piles used in building construction; the cell membrane is like a curtain wall on a building; the BB (brush border) myosin I is the attachment molecule for the cell membrane and is analogous to a structure used to hang the curtain walls in building construction.

These examples illustrate the fact that continuum models are used in modeling the structure of biological tissues at all levels from the macroscopic bending of whole bones and the flow of blood through arteries to the nanometer-size proteins that form subcellular structural networks and the flow of the fluid in which the nanometer-size proteins are immersed.

## 2.8. LUMPED PARAMETER MODELS

Lumped parameter models are extended rigid object models in which some of the elements are assumed not to be rigid, but to respond in simplified specific ways. The word "lumping" is used to imply that not all the properties are modeled exactly, but in a somewhat approximate way. For example, in a lumped parameter model the image of the object in Euclidean space, as shown in Figure 2.1, need not be an exact model of the object, just a model that contains the features the modeler desires. The mechanical concept of "Coulomb friction" is a "lumped" concept as it occurs in the formula of the French engineer Charles Augustin de Coulomb (1736–1806). The static friction formula of Coulomb is employed to express the force $F$ necessary to cause the motion of weight $W$ resting upon a frictional horizontal surface as $F = \mu W$, where $\mu$ represents the coefficient of friction. The sources of what is called "friction" between the surface and the weight $W$ are varied and include, among other things, the effect of surface adhesion, surface films, lubricants, and roughness; these effects are "lumped" together in the concept of Coulomb friction and expressed as a single coefficient, $\mu$.

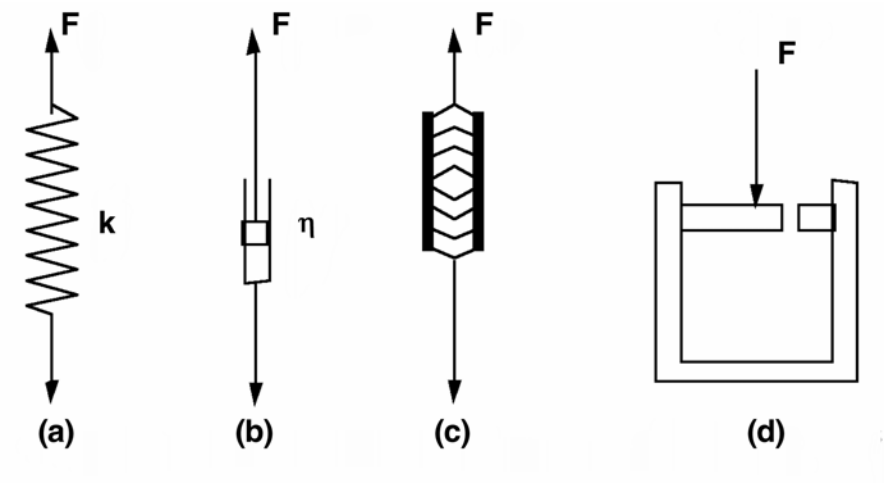



**Figure 2.13**. Four lumped parameter models: (a) the Hookian spring element, (b) the damping element or viscous dashpot, (c) the contractile element, and (d) the Darcy or permeability element.

When linear springs and dashpots are used as elements in a model they are "lumped" representations of an object's stiffness or damping. Their properties describe the constitution of the element and are called constitutive properties. The spring element is also called the Hookian model (Figure 2.13a) and is characterized by an equation that relates its overall lengthening or shortening, $x$, to the force applied to the spring, $F$, by a spring constant, $k$; thus, $F = kx$. This model is named after the English natural philosopher Robert Hooke (1635–1703). The dashpot is called the viscous model or damper (Figure 2.13b) and is characterized by an equation that relates the rate of its overall lengthening or shortening, $dx/dt$, to the force applied to the dashpot, $F$, by a damping constant, $\eta$; thus $F = \eta(dx/dt)$.

Lumped parameter models employing springs and dashpots are used extensively in the study of animal and human locomotion. These models are used to explain the material response phenomena called creep and stress relaxation. *Creep* is the increasing strain exhibited

by a material under constant loading as the time increases. A typical creep experiment on a piece of biological tissue is performed by placing a constant tensile load on the tissue and measuring the strain as a function of time. The function of time obtained by dividing the resulting strain against time data by a unit load is called the *creep function*. *Stress relaxation* is the reduction or decay of stress in a material under constant strain as the time increases. In a typical stress relaxation experiment on biological tissue a constant tensile strain is applied to a material specimen and the resultant stress recorded as a function of time. The function of time obtained by dividing the resulting stress against time data by a unit strain is called the *stress-relaxation function*. Equations for representing creep and stress relaxation will be obtained in the discussion of the standard linear solid model below. Materials that exhibit the time-dependent behaviors of creep and stress relaxation are called *viscoelastic*, indicating that they have some properties of both a viscous fluid and an elastic solid.

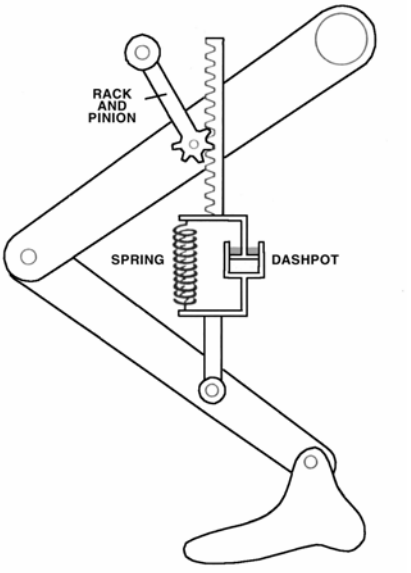



**Figure 2.14**. Schematic diagram showing the conceptual model of the leg used to predict the runner's performance on a compliant track. Descending commands from the cortex, brain stem, and spinal centers (acting to crank the rack and pinion) are assumed to be separate from the mechanical properties of the muscles plus local reflexes (parallel spring and dashpot). Reprinted with permission from McMahon and Greene (1979).

As an example of the use of a lumped parameter model, consider the question of determining the stiffness of elastic compliance of a running track so that the runner has the optimal advantage of the elastic rebound of the track surface. This question was answered using the spring and dashpot model of the lower limb shown in Figure 2.14. While running on soft surfaces like sod is easier on the body than running on hard surfaces like concrete, runners know that they run faster on the harder surface. The question of how hard the surface should be was answered (McMahon and Greene, 1978, 1979) by tuning the compliance of the track to the compliance of the model of the runner's leg shown in Figure 2.14. The half dozen or so run-

ning tracks that have been constructed on the basis of this model are known to runners as "fast" tracks.

The contractile element or force generator is a special lumped parameter model peculiar to biomechanics. It is employed to represent the "lumped" effects of the contractility of a muscle or muscle groups. A sketch of a muscle-testing experiment is shown in Figure 2.15. The electrically stimulated muscle contracts and exerts a force that is measured by the force transducer. The symbol (Figure 2.13c) for the contractile element is often the pinnate shape characteristic of some muscles (e.g., the crab claw muscle), but this symbolism has not been standardized.

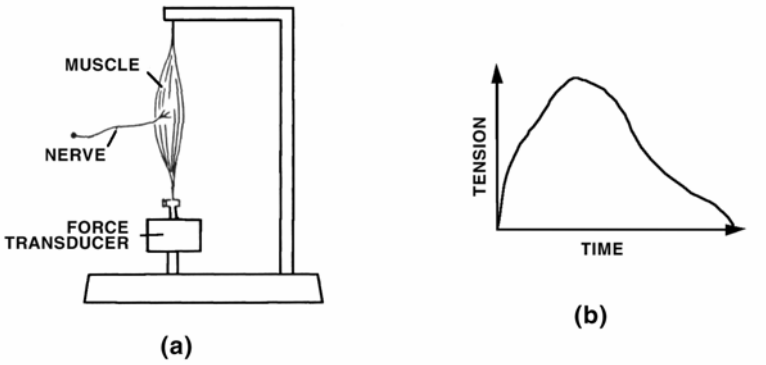



**Figure 2.15**. (a) Diagram of a muscle excitation experiment. The electrically stimulated muscle contracts and exerts a force that is measured by the force transducer. Reprinted with permission from McMahon and Greene (1978).

The tension generated by the contractile element $T$ is generally considered to be a function of the instantaneous length $\xi$ of the element, and the velocity of the contraction $v_c$, $T = T(\xi, v_c)$. The generated tension is assigned various properties depending upon the model, so possible constitutive equations for characterizing the contractile element are deferred to the chapter on skeletal muscle. The contractile element is a force generator in a spring-dashpot model of a biological system involving muscle action. For example, the model of Figures 2.8a–c is not a pure rigid object model because there is a contractile element in the form of a torque generator employed at the shoulder to drive the gymnast's motion. Another example is the model of the lower limb shown in Figure 2.16. This model was used in the simulation of a human vertical jump (Spägele et al., 1999), and it employs contractile elements as force generators. The time histories of the forces in the nine modeled muscle groups indicated in Figure 2.16 were the unknowns in this analysis; note that the symbol for the contractile element in Figure 2.16 is different from the pinnate element symbol of Figure 2.13c. The remaining skeletal elements of the lower limb were kinematically moved through the vertical jump, and an optimal control technique was used to determine the unknown muscle force histories necessarily exerted to make the motion possible. The fact that there are more algebraic unknowns than equations in problems of this type arises from the fact that there are many muscles and muscle groups that are potentially active. The solution is to use methods like optimal control to identify the muscles and muscle groups that are active.

Each of these lumped parameter models is an ideogram for a constitutive idea, e.g., elasticity, damping, or self-activated contraction. The Darcy or permeability element is a special

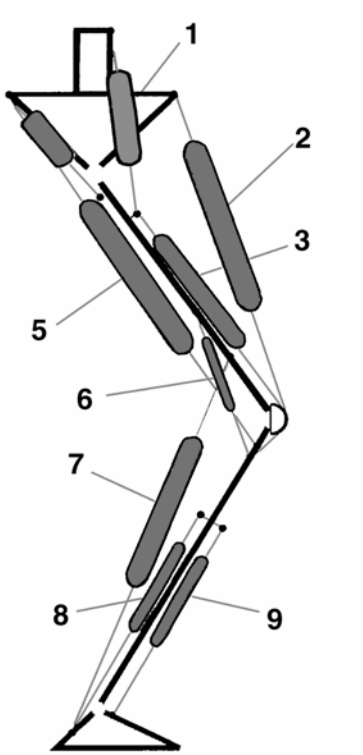



**Figure 2.16**. A model of the lower limb with nine muscle groups. Reprinted with permission from Spägele et al. (1999).

lumped parameter model peculiar to porous media. It was developed to explain the flow of fluids though porous media. Specifically, the city engineer of Dijon, France (Henri Philibert Gaspard Darcy, 1803–1858) in the middle of the 1800s developed the model to analyze the flow of water through a packed sand layer in a city fountain (Darcy, 1856). A sketch of the type of experiment that Darcy did is shown in Figure 2.17. A layer of sand of thickness $L$ is supported on a stiff wire mesh with mesh openings larger than the size of the typical fluid passages through the sand layer. On top of the layer of sand is a reservoir of water maintained at a constant height $h$. The constancy of this head pressure is maintained by providing a continuous supply of water to the reservoir and providing an overflow runoff passage. The domain at the bottom of the sand layer is open to the air again, as is the upper surface of the water reservoir; the air pressure is $p_o$. Thus, the decrease in water pressure across the sand layer is from $p + p_o$, where $p = \rho gh$, to $p_o$. The pressure gradient across the layer is then $p/L$, where $L$ is the layer thickness. The volume flux of water, that is to say the volume of water coming out of the sand layer per unit area per unit time, is denoted by $q$. If the cross-sectional area of the sand layer is denoted by $A_o$, then the volume flow per unit time is $A_o(dw/dt)$, where $dw/dt$ is the rate at which the surface of the water in the catchment basin of cross-sectional area $A_o$ below the sand layer is filling with water. The volume flux $q$ through the layer is then given by $q = (1/A_o)A_o(dw/dt) = (dw/dt)$. Darcy found that the volume flux $q$ through the sand layer was proportional to the pressure gradient across the sand layer, $p/L$. The constant of proportionality $\kappa$ is called the

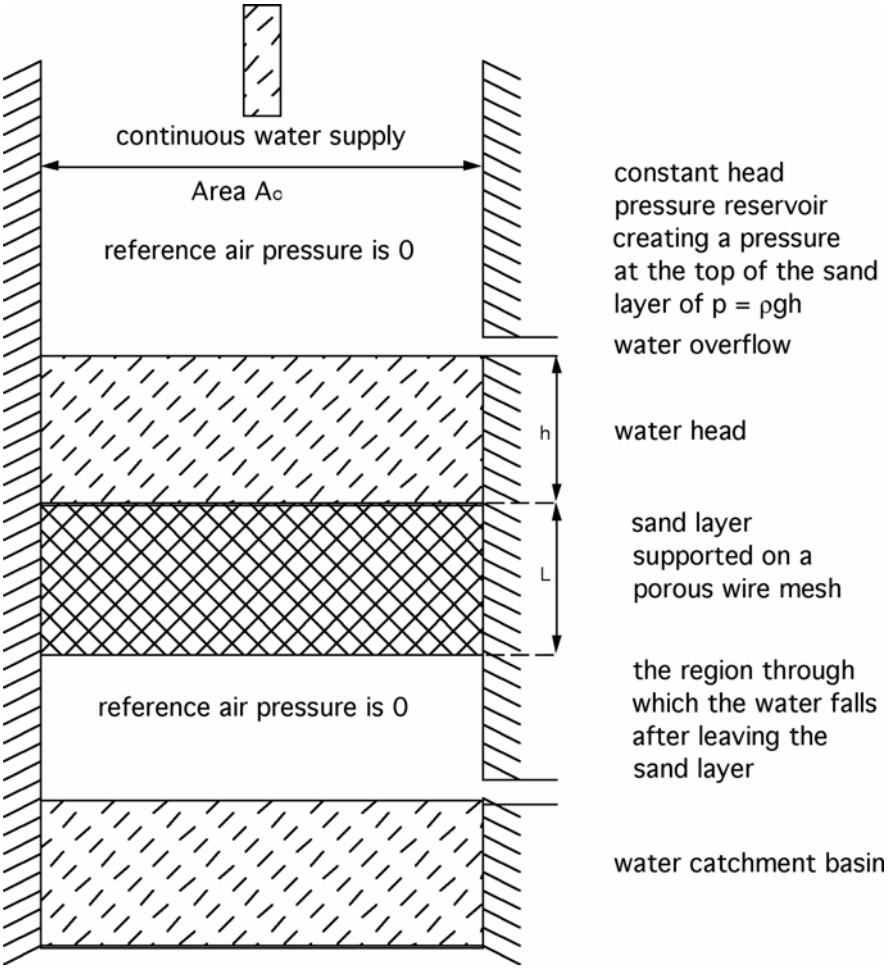



**Figure 2.17**. An illustration of an experimental determination of the permeability of a sand layer.

permeability and is calculated in the experiment described by the formula $\kappa = qL/p$. Replacing $p/L$ by the gradient $(\partial p/\partial L)$, Darcy's law is written as

$$q = -\kappa\,(\partial p/\partial x), \tag{2.6}$$

where $L$ has been replaced by the coordinate $x$ in formation of the one-dimensional gradient operator. The minus sign is placed in (2.6) so that permeability $\kappa$ is positive. The fluid flow is always from regions of higher fluid pressure to regions of lower fluid pressure, hence the pressure gradient in (2.6) is always negative. The combination of the minus sign in (2.6) and the always-negative pressure gradient means the volume flow rate $q$ is always positive.

The constitutive idea of the permeability element (Figure 2.13d) is that of a distributed volumetric resistance to flow throughout the layer thickness $L$ of the porous medium. When a compressive force $F$ is applied to the piston of the permeability element, the water in the chamber under the piston is subjected to a higher pressure and a pressure difference $p + p_o$ is created between the inside of the chamber and the air pressure $p_o$ outside. The water in the

chamber then flows from the high-pressure region $p + p_o$ to the low-pressure region $p_o$, and it passes out of the chamber through the hole in the piston. This process continues until all the water has been ejected from the chamber, the piston has moved to the bottom of the cylinder, and the chamber no longer exists. The volume flow rate $q$ is the uniform fluid velocity over the cross-section $A_o$ of the orifice in the piston. The pressure difference between the fluid chamber and the outside air is $p$; thus, $q = \kappa(p/L) = \kappa(\partial p/\partial L)$, where $\kappa$ is the permeability constant.

**Example 2.8.1**

**Problem**: Show that, from the viewpoint of the relationship between the applied force $F$ and the time rate of change of the deflection ($dx/dt$), that the permeability element is equivalent to a dashpot element characterized by the constant $\eta$. An equivalent statement of the problem would be to show that the dashpot constant $\eta$ of the permeability element (Figure 2.13d) is related to the permeability $\kappa$ by $\eta = \frac{A^2}{A_0}\frac{L}{\kappa}$, where $A$ is the area of the piston in the permeability element, $L$ is the thickness of the piston, and $A_o$ is the cross-sectional area of the orifice in the piston.

**Solution**: To show this, first note that a force balance applied to a free object diagram of the piston of the permeability element (Figure 2.13d) shows that $F = pA$, where $A$ is the cross-sectional area of the piston. If $dx/dt$ denotes the time rate of change of the downward movement of the piston and $q$ the volume flow rate through the orifice in the piston, then three different representations of the time rate of change of the fluid volume in the cylinder chamber are given by

$$\frac{dV}{dt} = -A\frac{dx}{dt} = -qA_0,$$

where $A_o$ is the cross-sectional area of the piston orifice. It follows that $q$, the volume flow rate per unit area through the orifice, may be expressed as

$$q = \frac{A}{A_o}\frac{dx}{dt}.$$

Combining this result with $F = pA$ and $q = \kappa(p/L)$, a constitutive relation for the dashpot of the form $F = \eta(dx/dt)$, is again obtained, but with

$$\eta = \frac{A^2}{A_o}\frac{L}{\kappa}.$$

This result identifies the source of the dashpot-like viscous loss in the permeability element as fluid movement. The velocity of the fluid movement and the fluid pressure are the primary parameters in the permeability element; the applied force and the piston deflection associated with the dashpot element are secondary. It will come as no surprise that the permeability element will often behave just like a dashpot element. However, the permeability element is not the same as the dashpot element because the source of the viscous loss is identified as fluid movement in the permeability element and is unspecified in the dashpot element.

Each of the four lumped parameter models described has been characterized by a single constitutive parameter, namely, the spring constant, the damping constant, the tension generated, or the permeability constant. The next higher level of lumped parameter models is char-

acterized by combinations of these elementary models with two constitutive parameters, and the level after that by three-parameter models. There are models with more than three parameters but they are less useful. The three two-parameter models of interest — the Maxwell model, the Voigt model, and the consolidation model — are illustrated in Figure 2.18. James Clerk Maxwell (1831–1879) was a Scottish natural philosopher who first formulated the basic equations of electromagnetism ("The Maxwell Equations"), and Woldemar Voigt (1850–1919) was a German theoretical physicist who wrote a classic volume on crystal physics. The Maxwell model is a combination of a spring and a dashpot in series. When a force applied to a Maxwell model is changed from zero to a finite value at an instant of time and held constant thereafter, there is an instantaneous initial elastic extension and then there is a continuous deformation as the damper in the dashpot is drawn through the dashpot cylinder. Thus, a Maxwell model exhibits the characteristics of a fluid with an initial elastic response.

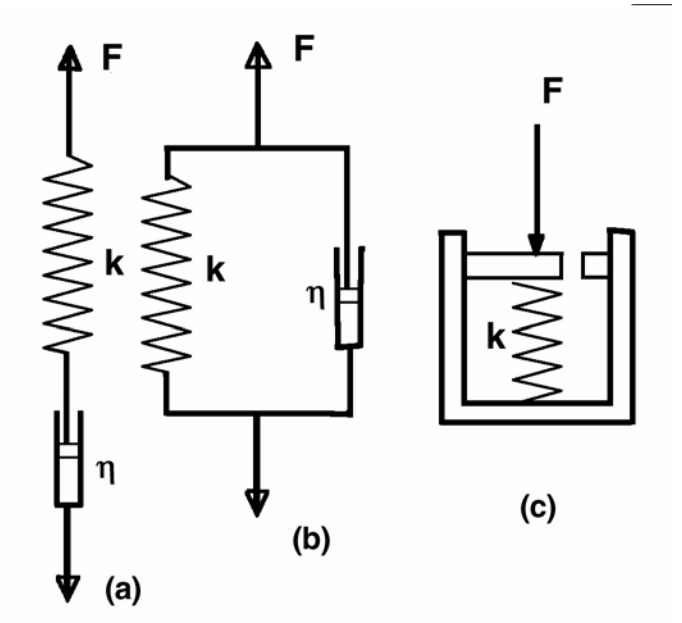



**Figure 2.18**. Lumped two-parameter models: (a) the Maxwell element; (b) the Voigt element; and (c) the consolidation or Terzaghi element.

The Maxwell model was used to represent the behavior of the contents of the leukocyte in a recovery experiment of Skalak et al. (1988) (see Figure 2.19). A leukocyte is a cell that circulates in the blood, and the vascular endothelium is the inside wall of a blood vessel. The passive deformation experiment on a leukocyte was accomplished by drawing it partially into a micropipette (Figure 2.19a). The cylindrical tip of the micropipette is indicated by the cross-hatched region in Figure 2.19a. In the short time deformation experiment, the leukocyte is deformed from its resting spherical shape into an axisymmetric shape with a portion of the cell projecting into the micropipette. In the recovery experiment, individual cells are originally aspirated into the large micropipette until they completely fit inside. The cell is assumed to be held in the micropipette in a sausage shape for a long time so that the interior shear stress is totally relaxed in the leukocyte model.

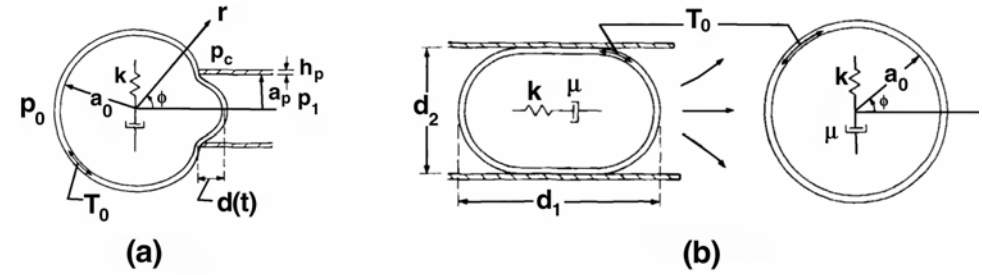



**Figure 2.19**. (a) Sketch of a cell in a micropipette aspiration test. In the short time deformation experiment using the micropipette method, the leukocyte is deformed from its resting spherical shape into an axisymmetric shape with a portion of the cell projecting into the micropipette. Reprinted with permission from Skalak et al. (1988). (b) Sketch of a leukocyte in a recovery test, before and after the spherical shape is recovered. In the recovery experiment, individual cells are originally aspirated into the large micropipette until they completely fit inside. The cell is assumed to be held in the micropipette in a sausage shape for a long time so that the interior shear stress is totally relaxed in the leukocyte model. Reprinted with permission from Skalak et al. (1988).

The Voigt model is a combination of a spring and a dashpot in parallel. When a force applied to a Voigt model is changed from zero to a finite value at an instant of time and then held constant thereafter, extension occurs only after the dashpot begins to move. Thus, the Voigt element is initially rigid, and it then begins to creep asymptotically under the constant applied load to a rest value. In parallel models like the Voigt model, the transverse or horizontal bars or connecting elements are required not to rotate, so the two parallel elements are constrained to always have the same extension in both elements at any instant of time. Neither the Maxwell model nor the Voigt model is considered to be a particularly good model of the force-deformation-time behavior of real materials, biological or non-biological.

The Terzaghi consolidation model element is a special lumped two-parameter model peculiar to soil mechanics (see, for example Terzaghi, 1943) that has applications in biomechanics to water flow in most tissues, although it has been primarily applied to articular cartilage and bone. It is formed by combining a spring element and a Darcy or permeability element in parallel (Figure 2.18c). It was developed by Karl Terzaghi (1883–1963) in 1923 to explain the settlement or consolidation of the soils under the foundations of buildings built on porous, water-saturated soils. The mechanical principles involved are easily illustrated by a sponge. If the sponge is waterlogged, then its compression under loading can only proceed as fast as the water can drain from the sponge. When a load is initially placed on the piston in Figure 2.18c the spring supporting the piston initially takes none of the load because it cannot deflect. It cannot deflect because the piston cannot move due to the fact that the cylinder chamber is filled with a relatively incompressible liquid (water). However, once the water has a chance to exit the cylinder through the orifice in the piston, then it is possible for the piston to begin to move downward under the action of the applied compressive loading. This process of consolidation or settlement proceeds until the spring has deflected an amount sufficient to create a force equal to the applied loading. The relation between the force $F$ applied to the piston of this model and the resulting displacement $x$ of the piston is given by the same constitutive equation that characterizes the Voigt model if the dashpot viscosity $\eta$ in the Voigt model is replaced by $(A^2/A_o)(L/\kappa)$. The application of this model to articular cartilage is illustrated in Figure 2.20. This figure illustrates the response of a sample of articular cartilage when a force applied to the sample is changed from zero to a finite value at an instant of time and held constant thereafter.

Like the Voigt element under the same loading, there is no instantaneous deflection, but a creeping deflection begins under the constant applied stress and proceeds asymptotically to a rest value.

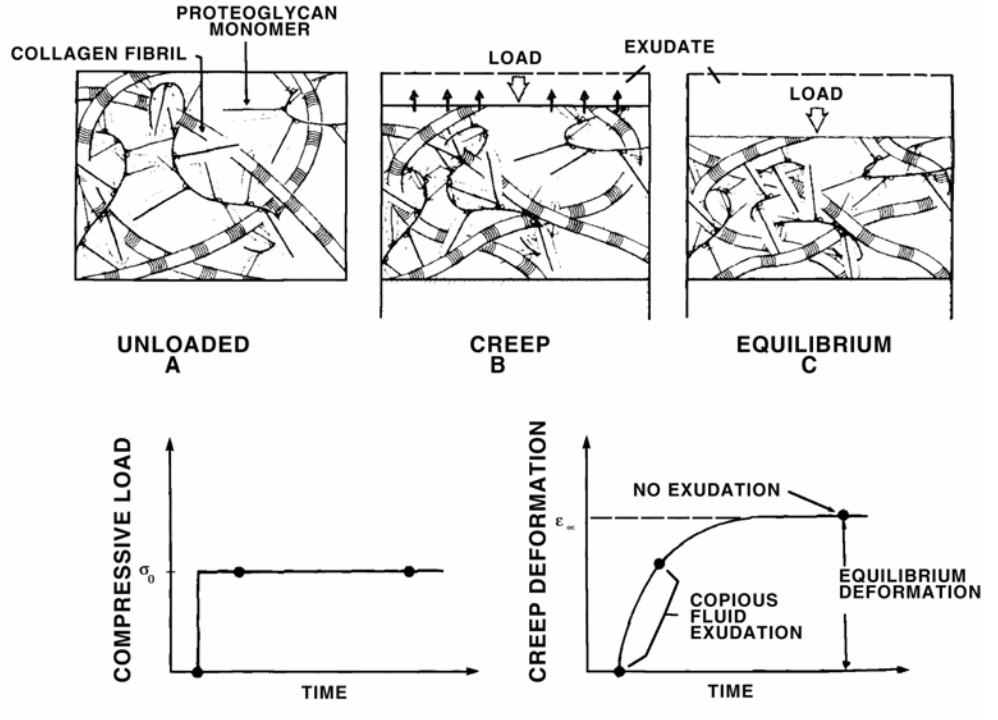



**Figure 2.20**. The application of the Terzaghi model to articular cartilage. On the bottom left the applied stress history is illustrated. A constant stress ($\sigma_0$) is applied to a sample of articular cartilage at an instant of time and held constant thereafter. The creep response of the sample under this loading is illustrated on the bottom right. At the top are drawings of the sample illustrating the tissue response. From these illustrations one can see that the creep is accompanied by exudation of the fluid from the sample and that the rate of exudation decreases over time from points A to B to C. At equilibrium the flow ceases and the load is borne entirely by the solid matrix (point C) and the water carries none of the load (due to the fact that any pressure in the water would cause it to flow out of the matrix). Reprinted with permission from Nordin and Frankel (1989).

There are only two lumped three-parameter elements of interest: the standard linear solid (SLS, Figure 2.21a) and the Hill model (Figure 2.21b) for muscle behavior. Archibald Vivian Hill (1886–1977) was an English physiologist who made many basic contributions to the understanding of muscle function. The pattern for these two three-element modes is similar; the only difference is that the Hill model has a contractile element where the standard linear solid has a dashpot element. These dissimilar elements are in series with a spring element, and the series combination is in parallel with another spring element (Figure 2.21). Another muscle model considered by McMahon (1984) is illustrated in Figure 2.22. The following example illustrates the effect of the contractive element in these models.

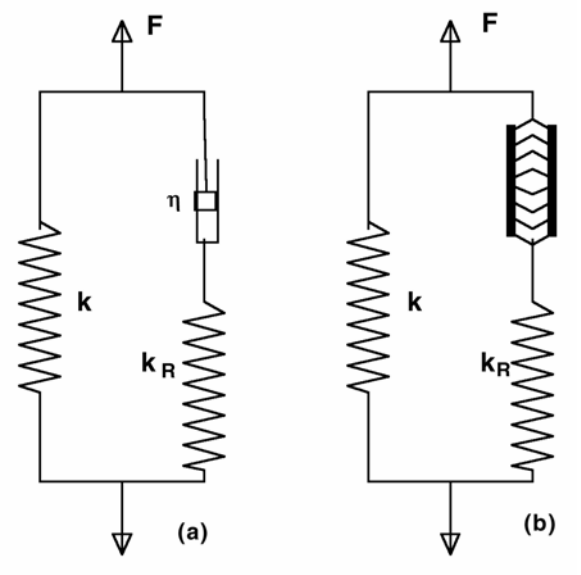



**Figure 2.21**. Lumped three-parameter models: (a) the standard linear solid; (b) the Hill model.

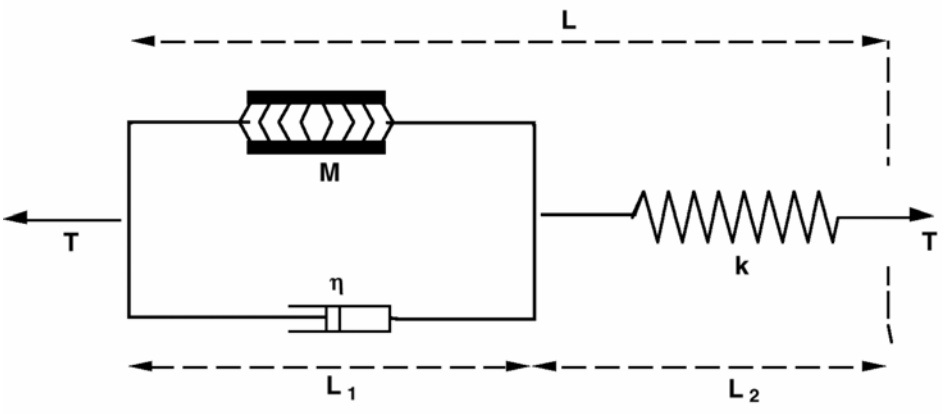



**Figure 2.22**. An idealized model of muscle behavior. See Problems 2.8.10 and 2.8.11.

**Example 2.8.2**

**Problem**: The unstretched length of the primitive muscle model shown in Figure 2.22 is denoted by $L_o$ and the stretched length by $L$. The unstretched length of the spring of constant $k$ in the primitive muscle model of Figure 2.22 is denoted by $L_{02}$ and the stretched length by $L_2$. Similarly the notation $L_{01}$ and $L_1$ apply to the ensemble of the dashpot of constant $\eta$ and the contractile element in series. The total unstretched length of the model *is* $L_0 = L_{01} + L_{02}$, and the total stretched length is $L(t) = L_1 + L_2$. The force exerted by the contractile element is $M(t)$. Consider the isometric functioning of this muscle model and let $T(t)$ denote the tension developed in the model by the isometric functioning. (a) Express the requirement that this system

function isometrically in terms of the notation introduced above. (b) What is the equation governing the series spring in terms of the notation introduced? (c) Express the total tension *T(t)* as the sum of the tensions in the two component elements that are arranged in parallel, the dashpot and the contractile element. (d) Derive the differential equation governing the tension *T(t)* in the muscle model in an isometric loading. The answer should be expressed in terms of the time *t*, tension *T(t)* and the muscle model properties, *k,* $\eta$, and *M(t)*. (e) Solve for the tension *T(t)* created by the muscle when the contractile element contracts by an impulse represented by a half sine wave between zero and $\pi$ in time, as shown in Figure 2.23a. Assume that $k/\eta = 2$. This half sine wave has the representation $M(t) = h(t)\sin t - h(t-\pi)\sin t$, where *h(t)* is the unit step function. (See Appendix 2A for the definition.)

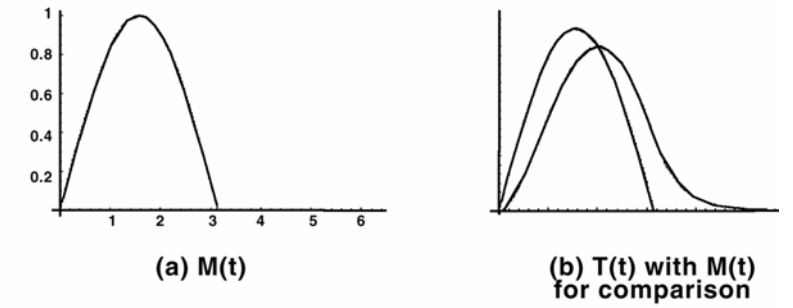



**Figure 2.23**. (a) A plot of the half-sine wave contraction. (b) A plot of the tension $T(t)$ generated by the muscle. $T(t) = (2/5)[e^{-2t} - \cos t + 2\sin t + (e^{2(\pi-t)} + \cos t - 2\sin t)\, h(t-\pi))]$.

**Solution**: (a) The requirement that this system function isometrically is $L_1 + L_2 = L_{01} + L_{02}$. (b) The equation governing the series spring is $k(L_2 - L_{02}) = T(t)$. (c) The total tension *T(t)* is given by $\eta(dL_1/dt) + M(t) = T(t)$. (d) The differential equation governing the tension *T(t)* in the muscle model is $(\eta/k)(dT/dt) + T = M(t)$. (e) From part (c) above the differential equation for *T(t)* due to this contraction is $dT/dt + 2T = 2h(t)\sin t - 2h(t-\pi)\sin t$. The solution to the Laplace transform of this differential equation using the initial condition $T(0) = 0$ is

$$\overline{T}(s) = \frac{2(1-e^{-\pi s})}{(2+s)(1+s^2)},$$

and the solution is given by

$$T(t) = \frac{2}{5}\left[e^{-2t} - \cos t + 2\sin t + (e^{2(\pi-t)} + \cos t - 2\sin t)h(t-\pi)\right].$$

This expression is plotted below in Figure 2.23b.

The standard linear solid considered is a reasonable first approximation of the force-deformation-time behavior of real materials, biological or non-biological. The linear first-order ordinary differential equation that characterizes the standard linear solid,

$$F + \frac{\eta}{k_R}\frac{dF}{dt} = kx + \eta\left(1 + \frac{k}{k_R}\right)\frac{dx}{dt}, \tag{2.7}$$

is derived in Exercise 2.8.3. This exercise is an illustration of the analysis and concepts associated with all the models containing only springs and dashpots.

**Example 2.8.3**

**Problem**: Using Figure 2.21a as a guide, derive the differential equation of the governing force-deflection relationship of the standard linear solid.

**Solution**: Let $F_L$ and $F_R$ denote the force in the two branches, left and right, of the standard linear solid; the total force $F$ is then given by $F = F_L + F_R$. Let $x$ denote the overall deflection of the standard linear solid element; the deflections in both branches must be equal; the horizontal cross-bars in spring-dashpot models are not allowed to rotate. The total deflection in the right branch is the sum, $x$, of the deflection of the dashpot, $x_D$, and the deflection of the spring, $x_S$; thus $x = x_D + x_S$. The equations describing the behavior of the three constituent elements are $F_L = kx$, $F_R = k_R x_S$ and $F_R = \eta(dx_D/dt)$, respectively. Note that the force in the two elements on the right branch must be the same. These equations are combined in the following manner. First, note that from $F_R = k_R x_S$ it follows that $(dx_S/dt) = (1/k_R)(dF_R/dt)$; from $F_R = \eta\,(dx_D/dt)$ it follows that $(dx_D/dt) = (1/\eta)F_R$; and from $x = x_D + x_S$ it follows that $(dx/dt) = (dx_D/dt) + (dx_S/dt)$. Combining these results it follows that

$$(dx/dt) = (1/\eta)F_R + (1/k_R)(dF_R/dt).$$

Now from the equation for the sum of the forces in the two branches ($F = F_L + F_R$) it follows that $F_R = F - F_L$ and since $F_L = kx$, $F_R = F - kx$. Substituting this equation for $F_R$ in the equation involving $F_R$ above it follows that

$$F + (\eta/k_R)(dF/dt) = kx + \eta\,(1 + k/k_R)\,(dx/dt).$$

The physical implications of the constant parameters characterizing the standard linear solid are easier to understand if the constants $\eta$ and $k_R$ are redefined in terms of time constants. To that end (2.7) is rewritten in the form

$$F + \tau_x\frac{dF}{dt} = k\left\{x + \tau_F\frac{dx}{dt}\right\}, \tag{2.8}$$

where $\tau_x$ and $\tau_F$ are material time constants defined by

$$\tau_x = \frac{\eta}{k_R} \text{ and } \tau_F = \frac{\eta}{k}\left\{1 + \frac{k}{k_R}\right\} = \frac{\eta}{k} + \tau_x. \tag{2.9}$$

These material time constants will be shown to have interpretations as the characteristic relaxation times of the load associated with a steady, constant deflection and the deflection associated with a steady, constant load, respectively. Note that, from the definitions, $\tau_F > \tau_x$ since $\eta$, $k$, and $k_R$ are positive.

The standard linear solid, characterized by linear differential equation (2.8), provides a reasonable first model for the phenomena of creep under constant load and stress relaxation under constant deflection, phenomena observed in many biological materials. The creep function is the increase in time of the deflection $x(t)$ when a unit force is applied to the element at $t$

= 0 and held constant forever. The relaxation function is the decrease in time of the force *F(t)* when a unit deflection is applied to the element at $t = 0$ and held constant forever. The creep and relaxation functions for the standard linear solid are obtained from solving the governing differential equation (2.8). In Appendix 2A the Laplace transform method for solving differential equation (2.8) is described; this is the simplest method of solution. In Appendix 2B the more complicated approach of using direct integration is described, and in Appendix 2C the possible electrical circuit analogs to the spring and dashpot models (or differential equations) are described. The creep function is the solution of (2.8) for *x(t)* when *F(t)* is specified to be the unit step function *h(t)* and the relaxation function is the solution of (2.8) for *F(t)* when *x(t)* is specified to be the unit step function *h(t)* (see Appendix 2A for a definition of the unit step function). The unit step function *h(t)* is therefore employed in the representation of deflection history *x(t)* to obtain the creep function *c(t)* as well as in the representation of the force history *F(t)* to obtain the relaxation function *r(t)*. The creep function *c(t)* for the standard linear solid is given by

$$c(t) = \frac{h(t)}{k}\left\{1 - \left(1 - \frac{\tau_x}{\tau_F}\right)e^{-t/\tau_F}\right\}. \tag{2.10}$$

From this result it may be seen that $\tau_F$ is indeed the characteristic relaxation time of the deflection at constant load. Plots of the creep function *c(t)* (multiplied by the spring constant *k*) against the dimensionless time ratio $t/\tau_F$ for different ratios of $\tau_x/\tau_F$ are shown in Figure 2.24.

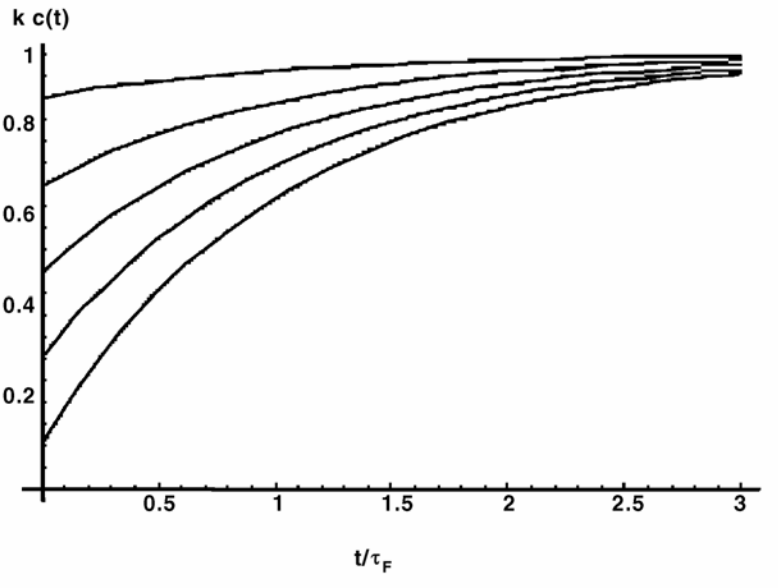



**Figure 2.24**. The creep function. This is a plot of the spring constant *k* times the creep function *c(t)* on the abscissa, against the dimensionless time ratio $t/\tau_F$ on the ordinate. See eq. (2.10). The five curves are for different ratios of $\tau_x/\tau_F$. Since $0 < \tau_x/\tau_F < 1$, the plots, from bottom to top, are for values of $\tau_x/\tau_F$ equal to 0.1, 0.3, 0.5, 0.7, and 0.9.

Because the values of $\tau_x/\tau_F$ are restricted by $0 < \tau/\tau_F < 1$, the plots in Figure 2.24 are, from bottom to top, for values of $\tau_x/\tau_F$ equal to 0.1, 0.3, 0.5, 0.7, and 0.9. The relaxation function for the standard linear solid is given by

$$r(t) = k\left\{1 + \left(\frac{\tau_F}{\tau_x} - 1\right)e^{-t/\tau_x}\right\}h(t)\,. \tag{2.11}$$

From this result it may be seen *that $\tau_x$ is indeed the characteristic relaxation time of the load at constant deflection. Plots* of the relaxation function *r(t)*, divided by the spring constant *k*, against the dimensionless time ratio $t/\tau_x$ for different ratios of $\tau_x/\tau_F$ are shown in Figure 2.25. The values of $\tau_x/\tau_F$ employed are 0.1, 0.3, 0.5, 0.7, and 0.9 — the same values as in Figure 2.24.

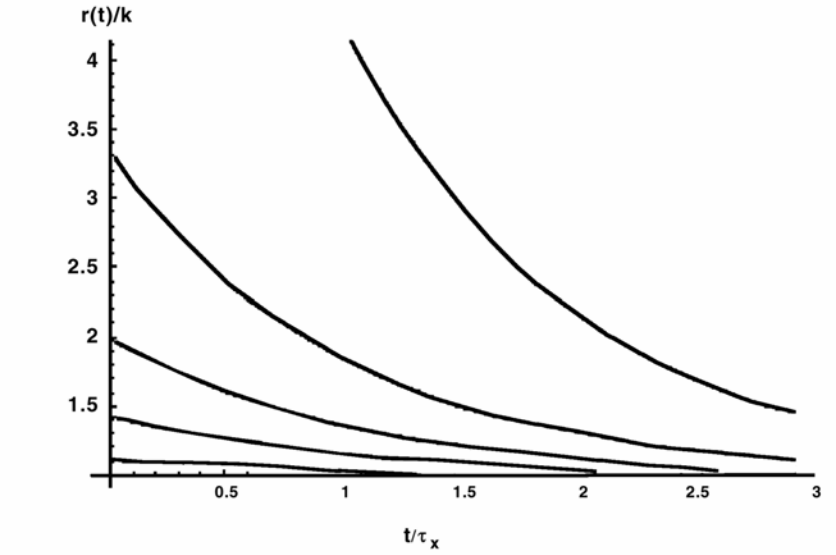



**Figure 2.25**. The relaxation function. This is a plot of the relaxation function *r*(*t*) divided by the spring constant *k*, against the dimensionless time ratio on the ordinate. See eq. (2.11). The five curves are for different ratios of $\tau_x/\tau_F$. Since $0 < \tau_x/\tau_F < 1$, the plots, from top to bottom, are for values of $\tau_x/\tau_F$ equal to 0.1, 0.3, 0.5, 0.7, and 0.9. The top curve, $\tau_x/\tau_F = 0.1$, will intersect the abscissa a little above the value $r(t)/k = 10$.

Higher-order lumped parameter models are obtained by combining the lower-order models described above. There is a strong caveat against the process of combining elementary lumped parameter models to build higher-order models. The caveat is that the number of parameters increases and defeats the advantage of simplicity of the lumped parameter model. Thus, the standard linear solid considered is the most reasonable for the spring and dashpot models as a first approximation of the force-deformation-time behavior of real materials, biological or non-biological. In the rapidly developing subject of biomechanics it appears possible that other lumped parameter models will be developed to represent mechanisms associated with growing objects or objects whose structure is developing in time or healing.

**Example 2.8.4**

**Problem**: The lunge stretch is an excellent exercise to stretch your inner thigh, hip, and calf. Stand with legs about two or more shoulder widths apart with feet pointed 45° away from your body. Lunge toward one side, never allowing the knee of that side to bend more than 90º, keeping it directly over your ankle (Figure 2.26). Allow the foot of the straight leg to point upward with heel on the floor. Hold stretch for 20 seconds. This is good for the gluteus maximus, the hip flexors (iliopsoas, sartorius, rectus femoris, tensor fasciae latae, pectineus) and the adductors (brevis, longus, magnus). It is assumed here that the passive behavior of these muscles may be modeled as a standard linear solid. The deflection time history of the standard linear solid is specified to be an imposed deflection of magnitude $x_{20}h(t)$ from $t = 0^-$ to $t = 20^-$, and it is unspecified for greater times. It is assumed that the dashpot is fully extended by $20^-$ s and that there is a temporally constant force $F_{20-}$ and deflection $x_{20-}$ at that time. The total force-time history across the standard linear solid is unspecified for $t$ less than 20 s; it is specified as zero force from $t = 20^+$ to all greater times. (a) Calculate the jump in the deflection, $\Delta x = x_{20-} - x_{20+}$, in the standard linear solid at 20 s, after the stretch has been released and before the dashpot begins to move. Express your answer in terms of the values of the spring constants, $k$ and $k_R$, of the standard linear solid, and $F_{20-}$ and $x_{20-}$. (b) Sketch the time history of the forces applied to the standard linear solid model of the muscle and time history of the resulting deflection of the standard linear solid model of the muscle. Note that the deflection of the model has been specified up until $t = 20^-$ and that the force applied to the model is specified as zero for $t = 20^+$ and all greater times as zero.



**Figure 2.26**. The lunge stretch. See Example 2.8.4. Reprinted with permission from http://orgs.jmu.edu/strength/JMU_Summer_2000_WebPage/JMU_Summer_2000_Sections/9_summer_dynamic_flexibilty.htm.

**Solution**: (a) At $t = 20^{-}$ s the standard linear solid model has a force of $F_{20-} = kx_{20-}$ in the side with the single spring $k$ and zero force in the side with both a spring and a dashpot. The force in the second arm is zero because the dashpot has fully extended to allow the spring in that arm to be undeflected. At $t = 20^{+}$ s the standard linear solid model has zero total force acting on it so the force in the two arms must balance each other, one in tension and the other in compression. The tensile force in the arm with the single spring is $kx_{20+}$ and the compressive force in the arm with both a spring and a dashpot is $k_R(x_{20+} - x_{20-})$, thus, $kx_{20+} = -k_R(x_{20+} - x_{20-})$ or $x_{20+} = (k_R/(k_R + k))x_{20-}$ and $(x_{20+} - x_{20-}) = (k/(k_R + k))x_{20-}$. (b) A sketch of the time history of the forces applied to the standard linear solid model of the muscle and time history of the resulting deflection is shown in Figure 2.27.

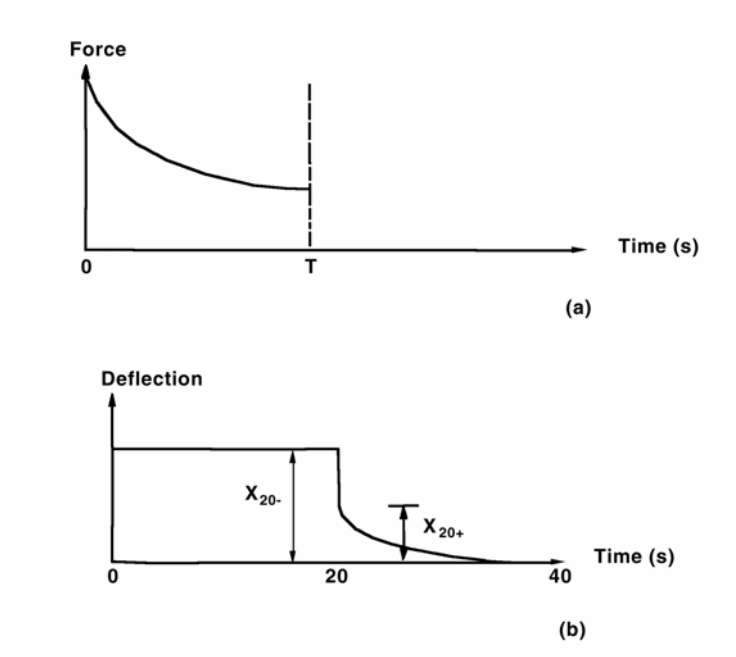



**Figure 2.27**. Sketches of the time history of the forces (a) applied to the standard linear solid model of the muscle and (b) the time history of the resulting deflection of the standard linear solid model of the muscle for the lunge stretch (Figure 2.26) in Example 2.8.4.

## Problems

2.8.1. Show that the constitutive relation governing the Maxwell element is $F + (\eta/k)(dF/dt) = \eta\,(dx/dt)$.

2.8.2. Show that the constitutive relation governing the Voigt element is $F = kx + \eta\,(dx/dt)$.

2.8.3. Show that the creep function for the Maxwell element is $c(t) = [(1/k) + (t/\eta)]h(t)$.

2.8.4. Show that the creep function for the Voigt element is expressed as $c(t) = (1/k)[1 - \exp(-kt/\eta)]h(t)$.

2.8.5. Show that the relaxation function for the Maxwell element is written as $r(t) = k[\exp(-kt/\eta)]h(t)$.

2.8.6. Show that the relation between the compressive force $F$ applied to the piston of the Terzaghi or consolidation element and the resulting compressive displacement $x$ of the piston is given by the same constitutive equation that characterizes the Voigt model, namely $F = kx + \eta\,(dx/dt)$, if the dashpot viscosity $\eta$ in the Voigt model is replaced by $(A^2/A_o)(h/\kappa)$, where $A$ is the cross-sectional area of the piston, $A_o$ is the cross-sectional area of the hole in the piston, $h$ the thickness of the piston, and $\kappa$ is the permeability constant.

2.8.7. Show that the relaxation function for the standard linear solid element is $r(t) = k[1 + ((\tau_F/\tau_x) - 1)\exp(-t/\tau_x)]\,h(t)$.

2.8.8. Sketch the deflection of each of the three models shown in Figure 2.18 to the following loading regime: before $t = 0$ the load is zero; at $t = 0$ the load is increased to $F$ and held at that value until $t = T$, when it is decreased to zero again and held at zero thereafter.

2.8.9. Is the stress relaxation function $r(t)$ or the creep function $c(t)$ a better analogy for the response of a runner's muscles when the runner performs the hamstring stretch? Please indicate the basis for your conclusion.

2.8.10. Solve for the tension $T(t)$ created by the muscle model illustrated in Figure 2.22 (see Example 2.8.2) when the contractile element contracts by a rectangular impulse of magnitude one between zero and 3 in time. Assume that $k/\eta = 4$. The representation of the rectangular impulse is $M(t) = h(t) - h(t - 3)$.

2.8.11. Solve again for the tension created by the muscle model illustrated in Figure 2.22 (see Example 2.8.2), but this time when the contractile element contracts by very short rectangular impulse of magnitude 1 between time 0 and 0.1. Assume again that $k/\eta = 4$. The representation of the rectangular impulse is $M(t) = h(t) - h(t - 0.1)$.

2.8.12. In Example 2.8.1 a calculation was presented that mathematically equated the permeability element and the dashpot element. However, the two elements are not physically the same. How do they differ?

## 2.9. STATISTICAL MODELS

Statistical models assume very idealized and simple structures for their basic elements. For example, the basic model of a molecule in the kinetic theory of gases is a sphere. That sphere may have different properties — rigid, elastic, or some more complicated force-deformation response — and its surface may be smooth or rough. The model of a gas in statistical mechanics is a large number of spheres in motion. The motion of each sphere in the collection may be in different directions with (possibly) different velocities. The impact of two spheres in the elementary statistical mechanics (kinetic theory) models is assumed to be a central impact, that is to say, that during impact the two spheres approach each other along a line joining their mass centers. It is the momentum of the spheres and their impact on a planar surface that creates the force per unit area we call pressure on the planar surface. An estimate of the numerical value of the material properties of the gas may be obtained from this simple model and a lot of calculational effort. For example, if the spheres are rigid and the impact central, the model predicts that the viscosity of the gas, $\mu$, and the coefficient of heat conduction of the gas, $k$, are given by

$$\mu = 0.1792\,(\sqrt{(k_B m\theta)})\sigma^2, \quad k = 2.522\mu c_v, \tag{2.12}$$

where $\theta$ is the temperature, $m$ is the mass of the molecule, $\sigma$ is the diameter of the molecule, $c_v$ is the specific heat at constant volume, and $k_B$ is Boltzmann's constant, $k_B = 1.38047 \times 10^{-16}$

erg/deg. The specific predictions of the simple model are coincident with experimental results for simple gases. This is relatively surprising given the weak assumptions that go into the model. Result (2.12) predicts that the viscosity of a gas is independent of density. Even more sophisticated kinetic theory models make the same prediction, a prediction that is generally consistent with experiment. The prediction that the viscosity of a gas varies with the square root of temperature is a bit off. Experiment shows that the variation in temperature is more rapid than the square root. For monatomic gases the result predicted for the coefficient of heat conduction of the gas compares very well with experimental values. The point of this discussion was to introduce the idea of statistical models and to show that, while the statistical mechanical models were quite specific and simple, they predict numerical values for the physical properties of gases (after a lot of calculation).

In general, statistical mechanical models are used to develop relationships between the macroscopic physical properties of systems composed of a large number of molecules and the properties of the individual molecular species in the system. A second example of such a system is the kinetic theory of rubber. The kinetic theory of rubber will be described in greater detail as similar models are used for proteins of interest, particularly collagen and elastin. Natural rubber, polyisoprene, is a hydrocarbon, that is to say a compound of hydrogen and carbon. Polyisoprene is a polymer and consists of many linked repeating units called isoprenes. A typical rubber molecule contains about 5000 isoprene units and is approximately a micron long. The description of the basic molecular model for rubber employed here is based on the simplified model devised by Müller (1985) to describe the nature of the kinetic theory of rubber. A rubber molecule will form a three-dimensional tangle, the two-dimensional projection of which might look like Figure 2.28. The links in the single molecule are the isoprenes. This

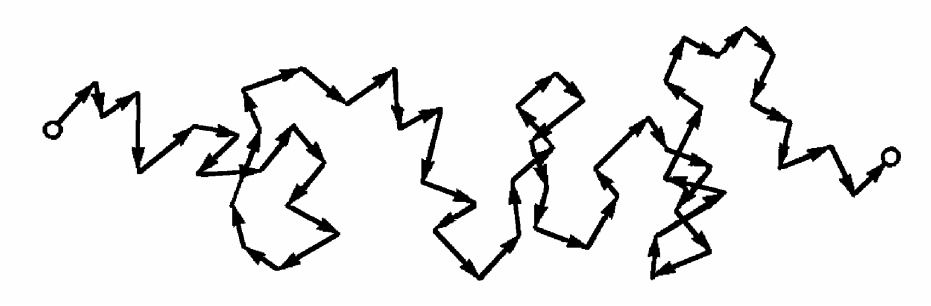


**Figure 2.28**. A rubber molecule in an unstretched, tangled state. Reprinted with permission from Müller (1985).

molecule is just one of many that form a network of chains in which the joints are formed by knots and loops where two chains inhibit each other's movement (Figure 2.29). This is the model upon which the kinetic theory of rubber is based. The model explains immediately the large extensibility of rubber and the proteins of interest here by partial disentanglement of the chains.

The kinetic theory for rubber provides a great deal of insight into the mechanical properties and physical behavior of rubber, but it does not provide a complete picture. Another part of the picture is provided by the theory of finite deformation elasticity theory and the two theories, taken together, provide the basic theoretical model for mechanical and thermal behavior of rubber employed today. The deformable continuum theory of finite deformation elasticity is

described later in this text; it is widely employed to model the behavior of soft tissues as well as the behavior of rubber. The two different types of models provide not only a theoretical basis for rubber behavior, but also for behavior of proteins, as will be illustrated later. These rubber models illustrate the fact that different types of mechanical models will illuminate different aspects of the physical behavior of materials; one type of model cannot be superior to another in general, but one can, in a specific instance, make a prediction that the other cannot.

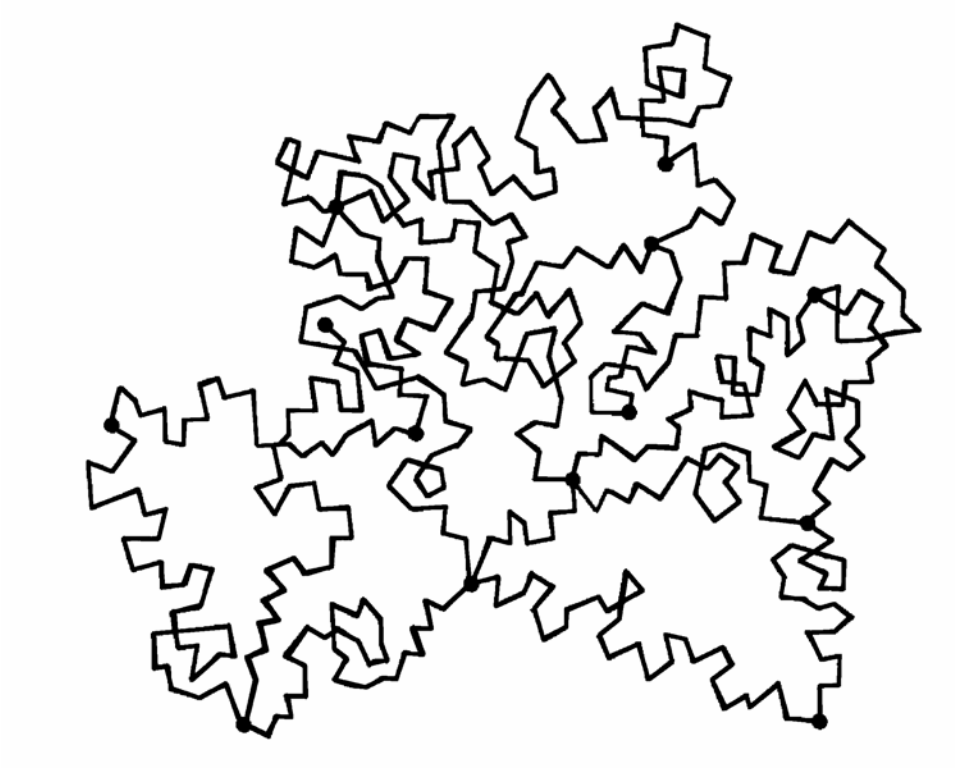


**Figure 2.29**. A network of rubber molecules in an unstretched, tangled state. Reprinted with permission from Müller (1985).

A comparison of statistical models with the deformable continuum models illustrates the advantages one model type has over the other in specific situations. In the remainder of this text, mostly concerned with continuum models, one will see that continuum models cannot predict the numerical values of the material parameters that appear in the model, whereas statistical models can, as illustrated above by (2.12). In continuum models the material parameters must be determined by experiment. On the other hand, the starting assumptions about the material properties, while precise in the statistical models, are relatively vague in the continuum model. For example, in the deformable continuum, the viscosity coefficient in the Newtonian law of viscosity is introduced as a constant of unspecified value because the model is potentially inclusive of many different types of fluids with different viscosities. This lack of specificity in the continuum model is its advantage. This is the mechanism by which contin-

uum theory is able to provide an aspect of the model that the statistical model missed. This point is illustrated by an argument over the numerical values of the elastic constants of materials that occupied much of the discussion of elasticity theory in the 19th century. In 1829 the French mathematician S. D. Poisson (1781–1840) published a molecular model of an elastic solid from which he calculated the value of the elastic constants. In the model he made the simplifying assumption that the interaction force between two molecules was central, that is to say, along the line connecting the mass centers of the two molecules. In the case of an isotropic elastic solid the model of Poisson predicted the value of a dimensionless elastic constant we now call Poisson's ratio to be 0.25. Guillaume Wertheim (1815–1861), an outstanding but little-known experimentalist who measured the mechanical properties of materials, determined the Poisson ratio for several isotropic elastic materials to be close to 0.33. (Incidentally, Wertheim was the first to measure the mechanical properties of most tissues, including bones, muscles, arteries, and nerves of the human body, which he did as a function of sex and age; his measured values for some of these tissues still appeared in medical publications over a hundred years after he published them in 1846.) After the appearance of the continuum formulation of the theory of elastic solids based on the conservation of energy by George Green (1793–1841) in 1839, it was seen that the value of the dimensionless elastic constant we now call Poisson's ratio did not have to be 0.25, and that that particular value was a consequence of the special molecular model Poisson had chosen for his analysis. This does not illustrate the superiority of the continuum model over the statistical model; it illustrates the need to sometimes consider more than one type of model for a physical situation.

## 2.10. CELLULAR AUTOMATA

The methods of calculation associated with the models described up to this point in this chapter have been based on the differential and integral calculus. In a large and extensively illustrated book, Wolfram (2002a) argues that the computational capabilities now available permit investigators to change their methods of calculation from calculus- to computational algorithm-based. Thus, equations are replaced by the simple step-by-step procedures of computer programs. In these algorithms time and space are no longer considered as continuous but as digital steps. The continuum is replaced by a grid or lattice. The algorithms that Wolfram proposes for the accomplishment of this objective are called cellular automata.

When one first encounters cellular automata they appear similar to a game of chess or checkers because they involve arrays of squares that look like a chess or checker board. The rules for any system, including chess or checkers, "can be viewed as corresponding to a program, so its behavior can be viewed as corresponding to a computation" (Wolfram 2002a, p. 165). The simplicity of cellular automata is extensively illustrated by Wolfram and in an associated illustrative CD (Wolfram 2002b) from which the following examples are taken.

Consider first the rule that Wolfram calls "rule 254" (Figure 2.30). The rule is represented graphically in the top panel of Figure 2.30, and in the lower panel there are ten steps represented by ten rows; the evolution of the computation is from steps 1 to 10. The progression from step 1 to step 2 works as follows: given the first row or step 1 with one black square in the middle of a row of white squares, rule 254 is used to calculate step 2. This calculation proceeds by considering all the sets of three contiguous squares in the first row and using the rules in the top panel to assign black or white as the color of the square in row 2 that lies in the second row directly underneath the middle square of the sets of three contiguous squares being considered in the first row. Consider first the leftmost sets of three contiguous squares in the first row. Since they are all white, the rightmost rule in the rule panel requires that white be the

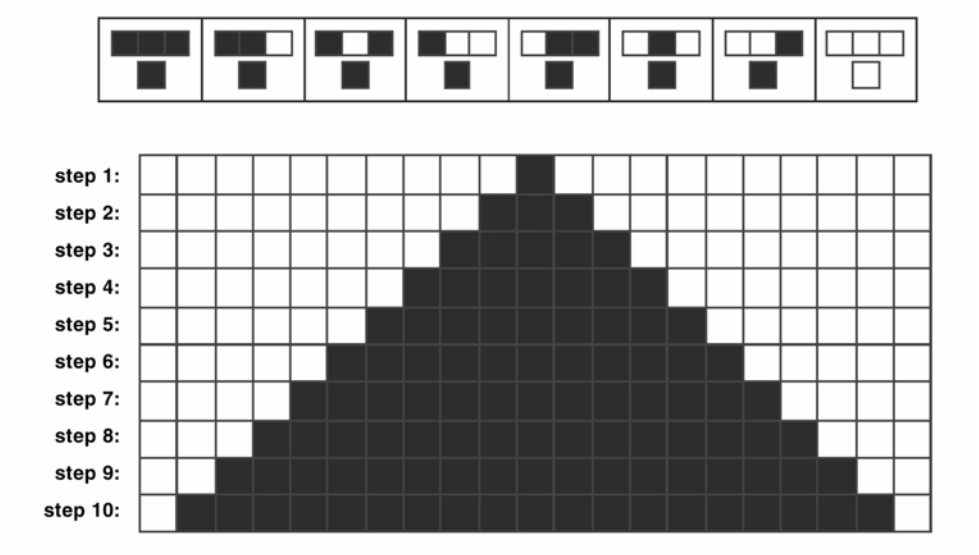



**Figure 2.30**. Ten steps executed using Wolfram rule 254 are shown in the bottom panel. The top panel gives the rule. See the text for further explanation. Reprinted with permission from Wolfram (2002b).

color of the second square from the left in row two. One can then consider the second set of three contiguous squares in the first row, and the result is that white is the color of the third square from the left in row two. This is repeated eight more times to show that the first nine squares in row 2 are white. The color of the tenth square in the second row is black because it is underneath a set of three contiguous squares in row 1 that are white, white and black, respectively, and the rule directly to the left of the rightmost rule in the rule panel (Figure 2.30) requires that that square be black. The color of the 11th square in the second row, the middle square, is again black because it is underneath a set of three contiguous squares in row 1 that are white, black, and white, respectively, and the rule third from the left of the rightmost rule in the rule panel (Figure 2.30) requires that that square be black. The color of the 12th square in the second row is again also black because it is underneath a set of three contiguous squares in row 1 that are black, white, and white, respectively, and the fourth rule from the left in the rule panel (Figure 2.30) requires that that square be black. The remainder of the squares in the second row are white due to the rightmost rule in the rule panel. The colors of the squares in the third row are then obtained by applying the rules to all the sets of three contiguous squares in the second row. In this way it is possible for the calculation to proceed indefinitely. Another two of Wolfram's rules are illustrated in Figures 2.31 and 2.32.

Wolfram (2002a) has applied this method to the solution of partial differential equations. He suggests (p. 165) that the cellular automata approach is superior to traditional numerical approaches because it is sometimes not clear if a feature of a solution is a consequence of the partial differential equation or "merely a reflection of the discretization procedure." Since cellular automata are fully discrete models, they are never subjected to a discretization procedure and are therefore not open to this source of error. A solution for a wave equation is illustrated in Figure 2.33 (§7.1 contains a brief discussion of the three types of partial differential equations). The parameter time is increasing in the direction toward the viewer in this figure, the transverse scale is a location and the vertical scale is the magnitude of the propagating impulse.

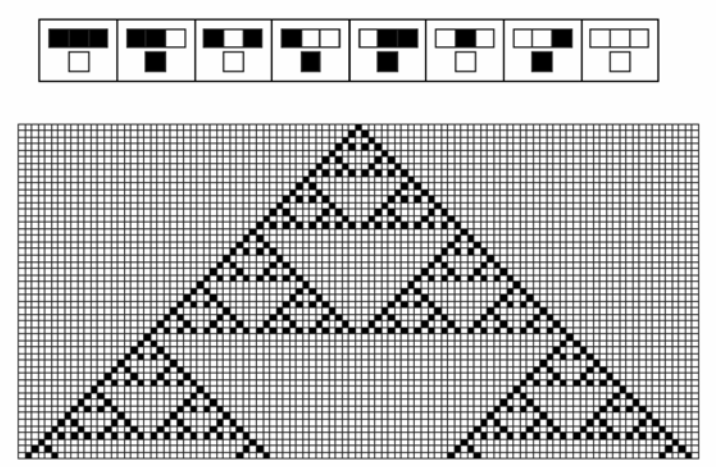


**Figure 2.31**, Fifty-one steps executed using Wolfram rule 90 are shown in the bottom panel. The top panel gives the rule. See the text for further explanation. Reprinted with permission from Wolfram (2002b).

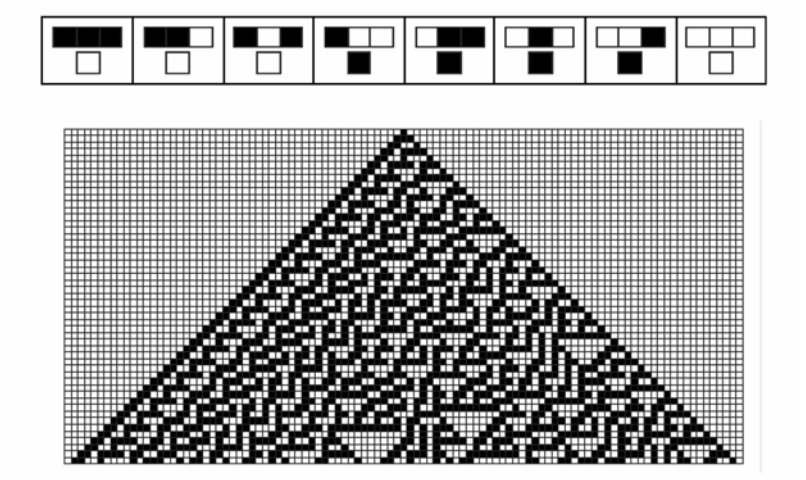


**Figure 2.32**. Fifty-one steps executed using Wolfram rule 30 are shown in the bottom panel. The top panel gives the rule. See the text for further explanation. This illustration is taken from Wolfram (2002b).

This is an illustration of, for example, the classical result that when a string is plucked the magnitude of pluck divides itself in two and each half heads off in an opposite direction along the string. A solution for a diffusion equation is illustrated in Figure 2.34. The parameter time is again increasing in the direction toward the viewer; the transverse scale is a location and the vertical scale is the magnitude of the concentration of the diffusing substance. This is an illustration of, for example, the diffusion from a point source of dye into a volume of clear liquid.

A model of a gas that employs a grid is called a lattice-gas. Lattice-gas cellular automata model the gas as a system of identical particles that transition from lattice point to lattice point, discrete distances at each discrete time step. When particles meet, they collide, but they always stay on the grid and all the appropriate physical laws are obeyed by the particles. An example

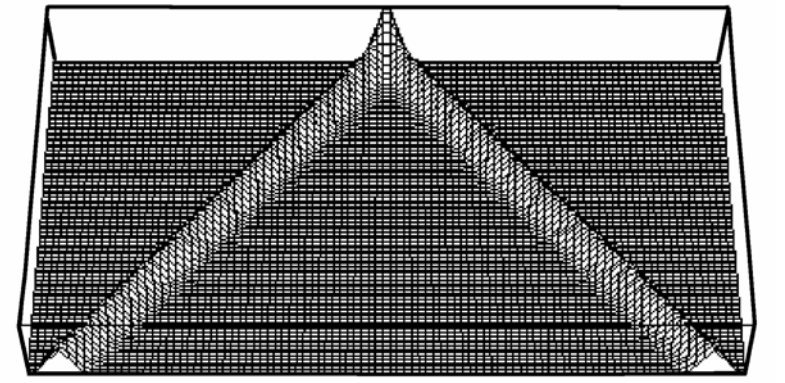


**Figure 2.33**. A solution for a wave equation. The parameter time is increasing in the direction toward the viewer; the transverse scale is a location and the vertical scale is the magnitude of the propagating impulse. Thus, one sees illustrated here, for example, the classical result when a string is plucked: the magnitude of pluck divides in two and each half heads off in an opposite direction along the string. Reprinted with permission from Wolfram (2002b).

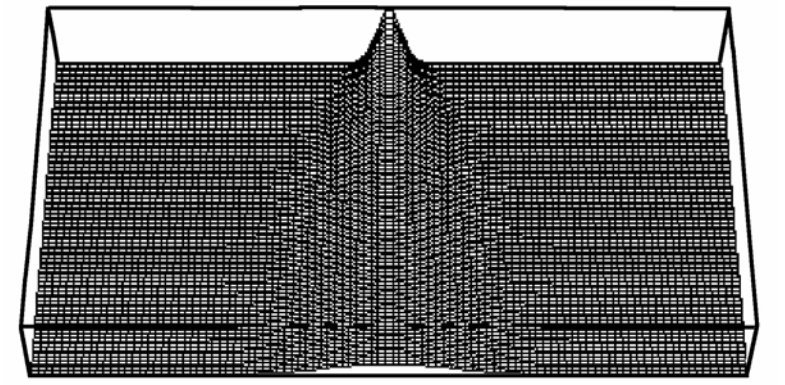


**Figure 2.34**. A solution for a diffusion equation. The parameter time is increasing in the direction toward the viewer; the transverse scale is a location and the vertical scale is the magnitude of the concentration of the diffusing substance. Thus, one sees illustrated here, for example, the diffusion from a point source of dye into a clear liquid. Reprinted with permission from Wolfram (2002b).

of one time step in the evolution of a model of a simple fluid on a hexagonal lattice is shown in Figure 2.35. Each arrow represents a particle of unit mass moving in the direction given by the arrow. Panel (a) represents the initial condition. Panel (b) represents the propagation, or free-streaming step: each particle has moved one lattice unit in the direction of its velocity. Panel (c) shows the result of collisions. The only collisions that have changed the configuration of particles are located in the middle row. Coarse-grained averages of the particle interactions on this hexagonal lattice can be shown to be asymptotically equivalent to the equations governing the flow of an incompressible viscous fluid, the (incompressible) Navier-Stokes equations (Rothman and Zaleski, 1997). The Navier-Stokes equations are derived in §7.4.

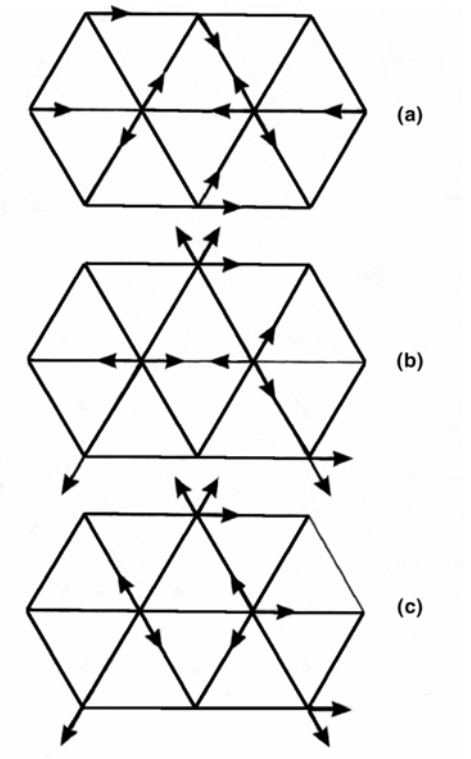



**Figure 2.35**. An example of one time step in the evolution of a model of a simple fluid. Each arrow represents a particle of unit mass moving in the direction given by the arrow. Panel (a) represents the initial condition. Panel (b) represents the propagation, or free-streaming step; each particle has moved one lattice unit in the direction of its velocity. Panel (c) shows the result of collisions. The only collisions that have changed the configuration of particles are located in the middle row. Reprinted with permission from Rothman and Zaleski (1997).

An exploratory application of the lattice-gas computational approach, called the lattice-Boltzmann method, to a study of the development of flow instabilities due to high Reynolds number flow in artificial heart valve geometries was reported by Krafczyk et al. (1998). These authors simulated three-dimensional transient physiological flows in fixed geometries similar to a CarboMedics bileaflet heart valve at different opening angles. The geometry of the simulated bileaflet heart valve is shown in Figure 2.36a, and the velocity vector plot at $t = 0.15$ s is shown in Figure 2.36b.

Two fluids are said to be immiscible if they do not mix, miscible if they do. The most well-known examples of immiscible fluids are oil and water. Immiscible lattice-gas models of immiscible fluids have been found to be very effective calculational tools. An example of one time step in the evolution of a lattice-gas model of immiscible fluids on a hexagonal lattice is shown in Figure 2.37. The three panels represent the microdynamics of the immiscible lattice-gas. Panel (a) represents the initial condition, panel (b) the propagation step. and panel (c) the collision step. The initial condition and propagation step are the same as in Figure 2.35, except that now some particles are represented by bold arrows while others are represented by double arrows. In the collision step, the particles are rearranged so that the flux of the particles indicated by bold arrows tends to be upward and the flux of the particles indicated by double

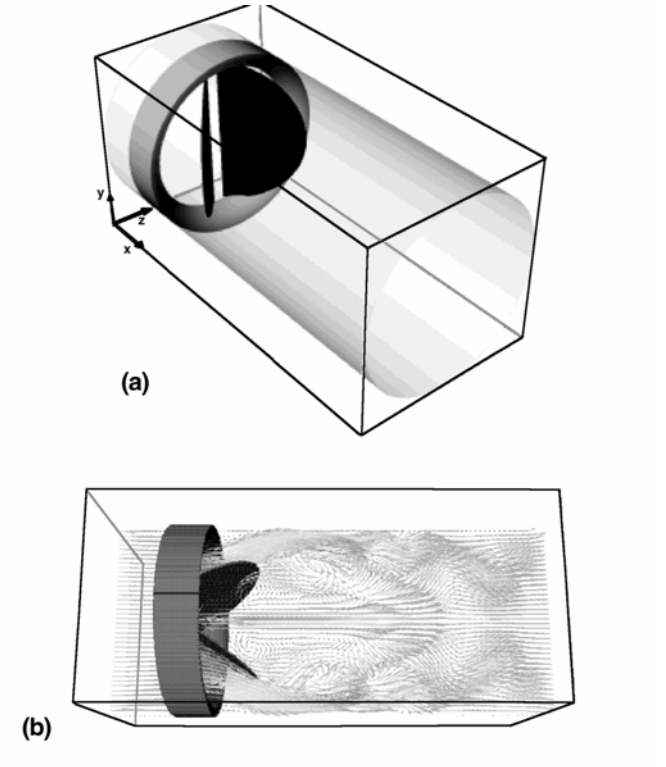



**Figure 2.36**. (a) Flow through a CarboMedics bileaflet heart valve using the lattice-Boltzmann method. Simulated CarboMedics bileaflet heart valve. Reprinted with permission from Krafczyk et al. (1998). (b) Flow through a CarboMedics bileaflet heart valve using the lattice-Boltzmann method. Plot of the velocity vector. Reprinted with permission from Krafczyk et al. (1998).

arrows tends to be downward, suggesting that the two fluids are sorting themselves out at this step. This separation of phases in the immiscible lattice-gas is illustrated in Figure 2.38. The initial condition for this calculation was a homogeneous random mixture with 50% dark particles and 50% grey particles. The number of time steps associated with each panel is shown. There are no walls bounding this lattice-gas; the boundary conditions are periodic, as one may verify by inspection. As time progresses, the dark and grey domains increase in size and tend to a steady state characterized by dark and grey stripes of similar size.

Immiscible fluids are of interest in the mechanical modeling of biological tissue development because cell sorting is analogous to the separation of phases in the immiscible fluids. Recall the differential adhesion hypothesis described in §1.6, the hypothesis that combinations of different cell types behave as immiscible liquids (e.g., oil and water) because of surface tension, but with the cell-to-cell adhesion forces playing the role of molecule–molecule attraction forces. Recall that in immiscible liquids a liquid with a higher surface tension will form droplets enclosed by drops of another liquid with lower surface tension. In combinations of different cell types, cells with higher surface tension will band more tightly together, forcing the cells with lower surface tension to the outside. The last statement is the differential adhesion hypothesis. This sorting was illustrated in Figure 1.15, repeated here as the top set of three panels in Figure 2.39. These three panels showed the experimental images from chicken

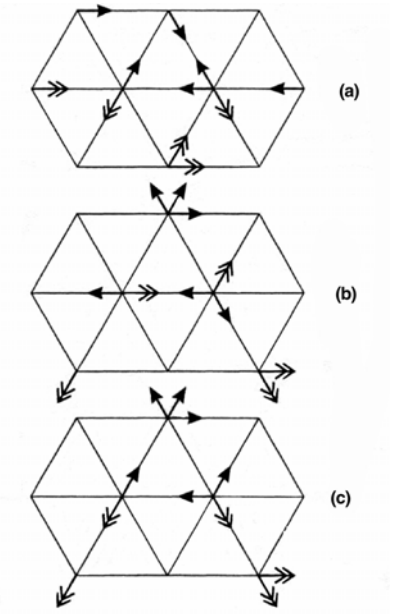



**Figure 2.37**. Microdynamics of the immiscible lattice gas, in which the initial condition (a), the propagation step (b), and collision step (c) are displayed as in Figure 2.35. The initial condition and propagation steps are the same as before, except that now some particles are represented by bold arrows while others are represented by double arrows. In the collision step the particles are rearranged so that the flux of the particles indicated by bold arrows tends to be upward and the flux of the particles indicated by double arrows tends to be downward, suggesting that the two fluids are sorting themselves out at this step. Reprinted with permission from Rothman and Zaleski (1997).

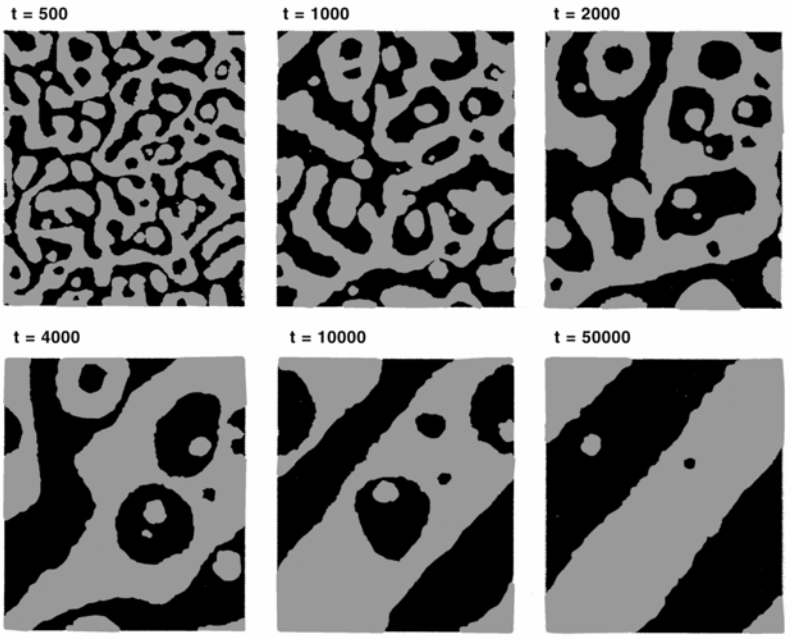



**Figure 2.38**. Phase separation in the immiscible lattice gas. The initial condition was a homogeneous random mixture, with 50% red (black) particles, and 50% blue (grey). Time t is given in time steps. Boundaries are periodic. Reprinted with permission from Rothman and Zaleski (1997).

embryo cells in culture. The light cells are neural retinal cells and the dark cells pigmented retinal cells. The initial situation, shown in the first of the three panels, is a random mixture of light and dark cells. The second panel shows the dark clusters formed by 10 hours, and the third panel shows the dark cell core surrounded by a light cell shell at 72 hours. The bottom set of three panels in Figure 2.39 shows the corresponding images from an immiscible lattice-gas simulation with three cells types: light, dark, and medium (Mombach et al., 1995; Alber et al., 2002).

There appears to be a great deal of potential for modeling the mechanics of biological tissue development using cellular automata, but it is only now being explored.

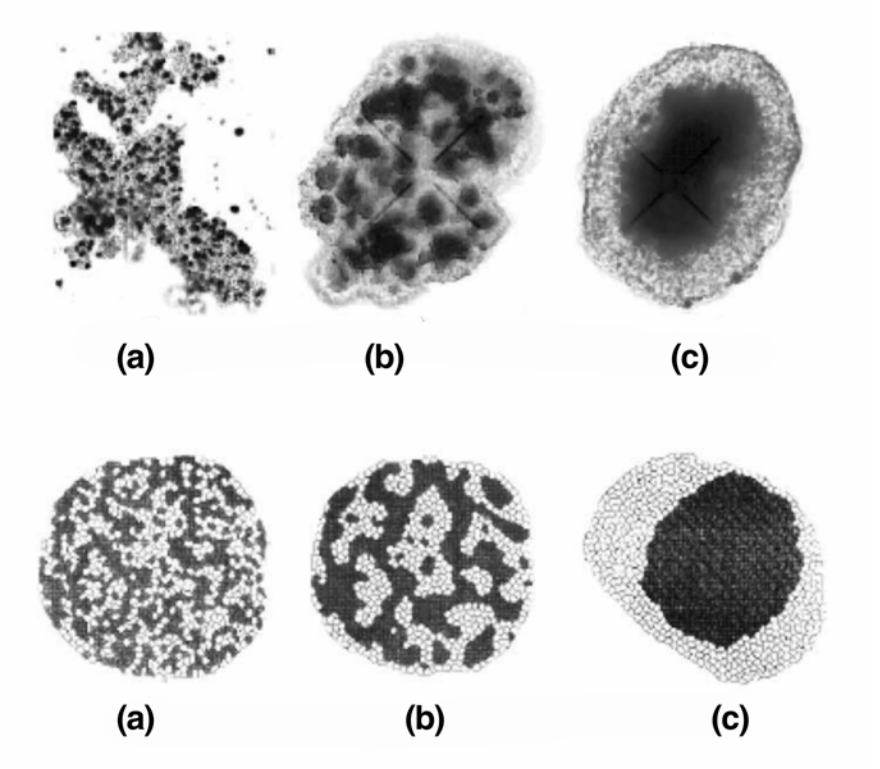



**Figure 2.39**. The top panel repeats Figure 1.15 and represents experimental images from chicken embryo cells in culture: light cells are neural retinal cells and dark cells are pigmented retinal cells. An initial random mixture of light and dark cells (a) forms dark clusters after around 10 hours (b), and eventually sorts to produce a dark cell core surrounded by light cells after around 72 hours. The bottom panels show the corresponding images from a simulation with three cells types: light cells, dark cells, and medium. Reprinted with permission from Alber et al. (2003). See also Mombach et al. (1995).

## 2.11. THE LIMITS OF REDUCTIONISM

A basic method of approach in science and engineering is reductionism. The philosophy of this approach is to decompose the object of study into its constituent parts, analyze each part sepa-

rately, then reconstruct the object and predict its response to stimuli from a knowledge of response of the constituent parts to stimuli. Mathematically, such a prediction of the response of the object from the superposition of the response of its constituent parts generally implies a linear model. An example is the stress analysis of a large bridge that is accomplished by decomposing the bridge into bars, beams, girders, and cables and analyzing the structural capacity of each of these constituents individually. Since reductionism is the philosophy followed in this book, it is appropriate to mention some general and some specific caveats. The prime caveat is that the mathematical model of the system may be nonlinear and that superposition of different responses from different stimuli is not a valid assumption. This is likely to be the case in a biological system. Further, although we can conceptually divide the body into its organs, the organs into tissues, and the tissues into cells and extracellular matrix in analogy with what would be done in the analysis of a bridge, we do not expect to be able to predict the response of the body to every loading of interest as we would in the case of a bridge. When it comes to predicting the response of biological structures, our objective will be a more modest one: to predict the response of the specific tissues to specific loadings of interest. Interpretation will then be necessary to understand how the specific result will influence the entire body.

## 2.12. REFERENCES


Alber MS, Kiskowski MA, Glazier JA, Jiang Y. 2002. On cellular automaton approaches to modeling biological cells. In *Mathematical systems theory in biology, communication, and finance*, ed. J Rosenthal, DS Gilliam. Institute for Mathematics and Its Applications, Vol 142, pp. 1–39. New York: Springer-Verlag.

Chaffin DB, Andersson GBJ. 1991. *Occupational biomechanics*, 2nd ed. New York: Wiley.

Darcy H. 1856. *Les fontains publiques de la ville de dijon*. Paris: Dalmont.

Furukawa R, Fechheimer M. 1997. The structure, function, and assembly of actin filament bundles. *Int Rev Cytol* **175**:29–90.

Harris AK. 1994. Multicellular mechanics in the creation of anatomical structures. In *Biomechanics of active movement and division of cells*, ed. N Akkas, pp. 87–129. New York: Springer-Verlag.

Kaplan W. 1958. *Ordinary differential equations*. Reading, MA: Addison Wesley.

Krafczyk M, Cerrolaza M, Schulz M, Rank E. 1998. Analysis of 3D transient blood flow passing through an artificial aortic valve by Lattice-Boltzmann methods. *J Biomech* **31**:453–462.

McMahon TA. 1984. *Muscles, reflexes, and locomotion*. Princeton: Princeton UP.

McMahon TA, Greene PR. 1978. Fast-running tracks. *Sci Am* **239**:148–163.

McMahon TA, Greene PR. 1979. The influence of track compliance upon running. *J Biomech* **12**:893–904.

Mombach J, Glazier JA, Raphael R, Zajac M. 1995. Quantitative comparison between differential adhesion models and cell sorting in the presence and absence of fluctuations. *Phys Rev Lett* **75**:2244–2247.

Müller I. 1985. *Thermodynamics*. Boston: Pitman.

Nordin M, Frankel VH. 1989. *Basic biomechanics of the musculoskeletal system*. 2nd ed. Philadelphia: Lea & Febiger.

Polya G. 1945. *How to solve it*. Princeton: Princeton UP.

Raven FH. 1966. *Mathematics of engineering systems*. New York: McGraw-Hill.

Rothman DH, Zaleski S. 1997. *Lattice–gas cellular automata*. Cambridge: Cambridge UP.

Schultz AB, Andersson GBJ. 1981. Analysis of loads on the lumbar spine. *Spine* **6**:76–82.

Schultz AB, Andersson GBJ, Örtengren R, Haderspeck K, Nachemson A. 1982. Loads on the lumbar spine. *J Bone Joint Surg* **64A**:713–720.

Skalak R, Sung K-LP, Schmid-Schönbein G, Chein S. 1988. Passive deformation analysis of human leukocytes. *J Biomech Eng* **110**:27–36.

Spägele T, Kistner A, Gollhofer A. 1999. A multiphase optimal control technique for the simulation of a human vertical jump. *J Biomech* **32**:87–91.

Sprigings EJ, Lanovaz JL, Watson LG, Russell KW. 1999. Removing swing from a handstand on rings using a properly timed backward giant circle: a simulation solution. *J Biomech* **32**:27–35.

Terzaghi K. 1943. *Theoretical soil mechanics*. New York: Wiley.

Thomson WT. 1960. *Laplace transformation*, 2nd ed. Englewood Cliffs, NJ: Prentice-Hall.

Weyl H. 1987. *The continuum*. Philadelphia: Thomas Jefferson UP.

Wolfram S. 2002a. *A new kind of science*. Champaign, IL: Wolfram Media.

Wolfram S. 2002b. *A new kind of science explorer* [CD]. Champaign, IL: Wolfram Media.

You L, Cowin SC, Schaffler M, Weinbaum S. 2001. A model for strain amplification in the actin cytoskeleton of osteocytes due to fluid drag on pericellular matrix. *J Biomech* **34**:1375–1386.

## APPENDIX 2A. LAPLACE TRANSFORM REFRESHER

The solution to the differential equations governing the lumped parameter models is accomplished most easily with the use of Laplace transforms and the Laplace transforms of discontinuous functions. Laplace transforms provide a method for representing and analyzing linear systems using algebraic methods. The Laplace transform variable $s$ can directly replace the $d/dt$ operator in differential equations involving functions whose value at time zero is 0. Most of the readers of this text will have been introduced to Laplace transforms at some time in their past and will find it convenient to have the salient points about these transforms refreshed in their minds before solving the differential equations in this chapter.

The Laplace transform of a function $f(t)$, $0 \le t \le \infty$, is defined by

$$\mathcal{L}\{f(t)\} = \tilde{f}(s) = \int_0^\infty f(t)e^{-st}dt\,. \tag{2A.1}$$

This integral is absolutely convergent if the function $f(t)$ is of exponential order $\alpha$, that is to say, if $f(t)$ is continuous for $0 \le t \le \infty$ and $|f(t)| < ce^{-\alpha t}$, where $c$ and $\alpha$ are constants. The notation for the inverse Laplace transform of the function $\tilde{f}(s)$ is

$$\mathcal{L}^{-1}\{\tilde{f}(s)\} = f(t)\,. \tag{2A.2}$$

The Laplace transforms of derivatives and integrals are some of the most useful properties of the transform. If the function $f(t)$ is of exponential order and the derivative of $f(t)$ is continuous, then for $s > \alpha$,

$$\mathcal{L}\{f'(t)\} = s\mathcal{L}\{f(t)\} - f(0) = s\tilde{f}(s) - f(0)\,, \tag{2A.3}$$

a result which, by repeated application, can be used to construct similar formulas for higher-order derivatives, for example,

$$\mathcal{L}\{f''(t)\} = s^2\mathcal{L}\{f(t)\} - sf'(0) - f(0)\,. \tag{2A.4}$$

The Laplace transform of an integral is given by

$$\mathcal{L}\left\{\int_0^t f(x)dx\right\} = \frac{1}{s}\tilde{f}(s)\,, \tag{2A.5}$$

for $s > \alpha$. It follows that, for a function whose value at $t = 0$ is zero, and whose higher-order derivatives are zero at $t = 0$, differentiation corresponds to multiplication by $s$ and integration corresponds to division by $s$. If the function *f(t)* is of exponential order, then

$$\mathcal{L}\{e^{-at}f(t)\} = \tilde{f}(s+a) \tag{2A.6}$$

for $s > \alpha - a$, and if $\tilde{f}(s)$ has derivatives of all orders for $s > \alpha$:

$$\tilde{f}\,'(s) = \mathcal{L}\{-tf(t)\} \text{ or } \tilde{f}^{(n)}(s) = \mathcal{L}\{(-t)^n f(t)\}\,. \tag{2A.7}$$

In the solution of differential equations using the Laplace transform it is often necessary to expand the transform into partial fractions before finding the inverse transform. The rational function *P(s)/Q(s)*, where *Q(s)* is a polynomial with *n* distinct zeros, $\alpha_1, \alpha_2, \ldots, \alpha_n$, and *P(s)* is a polynomial of degree less than *n*, can be written in the form

$$\frac{P(s)}{Q(s)} = \frac{A_1}{s-\alpha_1} + \frac{A_2}{s-\alpha_2} + \ldots + \frac{A_n}{s-\alpha_n} \tag{2A.8}$$

where the $A_i$ are constants. The constants $A_i$ are determined by multiplying both sides of the equation above by $s - \alpha_i$ and letting $s$ approach $\alpha_i$; thus,

$$A_i = \lim_{s->\alpha_i it} \frac{(s-\alpha_i)P(s)}{Q(s)} = \lim_{s->\alpha_i it} \frac{P(s)}{\dfrac{Q(s)-Q(\alpha_i)}{s-\alpha_i}} = \frac{P(\alpha_i)}{Q'(\alpha_i)}\,. \tag{2A.9}$$

Combining the two previous equations one may write

$$\frac{P(s)}{Q(s)} = \frac{P(\alpha_1)}{Q'(\alpha_1)}\frac{1}{s-\alpha_1} + \ldots + \frac{P(\alpha_n)}{Q'(\alpha_n)}\frac{1}{s-\alpha_n}\,, \tag{2A.10}$$

whose inverse Laplace transform is given by

$$\mathcal{L}^{-1}\left\{\frac{P(s)}{Q(s)}\right\} = \frac{P(\alpha_1)}{Q'(\alpha_1)}e^{\alpha_1 t} + \ldots + \frac{P(\alpha_n)}{Q'(\alpha_n)}e^{\alpha_n t}\,. \tag{2A.11}$$

The result above was obtained by using Table 2A.1 to verify that

$$\mathcal{L}^{-1}\{(s-\alpha_i)^{-1}\} = e^{\alpha_i t}\,.$$

**Example 2A.1**

**Problem**: Solve the differential equation $(dy/dt) - 5y = e^{3t} + 4$ for $y(0) = 0$ using Laplace transforms.

**Solution**: Noting that the Laplace transform of $e^{-at}$ is $1/s + a$ and that the Laplace transform of the derivative of a function is equal to $s$ times the Laplace transform of the function minus the value of the function at $t = 0$, the Laplace transform of $(dy/dt) - 5y = e^{3t} + 4$ is $s\hat{y}(s) - 5\hat{y}(s) = (1/[s-3]) + (4/s)$; thus,

$$\hat{y}(s) = \frac{5s-12}{s(s-3)(s-5)}.$$

By partial fractions $\frac{1}{s(s-3)(s-5)} = -\frac{4}{5s} - \frac{1}{2(s-3)} + \frac{13}{10(s-5)}$; thus $\hat{y}(s) = -\frac{4}{5s} - \frac{1}{2(s-3)} + \frac{13}{10(s-5)}$.

Using $\mathcal{L}^{-1}\{(s-a)^{-1}\} = e^{at}$, the inverse Laplace transform is

$$y(t) = -\frac{4}{5} - \frac{1}{2}e^{3t} + \frac{13}{10}e^{5t}.$$

**Table 2A.1**. A Very Short Table of Laplace Transforms

| Transform function | Object function | Conditions |
|---|---|---|
| $1/s$ | $1$ | $s > 0$ |
| $1/(s-a)$ | $e^{at}$ | $s > 0$ |
| $1/(s^2 + a^2)$ | $(1/a)\sin at$ | $a \neq 0, s > 0$ |
| $s/(s^2 + a^2)$ | $\cos at$ | $s > 0$ |
| $1/(s(s+a))$ | $(1/a)(1 - e^{-at})$ | $s > a$ |

The convolution of the functions *f(t)* and *g(t)* is indicated by $f(t) * g(t)$ and defined as the integral

$$f(t) * g(t) = \int_0^t f(t-x)g(x)dx. \tag{2A.12}$$

It can be demonstrated that the convolution is commutative ($f * g = g * f$), associative ($(f * g) * h = f * (g * h)$), and distributive ($f * (g + h) = f * g + f * h$). The Laplace transform of a convolution is the product of the Laplace transforms; thus,

$$\mathcal{L}\{f(t) * g(t)\} = \tilde{f}(s)\tilde{g}(s). \tag{2A.13}$$

**Example 2A.2**

**Problem**: Solve the differential equation $(dy/dt) - 5y = q(t)$ for $y(0) = 0$ in the general case where *q(t)* is not specified, other than it has a Laplace transform.

**Solution**: Noting that the Laplace transform of $e^{-at}$ is $1/(s+a)$ and that the Laplace transform of the derivative of a function is equal to *s* times the Laplace transform of the function minus the value of the function at $t = 0$, the Laplace transform of $(dy/dt) - 5y = q(t)$ is $s\tilde{y}(s) - 5\tilde{y}(s) = \tilde{q}(s)$, and thus $\tilde{y}(s) = [\tilde{q}(s)/(s-5)]$.

Observe that $\tilde{y}(s)$ is the product of two transformed functions like those that appear on the right-hand side of (2A.13) above; thus, from (2A.13) one can see by partial fractions that

$$\mathcal{L}\left\{\int_0^t e^{5(t-x)}q(x)dx\right\} = \frac{\tilde{q}(s)}{(s-5)} \text{ or } \int_0^5 e^{5(t-x)}q(x)dx = \mathcal{L}^{-1}\left\{\frac{\tilde{q}(s)}{(s-5)}\right\},$$

thus,

$$y(t) = \int_0^t e^{5(t-x)}q(x)dx\,.$$

This is a general integral to the differential equation for any function *q(t)*.

In the material above it was assumed for simplicity that the functions were continuous in the interval $0 \le t \le \infty$. However, one of the most attractive features of using Laplace transforms is their simplicity in dealing with functions that contain discontinuities. The unit or Heaviside step function $h(t - t_o)$ is defined as 0 for $t < t_o$ and as 1 for $t > t_o$. Since the function jumps from the value 0 to the value 1 on passage through $t = t_o$, the approach of $h(t - t_o)$ to the value $t_o$ is therefore different from below than it is from above:

$$h(t_o^-) = \lim_{t->t_o^-} h(t) = 0\,,\; h(t_o^+) = \lim_{t->t_o^+} h(t) = 1\,. \tag{2A.14}$$

The function $h(t - t_o)$ is multi-valued at $t = t_o$, and its value there depends on how the point $t = t_o$ is approached. The Laplace transform of the discontinuous function, because it integrates the function, removes the discontinuity, and thus

$$\mathcal{L}\{h(t-t_0)\} = \int_0^\infty h(t-t_0)e^{-st}dt = \int_{t_0}^\infty e^{-st}dt = \frac{e^{-st_0}}{s}\,. \tag{2A.15}$$

The derivative of the unit step function is the delta function $\delta(t)$ that has the value 0 for all values of $t$ except $t = t_o$. The function may be viewed as the limit as $\varepsilon$ tends to zero of a function that has the value $1/\varepsilon$ between 0 and $\varepsilon$ and is zero everywhere else. These properties of $\delta(t)$ are then

$$\frac{dh(t-t_o)}{dt} = \delta(t-t_o)\,,\; \delta(t-t_o) = 0 \text{ for } t \neq t_o, \text{ and } \int_0^\infty \delta(t-t_o)dt = 1\,. \tag{2A.16}$$

If the delta function is multiplied by any other function $f(t)$, the product is zero everywhere except at $t = t_o$ and it follows that

$$\int_0^\infty f(t)\delta(t-t_o)dt = f(t_o)\,. \tag{2A.17}$$

**Example 2A.3**

**Problem**: Use Laplace transforms to solve the ordinary differential equation representing the standard linear solid (2.8) for $\tilde{F}(s)$ as a function of $\tilde{x}(s)$ and vice versa assuming that $F(0^-)$ and $x(0^-)$ are equal to zero. Then determine the creep and relaxation functions from the result.

**Solution**: The Laplace transform of the differential equation for the standard linear solid (2.8) is given by

$$\frac{\tilde{F}(s)}{k}+\tau_x\frac{s\tilde{F}(s)}{k}=\tilde{x}(s)+\tau_F s\tilde{x}(s)\,. \tag{2A.18}$$

The solutions of this transformed equation for $\tilde{F}(s)$, and for $\tilde{x}(s)$, are

$$\frac{\tilde{F}(s)}{k}=\frac{(1+s\tau_F)}{(1+s\tau_x)}\tilde{x}(s) \quad \text{and} \quad \tilde{x}(s)=\frac{(1+s\tau_x)}{(1+s\tau_F)}\frac{\tilde{F}(s)}{k}, \tag{2A.19}$$

respectively. To obtain the creep function one sets $F(t) = h(t)$ in the second of the equations above; thus, by partial fractions,

$$k\tilde{x}(s)=\frac{(1+s\tau_x)}{(1+s\tau_F)}\frac{1}{s}=\frac{1}{s(1+s\tau_F)}+\frac{\tau_x}{(1+s\tau_F)}\,, \tag{2A.20}$$

and to obtain the relaxation function one sets $x(t) = h(t)$ in the first of the equations above; thus,

$$\frac{\tilde{F}(s)}{k}=\frac{(1+s\tau_F)}{s(1+s\tau_x)}=\frac{1}{s(1+s\tau_x)}+\frac{\tau_F}{(1+s\tau_x)}\,. \tag{2A.21}$$

Executing the inverse Laplace transforms of $\tilde{x}(s)$ given by (2A.20) and $\tilde{F}(s)$ given by (2A.21), using inverse transform results in Table 2A.1, the creep and relaxation functions (2.10) and (2.11) are obtained.

## APPENDIX 2B. DIRECT INTEGRATION OF FIRST-ORDER DIFFERENTIAL EQUATIONS

The ordinary differential equation representing the standard linear solid (2.8) may be solved for $F(t)$ given a specified $x(t)$ by direct integration of (2.8), recognizing that it is a first-order ordinary differential equation. For the direct integration method, note that all solutions to the linear first-order differential equation,

$$\frac{dx}{dt}+p(t)x=q(t) \tag{2B.1}$$

are given by

$$x(t)=\left(e^{\int -p(t)dt}\right)\left[\int q(t)e^{\int p(t)dt}dt+C\right], \tag{2B.2}$$

where $C$ is a constant of integration (Kaplan 1958). If one sets $p(t) = (1/\tau_F)$ and $q(t) = (1/k\tau_F)F + (\tau_x/k\tau_F)(dF/dt)$, then (2.8) may be rewritten in the form of differential equation (2B.1), and it follows from (2B.2) that

$$x(t)=(e^{-t/\tau_F})\left(\frac{1}{k\tau_F}\right)\left[\int_0^t F(t)e^{t/\tau_F}dt+\tau_x\int_0^t\left(\frac{dF}{dt}\right)e^{t/\tau_F}dt\right]+Ce^{-t/\tau_F}\,.$$

For both the creep and the relaxation functions the constant $C$ is evaluated using the fact that the dashpot in the standard linear solid cannot extend in the first instant, so the deflection at $t = 0$, $x_o$, is due only to the deflection of the two springs in the standard linear solid. The two springs must deflect the same amount, $x_o$, thus the initial force is $F_o = (k + k_R)x_o$. This relation-

ship may be rewritten in the form $F_o = (k\tau_F/\tau_x)x_o$, using the definitions in (2.9). For the creep function the initial force, $F_o$, is taken to be one unit of force; thus, the initial displacement is given by $x(0^+) = x_o = \tau_x/k\tau_F$. For the relaxation function the initial displacement, $x_o$, is taken to be one unit of displacement; thus, the initial force $F_o$ is given by $F(0^+) = F_o = k\tau_F/\tau_x$. To obtain the creep function one sets $F(t) = h(t)$; thus,

$$x(t) = (e^{-t/\tau_F})\left(\frac{1}{k\tau_F}\right)\left[\int_0^t h(t)e^{t/\tau_F}\,dt + \tau_x\int_0^t \delta(t)e^{t/\tau_F}\,dt\right] + Ce^{-t/\tau_F}.$$

The integrals in this equation may be evaluated with ease using the definition of the unit step function and integral formula (2.12), while the initial condition $x(0^+) = x_o = \tau_x/k\tau_F$ requires that $C = 0$; thus, the creep function $c(t)$ for the standard linear solid (2.10) is again recovered. The relaxation function for the standard linear solid is found by the same methods with some interchange in the roles of $F(t)$ and $x(t)$. In this case the selection of $p(t)$ and $q(t)$ in (2B.1) are such that $p(t) = (1/\tau_x)$ and $q(t) = (k/\tau_x)(x + \tau_F(dx/dt))$, then the solution of (2.8) for $F(t)$ is given by (2B.2) as

$$F(t) = (e^{-t/\tau_x})\left(\frac{k}{\tau_x}\right)\left[\int_0^t x(t)e^{t/\tau_x}\,dt + \tau_F\int_0^t \left(\frac{dx}{dt}\right)e^{t/\tau_x}\,dt\right] + Ce^{-t/\tau x}.$$

To obtain the relaxation function one sets $x(t) = h(t)$, and thus

$$F(t) = (e^{-t/\tau_x})\left(\frac{k}{\tau_x}\right)\left[\int_0^t h(t)e^{t/\tau_x}\,dt + \tau_F\int_0^t (\delta(t)e^{t/\tau_x}\,dt\right].$$

The integrals in this equation may again be evaluated using the definition of the unit step function and integral formula (2A.17). Thus, setting $F(t) = r(t)$ and using the fact that the initial condition, $F(0^+) = F_o = k\tau_F/\tau_x$ requires that $C = 0$, the relaxation function for a standard linear solid (2.10) is obtained again.

## APPENDIX 2C. ELECTRICAL ANALOGS OF THE SPRING AND DASHPOT MODELS

For a given spring and dashpot model it is possible to construct two different analogous electrical circuits whose differential equations have the same form. Similarly, two spring and dashpot model analogs may be constructed for an electrical circuit. This is true for the standard linear solid model. For a given circuit, one analog is obtained by replacing series elements by analogous elements in series, and, similarly, the parallel elements are replaced by analogous elements also in parallel. This type of analog is called a *direct analog.* The second analog is obtained by replacing the series elements in the given circuit by analogous elements in parallel, and the parallel elements are replaced by analogous elements in series. Because the connections are inverted, this type of analog is called an *inverse analog.*

To construct a direct analog between electrical and mechanical systems, series elements are replaced by series elements in accordance with the analogous relationships of Table 2C.1. Similarly, parallel elements are replaced by parallel elements in accordance with the Table 2C.1. Because force and voltage are analogous quantities, this type of analog is referred to as a *force-voltage analog.* The force-voltage electrical circuit analogs for the Maxwell model, the Voigt model, and the standard linear solid model are given in the middle panels of Figure 2.40a–c.

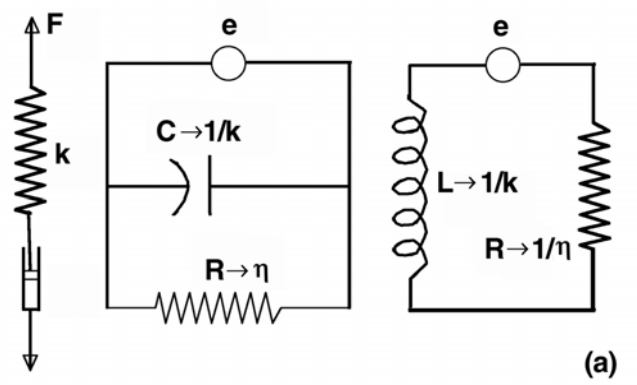



**Figure 2.40a**. The two electrical analogs for the Maxwell model. The left panel is the Maxwell model, the middle panel the force–voltage analog electrical circuit, and the right panel the force–current analog electrical circuit.

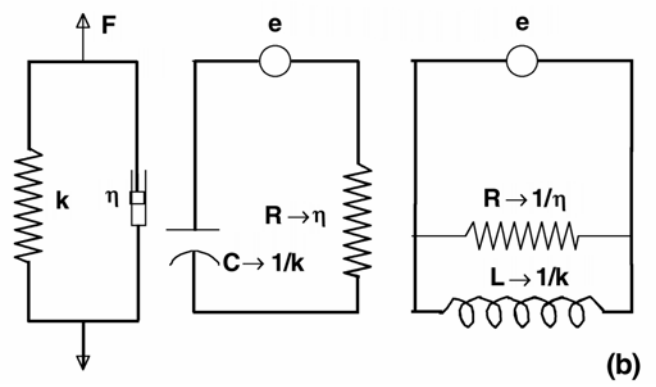



**Figure 2.40b**. The two electrical analogs for the Voigt model. The left panel is the Voigt model, the middle panel is force–voltage analog electrical circuit, and the right panel the force–current analog electrical circuit.

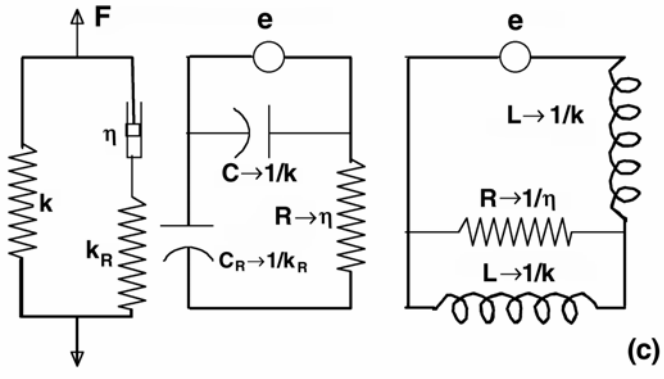



**Figure 2.40c**. The two electrical analogs for the standard linear solid model. The left panel is the standard linear solid model; the middle panel is the force–voltage analog electrical circuit; the right panel is the force–current analog electrical circuit.

**Table 2C.1**. Analogous Quantities for a Direct (Force–Voltage) Analog and the Inverse (Force–Current) Analog

| Mechanical system | Force–voltage analog | Force–current analog |
|---|---|---|
| $F$ Force | $e$ Voltage | $i$ Current |
| $x$ Displacement | Charge $q$ | Integral of voltage $\int e dt$ |
| OR ($dx/dt$) Velocity | Current $i$ | Voltage $e$ |
| $m$ Mass | $L$ Inductance | $C$ Capacitance |
| $\eta$ Dashpot | $R$ Resistance | $1/R$ Conductance |
| $k$ Spring | $1/C$ Inverse capacitance | $1/L$ Inverse inductance |

*Note that the third line is an alternative to the line above, and both lines contain the same deformation in alternate representations.

The other analog that exists between the spring and dashpot models and electrical circuits is the inverse analog. To construct an inverse analog, series elements are replaced by parallel elements, and vice versa. Because force and current are analogous quantities, this inverse analog is referred to as a *force-current analog*. The force-current electrical circuit analogs for the Maxwell model, the Voigt model, and the standard linear solid model are given in the right panels of Figure 2.40a–c.

Electrical analogs are not possible for all mechanical systems; they are limited to lumped spring-mass-damper systems. For further exploration of this topic see, for example, Thomson (1960) or Raven (1966).

# 3

# BASIC CONTINUUM KINEMATICS

The theme of this chapter was stated with exuberance and in an idealistic deterministic extreme by the Marquis Pierre-Simon de Laplace (1759–1827): "Thus, we must consider the present state of the universe as the effect of its previous state and as the cause of those states to follow. An intelligent being which, for a given point in time, knows all the forces acting upon the universe and the positions of the objects of which it is composed, supplied with facilities large enough to submit these data to numerical analysis, would include in the same formula the movements of the largest bodies of the universe and those of the lightest atom. Nothing would be uncertain for it, and the past and future would be known to it." [Trans. John H. Van Drie (http://www.johnvandrie.com)]

## 3.1. THE DEFORMABLE MATERIAL MODEL, THE CONTINUUM

In the deformable material model all types of motion are permitted, but the deformational motions are usually the major concern. Consider the image $O$ of an object in Euclidean space. The object is in a configuration $O(0)$ at $t = 0$ and in a configuration $O(t)$ at time t (Figure 3.1). The mathematical representation of the motion of a three-dimensional deformable continuum gives a complete history of the motion of each point $P$ on the object $O(0)$, $P \subset O(0)$; in words, $P \subset O(0)$ means all points $P$ contained in ($\subset$) the image of the object, $O$, at $t = 0$. In order to identify each point $P$ in the object $O(0)$ and follow the movement of that point in subsequent configurations of the object $O(t)$, each point on an object is given a reference location in a particular coordinate system, called the *reference coordinate system*. The selection of the reference configuration is the choice of the modeler; here the reference configuration is taken as the configuration of the object at time $t = 0$. To distinguish between the reference location of a point on an object and a location of the same point at a later time, the terminology of "particle" and "place" of a particle is introduced. Each point $P \subset O(0)$ in the continuum model of the object is labeled by its position in the reference configuration (Figure 3.2). This procedure assigns a location to each point in the object, and such points are called *particles*. A position vector of a point in a given coordinate system is a vector from the origin of coordinates to that point. In this case the reference configuration is a three-dimensional Cartesian coordinate system with base vectors $\mathbf{e}_\alpha$, $\alpha$ = I, II, III, and coordinates $X_\alpha$; the position of the particle is described by the vector

$$\mathbf{X} = \sum_{\alpha=1}^{\text{III}} X_\alpha \mathbf{e}_\alpha .$$

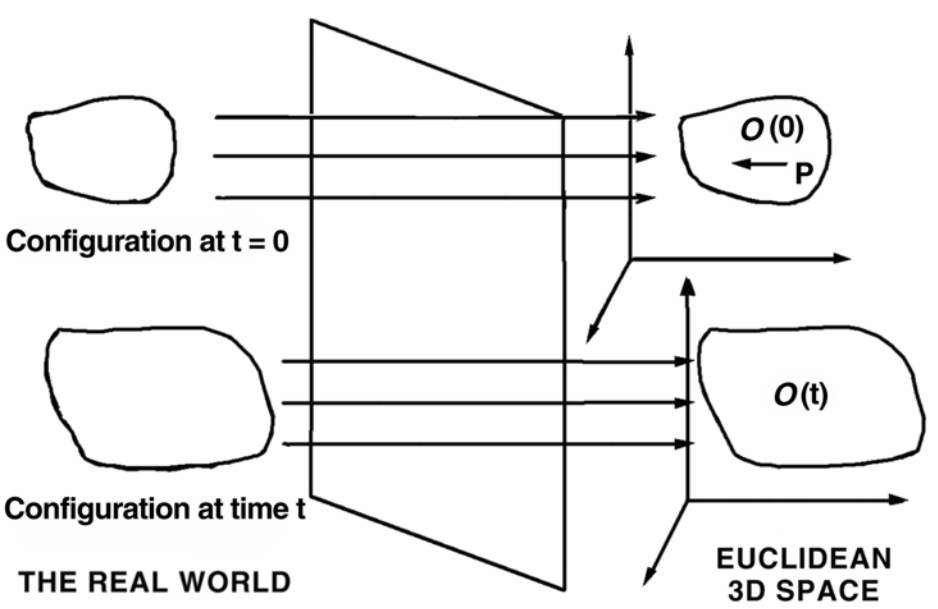



**Figure 3.1**. Representation of the motion of an object in Euclidean 3D space.

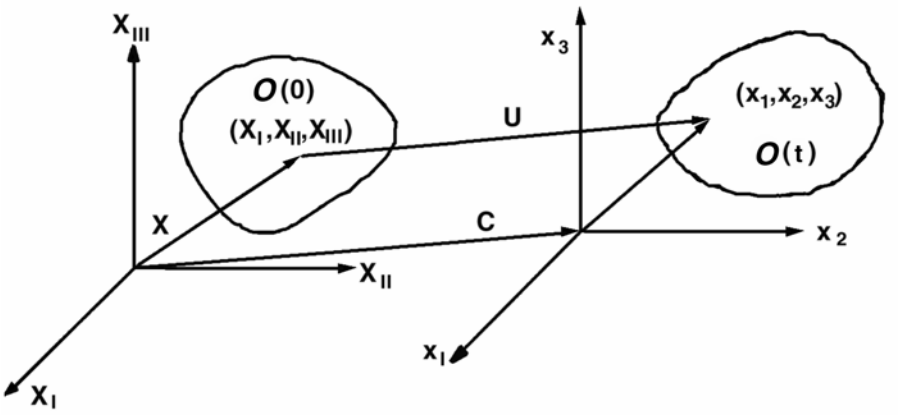



**Figure 3.2**. Details of the representation in Euclidean 3D space.

As a simplifying convention, instead of saying the vector $\mathbf{X}$ *describes the position* of a particle, we define it to *be* the particle. Thus the notation $\mathbf{X}$ has replaced the notation $P$, and one can speak of all $\mathbf{X} \subset O(0)$ as a complete representation of the object in the reference configuration.

If the motion of one particle $\mathbf{X}$ of an object can be represented, then the motion of all the particles of the object, $\mathbf{X} \subset O(0)$, can be represented. A second coordinate system with axes $x_i$, $i = 1, 2, 3$, and base vectors $\mathbf{e}_i$, $i = 1, 2, 3$, is introduced to represent the present position of the object $O(t)$; this also represents the present positions of the particles. The triplet $(x_1, x_2, x_3)$,

denoted in the shorthand direct notation by $\mathbf{x}$, represents the place at time $t$ of particle $\mathbf{X}$. The motion of particle $\mathbf{X}$ is then given by

$$x_1 = \chi_1(X_{\mathrm{I}}, X_{\mathrm{II}}, X_{\mathrm{III}}, t),\ \ x_2 = \chi_2(X_{\mathrm{I}}, X_{\mathrm{II}}, X_{\mathrm{III}}, t),\ \ x_3 = \chi_3(X_{\mathrm{I}}, X_{\mathrm{II}}, X_{\mathrm{III}}, t), \tag{3.1}$$

which is a set of three scalar-valued functions whose arguments are the particle $\mathbf{X}$ and time $t$ and whose values are the components of the place $\mathbf{x}$ at time $t$ of particle $\mathbf{X}$. Since $\mathbf{X}$ can be any particle in the object, $\mathbf{X} \subset O(0)$, the motion (3.1) describes the motion of the entire object $\mathbf{x} \subset O(\mathrm{t})$ and eq. (3.1) is thus referred to as the *motion* of the object $O$. In the direct shorthand or vector notation, (3.1) is written as

$$\mathbf{x} = \boldsymbol{\chi}(\mathbf{X}, t) \text{ for all } \mathbf{X} \subset O(0). \tag{3.2}$$

This is called the *material description of motion* because the material particles $\mathbf{X}$ are the independent variables. Generally the form of the motion, (3.1) or (3.2), is unknown in a problem, and the prime kinematic assumption for all continuum models is that such a description of the motion of an object is possible.

However, if the motion is known, then all the kinematic variables of interest concerning the motion of the object can be calculated from it; this includes velocities, accelerations, displacements, strains, rates of deformation, etc. The present, past, and future configurations of the object are all known. The philosophical concept embedded in the representation of a motion (3.2) is that of determinism. The determinism of the 18th century in physical theory was modified by humbler notions of "uncertainty" in the 19th century and by the discovery of extreme sensitivity to starting or initial conditions known by the misnomer "chaos" in the 20th century. The quote of the Marquis Pierre-Simon de Laplace (1759–1827) at the beginning of the chapter captures the idea of determinism underlying representation (3.2).

A translational rigid object motion is a special case of (3.2) represented by

$$\mathbf{x} = \mathbf{X} + \mathbf{h}(t) \text{ for all } \mathbf{X} \subset O(0), \tag{3.3}$$

where $\mathbf{h}(t)$ is a time-dependent vector. A rotational rigid object motion is a special case of (3.2), represented by

$$\mathbf{x} = \mathbf{Q}(t)\mathbf{X},\ \ \mathbf{Q}(t)\mathbf{Q}(t)^{\mathrm{T}} = \mathbf{1}, \text{ for all } \mathbf{X} \subset O(0), \tag{3.4}$$

where $\mathbf{Q}(t)$ is a time-dependent orthogonal transformation. It follows that a general rigid object motion is a special case of (3.2), represented by

$$\mathbf{x} = \mathbf{Q}(t)\mathbf{X} + \mathbf{h}(t),\ \ \mathbf{Q}(t)\mathbf{Q}(t)^{\mathrm{T}} = \mathbf{1}, \text{ for all } \mathbf{X} \subset O(0). \tag{3.5}$$

A motion of the form (3.2) is said to be a planar motion if the particles always remain in the same plane. In this case (3.2) becomes

$$x_1 = \chi_1(X_{\mathrm{I}}, X_{\mathrm{II}}, t),\ \ x_2 = \chi_2(X_{\mathrm{I}}, X_{\mathrm{II}}, t),\ \ x_3 = X_{\mathrm{III}}. \tag{3.6}$$

Another subset of the motion is a deformation of an object from one configuration to another, say from the configuration at $t = 0$ to the configuration at $t = t^*$. In this case the motion (3.2) becomes a deformation:

$$\mathbf{x} = \boldsymbol{\psi}(\mathbf{X}) \text{ for all } \mathbf{X} \subset O(0), \tag{3.7}$$

where

$$\boldsymbol{\psi}(\mathbf{X}) = \boldsymbol{\chi}(\mathbf{X}, t^*) \text{ for all } \mathbf{X} \subset O(0). \tag{3.8}$$

A 3D motion picture or 3D video of the motion of an object may be represented by a subset of the motion (3.2) because a discrete number of images (frames) per second are employed:

$$\mathbf{x} = \boldsymbol{\chi}(\mathbf{X}, n/\zeta) \text{ for all } \mathbf{X} \subset O(0), \ n = 0, 1, 2, \ldots, \tag{3.9}$$

where $\zeta$ is the number of images (frames) per second.

**Example 3.1.1**

Consider the special case of a planar motion given by

$$x_1 = A(t)X_{\mathrm{I}} + C(t)X_{\mathrm{II}} + E(t), \ x_2 = D(t)X_{\mathrm{I}} + B(t)X_{\mathrm{II}} + F(t), \ x_3 = X_{\mathrm{III}}, \tag{3.10}$$

where $A(t)$, $B(t)$, $C(t)$, $D(t)$, $E(t)$, $F(t)$ are arbitrary functions of time. Further specialize this motion by the selections

$$A(t) = 1 + t, \ C(t) = t, \ E(t) = 3t; \ B(t) = 1 + t, \ D(t) = t, \ F(t) = 2t, \tag{3.11}$$

for $A(t)$, $B(t)$, $C(t)$, $D(t)$, $E(t)$, and $F(t)$. With these selections the motion becomes

$$x_1 = (1 + t)X_{\mathrm{I}} + tX_{\mathrm{II}} + 3t, \ x_2 = tX_{\mathrm{I}} + (1 + t)X_{\mathrm{II}} + 2t, \ x_3 = X_{\mathrm{III}}. \tag{3.12}$$

The problem is to find the positions of the unit square whose corners are at the material points $(X_{\mathrm{I}}, X_{\mathrm{II}}) = (0,0)$, $(X_{\mathrm{I}}, X_{\mathrm{II}}) = (1,0)$, $(X_{\mathrm{I}}, X_{\mathrm{II}}) = (1,1)$, $(X_{\mathrm{I}}, X_{\mathrm{II}}) = (0,1)$ at times $t = 1$ and $t = 2$.

**Solution**: For convenience let the spatial $(x_1, x_2, x_3)$ and material $(X_{\mathrm{I}}, X_{\mathrm{II}}, X_{\mathrm{III}})$ coordinate systems coincide, and then consider the effect of the motion (3.12) on the unit square whose corners are at the material points $(X_{\mathrm{I}}, X_{\mathrm{II}}) = (0,0)$, $(X_{\mathrm{I}}, X_{\mathrm{II}}) = (1,0)$, $(X_{\mathrm{I}}, X_{\mathrm{II}}) = (1,1)$, $(X_{\mathrm{I}}, X_{\mathrm{II}}) = (0,1)$. At $t = 0$ the motion (3.12) specifies that $x_1 = X_{\mathrm{I}}$, $x_2 = X_{\mathrm{II}}$, and $x_3 = X_{\mathrm{III}}$, so that $t = 0$ has been taken as the reference configuration. The square at $t = 0$ is illustrated in Figure 3.1. At $t = 1$ the motion (3.12) specifies the places $\mathbf{x}$ of the particles $\mathbf{X}$ as follows:

$$x_1 = 2X_{\mathrm{I}} + X_{\mathrm{II}} + 3, \ x_2 = X_{\mathrm{I}} + 2X_{\mathrm{II}} + 2, \ x_3 = X_{\mathrm{III}}$$

Thus the particles at the four corners of the unit square have the following new places $\mathbf{x}$ at $t = 1$:

$$(3, 2) = \boldsymbol{\chi}(0, 0), \ (5, 3) = \boldsymbol{\chi}(1, 0), \ (6, 5) = \boldsymbol{\chi}(1, 1), \ (4, 4) = \boldsymbol{\chi}(0, 1).$$

A sketch of the deformed and translated unit square at $t = 1$ is shown in Figure 3.3. At $t = 2$ the motion (3.12) specifies the places $\mathbf{x}$ of the particles $\mathbf{X}$ as follows:

$$x_1 = 3X_{\mathrm{I}} + 2X_{\mathrm{II}} + 6, \ x_2 = 2X_{\mathrm{I}} + 3X_{\mathrm{II}} + 4, \ x_3 = X_{\mathrm{III}}.$$

Thus, the particles at the four corners of the unit square have the following new places at $t = 2$:

$$(6, 4) = \boldsymbol{\chi}(0, 0), \ (9, 6) = \boldsymbol{\chi}(1, 0), \ (11, 9) = \boldsymbol{\chi}(1, 1), \ (8, 7) = \boldsymbol{\chi}(0, 1).$$

A sketch of the deformed and translated unit square at $t = 2$ is shown in Figure 3.3.

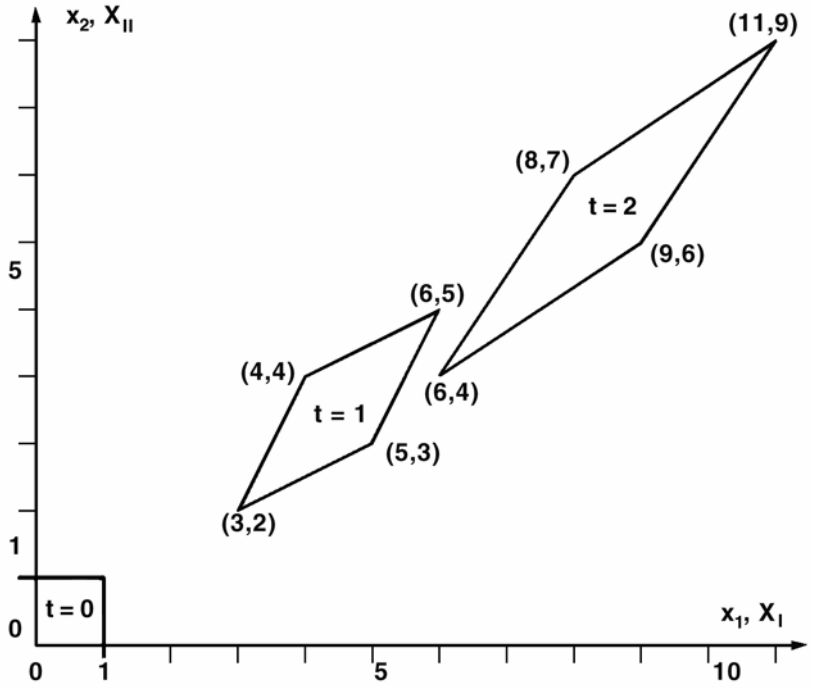



**Figure 3.3**. The movement of a square at $t = 0$ due to the motion describe by eq. (3.12).

**Example 3.1.2**

An experimental technique in widespread use in the measurement of the planar homogeneous motion of soft tissue is to place three markers (dots or beads) in a triangular pattern (so that the markers are not collinear) on the soft tissue before a motion. The initial locations of the three markers are recorded relative to a fixed laboratory frame of reference as $\left(X_{\mathrm{I}}^{(1)}, X_{\mathrm{II}}^{(1)}\right)$, $\left(X_{\mathrm{I}}^{(2)}, X_{\mathrm{II}}^{(2)}\right)$, and $\left(X_{\mathrm{I}}^{(3)}, X_{\mathrm{II}}^{(3)}\right)$ (see Figure 3.4). If the process is automated, a camera is used to follow the motion of the three markers with time and to digitize the data in real time. The instantaneous locations of the three markers at a time $t$ is recorded relative to a fixed laboratory frame of reference as $\left(x_1^{(1)}(t), x_1^{(2)}(t)\right)$, $\left(x_1^{(2)}(t), x_2^{(2)}(t)\right)$, and $\left(x_1^{(3)}(t), x_2^{(3)}(t)\right)$ (Figure 3.4). From these data the soft tissue experimentalist calculates the time-dependent coefficients *A(t), B(t), C(t), D(t), E(t)*, and *F(t)* of the homogeneous planar motion (3.10). Determine the formulas used in the calculation of the time-dependent coefficients *A(t), B(t), C(t), D(t), E(t)*, and *F(t)* from the data $\left(X_{\mathrm{I}}^{(1)}, X_{\mathrm{II}}^{(1)}\right)$, $\left(X_{\mathrm{I}}^{(2)}, X_{\mathrm{II}}^{(2)}\right)$, $\left(X_{\mathrm{I}}^{(3)}, X_{\mathrm{II}}^{(3)}\right)$, $\left(x_1^{(1)}(t), x_2^{(1)}(t)\right)$, ($\left(x_1^{(2)}(t), x_2^{(2)}(t)\right)$, and $\left(x_1^{(3)}(t), x_2^{(3)}(t)\right)$.

**Solution**: The data on the motion of each marker provide two equations that may be used for determination of the time-dependent coefficients. Since there are three markers, a total of six equations are obtained. Three markers are used because it is known that six equations will be needed to solve the linear system of equations for the six unknowns, *A(t), B(t), C(t), D(t), E(t)*, and *F(t)*. Using the notation for the data and the representation of the homogeneous planar motion (3.10), these six equations are as follows:

$$x_1^{(1)}(t) = A(t)X_{\mathrm{I}}^{(1)} + C(t)X_{\mathrm{II}}^{(1)} + E(t)\,, \quad x_2^{(1)}(t) = D(t)X_{\mathrm{I}}^{(1)} + B(t)X_{\mathrm{II}}^{(1)} + F(t)\,,$$

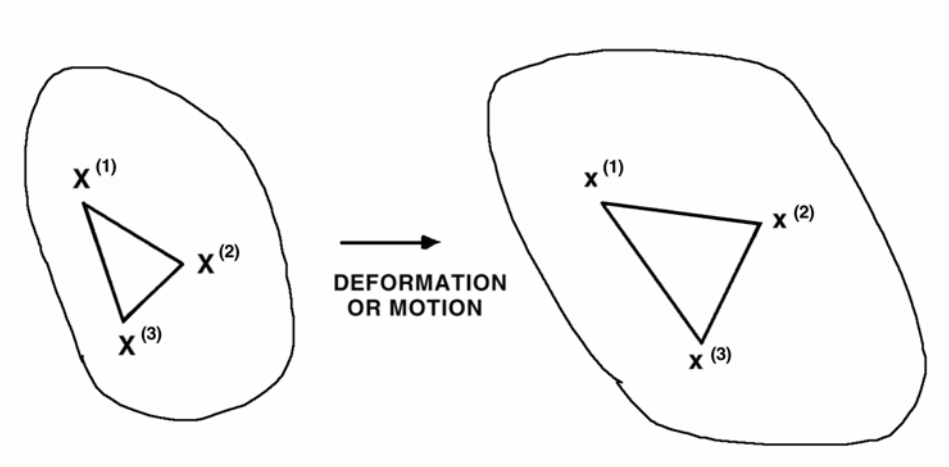



**Figure 3.4**. The experimental measurement of a planar homogeneous motion. The reference frame is the laboratory reference frame. The three initial positions ($\mathbf{X}^{(1)}$, $\mathbf{X}^{(2)}$, $\mathbf{X}^{(3)}$) of the markers are indicated as well as their positions ($\mathbf{x}^{(1)}$, $\mathbf{x}^{(2)}$, $\mathbf{x}^{(3)}$) at time $t$. In many experiments the markers are attached to a specimen of soft tissue that is undergoing a planar homogeneous motion in order to quantify the motion.

$$x_1^{(2)}(t) = A(t)X_{\mathrm{I}}^{(2)} + C(t)X_{\mathrm{II}}^{(2)} + E(t)\,, \quad x_2^{(2)}(t) = D(t)X_{\mathrm{I}}^{(2)} + B(t)X_{\mathrm{II}}^{(2)} + F(t)\,,$$

$$x_1^{(3)}(t) = A(t)X_{\mathrm{I}}^{(3)} + C(t)X_{\mathrm{II}}^{(3)} + E(t)\,, \quad x_2^{(3)}{}_{(t)} = D(t)X_{\mathrm{I}}^{(3)} + B(t)X_{\mathrm{II}}^{(3)} + F(t)\,.$$

The solution to these six equations is

$$A(t) = \frac{X_{\mathrm{II}}^{(1)}x_1^{(2)}(t) - X_{\mathrm{II}}^{(1)}x_1^{(3)}(t) - X_{\mathrm{II}}^{(2)}x_1^{(1)}(t) + X_{\mathrm{II}}^{(2)}x_1^{(3)}(t) + X_{\mathrm{II}}^{(3)}x_1^{(1)}(t) - X_{\mathrm{II}}^{(3)}x_1^{(2)}(t)}{X_{\mathrm{II}}^{(1)}X_{\mathrm{I}}^{(2)} - X_{\mathrm{II}}^{(1)}X_{\mathrm{I}}^{(3)} - X_{\mathrm{II}}^{(2)}X_{\mathrm{I}}^{(1)} + X_{\mathrm{II}}^{(2)}X_{\mathrm{I}}^{(3)} + X_{\mathrm{II}}^{(3)}X_{\mathrm{I}}^{(1)} - X_{\mathrm{II}}^{(3)}X_{\mathrm{I}}^{(2)}}\,,$$

$$B(t) = \frac{X_{\mathrm{I}}^{(2)}x_2^{(1)}(t) - X_{\mathrm{I}}^{(3)}x_2^{(1)}(t) - X_{\mathrm{I}}^{(1)}x_2^{(2)}(t) + X_{\mathrm{I}}^{(3)}x_2^{(2)}(t) + X_{\mathrm{I}}^{(1)}x_2^{(3)}(t) - X_{\mathrm{I}}^{(2)}x_2^{(3)}(t)}{X_{\mathrm{II}}^{(1)}X_{I}^{(2)} - X_{\mathrm{II}}^{(1)}X_{\mathrm{I}}^{(3)} - X_{\mathrm{II}}^{(2)}X_{\mathrm{I}}^{(1)} + X_{\mathrm{II}}^{(2)}X_{\mathrm{I}}^{(3)} + X_{\mathrm{II}}^{(3)}X_{\mathrm{I}}^{(1)} - X_{\mathrm{II}}^{(3)}X_{\mathrm{I}}^{(2)}}\,,$$

$$C(t) = \frac{-X_{\mathrm{I}}^{(1)}x_1^{(2)}(t) + X_{\mathrm{I}}^{(2)}x_1^{(1)}(t) + X_{\mathrm{I}}^{(1)}x_1^{(3)}(t) - X_{\mathrm{I}}^{(2)}x_1^{(3)}(t) - X_{\mathrm{I}}^{(3)}x_1^{(1)}(t) + X_{\mathrm{I}}^{(3)}x_1^{(2)}(t)}{X_{\mathrm{II}}^{(1)}X_{\mathrm{I}}^{(2)} - X_{\mathrm{II}}^{(1)}X_{\mathrm{I}}^{(3)} - X_{\mathrm{II}}^{(2)}X_{\mathrm{I}}^{(1)} + X_{\mathrm{II}}^{(2)}X_{\mathrm{I}}^{(3)} + X_{\mathrm{II}}^{(3)}X_{\mathrm{I}}^{(1)} - X_{\mathrm{II}}^{(3)}X_{\mathrm{I}}^{(2)}}\,,$$

$$D(t) = \frac{X_{\mathrm{II}}^{(1)}x_2^{(2)}(t) - X_{\mathrm{II}}^{(2)}x_2^{(1)}(t) - X_{\mathrm{II}}^{(1)}x_2^{(3)}(t) + X_{\mathrm{II}}^{(2)}x_2^{(3)}(t) + X_{\mathrm{II}}^{(3)}x_2^{(1)}(t) - X_{\mathrm{II}}^{(3)}x_2^{(2)}(t)}{X_{\mathrm{II}}^{(1)}X_{\mathrm{I}}^{(2)} - X_{\mathrm{II}}^{(1)}X_{\mathrm{I}}^{(3)} - X_{\mathrm{II}}^{(2)}X_{\mathrm{I}}^{(1)} + X_{\mathrm{II}}^{(2)}X_{\mathrm{I}}^{(3)} + X_{\mathrm{II}}^{(3)}X_{\mathrm{I}}^{(1)} - X_{\mathrm{II}}^{(3)}X_{\mathrm{I}}^{(2)}}\,,$$

$$E(t) = \frac{X_{\mathrm{II}}^{(1)}X_{\mathrm{I}}^{(2)}x_1^{(3)}(t) - X_{\mathrm{II}}^{(1)}X_{\mathrm{I}}^{(3)}x_1^{(2)}(t) - X_{\mathrm{I}}^{(1)}X_{\mathrm{II}}^{(2)}x_1^{(3)}(t)}{X_{\mathrm{II}}^{(1)}X_{\mathrm{I}}^{(2)} - X_{\mathrm{II}}^{(1)}X_{\mathrm{I}}^{(3)} - X_{\mathrm{II}}^{(2)}X_{\mathrm{I}}^{(1)} + X_{\mathrm{II}}^{(2)}X_{\mathrm{I}}^{(3)} + X_{\mathrm{II}}^{(3)}X_{\mathrm{I}}^{(1)} - X_{\mathrm{II}}^{(3)}X_{\mathrm{I}}^{(2)}} +$$

$$\frac{X_{\mathrm{II}}^{(2)}X_{\mathrm{I}}^{(3)}x_1^{(1)}(t) + X_{\mathrm{II}}^{(2)}X_{\mathrm{I}}^{(3)}x_1^{(2)}(t) - X_{\mathrm{I}}^{(2)}X_{\mathrm{II}}^{(3)}x_1^{(1)}(t)}{X_{\mathrm{II}}^{(1)}X_{\mathrm{I}}^{(2)} - X_{\mathrm{II}}^{(1)}X_{\mathrm{I}}^{(3)} - X_{\mathrm{II}}^{(2)}X_{\mathrm{I}}^{(1)} + X_{\mathrm{II}}^{(2)}X_{\mathrm{I}}^{(3)} + X_{\mathrm{II}}^{(3)}X_{\mathrm{I}}^{(1)} - X_{\mathrm{II}}^{(3)}X_{\mathrm{I}}^{(2)}}\,,$$

$$F(t) = \frac{-X_{II}^{(1)}X_{I}^{(3)}x_2^{(2)}(t) + X_{II}^{(2)}X_{I}^{(3)}x_2^{(1)}(t) + X_{I}^{(2)}X_{II}^{(1)}x_2^{(3)}(t)}{X_{II}^{(1)}X_{I}^{(2)} - X_{II}^{(1)}X_{I}^{(3)} - X_{II}^{(2)}X_{I}^{(1)} + X_{II}^{(2)}X_{I}^{(3)} + X_{II}^{(3)}X_{I}^{(1)} - X_{II}^{(3)}X_{I}^{(2)}} +$$

$$\frac{-X_{II}^{(2)}X_{I}^{(1)}x_2^{(3)}(t) - X_{II}^{(3)}X_{I}^{(2)}x_2^{(1)}(t) + X_{I}^{(1)}X_{II}^{(3)}x_2^{(2)}(t)}{X_{II}^{(1)}X_{I}^{(2)} - X_{II}^{(1)}X_{I}^{(3)} - X_{II}^{(2)}X_{I}^{(1)} + X_{II}^{(2)}X_{I}^{(3)} + X_{II}^{(3)}X_{I}^{(1)} - X_{II}^{(3)}X_{I}^{(2)}}.$$

**Example 3.1.3**

Consider again the experimental technique described in Example 3.1.2, but in this case a deformation rather than a motion (see Figure 3.4). Suppose that the initial locations of the markers are recorded relative to the fixed laboratory frame of reference as $\left(X_{I}^{(1)}, X_{II}^{(1)}\right) = (0,0)$, $\left(X_{I}^{(2)}, X_{II}^{(2)}\right) = (1, 0)$, and $\left(X_{I}^{(3)}, X_{II}^{(3)}\right) = (0, 1)$. The deformed locations of the three markers relative to the same fixed laboratory frame of reference are $\left(x_1^{(1)}, x_2^{(1)}\right) = (1, 2)$, $\left(x_1^{(2)}, x_2^{(2)}\right) = (3,3.25)$, and $\left(x_1^{(3)}, x_2^{(3)}\right) = (2.5, 3.75)$. From these data the constant coefficients *A, B, C, D, E*, and *F* of the homogeneous planar deformation (3.10) are determined.

**Solution**: The solution for the motion coefficients *A(t), B(t), C(t), D(t), E(t)*, and *F(t)* obtained in Example 3.1.2 may be used in the solution to this problem. One simply assigns the time-dependent positions in the formulas for *A(t), B(t), C(t), D(t), E(t)*, and *F(t)* to be fixed rather than time dependent by setting $\left(x_1^{(1)}(t), x_2^{(1)}(t)\right) = \left(x_1^{(1)}, x_2^{(1)}\right)$, $\left(x_1^{(2)}(t), x_2^{(2)}(t)\right) = \left(x_1^{(2)}, x_2^{(2)}\right)$, and $\left(x_1^{(3)}(t), x_2^{(3)}(t)\right) = \left(x_1^{(3)}, x_2^{(3)}\right)$. The coefficients are no longer functions of time, so they are denoted by *A, B, C. D, E*, and *F*. They are evaluated by substituting the initial and final locations of the set of particles, $\left(X_{I}^{(1)}, X_{II}^{(1)}\right) = (0, 0)$, $\left(X_{I}^{(2)}, X_{II}^{(2)}\right) = (1, 0)$, $\left(X_{I}^{(3)}, X_{II}^{(3)}\right) = (0, 1)$, and $\left(x_1^{(1)}, x_2^{(1)}\right) = (1, 2)$, $\left(x_1^{(2)}, x_2^{(2)}\right) = (3, 3.25)$, $\left(x_1^{(3)}, x_2^{(3)}\right) = (2.5, 3.75)$, respectively, into the last set of equations in Example 3.1.2. The values obtained are $A = 2$, $B = 1.75$, $C = 1.5$, $D = 1.25$, $E = 1$, and $F = 2$, and they are obtained by substituting the values for the relevant points given in the statement of the problem above into the last set of equations in Example 3.1.2. The planar homogeneous deformation then has the representation

$$x_1 = 2X_{I} + 1.5X_{II} + 1,\ x_2 = 1.25X_{I} + 1.75X_{II} + 2,\ x_3 = X_{III},$$

which is a particular case of (3.10). To double check this calculation one can check to see if each marker is mapped correctly from its initial position to its final position.

There are two coordinate systems with respect to which a gradient may be taken, either the spatial coordinate system $\mathbf{x}$, $(x_1, x_2, x_3)$, or the reference material coordinate system $\mathbf{X}$, $(X_{I}, X_{II}, X_{III})$. To distinguish between gradients with respect to these two systems, the usual gradient symbol $\nabla$ will be used to indicate a gradient with respect to the spatial coordinate system $\mathbf{x}$, and the gradient symbol $\nabla_o$ with a subscripted boldface $\mathbf{O}$ will indicate a gradient with respect to the material coordinate system $\mathbf{X}$. The (material) deformation gradient tensor $\mathbf{F}$ is defined by

$$\mathbf{F} = [\nabla_o \otimes \boldsymbol{\chi}(\mathbf{X}, t)]^T \text{ for all } \mathbf{X} \subset O(0). \tag{3.13}$$

The (spatial) inverse deformation gradient tensor $\mathbf{F}^{-1}$ is defined by

$$\mathbf{F}^{-1} = [\nabla \otimes \boldsymbol{\chi}^{-1}(\mathbf{x}, t)]^T \text{ for all } \mathbf{x} \subset O(t), \tag{3.14}$$

where

$$\mathbf{X} = \boldsymbol{\chi}^{-1}(\mathbf{x}, t) \text{ for all } \mathbf{x} \subset O(t) \tag{3.15}$$

is the inverse of the motion (3.2). The components of $\mathbf{F}$ and $\mathbf{F}^{-1}$ are

$$\mathbf{F} = \left[\frac{\partial x_i}{\partial X_\alpha}\right] = \begin{bmatrix} \frac{\partial x_1}{\partial X_{\mathrm{I}}} & \frac{\partial x_1}{\partial X_{\mathrm{II}}} & \frac{\partial x_1}{\partial X_{\mathrm{III}}} \\ \frac{\partial x_2}{\partial X_{\mathrm{I}}} & \frac{\partial x_2}{\partial X_{\mathrm{II}}} & \frac{\partial x_2}{\partial X_{\mathrm{III}}} \\ \frac{\partial x_3}{\partial X_{\mathrm{I}}} & \frac{\partial x_3}{\partial X_{\mathrm{II}}} & \frac{\partial x_3}{\partial X_{\mathrm{III}}} \end{bmatrix} \text{ and } \mathbf{F}^{-1} = \left[\frac{\partial X_\alpha}{\partial x_i}\right] = \begin{bmatrix} \frac{\partial X_{\mathrm{I}}}{\partial x_1} & \frac{\partial X_{\mathrm{I}}}{\partial x_2} & \frac{\partial X_{\mathrm{I}}}{\partial x_3} \\ \frac{\partial X_{\mathrm{II}}}{\partial x_1} & \frac{\partial X_{\mathrm{II}}}{\partial x_2} & \frac{\partial X_{\mathrm{II}}}{\partial x_3} \\ \frac{\partial X_{\mathrm{III}}}{\partial x_1} & \frac{\partial X_{\mathrm{III}}}{\partial x_2} & \frac{\partial X_{\mathrm{III}}}{\partial x_3} \end{bmatrix} \tag{3.16}$$

respectively. Using the chain rule for partial derivatives it is easy to verify that $\mathbf{F}^{-1}$ is indeed the inverse of $\mathbf{F}$,

$$\mathbf{F}\mathbf{F}^{-1} = \mathbf{F}^{-1}\mathbf{F} = 1. \tag{3.17}$$

Recall that any motion can be decomposed into a sum of a translational, rotational, and deformational motion. The deformation gradient tensors remove the translational motion, as may be easily seen because the translational motion is a separate function of time (c.f., e.g., eq. 3.3) that must be independent of the particle $\mathbf{X}$. Thus, only the rotational motion and the deformational motion determine $\mathbf{F}$. If $\mathbf{F} = \mathbf{1}$ there are no rotational or deformational motions. If $\mathbf{F} = \mathbf{Q}(t)$, $\mathbf{Q}(t)\mathbf{Q}(t)^{\mathrm{T}} = \mathbf{1}$, it follows from (3.4) that the motion is purely rotational and there is no deformational motion. The *deformation gradient* $\mathbf{F}$ is so named because it is a measure of the deformational motion as long as $\mathbf{F} \neq \mathbf{Q}(t)$. If $\mathbf{F} = \mathbf{Q}(t)$, then the motion is rotational and we replace $\mathbf{F}$ by $\mathbf{Q}(t)$.

The determinant of the tensor of deformation gradients, $J$, is the Jacobian of the transformation from $\mathbf{x}$ to $\mathbf{X}$; thus,

$$J \equiv \mathrm{Det}\ \mathbf{F} = 1/\ \mathrm{Det}\ \mathbf{F}^{-1}, \tag{3.18}$$

where it is required that

$$0 < J < \infty \tag{3.19}$$

so that a finite continuum volume always remains a finite continuum volume.

If $\mathbf{c}$ represents the position vector of the origin of the coordinate system used for the configuration at time $t$ relative to the origin of the coordinate system used for the configuration at $t = 0$, then the displacement vector $\mathbf{u}$ of the particle $\mathbf{X}$ is given by (Figure 3.2),

$$\mathbf{u} = \mathbf{x} - \mathbf{X} + \mathbf{c}. \tag{3.20}$$

The displacement vectors $\mathbf{u}$ for all the particles $\mathbf{X} \subset O(0)$ are given by

$$\mathbf{u}(\mathbf{X}, t) = \boldsymbol{\chi}(\mathbf{X}, t) - \mathbf{X} + \mathbf{c}(t), \quad \mathbf{X} \subset O(0), \tag{3.21}$$

or by

$$\mathbf{u}(\mathbf{x}, t) = \mathbf{x} - \boldsymbol{\chi}^{-1}(\mathbf{x}, t) + \mathbf{c}(t), \ \mathbf{x} \subset O(t). \tag{3.22}$$

Two gradients of the displacement field $\mathbf{u}$ may then be calculated, one with respect to the spatial coordinate system $\mathbf{x}$ denoted by the usual gradient symbol $\nabla$ and one with respect to the material coordinate system $\mathbf{X}$ denoted by the gradient symbol $\nabla_{\mathbf{o}}$; thus,

$$[\nabla_{\mathbf{o}} \otimes \mathbf{u}(\mathbf{X}, t)]^{\mathrm{T}} = \mathbf{F}(\mathbf{X}, t) - \mathbf{1} \text{ and } [\nabla \otimes \mathbf{u}(\mathbf{x}, t)]^{\mathrm{T}} = \mathbf{1} - \mathbf{F}^{-1}(\mathbf{x}, t) \tag{3.23}$$

when (3.13) and (3.14) are employed. Often the base vectors of the coordinate systems **X** and **x** are taken to coincide, in which case the position vector **c** of the origin of the **x** system relative to the **X** system is zero. The selection of the coordinate system is always the prerogative of the modeler and such selections are usually made to simplify the analysis of the resulting problem.

**Example 3.1.4**

Compute the deformation gradient and the inverse deformation gradient for the motion given by (3.12). Then compute the Jacobian of the motion and both the spatial and material gradients of the displacement vector.

**Solution**: The deformation gradients and the inverse deformation gradients for this motion are obtained from (3.16) and (3.12), thus

$$\mathbf{F}=\begin{bmatrix}1+t & t & 0\\ t & 1+t & 0\\ 0 & 0 & 1\end{bmatrix} \text{ and } \mathbf{F}^{-1}=\frac{1}{1+2t}\begin{bmatrix}1+t & -t & 0\\ -t & 1+t & 0\\ 0 & 0 & 1+2t\end{bmatrix},$$

a result that can be verified using $\mathbf{F}\mathbf{F}^{-1}=\mathbf{1}$ or $\mathbf{F}^{-1}\mathbf{F}=\mathbf{1}$. It is then easy to show that $J = 1 + 2t$. It also follows from (3.23) that

$$[\nabla_{\mathbf{O}}\otimes\mathbf{u}]^T=t\begin{bmatrix}1 & 1 & 0\\ 1 & 1 & 0\\ 0 & 0 & 0\end{bmatrix} \text{ and } [\nabla\otimes\mathbf{u}]^T=\frac{t}{1+2t}\begin{bmatrix}1 & 1 & 0\\ 1 & 1 & 0\\ 0 & 0 & 0\end{bmatrix}.$$

**Problems**

3.1.1. Sketch the shape and position of the unit square with corners at (0,0), (1,0), (1,1), and (0,1) subjected to the motion in eq. (3.10) for the seven special cases, (a) through (g), below. The shape and position are to be sketched for each of the indicated values of $t$.

3.1.1a. Translation. $A(t) = 1$, $B(t) = 1$, $C(t) = 0$, $D(t) = 0$, $E(t) = 3t$, $F(t) = 2t$, and values of $t = 0, 1, 2$.

3.1.1b. Uniaxial Extension. $A(t) = 1 + t$, $B(t) = 1$, $C(t) = 0$, $D(t) = 0$, $E(t) = 0$, $F(t) = 0$, and values of $t = 0, 1, 2, 3$.

3.1.1c. Biaxial Extension. $A(t) = 1 + t$, $B(t) = 1 + 2t$, $C(t) = 0$, $D(t) = 0$, $E(t) = 0$, $F(t) = 0$, and values of $t = 0, 1, 2$.

3.1.1d. Simple Shearing (R). $A(t) = 1$, $B(t) = 1$, $C(t) = t$, $D(t) = 0$, $E(t) = 0$, $F(t) = 0$, and values of $t = 0, 1, 2$.

3.1.1e. Simple Shearing (U). $A(t) = 1$, $B(t) = 1$, $C(t) = 0$, $D(t) = t$, $E(t) = 0$, $F(t) = 0$, and values of $t = 0, 1, 2$.

3.1.1f. Rigid Rotation (cw). $A(t) = \cos(\pi t/2)$, $B(t) = \cos(\pi t/2)$, $C(t) = \sin(\pi t/2)$, $D(t) = -\sin(\pi t/2)$, $E(t) = 0$, $F(t) = 0$, and values of $t = 0, 1, 2, 3, 4$.

3.1.1g. Rigid Rotation (ccw). $A(t) = \cos(\pi t/2)$, $B(t) = \cos(\pi t/2)$, $C(t) = -\sin(\pi t/2)$, $D(t) = \sin(\pi t/2)$, $E(t) = 0$, $F(t) = 0$, and values of $t = 0, 1, 2, 3, 4$.

3.1.2. Sketch the shape and position of the square with corners at (–1,–1), (1,–1), (1,1), and (–1,1) at times $t = 0, 1, 2, 3, 4$. The square is subjected to the motion in eq. (3.10) with the

values of *A(t), B(t), C(t), D(t), E(t)*, and *F(t)* being those given in 3.1.1f, the rigid rotation (clockwise) motion.

3.1.3. For the six motions of the form (3.10) given in Problem 3.1.1, namely 3.1.1a–3.1.1f, compute the deformation gradient tensor **F**, its Jacobian *J*, and its inverse $\mathbf{F}^{-1}$. Discuss briefly the significance of each of the tensors computed. In particular, explain the form or value of the deformation gradient tensor **F** in terms of the motion.

3.1.4. Using the planar homogenous deformation (3.10), with the values of *A, B, C, D, E*, and *F* calculated in Example 3.1.3, show that that deformation (3.10) predicts the final positions of the three markers when the initial marker locations $\left(X_{\mathrm{I}}^{(1)}, X_{\mathrm{II}}^{(1)}\right) = (0, 0)$, $\left(X_{\mathrm{I}}^{(2)}, X_{\mathrm{II}}^{(2)}\right) = (1, 0)$, and $\left(X_{\mathrm{I}}^{(3)}, X_{\mathrm{II}}^{(3)}\right) = (0, 1)$ are substituted into it.

3.1.5 In Example 3.1.3 an experimental technique in widespread use in the measurement of the planar homogeneous motion of soft tissue was described and a system of equations was set and solved to determine the time-dependent parameters appearing in the equations describing the planar homogeneous motion. Consider the same problem when the problem is not planar, but three-dimensional. How many markers are necessary in three dimensions and how must the markers be arranged so that they provide the information necessary to determine the time-dependent parameters appearing in the equations describing the three-dimensional homogeneous motion? Explain the process.

## 3.2. RATES OF CHANGE AND THE SPATIAL REPRESENTATION OF MOTION

The velocity **v** and acceleration **a** of a particle **X** are defined by

$$\mathbf{v} = \dot{\mathbf{x}} = \left.\frac{\partial \chi}{\partial t}\right|_{\mathbf{X}\text{ fixed}}, \quad \mathbf{a} = \ddot{\mathbf{x}} = \left.\frac{\partial^2 \chi}{\partial t^2}\right|_{\mathbf{X}\text{ fixed}} \tag{3.24}$$

where **X** is held fixed because it is the velocity or acceleration of that particular particle that is being determined. The *spatial description of motion* (as opposed to the *material description of motion* represented by (3.2)) is obtained by solving (3.2) for **X**,

$$\mathbf{X} = \boldsymbol{\chi}^{-1}(\mathbf{x}, t) \text{ for all } \mathbf{X} \subset O(0), \tag{3.25}$$

and substituting the result into the first of the expressions (3.24) for the velocity; thus $\mathbf{v} = \dot{\mathbf{x}} = \dot{\chi}(\mathbf{X}, t)$ becomes

$$\mathbf{v} = \dot{\mathbf{x}} = \dot{\chi}(\chi^{-1}(\mathbf{x}, t), t) = \mathbf{v}(\mathbf{x}, t)\,, \tag{3.26a}$$

or

$$\mathbf{v}(\mathbf{x}, t) = \mathbf{v}(\chi_1{}^{-1}(\mathbf{x}, t),\ \chi_2{}^{-1}(\mathbf{x}, t),\ \chi_3{}^{-1}(\mathbf{x}, t), t)\,, \tag{3.26b}$$

which emphasizes that the time dependence of the spatial representation of velocity is both explicit and implicit. This representation of the velocity with the places **x** as independent variables is called the *spatial representation of motion*. A quantity is said to be in the spatial representation if its independent variables are the places **x** and not the particles **X**. In the material representation the independent variables are the particles **X**; compare the material description of motion, (3.2), with (3.26). The *material time derivative* is the time derivative following the material particle **X**; it is denoted by a superposed dot or *D/Dt*, and it is defined as the partial

derivative with respect to time with **X** held constant. The material time derivative is easy to calculate in the material representation. It is more complicated to calculate in the spatial representation. To determine the acceleration in the spatial representation we must calculate the material time rate of the spatial representation of velocity (3.26). The notation D/Dt introduced above is illustrated using the definitions of (3.24):

$$\mathbf{a} = \left.\frac{\partial^2 \boldsymbol{\chi}}{\partial t^2}\right|_{\text{X fixed}} = \left.\frac{\partial \mathbf{v}}{\partial t}\right|_{\text{X fixed}} \equiv \frac{D\mathbf{v}}{Dt}. \tag{3.27}$$

A formula for $D\mathbf{v}/Dt$ is obtained by observing the explicit and implicit time dependence of the spatial representation of velocity (3.26b) and noting that the time derivative associated with the implicit dependencies may be obtained using the chain rule, thus

$$\frac{D\mathbf{v}}{Dt} = \left.\frac{\partial \mathbf{v}}{\partial t}\right|_{\mathbf{x}\text{ fixed}} + \sum_{i=1}^{3} \left.\frac{\partial \mathbf{v}}{\partial x_i}\frac{\partial x_i}{\partial t}\right|_{\text{X fixed}} = \left.\frac{\partial \mathbf{v}}{\partial t}\right|_{\text{x fixed}} + \sum_{i=1}^{3} \frac{\partial \mathbf{v}}{\partial x_i} v_i \,, \tag{3.28}$$

a result that may be written more simply as

$$\frac{D\mathbf{v}}{Dt} = \left.\frac{\partial \mathbf{v}}{\partial t}\right|_{\mathbf{x}\text{ fixed}} + \mathbf{v}\cdot\nabla\mathbf{v} \,. \tag{3.29}$$

The time rate computed by holding the places **x** fixed is called the local time rate. In general, the material time rate is related to the local time rate by the following operator expression that follows from (3.29),

$$\frac{D}{Dt} = \left.\frac{\partial}{\partial t}\right|_{\text{x fixed}} + \mathbf{v}\cdot\nabla \,, \tag{3.30}$$

where $D/Dt$ is the material time rate of change, $\partial/\partial t$ is the local time rate of change and $\mathbf{v}\cdot\nabla$ determines the convective change of the quantity.

The second-order tensor formed by taking the spatial gradient of the velocity field $\mathbf{v} = \mathbf{v}(\mathbf{x},t)$ is called the tensor of velocity gradients and is denoted by **L**; thus,

$$\mathbf{L} = \left[\nabla \otimes \mathbf{v}\right]^T = \left[\frac{\partial v_i}{\partial x_j}\right] = \begin{bmatrix} \frac{\partial v_1}{\partial x_1} & \frac{\partial v_1}{\partial x_2} & \frac{\partial v_1}{\partial x_3} \\ \frac{\partial v_2}{\partial x_1} & \frac{\partial v_2}{\partial x_2} & \frac{\partial v_2}{\partial x_3} \\ \frac{\partial v_3}{\partial x_1} & \frac{\partial v_3}{\partial x_2} & \frac{\partial v_3}{\partial x_3} \end{bmatrix}. \tag{3.31}$$

**L** is decomposed into a symmetric part **D**, called *the rate-of-deformation tensor*, and a skew symmetric part **W**, called the *spin tensor*; thus,

$$\mathbf{L} = \mathbf{D} + \mathbf{W},\ \mathbf{D} = (1/2)(\mathbf{L} + \mathbf{L}^{\mathrm{T}}),\ \ \mathbf{W} = (1/2)(\mathbf{L} - \mathbf{L}^{\mathrm{T}}). \tag{3.32}$$

The three nonzero components of **W** can be formed into an axial vector $(1/2)(\nabla \times \mathbf{v})$ which represents the local rotational motion and is called the angular velocity or one-half the vorticity.

The rate-of-deformation tensor **D**, defined by the second of (3.32), has the component representation

$$\mathbf{D} = \frac{1}{2}\left[\frac{\partial v_j}{\partial x_i} + \frac{\partial v_i}{\partial x_j}\right] = \frac{1}{2}\begin{bmatrix} 2\dfrac{\partial v_1}{\partial x_1} & \dfrac{\partial v_1}{\partial x_2} + \dfrac{\partial v_2}{\partial x_1} & \dfrac{\partial v_1}{\partial x_3} + \dfrac{\partial v_3}{\partial x_1} \\ \dfrac{\partial v_1}{\partial x_2} + \dfrac{\partial v_2}{\partial x_1} & 2\dfrac{\partial v_2}{\partial x_2} & \dfrac{\partial v_2}{\partial x_3} + \dfrac{\partial v_3}{\partial x_2} \\ \dfrac{\partial v_1}{\partial x_3} + \dfrac{\partial v_3}{\partial x_1} & \dfrac{\partial v_2}{\partial x_3} + \dfrac{\partial v_3}{\partial x_2} & 2\dfrac{\partial v_3}{\partial x_3} \end{bmatrix}. \tag{3.33}$$

The components of **D** along the diagonal are called normal rates of deformation and the components off the diagonal are called shear rates of deformation. The normal rates of deformation, $D_{11}$, $D_{22}$, and $D_{33}$, are measures of instantaneous time rate of change of the material filament instantaneously coincident with the 1, 2, and 3 axes, respectively, and the shear rates of deformation, $D_{23}$, $D_{13}$, and $D_{12}$, are equal to one-half the time rate of decrease in an originally right angle between material filaments instantaneously situated upon the 2 and 3 axes, the 1 and 3 axes, and the 1 and 2 axes, respectively.

The rate-of-deformation tensor **D** represents instantaneous rates of change, that is to say, how much a quantity is changing compared to its present size. Let $dx_1$ be a vector of infinitesimal length representing the present position of an infinitesimal material filament coinciding with the $x_1$ at time $t$ (see Figure 3.5). The instantaneous time rate of change of the material filament instantaneously coincident with $dx_1$ is $dv_1 = D_{11}dx_1$, a result that follows from the entry in the first column and first row of (3.33). The expression $dv_1 = D_{11}dx_1$ shows $dv_1$ as a linear function of $dx_1$ at any point **x** and time $t$. Thus, the geometric interpretation of $D_{11} = \left(d\dot{x}_1 / dx_1\right)$ is that it is the instantaneous time rate of change of $dx_1$ at time $t$ relative to $dx_1$ at time $t$. Similar geometric interpretations exist for $D_{22}$ and $D_{33}$.

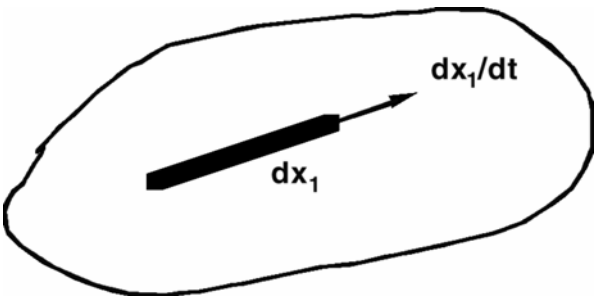



**Figure 3.5**. An illustration for geometric interpretation of the $D_{11}$ component of the rate-of-deformation tensor **D**. A vector of infinitesimal length representing the present position of an infinitesimal material filament coinciding with $x_1$ at time $t$ is denoted by $dx_1$. The instantaneous time rate of change of the material filament instantaneously coincident with $dx_1$ is $dv_1 = D_{11}dx_1$. The expression $dv_1 = D_{11}dx_1$ shows $dv_1$ as a linear function of $dx_1$ at any point **x** and time $t$. Thus, the geometric interpretation of $D_{11} = (d\dot{x}_1 / dx_1)$ is that it is the instantaneous time rate of change of $dx_1$ at time $t$ relative to $dx_1$ at time $t$.

The geometric interpretation of the normal rate of shearing components $D_{11}$, $D_{22}$, and $D_{33}$ is easily extended to obtain a geometric interpretation of the trace of **D**, which is also the diver-

gence of the velocity, tr**D** = **∇·v**. If $dv$ represents an element of volume in the spatial coordinate system, $dv = dx_1 dx_2 dx_3$ (Figure 3.6), the material time rate of change of $dv$ can be computed using the type of formula developed in the previous paragraph; $d\dot{x}_1 = D_{11}dx_1$, $d\dot{x}_2 = D_{22}dx_2$, and $d\dot{x}_3 = D_{33}dx_3$; thus.

$$d\dot{v} = \frac{D}{Dt}(dx_1 dx_2 dx_3) = (D_{11} + D_{22} + D_{33})dx_1 dx_2 dx_3 = (tr\mathbf{D})dv\,, \tag{3.34}$$

or, noting from the definition of **D** that

$$\text{tr}\mathbf{D} = D_{11} + D_{22} + D_{33} = \nabla\cdot\mathbf{v} = \text{div } \mathbf{v}, \tag{3.35}$$

it follows that

$$\text{tr}\mathbf{D} = \nabla\cdot\mathbf{v} = \frac{d\dot{v}}{dv}\,. \tag{3.36}$$

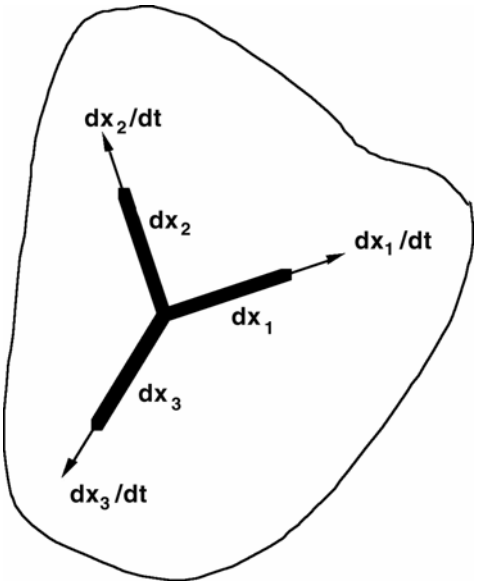



**Figure 3.6**. Illustration for geometric interpretation of the trace of rate-of-deformation tensor **D** as the instantaneous time rate of change of volume. The material time rate of change of an element of volume in the spatial coordinate system, $dv = dx_1 dx_2 dx_3$, is shown to be $d\dot{v} = tr\mathbf{D}dv = \nabla\cdot\mathbf{u}dv$ ; thus, $\nabla\cdot\mathbf{v}$ or tr**D** has a geometric interpretation as the instantaneous time rate of change of material volume.

Thus **∇·v** or tr**D** have the geometric interpretation as the instantaneous time rate of change of material volume. Another way of viewing this result is to say that the divergence of the velocity field is the time rate of change of a material volume relative to how large it is at an instant $t$.

The off-diagonal components of the rate-of-deformation tensor, for example $D_{12}$, represent rates of shearing. $D_{12}$ is equal to one half the time rate of decrease in an originally right angle

between the filaments $d\mathbf{x}(1)$ and $d\mathbf{x}(2)$ (see Figure 3.7). To see this, note that the dot product of material filaments $d\mathbf{x}(1)$ and $d\mathbf{x}(2)$ axes may be written as

$$d\mathbf{x}(1)\cdot d\mathbf{x}(2) = \left|d\mathbf{x}(1)\right| \ \left|d\mathbf{x}(2)\right|\cos\theta_{12}$$

where $\theta_{12}$ is the angle between the two filaments. In the calculation of the material time derivative of the dot product above, $d\mathbf{x}(1)\cdot d\mathbf{x}(2)$, we will employ the formula $dv_i = d\dot{x}_i = L_{ij}dx_j$ that follows from (3.31). The material time derivative of both sides of the equation above is then computed:

$$\frac{D}{Dt}(d\mathbf{x}(1)\cdot d\mathbf{x}(2)) = d\dot{\mathbf{x}}(1)\cdot d\mathbf{x}(2) + d\mathbf{x}(1)\cdot d\dot{\mathbf{x}}(2) =$$

$$L_{ij}dx_j(1)dx_2(2) + dx_i(1)L_{ij}dx_j(2) = 2D_{ij}dx_i(1)dx_j(2) =$$

$$\left|d\dot{\mathbf{x}}(1)\right| \ \left|d\mathbf{x}(2)\right|\cos\theta_{12} + \left|d\mathbf{x}(1)\right| \ \left|d\dot{\mathbf{x}}(2)\right|\cos\theta_{12} - \dot{\theta}_{12}\left|d\mathbf{x}(1)\right| \ \left|d\mathbf{x}(2)\right|\sin\theta_{12}$$

and, since we are interested in the instant that $\theta_{12} = \pi/2$, it follows that

$$2D_{ij}dx_i(1)dx_j(2) = -\dot{\theta}_{12}\left|d\mathbf{x}(1)\right| \ \left|d\mathbf{x}(2)\right| .$$

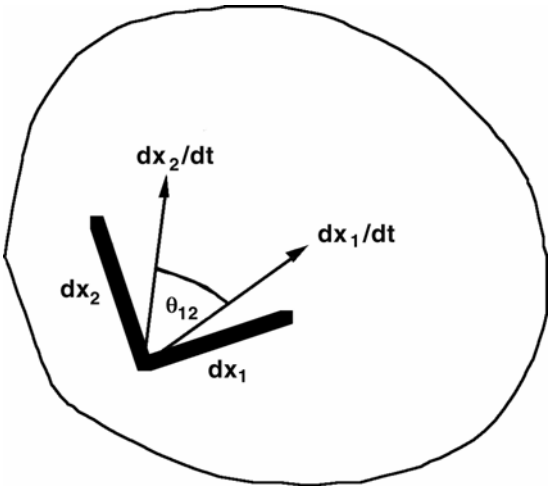



**Figure 3.7**. An illustration for geometric interpretation of the rate of shearing strain component $D_{12}$ of the rate-of-deformation tensor **D**. The heavy black lines represent two material filaments of infinitesimal length that are instantaneously perpendicular. The thin black lines represent the same two material filaments in the next instant. The instantaneous time rate of change of the angle between the two material filaments, the rate at which the two filaments are coming together or separating is $\dot{\theta}_{12}$. The geometric interpretation of $D_{12}$ is that it is half the instantaneous time of decrease in an originally right angle between $dx_1$ and $dx_2$, $D_{12} = -\dot{\theta}_{12}/2$.

Finally, if we take $d\mathbf{x}(1) = dx_1\mathbf{e}_1$ and $d\mathbf{x}(2) = dx_2\mathbf{e}_2$ it may be concluded that

$$D_{12} = -\frac{\dot{\theta}_{12}}{2},$$

confirming that $D_{12}$ is equal to one half the material time rate of decrease in an originally right angle between $dx_1$ and $dx_2$. The geometric interpretations of $D_{13}$ and $D_{23}$ are similar. These geometric interpretations of the components of **D** as the instantaneous time rate of change of filaments, angles, and volume are the rationale for calling **D** the *rate of deformation* tensor.

**Example 3.2.1**

Calculate the velocity and acceleration in the material representation of the motion (3.12) of Example 3.1.1; then determine the spatial representation. Verify that the acceleration computed in the spatial representation is the same as the acceleration computed in the material representation. Calculate the tensor of velocity gradients **L**, the rate of deformation tensor **D**, and the spin tensor **W** for this motion.

Solution: The velocity and acceleration for this motion are given by (3.24) as

$$\dot{x}_1 = X_{\mathrm{I}} + X_{\mathrm{II}} + 3,\ \ \dot{x}_2 = X_{\mathrm{I}} + X_{\mathrm{II}} + 2,\ \ \dot{x}_3 = 0,\ \ddot{x}_1 = \ddot{x}_2 = \ddot{x}_3 = 0.$$

In order to find the spatial representation for this motion we must invert the system of eqs. (3.12) representing the motion; thus,

$$X_{\mathrm{I}} = \frac{1}{1+2t}\left\{(1+t)x_1 - tx_2 - t^2 - 3t\right\},\ \ X_{\mathrm{II}} = \frac{1}{1+2t}\left\{-tx_1 + (1+t)x_2 + t^2 - 2t\right\},\ \ X_{\mathrm{III}} = x_3\,;$$

then, substituting these expressions into the previous equations for the velocities, the spatial representation of this motion is obtained:

$$v_1 = \frac{1}{1+2t}\{x_1 + x_2 + 3 + t\}\,,\ v_2 = \frac{1}{1+2t}\{x_1 + x_2 + 2 - t\}\,,\ \ v_3 = 0\,.$$

It is known from the first calculation in this example that this motion is one of zero acceleration, $\ddot{x}_1 = \ddot{x}_2 = \ddot{x}_3 = 0$. This may be verified by calculating the acceleration of the spatial representation of the motion above using the material time derivative (3.29), thus

$$a_1 = \frac{\partial v_1}{\partial t} + v_1\frac{\partial v_1}{\partial x_1} + v_2\frac{\partial v_1}{\partial x_2} + v_3\frac{\partial v_1}{\partial x_3} =$$

$$\frac{-2}{(1+2t)^2}\{x_1 + x_2 + 3 + t\} + \frac{1}{1+2t} + \frac{1}{(1+2t)^2}\{2(x_1 + x_2) + 5\} = 0\,,$$

$$a_2 = \frac{\partial v_2}{\partial t} + v_1\frac{\partial v_2}{\partial x_1} + v_2\frac{\partial v_2}{\partial x_2} + v_3\frac{\partial v_2}{\partial x_3} =$$

$$\frac{-2}{(1+2t)^2}\{x_1 + x_2 + 2 - t\} - \frac{1}{1+2t} + \frac{1}{(1+2t)^2}\{2(x_1 + x_2) + 5\} = 0\,.$$

The tensor of velocity gradients **L** for the motion (3.12) is obtained by substituting the spatial representation for the motion obtained above into (3.31); thus,

$$\mathbf{L} = \frac{1}{1+2t}\begin{bmatrix} 1 & 1 & 0 \\ 1 & 1 & 0 \\ 0 & 0 & 0 \end{bmatrix}.$$

The rate-of-deformation tensor **D** for this motion is equal to **L**. The spin tensor **W** is zero for this motion.

**Problems**

3.2.1. For the first six motions of the form (3.10) given in Problem 3.1.1, namely 3.1.1a–3.1.1f, determine the velocity and acceleration in the material (Lagrangian) representation, the velocity and acceleration in the spatial (Eulerian) representation, and the three tensors **L**, **D,** and **W**. Discuss briefly how these algebraic calculations relate to the geometry of the motion.

3.2.2. The motion of a continuum is given by: $x_1 = X_I + X_{II}t + X_{III}t^2$, $x_2 = X_{II} + X_{III}t + X_I t^2$, $x_3 = X_{III} + X_I t + X_{II}t^2$.

a. Find the inversion of this motion.

b. Determine the velocity and the acceleration in the material representation.

c. Find the velocity in the spatial (Eulerian) representation for this motion.

d. Find the three tensors **L**, **D** and **W** for this motion.

e. Find the tensor of deformation gradients **F** for this motion.

3.2.3. The motion of a continuum is given by:

$$x_1 = X_I + X_{II}\sin(\pi t),\ x_2 = X_{II} - X_I \sin(\pi t),\ x_3 = X_{III}.$$

a. Determine the deformation gradient **F** of this deformation.

b. Determine the instantaneous configuration image of the set of points $(X_I)^2 + (X_{II})^2 = 1$ in the reference configuration.

c. Describe the geometry of the set of points $(X_I)^2 + (X_{II})^2 = 1$ in the reference configuration and describe what happens to this set of points in the motion of the continuum as time t increases.

## 3.3. INFINITESIMAL MOTIONS

The term "infinitesimal motion" is used to describe the case when the deformation, including rotation, is small. This does not mean that the displacement vector is small; one can have large displacements but small strain infinitesimal motions. Large displacements associated with small strain infinitesimal motions occur in very thin long rods. The criterion for infinitesimal motion is that the square of the gradients of displacement be small compared to the gradients of displacement themselves. Thus, for infinitesimal motions, the squares and products of the nine quantities,

$$\frac{\partial u_1}{\partial x_1}, \frac{\partial u_1}{\partial x_2}, \frac{\partial u_1}{\partial x_3}, \frac{\partial u_2}{\partial x_1}, \frac{\partial u_2}{\partial x_2}, \frac{\partial u_2}{\partial x_3}, \frac{\partial u_3}{\partial x_1}, \frac{\partial u_3}{\partial x_2}, \frac{\partial u_3}{\partial x_3}, \tag{3.37}$$

must be small compared to their own values. This means, for example, $\{\partial u_2/\partial x_1\}^2$ is required to be much smaller than $\partial u_2/\partial x_1$; each such square and product of these nine quantities is so small that it may be neglected compared to the quantity itself. Using this criterion of smallness, rep-

resentations of the kinematics variables for infinitesimal motions will be developed in this section.

If the motion is infinitesimal the deformation gradient tensor **F** must not deviate significantly from the unit tensor **1**, the magnitude of the deviation being restricted by the criterion on the deformation gradients stated in the previous paragraph. The deformation gradient **F** may be expressed, using (3.23), in terms of $[\nabla_o \otimes \mathbf{u}]^T$, which is a matrix of components $[\partial u_i/\partial X_\alpha]$, as

$$\mathbf{F} = \mathbf{1} + [\nabla_o \otimes \mathbf{u}]^T. \tag{3.38}$$

Since

$$\nabla_o = \mathbf{F}^T \cdot \nabla, \text{ or } \frac{\partial}{\partial X_\alpha} = \frac{\partial}{\partial x_j}\frac{\partial x_j}{\partial X_\alpha} = \frac{\partial}{\partial x_j} F_{j\alpha} \tag{3.39}$$

it follows from (3.38) and a result obtained in Appendix A , namely, that $[\mathbf{AB}]^T = \mathbf{B}^T\mathbf{A}^T$, that

$$\mathbf{F} = \mathbf{1} + [\nabla \otimes \mathbf{u}]^T \cdot \mathbf{F}. \tag{3.40}$$

This result may be used as a recursion formula for **F**. In that role this formula for F can be substituted into itself once,

$$\mathbf{F} = \mathbf{1} + [\nabla \otimes \mathbf{u}]^T + [\nabla \otimes \mathbf{u}]^T \cdot [\nabla \otimes \mathbf{u}]^T \cdot \mathbf{F}, \tag{3.41}$$

and then again and again,

$$\mathbf{F} = \mathbf{1} + [\nabla \otimes \mathbf{u}]^T + [\nabla \otimes \mathbf{u}]^T \cdot [\nabla \otimes \mathbf{u}]^T + [\nabla \otimes \mathbf{u}]^T \cdot [\nabla \otimes \mathbf{u}]^T \cdot [\nabla \otimes \mathbf{u}]^T + \text{h.o.t}, \tag{3.42}$$

where h.o.t stands for "higher order terms." If the terms of second order according to the criterion (3.37) are neglected, the **F** is approximated by

$$\mathbf{F} \approx \mathbf{1} + [\nabla \otimes \mathbf{u}]^T. \tag{3.43}$$

From (3.23) it is known that

$$\mathbf{F}^{-1} = \mathbf{1} - [\nabla \otimes \mathbf{u}]^T, \tag{3.44}$$

a formula that is accurate in the approximation because $\mathbf{F} \cdot \mathbf{F}^{-1} = \mathbf{1}$ when terms of second order are neglected.

Two important conclusions may be made from this result. First, for infinitesimal motions the difference between the use of material and spatial coordinates is insignificant, thus **X** and **x** are equivalent as are the gradient operators $\nabla_o$ and $\nabla$. Concerning these operators note from (3.39) that

$$\nabla_o \otimes \mathbf{u} = \mathbf{F}^T \cdot [\nabla \otimes \mathbf{u}], \tag{3.45}$$

and, substituting for **F** using (3.43),

$$\nabla_o \otimes \mathbf{u} = \nabla \otimes \mathbf{u} + [\nabla \otimes \mathbf{u}] \cdot [\nabla \otimes \mathbf{u}];$$

thus, to neglect terms of second order,

$$\nabla_o \otimes \mathbf{u} \approx \nabla \otimes \mathbf{u}. \tag{3.46}$$

For infinitesimal motions, the movement of boundaries due to motion is neglected because the small movement is equivalent to the difference in the use of material and spatial coordinates,

which is insignificant. Therefore, in all the following considerations of infinitesimal motions the coordinates **x** will be used without reference to their material or spatial character, because the result is correct independent of their character. The second important conclusion is that, for infinitesimal motions, **F** has the representation

$$\mathbf{F} = \mathbf{1} + [\nabla \otimes \mathbf{u}(\mathbf{x}, t)]^{T}. \tag{3.47}$$

In the special case when the infinitesimal motion is a rigid object rotation, $\mathbf{F} = \mathbf{Q}$ and $\mathbf{Q} = \mathbf{1} + [\nabla \otimes \mathbf{u}]^{T}$. The requirement that **Q** be orthogonal, $\mathbf{Q}^{T}\cdot\mathbf{Q} = \mathbf{Q}\cdot\mathbf{Q}^{T} = \mathbf{1}$, $\mathbf{Q}\cdot\mathbf{Q}^{T} = (\mathbf{1} + [\nabla \otimes \mathbf{u}]^{T})\cdot(\mathbf{1} + [\nabla \otimes \mathbf{u}]^{T})^{T} = \mathbf{1} + [\nabla \otimes \mathbf{u}]^{T} + (\nabla \otimes \mathbf{u}) + (\nabla \otimes \mathbf{u})^{T}\cdot(\nabla \otimes \mathbf{u}) = \mathbf{1}$, means that

$$(\nabla \otimes \mathbf{u})^{T} + \nabla \otimes \mathbf{u} = 0, \tag{3.48}$$

since $(\nabla \otimes \mathbf{u})^{T}\cdot(\nabla \otimes \mathbf{u})$ represents second-order terms that are neglected. Defining the symmetric and skew symmetric parts of $\nabla \otimes \mathbf{u}$ as **E** and **Y**,

$$\mathbf{E} = (1/2)((\nabla \otimes \mathbf{u})^{T} + \nabla \otimes \mathbf{u}), \quad \mathbf{Y} = (1/2)((\nabla \otimes \mathbf{u})^{T} - \nabla \otimes \mathbf{u}), \tag{3.49}$$

it is seen from (3.48) that **E** must be zero when the infinitesimal motion is a rigid object rotation. It may also be seen that the orthogonal rotation **Q** characterizing the infinitesimal rigid object rotation is given by

$$\mathbf{Q} = \mathbf{1} + \mathbf{Y}, \tag{3.50}$$

where **Y**, defined by (3.49), is skew symmetric, $\mathbf{Y} = -\mathbf{Y}^{T}$, and $\mathbf{Y}\mathbf{Y}^{T}$ is a second-order term, since it is a square of the coefficients (3.37) that are neglected compared to the values of **Y**.

Returning to the total infinitesimal motion, the definitions (3.49) of **E** and **Y** may be used to rewrite (3.39) as

$$\mathbf{F} = \mathbf{1} + \mathbf{E} + \mathbf{Y}. \tag{3.51}$$

It has been established that **F** represents only the rotational and deformational motion because the translational portion of the motion, being independent of the coordinates, was removed by spatial or material differentiation. It has also been noted that the special case of $\mathbf{F} = \mathbf{1}$ corresponds to no rotational and no deformational motion. Further it has been shown (3.50) that **Y** is associated with pure rigid object rotation. This means that **E** must be the tensor representing the deformation. This is indeed the case, as will be shown below. **E** is called the *infinitesimal strain tensor* and **Y** is called the *infinitesimal rotation tensor*. The representation (3.51) for the tensor of deformation gradients then demonstrates that, for infinitesimal motions, $\mathbf{F} - \mathbf{1}$ may be decomposed into the sum of two terms, **E** and **Y**, which represent the deformational and rigid rotational characteristics of the infinitesimal motion, respectively.

The strain tensor **E**, defined by the first of (3.49), has the component representation

$$\mathbf{E} = \frac{1}{2}\left[\frac{\partial u_j}{\partial x_i} + \frac{\partial u_i}{\partial x_j}\right] = \frac{1}{2}\begin{bmatrix} 2\dfrac{\partial u_1}{\partial x_1} & \dfrac{\partial u_1}{\partial x_2} + \dfrac{\partial u_2}{\partial x_1} & \dfrac{\partial u_1}{\partial x_3} + \dfrac{\partial u_3}{\partial x_1} \\ \dfrac{\partial u_1}{\partial x_2} + \dfrac{\partial u_2}{\partial x_1} & 2\dfrac{\partial u_2}{\partial x_2} & \dfrac{\partial u_2}{\partial x_3} + \dfrac{\partial u_3}{\partial x_2} \\ \dfrac{\partial u_1}{\partial x_3} + \dfrac{\partial u_3}{\partial x_1} & \dfrac{\partial u_2}{\partial x_3} + \dfrac{\partial u_3}{\partial x_2} & 2\dfrac{\partial u_3}{\partial x_3} \end{bmatrix}. \tag{3.52}$$

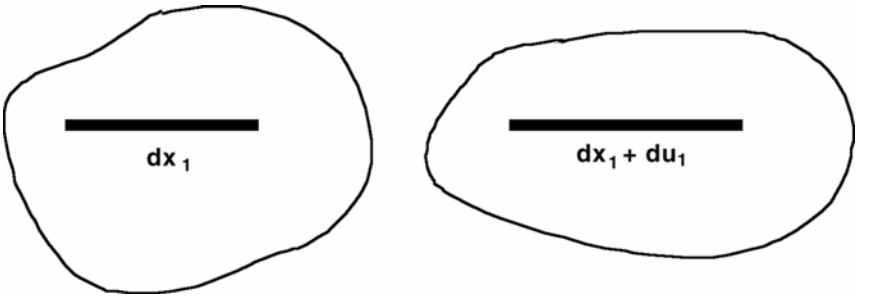



**Figure 3.8**. An illustration for geometric interpretation of normal strain component $E_{11}$. The left and right components of this figure represent the undeformed and deformed configurations, respectively. The heavy black line represents the same material filament in the two configurations. $E_{11}$ is equal to the change in length per unit length of the filament between the two configurations. The original length is $dx_1$ and the change in length due to the deformation is $du_1$, and thus $E_{11} = dx_1/du_1$.

The components of **E** along the diagonal are called normal strains and the components off the diagonal are called shear strains. The normal strains, $E_{11}$, $E_{22}$, and $E_{33}$, are measures of change in length per unit length along the 1, 2, and 3 axes, respectively, and the shear strains, $E_{23}$, $E_{13}$, and $E_{12}$, are half the changes in the angle between the 2 and 3 axes, the 1 and 3 axes, and the 1 and 2 axes, respectively.

The geometric interpretation of the components of the strain tensor **E** stated in the previous paragraph will be analytically developed here. Let $dx_1$ be a vector of infinitesimal length representing the present position of an infinitesimal material filament coinciding with $x_1$ at time $t$. The displacement of this material filament instantaneously coincident with $dx_1$ is $du_1 = E_{11}dx_1$, a result that follows from the entry in the first column and first row of (3.52). The expression $du_1 = E_{11}dx_1$ is the change in length of $dx_1$ as a consequence of the strain as illustrated in Figure 3.8. Thus the geometric interpretation of $E_{11} = (du_1/dx_1)$ is that it is the change in length per unit length of $dx_1$. Similar geometric interpretations exist for $E_{22}$ and $E_{33}$.

The geometric interpretation of the normal strain components $E_{11}$, $E_{22}$ and $E_{33}$ is easily extended to obtain a geometric interpretation of the trace of the small strain tensor tr**E**, or equivalently the divergence of the displacement field $\nabla\cdot\mathbf{u}$, tr$\mathbf{E} = \nabla\cdot\mathbf{u}$. If $dv_o = dx_1dx_2dx_3$ represents an undeformed element of volume (Figure 3.9), the deformed volume is given by $dv = (dx_1 + du_1)(dx_2 + du_2)(dx_3 + du_3)$. Using $du_1 = E_{11}dx_1$, $du_2 = E_{22}dx_2$ and $du_3 = E_{33}dx_3$, the deformed volume is given by $dv = (1 + E_{11})(1 + E_{22})(1 + E_{33})dv_o$. Expanding $dv = (1 + E_{11})(1 + E_{22})(1 + E_{33})dv_o$ and recognizing that the squares of displacement gradients (3.37) may be neglected, it follows that $dv = (1 + tr\mathbf{E})dv_o$. Thus the $tr\mathbf{E}$ represents the change in volume per unit volume, $(dv - dv_o)/dv_o$.

The off-diagonal components of the strain tensor, for example, $E_{12}$, represent the shearing strains. $E_{12}$ is equal to half the change in angle that was originally a right angle between the $x_1$ and $x_2$ axes. To construct this geometric result algebraically, the unit vectors $\mathbf{e}_1$ and $\mathbf{e}_2$ are considered (see Figure 3.10). After deformation these vectors are $\mathbf{Fe}_1$ and $\mathbf{Fe}_2$, respectively, or, since $\mathbf{F} = \mathbf{1} + \mathbf{E}$, the deformed vectors are given by $\mathbf{e}_1 + \mathbf{Ee}_1$ and $\mathbf{e}_2 + \mathbf{Ee}_2$, respectively. The dot product of the vectors $\mathbf{e}_1 + \mathbf{Ee}_1$ and $\mathbf{e}_2 + \mathbf{Ee}_2$ is $(\mathbf{e}_1 + \mathbf{Ee}_1)\cdot(\mathbf{e}_2 + \mathbf{Ee}_2) = \mathbf{e}_1\cdot\mathbf{e}_2 + \mathbf{e}_1\cdot\mathbf{Ee}_2 + \mathbf{e}_2\cdot\mathbf{Ee}_1 + \mathbf{Ee}_1\cdot\mathbf{Ee}_2$, but since the unit vectors $\mathbf{e}_1$ and $\mathbf{e}_2$ are orthogonal, $\mathbf{e}_1\cdot\mathbf{e}_2 = 0$, and also since $\mathbf{Ee}_1\cdot\mathbf{Ee}_2$ is a higher-order term because it contains the squares of the displacement gradients (3.37), this expression reduces to $(\mathbf{e}_1 + \mathbf{Ee}_1)\cdot(\mathbf{e}_2 + \mathbf{Ee}_2) = \mathbf{e}_1\cdot\mathbf{Ee}_2 + \mathbf{e}_2\cdot\mathbf{Ee}_1$. This result is further reduced by noting that $\mathbf{e}_1\cdot\mathbf{Ee}_2 = \mathbf{e}_2\cdot\mathbf{Ee}_1 = E_{12}$; thus, it follows that $(\mathbf{e}_1 + \mathbf{Ee}_1)\cdot(\mathbf{e}_2 + \mathbf{Ee}_2) = 2E_{12}$. Recalling the

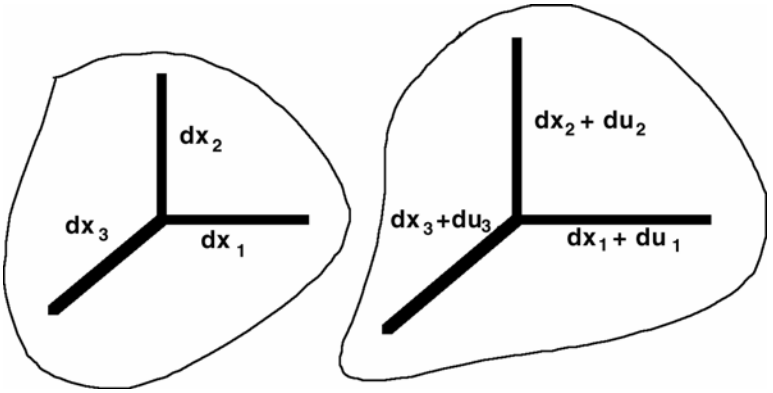



**Figure 3.9**. An illustration for geometric interpretation of the trace of strain tensor tr**E**, or the divergence of the displacement field, $\nabla\cdot\mathbf{u}$, $\mathrm{tr}\mathbf{E} = \nabla\cdot\mathbf{u}$. The left and right components of this figure represent the undeformed and deformed configurations, respectively. The heavy black lines represent the same material filaments in the two configurations. The volume element in the undeformed configuration is $dv_0 = dx_1dx_2dx_3$, and the deformed volume is given by $dv = (dx_1 + du_1)(dx_2 + du_2)(dx_3 + du_3)$. It may be shown (see text) that $dv = (1 + \mathrm{tr}\mathbf{E})dv_0$. Thus the $\mathrm{tr}\mathbf{E} = \nabla\cdot\mathbf{u}$ represents the change in volume per unit volume: $(dv - dv_0)/dv_0$.

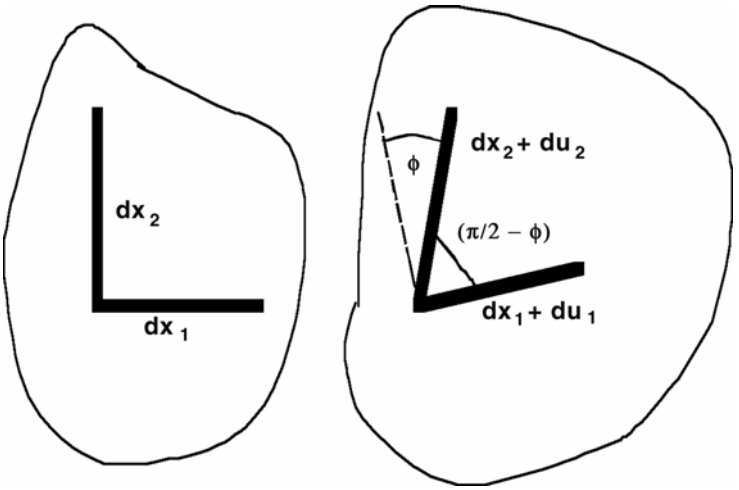



**Figure 3.10**. Illustration for geometric interpretation of shearing strain $E_{12}$. The left and right illustrations of this figure represent the undeformed and deformed configurations, respectively. The heavy black lines represent the same material filaments in the two configurations. $E_{12}$ is equal to half the change in angle that was originally a right angle between the $x_1$ and $x_2$ axes, $\phi/2$ in this figure.

formula (A61) for the dot product of two vectors, say **u** and **v**, as equal to the magnitude of the first times the magnitude of the second times the cosine of the angle (say $\zeta$) between them,

$$\mathbf{u}\cdot\mathbf{v} = \sum_{i=1}^{i=n} u_i v_i = |\mathbf{u}|\cdot|\mathbf{v}|\cos\zeta\,,$$

it follows that $2E_{12} = |\mathbf{e}_1 + \mathbf{E}\mathbf{e}_1|\,|\mathbf{e}_2 + \mathbf{E}\mathbf{e}_2| \cos(\pi/2 - \phi)$, where the angle $(\pi/2 - \phi)$ is illustrated in Figure 3.10. The magnitude of $|\mathbf{e}_1 + \mathbf{E}\mathbf{e}_1|$ is the square root of $(\mathbf{e}_1 + \mathbf{E}\mathbf{e}_1)\cdot(\mathbf{e}_1 + \mathbf{E}\mathbf{e}_1) = \mathbf{e}_1\cdot\mathbf{e}_1 + \mathbf{e}_1\cdot\mathbf{E}\mathbf{e}_1 + \mathbf{e}_1\cdot\mathbf{E}\mathbf{e}_1 + \mathbf{E}\mathbf{e}_1\cdot\mathbf{E}\mathbf{e}_1$, but since $\mathbf{e}_1\cdot\mathbf{e}_1 = 1$ and $\mathbf{E}\mathbf{e}_1\cdot\mathbf{E}\mathbf{e}_1$ is a higher-order term, this reduces to the square root of $1 + 2E_{11}$, by a parallel of the arguments used above to obtain the formula for $2E_{12}$. At this point a classical approximation is used. This approximation is that $1 + \varepsilon \approx \sqrt{(1 + 2\varepsilon)}$ if summands of the order $\varepsilon^2$ may be neglected; the proof of this approximation follows easily if one squares it. Then, since the square of $E_{11}$ is a higher-order term, the square root of $1 + 2E_{11}$ is given by $1 + E_{11}$; thus, $2E_{12} = (1 + E_{11})(1 + E_{22}) \cos(\pi/2 - \phi)$ or $2E_{12} = (1 + E_{11})(1 + E_{22}) \sin\phi$, or expanding; $2E_{12} = \sin\phi + (E_{11} + E_{22}) \sin\phi + E_{11}E_{22} \sin\phi$. Finally, since the angle $\phi$ is small, $\sin\phi$ is small, as are $E_{11}$ and $E_{22}$, thus the neglect of higher-order terms gives $2E_{12} = \phi$, and the interpretation of $E_{12}$ as half the change in an angle that was originally a right angle between the $x_1$ and $x_2$ axes (Figure 3.10). These geometric interpretations of the components of **E** as the change in the length of filaments, the change in angles, and the change in volume deformation between the undeformed and deformed configurations are the rationale for calling **E** the *strain tensor*.

**Example 3.3.1**

The deformation gradient and the inverse deformation gradient for the motion given by (3.12) were computed in Example 3.1.4. Determine the restriction on the motion given by (3.12) so the motion is infinitesimal. Find the strain tensor **E** and the rotation tensor **Y** for the infinitesimal motion.

**Solution**: Comparison of the expressions $\nabla_0 \otimes \mathbf{u}(\mathbf{X}, t)$ and $\nabla \otimes \mathbf{u}(\mathbf{x}, t)$ obtained in Example 3.1.4 shows that these two expressions coincide only for very small times $t$, only if $t^2$ is much less than $t$. In this case $\nabla_0 \otimes \mathbf{u}(\mathbf{X}, t) = \nabla \otimes \mathbf{u}(\mathbf{x}, t)$ and

$$\nabla \otimes \mathbf{u} = t\begin{bmatrix} 1 & 1 & 0 \\ 1 & 1 & 0 \\ 0 & 0 & 0 \end{bmatrix}.$$

From this expression for $\nabla \otimes \mathbf{u}$ and (3.49), the rotation tensor is determined to be $\mathbf{Y} = \mathbf{0}$, and the strain tensor **E** is given by

$$\mathbf{E} = t\begin{bmatrix} 1 & 1 & 0 \\ 1 & 1 & 0 \\ 0 & 0 & 0 \end{bmatrix}$$

as long as $t$ is small.

**Problems**

3.3.1. For the motions of the form (3.10) given in Problem 3.1.1, namely 3.1.1a–3.1.1g, determine the conditions under which the motion remains infinitesimal and compute the infinitesimal strain and rotation tensors, **E** and **Y**. Discuss briefly the significance of each of the seven strain tensors computed. In particular, explain the form or value of the strain tensor in terms of the motion.

## 3.4. THE STRAIN CONDITIONS OF COMPATIBILITY

Calculating the strain tensor **E** given the displacement field **u** is a relatively simple matter; one just substitutes the displacement field **u** into formula (3.49) for the strain displacement relations, $\mathbf{E} = (1/2)((\nabla\otimes\mathbf{u})^{\mathrm{T}} + \nabla\otimes\mathbf{u})$. Situations occur in which it is desired to calculate the displacement field **u** given the strain tensor **E**. This inverse problem is more difficult because the strain displacement relations, $\mathbf{E} = (1/2)((\nabla\otimes\mathbf{u})^{\mathrm{T}} + \nabla\otimes\mathbf{u})$, become a system of first-order partial differential equations for displacement field **u**. Given the significance of displacement field **u** in an object, we generally want to ensure that displacement field **u** is continuous and single valued. There are real situations in which displacement field **u** might be discontinuous and multiple valued, but these situations will be treated as special cases. In general it is desired that the integral of the strain-displacement relations, displacement field **u**, be continuous and single valued. The conditions of compatibility ensure this. The conditions of compatibility are equations that the strain tensor must satisfy so that when the strain-displacement relations are integrated the resulting displacement field **u**, is continuous and single valued. The conditions of compatibility may be written in the direct notation as

$$\nabla\times\mathbf{E}\times\nabla = 0\,, \tag{3.53}$$

or in the index notation as

$$\sum_{j=1}^{3}\sum_{k=1}^{3}\sum_{m=1}^{3}\sum_{n=1}^{3} e_{ijk}e_{pmn}\frac{\partial^2 E_{jm}}{\partial x_k \partial x_n} = 0, \tag{3.54}$$

or in scalar form as the following six equations:

$$\begin{aligned}
&\frac{\partial^2 E_{11}}{\partial x_2\partial x_3} = \frac{\partial}{\partial x_1}\left\{-\frac{\partial E_{23}}{\partial x_1}+\frac{\partial E_{31}}{\partial x_2}+\frac{\partial E_{12}}{\partial x_3}\right\}, \quad 2\frac{\partial^2 E_{12}}{\partial x_1\partial x_2} = \frac{\partial^2 E_{11}}{\partial x_2^2}+\frac{\partial^2 E_{22}}{\partial x_1^2}\\
&\frac{\partial^2 E_{22}}{\partial x_3\partial x_1} = \frac{\partial}{\partial x_2}\left\{-\frac{\partial E_{31}}{\partial x_2}+\frac{\partial E_{12}}{\partial x_3}+\frac{\partial E_{23}}{\partial x_1}\right\}, \quad 2\frac{\partial^2 E_{23}}{\partial x_2\partial x_3} = \frac{\partial^2 E_{22}}{\partial x_3^2}+\frac{\partial^2 E_{33}}{\partial x_2^2}\\
&\frac{\partial^2 E_{33}}{\partial x_1\partial x_2} = \frac{\partial}{\partial x_3}\left\{-\frac{\partial E_{12}}{\partial x_3}+\frac{\partial E_{23}}{\partial x_1}+\frac{\partial E_{31}}{\partial x_2}\right\}, \quad 2\frac{\partial^2 E_{31}}{\partial x_3\partial x_1} = \frac{\partial^2 E_{33}}{\partial x_1^2}+\frac{\partial^2 E_{11}}{\partial x_3^2}\,.
\end{aligned} \tag{3.55}$$

Equations (3.53) and (3.54) are symmetric second-rank tensors in three dimensions and therefore have the six components given by (3.55). It follows that each of the six scalar eqs. (3.55) must be satisfied in order to ensure compatibility. Conditions (3.53) are a direct consequence of the definition of strain, that is to say, that $\mathbf{E} = (1/2)((\nabla\otimes\mathbf{u})^{\mathrm{T}} + \nabla\otimes\mathbf{u}) = (1/2)(\mathbf{u}\otimes\nabla + \nabla\otimes\mathbf{u})$ implies that $\nabla\times\mathbf{E}\times\nabla = 0$. To see that this is true, consider the result of operating on $\mathbf{E} = (1/2)(\mathbf{u}\otimes\nabla + \nabla\otimes\mathbf{u})$ from the left by $\nabla\times$ and from the right by $\times\nabla$; one obtains the expression

$$2(\nabla\times\mathbf{E}\times\nabla) = \nabla\times\mathbf{u}\otimes\nabla\times\nabla + \nabla\times\nabla\otimes\mathbf{u}\times\nabla\,. \tag{3.56}$$

The operator $\nabla\times\nabla$, which occurs in both terms on the right-hand side of (3.56) is called the "curl grad"; the curl of the gradient applied to a function $f$ is zero, $\nabla\times\nabla f = 0$. In the indicial notation this is easy to see, $\nabla\times\nabla f = e_{ijk}(\partial f/\partial x_j\partial x_k)\mathbf{e}_i = 0$, because of the symmetry of the indices on the partial derivatives and skew-symmetry in the components of the alternator (see section A.9). Both terms on the right-hand side of (3.56) contain the operator curl grad, $\nabla\times\nabla$, applied to a function, hence $\nabla\times\mathbf{E}\times\nabla = 0$. It may also be shown that the

reverse is true, namely that $\nabla \times \mathbf{E} \times \nabla = 0$ implies that $\mathbf{E} = (1/2)((\nabla \otimes \mathbf{u})^{T} + \nabla \otimes \mathbf{u})$. Thus $\mathbf{E} = (1/2)((\nabla \otimes \mathbf{u})^{T} + \nabla \otimes \mathbf{u})$ is a necessary and sufficient condition that $\nabla \times \mathbf{E} \times \nabla = 0$.

**Problems**

3.4.1. For the motions of the form (3.10) given in Problem 3.1.1, namely, 3.1.1a–3.1.1g, determine if the infinitesimal strain tensors, **E**, calculated in 3.3.1 satisfy the conditions of compatibility.

3.4.2. Is the following strain state possible for an object in which the displacement field must be continuous and single valued? Justify your answer analytically.

$$\mathbf{e} = c \begin{bmatrix} x_3(x_1^2 + x_2^2) & x_1 x_2 x_3 & 0 \\ x_1 x_2 x_3 & x_3 x_2^2 & 0 \\ 0 & 0 & 0 \end{bmatrix}.$$

# 4

# CONTINUUM FORMULATIONS OF CONSERVATION LAWS

The theme for this chapter is captured by a quote from Herbert Callen's book on thermodynamics. Callen introduces the conservation of energy and the concept of internal energy in the following: "The development of the principle of conservation of energy has been one of the most significant achievements in the evolution of physics. The present form of the principle was not discovered in one magnificent stroke of insight but has been slowly and laboriously developed over two and a half centuries. The first recognition of a conservation principle, by Leibnitz in 1693, referred only to the sum of the kinetic energy ($(1/2)mv^2$) and the potential energy (mgh) of a simple mechanical mass point in the terrestrial gravitational field. As additional types of systems were considered, the established form of the conservation principle repeatedly failed, but in each case it was found possible to revive it by the addition of a new mathematical term — a "new kind of energy." Thus consideration of charged systems necessitated the addition of the Coulomb interaction energy ($Q_1Q_2/r$) and eventually of the energy of the electromagnetic field. In 1905 Einstein extended the principle to the relativistic region, adding such terms as the relativistic rest-mass energy. In the 1930s Enrico Fermi postulated the existence of a new particle, called the neutrino, solely for the purpose of retaining the energy conservation principle in nuclear reactions. Contemporary research in nuclear physics seeks the form of interaction between nucleons within a nucleus in order that the conservation principle may be formulated explicitly at the subnuclear level. Despite the fact that unsolved problems of this type remain, the energy conservation principle is now accepted as one of the most fundamental, general, and significant principles of physical theory."

## 4.1. THE CONSERVATION PRINCIPLES

Conservation principles will be cast here in the form of a balance or accounting statement for the time rate of change of a quantity in a system. On the plus side of the accountant's ledger are the amount of the quantity coming into the system and the quantity produced within the system. On the minus side are the amount of the quantity leaving the system and the quantity consumed within the system. The system will be either a fixed material system consisting always of the same set of particles or a fixed spatial (continuum) volume through which material is passing. The quantity will be either mass, linear momentum, angular momentum, or energy.

The focus of this chapter is the development of continuum formulations for the conservation principles of mass, linear momentum, angular momentum, and energy. The statement of conservation of mass is usually the statement that mass cannot be created or destroyed. The conservation of momentum is usually stated in the form of Newton's second law: the sum of the forces acting on an object is equal to the product of the mass of the object and the acceleration of the object. The conservation of angular momentum is the statement that the time rate of change of angular momentum must equal the sum of the applied moments. The conservation of energy is the requirement that the time rate of change of the sum of all the kinetic and internal energies must equal the mechanical power and heat power supplied to the object.

In the next section the continuum formulation of the conservation of mass is developed. In the following section the concept of stress is introduced and its important properties are derived and illustrated. The conservation of momentum, or the second law of Newton, when expressed in terms of stress, is called the *stress equation of motion.* The conservation of angular momentum is employed in the development of the stress equations of motion to show that the stress tensor is symmetric. In the last section the continuum formulation of the conservation of energy is developed.

## 4.2. THE CONSERVATION OF MASS

The total mass $M$ at time $t$ of an object $O$ is given by

$$M = \int_0 \rho(\mathbf{x},t)dv \,, \tag{4.1}$$

where $\rho(\mathbf{x}, t)$ is the mass density at the place $\mathbf{x}$ within the object at the time $t$. The statement of mass conservation for the object $O$ is that $M$ does not change with time:

$$\frac{DM}{Dt} = \frac{D}{Dt}\int_0 \rho(x,t)dv = 0 \,. \tag{4.2}$$

The material time derivative may be interchanged with the integration over the object $O$ since a fixed material volume is identified as the object:

$$\int_0 \dot{\rho}(\mathbf{x},t)dv + \rho(\mathbf{x},t)d\dot{v} = 0 \,. \tag{4.3}$$

Then, using the relationship relating the time rate of change in the volume to the present size of the volume from (3.36), $d\dot{v} = (\nabla \cdot \mathbf{v})dv$ , it follows that

$$\int_0 \rho(\mathbf{x},t) + \rho(\mathbf{x},t)(\nabla \bullet \mathbf{v})\, dv = 0 \,. \tag{4.4}$$

The next step in the development of this continuum representation of the conservation of mass is to employ the argument that the integral eq. (4.4) over the object $O$ may be replaced by the condition that the integrand in the integral eq. (4.4) be identically zero, thus

$$\dot{\rho} + \rho(\nabla \cdot \mathbf{v}) = 0 \,. \tag{4.5}$$

The argument that is used to go from (4.4) to (4.5) is an argument that will be employed three more times in this chapter. The argument is that any part or subvolume of an object $O$

may also be considered as an object and the result (4.4) also holds for that subobject. In Figure 4.1 an object and a portion of an object that may be considered as an object itself are illustrated. The argument for the transition (4.4)→(4.5) is as follows: suppose it is not true that the integrand of (4.4) is not zero everywhere (i.e., suppose the transition (4.4)→(4.5) is not true). If that is the case then there must exist domains of the object in which the integrand is positive and other domains in which the integrand is negative, so that when the integration is accomplished over the entire object the sum is zero. If that is the case, consider a domain of the object in which the integrand of (4.4) is always positive (or negative). Let this domain be an object. For the object chosen in this way the integral on the left-hand side of (4.4) cannot be zero. *This conclusion contradicts* (4.4) because (4.4) must be zero. It may therefore be concluded that the requirement that the integral (4.4) be zero for an object and all subobjects that can be formed from it means that the integrand must be zero everywhere in the object. Note that a very important transition has occurred in the argument that obtains (4.5) from (4.4). Integral statements such as (4.4) are global statements because they apply to an entire object. However the requirement (4.5) is a local, pointwise condition valid at the typical point (place) in the object. Thus, the transition (4.4)→(4.5) is from the global to the local or from the object to the point (or particle) in the object. Note also that the converse proof (4.5) →(4.4) is trivial.

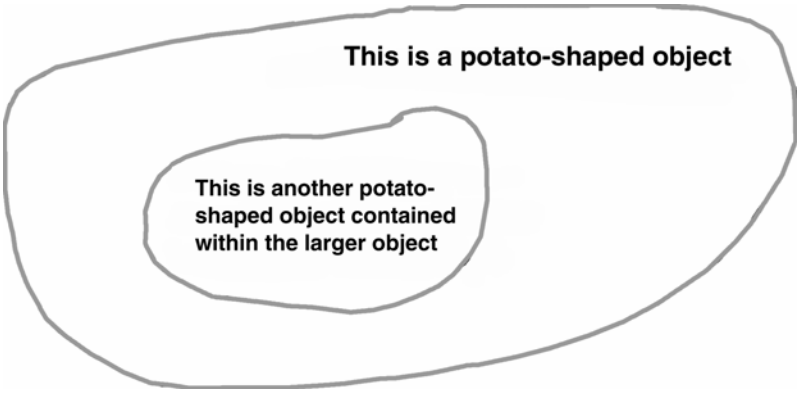



**Figure 4.1**. A potato-shaped object and a second potato-shaped object that is fully contained with the first potato-shaped object. All the conservation principles may be applied to both objects separately. Furthermore, one may select or define these objects as one chooses.

Note that (4.5) may be combined with (3.30), the expression decomposing the material time derivative into the sum of a local rate of change and a convective rate of change, to obtain this alternate local statement of mass conservation:

$$\frac{\partial \rho}{\partial t} + \nabla \cdot (\rho \mathbf{v}) = 0 \,. \tag{4.6}$$

Another consequence of the conservation of mass is a simple formula for the material time derivative of an integral of the form

$$K = \int_0 k(\mathbf{x},t)\rho(\mathbf{x},t)dv \,, \tag{4.7}$$

where $k(\mathbf{x}, t)$ is a physical quantity (temperature, momentum, etc.) of arbitrary scalar, vector, or tensor character, and $K$ is the value of the density times quantity $k(\mathbf{x}, t)$ integrated over the entire object $O$. Since, by (4.2), the material time rate of change of $\rho(\mathbf{x}, t)dv$ is zero, it follows that

$$\dot{K} = \int_0 \dot{k}(\mathbf{x},t)\rho(\mathbf{x},t)dv\,. \tag{4.8}$$

**Problem**

4.2.1. For the first six motions of the form (3.10) given in Problem 3.1.1, namely 3.1.1a–3.1.1f, determine the ratio of the time rate of change of density $\dot{\rho}$ to the instantaneous density $\rho$, $\dot{\rho}/\rho$.

4.2.2. In this section it was shown that one could derive the local statement of mass conservation (4.5) from the global statement of mass conservation, $DM/Dt = 0$. Reverse the direction of this derivation, and derive the global statement of mass conservation $DM/Dt = 0$ from the fact that the local statement (4.5) or (4.6) is true at all points in an object $O$.

## 4.3. THE STATE OF STRESS AT A POINT

Stress is a mental construct of humans to represent the internal interactions or internal forces on a material object. The concept of a stress will first be introduced as a vector. Consider the potato-shaped object shown in Figure 4.2. An imaginary plane $\Sigma$ characterized by its normal $\mathbf{n}$ divides the object into an upper portion U and a lower portion L. Considering L as a free object, the action of U upon L is statically equivalent to a resultant force $\mathbf{f}$ and couple $\mathbf{m}$. Assuming that the interaction is distributed across $\Sigma$, each area element $\Delta A_{(i)}$ of the intersection of $\Sigma$ and the object may be considered as transmitting a force $\Delta\mathbf{f}_{(i)}$ and a moment $\Delta\mathbf{m}_{(i)}$. The average stress vector, $\mathbf{t}^{A}_{(\mathbf{n})}(P)$, at the point $P$ acting on the plane whose normal is $\mathbf{n}$, is defined as the ratio

$$\mathbf{t}^{A}_{(\mathbf{n})}(P) = \frac{\Delta\mathbf{f}_{(i)}}{\Delta A_{(i)}}\,. \tag{4.9}$$

The quantity $\mathbf{t}^{A}_{(\mathbf{n})}$ is a vector because the force $\Delta\mathbf{f}_{(i)}$ is a vector and $\Delta A_{(i)}$ is a scalar. The average couple stress vector $\mathbf{c}^{A}_{(\mathbf{n})}(P)$ at the point $P$ acting on the plane whose normal is $\mathbf{n}$ is defined analogously by the ratio

$$\mathbf{c}^{A}_{(\mathbf{n})}(P) = \frac{\Delta\mathbf{m}_{(i)}}{\Delta A_{(i)}}\,. \tag{4.10}$$

These two definitions are illustrated in Figure 4.2. The stress vector $\mathbf{t}_{(\mathbf{n})}(P)$ acting at the point $P$ on the plane whose normal is $\mathbf{n}$ is defined as the limit of the average stress vector, $\mathbf{t}^{A}_{(\mathbf{n})}(P)$, as $\Delta A_{(i)}$ tends to zero through a sequence of progressively smaller areas, $\Delta A_{(1)}$, $\Delta A_{(2)}$, $\Delta A_{(3)}$, ..., $\Delta A_{(N)}$, ..., all containing the point $P$:

$$\mathbf{t}_{(\mathbf{n})}(P) = \lim_{\Delta A_{(i)} \to 0} \mathbf{t}^{A}_{(\mathbf{n})}(P)\,. \tag{4.11}$$

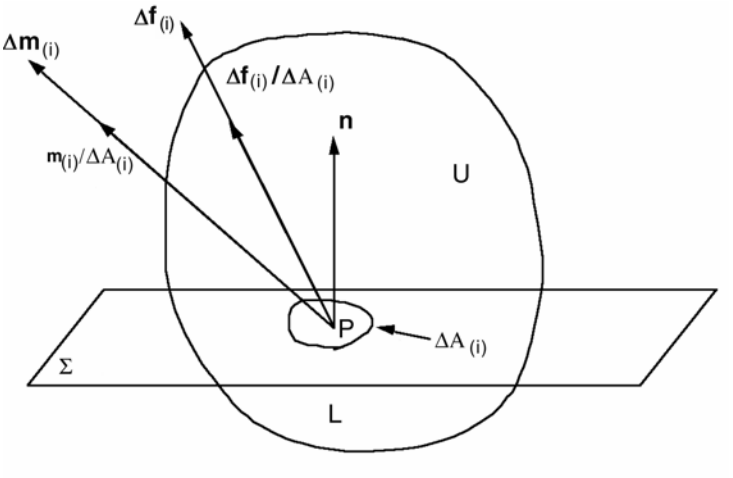



**Figure 4.2**. The force and moment acting across plane Σ, with normal **n**, passed through a point *P* in a potato-shaped object.

When a similar limit is applied to the average couple stress vector we assume that the limit is zero:

$$0 = \lim_{\Delta A_{(i)} \to 0} \mathbf{c}^{A}_{(\mathbf{n})}(P)\,. \tag{4.12}$$

In effect we are assuming that the forces involved are of finite magnitude and that the moment arm associated with $\Delta\mathbf{m}_{(i)}$ vanishes as $\Delta A_{(i)}$ tends to zero. For almost all continuum theories assumption (4.12) is adequate.

The internal force interaction at a point in an object is adequately represented by the stress vector $\mathbf{t}_{(\mathbf{n})}$ across the plane whose normal is **n**. However, there is a double infinity of distinct planes with normals **n** passing through a single point; thus, there is a double infinity of distinct stress vectors acting at each point. The multitude of stress vectors, $\mathbf{t}_{(\mathbf{n})}$, at a point are called the state of stress at the point. The totality of vectors $\mathbf{t}_{(\mathbf{n})}(P)$ at a fixed point *P*, and for all directions **n**, is called the *state of stress* at the point *P*. The representation of the state of stress at a point is simplified by proving that $\mathbf{t}_{(\mathbf{n})}(P)$ must be a linear function of the vector **n**, as will be done below. The coefficients of this linear relationship will be the stress tensor **T**. Thus, **T** will be a linear transformation that transforms **n** into $\mathbf{t}_{(\mathbf{n})}$, $\mathbf{t}_{(\mathbf{n})}(P) = \mathbf{T}(P)\cdot\mathbf{n}$. The proof that **T** is, in fact, a tensor and the coefficient of a linear transformation will also be provided below. However, even though it has not yet been proved, **T** will be referred to as a tensor. The stress tensor **T** has components relative to an orthonormal basis that are the elements of the matrix

$$\mathbf{T} = \begin{bmatrix} T_{11} & T_{12} & T_{13} \\ T_{21} & T_{22} & T_{23} \\ T_{31} & T_{32} & T_{33} \end{bmatrix}. \tag{4.13}$$

The component $T_{\mathrm{ij}}$ of the stress tensor is the component of the stress vector $\mathbf{t}_{(\mathbf{n})} = \mathbf{t}_{(j)}$ acting on the plane whose normal **n** is in the $\mathbf{e}_j$ direction, $\mathbf{n} = \mathbf{e}_j$, projected in the $\mathbf{e}_{\mathrm{i}}$ direction,

$$T_{ij} = \mathbf{e}_i \cdot \mathbf{t}_{(j)}. \tag{4.14}$$

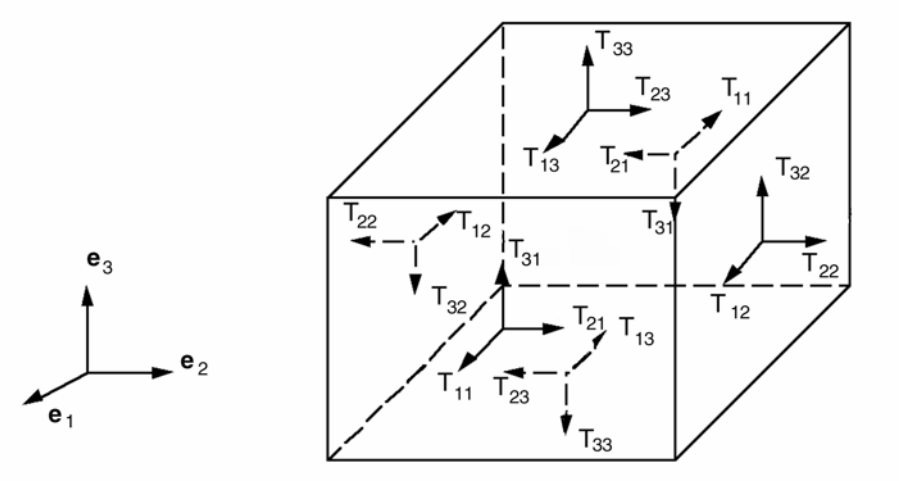



**Figure 4.3**. Cartesian components of stress acting on the faces of a small cubic element.

The nine components of the stress tensor defined by (4.14) and represented by (4.13) are therefore the $\mathbf{e}_1$, $\mathbf{e}_2$, and $\mathbf{e}_3$ components of the three stress vectors $\mathbf{t}_{(i)}$, $\mathbf{t}_{(j)}$ and $\mathbf{t}_{(k)}$ that act at the point $P$, on planes parallel to the three mutually perpendicular coordinate planes. This is illustrated in Figure 4.3. The components $T_{11}$, $T_{22}$, and $T_{33}$ are called *normal stresses*, and the remaining components — $T_{12}$, $T_{23}$, $T_{13}$, $T_{21}$, $T_{32}$, $T_{31}$ — are called *shearing stresses*. Each of these components has the dimension of force per unit area.

Recall that stress was defined as the force per unit area that the upper portion U exerts on the lower portion L. From this definition, it follows that if the exterior normal of the object is in the positive coordinate direction then positive normal and shear stresses will also be in the positive coordinate direction. If the exterior normal of the object is in the negative coordinate direction, however, positive normal and shear stresses will point in the negative coordinate direction. The rule for the signs of stress components is as follows: *the stress on a plane is positive if it points in a positive direction on a positive plane, or in a negative direction on a negative plane. Otherwise, it is negative.*

It will now be shown, following an 1822 result of Cauchy, that the nine components of stress are sufficient to characterize the entire state of stress at a point. Specifically, it will be shown that *the state of stress at a point P is completely determined if the stress vectors associated with three mutually perpendicular planes are known at P and are continuous in a neighborhood of P*. The stress vector $\mathbf{t}_{(\mathbf{n})}$ acting on any plane whose normal is $\mathbf{n}$ is given by

$$\begin{bmatrix} t_{(\mathbf{n})1} \\ t_{(\mathbf{n})2} \\ t_{(\mathbf{n})3} \end{bmatrix} = \begin{bmatrix} T_{11} & T_{12} & T_{13} \\ T_{21} & T_{22} & T_{23} \\ T_{31} & T_{32} & T_{33} \end{bmatrix} \begin{bmatrix} n_1 \\ n_2 \\ n_3 \end{bmatrix}. \tag{4.15a}$$

or

$$t_{(n)} = T \cdot n, \qquad t_{(\mathbf{n})i} = \sum_{j=1}^{j=3} T_{ij} n_j \,. \tag{4.15b}$$

This means that the stress tensor **T** can be considered as a linear transformation that transforms the unit normal **n** into the stress vector $\mathbf{t}_{(\mathbf{n})}$ acting on the plane whose normal is **n**.

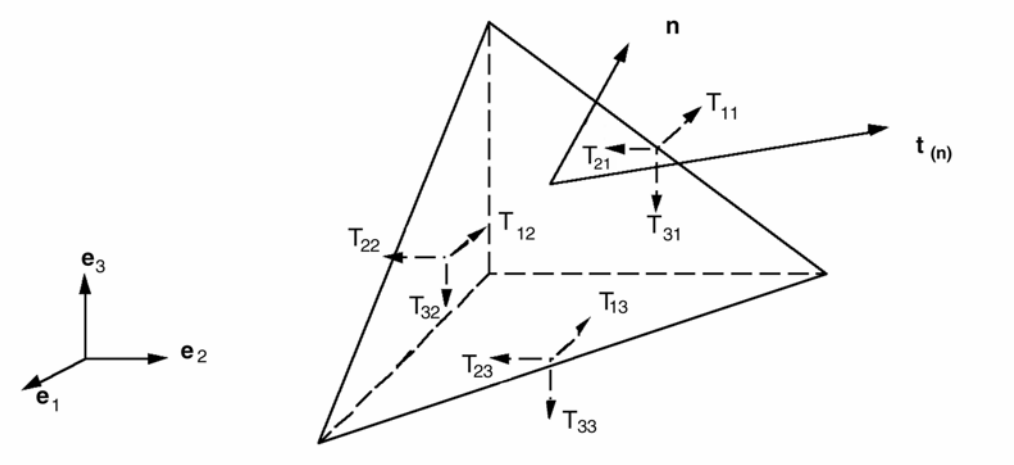



**Figure 4.4**. The surface tractions on a tetrahedron.

To prove this result we consider the tetrahedral element of an object shown in Figure 4.4 as a free object and apply Newton's second law to the force system acting on the tetrahedron. The tetrahedron is selected in such a way that the stress vectors acting on the mutually orthogonal faces are the stress vectors acting on the coordinate planes. Recall that we have represented the components of the stress vectors acting on the planes whose normals are $\mathbf{e}_1$, $\mathbf{e}_2$, and $\mathbf{e}_3$ by the components of the stress tensor. The three scalar equations of Newton's second law will suffice for determination of the unknown components of $\mathbf{t}_{(\mathbf{n})}$ acting on the fourth face. For simplicity we will only derive (4.15) in the $\mathbf{e}_1$ direction. We let $A$ be the area of the inclined face with normal **n** and $h$ the perpendicular distance from $P$ to the inclined face. The mean value of $\mathbf{t}_{(\mathbf{n})}$ will be denoted and defined by

$$\overline{\mathbf{t}}_{(\mathbf{n})1} = \frac{1}{A}\int_A \mathbf{t}_{(\mathbf{n})1} dA = \mathbf{t}_{(\mathbf{n})1}(Q)\,, \tag{4.16}$$

where, as a consequence of the mean value theorem, the point $Q$ lies inside $A$. Analogously defined mean values of the components of **T** over their respective areas will be denoted by $\overline{\mathbf{T}}$. The reason for requiring that the stress components be continuous in terms of position in a neighborhood of $P$ is to ensure that the mean values of the stress components actually occur at certain points always within the corresponding areas.

Since the area of the inclined face of the tetrahedron may be represented by the vector $A\mathbf{n}$, where $A$ is the magnitude of the area and **n** is the normal to the plane containing the area, the areas of the orthogonal faces are each given by $An_1$, $An_2$, $An_3$. The fact that the areas of four faces of a tetrahedron, where three of the faces of the tetrahedron are orthogonal, are $A$, $An_1$, $An_2$, and $An_3$ is a result from solid geometry. Summing forces in the $\mathbf{e}_1$ direction and setting the result equal to the mass times the acceleration of the tetrahedron we find that

$$\overline{t}_{(\mathbf{n})1}A - \overline{T}_{11}An_1 - \overline{T}_{12}An_2 - \overline{T}_{13}An_3 + \rho d_1 \frac{Ah}{3} = \rho\ddot{x}_1 \frac{Ah}{3}\,, \tag{4.17}$$

where $Ah/3$ is the volume of the tetrahedron, $d_1$ is the action-at-a-distance force (e.g., gravity) in the $\mathbf{e}_1$ direction and $\ddot{x}_1$ the acceleration of the tetrahedron in that direction. The next step in this development is to cancel $A$ throughout (4.17) and allow the plane whose normal is $\mathbf{n}$ to approach $P$, causing the volume of the tetrahedron to vanish as $h$ tends to zero. Before doing this, note that since $Q$ must always lie on $A$, as $h$ tends to zero, by the mean value theorem:

$$\mathbf{t}_{(\mathbf{n})}(P) = \lim_{h\to 0} \bar{\mathbf{t}}_{(\mathbf{n})1}(P) = \lim_{h\to 0} \mathbf{t}_{(\mathbf{n})1}(Q)\,, \quad \mathbf{T}(P) = \lim_{h\to 0} \bar{\mathbf{T}}(P) = \lim_{h\to 0} \mathbf{T}(Q)\,. \tag{4.18}$$

Canceling $A$ throughout (4.17) and taking the limiting process as $h$ tends to zero, noting that the object force and the acceleration vanish as the volume of the tetrahedron vanishes, it follows from (4.17) and (4.18) that

$$t_{(\mathbf{n})1} = T_{11}n_1 + T_{12}n_2 + T_{13}n_3\,. \tag{4.19}$$

Repeating this analysis for the $\mathbf{e}_2$ and $\mathbf{e}_3$ directions the result (4.15) is established.

Thus, we have shown that the double infinity of possible stress vectors $\mathbf{t}_{(\mathbf{n})}$, which constitute a state of stress at a point in an object, can be completely characterized by the nine components of $\mathbf{T}$. These nine components are simply the three components of three different stress vectors, one acting on each of the coordinate planes of a reference frame. Thus, in the matrix of tensor components (4.13) the first row consists of the components of the stress vector acting on a plane whose normal is in the $\mathbf{e}_1$ direction. A similar interpretation applies to the second and third rows. When the meaning is not obscured, we will drop the subscript $(\mathbf{n})$ in the equation $\mathbf{t}_{(\mathbf{n})} = \mathbf{T}\cdot\mathbf{n}$ and write it as $\mathbf{t} = \mathbf{T}\cdot\mathbf{n}$, with it being understood that the particular $\mathbf{t}$ depends upon $\mathbf{n}$. The normal stress on a plane is then given by $\mathbf{t}\cdot\mathbf{n} = \mathbf{n}\cdot\mathbf{T}\cdot\mathbf{n}$ and the shear stress in a direction $\mathbf{m}$ lying in the plane whose normal is $\mathbf{n}$, $\mathbf{m}\cdot\mathbf{n} = 0$, is given by $\mathbf{t}\cdot\mathbf{m} = \mathbf{m}\cdot\mathbf{T}\cdot\mathbf{n} = \mathbf{n}\cdot\mathbf{T}\cdot\mathbf{m}$. Note that if a vector $\mathbf{m}'$ is introduced that reverses the direction of $\mathbf{m}$, $\mathbf{m}' = -\mathbf{m}$, then the associated shear stress is given by $\mathbf{t}\cdot\mathbf{m}' = \mathbf{m}'\cdot\mathbf{T}\cdot\mathbf{n} = \mathbf{n}\cdot\mathbf{T}\cdot\mathbf{m}' = -\mathbf{t}\cdot\mathbf{m}$. This shows that, if the unit vector $\mathbf{m}$ is reversed in direction, the opposite value of the shear stress is obtained. Note also that if the unit vector $\mathbf{n}$ is reversed in direction, the opposite value of the shear stress is obtained. If both the unit vectors $\mathbf{n}$ and $\mathbf{m}$ are reversed in direction, the sign of the shear stress is unchanged. These conclusions are all consistent with the definition of the sign of the shear stress.

A short calculation will show that the stress matrix $\mathbf{T}$ is a tensor. Recall that, in order for $\mathbf{T}$ to be a tensor, its components in one coordinate system had to be related to the components in another coordinate system by

$$\mathbf{T}^{(L)} = \mathbf{Q}\cdot\mathbf{T}^{(G)}\cdot\mathbf{Q}^T \quad \text{and} \quad \mathbf{T}^{(G)} = \mathbf{Q}^T\cdot\mathbf{T}^{(L)}\cdot\mathbf{Q}\,. \qquad \text{(A83) repeated}$$

To show that the $\mathbf{T}$ in relationship (4.15), $\mathbf{t} = \mathbf{T}\cdot\mathbf{n}$, has the tensor property, the equation $\mathbf{t} = \mathbf{T}\cdot\mathbf{n}$ is specified in the Latin coordinate system, $\mathbf{t}^{(L)} = \mathbf{T}^{(L)}\cdot\mathbf{n}^{(L)}$. Then, using the vector transformation law (A73) for $\mathbf{t}$ and $\mathbf{n}$, $\mathbf{t}^{(L)} = \mathbf{Q}\cdot\mathbf{t}^{(G)}$ and $\mathbf{n}^{(L)} = \mathbf{Q}\cdot\mathbf{n}^{(G)}$, respectively, the expression $\mathbf{t}^{(L)} = \mathbf{T}^{(L)}\cdot\mathbf{n}^{(L)}$ is then rewritten as $\mathbf{Q}\cdot\mathbf{t}^{(G)} = \mathbf{T}^{(L)}\cdot\mathbf{Q}\cdot\mathbf{n}^{(G)}$, or $\mathbf{t}^{(G)} = \mathbf{Q}^{\mathrm{T}}\cdot\mathbf{T}^{(L)}\cdot\mathbf{Q}\cdot\mathbf{n}^{(G)}$. Finally, it can be noted from $\mathbf{t}^{(G)} = \mathbf{Q}^{\mathrm{T}}\cdot\mathbf{T}^{(L)}\cdot\mathbf{Q}\cdot\mathbf{n}^{(G)}$ that since $\mathbf{t}^{(G)} = \mathbf{T}^{(G)}\cdot\mathbf{n}^{(G)}$, it follows that $\mathbf{T}^{(G)} = \mathbf{Q}^{\mathrm{T}}\cdot\mathbf{T}^{(L)}\cdot\mathbf{Q}$. Since this is the transformation rule for a tensor (A83), $\mathbf{T}$ is a tensor.

**Example 4.3.1**

Determine the stress tensor representing the state of stress at a typical point in the uniform bar subjected to a uniform tensile stress (Figure 4.5). The applied tensile stress is of magnitude $\sigma$ and it is assumed that the stress state is the same at all points of the bar. Determine the stress

vector **t** acting on the plane whose normal is **n**, where **n** is given by $\mathbf{n} = \cos\theta\,\mathbf{e}_2 + \sin\theta\,\mathbf{e}_3$. Determine the normal stress on the plane whose normal is **n** and the shear stress in the direction **m**, $\mathbf{m}\cdot\mathbf{n} = 0$, $\mathbf{m} = -\sin\theta\,\mathbf{e}_2 + \cos\theta\,\mathbf{e}_3$, on the plane whose normal is **n**.

**Solution**: The components of the stress tensor **T** at a typical point in the bar and relative to the coordinate system shown in Figure 4.5, are given by

$$\mathbf{T} = \begin{bmatrix} 0 & 0 & 0 \\ 0 & 0 & 0 \\ 0 & 0 & \sigma \end{bmatrix},$$

thus the only nonzero component of the stress tensor is $T_{33}$. The stress vector **t** acting on the plane whose normal is **n** is then given by

$$\mathbf{t} = \mathbf{T}\mathbf{n} = \begin{bmatrix} 0 & 0 & 0 \\ 0 & 0 & 0 \\ 0 & 0 & \sigma \end{bmatrix} \begin{bmatrix} 0 \\ \cos\theta \\ \sin\theta \end{bmatrix} = \begin{bmatrix} 0 \\ 0 \\ \sigma\sin\theta \end{bmatrix}.$$

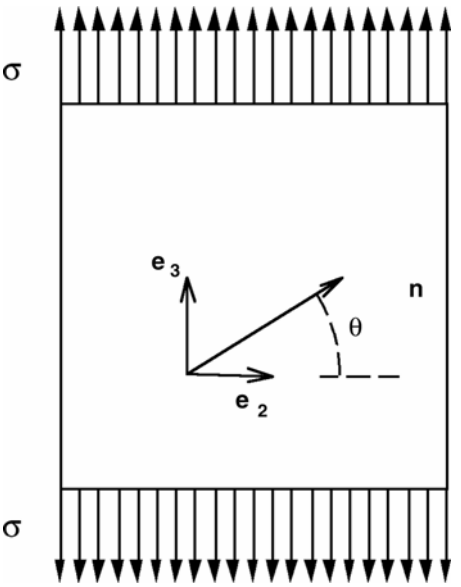



**Figure 4.5**. A uniform bar subjected to uniform stress σ.

Thus, this vector has only one nonzero component, namely, $t_3 = \sigma \sin\theta$. The normal stress on the plane whose normal is **n** is given by $\mathbf{t}\cdot\mathbf{n} = \sigma \sin^2\theta$. The shear stress on the plane whose normal is **n** in the direction **m**, $\mathbf{m}\cdot\mathbf{n} = 0$, $\mathbf{m} = -\sin\theta\,\mathbf{e}_2 + \cos\theta\,\boldsymbol{e}_3$ is given by $\mathbf{t}\cdot\mathbf{m} = \sigma\cos\theta\sin\theta$. (Note that one could choose $\mathbf{m}' = \sin\theta\,\boldsymbol{e}_2 - \cos\theta\,\boldsymbol{e}_3$ , where $\mathbf{m}' = -\mathbf{m}$, then $\mathbf{t}\cdot\mathbf{m}' = -\sigma\cos\theta\sin\theta = -\mathbf{t}\cdot\mathbf{m}$ and the direction of the shear stress is reversed). From these results it is seen that when the normal to the plane **n** coincides with the $\mathbf{e}_3$ direction ($\theta = \pi/2$), the stress component $t_3$ is equal to σ as one would expect, and when the normal to the plane **n** coincides

with the $\mathbf{e}_2$ direction, the stress component $t_2$ is zero. The shear stress $\mathbf{t}\cdot\mathbf{m} = \sigma \cos\theta \sin\theta$ has maxima of $\sigma/2$ at $\theta = \pi/4$ and $3\pi/4$.

**Problems**

4.3.1. The flat plate shown in Figure 4.6 has only two stresses acting on it. There is a uniform tensile stress $\sigma$ in the $\mathbf{e}_2$ direction and a uniform compressive stress $\sigma$ in the $\mathbf{e}_1$ direction. Find the stress vector and the components of the stress tensor acting on the planes whose normals are

$$\text{(a)}\ \frac{1}{\sqrt{2}}(\mathbf{e}_1+\mathbf{e}_2),\ \text{(b)}\ \frac{-1}{\sqrt{2}}(\mathbf{e}_1+\mathbf{e}_2),\ \text{(c)}\ \frac{1}{\sqrt{2}}(\mathbf{e}_1-\mathbf{e}_2),\ \text{(d)}\ \frac{1}{\sqrt{2}}(-\mathbf{e}_1+\mathbf{e}_2).$$

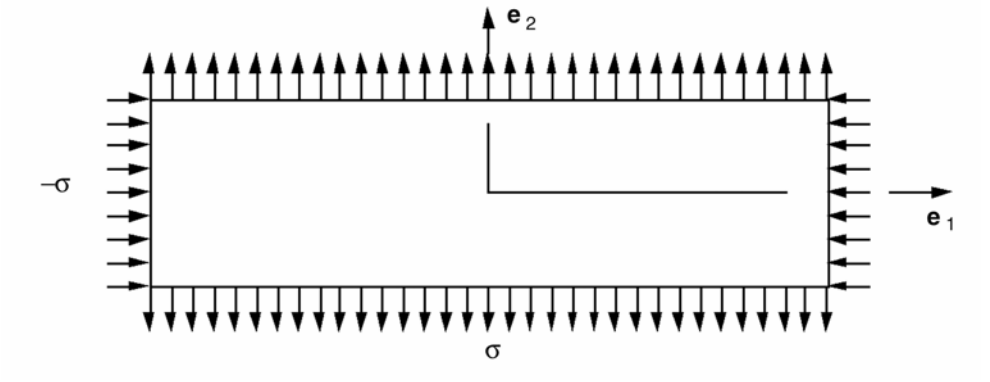



**Figure 4.6**. An illustration for Problem 4.3.1.

4.3.2. The flat plate shown in Figure 4.7 has shearing stresses $\tau$ acting on each of its four faces. Find the stress vector and the stress components acting on the planes whose normals are

$$\text{(a)}\ \mathbf{n} = \frac{1}{\sqrt{2}}(\mathbf{e}_1+\mathbf{e}_2),\ \text{(b)}\ \mathbf{n} = \frac{1}{\sqrt{2}}(\mathbf{e}_1-\mathbf{e}_2).$$

4.3.3. Repeat the arguments of this section and show that

$$t_{(\mathbf{n})2} = T_{21}n_1 + T_{22}n_2 + T_{23}n_3.$$

List each of the arguments and rules or facts used in the proof.

4.3.4. The roughly triangular-shaped region in Figure 4.8 with the included angle $\beta$ represents the upper portion of a dam. The zigzag lines at the bottom of the triangular region are an indication that the dam extends beyond those zigzags lines. Find the stress vectors acting on the face $x_1 = 0$ and on the slanted face of the wedge shown in the Figure 4.8. The stress matrix at the typical point $x_1, x_2, x_3$ of the wedge shown in Figure 4.8 is given by

$$T_{11} = -\gamma x_2,\quad T_{22} = \left(\frac{P}{\tan\beta} - \frac{2\gamma}{\tan^3\beta}\right)x_1 + \left(\frac{\gamma}{\tan^2\beta} - P\right)x_2,$$

$$T_{12} = T_{21} = \frac{-\gamma x_1}{\tan^2\beta},\quad T_{33} = T_{31} = T_{13} = T_{23} = T_{32} = 0.$$

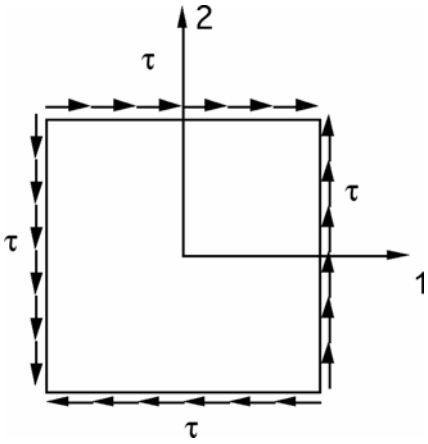



**Figure 4.7**. An illustration for Problem 4.3.2.

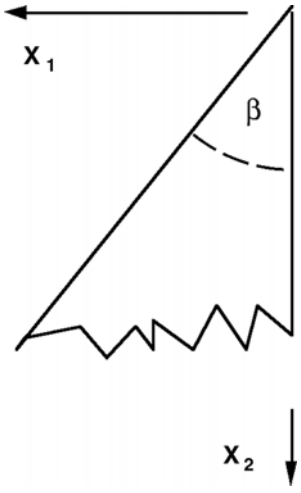



**Figure 4.8**. An illustration for Problem 4.3.4.

## 4.4. THE STRESS EQUATIONS OF MOTION

In continuum mechanics the stress equations of motion are the most useful form of the principles of balance of linear and angular momentum. The stress equations of motion are statements of Newton's second law (i.e., that force is equal to mass times acceleration) written in terms of stress.

The forces that act on the object in Figure 4.9 are the surface traction $\mathbf{t}(\mathbf{x},t)$, which acts at each boundary point, and the action-at-a-distance force $\rho\mathbf{d}$, which represents forces such as gravity and the effect of electromagnetic forces on charges within the object. For example, at the surface of the earth, in the absence of electromagnetic forces, $\mathbf{d} = -g\mathbf{e}_2$, where $\mathbf{e}_2$ is a posi-

tive unit normal to the surface of the earth and $g$ is the acceleration of gravity at the earth's surface. The total force $\Sigma\mathbf{F}$ acting on the object is given by

$$\Sigma\mathbf{F} = \int_{\partial 0} \mathbf{t}\,da + \int_{0} \rho\mathbf{d}\,dv\,, \tag{4.20}$$

where $\partial O$ is the surface of the object $O$. The total moment about the origin of the coordinate system illustrated is

$$\Sigma\mathbf{M} = \int_{\partial 0} \mathbf{x}\times\mathbf{t}\,da + \int_{0} \mathbf{x}\times\rho\mathbf{d}\,dv\,, \tag{4.21}$$

where $\mathbf{x}$ is a position vector from the origin. The linear momentum $\mathbf{p}$ and the angular momentum $\mathbf{H}$ of the object in Figure 4.9 are written as the following integrals over the object $O$:

$$\mathbf{p} = \int_{0} \rho\dot{\mathbf{x}}\,dv\,,\quad \mathbf{H} = \int_{0} \mathbf{x}\times\rho\dot{\mathbf{x}}\,dv\,. \tag{4.22}$$

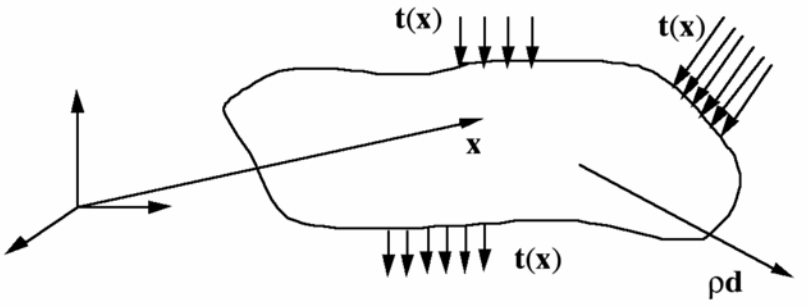



**Figure 4.9**. An object acted upon by action-at-a-distance force $\rho\mathbf{d}$ and system of surface tractions $\mathbf{t}(\mathbf{x})$.

The balance of linear momentum requires that the sum of the applied forces equals the time rate of change of the linear momentum, and the balance of angular momentum requires that the sum of the applied moments equals the time rate of change of the angular momentum. In computing the time rates of change of the integrals (4.22) we note that the object $O$ is material so that the material time derivative may be taken inside the integral sign and applied directly to the integrand with the density excluded, (4.8). The material time derivative applied to (4.22) yields

$$\dot{\mathbf{p}} = \int_{0} \rho\ddot{\mathbf{x}}\,dv\,,\quad \dot{\mathbf{H}} = \int_{0} \dot{\mathbf{x}}\times\dot{\mathbf{x}}\rho\,dv + \int_{0} \mathbf{x}\times\ddot{\mathbf{x}}\rho\,dv = \int_{0} \mathbf{x}\times\ddot{\mathbf{x}}\rho\,dv\,, \tag{4.23}$$

where the term in the square brackets vanishes because $\dot{\mathbf{x}}\times\dot{\mathbf{x}} = 0$. Equating $\dot{\mathbf{p}}$ to $\Sigma\mathbf{F}$ and $\dot{\mathbf{H}}$ to $\Sigma\mathbf{M}$ as required by the conservation of linear and angular momentum, respectively, we obtain from (4.20) and (4.23) that

$$\int_{0} \rho\ddot{\mathbf{x}}\,dv = \int_{\partial 0} \mathbf{t}\,da + \int_{0} \rho\mathbf{d}\,dv\,, \tag{4.24}$$

and from (4.21) and (4.23) that

$$\int_0 \mathbf{x}\times\ddot{\mathbf{x}}\rho dv = \int_{\partial 0} \mathbf{x}\times\mathbf{t}da + \int_0 \mathbf{x}\times\rho\mathbf{d}dv\,. \tag{4.25}$$

These integral forms of the balance of linear and angular momentum are the global forms of these principles. The global forms are stronger statements of these balance principles than are the point forms that we will now derive. We say that the point forms are weaker because it must be assumed that the stress is continuously differentiable and that $\rho\ddot{\mathbf{x}}$ and $\rho\mathbf{d}$ are continuous everywhere in the object in order to obtain the point forms from the global forms. The point form of the balance of linear momentum is obtained from (4.24) by first substituting (4.15b) into the surface integral in (4.24),

$$\int_0 \rho\ddot{\mathbf{x}}dv = \int_{\partial 0} \mathbf{T}\cdot\mathbf{n}da + \int_0 \rho\mathbf{d}dv\,, \tag{4.26}$$

then applying the divergence theorem (A184) to the surface integral in (4.26),

$$\int_0 \rho\ddot{\mathbf{x}}dv = \int_0 \nabla\cdot\mathbf{T}dv + \int_0 \rho\mathbf{d}dv\,. \tag{4.27}$$

The second step in obtaining the point form is to rewrite (4.27) as a single integral,

$$\int_0 (\rho\ddot{\mathbf{x}} - \nabla\cdot\mathbf{T} - \rho\mathbf{d})dv = 0\,, \tag{4.28}$$

and then employ the same argument as was employed in the transition from (4.4) to (4.5); see the discussion following (4.5). It follows then that

$$\rho\ddot{\mathbf{x}} = \nabla\cdot\mathbf{T} + \rho\mathbf{d} \tag{4.29}$$

at each point in the object $O$. There is one more point to make about (4.29) before it is complete. That point is that the stress tensor $\mathbf{T}$ is symmetric and thus the transposition in (4.29) is not necessary. In the next paragraph the conservation of angular momentum is used to show that the stress tensor $\mathbf{T}$ is symmetric.

The arguments to show that the stress tensor $\mathbf{T}$ is symmetric are algebraically simpler if we replace the statement of the conservation of angular momentum given above, (4.25), by the equivalent requirement that the skew-symmetric part of $\mathbf{Z}$,

$$\mathbf{Z} = \int_0 \mathbf{x}\otimes\ddot{\mathbf{x}}\rho dv - \int_{\partial 0} \mathbf{x}\otimes\mathbf{t}da - \int_0 \mathbf{x}\otimes\rho\mathbf{d}dv\,, \tag{4.30}$$

be zero:

$$\mathbf{Z} - \mathbf{Z}^{\mathrm{T}} = 0. \tag{4.31}$$

Equation (4.31) is equivalent to (4.25). The rationale for this equivalence is that the components of the cross-product of two vectors, say $\mathbf{a}$ x $\mathbf{b}$, are equal to the components of the skew-symmetric part of the open product of the two vectors, $\mathbf{a}\otimes\mathbf{b}$. Since (4.31) requires that $\mathbf{Z}$ be symmetric, it follows that the skew-symmetric part of $\mathbf{Z}$ is zero. Equation (4.25) is equivalent to the skew-symmetric part of $\mathbf{Z}$, and the equivalence is established.

The sequence of steps applied to the conservation of linear momentum in the paragraph before last are now applied to the expression (4.30) for **Z**. The point form of (4.30) is obtained by first substituting (4.15b) into the surface integral in (4.30):

$$\mathbf{Z} = \int_0 \mathbf{x} \otimes \ddot{\mathbf{x}} \rho dv - \int_{\partial 0} \mathbf{x} \otimes \mathbf{T} \cdot \mathbf{n} da - \int_0 \mathbf{x} \otimes \rho \mathbf{d} dv \,, \tag{4.32}$$

then applying the divergence theorem (A153) to the surface integral in (4.32):

$$\mathbf{Z} = \int_0 \mathbf{x} \otimes \ddot{\mathbf{x}} \rho dv - \int_0 \{(\nabla \otimes \mathbf{x}) \cdot \mathbf{T} + (\mathbf{x} \otimes \nabla \cdot \mathbf{T})\} dv - \int_0 \mathbf{x} \otimes \rho \mathbf{d} dv \,. \tag{4.33}$$

This result is simplified by observing that $\nabla \otimes \mathbf{x} = \mathbf{1}$ and collecting all the remaining integrals containing $\mathbf{x} \otimes$ together; thus,

$$\mathbf{Z} = \int_0 \mathbf{T} dv + \int_0 \mathbf{x} \otimes \{\rho \ddot{\mathbf{x}} - \nabla \cdot \mathbf{T} - \rho \mathbf{d}\} dv \,. \tag{4.34}$$

The second integral in (4.34) is exactly zero because its integrand contains the point form statement of linear momentum conservation (4.29); thus (4.34) and (4.31) show that

$$\int_0 (\mathbf{T} - \mathbf{T}^T) dv = 0 \,. \tag{4.35}$$

The final step in this development is to employ the same argument as was employed in the transition from (4.4) to (4.5); see the discussion following (4.5). It follows then that the stress tensor is symmetric,

$$\mathbf{T} = \mathbf{T}^T \,, \tag{4.36}$$

at each point in the object *O*.

The final form of the stress equations of motion is obtained from the combination of (4.36) and (4.29); thus,

$$\rho \ddot{\mathbf{x}} = \nabla \cdot \mathbf{T} + \rho \mathbf{d} \,, \quad \mathbf{T} = \mathbf{T}^T \,. \tag{4.37}$$

This local statement of Newton's second law retains aspects of the original. The mass times acceleration is represented by density times acceleration on the left-hand side. The sum of the forces is represented on the right-hand side by the gradient of the stress tensor and the action-at-a-distance force. The expanded scalar version of the stress equations of motion is

$$\begin{aligned}
\rho \ddot{x}_1 &= \frac{\partial T_{11}}{\partial x_1} + \frac{\partial T_{12}}{\partial x_2} + \frac{\partial T_{13}}{\partial x_3} + \rho d_1 \,, \\
\rho \ddot{x}_2 &= \frac{\partial T_{12}}{\partial x_1} + \frac{\partial T_{22}}{\partial x_2} + \frac{\partial T_{23}}{\partial x_3} + \rho d_2 \,, \\
\rho \ddot{x}_3 &= \frac{\partial T_{13}}{\partial x_1} + \frac{\partial T_{23}}{\partial x_2} + \frac{\partial T_{33}}{\partial x_3} + \rho d_3 \,,
\end{aligned} \tag{4.38}$$

where the symmetry of the stress tensor is expressed in the subscripted indices. For a two-dimensional motion the stress equations of motion reduce to

$$\rho\ddot{x}_1 = \frac{\partial T_{11}}{\partial x_1} + \frac{\partial T_{12}}{\partial x_2} + \rho d_1, \quad \rho\ddot{x}_2 = \frac{\partial T_{12}}{\partial x_1} + \frac{\partial T_{22}}{\partial x_2} + \rho d_2 . \tag{4.39}$$

**Example 4.4.1**

The stress tensor in an object is given by

$$\mathbf{T} = \begin{bmatrix} c_1x_1 + c_2x_2 & -c_4x_1 - c_1x_2 & 0 \\ -c_4x_1 - c_1x_2 & c_3x_1 + c_4x_2 + \rho g x_2 & 0 \\ 0 & 0 & c_5 \end{bmatrix},$$

where $c_i$, $i$ = 1, …, 5, are constants. This same object is subjected to an action-at a-distance force **d** with components [0, –$g$, 0]. Determine the components of the acceleration vector of this object.

**Solution**: Substitution of the given stress tensor **T** and the action-at-a-distance force **d** into the stress equations of motion (4.38) yields the fact that all the components of the acceleration are zero:

$$\rho\ddot{x}_1 = c_1 - c_1 + 0 = 0, \quad \rho\ddot{x}_2 = -c_4 + c_4 + \rho g - \rho g = 0, \quad \rho\ddot{x}_3 = 0 .$$

**Problems**

4.4.1. Derive the stress equations of motion in two dimensions, (4.39), from the less rigorous argument that consists of applying Newton's second law to the differential element of an object. This element is of length $dx_1$ and of width $dx_2$ (see Figure 4.10). The stresses acting on the element are all referred to the point ($x_1$, $x_2$) that is the lower left-hand corner of the element. Use the stresses to calculate the forces acting on the various faces of the element. In order to determine the stresses on opposite faces expand the stresses on one face in a one-term Taylor series about the first face. Please keep in mind that, even though the stress tensor is symmetric, the shear stress $T_{12}$ on a face with a normal in a positive direction is opposite in direction from the shear stress $T_{12}$ on a face with a normal in a negative direction.

4.4.2 The components of a stress matrix are

$$\mathbf{T} = \begin{bmatrix} A[x_2^2 + B(x_1^2 - x_2^2)] & -2ABx_1x_2 & 0 \\ -2ABx_1x_2 & A[x_1^2 + B(x_2^2 - x_1^2)] & 0 \\ 0 & 0 & A[B(x_1^2 + x_2^2)] \end{bmatrix},$$

where $A$ and $B$ are constants. Does this stress matrix satisfy the stress equations of motion? For what action-at-a-distance force field does it satisfy the stress equations of motion? Assume that the acceleration of the object is zero.

4.4.3. Using the equations of motion to determine the acceleration of an object for which $t$ = 2, $\mathbf{d} = 5\mathbf{e}_1 + 6\mathbf{e}_2 + 7\mathbf{e}_3$, the density, ρ, is 2 and and **T** is given by

$$\mathbf{T} = \begin{bmatrix} 3x_1 & x_3 & 3x_1 \\ x_3 & 4x_2 & 3x_3 \\ 3x_1 & 3x_3 & 7x_3 \end{bmatrix}.$$

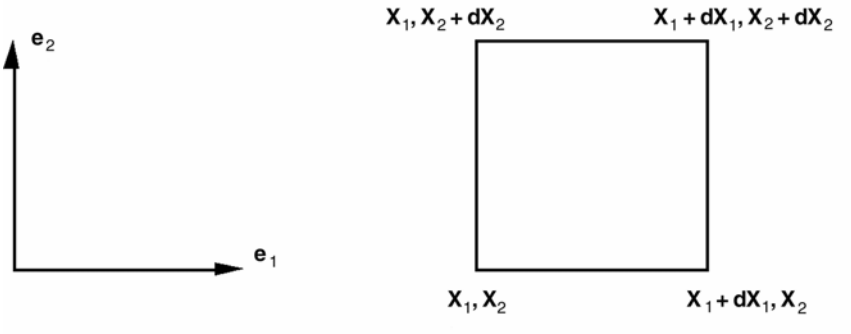



**Figure 4.10**. An illustration for Problem 4.4.1.

## 4.5. THE CONSERVATION OF ENERGY

The idea of energy and its balance or conservation is central in science, yet *energy* is not considered to be a precisely defined term. A precise definition would imply that all types of energy are known, and we do not think that they are. In this regard, review the quote from Herbert Callen at the beginning of the chapter. Some energies, such as kinetic energy, are well known and readily identified in any given situation. It is possible to define energy as any member of the set consisting of all energies which are recognized by science, energies such as heat energy, kinetic energy, atomic energy, chemical energy, electromagnetic energy, etc. As science identifies each new energy, it would become a member of this set of energies.

The conservation of energy is therefore viewed here more as a basic method of science rather than as a basic fact in the sense that the charge of an electron is a scientific fact. The conservation of energy is viewed here as a method of checking energetic interactions and discovering new energies. Whenever one approaches a new scientific problem, one tries to select or invent energies such that, by setting their sum equal to a constant, some aspect of the physical phenomenon is correctly described.

In the continuum theories, the known energies will include kinetic energy, heat energy, chemical energy, electromagnetic energy, and so forth. The *total energy E* of a system consists of the sum of all the energies we choose to recognize or define and the remainder of the total energy of a system is said to be the *internal energy U* of the system. That is to say, all the energies that are not singled out and explicitly defined are placed in the category of internal energy. The total energy $E$ of an object consists of a kinetic energy,

$$K = \frac{1}{2}\int_0 \rho(\mathbf{v}\cdot\mathbf{v})dv\,, \tag{4.40}$$

and an internal energy $U$,

$$E = K + U, \tag{4.41}$$

where $U$ consists of all energies except kinetic.

The principle of conservation of energy is the statement that the total energy of an object is constant. It is more convenient to reformulate the conservation of energy as a balance of rates: the rate of increase of the total energy of an object is equal to the rate of energy flux into the object. The flux of energy into an object occurs in two ways, first through the mechanical power $P$ of the surface tractions and action-at-a-distance forces and second through a direct flow of heat $Q$ into the object. With these definitions and conventions established, the conservation of energy may be written in the form

$$P + Q = \dot{K} + \dot{U} = \dot{E}\ , \tag{4.42}$$

where $P + Q$ is the rate of energy supply. Equation (4.42) is a global statement of energy conservation, and we will need a point form of the principle in continuum mechanics applications. In the point form representation all the variables will be intensive in the conventional thermodynamic use of that word. In thermodynamics an extensive variable is a variable that is additive over the system, e.g., volume or mass, and an intensive variable is a variable that is not additive over the system, e.g., pressure or temperature. To understand these definitions, consider adding together two identical masses occupying the same volume at the same temperature and pressure. When two masses have been added together the resulting system has double the volume and double the mass, but it still has the same temperature and pressure. Extensive variables can be made into intensive variables by dividing them by the density of the particle. Thus, density or specific volume (the reciprocal of density) is the intensive variable associated with the normally extensive variable mass. The internal energy $U$, an extensive variable, is represented in terms of the specific internal energy $\varepsilon$, an intensive variable, by the following volume integral

$$U = \int_0 \rho\, \varepsilon\, dv\ . \tag{4.43}$$

Integral representations of the mechanical power $P$ and the non-mechanical or heat power $Q$ supplied to an object $O$ are necessary in order to convert the global form of the energy conservation principle (4.42) to a point form. Heat is transferred into the object at a rate $-\mathbf{q}$ per unit area; the vector $\mathbf{q}$ is called the heat flux vector. The negative sign is associated with $\mathbf{q}$ because of the longstanding tradition in thermodynamics that heat coming out of a system is positive while heat going into a system is negative. The internal sources of heat such as chemical reactions and radiation are represented by the scalar field $r$ per unit mass. Using these representations the total non-mechanical power supplied to an object may be written as the sum of a surface integral and a volume integral:

$$Q = -\int_{\partial 0} \mathbf{q}\cdot\mathbf{n}\, da + \int_0 \rho r\, dv\ . \tag{4.44}$$

This integral representation for the heat supplied to the object distinguishes between the two possible sources of heat, the internal and the external. Applying the divergence theorem (A153) to the surface integral in (4.44), it is easy to see that $Q$ may also be represented by the volume integral

$$Q = \int_0 (\rho r - \nabla\cdot\mathbf{q})\, dv\ . \tag{4.45}$$

The mechanical power $P$ delivered to the object is represented in integral form by

$$P = \int_{\partial 0} \mathbf{t} \cdot \mathbf{v} da + \int_0 \rho \mathbf{d} \cdot \mathbf{v} dv \,, \tag{4.46}$$

where $\mathbf{t}$ is the surface traction acting on the surface of the object $O$, $\mathbf{d}$ is the action-at-a-distance force, and $\mathbf{v}$ is the velocity vector. The terms $\mathbf{t}\cdot\mathbf{v}da$ and $\rho\mathbf{d}\cdot\mathbf{v}dv$ both represent the rate at which mechanical work is done on the object, $\mathbf{t}\cdot\mathbf{v}da$ is the rate of work of surface forces and $\rho\mathbf{d}\cdot\mathbf{v}dv$ is the rate of work of action-at-a-distance forces. Substitution of (4.15b), $\mathbf{t} = \mathbf{T}\cdot\mathbf{n}$, into (4.46) and subsequent application of the divergence theorem (A153) to the surface integral in the resulting expression yields

$$P = \int_0 \{\nabla \cdot (\mathbf{T} \cdot \mathbf{v}) + \rho \mathbf{d} \cdot \mathbf{v}\} dv = \int_0 \{((\nabla \cdot \mathbf{T}) \cdot \mathbf{v}) + \mathbf{T} : (\nabla \otimes \mathbf{v}) + \rho \mathbf{d} \cdot \mathbf{v}\} dv \,,$$

or

$$P = \int_0 \{(\nabla \cdot \mathbf{T} + \rho \mathbf{d}) \cdot \mathbf{v} + \mathbf{T} : \mathbf{L}\} dv \,, \tag{4.47}$$

where $\mathbf{L}$ is the tensor of velocity gradients defined by (3.31). This result may be further reduced by using the stress equations of motion (4.37) to replace $\boldsymbol{\nabla}\cdot\mathbf{T} + \rho\mathbf{d}$ by $\rho\dot{\mathbf{v}}$ ; thus,

$$P = \int_0 \{\rho \dot{\mathbf{v}} \cdot \mathbf{v} + \mathbf{T} : \mathbf{L}\} dv \,. \tag{4.48}$$

Two more manipulations of this expression for $P$ will be performed. First, recall from (3.31) that $\mathbf{L} = [\nabla \otimes \mathbf{v}]^T$ , and from (3.32) that $\mathbf{L}$ is decomposed into a symmetric part $\mathbf{D}$ and a skew-symmetric part $\mathbf{W}$ by $\mathbf{L} = \mathbf{D} + \mathbf{W}$. It follows then that

$$\mathbf{T:L} = \mathbf{T:D} + \mathbf{T:W}, \tag{4.49}$$

but $\mathbf{T:W}$ is zero because $\mathbf{T}$ is symmetric by (4.36) and $\mathbf{W}$ is skew-symmetric, hence $\mathbf{T:L} = \mathbf{T:D}$. The second manipulation of (4.48) is to observe that the first integral in (4.48) is the material time rate of change of the kinetic energy $K$ defined by (4.40). To see that the first term in the integral of (4.48) is $\dot{K}$ , apply (4.8) to (4.40). With these two changes, the integral expression for $P$ (4.48) now has the form

$$P = \dot{K} + \int_0 \mathbf{T} : \mathbf{D} dv \,, \tag{4.50}$$

since, from (4.40),

$$\dot{K} = \int_0 \rho(\mathbf{v} \cdot \dot{\mathbf{v}}) dv \,.$$

Formula (4.50) shows that the total mechanical power supplied to the object is equal to the time rate of change of kinetic energy plus an integral representing power involved in deforming the object.

The point form statement of the principle of energy conservation will now be obtained by placing the integral representations for $U$, $Q$, and $P$, eqs. (4.43), (4.45), and (4.50), respectively, into the global statement (4.42), thus

$$\int_0 \{\mathbf{T} : \mathbf{D} + \rho r - \nabla \cdot \mathbf{q} - \rho \dot{\varepsilon}\} dv \,. \tag{4.51}$$

Now, for the last time in this chapter, the argument employed in the transition from (4.4) to (4.5) is employed (see the discussion following (4.5)); thus, the integrand of (4.51) must be zero everywhere in the object $O$:

$$\rho \dot{\varepsilon} = \mathbf{T} : \mathbf{D} + \rho r - \nabla \cdot \mathbf{q} \,. \tag{4.52}$$

This is the desired point form of the principle of energy conservation. It states that the time rate of change of the specific internal energy $\varepsilon$ multiplied by the density $\rho$ is equal to the sum of the stress power, the negative of the divergence of the heat flux, and the internal heat supply term.

Before leaving these considerations of energy, a formula for the quasi-static work done during loading of an object will be obtained. The mechanical power $P$ delivered to the object, (4.46), is the rate of work. The desired new formula relates to the work done rather than to the rate of doing work or power. A formula identical to formula (4.46) for the rate of work, in every regard except that the velocity is replaced by the displacement, is employed; thus,

$$W = \int_{\partial 0} \mathbf{t} \cdot \mathbf{u} da + \int_0 \rho \mathbf{d} \cdot \mathbf{u} dv \,. \tag{4.53}$$

$W$ is the mechanical work delivered to the object in a quasi-static loading, $\mathbf{t}$ is the surface traction acting on the surface of the object $O$, $\mathbf{d}$ is the action-at-a-distance force, and $\mathbf{u}$ is the displacement vector. The terms $\mathbf{t}\cdot\mathbf{u}da$ and $\rho\mathbf{d}\cdot\mathbf{u}dv$ both represent the mechanical work done on the object, $\mathbf{t}\cdot\mathbf{u}da$ is the work of surface forces, and $\rho\mathbf{d}\cdot\mathbf{u}dv$ is the work of action-at-a-distance forces. Substitution of (4.15b), $\mathbf{t} = \mathbf{T}\mathbf{n}$, into (4.53) and subsequent application of the divergence theorem (A153) to the surface integral in the resulting expression yields

$$W = \int_0 \{\nabla \cdot (\mathbf{T} \cdot \mathbf{u}) + \rho \mathbf{d} \cdot \mathbf{u}\} dv = \int_0 \{((\nabla \cdot \mathbf{T}) \cdot \mathbf{u}) + \mathbf{T} : (\nabla \otimes \mathbf{u}) + \rho \mathbf{d} \cdot \mathbf{u}\} dv \,,$$

or

$$W = \int_0 \{(\nabla \cdot \mathbf{T} + \rho \mathbf{d}) \cdot \mathbf{u} + \mathbf{T} : (\nabla \otimes \mathbf{u})\} dv \,. \tag{4.54}$$

This result may be further reduced by using the stress equations of motion (4.37) in the case when $\dot{\mathbf{v}} = 0$ to replace $\boldsymbol{\nabla}\cdot\mathbf{T} + \rho\mathbf{d}$ by 0, thus

$$W = \int_0 \mathbf{T} : (\nabla \otimes \mathbf{u}) dv \,. \tag{4.55}$$

Recall from (3.41) that $(\boldsymbol{\nabla}\otimes\mathbf{u})^T$ may be decomposed into a symmetric part $\mathbf{E}$ and a skew-symmetric part $\mathbf{Y}$ by $(\boldsymbol{\nabla}\otimes\mathbf{u})^T = \mathbf{E} + \mathbf{Y}$. It follows then that

$$\mathbf{T}:(\boldsymbol{\nabla}\otimes\mathbf{u}) = \mathbf{T}:\mathbf{E} + \mathbf{T}:\mathbf{Y}, \tag{4.56}$$

but $\mathbf{T}:\mathbf{Y}$ is zero because $\mathbf{T}$ is symmetric by (4.36) and $\mathbf{Y}$ is skew-symmetric; hence, $\mathbf{T}:(\boldsymbol{\nabla}\otimes\mathbf{u}) = \mathbf{T}:\mathbf{E}$. The work done on the object is then given by

$$W = \int_0 \mathbf{T} : \mathbf{E} dv \,. \tag{4.57}$$

This means that the local work done is **T:E**. This result will be of interest in the consideration of elastic objects.

**Problem**

4.5.1. In terms of the concepts introduced in this section, how would one specify a system that was functioning adiabatically globally but not locally? How would one specify a system that was adiabatic locally or point-wise? If a system is adiabatic locally, what type of energy is the mechanical work done on the object transferred into? If the system is not adiabatic and if the system's internal energy does not change as mechanical work is done on the system, into what type of energy is the mechanical work then converted?

## 4.6. REFERENCES

Callen HB. 1960. *Thermodynamics*. New York: Wiley.

Truesdell CA, Toupin RA. 1960. *The classical field theories*. In *Handbuch der Physik*, II/1, pp. 226–859. Ed S Flugge. Berlin: Springer Verlag.

# 5

# MODELING MATERIAL SYMMETRY

"A study of the symmetry of three-dimensional spaces is of great theoretical and practical significance, because symmetrical spaces include crystals (from which, of course, the majority of solids are formed), and all homogeneous fields without exception: electric, magnetic, gravitational, etc. A study of the structures of crystals is unthinkable without a knowledge of the laws governing symmetry of three-dimensional spaces" (from Shubnikov and Koptsik, 1974).

## 5.1. INTRODUCTION

The variation of material properties with respect to direction at a fixed point in a material is called *material symmetry*. If the material properties are the same in all directions, the properties are said to be *isotropic*. If the material properties are not isotropic, they are said to be *anisotropic*. The type of material anisotropy generally depends upon the size of the representative volume element (RVE). The RVE is a key concept in modeling material microstructure for inclusion in a continuum model. An RVE for a volume surrounding a point in a material is a statistically homogeneous representative of the material in the neighborhood of the point. The RVE concept, described briefly in the following section, is employed in this chapter, which addresses the modeling of material symmetry and, more extensively, in Chapter 8, which addresses the modeling of material microstructure.

The tensors that appear in linear transformations, for example, $\mathbf{A}$ in the three-dimensional linear transformation $\mathbf{r} = \mathbf{A} \cdot \mathbf{t}$, (A39), and $\hat{\mathbf{C}}$ in the six-dimensional linear transformation $\hat{\mathbf{T}} = \hat{\mathbf{C}} \cdot \hat{\mathbf{J}}$, (A160), often represent anisotropic material properties. Several examples of these linear transformations as constitutive equations will be developed in the next chapter. The purpose of this chapter is to present and record representations of $\mathbf{A}$ and $\hat{\mathbf{C}}$ that represent the effects of material symmetry. These results are recorded in Tables 5.3 and 5.4 for $\mathbf{A}$ and $\hat{\mathbf{C}}$, respectively. In these tables the forms of $\mathbf{A}$ and $\hat{\mathbf{C}}$ are given for all eight symmetries. Some background material is provided before the derivation of representations. First, there is a discussion of crystalline and textured materials in §5.3. Next the only symmetry operation considered here, the plane of mirror symmetry, is introduced in §5.4, and the symmetries of interest are defined in terms of mirror symmetry planes in §5.5. The symmetry representations for the forms of $\mathbf{A}$ and $\hat{\mathbf{C}}$ associated with the symmetries of interest are then obtained in §§5.6 and 5.7.

The primary interest here is only in about half of the eight material symmetries admitted by the tensor $\hat{\mathbf{C}}$ ; however, all of them are described for completeness (and because being complete requires little space). The eight material symmetries admitted by the tensor $\hat{\mathbf{C}}$ are triclinic, monoclinic, trigonal, tetragonal, orthotropic, transversely isotropic (or hexagonal), cubic, and isotropic symmetry. The main interest will be in the orthotropic, transversely isotropic, and isotropic symmetries with lesser interest in the triclinic, monoclinic, and trigonal symmetries.

Curvilinear and rectilinear anisotropy are described and compared in §5.8. The representation of the symmetry of a material with chirality (handedness) is considered in §5.9. The continuum modeling of material microstructures with vectors and tensors is described in §5.10, and §5.11 is a short guide to the literature on the subject matter of this chapter.

## 5.2. THE REPRESENTATIVE VOLUME ELEMENT (RVE)

The RVE is a very important conceptual tool for forming continuum models of materials and for establishing restrictions that might be necessary for a continuum model to be applicable. An RVE for a continuum particle $\mathbf{X}$ is a statistically homogeneous representative of the material in the neighborhood of $\mathbf{X}$, that is to say, a material volume surrounding $\mathbf{X}$. For purposes of this discussion, the RVE is taken to be a cube of side length $L_{\text{RVE}}$; it could be any shape, but it is necessary that it have a characteristic length scale. An RVE is shown in Figure 5.1; it is a homogenized or average image of a real material volume. Since the RVE image of the material object $O$ averages over the small holes and heterogeneous microstructures, overall it replaces a discontinuous real material object by a smooth continuum model $O$ of the object. The RVE for the representation of a domain of a porous medium by a continuum point is shown in Figure 5.2. The RVE is necessary in continuum models for all materials; the main question is how large must the length scale $L_{\text{RVE}}$ be to obtain a reasonable continuum model. The smaller the value of $L_{\text{RVE}}$ the better; in general, the value of $L_{\text{RVE}}$ should be much less than the characteristic

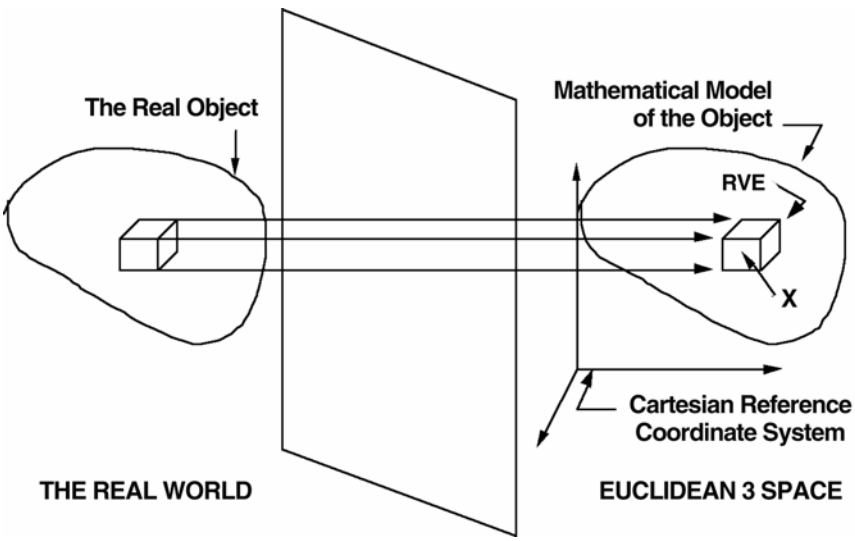



**Figure 5.1**. Image of a representative volume element (RVE).

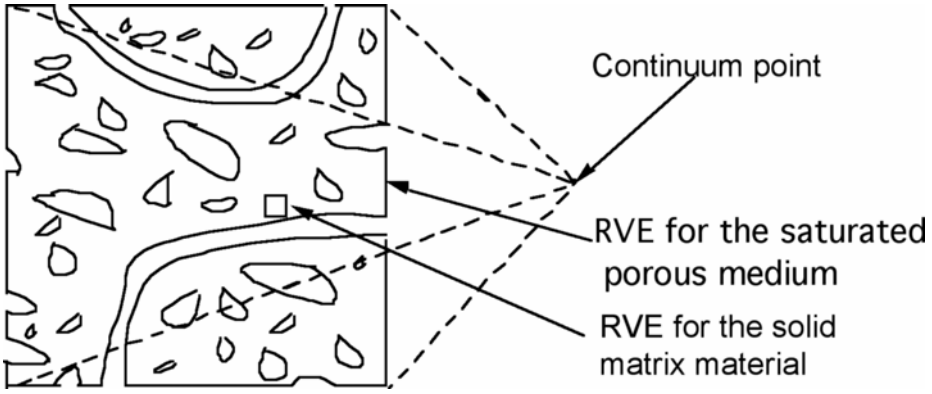



**Figure 5.2**. RVE for representation of a domain of a porous medium by a continuum point. Modified with permission from Cowin (1999).

dimension $L_P$ of the problem being modeled. On the other hand, $L_{\text{RVE}}$ should be much larger than the largest characteristic microstructural dimension, $L_M$, of the biological material being modeled; thus, $L_P >> L_{\text{RVE}} >> L_M$. In bone, for example, this can be a significant problem because there are some small bones and bone tissue has large microstructures. A human bone has a cortical thickness of, say, 2 cm while a typical bone tissue microstructure, the osteon, is about 200–350 microns in diameter (0.2 –0.3 millimeters) and the thickness of the cortex of some bones is on the order of two millimeters; thus, $L_P \approx 2$ cm and $L_M \approx 0.2$ mm = 0.02 cm; thus, 2 cm >> $L_{\text{RVE}}$ >> 0.02 cm for a typical stress analysis problem of a bone. For low-carbon structural steel the bounds on $L_{\text{RVE}}$ are much less restrictive, the characteristic size of the problem is greater, and the characteristic size of the material microstructure is much less. For many applications the bounds on $L_{\text{RVE}}$ are not seriously restrictive, although this is not generally the case with nanomechanical and biological problems. Both in biology and in nanomechanics there are structures that have a significant size range and the modeler must adjust the value of $L_{\text{RVE}}$ to the size range of the objects modeled. For example, in biomechanics, continuum models are often made of organs as well as of biological membranes. In the case of the membrane $L_{\text{RVE}}$ may be less than 0.01 nm, while in the case of the organ $L_{\text{RVE}}$ may be on the order of 0.01 mm or larger. The concept of stress is employed in both cases, with the modeler keeping in mind that the two $L_{\text{RVE}}$'s differ by a factor of 1,000,000. The concept of $L_{\text{RVE}}$ may, in this way, be used to justify the application of the concept of stress at different structural levels. The modeler usually does not write down the value of $L_{\text{RVE}}$ in a problem under consideration, hence it is a "hidden" parameter in many applications of continuum models.

The selection of different-sized RVEs is illustrated in Figure 5.2. A small RVE will just contain the solid matrix material while a much larger RVE will average over both the pores and the solid matrix. As another illustration of these different RVE sizes relative to a real material, consider a cross-section of trabecular bone shown in Figure 5.3. The white regions are the bone trabeculae and the darker regions are the pore spaces that are in vivo filled with marrow in the bone of young animals. First consider the small rectangular white region in the lower left quadrant as the first RVE for homogenization. This small rectangular white region is entirely within the trabecular bone domain and thus the properties will be those of trabecular bone. On the other hand, if the small RVE in the darker marrow region is entirely within the bone marrow domain, the properties will be those of the marrow. If the RVE or homogenization domain is taken to be one of the larger rectangles in Figure 5.3, the properties of the RVE

will reflect the properties of both the bone and the marrow, and their values will lie in between these two limits and be proportional to the ratio of the volume of marrow voids to the volume of bone in each rectangle.

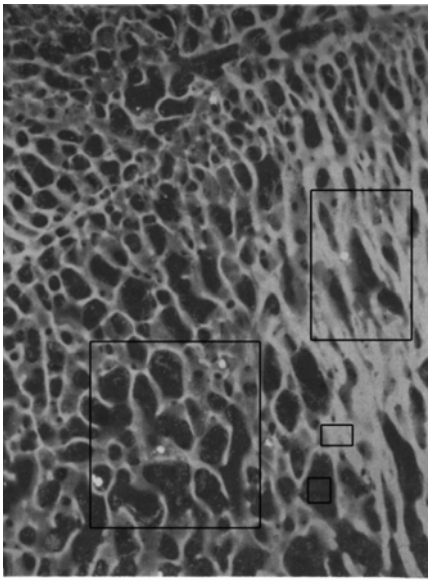


**Figure 5.3**. Illustration of a cross-section of trabecular bone. The whiter regions are the bone trabeculae and the darker regions the spaces occupied by the marrow in the bones of young animals. Rectangular regions represent various RVEs discussed in the text. Adapted with permission from Cowin and Mehrabadi (1989).

## 5.3. CRYSTALLINE MATERIALS AND TEXTURED MATERIALS

The difference between the crystalline materials and the textural materials is the difference between the types of force systems that determine the two different types of symmetry. Crystallographic symmetries are determined by the internal force systems that hold the material together in its solid form. These are force systems between atoms or molecules. The crystalline symmetry is determined by the lines of action of the forces in the force systems that structure the crystal. On the other hand, the symmetry of textured materials is determined mainly by external, rather than internal, force systems. For example, it is well known that geological materials have material symmetries associated with the stress state experienced by the material during its formative state. Sedimentary deposits are generally organized by the direction of gravity at the time of their formation. Similarly, the material symmetry of structural steel may be determined by the external force systems associated with its method of manufacture (extrusion, rolling, etc.) and not by the fact that it is composed of ferric polycrystals. Manmade composites are generally designed to survive in specific stress states and therefore can generally be considered as having a material symmetry designed for the external force systems they will experience. Plant and animal tissue are known to functionally adapt their local material structure to external loads. In each of these examples the macroscopic material symmetry of the textured material is determined by external force systems, even though at the microscopic level some constituents may have crystalline symmetries determined by internal force systems, as is the case with structural steel and bone tissue.

Crystals have the most clearly defined symmetries of all naturally occurring materials. In crystallography an ideal crystal is defined in terms of a lattice. A *lattice* is an infinite array of evenly spaced points that are all similarly situated. Points are regarded as "similarly situated" if the rest of the lattice appears the same and in the same orientation when viewed from them. An *ideal crystal* is then defined to be an object in which the points, or atoms, are arranged in a lattice. This means that the atomic arrangement appears the same and in the same orientation when viewed from all lattice points, and that the atomic arrangement viewed from any point that is not a lattice point is different from the atomic arrangement viewed from a lattice point. The form and orientation of the lattice are independent of the particular point in the crystal chosen as origin. An ideal crystal is infinite in extent. Real crystals are not only bounded but also depart from an ideal crystal by possessing imperfections. Crystals are held together by forces that act on the lines connecting the lattice points. The force systems that hold a crystal together and give it shape and form are internal force systems.

Most large samples of natural materials are not crystals. They are either not crystalline at all or are polycrystalline. Polycrystalline materials are composed of small randomly oriented crystalline regions separated by grain boundaries. The material symmetry of these materials is not determined by the crystal structure of their chemical components but by other factors. These factors include optional design for manmade composite materials, growth patterns and natural selection forces for biological materials, method of formation for geological materials, and method of manufacture for many manufactured materials. These factors are discussed in the following paragraphs. The selection of material symmetry for a model of a material depends upon the intended application of the model. For example, a common application of elasticity theory is to steels employed in large objects for structures. In this application steels are conventionally treated as materials with isotropic symmetry.

The basis for the isotropic symmetry selection is an RVE of a certain practical size that averages over many grains of the microstructure. Although each crystalline grain is oriented, their orientation is random and their average has no orientation; hence for a large enough RVE the material is isotropic. However, if the application of the model is to study the interaction between the crystalline grains, a much smaller RVE will be selected. If the RVE selected is entirely within a single crystalline grain, then this RVE selection would imply cubic material symmetry since ferrous materials are characterized by cubic symmetries. It follows that the selection of different-size RVEs can imply different material symmetries. The selection of a particular size RVE is at the discretion of the person making the model, and that selection should be determined by the model's intended use.

Manmade composite materials are often designed to be anisotropic because their intended use is to carry a particular type of loading that requires stiffness and strength in one direction more than in others. While many materials might have the stiffness and strength required, a composite material may have a lesser weight. A unidirectional fiber-reinforced lamina of a composite is illustrated in the top panel of Figure 5.4. The directions of the fibers in alternate layers can be crossed to obtain a laminar composite such as that shown in the remaining panels of Figure 5.4. It is possible to form cylinders and spheres from these laminae. Wood is a natural composite composed of cylindrical layers associated with each year's growth. These growth rings are illustrated in Figure 5.5. In Figure 5.6 there is an illustration of the microstructure of a biological material, a three-dimensional view of a nasturtium petiole. In each of these illustrations it is possible to see how the microstructure of the material will give the material a distinctive anisotropy. Such materials are often called natural composite materials. Bone tissue, bamboo, teeth, and muscles are other examples. These materials evolve their particular microstructures in response to the environmental forces of natural selection.

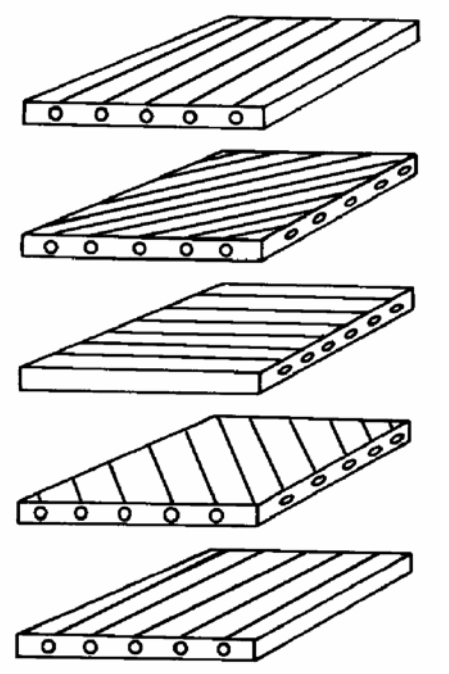


**Figure 5.4**. Layers of fibers alternated to obtain a laminar composite.

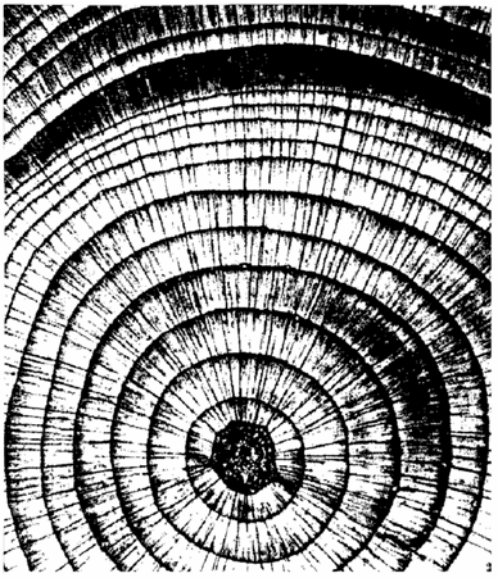


**Figure 5.5**. Cylindrical layers associated with each year's growth in wood; note the curvilinear orthotropic symmetry.

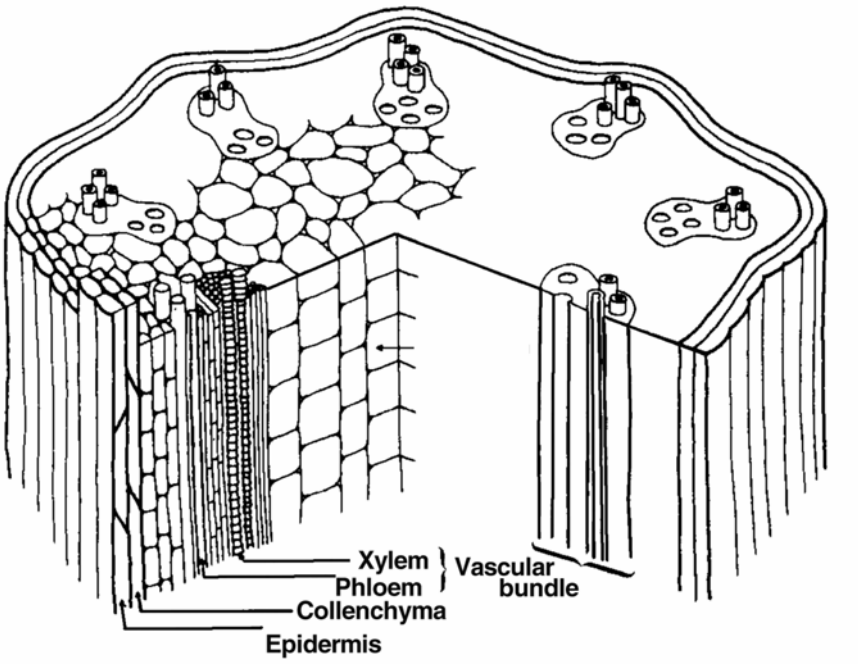



**Figure 5.6**. A three-dimensional view of a nasturtium petiole; note the curvilinear orthotropic symmetry. Reprinted with permission from Wainwright et al. (1976).

The method of formation of geological materials generally provides them with a definitive layering that makes them anisotropic. The layered structure is easily seen to be analogous to a layered composite. The deposition of layers is influenced by particle size, because different-size particles fall through liquids at different rates. Gravity is the force that gives geological sediments their initial layering. Plate tectonic forces then push these layers in directions other than that in which they were formed, which is why the layers are often viewed in situations where the normal to the plane of the layer is not the direction of gravity.

Macrocomposite manmade materials such as reinforced concrete beams, skis, and helicopter blades are easily seen to be elastically anisotropic. These materials are designed to be anisotropic. In the process of deformation or in the manufacturing process, anisotropy is induced in a material. Anisotropy is also induced in geological and biological materials by deformation. The manufacture of steel by extrusion or rolling induces anisotropy in the steel product as illustrated in Figure 5.7. Illustrated in Figure 5.8 is the anisotropy induced by deformation. The illustration in this figure might represent the fiber deformation in a fibrous composite manufacturing process. However, it could also represent deformation of the collagen fibers in the deformation of a soft tissue.

For non-crystalline materials there are only three material symmetries traditionally considered — orthotropy, transverse isotropy, and isotropy. However, the forms of $\hat{\mathbf{C}}$ for orthotropy and transverse isotropy are the same as the forms of $\hat{\mathbf{C}}$ for the rhombic and hexagonal crystal systems, respectively. Hence when the crystalline and the traditional non-crystalline elastic material symmetries are combined there are only eight distinct forms of $\hat{\mathbf{C}}$, one for each of the seven crystal systems and isotropy.

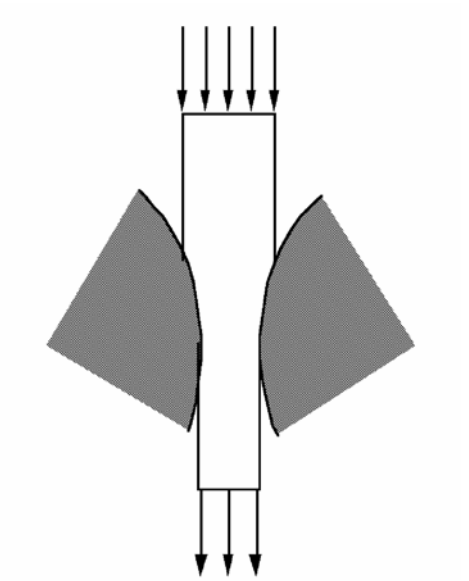


**Figure 5.7**. Extrusion or rolling induces anisotropy in a steel product.

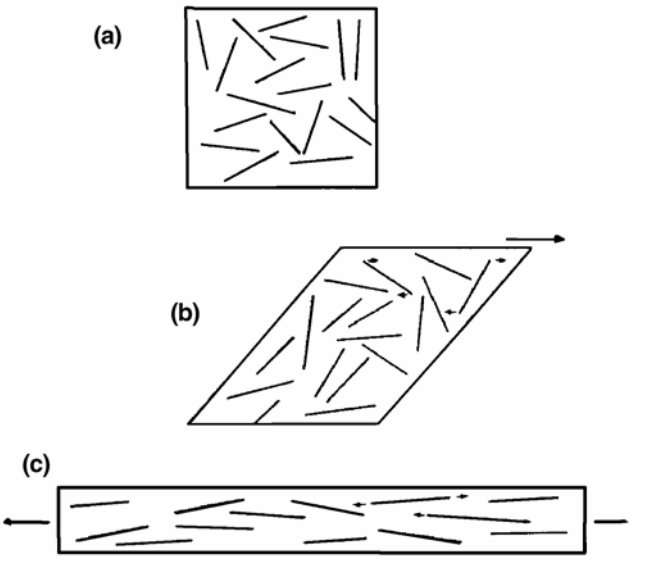



**Figure 5.8**. Material anisotropy induced by deformation. Reprinted with permission from Hull (1981).

## 5.4. PLANES OF MIRROR SYMMETRY

Symmetry elements are operations used in the analysis of symmetry. The principal symmetry element of interest here is the plane of mirror or reflective symmetry. We begin with a discussion of congruence and mirror symmetry. Two objects are geometrically congruent if they can be superposed upon one another so that they coincide. The two tetrahedra at the top of Figure 5.9 are congruent. Congruence of two shapes is a necessary but not sufficient condition for mirror symmetry. A pair of congruent geometric objects is said to have mirror symmetry with respect to a plane if for each point of either object there is a point of the other object such that the pair of points is symmetric with respect to the plane. The two congruent tetrahedra at the bottom of Figure 5.9 have the special relationship of mirror symmetry with respect to the plane whose end view is indicated by an m. Each congruent geometric object is said to be the reflection of the other. The relationship between the two objects with respect to the symmetry plane is said to be *achiral* (i.e., the objects are mirror images). If the objects are not reflections of one another they are said to be *chiral*. The plane with respect to which two objects have mirror symmetry is called their *plane of reflective symmetry* . A material is said to have a *plane of reflective symmetry* or a *mirror plane* at a point in the material if the structure of the material has mirror symmetry with respect to a plane passing through the point.

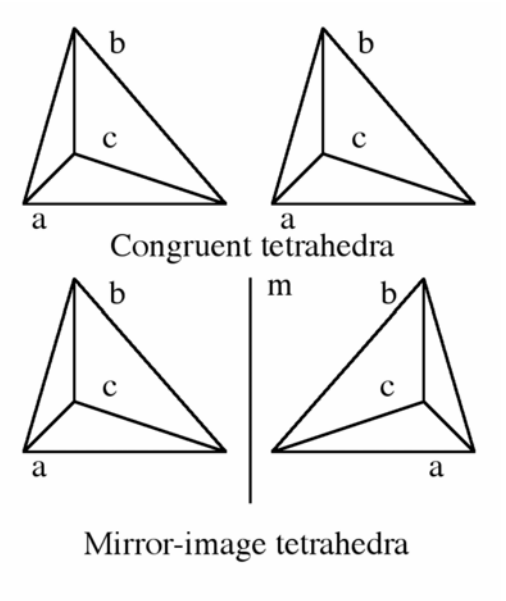



**Figure 5.9**. Illustrations of mirror symmetry.

In the following three sections the concept of a plane of reflective symmetry will now be used to classify the various types of anisotropy possible in the 3D and 6D symmetric linear transformations, the $\mathbf{A}$ in the three-dimensional linear transformation $\mathbf{r} = \mathbf{A} \cdot \mathbf{t}$ (A39), and $\hat{\mathbf{C}}$ in the six-dimensional linear transformation $\hat{\mathbf{T}} = \hat{\mathbf{C}} \cdot \hat{\mathbf{J}}$ (A160). Recall that matrices $\mathbf{A}$ and $\hat{\mathbf{C}}$ transform according to rules (A83) and (A162), respectively, when the coordinate system is changed. In order to apply the restrictions of reflective symmetry to (A162), it is necessary to have a representation for a plane of reflective symmetry for orthogonal transformations $\mathbf{Q}$ and $\hat{\mathbf{Q}}$ . In order to construct such representations, let $\mathbf{a}$ be a unit vector representing the normal

to a plane of reflective symmetry and let **b** be any vector perpendicular to **a**; then **a**·**b** = **0** for all **b**. An orthogonal transformation with the properties

$$\mathbf{R}^{(\mathbf{a})}\cdot\mathbf{a}=-\mathbf{a}\,,\quad \mathbf{R}^{(\mathbf{a})}\cdot\mathbf{b}=\mathbf{b} \tag{5.1}$$

represents a plane of reflective, or mirror, symmetry. Transformation (5.1) carries every vector parallel to vector **a**, the normal to the plane of mirror symmetry, into direction **–a,** and it carries every vector **b** parallel to the plane into itself. The orthogonal transformation with the property (5.1) is given by

$$\mathbf{R}^{(\mathbf{a})}=\mathbf{1}-2\mathbf{a}\otimes\mathbf{a}\,,\quad \left(R_{ij}^{(\mathbf{a})}=\delta_{ij}-2a_ia_j\right), \tag{5.2}$$

as may be verified directly. The reflective transformation in six dimensions, denoted $\hat{\mathbf{R}}^{(\mathbf{a})}$, is constructed from $\mathbf{R}^{(\mathbf{a})}$ using (A142), and thus

$$\hat{\mathbf{R}}^{(\mathbf{a})}=2\sqrt{2}\begin{bmatrix}
\frac{(1-2a_1^2)^2}{2\sqrt{2}} & \frac{2a_1^2a_2^2}{2\sqrt{2}} & \frac{2a_1^2a_3^2}{2\sqrt{2}} & 2a_1^2a_2a_3 & a_1a_3(2a_1^2-1) & a_1a_2(2a_1^2-1)\\
\frac{2a_1^2a_2^2}{2\sqrt{2}} & \frac{(1-2a_2^2)^2}{2\sqrt{2}} & \frac{2a_2^2a_3^2}{2\sqrt{2}} & a_2a_3(2a_2^2-1) & 2a_1a_2^2a_3 & a_1a_2(2a_2^2-1)\\
\frac{2a_1^2a_3^2}{2\sqrt{2}} & \frac{2a_2^2a_3^2}{2\sqrt{2}} & \frac{(1-2a_3^2)^2}{2\sqrt{2}} & a_2a_3(2a_3^2-1) & a_1a_3(2a_3^2-1) & 2a_1a_2a_3^2\\
2a_1^2a_2a_3 & a_2a_3(2a_2^2-1) & a_2a_3(2a_3^2-1) & \frac{2a_1^2+8a_2^2a_3^2-1}{2\sqrt{2}} & \frac{2a_1a_2(4a_3^2-1)}{2\sqrt{2}} & \frac{2a_1a_3(4a_2^2-1)}{2\sqrt{2}}\\
a_1a_3(2a_1^2-1) & 2a_1a_2^2a_3 & a_1a_3(2a_3^2-1) & \frac{2a_1a_2(4a_3^2-1)}{2\sqrt{2}} & \frac{2a_2^2+8a_1^2a_3^2-1}{2\sqrt{2}} & \frac{2a_2a_3(4a_1^2-1)}{2\sqrt{2}}\\
a_1a_2(2a_1^2-1) & a_1a_2(2a_2^2-1) & 2a_1a_2a_3^2 & \frac{2a_1a_3(4a_2^2-1)}{2\sqrt{2}} & \frac{2a_2a_3(4a_1^2-1)}{2\sqrt{2}} & \frac{2a_3^2+8a_2^2a_1^2-1}{2\sqrt{2}}
\end{bmatrix} \tag{5.3}$$

As an example of the application of result (5.3), the six-dimensional transformations corresponding to planes of mirror symmetry in the $\mathbf{e}_1$ and $\mathbf{e}_2$ directions,

$$\mathbf{R}^{(\mathbf{e}_1)}=\begin{bmatrix}-1&0&0\\0&1&0\\0&0&1\end{bmatrix},\quad \mathbf{R}^{(\mathbf{e}_2)}=\begin{bmatrix}1&0&0\\0&-1&0\\0&0&1\end{bmatrix}, \tag{5.4}$$

respectively, are given by

$$\hat{\mathbf{R}}^{(\mathbf{e}_1)}=\begin{bmatrix}1&0&0&0&0&0\\0&1&0&0&0&0\\0&0&1&0&0&0\\0&0&0&1&0&0\\0&0&0&0&-1&0\\0&0&0&0&0&-1\end{bmatrix},\quad \hat{\mathbf{R}}^{(\mathbf{e}_2)}=\begin{bmatrix}1&0&0&0&0&0\\0&1&0&0&0&0\\0&0&1&0&0&0\\0&0&0&-1&0&0\\0&0&0&0&1&0\\0&0&0&0&0&-1\end{bmatrix}, \tag{5.5}$$

respectively. Other examples are the cases when the normals to the plane of reflective symmetry are vectors in the $\mathbf{e}_1$, $\mathbf{e}_2$ plane, $\mathbf{a} = \cos\theta\,\mathbf{e}_1 + \sin\theta\,\mathbf{e}_2$, or the $\mathbf{e}_2$, $\mathbf{e}_3$ plane, $\mathbf{a} = \cos\theta\,\mathbf{e}_2 + \sin\theta\,\mathbf{e}_3$. In these cases $\mathbf{R}^{(\theta_{12})}$ and $\mathbf{R}^{(\theta_{23})}$ are given by

$$\mathbf{R}^{(\theta_{12})} = \begin{bmatrix} -\cos 2\theta & -\sin 2\theta & 0 \\ -\sin 2\theta & \cos 2\theta & 0 \\ 0 & 0 & 1 \end{bmatrix}, \quad \mathbf{R}^{(\theta_{23})} = \begin{bmatrix} 1 & 0 & 0 \\ 0 & -\cos 2\theta & -\sin 2\theta \\ 0 & -\sin 2\theta & \cos 2\theta \end{bmatrix}, \tag{5.6}$$

respectively, and $\hat{\mathbf{R}}^{(\theta_{12})}$ and $\hat{\mathbf{R}}^{(\theta_{23})}$ are given by

$$\begin{bmatrix} \cos^2 2\theta & \sin^2 2\theta & 0 & 0 & 0 & \sqrt{2}\sin 2\theta\cos 2\theta \\ \sin^2 2\theta & \cos^2 2\theta & 0 & 0 & 0 & -\sqrt{2}\sin 2\theta\cos 2\theta \\ 0 & 0 & 1 & 0 & 0 & 0 \\ 0 & 0 & 0 & \cos 2\theta & -\sin 2\theta & 0 \\ 0 & 0 & 0 & -\sin 2\theta & -\cos 2\theta & 0 \\ \sqrt{2}\sin 2\theta\cos 2\theta & -\sqrt{2}\sin 2\theta\cos 2\theta & 0 & 0 & 0 & \sin^2 2\theta - \cos^2 2\theta \end{bmatrix}$$

and

$$\begin{bmatrix} 1 & 0 & 0 & 0 & 0 & 0 \\ 0 & \cos^2 2\theta & \sin^2 2\theta & \sqrt{2}\sin 2\theta\cos 2\theta & 0 & 0 \\ 0 & \sin^2 2\theta & \cos^2 2\theta & -\sqrt{2}\sin 2\theta\cos 2\theta & 0 & 0 \\ 0 & \sqrt{2}\sin 2\theta\cos 2\theta & -\sqrt{2}\sin 2\theta\cos 2\theta & \sin^2 2\theta - \cos^2 2\theta & 0 & 0 \\ 0 & 0 & 0 & 0 & \cos 2\theta & -\sin 2\theta \\ 0 & 0 & 0 & 0 & -\sin 2\theta & -\cos 2\theta \end{bmatrix} \tag{5.7}$$

respectively. Formulas (5.1)–(5.7) provide the 3D and 6D orthogonal transformations for a plane of reflective symmetry. These mirror symmetry transformations will be used in §§ 5.6 and 5.7 to develop the representations in Tables 5.3 and 5.4 for matrices $\mathbf{A}$ and $\hat{\mathbf{C}}$, respectively, for the various material symmetries.

**Problems**

5.4.1. Verify that transformation (5.2), $\mathbf{R}^{(\mathbf{a})} = \mathbf{1} - 2\mathbf{a} \otimes \mathbf{a}$, retains the properties of (5.1), $\mathbf{R}^{(\mathbf{a})} \cdot \mathbf{a} = -\mathbf{a}$ and $\mathbf{R}^{(\mathbf{a})} \cdot \mathbf{b} = \mathbf{b}$, where $\mathbf{a} \cdot \mathbf{b} = \mathbf{0}$ for all $\mathbf{b}$.

5.4.2. Construct orthogonal transformations $\mathbf{R}^{(\mathbf{e}_3)}$ and $\hat{\mathbf{R}}^{(\mathbf{e}_3)}$, and then verify their orthogonality.

5.4.3. Construct orthogonal transformations $\mathbf{R}^{(\theta_{13})}$ and $\hat{\mathbf{R}}^{(\theta_{13})}$ associated with vector $\mathbf{a} = \cos\theta\,\mathbf{e}_1 + \sin\theta\,\mathbf{e}_3$, and verify their orthogonality.

5.4.4. Show that reflections $\mathbf{R}^{(\theta_{12})}$ and $\hat{\mathbf{R}}^{(\theta_{12})}$ when evaluated at $\theta = 0$ coincide with reflections $\mathbf{R}^{(\mathbf{e}_1)}$ and $\hat{\mathbf{R}}^{(\mathbf{e}_1)}$, and when evaluated at $\theta = \pi/2$ they coincide with reflections $\mathbf{R}^{(\mathbf{e}_2)}$ and $\hat{\mathbf{R}}^{(\mathbf{e}_2)}$.

5.4.5. Show that reflections $\mathbf{R}^{(\theta_{23})}$ and $\hat{\mathbf{R}}^{(\theta_{23})}$ when evaluated at $\theta = 0$ coincide with reflections $\mathbf{R}^{(\mathbf{e}_2)}$ and $\hat{\mathbf{R}}^{(\mathbf{e}_2)}$, and when evaluated at $\theta = \pi/2$ they coincide with reflections $\mathbf{R}^{(\mathbf{e}_3)}$ and $\hat{\mathbf{R}}^{(\mathbf{e}_3)}$.

5.4.6. Construct the three- and six-dimensional reflective transformations for each of four normal vectors: $\mathbf{k} = (1/2)(\mathbf{e}_1 + (\sqrt{3})\mathbf{e}_2)$, $\mathbf{p} = (1/2)(-\mathbf{e}_1 + (\sqrt{3})\mathbf{e}_2)$, $\mathbf{m} = (1/2)( (\sqrt{3})\mathbf{e}_1 + \mathbf{e}_2)$, and $\mathbf{n} = (1/2)( (\sqrt{3})\mathbf{e}_1 - \mathbf{e}_2)$. Show that the set of six vectors — $\mathbf{k}$, $\mathbf{p}$, $\mathbf{m}$, $\mathbf{n}$, $\mathbf{e}_1$, and $\mathbf{e}_2$ — forms a set that makes a pattern. The pattern is such that each vector of the set points in one of six different directions and makes angles that are each multiples of $\pi/6$ with the other vectors.

## 5.5. CHARACTERIZATION OF MATERIAL SYMMETRIES BY PLANES OF SYMMETRY

In this section the number and orientation of the planes of reflective symmetry possessed by each linear elastic material symmetry will be used to define it. These material symmetries include isotropic symmetry and the seven anisotropic symmetries — triclinic, monoclinic, trigonal, orthotropic, hexagonal (transverse isotropy), tetragonal, and cubic. These symmetries may be classified strictly on the basis of the number and orientation of their planes of mirror symmetry. Figure 5.10 illustrates the relationship between the various symmetries; it is organized so that the lesser symmetries are at the upper left and as one moves to the lower right one sees crystal systems with greater and greater symmetry. The number of planes of symmetry for each material symmetry is given in Table 5.1, and, relative to a selected reference coordinate

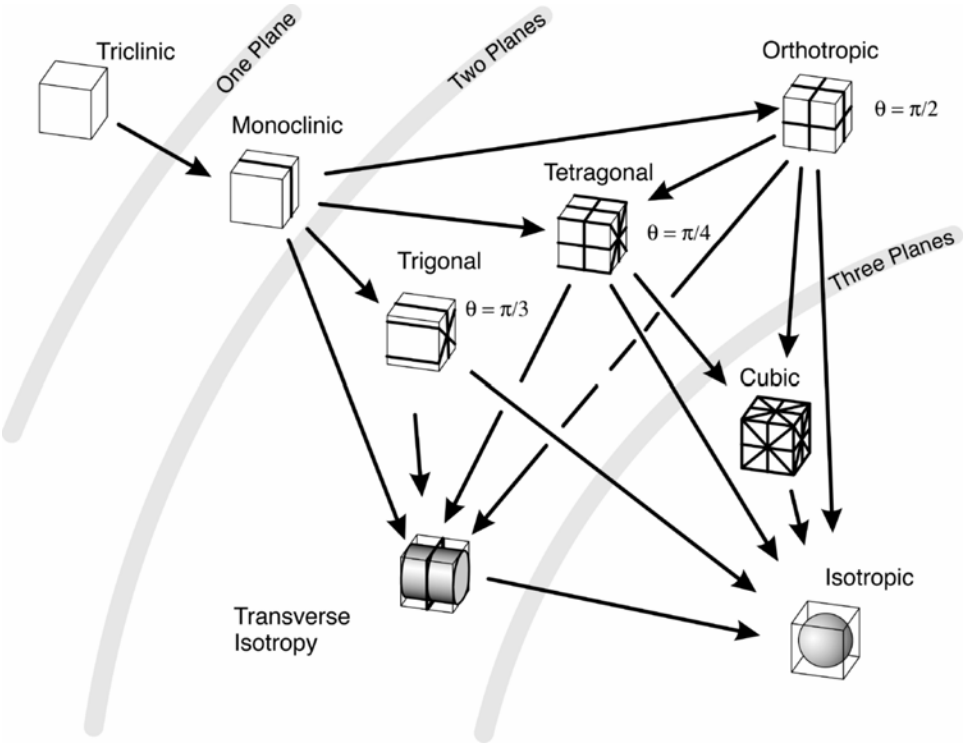



**Figure 5.10**. The hierarchical organization of the eight material symmetries of linear elasticity. This figure is organized so that the lower symmetries are at the upper left; as one moves down and across the table to the right one encounters crystal systems with greater and greater symmetry. Reprinted with permission from Chadwick et al. (2001).

**Table 5.1**. The Distinct Symmetries of Linear Anisotropic Elasticity

| Type of material symmetry | Number of planes of mirror symmetry | Number of planes of isotropy | Number of independent elastic coefficients |
|---|---|---|---|
| Triclinic | 0 | 0 | 18 (21) |
| Monoclinic | 1 | 0 | 12 (13) |
| Orthotropic or orthorhombic | 3 | 0 | 9 |
| Tetragonal | 5 | 0 | 6 (7) |
| Cubic | 9 | 0 | 3 |
| Trigonal | 3 | 0 | 6 (7) |
| Hexagonal | 7 | 0 | 5 |
| Transverse isotropy | $1 + \infty$ | 1 | 5 |
| Isotropy | $\infty^2$ | $\infty^2$ | 2 |

**Table 5.2**. Normals to the Planes of Symmetry of the Indicated Symmetry

| Type of material symmetry | Normals to the planes of symmetry of the indicated symmetry |
|---|---|
| Triclinic | none |
| Monoclinic | $\mathbf{e}_1$ |
| Orthotropic | $\mathbf{e}_1, \mathbf{e}_2, \mathbf{e}_3$ |
| Tetragonal | $\mathbf{e}_1, \mathbf{e}_2, \mathbf{e}_3, (1/\sqrt{2})(\mathbf{e}_1 + \mathbf{e}_2)$ and $(1/\sqrt{2})(\mathbf{e}_1 - \mathbf{e}_2)$ |
| Cubic | $\mathbf{e}_1, \mathbf{e}_2, \mathbf{e}_3, (1/\sqrt{2})(\mathbf{e}_1 + \mathbf{e}_2), (1/\sqrt{2})(\mathbf{e}_1 - \mathbf{e}_2), (1/\sqrt{2})(\mathbf{e}_1 + \mathbf{e}_3), (1/\sqrt{2})(\mathbf{e}_1 - \mathbf{e}_3), (1/\sqrt{2})(\mathbf{e}_2 + \mathbf{e}_3), (1/\sqrt{2})(\mathbf{e}_2 - \mathbf{e}_3)$ |
| Trigonal | $\mathbf{e}_1, (1/2)(\mathbf{e}_1 + \sqrt{3}\,\mathbf{e}_2)$ and $(1/2)(\mathbf{e}_1 - \sqrt{3}\,\mathbf{e}_2)$ |
| Hexagonal | $\mathbf{e}_1, \mathbf{e}_2, \mathbf{e}_3, (1/2)(\sqrt{3}\,\mathbf{e}_1 + \mathbf{e}_2), (1/2)(\sqrt{3}\,\mathbf{e}_1 - \mathbf{e}_2), (1/2)(\mathbf{e}_1 + \sqrt{3}\,\mathbf{e}_2)$ and $(1/2)(\mathbf{e}_1 - \sqrt{3}\,\mathbf{e}_2)$ |
| Transverse isotropy | $\mathbf{e}_3$ and any vector lying in the $\mathbf{e}_1$ , $\mathbf{e}_2$ plane |
| Isotropy | any vector |

system, the normals to the planes of symmetry for each material symmetry are specified in Table 5.2. *Triclinic symmetry* has no planes of reflective symmetry, so there are no symmetry restrictions for a triclinic material. *Monoclinic symmetry* has exactly one plane of reflective symmetry. *Trigonal symmetry* has three planes of symmetry whose normals all lie in the same plane and make angles of 120° with each other; its threefold character stems from this relative orientation of its planes of symmetry. *Orthotropic symmetry* has three mutually perpendicular planes of reflective symmetry, but the existence of the third plane is implied by the first two. That is to say, if there exist two perpendicular planes of reflective symmetry, there will automatically be a third one perpendicular to both of the first two. *Tetragonal symmetry* has the five planes of symmetry ($\boldsymbol{a}_1$–$\boldsymbol{a}_5$) illustrated in Figure 5.11; four of the five planes of symmetry have normals that all lie in the same plane and make angles of 90° with each other; its fourfold

character stems from this relative orientation of its planes of symmetry. The fifth plane of symmetry is the plane containing the normals to the other four planes of symmetry. *Hexagonal symmetry* has seven planes of symmetry, six of which have normals that all lie in the same plane and make angles of 60° with each other; its sixfold character stems from this relative orientation of its planes of symmetry. The seventh plane of symmetry is the plane containing the normals to the other six planes of symmetry. The illustration for hexagonal symmetry is similar to that for tetragonal symmetry shown in Figure 5.11; the difference is that there are six rather than four planes with normals all lying in the same plane and that those normals make angles of 60° rather than 90° with each other. *Cubic symmetry* has the nine planes of symmetry illustrated in Figure 5.12. The positive octant at the front of Figure 5.12 is bounded by three of the symmetry planes with normals $\boldsymbol{a}_1$, $\boldsymbol{a}_2$, and $\boldsymbol{a}_3$ and contains traces of the six other planes of symmetry.

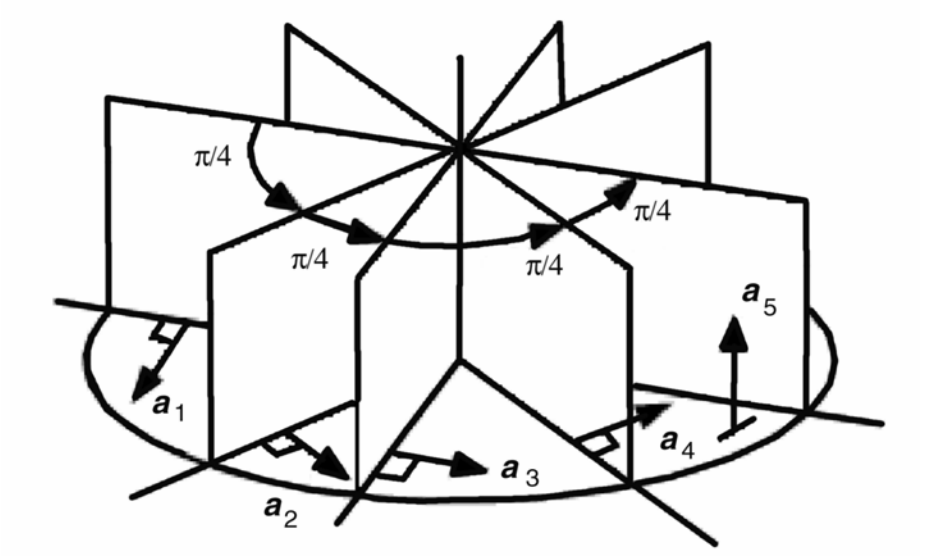



**Figure 5.11**. Illustration of the five planes of symmetry characterizing tetragonal symmetry. The normals to the five planes are denoted by $\boldsymbol{a}_1$–$\boldsymbol{a}_5$. Four of the five planes of symmetry have normals that all lie in the same plane and make angles of 90° with each other. The fourfold character of the symmetry stems from the relative orientation of its planes of symmetry. The fifth plane of symmetry is the plane containing the normals to the other four planes of symmetry. Modified with permission from Rovati and Taliercio (2003).

If every vector in a plane is a normal to a plane of reflective symmetry, the plane is called a *plane of isotropy*. It can be shown that a plane of isotropy is itself a plane of reflective symmetry. The material symmetry characterized by a single plane of isotropy is said to be *transverse isotropy*. In the case of linear elasticity the $\hat{\mathbf{C}}$ matrix for transversely isotropic symmetry is the same as the $\hat{\mathbf{C}}$ matrix for hexagonal symmetry, and so a distinction is not made between these two symmetries. *Isotropic symmetry* is characterized by every direction being the normal to a plane of reflective symmetry, or equivalently, every plane being a plane of isotropy.

In this presentation the reference coordinate system for the elastic symmetries is selected so that there are only 18 distinct components of $\hat{\mathbf{C}}$ for triclinic symmetry and 12 for monoclinic, so that the seven constant tetragonal and trigonal symmetries are the same as the six constant tetragonal and trigonal symmetries, respectively. This selection of the coordinate sys-

tem is always possible without restricting the generality of the matrix representations (Fedorov, 1968; Cowin, 1995).

This classification of the types of linear elastic material symmetries by the number and orientation of the normals to the planes of material symmetry is fully equivalent to the crystallographic method using group theory (Chadwick et al., 2001).

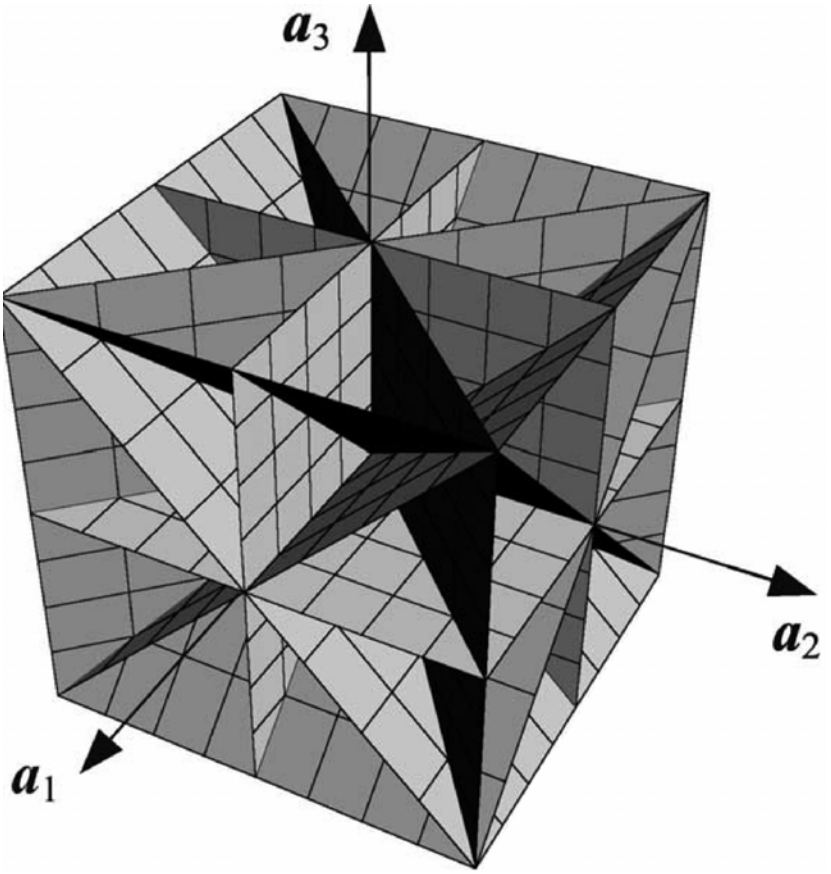



**Figure 5.12**. An illustration of the nine planes of symmetry characterizing cubic symmetry. The positive octant at the front of the perspective is bounded by three of the symmetry planes with normals $\boldsymbol{a}_1$, $\boldsymbol{a}_2$, and $\boldsymbol{a}_3$ and contains traces of the six other planes of symmetry. Reprinted with permission from Rovati and Taliercio (2003).

**Problems**

5.5.1. Construct diagrams of the number and orientation of the normals to the planes of reflective symmetry for six of the eight material symmetries (diagrams for the other two, tetragonal and cubic, and prose descriptions for all the symmetries are given in the text); the triclinic, monoclinic, orthotropic, hexagonal, transverse isotropic, and isotropic material symmetries.

5.5.2. Construct a diagram for the set of normals to the planes of reflective symmetry given in Problem 5.4.6, with the addition of normal $\mathbf{e}_3$ so that the set now consists of seven vectors: **k**, **p**, **m**, **n**, $\mathbf{e}_1$, $\mathbf{e}_2$, and $\mathbf{e}_3$.

## 5.6. THE FORMS OF THE SYMMETRIC THREE-DIMENSIONAL LINEAR TRANSFORMATION A

In this section the definitions of the material symmetries given in §5.5 are used in conjunction with orthogonal transformation (5.2) characterizing a plane of reflective symmetry and transformation law (A83) to derive the forms of three-dimensional linear transformation **A** for the material symmetries of interest. First, since triclinic symmetry has no planes of reflective symmetry, there are no symmetry restrictions for a triclinic material and linear transformation **A** is unrestricted. This conclusion is recorded in Table 5.3.

Monoclinic symmetry has exactly one plane of reflective symmetry. This means that the material coefficients appearing in **A** must be unchanged by one reflective symmetry transformation. Let $\mathbf{e}_1$ be the normal to the plane of reflective symmetry so the reflective symmetry transformation is $\mathbf{R}^{(\mathbf{e}_1)}$, given by the first of (5.4). The tensor **A** is subject to transformation

$$\mathbf{A}^{(L)} = \mathbf{R}^{(\mathbf{e}_1)} \cdot \mathbf{A}^{(G)} \cdot \mathbf{R}^{(\mathbf{e}_1)T} \tag{5.8}$$

which follows from the first of (A83) by setting $\mathbf{T} = \mathbf{A}$ and $\mathbf{Q} = \mathbf{R}^{(\mathbf{e}_1)}$. Substituting for **A** and $\mathbf{R}^{(\mathbf{e}_1)}$ in this equation, one finds that

$$\begin{bmatrix} A_{11} & A_{12} & A_{13} \\ A_{21} & A_{22} & A_{23} \\ A_{31} & A_{32} & A_{33} \end{bmatrix} = \begin{bmatrix} -1 & 0 & 0 \\ 0 & 1 & 0 \\ 0 & 0 & 1 \end{bmatrix} \begin{bmatrix} A_{11} & A_{12} & A_{13} \\ A_{21} & A_{22} & A_{23} \\ A_{31} & A_{32} & A_{33} \end{bmatrix} \begin{bmatrix} -1 & 0 & 0 \\ 0 & 1 & 0 \\ 0 & 0 & 1 \end{bmatrix},$$

or

$$\begin{bmatrix} A_{11} & A_{12} & A_{13} \\ A_{21} & A_{22} & A_{23} \\ A_{31} & A_{32} & A_{33} \end{bmatrix} = \begin{bmatrix} A_{11} & -A_{12} & -A_{13} \\ -A_{21} & A_{22} & A_{23} \\ -A_{31} & A_{32} & A_{33} \end{bmatrix}. \tag{5.9}$$

Transformation (5.8) or (5.9) is thus seen to leave tensor **A** unchanged by the reflection only if $A_{12} = A_{21} = A_{13} = A_{31} = 0$. It follows then that the form of tensor **A** consistent with monoclinic symmetry characterized by a plane of reflective symmetry normal to the $\mathbf{e}_1$ base vector must satisfy the conditions $A_{12} = A_{21} = A_{13} = A_{31} = 0$. This result for monoclinic symmetry is recorded in Table 5.1.

Orthotropic symmetry is characterized by three mutually perpendicular planes of reflective symmetry, but the third plane is implied by the first two. This means that the material coefficients appearing in the representation of **A** for monoclinic symmetry must be unchanged by one more perpendicular reflective symmetry transformation. Let $\mathbf{e}_2$ be the normal to the plane of reflective symmetry so the reflective symmetry transformation is $\mathbf{R}^{(\mathbf{e}_2)}$ is given by the second of (5.4). The monoclinic form of tensor **A** is subject to transformation

$$\mathbf{A}^{(L)} = \mathbf{R}^{(\mathbf{e}_2)} \cdot \mathbf{A}^{(G)} \cdot \mathbf{R}^{(\mathbf{e}_2)T} \tag{5.10}$$

**Table 5.3.** The Forms of Three-Dimensional Symmetric Linear Transformation **A** for the Different Material Symmetries

| Type of material symmetry | Form of linear transformation **A** |
|---|---|
| Triclinic | $\begin{bmatrix} A_{11} & A_{12} & A_{13} \\ A_{21} & A_{22} & A_{23} \\ A_{31} & A_{32} & A_{33} \end{bmatrix}$ |
| Monoclinic | $\begin{bmatrix} A_{11} & 0 & 0 \\ 0 & A_{22} & A_{23} \\ 0 & A_{32} & A_{33} \end{bmatrix}$ |
| Orthotropic | $\begin{bmatrix} A_{11} & 0 & 0 \\ 0 & A_{22} & 0 \\ 0 & 0 & A_{33} \end{bmatrix}$ |
| Hexagonal, trigonal. tetragonal (some crystal classes) | $\begin{bmatrix} A_{11} & A_{12} & 0 \\ -A_{12} & A_{11} & 0 \\ 0 & 0 & A_{33} \end{bmatrix}$ |
| Transversely isotropic, hexagonal, trigonal. tetragonal (the other crystal classes) | $\begin{bmatrix} A_{11} & 0 & 0 \\ 0 & A_{11} & 0 \\ 0 & 0 & A_{33} \end{bmatrix}$ |
| Isotropic and cubic | $\begin{bmatrix} A_{11} & 0 & 0 \\ 0 & A_{11} & 0 \\ 0 & 0 & A_{11} \end{bmatrix}$ |

which follows from the first of (A83) by setting $\mathbf{T} = \mathbf{A}$ and $\mathbf{Q} = \mathbf{R}^{(\mathbf{e}_2)}$. Substituting into (5.10) the representation for the monoclinic form for **A** and the representation for $\mathbf{R}^{(\mathbf{e}_2)}$, one finds that

$$\begin{bmatrix} A_{11} & 0 & 0 \\ 0 & A_{22} & A_{23} \\ 0 & A_{32} & A_{33} \end{bmatrix} = \begin{bmatrix} 1 & 0 & 0 \\ 0 & -1 & 0 \\ 0 & 0 & 1 \end{bmatrix} \begin{bmatrix} A_{11} & 0 & 0 \\ 0 & A_{22} & A_{23} \\ 0 & A_{32} & A_{33} \end{bmatrix} \begin{bmatrix} 1 & 0 & 0 \\ 0 & -1 & 0 \\ 0 & 0 & 1 \end{bmatrix},$$

or

$$\begin{bmatrix} A_{11} & 0 & 0 \\ 0 & A_{22} & A_{23} \\ 0 & A_{32} & A_{33} \end{bmatrix} = \begin{bmatrix} A_{11} & 0 & 0 \\ 0 & A_{22} & -A_{23} \\ 0 & -A_{32} & A_{33} \end{bmatrix}. \tag{5.11}$$

Transformation (5.10) or (5.11) is thus seen to leave the monoclinic form of tensor **A** unchanged by the reflection only if $A_{32} = A_{23} = 0$. It follows then that the form of tensor **A** consistent with an orthotropic symmetry characterized by planes of reflective symmetry normal to the $\mathbf{e}_1$ and $\mathbf{e}_2$ base vectors must satisfy the conditions $A_{32} = A_{23} = 0$. It is then possible to show that this restriction also permits the existence of a third plane of reflective symmetry perpendicular to the first two. This result for orthotropic symmetry is recorded in Table 5.3.

A transversely isotropic material is one with a plane of isotropy. A plane of isotropy is a plane in which every vector is the normal to a plane of reflective symmetry. This means that the material coefficients appearing in the representation of **A** for orthotropic symmetry must be unchanged by any reflective symmetry transformation characterized by any unit vector in a specified plane. Let the plane be the $\mathbf{e}_1$, $\mathbf{e}_2$, plane and let the unit vectors be $\mathbf{a} = \cos\theta\mathbf{e}_1 + \sin\theta\mathbf{e}_2$ for any and all values of $\theta$; then the reflective symmetry transformations of interest are $\mathbf{R}^{(\theta_{12})}$ given by the first of (5.6). The orthotropic form of the tensor **A** is subject to the transformation

$$\mathbf{A}^{(L)} = \mathbf{R}^{(\theta_{12})} \cdot \mathbf{A}^{(G)} \cdot \mathbf{R}^{(\theta_{12})T} \tag{5.12}$$

which follows from the first of (A83) by setting $\mathbf{T} = \mathbf{A}$ and $\mathbf{Q} = \mathbf{R}^{(\theta_{12})}$. Substituting for $\mathbf{R}^{(\theta_{12})}$ and the orthotropic form for **A** into this equation, one finds that

$$\begin{bmatrix} A_{11} & 0 & 0 \\ 0 & A_{22} & 0 \\ 0 & 0 & A_{33} \end{bmatrix} = \begin{bmatrix} -\cos 2\theta & -\sin 2\theta & 0 \\ -\sin 2\theta & \cos 2\theta & 0 \\ 0 & 0 & 1 \end{bmatrix} \begin{bmatrix} A_{11} & 0 & 0 \\ 0 & A_{22} & 0 \\ 0 & 0 & A_{33} \end{bmatrix} \begin{bmatrix} -\cos 2\theta & -\sin 2\theta & 0 \\ -\sin 2\theta & \cos 2\theta & 0 \\ 0 & 0 & 1 \end{bmatrix}$$

or

$$\begin{bmatrix} A_{11} & 0 & 0 \\ 0 & A_{22} & 0 \\ 0 & 0 & A_{33} \end{bmatrix} = \begin{bmatrix} A_{11}\cos^2 2\theta + A_{22}\sin^2 2\theta & \frac{1}{4}\sin 4\theta(A_{11} - A_{22}) & 0 \\ \frac{1}{4}\sin 4\theta(A_{11} - A_{22}) & A_{11}\sin^2 2\theta + A_{22}\cos^2 2\theta & 0 \\ 0 & 0 & A_{33} \end{bmatrix}. \tag{5.13}$$

Transformation (5.12) or (5.13) is thus seen to leave the transversely isotropic form of tensor **A** unchanged by the reflection only if $A_{11} = A_{22}$. It follows then that the transversely isotropic form of tensor **A** consistent with transversely isotropic symmetry characterized by a plane of isotropy in the $\mathbf{e}_1$, $\mathbf{e}_2$ plane must satisfy the conditions $A_{11} = A_{22}$. This result for transversely isotropic symmetry is recorded in Table 5.3. Algebraic procedures identical with those described above may be used to show that the forms of tensor **A** consistent with the trigonal, tetragonal, and hexagonal symmetries are each identical with that for transversely isotropic symmetry.

Isotropic symmetry is characterized by every direction being the normal to a plane of reflective symmetry or, equivalently, every plane being a plane of isotropy. This means that the material coefficients appearing in the representation of **A** for transversely isotropic symmetry

must be unchanged by any reflective symmetry transformation characterized by any unit vector in any direction. In addition to the $\mathbf{e}_1$, $\mathbf{e}_2$ plane considered as the plane of isotropy for transversely isotropic symmetry, it is required that the $\mathbf{e}_2$, $\mathbf{e}_3$ plane be a plane of isotropy. The second plane of isotropy is characterized by the unit vectors $\mathbf{a} = \cos\theta\mathbf{e}_2 + \sin\theta\mathbf{e}_3$ for any and all values of $\theta$; then the reflective symmetry transformations of interest is $\mathbf{R}^{(\theta_{23})}$ given by the second of (5.6). The transversely isotropic form of the tensor $\mathbf{A}$ must be invariant under transformation

$$\mathbf{A}^{(L)} = \mathbf{R}^{(\theta_{23})} \cdot \mathbf{A}^{(G)} \cdot \mathbf{R}^{(\theta_{23})T} \tag{5.14}$$

which follows from the first of (A83) by setting $\mathbf{T} = \mathbf{A}$ and $\mathbf{Q} = \mathbf{R}^{(\theta_{23})}$. Substitution of $\mathbf{R}^{(\theta_{23})}$ and the transversely isotropic form for $\mathbf{A}$ into this equation, one finds that

$$\begin{bmatrix} A_{11} & 0 & 0 \\ 0 & A_{11} & 0 \\ 0 & 0 & A_{33} \end{bmatrix} = \begin{bmatrix} 1 & 0 & 0 \\ 0 & -\cos 2\theta & -\sin 2\theta \\ 0 & -\sin 2\theta & \cos 2\theta \end{bmatrix} \begin{bmatrix} A_{11} & 0 & 0 \\ 0 & A_{11} & 0 \\ 0 & 0 & A_{33} \end{bmatrix} \begin{bmatrix} 1 & 0 & 0 \\ 0 & -\cos 2\theta & -\sin 2\theta \\ 0 & -\sin 2\theta & \cos 2\theta \end{bmatrix}$$

or

$$\begin{bmatrix} A_{11} & 0 & 0 \\ 0 & A_{11} & 0 \\ 0 & 0 & A_{33} \end{bmatrix} = \begin{bmatrix} A_{11} & 0 & 0 \\ 0 & A_{11}\cos^2 2\theta + A_{33}\sin^2 2\theta & \frac{1}{4}\sin 4\theta(A_{11} - A_{33}) \\ 0 & \frac{1}{4}\sin 4\theta(A_{11} - A_{33}) & A_{11}\sin^2 2\theta + A_{33}\cos^2 2\theta \end{bmatrix}. \tag{5.15}$$

Transformation (5.14) or (5.15) is thus seen to leave the isotropic form of tensor $\mathbf{A}$ unchanged by the reflection only if $A_{11} = A_{33}$. It follows then that the isotropic form of tensor $\mathbf{A}$ consistent with isotropic symmetry characterized by planes of isotropy in the $\mathbf{e}_1$, $\mathbf{e}_2$ and $\mathbf{e}_2$, $\mathbf{e}_3$ planes must satisfy the conditions $A_{11} = A_{33}$. Actually, there are many ways to make the transition from transversely isotropic symmetry to isotropic symmetry other than the method chosen here. Any plane of reflective symmetry added to the plane of isotropy of transversely isotropic symmetry, and not coincident with the plane of isotropy, will lead to isotropic symmetry. This result for isotropic symmetry is recorded in Table 5.3. Algebraic procedures identical with those described above may be used to show that the form of tensor $\mathbf{A}$ consistent with cubic symmetry is identical with that for isotropic symmetry.

**Problems**

5.6.1. Show that the orthotropic form of tensor $\mathbf{A}$ given in Table 5.3 is invariant under transformation $\mathbf{R}^{(\mathbf{e}_3)}$ constructed in Problem 5.4.2.

5.6.2. Show that the isotropic form of tensor $\mathbf{A}$ given in Table 5.3 is invariant under transformation $\mathbf{R}^{(\theta_{13})}$ constructed in Problem 5.4.3.

5.6.3. Construct a representation for $\mathbf{A}$ that is invariant under the seven reflective transformations formed from the set of normals to the planes of reflective symmetry given in Problem 5.5.2: $\mathbf{k}$, $\mathbf{p}$, $\mathbf{m}$, $\mathbf{n}$, $\mathbf{e}_1$, $\mathbf{e}_2$, and $\mathbf{e}_3$. Does the result coincide with one of the representations already in Table 5.3? If it does, please explain.

## 5.7. THE FORMS OF THE SYMMETRIC SIX-DIMENSIONAL LINEAR TRANSFORMATION $\hat{\mathbf{C}}$

In this section the definitions of the material symmetries given in §5.5 are used in conjunction with six-dimensional orthogonal transformation (5.3) characterizing a plane of reflective symmetry and transformation law (A162) to derive the forms of three-dimensional linear transformation $\hat{\mathbf{C}}$ for different material symmetries. The developments in this section parallel those in the previous section step for step. The matrices are different, and the results are different, but the arguments are identical. However, since this topic involves 6-by-6 rather than 3-by-3 matrices, a computational symbolic algebra program (e.g., Maple, Mathematica, Matlab, MathCad, etc.) is required to make the calculations simple. One should work through this section with such a program on a nearby computer.

First, since triclinic symmetry has no planes of reflective symmetry, there are no symmetry restrictions for a triclinic material and linear transformation $\hat{\mathbf{C}}$ is unrestricted. This conclusion is recorded in Table 5.4. Monoclinic symmetry has exactly one plane of reflective symmetry. This means that the material coefficients appearing in $\hat{\mathbf{C}}$ must be unchanged by one reflective symmetry transformation. Let $\mathbf{e}_1$ be the normal to the plane of reflective symmetry, so the reflective symmetry transformation is $\hat{\mathbf{R}}^{(\mathbf{e}_1)}$, given by the first of (5.5). Tensor $\hat{\mathbf{C}}$ must be invariant under transformation

$$\hat{\mathbf{C}}^{(L)} = \hat{\mathbf{R}}^{(\mathbf{e}_1)} \cdot \hat{\mathbf{C}}^{(G)} \cdot \hat{\mathbf{R}}^{(\mathbf{e}_1)T}, \tag{5.16}$$

which follows from the first of (A162) by setting $\hat{\mathbf{Q}} = \hat{\mathbf{R}}^{(\mathbf{e}_1)}$. The pattern of this calculation follows the pattern of calculation in (5.9). That pattern is the substitution for $\hat{\mathbf{C}}$ and $\hat{\mathbf{R}}^{(\mathbf{e}_1)}$ into this equation and the execution of matrix multiplication. The resulting matrices are not documented here. As mentioned above, they may be easily obtained with any symbolic algebra program. The result is that tensor $\hat{\mathbf{C}}$ is unchanged by the reflection only if $\hat{C}_{15} = \hat{C}_{51} = \hat{C}_{16} = \hat{C}_{61} = \hat{C}_{25} = \hat{C}_{52} = \hat{C}_{26} = \hat{C}_{62} = \hat{C}_{35} = \hat{C}_{53} = \hat{C}_{36} = \hat{C}_{63} = \hat{C}_{45} = \hat{C}_{54} = \hat{C}_{46} = \hat{C}_{64} = 0$. It follows then that the form of tensor $\hat{\mathbf{C}}$ consistent with monoclinic symmetry characterized by a plane of reflective symmetry normal to the $\mathbf{e}_1$ base vector must satisfy the conditions $\hat{C}_{15} = \hat{C}_{51} = \hat{C}_{16} = \hat{C}_{61} = \hat{C}_{25} = \hat{C}_{52} = \hat{C}_{26} = \hat{C}_{62} = \hat{C}_{35} = \hat{C}_{53} = \hat{C}_{36} = \hat{C}_{63} = \hat{C}_{45} = \hat{C}_{54} = \hat{C}_{46} = \hat{C}_{64} = 0$. This result for monoclinic symmetry is recorded in Table 5.4.

Orthotropic symmetry is characterized by three mutually perpendicular planes of reflective symmetry, but the third plane in implied by the first two. This means that the material coefficients appearing in the representation of $\hat{\mathbf{C}}$ for monoclinic symmetry must be unchanged by another perpendicular reflective symmetry transformation. Let $\mathbf{e}_2$ be the normal to the plane of reflective symmetry so the reflective symmetry transformation is $\hat{\mathbf{R}}^{(\mathbf{e}_2)}$, as given by the second of (5.5). The monoclinic form of tensor $\hat{\mathbf{C}}$ must be invariant under transformation

$$\hat{\mathbf{C}}^{(L)} = \hat{\mathbf{R}}^{(\mathbf{e}_2)} \cdot \hat{\mathbf{C}}^{(G)} \cdot \hat{\mathbf{R}}^{(\mathbf{e}_2)T}, \tag{5.17}$$

which follows from the first of (A162) by setting $\hat{\mathbf{Q}} = \hat{\mathbf{R}}^{(\mathbf{e}_2)}$. The pattern of this calculation follows the pattern of calculation in (5.11). That pattern is the substitution of the monoclinic form for $\hat{\mathbf{C}}$ and $\hat{\mathbf{R}}^{(\mathbf{e}_2)}$ into this equation and execution of matrix multiplication. The resulting matrices are not documented here; they may be easily obtained with any symbolic algebra program. The result is that tensor $\hat{\mathbf{C}}$ is unchanged by the reflection only if $\hat{C}_{14} = \hat{C}_{41} = \hat{C}_{24} = \hat{C}_{42} = \hat{C}_{34} = \hat{C}_{43} = \hat{C}_{56} = \hat{C}_{65} = 0$. It follows then that the form of tensor $\hat{\mathbf{C}}$ consistent with orthotropic symmetry characterized by planes of reflective symmetry normal to the $\mathbf{e}_1$ and $\mathbf{e}_2$ base vectors must satisfy the conditions $\hat{C}_{14} = \hat{C}_{41} = \hat{C}_{24} = \hat{C}_{42} = \hat{C}_{34} = \hat{C}_{43} = \hat{C}_{56} = \hat{C}_{65} = 0$. This result for orthotropic symmetry is recorded in Table 5.4.

A transversely isotropic material is one with a plane of isotropy. This means that the material coefficients appearing in the representation of $\hat{\mathbf{C}}$ for orthotropic symmetry must be unchanged by any reflective symmetry transformation characterized by any unit vector in a specified plane. Let the designated plane of isotropy be the $\mathbf{e}_1$, $\mathbf{e}_2$ plane and let the unit vector be $\mathbf{a} = \cos\theta\,\mathbf{e}_1 + \sin\theta\,\mathbf{e}_2$ for any and all values of $\theta$; then the reflective symmetry transformation of interest is $\hat{\mathbf{R}}^{(\theta_{12})}$, given by the first of (5.7). The orthotropic form of tensor $\hat{\mathbf{C}}$ must be invariant under transformation

$$\hat{\mathbf{C}}^{(L)} = \hat{\mathbf{R}}^{(\theta_{12})} \cdot \hat{\mathbf{C}}^{(G)} \cdot \hat{\mathbf{R}}^{(\theta_{12})T}, \tag{5.18}$$

which follows from the first of (A162) by setting $\hat{\mathbf{Q}} = \hat{\mathbf{R}}^{(\theta_{12})}$. The pattern of this calculation follows the pattern of calculation in (5.12). That pattern is substitution of the orthotropic form for $\hat{\mathbf{C}}$ and $\hat{\mathbf{R}}^{(\theta_{12})}$ into this equation and execution of matrix multiplication. The resulting matrices are not documented here. They may be easily obtained with any symbolic algebra program. The result is that tensor $\hat{\mathbf{C}}$ is unchanged by the reflection only if $\hat{C}_{22} = \hat{C}_{11}$, $\hat{C}_{21} = \hat{C}_{12}$, $\hat{C}_{23} = \hat{C}_{13}$, $\hat{C}_{32} = \hat{C}_{31}$, $\hat{C}_{55} = \hat{C}_{44}$, $\hat{C}_{66} = \hat{C}_{11} - \hat{C}_{12}$. It follows then that the form of tensor $\hat{\mathbf{C}}$ consistent with transversely isotropic symmetry characterized by a plane of isotropy whose normal is in the $\mathbf{e}_3$ direction must satisfy the conditions $\hat{C}_{22} = \hat{C}_{11}$, $\hat{C}_{21} = \hat{C}_{12}$, $\hat{C}_{23} = \hat{C}_{13}$, $\hat{C}_{32} = \hat{C}_{31}$, $\hat{C}_{55} = \hat{C}_{44}$, $\hat{C}_{66} = \hat{C}_{11} - \hat{C}_{12}$. This result for transversely isotropic symmetry is recorded in Table 5.4.

Isotropic symmetry is characterized by every direction being the normal to a plane of reflective symmetry or, equivalently, every plane being a plane of isotropy. This means that the material coefficients appearing in the representation of $\hat{\mathbf{C}}$ for transversely isotropic symmetry must be unchanged by any reflective symmetry transformation characterized by any unit vector in any direction. In addition to the $\mathbf{e}_1$, $\mathbf{e}_2$ plane considered for transversely isotropic symmetry, it is required that the $\mathbf{e}_2$, $\mathbf{e}_3$ plane be a plane of isotropy. The second plane of isotropy is characterized by the unit vectors $\mathbf{a} = \cos\theta\,\mathbf{e}_2 + \sin\theta\,\mathbf{e}_3$, for any and all values of $\theta$, then the reflective symmetry transformations of interest are $\hat{\mathbf{R}}^{(\theta_{23})}$ given by the second of (5.7). The form of tensor $\hat{\mathbf{C}}$ representing transversely isotropic symmetry must be invariant under transformation

$$\hat{\mathbf{C}}^{(L)} = \hat{\mathbf{R}}^{(\theta_{23})} \cdot \hat{\mathbf{C}}^{(G)} \cdot \hat{\mathbf{R}}^{(\theta_{23})T}, \tag{5.19}$$

which follows from the first of (A162) by setting $\hat{\mathbf{Q}} = \hat{\mathbf{R}}^{(\theta_{23})}$. The pattern of this calculation follows the pattern of calculation in (5.14) and (5.15). That pattern is the substitution of the transversely isotropic form for $\hat{\mathbf{C}}$ and $\hat{\mathbf{R}}^{(\theta_{23})}$ into this equation and execution of matrix multiplication. The resulting matrix is not recorded here; it may be easily obtained with any symbolic algebra program. The result is that tensor $\hat{\mathbf{C}}$ is unchanged by any of the reflections whose normals lie in the plane perpendicular to $\mathbf{e}_1$ only if the transversely isotropic form for $\hat{\mathbf{C}}$ satisfies additional restrictions: $\hat{C}_{33} = \hat{C}_{11}$, $\hat{C}_{31} = \hat{C}_{12}$, $\hat{C}_{31} = \hat{C}_{12}$, $\hat{C}_{13} = \hat{C}_{12}$, $\hat{C}_{44} = \hat{C}_{11} - \hat{C}_{12}$. It follows then that the transversely isotropic form of tensor $\hat{\mathbf{C}}$ consistent with isotropic symmetry characterized by two perpendicular planes of isotropy must satisfy conditions $\hat{C}_{33} = \hat{C}_{11}$, $\hat{C}_{31} = \hat{C}_{12}$, $\hat{C}_{31} = \hat{C}_{12}$, $\hat{C}_{13} = \hat{C}_{12}$, $\hat{C}_{44} = \hat{C}_{11} - \hat{C}_{12}$. This result for isotropic symmetry is recorded in Table 5.4. An algebraic procedure identical with those described above may be used to obtain the forms of tensor $\hat{\mathbf{C}}$ consistent with the trigonal, tetragonal, and cubic symmetries listed in Table 5.4.

**Table 5.4**. The forms of Six-Dimensional Linear Transformation $\hat{\mathbf{C}}$ for the Triclinic, Monoclinic, and Orthotropic Material Symmetries

| Type of material symmetry | Form of the six-dimensional linear transformation $\hat{\mathbf{C}}$ |
|---|---|
| Triclinic | $\begin{bmatrix} \hat{C}_{11} & \hat{C}_{12} & \hat{C}_{13} & \hat{C}_{14} & \hat{C}_{15} & \hat{C}_{16} \\ \hat{C}_{21} & \hat{C}_{22} & \hat{C}_{23} & \hat{C}_{24} & \hat{C}_{25} & \hat{C}_{26} \\ \hat{C}_{31} & \hat{C}_{32} & \hat{C}_{33} & \hat{C}_{34} & \hat{C}_{35} & \hat{C}_{36} \\ \hat{C}_{41} & \hat{C}_{42} & \hat{C}_{43} & \hat{C}_{44} & \hat{C}_{45} & \hat{C}_{46} \\ \hat{C}_{51} & \hat{C}_{52} & \hat{C}_{53} & \hat{C}_{54} & \hat{C}_{55} & \hat{C}_{56} \\ \hat{C}_{61} & \hat{C}_{62} & \hat{C}_{63} & \hat{C}_{64} & \hat{C}_{65} & \hat{C}_{66} \end{bmatrix}$ |
| Monoclinic | $\begin{bmatrix} \hat{C}_{11} & \hat{C}_{12} & \hat{C}_{13} & \hat{C}_{14} & 0 & 0 \\ \hat{C}_{21} & \hat{C}_{22} & \hat{C}_{23} & \hat{C}_{24} & 0 & 0 \\ \hat{C}_{31} & \hat{C}_{32} & \hat{C}_{33} & \hat{C}_{34} & 0 & 0 \\ \hat{C}_{41} & \hat{C}_{42} & \hat{C}_{43} & \hat{C}_{44} & 0 & 0 \\ 0 & 0 & 0 & 0 & \hat{C}_{55} & \hat{C}_{56} \\ 0 & 0 & 0 & 0 & \hat{C}_{65} & \hat{C}_{66} \end{bmatrix}$ |
| Orthotropic | $\begin{bmatrix} \hat{C}_{11} & \hat{C}_{12} & \hat{C}_{13} & 0 & 0 & 0 \\ \hat{C}_{21} & \hat{C}_{22} & \hat{C}_{23} & 0 & 0 & 0 \\ \hat{C}_{31} & \hat{C}_{32} & \hat{C}_{33} & 0 & 0 & 0 \\ 0 & 0 & 0 & \hat{C}_{44} & 0 & 0 \\ 0 & 0 & 0 & 0 & \hat{C}_{55} & 0 \\ 0 & 0 & 0 & 0 & 0 & \hat{C}_{66} \end{bmatrix}$ |
| Trigonal | $\begin{bmatrix} \hat{C}_{11} & \hat{C}_{12} & \hat{C}_{13} & \hat{C}_{14} & 0 & 0 \\ \hat{C}_{12} & \hat{C}_{22} & \hat{C}_{23} & -\hat{C}_{14} & 0 & 0 \\ \hat{C}_{13} & \hat{C}_{23} & \hat{C}_{33} & 0 & 0 & 0 \\ \hat{C}_{41} & -\hat{C}_{41} & 0 & \hat{C}_{44} & 0 & 0 \\ 0 & 0 & 0 & 0 & \hat{C}_{44} & \sqrt{2}\hat{C}_{14} \\ 0 & 0 & 0 & 0 & \sqrt{2}\hat{C}_{41} & (\hat{C}_{11} - \hat{C}_{12}) \end{bmatrix}$ |

**Table 5.4**. (cont'd)

| Type of material symmetry | Form of the six-dimensional linear transformation $\hat{\mathbf{C}}$ |
|---|---|
| Tetragonal | $\begin{bmatrix} \hat{C}_{11} & \hat{C}_{12} & \hat{C}_{13} & 0 & 0 & 0 \\ \hat{C}_{12} & \hat{C}_{11} & \hat{C}_{13} & 0 & 0 & 0 \\ \hat{C}_{31} & \hat{C}_{31} & \hat{C}_{33} & 0 & 0 & 0 \\ 0 & 0 & 0 & \hat{C}_{44} & 0 & 0 \\ 0 & 0 & 0 & 0 & \hat{C}_{44} & 0 \\ 0 & 0 & 0 & 0 & 0 & \hat{C}_{66} \end{bmatrix}$ |
| Transversely isotropic, hexagonal | $\begin{bmatrix} \hat{C}_{11} & \hat{C}_{12} & \hat{C}_{13} & 0 & 0 & 0 \\ \hat{C}_{12} & \hat{C}_{11} & \hat{C}_{13} & 0 & 0 & 0 \\ \hat{C}_{31} & \hat{C}_{31} & \hat{C}_{33} & 0 & 0 & 0 \\ 0 & 0 & 0 & \hat{C}_{44} & 0 & 0 \\ 0 & 0 & 0 & 0 & \hat{C}_{44} & 0 \\ 0 & 0 & 0 & 0 & 0 & \hat{C}_{11} - \hat{C}_{12} \end{bmatrix}$ |
| Cubic | $\begin{bmatrix} \hat{C}_{11} & \hat{C}_{12} & \hat{C}_{12} & 0 & 0 & 0 \\ \hat{C}_{12} & \hat{C}_{11} & \hat{C}_{12} & 0 & 0 & 0 \\ \hat{C}_{12} & \hat{C}_{12} & \hat{C}_{11} & 0 & 0 & 0 \\ 0 & 0 & 0 & \hat{C}_{44} & 0 & 0 \\ 0 & 0 & 0 & 0 & \hat{C}_{44} & 0 \\ 0 & 0 & 0 & 0 & 0 & \hat{C}_{44} \end{bmatrix}$ |
| Isotropic | $\begin{bmatrix} \hat{C}_{11} & \hat{C}_{12} & \hat{C}_{12} & 0 & 0 & 0 \\ \hat{C}_{12} & \hat{C}_{11} & \hat{C}_{12} & 0 & 0 & 0 \\ \hat{C}_{12} & \hat{C}_{12} & \hat{C}_{11} & 0 & 0 & 0 \\ 0 & 0 & 0 & \hat{C}_{11} - \hat{C}_{12} & 0 & 0 \\ 0 & 0 & 0 & 0 & \hat{C}_{11} - \hat{C}_{12} & 0 \\ 0 & 0 & 0 & 0 & 0 & \hat{C}_{11} - \hat{C}_{12} \end{bmatrix}$ |

**Problems**

5.7.1. Show that the representation for orthotropic symmetry in Table 5.4 is also invariant under transformation $\hat{\mathbf{R}}^{(\mathbf{e}_3)}$ constructed in Problem 5.4.2.

5.7.2. Show that the representation for isotropic symmetry in Table 5.4 is also invariant under transformation $\hat{\mathbf{R}}^{(\theta_{13})}$ constructed in Problem 5.4.3.

5.7.3. Construct a representation for $\hat{\mathbf{C}}$ that is invariant under the seven reflective transformations formed from the set of normals to the planes of reflective symmetry given in Problem 5.5.2: $\mathbf{k}$, $\mathbf{p}$, $\mathbf{m}$, $\mathbf{n}$, $\mathbf{e}_1$, $\mathbf{e}_2$, and $\mathbf{e}_3$. Does the result coincide with one of the representations already in Table 5.4? If it does, please explain.

## 5.8. CURVILINEAR ANISOTROPY

In the case where the type of textured material symmetry is the same at all points in an object, it is still possible for the normals to the planes of mirror symmetry to rotate as a path is traversed in the material. This type of anisotropy is referred to as *curvilinear anisotropy*. The cross-section of the tree illustrated in Figure 5.5 and the nasturtium petiole in Figure 5.6 have curvilinear anisotropy. At any point the tree has orthotropic symmetry, but as a path across a cross-section of the tree is followed the normals to the planes of symmetry rotate. In the cross-section the normals to the planes of symmetry are perpendicular and tangent to the growth rings. Curvilinear anisotropy, particularly curvilinear orthotropy and curvilinear transverse isotropy, are found in many manmade materials and in biological materials. Wood and plane tissue are generally curvilinearly orthotropic, as are fiber-wound composites. Only textured symmetries can be curvilinear. Crystalline symmetries are rectilinear, that is to say, the planes of symmetry cannot rotate as a linear path is traversed in the material.

Curvilinear anisotropies such as those based on the ideal cylindrical and spherical coordinate systems may have mathematical singularities. For example, a curvilinear orthotropy characterized by an ideal cylindrical coordinate system has a singularity at the origin (Tarn, 2002). This is due to the fact that the modulus associated with the radial direction is different from that associated with the circumferential or hoop direction (cf., Figure 5.5). The singularity at the origin arises from the fact that the radial direction and the circumferential or hoop direction are indistinguishable at the origin yet they have different moduli. A simple resolution of the mathematical singularity in the model is possible with proper physical interpretation of its significance in the real material. One such proper physical interpretation of such singular points is to note that a volume element containing such a singular point is ***not*** a typical representative volume element (RVE) and must be treated in a special manner. This is basically the approach of Tarn (2002), who constructs a special volume element, with transversely isotropic symmetry, enclosing the singularity in the cylindrical coordinate system. The mathematical singularity in the model is, in this way, removed and the model corresponds more closely to the real material (see Cowin and Fraldi, 2004).

**Problems**

5.8.1. Sketch the curvilinear nature of the set of three normals to the planes of reflective symmetry that characterize the wood tissue of a tree.

## 5.9. SYMMETRIES THAT PERMIT CHIRALITY

Thus far in the consideration of material symmetries the concern has been with the number and orientation of the planes of material symmetry. In this section the consideration is of those material symmetries that have planes that are ***not*** normals to planes of reflective symmetry. The triclinic, monoclinic, and trigonal symmetries are the only three of the eight elastic symmetries that permit directions that are not normals to planes of reflective symmetry. Every direction in triclinic symmetry is a direction in which a normal to the plane of material symmetry is *not* permitted. Every direction that lies in the single symmetry plane in monoclinic symmetry is a direction in which a normal to the plane of material symmetry is *not* permitted. The only direction in trigonal symmetry in which a normal to the plane of material symmetry is not permitted is the direction normal to a plane of threefold symmetry. There are *not* other such directions. The triclinic, monoclinic, and trigonal symmetries are also the only three of the eight elastic symmetries that, in their canonical symmetry coordinate system, retain nonzero components in their upper right and lower left 3-by-3 submatrices of the 6-by-6 matrices shown in Table 5.4. The nonzero components in these upper right and lower left 3-by-3 submatrices and the directions that are not normals to planes of reflective symmetry are directly related; such planes disappear when these components are zero. It is the existence of such planes and associated nonzero components that allow chirality such as structural gradients and handedness.

Trigonal symmetry — because it is the highest symmetry of the three symmetries — admits a direction that is not a direction associated with a normal to a plane of reflective symmetry, nor any projected component of a normal to a plane of reflective symmetry. An interesting aspect of trigonal symmetry is the chiral or symmetry-breaking character of nonzero constant $\hat{c}_{14}$. Note that $\hat{c}_{14}$ is not constrained to be of one sign; the sign restriction on $\hat{c}_{14}$ from the positive definiteness of matrix $\hat{\mathbf{c}}$ is

$$-\sqrt{\frac{\hat{c}_{44}(\hat{c}_{11}-\hat{c}_{12})}{2}} < \hat{c}_{14} < \sqrt{\frac{\hat{c}_{44}(\hat{c}_{11}-\hat{c}_{12})}{2}}\,. \tag{5.20}$$

If $\hat{c}_{14}$ vanishes, the $\hat{\mathbf{c}}$ matrix for triginal symmetry in Table 5.4 becomes that for hexagonal or transversely isotropic symmetry. Hexagonal symmetry is a sixfold symmetry with seven planes of mirror symmetry. Six of the normals to these seven planes all lie in the seventh plane and make angles of 30º with one another. Transversely isotropic symmetry is characterized by a *single plane of isotropy*. A *plane of isotropy* is a plane of mirror symmetry in which every vector is itself a normal to a plane of mirror symmetry. Since a *plane of isotropy* is also a plane of symmetry, there are an infinity plus one planes of symmetry associated with transverse isotropy.

A simple thought model is possible for visualization of the symmetry-breaking character of nonzero constant component $\hat{c}_{14}$. This constant could be described as a chiral constant, chiral being a word created by Lord Kelvin (Thompson, 1904) (*"I call any geometrical figure, or group of points, chiral, and say it has chirality, if its image in a plane mirror, ideally realized, cannot be brought to coincide with itself."*) and widely used in describing the structure of molecules. It means that a structure cannot be superposed on its mirror image, that the structure has handedness. For example, helical spirals are chiral; they are either left- or right-handed. A composite structure of alternate left- and right-handed helical spirals is illustrated in Figure 5.13. Consider a composite material constructed of an isotropic matrix material reinforced by only right-handed spiral helices whose long axes are all parallel. These helical spirals may be either touching or separated by matrix material (Figure 5.14). Let the helical angle

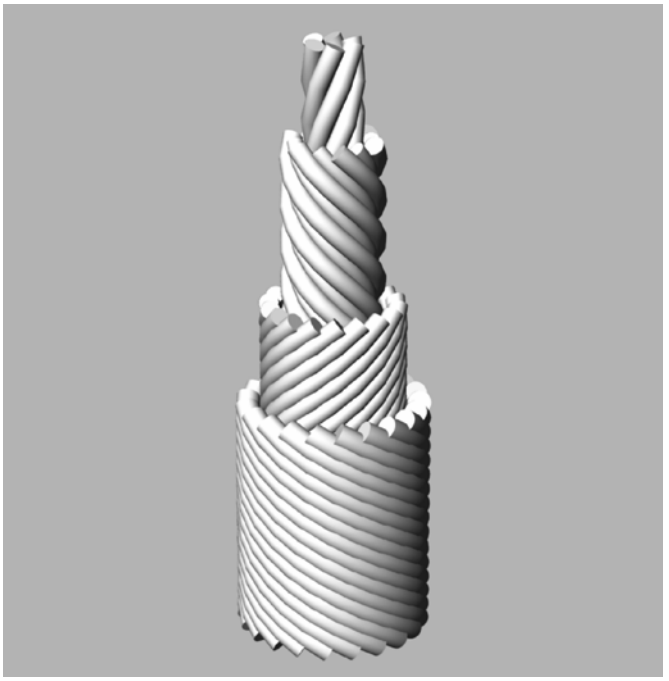


**Figure 5.13**. A composite structure composed from sets of left- and right-handed helically wound fibrous laminae that are in the form of concentric coaxial cylinders; the fibers of each lamina or component cylinder are characterized by a different helical angle. The angle of the helices often rotates regularly from one cylinder to the next. This type of structure is called elicoidal and is described as a cylinder made of twisted plywood. Reprinted with permission from Fraldi and Cowin (2002).

be $\theta$ (Figure 5.14), and let negative values of $\theta$ correspond to otherwise similar left-handed helices; the vanishing of $\theta$ then corresponds to a straight reinforcement fiber. Assume that when the effective elastic constants for this material are calculated, the sign of $\hat{C}_{14}$ is determined by the sign of $\theta$ and vanishes when $\theta$ is zero. It is then possible to geometrically visualize the chiral, symmetry-breaking character of $\hat{C}_{14}$ as it passes from positive to negative (or negative to positive) values through zero as the vanishing of a helical angle of one handedness occurs and the initiating of a helical angle of the opposite handedness commences. At the dividing line between the two types of handedness, the reinforcing fibers are straight. In terms of the material symmetry, as $\hat{C}_{14}$ passes from positive to negative (or negative to positive) values through zero, the material is first a trigonal material of a certain chirality, then a transversely isotropic (or hexagonal) material, and then a trigonal material of an opposite chirality. A *representative volume element* (RVE) of the composite in Figure 5.13 may be constructed using a set of the helicoidal fibers all having identical circular cross-sections and using the periodicity of the helix (Figure 5.14, inset). This construction provides an RVE with a material neighborhood large enough to adequately average over the microstructure and small enough to ensure that the structural gradient across it is negligible. An examination of Figure 5.14 shows that, in the plane orthogonal to the $x_3$ axis, the threefold symmetry characteristic of trigonal symmetry arises naturally.

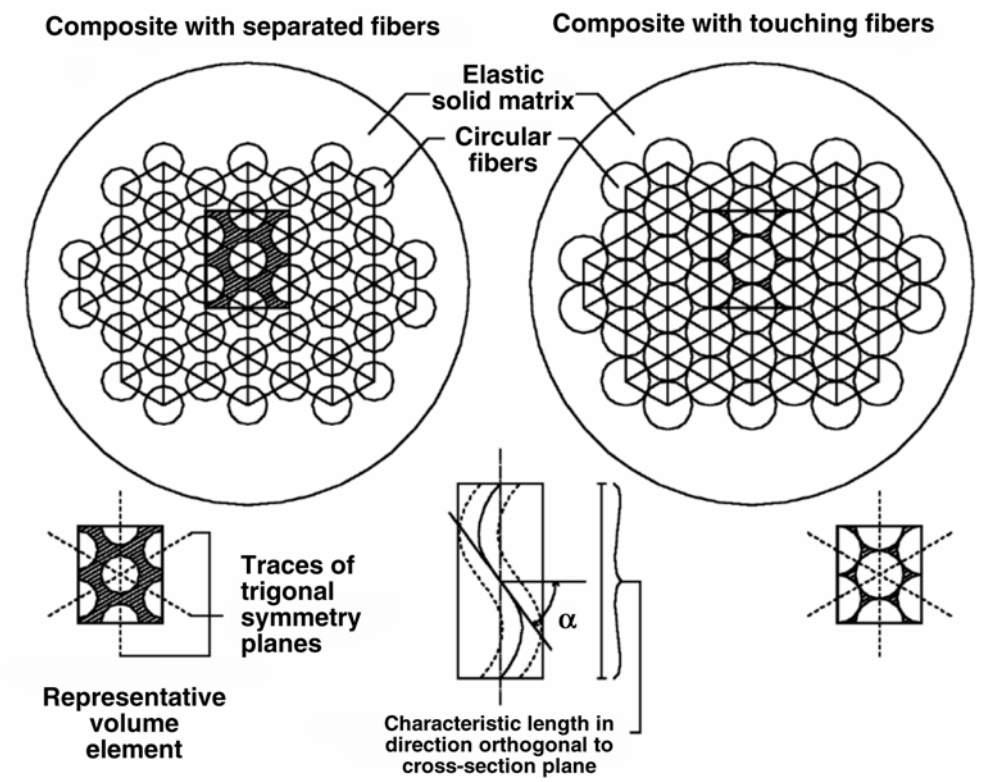



**Figure 5.14**. Two examples of composites formed from an elastic matrix and embedded helicoidal circular fibers. The two large circular diagrams illustrate the characteristic threefold trigonal symmetry in the cross-sectional plane. The possible representative volume elements (RVEs) and their characteristic helical angles are also depicted. Reprinted with permission from Fraldi and Cowin (2002).

This example illustrates how chirality is created in a material with a helical structure. It also demonstrates that the symmetry-breaking chiral constant in trigonal symmetry is proportional to the angle of the helical structure of the material, if the material has a helical structure. Further, it again illustrates how different levels of RVEs are associated with different types of material symmetry. In this example the smaller RVE is associated with orthotropic material symmetry, and the larger RVE (obtained by volume averaging over the domain of the smaller RVE) is associated with monoclinic symmetry. The result demonstrates that a material symmetry that permits chirality (i.e., trigonal, monoclinic, or triclinic symmetry) is obtained by averaging over a domain that is characterized by a symmetry that does not permit chirality (i.e., isotropic, cubic, transverse isotropic, tetragonal, and orthotropic). Clearly the result presented depends on the fact that the (achiral) orthotropic material symmetry is helically curvilinear. The association of the microgeometric chiral character of $\hat{C}_{14}$ with a helix is not a unique association. The basic property of $\hat{C}_{14}$ is its symmetry-breaking character, and it may be associated with structural gradients in the material (Cowin, 2002; Fraldi and Cowin, 2002).

There are many natural and manmade examples of both chiral materials as structures and as local components in globally achiral composites. Chiral materials that form chiral structures occur in nature (Neville, 1995). Perhaps the most famous is the tusk of the narwhal

(in the Middle Ages the tusk of the narwhal was thought to be the horn of the mythical unicorn). This whale is edentulous except for the upper lateral incisors. The right incisor normally remains embedded in the jaw, but in adult males the left tooth forms a tusk, which can in large specimens reach a length of 2.4 m and have a diameter of 8 cm at the point of eruption. Normally the tusk is imprinted with the curvature of the bone socket as it erupts or extrudes itself from a bone socket. However, if the tusk slowly twists in the socket as it grows, the imprinted curvature will be neutralized or averaged and the tusk will grow straight with the spiral structure. A second example of a natural chiral structure occurs in trees, both hardwoods and softwoods, due to a combination of genetic and environmental factors. The spiral structure in trees causes a practical problem with telephone and power poles. Changes in the moisture content of the wood of the pole causes the pole to twist after it has been employed as part of a transmission network.

Chiral materials that form chiral and non-chiral structures occur very frequently in nature (Neville, 1995). A typical such natural structure is illustrated in Figure 5.13. The structure is a set of concentric coaxial cylinders, each lamina or cylinder characterized by a different helical angle. The angle of the helices often rotates regularly from one cylinder to the next. This type of structure is called helicoidal and described as a cylinder made of "twisted plywood" (see Figures 10.33 and 10.34). The helical fibers may or may not be touching, as illustrated in Figure 5.14. The examples of this structure in nature are numerous and include fish scales and plant stem walls. Man also uses cylinders made of "twisted plywood" to create structures.

## 5.10. RELEVANT LITERATURE

A very interesting and perceptive book on symmetry in general, but including all the symmetries of interest in the present text, is the book by Weyl (1952) with the title *Symmetry*. Material symmetry is well explained in the books of Nye (1957) and Fedorov (1968). Some material in this chapter was originally developed by the first author of the present book and coworkers. The treatment of material symmetry in this chapter does not follow the standard treatments of material symmetry contained, for example, in the books on anisotropic elasticity mentioned in the literature notes at the end of Chapter 7. In the first section of this chapter it was stated that one of the purposes of this chapter was to obtain and record representations of $\mathbf{A}$ and $\hat{\mathbf{C}}$ that represent the effects of material symmetry. This has been done, and the results are recorded in Tables 5.3 and 5.4 for $\mathbf{A}$ and $\hat{\mathbf{C}}$, respectively. The representations in these tables were developed with the minimum algebraic manipulation invoked and with the minimum rigor but, we think, with the most concise method. The method employed to obtain these representations is new. Cowin and Mehrabadi (1987) first pursued using reflections to characterize the elastic symmetries. Later Cowin and Mehrabadi (1995) developed all the linear elastic symmetries from this viewpoint. Here we have not generally bothered to demonstrate invariance of these representations for all the reflective symmetries that they enjoy. In this presentation we have been content to use the minimum number of reflective symmetries necessary to obtain the symmetry representations. So we do not show the reader that further admissible reflective symmetries will not alter the representation obtained, but it happens to be true.

The established and more general method to obtain these representations is to use the symmetry groups associated with each of these symmetries. The disadvantage of that path in the present text is that it takes too much text space and distracts the reader from the main topic because it requires the introduction of the group concept and then the concept of the material symmetry group, etc. In the method of presentation employed, only the concept of the plane of mirror or reflective symmetry is necessary. The reflective symmetry approach is equivalent to

the group theory approach for tensors $\mathbf{A}$ and $\hat{\mathbf{C}}$ (Chadwick et al., 2001), but it may not be so for nonlinear relationships between these tensors. It does, however, not provide all the representations for the second rank $\mathbf{A}$ if $\mathbf{A}$ is not symmetric (Cowin, 2003).

## References


Chadwick P, Vianello M, Cowin SC. 2001. A proof that the number of linear anisotropic elastic symmetries is eight. *J Mech Phys Solids* **49**:2471–2492.

Cowin SC. 1995. On the number of distinct elastic constants associated with certain anisotropic elastic symmetries. In Theoretical, experimental, and numerical contributions to the mechanics of fluids and solids — a collection of papers in honor of Paul M. Naghdi, ed. J Casey, MJ Crochet, Z Ang Math Phys [Special Issue] **46**:S210–S214.

Cowin SC. 1999. Bone poroelasticity. *J Biomec*h **32**:218–238.

Cowin SC. 2002. Elastic symmetry restrictions from structural gradients. In rational continua, classical and new — a collection of papers dedicated to Gianfranco Capriz on the occasion of his 75th birthday, pp. 51–66, ed. P Podio-Guidugli, M Brocato. New York: Springer-Verlag.

Cowin SC. 2003. Symmetry plane classification criteria and the symmetry group classification criteria are not equivalent in the case of asymmetric second order tensors. *Chinese J Mech* **19**:9–14.

Cowin SC, Fraldi M. 2005. On singularities associated with the curvilinear anisotropic elastic symmetries. *Int J Nonlinear Mech* **40**:361–371.

Cowin SC, Mehrabadi MM. 1987. On the identification of material symmetry for anisotropic elastic materials. *Q J Mech Appl Math* **40**:451–476.

Cowin SC, Mehrabadi MM. 1989. Identification of the elastic symmetry of bone and other materials. *J Biomech* **22**:503–515.

Cowin SC, Mehrabadi MM. 1995. Anisotropic symmetries of linear elasticity. *Appl Mech Rev* **48**:247–285.

Fedorov FI. 1968. *Theory of elastic waves in crystals*. New York: Plenum Press.

Fraldi M, Cowin SC. 2002. Chirality in the torsion of cylinders with trigonal material symmetry. *J Elast* **69**:121–148.

Hull D. 1981. *An introduction to composite materials*. Cambridge: Cambridge UP.

Neville C. 1993. *Biology of fibrous composites*. Cambridge: Cambridge UP.

Nye JF. 1957. *Physical properties of crystals*. Oxford: Clarendon Press.

Rovati M, Taliercio A. 2003. Stationarity of the strain energy density for some classes of anisotropic solids. *Int J Solids Struct* **40**:6043–6075.

Shubnikov AV, Koptsik VA. 1974. *Symmetry in science and art*. New York: Plenum.

Tarn JQ. 2002. Stress singularity in an elastic cylinder of cylindrically anisotropic materials. *J Elast* **69**:1–13.

Thompson W (Lord Kelvin). 1904. Baltimore lectures on molecular dynamics and the wave theory of light. London: CJ Clay & Sons.

Wainwight SA, Biggs WD, Currey JD, Gosline JM. 1976. *Mechanical design in organisms*. London: Arnold.

Weyl H. 1952. *Symmetry*. Princeton: Princeton UP.

# 6

# FORMULATION OF CONSTITUTIVE EQUATIONS

The theme for this chapter is contained in a quote from Truesdell and Noll's volume on the *Non-Linear Field Theories of Mechanics*: "The general physical laws in themselves do not suffice to determine the deformation or motion of … an object ... subject to given loading. Before a determinate problem can be formulated, it is usually necessary to specify the material of which the ... object ... is made. In the program of continuum mechanics, such specification is stated by constitutive equations, which relate the stress tensor and the heat-flux vector to the motion. For example, the classical theory of elasticity rests upon the assumption that the stress tensor at a point depends linearly on the changes of length and mutual angle suffered by elements at that point, reckoned from their configurations in a state where the external and internal forces vanish, while the classical theory of viscosity is based on the assumption that the stress tensor depends linearly on the instantaneous rates of change of length and mutual angle. These statements cannot be universal laws of nature, since they contradict one another. Rather, they are definitions of ideal materials. The former expresses in words the constitutive equation that defines a linearly and infinitesimally elastic material; the latter, a linearly viscous fluid. Each is consistent, at least to within certain restrictions, with the general principles of continuum mechanics, but in no way a consequence of them. There is no reason a priori why either should ever be physically valid, but it is an empirical fact, established by more than a century of test and comparison, that each does indeed represent much of the mechanical behavior of many natural substances of the most various origin, distribution, touch, color, sound, taste, smell, and molecular constitution. Neither represents all the attributes, or suffices even to predict all the mechanical behavior, of any one natural material. No natural ... object ... is perfectly elastic, or perfectly fluid, any more than any is perfectly rigid or perfectly incompressible. These trite observations do not lessen the worth of the two particular constitutive equations just mentioned. That worth is twofold: First, each represents in ideal form an aspect, and a different one, of the mechanical behavior of nearly all natural materials, and, second, each does predict with considerable though sometimes not sufficient accuracy the observed response of many different natural materials in certain restricted situations."

## 6.1. GUIDELINES FOR THE FORMULATION OF CONSTITUTIVE EQUATIONS

The conservation principles of mass, linear momentum, angular momentum, and energy do not yield, in general, a sufficient number of equations to determine all the unknown variables for a physical system. These conservation principles must hold for all materials and therefore give no information about the particular material of which the system is composed, be it fluid or solid, bone, concrete or steel, blood, oil, honey, or water. Additional equations must be developed to describe the material of the system and to complete the set of equations involving the variables of the system so that the set of equations consisting of these additional equations and the conservation equations are solvable for the variables.

Equations that characterize the physical properties of the material of a system are called "constitutive equations." Each material has a different constitutive equation to describe each of its physical properties. Thus, there is one constitutive equation to describe the mechanical response of steel to applied stress and another to describe the mechanical response of water to applied stress. Constitutive equations are contrasted with conservation principles in that conservation principles must hold for all materials while constitutive equations only hold for a particular property of a particular material. The purpose of this chapter is to present the guidelines generally used in the formulation of constitutive equations, and to illustrate their application by developing four classical continuum constitutive relations — namely, Darcy's law for mass transport in a porous medium, Hooke's law for elastic materials, the Newtonian law of viscosity, and the constitutive relations for viscoelastic materials.

## 6.2. CONSTITUTIVE IDEAS

The basis for a constitutive equation is a constitutive idea, that is to say, an idea taken from physical experience or experiment that describes how real materials behave under a specified set of conditions. For example, the constitutive idea of the elongation of a bar being proportional to the axial force applied to the ends of the bar is expressed mathematically by the constitutive equation called Hooke's law. Another example of a constitutive idea is that, in a saturated porous medium the fluid flows from regions of higher pressure to regions of lower pressure; this idea is expressed mathematically by the constitutive equation called Darcy's law for fluid transport in a porous medium. It is not a simple task to formulate a constitutive equation from a constitutive idea. The constitutive idea expresses a notion concerning some aspect of the behavior of real materials, a notion based on the physics of the situation that might be called physical insight. The art of formulating constitutive equations is to turn the physical insight into a mathematical equation. The conversion of insight into equation can never be exact because the equation is precise and limited in the amount of information it can embody while the constitutive idea is embedded in one's entire understanding of the physical situation. The fine art in the formulation of constitutive equations is to extract from the physical situation under consideration the salient constitutive idea and then express its essence in an equation.

The four classical constitutive ideas employed here as examples are described in this paragraph. Darcy's law for mass transport in a porous medium may be considered as arising from the idea that, in a saturated porous medium, fluid flows from regions of higher pressure to those of lower pressure. Let $\rho_f$ denote the density of the fluid in the pores of the porous medium, $\rho_o$ denote a constant reference fluid density, and $\phi$ denote the porosity of the medium. The velocity of the fluid $\mathbf{v}$ passing through the pores is the velocity relative to the solid porous matrix. This constitutive idea is that the fluid volume flux $\mathbf{q} = \phi\rho_f\mathbf{v}/\rho_o$ through the pores, at a

particle **X**, is a function of the pressure variation in the neighborhood of **X**, N(**X**). If $p(\mathbf{X}, t)$ represents the pressure at particle **X** at time $t$, then this constitutive idea is expressed as

$$\mathbf{q} = \phi\rho_f\mathbf{v}/\rho_o = \mathbf{q}(p(\mathbf{X}, t), \mathbf{X}), \text{ all } \mathbf{X}^* \text{ in } N(\mathbf{X}). \tag{6.1D}$$

Note that **q** has the dimensions of volume flow per unit area, which means it is the volume flow rate of fluid across a certain surface area. The volume flow rate, **q**, is the flow rate relative to the solid porous matrix. The constitutive idea for Fourier's law of heat conduction and Fick's law for diffusion of a solute in a solvent have the same mathematical structure as Darcy's law for mass transport in a porous medium. The constitutive idea for Fourier's law of heat conduction is that heat flows from regions of higher temperature to those of lower temperature. The constitutive idea for Fick's law for diffusion of a solute in a solvent is that a solute diffuses from regions of higher solute concentration to those of lower solute concentration. The development of Fourier's law and Fick's law is parallel to the development of Darcy's law. For the Fourier law the volume flux per unit area, **q**, is replaced by the heat flux vector and the pressure is replaced by the temperature. For Fick's law for diffusion of a solute in a solvent the volume flux per unit area, **q**, is replaced by the diffusion flux vector and the pressure is replaced by the concentration of the solute. These substitutions will extend most of what is recorded in this chapter about Darcy's law to the Fourier and Fick laws.

In the development of the remaining constitutive equations, those that assume that stress is a function of different kinematic variables, the stress will be denoted as a vector in six dimensions, $\hat{\mathbf{T}}$, rather than a tensor in three dimensions, **T** (see §A.11). The six-dimensional representation has advantages in the formulation of constitutive equations. The main advantage in the present chapter is that all the constitutive ideas to be developed will then have a similar structure except that some will be in three dimensions and the rest in six dimensions. The constitutive idea for Hooke's law is that of a spring. If a force displaces the end of a spring, there is a relationship between the force and the resulting displacement. Thus, to develop Hooke's law, stress $\hat{\mathbf{T}}$ at particle **X** is expressed as a function of the variation in the displacement field $\mathbf{u}(\mathbf{X}, t)$ in the neighborhood of **X**, N(**X**),

$$\hat{\mathbf{T}} = \hat{\mathbf{T}}(\mathbf{u}(\mathbf{X}, t), \mathbf{X}), \text{ all } \mathbf{X}^* \text{ in } N(\mathbf{X}). \tag{6.1H}$$

The constitutive idea for the Newtonian law of viscosity is that of the dashpot or damper, namely, that the force is proportional to the rate at which the deformation is accomplished rather than to the size of the deformation itself. The total stress in a viscous fluid is the sum of the viscous stresses, $\mathbf{T}_v$, plus the fluid pressure $p$: $\mathbf{T} = -p\mathbf{1} + \mathbf{T}_v$. The constitutive idea for the Newtonian law of viscosity is that stress $\hat{\mathbf{T}}_v$, due to the viscous effects at particle **X**, is expressed as a function of the variation in the velocity field, $\mathbf{v}(\mathbf{X}, t)$ in the neighborhood of **X**, N(**X**). The expression for the total stress in a fluid is the pressure plus the viscous stresses:

$$\hat{\mathbf{T}} = -p\hat{\mathbf{U}} + \hat{\mathbf{T}}_v(\mathbf{v}(\mathbf{X}, t), \mathbf{X}), \text{ all } \mathbf{X}^* \text{ in } N(\mathbf{X}). \tag{6.1N}$$

Recall that $\hat{\mathbf{U}}$ is the six-dimensional vector with components {1,1,1,0,0,0}; it is the image of three-dimensional unit tensor **1** in six dimensions. Each of the three constitutive ideas described yields the value of a flux or stress at time $t$ due to the variation in a field (temperature, pressure, displacement, velocity) at particle **X** at time $t$. The constitutive idea for viscoelasticity is different in that the stress at time $t$ is assumed to depend upon the entire history of a field, the displacement field. Thus, while the first three constitutive ideas are expressed as functions, the constitutive idea for viscoelasticity is expressed as a functional of the history of the displacement field. A functional is like a function, but rather than being evaluated at a particular

value of its independent variables like a function, it requires an entire function to be evaluated; a functional is a function of function(s). An example of a functional is the value of an integral in which the integrand is a variable function. The constitutive idea for a viscoelastic material is that stress $\hat{\mathbf{T}}$ at particle $\mathbf{X}$ is a function of the variation in the history of the velocity field $\mathbf{v}(\mathbf{X}, t)$ in the neighborhood of $\mathbf{X}$, $\mathsf{N}(\mathbf{X})$,

$$\hat{\mathbf{T}} = \int_{s=0}^{\infty} \hat{\mathbf{T}}(\mathbf{v}(\mathbf{X}, t-s), s, \mathbf{X}) ds, \text{ all } \mathbf{X}^* \text{ in } \mathsf{N}(\mathbf{X}), \tag{6.1V}$$

where $s$ is a backward running time variable that is 0 at the present instant and increases with events more distant in the past. Thus stress $\hat{\mathbf{T}}$ at particle $\mathbf{X}$ is a function of the entire history of the displacement of the particle; to evaluate the stress, a knowledge of the entire history is required. In the sections that follow this one, these four constitutive ideas will be developed into linear constitutive equations.

**Problem**

6.2.1. Record a rigorous definition of the neighborhood of particle $\mathbf{X}$, $\mathsf{N}(\mathbf{X})$, using reference particle $\mathbf{X}^*$, small positive number $\varepsilon$, and length measure $\|\mathbf{X} - \mathbf{X}^*\|$. Note that this neighborhood is, in general, a three-dimensional neighborhood.

## 6.3. LOCALIZATION

A constitutive equation valid at particle $\mathbf{X}$ of a material object can depend upon the behavior of the material in the neighborhood of particle $\mathbf{X}$, $\mathsf{N}(\mathbf{X})$, but is unlikely to depend upon the behavior of the material in regions of the object far removed from particle $\mathbf{X}$. The localization guideline for the development of constitutive relations restricts the dependence of constitutive equations valid for particle $\mathbf{X}$ to events that occur in $\mathsf{N}(\mathbf{X})$. The application of the localization guideline to the four constitutive equations described in the previous section is described in the next paragraph.

The constitutive idea for Darcy's law is considered first. Pressure field $p(\mathbf{X}^*, t)$ at particle $\mathbf{X}^*$ in $\mathsf{N}(\mathbf{X})$ may be related to pressure field $\mathrm{p}(\mathbf{X}, t)$ at particle $\mathbf{X}$ by a Taylor series expansion about the point by

$$p(\mathbf{X}^*, t) = p(\mathbf{X}, t) + (\nabla p(\mathbf{X}, t))\cdot(\mathbf{X} - \mathbf{X}^*) + \text{higher-order terms}, \tag{6.2}$$

where it is assumed that the pressure field is sufficiently smooth to permit this differentiation. With the Taylor theorem as justification, $\mathsf{N}(\mathbf{X})$ may always be selected sufficiently small so that the value of pressure field $p(\mathbf{X}^*, t)$ at particle $\mathbf{X}^*$ in $\mathsf{N}(\mathbf{X})$ may be represented by $p(\mathbf{X}, t)$ and $\nabla p(\mathbf{X}, t)$. Thus, by localization, (6.1D) may be rewritten as

$$\mathbf{q} = \phi\rho_f\mathbf{v}/\rho_o = \mathbf{q}(p(\mathbf{X}, t), \nabla p(\mathbf{X}, t), \mathbf{X}). \tag{6.3D}$$

Exactly the same argument is applicable to the other three constitutive ideas; thus, we have that

$$\hat{\mathbf{T}} = \hat{\mathbf{T}}(\mathbf{u}(\mathbf{X}, t), \nabla\otimes\mathbf{u}(\mathbf{X}, t), \mathbf{X}), \tag{6.3H}$$

$$\hat{\mathbf{T}} = -p\hat{\mathbf{U}} + \hat{\mathbf{T}}_v(\mathbf{v}(\mathbf{X}, t), \nabla\otimes\mathbf{v}(\mathbf{X}, t), \mathbf{X}), \tag{6.3N}$$

and,

$$\hat{\mathbf{T}} = \int_{s=0}^{\infty} \hat{\mathbf{T}}(\mathbf{v}(\mathbf{X},t-s),\, \nabla \otimes \mathbf{v}(\mathbf{X},t-s),\mathbf{X},s)\, ds\,. \tag{6.3V}$$

**Problem**

6.3.1. Record a complete statement of Taylor's theorem in the case of three independent variables for function $f(\mathbf{X})$ using point $\mathbf{X}_o$ as the point about which the expansion occurs.

## 6.4. INVARIANCE UNDER RIGID OBJECT MOTIONS

This guideline for the development of constitutive relations restricts the independent variables and functional dependence of constitutive equations for material behavior by requiring that the constitutive equations be independent of the motions of the object that do not deform the object. The motions of the object that do not deform the object are rigid object motions. This guideline requires that constitutive equations for material behavior be independent of, that is to say unchanged by, superposed rigid object motions. As an illustration consider the object shown in Figure 6.1. If the object experiences a translation and a rigid object rotation such that the force system acting on the object is also translated and rotated, then the state of stress $\mathbf{T}(\mathbf{X}, t)$ at any particle $\mathbf{X}$ is unchanged. As a second example, recall that volume flow rate $\mathbf{q}$ is the flow rate relative to the solid porous matrix. It follows that volume flow rate $\mathbf{q}$ in a porous medium is unchanged by (virtual or very slow) superposed rigid object motions.

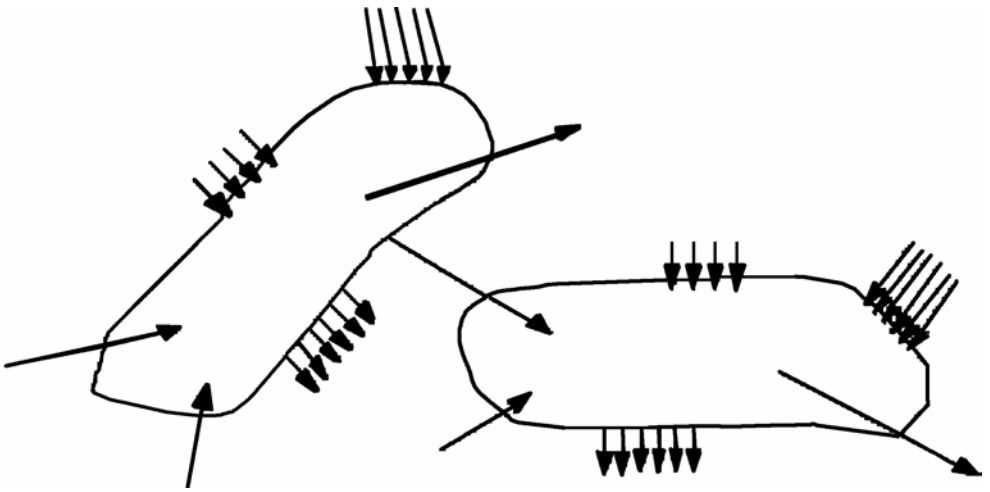


**Figure 6.1**. A rigid object rotation of an object, a rotation that includes the force system that acts upon the object.

Application of this guideline of invariance under rigid object motions is illustrated by application to the three constitutive ideas involving stress. The two constitutive ideas involving fluxes automatically satisfy this guideline because the fluxes are defined relative to the mate-

rial object and the rigid motion does not change the temperature field or the pressure field. The constitutive idea for Hooke's law (6.3H) may be rewritten as

$$\hat{\mathbf{T}} = \hat{\mathbf{T}}\,(\mathbf{u}(\mathbf{X}, t), \mathbf{E}(\mathbf{X}, t), \mathbf{Y}(\mathbf{X}, t), \mathbf{X}), \tag{6.4H}$$

where the tensor of displacement gradients, $\nabla\otimes\mathbf{u}(\mathbf{X}, t)$, has been replaced by its symmetric part, infinitesimal strain tensor $\mathbf{E}(\mathbf{X}, t)$, defined by (3.41), and its skew symmetric part, infinitesimal rotation tensor $\mathbf{Y}(\mathbf{X}, t)$, also defined by (3.41). In a similar way, the tensor of velocity gradients, $\nabla\otimes\mathbf{v}(\mathbf{X}, t)$, may be replaced by its symmetric part, rate of deformation tensor $\mathbf{D}(\mathbf{X}, t)$ defined by (3.32), and its skew symmetric part, spin tensor $\mathbf{W}(\mathbf{X}, t)$, also defined by (3.32):

$$\hat{\mathbf{T}} = -p\,\hat{\mathbf{U}} + \hat{\mathbf{T}}_v\ (\mathbf{v}(\mathbf{X}, t), \mathbf{D}(\mathbf{X}, t), \mathbf{W}(\mathbf{X}, t), \mathbf{X}). \tag{6.4N}$$

Finally, decomposing the tensor of velocity gradients, $\nabla\otimes\mathbf{v}(\mathbf{X}, t - s)$, as in the case of the Newtonian law of viscosity, the viscoelastic constitutive relation (6.3V) takes the form

$$\hat{\mathbf{T}} = \int_{s=0}^{\infty} \hat{\mathbf{T}}(\mathbf{v}(\mathbf{X}, t-s), \mathbf{D}(\mathbf{X}, t-s), \mathbf{W}(\mathbf{X}, t-s), \mathbf{X}, s)ds\ . \tag{6.4V}$$

This guideline requires that constitutive equations remain unchanged by superposed rigid object motions; thus, measures of translational motion, like displacement $\mathbf{u}(\mathbf{X}, t)$ and velocity $\mathbf{v}(\mathbf{X}, t)$, and measures of rotational motion, like infinitesimal rotation tensor $\mathbf{Y}(\mathbf{X}, t)$ and spin tensor $\mathbf{W}(\mathbf{X}, t)$, must be excluded from the equations above. Using this guideline the form of these three constitutive ideas is then reduced to

$$\hat{\mathbf{T}} = \hat{\mathbf{T}}(\hat{\mathbf{E}}(\mathbf{X}, t), \mathbf{X}), \tag{6.5H}$$

$$\hat{\mathbf{T}} = -p\hat{\mathbf{U}} + \hat{\mathbf{T}}_v(\hat{\mathbf{D}}(\mathbf{X}, t), \mathbf{X}), \tag{6.5N}$$

and

$$\hat{\mathbf{T}} = \int_{s=0}^{\infty} \hat{\mathbf{T}}(\hat{\mathbf{D}}(\mathbf{X}, t-s), \mathbf{X}, s)ds\ , \tag{6.5V}$$

where three-dimensional tensors $\mathbf{E}(\mathbf{X},t)$ and $\mathbf{D}(\mathbf{X},t)$ have been replaced by their six-dimensional vector equivalents, $\hat{\mathbf{E}}(\mathbf{X},t)$ and $\hat{\mathbf{D}}(\mathbf{X},t)$, respectively.

## 6.5. DETERMINISM

A constitutive equation valid for a material at time $t$ must depend upon events that are occurring to the material at instant $t$ and upon events that have occurred to the material in the past. The constitutive equation cannot depend upon events that will occur to the material in the future. For example, the constitutive assumption for elastic materials is that the stress depends upon the strain between a previous unstressed reference configuration and the instantaneous configuration of the object. All four of the constitutive equations satisfy this guideline. The first four satisfy it because all the variables entering the relationships are at time $t$. The viscoelastic constitutive relation satisfies the guideline by only depending upon past events.

## 6.6. LINEARIZATION

Each of the constitutive ideas considered has been reduced to the form of a vector-valued ($\mathbf{q}$ or $\hat{\mathbf{T}}$) function or functional of another vector ($\nabla p$, $\hat{\mathbf{E}}$ or $\hat{\mathbf{D}}$), $\mathbf{X}$, and some scalar parameters. It is assumed that each of these vector-valued functions is linear in the vector argument, thus each may be represented by a linear transformation. For Darcy's law the second-order tensor in three dimensions represents the coefficients of the linear transformation and, due to the dependence of the volume flow rate upon pressure, this second-order tensor admits the functional dependency indicated:

$$\mathbf{q} = \phi\rho_f\mathbf{v}/\rho_o = -\mathbf{H}(p, \mathbf{X})\cdot\nabla p(\mathbf{X}, t). \tag{6.6D}$$

The minus sign was placed in (6.6D) to indicate that volume fluid flux $\mathbf{q}$ will be directed down the pressure gradient, from domains of higher pore fluid pressure to domains of lower pressure.

For the three constitutive ideas involving stress vector $\hat{\mathbf{T}}$, second-order tensors in six dimensions represent the coefficients of the linear transformation:

$$\hat{\mathbf{T}} = \hat{\mathbf{C}}(\mathbf{X})\cdot\hat{\mathbf{E}}(\mathbf{X},t), \tag{6.6H}$$

$$\hat{\mathbf{T}} = -p\hat{\mathbf{U}} + \hat{\mathbf{N}}(\mathbf{X})\cdot\hat{\mathbf{D}}(\mathbf{X},t), \tag{6.6N}$$

and

$$\hat{\mathbf{T}} = \int_{s=0}^{\infty} \hat{\mathbf{G}}(\mathbf{X},s)\cdot\hat{\mathbf{D}}(\mathbf{X},t-s)ds. \tag{6.6V}$$

Six-dimensional second-order tensors $\hat{\mathbf{C}}(\mathbf{X})$ and $\hat{\mathbf{N}}(\mathbf{X})$ are for Hooke's law and the Newtonian law of viscosity, respectively. Six-dimensional second-order tensor function $\hat{\mathbf{G}}(\mathbf{X},s)$ represents the viscoelastic coefficients.

**Problem**

6.6.1. Record the explicit matrix form for the constitutive relation for the Darcy medium (6.6D) and for Hooke's law (6.6H).

## 6.7. COORDINATE INVARIANCE

Since the representation of physical phenomena must be independent of the observer, it is necessary to express physical quantities in ways that are independent of coordinate systems. This is because different observers may select different coordinate systems. It therefore becomes a requirement that physical quantities be invariant of the coordinate system selected to express them. On the other hand, in order to work with these physical quantities, it is necessary to refer physical quantities to coordinate systems. In particular, a constitutive equation should be expressed by a relation that holds in all admissible coordinate systems at a fixed time. The admissible coordinate systems may be any coordinate system possible in a Euclidean three-dimensional space. A sufficient condition for the satisfaction of this requirement is to state the constitutive equations in tensorial form since tensors are independent of any particular coordinate system, although their components may be written relative to any particular one. In classical mechanics the essential concepts of force, velocity, and acceleration are all vectors; hence,

the mathematical language of classical mechanics is that of vectors. In the mechanics of deformable media the essential concepts of stress, strain, rate of deformation, etc., are all second-order tensors; thus, by analogy, one can expect to deal quite frequently with second-order tensors in this branch of mechanics. The constitutive ideas that are developed in this chapter satisfy the requirement of coordinate invariance by virtue of being cast as tensorial expressions.

## 6.8. HOMOGENEOUS VERSUS INHOMOGENEOUS CONSTITUTIVE MODELS

A material property is said to be *homogeneous* when it is the same at all particles $\mathbf{X}$ in the object, and *inhomogeneous* if it varies from particle to particle in an object. Most biological materials are inhomogeneous, and many manufactured materials are considered to be homogeneous. Each of constitutive relations (6.6D), (6.6H), (6.6N), and (6.6V) is presented as inhomogeneous because the tensors representing their material coefficients, $\mathbf{H}(p,\mathbf{X})$, $\hat{\mathbf{C}}(\mathbf{X})$, $\hat{\mathbf{N}}(\mathbf{X})$, and $\hat{\mathbf{G}}(\mathbf{X},s)$, respectively, are allowed to depend upon particle $\mathbf{X}$. If the dependence upon $\mathbf{X}$ does not occur, or can be neglected, then the material is homogeneous and constitutive equations (6.6D), (6.6H), (6.6N), and (6.6V) take the form

$$\mathbf{q} = \phi\rho_f\mathbf{v}/\rho_o = -\mathbf{H}(p)\cdot\nabla p(\mathbf{x}, t), \tag{6.7D}$$

$$\hat{\mathbf{T}} = \hat{\mathbf{C}}\cdot\hat{\mathbf{E}}(\mathbf{x},t)\,, \tag{6.7H}$$

$$\hat{\mathbf{T}} = -p\hat{\mathbf{U}} + \hat{\mathbf{N}}\cdot\hat{\mathbf{D}}(\mathbf{x},t)\,, \tag{6.7N}$$

and

$$\hat{\mathbf{T}} = \int_{s=0}^{\infty} \hat{\mathbf{G}}(s)\cdot\hat{\mathbf{D}}(\mathbf{x},t-s)ds\,. \tag{6.7V}$$

Note that, in the constitutive expressions above, not only has the dependence of the material coefficient tensors been removed by eliminating their dependence upon particle $\mathbf{X}$, but also $\mathbf{X}$ has been replaced by $\mathbf{x}$ everywhere else. For the two constitutive relations restricted to infinitesimal motions, (6.7H) and (6.7V), and the constitutive relations based on a rigid continuum, (6.7D), there is no difference between $\mathbf{X}$ and $\mathbf{x}$ (see §3.4), hence $\mathbf{x}$ could have been used from the beginning of the chapter. For the Newtonian law of viscosity, however, the assumption of homogeneity is much more significant because it permits elimination of $\mathbf{X}$ from the entire constitutive relation, a constitutive relation that is not restricted to infinitesimal deformations. Thus, even though (6.7N) applies for large deformations, it is independent of $\mathbf{X}$. The Newtonian law is different from the other four constitutive relations in another way, detailed in the next section.

## 6.9. RESTRICTIONS DUE TO MATERIAL SYMMETRY

The results of the previous chapter are used in this section to further specify the form of the constitutive relations. Isotropy, or any type of anisotropy, is possible for three constitutive relations, (6.7D), (6.7H) and (6.7V), that are, or may be, applied to solid or semi-solid materials. The type of anisotropy is expressed in the forms of the tensors of material coefficients, $\mathbf{H}$, $\hat{\mathbf{C}}$, and $\hat{\mathbf{G}}(s)$, respectively. Once the type of anisotropy possessed by the solid or semi-solid mate-

rial to be modeled has been determined, the appropriate form of $\mathbf{H}$ may be selected from Table 5.3 or the form of $\hat{\mathbf{C}}$ or $\hat{\mathbf{G}}(s)$ from Table 5.4. Thus, for these three constitutive relations any type of material symmetry is possible.

The concepts of anisotropy and inhomogeneity of materials are sometimes confused. A constitutive relation is inhomogeneous or homogeneous depending upon whether the material coefficients (i.e., $\mathbf{H}$, $\hat{\mathbf{C}}$, and $\hat{\mathbf{G}}(s)$) depend upon $\mathbf{X}$ or not. The type of material symmetry, that is to say either isotropy or the type of anisotropy characterizing a constitutive, relation is reflected in the form of the material coefficient tensors ($\mathbf{H}$, $\hat{\mathbf{C}}$ or $\hat{\mathbf{G}}(s)$), for example, the forms listed in Tables 5.3 and 5.4. Tensor $\mathbf{H}$ may have any of the forms in Table 5.3 and tensor $\hat{\mathbf{C}}$ may have any of the forms in Table 5.4. Material symmetry, that is to say the isotropy or type of anisotropy, is the property of a constitutive relation at particle $\mathbf{X}$, while inhomogeneity or homogeneity of materials relates to how the material properties change from particle to particle. Thus, a constitutive relation may be either anisotropic and homogeneous or anisotropic and inhomogeneous. The most mathematically simplifying assumptions are those of an isotropic symmetry and homogeneous material.

The Newtonian law of viscosity, (6.7N), is characterized by these most simplifying assumptions: homogeneity and isotropy. These assumptions are easily justified when one thinks about the structure of, say, distilled water. Absent gravity, there is no preferred direction in distilled water, and distilled water has the same mechanical and thermal properties at all locations in the volume and in all volumes of distilled water. One can then generalize this thought process to see that most fluids are isotropic.

The isotropic form of the Newtonian law of viscosity, (6.7N), is obtained by using the representation for the isotropic form of $\hat{\mathbf{N}}$ obtained from Table 5.4, thus

$$\begin{bmatrix} \hat{T}_1 + p \\ \hat{T}_2 + p \\ \hat{T}_3 + p \\ \hat{T}_4 \\ \hat{T}_5 \\ \hat{T}_6 \end{bmatrix} = \begin{bmatrix} \hat{N}_{11} & \hat{N}_{12} & \hat{N}_{12} & 0 & 0 & 0 \\ \hat{N}_{12} & \hat{N}_{11} & \hat{N}_{12} & 0 & 0 & 0 \\ \hat{N}_{12} & \hat{N}_{12} & \hat{N}_{11} & 0 & 0 & 0 \\ 0 & 0 & 0 & \hat{N}_{11} - \hat{N}_{12} & 0 & 0 \\ 0 & 0 & 0 & 0 & \hat{N}_{11} - \hat{N}_{12} & 0 \\ 0 & 0 & 0 & 0 & 0 & \hat{N}_{11} - \hat{N}_{12} \end{bmatrix} \begin{bmatrix} \hat{D}_1 \\ \hat{D}_2 \\ \hat{D}_3 \\ \hat{D}_4 \\ \hat{D}_5 \\ \hat{D}_6 \end{bmatrix}, \tag{6.8N}$$

This six-dimensional representation is converted to the three-dimensional representation by employing relations (A163) and introducing the following new notation for the two distinct elements of the 6-by-6 matrix in (6.8N):

$$\hat{N}_{11} = \lambda + 2\mu\,,\ \hat{N}_{12} = \lambda\,, \tag{6.9N}$$

then

$$\begin{bmatrix} T_{11} + p \\ T_{22} + p \\ T_{33} + p \\ \sqrt{2}T_{23} \\ \sqrt{2}T_{13} \\ \sqrt{2}T_{12} \end{bmatrix} = \begin{bmatrix} \lambda + 2\mu & \lambda & \lambda & 0 & 0 & 0 \\ \lambda & \lambda + 2\mu & \lambda & 0 & 0 & 0 \\ \lambda & \lambda & \lambda + 2\mu & 0 & 0 & 0 \\ 0 & 0 & 0 & 2\mu & 0 & 0 \\ 0 & 0 & 0 & 0 & 2\mu & 0 \\ 0 & 0 & 0 & 0 & 0 & 2\mu \end{bmatrix} \begin{bmatrix} D_{11} \\ D_{22} \\ D_{33} \\ \sqrt{2}D_{23} \\ \sqrt{2}D_{13} \\ \sqrt{2}D_{12} \end{bmatrix}, \tag{6.10N}$$

or

$$T_{11} + p = \lambda \mathrm{tr}\mathbf{D} + 2\mu D_{11},\ T_{22} + p = \lambda \mathrm{tr}\mathbf{D} + 2\mu D_{22},\ T_{33} + p = \lambda \mathrm{tr}\mathbf{D} + 2\mu D_{33},$$

$$T_{23} = 2\mu D_{23},\ T_{13} = 2\mu D_{13},\ T_{12} = 2\mu D_{12},$$

where $\lambda$ and $\mu$ are viscosity coefficients. It is easy to see that the constitutive relation may be rewritten in three dimensions as

$$\mathbf{T} + p\mathbf{1} = \lambda(\mathrm{tr}\mathbf{D})\mathbf{1} + 2\mu\mathbf{D}. \tag{6.11N}$$

This is the form of the constitutive equation for a viscous fluid, the pressure plus the Newtonian law of viscosity, which will be used in the remainder of the text.

**Problems**

6.9.1. Record the explicit matrix form for the constitutive relation for a Darcy porous medium in an inhomogeneous transversely isotropic material.

6.9.2. Record the explicit matrix form for the constitutive relation for Darcy's law in a homogeneous isotropic material.

6.9.3. Record the explicit matrix form for the constitutive relation for Hooke's law in a homogeneous orthotropic material.

6.9.4. Record the explicit matrix form for the constitutive relation for a transversely isotropic, homogeneous viscoelastic material.

6.9.5. Show that the eigenvalues of (6.10N) are $3\lambda + 2\mu$ and $2\mu$ and specify how many times each is repeated.

6.9.6. Describe the criteria for the selection of an RVE (and associated $L_{\mathrm{RVE}}$) to be employed for a porous medium to which Darcy's law is to be applied.

## 6.10. THE SYMMETRY OF THE MATERIAL COEFFICIENT TENSORS

In this section the question of the symmetry of the matrices of the tensors of material coefficients, $\mathbf{H}$, $\hat{\mathbf{C}}$, $\hat{\mathbf{N}}$, and $\hat{\mathbf{G}}(s)$, is considered. Consider first tensor of material coefficients $\hat{\mathbf{N}}$ for a Newtonian viscous fluid. In the previous section it was assumed that a Newtonian viscous fluid was isotropic; therefore, from Table 5.3, tensor of material coefficients $\hat{\mathbf{N}}$ is symmetric. In this case the material symmetry implied the symmetry of the tensor of material coefficients. A similar symmetry result emerges for permeability tensor $\mathbf{H}$ if only orthotropic symmetry or greater symmetry is considered. To see that material symmetry implies the symmetry of tensor of material coefficients $\mathbf{H}$, if only orthotropic symmetry or greater symmetry is considered, one need only consult Table 5.3. The symmetry of $\mathbf{H}$ is also true for symmetries less than orthotropic, namely monoclinic and triclinic, but the proof will not be given here. Finally, $\hat{\mathbf{G}}(s)$ is never symmetric unless the viscoelastic model is in the limiting cases of $\hat{\mathbf{G}}(0)$ or $\hat{\mathbf{G}}(\infty)$, where the material behavior is elastic.

The symmetry of tensor of elastic material coefficients $\hat{\mathbf{C}}$ is the only coefficient tensor symmetry remaining to be demonstrated in this section. In this development, the inverse of (6.7H), the strain–stress relation, rather than the stress-strain relation, is employed

$$\hat{\mathbf{E}} = \hat{\mathbf{S}} \cdot \hat{\mathbf{T}},\quad \hat{\mathbf{S}} = \hat{\mathbf{C}}^{-1}, \tag{6.12H}$$

where $\hat{\mathbf{S}}$ is the compliance tensor of elastic material coefficients. The form and symmetry of $\hat{\mathbf{C}}$ and $\hat{\mathbf{S}}$ are identical for any material, and it is easy to show that the symmetry of one implies the symmetry of the other. The symmetry of $\hat{\mathbf{C}}$ and $\hat{\mathbf{S}}$ follows from the requirement that the work done on an elastic material in a closed cycle vanish. This requirement stems from the argument that if work can be done on the material in some closed cycle, then the cycle can be reversed and the material can do work in the reversed closed cycle. This would imply that work could be extracted from the material in a closed loading cycle. Thus, one would be able to take an inert elastic material and extract work from it. This situation is not logical, and it is therefore required that the work done on an elastic material in a closed loading cycle vanish. We express the work done on the material between strain $\hat{\mathbf{E}}^{(1)}$ and strain $\hat{\mathbf{E}}^{(2)}$ by

$$W_{12} = \int_1^2 \hat{\mathbf{T}} \cdot d\hat{\mathbf{E}} \,, \tag{6.13H}$$

and for a closed loading cycle it is required that

$$\oint \hat{\mathbf{T}} \cdot d\hat{\mathbf{E}} = 0 \,. \tag{6.14H}$$

Consider the work done in a closed loading cycle applied to a unit cube of a linear anisotropic elastic material. The loading cycle begins from an unstressed state and contains the following four loading sequences (Figure 6.2a): $0 \rightarrow$ A, the stress is increased slowly from 0 to $\hat{T}_i^A$; $A \rightarrow B$, holding stress state $\hat{T}_i^A$ constant, the second stress is increased slowly from $\hat{T}_i^A$ to $\hat{T}_i^A + \hat{T}_i^B$, $\hat{T}_i^B \neq \hat{T}_i^A$; $B \rightarrow C$, holding second stress state $\hat{T}_i^B$ constant, the first stress is decreased slowly from $\hat{T}_i^A + \hat{T}_i^B$ to $\hat{T}_i^B$; and $C \rightarrow 0$, the stress is decreased slowly from $\hat{T}_i^B$ to 0. At the end of this loading cycle the object is again in an unstressed state. The work done in (6.13H) on each of these loading sequences is expressed as an integral in stress:

$$W_{12} = \int_1^2 \hat{\mathbf{T}} \cdot d\hat{\mathbf{E}} = \int_1^2 \hat{\mathbf{E}} \cdot d\hat{\mathbf{T}} \,. \tag{6.15H}$$

The integral over the first loading sequence of the cycle, from 0 to $\hat{T}_i^A$, is given by

$$W_{OA} = \int_O^A \hat{\mathbf{E}} \cdot d\hat{\mathbf{T}} = \int_O^A \sum_1^6 \hat{E}_i d\hat{T}_i = \sum_{i=1}^6 \int_O^A \hat{E}_i d\hat{T}_i = \sum_{i,j=1}^6 \int_O^A \hat{\mathbf{S}}_{ij} \hat{T}_j d\hat{T}_i = \frac{1}{2} \sum_{i,j=1}^6 \hat{\mathbf{S}}_{ij} \hat{T}_j^{(A)} \hat{T}_i^{(A)} \,. \tag{6.16H}$$

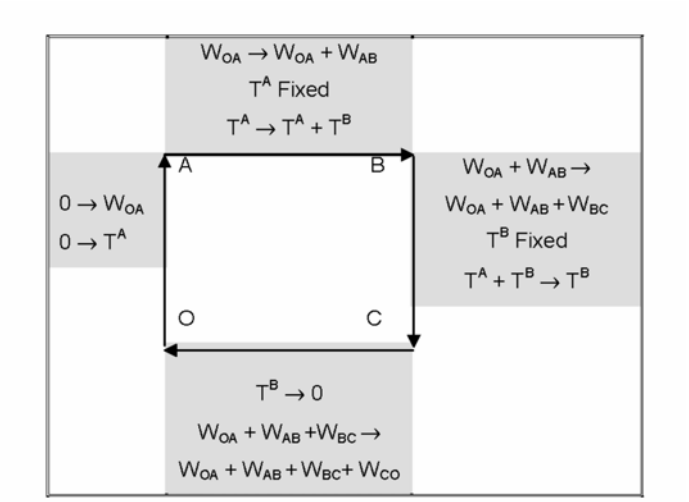
The integral over the second loading sequence of the cycle, from $\hat{T}_i^A$ to $\hat{T}_i^A + \hat{T}_i^B$, $\hat{T}_i^B \neq \hat{T}_i^A$, is a bit more complicated because the loading of the object begins from a state in which it is subjected to stress $\hat{T}_i^A$, which is held constant during this leg of the cycle. During the second loading sequence the strain is given by

$$\hat{E}_i = \sum_{j=1}^6 \hat{\mathbf{S}}_{ij} (\hat{T}_j^{(A)} + \hat{T}_j) \,, \quad 0 \leq \hat{T}_j \leq \hat{T}_j^{(B)} \tag{6.17H}$$

and the work done from $\hat{T}_i^A$ to $\hat{T}_i^A + \hat{T}_i^B$ is

$$W_{AB} = \sum_{i,j=1}^6 \int_O^B \hat{\mathbf{S}}_{ij} (\hat{T}_j^{(A)} + \hat{T}_j) d\hat{T}_i = \sum_{i,j=1}^6 \hat{\mathbf{S}}_{ij} \hat{T}_j^{(A)} \hat{T}_i^{(B)} + \frac{1}{2} \sum_{i,j=1}^6 \hat{\mathbf{S}}_{ij} \hat{T}_j^{(B)} \hat{T}_i^{(B)} \tag{6.18H}$$

where the factor of one-half does not appear before the first term on the right-hand side because $\hat{T}_i^A$ is held fixed during the second loading sequence in this leg of the loading cycle.



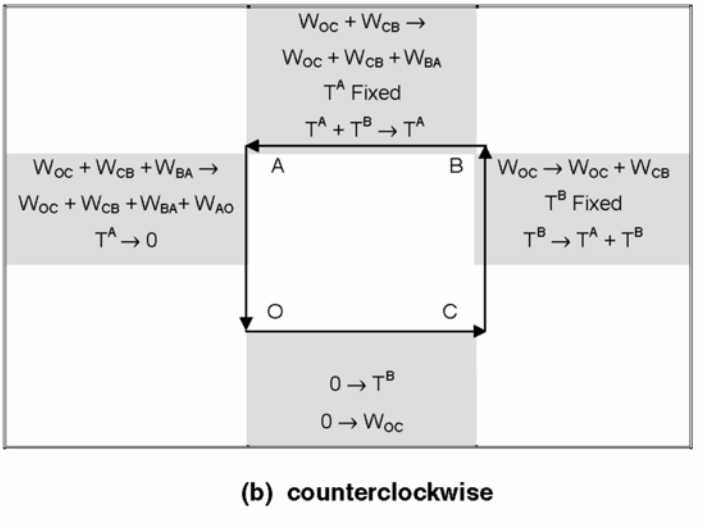




**Figure 6.2**. Illustrations of closed loading cycles. (a) clockwise cycle 0 → A → B → C → 0; (b) counterclockwise cycle 0 → C → B → A → 0. See the text for further explanation.

During the third loading sequence stress $\hat{T}_i^B$ is held fixed; the strain is given by

$$\hat{E}_i = \sum_{j=1}^{6} \hat{\mathbf{S}}_{ij} (\hat{T}_j^{(B)} + \hat{T}_j), \quad 0 \le \hat{T}_j \le \hat{T}_j^{(A)}. \tag{6.19H}$$

The work done during the third loading sequence of the cycle, from $\hat{T}_i^A + \hat{T}_i^B$ to $\hat{T}_i^B$ is then

$$W_{BC} = \sum_{i,j=1}^{6} \int_{A}^{O} \hat{\mathbf{S}}_{ij} (\hat{T}_j^{(B)} + \hat{T}_j) d\hat{T}_i = -\sum_{i,j=1}^{6} \hat{\mathbf{S}}_{ij} \hat{T}_j^{(B)} \hat{T}_i^{(A)} - \frac{1}{2} \sum_{i,j=1}^{6} \hat{\mathbf{S}}_{ij} \hat{T}_j^{(A)} \hat{T}_i^{(A)} . \tag{6.20H}$$

The work done during the final loading sequence, from $\hat{T}_i^B$ to 0, is then

$$W_{CO} = \sum_{i,j=1}^{6} \int_{B}^{O} \hat{\mathbf{S}}_{ij} \hat{T}_j d\hat{T}_i = -\frac{1}{2} \sum_{i,j=1}^{6} \hat{\mathbf{S}}_{ij} \hat{T}_j^{(B)} \hat{T}_i^{(B)} . \tag{6.21H}$$

The work done in the closed cycle is the sum $W_{OO} = W_{OA} + W_{AB} + W_{BC} + W_{CO}$, given by

$$W_{OO} = \sum_{i,j=1}^{6} \hat{\mathbf{S}}_{ij} \hat{T}_j^{(A)} \hat{T}_i^{(B)} - \sum_{i,j=1}^{6} \hat{\mathbf{S}}_{ij} \hat{T}_j^{(B)} \hat{T}_i^{(A)} = \sum_{i,j=1}^{6} (\hat{\mathbf{S}}_{ij} - \hat{\mathbf{S}}_{ji}) \hat{T}_j^{(A)} \hat{T}_i^{(B)} . \tag{6.22H}$$

If the cycle is traversed in reverse (Figure 6.2b), then

$$W_{OO} = -\sum_{i,j=1}^{6} (\hat{\mathbf{S}}_{ij} - \hat{\mathbf{S}}_{ji}) \hat{T}_j^{(A)} \hat{T}_i^{(B)} . \tag{6.23H}$$

This result suggests that, if work is required to traverse the loading cycle in one direction, then work may be extracted by traversing the cycle in the reverse direction. It is common knowledge, however, that it is not possible to extract work from an inert material by mechanical methods. If it were, the world would be a different place. To prevent the possibility of extracting work from an inert material, it is required that $\hat{\mathbf{C}}$ and $\hat{\mathbf{S}}$ be symmetric:

$$\hat{\mathbf{S}} = \hat{\mathbf{S}}^T , \ \hat{\mathbf{C}} = \hat{\mathbf{C}}^T . \tag{6.24H}$$

There are further restrictions on the tensors of material coefficients, and some of them will be discussed in the next section.

The definition of a linear elastic material includes not only the stress–strain relation, $\hat{\mathbf{T}} = \hat{\mathbf{C}} \cdot \hat{\mathbf{E}}(\mathbf{x}, t)$, but also symmetry restriction $\hat{\mathbf{C}} = \hat{\mathbf{C}}^T$, (6.7H) and (6.24H), respectively. Symmetry restriction $\hat{\mathbf{C}} = \hat{\mathbf{C}}^T$ is equivalent to the requirement that the work done on an elastic material in a closed loading cycle is zero (6.14H). The restriction on the work done allows for introduction of a potential, the strain energy $U$. Since the work done on an elastic material in a closed loading cycle is zero, this means that the work done on the elastic material depends only on the initial and final states of stress (strain) and not on the path followed from the initial to the final state. From an initial state of zero stress or strain, strain energy $U$ is defined as the work done (6.15H):

$$U = \int \hat{\mathbf{T}} \cdot d\hat{\mathbf{E}} = \int \hat{\mathbf{E}} \cdot d\hat{\mathbf{T}} . \tag{6.25H}$$

Strain energy $U$ may be considered as a function of either $\hat{\mathbf{T}}$ or $\hat{\mathbf{E}}$, $U(\hat{\mathbf{T}})$ or $U(\hat{\mathbf{E}})$. From (6.25H) and the fundamental theorem of the integral calculus, namely, that the derivative of an integral with respect to its parameter of integration yields the integrand, we have

$$\hat{\mathbf{T}} = \frac{\partial U}{\partial \hat{\mathbf{E}}} \text{ and } \hat{\mathbf{E}} = \frac{\partial U}{\partial \hat{\mathbf{T}}} \quad \left( \text{or } \mathbf{T} = \frac{\partial U}{\partial \mathbf{E}} \text{ and } \mathbf{E} = \frac{\partial U}{\partial T} \right). \tag{6.26H}$$

The following expressions for $U$ are obtained substituting Hooke's law (6.7H) into (6.25H) and then integrating both of the expressions for $U$ in (6.25H):

$$U = \frac{1}{2}\hat{\mathbf{E}}\cdot\hat{\mathbf{C}}\cdot\hat{\mathbf{E}} \text{ and } U = \frac{1}{2}\hat{\mathbf{T}}\cdot\hat{\mathbf{S}}\cdot\hat{\mathbf{T}} \ . \tag{6.27H}$$

It is easy to verify that the linear form of Hooke's law is recovered if the representations (6.27H) for $U$ are differentiated with respect to $\hat{\mathbf{T}}$ and $\hat{\mathbf{E}}$, respectively, as indicated by (6.27H). *It then follows that (6.26H) and (6.27H) constitute an equivalent definition of a linear elastic material*. The definition of the most important type of nonlinear elastic material model, the hyperelastic material, is that the stress is the derivative of the strain energy with respect to strain, as in (6.26H). In the nonlinear case the strain energy is not specified by an expression as simple as (6.27H).

**Problems**

6.10.1. Consider the work done in a closed loading cycle applied to a unit cube of a linear anisotropic elastic material. The loading cycle this cube will be subjected to begins from an unstressed state and contains the following four loading sequences: $0 \rightarrow A$, the stress in the $x_1$ direction is increased slowly from 0 to $T_A$; $A \rightarrow B$, holding the stress in the $x_1$ direction, $T_A$, constant, the stress in the $x_2$ direction is increased slowly from 0 to $T_B$; $B \rightarrow C$, holding the stress in the $x_2$ direction constant, the stress in the $x_1$ direction is decreased slowly from $T_A$ to 0; $C \rightarrow 0$, the stress in the $x_2$ direction is decreased slowly from $T_B$ to 0. At the end of this loading cycle the object is again in an unstressed state. Show that the work done on each of these loading sequences is given by

$$W_{OA} = \frac{1}{2}\hat{\mathbf{S}}_{11}(\hat{T}_1^{(A)})^2 \ , \ \ W_{AB} = \frac{1}{2}\hat{\mathbf{S}}_{22}(\hat{T}_2^{(B)})^2 + \hat{\mathbf{S}}_{21}T_1^{(A)}\hat{T}_2^{(B)}$$

$$W_{BC} = -\frac{1}{2}\hat{\mathbf{S}}_{11}(\hat{T}_1^{(A)})^2 - \hat{\mathbf{S}}_{12}T_1^{(A)}\hat{T}_2^{(B)} \ , \ \ W_{CO} = -\frac{1}{2}\hat{\mathbf{S}}_{22}(\hat{T}_2^{(B)})^2$$

and show that the work done around the closed cycle is given by

$$W_{OO} = (\hat{\mathbf{S}}_{21} - \hat{\mathbf{S}}_{12})\hat{T}_1^{(A)}\hat{T}_2^{(B)} \ .$$

Show that one may therefore argue that $\hat{\mathbf{S}}_{12} = \hat{\mathbf{S}}_{21}$.

6.10.2. Show that $\hat{\mathbf{S}} = \hat{\mathbf{S}}^T$ implies $\hat{\mathbf{C}} = \hat{\mathbf{C}}^T$.

## 6.11. RESTRICTIONS ON THE COEFFICIENTS REPRESENTING MATERIAL PROPERTIES

In this section other restrictions on the four tensors of material coefficients are considered. Consider first that the dimensions of the material coefficients contained in the tensor must be consistent with the dimensions of the other terms occurring in the constitutive equation. The constitutive equation must be invariant under changes in gauge of the basis dimensions as would be affected, for example, by a change from SI units to the English foot-pound system.

It will be shown here that all the tensors of material coefficients are positive definite as well as symmetric except for viscoelastic tensor function $\hat{\mathbf{G}}(s)$. To see that permeability tensor

$\mathbf{H}(p)$ is positive definite, let $\nabla p = \mathbf{n}(\partial p/\partial w)$, where $w$ is a scalar length parameter in the $\mathbf{n}$ direction. The volume flow rate, $\mathbf{q} = \phi\rho_f\mathbf{v}/\rho_o$, projected in the $\mathbf{n}$ direction, $\phi\rho_f\mathbf{n}\cdot\mathbf{v}/\rho_o$, is then given by

$$\phi\rho_f\mathbf{n}\cdot\mathbf{v}/\rho_o = -(\partial p/\partial w)\,\mathbf{n}\cdot\mathbf{H}\cdot\mathbf{n}. \tag{6.28D}$$

In order for the volume flux per unit area, $\mathbf{q} = \phi\rho_f\mathbf{v}/\rho_o$, in the $\mathbf{n}$ direction to be pointed in the direction of decreasing pressure, it is necessary to require that

$$\mathbf{n}\cdot\mathbf{H}\cdot\mathbf{n} > 0 \quad \text{for all unit vectors } \mathbf{n}. \tag{6.29D}$$

If the fluid flowed the other way, all the mass of the fluid would concentrate itself at the highest pressure location, and we know that does not happen. Condition (6.29D) is the condition that symmetric tensor $\mathbf{H}$ be positive definite. This condition is satisfied if all the eigenvalues of $\mathbf{H}$ are positive.

The tensor of material coefficients for the Newtonian law of viscosity is positive definite also. To see this, the local stress power, $\mathrm{tr}(\mathbf{T}\cdot\mathbf{D}) = \mathbf{T}:\mathbf{D}$ (eq. (4.50), is calculated using constitutive equation (6.11N) and decomposition (A18) of the rate of deformation tensor :

$$\mathbf{D} = (1/3)(\mathrm{tr}\mathbf{D})\mathbf{1} + \mathrm{dev}\mathbf{D},\ \mathrm{dev}\mathbf{D} = \mathbf{D} - (1/3)(\mathrm{tr}\mathbf{D})\mathbf{1}. \tag{6.30N}$$

The stress due to viscous stresses may be recast in the form

$$\mathbf{T} + p\mathbf{1} = ((3\lambda + 2\mu)(\mathrm{tr}\mathbf{D})\mathbf{1} + 2\mu\,\mathrm{dev}\mathbf{D}, \tag{6.31N}$$

using (6.11N) and (6.30N). Calculation of the viscous stress power, $\mathrm{tr}\{(\mathbf{T} + p\mathbf{1})\mathbf{D}\}$, using the two equations above then yields

$$(\mathbf{T} + p\mathbf{1}):\mathbf{D} = ((3\lambda + 2\mu)/3)(\mathrm{tr}\mathbf{D})^2 + 2\mu\mathrm{tr}(\mathrm{dev}\mathbf{D})^2. \tag{6.32N}$$

Note that the terms in (6.32N) involving $\mathbf{D}$ are squared, and multiply expressions $3\lambda + 2\mu$ and $2\mu$; thus, if the viscous stress power, $\mathrm{tr}\{(\mathbf{T} + p\mathbf{1})\cdot\mathbf{D}\} = (\mathbf{T} + p\mathbf{1}):\mathbf{D}$ is to be positive it is necessary that

$$3\lambda + 2\mu > 0, \quad 2\mu > 0. \tag{6.33N}$$

The viscous stress power, $(\mathbf{T} + p\mathbf{1}):\mathbf{D}$, must be positive for an inert material as the world external to the material is working on the inert material, not the reverse. The inequalities restricting viscosities (6.33N) also follow for the condition that 6-by-6 matrix (6.10N) be positive definite. Finally, to see that the tensor of elastic coefficients is positive definite, the local form of the work done expressed in terms of stress and strain, $\mathbf{T}:\mathbf{E} = \hat{\mathbf{T}}\cdot\hat{\mathbf{E}}$, is employed (see (4.57) and (A141)). Since $\hat{\mathbf{T}} = \hat{\mathbf{C}}\cdot\hat{\mathbf{E}}$, it follows that $\mathbf{T}:\mathbf{E} = \hat{\mathbf{T}}\cdot\hat{\mathbf{E}} = \hat{\mathbf{E}}\cdot\hat{\mathbf{C}}\cdot\hat{\mathbf{E}}$; thus, from the requirement that the local work done on an inert material be positive, $\mathbf{T}:\mathbf{E} = \hat{\mathbf{T}}\cdot\hat{\mathbf{E}} > 0$, it follows that

$$\hat{\mathbf{E}}\cdot\hat{\mathbf{C}}\cdot\hat{\mathbf{E}} > 0 \text{ for all non-zero strains } \hat{\mathbf{E}}. \tag{6.34H}$$

Thus, it follows that $\hat{\mathbf{C}}$ is a positive definite symmetric tensor, $\hat{\mathbf{C}} = \hat{\mathbf{C}}^T$ and $\hat{\mathbf{E}}\cdot\hat{\mathbf{C}}\cdot\hat{\mathbf{E}} > 0$ for all nonzero strains $\hat{\mathbf{E}}$.

## 6.12. SUMMARY OF RESULTS

In this chapter a progressive development of four constitutive relations has been presented. Beginning with the constitutive idea, restrictions associated with the notions of localization,

invariance under rigid object motions, determinism, coordinate invariance, and material symmetry were imposed. In the development the constitutive equations were linearized and the definition of homogeneous versus inhomogeneous constitutive models reviewed. Restrictions due to material symmetry, the symmetry of the material coefficient tensors, and restrictions on the coefficients representing material properties were developed. The results of these considerations are the following constitutive equations:

$$\mathbf{q} = \phi\rho_f\mathbf{v}/\rho_o = -\mathbf{H}(p)\cdot\nabla p(\mathbf{x}, t),\ \mathbf{H}(p) = \mathbf{H}^T(p), \tag{6.36D}$$

$$\hat{\mathbf{T}} = \hat{\mathbf{C}}\cdot\hat{\mathbf{E}}\ ,\ \text{where}\ \ \hat{\mathbf{C}} = \hat{\mathbf{C}}^T\ , \tag{6.36H}$$

where $\mathbf{H}(p)$ and $\hat{\mathbf{C}}$ are positive definite, and

$$\mathbf{T} = -p\mathbf{1} + \lambda(\text{tr}\mathbf{D})\mathbf{1} + 2\mu\mathbf{D}, \tag{6.36N}$$

where $p$ is the fluid pressure and $\lambda$ and $\mu$ are viscosity coefficients ($3\lambda + 2\mu > 0,\ 2\mu > 0$), and

$$\hat{\mathbf{T}} = \int_{s=0}^{\infty} \hat{\mathbf{G}}(s)\cdot\hat{\mathbf{D}}(\mathbf{x}, t-s)ds\ , \tag{6.36V}$$

where there are no symmetry restrictions on $\hat{\mathbf{G}}(s)$. All the constitutive equations developed in this chapter, including Darcy's law, can be developed from many different arguments. Darcy's law can also be developed from experimental or empirical results for seepage flow in nondeformable porous media; all of the other constitutive equations in this chapter have experimental or empirical basis. Analytical arguments for these constitutive equations are presented so that it is understood by the reader that they also have an analytical basis for their existence. Darcy's law is a form of the balance of linear momentum and could include a body force term; however, such a body force would normally be a constant, and since it is only the divergence of $\mathbf{q} = \phi\rho_f\mathbf{v}/\rho_o$ that appears in the theory, such a body force would not appear in the final theory. In particular, Darcy's law could also be developed from the conservation of linear momentum, or from the Navier-Stokes equations that, as will be shown in the Chapter 8, is a combination of the stress equations of motion and the Newtonian law of viscosity (section 6.5).

## 6.13. RELEVANT LITERATURE

Christensen RM. 1971. *Theory of viscoelasticity*. New York: Academic Press.

Darcy H. 1856. *Les fontains publiques de la ville de Dijon*. Paris: Dalmont.

Gurtin ME. 1972. The linear theory of elasticity. In *Handbuch der Physik*, ed. S Flugge, pp. 1–296. Berlin: Springer-Verlag.

Lockett FJ. 1972. *Nonlinear viscoelastic solids*. New York: Academic Press.

Sokolnikoff IS. 1956. *Mathematical theory of elasticity*. New York: McGraw-Hill.

Truesdell CA, Toupin RA. 1960. The classical field theories. In *Handbuch der Physik*, ed. S Flugge, pp. 226–902. Berlin: Springer-Verlag.

Truesdell CA, Noll W. 1965. The non-linear field theories of mechanics. In *Handbuch der Physik*, ed. S Flugge, pp. 1–602. Berlin: Springer-Verlag.

# 7

# FOUR LINEAR CONTINUUM THEORIES

Four linear theories are considered in this chapter. Each has a distinctive and interesting history. Each one of the theories was originally formulated between 1820 and 1860. Representative of the theme of this chapter are the opening lines of the Historical Introduction in A.E.H. Love's *Theory of Elasticity* (original edition, 1892): "The Mathematical Theory of Elasticity is occupied with an attempt to reduce to calculation the state of strain, or relative displacement, within a solid … object ... which is subject to the action of an equilibrating system of forces, or is in a state of slight internal relative motion, and with endeavours to obtain results which shall be practically important in applications to architecture, engineering, and all other useful arts in which the material of construction is solid."

## 7.1. FORMATION OF CONTINUUM THEORIES

Four linear continuum theories are developed in this chapter. These are the theories of fluid flow through rigid porous media, of elastic solids, of viscous fluids, and of viscoelastic materials. There are certain features that are common to the development of each of these theories: they all involve at least one conservation principle and one constitutive equation, and for each it is necessary to specify boundary or initial conditions to properly formulate boundary value problems. Some of the continuum theories involve more than one conservation principle, more than one constitutive equation, and some kinematics relations. Thus, this chapter draws heavily upon the material in the previous chapters and serves to integrate the kinematics, the conservation principles, and the constitutive equations into theories that may be applied to physical situations to explain physical phenomena. This is generally accomplished by the solution of differential equations in the context of specific theories.

The differential equations that are formulated from these linear theories are usually the familiar, fairly well-understood differential equations, and they represent each of the three major types of second-order partial differential equations — the elliptic, the parabolic, and the hyperbolic. These three types of differential equations are characteristic of three different types of physical situations. Elliptic partial differential equations typically occur in equilibrium or steady-state situations where time does not enter the problem. Laplace's equation,

$$\nabla^2 f(x,y,z) = \frac{\partial^2 f}{\partial x^2} + \frac{\partial^2 f}{\partial y^2} + \frac{\partial^2 f}{\partial z^2} = 0\,, \tag{7.1}$$

and Poisson's equation, $\nabla^2 f(x, y, z) = g(x, y, z)$, are typical elliptic partial differential equations. Parabolic partial differential equations,

$$\nabla^2 f(x,y,z) = \frac{\partial f}{\partial t}\,, \tag{7.2}$$

typically occur in diffusion problems, such as fluid pressure diffusion in a rigid porous medium, as will be seen in the following section. Hyperbolic partial differential equations,

$$\nabla^2 f(x,y,z) = \frac{\partial^2 f}{\partial t^2}\,, \tag{7.3}$$

often characterize dynamic situations with propagating waves; hence they are called *wave equations*. A *boundary-value problem* is the problem of finding a solution to a differential equation or to a set of differential equations subject to certain specified boundary and/or initial conditions. The theories developed in this chapter all lead to boundary-value problems. Thus, in this chapter, conservation principles, constitutive equations, and some kinematics relations from the previous chapters are employed to formulate continuum theories that lead to physically motivated and properly formulated boundary-value problems.

## 7.2. THE THEORY OF FLUID FLOW THROUGH RIGID POROUS MEDIA

The theory of fluid flow through rigid porous media reduces to a typical diffusion problem: the diffusion of the pore fluid pressure through the porous medium. The continuum is assumed to be porous, rigid, and stationary, so that both the strain and rate of deformation are zero. The pores in the solid cannot be closed — most of them must be open and connected, so it is possible for the pore fluid to flow about the medium. The assumption of an immobile rigid porous continuum is not necessary, as the constitutive equation for the porous medium may be combined with the equations of elasticity to form a theory for poroelastic materials (see Chapter 9). Recall that $\rho_f$ denotes the density of the fluid in the pores of the porous medium, $\rho_0$ a reference value of density, $\mathbf{v}$ the velocity of the fluid passing through the pore, $\phi$ the porosity of the medium, and $\mathbf{q}$ the volume flux of fluid per unit area, $\mathbf{q} = \phi\rho_f\mathbf{v}/\rho_0$, through the pores. This constitutive idea is that the fluid volume flux, $\mathbf{q} = \phi\rho_f\mathbf{v}/\rho_0$, at particle $\mathbf{X}$ is a function of the pressure variation in the neighborhood of $\mathbf{X}$, $\mathcal{N}(\mathbf{X})$. The constitutive relation for the rigid porous continuum is Darcy's law, which relates the fluid volume flow rate, $\mathbf{q} = \phi\rho_f\mathbf{v}/\rho_0$, to the gradient ($\nabla p$) of pore pressure $p$:

$$\mathbf{q} = \phi\rho_f\mathbf{v}/\rho_0 = -\mathbf{H}(p)\cdot\nabla p(\mathbf{x}, t), \quad \mathbf{H}(p) = \mathbf{H}^T(p), \qquad \text{(6.36D) repeated}$$

where the symmetry in material tensor $\mathbf{H}$ has been shown in Chapter 5 to hold for material symmetries greater than monoclinic. The conservation law that is combined with Darcy's law is the conservation of mass (4.6) in a slightly rearranged form. In (4.6) the density $\rho$ is replaced by the product of the porosity and the fluid density, $\phi\rho_f$, in order to account for the fact that the fluid is only in the pores of the medium, and the resulting mass balance equation is divided throughout by $\rho_0$; thus,

$$\frac{1}{\rho_0}\frac{\partial \phi \rho_f}{\partial t} + \nabla \cdot (\phi \rho_f \mathbf{v} / \rho_0) = 0 \,. \tag{7.4}$$

In the case of compressible fluids it is reasonable to assume that the fluid is barotropic, that is to say, that fluid density $\rho_f$ is a function of pressure, $\rho_f = \rho_f(p)$, in which case (7.4) may be written as

$$\frac{\phi}{\rho_o}\frac{\partial \rho_f}{\partial p}\frac{\partial p}{\partial t} + \nabla \cdot \mathbf{q} = 0 \,, \tag{7.5}$$

where $\phi\rho_f\mathbf{v}/\rho_o$ has been replaced by $\mathbf{q}$ and where it has been assumed that porosity $\phi$ is not a function of time. Substituting (6.36D) into (7.5), and multiplying through by the inverse of the factor multiplying the partial derivative of pressure $p$ with respect to time, a differential equation for the pore pressure is obtained:

$$\frac{\partial p}{\partial t} = \left(\frac{\rho_0}{\phi}\frac{\partial p}{\partial \rho_f}\right)\nabla \cdot (\mathbf{H} \cdot \nabla p) \,. \tag{7.6}$$

If it is assumed that $\mathbf{H}$ and $\partial p / \partial \rho_f$ are constants, and if viscosity $\mu$ of the pore fluid is introduced by the substitution

$$\mathbf{H} \equiv \frac{1}{\mu}\mathbf{K} \,, \tag{7.7}$$

then

$$\frac{\partial p}{\partial t} = \frac{1}{\tau}\mathbf{K} : (\nabla \otimes \nabla) p \,, \tag{7.8}$$

where

$$\tau = \mu \frac{\phi}{\rho_0}\frac{\partial \rho_f}{\partial p} \tag{7.9}$$

is a material constant of dimension time. The time constant, $\tau$, depends upon the porosity of the medium and the viscosity and barotropic character of the pore fluid. The constant intrinsic permeability tensor, $\mathbf{K}$, is of dimension length squared; it depends only upon the arrangement and size of the pores in the medium and, in particular, is independent of the pore fluid properties. Differential equation (7.8) is a typical diffusion equation for an anisotropic medium; in the case of an isotropic medium differential equation (7.8) becomes

$$\frac{\partial p}{\partial t} = \frac{k}{\tau}\nabla^2 p \,, \tag{7.10}$$

where $\mathbf{K} = k\mathbf{1}$. Mathematically equivalent differential equations for anisotropic and isotropic heat conductors are obtained from the Fourier law of heat conduction and the conservation of energy. Pore fluid density $\rho_f$ satisfies the same diffusion equation (7.8) as the pore fluid pressure $p$:

$$\frac{\partial \rho_f}{\partial t} = \frac{1}{\tau}\mathbf{K} : (\nabla \otimes \nabla)\rho_f \,, \tag{7.11}$$

a result that follows from the assumed barotropic character, $\rho_f = \rho_f(p)$, of the pore fluid, and the assumption that $\partial\rho / \partial q_f$ is constant.

The boundary conditions on the pore pressure field customarily employed in the solution of differential equation (7.8) are (i) that external pore pressure $p$ is specified at the boundary (a lower pressure on one side of the boundary permits flow across the boundary), (ii) that pressure gradient $\nabla p$ at the boundary is specified (a zero pressure gradient permits no flow across the boundary), and (iii) that some linear combination of (i) and (ii) is specified. The complete theory for the flow of a fluid through a rigid porous medium consists of this differential equation (7.8) specified for object $O$ and boundary and initial conditions. The boundary conditions include the prescription of some combination of the pressure and the mass flux normal to boundary $\partial O$ as a function of time: $\mathbf{n}\cdot\mathbf{q} = \phi\rho_f\, \mathbf{n}\cdot\mathbf{v}(\boldsymbol{x}^*, t)/\rho_o = -(1/\mu)\, \mathbf{n}\cdot\mathbf{K}\cdot\nabla p(\boldsymbol{x}^*, t)$, $\boldsymbol{x}^* \subset \partial O$, so that

$$-(c_1/\mu)\, \mathbf{n}\cdot\mathbf{K}\cdot\nabla p(\boldsymbol{x}^*, t) + c_2 p(\boldsymbol{x}^*, t) = f(\boldsymbol{x}^*, t), \quad \boldsymbol{x}^* \subset \partial O, \tag{7.12}$$

where $c_1$ and $c_2$ are constants and $f(\boldsymbol{x}^*, t)$ is a function specified on $\partial O$. In the case when $c_1$ is zero, this condition reduces to a restriction of the boundary pressure, and in the case when $c_2$ is zero it is a restriction on the component of the mass flux vector normal to the boundary.

The basic pore fluid flow problem described by (7.8) and (7.12) may be simplified by specifying the type of material symmetry. If the material has orthotropic symmetry, employing a representation from Table 5.3 and the principal coordinate system for orthotropic symmetry, (7.8) and (7.12) become

$$\frac{\partial p}{\partial t} = \frac{K_{11}}{\tau}\frac{\partial^2 p}{\partial x_1^2} + \frac{K_{22}}{\tau}\frac{\partial^2 p}{\partial x_2^2} + \frac{K_{33}}{\tau}\frac{\partial^2 p}{\partial x_3^2} \text{ in } O, \tag{7.13}$$

$$-c_1 n_1 K_{11}\left\{\frac{\partial p}{\partial x_1}\right\}_{\mathbf{x}^*} - c_1 n_2 K_{22}\left\{\frac{\partial p}{\partial x_2}\right\}_{\mathbf{x}^*} - c_1 n_3 K_{33}\left\{\frac{\partial p}{\partial x_3}\right\}_{\mathbf{x}^*} + c_2 p(\mathbf{x}^*, t) = f(\mathbf{x}^*, t)$$

$$\boldsymbol{x}^* \subset \partial O, \tag{7.14}$$

and, if the material is isotropic, it follows from a representation in Table 5.3 that (7.13) reduces to (7.10) and (7.12) may be specialized as follows:

$$-c_1 K\, \mathbf{n}\cdot\nabla p(\mathbf{x}^*, t) + c_2 p(\mathbf{x}^*, t) = f(\mathbf{x}^*, t), \mathbf{x}^* \subset \partial O. \tag{7.15}$$

The coordinate system may be rescaled so that the differential equation and boundary conditions are those of distorted heat conduction objects with isotropic material symmetry. To accomplish this, the coordinates $x_1$, $x_2$, and $x_3$ are rescaled by

$$x = \left(\sqrt{\frac{k}{K_{11}}}\right)x_1, \quad y = \left(\sqrt{\frac{k}{K_{22}}}\right)x_2, \quad z = \left(\sqrt{\frac{k}{K_{33}}}\right)x_3, \tag{7.16a}$$

where

$$k^3 = K_{11}K_{22}K_{33}\,. \tag{7.16b}$$

Then differential equation (7.10) for an isotropic medium applies in the *distorted or stretched* $O$, and boundary conditions (7.14) are

$$-c_1 n_1 \sqrt{kK_{11}} \left\{\frac{\partial p}{\partial x}\right\}_{\mathbf{x}^*} - c_1 n_2 \sqrt{kK_{22}} \left\{\frac{\partial p}{\partial y}\right\}_{\mathbf{x}^*} - c_1 n_3 \sqrt{kK_{33}} \left\{\frac{\partial p}{\partial z}\right\}_{\mathbf{x}^*} +$$

$$c_2 p(\mathbf{x}^*, t) = f(\mathbf{x}^*, t)\,,\ \boldsymbol{x}^* \subset \text{distorted } \partial O. \tag{7.17}$$

In this restatement of the anisotropic problem one trades a slightly more complicated differential equation (7.8) for a simpler one (7.10) and obtains the slightly more complicated boundary conditions (7.17).

**Example 7.2.1**

A layer of thickness $h$ of a rigid porous material is between two fluid reservoirs both containing the same fluid at the same pressure $p_o$. Let $x_1$ be a coordinate that transverses the perpendicular distance between two layers; one reservoir is located at $x_1 = 0$ and the other reservoir is located at $x_1 = h$. At $t = 0$ the pore fluid pressure in the reservoir at $x_1 = h$ is raised from $p_o$ to $p_1$ and held at $p_1$ for all subsequent times, $\infty > t > 0$. The pressure in the reservoir at $x_1 = 0$ is held at $p_o$ for all times, $\infty > t > -\infty$. (a) Show that the steady-state solution (that is to say, after the startup effects of the pressure changes at $t = 0$ have vanished) is a linear variation in the pore fluid pressure from $p_o$ at $x = 0$ to $p_1$ at $x_1 = h$. (b) How does pressure $p(x_1, t)$ in the layer evolve in time to the linear long-term steady-state solution?

**Solution**: The problem is one dimensional in the direction of $x_1$. The one-dimensional form of differential equation (7.8) is

$$\frac{\partial p}{\partial t} = \frac{K_{11}}{\tau}\frac{\partial^2 p}{\partial x_1^2}\,. \qquad \text{(a) unsteady}$$

In the special case of steady states it reduces to

$$\frac{\partial^2 p}{\partial x_1^2} = 0\,. \qquad \text{(b) steady}$$

The solution to steady-state equation (b) subject to the condition that $p = p_o$ at $x_1 = 0$ and $p = p_1$ at $x_1 = h$ for all $t$ for all times, $\infty > t >> 0$, is $p(x_1) = (p_1 - p_o)(x_1/h) + p_o$. This result represents a linear variation in the pore fluid pressure from $p_0$ at $x_1 = 0$ to $p_1$ at $x_1 = h$.

(b) In the case of unsteady flow a solution to differential equation (a) is sought, subject to the conditions that $p = p_o$ everywhere in the medium and on its boundaries for $t < 0$, that $p = p_o$ at $x = 0$ for all $\infty > t > 0$ and $p = p_1$ at $L = h$ for all $\infty > t > 0$. Before solving differential equation (a) it is first rendered dimensionless by introducing dimensionless pressure ratio $P$, dimensionless coordinate $X$, and dimensionless time parameter $T$; thus,

$$P = \frac{p - p_0}{p_1 - p_0}\,,\quad X = \frac{x_1}{h}\,,\ \text{ and }\ T = \frac{K_{11}}{h^2}\frac{t}{\tau}\,,$$

respectively. These equations are solved for $p$, $x_1$, and $t$:

$$p = (p_1 - p_0)P + p_0 , \quad x_1 = hX , \text{ and } \quad t = \frac{h^2 \tau}{K_{11}} T ,$$

and substituted into (a), which then converts to the dimensionless version of this differential equation:

$$\frac{\partial P}{\partial T} = \frac{\partial^2 P}{\partial X^2} .$$

The solution to this dimensionless differential equation for $t \geq 0$ subject to these boundary and initial conditions is

$$P = X - \frac{2}{\pi} \sum_{n=1}^{n=\infty} \frac{1}{n} (-1)^{n-1} e^{-n^2 \pi^2 T} \sin(n\pi X) .$$

The temporal evolution of the steady-state linear distribution of pore fluid pressure across the layer of rigid porous material is illustrated in Figure 7.1. The vertical scale is dimensionless pressure $P$ with a range of 0 to 1. The front horizontal scale is dimensionless coordinate $X$, also with a range of 0 to 1; it traverses the porous layer. Dimensionless time constant $T$ is plotted from 0 to 0.2 in the third direction.

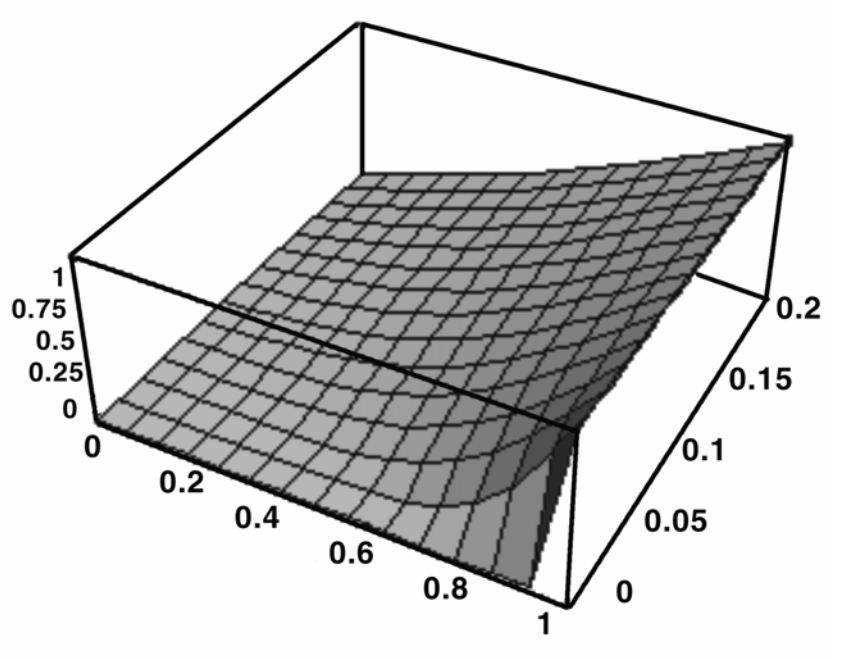



**Figure 7.1**. The temporal evolution of the pressure distribution in a layer of rigid porous material. The vertical scale is the dimensionless pressure $P$ with a range of 0 to 1. The front horizontal scale is the dimensionless coordinate $X$, also with a range of 0 to 1; it traverses the porous layer. The dimensionless time constant $T$ is plotted from 0 to 0.2 in the third direction. The purpose of the plot is to illustrate the evolution of the steady-state linear distribution of pressure across the layer of rigid porous material.

**Problems**

7.2.1. Show that pore fluid density $\rho_f$ satisfies the same differential equation for diffusion, (7.11), as pore fluid pressure $p$ (7.8).

7.2.2. Verify that the form of rescaled eqs. (7.10) and (7.17) follow from (7.13) and (7.14). Describe the shape of a homogeneous orthotropic material object, $O$, that is in the form of a cube after it is rescaled and distorted so that the differential equation is isotropic.

7.2.3. Show that the solution to the dimensionless differential equation $\partial P / \partial T = \partial^2 P / \partial X^2$ and the prescribed boundary and initial conditions, that $p = p_0$ at $x = 0$ for all $\infty > t > -\infty$ and $p = p_1$ at $L = h$ for all $\infty > t > 0$, is given by

$$P = X - \frac{2}{\pi} \sum_{n=1}^{n=\infty} \frac{1}{n} (-1)^{n-1} e^{-n^2 \pi^2 T} \sin(n\pi X) .$$

## 7.3. THE THEORY OF ELASTIC SOLIDS

An overview of the theory of linear elastic solids can be obtained by considering it as a system of fifteen equations in fifteen scalar unknowns. The fifteen scalar unknowns are the six components of stress tensor **T**, the six components of strain tensor **E**, and the three components of displacement vector **u**. The parameters of an elasticity problem are the tensor of elastic coefficients, $\hat{\mathbf{C}}$, density $\rho$, and action-at-a-distance force **d**, which are assumed to be known. The system of fifteen equations consists of stress–strain relations from the anisotropic Hooke's law:

$$\hat{\mathbf{T}} = \hat{\mathbf{C}} \cdot \hat{\mathbf{E}} , \text{ where } \hat{\mathbf{C}} = \hat{\mathbf{C}}^T , \qquad \text{(6.36H) repeated}$$

the six strain-displacement relations,

$$\mathbf{E} = (1/2)((\nabla \otimes \mathbf{u})^{\mathrm{T}} + \nabla \otimes \mathbf{u}), \qquad \text{(3.49) repeated}$$

and the three stress equations of motion:

$$\rho \ddot{\mathbf{u}} = \nabla \cdot \mathbf{T} + \rho \mathbf{d} , \mathbf{T} = \mathbf{T}^T . \qquad (7.18)$$

This form of the stress equations of motion differs from (4.37) only in notation: the acceleration is here represented by $\ddot{\mathbf{u}}$ rather than $\ddot{\mathbf{x}}$, a result that follows from (3.21) by taking the time derivative twice and assuming that the material and spatial reference frames are not accelerating relative to one another. The system of fifteen equations in fifteen scalar unknowns may be reduced to a system of three equations in three scalar unknowns by accomplishing the following algebraic steps: (1) substitute strain-displacement relations (3.49) into stress–strain relations (6.36H), then (2) substitute the resulting expression relating the stress to the first derivatives of the displacement into the three stress equations of motion (7.18). The result is a system of three equations in three scalar unknowns, the three components of the displacement vector. This algebraic simplification will be accomplished in the case of an isotropic material after Hooke's law for isotropic materials is developed in the next paragraph.

The stress–strain and strain–stress relations of anisotropic Hooke's law (6.36H) are developed next. It has been shown that the tensor of elastic material coefficients, $\hat{\mathbf{C}}$, is symmetric and positive definite, as is its inverse, $\hat{\mathbf{S}}$, the compliance tensor of elastic material coefficients. The strain–stress relations (as opposed to the stress-strain relations) are

$$\hat{\mathbf{E}} = \hat{\mathbf{S}} \cdot \hat{\mathbf{T}}\,, \hat{\mathbf{S}} = \hat{\mathbf{C}}^{-1}\,. \qquad \text{(6.12H) repeated}$$

The form and symmetry of $\hat{\mathbf{C}}$ and $\hat{\mathbf{S}}$ are identical for any material symmetry, and, for the material symmetries of interest, the form appropriate to the material symmetry is given in Table 5.4. The notation employed thus far for $\hat{\mathbf{C}}$ and $\hat{\mathbf{S}}$, the notation that allows their representation as second-order tensors in six dimensions, is not the traditional notation. To obtain the traditional notation, Hooke's law (6.36H) is expressed in its matrix format:

$$\begin{bmatrix} \hat{T}_1 \\ \hat{T}_2 \\ \hat{T}_3 \\ \hat{T}_4 \\ \hat{T}_5 \\ \hat{T}_6 \end{bmatrix} = \begin{bmatrix} \hat{C}_{11} & \hat{C}_{12} & \hat{C}_{13} & \hat{C}_{14} & \hat{C}_{15} & \hat{C}_{16} \\ \hat{C}_{21} & \hat{C}_{22} & \hat{C}_{23} & \hat{C}_{24} & \hat{C}_{25} & \hat{C}_{26} \\ \hat{C}_{31} & \hat{C}_{32} & \hat{C}_{33} & \hat{C}_{34} & \hat{C}_{35} & \hat{C}_{36} \\ \hat{C}_{41} & \hat{C}_{42} & \hat{C}_{43} & \hat{C}_{44} & \hat{C}_{45} & \hat{C}_{46} \\ \hat{C}_{51} & \hat{C}_{52} & \hat{C}_{53} & \hat{C}_{54} & \hat{C}_{55} & \hat{C}_{56} \\ \hat{C}_{61} & \hat{C}_{62} & \hat{C}_{63} & \hat{C}_{64} & \hat{C}_{65} & \hat{C}_{66} \end{bmatrix} \begin{bmatrix} \hat{E}_1 \\ \hat{E}_2 \\ \hat{E}_3 \\ \hat{E}_4 \\ \hat{E}_5 \\ \hat{E}_6 \end{bmatrix}, \tag{7.19}$$

and then converted to the traditional three-dimensional component representation by employing relations (A163):

$$\begin{bmatrix} T_{11} \\ T_{22} \\ T_{33} \\ \sqrt{2}T_{23} \\ \sqrt{2}T_{13} \\ \sqrt{2}T_{12} \end{bmatrix} = \begin{bmatrix} c_{11} & c_{12} & c_{13} & \sqrt{2}c_{14} & \sqrt{2}c_{15} & \sqrt{2}c_{16} \\ c_{12} & c_{22} & c_{23} & \sqrt{2}c_{24} & \sqrt{2}c_{25} & \sqrt{2}c_{26} \\ c_{13} & c_{23} & c_{33} & \sqrt{2}c_{34} & \sqrt{2}c_{35} & \sqrt{2}c_{36} \\ \sqrt{2}c_{14} & \sqrt{2}c_{24} & \sqrt{2}c_{34} & 2c_{44} & 2c_{45} & 2c_{46} \\ \sqrt{2}c_{15} & \sqrt{2}c_{25} & \sqrt{2}c_{35} & 2c_{45} & 2c_{55} & 2c_{56} \\ \sqrt{2}c_{16} & \sqrt{2}c_{26} & \sqrt{2}c_{36} & 2c_{46} & 2c_{56} & 2c_{66} \end{bmatrix} \begin{bmatrix} E_{11} \\ E_{22} \\ E_{33} \\ \sqrt{2}E_{23} \\ \sqrt{2}E_{13} \\ \sqrt{2}E_{12} \end{bmatrix}, \tag{7.20}$$

and introducing matrix coefficients $c_{ij}$, $i, j = 1, \ldots, 6$, defined in Table 7.1. It is easy to verify that matrix equation (7.20) may be rewritten as

$$\begin{bmatrix} T_{11} \\ T_{22} \\ T_{33} \\ T_{23} \\ T_{13} \\ T_{12} \end{bmatrix} = \begin{bmatrix} c_{11} & c_{12} & c_{13} & c_{14} & c_{15} & c_{16} \\ c_{12} & c_{22} & c_{23} & c_{24} & c_{25} & c_{26} \\ c_{13} & c_{23} & c_{33} & c_{34} & c_{35} & c_{36} \\ c_{14} & c_{24} & c_{34} & c_{44} & c_{45} & c_{46} \\ c_{15} & c_{25} & c_{35} & c_{45} & c_{55} & c_{56} \\ c_{16} & c_{26} & c_{36} & c_{46} & c_{56} & c_{66} \end{bmatrix} \begin{bmatrix} E_{11} \\ E_{22} \\ E_{33} \\ 2E_{23} \\ 2E_{13} \\ 2E_{12} \end{bmatrix}. \tag{7.21}$$

This matrix represents the classical notation of Voigt (1910) for the anisotropic stress–strain relations. Unfortunately, matrix $\mathbf{c}$ appearing in (7.21) does not represent the components of a tensor, while symmetric matrices $\hat{\mathbf{C}}$ and $\hat{\mathbf{S}}$ do represent the components of a second-order tensor in a 6-dimensional space. A chart relating the component notations of matrix $\mathbf{c}$ (and its inverse $\mathbf{s}$) to the component notations for $\hat{\mathbf{C}}$ and $\hat{\mathbf{S}}$ is given in Table 7.1. Table 7.1 also relates these coefficients to the traditional notation for representation of these tensors as fourth-order

**Table 7.1**. Elasticity and Compliance in Different Notations*

| 1 | 2 | 3 | 1 | 2 | 3 |
|---|---|---|---|---|---|
| $C_{1111}$ | $c_{11}$ | $\hat{C}_{11}$ | $S_{1111}$ | $s_{11}$ | $\hat{S}_{11}$ |
| $C_{2222}$ | $c_{22}$ | $\hat{C}_{22}$ | $S_{2222}$ | $s_{22}$ | $\hat{S}_{22}$ |
| $C_{3333}$ | $c_{33}$ | $\hat{C}_{33}$ | $S_{3333}$ | $s_{33}$ | $\hat{S}_{33}$ |
| $C_{1122}$ | $c_{12}$ | $\hat{C}_{12}$ | $S_{1122}$ | $s_{12}$ | $\hat{S}_{12}$ |
| $C_{1133}$ | $c_{13}$ | $\hat{C}_{13}$ | $S_{1133}$ | $s_{13}$ | $\hat{S}_{13}$ |
| $C_{2233}$ | $c_{23}$ | $\hat{C}_{23}$ | $S_{2233}$ | $s_{23}$ | $\hat{S}_{23}$ |
| $C_{2323}$ | $c_{44}$ | $\frac{1}{2}\hat{C}_{44}$ | $S_{2323}$ | $\frac{1}{4}s_{44}$ | $\frac{1}{2}\hat{S}_{44}$ |
| $C_{1313}$ | $c_{55}$ | $\frac{1}{2}\hat{C}_{55}$ | $S_{1313}$ | $\frac{1}{4}s_{55}$ | $\frac{1}{2}\hat{S}_{55}$ |
| $C_{1212}$ | $c_{66}$ | $\frac{1}{2}\hat{C}_{66}$ | $S_{1212}$ | $\frac{1}{4}s_{66}$ | $\frac{1}{2}\hat{S}_{66}$ |
| $C_{1323}$ | $c_{54}$ | $\frac{1}{2}\hat{C}_{54}$ | $S_{1323}$ | $\frac{1}{4}s_{54}$ | $\frac{1}{2}\hat{S}_{54}$ |
| $C_{1312}$ | $c_{56}$ | $\frac{1}{2}\hat{C}_{56}$ | $S_{1312}$ | $\frac{1}{4}s_{56}$ | $\frac{1}{2}\hat{S}_{56}$ |
| $C_{1223}$ | $c_{64}$ | $\frac{1}{2}\hat{C}_{64}$ | $S_{1223}$ | $\frac{1}{4}s_{64}$ | $\frac{1}{2}\hat{S}_{64}$ |
| $C_{2311}$ | $c_{41}$ | $\frac{1}{\sqrt{2}}\hat{C}_{41}$ | $S_{2311}$ | $\frac{1}{2}s_{41}$ | $\frac{1}{2}\hat{S}_{41}$ |
| $C_{1311}$ | $c_{51}$ | $\frac{1}{\sqrt{2}}\hat{C}_{51}$ | $S_{1311}$ | $\frac{1}{2}s_{51}$ | $\frac{1}{\sqrt{2}}\hat{S}_{51}$ |
| $C_{1211}$ | $c_{61}$ | $\frac{1}{\sqrt{2}}\hat{C}_{61}$ | $S_{1211}$ | $\frac{1}{2}s_{61}$ | $\frac{1}{\sqrt{2}}\hat{S}_{61}$ |
| $C_{2322}$ | $c_{42}$ | $\frac{1}{\sqrt{2}}\hat{C}_{42}$ | $S_{2322}$ | $\frac{1}{2}s_{42}$ | $\frac{1}{\sqrt{2}}\hat{S}_{42}$ |
| $C_{1322}$ | $c_{52}$ | $\frac{1}{\sqrt{2}}\hat{C}_{52}$ | $S_{1322}$ | $\frac{1}{2}s_{52}$ | $\frac{1}{\sqrt{2}}\hat{S}_{52}$ |
| $C_{1222}$ | $c_{62}$ | $\frac{1}{\sqrt{2}}\hat{C}_{62}$ | $S_{1222}$ | $\frac{1}{2}s_{62}$ | $\frac{1}{\sqrt{2}}\hat{S}_{62}$ |
| $C_{2333}$ | $c_{43}$ | $\frac{1}{\sqrt{2}}\hat{C}_{43}$ | $S_{2333}$ | $\frac{1}{2}s_{43}$ | $\frac{1}{\sqrt{2}}\hat{S}_{43}$ |
| $C_{1333}$ | $c_{53}$ | $\frac{1}{\sqrt{2}}\hat{C}_{53}$ | $S_{1333}$ | $\frac{1}{2}s_{53}$ | $\frac{1}{\sqrt{2}}\hat{S}_{53}$ |
| $C_{1233}$ | $c_{63}$ | $\frac{1}{\sqrt{2}}\hat{C}_{63}$ | $S_{1233}$ | $\frac{1}{2}s_{63}$ | $\frac{1}{\sqrt{2}}\hat{S}_{63}$ |

*Column 1 illustrates the Voigt notation of these quantities as fourth-order tensor components in a three-dimensional Cartesian space. Column 2 represents the Voigt matrix or double index notation. Column 3 illustrates the Kelvin-inspired notation for these quantities as second-order tensor components in a six-dimensional Cartesian space.

tensors in a three-dimensional space, a notation that is not employed in this text. The various components in Table 7.1 are either equal or differ by multiples of $\sqrt{2}$ from each other. In the case of orthotropic symmetry it follows from Table 5.4 and (7.19)–(7.21) that

$$\begin{bmatrix} T_{11} \\ T_{22} \\ T_{33} \\ T_{23} \\ T_{13} \\ T_{12} \end{bmatrix} = \begin{bmatrix} c_{11} & c_{12} & c_{13} & 0 & 0 & 0 \\ c_{12} & c_{22} & c_{23} & 0 & 0 & 0 \\ c_{13} & c_{23} & c_{33} & 0 & 0 & 0 \\ 0 & 0 & 0 & c_{44} & 0 & 0 \\ 0 & 0 & 0 & 0 & c_{55} & 0 \\ 0 & 0 & 0 & 0 & 0 & c_{66} \end{bmatrix} \begin{bmatrix} E_{11} \\ E_{22} \\ E_{33} \\ 2E_{23} \\ 2E_{13} \\ 2E_{12} \end{bmatrix}, \tag{7.22a}$$

or

$$\begin{bmatrix} T_{11} \\ T_{22} \\ T_{33} \end{bmatrix} = \begin{bmatrix} c_{11} & c_{12} & c_{13} \\ c_{12} & c_{22} & c_{23} \\ c_{13} & c_{23} & c_{33} \end{bmatrix} \begin{bmatrix} E_{11} \\ E_{22} \\ E_{33} \end{bmatrix},$$

$$T_{23} = 2c_{44}E_{23}, \;\; T_{13} = 2c_{55}E_{13}, \;\; T_{12} = 2c_{66}E_{12}, \tag{7.22b}$$

and, in the case of isotropic symmetry, it follows again from Table 5.4 and (7.19)–(7.21) that

$$\begin{bmatrix} T_{11} \\ T_{22} \\ T_{33} \\ T_{23} \\ T_{13} \\ T_{12} \end{bmatrix} = \begin{bmatrix} \lambda+2\mu & \lambda & \lambda & 0 & 0 & 0 \\ \lambda & \lambda+2\mu & \lambda & 0 & 0 & 0 \\ \lambda & \lambda & \lambda+2\mu & 0 & 0 & 0 \\ 0 & 0 & 0 & \mu & 0 & 0 \\ 0 & 0 & 0 & 0 & \mu & 0 \\ 0 & 0 & 0 & 0 & 0 & \mu \end{bmatrix} \begin{bmatrix} E_{11} \\ E_{22} \\ E_{33} \\ 2E_{23} \\ 2E_{13} \\ 2E_{12} \end{bmatrix}, \tag{7.23}$$

where coefficients $c_{11}$ and $c_{12}$ are expressed in terms of the Lamé moduli of elasticity, $\lambda$ and $\mu$; $c_{11} = \lambda + 2\mu$ and $c_{12} = \lambda$ (note that $\hat{c}_{11} = \lambda + 2\mu$ and $\hat{c}_{12} = \lambda$. In eq. (6.11N) the Greek letters $\lambda$ and $\mu$ are also used to denote the viscosity coefficients. This dual use for these Greek letters will continue throughout the text, as they are traditional notations in elasticity theory and in viscous fluid theory. The reader should keep in mind that the significance of $\lambda$ and $\mu$ will depend upon context — viscous fluid or elastic solid. Developing the six scalar equations that come from matrix equation (7.23) in algebraic analogy with the transition from (6.8N) to (6.11N), a result algebraically equivalent to (6.11N) then follows:

$$\mathbf{T} = \lambda(tr\mathbf{E})\mathbf{1} + 2\mu\mathbf{E}. \tag{7.24}$$

For an isotropic linear elastic material there are just two independent elastic constants. These two constants are represented, for example, by Lamé moduli $\lambda$ and $\mu$. Another set of isotropic elastic constants in common use are Young's modulus $E$, shear modulus $G$ (= $\mu$), and Poisson's ratio $\nu$, where the three constants are related by $2G(1+\nu) = E$, so that only two are independent. Any single isotropic elastic constant can be expressed in terms of any two other isotropic elastic constants, as documented by Table 7.2, which contains expressions for most of the usual isotropic elastic constants in terms of different pairs of the other isotropic elastic constants. A frequently employed isotropic elastic constant is bulk modulus $k$, which represents the ratio of an applied mean hydrostatic stress, $-p = (\mathrm{tr}\mathbf{T})/3$, to a volumetric strain. Recall that $\mathrm{tr}\mathbf{E}$ represents the volumetric strain per unit volume. The relationship between volumetric strain per unit volume and the mean hydrostatic stress, $-p = (\mathrm{tr}\mathbf{T})/3$, is obtained by taking the trace of (7.24), and thus $-3p = (3\lambda + 2\mu)\,\mathrm{tr}\mathbf{E}$. Bulk modulus $k$ is then given by the following different representations:

$$k \equiv \frac{-p}{tr\mathbf{E}} = \lambda + \frac{2\mu}{3} = \frac{E}{3(1-2\nu)}; \tag{7.25}$$

the equivalence of the last equality for bulk modulus $k$ may be seen from the last column of Table 7.2. The isotropic strain–stress relations are obtained from (7.24), so that

$$\mathbf{E} = \frac{1}{E}\{(1+\nu)\mathbf{T} - \nu(tr\mathbf{T})\mathbf{1}\}. \tag{7.26}$$

**Table 7.2**. Isotropic Elastic Constants Expressed in Terms of Certain Pairs of Other Isotropic Elastic Constants

| | $\lambda$ | $\mu$ | $E$ | $\nu$ | $k$ |
|---|---|---|---|---|---|
| $\lambda, \mu$ | – | – | $\frac{\mu(3\lambda+2\mu)}{\lambda+\mu}$ | $\frac{\lambda}{2(\lambda+\mu)}$ | $\frac{3\lambda+2\mu}{3}$ |
| $\lambda, \nu$ | – | $\frac{\lambda(1-2\nu)}{2\nu}$ | $\frac{\lambda(1+\nu)(1-2\nu)}{\nu}$ | – | $\frac{\lambda(1+\nu)}{3\nu}$ |
| $\lambda, k$ | – | $\frac{3(k-\lambda)}{2}$ | $\frac{9k(k-\lambda)}{3k-\lambda}$ | $\frac{\lambda}{3k-\lambda}$ | – |
| $\mu, E$ | $\frac{(2\mu-E)\mu}{(E-3\mu)}$ | – | – | $\frac{(E-2\mu)}{2\mu}$ | $\frac{\mu E}{3(3\mu-E)}$ |
| $\mu, \nu$ | $\frac{2\mu\nu}{1-2\nu}$ | – | $2\mu(1+\nu)$ | – | $\frac{2\mu(1+\nu)}{3(1-2\nu)}$ |
| $\mu, k$ | $\frac{3k-2\mu}{3}$ | – | $\frac{9k\mu}{3k+\mu}$ | $\frac{3k-2\mu}{6k+2\mu}$ | – |
| $E, \nu$ | $\frac{\nu E}{(1+\nu)(1-2\nu)}$ | $\frac{E}{2(1+\nu)}$ | – | – | $\frac{E}{3(1-2\nu)}$ |
| $E, k$ | $\frac{3k(3k-E)}{9k-E}$ | $\frac{3kE}{9k-E}$ | – | $\frac{(3k-E)}{6k}$ | – |
| $\nu, k$ | $\frac{3k\nu}{1+\nu}$ | $\frac{3k(1-2\nu)}{2(1+\nu)}$ | $3k(1-2\nu)$ | – | – |

Reverting briefly to the case of orthotropic symmetry, the strain–stress relations may be written in the form

$$\begin{bmatrix} E_{11} \\ E_{22} \\ E_{33} \end{bmatrix} = \begin{bmatrix} \frac{1}{E_1} & \frac{-\nu_{21}}{E_2} & \frac{-\nu_{31}}{E_3} \\ \frac{-\nu_{12}}{E_1} & \frac{1}{E_2} & \frac{-\nu_{32}}{E_3} \\ \frac{-\nu_{13}}{E_1} & \frac{-\nu_{23}}{E_2} & \frac{1}{E_3} \end{bmatrix} \begin{bmatrix} T_{11} \\ T_{22} \\ T_{33} \end{bmatrix}$$

$$E_{23} = \frac{T_{23}}{2G_{23}}, \quad E_{13} = \frac{T_{13}}{2G_{13}}, \quad E_{12} = \frac{T_{12}}{2G_{12}}, \tag{7.27}$$

where $E_1$, $E_2$, $E_3$ represent the Young's moduli in the $x_1$, $x_2$, $x_3$ directions; $G_{23}$, $G_{31}$, $G_{12}$ represent the shear moduli about the $x_1$, $x_2$, $x_3$ axes and $\nu_{23}$, $\nu_{31}$, $\nu_{12}$, $\nu_{32}$, $\nu_{13}$, and $\nu_{21}$ are Poisson's ratios. Poisson ratio $\nu_{21}$ represents the strain in the $x_1$ direction due to the normal strain in the $x_2$ direction and where symmetry of the compliance tensor requires that

$$\frac{-\nu_{12}}{E_1}=\frac{-\nu_{21}}{E_2},\quad \frac{-\nu_{13}}{E_1}=\frac{-\nu_{31}}{E_3},\quad \frac{-\nu_{23}}{E_2}=\frac{-\nu_{32}}{E_3}. \tag{7.28}$$

**Biomedical Historical Note**: Thomas Young (1773–1829) was a child prodigy, a well-educated physician, a physicist, and a student of languages who attempted to decipher Egyptian hieroglyphics, and who translated the Rosetta Stone. Although he is well known for his concept of the modulus of elasticity, he did significant work in explaining how the eye functions. He argued that the lens of an eye changes shape to focus light as necessary. He suggested that the retina responds to three principal colors that combined to form all the other colors. More generally he considered the nature of light and discovered the principle of interference of light.

As noted in the introductory paragraph of this section, the system of 15 equations in 15 unknowns can be reduced to a set of three equations in three unknowns or, equivalently, to a single vector equation in three dimensions. The resulting equations are known as the Navier equations of elasticity, and they are similar in form to the Navier-Stokes equations of viscous fluid theory developed in the following section. To obtain these equations for an isotropic material one substitutes (3.49) into (7.24) and then places modified (7.24) for the stresses in terms of the components of the displacement vector into equations of motion (7.18), thus

$$\rho\ddot{\mathbf{u}}=(\lambda+\mu)\nabla(\nabla\cdot\mathbf{u})+\mu\nabla^2\mathbf{u}+\rho\mathbf{d}\,. \tag{7.29}$$

This is the Navier equation. If the Navier equation is solved for displacement field **u**, then strain field **E** can be determined from (3.49) and stress field **T** from (7.24). The resulting stress field will satisfy stress equations of motion (7.18) because (7.29) is an alternate statement of the equations of motion.

Consider now the special case when one chooses the stress (or the strain) as the unknown and the displacement is to be calculated last from the determined strain tensor. In this case one must consider the strain-displacement relations (3.49) to be a system of first-order partial differential equations to be solved for the components of displacement vector **u** given the components of strain tensor **E** (see §3.4). The *conditions of compatibility* in terms of strain — (3.53), (3.54), or (3.55) — are a set of necessary and sufficient conditions that first-order partial differential equations (3.49) must satisfy in order that (3.49) have a single valued and continuous solution **u**.

The general problem associated with the basic system of fifteen equations is to find the fields $\mathbf{T}(\mathbf{x}, t)$, $\mathbf{E}(\mathbf{x}, t)$, and $\mathbf{u}(\mathbf{x}, t)$ for all $\mathbf{x} \in O$ and $t \in [0, t]$ given a particular object $O$ of density $\rho$ and elastic coefficients $\hat{\mathbf{C}}$ (or, in the case of isotropy, $\lambda$ and $\mu$) acted upon by action-at-a-distance force **d** and some surface loading or specified displacements at the boundary during specified time interval $[0, t]$. Such problems are called the *boundary value problems* of the theory of elasticity, and they are classified in several ways. First, they are classified as either elastostatic, elastoquasi-static, or elastodynamic. The *elastostatic boundary value problems* are those in which $\mathbf{T}(\mathbf{x})$, $\mathbf{E}(\mathbf{x})$, and $\mathbf{u}(\mathbf{x})$ are independent of time, and the inertia term in the stress equations of motion, $\rho\ddot{\mathbf{u}}$, is zero. The *elastoquasi-static problems* are those in which $\mathbf{T}(\mathbf{x}, t)$, $\mathbf{E}(\mathbf{x}, t)$, and $\mathbf{u}(\mathbf{x}, t)$ are time dependent, but the inertia term in the stress equations of motion, $\rho\ddot{\mathbf{u}}$, is small enough to be neglected. The *elastodynamic boundary value problems* are those in which $\mathbf{T}(\mathbf{x}, t)$, $\mathbf{E}(\mathbf{x}, t)$, and $\mathbf{u}(\mathbf{x}, t)$ are time dependent and the inertia term in the stress equations of motion, $\rho\ddot{\mathbf{u}}$, is neither zero nor negligible.

The formulation of boundary-value problems is considered next. The boundary-value problems are classified as displacement, traction, mixed or mixed-mixed boundary-value prob-

lems. An object, $O$, with boundary $\partial O$ is illustrated in Figure 7.2. The total boundary of object $O$ is divided into the sum of two boundaries, displacement boundary $\partial O_{\mathbf{u}}$ over which the boundary conditions are specified in terms of displacement and traction boundary $\partial O_{\mathbf{t}}$ over which the boundary conditions are specified in terms of surface tractions $\mathbf{t}$. It is required for some problems to further subdivide the boundaries to include the situation in which the normal tractions and transverse displacements, or transverse tractions and normal displacements, are specified over portions of the object boundary, but that is not done here. The rigid wall indicated in Figure 7.2 is intended to suggest a boundary upon which the boundary condition on the displacement is specified and the other surface is intended to suggest a boundary on which the (zero or nonzero)surface tractions are specified.

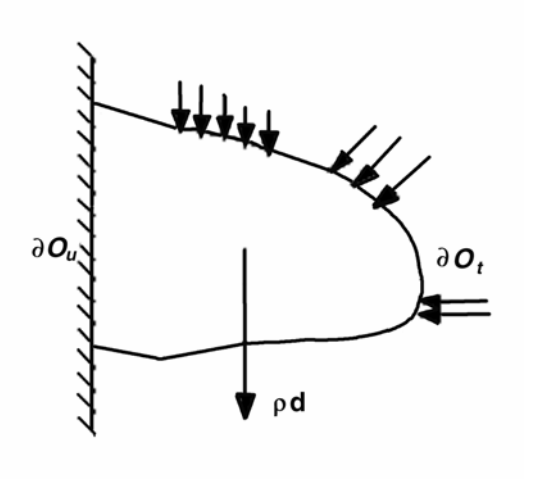



**Figure 7.2**. An object denoted by $O$ whose total boundary is divided into traction and displacement boundaries denoted by $\partial O_t$ and $\partial O_u$, respectively.

In the *displacement boundary value problem* the continuous surface displacement $\mathbf{u}(\mathbf{x}^*, t)$ is specified on boundary $\partial O$ for $[0, t]$, $\mathbf{x}^* \in \partial O$, where $[0, t]$ is the time interval for which a solution is desired, and the continuous initial displacement field $\mathbf{u}^o(\mathbf{x})$ is specified for all $\mathbf{x} \in O$. The displacement boundary value problem is the following; given particular object $O$ of density $\rho$ and elastic coefficients $\hat{\mathbf{C}}$ (or, in the case of isotropy, $\lambda$ and $\mu$) acted upon by an action-at-a-distance force $\mathbf{d}$, determine fields $\mathbf{u}(\mathbf{x}, t)$, $\mathbf{T}(\mathbf{x}, t)$, and $\mathbf{E}(\mathbf{x}, t)$, which satisfy system of equations (3.49), (7.18) and some form of Hooke's law (6.36H), with initial conditions

$$\mathbf{u}(\mathbf{x}, 0) = \mathbf{u}(\mathbf{x}), \quad \dot{\mathbf{u}}(\mathbf{x}, 0) = \dot{\mathbf{u}}(\mathbf{x}), \quad \mathbf{x} \in O, \tag{7.30}$$

and displacement boundary condition

$$\mathbf{u}(\mathbf{x}, t) = \mathbf{u}^*(\mathbf{x}^*, t), \ \mathbf{x}^* \in \partial O, \ t \in [0, t]. \tag{7.31}$$

In the *traction boundary-value problem* the specification of surface displacement (7.31) is replaced by specification of surface traction $\mathbf{t}(\mathbf{x}^*, t)$ for all $\mathbf{x}^* \in \partial O$ and $t \in [0, t]$; thus,

$$\mathbf{t}(\mathbf{x}^*, t) = \mathbf{T}(\mathbf{x}^*, t) \cdot \mathbf{n}, \ \mathbf{n} \perp \partial O, \ \mathbf{x}^* \in \partial O, \ t \in [0, t], \tag{7.32}$$

where $\mathbf{n}$ is the unit exterior normal to the boundary. In a *mixed boundary-value problem* there is a portion of the boundary on which the displacements are specified and a portion of the boundary on which the surface tractions are specified. These portions of the boundary are denoted in Figure 7.2 by $\partial O_{\mathbf{u}}$ and $\partial O_{\mathbf{t}}$, and they are nonempty, nonintersecting portions of the boundary whose union is the entire boundary, $\partial O$. The typical mixed boundary-value problem must satisfy condition (7.31) on $\partial O_{\mathbf{u}}$ and the surface traction condition (7.32) on $\partial O_{\mathbf{t}}$. The mixed-mixed boundary-value problem of elasticity is characterized by boundaries where the two types of boundary conditions appear on the same portion of the boundary. For example, the normal displacement is specified and the shear stress is specified on the same portion of the boundary, or the normal stress and the tangential displacement are specified on the same portion of the boundary. The mixed-mixed boundary-value problems are complicated and are not considered here.

Any solution to an elasticity problem is unique. That is to say that, for a specific object of a specified material acted upon by a specified action-at-a-distance force and subject to specific boundary conditions, there is one and only one solution to the set of 15 equations in 15 unknowns. The common strategy for proving uniqueness theorems is to assume non-uniqueness, that is to say, assume there are two, and then prove that the two must be equal. The uniqueness theorem for linear elasticity is proved using this strategy. Assume that there are two solutions — $\mathbf{u}^{(1)}(\mathbf{x}, t)$, $\mathbf{T}^{(1)}(\mathbf{x}, t)$, $\mathbf{E}^{(1)}(\mathbf{x}, t)$, and $\mathbf{u}^{(2)}(\mathbf{x}, t)$, $\mathbf{T}^{(2)}(\mathbf{x}, t)$, $\mathbf{E}^{(2)}(\mathbf{x}, t)$ — to the same elasticity problem, that is to say, a problem in which the object, the material, the action-at-a-distance force, and the boundary conditions to which the object is subjected are all specified. The linearity of the system of equations for linear elasticity permits one problem solution for a specified object and material, action-at-a-distance force, traction boundary conditions, and displacement boundary conditions, to be superposed upon a second solution for the same specified object, material, and displacement boundary conditions, but for a different action-at-a-distance force, different traction boundary conditions, and different displacement boundary conditions. Thus, for example, two solutions — $\mathbf{u}^{(1)}(\mathbf{x}, t)$, $\mathbf{T}^{(1)}(\mathbf{x}, t)$, $\mathbf{E}^{(1)}(\mathbf{x}, t)$, and $\mathbf{u}^{(2)}(\mathbf{x}, t)$, $\mathbf{T}^{(2)}(\mathbf{x}, t)$, $\mathbf{E}^{(2)}(\mathbf{x}, t)$ — for the same specified object and material, traction boundary conditions, and displacement boundary conditions, but different action-at-a-distance forces, $\mathbf{d}^{(1)}$ and $\mathbf{d}^{(2)}$, may be added together — $\mathbf{u}^{(1)}(\mathbf{x}, t) + \mathbf{u}^{(2)}(\mathbf{x}, t)$, $\mathbf{T}^{(1)}(\mathbf{x}, t) + \mathbf{T}^{(2)}(\mathbf{x}, t)$, $\mathbf{E}^{(1)}(\mathbf{x}, t) + \mathbf{E}^{(2)}(\mathbf{x}, t)$ — to obtain the solution for specified object and material, traction boundary conditions, and displacement boundary conditions, subject to different action-at-a-distance force $\mathbf{d}^{(1)} + \mathbf{d}^{(2)}$. In the proof of uniqueness the principle of superposition is used to define the difference problem obtained by subtracting the two (possibly different) solutions — $\mathbf{u}^{(1)}(\mathbf{x}, t)$, $\mathbf{T}^{(1)}(\mathbf{x}, t)$, $\mathbf{E}^{(1)}(\mathbf{x}, t)$, and $\mathbf{u}^{(2)}(\mathbf{x}, t)$, $\mathbf{T}^{(2)}(\mathbf{x}, t)$, $\mathbf{E}^{(2)}(\mathbf{x}, t)$ — to the same elasticity problem. The difference problem to which the fields $\mathbf{u}^{(1)}(\mathbf{x}, t) - \mathbf{u}^{(2)}(\mathbf{x}, t)$, $\mathbf{T}^{(1)}(\mathbf{x}, t) - \mathbf{T}^{(2)}(\mathbf{x}, t)$, and $\mathbf{E}^{(1)}(\mathbf{x}, t) - \mathbf{E}^{(2)}(\mathbf{x}, t)$ are a solution is thus a problem for the same specified object and material but for a zero action-at-a-distance force and for zero stress boundary conditions on $\partial O_{\mathbf{t}}$ and zero displacement boundary conditions on $\partial O_{\mathbf{u}}$. The objective is to obtain the solution to this difference problem by considering the work done on a linearly elastic object by the surface tractions, and the action-at-a-distance force does this most efficiently. The relation between the work done by the surface tractions and by the "action-at-a-distance force" on the object may be expressed as an integral over the object of the local work done per unit volume, tr$\mathbf{TE}$ (see (4.53) and (4.57))**:**

$$\int_{\partial 0} \mathbf{t} \cdot \mathbf{u} da + \int_0 \rho \mathbf{d} \cdot \mathbf{u} dv = \int_0 tr\{\mathbf{T} \cdot \mathbf{E}\} dv = \int_0 \mathbf{T} : \mathbf{E} dv = \int_0 \hat{\mathbf{T}} \cdot \hat{\mathbf{E}} dv \,. \tag{7.33}$$

The local work done is tr**T**·**E,** which also has the representation **T:E** = $\hat{\mathbf{T}}\cdot\hat{\mathbf{E}}$ (see (4.57) and (A164)). Partitioning the two types of boundaries being considered here, (7.33) may be rewritten as

$$\int_{\partial 0_t} \mathbf{t}\cdot\mathbf{u}da + \int_{\partial 0_u} \mathbf{t}\cdot\mathbf{u}da + \int_0 \rho\mathbf{d}\cdot\mathbf{u}dv = \int_0 \hat{\mathbf{T}}\cdot\hat{\mathbf{E}}dv\,. \tag{7.34}$$

Each of the three integrals on the left-hand side of (7.34) is zero. The first one is zero because the difference in boundary surface tractions is zero for the difference problem. The second one is zero because the difference in boundary surface displacements is zero for the difference problem. The third one is zero because the difference in action-at-a-distance forces is zero for the difference problem. Since the left-hand side of (7.34) is zero and since Hooke's law relates the stress and strain by $\hat{\mathbf{T}} = \hat{\mathbf{C}}\cdot\hat{\mathbf{E}}$, it follows that tr(**T**·**E**) = $\hat{\mathbf{T}}\cdot\hat{\mathbf{E}} = \hat{\mathbf{E}}\cdot\hat{\mathbf{C}}\cdot\hat{\mathbf{E}}$; thus, for the special case of the difference solution:

$$\int_0 (\hat{\mathbf{E}}\cdot\hat{\mathbf{C}}\cdot\hat{\mathbf{E}})dv = 0\,. \tag{7.35}$$

The final step in this proof of uniqueness is to recall that $\hat{\mathbf{C}}$ is positive definite; $\hat{\mathbf{E}}\cdot\hat{\mathbf{C}}\cdot\hat{\mathbf{E}} > 0$ for all nonzero strains $\hat{\mathbf{E}}$, (6.34H). There is a contradiction between (7.35) and the requirement that $\hat{\mathbf{C}}$ be positive definite, $\hat{\mathbf{E}}\cdot\hat{\mathbf{C}}\cdot\hat{\mathbf{E}} > 0$, everywhere in the object unless $\hat{\mathbf{E}} = 0$. This shows that the strain, and therefore the stress, in the difference solution is zero. It does not show that the displacement is zero, however. If fact, the displacement may represent any rigid object motion. Thus, a solution to a linear elasticity problem is only unique up to a rigid object motion.

The uniqueness theorem of linear elasticity theory is a very important tool in solution of elasticity problems. From it the elasticity problem solver knows that if a candidate solution satisfies all the boundary conditions as well as all the 15 elasticity equations, then the candidate solution is a unique solution to the problem. In particular, it allows the elasticity problem solver to guess candidate solutions to elasticity problems, or to make partial guesses. The literature of elasticity does not describe these guessing or semi-guessing methods as guessing; rather, it uses more dignified terminology like "the semi-inverse method." The following example is an illustration.

**Example 7.3.1**

Consider the problem of pure bending of a beam of orthotropic elastic material. The long axis of the beam coincides with the $x_3$ direction and the bending moment is applied about the $x_1$ axis (Figure 7.3). The coordinate system has its origin at the centroid of the cross-sectional area and the 1, 2 axes coincide with the principal axes of the area moment of inertia. Determine formulas for the stress components in terms of the applied moment $M_1$ and the geometric properties of the cross-section.

**Solution**: To obtain this solution, it is necessary to account only for the bending moment about the $x_1$ axis, $M_1$, and the fact that the lateral surfaces of this beam, that is to say, the surfaces other than the ends normal to the $x_3$ axis, are unloaded, that is to say, that there are no surface tractions applied. Because the lateral boundaries are unloaded we are going to guess that stresses that could act on the lateral boundaries are zero everywhere in the object, and thus

$$T_{11} = T_{22} = T_{12} = T_{13} = T_{23} = 0\,.$$

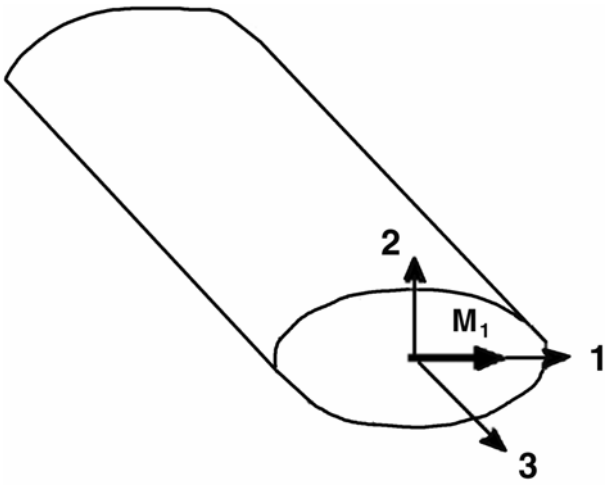



**Figure 7.3**. A beam subjected to pure bending loading. The bending moment $\mathbf{M}_1$ is applied about the 1-axis. There are no other loads. The origin of coordinates is at the centroid of the cross-section. The coordinate axes coincide with the principal axes of the area moment of inertia.

The only nonzero stress is then axial stress $T_{33}$. Moment $M_1$ must then be balanced by a distribution of axial stress $T_{33}$ in the beam. In general, $T_{33} = T_{33}(x_1, x_2, x_3)$; however, this may be reduced to $T_{33} = T_{33}(x_1, x_2)$ by observing that $T_{33}$ must be independent of $x_3$. The argument for $T_{33}$ being independent of $x_3$ is a physical one. Consider a free object diagram at any location along the length of the beam in Figure 7.3. The reactive force system at that (any) location must be equal to moment $M_1$ applied at the end. Thus, the stress distribution must be the same along the entire length of the beam. The only nonzero strains due to $T_{33}$ are then computed from (7.27):

$$E_{11}(x_1,x_2) = \frac{-\nu_{13}}{E_1} T_{33}(x_1,x_2)\,, \quad E_{22}(x_1,x_2) = \frac{-\nu_{23}}{E_2} T_{33}(x_1,x_2)\,,$$

$$E_{33}(x_1,x_2) = \frac{1}{E_3} T_{33}(x_1,x_2)\,.$$

When the compatibility equations (3.55) are applied to these three strains, the following differential equations for $T_{33}$ are obtained:

$$\frac{\partial^2 T_{33}}{\partial x_1^2} = \frac{\partial^2 T_{33}}{\partial x_2^2} = \frac{\partial^2 T_{33}}{\partial x_1 \partial x_2} = 0\,.$$

The solution to this system of differential equations is $T_{33} = c_0 + c_1 x_1 + c_2 x_2$, where $c_0$, $c_1$, and $c_2$ are constants. The next step in the solution to this problem is to require that stress distribution $T_{33}$ satisfy the conditions that the axial load on the beam is zero, that the bending moment about the $x_1$ axis is equal to $M_1$, and that the bending moment about the $x_2$ axis is equal to 0. The respective integrals in the 1, 2 plane over the cross-sectional area are given by

$$\int_A T_{33}\,dA = 0\,, \quad \int_A T_{33} x_2\,dA = M_1\,, \quad \int_A T_{33} x_1\,dA = 0\,.$$

The second integral equates $M_1$ to the couple generated by the integral of the moment of stress $T_{33}$ times the area patch at location $x_2$. The positive direction is determined by the right-hand rule. Substituting $T_{33} = c_o + c_1x_1 + c_2x_2$ into these three integrals, it follows that

$$c_o\int_A dA + c_1\int_A x_1 dA + c_2\int_A x_2 dA = 0\,,\quad c_o\int_A x_2 dA + c_1\int_A x_1x_2 dA + c_2\int_A x_2^2 dA = M_1$$

$$c_o\int_A x_1 dA + c_1\int_A x_1^2 dA + c_2\int_A x_1x_2 dA = 0\,.$$

These results are simplified by denoting the cross-sectional area $A$, $x_i$, $i = 1, 2$, centroid of the cross-sectional area, denoted by $\bar{x}_i$, and the components of the area moment of inertia tensor, $I_{11}$, $I_{22}$, $I_{12}$:

$$A = \int_A dA\,,\quad \bar{x}_i = \frac{1}{A}\int_A x_i dA\,,\quad I_{11} = \int_A x_2^2 dA\,,\quad I_{22} = \int_A x_1^2 dA\,,\quad I_{12} = -\int_A x_1x_2 dA\,.$$

Since the origin of coordinates was selected at the centroid, it follows that $\bar{x}_i$ are zero; thus, $c_o = 0$. Then, since the coordinate system has been chosen to be the principal axes of the area moment of inertia, it follows that the product of inertia $I_{12}$ vanishes, and so $c_2 = M_1/I_{11}$ and $c_1 = 0$. It follows that $T_{33} = M_1x_2/I_{11}$.

The solution of the stresses is then $T_{11} = T_{22} = T_{12} = T_{13} = T_{23} = 0$ and $T_{33} = M_1x_2/I_{11}$. The solution for the strains is

$$E_{11} = \frac{-\nu_{13}M_1x_2}{E_1I_{11}}\,,\quad E_{22} = \frac{-\nu_{23}M_1x_2}{E_2I_{11}}\,,\quad E_{33} = \frac{M_1x_2}{E_3I_{11}}\,,\quad E_{12} = E_{13} = E_{23} = 0\,,$$

and the solution for the displacements may be obtained from the solution for the strains and integration of strain displacement relations (3.49). This solution satisfies each of the 15 equations of elasticity and the boundary conditions specified for this problem; thus, by the uniqueness theorem, it is the unique solution to this bending problem.

**Example 7.3.2**

For the problem considered in Example 7.3.1, determine the solution for displacement field $\mathbf{u}(\mathbf{x}, t)$ from the solution for the strains:

$$E_{11} = \frac{-\nu_{13}M_1x_2}{E_1I_{11}}\,,\quad E_{22} = \frac{-\nu_{23}M_1x_2}{E_2I_{11}}\,,\quad E_{33} = \frac{M_1x_2}{E_3I_{11}}\,,\quad E_{12} = E_{13} = E_{23} = 0\,,$$

by integration of strain displacement relations (3.49).

**Solution**: From this strain solution and strain displacement relations (3.49), a system of six first-order partial differential equations for the components of the displacement vector are obtained:

$$\frac{\partial u_1}{\partial x_1} = \frac{-\nu_{13}M_1x_2}{E_1I_{11}}\,,\quad \frac{\partial u_2}{\partial x_2} = \frac{-\nu_{23}M_1x_2}{E_2I_{11}}\,,\quad \frac{\partial u_3}{\partial x_3} = \frac{M_1x_2}{E_3I_{11}}\,,$$

$$\frac{\partial u_1}{\partial x_2} + \frac{\partial u_2}{\partial x_1} = 0\,,\quad \frac{\partial u_1}{\partial x_3} + \frac{\partial u_3}{\partial x_1} = 0\,,\quad \frac{\partial u_3}{\partial x_2} + \frac{\partial u_2}{\partial x_3} = 0\,.$$

Integration of the first three of these equations yields

$$u_1 = \frac{-\nu_{13} M_1 x_2 x_1}{E_1 I_{11}} + w_1(x_2, x_3), \quad u_2 = \frac{-\nu_{23} M_1 x_2^2}{2E_2 I_{11}} + w_2(x_1, x_3),$$

$$u_3 = \frac{M_1 x_2 x_3}{E_3 I_{11}} + w_3(x_1, x_2).$$

This representation for the components of **u** can then be substituted into the second set of three equations above, and thus

$$\frac{\partial w_1(x_2, x_3)}{\partial x_2} + \frac{\partial w_2(x_1, x_3)}{\partial x_1} = \frac{\nu_{13} M_1 x_1}{E_1 I_{11}}, \quad \frac{\partial w_1(x_2, x_3)}{\partial x_3} + \frac{\partial w_3(x_1, x_2)}{\partial x_1} = 0$$

$$\frac{\partial w_3(x_1, x_2)}{\partial x_2} + \frac{\partial w_2(x_1, x_3)}{\partial x_3} = -\frac{M_1 x_3}{E_1 I_{11}}.$$

The problem of determining displacement field **u** is now the problem of determining functions $w_1(x_2, x_3)$, $w_2(x_1, x_3)$, and $w_3(x_1, x_2)$. Differentiating the first equation above with respect to $x_3$, the second equation above with respect to $x_2$, and the third equation above with respect to $x_1$, one obtains the following:

$$\frac{\partial^2 w_1(x_2, x_3)}{\partial x_2 \partial x_3} = -\frac{\partial^2 w_2(x_1, x_3)}{\partial x_1 \partial x_3}, \quad \frac{\partial^2 w_1(x_2, x_3)}{\partial x_2 \partial x_3} = -\frac{\partial^2 w_3(x_1, x_2)}{\partial x_1 \partial x_2}$$

$$\frac{\partial^2 w_3(x_1, x_2)}{\partial x_1 \partial x_2} = -\frac{\partial^2 w_2(x_1, x_3)}{\partial x_1 \partial x_3},$$

from which we conclude that

$$\frac{\partial^2 w_1(x_2, x_3)}{\partial x_2 \partial x_3} = \frac{\partial^2 w_2(x_1, x_3)}{\partial x_1 \partial x_3} = \frac{\partial^2 w_3(x_1, x_2)}{\partial x_1 \partial x_2} = 0.$$

It follows that each component of **w** must be the sum of two functions, each of a different single variable, and so

$$w_1(x_2, x_3) = f_{12}(x_2) + f_{13}(x_3), \quad w_2(x_1, x_3) = f_{21}(x_1) + f_{23}(x_3),$$

$$w_3(x_1, x_2) = f_{31}(x_1) + f_{32}(x_2).$$

Substitution of these representations for **w** back into the differential equations above yields the following:

$$\frac{\partial f_{12}(x_2)}{\partial x_2} + \frac{\partial f_{21}(x_1)}{\partial x_1} = \frac{\nu_{13} M_1 x_1}{E_1 I_{11}}, \quad \frac{\partial f_{13}(x_3)}{\partial x_3} + \frac{\partial f_{31}(x_1)}{\partial x_1} = 0,$$

$$\frac{\partial f_{31}(x_1)}{\partial x_2} + \frac{\partial f_{23}(x_3)}{\partial x_3} = -\frac{M_1 x_3}{E_3 I_{11}}.$$

A study of the equations above shows that certain combinations of terms are constants, denoted by $c_{12}$, $c_{13}$, and $c_{32}$:

$$\frac{\partial f_{12}(x_2)}{\partial x_2} = -Y_{12}^0 = -\frac{\partial f_{21}(x_1)}{\partial x_1} + \frac{\nu_{13} M_1 x_1}{E_1 I_{11}}, \quad \frac{\partial f_{13}(x_3)}{\partial x_3} = -Y_{13}^0 = -\frac{\partial f_{31}(x_1)}{\partial x_1},$$

$$\frac{\partial f_{32}(x_2)}{\partial x_2} = Y_{23}^0 = -\frac{\partial f_{23}(x_3)}{\partial x_3} - \frac{M_1 x_3}{E_1 I_{11}},$$

and thus

$$f_{12}(x_2) = -Y_{12}^0 x_2 + c_{12}, \quad f_{21}(x_1) = Y_{12}^0 x_1 + \frac{\nu_{13} M_1 x_1^2}{2E_1 I_{11}} + c_{21},$$

$$f_{13}(x_3) = -Y_{13} x_3 + c_{13}, \quad f_{31}(x_1) = Y_{13}^0 x_1 + c_{13},$$

$$f_{32}(x_2) = Y_{23}^0 x_2 + c_{32}, \quad f_{23}(x_3) = -Y_{23}^0 x_3 - \frac{M_1 x_3^2}{2E_3 I_{11}} + c_{23}.$$

Substitution of these results into the formulas for **w**,

$$w_1(x_2, x_3) = -Y_{12}^0 x_2 - Y_{13}^0 x_3 + c_{12} + c_{13},$$

$$w_2(x_1, x_3) = \frac{\nu_{13} M_1 x_1^2}{2E_1 I_{11}} - \frac{M_1 x_3^2}{2E_3 I_{11}} + Y_{12}^0 x_1 - Y_{23}^0 x_3 + c_{21} + c_{23},$$

$$w_3(x_1, x_2) = Y_{23}^0 x_2 + Y_{13}^0 x_1 + c_{13} + c_{32},$$

and then into the results of the first integration above, the components of **u** are obtained:

$$u_1 = \frac{-\nu_{13} M_1 x_2 x_1}{E_1 I_{11}} - Y_{12}^0 x_2 - Y_{13}^0 x_3 + u_1^0,$$

$$u_2 = -\frac{M_1}{2I_{11}}\left(\frac{x_3^2}{E_3} - \frac{\nu_{23} x_2^2}{E_2} + \frac{\nu_{13} x_1^2}{E_1}\right) + Y_{12}^0 x_1 - Y_{23}^0 x_3 + u_2^0,$$

$$u_3 = \frac{M_1 x_2 x_3}{E_1 I_{11}} + Y_{23}^0 x_2 + Y_{13}^0 x_1 + u_3^0,$$

where $u_1^0 = c_{12} + c_{13}$, $u_2^0 = c_{21} + c_{23}$, $u_3^0 = c_{13} + c_{32}$. Vector $\mathbf{u}^\circ$ represents a superposed rigid object translation, as one can see from the fact that $\mathbf{u}^\circ$ are the constant components of **u**; they are the values of **u** at the origin. The rigid object rotation, **Y,** may be determined from displacement field **u** using (3.49), and thus

$$Y_{12} = Y_{12}^0, \quad Y_{13} = Y_{13}^0, Y_{23} = \frac{M_1 x_3}{I_{11}}\left(\frac{1}{E_1} + \frac{1}{E_3}\right) + Y_{23}^0.$$

Constants $Y_{12}^0$, $Y_{13}^0$, $Y_{23}^0$ therefore represent the superposed rigid object rotation, the values of the rigid object rotation at the origin. If the superposed rigid object translation and rotation are zero, then the displacement field **u** is given by

$$u_1 = \frac{-\nu_{13} M_1 x_2 x_1}{E_1 I_{11}}, \quad u_2 = -\frac{M_1}{2I_{11}}\left(\frac{x_3^2}{E_3} - \frac{\nu_{23} x_2^2}{E_2} + \frac{\nu_{13} x_1^2}{E_1}\right), \quad u_3 = \frac{M_1 x_2 x_3}{E_1 I_{11}},$$

and rigid object rotation **Y** has only one nonzero component:

$$Y_{23} = \frac{M_1 x_3}{I_{11}}\left(\frac{1}{E_1} + \frac{1}{E_3}\right),$$

which represents the rotation along the beam as the distance increases from the beam end at the origin of coordinates. The total rotation between the two ends of the bent beam of length $L$ is then given by

$$Y_{23}^{\text{Total end-to-end rotation}} = \frac{M_1 L}{I_{11}}\left(\frac{1}{E_1} + \frac{1}{E_3}\right).$$

**Example 7.3.3**

In mechanics of materials the deflection curve for a beam is considered to be the deflection curve for the neutral axis, the neutral axis being by definition the curve that coincides with the centroid of the cross-section at each cross-section. Using the results of the problem considered in Examples 7.3.1 and 7.3.2, determine the formula for the deflection curve for a beam subject to pure bending

**Solution**: The displacement of the neutral axis of a beam subjected to pure bending may be determined from the formulas for the displacement field given in Example 7.3.2 above:

$$u_1 = \frac{-\nu_{13} M_1 x_2 x_1}{E_1 I_{11}}, \quad u_2 = -\frac{M_1}{2I_{11}}\left(\frac{x_3^2}{E_3} - \frac{\nu_{23} x_2^2}{E_2} + \frac{\nu_{13} x_1^2}{E_1}\right), u_3 = \frac{M_1 x_2 x_3}{E_1 I_{11}}.$$

The centroid of the beam's cross-section in Examples 7.3.1 was set at the origin of coordinates in the planar cross-section; thus, for the centroid, $x_1$ and $x_2$ are zero and

$$u_1 = 0, \quad u_2 = -\frac{M_1 x_3^2}{2I_{11} E_3}, u_3 = 0.$$

Displacement $u_2$ represents the displacement curve. In the case of isotropy, and in the notation customary of mechanics of materials, the deflection curve is given by

$$y(x) = -\frac{Mx^2}{2EI}.$$

**Example 7.3.4**

This problem concerns the propagation of elastic plane waves. The problem is to determine the wave speed of a plane wave propagating in a symmetry direction in an orthotropic material.

Two kinds of plane waves are to be considered, one in which the oscillating displacement component varies in the direction of propagation and the other in which it varies in a direction perpendicular to the direction of propagation. Let the direction of propagation be the $x_1$ direction and let the direction perpendicular to the direction of propagation be the $x_2$ direction. Both the $x_1$ and the $x_2$ directions are directions of the symmetry axes of the orthotropic material. The displacement that varies in the direction of its propagation is $u_1 = u_1(x_1,t)$ and represents a time-varying longitudinal motion of axial compression or tension or some combination of the two. The displacement that varies in the perpendicular direction is $u_2 = u_2(x_1,t)$ and represents a time varying shearing motion. The motion $u_1 = u_1(x_1,t)$ is called the longitudinal (L) motion and $u_2 = u_2(x_1,t)$, the shear (S) motion. Neglect the action-at-a-distance force.

**Solution**: The differential equations governing these two motions are obtained from the governing set of elasticity equations, the first three equations in this section. First, from the strain-displacement relations (3.49) it follows that all the strain components but one is zero for both the longitudinal and shearing motions and that the non-zero components are given by

$$E_{11} = \frac{\partial u_1}{\partial x_1} \text{ for (L) and } E_{12} = \frac{1}{2}\frac{\partial u_2}{\partial x_1} \text{ for (S).}$$

Second, using these two results in the stress-strain relations for orthotropic materials (7.22), it follows that

$$T_{11} = c_{11}\frac{\partial u_1}{\partial x_1},\ T_{22} = c_{12}\frac{\partial u_1}{\partial x_1},\ T_{33} = c_{13}\frac{\partial u_1}{\partial x_1}, \text{ for (L) and } T_{12} = c_{66}\frac{\partial u_2}{\partial x_1} \text{ for (S).}$$

Third, upon substitution of these stresses and the functional form of the two motions, $u_1 = u_1(x_1,t)$ and $u_2 = u_2(x_1,t)$, in the stress equations of motion (7.18), one obtains the differential equations

$$\frac{\partial^2 u_1}{\partial t^2} = c_L^2\frac{\partial^2 u_1}{\partial x_1^2} \text{ for (L) and } \frac{\partial^2 u_2}{\partial t^2} = c_S^2\frac{\partial^2 u_2}{\partial x_1^2} \text{ for (S),}$$

where the notations

$$c_L^2 = \frac{c_{11}}{\rho} \text{ for (L) and } c_S^2 = \frac{c_{66}}{\rho} \text{ for (S)}$$

have been introduced. The solution of these equations is so very similar that only the longitudinal case is considered. These are differential equations whose solutions can be explicitly calculated. Consider the differential equation for the longitudinal wave and let $\xi = x_1 + c_L t$ and $\eta = x_1 - c_L t$. The second derivatives that appear in the differential equation are obtained using the chain rule, thus

$$\frac{\partial^2 u_1}{\partial x_1^2} = \frac{\partial^2 u_1}{\partial \xi^2} + 2\frac{\partial^2 u_1}{\partial \xi \partial \eta} + \frac{\partial^2 u_1}{\partial \eta^2} \text{ and } \frac{\partial^2 u_1}{\partial t^2} = c_L^2\left[\frac{\partial^2 u_1}{\partial \xi^2} - 2\frac{\partial^2 u_1}{\partial \xi \partial \eta} + \frac{\partial^2 u_1}{\partial \eta^2}\right].$$

When these expressions are substituted into the differential equation for the longitudinal wave it reduces to

$$\frac{\partial^2 u_1}{\partial \xi \partial \eta} = 0\,,$$

which has the solution

$$u_1 = p(\xi) + q(\eta) = p(x_1 + c_L t) + q(x_1 - c_L t)\,.$$

The transformation $\xi = x_1 + c_L t$ represents a translation of the coordinate system to the left by the amount $c_L t$. Since this translation is proportional to the time, a point $\xi$ = constant moves to the left with speed $c_L$. A solution of the form $u_1 = p(\xi) = p(x_1 + c_L t)$ represents a wave traveling with velocity - $c_L$ without changing its shape. Similarly, $u_1 = q(\eta) = q(x_1 - c_L t)$ represents a wave traveling with velocity + $c_L$ without changing its shape. Thus the solution $u_1 = p(x_1 + c_L t) + q(x_1 - c_L t)n$ is the sum of a wave traveling to the left with velocity $-c_L$ and one traveling to the right with velocity + $c_L$, and since the two waves travel in opposite directions, the shape of $u_1(x_1, t)$ will in general change with time.

The initial-boundary value problem is composed of the differential equation for the longitudinal wave and the initial conditions $u_1(x_1, 0) = f(x_1)$ and $\partial u_1 / \partial t(x_1, 0) = g(x_1)$ for $0 \le x_1 < \infty$. These initial conditions determine the form of the functions $p$ and $q$ in the solution. From the solution $u_1 = p(x_1 + c_L t) + q(x_1 - c_L t)$ and using the chain rule it follows that

$$p(x_1) + q(x_1) = f(x_1) \text{ and } c_L p'(x_1) - c_L q'(x_1) = g(x_1) \text{ for } 0 \le x_1 < \infty\,.$$

Combining these two equations, it follows that $2c_L p'(x_1) = c_L f'(x_1) + g(x_1)$ or, following integration,

$$p(\xi) = \frac{1}{2} f(\xi) + \frac{1}{2c_L} \int_0^{\xi} g(\zeta)\, d\zeta + \text{constant}\,.$$

From $p(x_1) + q(x_1) = f(x_1)$ it follows that

$$q(\eta) = \frac{1}{2} f(\eta) - \frac{1}{2c_L} \int_0^{\eta} g(\zeta)\, d\zeta - \text{constant}\,;$$

thus,

$$u_1 = p(x_1 + c_L t) + q(x_1 - c_L t) =$$

$$\frac{1}{2}\left[f(x_1 + c_L t) + f(x_1 - c_L t)\right] + \frac{1}{2c_L} \int_0^{x_1 + c_L t} g(\zeta)\, d\zeta - \int_0^{x_1 - c_L t} g(\zeta)\, d\zeta \;=$$

$$\frac{1}{2}\left[f(x_1 + c_L t) + f(x_1 - c_L t)\right] + \frac{1}{2c_L} \int_{x_1 - c_L t}^{x_1 + c_L t} g(\zeta)\, d\zeta\,.$$

A similar result holds for the S wave; one has only to change the $c_L$ to $c_S$ and the subscript on $u_1$ from 1 to 2 to obtain the S result. The difference between the two results is that the shear or S wave is a propagating shearing motion, as opposed to a propagating compression/tension motion, and that it travels at a different wave speed. If the same results were obtained for an isotropic elastic material, the wave speeds would be

$$c_L^2 = \frac{\lambda + 2\mu}{\rho} \text{ for (L) and } c_S^2 = \frac{2\mu}{\rho} \text{ for (S).}$$

**Problems**

7.3.1. Verify that (7.21) may be determined directly from (7.20).

7.3.2. Record the form of (7.22) for transversely isotropic materials.

7.3.3. Calculate (7.24) from (7.23).

7.3.4. Verify Navier equation (7.29) for isotropic linear elasticity. Accomplish this by substituting (3.49) into (7.24) and then place modified (7.24) for the stresses in terms of the components of the displacement vector into equations of motion (7.18).

7.3.5. Show that, in an isotropic elastic material the principal axes of stress and strain always coincide. {Hint: Recall that the principal axes of stress (strain) are characterized by vanishing of the shearing stresses (shearing strains)}.

7.3.6. Prove that the principal axes of stress and the principal axes of strain cannot coincide in a triclinic material.

7.3.7. Under what conditions do the principal axes of stress and the principal axes of strain not coincide for an orthotropic elastic material?

7.3.8. As an extension of Example 7.3.1, show that if the beam in Figure 7.3 is bent about both the $x_1$ and the $x_2$ axes, and it is also subjected to an axial tensile load of magnitude $P$, then $T_{33} = P/A + M_1 x_2/I_{11} - M_2 x_1/I_{22}$.

7.3.9. Show that differential equation

$$\frac{\partial^2 u_1}{\partial t^2} = c_S^2 \frac{\partial^2 u_1}{\partial x_2^2}$$

and the initial conditions that require that the displacement and velocity at time $t = 0$ to be given by $u_1(x_2, 0)$ and $(\partial u_1/\partial t)(x_2, 0)$ are identically satisfied by solution

$$u_1(x_2,t) = \frac{1}{2}\{u_1(x_2 + c_S t, 0) + u_1(x_2 - c_S t, 0)\} + \frac{1}{2c_S}\int_{x_2 - c_S t}^{x_2 + c_S t} \frac{\partial u_1}{\partial t}(\xi, 0)\, d\xi \,.$$

## 7.4. THE THEORY OF VISCOUS FLUIDS

An overview of the theory of viscous fluids, without temperature effects, can be obtained by considering it as a system of seventeen equations in seventeen scalar unknowns. The seventeen scalar unknowns are the six components of stress tensor **T**, fluid pressure $p$, fluid density $\rho$, the six components of rate-of-deformation tensor **D**, and the three components of velocity vector **v**. The parameters of a viscous fluid problem are the viscosity coefficients $\lambda$ and $\mu$ ($3\lambda + 2\mu > 0$, $2\mu > 0$) and action-at-a-distance force **d**, which are assumed to be known. The system of seventeen equations consists of a constitutive equation relating density $\rho$ to pressure $p$, $\rho = \rho(p)$ (and, in thermal-viscous problems, to the temperature), the six equations of the Newtonian law of viscosity,

$$\mathbf{T} = -p\mathbf{1} + \lambda(\mathrm{tr}\mathbf{D})\mathbf{1} + 2\mu\mathbf{D}, \qquad \text{(6.36N) repeated}$$

the six rate-of-deformation-velocity relations,

$$\mathbf{D} = (1/2)((\nabla \otimes \mathbf{v})^{\mathrm{T}} + \nabla \otimes \mathbf{v}), \qquad \text{(3.32) repeated}$$

the one equation of the conservation of mass,

$$\dot{\rho} + \rho(\nabla \cdot \mathbf{v}) = 0\,, \qquad \text{(4.5) repeated}$$

and the three stress equations of motion,

$$\rho\dot{\mathbf{v}} = \nabla\cdot\mathbf{T} + \rho\mathbf{d}\,,\ \mathbf{T} = \mathbf{T}^T\,. \tag{7.36}$$

This form of the stress equations of motion differs from (4.37) and (7.18) only in notation: the acceleration is here represented by $\dot{\mathbf{v}}$ rather than $\ddot{\mathbf{x}}$ or $\ddot{\mathbf{u}}$, respectively, a result that follows from (3.24). The system of seventeen equations in seventeen scalar unknowns may be reduced to a system of four equations in four scalar unknowns, pressure $p$, and the three components of velocity $\mathbf{v}$ by accomplishing the following algebraic steps: (1) substitute rate-of-deformation-velocity (3.32) into stress–strain relations (6.36N), and then (2) substitute the resulting expression relating the stress to the first derivatives of the velocity into the three stress equations of motion (7.36). The result is a system of three equations in three scalar unknowns, the three components of the velocity vector $\mathbf{v}$:

$$\rho\dot{\mathbf{v}} = -\nabla p + (\lambda+\mu)\nabla(\nabla\cdot\mathbf{v}) + \mu\nabla^2\mathbf{v} + \rho\mathbf{d}\,. \tag{7.37}$$

This is the Navier-Stokes equation for viscous fluid flow. Substituting barotropic relation $\rho = \rho(p)$ into the conservation of mass (4.5) yields the fourth equation in the set of four equations for the four unknowns, $p$, and the components of $\mathbf{v}$:

$$\frac{\partial\rho}{\partial p}\dot{p} + \rho(p)(\nabla\cdot\mathbf{v}) = 0\,. \tag{7.38}$$

This system of equations will become more complicated if thermal effects are considered. They may also be simplified in different ways. An easy simplification is to assume that the viscosity of the fluid is small and can be neglected (that is to say, the fluid is assumed to be inviscid), then $\lambda$ and $\mu$ are set equal to zero, (7.37) becomes

$$\rho\dot{\mathbf{v}} = -\nabla p + \rho\mathbf{d}\,, \tag{7.39}$$

and (7.38) is unchanged. System of equations (7.37) and (7.38) may also be simplified using the assumption of incompressibility of the fluid. An incompressible material is one which is not permitted to have changes in its volume, $\mathrm{tr}\mathbf{D} = \nabla\cdot\mathbf{v} = 0$. If the volume cannot change, density $\rho$ of the fluid cannot change. It follows that barotropic relationship $\rho = \rho(p)$ is not appropriate and the pressure is no longer determined by the density. Pressure field $p$ in an incompressible material is a Lagrange multiplier (see Example 7.4.1) that serves the function of maintaining the incompressibility constraint, $\nabla\cdot\mathbf{v} = 0$. Because the volume of the fluid cannot change, $p$ does no work on the fluid; it is a function of $\mathbf{x}$ and $t$, $p(\mathbf{x}, t)$, to be determined by solution of the system of differential equations and boundary/initial conditions. The reduced Navier-Stokes equation for viscous fluid flow and incompressibility constraint now becomes a system of four equations:

$$\rho\dot{\mathbf{v}} = -\nabla p + \mu\nabla^2\mathbf{v} + \rho\mathbf{d}\,,\quad \nabla\cdot\mathbf{v} = 0, \tag{7.40}$$

for the four unknown fields: the three components of $\mathbf{v}(\mathbf{x}, t)$ and $\mathrm{p}(\mathbf{x}, t)$. The typical boundary condition applied in viscous fluid theory is the "no slip" condition. This condition requires that a viscous fluid at a solid surface must stick to the surface and have no velocity, $\mathbf{v}(\mathbf{x}^*, t) = 0$ for $\mathbf{x}^* \in \partial O_s$, where $\partial O_s$ stands for the solid boundary of the fluid domain.

**Example 7.4.1. Pressure as a Lagrange multiplier in incompressible fluids**

The constraint of incompressibility is imposed using a Lagrange multiplier. In order to describe what this means and how it is accomplished, Lagrange's method of calculating extrema in problems in which there is a constraint is summarized briefly. Lagrange's method is for solution of a type of problem in which one must find the extremal values of function $f(x, y, z)$ subject to constraint $g(x, y, z) = c$. The solution to the problem is obtained by forming function $q(x, y, z) = f(x, y, z) + \lambda g(x, y, z)$, where $\lambda$ is a constant, called the Lagrange multiplier, whose value is to be determined. Treating $x$, $y$, and $z$ as independent variables, four independent conditions — $\partial q/\partial x = 0$, $\partial q/\partial y = 0$, $\partial q/\partial z = 0$, and $g(x, y, z) = c$ — are available to find the four unknowns, $x, y, z$, and $\lambda$. As an example of application of Lagrange's method, consider the problem of finding the maximum or minimum distance from point $(a, b, c)$ to a point on the surface of the unit sphere, $x^2 + y^2 + z^2 = 1$. The function that is to be extremized is the square of the distance between $(x, y, z)$ and $(a, b, c)$, $f(x, y, z) = (x - a)^2 + (y - b)^2 + (z - c)^2$. This function is to be extremized subject to the constraint that $(x, y, z)$ be a point on the surface of the unit sphere, $x^2 + y^2 + z^2 = 1$, thus $q(x, y, z) = (x - a)^2 + (y - b)^2 + (z - c)^2 + \lambda(x^2 + y^2 + z^2 - 1)$. Setting the derivatives of $q(x, y, z)$ with respect to $x$, $y$, and $z$ equal to zero, it follows that $x = a/(\lambda + 1)$, $y = b/(\lambda + 1)$, and $z = c/(\lambda + 1)$. From constraint condition $x^2 + y^2 + z^2 = 1$, it follows that $(\lambda + 1) = \pm\sqrt{(a^2 + b^2 + c^2)}$. In the special case when $(a, b, c) = (2, 0, 0)$, $(\lambda + 1) = \pm 2$, and $(x, y, z) = (1, 0, 0)$ or $(x, y, z) = (-1, 0, 0)$; thus, the point on the unit sphere closest to (2, 0, 0) is (1, 0, 0) and the point on the unit sphere furthest from (2, 0, 0) is (–1, 0, 0).

With this background the problem is to employ Lagrange's method to minimize the dissipation due to the rate of volume change, as opposed to the dissipation due to the shearing motion, in a viscous fluid. From eq. (6.32N) the stress power or dissipation is represented by $\mathbf{T}:\mathbf{D} = -p(\mathrm{tr}\mathbf{D}) + ((3\lambda + 2\mu)/3)(\mathrm{tr}\mathbf{D})^2 + 2\mu\mathrm{tr}(\mathrm{dev}\mathbf{D})^2$, and the stress power or dissipation due to the rate of volume change only is given by $\mathbf{T}:\mathbf{D} = -p(\mathrm{tr}\mathbf{D}) + ((3\lambda + 2\mu)/3)(\mathrm{tr}\mathbf{D})^2$ since deviatoric term dev$\mathbf{D}$ is dropped. The constraint condition is that tr$\mathbf{D} = 0$. The problem is to show that when this constraint is imposed, the pressure becomes a constant Lagrange multiplier.

**Solution**: In this case $q(\mathrm{tr}\mathbf{D}) = -p(\mathrm{tr}\mathbf{D}) + ((3\lambda + 2\mu)/3)(\mathrm{tr}\mathbf{D})^2 + \lambda(\mathrm{tr}\mathbf{D})$; thus, from $\partial q/\partial(\mathrm{tr}\mathbf{D}) = (\lambda - p) + (2(3\lambda + 2\mu)/3)(\mathrm{tr}\mathbf{D}) = 0$, and constraint condition tr$\mathbf{D} = 0$, it follows that $\lambda = p$.

In an 1883 paper Sir Osborne Reynolds showed that the transition between laminar flow governed by the Newtonian law of viscosity, and the form of the Navier-Stokes equations considered here, and the chaotic flow called turbulence depended upon a dimensionless number that is now called the Reynolds number. Reynolds number $R$ is equal to $\rho Vd/\mu$, where $\rho$ and $\mu$ are the density and viscosity of the fluid, respectively, and $V$ and $d$ are a representative velocity and a representative length of the problem under consideration, respectively. Only laminar flows of viscous fluids are considered in this book, and so there is always a certain value of a Reynolds number for which the solution no longer describes the physical situation accurately.

**Example 7.4.2. Couette flow**

Consider an incompressible viscous fluid of viscosity $\mu$ in the domain between two infinite flat solid plates at $x_2 = \pm h/2$. Action-at-a-distance forces are not present and the plate at $x_2 = h/2$ is moving at constant velocity $V$ in the positive $x_1$ direction. There is no pressure gradient. Determine the velocity distribution and the stress that must be applied to the top plate to maintain its motion.

**Solution**: Assume that the only nonzero velocity component is in the $x_1$ direction and that it depends only upon the $x_2$ coordinate, $v_1 = v_1(x_2)$. This velocity field automatically satisfies the incompressibility condition, $\nabla\cdot\mathbf{v} = 0$, and the reduced Navier Stokes equations are

$$\frac{\partial^2 v_1}{\partial x_2^2} = 0 \text{ and } \nabla p = 0.$$

The solution to the first of these differential equations, which is in fact an ordinary differential equation, is given by $v_1(x_2) = c_1 x_2 + c_2$. The no-slip boundary conditions are that $v_1(-h/2) = 0$ and $v_1(h/2) = V$, and thus $c_1 = V/h$ and $c_2 = V/2$, and thus $v_1(x_2) = (V/h)(x_2 + h/2)$. The solution to the second of these differential equations is that $p$ is a constant. The stress at the top plate is given by the $T_{12}$ component of (6.36N):

$$T_{12} = \mu \frac{\partial v_1}{\partial x_2} = \frac{\mu V}{h}.$$

**Example 7.4.3 Plane Poiseuille flow**

Consider an incompressible viscous fluid of viscosity $\mu$ in the domain between two infinite flat solid plates at $x_2 = \pm h/2$. Action-at-a-distance forces are not present and the plates are not moving. The flow is steady and there is a constant pressure drop in the $x_1$ direction given by $\partial p/\partial x_1$. Determine the velocity distribution.

**Solution**: As in the previous example, assume that the only nonzero velocity component is in the $x_1$ direction and that it depends only upon the $x_2$ coordinate, $v_1 = v_1(x_2)$. This velocity field automatically satisfies the incompressibility condition, $\nabla \cdot \mathbf{v} = 0$, and the reduced Navier Stokes equation is

$$\mu \frac{\partial^2 v_1}{\partial x_2^2} = \frac{\partial p}{\partial x_1}.$$

The solution to this differential equation, which is again an ordinary differential equation, is given by

$$v_1 = \frac{1}{2\mu} \frac{\partial p}{\partial x_1} x_2^2 + c_3 x_2 + c_4.$$

The boundary conditions are that $v_1(\pm h/2) = 0$, and thus $c_3 = 0$ and $c_4 = -\frac{1}{2\mu} \frac{\partial p}{\partial x_1} \left(\frac{h}{2}\right)^2$, and it follows that the velocity profile is parabolic in shape:

$$v_1 = \frac{1}{2\mu} \left(-\frac{\partial p}{\partial x_1}\right) \left\{ \left(\frac{h}{2}\right)^2 - x_2^2 \right\},$$

which is written with a minus sign in front of the pressure gradient to emphasize that the pressure gradient is negative in the direction of flow or, equivalently, the pressure is dropping in the direction of flow. The volume flow rate per unit length, $Q$, is given by

$$Q = \int_{-h/2}^{h/2} v_1 dx_2 = \frac{1}{2\mu} \left(-\frac{\partial p}{\partial x_1}\right) \int_{-h/2}^{h/2} \left\{ \left(\frac{h}{2}\right)^2 - x_2^2 \right\} dx_2 = \left(-\frac{\partial p}{\partial x_1}\right) \frac{h^3}{12\mu}.$$

In the case of pipe flow, the differential equation corresponding to $\mu \frac{\partial^2 v_1}{\partial x_2^2} = \frac{\partial p}{\partial x_1}$ is, in cylindrical coordinates $r$ and $z$ (see §A.13), given by $\frac{\mu}{r}\frac{\partial v_z}{\partial r}\ r\frac{\partial v_z}{\partial r}\ = \frac{\partial p}{\partial z}$, where the pressure gradient is assumed to be a constant. The solution to this equation in cylindrical coordinates, subject to the 'no slip" boundary condition at the pipe wall, is a similar parabolic profile to that obtained above

$$v_z = -\frac{\partial p}{\partial z}\ \frac{r_o^2}{4\mu}\ 1-\frac{r^2}{r_o^2}\ ,$$

where $r_o$ is the radius of the pipe and r and z are two of the three cylindrical coordinates. The volume flow rate is given by

$$Q = 2\pi \int_0^{r_o} r v_z dr = \overline{v}\pi r_o^2 = -\frac{\partial p}{\partial z}\ \frac{\pi r_o^4}{8\mu},$$

where $\overline{v}$ is the mean velocity.

**Biomedical Historical Note**: Solution to the Navier-Stokes equations for steady flow in a pipe is called Poiseuille flow after Jean-Louis-Marie Poiseuille (1799–1869), a Parisian physician and physiologist interested in the flow of blood. Poiseuille received his medical degree in 1828 and established his practice in Paris. He developed an improved method for measuring blood pressure. He also is believed to be the first to have used the mercury manometer to measure blood pressure. In the 1840s Poiseuille experimentally determined the basic properties of steady laminar pipe flow using water as a substitute for blood. The formula for $Q$ above is rewritten below with the negative pressure gradient expressed as the change in pressure $\Delta p$ along the entire length of pipe divided by the pipe length L, and thus

$$Q = \overline{v}\pi r_o^2 = \frac{\Delta p \pi r_o^4}{8\mu L}.$$

This formula had not been derived when Poiseuille did his very careful experimental work, which demonstrated its principal features using capillary tubes of glass (models of the blood capillary vessels). Poiseuille showed that volume flow rate $Q$ was proportional to the pressure drop along the pipe, $\Delta p$, to the fourth power of radius $r_0$ of the pipe and inversely proportional to the length of the pipe, $L$. In honor of Poiseuille the unit of viscosity is call the poise. The poise has the symbol $P$ and is equal to one (dyne-second)/(centimeter)$^2$ or 0.1 Pa-s.

**Problems**

7.4.1. Verify the calculation of Navier-Stokes equations (7.37) by (1) substituting rate-of-deformation-velocity (3.32) into stress–strain relations (6.36N), then (2) substituting the resulting expression relating the stress to the first derivatives of the velocity into the three stress equations of motion (7.36).

7.4.2. Determine the shear stress acting on the lower plate in Example 7.4.2.

7.4.3. Determine the volume flux per unit length in the direction of flow in Example 7.4.3

7.4.4. Determine a formula for the stress exerted upon the upper plate during plane Poiseuille flow.

7.4.5 Consider a viscous fluid layer between two parallel flat plates. A reference coordinate system with $x_1$ in the plane of the plates and $x_2$ as the direction perpendicular to the plane of the plates is to be employed. Relative to this coordinate system the plates are located at $x_2 = \pm h/2$ (see Figure 7.4). For Couette flow the velocity distribution is $v_1 = (V/h)(x_2 + h/2)$ and for plane Poiseuille flow the velocity distribution is $v_1 = \frac{1}{2\mu}\left(-\frac{\partial p}{\partial x_1}\right)\left(\frac{h}{2}\right)^2 - x_2^2$ .

a. Determine formulas for the shear stress in the fluid for Couette flow and for Poiseuille flow.

b. On the graph of the type shown in Figure 7.4 plot the shear stress in the fluid as a function of $x_2$ for Couette flow. In this case let he units of shear stress on the graph be multiples of $\mu V/h$.

c. On the graph of the type shown in Figure 7.4 plot the shear stress in the fluid as a function of $x_2$ for Poiseuille flow. In this case let he units of shear stress on the graph be multiples of $-\frac{h}{2}\frac{\partial p}{\partial x_1}$.

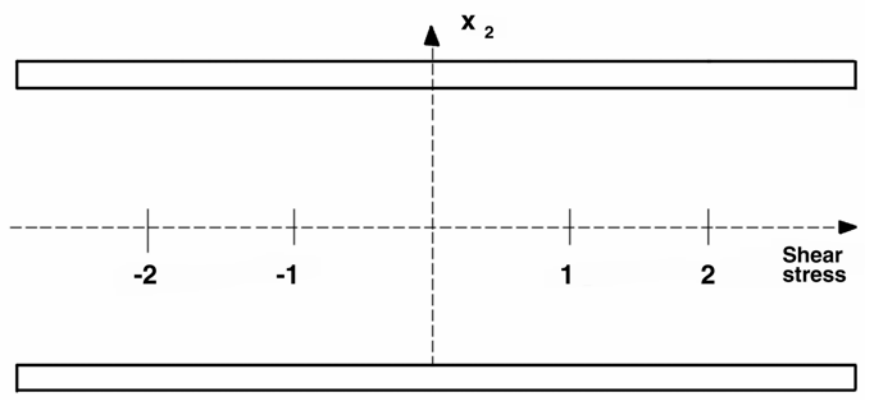



**Figure 7.4.** The two identical long rectangles represent flat plates that bound the domain occupied by a viscous fluid. As part of Problem 7.4.5, one is asked to plot the shear stress in the fluid as a function of $x_2$ for Couette flow on a graph of this kind and on another graph of this kind to do the same for Poiseuille flow.

## 7.5. THE THEORY OF VISCOELASTIC MATERIALS

An algebraic overview of the theory of linear viscoelastic materials can be obtained by considering it as a system of fifteen equations in fifteen unknown functions of time. The fifteen unknown functions of time are the six components of stress tensor **T**, the six components of strain tensor **E**, and the three components of displacement vector **u**. The parameter functions of

a viscoelasticity problem are tensor of viscoelastic coefficients $\hat{\mathbf{G}}(s)$, called the tensor of *relaxation functions*, density $\rho(s)$, and action-at-a-distance force $\mathbf{d}(s)$, which are assumed to be known. The system of fifteen equations consists of viscoelastic stress-strain relations,

$$\hat{\mathbf{T}}(\mathbf{x}, t) = \int_{s=-\infty}^{s=t} \hat{\mathbf{G}}(t-s)\cdot\hat{\mathbf{D}}(\mathbf{x},s)ds = \int_{s=-\infty}^{s=t} \hat{\mathbf{G}}(t-s)\cdot\frac{D\hat{\mathbf{E}}}{Ds}(\mathbf{x},s)ds\,, \qquad \text{(6.36V) repeated}$$

the six strain-displacement relations,

$$\mathbf{E} = (1/2)((\nabla\otimes\mathbf{u})^{\mathrm{T}} + \nabla\otimes\mathbf{u}), \qquad \text{(3.49) repeated}$$

and the three stress equations of motion,

$$\rho\ddot{\mathbf{u}} = \nabla\cdot\mathbf{T} + \rho\mathbf{d}\,,\ \mathbf{T} = \mathbf{T}^{T}\,. \qquad \text{(7.18) repeated}$$

Interchanging the roles of stress and strain, the current strain is expressed as a function of the past history of stress by

$$\hat{\mathbf{E}}(\mathbf{x}, t) = \int_{s=-\infty}^{s=t} \hat{\mathbf{J}}(t-s)\cdot\frac{D\hat{\mathbf{T}}}{Ds}(\mathbf{x},s)ds\,, \qquad (7.41)$$

where $\hat{\mathbf{J}}(s)$ is called the tensor of creep function.

The physical significance of the creep and relaxation functions, $\hat{\mathbf{J}}(s)$ and $\hat{\mathbf{G}}(s)$, are best illustrated by one-dimensional examples; uniaxial one-dimensional examples will be used here. A uniaxial tension specimen of homogeneous material is subjected to step increase in stress, $\hat{T}_1 = T_o h(t)$, where $h(t)$ is the unit step function, $h(t) = 0$ for $t < 0$ and $h(t) = 1$ for $t > 0$. Loading function $\hat{T}_1 = T_o h(t)$ is plotted in the top panel of Figure 7.5. Creep function $\hat{J}_{11}(s)$ is the uniaxial strain-versus-time response of the uniaxially stressed specimen to the step increase in stress, $\hat{T}_1 = T_o h(t)$. Function $\hat{J}_{11}(s)$ is illustrated in the lower panel of Figure 7.5. The strain response is given by $\hat{E}_1 = T_o\hat{J}_{11}(t)$. The creep function defined and measured in this way may be used to predict the creep response to a more complicated stress history. Suppose, for example, the stress history is a long series of step jumps rather than just one step jump (Figure 7.6). The creep strain response to this new stress history may be built up by repeated application of the basic result, $\hat{E}_1 = T_o\hat{J}_{11}(t)$, to each step, and subsequent summation of strains associated with each step,

$$\hat{E}_1(t) = \hat{J}_{11}(t)\Delta\hat{T}_1(0) + \hat{J}_{11}(t-t_1)\Delta\hat{T}_1(t_1) + \cdots + \hat{J}_{11}(t-t_n)\Delta\hat{T}_1(t_n) + \cdots\,. \qquad (7.42)$$

The multiple step plot of Figure 7.5 is familiar from the introductory presentations to the process of integration in which a horizontal axis is divided into segments and the curve is approximated by different level steps drawn horizontally for each segment so that the curve is approximated by a series of various-sized steps. It follows that any curve representing a stress history could be approximated arbitrarily closely by a set of various-sized steps like those illustrated in Figure 7.6 and represented analytically by an equation of type (7.42). In preparation for a passage to the limit of the type used in the integral calculus, (7.42) is rewritten as

$$\hat{E}_1(t) = \sum_{i=1}^{n} \hat{J}_{11}(t-t_i)\Delta\hat{T}_1(t_i)\,. \qquad (7.43)$$

In the passage to the limit the series of times $t_i$, $i = 1, \ldots, n$, will be replaced by continuous parameter $s$, and the step in the stress by $\Delta\hat{T}_1(t_i)$ by $(d\hat{T}_1/ds)ds$, and thus

$$\hat{E}_1(t) = \int^{t} \hat{J}_{11}(t-t_s)\frac{d\hat{T}_1}{ds}ds \,. \tag{7.44}$$

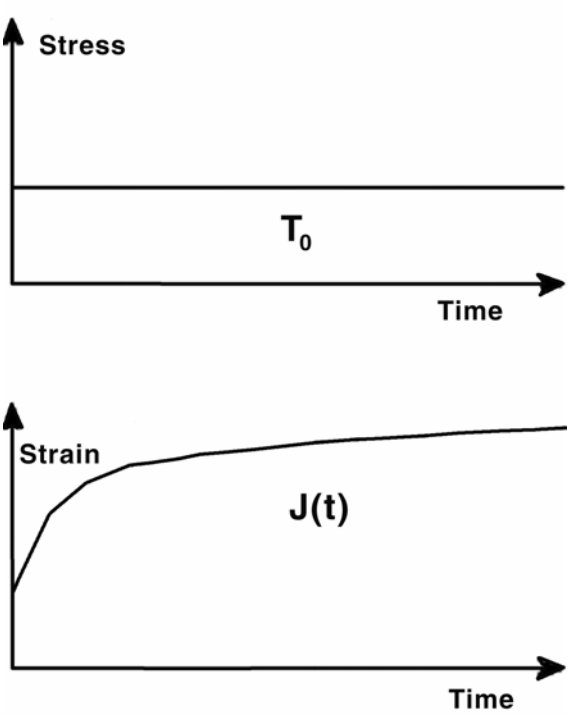



**Figure 7.5**. Creep function $J(t)$. The creep function is the strain response to a step input of stress at $t = 0$.

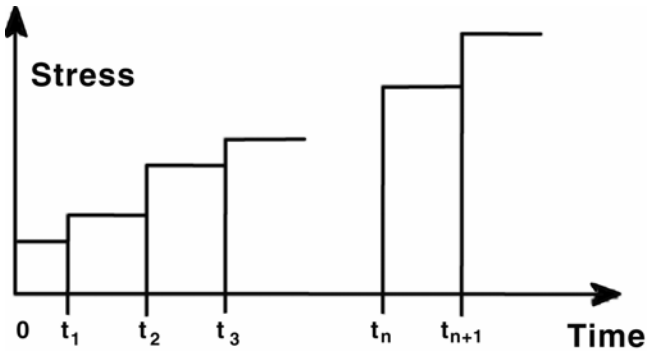



**Figure 7.6**. A plot of stress increments applied at specific time increments.

Finally, going back to the beginning of this development, there was nothing special about applying the loading at $t = 0$; it could have been started at any time; thus, we set it back to the beginning of time:

$$\hat{E}_1(t) = \int_{s=-\infty}^{s=t} \hat{J}_{11}(t-s)\frac{d\hat{T}_1}{ds}ds \,. \tag{7.45}$$

It is now clear that (7.45) is a special case of (7.41). The physical significance of creep function $\hat{J}_{11}(s)$ is the following: it is the uniaxial normal strain, $\hat{E}_1(t)$, versus time response of a specimen subjected to a step increase in the normal stress in the same direction, $\hat{T}_1 = T_0 h(t)$.

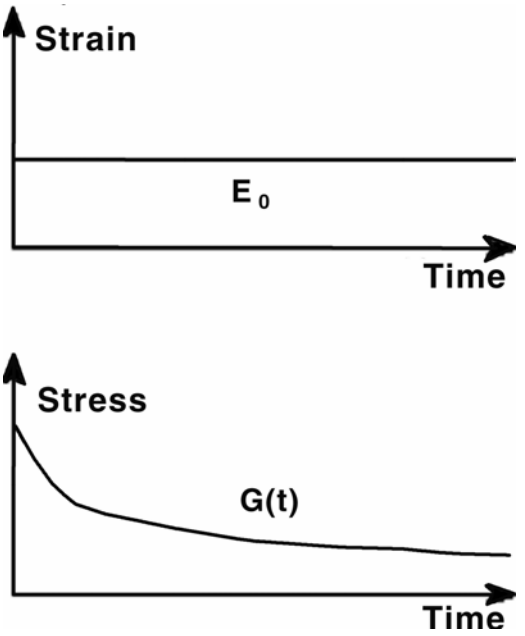



**Figure 7.7**. Relaxation function $G(t)$. The relaxation function is the stress response to a step input of strain at $t = 0$.

The physical significance of relaxation function $\hat{G}_{11}(s)$ can be developed in a similar manner by reversing the roles of stress and strain used in the case of the creep function. A uniaxial tension specimen of homogeneous material is subjected to a step increase in strain, $\hat{E}_1 = E_0 h(t)$. Strain loading function $\hat{E}_1 = E_0 h(t)$ is plotted in the top panel of Figure 7.7. Relaxation function $\hat{G}_{11}(s)$ is the uniaxial stress-versus-time response of the uniaxially strained specimen to the step increase in strain, $\hat{E}_1 = E_0 h(t)$. Function $\hat{G}_{11}(s)$ is illustrated in the lower panel of Figure 7.7. The stress response is given by $\hat{T}_1 = \hat{G}_{11}(t)\hat{E}_0$. The relaxation function defined and measured in this way may be used to predict the relaxation response to a more complicated strain history, as described above for the creep function. Following completely analogous steps, one finds that

$$\hat{T}_1(t) = \int_{s=-\infty}^{s=t} \hat{G}_{11}(t-s)\frac{d\hat{E}_1}{ds}ds \,. \tag{7.46}$$

Result (7.46) is a special case of (6.36V). The physical significance of relaxation function $\hat{G}_{11}(s)$ is the following: it is the uniaxial normal stress, $\hat{T}_1(t)$, versus time response of a specimen subjected to a step increase in the normal strain in the same direction, $\hat{E}_1 = E_0 h(t)$.

The creep and relaxation functions, $\hat{\mathbf{J}}(s)$ and $\hat{\mathbf{G}}(s)$, are hypothesized to have a property called *fading memory*. The fading memory hypothesis for $\hat{\mathbf{J}}(s)$ ($\hat{\mathbf{G}}(s)$) is that the strain (stress) depends more strongly upon the recent history than it does upon the distant history of the value of stress (strain). Mathematically this is the requirement that functions $\hat{\mathbf{J}}(s)$ and $\hat{\mathbf{G}}(s)$ are continuously decreasing functions of backward running time parameter $s$. This then decreases the influence of the more distant events. For each component of the viscoelastic strain–stress relations to possess this fading memory behavior, it is sufficient that the magnitude of the slope of each component of the creep function tensor be a continuously decreasing function of time, and thus

$$\left|\frac{D\hat{\mathbf{J}}_{ij}(s)}{Ds}\right|_{s=s_1} < \left|\frac{D\hat{\mathbf{J}}_{ij}(s)}{Ds}\right|_{s=s_2} \quad \text{for all } i, j = 1, 2, \ldots 6, \text{ and for } s_1 > s_2 > 0. \tag{7.47}$$

For each component of the viscoelastic stress-strain relations a similar fading memory hypothesis holds, thus

$$\left|\frac{D\hat{\mathbf{G}}_{ij}(s)}{Ds}\right|_{s=s_1} < \left|\frac{D\hat{\mathbf{G}}_{ij}(s)}{Ds}\right|_{s=s_2} \quad \text{for all } i, j = 1, 2, \ldots 6, \text{ and for } s_1 > s_2 > 0. \tag{7.48}$$

The isotropic form of viscoelastic stress–strain relations (6.36V) is obtained by using the representation for the isotropic form of $\hat{\mathbf{G}}(s)$ obtained from Table 5.4, and thus

$$\hat{\mathbf{G}}(s) = \begin{bmatrix} \hat{G}_{11}(s) & \hat{G}_{12}(s) & \hat{G}_{12}(s) & 0 & 0 & 0 \\ \hat{G}_{12}(s) & \hat{G}_{11}(s) & \hat{G}_{12}(s) & 0 & 0 & 0 \\ \hat{G}_{12}(s) & \hat{G}_{12}(s) & \hat{G}_{11}(s) & 0 & 0 & 0 \\ 0 & 0 & 0 & \hat{G}_{11}(s)-\hat{G}_{12}(s) & 0 & 0 \\ 0 & 0 & 0 & 0 & \hat{G}_{11}(s)-\hat{G}_{12}(s) & 0 \\ 0 & 0 & 0 & 0 & 0 & \hat{G}_{11}(s)-\hat{G}_{12}(s) \end{bmatrix}$$

This six-dimensional representation is converted to a three-dimensional representation by employing the relations in Table 7.1 and introducing the following new notation for the two distinct elements of this 6-by-6 matrix, and so

$$\hat{G}_{11}(s) = \frac{k_{tr}(s) + 2G_{dev}(s)}{3}, \quad \hat{G}_{12}(s) = \frac{k_{tr}(s) - G_{dev}(s)}{3}. \tag{7.49}$$

The isotropic form of the viscoelastic stress-strain relations (6.36V) may then be rewritten in three dimensions as

$$\text{tr}\mathbf{T}(\mathbf{x}, \text{t}) = \int_{s=-\infty}^{s=t} k_{tr}(t-s)\frac{D}{Ds}\{tr\mathbf{E}(\mathbf{x}, s)\}ds \tag{7.50}$$

and

$$\text{dev}\mathbf{T}(\mathbf{x}, \text{t}) = \int_{s=-\infty}^{s=t} G_{dev}(t-s)\frac{D}{Ds}\{dev\mathbf{E}(\mathbf{x}, s)\}ds\,, \tag{7.51}$$

where $k_{tr}(s)$ and $G_{dev}(s)$ represent independent relaxation functions. In a similar set of arguments it may be shown that the isotropic form of viscoelastic strain–stress relations (7.41) may be expressed in terms of two isotropic creep functions, $j_{tr}(s)$ and $J_{dev}(s)$, and thus

$$\mathrm{tr}\mathbf{E}(\mathbf{x}, \mathrm{t}) = \int_{s=-\infty}^{s=t} j_{tr}(t-s)\frac{D}{Ds}\{tr\mathbf{T}(\mathbf{x}, s)\}ds \tag{7.52}$$

and

$$\mathrm{dev}\mathbf{E}(\mathbf{x}, \mathrm{t}) = \int_{s=-\infty}^{s=t} J_{dev}(t-s)\frac{D}{Ds}\{dev\mathbf{T}(\mathbf{x}, s)\}ds\,. \tag{7.53}$$

Viscoelastic materials have properties characteristic of both fluids and solids, and it is sometimes important to distinguish between viscoelastic fluids and viscoelastic solids. One aspect of fluid behavior is that a fluid is usually isotropic while a solid may be anisotropic. A second characteristic of a fluid, a characteristic that aids in distinguishing isotropic viscoelastic solids from isotropic viscoelastic fluids, is the asymptotic value of $G_{dev}(t)$ as $t$ tends to infinity. A necessary and sufficient condition that an isotropic viscoelastic material be a solid is that $G_{dev}(t)$ tend to a nonzero constant as $t$ tends to infinity. A necessary but not sufficient condition, that an isotropic viscoelastic material be a fluid is that $G_{dev}(t)$ tend to zero as $t$ tends to infinity. It is convenient to define

$$G^0_{\mathrm{dev}} \equiv \lim_{t\to\infty} G_{\mathrm{dev}}(t)\,, \tag{7.54}$$

then

$$G_{\mathrm{dev}}(t) \equiv G^0_{\mathrm{dev}} + G^\infty_{\mathrm{dev}}(t)\,, \tag{7.55}$$

where

$$\lim_{t\to\infty} G^\infty_{\mathrm{dev}}(t) = 0\,. \tag{7.56}$$

Thus, if $G^0_{\mathrm{dev}} \neq 0$ the material is a viscoelastic solid, and if $G^0_{\mathrm{dev}} = 0$ it may be a fluid.

Viscoelastic materials differ from the other materials considered in this chapter because their material properties are determined by material functions rather than material constants. The material functions are functions of time, or of time transformed, that is to say, frequency. Viscoelastic materials are probed with various dynamical test systems in order to evaluate the forms of the material functions, their peaks and valleys. Different dynamical test systems are effective for determining the material functions for different frequency ranges (see Figure 7.8). Both free and resonant vibrations and pulse and harmonic wave propagation techniques have the ranges of effectiveness indicated in Figure 7.8. One of the easiest probing tests for a viscoelastic material is to subject the material to forced steady-state oscillations. This testing method is effective over a wide range of frequencies (Figure 7.8).

In the special case of forced steady-state oscillations, special forms of the stress–strain relations emerge. As an example we consider the case of the deviatoric part of isotropic stress–strain relations (7.51). It is assumed that the material is subjected to a forced deviatoric strain specified as a harmonic function of time:

$$\mathrm{dev}\mathbf{E}(\mathrm{t}) = \{\mathrm{dev}\mathbf{E}_o\}\mathrm{e}^{\mathrm{i}\omega\mathrm{t}} = \{\mathrm{dev}\mathbf{E}_o\}\{\cos\omega t + i\sin\omega t\}. \tag{7.57}$$

Upon substitution of strain (7.57) into viscoelastic stress-strain relation (7.51), along with decomposition of $G_{\text{dev}}(t)$ given by (7.55), it follows that

$$\text{dev}\mathbf{T}(\mathbf{x}, \text{t}) = G^0_{\text{dev}}\text{dev}\mathbf{E}_0 e^{i\omega s} + i\omega\ \text{dev}\mathbf{E}_o \int_{s=-\infty}^{s=t} G^{\infty}_{\text{dev}}(t-s)e^{i\omega s} ds\ . \tag{7.58}$$

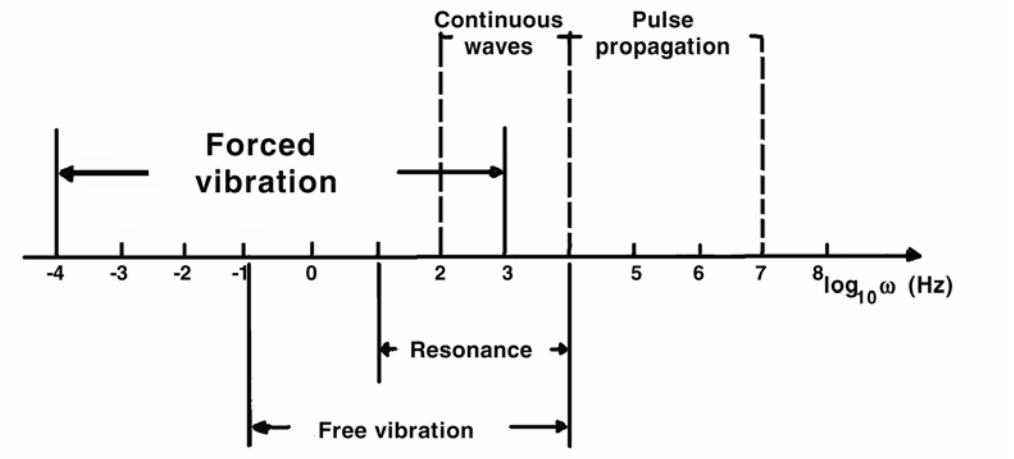



**Figure 7.8**. Frequency ranges that are most effective for the various types of dynamical mechanical tests. Reprinted with permission from Lockett (1972).

Now, making a change of variable, $t - s = \eta$,

$$\text{dev}\mathbf{T}(\mathbf{x}, \text{t}) = \left\{ G^0_{\text{dev}} + \omega \int_0^{\infty} \sin\omega\eta\ G^{\infty}_{\text{dev}}(\eta) d\eta + i\omega \int_0^{\infty} \cos\omega\eta\ G^{\infty}_{\text{dev}}(\eta) d\eta \right\} \text{dev}\ \mathbf{E}_0 e^{i\omega t}\ , \tag{7.59}$$

or

$$\text{dev}\mathbf{T}(\mathbf{x}, \text{t}) = G^{*}_{\text{dev}}(i\omega)\text{dev}\mathbf{E}_0 e^{i\omega t}\ , \tag{7.60}$$

where

$$G^{*}_{\text{dev}}(i\omega) = G^{'}_{\text{dev}}(\omega) + iG^{''}_{\text{dev}}(\omega)\ , \tag{7.61}$$

and

$$G^{'}_{\text{dev}}(\omega) = G^0_{\text{dev}} + \omega \int_0^{\infty} \sin\omega\eta\ G^{\infty}_{\text{dev}}(\eta) d\eta\ ,\quad G^{''}_{\text{dev}}(\omega) = \omega \int_0^{\infty} \cos\omega\eta\ G^{\infty}_{\text{dev}}(\eta) d\eta\ . \tag{7.62}$$

Functions $G^{'}_{\text{dev}}(\omega)$ and $G^{''}_{\text{dev}}(\omega)$ are called the storage and loss moduli, respectively. Formulas (7.62) show that the real and complex parts of complex modulus $G^{*}_{\text{dev}}(i\omega)$, the only material function in specialized steady-state oscillatory viscoelastic stress–strain relation (7.60), are determined by relaxation function, $G_{\text{dev}}(t)$. Stress–strain relations (7.60) may also be written as

$$\mathrm{dev}\mathbf{T}(\mathbf{x}, t) = \left|G^{*}_{\mathrm{dev}}(i\omega)\right| \mathrm{dev}\mathbf{E}_{o} e^{i(\omega t + \varphi_{\mathrm{dev}})}, \tag{7.63}$$

where phase angle $\varphi_{\mathrm{dev}}(\omega)$ is given by

$$\varphi_{\mathrm{dev}}(\omega) = \tan^{-1}\left\{\frac{G^{''}_{\mathrm{dev}}(\omega)}{G^{'}_{\mathrm{dev}}(\omega)}\right\}. \tag{7.64}$$

Quantity $\tan\varphi_{\mathrm{dev}}(\omega)$ is called the loss tangent. The steady-state harmonic strain lags behind the stress by phase angle $\varphi_{\mathrm{dev}}(\omega)$. Typical plots of the storage and loss moduli, $G^{'}_{\mathrm{dev}}(\omega)$ and $G^{''}_{\mathrm{dev}}(\omega)$, respectively as a function of $\omega$ are shown in Figure 7.9. However, these curves for real material seldom look exactly like these examples.

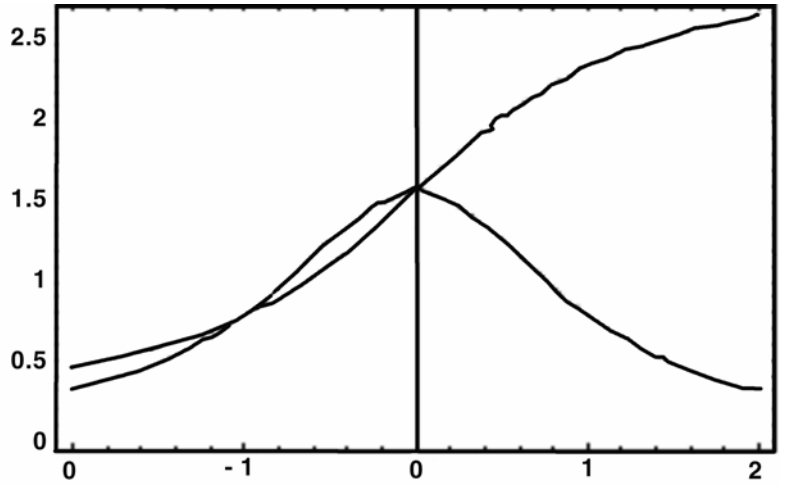



**Figure 7.9**. Complex modulus $G^{*}(i\omega)$. The vertical scale represents both the real and imaginary parts of $G^{*}(i\omega)$, which have the dimensions of 1 upon stress. The horizontal scale is the log of the frequency, log $\omega$. The monotonically increasing curve represents $G'(\omega)$, the real part of $G^{*}(i\omega)$, and the curve with a peak represents G"($\omega$), the imaginary part of $G^{*}(i\omega)$.

**Example 7.5.1**

An isotropic viscoelastic material is subjected to a step loading in shear strain $E_{12}$. The magnitude of step loading is $E_o$. Unit step function $h(t)$ is used to represent the step loading, $E_{12} = E_o h(t)$. Recall that $h(t)$ is a function that is defined as 0 for $t < 0$ and as 1 for $t > 0$. The derivative of the unit step function is delta function $\delta(t)$, $d/dt(h(t)) = \delta(t)$, where the delta function has the property that

$$f(t^{*}) = \int_{-\infty}^{\infty} \delta(t - t^{*}) f(t) dt \, .$$

Determine the stress response to the strain loading, $E_{12} = E_o h(t)$.

**Solution**: Substitution of strain loading $E_{12} = E_o h(t)$ into appropriate stress–strain relation (7.51) yields the following simple formula:

$$T_{12} = \int_{s=-\infty}^{s=t} G_{\text{dev}}(t-s)E_o\delta(s)ds = G_{\text{dev}}(t)E_o\,.$$

It follows then that the relaxation function is just the value of the resulting stress divided by $E_o$:

$$G_{\text{dev}}(t) = (1/E_o)T_{12}\,.$$

This result can then be used as the basis of an experiment to determine relaxation function $G_{\text{dev}}(t)$. Typical relaxation functions are of the form of decaying functions of time like that shown in Figure 7.10. Decaying with time is consistent with the hypothesis of fading memory.

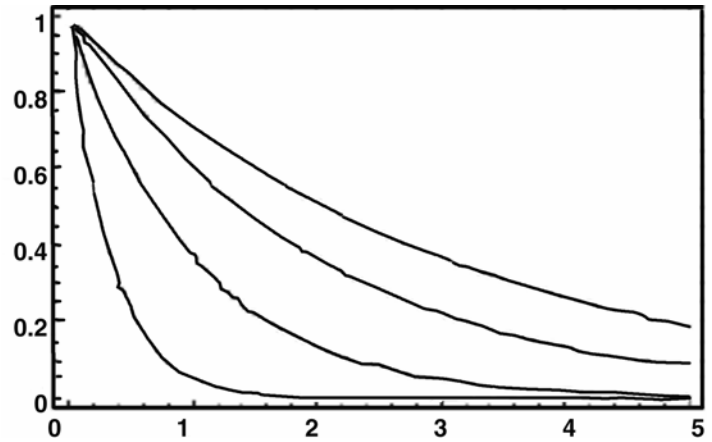



**Figure 7.10**. Four typical relaxation functions $G(t)$. The vertical scale is the relaxation function $G(t)$ that has the dimensions of stress. The horizontal scale is time.

**Example 7.5.2**

The Maxwell model is a lumped viscoelastic model that is a combination of a spring and a dashpot in series (Figure 2.18a). When a force applied to a Maxwell model is changed from zero to a finite value at an instant of time and held constant thereafter, there is an instantaneous initial elastic extension and then there is a continued deformation forever as the damper in the dashpot is drawn through the dashpot cylinder. Thus, a Maxwell model exhibits the characteristics of a fluid with an initial elastic response. In this model, in general, the deflection represents the strain and the force represents the stress. In this particular illustration the deflection represents the shearing strain and the force represents the shearing stress. The differential equation for a Maxwell model is formed by adding together the rate of strain of the spring, obtained by differentiating Hooke's law in isotropic shear, $E_{12} = (1/G_0)T_{12}$, with respect to time, $(d/dt)E_{12} = (1/G_0)(d/dt)T_{12}$, and the dashpot $(d/dt)E_{12} = (1/\tau_r G_0)T_{12}$, where $\tau_r G_0$ represents the viscosity of the dashpot), and thus

$$\frac{dE_{12}}{dt} = \frac{1}{\tau_r G_0}T_{12} + \frac{1}{G_0}\frac{dT_{12}}{dt}\,.$$

The problem is to determine the response of the Maxwell model to a step loading in shearing strain $E_{12}$. The magnitude of the step loading is $E_o$. This example is formally similar to the previous example, the only change being in the model. The solution of the problem requires solution of a first-order ordinary differential equation subject to the case when the strain history is given by $E_{12} = E_o h(t)$, and no other loading is applied to the model. Determine the stress response to this strain history loading.

**Solution**: The general solution to the first-order ordinary differential equation

$$\frac{dy}{dt} + f(t)y = g(t)$$

is

$$y(t) = e^{-F}(c + \int_{t_0}^{t} g(s)e^{F}\,ds)\,, \text{ where } F(t) = \int_{t_o}^{t} f(s)ds\,,$$

and where $c$ is a constant of integration. In the differential equation of interest $y(t) = T_{12}(t)$, $F(t) = (t/\tau_r)$, $g(s) = (d/dt)E_{12} = (d/dt)(E_0 h(s))$, and, due to the initial condition $c = 0$; thus,

$$T_{12}(t) = e^{-t/\tau_r}\left(\int_0^t G_0 E_0 \frac{dh(s)}{ds} e^{s/\tau_r}\,ds\right) = e^{-t/\tau_r}\left(\int_0^t G_0 E_0 \delta(s) e^{s/\tau_r}\,ds\right) = G_0 E_0 h(t) e^{-t/\tau_r}\,.$$

The special form of the relaxation function for the Maxwell model may then be identified as

$$G_{dev}(t) = (1/E_o)T_{12} = G_0 h(t) e^{-t/\tau_r}\,.$$

**Problems**

Problem 7.5.1. Derive (7.50) and (7.51) from (6.36V).

Problem 7.5.2. Derive (7.52) and (7.53) from (7.41).

Problem 7.5.3. Determine the strain response to this stress loading for an isotropic viscoelastic material subjected to a step loading in shear stress $T_{12}$. The magnitude of the step loading is $T_o$. This problem is formally similar to Example 7.5.1, the only change being that the step loading is now in shear stress rather than shear strain. The step loading is represented by $T_{12} = T_o h(t)$. Show that the creep function is just the value of the resulting strain divided by $T_o$. Note that typical creep functions are of the form of increasing functions of time like that shown in Figure 7.11.

Problem 7.5.4. The Voigt model is a lumped viscoelastic model that is a combination of a spring and a dashpot in parallel (Figure 2.18b). When a force applied to a Voigt model is changed from zero to a finite value at an instant of time and then held constant thereafter, extension occurs only after the dashpot begins to move. Thus, the Voigt model is initially rigid; then it begins to creep asymptotically under the constant applied load to a rest value. In parallel models like the Voigt model, the transverse or horizontal bars or connecting elements are required not to rotate, so the two parallel elements are constrained to always have the same extension in both elements at any instant of time. In these spring and dashpot models, in general, the deflection represents the strain and the force represents the stress. In this particular illustration the deflection represents the shearing strain and the force the shearing stress. The differen-

tial equation for a Voigt model is formed by adding together the stress in the two parallel branches, $T_{12} = (1/J_o)E_{12}$ for the spring and $T_{12} = (\tau_r/J_o)(d/dt)(E_{12})$ for the dashpot, and so

$$T_{12} = \frac{1}{J_0} E_{12} + \frac{\tau_c}{J_0} \frac{dE_{12}}{dt} .$$

The problem is to determine the response of the Voigt model to a step loading in shearing stress $T_{12}$. The magnitude of the step loading is $T_o$. This problem is formally similar to Example 7.5.2, the only change being in the model. The solution of the problem requires the solution of a first-order ordinary differential equation subject to the case when the stress history is given by $T_{12} = T_o h(t)$, and no other loading is applied to the model. Determine the stress response to this strain history loading and show that, for this model, the creep function is given by $J(t) = (1/T_o)E_{12} = J_0 h(t)(1 - e^{-t/\tau_c})$. Typical creep functions are shown in Figure 7.11.

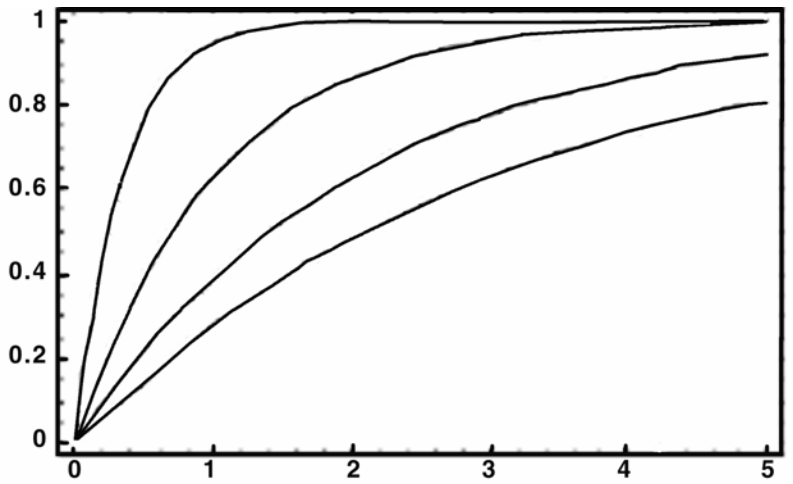



**Figure 7.11**. Four typical creep functions $J(t)$. The vertical scale is the creep function $J(t)$ that has the dimensions of one upon stress. The horizontal scale is time.

Problem 7.5.5. A three-parameter viscoelastic model is shown in Figure 7.12. The model consists of two branches: the lower branch with a spring and the upper branch with a spring and a dashpot. These two branches are connected by two transverse elements that are indicated by vertical lines. The rules for formulating the overall force-deformation ($F - \delta$) relation for these spring and dashpot models are: (1) the transverse elements that connect the two branches remain parallel as the system is deformed; (2) the springs follow the rule that $F = k\delta$ ($F = k_D\delta$), and the dashpots follow the rule that $F = \eta(d\delta/dt)$. Let $F_L$ and $F_U$ denote the forces in the lower and upper branches, respectively, $\delta_D$ the deflection of the dashpot, and $\delta_s$ the deflection of the spring in series with the dashpot. Construct the overall force-deformation ($F - \delta$) relation for this spring and dashpot model. List each step of your argument and explain its rationale.

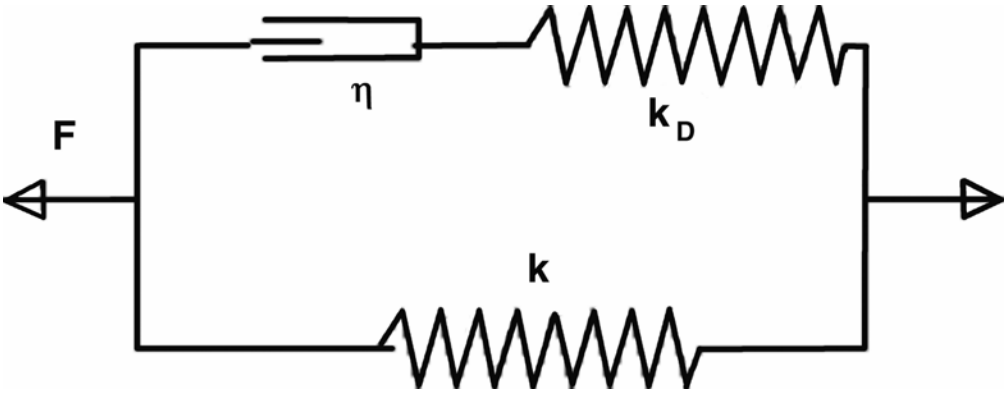



**Figure 7.12**. A three-parameter viscoelastic model.

## 7.6. RELEVANT LITERATURE

This chapter presents brief descriptions of four theories of material behavior. There are many volumes written on each of these theories, and there are entire periodicals devoted to publishing recent results in each of these theories. The purpose of this section is to mention some of the general literature associated with each of these four theories, particularly that drawn upon in the writing of this chapter.

Flow through porous media is addressed in books by Bear (1972), Carman (1956), Scheidegger (1960), and others. Several of the books on poroelasticity mentioned in Chapter 9 contain much related material. The related journals include *Transport in Porous Media*, *Water Resources Research*, and the *Journal of Hydrology*.

The theory of elastic solids is described in the classical text of Love (1927), and in Timoshenko and Goodier (1951), Sokolnikoff (1956), Saada (1974) and Gurtin (1972). Anisotropic elasticity is the subject of books by Hearmon (1961), Lekhnitskii (1963), and Fedorov (1968). Current publications on elasticity theory may be found in the *Journal of Elasticity* and in many related journals such as the *International Journal of Solids and Structures*, the *Journal of the Mechanics and Physics of Solids*, and the ASME *Journal of Applied Mechanics*.

The theories associated with fluid behavior are described in the classical books by Lamb (1932), Prandtl and Tietjens (1934a,b), and Schlichting (1960); Langois (1964) offers an introduction to slow viscous flow. The current widely used text is Batchelor (2000). There are many journals specializing in fluid mechanics; the most broad and most successful is the *Journal of Fluid Mechanics*.

The books that deal with viscoelasticity theory include Christensen (1971), Lakes (1999), Lockett (1972), Pipkin (1972), and the contemporary work of Wineman and Rajagopal (2000). Journals in this area include *Rheologica Acta*, *Journal of Rheology*, and *Biorheology*.

### Theory of Rigid Porous Media

Bear J. 1972. *Dynamics of fluids in porous media*. New York: Elsevier.
Carman PC. 1956. *Flow of gases through porous media*. London: Butterworths.
Scheidegger AE. 1960. *The physics of flow through porous media*, 2nd ed. Toronto: U Toronto P.

### Elasticity Theory (Classical)

Gurtin ME. 1972. The linear theory of elasticity. In *Handbuch der physik*, ed. S Flugge, pp. 1–296. Berlin: Springer-Verlag.
Love AEH. 1927. *Elasticity*. New York: Dover.
Saada AS. 1974. *Elasticity theory and applications*. Oxford: Pergamon.
Sokolnikoff IS. 1956. *Mathematical theory of elasticity*. New York: McGraw-Hill.
Timoshenko SP, Goodier JN. 1951. *Theory of elasticity*. New York: McGraw-Hill.

### Elasticity Theory (Anisotropic)

Fedorov FI. 1968. *Theory of elastic waves in crystals*. New York: Plenum Press.
Hearmon RFS. 1961. *An introduction to applied anisotropic elasticity*. Oxford: Oxford UP.
Lekhnitskii SG. 1963. *Theory of elasticity of an anisotropic elastic body*. San Francisco: Holden Day.
Ting TCT. 1996. *Anisotropic elasticity — theory and applications*. New York: Oxford UP.

### Classical Fluid Theory

Batchelor GK. 2000. *An introduction to fluid mechanics*. Cambridge: Cambridge.
Lamb H. 1932. *Hydrodynamics*. New York: Dover.
Langois WE. 1964. *Slow viscous flow*. New York: Macmillan.
Prandtl L, Tietjens OG. 1934a. *Fundamentals of hydro- and aeromechanics*. New York: McGraw-Hill.
Prandtl L, Tietjens OG. 1934b. *Applied hydro- and aeromechanics*. New York: McGraw-Hill.
Schlichting H. 1960. *Boundary layer theory*. New York: McGraw-Hill.

### Viscoelasticity Theory

Christensen RM. 1971. *Theory of viscoelasticity*. New York: Academic Press.
Lakes RS. 1999. *Viscoelastic solids*. Boca Raton, FL: CRC Press.
Lockett FJ. 1972. *Nonlinear viscoelastic solids*. New York: Academic Press.
Pipkin AC. 1972. *Lectures on viscoelasticity theory*. New York: Springer.
Wineman AS, Rajagopal KR. 2000. *Mechanical response of polymers*. Cambridge: Cambridge UP.

# 8

# MODELING MATERIAL MICROSTRUCTURE

"Continuum mechanics deals with idealized materials consisting of material points and material neighborhoods. It assumes that the material distribution, the stresses, and the strains within an infinitesimal material neighborhood of a typical particle (or a material element) can be regarded as essentially uniform. On the microscale, however, the infinitesimal material neighborhood, in general, is not uniform, consisting of various constituents with differing properties and shapes, i.e., an infinitesimal material element has its own complex and, in general, evolving microstructure. Hence, the stress and strain fields within the material element likewise are not uniform at the microscale level. One of the main objectives of micromechanics is to express in a systematic and rigorous manner the continuum quantities associated with an infinitesimal material neighborhood in terms of the parameters that characterize the microstructure and properties of the micro-constituents of the material neighborhood." [From Nemat-Nasser and Hori (1999, p. 11).]

## 8.1. INTRODUCTION

The heterogeneity of biological materials is obvious at all levels of their hierarchical structure, including the smallest level. At the smallest level there are spaces between the atoms or molecules that constitute holes in the material making the material discontinuous. One purpose of this chapter is to reconcile this fact with the continuity assumption of the continuum models described in the preceding chapters so that one will understand how these continuum models are applied to biological tissues. A second purpose is to relate the effective material parameters and material symmetry used in continuum models to the material microstructure.

The key concept in modeling material microstructure, as well as for modeling material symmetry, for inclusion in a continuum model is the representative volume element (RVE). The discussion of the RVE contained in Chapter 5, particularly §5.2, is further developed in §8.2. A material composed of two or more distinct constituent materials is called a composite material. Most natural materials are composite materials. Many think that the first manmade composite material was the reinforced brick constructed by using straw to reinforce the clay of the brick. Dried clay is satisfactory in resisting compression, but not very good in tension. The straw endows the brick with the ability to sustain greater tensile forces. Most structural soft tissues in animals can carry tensile forces adequately but do not do well with compressive

forces. In particular, due to their great flexibility they may deform greatly under compressive forces. The mineralization of the collagenous tissues provides those tissues with the ability to resist compressive forces; thus, bone and teeth are composites of an organic phase, primarily collagen, and an inorganic or mineral phase. Effective material parameters for composite materials, defined in §8.3, are generally determined by expressions that depend upon the phase or constituent-specific material parameters and their geometries. Examples of effective elastic constants and effective permeabilities are developed in §§8.4 and 8.5, respectively. Restrictions on the RVE for a material gradient in its material structural is considered in §8.6. The continuum modeling of material microstructures with vectors and tensors is described in §8.7 and §8.8 considers the relevant literature.

## 8.2. THE REPRESENTATIVE VOLUME ELEMENT (RVE)

Recall from §5.2 that, for this presentation, the RVE is taken to be a cube of side length $L_{\text{RVE}}$; it could be any shape, but it is necessary that it have a characteristic length scale (Figure 5.1). The RVE for the representation of a domain of a porous medium by a continuum point was illustrated in Figure 5.2. We begin here by picking up the question of how large must the length scale $L_{\text{RVE}}$ be to obtain a reasonable continuum model. The $L_{\text{RVE}}$ should be much larger than the largest characteristic microstructural dimension $L_{\text{M}}$ of the biological material being modeled and smaller than the characteristic dimension of the problem to be addressed, $L_{\text{P}}$, and thus $L_{\text{P}} >> L_{\text{RVE}} >> L_{\text{M}}$.

The question of the size of $L_{\text{RVE}}$ can also be posed in the following way: How large a hole is no hole? The value of $L_{\text{RVE}}$ selected determines what the modeler has selected as too small a hole, or too small an inhomogeneity or microstructure, to influence the result the modeler is seeking. An interesting aspect of the RVE concept is that it provides a resolution of a paradox concerning stress concentrations around circular holes in elastic materials. The stress concentration factor associated with the hole in a circular elastic plate in a uniaxial field of otherwise uniform stress is three times the uniform stress (Figure 8.1). This means that the stress at certain points in the material on the edge of the hole is three times the stress five or six hole diameters away from the hole. The hole has a concentrating effect of magnitude 3. The paradox is that the stress concentration factor of 3 is independent of the size of the hole. Thus, no matter how small the hole, there is a stress concentration factor of 3 associated with the hole in a field of uniaxial tension or compression. One way to resolve the paradox described above is to observe that the modeler has decided how big a hole is no hole by choosing to recognize a hole of a certain size and selecting a value of $L_{\text{RVE}}$ to be much less. Let the size of the largest hole in the plate be $d_{\text{L}}$ and assume that the plate has a dimension of $100d_{\text{L}}$, and thus $d_{\text{L}} \geq L_{\text{RVE}} \geq L_{\text{M}}$. Let $d_{\text{S}}$ denote the dimension of the largest of the other holes in the plate. Thus, any hole whose dimension is less than $L_{\text{M}} = d_{\text{S}}$ will not appear in the model although it is in the real object. The interpretation of the solution to the problem illustrated by Figure 8.1 is that there is only one hole in the model of radius $d_{\text{L}}$, no holes of size less than $d_{\text{L}}$ and greater than $L_{\text{M}} = d_{\text{S}}$, and all holes in the real object of size less than $L_{\text{M}} = d_{\text{S}}$ have been "homogenized" or averaged over.

The macro or continuum properties that are employed in continuum models are micro material properties that have been averaged over an RVE. Let $\rho$ denote the microdensity field and $\mathbf{T}$ the micro stress field; then the average or macrodensity field $\langle \rho \rangle$ and the macro stress tensor $\langle \mathbf{T} \rangle$ field are obtained by volume averaging over the microscale. The averaging integral operator $\langle f \rangle$ of micro field $f$ is given by

$$\langle f \rangle = \frac{1}{V_{\text{RVE}}} \oint_{V} f dv \, . \tag{8.1}$$

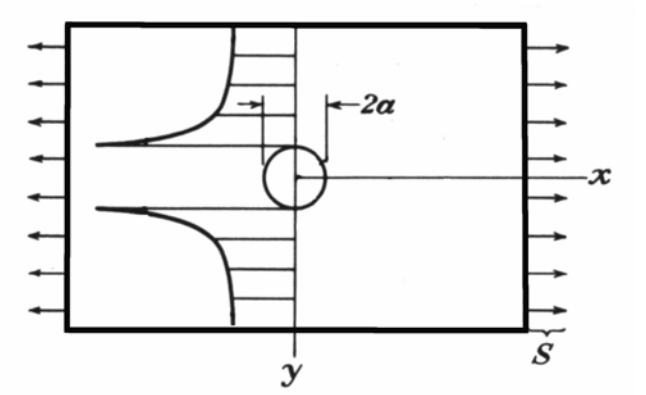



**Figure 8.1**. An illustration of the stress concentration (by a factor of 3) associated with the hole in a circular plate in a uniaxial field of otherwise uniform stress, *S*. Reprinted with permission from Cowin (2002).

Equation (8.1) represents the *homogenization* of the local or micro material parameter fields. That is to say, in volume $V_{\mathrm{RVE}}$ average field $\langle f \rangle$ replaces inhomogeneous field $f$ in the RVE. The length scale over which the homogenization is accomplished is $L_{\mathrm{RVE}}$ or the cube root of volume $V_{\mathrm{RVE}}$, which is intended to be the largest dimension of the unit cell over which integration (8.1) is accomplished. A plot of the values of macrodensity $\langle \rho \rangle$ as a function of the size of the RVE is sketched in Figure 8.2. Note that as the size of volume $V_{\mathrm{RVE}}$ or $L_{\mathrm{RVE}}$ is decreased, the value of density $\langle \rho \rangle$ begins to oscillate because the small volume of dense solid material in volume $V_{\mathrm{RVE}}$ is greatly influenced by the occurrence of small voids. On the other hand, as the size of volume $V_{\mathrm{RVE}}$ or $L_{\mathrm{RVE}}$ is increased, the value of the density tends to a constant, stable value.

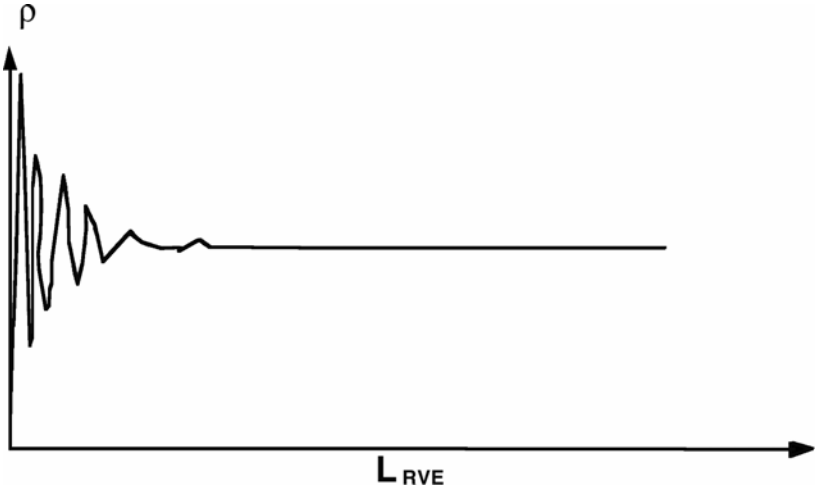



**Figure 8.2**. A plot of the values of the macrodensity as a function of the size $L_{\mathrm{RVE}}$ of the RVE. Note that as the size of the volume, $V_{\mathrm{RVE}} = (L_{\mathrm{RVE}})^3$, is decreased, the value of the density begins to oscillate because the amount of dense solid material in the volume, $V_{\mathrm{RVE}}$, is greatly influenced by the occurrence of small voids. On the other hand, as the size of the volume, $V_{\mathrm{RVE}} = (L_{\mathrm{RVE}})^3$, is increased, the value of the density tends to a constant, stable value. The concept for this plot is taken from Prandtl and Tietjens (1934). Prandtl used this type of diagram to illustrate density in the transition from rarefied gases in the upper atmosphere to denser air.

As another illustration of these ideas, consider the cross-section of trabecular bone shown in Figure 5.3. As noted in §5.2, the white regions are the bone trabeculae and the darker regions the pore spaces that are in vivo filled with marrow in the bone of young animals. First consider the small rectangular white region in the lower left quadrant as the first RVE for homogenization. This small rectangular white region is entirely within the trabecular bone domain and thus the global or macrodensity $\langle\rho\rangle$ and stress tensor $\langle\mathbf{T}\rangle$ obtained by volume averaging over microscale density $\rho$ and stress tensor $\mathbf{T}$ will be those for trabecular bone. On the other hand, if the small RVE in the darker marrow region is entirely within the whole domain, global or macrodensity $\langle\rho\rangle$ and stress tensor $\langle\mathbf{T}\rangle$ obtained by volume averaging will be those associated with marrow. If the RVE or homogenization domain is taken to be one of the larger rectangles in Figure 5.3, global or macrodensity $\langle\rho\rangle$ and stress tensor $\langle\mathbf{T}\rangle$ obtained by volume averaging over the microscale will be different from microscale density $\rho$ and stress tensor $\mathbf{T}$ for both bone and marrow, and their values will lie in between these two limits and be proportional to the ratio of the volume of marrow voids to the volume of bone in each rectangle.

**Problems**

8.2.1. Find average density $\langle\rho\rangle$ of a cube of volume $b^3$ if one-half the cube has a density of $\rho_0$ and the other half of the cube has density $\omega\rho_0$.

8.2.2. Find average density $\langle\rho\rangle$ of a sphere of radius $a$ whose density $\rho$ is given by $\rho = k\rho_o r$, where $r$ is the radial spherical coordinate.

## 8.3. EFFECTIVE MATERIAL PARAMETERS

One of the prime objectives in the discipline of composite materials, a discipline that has developed over the last half-century, is to evaluate the effective material parameters of a composite in terms of the material parameters and configurational geometries of its constituent components or phases. The purpose of this section is to show that the effective material properties may be expressed in terms of integrals over the surface of the RVE. The conceptual strategy is to average the heterogeneous properties of a material volume and conceptually replace that material volume with an equivalent homogenous material that will provide exactly the same property volume averages as the real heterogeneous material, allowing calculation of the material properties of equivalent homogeneous material. The material volume selected for averaging is the RVE, and the material properties of equivalent homogeneous material are then called the effective properties of the RVE. The calculational objective is to compute the effective material properties in terms of an average of the real constituent properties. This is accomplished by requiring that the integrals of the material parameters over the bounding surface of the RVE for the real heterogeneous material equal those same integrals obtained when the RVE consists of the equivalent homogeneous material. Thus, we seek to express the physical fields of interest for a particular RVE in terms of RVE boundary integrals.

In order to construct an effective anisotropic Hooke's law it is necessary to represent the global or macro stress and strain tensors, $\langle\mathbf{E}\rangle$ and $\langle\mathbf{T}\rangle$, respectively, as integrals over the boundary of the RVE. To accomplish this for the stress tensor we begin by noting the easily verified identity (see the Appendix, especially Problem A.3.3)

$$(\nabla \otimes \mathbf{x})^T = \frac{\partial x_i}{\partial x_j} e_i \otimes e_j = \mathbf{1}. \tag{8.2}$$

Using identity (8.2), a second identity involving the stress is constructed:

$$\mathbf{T} = \mathbf{1}\cdot\mathbf{T} = (\nabla \otimes \mathbf{x})^T \cdot \mathbf{T} = \{\nabla\cdot(\mathbf{T}\otimes\mathbf{x})\}^T . \tag{8.3}$$

The derivation of the last equality in (8.3) employs the fact that the divergence of the stress tensor is assumed to be zero, $\nabla\cdot\mathbf{T} = 0$. This restriction on the stress tensor follows from the stress equation of motion (4.29) when the acceleration and action-at-a-distance forces are zero. The result (8.3) has a restriction that the divergence $\nabla\cdot(\mathbf{T}\otimes\mathbf{x})$ is calculated with respect to **T**, not with respect to **x**; thus,

$$\nabla\cdot(\mathbf{T}\otimes\mathbf{x}) = \nabla\cdot\mathbf{T}\otimes\mathbf{x} + \mathbf{T}\cdot(\nabla\otimes\mathbf{x}) = \mathbf{T}$$

since $\nabla\cdot\mathbf{T} = 0$ and $\nabla\otimes\mathbf{x} = \mathbf{1}$. In the indicial notation this is written

$$\frac{\partial}{\partial x_j}(x_i T_{jk}) = x_i \frac{\partial T_{jk}}{\partial x_j} + T_{jk}\frac{\partial x_i}{\partial x_j} = T_{ik}$$

since

$$\frac{\partial T_{jk}}{\partial x_j} = 0 \quad \text{and} \quad \frac{\partial x_i}{\partial x_j} = \delta_{ij} .$$

The alternative and, in this case incorrect, interpretation of the divergence $\nabla\cdot(\mathbf{T}\otimes\mathbf{x})$ is calculated with respect to **x**, not with respect to **T**; thus,

$$\nabla\cdot(\mathbf{T}\otimes\mathbf{x}) = (\nabla\cdot\mathbf{x})\mathbf{T} + \mathbf{x}\cdot\nabla\otimes\mathbf{T} = 3\mathbf{T} + \mathbf{x}\cdot\nabla\otimes\mathbf{T} ,$$

or, in the indicial notation,

$$\frac{\partial}{\partial x_i}(x_i T_{jk}) = \frac{\partial x_i}{\partial x_i}T_{jk} + x_i\frac{\partial T_{jk}}{\partial x_i} = 3T_{jk} + x_i\frac{\partial T_{jk}}{\partial x_i} .$$

Substitution of identity (8.3) into the definition for $\langle\mathbf{T}\rangle$ yields

$$\langle\mathbf{T}\rangle = \frac{1}{V_{\text{RVE}}}\oint_V \mathbf{T}dv = \frac{1}{V_{\text{RVE}}}\oint_V \{\nabla\cdot(\mathbf{T}\otimes\mathbf{x})\}^T dv , \tag{8.4}$$

and subsequent application of divergence theorem (A183) converts the last volume integral in (8.4) to the following surface integral:

$$\langle\mathbf{T}\rangle = \frac{1}{V_{\text{RVE}}}\oint_{\partial V} \{\mathbf{n}\cdot(\mathbf{T}\otimes\mathbf{x})\}^T ds . \tag{8.5}$$

Finally, employing Cauchy relation (4.15), $\mathbf{t} = \mathbf{T}\cdot\mathbf{n}$, provides a relationship between $\langle\mathbf{T}\rangle$ and the integral over the boundary of the RVE depending only upon stress vector **t** acting on the boundary:

$$\langle\mathbf{T}\rangle = \frac{1}{V_{\text{RVE}}}\oint_{\partial V} \mathbf{x}\otimes\mathbf{t}ds . \tag{8.6}$$

This is the desired relationship because it expresses $\langle\mathbf{T}\rangle$ in terms only of boundary information, the surface tractions **t** acting on the boundary.

It is even easier to construct a similar representation of $\langle \mathbf{E} \rangle$ as an integral over the boundary of the RVE. To accomplish this set $f$ in (8.1) equal to $\nabla \otimes \mathbf{u}$ and then employ the divergence theorem in the form (A184), and thus

$$\langle \nabla \otimes \mathbf{u} \rangle = \frac{1}{V_{\text{RVE}}} \oint_V (\nabla \otimes \mathbf{u}) dv = \frac{1}{V_{\text{RVE}}} \oint_{\partial V} (\mathbf{n} \otimes \mathbf{u}) ds \,. \tag{8.7}$$

The final result is achieved immediately by recalling the definition of small strain tensor $\mathbf{E} = (1/2)((\nabla \otimes \mathbf{u})^{\mathrm{T}} + \nabla \otimes \mathbf{u})$; thus, from (8.7):

$$\langle \mathbf{E} \rangle = \frac{1}{V_{\text{RVE}}} \oint_{\partial V} \frac{1}{2} (\mathbf{n} \otimes \mathbf{u} + \mathbf{u} \otimes \mathbf{n}) ds \,. \tag{8.8}$$

With representations (8.6) and (8.8) for the global or macro stress and strain tensors, $\langle \mathbf{E} \rangle$ and $\langle \mathbf{T} \rangle$, respectively, effective anisotropic elastic constants $\widehat{\mathbf{C}}^{\text{eff}}$ are defined by relation

$$\langle \hat{\mathbf{T}} \rangle \equiv \widehat{\mathbf{C}}^{\text{eff}} \langle \hat{\mathbf{E}} \rangle \,. \tag{8.9}$$

This formula provides the tool for evaluation of the effective material elastic constants of a composite in terms of the material parameters of its constituent components or phases and the arrangement and geometry of the constituent components. In the next section results obtained using this formula are recorded in the cases of spherical inclusions in a matrix material and aligned cylindrical voids in a matrix material.

As a second example of this averaging process for material parameters, the permeability coefficients in Darcy's law are considered. In this case the vectors representing volume averages of the mass flow rates, $\langle \mathbf{q} \rangle$, and the pressure gradient, $\langle \nabla p \rangle$, have to be expressed in terms of surface integrals over the RVE. Obtaining such a formula for pressure gradient $\langle \nabla p \rangle$ is straightforward. Substitute $\mathbf{r} = p\mathbf{c}$, where $\mathbf{c}$ is a constant vector, into the divergence theorem in the form (A183), and then remove the constant vector from the integrals; thus,

$$\mathbf{c} \cdot \left( \oint_V \nabla p dv - \oint_{\partial V} (\mathbf{n} p dv) \right) = 0 \,; \tag{8.10}$$

then, since (8.10) must hold for all vectors $\mathbf{c}$, it follows from (8.10) and (8.1) that

$$\langle \nabla p \rangle = \frac{1}{V_{\text{RVE}}} \oint_{\partial V} \mathbf{n} p ds \,. \tag{8.11}$$

Obtaining a surface integral representation for the mass flow rates $\langle \mathbf{q} \rangle$ is slightly more complicated. To start, consider the expression $\nabla \cdot (\mathbf{x} \otimes \mathbf{q})$ and recall the comment in the text following equation (8.3) requiring the divergence $\nabla \cdot (\mathbf{T} \otimes \mathbf{x})$ to be interpreted as the divergence calculated with respect to $\mathbf{T}$, not with respect to $\mathbf{x}$. A similar restriction applies to $\nabla \cdot (\mathbf{x} \otimes \mathbf{q})$; the divergence is to be calculated with respect to $\mathbf{q}$ not with respect to $\mathbf{x}$; and thus, $\nabla \cdot (\mathbf{x} \otimes \mathbf{q}) = (\nabla \cdot \mathbf{q})\mathbf{x} + \mathbf{q}$. Set the second-rank tensor in the divergence theorem in the form (A184) equal to $\mathbf{x} \otimes \mathbf{q}$; the divergence of $\mathbf{x} \otimes \mathbf{q}$ is then equal to $\mathbf{x}(\nabla \cdot \mathbf{q}) + \mathbf{q}$, and (A184) yields

$$\oint_V \mathbf{q} + \mathbf{x}(\nabla \cdot \mathbf{q}) dv = \oint_{\partial V} (\mathbf{q} \cdot \mathbf{n}) \mathbf{x} dv \,. \tag{8.12}$$

A second integral formula involving $\mathbf{q}$ is obtained by setting $\mathbf{r}$ in the divergence theorem in the form (A183) equal to $\mathbf{q}$, thus

$$\oint_V \nabla \cdot \mathbf{q} dv = \oint_{\partial V} \mathbf{q} \cdot \mathbf{n} dv \,. \tag{8.13}$$

Now, if it is assumed that there are no sources or sinks in the volume $V$ and that the fluid is incompressible, then $\nabla\cdot\,\mathbf{q} = 0$ everywhere in the region and (8.12) yields

$$\langle \mathbf{q} \rangle = \frac{1}{V_{\text{RVE}}} \oint_{\partial V} (\mathbf{n}\cdot\mathbf{q})\mathbf{x}\,ds\,. \tag{8.14}$$

Using representations (8.14) and (8.11) for the volume averages of mass flow rates $\langle \mathbf{q} \rangle$ and pressure gradient $\langle \nabla p \rangle$, respectively, effective anisotropic permeability constants $\mathbf{H}^{\text{eff}}$ are defined by relation

$$\langle \mathbf{q} \rangle \equiv -\mathbf{H}^{\text{eff}} \langle \nabla p \rangle\,. \tag{8.15}$$

This formula provides the tool for evaluation of the effective permeability of a porous material in terms of the porous architecture of the solid phase and the properties of the fluid in those pores. In the section after next result (8.15) is used to evaluate effective permeability in a simple uniaxial model with multiple aligned cylindrical channels.

Although it is frequently not stated, all continuum theories employ local effective constitutive relations such as those defined by (8.9) and (8.15). This is necessarily the case because it is always necessary to replace the real material by a continuum model that does not contain the small-scale holes and inhomogeneities the real material contains, but which are not relevant to the concerns of the modeler. In the presentations of many continuum theories the substance of this modeling procedure is incorporated in a shorthand statement to the effect that a continuum model is (or will be) employed.

This approach is reasonable because, for many continuum theories, the averaging arguments are intuitively justifiable. This is generally not the case for biological tissues and nanomechanics in general. In almost all continuum theories the notation for RVE averaging, such as $\langle f \rangle$ for the RVE average of $f$, and notation $f$ really means $\langle f \rangle$. In particular, in any continuum theory involving the use of stress tensor $\mathbf{T}$, it is really the RVE averaged, $\langle \mathbf{T} \rangle$, that is being represented, even though an RVE has not been specified.

**Problem**

8.3.1 Find average stress $\langle \mathbf{T} \rangle$ in a heterogeneous cube of volume $b^3$ if each face of the cube is subjected to a different pressure. The pressure on the face normal to $\mathbf{e}_1$ and $-\mathbf{e}_1$ is $p_1$, $\mathbf{e}_2$ and $-\mathbf{e}_2$ is $p_2$, $\mathbf{e}_3$ and $-\mathbf{e}_3$ is $p_3$. Find average stress $\langle \mathbf{T} \rangle$ in a heterogeneous cube when all the surfaces are subjected to the same pressure.

## 8.4. EFFECTIVE ELASTIC CONSTANTS

As a first example of effective Hooke's law (8.9), consider a composite material in which the matrix material is isotropic and the inclusions are spherical in shape, sparse in number (dilute), and of a material with different isotropic elastic constants. In this case the effective elastic material constants are also isotropic and the bulk and shear moduli, $K^{\text{eff}}$ and $G^{\text{eff}}$, are related to the matrix material bulk and shear moduli, $K_m$ and $G_m$, and Poisson's ratio $\nu_m$, and to inclusion bulk and shear moduli, $K_i$ and $G_i$, by (Christensen, 1971, pp. 46–47):

$$\frac{K^{\text{eff}}}{K_m} = 1 + \frac{\left(\dfrac{K_i}{K_m} - 1\right)\phi_s}{1 + \dfrac{K_i - K_m}{K_m + (4/3)G_m}}, \quad \frac{G^{\text{eff}}}{G_m} = 1 - \frac{15(1-\nu_m)\left(1 - \dfrac{G_i}{G_m}\right)\phi_s}{7 - 5\nu_m + 2(4-5\nu_m)\dfrac{G_i}{G_m}}\,, \tag{8.16}$$

where $\phi_s$ is the porosity associated with the spherical pores. Thus if porosity $\phi_s$ and matrix and inclusion constants $K_m$, $G_m$, $K_i$, and $G_i$ are known, formulas (8.16) may be used to determine the effective bulk and shear moduli, $K^{\text{eff}}$ and $G^{\text{eff}}$, recalling that for an isotropic material Poisson's ratio $\nu_m$ is related to $K_m$ and $G_m$ by $\nu_m = (3K_m - 2G_m)/(6K_m + 2G_m)$ (see Table 7.2).

As a simple example of these formulas, consider the case when $\nu_m = 1/3$ and, since there are only two independent isotropic elastic constants, $G_m$ and $K_m$ are related. A formula from Table 7.2 may be used to show that $G_m = (3/8)K_m$. Substituting $\nu_m = 1/3$ and $G_m = (3/8)K_m$ in eq. (8.16), they simplify as follows:

$$\frac{K^{\text{eff}}}{K_m} = 1 + \frac{\left(\frac{K_i}{K_m} - 1\right)\phi_s}{1 + \frac{2}{3}\left(\frac{K_i}{K_m} - 1\right)}, \quad \frac{G^{\text{eff}}}{G_m} = 1 - \frac{15\left(1 - \frac{G_i}{G_m}\right)\phi_s}{8 + 7\frac{G_i}{G_m}}. \tag{8.17}$$

The ratio of the effective bulk modulus to the matrix bulk modulus, in the limiting cases when as the ratio of inclusion bulk modulus to the matrix bulk modulus tends to zero and infinity, are given by

$$\lim_{\frac{K_i}{K_m} \to 0} \frac{K^{\text{eff}}}{K_m} = 1 - 3\phi_s \quad \text{and} \quad \lim_{\frac{K_i}{K_m} \to \infty} \frac{K^{\text{eff}}}{K_m} = 1 + \frac{3\phi_s}{2}, \tag{8.18}$$

respectively. The ratio of effective shear modulus to the matrix shear modulus, in the limiting cases when as the ratio of inclusion shear modulus to the matrix shear modulus tends to zero and infinity, are given by

$$\lim_{\frac{G_i}{G_m} \to 0} \frac{G^{\text{eff}}}{G_m} = 1 - \frac{15\phi_s}{8} \quad \text{and} \quad \lim_{\frac{G_i}{G_m} \to \infty} \frac{G^{\text{eff}}}{G_m} = 1 + \frac{15\phi_s}{7}, \tag{8.19}$$

respectively. These results illustrate certain intuitive properties of effective moduli. As the moduli of inclusion decrease (increase) relative to the moduli of the matrix material, the effective elastic constants decrease (increase) relative to the elastic constants of the matrix material. If the inclusions are voids, formulas (8.16) simplify to

$$\frac{K^{\text{eff}}}{K_m} = 1 + \frac{\phi_s}{1 - \frac{K_m}{K_m + (4/3)G_m}}, \quad \frac{G^{\text{eff}}}{G_m} = 1 - \frac{15(1 - \nu_m)\phi_s}{7 - 5\nu_m}. \tag{8.20}$$

In the case when $\nu_m = 1/3$ these two formulas reduce to the first of (8.18) and the first of (8.19), respectively. The first equation of (8.20) is given by Nemat-Nasser and Hori (1999) as their eq. (5.2.6b).

If the material of the inclusion is a fluid, (8.16) simplifies to the following:

$$\frac{K^{eff}}{K_m} = 1 + \frac{\left(1 - \frac{K_f}{K_m}\right)\phi_s}{1 + \frac{K_f - K_m}{K_m + (4/3)G_m}}, \quad \frac{G^{eff}}{G_m} = 1 - \frac{15(1 - \nu_m)\phi_s}{7 - 5\nu_m}, \tag{8.21}$$

where $K_f$ represents the bulk modulus of the fluid.

**Exercise 8.4.1**

**Problem**: Calculate effective bulk modulus $K^{\text{eff}}$, shear modulus $G^{\text{eff}}$, and Young's modulus $E^{\text{eff}}$ for a composite material consisting of a steel matrix material and spherical inclusions. The spherical inclusions are made of magnesium, have radius $r$, and are contained within unit cells that are cubes with dimension $5r$. The Young's modulus of steel (magnesium) is 200 GPa (45 GPa), and the shear modulus of steel (magnesium) is 77 GPa (16 GPa).

**Solution**: Isotropic bulk modulus $K$ of a material may be determined from Young's modulus $E$ and shear modulus $G$ by use of formula $K = EG/(9G - 3E)$, given in Table 7.2. The bulk modulus of steel (magnesium) is 166 GPa (80 GPa). The volume fraction of the spherical inclusions is the ratio of the volume of one sphere, $(4/3)\pi r^3$, to the volume of the unit cell, $(5r)^3$, and thus $\phi_c = 0.0335$. Substituting the accumulated information into formulas (8.16), one finds that $K^{\text{eff}}$ and $G^{\text{eff}}$ are given by 161 and 74 GPa, respectively. Effective Young's modulus $E^{\text{eff}}$ is determined to be 103 GPa from formula $E = 9KG/(6K + G)$, given in Table 7.2.

As a second example of effective Hooke's law (8.9), consider a composite made up of a linear elastic homogenous and isotropic solid matrix material containing cylindrical cavities aligned in the $x_3$ direction (Figure 8.3). Although the matrix material is assumed to be isotropic, the cylindrical cavities aligned in the $x_3$ direction require that the material symmetry of the composite be transverse isotropy (Chapter 5, Table 5.4). Matrix of tensor compliance components $\hat{\mathbf{S}}$ for the effective transversely isotropic engineering elastic constants is in the following form:

$$\hat{\mathbf{S}} = \begin{bmatrix} \frac{1}{E_1^{\text{eff}}} & \frac{-\nu_{12}^{\text{eff}}}{E_1^{\text{eff}}} & \frac{-\nu_{13}^{\text{eff}}}{E_3^{\text{eff}}} & 0 & 0 & 0 \\ \frac{-\nu_{12}^{\text{eff}}}{E_1^{\text{eff}}} & \frac{1}{E_1^{\text{eff}}} & \frac{-\nu_{13}^{\text{eff}}}{E_3^{\text{eff}}} & 0 & 0 & 0 \\ \frac{-\nu_{13}^{\text{eff}}}{E_3^{\text{eff}}} & \frac{-\nu_{13}^{\text{eff}}}{E_3^{\text{eff}}} & \frac{1}{E_3^{\text{eff}}} & 0 & 0 & 0 \\ 0 & 0 & 0 & \frac{1}{2G_{23}^{\text{eff}}} & 0 & 0 \\ 0 & 0 & 0 & 0 & \frac{1}{2G_{23}^{\text{eff}}} & 0 \\ 0 & 0 & 0 & 0 & 0 & \frac{1+\nu_{12}^{\text{eff}}}{E_1^{\text{eff}}} \end{bmatrix}.$$

The effective elastic constants are expressed in terms of the matrix elastic constants and the volume fraction of cylindrical cavities, which is denoted by $\phi_c$. Volume fraction $\phi_c$ is assumed to be small and the distribution of cavities dilute and random. Terms proportional to the square and higher orders of $\phi_c$ are neglected. When $\phi_c$ is this small, several different averaging methods show, using a plane stress assumption in the $x_1$, $x_2$ plane, that the effective elastic constants are given by (Nemat-Nasser and Hori, 1999; chap. 5, eqs. (5.1.18a,b,c,d) and (5.1.27a,c)):

$$\frac{G_{13}^{\text{eff}}}{G_m} = \frac{G_{23}^{\text{eff}}}{G_m} = 1 - \frac{4\phi_c}{1+\nu_m}, \quad \frac{E_1^{\text{eff}}}{E_m} = \frac{E_2^{\text{eff}}}{E_m} = 1 - 3\phi_c, \quad \frac{E_3^{\text{eff}}}{E_{\text{m}}} = 1 - \phi_c,$$

$$\frac{\nu_{12}^{\text{eff}}}{\nu_{\text{m}}} = \frac{\nu_{21}^{\text{eff}}}{\nu_{\text{m}}} = 1 - (3 - \frac{1}{\nu_{\text{m}}})\phi_c, \quad \frac{\nu_{31}^{\text{eff}}}{\nu_{\text{m}}} = \frac{\nu_{32}^{\text{eff}}}{\nu_{\text{m}}} = 1, \quad \frac{\nu_{13}^{\text{eff}}}{\nu_{\text{m}}} = \frac{\nu_{23}^{\text{eff}}}{\nu_{\text{m}}} = 1 - 2\phi_c. \qquad (8.22)$$

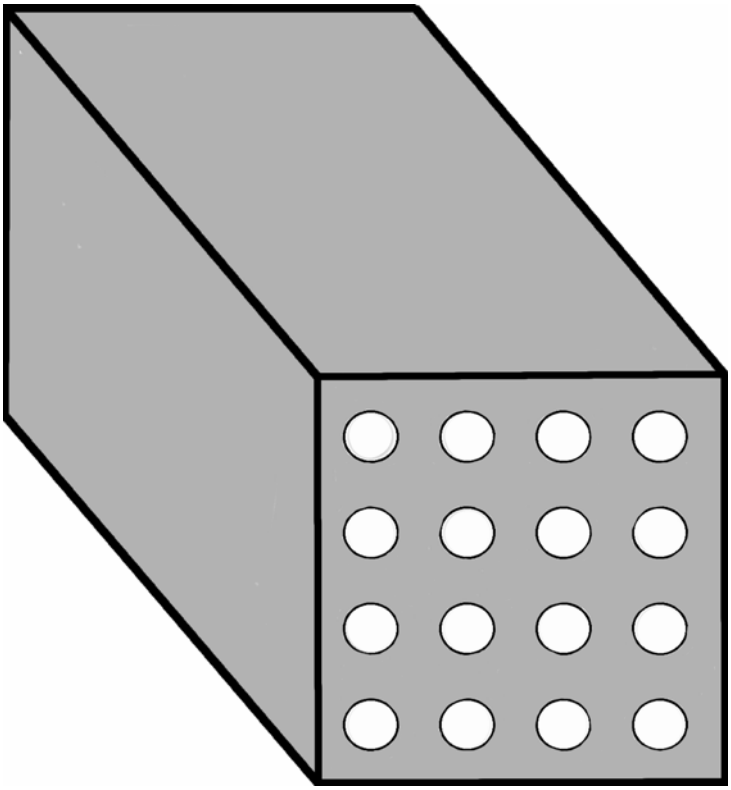


**Figure 8.3**. An illustration of a block of a homogeneous material containing cylindrical pores all aligned in one direction.

As noted, the cylindrical cavities aligned in the $x_3$ direction change that material symmetry but the isotropy in the plane perpendicular to the $x_3$ direction is retained. The material in the plane perpendicular to the $x_3$ direction is isotropic; all the elastic constants associated with that plane will be isotropic, as shown in the following exercise.

**Exercise 8.4.2**

**Problem**: Effective elastic constants (8.19) for the composite composed of an isotropic matrix material containing cylindrical cavities aligned in the $x_3$ direction are isotropic in the plane perpendicular to the $x_3$ direction. Verify that this is the case showing that if the matrix material satisfies isotropy relationship $2G_{\mathrm{m}} = E_{\mathrm{m}}/(1 + \nu_{\mathrm{m}})$, effective elastic constants $G_{13}^{\mathrm{eff}} = G_{23}^{\mathrm{eff}}$, $E_1^{\mathrm{eff}} = E_2^{\mathrm{eff}}$ and $\nu_{12}^{\mathrm{eff}} = \nu_{21}^{\mathrm{eff}}$ also satisfy the isotropy relationship. However, due to the notation, there is a multitude of equivalent forms: $2G_{13}^{\mathrm{eff}} = 2G_{23}^{\mathrm{eff}} = E_1^{\mathrm{eff}}/(1+\nu_{12}^{eff}) = E_2^{\mathrm{eff}}/(1+\nu_{12}^{\mathrm{eff}}) = E_1^{\mathrm{eff}}/(1+\nu_{21}^{eff}) = E_2^{\mathrm{eff}}/(1+\nu_{21}^{eff})$.

**Solution**: The first formula of (8.22) is rewritten as $2G_{13}^{\mathrm{eff}} = 2G_{23}^{\mathrm{eff}} = 2G_{\mathrm{m}} - \dfrac{8G_{\mathrm{m}}\phi_c}{1+\nu_m}$, then from $2G_{\mathrm{m}} = E_{\mathrm{m}}/(1 + \nu_{\mathrm{m}})$ it follows that $2G_{13}^{\mathrm{eff}} = 2G_{23}^{\mathrm{eff}} = E_{\mathrm{m}}(1+\nu_{\mathrm{m}} - 4\phi_c)$. From the second

formula of (8.22) one can see that $E_{\mathrm{m}} = \dfrac{E_1^{\mathrm{eff}}}{1-3\phi_c}$; thus, $2G_{13}^{\mathrm{eff}} = 2G_{23}^{\mathrm{eff}} = \dfrac{E_1^{\mathrm{eff}}(1+\nu_{\mathrm{m}}-4\phi_c)}{1-3\phi_c}$, or to the neglect of squared terms in $\phi_c$, $2G_{13}^{\mathrm{eff}} = 2G_{23}^{\mathrm{eff}} = E_1^{\mathrm{eff}}(1+\nu_{\mathrm{m}}-(3\nu_{\mathrm{m}}-1)\phi_c)$. From the fourth formula of (8.22) one can write $\nu_{12}^{eff} = \nu_{21}^{eff} = \nu_{\mathrm{m}}-(3\nu_{\mathrm{m}}-1)\phi_c$; thus, obtaining the desired result: $2G_{13}^{\mathrm{eff}} = 2G_{23}^{\mathrm{eff}} = E_1^{\mathrm{eff}}(1+\nu_{12}^{eff})$.

In the special case when $\nu_{\mathrm{m}}$ is 1/3, the expressions for the effective constants (8.22) simplify to

$$\frac{G_{13}^{\mathrm{eff}}}{G_{\mathrm{m}}} = \frac{G_{23}^{\mathrm{eff}}}{G_{\mathrm{m}}} = \frac{E_1^{\mathrm{eff}}}{E_{\mathrm{m}}} = \frac{E_2^{\mathrm{eff}}}{E_{\mathrm{m}}} = 1-3\phi_c\,, \quad \frac{E_3^{\mathrm{eff}}}{E_{\mathrm{m}}} = 1-\phi_c\,,$$

$$\frac{\nu_{12}^{\mathrm{eff}}}{\nu_{\mathrm{m}}} = \frac{\nu_{21}^{\mathrm{eff}}}{\nu_{\mathrm{m}}} = 1\,, \quad \frac{\nu_{31}^{\mathrm{eff}}}{\nu_{\mathrm{m}}} = \frac{\nu_{32}^{\mathrm{eff}}}{\nu_{\mathrm{m}}} = 1\,, \quad \frac{\nu_{13}^{\mathrm{eff}}}{\nu_{\mathrm{m}}} = \frac{\nu_{23}^{\mathrm{eff}}}{\nu_{\mathrm{m}}} = 1-2\phi_c\,. \tag{8.23}$$

From these results it is apparent that Young's modulus and the shear modulus in the transverse plane are more severely reduced than the axial Young's modulus as the porosity increases. In the example below, the second of (8.23), $E_{\mathrm{m}}^{\mathrm{eff}} / E_{\mathrm{m}} = 1-\phi_c$, is constructed from a mechanics of materials argument.

**Exercise 8.4.3**

**Problem**: Recall the mechanics of materials formula for deflection $\delta = PL/AE$ of a bar of cross-sectional area $A$, length $L$, and modulus $E$ subjected to axial force $P$. Apply this formula to the bar with axially aligned cylindrical cavities illustrated in Figure 8.3 to show that $E_{\mathrm{m}}^{\mathrm{eff}} / E_{\mathrm{m}} = 1-\phi_c$. The bar and the cylindrical cavities are aligned in the $x_3$ direction.

**Solution**: Formula $\delta = PL/AE$ will be applied in two ways to the bar with axially aligned cylindrical cavities illustrated in Figure 8.3 and subjected to axial force $P$. First apply the formula to the matrix material imagining a reduced cross-sectional area, $A_{\mathrm{m}}$, not containing the voids; thus, $E_{\mathrm{m}} = PL/A_{\mathrm{m}}\delta$. Next apply the formula to the entire bar containing the voids, and thus $E_3^{\mathrm{eff}} = PL/A\delta$. The relationship between cross-sectional total area $A$ and cross-sectional area $A_{\mathrm{m}}$ occupied by the matrix material is $A_{\mathrm{m}} = A(1 - \phi_c)$. The desired result is established by eliminating $P$, $L$, $\delta$, $A$, and $A_{\mathrm{m}}$ between these three formulas.

**Problems**

8.4.1. Calculate the effective bulk modulus, $K^{\mathrm{eff}}$, shear modulus $G^{\mathrm{eff}}$, and Young's modulus $E^{\mathrm{eff}}$ for a composite material consisting of a steel matrix material with spherical inclusions that contain water. The spherical inclusions, which have radius $r$, are contained within unit cells that are cubes with dimension $4r$. The Young's modulus of steel is 200 Gpa, and the shear modulus of steel is 77 GPa. The bulk modulus of water is 2.3 GPa.

8.4.2. Calculate the effective bulk modulus, $K^{\mathrm{eff}}$, shear modulus $G^{\mathrm{eff}}$, and Young's modulus $E^{\mathrm{eff}}$ for a composite material consisting of a magnesium matrix material and spherical inclusions. The spherical inclusions are made of steel, have radius $r$, and are contained within unit cells that are cubes with dimension $5r$. The Young's modulus of steel (magnesium) is 200 GPa (45 GPa) and the shear modulus of steel (magnesium) is 77 GPa (16 GPa).

8.4.3. Calculate the effective moduli for a composite material consisting of a steel matrix material and cylindrical voids of radius $r$ contained in unit squares $8r$ by $8r$. The Young's modulus of steel is 77 GPa and its Poisson's ratio 0.33.

8.4.4. Considering the effective moduli for a composite material consisting of a matrix material and aligned cylindrical voids, show that for small values of the volume fraction the in-plane effective shear moduli and the in-plane effective Young's moduli decrease more rapidly with increasing porosity than the out-of-plane effective Young's moduli. For simplicity, consider the case when $\nu_m$ is 1/3.

## 8.5. EFFECTIVE PERMEABILITY

In this section the effective axial permeability of the bar with axially aligned cylindrical cavities illustrated in Figure 8.3 is calculated. The method used is the simplest one available to show that Darcy's law is a consequence of application of the Newtonian law of viscosity to a porous medium with interconnected pores. Navier-Stokes equations (7.37) are a combination of Newtonian law of viscosity (6.36N) and stress equations of motion (4.37), as will be shown in the next chapter. Thus, one can say that Darcy's law is a consequence of application of either the Newtonian law of viscosity or the Navier-Stokes equations to a porous medium with interconnected pores. There are a number of more general, more rigorous, and more elegant proofs of this result (Ene and Sanchez-Palencia, 1975; Sanchez-Palencia, 1980; Burridge and Keller, 1981) but the one presented below suffices to make the point.

Consider the bar with axially aligned cylindrical cavities illustrated in Figure 8.3 as a porous medium, the pores being the axially aligned cylindrical cavities. Each pore is identical and can be treated as a pipe for the purpose of determining the fluid flow through it. In the case of pipe flow under steady pressure gradient $\partial p / \partial x_3$, the velocity distribution predicated by the Navier-Stokes equations is a parabolic profile (compare the paragraph following Example 7.4.3):

$$v_3 = -\left(\frac{\partial p}{\partial x_3}\right)\frac{r_o^2}{4\mu}\left(1-\frac{r^2}{r_o^2}\right), \tag{8.24}$$

where $\mu$ is the viscosity, $r_o$ is the radius of the pipe, and $r$ and $x_3$ are two of the three cylindrical coordinates. The volume flow rate through the pipe is given by

$$Q = 2\pi\int_0^{r_o} r v_3 dr = -\left(\frac{\partial p}{\partial x_3}\right)\frac{\pi r_o^4}{8\mu}, \tag{8.25}$$

which, multiplied by the total number of axially aligned cylindrical cavities per unit area, $n_c$, gives the average volume flow rate per unit area along the bar:

$$\langle \mathbf{q} \rangle = \frac{1}{V_{\text{RVE}}}\oint_{\partial V} (\mathbf{n}\cdot\mathbf{q})\mathbf{x} ds = \left(-\frac{\partial p}{\partial x_3}\right) n_c \frac{\pi r_o^4}{8\mu}. \tag{8.26}$$

Pressure gradient $\partial p / \partial x_3$ is a constant in the bar, hence the average of the pressure gradient over the bar is given by the constant value

$$\langle \nabla p \rangle = \frac{1}{V_{\text{RVE}}}\oint_V \nabla p dv = \frac{\partial p}{\partial x_3}, \tag{8.27}$$

a result that, combined with (8.26), yields

$$\langle \mathbf{q} \rangle = -n_c \frac{\pi r_o^4}{8\mu} \langle \nabla p \rangle . \tag{8.28}$$

A comparison of this representation for $\langle \mathbf{q} \rangle$ with that of (8.15) yields a representation for effective permeability $\mathsf{H}_{33}^{\text{eff}}$ in the $x_3$ direction:

$$\mathsf{H}_{33}^{\text{eff}} = n_c \frac{\pi r_o^4}{8\mu} . \tag{8.29}$$

This derivation has demonstrated that the effective permeability depends upon viscosity of the fluid $\mu$ and the geometry of the pores. The effective intrinsic permeability is defined as the regular effective permeability times the viscosity of the fluid in the pores, $\mathsf{K}_{33}^{\text{eff}} = \mu \mathsf{H}_{33}^{\text{eff}} = n_c(\pi r_0^4/8)$. Intrinsic effective permeability $\mathsf{K}_{33}^{\text{eff}} = n_c(\pi r_0^4/8)$ is of dimension length squared; it is independent of the type of fluid in the pores and dependent only upon the size and geometrical arrangement of the pores in the medium. The comments above concerning the connection between, and the relative properties of, the intrinsic (effective) permeability and the (effective) permeability are general and not tied to the particular model used here to calculate effective permeability $\mathsf{H}_{33}^{\text{eff}}$.

## 8.6. STRUCTURAL GRADIENTS

A material containing a structural gradient, such as increasing/decreasing porosity, is said to be a gradient material. Figure 8.4 is an illustration of an example material with a layered structural gradient. Spheres of varying diameters and one material type are layered in a matrix material of another type. As a special case, the spheres may be voids. Figure 8.5 is an illustration of a material with an unlayered structural gradient. Spheres of varying diameters and one material type are graded in a size distribution in a material of another type. Again, as a special case, the spheres may be voids. Gradient materials may be manmade, but they also occur in nature. Examples of natural materials with structural gradients include cancellous bone and the growth rings of trees.

The RVE plays an important role in determining the relationship between the structural gradient and the material symmetry. In a material with a structural gradient, if it is not possible to select an RVE so that it is large enough to adequately average over the microstructure and *also* small enough to ensure that the structural gradient across the RVE is negligible, then it is necessary to restrict the material symmetry to accommodate the gradient. However, in a material with a structural gradient, if an RVE may be selected so that it is large enough to adequately average over the microstructure and small enough to ensure that the structural gradient across the RVE is negligible, then it is not necessary to restrict the material symmetry to accommodate the gradient.

It is easy to see that a structural gradient is incompatible with a plane of symmetry. If a given direction is the direction of a structural gradient, it cannot also be the direction of a normal to a plane of symmetry, nor any projected component of a normal to a plane of reflective symmetry, because the increasing or decreasing structure with increasing distance from the reference plane, such as the layered spherical inclusions in Figure 8.4, would be increasing on one side of the plane and decreasing on the other side of the plane violating mirror symmetry. Gradient materials are thus a type of chiral material described in §5.9. The point is that, on the

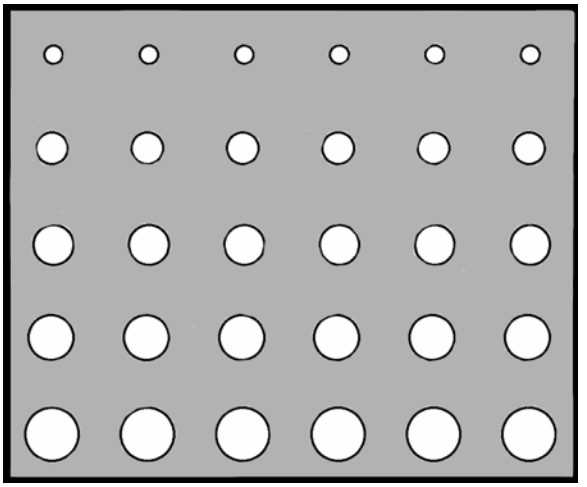


**Figure 8.4**. An illustration of a material with a layered structural gradient. Spheres of varying diameters and one material type are layered in a material of another type. As a special case, the spheres may be voids. Reprinted with permission from Cowin (2002).

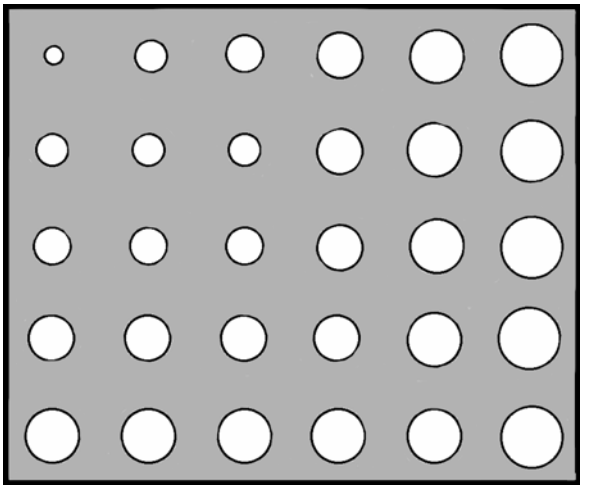


**Figure 8.5**. An illustration of a material with an unlayered structural gradient. Spheres of varying diameter and one material type are graded in a size distribution in a material of another type. As a special case, the spheres may be voids. Reprinted with permission from Cowin (2002).

same scale, the normal to a plane of symmetry and a material structural gradient are incompatible unless they are perpendicular. This incompatibility restricts the type of symmetries possible for gradient materials to those possible for chiral materials (§5.9), namely, trigonal, monoclinic, and triclinic symmetries (cf. Figure 5.10). In a material with a structural gradient, if an RVE may be selected so that it is large enough to adequately average over the microstructure and small enough to ensure that the structural gradient across the RVE is negligible, then it is not necessary to restrict the material symmetry to accommodate the gradient. However, in a material with a structural gradient, if an RVE cannot be selected such that the structural gra-

dient across an adequately sized RVE is negligible, then it is not necessary to restrict the material symmetry to accommodate the structural gradient.

The normal to a plane of material symmetry can only be perpendicular to the direction of a uniform structural gradient. The argument for this conclusion is a purely geometrical one. First note that the direction of a normal to a plane of material symmetry cannot be coincident with the direction of the structural gradient because the structural gradient is inconsistent with the reflective structural symmetry required by a plane of mirror symmetry. Next consider the case when the normal to a plane of material symmetry is inclined, but not perpendicular, to the direction of the structural gradient. In this case, the same situation prevails because the structural gradient is still inconsistent with the reflective structural symmetry required by a plane of mirror symmetry. The only possibility is that the normal to a plane of material symmetry is perpendicular to the direction of the structural gradient. Thus, it is concluded that the only symmetries permitted in a material containing a structural gradient are those symmetries characterized by having all their normals to their planes of mirror or reflective symmetry perpendicular to the structural gradient. The caveat to this conclusion is that the structural gradient and the material symmetry are at the same structural scale in the material. Only the three symmetries — triclinic, monoclinic, and trigonal — satisfy the condition that they admit a direction perpendicular to all the normals to their planes of mirror or reflective symmetry. Trigonal symmetry has the highest symmetry of the three symmetries and admits a direction that is not a direction associated with a normal to a plane of reflective symmetry, nor any projected component of a normal to a plane of reflective symmetry.

## 8.7. TENSORIAL REPRESENTATIONS OF MICROSTRUCTURE

The description and measurement of the microstructure of a material with multiple distinct constituents is called quantitative stereology (Underwood, 1969) or texture analysis (Bunge, 1982) or, in the case of biological tissues, it becomes part of histology. The concern here is primarily with the modeling of the material microstructure and only secondarily with techniques for its measurement.

It is recognized that the volume fraction of a constituent material is the primary geometric measure of local material structure in a material with multiple distinct constituents. This means that in the purely geometric kinematic description of the arrangement of the microstructure the volume fraction of a constituent material is the primary parameter in the geometric characterization of the microstructure.

The volume fraction of a constituent in a multiconstituent material does not provide information on the arrangement or architecture of microstructure of the multiconstituent material, only information on the volume of the constituent present. The second best measure of local material microstructure depends upon the type of material microstructure being modeled and the objective of the modeler. One approach to modeling of material microstructures is to use tensors to characterize the microstructural architecture.

Modeling of the microstructural architecture of a material with two distinct constituents, one dispersed in the other, has been accomplished using a second-rank tensor called the fabric tensor. Fabric tensors may be defined in a number of ways; it is required only that the fabric tensor be a positive definite tensor that is a quantitative stereological measure of the microstructural architecture, a measure whose principal axes are coincident with the principal microstructural directions and whose eigenvalues are proportional to the distribution of the microstructure in the associated principal direction. The fabric tensor is a continuum point property

(as usual, its measurement requires a finite test volume or RVE) and is therefore considered to be a continuous function of position in the material.

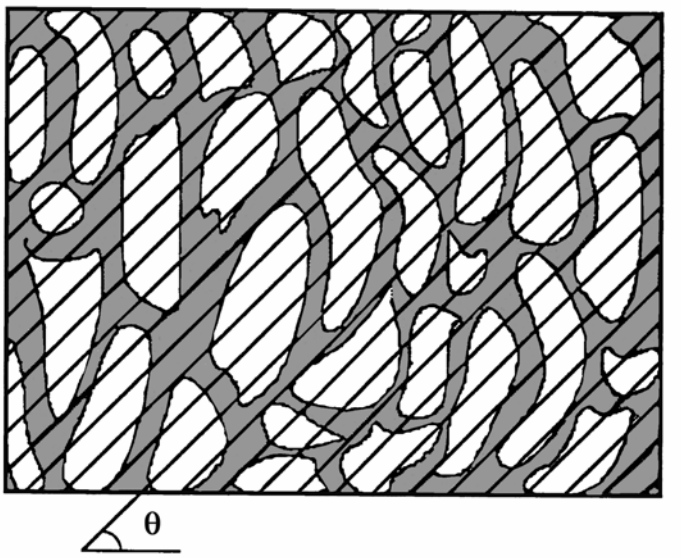



**Figure 8.6**. Test lines superimposed on a cancellous bone specimen. The test lines are oriented at angle θ. The mean intercept length measured at this angle is denoted $L(\theta)$. Reprinted with permission from Cowin and Mehrabadi (1989).

One type of fabric tensor is the mean intercept length (MIL) tensor. The MIL in a material is the average distance, measured along a particular straight line, between two interfaces of the two phases or constituents (Figure 8.6). The value of the mean intercept length is a function of the slope of the line, θ, along which the measurement is made in a specified plane. A grid of parallel lines is overlaid on the plane through the specimen of the binary material and the distance between changes of phase, first material to second material or second material to first material, are counted. The average of these lengths is the mean intercept length at angle θ, the angle characterizing the orientation of the set of parallel lines. Figure 8.6 illustrates such measurements. If, when the mean intercept lengths measured in the selected plane passing through a particular point in the specimen are plotted in a polar diagram as a function of θ, the polar diagram produced ellipses, the values of all MILs in the plane may be represented by a second-order tensor in two dimensions. If the test lines are rotated through several values of θ and the corresponding values of mean intercept length $L(\theta)$ are measured, the data are found to fit the equation for an ellipse very closely,

$$(1/L^2(\theta)) = M_{11}\cos^2\theta + M_{22}\sin^2\theta + 2M_{12}\sin\theta\cos\theta, \tag{8.30}$$

where $M_{11}$, $M_{22}$, and $M_{12}$ are constants when the reference line from which angle θ is measured is constant. Subscripts 1 and 2 indicate the axes of the $x_1$, $x_2$ coordinate system to which the measurements are referred. The ellipse is shown superposed on the binary microstructure it represents in Figure 8.7. Examples of this process for cancellous bone specimens are shown in Figure 8.8. The mean intercept lengths in all directions in a three-dimensional binary microstructure structure would be represented by an ellipsoid and would therefore be equivalent to a

positive definite second rank tensor. Constants $M_{11}$, $M_{22}$, and $M_{12}$ introduced in the foregoing are then the components in a matrix representing tensor $M$ that are related to mean intercept length $L(\mathbf{n})$, where $\mathbf{n}$ is a unit vector in the direction of the test line, by $(1/L^2(\mathbf{n})) = \mathbf{n} \cdot \mathbf{M}\, \mathbf{n}$.

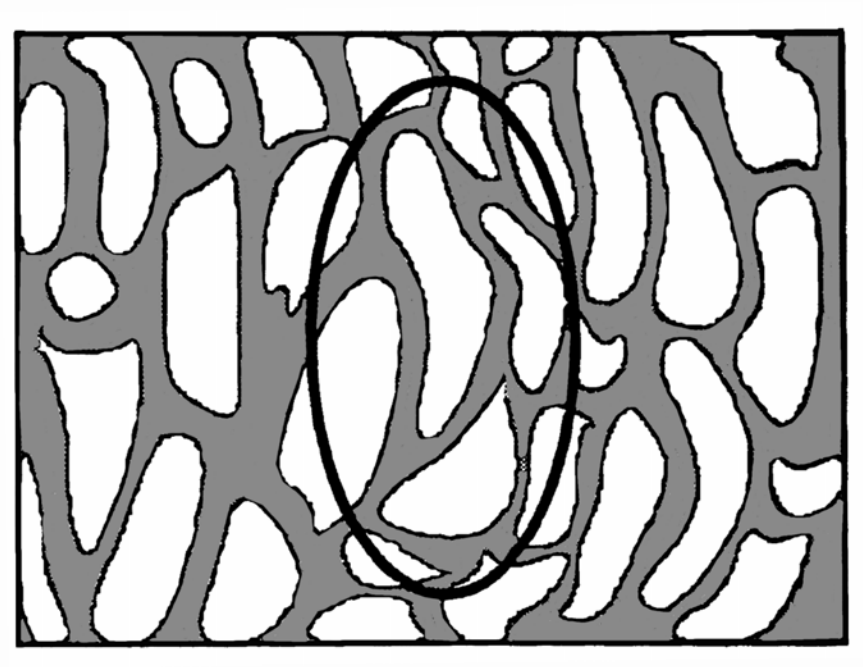


**Figure 8.7**. An ellipse constructed by making a polar pole of the average value of the mean intercept length $L(\theta)$ for each value of angle $\theta$. Reprinted with permission from Cowin and Mehrabadi (1989).

A number of ways of constructing a fabric tensor for a material with two distinct constituents are described by Odgaard (1997; 2001) for a particular porous material, cancellous bone. These methods are applicable to any material with at least two distinct constituents and include the stereological methods known as the mean intercept length method, the volume orientation method and star volume distribution method. In multiphase materials such as cellular materials, foams, and cancellous bone, the unit vectors may represent the orientation of the interface surface area or the inclusion volume orientation (Hilliard, 1967). As pointed out by Odgaard et al. (1997), for the same microstructural architecture these different fabric tensor definitions each lead to representations of the data that are, effectively, the same.

The existence of a mean intercept or fabric ellipsoid for an anisotropic porous material suggests elastic orthotropic symmetry. To visualize this result, consider an ellipse, illustrated in Figure 8.9, that is one of the three principal planar projections of the mean intercept length ellipsoid. The planes perpendicular to the major and minor axes of the ellipse illustrated in Figure 8.9b are planes of mirror symmetry because the increasing or decreasing direction of the mean intercept length, indicated by the arrowheads, is the same with respect to either of these planes. On the other hand, if one selects an arbitrary direction such as that illustrated in Figure 8.9a, it is easy to see that the selected direction is not a normal direction for a plane of mirror symmetry because the direction of increasing mean intercept length is reversed from its appropriate mirror image position. Therefore, there are only two planes of mirror symmetry

associated with the ellipse. Considering the other two ellipses that are planar projections of the mean intercept ellipsoid, the same conclusion is reached. Thus, only the three perpendicular principal axes of the ellipsoids are normals to the planes of mirror symmetry. This means that, if the structural materials involved are isotropic, the material symmetry will be determined only by the fabric ellipsoid and that the material symmetry will be orthotropic or of greater symmetry. If two of the principal axes of the mean intercept length ellipsoid were equal (i.e., an ellipsoid of revolution or, equivalently, a spheroid, either oblate or prolate), then the elastic symmetry of the material is transversely isotropic. If the fabric ellipsoid degenerates to a sphere, the elastic symmetry of the material is isotropic.

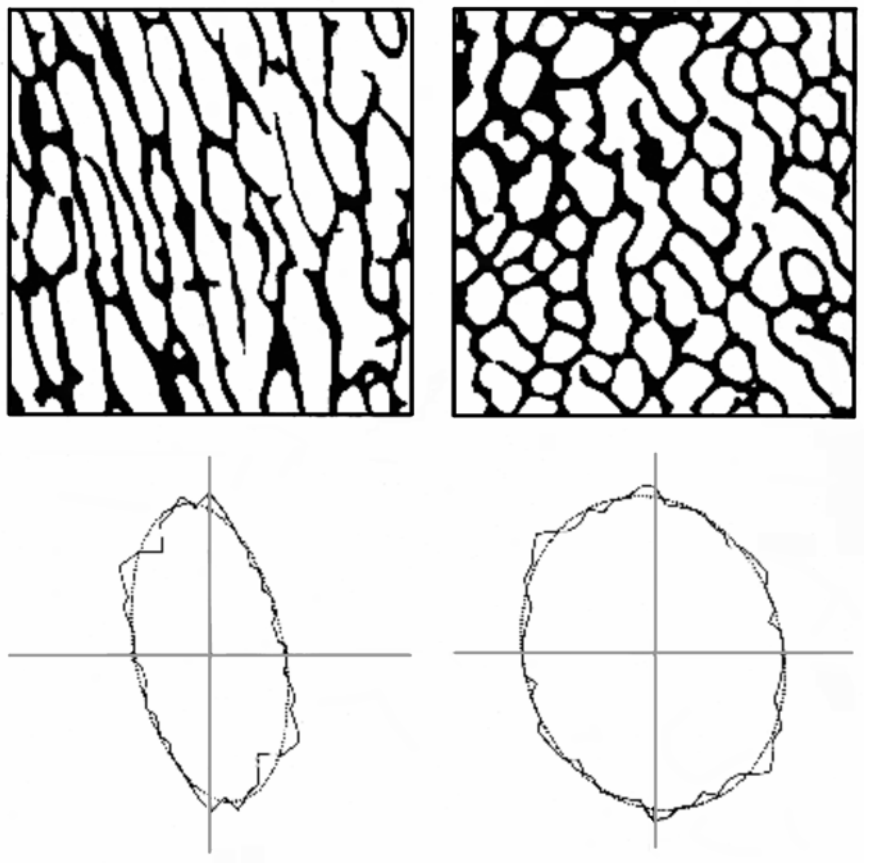


**Figure 8.8**. Illustrations of two different regions of cancellous bone in the horse (top) and the fabric ellipses for each of these regions constructed from these planar images (below). Courtesy of John Currey.

The fabric tensor employed here is denoted by **H** and is related to mean intercept length tensor **M** by $\mathbf{H} = \mathbf{M}^{-1/2}$. The positive square root of the inverse of **M** is well defined because **M** is a positive definite symmetric tensor. The principal axes of **H** and **M** coincide; only the shape of the ellipsoid changes. **M** is a positive definite symmetric tensor because it represents an ellipsoid. The fabric tensor or mean intercept ellipsoid can be measured using the techniques described above for a cubic specimen. On each of three orthogonal faces of a cubic specimen

of cancellous bone an ellipse will be determined from the directional variation of mean intercept length on that face. The mean intercept length tensor or the fabric tensor can be constructed from these three ellipses that are projections of the ellipsoid on three perpendicular planes of the cube.

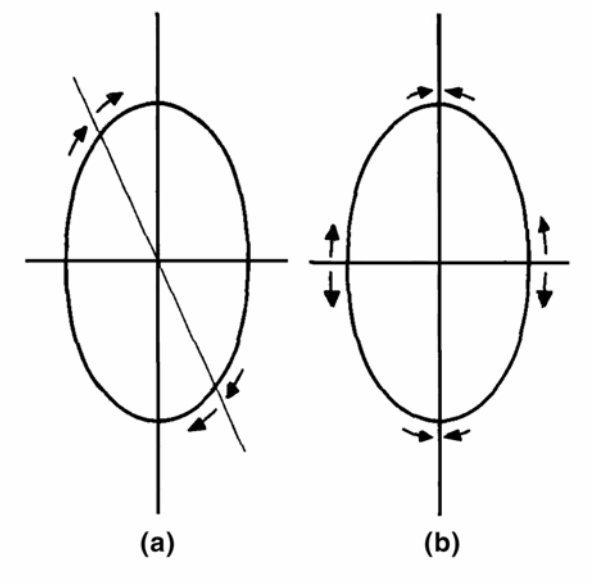



**Figure 8.9**. The mean intercept length ellipse as an indicator of the normals to planes of mirror symmetry: (a) the direction of the skewed line cannot be a normal to a plane of mirror symmetry because the direction of increasing mean intercept length has an anti-mirror symmetry; (b) the directions of the major and minor axes of the ellipse are normals to planes of mirror symmetry. Reprinted with permission from Cowin and Mehrabadi (1989).

As an example of how fabric tensor **H** may be employed, consider a porous medium that may be satisfactorily modeled as an orthotropic, linearly elastic material. Six-dimensional second-rank elasticity tensor $\hat{\mathbf{C}}$ relates the six-dimensional stress vector to the six-dimensional infinitesimal strain vector in the linear anisotropic form of Hooke's law, (6.36H). Elasticity tensor $\hat{\mathbf{C}}$ completely characterizes the linear elastic mechanical behavior of the porous medium. If it is assumed that all the anisotropy of the porous medium is due to the anisotropy of its solid matrix pore structure, that is to say, that the matrix material is itself isotropic, then a relationship between the components of elasticity tensor $\hat{\mathbf{C}}$ and **H** can be constructed. From previous studies of porous media it is known that its elastic properties are strongly dependent upon its apparent density or, equivalently, the solid volume fraction of matrix material. This solid volume fraction is denoted by $\nu$ and is defined as the volume of matrix material per unit bulk volume of the porous medium. Thus, $\hat{\mathbf{C}}$ will be a function of $\nu$ as well as **H**. A general representation of $\hat{\mathbf{C}}$ as a function of $\nu$ and **H** was developed based on the assumption that the matrix material of the porous medium is isotropic and that the anisotropy of the porous medium itself is due only to the geometry of the microstructure represented by fabric tensor **H**. The mathematical statement of this notion is that stress tensor **T** is an isotropic function of strain tensor **E** and fabric tensor **H** as well as solid volume fraction $\nu$. Thus, tensor valued function

$$\mathbf{T} = \mathbf{T}(\nu, \mathbf{E}, \mathbf{H}), \tag{8.31}$$

has the property that

$$\mathbf{Q}\mathbf{T}\mathbf{Q}^{T} = \mathbf{T}(\nu, \mathbf{Q}\mathbf{E}\mathbf{Q}^{T}, \mathbf{Q}\mathbf{H}\mathbf{Q}^{T}), \tag{8.32}$$

for all orthogonal tensors $\mathbf{Q}$. The most general form of the relationship between the stress tensor and the strain and the fabric tensors consistent with the isotropy assumption (8.32) is

$$\begin{aligned}\mathbf{T} = {} & a_1\mathbf{1}\mathrm{tr}\,\mathbf{E} + a_2(\mathbf{H}\mathrm{tr}\mathbf{E} + \mathbf{1}\mathrm{tr}\,[\mathbf{E}\cdot\mathbf{H}]) + a_3(\mathbf{1}\mathrm{tr}[\mathbf{H}\cdot\mathbf{E}\cdot\mathbf{H}] + (\mathrm{tr}\mathbf{E})\mathbf{H}^2) + b_1\mathbf{H}\mathrm{tr}[\mathbf{H}\cdot\mathbf{E}] \\ & + b_2(\mathbf{H}\mathrm{tr}[\mathbf{H}\cdot\mathbf{E}\cdot\mathbf{H}] + (\mathrm{tr}\mathbf{E}\cdot\mathbf{H})\mathbf{H}^2) + b_3(\mathbf{H}^2\mathrm{tr}[\mathbf{H}\cdot\mathbf{E}\cdot\mathbf{H}]) \\ & + 2c_1\mathbf{E} + 2c_2(\mathbf{H}\cdot\mathbf{E} + \mathbf{E}\cdot\mathbf{H}) + 2c_3(\mathbf{H}^2\cdot\mathbf{E} + \mathbf{E}\cdot\mathbf{H}^2)\end{aligned} \tag{8.33}$$

where $a_1$, $a_2$, $a_3$, $b_1$, $b_2$, $b_3$, $c_1$, $c_2$, and $c_3$ are functions of $\nu$, $\mathrm{tr}\mathbf{H}$, $\mathrm{tr}\mathbf{H}^2$, and $\mathrm{tr}\mathbf{H}^3$. This representation will be used in Chapter 11 to represent the elastic behavior of highly porous bone tissue.

## 8.8. RELEVANT LITERATURE

Good discussions of the representative volume element (RVE) concept appear in the books by Christensen (1979) and Nemat-Nasser and Hori (1999). The opening quote of Chapter 8 describes a very early application of the RVE concept by Maurice Biot (1941) to poroelasticity.

The books on composite materials by Jones (1975), Tsai and Hahn (1980), Hull (1981), and Halpin (1984) tend to specialize in laminated composites, that is, to composites constructed in the manner illustrated in Figure 8.7. The early book of Spencer (1972), which develops the theory of fiber reinforced materials, has been used in developing mathematical models for several biological tissues. Early rigorous summaries of composite material modeling were given by Sendeckyj (1974) and Christensen (1979); a contemporary rigorous and exhaustive development of elastic composite theory is contained in Nemat-Nasser and Hori (1999). Torquato (2002) presents a general, contemporary, rigorous, and exhaustive development of the quantification and modeling of microstructure.

Wainwright et al. (1976) and Neville (1993) are two interesting books on biological composites, both plant and animal natural composites. Neville's book explores nature's wide use of the helicoidal structure as a composite building geometry. The book of Vincent (1982) is of more restricted scope. Wood is the most widely analyzed natural composite material, and its mechanics and microstructure are described in an abundant literature, for example, Kollmann and Côte (1968) and Bodig and Jayne (1982). The book by Niklaus (1992) on plant biomechanics covers a wider range of the plant world, but it also deals with mechanism and microstructure.

The quantification and measurement of material microstructure is not addressed in the present book, but it is addressed in books on histology, metallurgy, and materials science. The book of Underwood (1969) on quantitative stereology, that of Bunge (1982) on texture analysis in material science, and any standard textbook on histology are examples of this literature.

### References

Biot MA. 1941. General theory of three-dimensional consolidation. *J Appl Phys* **12**:155–164.
Bodig J, Jayne BA. 1982. *Mechanics of wood and wood composites*. New York: Van Nostrand.
Bunge HJ. 1982. *Texture analysis in materials science*. London: Butterworths.

Burridge R, Keller JB. 1981. Poroelasticity equations derived from microstructure. *J Acoust Soc Am* **70**:1140–1146.

Christensen RM. 1979. *Mechanics of composite materials*. New York: Wiley.

Cowin SC. 2002. Elastic symmetry restrictions from structural gradients. In *Rational continua, classical and new — a collection of papers dedicated to Gianfranco Capriz on the occasion of his 75th birthday*, eds. P Podio-Guidugli, M Brocato. New York: Springer-Verlag. ISBN 88-470-0157-9.

Cowin SC, Mehrabadi MM. 1989. Identification of the elastic symmetry of bone and other materials. *J Biomech* **22**:503–515.

Ene HJ, Sanchez-Palencia E. 1975. Equations et phénoménes di surface pour l'écoulement dans unmodèle de milieu poreux. *J Mécanique* **14**:73–81.

Halpin JC. 1984. *Primer on composite materials: analysis*. Lancaster PA: Technomic Publishers.

Hilliard JE. 1967. Determination of structural anisotropy. In *Stereology — Proc. 2nd Int. Congress for Stereology, Chicago*, p.219. Berlin: Springer.

Hull D. 1981. *An introduction to composite materials*. Cambridge: Cambridge UP.

Jones RM. 1975. *Mechanics of composite materials*. Washington, DC: Scripta.

Kollmann FFP, Cote WA. 1968. *Principles of wood science and technology*. New York: Springer-Verlag.

Nemat-Nasser S, Hori M. 1999. *Micromechanics: overall properties of heterogeneous materials*. Amsterdam: Elsevier.

Neville C. 1993. *Biology of fibrous composites*. Cambridge: Cambridge UP.

Niklas KJ. 1992. *Plant biomechanics*. Chicago: U Chicago P.

Odgaard A. 1997. Three-dimensional methods for quantification of cancellous bone architecture. *Bone* **20**:315–328.

Odgaard A. 2001. Quantification of cancellous bone architecture. In *Bone mechanics handbook*, ed. SC Cowin. Boca Raton, FL: CRC Press.

Prandtl L, Tietjens OG. 1934. *Fundamentals of hydro- and aeromechanics*. New York: Dover.

Sanchez-Palencia E. 1980. *Non-homogeneous media and vibration theory*. Berlin: Springer.

Sendeckyj GP. 1974. Elastic behavior of composites. In *Mechanics of composite materials*, ed. GP Sendeckyj, **2**:46–83. New York and London: Academic Press.

Spencer AJM. 1972. *Deformations of fibre-reinforced materials*. Oxford: Clarendon Press.

Torquato S. 2002. *Random heterogeneous materials*. New York: Springer.

Tsai SW, Hahn HT. 1980. *Introduction to composite materials*. Westport, CT: Technomic Publishers.

Underwood EE. 1969. *Quantitative stereology*. Reading, MA: Addison-Wesley.

Vincent JFV. 1982. *Structural biomaterials*. New York: Wiley.

Wainwright SA, Biggs WD, Currey JD, Gosline JM. 1976. *Mechanical design in organisms*. London: Edward Arnold.

# 9

# POROELASTICITY

The theme of this chapter is contained in a quote from the 1941 paper of M.A. Biot that clearly describes an RVE: "Consider a small cubic element of soil, its sides being parallel with the coordinate axes. This element is taken to be large enough compared to the size of the pores so that it may be treated as homogeneous, and at the same time small enough, compared to the scale of the macroscopic phenomena in which we are interested, so that it may be considered as infinitesimal in the mathematical treatment."

## 9.1. POROELASTIC MATERIALS

An intuitive sense of the response of a saturated elastic porous medium to mechanical loading can be developed by thinking about, or experimenting with, a fluid-saturated sponge. If a fluid-saturated sponge is compressed, fluid will flow from the sponge. If the sponge is in a fluid reservoir and compressive pressure is subsequently removed, the sponge will reimbibe the fluid and expand. The volume of the sponge will also increase if its exterior openings are sealed and the pore fluid pressure is increased. The basic ideas underlying the theory of poroelastic materials are that the pore fluid pressure contributes to the total stress in the porous matrix medium and that the pore fluid pressure alone can strain the porous matrix medium. There is fluid movement in a porous medium due to differences in pore fluid pressure created by different pore volume strains associated with mechanical loading of the porous medium.

Poroelastic theory is a useful model in many tissues because almost all tissues have an interstitial fluid in their pores. The interstitial fluid has many functions, one important function being to transport nutrients from the vasculature to the cells in the tissue and to transport waste products for removal. In some tissues the pore fluid pressure creates a turgor that stiffens a soft tissue structure, and in other tissues it is part of the intercellular communication system. In tissues deformation of the porous medium has a significant effect on the movement of pore fluid, although fluid pressure and fluid movement generally have only a small effect on deformation of the porous medium; porous medium deformation generally pushes the fluid around, not vice-versa. The pore fluid pressure stays relatively low in tissues because a higher pressure could collapse blood vessels and render the tissue ischemic. However, the pore fluid pressure does not have to stay low in tissues like articular cartilage that are avascular. One could speculate that the reason articular cartilage is avascular is to avoid the collapse of blood vessels. Many of these effects have been, or will be, modeled using poroelasticity theory.

The poroelastic theory developed in this chapter is a combination and modification of three of the four theories — those for elastic solids, viscous fluids, and flow through porous media — developed in Chapter 7. The development of the theory is strongly dependent on the microstructural modeling concepts described in Chapter 8. In fact, much of the material that has preceded this chapter has been laying the foundation for the present chapter. Laying this foundation began with the discussion of the Terzaghi and Darcy lumped parameter models in Chapter 2.

Two cases associated with the effects of fluid pressure are considered for the purpose of measuring the elastic constants in a poroelastic material: drained and undrained. In the *drained* case the fluid pressure in the pores is zero; this is achieved by draining all the pores before the test or doing the test so slowly that the pores will drain from a negligible fluid pressure. In a porous medium the pores are assumed to be connected; there are no unconnected pores that prevent the flow of fluid through them. In the *undrained* case the pores that permit fluid to exit the test specimen are sealed; thus, pressure will build in the specimen when other forces load it, but the pressure cannot cause the fluid to move out of the specimen. Paraphrasing the opening quote of this chapter, the representative volume element (RVE) for a porous medium (Figure 5.2) is considered as a small cube (Figure 5.1) that is large enough, compared to the size of the largest pores, that it may be treated as homogeneous, and at the same time small enough, compared to the scale of the macroscopic phenomena that are of interest, that it may be considered infinitesimal in the mathematical treatment. The creator of the poroelastic theory advanced this description of the RVE for a saturated porous medium before the terminology RVE came into wide usage. Maurice Anthony Biot (1905–1985), a Belgian-American engineer who made many theoretical contributions to mechanics, developed poroelastic theory. It is his 1941 paper (Biot, 1941) that is the basis of the isotropic form of the theory described here.

There are three sets of elastic constants employed in this poroelasticity theory, the drained, $\hat{\mathbf{S}}^{\mathrm{d}}$, the undrained, $\hat{\mathbf{S}}^{\mathrm{u}}$, and those of the matrix material, $\hat{\mathbf{S}}^{\mathrm{m}}$. The RVE associated with the large box in Figure 5.2 is used for determination of the drained and undrained elastic constants, while the RVE associated with the smallest box is used for characterization of the matrix elastic constants. Unlike the large-box RVE, the small-box RVE contains no pores. Elastic compliance matrices $\hat{\mathbf{S}}^{\mathrm{u}}$, $\hat{\mathbf{S}}^{\mathrm{d}}$, and $\hat{\mathbf{S}}^{\mathrm{m}}$ for these materials have a similar representation:

$$\hat{\mathbf{S}}^{\mathrm{x}} = \begin{bmatrix} \hat{S}^x_{11} & \hat{S}^x_{12} & \hat{S}^x_{13} & \hat{S}^x_{14} & \hat{S}^x_{15} & \hat{S}^x_{16} \\ \hat{S}^x_{12} & \hat{S}^x_{22} & \hat{S}^x_{23} & \hat{S}^x_{24} & \hat{S}^x_{25} & \hat{S}^x_{26} \\ \hat{S}^x_{13} & \hat{S}^x_{23} & \hat{S}^x_{33} & \hat{S}^x_{34} & \hat{S}^x_{35} & \hat{S}^x_{36} \\ \hat{S}^x_{14} & \hat{S}^x_{24} & \hat{S}^x_{34} & \hat{S}^x_{44} & \hat{S}^x_{45} & \hat{S}^x_{46} \\ \hat{S}^x_{15} & \hat{S}^x_{25} & \hat{S}^x_{35} & \hat{S}^x_{45} & \hat{S}^x_{55} & \hat{S}^x_{56} \\ \hat{S}^x_{16} & \hat{S}^x_{26} & \hat{S}^x_{36} & \hat{S}^x_{46} & \hat{S}^x_{56} & \hat{S}^x_{66} \end{bmatrix},$$

where $x = d$, $u$, or $m$ stands for drained, undrained, or matrix, respectively. The special forms of $\hat{\mathbf{S}}^{\mathrm{x}}$ associated with particular elastic symmetries are listed in Table 5.4.

There are seven scalar stress variables and seven scalar strain variables in poroelasticity. The seven scalar stress variables are the six components of stress tensor $\mathbf{T}$ and fluid pressure $p$ in the pores. The seven scalar strain variables are the components of strain tensor $\mathbf{E}$ and variation in fluid content $\zeta$, a dimensionless measure of the fluid mass per unit volume of the porous material due to diffusive fluid mass transport. This set of variables may be viewed as conjugate pairs of stress measures ($\mathbf{T}$, $p$) and strain measures ($\mathbf{E}$, $\zeta$) appearing in the following form in an expression for work done on the poroelastic medium: $dW = \mathbf{T}: d\mathbf{E} + p d\zeta$. The linear stress–strain–pore pressure constitutive relation, $\mathbf{E} = \mathbf{E}(\mathbf{T}, p)$, consisting of six scalar equa-

tions, is described in §9.2, and the single-scalar-linear equation fluid content-stress-pore pressure constitutive relation, $\zeta = \zeta(\mathbf{T}, p)$, is described in §9.3. Thus, the seven scalar stress variables will be linearly related to the seven scalar strain variables. The poroelastic theory considered here is fully saturated, which means that the volume fraction of fluid is equal to the porosity, $\phi$, of the solid matrix. Darcy's law, which relates the gradient of the pore pressure to the mass flow rate, is the subject of §9.4. The special form of poroelasticity theory in the case when both the matrix material and the pore fluid are considered to be incompressible is developed in §9.5. Formulas for undrained elastic coefficients $\hat{\mathbf{S}}^{\mathrm{u}}$ as functions of $\phi$, the bulk modulus of the pore fluid, $K_f$, and drained and matrix elastic constants $\hat{\mathbf{S}}^{\mathrm{d}}$ and $\hat{\mathbf{S}}^{\mathrm{m}}$, respectively, $\hat{\mathbf{S}}^{\mathrm{u}} = \hat{\mathbf{S}}^{\mathrm{u}}\ (\hat{\mathbf{S}}^{\mathrm{d}}, \hat{\mathbf{S}}^{\mathrm{m}}, \phi, K_f)$, are developed in §9.6. The objective of §§9.2–9.7 is to develop the background for the basic system of equations for poroelasticity recorded in §§9.8–9.9. If the reader would like to have a preview of where the §§9.2–9.8 are leading, they can peruse §9.9 and observe how the various elements in §§9.2–9.8 are combined with the conservation of mass (4.6) and the conservation of momentum (4.37) to form poroelasticity theory. Examples of the solutions to poroelastic problems are given in §§9.10 and 9.11, and a summary of the literature, with references, appears in §9.12.

## 9.2. THE STRESS–STRAIN-PORE PRESSURE CONSTITUTIVE RELATION

The basic hypothesis is that average strain $\hat{\mathbf{E}}$ in the RVE of the saturated porous medium is related, not only to average stress $\hat{\mathbf{T}}$ in the RVE, but also to fluid pressure p in the fluid-filled pores. Thus, the stress–strain-pore pressure constitutive relation for a saturated porous medium linearly relates strain $\hat{\mathbf{E}}$ in the saturated porous medium not only to stress $\hat{\mathbf{T}}$ but also to fluid pressure $p$ in the fluid-filled pores; this is expressed as the strain–stress-pore pressure relation:

$$\hat{\mathbf{E}} = \hat{\mathbf{S}}^{\mathrm{d}} \cdot \hat{\mathbf{T}} + \hat{\mathbf{S}}^{\mathrm{d}} \cdot \hat{\mathbf{A}} p \tag{9.1}$$

or the stress-pore-pressure strain relation:

$$\hat{\mathbf{T}} + \hat{\mathbf{A}} p = \hat{\mathbf{C}}^{\mathrm{d}} \cdot \hat{\mathbf{E}}\,, \tag{9.2}$$

where $\hat{\mathbf{S}}^{\mathrm{d}}$ represents the drained anisotropic compliance elastic constants of the saturated porous medium and $\hat{\mathbf{C}}^{\mathrm{d}}$ is its reciprocal, the drained anisotropic elasticity tensor. This constitutive equation is a modification of (6.12H) to include the effect of pore pressure $p$. The six-dimensional vector (three-dimensional symmetric second-order tensor), $\hat{\mathbf{A}}$, is called the Biot effective stress coefficient tensor. When $p = 0$ stress–strain-pore pressure relation (9.1) coincides with (6.12H). The porous elastic material is treated as a composite of an elastic solid and a pore fluid. Biot effective stress coefficient vector $\hat{\mathbf{A}}$ is related not only to the drained effective elastic constants of porous matrix material $\hat{\mathbf{S}}^{\mathrm{d}}$ but also to elastic constants of the solid matrix material $\hat{\mathbf{S}}^{\mathrm{m}}$. The solid matrix material elastic constants of the porous material are based on an RVE that is so small that it contains none of the pores (Figure 5.2). Biot effective stress coefficient tensor $\hat{\mathbf{A}}$ is related to the difference between effective drained elastic constants $\hat{\mathbf{S}}^{\mathrm{d}}$ and solid matrix material elastic compliance tensor $\hat{\mathbf{S}}^{\mathrm{m}}$ by the following formula:

$$\hat{\mathbf{A}} = (\hat{\mathbf{I}} - \hat{\mathbf{C}}^{\mathrm{d}} \cdot \hat{\mathbf{S}}^{\mathrm{m}}) \cdot \hat{\mathbf{U}}\,, \tag{9.3}$$

where $\hat{\mathbf{U}} = [1,1,1,0,0,0]^{\mathrm{T}}$ is the six-dimensional vector representation of three-dimensional unit tensor $\mathbf{1}$. A derivation of (9.3) is given at the end of this section. Note that symbol $\hat{\mathbf{U}}$ is distinct from the unit tensor in six dimensions that is denoted by $\hat{\mathbf{I}}$; $\hat{\mathbf{U}}$ is described in further

detail in §A11. The components of $\hat{\mathbf{A}}$ depend upon both the matrix and drained elastic constants. The assumption concerning the symmetry of $\hat{\mathbf{S}}^{\mathrm{m}}$ is interesting and complex. If the symmetry of $\hat{\mathbf{S}}^{\mathrm{m}}$ is less than transversely isotropic and/or its axis of symmetry is not coincident with the transversely isotropic axis of symmetry of $\hat{\mathbf{C}}^{\mathrm{d}}$, then 6D vector $\hat{\mathbf{C}}^{\mathrm{d}} \cdot \hat{\mathbf{S}}^{\mathrm{m}} \cdot \hat{\mathbf{U}}$ in expression (9.3) has, in general, six nonzero components and the solution to problems is more complicated. However, if both $\hat{\mathbf{C}}^{\mathrm{d}}$ and $\hat{\mathbf{S}}^{\mathrm{m}}$ are transversely isotropic with respect to a common axis, then

$$\hat{\mathbf{A}} = [\hat{A}_1, \hat{A}_1, \hat{A}_3, 0, 0, 0]^T \tag{9.4}$$

where

$$\hat{A}_1 = 1 - (\hat{C}^d_{11} + \hat{C}^d_{12})(\hat{S}^m_{11} + \hat{S}^m_{12} + \hat{S}^m_{13}) - \hat{C}^d_{13}(2\hat{S}^m_{13} + \hat{S}^m_{33}),$$

$$\hat{A}_3 = 1 - 2\hat{C}^d_{13}(\hat{S}^m_{11} + \hat{S}^m_{12} + \hat{S}^m_{13}) - \hat{C}^d_{33}(2\hat{S}^m_{13} + \hat{S}^m_{33}).$$

In the case when both $\hat{\mathbf{C}}^{\mathrm{d}}$ and $\hat{\mathbf{S}}^{\mathrm{m}}$ are isotropic, it follows that $\hat{\mathbf{A}}$ is given by $\alpha\hat{\mathbf{U}}$ ($\alpha\mathbf{1}$ in 3D):

$$\hat{\mathbf{A}} = \alpha\hat{\mathbf{U}} \quad \text{where} \quad \alpha = [1 - (K^d/K^m)], \tag{9.5}$$

where $\alpha$ is called the isotropic effective stress coefficient. In most situations there appears to be little disadvantage in assuming that $\hat{\mathbf{S}}^{\mathrm{m}}$ is isotropic. The assumption does not mean that the real matrix material is actually isotropic; it only means that there is little error in assuming that it is isotropic because the principal determinant of the symmetry of the drained elastic constants, $\hat{\mathbf{C}}^{\mathrm{d}}$, is the arrangement of pores; the symmetry of the material surrounding the pores, $\hat{\mathbf{S}}^{\mathrm{m}}$, has only a minor effect. These low consequences of the isotropy assumption for the symmetry of $\hat{\mathbf{S}}^{\mathrm{m}}$ have been discussed by several authors (Shafiro and Kachanov, 1997; Kachanov, 1999; Sevostianov and Kachanov, 2001; Cowin. 2004). *Biot effective stress coefficient tensor* $\hat{\mathbf{A}}$ is so named because it is employed in the definition of effective stress $\hat{\mathbf{T}}^{\mathrm{eff}}$:

$$\hat{\mathbf{T}}^{\mathrm{eff}} = \hat{\mathbf{T}} + \hat{\mathbf{A}}p. \tag{9.6}$$

This definition of effective stress reduces stress–strain-pressure relation (9.1) to the same form as (6.12H), and thus

$$\hat{\mathbf{E}} = \hat{\mathbf{S}}^{\mathrm{d}} \cdot \hat{\mathbf{T}}^{\mathrm{eff}}. \tag{9.7}$$

The advantage of representation (9.7) is that the fluid-saturated porous material may be thought of as an ordinary elastic material, but one subjected to "effective stress" $\hat{\mathbf{T}}^{\mathrm{eff}}$ rather than (ordinary) stress $\hat{\mathbf{T}}$.

Matrix elastic compliance tensor $\hat{\mathbf{S}}^{\mathrm{m}}$ may be evaluated from knowledge of drained elastic compliance tensor $\hat{\mathbf{S}}^{\mathrm{d}}$ using composite or effective medium theory described in Chapter 8. For example, if the matrix material is isotropic and the pores are dilute and spherical in shape, then the drained elastic material is isotropic and the bulk and shear moduli, $K^d$ and $G^d$, are related to the matrix bulk and shear moduli, $K^m$ and $G^m$, and Poisson's ratio $\nu^m$ by

$$K^d = K^m - \frac{\phi K^m}{1 - \dfrac{K^m}{K^m + (\dfrac{4}{3})G^m}}, \quad \frac{G^d}{G^m} = 1 - \frac{15(1-\nu^m)\phi}{7 - 5\nu^m}, \tag{9.8}$$

where $\phi$ is the porosity associated with the spherical pores. A problem at the end of this section derives expressions (9.8) from formulas (8.16). If porosity $\phi$ and drained constants $K^d$ and $G^d$ are known, formulas (9.8) may be used to determine the matrix bulk and shear moduli, $K^m$ and $G^m$, recalling that for an isotropic material Poisson's ratio $\nu^m$ is related to $K^m$ and $G^m$ by $\nu^m = (3K^m - 2G^m)/(6K^m + 2G^m)$ (see Table 7.2). As an example, if $K^d = 11.92$ GPa, $G^d = 4.98$ Gpa, and $\phi = 0.5$, then $K^m = 16.9$ GPa and $G^m = 5.48$ GPa.

The final consideration in this section is derivation of formula (9.3) for *Biot effective stress coefficient tensor* $\hat{\mathbf{A}}$. The material in this paragraph follows derivation of the formula by Carroll (1979). In his proof, which generalized the proof of Nur and Byerlee (1971) from the isotropic case to the anisotropic case, Carroll (1979) begins by noting that the response of the fluid-saturated porous material may be related to that of the drained material by considering the loading:

$$\mathbf{t} = \mathbf{T}\cdot\mathbf{n} \text{ on } O_o, \quad \mathbf{t} = -p\mathbf{n} \text{ on } O_p,$$

where $O_o$ and $O_p$ represent the outer boundary of the porous medium and the pore boundary, respectively. It is convenient to treat this as a superposition of two separate loadings:

$$\mathbf{t} = -p\mathbf{n} \text{ on } O_o, \quad \mathbf{t} = -p\mathbf{n} \text{ on } O_p, \qquad \text{loading (a)}$$

and

$$\mathbf{t} = \mathbf{T}\cdot\mathbf{n} + p\mathbf{n} \text{ on } O_o, \quad \mathbf{t} = 0 \text{ on } O_p. \qquad \text{loading (b)}$$

Loading (a) creates uniform hydrostatic pressure $p$ in the matrix material and, consequently, a uniform strain if the porous material is homogeneous. The strain in the porous material is then the same as that in the matrix material; in effect, uniform straining of the matrix material results in the same straining of the pore space. Nur and Byerlee (1971) illustrate this clearly by pointing out that loading (a) of the solid is achieved by filling the pores with the matrix material. Resulting strain $\hat{\mathbf{E}}^{(a)}$ in the homogeneous matrix material is then uniform, and it is given, in the present case, by

$$\hat{\mathbf{E}}^{(a)} = -p\hat{\mathbf{S}}^{\mathrm{m}}\cdot\hat{\mathbf{U}},$$

where tensor equation $\mathbf{T} = -p\mathbf{1}$ in 3D has been written in 6D as $\hat{\mathbf{T}} = -p\hat{\mathbf{U}}$. Since the pore pressure in loading (b) is zero, the exterior surface loading ($\mathbf{t} = \mathbf{T}\cdot\mathbf{n} + p\mathbf{n}$ on $O_o$) may be considered as being applied to the drained elastic material. Resulting strain $\hat{\mathbf{E}}^{(b)}$ is given by

$$\hat{\mathbf{E}}^{(b)} = \hat{\mathbf{S}}^{\mathrm{d}}\cdot(\hat{\mathbf{T}} + p\hat{\mathbf{U}}),$$

and the total strain due to the loadings (a) plus (b) is

$$\hat{\mathbf{E}} = \hat{\mathbf{E}}^{(a)} + \hat{\mathbf{E}}^{(b)} = \hat{\mathbf{S}}^{\mathrm{d}}\cdot\hat{\mathbf{T}} + p(\hat{\mathbf{S}}^{\mathrm{d}} - \hat{\mathbf{S}}^{\mathrm{m}})\cdot\hat{\mathbf{U}},$$

or, rewriting the last expression, it follows that

$$\hat{\mathbf{E}} = \hat{\mathbf{S}}^{\mathrm{d}}\cdot(\hat{\mathbf{T}} + (\hat{\mathbf{1}} - \hat{\mathbf{C}}^{\mathrm{d}}\hat{\mathbf{S}}^{\mathrm{m}})\cdot\hat{\mathbf{U}}p).$$

Comparing this result with (9.1), it may be seen that *Biot effective stress coefficient tensor* $\hat{\mathbf{A}}$ is given by (9.3). Note that this proof is based on superposition that is a characteristic of linear

systems and thus applies to all the considerations of this chapter, but fails when deformations are no longer infinitesimal.

**Problems**

9.2.1. Show that representation (9.4) for $\hat{\mathbf{A}}$ in the case when both $\hat{\mathbf{C}}^{\mathrm{d}}$ and $\hat{\mathbf{S}}^{\mathrm{m}}$ are transversely isotropic with respect to a common axis reduces to (9.5) when both $\hat{\mathbf{C}}^{\mathrm{d}}$ and $\hat{\mathbf{S}}^{\mathrm{m}}$ are isotropic.

9.2.2. Derive expressions (9.8) for $K^d$ and $G^d$ in terms of volume fraction $\phi$, the matrix bulk and shear moduli, $K^m$ and $G^m$, and Poisson's ratio $\nu^m$ from formulas (8.16).

## 9.3. THE FLUID CONTENT-STRESS-PORE PRESSURE CONSTITUTIVE RELATION

The basic field variables for poroelasticity are total stress $\hat{\mathbf{T}}$, pore pressure $p$, strain in the solid matrix $\hat{\mathbf{E}}$, and variation in (dimensionless) fluid content $\zeta$. The variation in fluid content $\zeta$ is the variation of the fluid mass per unit volume of the porous material due to diffusive fluid mass transport. This set of variables may be viewed as the conjugate pairs of stress measures ($\hat{\mathbf{T}}$, $p$) and strain measures ($\hat{\mathbf{E}}$, $\zeta$) appearing in the following form in an expression for work done on the poroelastic medium:

$$dW = \hat{\mathbf{T}} \cdot \mathrm{d}\hat{\mathbf{E}} + p d\zeta. \tag{9.9}$$

Thus, pressure $p$ is viewed as another component of stress, and variation in fluid content $\zeta$ is viewed as another component of strain; the one conjugate to pressure is the expression for work. It follows that variation in fluid content $\zeta$ is linearly related to both stress $\hat{\mathbf{T}}$ and pore pressure $p$:

$$\zeta = \hat{\mathbf{A}} \cdot \hat{\mathbf{S}}^{\mathrm{d}} \cdot \hat{\mathbf{T}} + C^d_{\mathrm{eff}} p, \quad \text{where} \quad C^d_{\mathrm{eff}} = \frac{1}{K^d_{\mathrm{Reff}}} - \frac{1}{K^m_{\mathrm{Reff}}} + \phi \left( \frac{1}{K^f} - \frac{1}{K^m_{\mathrm{Reff}}} \right) \tag{9.10}$$

or related, using (9.2), to both strain $\hat{\mathbf{E}}$ and pressure $p$, by

$$\zeta = \hat{\mathbf{A}} \cdot \hat{\mathbf{E}} + \Lambda p, \ \Lambda = C^d_{\mathrm{eff}} - \hat{\mathbf{A}} \cdot \hat{\mathbf{S}}^{\mathrm{d}} \cdot \hat{\mathbf{A}} \tag{9.11}$$

and where the various super- and subscripted *K's* are different bulk moduli; for example, $K^f$ is the bulk modulus of the pore fluid. Before introducing formulas for the other two bulk moduli in (9.10), note that isotropic elastic compliance tensor $\hat{\mathbf{S}}$ twice contracted with $\hat{\mathbf{U}}$, the six-dimensional vector representation of three-dimensional unit tensor $\mathbf{1}$, $\hat{\mathbf{U}} \cdot \hat{\mathbf{S}} \cdot \hat{\mathbf{U}}$ (see eq. (A166)), is equal to $3(1 - 2\nu)E^{-1}$, which, in turn, is the reciprocal of the bulk modulus (see Table 7.2):

$$\hat{\mathbf{U}} \cdot \hat{\mathbf{S}} \cdot \hat{\mathbf{U}} = \frac{3(1-2\nu)}{E} \equiv \frac{1}{K}. \tag{9.12}$$

Hill (1952) showed that $K_{\mathrm{Reff}} = (\hat{\mathbf{U}} \cdot \hat{\mathbf{S}} \cdot \hat{\mathbf{U}})^{-1}$, where $\hat{\mathbf{S}}$ is now the anisotropic elastic compliance tensor, is the Reuss lower bound on effective (isotropic) bulk modulus of the anisotropic elastic material $\hat{\mathbf{S}}$, and that the Voigt effective bulk modulus of an anisotropic elastic material, $K_{\mathrm{Veff}} = (\hat{\mathbf{U}} \cdot \hat{\mathbf{S}}^{-1} \cdot \hat{\mathbf{U}})/9$, is the upper bound,

$$(\hat{\mathbf{U}}\cdot\hat{\mathbf{S}}\cdot\hat{\mathbf{U}})^{-1} = K_{\text{Reff}} \le K_{\text{eff}} \le K_{\text{Veff}} = (\hat{\mathbf{U}}\cdot\hat{\mathbf{S}}^{-1}\cdot\hat{\mathbf{U}})/9\,.$$

In the case of isotropy the two bounds coincide with the isotropic bulk modulus, $K$, and thus:

$$\frac{1}{K_{\text{Reff}}} = \frac{1}{K_{\text{R}}} = \frac{1}{K_{\text{eff}}} = \frac{1}{K_{\text{Veff}}} = \frac{1}{K_{\text{V}}} = (\hat{\mathbf{U}}\cdot\hat{\mathbf{S}}\cdot\hat{\mathbf{U}})^{-1} = \frac{\hat{\mathbf{U}}\cdot\hat{\mathbf{S}}^{-1}\cdot\hat{\mathbf{U}}}{9} = \frac{3(1-2\nu)}{E} \equiv \frac{1}{K}$$

where $E$ is the isotropic Young's modulus and $\nu$ is Poisson's ratio, and where subscript eff is no longer applicable because these $K$'s are the actual bulk moduli rather than the effective bulk moduli. The Reuss effective bulk modulus of an anisotropic elastic material, $K_{\text{Reff}}$, occurs naturally in anisotropic poroelastic theory as shown, but not noted, by Thompson and Willis (1991). In analogy with this result (9.12), $\hat{\mathbf{U}}\cdot\hat{\mathbf{S}}\cdot\hat{\mathbf{U}}$ is defined as the inverse of the effective bulk modulus ($1/K$) when the material is not isotropic. Thus, for orthotropic drained elastic compliance tensor $\hat{\mathbf{S}}^{\text{d}}$, and matrix of the orthotropic elastic compliance tensor $\hat{\mathbf{S}}^{\text{m}}$, the following definitions, which were employed in (9.10), are introduced:

$$\frac{1}{K^d_{\text{eff}}} = \hat{\mathbf{U}}\cdot\hat{\mathbf{S}}^{\text{d}}\cdot\hat{\mathbf{U}} = \frac{1}{E^d_1} + \frac{1}{E^d_2} + \frac{1}{E^d_3} - \frac{2\nu^d_{23}}{E^d_2} - \frac{2\nu^d_{31}}{E^d_3} - \frac{2\nu^d_{12}}{E^d_1}\,, \tag{9.13}$$

$$\frac{1}{K^m_{\text{eff}}} = \hat{\mathbf{U}}\cdot\hat{\mathbf{S}}^{\text{m}}\cdot\hat{\mathbf{U}} = \frac{1}{E^m_1} + \frac{1}{E^m_2} + \frac{1}{E^m_3} - \frac{2\nu^m_{23}}{E^m_2} - \frac{2\nu^m_{31}}{E^m_3} - \frac{2\nu^m_{12}}{E^m_1}\,. \tag{9.14}$$

Using these notations, the formula for $\Lambda$, (9.11), may be recast in terms of the effective bulk moduli. Using (9.3) note that

$$\hat{\mathbf{A}}\cdot\hat{\mathbf{S}}^{\text{d}}\cdot\hat{\mathbf{A}} = \frac{1}{K^d_{\text{Reff}}} - \frac{1}{K^m_{\text{Reff}}} + \hat{\mathbf{U}}\cdot\hat{\mathbf{S}}^{\text{m}}\cdot\hat{\mathbf{C}}^{\text{d}}\cdot\hat{\mathbf{S}}^{\text{m}}\cdot\hat{\mathbf{U}}\,, \tag{9.15}$$

where (9.12) and (9.13) have been employed. Substituting this result into (9.11) and employing (9.10) to remove $C^d_{\text{eff}}$, it follows that

$$\Lambda = \phi\left(\frac{1}{K^f} - \frac{1}{K^m_{\text{Reff}}}\right) - \hat{\mathbf{U}}\cdot\hat{\mathbf{S}}^{\text{m}}\cdot\hat{\mathbf{C}}^{\text{d}}\cdot\hat{\mathbf{S}}^{\text{m}}\cdot\hat{\mathbf{U}}\,. \tag{9.16}$$

**Problems**

9.3.1. Prove that $\hat{\mathbf{U}}\cdot\hat{\mathbf{T}} = tr\mathbf{T}$.

9.3.2. Show that isotropic elastic compliance tensor $\hat{\mathbf{S}}$, twice contracted with $\hat{\mathbf{U}}$, the six-dimensional vector representation of three-dimensional unit tensor $\mathbf{1}$, $\hat{\mathbf{U}}\cdot\hat{\mathbf{S}}\cdot\hat{\mathbf{U}}$, is given by (9.12).

9.3.3. Show that, in the case of isotropy, $\hat{\mathbf{A}}$ is given by $\alpha\hat{\mathbf{U}}$, where $\alpha$ is the isotropic effective stress coefficient given by $\alpha = [1 - (K^d/K^m)]$.

9.3.4. In the case of isotropy show that $\hat{\mathbf{U}}\cdot\hat{\mathbf{S}}^{\text{m}}\cdot\hat{\mathbf{C}}^{\text{d}}\cdot\hat{\mathbf{S}}^{\text{m}}\cdot\hat{\mathbf{U}}$ is equal to $K^d_{\text{Reff}}/(K^m_{\text{Reff}})^2$, and thus $\hat{\mathbf{A}}\cdot\hat{\mathbf{S}}^{\text{d}}\cdot\hat{\mathbf{A}}$ is given by

$$\hat{\mathbf{A}}\cdot\hat{\mathbf{S}}^{\text{d}}\cdot\hat{\mathbf{A}} = \frac{1}{K^d} - \frac{\alpha}{K^m} \quad \text{and} \quad \Lambda = \phi\left(\frac{1}{K^f} - \frac{1}{K^m}\right) - \frac{K^d}{(K^m)^2}\,.$$

## 9.4. DARCY'S LAW

The constitutive equations of poroelasticity developed thus far are strain–stress-pore pressure relations (9.1) and fluid content-stress-pore pressure relation (9.10). The other constitutive relation of poroelasticity is Darcy's law, which relates the fluid mass flow rate, $\rho_f \mathbf{v}$, to the gradient ($\nabla p$) of pore pressure $p$:

$$\rho_f \mathbf{v} = -\mathbf{H}(p)\nabla p(\mathbf{x}, t), \quad \mathbf{H}(p) = \mathbf{H}^T(p), \qquad \text{(6.36D) repeated}$$

where the symmetry in $\mathbf{H}$ has been shown to hold for material symmetries greater than monoclinic. It will be assumed that $\mathbf{H}$ is independent of pore fluid pressure and that $\mathbf{H} = \rho_{f0}\mathbf{K}/\phi\mu$, where $\mathbf{K}$ is the intrinsic Darcy's law permeability tensor, $\rho_{f0}$ is a reference value of the fluid density, and $\mu$ is the fluid viscosity. Intrinsic permeability tensor $\mathbf{K}$ has units of length squared and is a function of the porous structure only, not the fluid in the pores; thus, Darcy's law takes the form

$$\mathbf{q} = (\phi\rho_f/\rho_{fo})\mathbf{v} = -(1/\mu)\mathbf{K}\nabla p(\mathbf{x}, t), \quad \mathbf{K} = \mathbf{K}^T, \tag{9.17}$$

where it has been shown that the symmetry in $\mathbf{K}$ holds for material symmetries greater than monoclinic and where volume flux $\mathbf{q}$ has the dimension of velocity because it is the volume flow rate per unit area. In the case of isotropy Darcy's law is written in the form

$$\mathbf{q} = (\phi\rho_f/\rho_{f0})\mathbf{v} = -(k/\mu)\,\nabla p(\mathbf{x}, t). \tag{9.18}$$

Recall from §2.8 the lumped parameter model for Darcy's law and consider that idea again in the present context. Also, recall from §8.5 that it was shown how the Darcy permeability law could be obtained from a model for the flow of a viscous fluid through a rigid porous solid. These ideas, plus the example of the compressed, fluid saturated sponge described in §9.1, convey the physical meaning of Darcy's law in three different models.

## 9.5. MATRIX MATERIAL AND PORE FLUID INCOMPRESSIBILITY CONSTRAINTS

The two incompressibility constituent specific constraints for poroelasticity are that matrix material and the pore fluid be incompressible. These two incompressibility constraints are kinematic in nature, requiring that both materials experience no volume change at any stress level. Constraints of this type introduce an indeterminate pressure in both the fluid and the matrix material that must be equal in both materials at any location from the requirement of local force equilibrium. Thus the two assumptions are compatible.

The requirement that the fluid be incompressible is implemented by requiring that the reciprocal of the bulk modulus of the fluid tends to zero as the instantaneous density tends to the initial density,

$$\lim_{\rho_f \to \rho_{f_o}} \frac{1}{K^f} \to 0\,, \tag{9.19}$$

or by imposing the condition that fluid density $\rho_f$ be a constant; thus, $\rho_f$ and its initial value, $\rho_{f0}$, are equal. When $\rho_f = \rho_{f0}$, Darcy's law (9.17) may be written in the form

$$\mathbf{q} = \phi\mathbf{v} = -(1/\mu)\mathbf{K}\nabla p(\mathbf{x}, t), \quad \mathbf{K} = \mathbf{K}^T. \tag{9.20}$$

The requirement that the matrix material be incompressible involves a slightly longer development. Hooke's law for the matrix material is written in the form

$$\hat{\mathbf{E}}^{\mathrm{m}} = \hat{\mathbf{S}}^{\mathrm{m}}\hat{\mathbf{T}}^{\mathrm{m}}, \tag{9.21}$$

and the incompressibility constraint for the matrix material is the requirement that the dilatational strain,

$$\hat{\mathbf{U}}\cdot\hat{\mathbf{E}}^{\mathrm{m}} = tr\mathbf{E}^{\mathrm{m}} = E^{m}_{kk} = \hat{\mathbf{U}}\cdot\hat{\mathbf{S}}^{\mathrm{m}}\cdot\hat{\mathbf{T}}^{\mathrm{m}} = \hat{\mathbf{T}}^{\mathrm{m}}\cdot\hat{\mathbf{S}}^{\mathrm{m}}\cdot\hat{\mathbf{U}}, \tag{9.22}$$

vanish for all possible stress states $\hat{\mathbf{T}}^{\mathrm{m}}$; thus,

$$\hat{\mathbf{U}}\cdot\hat{\mathbf{E}}^{\mathrm{m}} = 0 \Rightarrow \hat{\mathbf{U}}\cdot\hat{\mathbf{S}}^{\mathrm{m}} = \hat{\mathbf{S}}^{\mathrm{m}}\cdot\hat{\mathbf{U}} = 0. \tag{9.23}$$

The components of vector $\hat{\mathbf{U}}\cdot\hat{\mathbf{S}}^{\mathrm{m}} = \hat{\mathbf{S}}^{\mathrm{m}}\cdot\hat{\mathbf{U}}$ are given by

$$\hat{\mathbf{U}}\cdot\hat{\mathbf{S}}^{\mathrm{m}} = \frac{1}{3}\left[\frac{1}{K^{m}_{1}},\frac{1}{K^{m}_{2}},\frac{1}{K^{m}_{3}},\frac{1}{K^{m}_{4}},\frac{1}{K^{m}_{5}},\frac{1}{K^{m}_{6}}\right], \tag{9.24a}$$

where

$$\frac{1}{K^{m}_{\alpha}} = S^{m}_{\alpha 1} + S^{m}_{\alpha 2} + S^{m}_{\alpha 3}\ (\alpha = 1,..,6), \tag{9.24b}$$

in the case of no (triclinic) symmetry, and by

$$\hat{\mathbf{U}}\cdot\hat{\mathbf{S}}^{\mathrm{m}} = \frac{1}{3}\left[\frac{1}{K^{m}_{1}},\frac{1}{K^{m}_{2}},\frac{1}{K^{m}_{3}},0,0,0\right],\quad \frac{1}{3K^{m}_{1}} = \frac{1-\nu^{m}_{12}-\nu^{m}_{13}}{E^{m}_{1}},$$

$$\frac{1}{3K^{m}_{2}} = \frac{1-\nu^{m}_{21}-\nu^{m}_{23}}{E^{m}_{2}},\quad \frac{1}{3K^{m}_{3}} = \frac{1-\nu^{m}_{13}-\nu^{m}_{32}}{E^{m}_{3}},$$

$$\hat{\mathbf{U}}\cdot\hat{\mathbf{S}}^{\mathrm{m}} = \frac{1}{3}\left[\frac{1}{K^{m}_{1}},\frac{1}{K^{m}_{1}},\frac{1}{K^{m}_{3}},0,0,0\right],\quad \frac{1}{3K^{m}_{3}} = \frac{1-2\nu^{m}_{31}}{E^{m}_{3}}$$

$$\frac{1}{3K^{m}_{1}} = \frac{1}{3K^{m}_{2}} = \frac{1-\nu^{m}_{12}-\nu^{m}_{13}}{E^{m}_{1}} = \frac{1-\nu^{m}_{21}-\nu^{m}_{23}}{E^{m}_{2}},$$

$$\hat{\mathbf{U}}\cdot\hat{\mathbf{S}}^{\mathrm{m}} = \frac{1}{3K^{m}}[1,1,1,0,0,0],\ \frac{1}{3K^{m}} = \frac{1-2\nu^{m}}{E^{m}} \tag{9.25}$$

in the cases of orthotropic, transversely isotropic, and isotropic symmetries, respectively. As may be seen from (9.24), the incompressibility condition, $\hat{\mathbf{U}}\cdot\hat{\mathbf{S}}^{\mathrm{m}} = \hat{\mathbf{S}}^{\mathrm{m}}\cdot\hat{\mathbf{U}} = 0$, requires that $\hat{\mathbf{S}}^{\mathrm{m}}$ be singular, $\mathrm{Det}\,\hat{\mathbf{S}}^{\mathrm{m}} = 0$. From (9.23) and (9.25), incompressibility condition $\hat{\mathbf{U}}\cdot\hat{\mathbf{S}}^{\mathrm{m}} = \hat{\mathbf{S}}^{\mathrm{m}}\cdot\hat{\mathbf{U}} = 0$ is expressed in terms of Poisson's ratios for the orthotropic, transversely isotropic, and isotropic symmetries by

$$\nu_{12}^m = \frac{1}{2}\left(1+\frac{E_1^m}{E_2^m}-\frac{E_1^m}{E_3^m}\right),\ \nu_{13}^m = \frac{1}{2}\left(1+\frac{E_1^m}{E_3^m}-\frac{E_1^m}{E_2^m}\right),\ \nu_{23}^m = \frac{1}{2}\left(1+\frac{E_2^m}{E_3^m}-\frac{E_2^m}{E_1^m}\right), \tag{9.26}$$

$$\nu_{12}^m = 1-\frac{E_1^m}{2E_3^m},\ \ \nu_{13}^m = \frac{E_1^m}{2E_3^m},\ \ \nu_{31}^m = \frac{1}{2}, \tag{9.27}$$

and $\nu^m = 1/2$, respectively.

Only two of three sets of poroelastic constitutive equations described in the previous section are influenced by these two incompressibility constraints. Darcy's law is unchanged because in both cases it is based on an assumption that the movement of the boundaries of the pores is a higher-order term that is negligible, and thus the law has the same form in the compressible and incompressible cases as it would have in a rigid porous material. The stress–strain-pore pressure and the fluid content-stress-pore pressure are modified in the case of incompressibility from their forms in the compressible case. Stress–strain-pore pressure relation (9.1) for the incompressible case is given by

$$\hat{\mathbf{E}} = \hat{\mathbf{S}}^{\mathrm{d}} \cdot (\hat{\mathbf{T}} + \hat{\mathbf{U}}p) \tag{9.28}$$

for $\hat{\mathbf{U}} \cdot \hat{\mathbf{S}}^{\mathrm{m}} = 0$ since Biot effective stress coefficient tensor $\hat{\mathbf{A}}$ given by (9.3) takes the form

$$\hat{\mathbf{A}} = \hat{\mathbf{U}}, \tag{9.29}$$

for $\hat{\mathbf{U}} \cdot \hat{\mathbf{S}}^{\mathrm{m}} = 0$. The definition of effective stress $\hat{\mathbf{T}}^{\mathrm{eff}}$,

$$\hat{\mathbf{T}}^{\mathrm{eff}} = \hat{\mathbf{T}} + \hat{\mathbf{U}}p, \tag{9.30}$$

changes for the incompressible case, and Hooke's law (9.7) holds in the incompressible case with this revised definition of $\hat{\mathbf{T}}^{\mathrm{eff}}$.

Since the reciprocals of $K_{\mathrm{Reff}}^m$ and $K^f$ vanish in the case of incompressibility, fluid content-stress-pore pressure relation (9.10) is modified in the case of incompressibility to the form

$$\zeta = \hat{\mathbf{U}} \cdot \hat{\mathbf{S}}^{\mathrm{d}} \cdot \hat{\mathbf{T}} + \frac{p}{K_{\mathrm{Reff}}^d} \text{ where } C_{\mathrm{eff}}^d = \frac{1}{K_{\mathrm{Reff}}^d} = \hat{\mathbf{U}} \cdot \hat{\mathbf{S}}^{\mathrm{d}} \cdot \hat{\mathbf{U}}; \tag{9.31}$$

and thus, from (9.11), (9.29), and (9.31), and the vanishing of the reciprocals of the bulk moduli of the fluid and the matrix material it follows that

$$\zeta = \hat{\mathbf{U}} \cdot \hat{\mathbf{E}} \text{ and } \Lambda = 0. \tag{9.32}$$

Specialization of (9.14) to the case of incompressibility recovers the obvious consequence of the assumption of material matrix incompressibility:

$$\frac{1}{K_{\mathrm{Reff}}^m} = \hat{\mathbf{U}}^T \cdot \hat{\mathbf{S}}^{\mathrm{m}} \cdot \hat{\mathbf{U}} = 0, \tag{9.33}$$

for $\hat{\mathbf{U}} \cdot \hat{\mathbf{S}}^{\mathrm{m}} = 0$. The pore pressure is given by (9.11) as

$$p = \frac{1}{\Lambda}[\zeta - (\hat{\mathbf{A}} \cdot \hat{\mathbf{E}})], \tag{9.34}$$

and one can observe from the preceding that, for incompressibility,

$$\Lambda -> 0 \text{ and } [\zeta - (\hat{\mathbf{A}} \cdot \hat{\mathbf{E}})] -> 0\,, \tag{9.35}$$

and it follows that pressure $p$ given by (9.34) becomes indeterminate in formula (9.34) as the porous medium constituents become incompressible. A Lagrange multiplier (see Example 7.4.1) is then introduced, so that (9.30) above now applies. The convention that there are two very different meanings associated with the symbol for pore pressure $p$ is maintained here. In the compressible case $p$ is a thermodynamic variable determined by an equation of state that includes the temperature and the specific volume of the fluid as variables, but in the incompressible case $p$ is a Lagrange multiplier whose value is determined by the boundary conditions independent of the temperature and the specific volume of the fluid.

**Problems**

9.5.1. Show that (9.10) reduces to $\zeta = \hat{\mathbf{A}} \cdot \hat{\mathbf{S}}^{\mathrm{d}} \cdot \hat{\mathbf{T}} + \left(\alpha p / K^{d}_{\mathrm{Reff}}\right)$, where $C^{d}_{\mathrm{eff}} = \alpha / K^{d}_{\mathrm{Reff}}$ when the bulk moduli of the matrix material and the fluid are equal.

9.5.2. Show that (9.10) reduces to (9.31) when the matrix material and the fluid are assumed to be incompressible.

## 9.6. THE UNDRAINED ELASTIC COEFFICIENTS

If no fluid movement in the poroelastic medium is possible, then the variation in fluid content, $\zeta$, that is to say, the variation of the fluid volume per unit volume of the porous material due to diffusive fluid mass transport, is zero. In this situation (9.10) may be solved for $p$; thus, the pore pressure is related to solid stress $\hat{\mathbf{T}}$ by $p = -\hat{\mathbf{B}} \cdot \hat{\mathbf{T}}$, where

$$\hat{\mathbf{B}} = \frac{1}{C^{d}_{\mathrm{eff}}} \hat{\mathbf{S}}^{\mathrm{d}} \cdot \hat{\mathbf{A}} = \frac{1}{C^{d}_{\mathrm{eff}}} (\hat{\mathbf{S}}^{\mathrm{d}} - \hat{\mathbf{S}}^{\mathrm{m}}) \cdot \hat{\mathbf{U}}\,. \tag{9.36}$$

Skempton (1954) first introduced the components of tensor $\hat{\mathbf{B}}$, and thus it is reasonable to call tensor $\hat{\mathbf{B}}$ the Skempton compliance difference tensor. In the case of incompressibility, it follows from (9.36), (9.31), and (9.23) that the Skempton compliance difference tensor in the incompressible case is given by

$$\hat{\mathbf{B}} = K^{d}_{\mathrm{Reff}} \hat{\mathbf{S}}^{\mathrm{d}} \cdot \hat{\mathbf{U}}\,, \tag{9.37}$$

from which it follows, with use of (9.13), that

$$\hat{\mathbf{U}} \cdot \hat{\mathbf{B}} = K^{d}_{\mathrm{Reff}} \hat{\mathbf{U}} \cdot \hat{\mathbf{S}}^{\mathrm{d}} \cdot \hat{\mathbf{U}} = 1 \tag{9.38}$$

in the incompressible case. In the case of the isotropic compressible case, the Skempton compliance difference tensor has the form

$$\hat{\mathbf{B}} = \frac{S}{3}\hat{\mathbf{U}}\,, \text{ or } \hat{B}_1 = \hat{B}_2 = \hat{B}_3 = \frac{S}{3},\ \hat{B}_4 = \hat{B}_5 = \hat{B}_6 = 0\,, \tag{9.39}$$

where $S$ is the Skempton parameter:

$$S = \frac{\alpha}{C^d K^d}\,. \tag{9.40}$$

Subscript eff is removed from $C^d_{\text{eff}}$ as well as all the $K$'s in eq. (9.10) because these $K$'s are the actual bulk moduli for the isotropic material rather than the effective isotropic bulk moduli of an anisotropic material. It follows from $p = -\hat{\mathbf{B}}\cdot\hat{\mathbf{T}}$ that, in case of an isotropic and compressible medium, $p = -(S/3)\hat{\mathbf{U}}\cdot\hat{\mathbf{T}} = -(S/3)tr\mathbf{T}$. Note that if $K^f = K^m$, then $C^d = \alpha / K^d$ and $S = 1$ whether or not these constituents are incompressible. In the isotropic compressible case, (9.36) may be used to show that $\hat{\mathbf{A}} = SK^dC^d\hat{\mathbf{U}}$. In the isotropic incompressible case Skempton parameter $S$ is equal to 1, and thus $p = -(1/3)\hat{\mathbf{U}}\cdot\hat{\mathbf{T}} = -(1/3)tr\mathbf{T}$. It also follows in the isotropic incompressible case that $K^d = 1/C^d$ and $\hat{\mathbf{A}} = \hat{\mathbf{U}}$, as shown by (9.29).

In the case of compressibility, undrained elastic coefficients $\hat{\mathbf{S}}^{\text{u}}$ are related to drained elastic constants $\hat{\mathbf{S}}^{\text{d}}$ and tensor $\hat{\mathbf{A}}$ by

$$\hat{\mathbf{S}}^{\text{u}} = \hat{\mathbf{S}}^{\text{d}} - \hat{\mathbf{S}}^{\text{d}}\cdot\hat{\mathbf{A}}\otimes\hat{\mathbf{B}} = \hat{\mathbf{S}}^{\text{d}} - \frac{1}{C^d_{\text{eff}}}(\hat{\mathbf{S}}^{\text{d}}\cdot\hat{\mathbf{A}}\otimes\hat{\mathbf{S}}^{\text{d}}\cdot\hat{\mathbf{A}})\,. \tag{9.41}$$

In the case of incompressibility, undrained elastic coefficients $\hat{\mathbf{S}}^{\text{u}}$ are related to drained elastic constants $\hat{\mathbf{S}}^{\text{d}}$ by

$$\hat{\mathbf{S}}^{\text{u}} = \hat{\mathbf{S}}^{\text{d}} - K^d_{\text{Reff}}(\hat{\mathbf{S}}^{\text{d}}\cdot\hat{\mathbf{U}}\otimes\hat{\mathbf{S}}^{\text{d}}\cdot\hat{\mathbf{U}})\,, \tag{9.42}$$

a result that follows from (9.40) with application of (9.31) and (9.32). When (9.42) is dotted with $\hat{\mathbf{U}}$ and (9.32) again employed, it follows that the undrained elastic coefficients are also incompressible in the case of assumed incompressibility of the matrix material and the fluid, as one would anticipate:

$$\hat{\mathbf{U}}\cdot\hat{\mathbf{S}}^{\text{u}} = \hat{\mathbf{U}}\cdot\hat{\mathbf{S}}^{\text{d}} - K^d_{\text{Reff}}(\hat{\mathbf{U}}\cdot\hat{\mathbf{S}}^{\text{d}}\cdot\hat{\mathbf{U}}\otimes\hat{\mathbf{S}}^{\text{d}}\cdot\hat{\mathbf{U}}) = \hat{\mathbf{U}}\cdot\hat{\mathbf{S}}^{\text{d}} - \hat{\mathbf{S}}^{\text{d}}\cdot\hat{\mathbf{U}} = 0\,. \tag{9.43}$$

In the isotropic compressible case, (9.40) reduces to formulas for undrained bulk modulus $K^u$ ($K^u = (\hat{\mathbf{U}}^T\cdot\hat{\mathbf{S}}^{\text{u}}\cdot\hat{\mathbf{U}})^{-1}$) and undrained Poisson's ratio $\nu^{\text{u}}$ in terms of $\nu^d$, $K^d$, $K^f$, $K^m$, and $\phi$, and thus

$$K^u = K^d + \frac{K^f(1-\frac{K^d}{K^m})^2}{\frac{K^f}{K^m}(1-\frac{K^d}{K^m}-\phi)+\phi} \text{ and } \nu^u = \frac{3\nu^d + S(1-2\nu^d)(1-\frac{K^d}{K^m})}{3 - S(1-2\nu^d)(1-\frac{K^d}{K^m})}\,. \tag{9.44}$$

In the isotropic incompressible case, (9.44) reduces to $1/K^u = 0$ and $\nu^u = 1/2$, consistent with the general result for incompressibility for the undrained constant set. It follows that $E^u = 3G$.

**Problems**

9.6.1. Expand the second equality in (9.41) as a six-by-six matrix equation.

9.6.2. Expand the second equality in (9.41) as a six-by-six matrix equation for the special case of transversely isotropic symmetry using the technical elastic constants, i.e., Young's moduli and Poisson's ratios.

9.6.3. Show that (9.44) are a consequence of the two equations (8.16). Do this by working backward; start with (9.44) and substitute $K^d$ and $G^d$ from (9.8), $\alpha = [1 - (K^d/K^m)]$ and employ the relations between the elastic isotropic constants listed in Table 7.2. The mechanics of solving this problem is straightforward algebraic substitution. However, it can become a task if one is not careful to keep the algebraic objective in view. Try using a symbolic algebra program.

## 9.7. EXPRESSIONS OF MASS AND MOMENTUM CONSERVATION

The conservation of mass is expressed by the equation of continuity,

$$\frac{\partial \rho}{\partial t} + \nabla \cdot (\rho \mathbf{v}) = 0 \,. \qquad \text{(4.6) repeated}$$

The form of mass conservation equation (4.6) is altered to apply to the pore fluid volume by first replacing $\rho$ by $\phi\rho_f$ in (4.6) and then dividing the equation through by $\rho_{fo}$; thus,

$$\frac{1}{\rho_{fo}} \frac{\partial \phi \rho_f}{\partial t} + \frac{1}{\rho_{fo}} \nabla \cdot (\phi \rho_f \mathbf{v}) = 0 \,. \qquad (9.45)$$

The form of (9.45) is changed by use of (9.17) and setting

$$\frac{\partial \zeta}{\partial t} = \frac{1}{\rho_{fo}} \frac{\partial \phi \rho_f}{\partial t} \,;$$

thus,

$$\partial \zeta / \partial t + \nabla \cdot \mathbf{q} = 0. \qquad (9.46)$$

In the case of incompressibility, $\rho_f = \rho_{f0}$, and (9.45) becomes

$$\frac{\partial \phi}{\partial t} + \nabla \cdot (\phi \mathbf{v}) = 0 \,. \qquad (9.47)$$

The stress equations of motion in three dimensions,

$$\rho \ddot{\mathbf{u}} = \nabla \cdot \mathbf{T} + \rho \mathbf{d} \,, \quad \mathbf{T} = \mathbf{T}^T \,, \qquad \text{(4.37) repeated}$$

have no simple representation in 6D vector notation, and the conventional notation is employed; $\ddot{\mathbf{u}}$ represents acceleration and $\mathbf{d}$ the action-at-a-distance force.

**Problem**

9.7.1. Evaluate each of the following formulas in the limit as $\phi \to 0$ (note that $\phi \to 0$ implies $\phi_0 \to 0$): (a) (9.8), (b) (9.10), (c) (9.13), (d) (9.17), (e) (9.40), (f) (9.41), (g) (9.44), (h) (9.45).

## 9.8. THE BASIC EQUATIONS OF POROELASTICITY

An overview of the theory of poroelastic materials can be obtained by considering it as a system of eighteen equations in eighteen scalar unknowns. This system of equations and unknowns, a combination of conservation principles and constitutive equations, is described in this section. The eighteen scalar unknowns are the six components of stress tensor **T**, fluid pressure p, fluid density $\rho_f$, variation in fluid content $\zeta$, the six components of strain tensor **E,** and the three components of displacement vector **u**. The eighteen scalar equations of the theory of poroelastic solids are the six equations of strain–stress-pressure relation (9.1), six strain displacement relations (3.49), $2\mathbf{E} = ((\nabla\otimes\mathbf{u})^{\mathrm{T}} + \nabla\otimes\mathbf{u})$, three equations of motion (4.37), one fluid content-stress-pressure relation (9.10) (or one fluid content-strain-pressure relation (9.11)) and one mass conservation equation (9.46), and a relation between the fluid pressure and the density, $p = p(\rho_f)$, that is not specified here. The parameters of a poroelasticity problem are drained effective elastic constants of porous matrix material $\hat{\mathbf{S}}$, Biot effective stress coefficients $\hat{\mathbf{A}}$, $C^d_{\mathrm{eff}}$, fluid viscosity $\mu$, intrinsic permeability tensor **K**, and action-at-a-distance force **d**, which are all assumed to be known. If displacement vector **u** is taken as the independent variable, no further equations are necessary. However, if it is not, use of compatibility equations (3.56) are necessary to ensure that the displacements are consistent.

There are many methods of approach to solution of poroelastic problems for compressible media. The method selected depends upon the information provided and the fields to be calculated. One approach that has been effective is to solve for variation in fluid content $\zeta$ if the stress or strain field is known or may be calculated without reference to $\zeta$. The diffusion equation for the variation in volume fraction is obtained by first substituting Darcy's law (9.17) into expression (9.46) for conservation of mass and subsequently eliminating the pore pressure by use of (9.34); thus,

$$\frac{\partial\zeta}{\partial t} - \frac{1}{\mu\Lambda}\hat{\mathbf{K}}\cdot\hat{\mathbf{O}}\zeta = -\frac{1}{\mu\Lambda}\hat{\mathbf{K}}\cdot\hat{\mathbf{O}}[\hat{\mathbf{A}}\cdot\hat{\mathbf{E}}]. \tag{9.48}$$

This shows that time rate of change of fluid content $\zeta$ is due either to fluid flux or to volume changes caused by the strain field. It is possible to replace the strain on the right-hand side of (9.48) by stress, in which case (9.48) becomes

$$\frac{\partial\zeta}{\partial t} - \frac{1}{\mu C^d_{\mathrm{eff}}}\hat{\mathbf{K}}\cdot\hat{\mathbf{O}}\zeta = -\frac{1}{\mu C^d_{\mathrm{eff}}}\hat{\mathbf{K}}\cdot\hat{\mathbf{O}}[\hat{\mathbf{A}}\cdot\hat{\mathbf{S}}^{\mathrm{d}}\cdot\hat{\mathbf{T}}]. \tag{9.49}$$

Diffusion equations for the pressure field are also employed in the solution of poroelastic problems. The first diffusion equation for the pore pressure field is obtained by substituting Darcy's law (9.17) into expression (9.46) for the conservation of mass and subsequently eliminating variation in fluid content $\zeta$ by use of (9.10), and thus

$$\frac{\partial p}{\partial t} - \frac{1}{\mu\Lambda}\hat{\mathbf{K}}\cdot\hat{\mathbf{O}}p = -\frac{1}{\Lambda}\hat{\mathbf{A}}\cdot\frac{\partial\hat{\mathbf{E}}}{\partial t}. \tag{9.50}$$

The alternative diffusion equation for the pore pressure field is obtained by replacing the strain on the right hand side of (9.50) by stress:

$$\frac{\partial p}{\partial t} - \frac{1}{\mu C^d_{\text{eff}}} \hat{\mathbf{K}} \cdot \hat{\mathbf{O}} p = \frac{1}{C^d_{\text{eff}}} (\hat{\mathbf{U}} \cdot (\hat{\mathbf{S}}^{\text{m}} - \hat{\mathbf{S}}^{\text{d}}) \cdot \frac{\partial \hat{\mathbf{T}}}{\partial t}) . \tag{9.51}$$

For an orthotropic material, eq. (9.51) may be written in the following form:

$$\begin{aligned} C_{\text{eff}} \frac{\partial p}{\partial t} - \frac{1}{\mu} K_{11} \frac{\partial^2 p}{\partial x_1^2} - \frac{1}{\mu} K_{22} \frac{\partial^2 p}{\partial x_2^2} - \frac{1}{\mu} K_{33} \frac{\partial^2 p}{\partial x_3^2} = \\ - \left\{ \left( \frac{1}{E_1^d} - \frac{\nu_{12}^d}{E_1^d} - \frac{\nu_{31}^d}{E_3^d} - \frac{1}{E_1^m} + \frac{\nu_{12}^m}{E_1^m} + \frac{\nu_{31}^m}{E_3^m} \right) \frac{\partial T_{11}}{\partial t} + \right. \\ \left( \frac{1}{E_2^d} - \frac{\nu_{12}^d}{E_1^d} - \frac{\nu_{23}^d}{E_2^d} - \frac{1}{E_2^m} + \frac{\nu_{12}^m}{E_1^m} + \frac{\nu_{23}^m}{E_2^m} \right) \frac{\partial T_{22}}{\partial t} + \\ \left. \left( \frac{1}{E_3^d} - \frac{\nu_{23}^d}{E_2^d} - \frac{\nu_{31}^d}{E_3^d} - \frac{1}{E_3^m} + \frac{\nu_{23}^m}{E_2^m} + \frac{\nu_{31}^m}{E_3^m} \right) \frac{\partial T_{33}}{\partial t} \right\} . \end{aligned} \tag{9.52}$$

The boundary conditions on the pore pressure field customarily employed in the solution of this differential equation are (i) that external pore pressure $p$ is specified at the boundary (a lower pressure permits flow across the boundary), (ii) that pressure gradient $\nabla p$ at the boundary is specified (a zero pressure gradient permits no flow across the boundary), and (iii) that some linear combination of (i) and (ii) is specified.

**Problem**

9.8.1. Verify that (9.52) follows from (9.51) once the assumption of orthotropy is made. Record the form of (9.52) for transversely isotropic symmetry.

## 9.9. THE BASIC EQUATIONS OF INCOMPRESSIBLE POROELASTICITY

In this section the development of compressible poroelasticity as a system of eighteen equations in eighteen scalar unknowns presented in the previous section is specialized to the case of incompressibility. The result is a system of seventeen equations in seventeen scalar unknowns because fluid density $\rho_{\text{f}}$ is a constant, $\rho_f = \rho_{\text{f0}}$, and no longer an unknown, and an equation relating the fluid pressure to the fluid density, $p = p(\rho_{\text{f}})$, does not exist. The other seventeen equations in seventeen scalar unknowns are the same except for the constraint of matrix material incompressibility. It is important to note that only algebraic coefficients of terms are changed by the transition to incompressible components; the order of the differential equations is unchanged. Diffusion equation (9.51) makes an easy transition to the incompressible case. Recognizing (9.20) and (9.27), (9.51) reduces to

$$\frac{\partial p}{\partial t} - \frac{K^d_{\text{Reff}}}{\mu} \hat{\mathbf{K}} \cdot \hat{\mathbf{O}} p = -K^d_{\text{Reff}} (\hat{\mathbf{U}} \cdot \hat{\mathbf{S}}^{\text{d}} \cdot \frac{\partial \hat{\mathbf{T}}}{\partial t}) , \tag{9.53}$$

and for an orthotropic material equation (9.53) may be written in the following form:

$$\frac{1}{K^d_{\text{Reff}}}\frac{\partial p}{\partial t}-\frac{1}{\mu}K_{11}\frac{\partial^2 p}{\partial x_1^2}-\frac{1}{\mu}K_{22}\frac{\partial^2 p}{\partial x_2^2}-\frac{1}{\mu}K_{33}\frac{\partial^2 p}{\partial x_3^2}=-\left\{\left(\frac{1}{E_1^d}-\frac{\nu_{12}^d}{E_1^d}-\frac{\nu_{13}^d}{E_3^d}\right)\frac{\partial T_{11}}{\partial t}+\right.$$

$$\left.\left(\frac{1}{E_2^d}-\frac{\nu_{12}^d}{E_1^d}-\frac{\nu_{23}^d}{E_2^d}\right)\frac{\partial T_{22}}{\partial t}+\left(\frac{1}{E_3^d}-\frac{\nu_{23}^d}{E_2^d}-\frac{\nu_{31}^d}{E_3^d}\right)\frac{\partial T_{33}}{\partial t}\right\}. \tag{9.54}$$

The boundary conditions on the pore pressure field are coincident with those described at the end of the previous section.

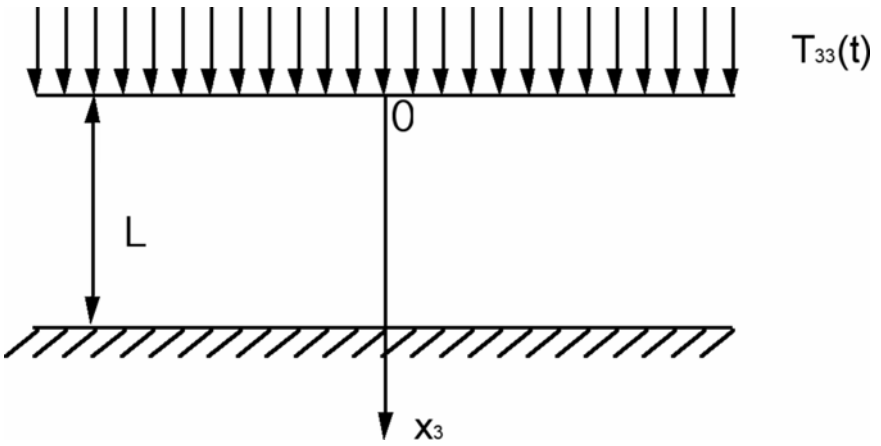



**Figure 9.1**. Illustration of a layer of poroelastic material resting on a stiff impermeable base subjected to a uniform time-varying surface loading.

## 9.10. SOME EXAMPLE ISOTROPIC POROELASTIC PROBLEMS

**Example 9.10.1**

Formulate the differential equations governing the problem of determining the vertical surface settlement of a layer of poroelastic material resting on a stiff impermeable base subjected to a constant surface loading. The layer, illustrated in Figure 9.1, is in the $x_1$, $x_2$ plane, and the $x_3$ positive coordinate is in the thickness direction, and it is pointed downward in Figure 9.1. The surface is subjected to an applied compressive stress, $T_{33} = -P(t)$, the only nonzero strain component is $E_{33}$. The free surface of the layer permits passage of fluid out of the layer.

**Solution**: First, since the free surface of the layer permits the passage of fluid and the supporting base of the layer is impermeable, the boundary conditions on the pore pressure field are $p = 0$ at $x_3 = 0$, $\partial p / \partial x_3 = 0$ at $x_3 = L$. Next, using the fact that the only nonzero strain component is $E_{33}$ ($E_{33} = \partial u_3 / \partial x_3$ from (3.52)) and that the applied compressive stress, $T_{33} = -P(t)$ is uniform throughout the layer, strain–stress-pressure relations (9.1) specialize to the following:

$$0 = \frac{1}{E^d}\left\{(1+\nu^d)T_{11} - \nu^d tr\mathbf{T} + (1-2\nu^d)\alpha p\right\},$$

$$0 = \frac{1}{E^d}\left\{(1+\nu^d)T_{22} - \nu^d tr\mathbf{T} + (1-2\nu^d)\alpha p\right\},$$

$$\frac{\partial u_3}{\partial x_3} = \frac{1}{E^d}\left\{-(1+\nu^d)P(t) - \nu^d tr\mathbf{T} + (1-2\nu^d)\alpha p\right\}.$$

The solutions of these equations for $T_{11}$, $T_{22}$, $tr\mathbf{T}$, and $T_{33}$ are

$$T_{11} = T_{22} = -\frac{\nu^d}{(1-\nu^d)}P(t) - \frac{(1-2\nu^d)}{(1-\nu^d)}\alpha p\,,$$

$$\mathrm{tr}\mathbf{T} = \frac{E^d}{(1-2\nu^d)}\frac{\partial u_3}{\partial x_3} - 3\alpha p = -\frac{(1+\nu^d)}{(1-\nu^d)}P(t) - \frac{2(1-2\nu^d)}{(1-\nu^d)}\alpha p\,,$$

and

$$T_{33} = -P(t) = 3K^d\frac{(1-\nu^d)}{(1+\nu^d)}\frac{\partial u_3}{\partial x_3} - \alpha p\,,$$

and the single strain component, $E_{33}$, is given by

$$E_{33} = \frac{\partial u_3}{\partial x_3} = \frac{(1+\nu^d)}{3K^d(1-\nu^d)}(-P(t) + \alpha p)\,.$$

Stress equations of motion (4.37) or (4.38), or equilibrium in this case, reduce to the condition that the derivative of the $T_{33}$ stress component with respect to $x_3$ must vanish, and thus from the equation directly above,

$$\frac{\partial}{\partial x_3}\left\{3K^d\frac{(1-\nu^d)}{(1+\nu^d)}\frac{\partial u_3}{\partial x_3} - \alpha p\right\} = 0\,.$$

Since $\mathrm{tr}\mathbf{E} = E_{33}$, substitution of $E_{33}$ into pressure diffusion equation (9.50), and use of $\hat{\mathbf{A}} = SK^dC^d\hat{\mathbf{U}}$ and (9.25) for both material and drained constants yields

$$\frac{\partial p}{\partial t} - c\frac{\partial^2 p}{\partial x_3^2} = W\frac{\partial P}{\partial t}\,,$$

where

$$c = \frac{c_I W}{SK^dC^d}\,,\quad W = \frac{SC^d(1+\nu^d)}{(3\Lambda(1-\nu^d) + \alpha SC^d(1+\nu^d))}$$

and $c_I$ represents the value of constant $c$ when the matrix material and the pore fluid are incompressible:

$$c_I = \frac{K_{11} 3K^d (1-\nu^d)}{\mu(1+\nu^d)}.$$

In the special case when if $K^f = K^m$ (hence $S = 1$, $C^d = \alpha / K^d$, $\Lambda = \alpha / K^m$)

$$c = \frac{c_I W}{\alpha}, \text{ and } W = \frac{(1+\nu^d)}{(3(1-\nu^d) - 2\alpha(1-2\nu^d))},$$

and when the matrix material and the fluid are incompressible, $c = c_I$ and $W = 1$. For the special cases of $K^f = K^m$ it may be shown that $1 \geq W \geq 1/3$ and $\infty \geq c/c_I \geq 1$. The two following examples examine special solutions of these equations, which may then be specialized to these more special assumptions by appropriate selection of $c$ and $W$.

**Example 9.10.2**

Determine the vertical surface settlement of a layer of poroelastic material resting on a stiff impermeable base subjected to a constant surface loading, $T_{33} = -P(t) = -p_o h(t)$. The layer, illustrated in Figure 9.1, is in the $x_1$, $x_2$ plane and the $x_3$ positive coordinate direction is downward. The conditions for drainage of the layer are described in Example 9.10.1.

**Solution**: Substituting the surface loading, $P(t) = p_o h(t)$, into the pressure diffusion equation above, the equation may be rewritten as

$$\frac{\partial p}{\partial t} - c\frac{\partial^2 p}{\partial x_3^2} = W p_o \delta(t).$$

Since the surface loading appears in this differential equation as an impulse, and since we are avoiding Laplace transforms in this presentation, we consider only time $t > 0^+$; thus, the equation simplifies to a classical diffusion equation in $p$:

$$\frac{\partial p}{\partial t} - c\frac{\partial^2 p}{\partial x_3^2} = 0.$$

Now, in order to account for step loading, with the initial pressure distribution (at $t = 0$), it is assumed that there is a pore pressure set up in a layer by the surface loading at the first instant when there has been no reduction in the pressure due to fluid movement. This pressure is calculated from the assumption that the layer is undrained. Thus, from (9.20), using the formula for tr**T** given above and definition of the constant $W$ given above, the initial pore pressure is $p(0) = Wp_o$. This initial pressure distribution is the pressure in the undrained layer at $t = 0$. The solution $p(X, \tau)$ to this diffusion equation is accomplished by the method of separation of variables and is subject to boundary conditions $p = 0$ at $x_3 = 0$ for $t > 0$, $\partial p / \partial x_3 = 0$ at $x_3 = L$ for all $t$ and initial condition $p(0) = Wp_0$, and thus

$$p(X,\tau) = \sum_{m=0}^{\infty} \frac{4Wp_o}{(1+2m)\pi} \sin\left\{\frac{(1+2m)\pi X}{2}\right\} e^{-(1+2m)^2\pi^2\tau}$$

where a dimensionless time parameter, $\tau = ct/4L^2$, and a dimensionless layer coordinate, $X = x_3/L$, have been introduced. Dimensionless pressure $p(X,\tau)/Wp_0$ is plotted in Figure 9.2a for the entire range of dimensionless layer coordinate $X = x_3/L$ from 0 to 1 and for dimensionless times $\tau$ of 0, 0.0001,0.001, 0.01, 0.1, and 1. A three-dimensional plot (Figure 9.2b) of dimen-

sionless pressure $p(X,\tau)/Wp_0$ against both the entire range of dimensionless layer coordinate $X = x_3/L$ from 0 to 1 and dimensionless times $\tau$ between 0 and 0.01 provides a second perspective on the behavior of the pressure across the layer for the significant early times. Function $p(X,\tau)/Wp_0$ is seen to have a peak value at the surface, $x_3 = 0$ ($X = 0$) at $t = 0$ ($\tau = 0$) and then to decay in both space and time to a uniform value of zero. At $t = 0$ the pore pressure carries most of surface stress $P$, but as the pore pressure diminishes and the layer settles surface stress $P$ is transferred to the solid matrix structure.

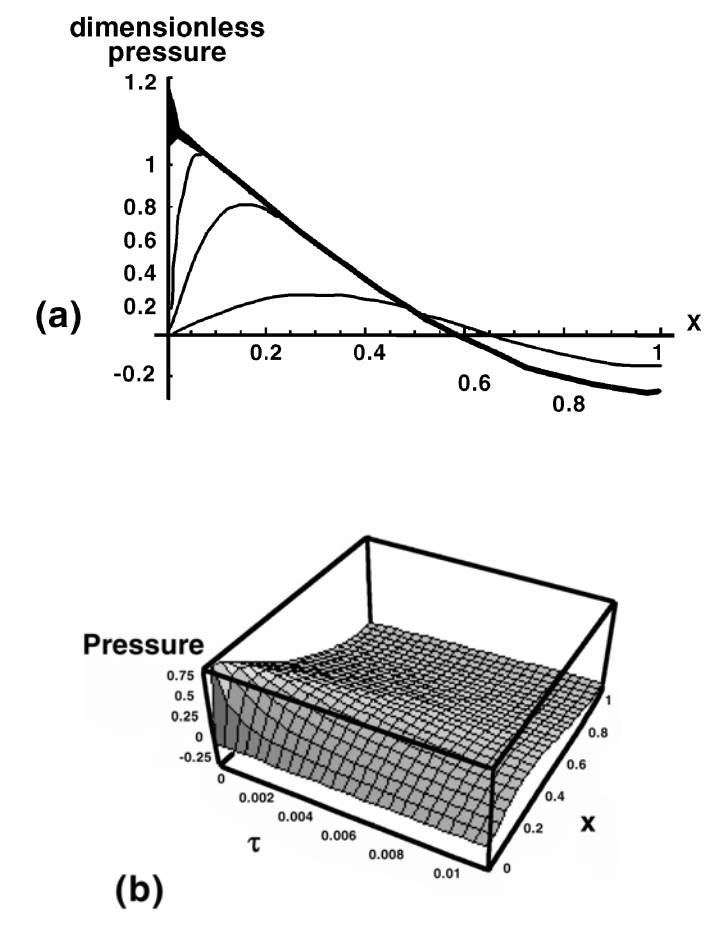



**Figure 9.2**. Illustration of decay of the pressure with time in a layer of poroelastic material resting on a stiff impermeable base subjected to a constant surface loading. (a) The dimensionless pressure $p(X,\tau)/Wp_0$ is plotted (ordinate) against the entire range of the dimensionless layer coordinate $X = x_3/L$ from 0 to 1 (abscissa) for dimensionless time $t$ values of 0, 0.0001, 0.001, 0.01, 0.1, and 1. The top curve with the sinusoidal oscillations is the curve for $\tau = 0$. The sinusoidal oscillations arise because only a finite number of terms (200) of the Fourier series were used to determine the plot. It is important to note that this curve begins at the origin and very rapidly rises to the value 1, then begins a (numerically oscillating) decay that is easily visible. The curves for values of $t$ of 0.0001, 0.001, and 0.01 are the first, second, and third curves below and to the right of the one for $\tau = 0$. The curves for values of $\tau$ of 0.1 and 1 both appear as $p(X,\tau)/Wp_0 = 0$ in this plot. (b) The dimensionless pressure $p(X,\tau)/Wp_0$ is plotted against the entire range of the dimensionless layer coordinate $X = x_3/L$ from 0 to 1 (abscissa) and the range of dimensionless time $\tau$ from 0 to 0.01.

Total displacement $u_3(x_3, t)$ must satisfy boundary condition $u_3(L, t) = 0$, and the desired settlement of the free surface is given by $u_3(0, t)$. In order to calculate $u_3(0, t)$, $u_3(x_3, t)$ must first be calculated. Displacement $u_3(x_3, t)$ is obtained from the pressure solution obtained above and the equilibrium condition that the derivative of the $T_{33}$ stress component with respect to $x_3$ must vanish:

$$\frac{\partial}{\partial x_3}\left\{3K^d\,\frac{(1-\nu^d)}{(1+\nu^d)}\,\frac{\partial u_3}{\partial x_3}-\alpha p\right\}=0\,.$$

Total displacement $u_3(x_3, t)$ of the points in the layer is decomposed into two components — the initial displacement at $t = 0$, $u_3(x_3,0)$, and the transient displacement $u_3^t(x_3,t)$; thus,

$$u_3(x_3,t)=u_3(x_3,0)+u_3^t(x_3,t)\,.$$

The initial displacement at $t = 0$, $u_3(x_3,0)$, is determined from the equilibrium condition for $T_{33}$ above; thus,

$$u_3(x_3,0)=\frac{\alpha(1+\nu^d)WLp_o}{3K^d(1-\nu^d)}\left(1-\frac{x_3}{L}\right).$$

Transient displacement $u_3^t(x_3,t)$ is obtained from the pressure solution for $p$ obtained above and the same equilibrium condition for $T_{33}$, and thus

$$u_3^t(X,\tau)=\frac{\alpha(1+\nu^d)WLp_o}{3K^d(1-\nu^d)}\left\{\sum_{m=0}^{\infty}\frac{8}{(1+2m)^2\pi^2}\cos\left(\frac{(1+2m)\pi X}{2}\right)\left[1-e^{-(1+2m)^2\pi^2\tau}\right]\right\}.$$

The desired settlement of the free surface, $u_3(0, t)$, may now be calculated. The sum of the initial displacement at $x_3 = 0$, $u_3(0,0)$, and the transient displacement at $x_3 = 0$, $u_3^t(0,\tau)$, is given by

$$u_3(0,\tau)=u_3(0,0)+u_3^t(0,\tau)=\frac{\alpha(1+\nu^d)WLp_o}{3K^d(1-\nu^d)}\{1+g(\tau)\}\,,$$

where

$$g(\tau)=\sum_{m=0}^{\infty}\frac{8}{(1+2m)^2\pi^2}\left[1-e^{-(1+2m)^2\pi^2\tau}\right].$$

A plot against time on a log scale of function $g(\tau)$ governing the settlement of the free surface $u_3(0, t)$ is shown in Figure 9.3. The function has a range from 0 to 1. The curve underneath the top curve is for a layer twice as thick as the layer of the top curve. The two curves below are for layers that are five and ten times as thick, respectively, as the layer associated with the top curve. However, since the equation for $u_3(0, t)$ above is proportional to layer thickness $L$, the surface settlement estimates must be multiplied by factors of 1, 2, 5, and 10 for the four curves in Figure 9.3, the four factors applying in descending order from top to bottom of the curve set. The curves in Figure 9.3 show that the time period for layer consolidation increases with layer thickness and that, at a fixed time in the consolidation process, the drainage of the thicker layers is at an earlier stage than drainage of the thinner layers. These curves are all for the vertical settlement of a layer of poroelastic material resting on a stiff impermeable base subjected to a constant surface loading.

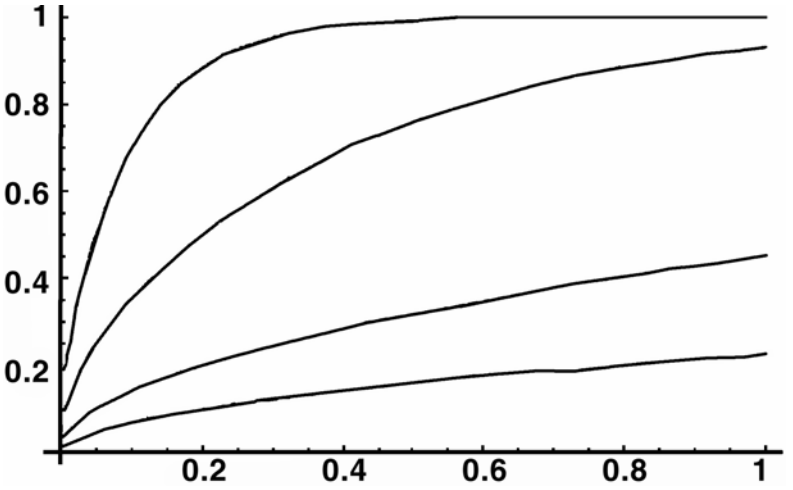



**Figure 9.3**. Illustration of vertical settlement of a layer of poroelastic material resting on a stiff impermeable base subjected to a constant surface loading. This is a plot of function $g(t)$ against time. The curve underneath the top curve is for a layer twice as thick as the layer of the top curve. The two curves below are for layers that are five and ten times as thick, respectively, as the layer associated with the top curve. Compare with Figure 2.20c.

**Example 9.10.3**

Determine the vertical surface settlement of a layer of poroelastic material resting on a stiff impermeable base subjected to a harmonic surface loading $T_{33} = -P(t) = -p_o e^{i\omega t}$. The layer, illustrated in Figure 9.1, is in the $x_1$, $x_2$ plane and the $x_3$ positive coordinate direction is downward. The conditions for drainage of the layer are described in Example 9.10.1.

**Solution**: Substituting the surface loading, $P(t) = p_0 e^{i\omega t}$ into the pressure diffusion equation in Example 9.10.1, the diffusion takes the form

$$\frac{\partial p}{\partial t} - c\frac{\partial^2 p}{\partial x_3^2} = i\omega W p_o e^{i\omega t}.$$

The solution is obtained by assuming that pressure $p$ is of the form $p(x_3, t) = f(x_3)e^{i\omega t}$, and thus the partial differential equation above reduces to an ordinary differential equation:

$$i\omega f(x_3) - c\frac{d^2 f}{dx_3^2} = i\omega W p_o,$$

after dividing through by $e^{i\omega t}$. The solution to this ordinary differential equation is

$$f(x_3) = Wp_o + A\sinh\frac{x_3}{L}\sqrt{\frac{i\omega L^2}{c}} + B\cosh\frac{x_3}{L}\sqrt{\frac{i\omega L^2}{c}}.$$

The boundary conditions of the previous example, namely, that the pressure is zero at $x_3 = 0$ and that the pressure gradient is zero at $x_3 = L$, yield the following solution to the original partial differential equation above, and thus

$$p(x_3,t) = Wp_o\left[1+\tanh\sqrt{\frac{i\omega L^2}{c}}\sinh\frac{x_3}{L}\sqrt{\frac{i\omega L^2}{c}}-\cosh\frac{x_3}{L}\sqrt{\frac{i\omega L^2}{c}}\right]e^{i\omega t}\,.$$

The solution to the problem of semi-infinite domain of poroelastic material subjected to a harmonic surface loading, $T_{33} = -P(t) = -p_o e^{i\omega t}$, may also be obtained without difficulty. This problem is also illustrated in Figure 9.1 if the stiff impermeable base is removed. The solution to the original differential equation above with the boundary conditions that the pressure is zero at $x_3 = 0$ and that the pressure gradient tends to zero as $x_3$ becomes large, is

$$p(x_3,t) = Wp_o a(x_3)e^{i\omega t}\,,\ \text{where}\ \ a(x_3) = [1-e^{-x_3\sqrt{\frac{i\omega}{c}}}]\,.$$

The derivation of this solution is a problem at the end of the section. The real part of $a(x_3)$ is plotted in Figure 9.4. This plot has a peak of 1.06702 at $x_3 = 3.33216$, and then it is asymptotic to the value one as $x_3$ tends to infinity. This indicates that the depth beyond $\delta = 3.33216\sqrt{c/\omega}$ from the surface, where $a(x_3)$ has an almost constant value of one, and pore pressure $p$ is in phase with the surface loading and proportional to it by factor $W$. The interpretation of this result is that departure of the pore pressure fluctuations from the undrained solution is confined to a boundary layer of thickness $\delta$. The semi-infinite domain solution is therefore applicable to the finite-layer problem under consideration provided $\delta < L$.

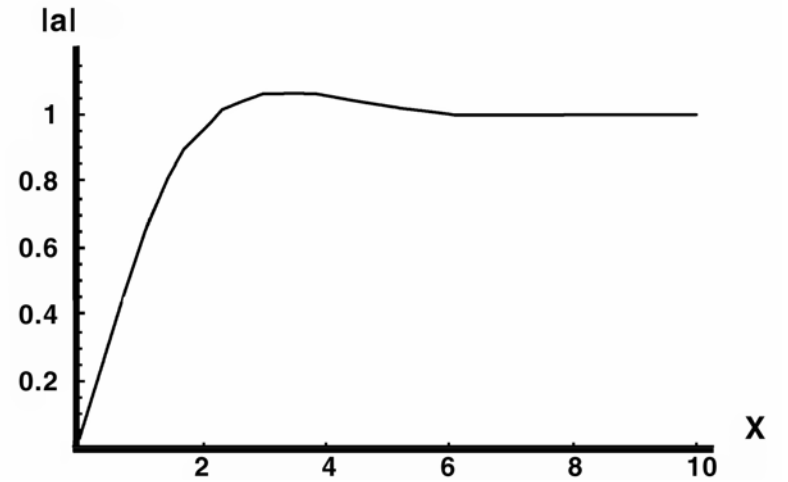



**Figure 9.4**. Plot of function $|a(x_3)|$ against $x_3$. This plot has a peak of 1.06702 at $x_3 = 3.33216$ and then is asymptotic to the value 1 as $x_3$ tends to infinity.

The desired settlement of the free surface, $u_3(0, t)$, is calculated following the method of Example 9.10.2, and thus

$$u(0,t) = \frac{\alpha(1+\nu^d)WLp_o}{3K^d(1-\nu^d)}\sqrt{\frac{c}{i\omega L^2}}\tanh\sqrt{\frac{i\omega L^2}{c}}]e^{i\omega t}\,.$$

A plot against frequency of the absolute value of function

$$\sqrt{\frac{c}{i\omega L^2}}\tanh\sqrt{\frac{i\omega L^2}{c}}$$

determining the amplitude of the settlement of the free surface, $u_3(0, t)$, is shown in Figure 9.5. At very large frequency the poroelastic layer behaves as if it were undrained, that is to say, $|u(0, t)| \to 1$ as $\omega \to \infty$. At low frequencies it behaves as if it were drained, that is to say, $|u(0, t)| \to 0$ as $\omega \to 0$.

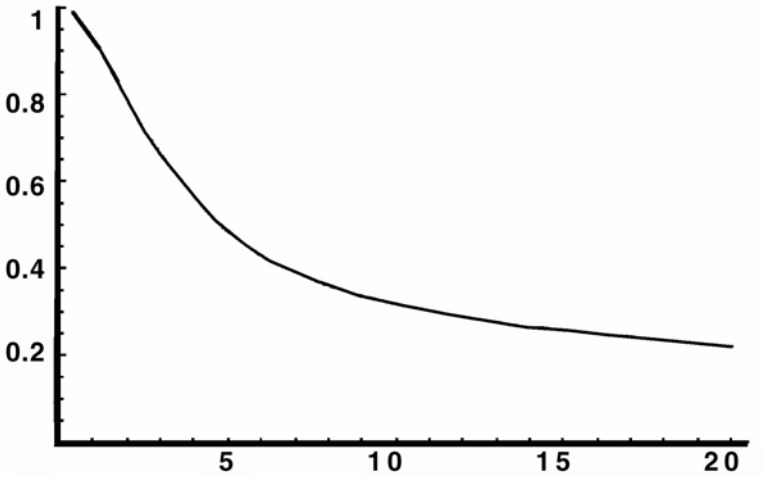



**Figure 9.5**. Illustration of the vertical settlement of a layer of poroelastic material resting on a stiff impermeable base subjected to a harmonic surface loading. A plot of the absolute value of the function $\sqrt{c/i\omega L^2}\tanh\sqrt{i\omega L^2/c}$ against frequency. See Example 9.8.3.

**Problems**

9.10.1. Using the assumptions of Example 9.10.1 and eq. (9.50), derive pressure diffusion equation

$$\frac{\partial p}{\partial t} - c\frac{\partial^2 p}{\partial x_3^2} = W\frac{\partial P}{\partial t},$$

where $c$, $c_I$, and $W$ are given by

$$c = \frac{c_I W}{SK^d C^d},\quad c_I = \frac{K_{11}3K^d(1-\nu^d)}{\mu(1+\nu^d)},\quad W = \frac{SC^d(1+\nu^d)}{(3\Lambda(1-\nu^d)+\alpha SC^d(1+\nu^d))}.$$

9.10.2. Verify that the solution to the pressure diffusion differential equation in Example 9.10.2 satisfies the specified form of the differential equation and the appropriate boundary and initial conditions.

9.10.3. Determine flux $q_3$ of the pore fluid from out of the top surface of the layer in Example 9.10.2.

9.10.4. Verify that the solution to the pressure diffusion differential equation in Example 9.10.3 satisfies the specified form of the differential equation and the appropriate boundary conditions.

9.10.5 Determine the pressure distribution in a semi-infinite domain of poroelastic material subjected to a harmonic surface loading $T_{33} = -P(t) = -p_o e^{i\omega t}$. The surface of the domain is in the $x_1$, $x_2$ plane, and the $x_3$ positive coordinate direction is downward. Drainage of the semi-infinite domain is only allowed at the surface. The solution to the pressure diffusion equation,

$$\frac{\partial p}{\partial t} - c\frac{\partial^2 p}{\partial x_3^2} = W\frac{\partial P}{\partial t},$$

for the semi-infinite domain will determine the pressure field.

9.10.6 Determine flux $q_3$ of the pore fluid from out of the top surface of the layer in Example 9.10.3.

## 9.11. AN EXAMPLE: THE UNCONFINED COMPRESSION OF AN ANISOTROPIC DISK

### Example 9.11.1

This example concerns the boundary-value problem that is a model for the unconfined compression of a disk-shaped specimen. The material of the disk is assumed to be transversely isotropic. In unconfined compression tests a thin cylinder is compressed between two parallel rigid and impermeable smooth plates, but the specimen is assumed to have no frictional contact with the end plates, so that it is free to expand radially; there are thus assumed to be no end effects (Figure 9.6). The passage of fluid is free across the lateral boundaries (the curved surfaces of the thin cylinder), while it is not permitted across the boundaries forming the flat end plates of the thin cylinder due to the two parallel rigid and impermeable smooth plates that are squeezing the thin cylinder. In this test either a step in end plate displacement may be applied, which would constitute a stress relaxation test for the material of the thin cylinder, or a step in total applied end force load may be applied, which would constitute a creep test. This test is used in the biomechanics of articular cartilage, and it is illustrated in the papers of Armstrong et al. (1984) and Cohen et al. (1998). In those papers the solution for the unconfined compression tests of a thin cylinder of an incompressible material were presented; Armstrong et al. (1984) considered the isotropic incompressible case and Cohen et al. (1998) the transversely isotropic incompressible case. Cowin and Mehrabadi (2006) obtained the solution for transversely isotropic compressible material and showed that it specialized to these earlier solutions.

Formulation of the mathematical problem begins with assumptions concerning the functional dependence of variables. Cylindrical coordinates are employed and the displacement field components, the pressure, and the variation in fluid content are assumed to have the functional dependencies indicated below:

$$u_r = u(r,t), \quad u_z = z\varepsilon(t), \quad p = p(r,t), \quad \zeta = \zeta(r,t).$$

The formulas for the stress equations of equilibrium and the strain displacement relations in cylindrical coordinates are given in the Appendix, §A.13. If both $\hat{\mathbf{C}}^{\mathrm{d}}$ and $\hat{\mathbf{S}}^{\mathrm{m}}$ are transversely

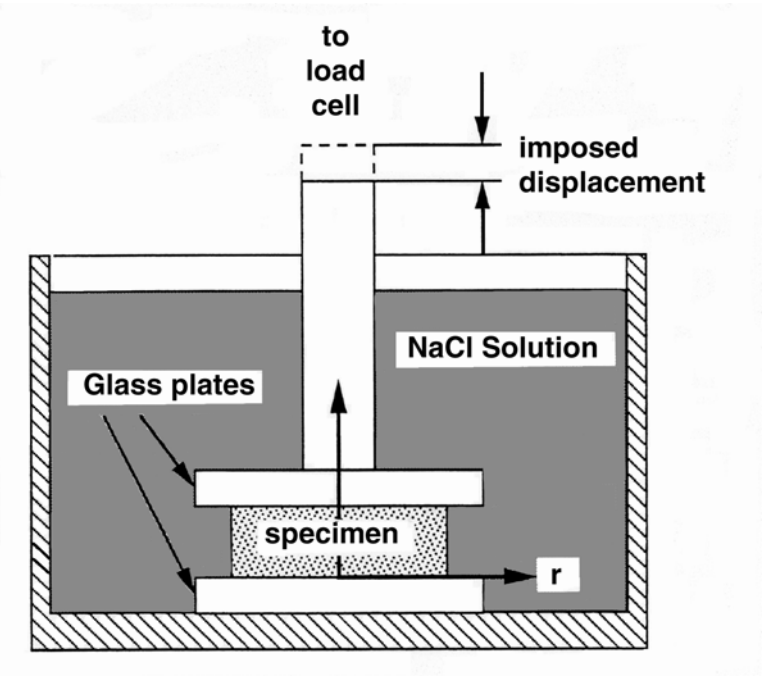



**Figure 9.6**. Schematic of an unconfined compression test. Reprinted with permission from Cohen et al. (1998).

isotropic with respect to a common axis, formulas (9.4) may be written in cylindrical coordinates as

$$\hat{\mathbf{A}} = [\hat{A}_r, \hat{A}_r, \hat{A}_z, 0, 0, 0]^T ,$$

where

$$\hat{A}_r = 1 - (\hat{C}^d_{rr} + \hat{C}^d_{r\theta})(\hat{S}^m_{rr} + \hat{S}^m_{r\theta} + \hat{S}^m_{rz}) - \hat{C}^d_{rz}(2\hat{S}^m_{rz} + \hat{S}^m_{zz}) ,$$

$$\hat{A}_z = 1 - 2\hat{C}^d_{rz}(\hat{S}^m_{rr} + \hat{S}^m_{r\theta} + \hat{S}^m_{rz}) - \hat{C}^d_{zz}(2\hat{S}^m_{rz} + \hat{S}^m_{zz}) .$$

This result may easily be specialized to the case where $\hat{\mathbf{S}}^{\mathrm{m}}$ is isotropic ( $\hat{S}^m_{rr} = \hat{S}^m_{zz}$, $\hat{S}^m_{r\theta} = \hat{S}^m_{rz}$ ) or $\hat{\mathbf{S}}^{\mathrm{m}}$ is incompressible ( $\hat{\mathbf{U}} \cdot \hat{\mathbf{S}}^{\mathrm{m}} = 0 \Rightarrow \hat{S}^m_{rr} + \hat{S}^m_{r\theta} + \hat{S}^m_{rz} = 0,\ 2\hat{S}^m_{rz} + \hat{S}^m_{zz} = 0, \hat{\mathbf{A}} = \hat{\mathbf{U}}$ ). If $\hat{\mathbf{C}}^{\mathrm{d}}$ and $\hat{\mathbf{S}}^{\mathrm{m}}$ do not have the relationship indicated, the solution of the problem under consideration would be much more difficult because $\hat{A}_r \neq \hat{A}_\theta$ , although the last three nonzero components of $\hat{\mathbf{A}}$ have no effect on the present solution. The expressions above for $\hat{A}_r$ and $\hat{A}_z$ may be rewritten in terms of the drained engineering elastic constants as

$$\hat{A}_r = 1 - \frac{E^d_1}{3(1 - \nu^d_{12} - 2\nu^d_{13}\nu^d_{31})}\left(\frac{1}{K^m_1} + \frac{\nu^d_{31}}{K^m_3}\right)$$

and

$$\hat{A}_z = 1 - \frac{E^d_3}{3(1 - \nu^d_{12} - 2\nu^d_{13}\nu^d_{31})}\left(\frac{2\nu^d_{13}}{K^m_1} + \frac{1 - \nu^d_{12}}{K^m_3}\right),$$

where the notation for $K_\alpha^m$ introduced in (9.24b) has been employed.

Quantity $\hat{\mathbf{A}}\cdot\hat{\mathbf{S}}^{\mathrm{d}}\cdot\hat{\mathbf{A}}$ appearing in the definition of $C_{\mathrm{eff}}^d$ in (9.11) has the form

$$\hat{\mathbf{A}}\cdot\hat{\mathbf{S}}^{\mathrm{d}}\cdot\hat{\mathbf{A}} = \frac{2(1-\nu_{12}^d)}{E_1^d}\hat{A}_r{}^2 - \frac{4\nu_{13}^d}{E_1^d}\hat{A}_r\hat{A}_z + \frac{1}{E_3^d}\hat{A}_z{}^2$$

$$= \frac{2\hat{C}_{zz}^d\hat{A}_r{}^2 - 4\hat{C}_{rz}^d\hat{A}_r\hat{A}_z + (\hat{C}_{rr}^d + \hat{C}_{r\theta}^d)\hat{A}_z{}^2}{(\hat{C}_{rr}^d + \hat{C}_{r\theta}^d)\hat{C}_{zz}^d - 2\hat{C}_{rz}^{d\,2}}.$$

Substituting the expression above for $\hat{A}_r$ and $\hat{A}_z$ in the first expression directly above for $\hat{\mathbf{A}}\cdot\hat{\mathbf{S}}^{\mathrm{d}}\cdot\hat{\mathbf{A}}$ yields

$$\hat{\mathbf{A}}\cdot\hat{\mathbf{S}}^{\mathrm{d}}\cdot\hat{\mathbf{A}} = \frac{1}{K_{\mathrm{Reff}}^{\mathrm{d}}} - \frac{2}{K_{\mathrm{Reff}}^m} - \frac{1}{9(1-\nu_{12}^d-2\nu_{13}^d\nu_{31}^d)}\left[\frac{2E_1^d}{K_1^{m2}} + \frac{4E_1^d\nu_{31}^d}{K_1^mK_3^m} + \frac{E_3^d(1-\nu_{12}^d)}{K_3^{m2}}\right].$$

A comparison of the formula for $\hat{\mathbf{A}}\cdot\hat{\mathbf{S}}^{\mathrm{d}}\cdot\hat{\mathbf{A}}$ above and (9.15) yields an expression for $\hat{\mathbf{U}}\cdot\hat{\mathbf{S}}^{\mathrm{m}}\cdot\hat{\mathbf{C}}^{\mathrm{d}}\cdot\hat{\mathbf{S}}^{\mathrm{m}}\cdot\hat{\mathbf{U}}$:

$$\hat{\mathbf{U}}\cdot\hat{\mathbf{S}}^{\mathrm{m}}\cdot\hat{\mathbf{C}}^{\mathrm{d}}\cdot\hat{\mathbf{S}}^{\mathrm{m}}\cdot\hat{\mathbf{U}} = \frac{1}{9(1-\nu_{12}^d-2\nu_{13}^d\nu_{31}^d)}\left[\frac{2E_1^d}{K_1^{m2}} + \frac{4E_1^d\nu_{31}^d}{K_1^mK_3^m} + \frac{E_3^d(1-\nu_{12}^d)}{K_3^{m2}}\right].$$

The formula for $\hat{\mathbf{A}}\cdot\hat{\mathbf{S}}^{\mathrm{d}}\cdot\hat{\mathbf{A}}$ above and the second of (9.11) then may be combined to show that

$$\Lambda = C_{\mathrm{eff}}^d - \frac{1}{K_{\mathrm{Reff}}^d} + \frac{2}{K_{\mathrm{Reff}}^m} - \frac{1}{9(1-\nu_{12}^d-2\nu_{13}^d\nu_{31}^d)}\left[\frac{2E_1^d}{K_1^{m2}} + \frac{4E_1^d\nu_{31}^d}{K_1^mK_3^m} + \frac{E_3^d(1-\nu_{12}^d)}{K_3^{m2}}\right].$$

It is easy to verify that for an isotropic, compressible poroelastic solid,

$$\Lambda = C_{\mathrm{eff}}^d(1-S^2K^dC_{\mathrm{eff}}^d).$$

The key variables are taken to be *u(t), p(t), ζ(t), ε(t),* and *P(t)*, and the direct reference to stress $\hat{\mathbf{T}}$ and strain $\hat{\mathbf{E}}$ is eliminated in the remainder of the calculation. This elimination is achieved by expressing $\hat{\mathbf{E}}$ in terms of *u(t)* and *ε(t)* using strain-displacement relations (3.52) and the assumptions made above, namely, that $u_r = u(r,t)$ and $u_z = z\varepsilon(t)$, and thus, from (A196),

$$\hat{\mathbf{E}} = [\hat{E}_1,\hat{E}_2,\hat{E}_3,\hat{E}_4,\hat{E}_5,\hat{E}_6]^T = \left[\frac{\partial u}{\partial r},\frac{u}{r},\varepsilon(t),0,0,0\right]^T.$$

It follows from this representation of strain and stress–strain relations (9.1) that, since the shearing strains are zero, the shear stresses are zero, and thus

$$\hat{\mathbf{T}} = [\hat{T}_1,\hat{T}_2,\hat{T}_3,\hat{T}_4,\hat{T}_5,\hat{T}_6]^T = [T_{rr},T_{\theta\theta},T_{zz},0,0,0]^T.$$

The assumed transversely isotropic material symmetry of $\hat{\mathbf{C}}^{\mathrm{d}}$ is expressed as

$$\hat{\mathbf{C}}^{\mathrm{d}} = \begin{bmatrix} \hat{C}^d_{rr} & \hat{C}^d_{r\theta} & \hat{C}^d_{rz} & 0 & 0 & 0 \\ \hat{C}^d_{r\theta} & \hat{C}^d_{rr} & \hat{C}^d_{rz} & 0 & 0 & 0 \\ \hat{C}^d_{rz} & \hat{C}^d_{rz} & \hat{C}^d_{zz} & 0 & 0 & 0 \\ 0 & 0 & 0 & \hat{C}^d_{44} & 0 & 0 \\ 0 & 0 & 0 & 0 & \hat{C}^d_{44} & 0 \\ 0 & 0 & 0 & 0 & 0 & \hat{C}^d_{66} \end{bmatrix},$$

and, due to the assumption that both $\hat{\mathbf{C}}^{\mathrm{d}}$ and $\hat{\mathbf{S}}^{\mathrm{m}}$ are transversely isotropic with respect to a common axis, $\hat{\mathbf{A}}$ is given by $\hat{\mathbf{A}} = [\hat{A}_r, \hat{A}_r, \hat{A}_z, 0, 0, 0]^T$. It follows from this representation of $\hat{\mathbf{A}}$ and

$$\hat{\mathbf{E}} = \left[\frac{\partial u}{\partial r}, \frac{u}{r}, \varepsilon(t), 0, 0, 0\right]^T$$

that

$$\hat{\mathbf{A}} \cdot \hat{\mathbf{E}} = \hat{A}_r \left(\frac{\partial u}{\partial r} + \frac{u}{r}\right) + \hat{A}_z \varepsilon(t).$$

The nonzero stress components are then determined from (9.2) using the $\hat{\mathbf{C}}^{\mathrm{d}}$ given above and the formula for

$$\hat{\mathbf{E}} = \left[\frac{\partial u}{\partial r}, \frac{u}{r}, \varepsilon(t), 0, 0, 0\right]^T,$$

and thus

$$T_{rr} = -\hat{A}_r p + \hat{C}^d_{rr} \frac{\partial u}{\partial r} + \hat{C}^d_{r\theta} \frac{u}{r} + \hat{C}^d_{rz} \varepsilon(t),$$

$$T_{\theta\theta} = -\hat{A}_r p + \hat{C}^d_{r\theta} \frac{\partial u}{\partial r} + \hat{C}^d_{rr} \frac{u}{r} + \hat{C}^d_{rz} \varepsilon(t),$$

$$T_{zz} = -\hat{A}_z p + \hat{C}^d_{rz} \left(\frac{\partial u}{\partial r} + \frac{u}{r}\right) + \hat{C}^d_{zz} \varepsilon(t).$$

The only equation of equilibrium (A197) that is not satisfied automatically is

$$\frac{\partial T_{rr}}{\partial r} + \frac{T_{rr} - T_{\theta\theta}}{r} = 0.$$

Substitution of the nonzero stress components above into this equilibrium equation yields an expression which, when integrated with respect to $r$, takes the following form:

$$\left(\frac{\partial u}{\partial r} + \frac{u}{r}\right) = \frac{1}{r} \frac{\partial}{\partial r}(ru) = \frac{\hat{A}_r}{\hat{C}^d_{rr}} p(r,t) + f(t),$$

where *f(t)* is an arbitrary function of time obtained in the integration with respect to *r*. This expression for $(\partial u/\partial r)+(u/r)=(1/r)(\partial/\partial r)(ru)$ may be used to calculate two expressions for quantity $\hat{\mathbf{A}}\cdot\hat{\mathbf{E}}$, defined above, one in terms of variation in fluid content $\zeta$ and the other in terms of pressure *p*. These expressions are needed in the diffusion equations for $\zeta$ and *p*, respectively, to be obtained below. To find $\hat{\mathbf{A}}\cdot\hat{\mathbf{E}}$ in terms of *p*, substitute the formula obtained above for $(\partial u/\partial r)+(u/r)=(1/r)(\partial/\partial r)(ru)$ into the expression for $\hat{\mathbf{A}}\cdot\hat{\mathbf{E}}$ to obtain

$$\hat{\mathbf{A}}\cdot\hat{\mathbf{E}}=\frac{\hat{A}_r\hat{A}_r}{\hat{C}^d_{rr}}p(r,t)+\hat{A}_z\varepsilon(t)+\hat{A}_r f(t)\,,$$

and to find $\hat{\mathbf{A}}\cdot\hat{\mathbf{E}}$ in terms of $\zeta$, eliminate *p* in the equation above using (9.11). This elimination yields

$$\hat{\mathbf{A}}\cdot\hat{\mathbf{E}}=\frac{1}{J}\left\{\hat{A}_r^2\zeta+\Lambda\hat{C}^d_{rr}[\hat{A}_z\varepsilon(t)+\hat{A}_r f(t)]\right\}$$

where dimensionless quantity *J* is introduced:

$$J\equiv\hat{A}_r{}^2+\Lambda\hat{C}^d_{rr}\,.$$

Note that this quantity *J* is equal to 1 in the case of incompressibility ($\Lambda = 0$, $\hat{\mathbf{A}}=\hat{\mathbf{U}}$). In the compressible, transversely anisotropic case, an expression for *J* can be obtained by substituting for $\hat{A}_r$ and converting to the drained engineering elastic constants, and thus

$$J=\left[1-\frac{E^d_1}{3(1-\nu^d_{12}-2\nu^d_{31}\nu^d_{13})}\left(\frac{1}{K^m_1}+\frac{\nu^d_{31}}{K^m_3}\right)\right]^2+\Lambda\frac{E^d_1(1-\nu^d_{13}\nu^d_{31})}{(1+\nu^d_{12})(1-\nu^d_{12}-2\nu^d_{31}\nu^d_{13})}\,.$$

A diffusive differential equation for the pore pressure is obtained by substituting the expression before last for $\hat{\mathbf{A}}\cdot\hat{\mathbf{E}}$ into (9.50); thus,

$$\frac{\partial^2 p}{\partial r^2}+\frac{1}{r}\frac{\partial p}{\partial r}-\frac{1}{c}\frac{\partial p}{\partial t}=\frac{\mu}{K_{rr}}\left(\hat{A}_z\frac{\partial\varepsilon}{\partial t}+\hat{A}_r\frac{\partial f}{\partial t}\right)$$

and a diffusive differential equation for the variation in fluid content is obtained by substituting the expression for $\hat{\mathbf{A}}\cdot\hat{\mathbf{E}}$ into (9.48), and thus

$$\frac{\partial^2\zeta}{\partial r^2}+\frac{1}{r}\frac{\partial\zeta}{\partial r}-\frac{1}{c}\frac{\partial\zeta}{\partial t}=0\,.$$

In both of these cases, the fact that

$$\hat{\mathbf{K}}\cdot\hat{\mathbf{O}}=K_{rr}\left(\frac{\partial^2}{\partial r^2}+\frac{1}{r}\frac{\partial}{\partial r}\right)$$

has been used as well as the formula for *c* given by

$$c=\frac{K_{rr}\hat{C}^d_{rr}}{\mu J}\,.$$

A comparison of the differential equations above shows that both the pore pressure and the variation in fluid content satisfy the same differential equation, but the differential equation for pressure has an inhomogeneous part while that for the variation in fluid content does not. In fact, instead of solving both of these equations one can solve for $\zeta(r,t)$ and then find $p(r, t)$ by equating the two expressions above for $\hat{\mathbf{A}}\cdot\hat{\mathbf{E}}$. This latter operation yields an equation that can be solved for pressure $p(r, t)$ in terms of variation in fluid content $\zeta(r, t)$ and the strain applied to the plates, $\varepsilon(t)$:

$$p(r,t)=\frac{\hat{C}^d_{rr}}{J}[\zeta(r,t)-\hat{A}_z\varepsilon(t)-\hat{A}_r f(t)]$$

Substituting this expression for pressure $p(r,t)$ into the formula for $\partial u/\partial r+u/r$ above, a differential equation for displacement field $u(r,t)$ in terms of variation in fluid content $\zeta(r, t)$ and the strain applied to the plates, $\varepsilon(t)$, is obtained:

$$\frac{\partial u}{\partial r}+\frac{u}{r}=\frac{1}{r}\frac{\partial}{\partial r}(ru)=\frac{1}{J}\left\{\hat{A}_r\zeta(r,t)-\hat{A}_r\hat{A}_z\varepsilon(t)+\Lambda\hat{C}^d_{rr}f(t)\right\}.$$

The differential equation for variation in fluid content $\zeta(r,t)$ above is expressed in terms of dimensionless arguments by introducing dimensionless time $\tau$ and dimensionless radius $\lambda$, and thus

$$\tau=\frac{ct}{b^2},\quad \lambda=\frac{r}{b},$$

and a dimensionless differential equation is obtained:

$$\frac{\partial^2\zeta}{\partial\lambda^2}+\frac{1}{\lambda}\frac{\partial\zeta}{\partial\lambda}-\frac{\partial\zeta}{\partial\tau}=0,$$

The Laplace transform of a function will be indicated by a tilde (˜) over the function whose independent variable will shift from $\tau$ to $s$. The Laplace transform of the differential equation above yields a Bessel differential equation in variation in fluid content $\zeta(\lambda, s)$:

$$\frac{\partial^2\tilde{\zeta}}{\partial\lambda^2}+\frac{1}{\lambda}\frac{\partial\tilde{\zeta}}{\partial\lambda}-s\tilde{\zeta}=0.$$

The solution to this equation is

$$\tilde{\zeta}(\lambda,s)=Jg(s)I_o(\lambda\sqrt{s}),$$

where $I_0$ is a modified Bessel function of the first kind, $g(s)$ is an arbitrary function of the transformed variable to be determined, and where the coefficient is $J$ defined above and introduced here for convenience. This solution for $\tilde{\zeta}$ also contains a term proportional to a modified Bessel function of the second kind, but since the function has a singularity as $\lambda$ tends to *0*, the requirement for a finite solution at $\lambda = 0$ justifies the setting of the arbitrary function of the transformed variable associated with the second kind of Bessel function equal to zero.

We are now in a position to use the boundary condition on the pore pressure at $\lambda = 1$ to eliminate function $f(\tau)$ or, actually, its Laplace transform, $\tilde{f}(s)$. The Laplace transform of the formula given above for the pressure, $p(r,t)=\left(\hat{C}^d_{rr}/J\right)[\zeta(r,t)-\hat{A}_z\varepsilon(t)-\hat{A}_r f(t)]$, with the use of

the solution for $\tilde{\zeta}$ directly above yields the following formula for the Laplace transform of pressure $\tilde{p}(r,s)$:

$$\tilde{p}(\lambda,s)=\frac{\hat{C}^d_{rr}}{J}\Big[Jg(s)I_o(\lambda\sqrt{s})-\hat{A}_z\tilde{\varepsilon}(s)-\hat{A}_r\tilde{f}(s)\Big].$$

It is easy to verify that this formula gives the solution to the Laplace transform of the differential equation for $p(r, t)$ given above (cf. Cohen et al., 1998; Armstrong et al., 1984). Function $\tilde{f}(s)$ is determined by the condition that the pore fluid pressure be zero at curved lateral surface $\lambda = 1$, and thus

$$\tilde{f}(s)=\frac{1}{\hat{A}_r}\Big[Jg(s)I_o(\sqrt{s})-\hat{A}_z\tilde{\varepsilon}(s)\Big],$$

then the Laplace transform of pressure $\tilde{p}(\lambda,s)$ is given by

$$\tilde{p}(\lambda,s)=\hat{C}^d_{rr}g(s)\Big[I_o(\lambda\sqrt{s})-I_o(\sqrt{s})\Big].$$

Substitution of solution $\tilde{\zeta}(\lambda,s)=Jg(s)I_o(\lambda\sqrt{s})$ for the Laplace transform of the variation in fluid content, $\tilde{\zeta}(\lambda,s)$, into the Laplace transform of differential equation

$$\frac{\partial u}{\partial r}+\frac{u}{r}=\frac{1}{r}\frac{\partial}{\partial r}(ru)=\frac{1}{J}\{\hat{A}_r\zeta(r,t)-\hat{A}_r\hat{A}_z\varepsilon(t)+\Lambda\hat{C}^d_{rr}f(t)\}$$

for displacement $\tilde{u}(r,s)$, and subsequently employing the formula for the Laplace transform of $\tilde{f}(s)$ given above, leads one to the following differential equation:

$$\frac{1}{b\lambda}\frac{\partial}{\partial\lambda}(\lambda\tilde{u})=\hat{A}_r g(s)I_o(\lambda\sqrt{s})-\frac{\hat{A}_z}{\hat{A}_r}\tilde{\varepsilon}(s)+\frac{\Lambda\hat{C}^d_{rr}}{\hat{A}_r}g(s)I_o(\sqrt{s}).$$

Integration of this differential equation yields

$$\tilde{u}(\lambda,s)=\frac{1}{2}b\lambda\left\{\hat{A}_r g(s)\left[2h(\lambda,s)+\frac{\Lambda}{\hat{A}_r^{\,2}}\hat{C}^d_{rr}\right]I_o(\sqrt{s})-\frac{\hat{A}_z}{\hat{A}_r}\tilde{\varepsilon}(s)\right\},$$

where function $h(\lambda,s)$,

$$h(\lambda,s)\equiv\frac{I_1(\lambda\sqrt{s})}{\lambda\sqrt{s}I_o(\sqrt{s})},$$

has been introduced. This function monotonically decreases from a value of one-half at $s = 0$ to a value of 0 as $s$ tends to infinity. Function $g(s)$ is evaluated by calculating stress $T_{rr}$ on the curved lateral boundary at $\lambda = 1$ and requiring that it be zero. To that end, the formula directly above for $\tilde{u}(\lambda,s)$, and the formula for $\tilde{p}(r,s)$ above, are substituted in the Laplace transform of the expression given above for radial stress

$$T_{rr}=-\hat{A}_r p+\hat{C}^d_{rr}\frac{\partial u}{\partial r}+\hat{C}^d_{r\theta}\frac{u}{r}+\hat{C}^d_{rz}\varepsilon(t);$$

function $g(s)$ is found to be given by

$$g(s) = \frac{B\tilde{\varepsilon}(s)}{[C - D\,h(1,s)]I_o(\sqrt{s})}$$

where $B$, $C$, and $D$ are given by (see Tables 9.1 and 9.2 for formulas for various special cases)

$$B = \frac{1}{2\hat{C}^d_{rr}}[(\hat{C}^d_{rr} + \hat{C}^d_{r\theta})\hat{A}_z - 2\hat{C}^d_{rz}\hat{A}_r] = \frac{1}{2\Delta_2}(\hat{A}_z - 2\nu_{31}\hat{A}_r)$$

$$C = \hat{A}_r{}^2 + \frac{\Lambda}{2}(\hat{C}^d_{rr} + \hat{C}^d_{r\theta}) = \hat{A}_r{}^2 + \frac{\Lambda E_1}{2\Delta_1}, \quad D = \hat{A}_r^2\frac{\hat{C}^d_{rr} - \hat{C}^d_{r\theta}}{\hat{C}^d_{rr}} = \frac{\hat{A}_r^2}{\Delta_2}(2\Delta_2 - 1),$$

and where $\Delta_1$ and $\Delta_2$ are defined by

$$\Delta_1 = 1 - \nu^d_{12} - 2\nu^d_{31}\nu^d_{13} \text{ and } \Delta_2 = \frac{1 - \nu^d_{13}\nu^d_{31}}{1 + \nu^d_{12}}.$$

Using this expression for $g(s)$, formula $\tilde{\zeta}(\lambda, s) = Jg(s)I_o(\lambda\sqrt{s})$ for the Laplace transform of variation in fluid content $\tilde{\zeta}(\lambda, s)$ may be written as

$$\tilde{\zeta}(\lambda, s) = \frac{CI_o(\lambda\sqrt{s})\tilde{\varepsilon}(s)}{HI_o(\sqrt{s}) - \dfrac{D}{\sqrt{s}}I_1(\sqrt{s})},$$

and the formula almost directly above for the Laplace transform of the radial displacement may be written as

$$\tilde{u}(\lambda, s) = -\frac{b\lambda}{2\hat{A}_r}\left[\hat{A}_z - B\frac{\Lambda\hat{C}^d_{rr} + 2\hat{A}_r^2 h(\lambda, s)}{C - D\,h(1,s)}\right]\tilde{\varepsilon}(s).$$

Similar substitutions provide a formula for $\tilde{p}(s,t)$:

$$\frac{\tilde{p}(\lambda, s)}{\hat{C}^d_{rr} - \hat{C}^d_{r\theta}} = \frac{B\hat{A}_r{}^2}{D}\left[\frac{I_o(\lambda\sqrt{s})}{I_o(\sqrt{s})} - 1\right]\frac{\tilde{\varepsilon}(s)}{C - D\,h(1,s)}.$$

As a first step in calculating total force *P(t)* applied to the circular flat plate, a formula for stress component $T_{zz}$ in terms of only *p(r, t)* and $\varepsilon(t)$ is obtained. The formula for

$$\frac{\partial u}{\partial r} + \frac{u}{r} = \frac{1}{r}\frac{\partial}{\partial r}(ru)$$

is substituted into the expression above for the third of the stress components, $T_{zz}$, and thus

$$T_{zz} = -\frac{\hat{A}_z\hat{C}^d_{rr} - \hat{A}_r\hat{C}^d_{rz}}{\hat{C}^d_{rr}}p(r,t) + \hat{C}^d_{zz}\varepsilon(t) + \hat{C}^d_{rz}f(t).$$

Total force *P(t)* applied to the circular flat plate is then given by

$$P(t) = 2\pi\int_0^b T_{zz}rdr = -\frac{2\pi}{\hat{C}^d_{rr}}(\hat{A}_z\hat{C}^d_{rr} - \hat{A}_r\hat{C}^d_{rz})\int_0^b prdr + \pi b^2\hat{C}^d_{zz}\varepsilon(t) + \pi b^2\hat{C}^d_{rz}f(t).$$

**Table 9.1**. Values of Various Bulk Moduli and Constants $C^d_{\text{eff}}$, $\Lambda$, and $J$, Defined for Convenience, for Cases of Different Material Models

| | Transverse isotropy, compressible | Transverse isotropy, incompressible | Isotropy, compressible | Isotropy, incompressible |
|---|---|---|---|---|
| $\frac{1}{K^m_1}$ | $\frac{3(1-\nu^m_{12}-\nu^m_{13})}{E^m_1}$ | 0 | $\frac{1}{K^m}=\frac{3(1-2\nu^m)}{E^m}$ | 0 |
| $\frac{1}{K^m_3}$ | $\frac{3(1-2\nu^m_{31})}{E^m_3}$ | 0 | $\frac{1}{K^m}$ | 0 |
| $\frac{1}{K^m_{Reff}}$ | $\frac{2}{3K^m_1}+\frac{1}{3K^m_3}$ | 0 | $\frac{1}{K^m}$ | 0 |
| $\frac{1}{K^d_{Reff}}$ | $\frac{2(1-\nu^d_{12}-\nu^d_{13})}{E^d_1}+\frac{1-2\nu^d_{31}}{E^d_3}$ | $\frac{2(1-\nu^d_{12}-\nu^d_{13})}{E^d_1}+\frac{1-2\nu^d_{31}}{E^d_3}$ | $\frac{1}{K^d}=\frac{3(1-2\nu^d)}{E^d}$ | $\frac{1}{K^d}=\frac{3(1-2\nu^d)}{E^d}$ |
| $C^d_{\text{eff}}$ | $\frac{1}{K^d_{Reff}}-\frac{1}{K^m_{Reff}}+\phi\left(\frac{1}{K^f}-\frac{1}{K^m_{Reff}}\right)$ | $\frac{1}{K^d_{Reff}}$ | $\frac{1}{K^d}-\frac{1}{K^m}+\phi\left(\frac{1}{K^f}-\frac{1}{K^m}\right)$ | $\frac{1}{K^d}$ |
| $\Lambda$ | $C^d_{\text{eff}}-\frac{1}{K^d_{Reff}}+\frac{2}{K^m_{Reff}}-\frac{1}{9\Delta_1}\left(\frac{2E^d_1}{K^{m2}_1}+\frac{4E^d_1\nu^d_{31}}{K^m_1K^m_3}+\frac{E^d_3(1-\nu^d_{12})}{K^{m2}_3}\right)$ | 0 | $C^d_{\text{eff}}(1-S^2K^dC^d_{\text{eff}})$ | 0 |
| $J$ | $1-\frac{E^d_1}{3\Delta_1}\left(\frac{1}{K^m_1}+\frac{\nu^d_{31}}{K^m_3}\right)^2+\Lambda\frac{E^d_1\Delta_2}{\Delta_1}$ | 1 | $\frac{1}{1+\nu^d}[3(1-\nu^d)-2(1-2\nu^d)S^2K^dC^d_{\text{eff}}]K^dC^d_{\text{eff}}$ | 1 |

The material constants $\Delta_1$ and $\Delta_2$ appearing in the table are defined by the first two equations of (99): $\Delta_1=1-\nu^d_{12}-2\nu^d_{31}\nu^d_{13}$ and $\Delta_2=(1-\nu^d_{13}\nu^d_{31})/(1+\nu^d_{12})$.

**Table 9.2**. Values of the Biot Effective Coefficient, $\hat{\mathbf{A}}$, the Constants Defined for Convenience ($B$, $C$, $D$, $M$, $N$), and Diffusion Constant $c$ in the Unconfined Compression Problem of a Disk

| | Transverse isotropy, compressible | Transverse isotropy, incompressible | Isotropy, compressible | Isotropy, incompressible |
|---|---|---|---|---|
| $\hat{A}_r$ | $1-\frac{E_1^d}{3\Delta_1}\left(\frac{1}{K_1^m}+\frac{\nu_{31}^d}{K_3^m}\right)$ | 1 | $1-\frac{K^d}{K^m}=SK^dC_{eff}^d$ | 1 |
| $\hat{A}_z$ | $1-\frac{E_3^d}{3\Delta_1}\left(\frac{2\nu_{13}^d}{K_1^m}+\frac{1-\nu_{12}^d}{K_3^m}\right)$ | 1 | $1-\frac{K^d}{K^m}=SK^dC_{eff}^d$ | 1 |
| $B$ | $\frac{1}{2\Delta_2}(\hat{A}_z-2\nu_{31}^d\hat{A}_r)$ | $\frac{1}{2\Delta_2}(1-2\nu_{31}^d)$ | $\frac{1-2\nu^d}{2(1-\nu^d)}SK^dC_{eff}^d$ | $\frac{1-2\nu^d}{2(1-\nu^d)}$ |
| $C$ | $\hat{A}_r^{\,2}+\frac{\Delta E_1}{2\Delta_1}$ | 1 | $\frac{1}{2(1+\nu^d)}[3-(1-2\nu^d)S^2K^dC_{eff}^d]K^dC_{eff}^d$ | 1 |
| $D$ | $\frac{\hat{A}_r^2}{\Delta_2}(2\Delta_2-1)$ | $\frac{1}{\Delta_2}(2\Delta_2-1)$ | $\frac{1-2\nu^d}{1-\nu^d}(SK^dC_{eff}^d)^2$ | $\frac{1-2\nu^d}{1-\nu^d}$ |
| $M$ | $C_{eff}^d\frac{E_3}{2\Delta_2-1}$ | $\frac{1}{K_{Reff}^d}\frac{E_3}{2\Delta_2-1}$ | $3K^dC_{eff}^d$ | 3 |
| $N$ | $\frac{2E_3}{2\Delta_2-1}\left(C_{eff}^d-\frac{J\Delta_1}{E_1\Delta_2}\right)$ | $\frac{2E_3}{2\Delta_2-1}\left(\frac{1}{K_{Reff}^d}-\frac{\Delta_1}{E_1\Delta_2}\right)$ | $\frac{4(1-2\nu^d)}{1-\nu^d}(SK^dC_{eff}^d)^2$ | $\frac{4(1-2\nu^d)}{1-\nu^d}$ |
| $c$ | $\frac{K_{rr}\hat{C}_{rr}^d}{\mu J}$ | $\frac{K_{rr}\hat{C}_{rr}^d}{\mu}$ | $\frac{3k(1-\nu^d)}{\mu[3(1-\nu^d)-2(1-2\nu^d)S^2K^dC_{eff}^d]C_{eff}^d}$ | $\frac{3k(1-\nu^d)}{\mu(1+\nu^d)}K^d$ |

Results are given in the table are for the cases of different material models; compressible isotropy and transverse isotropy and incompressible isotropy and transverse isotropy. The material constants $\Delta_1$ and $\Delta_2$ appearing in the table are defined by $\Delta_1=1-\nu_{12}^d-2\nu_{31}^d\nu_{13}^d$ and $\Delta_2=(1-\nu_{13}^d\nu_{31}^d)/(1+\nu_{12}^d)$.

Substituting the expression above for $\tilde{p}(\lambda,s)$ and the formula above for $\tilde{f}(s)$ into the Laplace transform of the equation directly above, one obtains

$$\tilde{P}(s)=2\pi b^2\int_0^1\tilde{T}_{zz}\lambda d\lambda=-\frac{2\pi b^2}{\hat{C}^d_{rr}}(\hat{A}_z\hat{C}^d_{rr}-\hat{A}_r\hat{C}^d_{rz})\int_0^1\tilde{p}\lambda d\lambda+\pi b^2\hat{C}^d_{zz}\tilde{\varepsilon}(s)+\pi b^2\hat{C}^d_{rz}\tilde{f}(s)$$

and after some rearrangement of terms,

$$\frac{2\tilde{P}(s)}{\pi b^2(\hat{C}^d_{rr}-\hat{C}^d_{r\theta})}=\frac{M-N\,h(1,s)}{C-D\,h(1,s)}\tilde{\varepsilon}(s)$$

where $C$ and $D$ are given above, and $M$ and $N$ are defined by relations (see Table 9.2 for formulas for various special cases)

$$M=\frac{1}{\hat{C}^d_{rr}-\hat{C}^d_{r\theta}}[2\hat{C}^d_{zz}\hat{A}_r^2-4\hat{C}^d_{rz}\hat{A}_r\hat{A}_z+(\hat{C}^d_{rr}+\hat{C}^d_{r\theta})\hat{A}_z^2+\Lambda(\hat{C}^d_{rr}\hat{C}^d_{zz}+\hat{C}^d_{r\theta}\hat{C}^d_{zz}-2\hat{C}^{d\,2}_{rz})]$$

$$=C^d_{eff}\,\frac{(\hat{C}^d_{rr}+\hat{C}^d_{r\theta})\hat{C}^d_{zz}-2\hat{C}^{d\,2}_{rz}}{\hat{C}^d_{rr}-\hat{C}^d_{r\theta}}=C^d_{eff}\,\frac{E_3}{2\Delta_2-1},$$

$$N=\frac{2}{\hat{C}^d_{rr}(\hat{C}^d_{rr}-\hat{C}^d_{r\theta})}[(\hat{C}^d_{rr}\hat{C}^d_{zz}-\hat{C}^d_{r\theta}\hat{C}^d_{zz}+2\hat{C}^{d\,2}_{rz})\hat{A}_r^2-4\hat{C}^d_{rr}\hat{C}^d_{rz}\hat{A}_r\hat{A}_z+\hat{C}^d_{rr}(\hat{C}^d_{rr}+\hat{C}^d_{r\theta})\hat{A}_z^2]$$

$$=2(\hat{C}^d_{rr}C^d_{eff}-J)\frac{(\hat{C}^d_{rr}+\hat{C}^d_{r\theta})\hat{C}^d_{zz}-2\hat{C}^{d\,2}_{rz}}{\hat{C}^d_{rr}(\hat{C}^d_{rr}-\hat{C}^d_{r\theta})}=\frac{2E_3}{2\Delta_2-1}(C^d_{eff}-J\frac{\Delta_1}{E_1\Delta_2}).$$

Note that definition (9.11) of $C^d_{\text{eff}}$ and the second relation in the double equality for quantity $\hat{\mathbf{A}}\cdot\hat{\mathbf{S}}^{\text{d}}\cdot\hat{\mathbf{A}}$ have been used to write the second equalities for both $M$ and $N$.

Using the Laplace-transformed representation above, total load $P(t)$ generated on a specimen by an arbitrary strain history $\varepsilon(t)$ can be determined. Alternatively, if load history $P(t)$ is prescribed, then the equation above can be used to determine $\varepsilon(t)$. Displacement field $\tilde{u}(\lambda,s)$ and pore pressure field $\tilde{p}(\lambda,s)$ may be evaluated for an imposed load history, as opposed to an imposed displacement history, by solving the equation directly above for $\tilde{\varepsilon}(s)$ and then substituting the result into equations for displacement field $\tilde{u}(\lambda,s)$ and pore pressure field $\tilde{p}(\lambda,s)$, respectively. Thus, the solution for the linear poroelastic, transversely isotropic, unconfined-compression, creep, and stress-relaxation analysis is completed. Before inverting these expressions and presenting numerical results, it is helpful to observe some mathematical properties pertaining to the Laplace transform solution equations for $\tilde{u}(\lambda,s)$, $\tilde{p}(\lambda,s)$, and $\tilde{P}(s)$.

Laplace transform theory includes two theorems that are used here to gain some insight into these results without accomplishing the complete inversion process. The final and initial value theorems are characterized by the following two respective formulas (Thomson, 1960, pp. 20–21):

$$\lim_{s\to o}s\tilde{f}(s)=\lim_{t\to\infty}f(t)\ \text{ and }\ \lim_{s\to\infty}s\tilde{f}(s)=\lim_{t\to 0}f(t).$$

The conditions that functions $f(t)$ and $\tilde{f}(s)$ must satisfy are assumed to be satisfied by the solutions for $\tilde{u}(s,r)$, $\tilde{p}(s,r)$, and $\tilde{P}(s)$ given above. The case considered as an example is ap-

plied step loading , $\varepsilon(t) = \varepsilon_0 h(t)$, which has Laplace transform $\tilde{\varepsilon}(s) = \varepsilon_0 / s$. Applying the initial and final value theorems to $\tilde{u}(s,r)$, it is easy to show that

$$u(1,0) = -\frac{b\varepsilon_o}{2\hat{A}_r}\left(\hat{A}_z - \frac{B}{C}\Lambda\hat{C}^d_{rr}\right) \text{ and } u(1,\infty) = -\frac{b\varepsilon_o}{2\hat{A}_r}\left(\hat{A}_z - \frac{2BJ}{2C-D}\right),$$

from which it is seen that the displacement at the outer boundary of the disk is initially larger that the final displacement: $u(1,0) > u(1,\infty)$. The physical reason for this is that there is no fluid flow at the first instance, and so the disk is functioning as an incompressible object whose elasticity is determined by the undrained elastic constants. Thus, the volume by which the disk is diminished in the axial direction by compressive loading from the plates must be balanced by an equal volume of expansion in the radial direction. As time increases, the fluid flows from the disk across the lateral boundaries, and the displacement of the outer boundary of the disk diminishes to an equilibrium value determined by the drained elastic constants. In the isotropic, incompressible case these formulas for the displacement at the outer boundary of the disk simplify to

$$u(1,0) = -\frac{b\varepsilon_o}{2} \text{ and } u(1,\infty) = -\nu^d b\varepsilon_0 .$$

The correctness of these results may be verified by simpler mechanics arguments. In the case of the initial deformation, the volume of the decrease in height of the cylinder, $\pi b^2\varepsilon_o L$, must equal the volume expansion in the radial direction, $2\pi bL,\ u(1,0)$, so that the result on the left above follows. Verification of the correctness of the formula on the right is one of the problems at the end of the section. These and the other values of $u(1,0)$ and $u(1,\infty)$ for specializations to isotropy or transverse isotropy and compressible or incompressible materials are recorded in Table 9.2. Also recorded in Table 9.3 are the corresponding results for $P(0)$, $P(\infty)$, $p(0,0)$, and $p(0,\infty)$.

The inverse Laplace transforms of equations representing solutions $\tilde{u}(s,r)$, $\tilde{p}(s,r)$, and $\tilde{P}(s)$ may be obtained easily by standard methods. We note that $\tilde{u}(s,r)$, $\tilde{p}(s,r)$, and $\tilde{P}(s)$ are all of fractional form *p(s)/q(s),* the inverse of which is

$$\mathcal{L}^{-1}\left[\frac{p(s)}{q(s)}\right] = \sum_{n=1}^{\infty}\frac{p(\alpha_n)}{q'(\alpha_n)}e^{\alpha_n ct/b^2},$$

where *p(s)* and *q(s)* are analytic at $s = \alpha_n$, $p(\alpha_n) \neq 0$, and $\alpha_n$ are simple poles of *p/q*.

In stress relaxation, the axial compressive strain history is given by $\varepsilon(t) = \varepsilon_0 h(t)$, where *h(t)* is the Heaviside step function, and $\tilde{\varepsilon}(s) = \varepsilon_0 / s$. The resulting dimensional load history, *P(t)*, may then be calculated using the method described in Armstrong et al. (1984) for the isotropic incompressible case and in Cohen et al. (1998) for the transversely isotropic incompressible case. Application of this method to the case of a transversely isotropic poroelastic material with compressible constituents subjected to a step loading will yield

$$\frac{P(t)}{\pi b^2} = E^d_3\varepsilon_o + E^d_1\varepsilon_o(b^2/c)\Delta'_3\sum_{n=1}^{\infty}A_n e^{-ct\alpha_n^2/b^2}$$

where $\alpha_n$ are the roots of the characteristic equation $J_1(x) - (C/D)xJ_0(x) = 0$, where $J_o(x)$ and $J_1(x)$ are Bessel functions, and

$$A_n = \frac{(2C-D)^2}{C^2\alpha_n^2 - D(2C-D)} = \frac{1}{C^2\Delta_2'^2\alpha_n^2 - \Delta_1'/(1+\nu_{12})}$$

**Table 9.3**. Values at $t = 0$ and as $t \to \infty$ of Key Parameters for the case of Unconfined Compression of a Disk Subjected to Axial Step Loading in Strain at $t = 0$

| | Transverse isotropy, compressible | Transverse isotropy, incompressible | Isotropy, compressible | Isotropy, incompressible |
|---|---|---|---|---|
| $u(1,0)$ | $-\frac{b\varepsilon_o}{2\hat{A}_r}\ \hat{A}_z - \frac{B}{C}\Lambda\hat{C}^d_{rr}$ | $-\frac{b\varepsilon_o}{2}$ | $-b\varepsilon_o\ \frac{3\nu^d + (1-2\nu^d)S^2K^dC^d_{\text{eff}}}{3-(1-2\nu^d)S^2K^dC^d_{\text{eff}}}$ | $-\frac{b\varepsilon_o}{2}$ |
| $u(1,\infty)$ | $-\frac{b\varepsilon_o}{2\hat{A}_r}\ \hat{A}_z - \frac{2B}{2C-D}$ | $-\nu^d_{31}b\varepsilon_o$ | $-\nu^d b\varepsilon_o$ | $-\nu^d b\varepsilon_o$ |
| $\frac{P(0)}{\pi b^2}$ | $-\frac{1}{2}\hat{C}^d_{rr}\varepsilon_o DM / C\hat{A}^2_r$ | $-\frac{1}{2}\hat{C}^d_{rr}\varepsilon_o DM$ | $\frac{-9\varepsilon_o(1-2\nu^d)K^d}{3-(1-2\nu^d)S^2K^dC^d_{\text{eff}}}$ | $-3G^d\varepsilon_o$ |
| $\frac{P(\infty)}{\pi b^2}$ | $-\frac{1}{2}\hat{C}^d_{rr}\varepsilon_o(2M-N)D/(2C-D)\hat{A}^2_r$ | $-E^d_3\varepsilon_o$ | $-E^d\varepsilon_o$ | $-E^d\varepsilon_o$ |
| $p(0,0)$ | $-\frac{\hat{C}^d_{rr}\varepsilon_o B}{C}$ | $-\hat{C}^d_{rr}\varepsilon_o B$ | $-\frac{3(1-2\nu^d)K^d\varepsilon_o}{3-(1-2\nu^d)S^2K^dC^d_{\text{eff}}}$ | $-G^d\varepsilon_o$ |
| $p(0,\infty)$ | 0 | 0 | 0 | 0 |

Values given are those of the radial displacement at the outer boundary of the disk at $t = 0$ and as $t \to \infty$; the values of the required axial force applied to the disk at $t = 0$ and as $t \to \infty$; and the values of the pore pressure at the center of the disk at $t = 0$ and as $t \to \infty$.

and

$$\Delta_3' = \frac{CN - DM}{(1+\nu_{12}^d)(2C-D)^2} = \Delta_3 \frac{\nu_{31}\Delta_1}{\nu_{13}(1-2\nu_{31})^2 J^2}\left(C_{eff}^d J \frac{E_1}{\Delta_1} - 2J + \Lambda \frac{E_1}{1+\nu_{12}}\right)$$

$$\Delta_1' = \frac{(1+\nu_{12}^d)D}{2C-D} = \Delta_1 \frac{\hat{A}_r^2}{J},\ \Delta_2' = \frac{1}{2C-D} = \Delta_2 \frac{1}{J}$$

and where $\Delta_1$, $\Delta_2$, and $\Delta_3$ are defined by

$$\Delta_1 = 1 - \nu_{12}^d - 2\nu_{31}^d \nu_{13}^d,\ \ \Delta_2 = \frac{1-\nu_{13}^d \nu_{31}^d}{1+\nu_{12}^d},\ \ \Delta_3 = \frac{(1-2\nu_{31}^d)^2 \Delta_2}{\Delta_1}.$$

When incompressibility of the constituents is assumed, the expressions in the above equations are simplified by the following equalities:

$$\Delta_3' = \Delta_3,\quad \Delta_1' = \Delta_1,\quad \Delta_2' = \Delta_2,$$

where $J = \hat{A}_r{}^2 + \Lambda \hat{C}_{rr}^d$ has been employed and the values of $\Lambda = 0$ and $C = \hat{A}_r^2 = J = 1$ (see Tables 9.1 and 9.2) have been employed. For the incompressible case *P(t)* is given by

$$\frac{P(t)}{\pi b^2} = E_3^d \varepsilon_o + E_1^d \varepsilon_o \Delta_3 (b^2/c) \sum_{n=1}^{\infty} \frac{1}{\Delta_2^2 \alpha_n^2 - \Delta_1/(1+\nu_{12})} e^{-ct\alpha_n^2/b^2}.$$

This expression for *P(t)* was obtained by Cohen et al. (1998).

Cohen et al. (1998) also obtained an analytical solution for the experimentally significant case of a ramp loading for a transversely isotropic incompressible material. Ramp loading is characterized by constant strain rate $\dot{\varepsilon}_o$ and period of duration $t_0$ during which the applied strain is rising linearly from a value of 0 to $t_o\dot{\varepsilon}_o$. After time $t_0$ the value of $\varepsilon(t)$ is constant at $t_o\dot{\varepsilon}_o$. In terms of Heaviside step function *H(t)*,

$$\varepsilon(t) = \dot{\varepsilon}_o [tH(t) - (t-t_o)H(t-t_o)].$$

For the specified ramp loading, the solution for $P(t)$ is given by

$$\frac{P(t)}{\pi b^2} = \dot{\varepsilon}_o E_3^d t + E_1^d \varepsilon_o (b^2/c)\Delta_3' \left[\frac{1}{8} - \sum_{n=1}^{\infty} \frac{A_n}{\alpha_n^2} e^{-ct\alpha_n^2/b^2}\right],$$

for $0 < t < t_0$, and

$$\frac{P(t)}{\pi b^2} = \dot{\varepsilon}_0 E_3^d t_0 - E_1^d \dot{\varepsilon}_0 (b^2/c)\Delta_3' \left\{\sum_{n=1}^{\infty} \frac{A_n}{\alpha_n^2}\left[e^{-ct\alpha_n^2/b^2} - e^{-c(t-t_o)\alpha_n^2/b^2}\right]\right\},$$

for $t > t_0$. It is easy to show that these for *P(t)* reduce to the corresponding equations of Cohen et al. (1998) (see their eqs. (20a) and (20b)) for the incompressible case when the equalities valid for incompressibility, $\Delta_3' = \Delta_3,\ \ \Delta_1' = \Delta_1,\ \ \Delta_2' = \Delta_2$, are employed. The stress relaxation time history in an unconfined compression test in response to this ramped displacement is shown in Figure 9.7 for various values of dimensionless time variable $ct_0/b^2$. The vertical scale in this figure is the nondimensional load intensity obtained by dividing *P(t)* by $\pi b^2 \dot{\varepsilon}_o E_z^d t_o$.

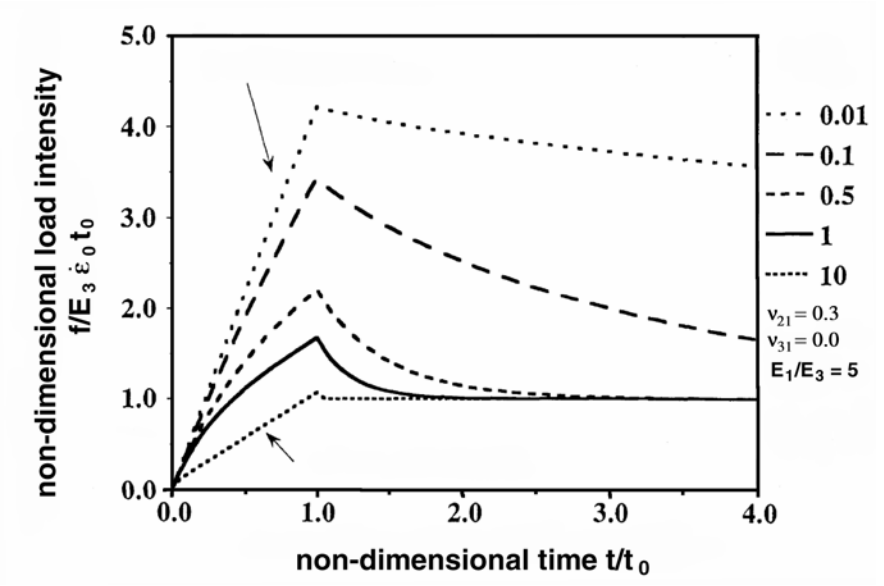



**Figure 9.7**. Stress relaxation time history in an unconfined compression test in response to a ramped displacement for various values of the dimensionless time variable $ct_0/b^2$. The quantity $b^2/c$ is a characteristic time of the disk obtained from the ratio of the disk radius squared, $b^2$, to the diffusion constant $c$, and $t_0$ is the ramp time in the ramped displacement $\varepsilon(t) = \dot{\varepsilon}[\text{th}(t) - (t - t_0)h(t - t_0)]$ . The vertical scale is the non-dimensional load intensity obtained by dividing $P(t)$ by $\pi b^2 \dot{\varepsilon}_0 E_z^d t_0$ . Reprinted with permission from Cohen et al. (1998).

Typical stress-relaxation time histories in an unconfined compression test in response to this ramped displacement are plotted in Figure 9.8. The plots are curve fits of the same data to both isotropic and transversely isotropic models and demonstrate the advantage of the transversely isotropic model in this situation. Not surprisingly, using the data provided by Cohen et al. (1998), these plots are almost identical to the plots obtained on the basis of the expressions for *P(t)* above.

The differences between predictions of the solutions for ramp loading in the case of compressible vs. incompressible constituents is illustrated by evaluation of the two solutions for bone tissue. The bone tissue selected is that containing only the small-dimensioned lacunar-canalicular porosity and not the larger-sized vascular porosity. The approximate transversely isotropic poroelastic constants for this level of bone tissue are assumed to be $E_1^m = E_2^m$ = 18.26 GPa, $E_3^m$ = 22.32 GPa, $\nu_{12}^m = \nu_{21}^m$ = 0.332, $\nu_{13}^m = \nu_{23}^m$ = 0.255, $\nu_{31}^m = \nu_{32}^m$ = 0.312, $G_{12}^m$ = 7.28 Gpa, and $G_{13}^m = G_{23}^m$ = 7.6 GPa for the matrix material; $E_1^d = E_2^d$ = 15.17 GPa, $E_3^d$ = 15.96 GPa, $\nu_{12}^d = \nu_{21}^d$ = 0.270, $\nu_{13}^d = \nu_{23}^d$ = 0.270, $\nu_{31}^d = \nu_{32}^d$ = 0.285, $G_{12}^d$ = 5.97 Gpa, and $G_{13}^d = G_{23}^d$ = 6.74 GPa for the drained elastic constants. The lacunar-canalicular intrinsic permeability is taken to be $k$ = 2 x $10^{-20}$ $m^2$. The lacunar-canalicular porosity, $\phi$, is 0.05, the compressibility of water is $K^f$ = 2.3 Gpa, and the viscosity of water $\mu$ = 1 centi-Poise (cP) = 0.01 poise = 0.01 dyne-s/$cm^2$. In Figure 9.9 the stress levels in the bone tissue for three different strain-rates — 3.85 x $10^{-4}$ (1/s), 1.92 x $10^{-4}$(1/s), and 0.962 x $10^{-4}$(1/s) — and for rise time $t_o$ of 1.3 s are shown. The strains produced in the poroelastic solid at $t_o$ = 1.3 s as a result of applying these three strain-rates are, respectively, 5 x $10^{-4}$, 2.5 x $10^{-4}$, and 1.25 x $10^{-4}$. In all three cases, Figure 9.9 shows that the compressible model predicts a slight nonlinear increase in stress, with increasing time, after straining stops at $t_o$. On the other hand, the incompressible model pre-

dicts relaxation of stress after rise time $t_o$ of 1.3 s. In these and all other cases examined, as the stress relaxation proceeds, the stress in the incompressible case approaches the value of stress for the compressible solid.

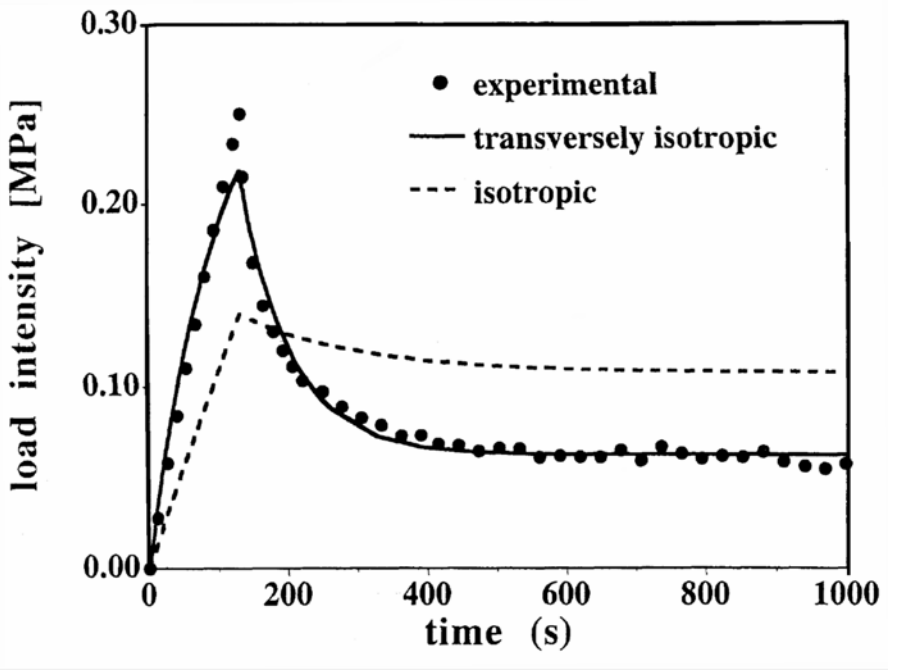



**Figure 9.8**. A typical stress relaxation time history in an unconfined compression test in response to a ramped displacement. The ramped displacement is $\epsilon(t) = (0.13/131)[th(t) - (t - 131)h(t - 131)]$, or 10% compressive strain at 131 seconds. The plots are curve fits of the same data to both isotropic and transversely isotropic models. Reprinted with permission from Cohen et al. (1998).

In order to illustrate the effect of varying the porosity, the data for the bone containing the lacunar-canalicular porosity was plotted again (Figure 9.10) for the same poroelastic and ramp-loading parameters, but with a changed porosity of $\phi = 0.55$. (This value of $\phi$ is unrealistic for the tissue considered, but its use is effective for illustrating the effect of varying the porosity.) The stress levels predicted by the incompressible constituent model were always greater than or equal to those predicted by the compressible constituent model when the porosity is 0.05 (Figure 9.9); however, the situation is reversed when the porosity is 0.55 (Figure 9.10). All of the plots in Figure 9.10 show stress relaxation in the period following rise time $t_o$; however, the peak values of stress predicted for the compressible case are more than twice the poroelastic solid with incompressible constituents. For values of $\phi$ between 0.05 and 0.55 (or higher) the trend suggested by Figures 9.9 and 9.10 continues smoothly, showing that the compressible model is very sensitive to the value of the porosity in the poroelastic material.

**Problems**

9.11.1. Prove formula $u(1,\infty) = \nu^d b\varepsilon_o$, which appears in the text of Example 9.11.1 and in Table 9.3, for displacement of the external boundary of a disk-shaped specimen in unconfined

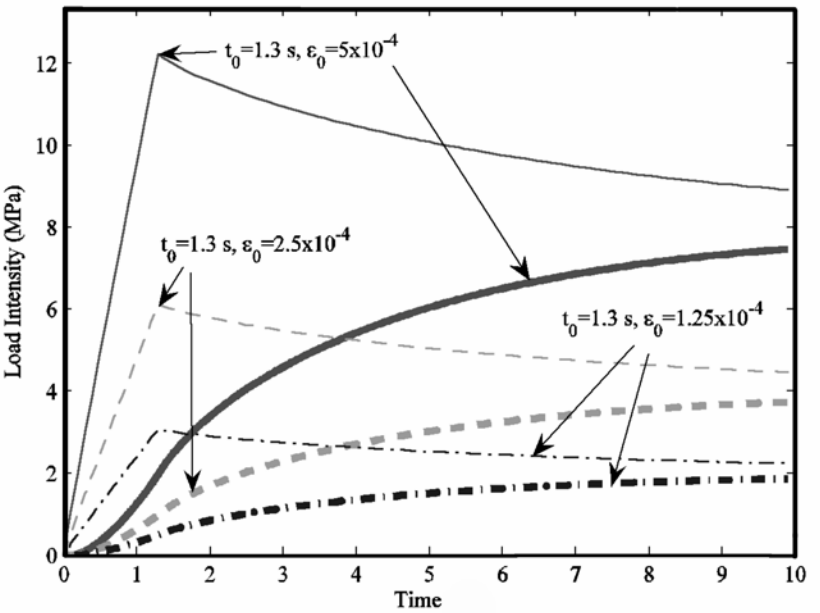



**Figure 9.9**. Typical stress relaxation time history in an unconfined compression test in response to a ramped displacement for a poroelastic solid with compressible constituents (thick solid, dashed, and dash-dotted lines) and a poroelastic solid with incompressible constituents (thin solid, dashed, and dash-dotted lines) for a porosity of $\phi = 0.05$. In each case, the solids are strained at three different rates: 3.85 x $10^{-4}$ (1/s), 1.92 x $10^{-4}$ (1/s), and 0.962 x $10^{-4}$ (1/s) until $t_0 = 1.3$ s, at which time the strains produced in the solid are 5 x $10^{-4}$, 2.5 x $10^{-4}$, and 1.25 x $10^{-4}$, respectively. In all three cases, the compressible model predicts a slight nonlinear increase in stress, with increasing time, after straining stops at $t_0$. On the other hand, the incompressible model predicts relaxation of the stress after the rise time $t_0$ of 1.3 s. As stress relaxation proceeds, the stress in the incompressible case approaches the value of stress for the compressible solid.

compression, subjected to a Heaviside step loading at $t = 0$, as time becomes great. The material of the disk is assumed to be isotropic and incompressible. Proof of this result requires only the use of Hooke's law.

## 9.12. RELEVANT LITERATURE

There is only one text on poroelasticity, Coussy (1995), but there is much related material in Bear (1972). There is also a book on the very interesting historical development of the theory, de Boer (2000), which also presents a noteworthy presentation of the theory. The presentation of poroelasticity in this chapter was taken from the following papers: Biot (1941), Rice and Cleary (1976), Rudnicki (1985), Thompson and Willis (1991), Cowin (2002), and the excellent summary of Detournay and Cheng (1993). The particular development of anisotropic poroelasticity followed here, and the solution of the problem of the unconfined compression of a porous saturated disk in §9.11, are from Cowin and Mehrabadi (2006). In these papers the proofs omitted in this chapter, as well as some technical restrictions or assumptions underlying those proofs, are documented. The exception to the inclusion of proofs occurred at the end of §9.2.

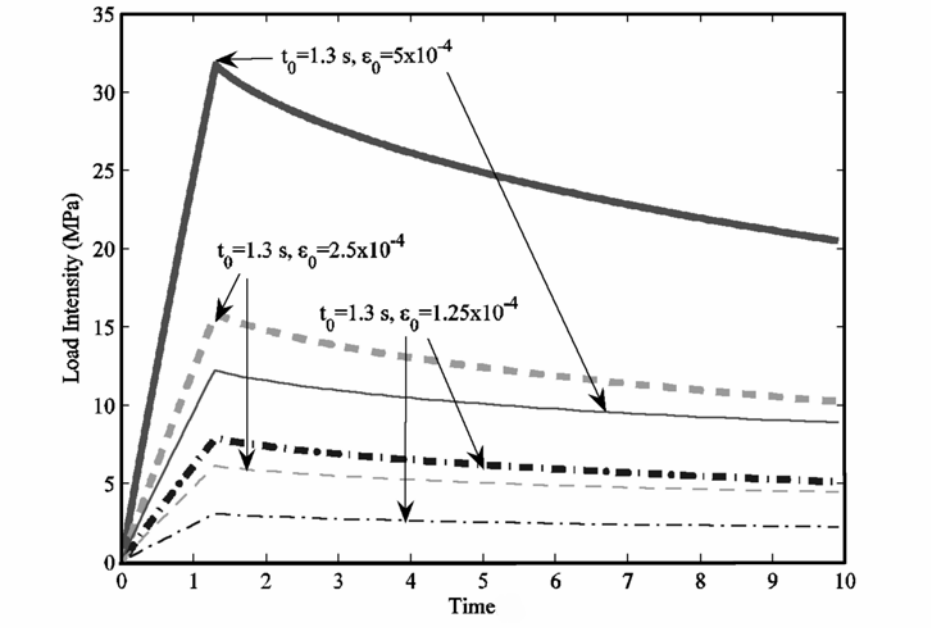



**Figure 9.10**. A typical stress relaxation time history in an unconfined compression test in response to a ramped displacement for a poroelastic solid with compressible constituents (thick solid, dashed, and dotted lines) and a poroelastic solid with incompressible constituents (thin solid, dashed, and dotted lines) for a porosity of $\phi$ = 0.55. In each case, the solids are strained at three different rates: 3.85 x $10^{-4}$ (1/s), 1.92 x $10^{-4}$ (1/s), and 0.962 x $10^{-4}$ (1/s) until $t_0$ = 1.3 s, at which time the strains produced in the solid are 5 x $10^{-4}$, 2.5 x $10^{-4}$, and 1.25 x $10^{-4}$, respectively. The peak values of stress induced in the compressible case are predicted to be more than twice the incompressible case.

The proof included was derivation of formula (9.3) for *Biot effective stress coefficient tensor* $\hat{\mathbf{A}}$ . This formula has an interesting history. It was suggested by Geertsma (1957) and by Skempton (1961), then proved with increasing generality by Nur and Byerlee (1971), Carroll (1979), and Thompson and Willis (1991). The material in this paragraph follows the elegant derivation of the formula by Nur and Byerlee (1971) in the isotropic case and by Carroll (1979) for the anisotropic case.

The problems described in §§9.10 and 9.11 were taken from Detournay and Cheng (1993), Armstrong et al. (1984), Cohen et al. (1998), and Cowin and Mehrabadi (2006).

## References

Armstrong GC, Lai WM, Mow VC. 1984. An analysis of the unconfined compression of articular cartilage. *J Biomech Eng* **106**:165–173.

Bear J. 1972. *Dynamics of fluids in porous media*. New York: Elsevier.

Biot MA. 1941. General theory of three-dimensional consolidation. *J Appl Phys* **12**:155–164.

Carroll MM. 1979. An effective stress law for anisotropic elastic deformation. *J Geophys Res* **84**:7510–7512.

Cohen, B, Lai, WM, Mow VC. 1998. A transversely isotropic biphasic model for unconfined compression of growth plate and chondroepiphysis. *J Biomech Eng* **120**:491–496.

Coussy O. 1995. *Mechanics of porous continua*. New York: Wiley.

Cowin SC. 2003. A recasting of anisotropic poroelasticity in matrices of tensor components. *Transport Porous Media* **50**:35–56.

Cowin SC. 2004. Anisotropic poroelasticity: fabric tensor formulation. *Mech Mater* **36**:665–677.

Cowin SC, Mehrabadi MM. 2006. Compressible and incompressible constituents in anisotropic poroelasticity: the problem of unconfined compression of a disk. *J Mech Phys Solids*. In press.

de Boer R. 2000. *Theory of porous media*. Berlin: Springer.

Detournay E, Cheng H-DA. 1993. Fundamentals of poroelasticity. In *Comprehensive rock engineering: principles, practice and projects*. ed. JA Hudson, pp. 113–171. Oxford: Pergamon.

Geertsma J. 1957. The effect of fluid pressure decline on volumetric changes of porous rocks. *J Appl Mech* **24**:594–601.

Kachanov M. 1999. Solids with cracks and non-spherical pores: proper parameters of defect density and effective elastic properties. *Int J Fracture* **97**:1–32.

Nur A, Byerlee JD. 1971. An exact effective stress law for elastic deformation of rock with fluids. *J Geophys Res* **76**:6414.

Rice JR, Cleary MP. 1976. Some basic stress diffusion solutions for fluid-saturated elastic porous media with compressible constituents. *Rev Geophys Space Phys* **14**:227–241.

Rudnicki JW. 1985. Effect of pore fluid diffusion on deformation and failure of rock. In *Mechanics of geomaterials*, ed. Z Bazant, pp. 315–347. New York: Wiley.

Shafiro B, Kachanov M. 1997. Materials with fluid filled pores of various shapes: effective elastic properties and fluid pressure polarization. *Int J Solids Struct* 34:3517–3540.

Skempton AW. 1954. The pore pressure coefficients A and B. *Géotechnique* **4**:143–147.

Skempton AW. 1961. Effective stress in soils, concrete and rock. In *Pore pressure and suction in soils*, pp. 4–16. Butterworths, London.

Sevostianov I, Kachanov M. 2001. Author's response. *J Biomech* **34**:709–710.

Thompson M, Willis JR. 1991. A reformation of the equations of anisotropic poroelasticity. *J Appl Mech* **58**:612–616.

Thomson WT. 1960. *Laplace transformation*, 2nd ed. Engelwood Cliffs, NJ: Prentice-Hall.

APPENDIX

# MATRICES AND TENSORS

## A.1. INTRODUCTION AND RATIONALE

The purpose of this appendix is to present the notation and most of the mathematical techniques that are used in the body of the text. The audience is assumed to have been through several years of college-level mathematics, which included the differential and integral calculus, differential equations, functions of several variables, partial derivatives, and an introduction to linear algebra. Matrices are reviewed briefly, and determinants, vectors, and tensors of order two are described. The application of this linear algebra to material that appears in undergraduate engineering courses on mechanics is illustrated by discussions of concepts like the area and mass moments of inertia, Mohr's circles, and the vector cross and triple scalar products. The notation, as far as possible, will be a matrix notation that is easily entered into existing symbolic computational programs like Maple, Mathematica, Matlab, and Mathcad. The desire to represent the components of three-dimensional fourth-order tensors that appear in anisotropic elasticity as the components of six-dimensional second-order tensors and thus represent these components in matrices of tensor components in six dimensions leads to the nontraditional part of this appendix. This is also one of the nontraditional aspects in the text of the book, but a minor one. This is described in §A.11, along with the rationale for this approach.

## A.2. DEFINITION OF SQUARE, COLUMN, AND ROW MATRICES

An $r$-by-$c$ matrix, **M,** is a rectangular array of numbers consisting of $r$ rows and $c$ columns:

$$\mathbf{M} = \begin{bmatrix} M_{11} & M_{12} & . & . & . & M_{1c} \\ M_{21} & M_{22} & . & . & . & M_{2c} \\ . & . & . & . & . & . \\ M_{r1} & . & . & . & . & M_{rc} \end{bmatrix}. \tag{A1}$$

The typical element of the array, $M_{ij}$, is the $i$th element in the $j$th column; in this text elements $M_{ij}$ will be real numbers or functions whose values are real numbers. The transpose of matrix **M** is denoted by $\mathbf{M}^{\mathrm{T}}$ and is obtained from **M** by interchanging the rows and columns:

$$\mathbf{M}^{T} = \begin{bmatrix} M_{11} & M_{21} & . & . & . & M_{r1} \\ M_{12} & M_{22} & . & . & . & M_{r2} \\ . & . & . & . & . & . \\ M_{1c} & . & . & . & . & M_{rc} \end{bmatrix}. \tag{A2}$$

The operation of obtaining $\mathbf{M}^T$ from $\mathbf{M}$ is called transposition. In this text we are interested in special cases of $r$-by-$c$ matrix $\mathbf{M}$. These special cases are those of the square matrix, $r = c = n$, the case of the row matrix, $r = 1$, $c = n$, and the case of the column matrix, $r = n$, $c = 1$. Further, the special subcases of interest are $n = 2$, $n = 3$, and $n = 6$; subcase $n = 1$ reduces all three special cases to the trivial situation of a single number or scalar. Square matrix $\mathbf{A}$ has the form

$$\mathbf{A} = \begin{bmatrix} A_{11} & A_{12} & . & . & . & A_{1n} \\ A_{21} & A_{22} & . & . & . & A_{2n} \\ . & . & . & . & . & . \\ A_{n1} & . & . & . & . & A_{nn} \end{bmatrix}, \tag{A3}$$

while row and column matrices $\mathbf{r}$ and $\mathbf{c}$ have the forms

$$\mathbf{r} = \begin{bmatrix} r_1 & r_2 & . & . & . & r_n \end{bmatrix}, \quad \mathbf{c} = \begin{bmatrix} c_1 \\ c_2 \\ . \\ . \\ . \\ c_n \end{bmatrix}, \tag{A4}$$

respectively. The transpose of a column matrix is a row matrix, and thus

$$\mathbf{c}^T = \begin{bmatrix} c_1 & c_2 & . & . & . & c_n \end{bmatrix}. \tag{A5}$$

To save space in books and papers, the form of $\mathbf{c}$ in (A5) is used more frequently than the form in the second of (A4). Wherever possible, square matrices will be denoted by upper-case boldface Latin letters, while row and column matrices will be denoted by lower-case boldface Latin letters, as is the case in eqs. (A3) and (A4).

## A.3. THE TYPES AND ALGEBRA OF SQUARE MATRICES

The elements of square matrix $\mathbf{A}$ given by (A3) for which the row and column indices are equal, namely elements $A_{11}, A_{22}, \ldots, A_{nn}$, are called diagonal elements. A matrix with only diagonal elements is called a diagonal matrix:

$$\mathbf{A} = \begin{bmatrix} A_{11} & 0 & . & . & . & 0 \\ 0 & A_{22} & . & . & . & 0 \\ . & . & . & . & . & . \\ 0 & . & . & . & . & A_{nn} \end{bmatrix}. \tag{A6}$$

The sum of the diagonal elements of a matrix is a scalar called the trace of the matrix and, for matrix $\mathbf{A}$, it is denoted by tr$\mathbf{A}$:

$$\text{tr}\mathbf{A} = A_{11} + A_{22} + \ldots + A_{nn}. \tag{A7}$$

If the trace of a matrix is zero, the matrix is said to be traceless. Note also that tr$\mathbf{A}$ = tr$\mathbf{A}^T$.

The zero and the unit matrix, **0** and **1**, respectively, constitute the null element, the 0, and the unit element, the 1, in the algebra of square matrices. The zero matrix is a matrix whose every element is zero and the unit matrix is a diagonal matrix whose diagonal elements are all one:

$$\mathbf{0} = \begin{bmatrix} 0 & 0 & . & . & . & 0 \\ 0 & 0 & . & . & . & 0 \\ . & . & . & . & . & . \\ 0 & . & . & . & . & 0 \end{bmatrix}, \quad \mathbf{1} = \begin{bmatrix} 1 & 0 & . & . & . & 0 \\ 0 & 1 & . & . & . & 0 \\ . & . & . & . & . & . \\ 0 & . & . & . & . & 1 \end{bmatrix}. \tag{A8}$$

A special symbol, the Kronecker delta, $\delta_{ij}$, is introduced to represent the components of the unit matrix. When $i = j$ the value of the Kronecker delta is 1, $\delta_{11} = \delta_{22} = \ldots = \delta_{nn} = 1$, and when $i \neq j$ the value of the Kronecker delta is 0, $\delta_{12} = \delta_{21} = \ldots = \delta_{n1} = \delta_{1n} = 0$. Multiplication of matrix **A** by a scalar is defined as multiplication of every element of matrix **A** by scalar $\alpha$; thus,

$$\alpha\mathbf{A} \equiv \begin{bmatrix} \alpha A_{11} & \alpha A_{12} & . & . & . & \alpha A_{1n} \\ \alpha A_{21} & \alpha A_{22} & . & . & . & \alpha A_{2n} \\ . & . & . & . & . & . \\ \alpha A_{n1} & . & . & . & . & \alpha A_{nn} \end{bmatrix}. \tag{A9}$$

It is then easy to show that $1\mathbf{A} = \mathbf{A}$, $-1\mathbf{A} = -\mathbf{A}$, $0\mathbf{A} = \mathbf{0}$, and $\alpha\mathbf{O} = \mathbf{0}$.The addition of square matrices is defined only for matrices with the same number of rows (or columns). The sum of two matrices, **A** and **B**, is denoted by **A + B**, where

$$\mathbf{A} + \mathbf{B} \equiv \begin{bmatrix} A_{11} + B_{11} & A_{12} + B_{12} & . & . & . & A_{1n} + B_{1n} \\ A_{21} + B_{21} & A_{22} + B_{22} & . & . & . & A_{2n} + B_{2n} \\ . & . & . & . & . & . \\ A_{n1} + B_{n1} & . & . & . & . & A_{nn} + B_{nn} \end{bmatrix}. \tag{A10}$$

Matrix addition is commutative and associative,

$$\mathbf{A} + \mathbf{B} = \mathbf{B} + \mathbf{A} \quad \text{and} \quad \mathbf{A} + (\mathbf{B} + \mathbf{C}) = (\mathbf{A} + \mathbf{B}) + \mathbf{C}\,, \tag{A11}$$

respectively. The following distributive laws connect matrix addition and matrix multiplication by scalars:

$$\alpha(\mathbf{A} + \mathbf{B}) = \alpha\mathbf{A} + \alpha\mathbf{B} \quad \text{and} \quad (\alpha + \beta)\mathbf{A} = \alpha\mathbf{A} + \beta\mathbf{A}\,, \tag{A12}$$

where $\alpha$ and $\beta$ are scalars. Negative square matrices may be created by employing the definition of matrix multiplication by scalar (A8) in the special case when $\alpha = -1$. In this case the definition of addition of square matrices (A10) can be extended to include subtraction of square matrices, **A** – **B**.

A matrix for which $\mathbf{B} = \mathbf{B}^{\mathrm{T}}$ is said to be a symmetric matrix, while a matrix for which $\mathbf{C} = -\mathbf{C}^{\mathrm{T}}$ is said to be a skew-symmetric or anti-symmetric matrix. The symmetric and skew-symmetric parts of a matrix, say **A**, are constructed from **A** as follows:

$$\text{symmetric part of } \mathbf{A} \equiv \left(\frac{1}{2}\right)(\mathbf{A} + \mathbf{A}^T)\,, \quad \text{and} \tag{A13}$$

$$\text{skew-symmetric part of } \mathbf{A} \equiv \left(\frac{1}{2}\right)(\mathbf{A} - \mathbf{A}^T)\,. \tag{A14}$$

It is easy to verify that the symmetric part of **A** is a symmetric matrix and that the skew-symmetric part of **A** is a skew-symmetric matrix. The sum of the symmetric part of **A** and the skew-symmetric part of **A** is **A**:

$$\mathbf{A} = \left(\frac{1}{2}\right)(\mathbf{A} + \mathbf{A}^T) + \left(\frac{1}{2}\right)(\mathbf{A} - \mathbf{A}^T). \tag{A15}$$

This result shows that any square matrix can be decomposed into the sum of a symmetric and a skew-symmetric matrix. Using the trace operation introduced above, representation (A15) can be extended to three-way decomposition of matrix **A**:

$$\mathbf{A} = \frac{(\mathrm{tr}\mathbf{A})}{n}\mathbf{1} + \left(\frac{1}{2}\right)\left[(\mathbf{A}+\mathbf{A}^T) - 2\left(\frac{(\mathrm{tr}\mathbf{A})}{n}\right)\right] + \left(\frac{1}{2}\right)(\mathbf{A} - \mathbf{A}^T). \tag{A16}$$

The last term in this decomposition is still the skew-symmetric part of the matrix. The second term is the traceless symmetric part of the matrix, and the first term is simply the trace of the matrix multiplied by the unit matrix.

**Example A.3.1**

Construct the three-way decomposition of matrix **A** given by

$$\mathbf{A} = \begin{bmatrix} 1 & 2 & 3 \\ 4 & 5 & 6 \\ 7 & 8 & 9 \end{bmatrix}.$$

**Solution**: The symmetric and skew-symmetric parts of **A**, as well as the trace of **A** are calculated:

$$\left(\frac{1}{2}\right)(\mathbf{A} + \mathbf{A}^T) = \begin{bmatrix} 1 & 3 & 5 \\ 3 & 5 & 7 \\ 5 & 7 & 9 \end{bmatrix}, \ \left(\frac{1}{2}\right)(\mathbf{A} - \mathbf{A}^T) = \begin{bmatrix} 0 & -1 & -2 \\ 1 & 0 & -1 \\ 2 & 1 & 0 \end{bmatrix}, \ \mathrm{tr}\mathbf{A} = 15;$$

then, since $n = 3$, it follows from (A16) that

$$\mathbf{A} = \begin{bmatrix} 5 & 0 & 0 \\ 0 & 5 & 0 \\ 0 & 0 & 5 \end{bmatrix} + \begin{bmatrix} -4 & 3 & 5 \\ 3 & 0 & 7 \\ 5 & 7 & 4 \end{bmatrix} + \begin{bmatrix} 0 & -1 & -2 \\ 1 & 0 & -1 \\ 2 & 1 & 0 \end{bmatrix}.$$

Introducing the notation for the deviatoric part of $n$-by-$n$ square matrix **A**,

$$\mathrm{dev}\mathbf{A} = \mathbf{A} - \frac{(\mathrm{tr}\mathbf{A})}{n}\mathbf{1}, \tag{A17}$$

the representation for matrix **A** given by (A16) may be rewritten as

$$\mathbf{A} = \mathbf{H} + \mathbf{D} + \mathbf{S}, \tag{A18}$$

where **H** is called the hydrostatic component, **D** is called the deviatoric component, and **S** is the skew-symmetric component,

$$\mathbf{H} = \frac{(\mathrm{tr}\mathbf{A})}{n}\mathbf{1}, \quad \mathbf{D} = \left(\frac{1}{2}\right)(\mathrm{dev}\mathbf{A} + \mathrm{dev}\mathbf{A}^{\mathrm{T}}), \quad \mathbf{S} = \left(\frac{1}{2}\right)(\mathbf{A} - \mathbf{A}^{\mathrm{T}}). \tag{A19}$$

**Example A.3.2**

Show that tr(dev**A**) = 0.

**Solution**: Applying the trace operation to both sides of (A17), one obtains tr(dev**A**) = tr**A** – (1/*n*)tr**A** tr**1**; then, since tr**1** = *n*, it follows that tr(dev**A**) = 0.

The product of two square matrices, **A** and **B**, with equal numbers of rows (columns) is a square matrix with the same number of rows (columns). The matrix product is written as **A**·**B** where **A**·**B** is defined by

$$(\mathbf{A}\cdot\mathbf{B})_{ij} = \sum_{k=1}^{k=n} A_{ik}B_{kj}\ ; \tag{A20}$$

thus, for example, the element in the *r*th row and *c*th column of product **A**·**B** is given by

$$(\mathbf{A}\cdot\mathbf{B})_{rc} = A_{r1}B_{1c} + A_{r2}B_{2c} + ... + A_{rn}B_{nc}\ .$$

The dot inside matrix product **A**·**B** indicates that one index from **A** and one index from **B** are to be summed over. The positioning of the summation index on the two matrices involved in a matrix product is critical and is reflected in the matrix notation by the transpose. In the three equations below, (A21), study carefully how the positions of the summation indices within the summation sign change in relation to the position of the transpose on the matrices in the associated matrix product:

$$(\mathbf{A}\cdot\mathbf{B}^T)_{ij} = \sum_{k=1}^{k=n} A_{ik}B_{jk},\ \ (\mathbf{A}^T\cdot\mathbf{B})_{ij} = \sum_{k=1}^{k=n} A_{ki}B_{kj},\ \ (\mathbf{A}^T\cdot\mathbf{B}^T)_{ij} = \sum_{k=1}^{k=n} A_{ki}B_{jk}\ . \tag{A21}$$

A widely used notational convention, called the Einstein summation convention, drops the summation symbol in (A20) and writes

$$(\mathbf{A}\cdot\mathbf{B})_{ij} = A_{ik}B_{kj}\,, \tag{A22}$$

where the convention is the understanding that the repeated index, *k*, is to be summed over its *range* of admissible values from 1 to *n*. For *n* = 6, the range of admissible values is 1 to 6, including 2, 3, 4, and 5. The two *k* indices are the *summation* or *dummy* indices. A summation index is defined as an index that occurs in a summand twice and only twice. Note that *summands* are terms in equations separated from each other by plus, minus, or equal signs. The existence of summation indices in a summand requires that the summand be summed with respect to those indices over the entire range of admissible values. Note that the summation index is only a means of stating that a term must be summed, and the letter used for this index is immaterial; thus $A_{im}B_{mj}$ has the same meaning as $A_{ik}B_{kj}$. The other indices in formula (A22), the *i* and *j* indices, are called free indices. A free index is *free* to take on any one of its *range* of admissible values from 1 to *n*. For example, if n were 3, the free index could be 1, 2 or 3. A *free* index is formally defined as an index that occurs once and only once in every summand of an equation. A free index may take on any or all of its *admissible values*; the total number of equations that may be represented by an equation with one free index is the range of admissible values. Thus, equation (A22) represents $n^2$ separate equations. For two 2-by-2 matrices **A** and **B**, the product is written as

$$\mathbf{A}\cdot\mathbf{B} = \begin{bmatrix} A_{11} & A_{12} \\ A_{21} & A_{22} \end{bmatrix}\begin{bmatrix} B_{11} & B_{12} \\ B_{21} & B_{22} \end{bmatrix} = \begin{bmatrix} A_{11}B_{11} + A_{12}B_{21} & A_{11}B_{12} + A_{12}B_{22} \\ A_{21}B_{11} + A_{22}B_{21} & A_{21}B_{12} + A_{22}B_{22} \end{bmatrix}, \tag{A23}$$

where, in this case, products (A20) and (A22) stand for $n^2 = 2^2 = 4$ separate equations, the right-hand sides of which are the four elements of the last matrix in (A23).

A very significant feature of matrix multiplication is noncommutativity, that is to say, $\mathbf{A}\cdot\mathbf{B} \neq \mathbf{B}\cdot\mathbf{A}$. Note, for example, that transposed product $\mathbf{B}\cdot\mathbf{A}$ of the multiplication represented in (A23),

$$\mathbf{B}\cdot\mathbf{A} = \begin{bmatrix} B_{11} & B_{12} \\ B_{21} & B_{22} \end{bmatrix}\begin{bmatrix} A_{11} & A_{12} \\ A_{21} & A_{22} \end{bmatrix} = \begin{bmatrix} B_{11}A_{11} + B_{12}A_{21} & B_{11}A_{12} + B_{12}A_{22} \\ B_{21}A_{11} + B_{22}A_{21} & B_{21}A_{12} + B_{22}A_{22} \end{bmatrix}, \tag{A24}$$

is an illustration of the fact that $\mathbf{A}\cdot\mathbf{B} \neq \mathbf{B}\cdot\mathbf{A}$, in general. If $\mathbf{A}\cdot\mathbf{B} = \mathbf{B}\cdot\mathbf{A}$, matrices $\mathbf{A}$ and $\mathbf{B}$ are said to commute. Finally, matrix multiplication is associative:

$$\mathbf{A}\cdot(\mathbf{B}\cdot\mathbf{C}) = (\mathbf{A}\cdot\mathbf{B})\cdot\mathbf{C}\,, \tag{A25}$$

and matrix multiplication is distributive with respect to addition:

$$\mathbf{A}\cdot(\mathbf{B}+\mathbf{C}) = \mathbf{A}\cdot\mathbf{B} + \mathbf{A}\cdot\mathbf{C} \quad \text{and} \quad (\mathbf{B}+\mathbf{C})\cdot\mathbf{A} = \mathbf{B}\cdot\mathbf{A} + \mathbf{C}\cdot\mathbf{A}\,, \tag{A26}$$

provided the results of these operations are defined.

**Example A.3.3**

Construct products $\mathbf{A}\cdot\mathbf{B}$ and $\mathbf{B}\cdot\mathbf{A}$ of matrices $\mathbf{A}$ and $\mathbf{B}$ given by

$$\mathbf{A} = \begin{bmatrix} 1 & 2 & 3 \\ 4 & 5 & 6 \\ 7 & 8 & 9 \end{bmatrix}, \quad \mathbf{B} = \begin{bmatrix} 10 & 11 & 12 \\ 13 & 14 & 15 \\ 16 & 17 & 18 \end{bmatrix}.$$

**Solution**: Products $\mathbf{A}\cdot\mathbf{B}$ and $\mathbf{B}\cdot\mathbf{A}$ are given by

$$\mathbf{A}\cdot\mathbf{B} = \begin{bmatrix} 84 & 90 & 96 \\ 201 & 216 & 231 \\ 318 & 342 & 366 \end{bmatrix}, \quad \mathbf{B}\cdot\mathbf{A} = \begin{bmatrix} 138 & 171 & 204 \\ 174 & 216 & 258 \\ 210 & 261 & 312 \end{bmatrix}.$$

Observe that $\mathbf{A}\cdot\mathbf{B} \neq \mathbf{B}\cdot\mathbf{A}$.

The colon or double dot notation between the two second-order tensors is an extension of the single dot notation between the matrices, $\mathbf{A}\cdot\mathbf{B}$, and indicates that one index from $\mathbf{A}$ and one index from $\mathbf{B}$ are to be summed over; the double dot notation between the matrices, $\mathbf{A}:\mathbf{B}$, indicates that both indices of $\mathbf{A}$ are to be summed with different indices from $\mathbf{B}$, and thus

$$\mathbf{A}:\mathbf{B} \equiv \sum_{i=1}^{1=n}\sum_{k=1}^{k=n} A_{ik}B_{ki}\,.$$

This colon notation stands for the same operation as the trace of the product, $\mathbf{A}:\mathbf{B} = \text{tr}(\mathbf{A}\cdot\mathbf{B})$. Although $\text{tr}(\mathbf{A}\cdot\mathbf{B})$ and $\mathbf{A}:\mathbf{B}$ mean the same thing, $\mathbf{A}:\mathbf{B}$ involves fewer characters and it will be the notation of choice. Note that $\mathbf{A}:\mathbf{B} = \mathbf{A}^{\mathrm{T}}:\mathbf{B}^{\mathrm{T}}$ and $\mathbf{A}^{\mathrm{T}}:\mathbf{B} = \mathbf{A}:\mathbf{B}^{\mathrm{T}}$ but that $\mathbf{A}:\mathbf{B} \neq \mathbf{A}^{\mathrm{T}}:\mathbf{B}$ in general.

In the considerations of mechanics, matrices are often functions of coordinate positions $x_1$, $x_2$, $x_3$ and time $t$. In this case the matrix is written $\mathbf{A}(x_1, x_2, x_3, t)$, which means that each element of $\mathbf{A}$ is a function of $x_1$, $x_2$, $x_3$ and $t$:

$$\mathbf{A}(x_1,x_2,x_3,t)=$$

$$\begin{bmatrix} A_{11}(x_1,x_2,x_3,t) & A_{12}(x_1,x_2,x_3,t) & . \ . \ . & A_{1n}(x_1,x_2,x_3,t) \\ A_{21}(x_1,x_2,x_3,t) & A_{22}(x_1,x_2,x_3,t) & . \ . \ . & A_{2n}(x_1,x_2,x_3,t) \\ . & . & . \ . \ . & . \\ A_{n1}(x_1,x_2,x_3,t) & . & . \ . \ . & A_{nn}(x_1,x_2,x_3,t) \end{bmatrix}. \tag{A27}$$

Let operator $\Diamond$ stand for a total derivative, or a partial derivative with respect to $x_1$, $x_2$, $x_3$, or $t$, or a definite or indefinite (single or multiple) integral; then the operation of the operator on the matrix follows the same rule as multiplication of a matrix by a scalar (A9); thus,

$$\Diamond\mathbf{A}(x_1,x_2,x_3,t)=$$

$$\begin{bmatrix} \Diamond A_{11}(x_1,x_2,x_3,t) & \Diamond A_{12}(x_1,x_2,x_3,t) & . \ . \ . & \Diamond A_{1n}(x_1,x_2,x_3,t) \\ \Diamond A_{21}(x_1,x_2,x_3,t) & \Diamond A_{22}(x_1,x_2,x_3,t) & . \ . \ . & \Diamond A_{2n}(x_1,x_2,x_3,t) \\ . & . & . \ . \ . & . \\ \Diamond A_{n1}(x_1,x_2,x_3,t) & . & . \ . \ . & \Diamond A_{nn}(x_1,x_2,x_3,t) \end{bmatrix}. \tag{A28}$$

The following distributive laws connect matrix addition and operator operations:

$$\Diamond(\mathbf{A}+\mathbf{B})=\Diamond\mathbf{B}+\Diamond\mathbf{A} \ \text{ and } \ (\Diamond_1+\Diamond_2)\mathbf{A}=\Diamond_1\mathbf{A}+\Diamond_2\mathbf{A}\,, \tag{A29}$$

where $\Diamond_1$ and $\Diamond_2$ are two different operators.

**Problems**

A.3.1. Simplify the following expression by using the summation index convention:

$$0=r_1w_1+r_2w_2+r_3w_3\,,$$

$$\psi=(u_1v_1+u_2v_2+u_3v_3)(u_1v_1+u_2v_2+u_3v_3)\,,$$

$$\phi=A_{11}x_1^2+A_{12}x_1x_2+A_{21}x_2x_1+A_{13}x_1x_3+A_{31}x_3x_1 +A_{22}x_2^2+A_{32}x_3x_2+A_{23}x_2x_3+A_{33}x_3^2.$$

A.3.2. Matrix **M** has the numbers 4, 5, –5 in its first row, –1, 3, –1 in its second row, and 7, 1, 1 in its third row. Find the transpose of **M**, the symmetric part of **M**, and the skew-symmetric part of **M**.

A.3.3. Prove that $\partial x_i/\partial x_j=\delta_{ij}$.

A.3.4. Consider hydrostatic component **H**, deviatoric component **D,** and skew-symmetric component **S** of square *n*-by-*n* matrix **A** defined by (A17) and (A18). Evaluate the following: tr**H**, tr**D**, tr**S**, tr(**H**·**D**) = **H:D**, tr(**H**·**S**) = **H:S**, and tr(**S**·**D**) = **S:D**.

A.3.5. For the matrices in Example A3.3 show that tr**A**·**B** = tr**B**·**A** = 666. In general, will **A:B** = **B:A**, or is this a special case?

A.3.6. Prove that **A:B** is zero if **A** is symmetric and **B** is skew-symmetric.

A.3.7. Calculate $\mathbf{A}^{\mathrm{T}}\cdot\mathbf{B}$, $\mathbf{A}\cdot\mathbf{B}^{\mathrm{T}}$ and $\mathbf{A}^{\mathrm{T}}\cdot\mathbf{B}^{\mathrm{T}}$ for matrices **A** and **B** of Example A.3.3.

A.3.8. Find the derivative of matrix $\mathbf{A}(t)$ with respect to $t$:

$$\mathbf{A}(t)=\begin{bmatrix} t & t^2 & \sin\omega t \\ \cosh t & \ln t & 17t \\ 1/t & 1/t^2 & \ln t^2 \end{bmatrix}.$$

A.3.9. Show that $(\mathbf{A}\cdot\mathbf{B})^T = \mathbf{B}^T\cdot\mathbf{A}^T$.
A.3.10. Show that $(\mathbf{A}\cdot\mathbf{B}\cdot\mathbf{C})^T = \mathbf{C}^T\cdot\mathbf{B}^T\cdot\mathbf{A}^T$.

## A.4. THE ALGEBRA OF *N*-TUPLES

The algebra of column matrices is the same as the algebra of row matrices. The column matrices need only be transposed to be equivalent to row matrices, as illustrated in eqs. (A3) and (A4). A phrase that describes both row and column matrices is *n*-tuples. This phrase will be used here because it is descriptive and inclusive. A zero *n*-tuple is an *n*-tuple whose entries are all zero; it is denoted by $\mathbf{0} = [0, 0, \ldots, 0]$. The multiplication of *n*-tuple **r** by scalar $\alpha$ is defined as multiplication of every element of *n*-tuple **r** by scalar $\alpha$, and thus $\alpha\mathbf{r} = [\alpha r_1, \alpha r_2, \ldots, \alpha r_n]$. As with square matrices, it is then easy to show for *n*-tuples that $1\mathbf{r} = \mathbf{r}$, $-1\mathbf{r} = -\mathbf{r}$, $0\mathbf{r} = \mathbf{0}$, and $\alpha\mathbf{0} = \mathbf{0}$. Addition of *n*-tuples is only defined for *n*-tuples with the same *n*. The sum of two *n*-tuples, **r** and **t**, is denoted by $\mathbf{r} + \mathbf{t}$, where $\mathbf{r} + \mathbf{t} = [r_1 + t_1, r_2 + t_2, \ldots, r_n + t_n]$. Row-matrix addition is commutative, $\mathbf{r} + \mathbf{t} = \mathbf{t} + \mathbf{r}$, and associative, $\mathbf{r} + (\mathbf{t} + \mathbf{u}) = (\mathbf{r} + \mathbf{t}) + \mathbf{u}$. The following distributive laws connect *n*-tuple addition and *n*-tuple multiplication by scalars; thus, $\alpha(\mathbf{r} + \mathbf{t}) = \alpha\mathbf{r} + \alpha\mathbf{t}$ and $(\alpha + \beta)\mathbf{r} = \alpha\mathbf{r} + \beta\mathbf{r}$, where $\alpha$ and $\beta$ are scalars. Negative *n*-tuples may be created by employing the definition of *n*-tuple multiplication by a scalar, $\alpha\mathbf{r} = [\alpha r_1, \alpha r_2, \ldots, \alpha r_n]$, in the special case when $\alpha = -1$. In this case the definition of addition of *n*-tuples, $\mathbf{r} + \mathbf{t} = [r_1 + t_1, r_2 + t_2, \ldots, r_n + t_n]$, can be extended to include subtraction of *n*-tuples, $\mathbf{r} - \mathbf{t}$, and the difference between *n*-tuples, $\mathbf{r} - \mathbf{t}$.

Two *n*-tuples may be employed to create a square matrix. The square matrix formed from **r** and **t** is called the *open* product of n-tuples **r** and **t**; it is denoted by $\mathbf{r} \otimes \mathbf{t}$, and defined by

$$\mathbf{r}\otimes\mathbf{t} = \begin{bmatrix} r_1t_1 & r_1t_2 & . & . & . & r_1t_n \\ r_2t_1 & r_2t_2 & . & . & . & r_2t_n \\ . & . & . & . & . & . \\ r_nt_1 & . & . & . & . & r_nt_n \end{bmatrix}. \tag{A30}$$

The American physicist J. Willard Gibbs introduced the concept of the open product of vectors, calling the product a *dyad*. This terminology is still used in some books, and the notation is spoken of as the *dyadic* notation. The trace of this square matrix, $\mathrm{tr}\{\mathbf{r} \otimes \mathbf{t}\}$ is the scalar product of **r** and **t**:

$$tr\{\mathbf{r}\otimes\mathbf{t}\} = \mathbf{r}\cdot\mathbf{t} = r_1t_1 + r_2t_2 + \ldots + r_nt_n\,. \tag{A31}$$

In the special case of $n = 3$, the skew-symmetric part of open product $\mathbf{r}\otimes\mathbf{t}$,

$$\frac{1}{2}\begin{bmatrix} 0 & r_1t_2 - r_2t_1 & r_1t_3 - r_3t_1 \\ r_2t_1 - r_1t_2 & 0 & r_2t_3 - r_3t_2 \\ r_3t_1 - r_1t_3 & r_3t_2 - r_2t_3 & 0 \end{bmatrix}, \tag{A32}$$

provides the components of the cross product of **r** and **t**, denoted by **r** x **t**, and written as $\mathbf{r} \times \mathbf{t} = [r_2t_3 - r_3t_2, r_3t_1 - r_1t_3, r_1t_2 - r_2t_1]$. These points concerning dot product $\mathbf{r}\cdot\mathbf{t}$ and cross product **r** x **t** will be revisited later in this Appendix.

**Example A.4.1**

Given *n*-tuples $\mathbf{a} = [1, 2, 3]$ and $\mathbf{b} = [4, 5, 6]$, construct open product matrix $\mathbf{a}\otimes\mathbf{b}$, the skew-symmetric part of the open product matrix, and trace of the open product matrix.

**Solution**:

$$\mathbf{a}\otimes\mathbf{b}=\begin{bmatrix}4 & 5 & 6\\ 8 & 10 & 12\\ 12 & 15 & 18\end{bmatrix},\quad \left(\frac{1}{2}\right)(\mathbf{a}\otimes\mathbf{b}-\mathbf{a}\otimes\mathbf{b}^{T})=\left(\frac{3}{2}\right)\begin{bmatrix}0 & -1 & -2\\ 1 & 0 & -1\\ 2 & 1 & 0\end{bmatrix}.$$

and tr{$\mathbf{a}\otimes\mathbf{b}$} = $\mathbf{a}\cdot\mathbf{b}$ =32.

Frequently, *n*-tuples are considered as functions of coordinate positions $x_1$, $x_2$, $x_3$ and time *t*. In this case the *n*-tuple is written $\mathbf{r}(x_1, x_2, x_3, t)$, which means that each element of $\mathbf{r}$ is a function of $x_1$, $x_2$, $x_3$, and *t*:

$$\mathbf{r}(x_1,x_2,x_3,t)=[r_1(x_1,x_2,x_3,t),r_2(x_1,x_2,x_3,t),...,r_n(x_1,x_2,x_3,t)]\,. \tag{A33}$$

Again, letting the operator $\Diamond$ stand for a total derivative, or a partial derivative with respect to $x_1$, $x_2$, $x_3$, or *t*, or a definite or indefinite (single or multiple) integral, then the operation of the operator on the *n*-tuple follows the same rule as the multiplication of an *n*-tuple by a scalar (A9), and thus

$$\Diamond\mathbf{r}(x_1,x_2,x_3,t)=[\Diamond r_1(x_1,x_2,x_3,t),\Diamond r_2(x_1,x_2,x_3,t),...,\Diamond r_n(x_1,x_2,x_3,t)]\,. \tag{A34}$$

The following distributive laws connect matrix addition and operator operations:

$$\Diamond(\mathbf{r}+\mathbf{t})=\Diamond\mathbf{r}+\Diamond\mathbf{t}\quad\text{and}\quad(\Diamond_1+\Diamond_2)\mathbf{r}=\Diamond_1\mathbf{r}+\Diamond_2\mathbf{r}\,, \tag{A35}$$

where $\Diamond_1$ and $\Diamond_2$ are two different operators.

**Problems**

A.4.1. Find the derivative of *n*-tuple $\mathbf{r}(x_1, x_2, x_3, t) = [x_1x_2x_3, 10x_1x_2, \cosh \alpha x_3]^T$ with respect to $x_3$.

A.4.2. Find the symmetric and skew-symmetric parts of matrix $\mathbf{r}\otimes\mathbf{s}$, where $\mathbf{r}$ = [1, 2, 3,4] and $\mathbf{s}$ = [5, 6,7,8].

## A.5. LINEAR TRANSFORMATIONS

A system of linear equations,

$$\begin{aligned} r_1 &= A_{11}t_1 + A_{12}t_2 + ... + A_{1n}t_n\,,\\ r_2 &= A_{21}t_1 + A_{22}t_2 + ... + A_{2n}t_n\,,\\ &\cdots\\ r_n &= A_{n1}t_1 + A_{n2}t_2 + ... + A_{nn}t_n\,, \end{aligned} \tag{A36}$$

may be contracted horizontally using the summation symbol, and thus

$$\begin{aligned} r_1 &= \sum_{k=1}^{k=n} A_{1k}t_k\,,\\ r_2 &= \sum_{k=1}^{k=n} A_{2k}t_k\,,\\ &\cdots\\ r_n &= \sum_{k=1}^{k=n} A_{nk}t_k\,. \end{aligned} \tag{A37}$$

Introduction of the free index convention condenses this system of equations vertically:

$$r_i = \sum_{k=1}^{k=n} A_{ik} t_k \ . \tag{A38}$$

This result may also be represented in matrix notation as a combination of $n$-tuples, $\mathbf{r}$ and $\mathbf{t}$, and square matrix $\mathbf{A}$:

$$\mathbf{r} = \mathbf{A} \cdot \mathbf{t} \ , \tag{A39}$$

where the dot between $\mathbf{A}$ and $\mathbf{t}$ indicates that summation is with respect to one index of $\mathbf{A}$ and one index of $\mathbf{t}$, or

$$\begin{bmatrix} r_1 \\ r_2 \\ . \\ . \\ . \\ r_n \end{bmatrix} = \begin{bmatrix} A_{11} & A_{12} & . & . & . & A_{1n} \\ A_{21} & A_{22} & . & . & . & A_{2n} \\ . & . & . & . & . & . \\ A_{n1} & . & . & . & . & A_{nn} \end{bmatrix} \begin{bmatrix} t_1 \\ t_2 \\ . \\ . \\ . \\ t_n \end{bmatrix} \tag{A40}$$

if the operation of matrix $\mathbf{A}$ upon column matrix $\mathbf{t}$ is interpreted as the operation of the square matrix upon the $n$-tuple defined by (A38). This is an operation very similar to square matrix multiplication. This may be seen easily by rewriting the $n$-tuple in (A40) as the first column of a square matrix whose entries are all otherwise zero; thus, the operation is one of multiplication of one square matrix by another:

$$\begin{bmatrix} r_1 \\ r_2 \\ . \\ . \\ . \\ r_n \end{bmatrix} = \begin{bmatrix} A_{11} & A_{12} & . & . & . & A_{1n} \\ A_{21} & A_{22} & . & . & . & A_{2n} \\ . & . & . & . & . & . \\ A_{n1} & . & . & . & . & A_{nm} \end{bmatrix} \begin{bmatrix} t_1 & 0 & . & . & . & 0 \\ t_2 & 0 & . & . & . & 0 \\ . & . & . & . & . & . \\ t_n & . & . & . & . & 0 \end{bmatrix} . \tag{A41}$$

The operation of square matrix $\mathbf{A}$ on $n$-tuple $\mathbf{t}$ is called a *linear transformation* of $\mathbf{t}$ into $n$-tuple $\mathbf{r}$. The linearity property is reflected in the property that $\mathbf{A}$ applied to the sum $(\mathbf{r} + \mathbf{t})$ follows a distributive law $\mathbf{A} \cdot (\mathbf{r} + \mathbf{t}) = \mathbf{A} \cdot \mathbf{r} + \mathbf{A} \cdot \mathbf{t}$ and that multiplication by scalar $\alpha$ follows rule $\alpha(\mathbf{A} \cdot \mathbf{r}) = \mathbf{A} \cdot (\alpha \mathbf{r})$. These two properties may be combined into one, $\mathbf{A} \cdot (\alpha \mathbf{r} + \beta \mathbf{t}) = \alpha \mathbf{A} \cdot \mathbf{r} + \beta \mathbf{A} \cdot \mathbf{t}$, where $\alpha$ and $\beta$ are scalars. The composition of linear transformations is again a linear transformation. Consider linear transformation $\mathbf{t} = \mathbf{B} \cdot \mathbf{u}$, $\mathbf{u} \rightarrow \mathbf{t}$ (meaning $\mathbf{u}$ is transformed into $\mathbf{t}$), which is combined with linear transformation (A39), $\mathbf{r} = \mathbf{A} \cdot \mathbf{t}$, $\mathbf{t} \rightarrow \mathbf{r}$, to transform $\mathbf{u} \rightarrow \mathbf{r}$, and thus $\mathbf{r} = \mathbf{A} \cdot \mathbf{B} \cdot \mathbf{u}$, and if we let $\mathbf{C} \equiv \mathbf{A} \cdot \mathbf{B}$, then $\mathbf{r} = \mathbf{C} \cdot \mathbf{u}$. The result of the composition of the two linear transformations, $\mathbf{r} = \mathbf{A} \cdot \mathbf{t}$ and $\mathbf{t} = \mathbf{B} \cdot \mathbf{u}$, is then a new linear transformation, $\mathbf{r} = \mathbf{C} \cdot \mathbf{u}$, where square matrix $\mathbf{C}$ is given by matrix product $\mathbf{A} \cdot \mathbf{B}$. To verify that it is, in fact, a matrix multiplication, the composition of transformations is done again in the indicial notation. Transformation $\mathbf{t} = \mathbf{B} \cdot \mathbf{u}$ in the indicial notation,

$$t_k = \sum_{m=1}^{m=n} B_{km} u_m \ , \tag{A42}$$

is substituted into $\mathbf{r} = \mathbf{A}\cdot\mathbf{t}$ in indicial notation (A38),

$$r_i = \sum_{k=1}^{k=n} A_{ik} \sum_{m=1}^{m=n} B_{km} u_m \,, \tag{A43}$$

which may be rewritten as

$$r_i = \sum_{m=1}^{m=n} C_{im} u_m \,, \tag{A44}$$

where $\mathbf{C}$ is defined by

$$C_{im} = \sum_{k=1}^{k=n} A_{ik} B_{km} \,. \tag{A45}$$

Comparison of (A45) with (A20) shows that $\mathbf{C}$ is the matrix product of $\mathbf{A}$ and $\mathbf{B}$, $\mathbf{C} = \mathbf{A}\cdot\mathbf{B}$. The calculation from (A42) to (A45) may be repeated using the Einstein summation convention. The calculation will be similar to the one above, with the exception that the summation symbols will not appear.

**Example A.5.1**

Determine result $\mathbf{r} = \mathbf{C}\cdot\mathbf{u}$ of the composition of the two linear transformations, $\mathbf{r} = \mathbf{A}\cdot\mathbf{t}$ and $\mathbf{t} = \mathbf{B}\cdot\mathbf{u}$, where $\mathbf{A}$ and $\mathbf{B}$ are given by

$$\mathbf{A} = \begin{bmatrix} 1 & 2 & 3 \\ 4 & 5 & 6 \\ 7 & 8 & 9 \end{bmatrix}, \quad \mathbf{B} = \begin{bmatrix} 10 & 11 & 12 \\ 13 & 14 & 15 \\ 16 & 17 & 18 \end{bmatrix}.$$

**Solution**: Square matrix $\mathbf{C}$ representing the composed linear transformation is given by the matrix product $\mathbf{A}\cdot\mathbf{B}$:

$$\mathbf{A}\cdot\mathbf{B} = \begin{bmatrix} 84 & 90 & 96 \\ 201 & 216 & 231 \\ 318 & 342 & 366 \end{bmatrix}.$$

It is important to be able to construct the inverse of linear transformation $\mathbf{r} = \mathbf{A}\cdot\mathbf{t}$, $\mathbf{t} = \mathbf{A}^{-1}\cdot\mathbf{r}$, if it exists. The inverse transformation exists if inverse matrix $\mathbf{A}^{-1}$ can be constructed from matrix $\mathbf{A}$. The construction of the inverse of a matrix involves the determinant of the matrix and the matrix of the cofactors. The determinant of $\mathbf{A}$ is denoted by Det$\mathbf{A}$. A matrix is said to be *singular* if its determinant is zero, *non-singular* if it is not. The cofactor of element $A_{ij}$ of $\mathbf{A}$ is denoted by $\mathrm{coA}_{ij}$ and is equal to $(-1)^{i+j}$ times the determinant of a matrix constructed from matrix $\mathbf{A}$ by deleting the row and column in which element $A_{ij}$ occurs. A matrix formed of cofactors $\mathrm{coA}_{ij}$ is denoted by **coA**.

**Example A.5.2**

Compute the matrix of cofactors of $\mathbf{A}$:

$$\mathbf{A} = \begin{bmatrix} a & d & e \\ d & b & f \\ e & f & c \end{bmatrix}.$$

**Solution**: The cofactors of the distinct elements of matrix **A** are co$a$ = ($bc$ – f$^2$), co$b$ = ($ac$ – $e^2$), co$c$ = ($ab$ – $d^2$), co$d$ = –($dc$ – $fe$), co$e$ = ($df$ – $eb$), and co$f$ = –($af$ – $de$); thus, the matrix of cofactors of **A** is

$$\mathbf{coA} = \begin{bmatrix} bc-f^2 & -(dc-fe) & (df-eb) \\ -(dc-fe) & ac-e^2 & -(af-de) \\ (df-eb) & -(af-de) & ab-d^2 \end{bmatrix}.$$

The formula for the inverse of **A** is written in terms of **coA** as

$$\mathbf{A}^{-1} = \frac{(\mathbf{coA})^T}{\text{Det}\,\mathbf{A}}, \tag{A46}$$

where $(\mathbf{coA})^T$ is the matrix of cofactors transposed. The inverse of a matrix is not defined if the matrix is singular. For every nonsingular square matrix **A** the inverse of **A** can be constructed, and thus

$$\mathbf{A}\cdot\mathbf{A}^{-1} = \mathbf{A}^{-1}\cdot\mathbf{A} = \mathbf{1}. \tag{A47}$$

It follows then that the inverse of linear transformation $\mathbf{r} = \mathbf{A}\cdot\mathbf{t}$, $\mathbf{t} = \mathbf{A}^{-1}\cdot\mathbf{r}$, exists if matrix **A** is nonsingular, Det**A** ≠ 0.

**Example A.5.3**

Show that the determinant of a 3-by-3 open product matrix, **a**⊗**b**, is zero.

**Solution**:

$$\text{Det}\{\mathbf{a}\otimes\mathbf{b}\} = \text{Det}\begin{bmatrix} a_1b_1 & a_1b_2 & a_1b_3 \\ a_2b_1 & a_2b_2 & a_2b_3 \\ a_3b_1 & a_3b_2 & a_3b_3 \end{bmatrix} = a_1b_1(a_2b_2a_3b_3 - a_2b_3a_3b_2)$$
$$-a_1b_2(a_2b_1a_3b_3 - a_3b_1a_2b_3) + a_1b_3(a_2b_1a_3b_2 - a_3b_1a_2b_2) = 0.$$

**Example A.5.4**

Find the inverse of matrix

$$\mathbf{A} = \begin{bmatrix} 18 & 6 & 6 \\ 6 & 15 & 0 \\ 6 & 0 & 21 \end{bmatrix}$$

**Solution**: The matrix of cofactors is given by

$$\text{co}\mathbf{A} = \begin{bmatrix} 315 & -126 & -90 \\ -126 & 342 & 36 \\ -90 & 36 & 234 \end{bmatrix};$$

thus, the inverse of **A** is then given by

$$\mathbf{A}^{-1} = \frac{\text{co}\mathbf{A}^T}{\text{Det}\,\mathbf{A}} = \frac{1}{243}\begin{bmatrix} 17.5 & -7 & -5 \\ -7 & 19 & 2 \\ -5 & 2 & 13 \end{bmatrix}.$$

The eigenvalue problem for linear transformation $\mathbf{r} = \mathbf{A}\cdot\mathbf{t}$ addresses the question of *n*-tuple $\mathbf{t}$ being transformed by $\mathbf{A}$ into some scalar multiple of itself, $\lambda\mathbf{t}$. Specifically, for what values of $\mathbf{t}$ and $\lambda$ does $\lambda\mathbf{t} = \mathbf{A}\cdot\mathbf{t}$? If such values of $\lambda$ and $\mathbf{t}$ exist, they are called eigenvalues and eigen *n*-tuples of matrix $\mathbf{A}$, respectively. The eigenvalue problem is then to find solutions to the equation

$$(\mathbf{A} - \lambda\mathbf{1})\cdot\mathbf{t} = 0\,. \tag{A48}$$

This is a system of linear equations for the elements of *n*-tuple $\mathbf{t}$. For the case of $n = 3$ it may be written in the form

$$\begin{aligned} (A_{11} - \lambda)t_1 + A_{12}t_2 + A_{13}t_3 &= 0\,, \\ A_{21}t_1 + (A_{22} - \lambda)t_2 + A_{23}t_3 &= 0\,, \\ A_{31}t_1 + A_{32}t_2 + (A_{33} - \lambda)t_3 &= 0\,. \end{aligned} \tag{A49}$$

The standard approach to the solution of a system of linear equations like (A48) is Cramer's rule. For a system of three equations in three unknowns, (A36) with $n = 3$,

$$\begin{aligned} r_1 &= A_{11}t_1 + A_{12}t_2 + A_{13}t_3\,, \\ r_2 &= A_{21}t_1 + A_{22}t_2 + A_{23}t_3\,, \\ r_3 &= A_{31}t_1 + A_{32}t_2 + A_{33}t_3\,. \end{aligned} \tag{A50}$$

Cramer's rule provides the solution for *n*-tuple $\mathbf{t} = [t_1, t_2, t_3]$:

$$t_1 = \frac{\begin{vmatrix} r_1 & A_{12} & A_{13} \\ r_2 & A_{22} & A_{23} \\ r_3 & A_{32} & A_{33} \end{vmatrix}}{\text{Det}A}, \quad t_2 = \frac{\begin{vmatrix} A_{11} & r_1 & A_{13} \\ A_{21} & r_2 & A_{23} \\ A_{31} & r_3 & A_{33} \end{vmatrix}}{\text{Det}A}, \quad t_3 = \frac{\begin{vmatrix} A_{11} & A_{12} & r_1 \\ A_{21} & A_{22} & r_2 \\ A_{31} & A_{32} & r_3 \end{vmatrix}}{\text{Det}A}. \tag{A51}$$

Considering the case where $n = 3$ and applying Cramer's rule to system of equations (A49), we find that

$$t_1 = \frac{\begin{vmatrix} 0 & A_{12} & A_{13} \\ 0 & A_{22} - \lambda & A_{23} \\ 0 & A_{32} & A_{33} - \lambda \end{vmatrix}}{\text{Det}[\mathbf{A} - \lambda\mathbf{1}]}, \quad t_2 = \frac{\begin{vmatrix} A_{11} - \lambda & 0 & A_{13} \\ A_{21} & 0 & A_{23} \\ A_{31} & 0 & A_{33} - \lambda \end{vmatrix}}{\text{Det}[\mathbf{A} - \lambda\mathbf{1}]}, \quad t_3 = \frac{\begin{vmatrix} A_{11} - \lambda & A_{12} & 0 \\ A_{21} & A_{22} - \lambda & 0 \\ A_{31} & A_{32} & 0 \end{vmatrix}}{\text{Det}[\mathbf{A} - \lambda\mathbf{1}]}$$

which shows, due to the column of zeros in each numerator determinant, that the only solution is that $\mathbf{t} = [0, 0, 0]$, unless $\text{Det}[\mathbf{A} - \lambda\mathbf{1}] = 0$. If $\text{Det}[\mathbf{A} - \lambda\mathbf{1}] = 0$, the values of $t_1$, $t_2$, and $t_3$ are all of the form 0/0 and therefore undefined. In this case Cramer's rule provides no information. In

order to avoid trivial solution $\mathbf{t} = [0, 0, 0]$, the value of $\lambda$ is selected so that $\mathrm{Det}[\mathbf{A} - \lambda\mathbf{1}] = 0$. While the argument was specialized to $n = 3$ in order to conserve page space, result

$$\mathrm{Det}[\mathbf{A} - \lambda\mathbf{1}] = 0 \tag{A52}$$

holds for all $n$. This condition forces matrix $[\mathbf{A} - \lambda\mathbf{1}]$ to be singular and forces system of equations (A48) to be linearly dependent. The further solution of (A52) is explored, retaining the assumption of $n = 3$ for convenience, but it should noted that all the manipulations can be accomplished for any $n$, including the values of $n$ of interest here — 2, 3, and 6. In the case of $n = 3$, (A52) is written in the form

$$\begin{vmatrix} A_{11} - \lambda & A_{12} & A_{13} \\ A_{21} & A_{22} - \lambda & A_{23} \\ A_{31} & A_{32} & A_{33} - \lambda \end{vmatrix} = 0\,, \tag{A53}$$

and, when the determinant is expanded, one obtains a cubic equation for $\lambda$:

$$\lambda^3 - I_{\mathbf{A}}\lambda^2 + II_{\mathbf{A}}\lambda - III_{\mathbf{A}} = 0 \tag{A54}$$

where

$$I_{\mathbf{A}} = \mathrm{tr}\mathbf{A} = \sum_{k=1}^{k=3} A_{kk} = A_{kk} = A_{11} + A_{22} + A_{33}\,, \tag{A55}$$

$$II_{\mathbf{A}} = \begin{vmatrix} A_{11} & A_{12} \\ A_{21} & A_{22} \end{vmatrix} + \begin{vmatrix} A_{11} & A_{13} \\ A_{31} & A_{33} \end{vmatrix} + \begin{vmatrix} A_{22} & A_{23} \\ A_{32} & A_{33} \end{vmatrix}, \tag{A56}$$

$$III_{\mathbf{A}} = \mathrm{Det}\mathbf{A} = \begin{vmatrix} A_{11} & A_{12} & A_{13} \\ A_{21} & A_{22} & A_{23} \\ A_{31} & A_{32} & A_{33} \end{vmatrix}. \tag{A57}$$

This argument then generates a set of three $\lambda$'s that allow determinant (A53) to vanish. We note again that the vanishing of the determinant makes set of equations (A49) linearly dependent. Since the system is linearly dependent, all of the components of $\mathbf{t}$ cannot be determined from (A49). Thus, for each value of $\lambda$ that is a solution to (A54), we can find only two ratios of the elements of $\mathbf{t}$ — $t_1$, $t_2$, and $t_3$. It follows that, for each eigen $n$-tuple, there will be one scalar unknown.

In this text we will only be interested in the eigenvalues of symmetric matrices. In §A.7 it is shown that a necessary and sufficient condition for all the eigenvalues to be real is that the matrix be symmetric.

**Example A.5.5**

Find the eigenvalues and construct the ratios of the eigen $n$-tuples of matrix

$$\mathbf{A} = \begin{bmatrix} 18 & 6 & 6 \\ 6 & 15 & 0 \\ 6 & 0 & 21 \end{bmatrix}. \tag{A58}$$

**Solution**: The cubic equation associated with this matrix is, from (A54), (A55), (A56). and (A57),

$$\lambda^3 - 54\lambda^2 + 891\lambda - 4374 = 0\,, \tag{A59}$$

which has three roots — 27, 18, and 9. The eigen *n*-tuples are constructed using these eigenvalues. The first eigen *n*-tuple is obtained by substitution of (A58) and $\lambda = 27$ into (A49), and thus

$$-9t_1 + 6t_2 + 6t_3 = 0,\;\; 6t_1 - 12t_2 = 0,\;\; 6t_1 - 6t_3 = 0. \tag{A60}$$

Note the linear dependence of this system of equations; the first equation is equal to the second multiplied by (–1/2) and added to the third multiplied by (–1). Since there are only two independent equations, the solution to this system of equations is $t_1 = t_3$ and $t_1 = 2t_2$, leaving an undetermined parameter in eigen *n*-tuple **t**. Similar results are obtained by taking $\lambda = 18$ and $\lambda = 9$.

**Problems**

A.5.1. Show that the eigenvalues of matrix

$$\mathbf{G} = \begin{bmatrix} 1 & 2 & 3 \\ 2 & 4 & 5 \\ 3 & 5 & 6 \end{bmatrix}$$

are 11.345, 0.171, and –0.516.

A.5.2. Construct the inverse of matrix **A**, where

$$\mathbf{A} = \begin{bmatrix} a & b \\ b & c \end{bmatrix}.$$

A.5.3. Show that the inverse of matrix **G** of Problem A.5.1 is given by

$$\mathbf{G}^{-1} = \begin{bmatrix} 1 & -3 & 2 \\ -3 & 3 & -1 \\ 2 & -1 & 0 \end{bmatrix}.$$

A.5.4. Show that the eigenvalues of matrix $\mathbf{G}^{-1}$ of Problem A.5.3 are the inverse of the eigenvalues of matrix **G** of Problem A.5.1.

A.5.5. Solve matrix equation $\mathbf{A}^2 = \mathbf{A}\cdot\mathbf{A} = \mathbf{A}$ for **A** assuming that **A** is nonsingular.

A.5.6. Why is it not possible to construct the inverse of an open product matrix, $\mathbf{a}\otimes\mathbf{b}$?

A.5.7. Construct a compositional transformation based on matrix **G** of Problem A.5.1 and the open product matrix, $\mathbf{a}\otimes\mathbf{b}$, where the *n*-tuples are $\mathbf{a} = [1, 2, 3]$ and $\mathbf{b} = [4, 5, 6]$.

A.5.8. If **F** is a square matrix and **a** is an *n*-tuple, show that $\mathbf{a}^{\mathrm{T}}\cdot\mathbf{F}^{\mathrm{T}} = \mathbf{F}\cdot\mathbf{a}$.

## A.6. VECTOR SPACES

Loosely, vectors are defined as *n*-tuples that follow the *parallelogram law of addition.* More precisely, vectors are defined as elements of a vector space called the *arithmetic n-space*. Let $A^n$ denote the set of all *n*-tuples, $\mathbf{u} = [u_1, u_2, u_3, ..., u_N]$, $\mathbf{v} = [v_1, v_2, v_3, ..., v_N]$ , etc., includ-

ing the zero n-tuple, $\mathbf{0} = [0, 0, 0, ..., 0]$, and the negative $n$-tuple, $-\mathbf{u} = [-u_1, -u_2, -u_3, ..., -u_N]$. An *arithmetic n-space* consists of set $A^n$ together with the additive and scalar multiplication operations defined by $\mathbf{u} + \mathbf{v} = [u_1 + v_1, u_2 + v_2, u_3 + v_3,..., u_N + v_N]$ and $\alpha\mathbf{u} = [\alpha u_1, \alpha u_2, \alpha u_3, ..., \alpha u_N]$, respectively. The additive operation defined by $\mathbf{u} + \mathbf{v} = [u_1 + v_1, u_2 + v_2, u_3 + v_3,..., u_N + v_N]$ is the *parallelogram law of addition*. The parallelogram law of addition was first introduced and proved experimentally for forces. A vector is defined as an element of a vector space, in our case a particular vector space called the arithmetic $n$-space.

The scalar product of two vectors in $n$ dimensions was defined earlier, (A31). This definition provided a formula for calculating scalar product $\mathbf{u}\cdot\mathbf{v}$ and the magnitude of vectors $\mathbf{u}$ and $\mathbf{v}$, $|\mathbf{u}| = \sqrt{\mathbf{u}\cdot\mathbf{u}}$ and $|\mathbf{v}| = \sqrt{\mathbf{v}\cdot\mathbf{v}}$. Thus, one can consider the elementary definition of the scalar product below as the definition of angle $\zeta$:

$$\mathbf{u}\cdot\mathbf{v} = \sum_{i=1}^{i=n} u_i v_i = |\mathbf{u}|\cdot|\mathbf{v}|\cos\zeta\,. \tag{A61}$$

Recalling that there is a geometric interpretation of $\zeta$ as the angle between two vectors $\mathbf{u}$ and $\mathbf{v}$ in two or three dimensions, it may seem strange to have cos $\zeta$ appear in formula (A61), which is valid in $n$ dimensions. However, since $\mathbf{u}\cdot\mathbf{v}$ divided by $|\mathbf{u}|\cdot|\mathbf{v}|$ is always less than one, and thus definition (A61) is reasonable not only for two and three dimensions, but for a space of any finite dimension. It is only in two and three dimensions that angle $\zeta$ may be interpreted as the angle between the two vectors.

**Example A.6.1**

Show that the magnitude of the sum of two unit vectors $\mathbf{e}_1 = [1,0]$ and $\mathbf{e}_2 = [\cos\alpha, \sin\alpha]$ can vary in magnitude from 0 to 2, depending on the value of angle $\alpha$.

**Solution**: $\mathbf{e}_1 + \mathbf{e}_2 = [1 + \cos\alpha, \sin\alpha]$, and thus $|\mathbf{e}_1 + \mathbf{e}_2| = \sqrt{2(1+\cos\alpha)}$. It follows that $|\mathbf{e}_1 + \mathbf{e}_2| = 2$ when $\alpha = 0$, $|\mathbf{e}_1 + \mathbf{e}_2| = 0$ when $\alpha = \pi$, and $|\mathbf{e}_1 + \mathbf{e}_2| = \sqrt{2}$ when $\alpha = \pi/2$. Thus, the sum of two unit vectors in two dimensions can point in any direction in the two dimensions and can have a magnitude between 0 and 2.

A set of unit vectors $\mathbf{e}_i$, $i = 1, 2,..., n$, is called an *orthonormal basis* of the vector space if all the base vectors are of unit magnitude and are orthogonal to each other, $\mathbf{e}_i\cdot\mathbf{e}_j = \delta_{ij}$ for $i, j$ having range $n$. From the definition of orthogonality one can see that, when $i \neq j$, unit vectors $\mathbf{e}_i$ and $\mathbf{e}_j$ are orthogonal. In the case where $i = j$ the restriction reduces to the requirement that the $\mathbf{e}_i$'s be unit vectors. The elements of $n$-tuples $v = [v_1, v_2, v_3, ..., v_n]$ referred to an orthonormal basis are called components. An important question concerning vectors is the manner in which their components change as their orthonormal basis is changed. In order to distinguish between the components referred to two different bases of a vector space we introduce two sets of indices. The first set of indices is composed of lowercase Latin letters *i, j, k, m, n, p*, etc. which have admissible values 1, 2, 3, ..., $n$ as before; the second set is composed of lowercase Greek letters $\alpha, \beta, \gamma, \delta,$ ..., etc., whose set of admissible values are Roman numerals I, II, III, ..., $n$. The Latin basis refers to base vectors $\mathbf{e}_i$ while the Greek basis refers to base vectors $\mathbf{e}_\alpha$. The components of vector $\mathbf{v}$ referred to a Latin basis are then $v_i$, $i = 1, 2, 3, ..., n$, while the components of the same vector referred to a Greek basis are $v_\alpha$, $\alpha = \text{I, II, III, ..., } n$. It should be clear that $\mathbf{e}_1$ is not the same as $\mathbf{e}_\text{I}$, $v_2$ is not the same as $v_\text{II}$, etc., that $\mathbf{e}_1$, $v_2$ refer to the Latin basis while $\mathbf{e}_\text{I}$, $v_\text{II}$ refer to the Greek basis. The terminology of calling a set of indices "Latin" and the other "Greek" is arbitrary; we could have introduced the second set of indices as *i', j', k', m', n',*

*p'*, etc., which would have had admissible values of 1', 2', 3', ..., *n*, and subsequently spoken of the unprimed and primed sets of indices.

The range of the indices in the Greek and Latin sets must be the same since both sets of base vectors $\mathbf{e}_i$ and $\mathbf{e}_\alpha$ occupy the same space. It follows then that the two sets, $\mathbf{e}_i$ and $\mathbf{e}_\alpha$, taken together are linearly dependent and therefore we can write that $\mathbf{e}_i$ is a linear combination of the $\mathbf{e}_\alpha$'s and vice versa. These relationships are expressed as linear transformations:

$$\mathbf{e}_i = \sum_{\alpha=1}^{\alpha=n} Q_{i\alpha}\mathbf{e}_\alpha \text{ and } \mathbf{e}_\alpha = \sum_{i=1}^{i=n} Q_{i\alpha}^{-1}\mathbf{e}_i , \tag{A62}$$

where $\mathbf{Q} = [Q_{i\alpha}]$ is the matrix characterizing the linear transformation. In the case of $n = 3$ the first of these equations may be expanded into a system of three equations:

$$\begin{aligned}
\mathbf{e}_1 &= Q_{1\mathrm{I}}\mathbf{e}_\mathrm{I} + Q_{1\mathrm{II}}\mathbf{e}_\mathrm{II} + Q_{1\mathrm{III}}\mathbf{e}_\mathrm{III} ,\\
\mathbf{e}_2 &= Q_{2\mathrm{I}}\mathbf{e}_\mathrm{I} + Q_{2\mathrm{II}}\mathbf{e}_\mathrm{II} + Q_{2\mathrm{III}}\mathbf{e}_\mathrm{III} ,\\
\mathbf{e}_3 &= Q_{3\mathrm{I}}\mathbf{e}_\mathrm{I} + Q_{3\mathrm{II}}\mathbf{e}_\mathrm{II} + Q_{3\mathrm{III}}\mathbf{e}_\mathrm{III} .
\end{aligned} \tag{A63}$$

If one takes the scalar product of $\mathbf{e}_\mathrm{I}$ with each of these equations and notes that since the $\mathbf{e}_\alpha$ , $\alpha$ = I, II, III, form an orthonormal basis, then $\mathbf{e}_\mathrm{I}\cdot\mathbf{e}_\mathrm{II} = \mathbf{e}_\mathrm{I}\cdot\mathbf{e}_\mathrm{III} = 0$, and $Q_{1\mathrm{I}} = \mathbf{e}_1\cdot\mathbf{e}_\mathrm{I} = \mathbf{e}_\mathrm{I}\cdot\mathbf{e}_1$, $Q_{2\mathrm{I}} = \mathbf{e}_2\cdot\mathbf{e}_\mathrm{I} = \mathbf{e}_\mathrm{I}\cdot\mathbf{e}_2$, and $Q_{3\mathrm{I}} = \mathbf{e}_3\cdot\mathbf{e}_\mathrm{I} = \mathbf{e}_\mathrm{I}\cdot\mathbf{e}_3$. Repeating the scalar product operation for $\mathbf{e}_{\mathrm{I}\,\mathrm{I}}$ and $\mathbf{e}_{\mathrm{I}\,\mathrm{II}}$ shows that, in general, $Q_{i\alpha} = \mathbf{e}_i\cdot\mathbf{e}_\alpha = \mathbf{e}_\alpha\cdot\mathbf{e}_i$. Recalling that the scalar product of two vectors is the product of magnitudes of each vector and the cosine of the angle between the two vectors (A61), and that the base vectors are unit vectors, it follows that $Q_{i\alpha} = \mathbf{e}_i\cdot\mathbf{e}_\alpha = \mathbf{e}_\alpha\cdot\mathbf{e}_i$ are just the cosines of angles between the base vectors of the two bases involved. Thus, the components of linear transformation $\mathbf{Q} = [Q_{i\alpha}]$ are the cosines of the angles between the base vectors of the two bases involved. Because the definition of scalar product (A61) is valid in *n* dimensions, all these results are valid in *n* dimensions even though the two- and three- dimensional geometric interpretation of the components of linear transformation **Q** as the cosines of the angles between coordinate axes is no longer valid.

The geometric analogy is very helpful, so considerations in three dimensions are continued. Three-dimensional Greek and Latin coordinate systems are illustrated on the left-hand side of Figure A.1. Matrix **Q** with components $Q_{i\alpha} = \mathbf{e}_i\cdot\mathbf{e}_\alpha$ relates the components of vectors and base vectors associated with the Greek system to those associated with the Latin system:

$$\mathbf{Q} = [Q_{i\alpha}] = [\mathbf{e}_i\cdot\mathbf{e}_\alpha] = \begin{bmatrix} \mathbf{e}_1\cdot\mathbf{e}_\mathrm{I} & \mathbf{e}_1\cdot\mathbf{e}_\mathrm{II} & \mathbf{e}_1\cdot\mathbf{e}_\mathrm{III} \\ \mathbf{e}_2\cdot\mathbf{e}_\mathrm{I} & \mathbf{e}_2\cdot\mathbf{e}_\mathrm{II} & \mathbf{e}_2\cdot\mathbf{e}_\mathrm{III} \\ \mathbf{e}_3\cdot\mathbf{e}_\mathrm{I} & \mathbf{e}_3\cdot\mathbf{e}_\mathrm{II} & \mathbf{e}_3\cdot\mathbf{e}_\mathrm{III} \end{bmatrix}. \tag{A64}$$

In the special case when the $\mathbf{e}_1$ and $\mathbf{e}_\mathrm{I}$ are coincident, the relative rotation between the two observers' frames is a rotation about that particular selected and fixed axis, and matrix **Q** has the special form

$$\mathbf{Q} = \begin{bmatrix} 1 & 0 & 0 \\ 0 & \cos\theta & -\sin\theta \\ 0 & \sin\theta & \cos\theta \end{bmatrix}. \tag{A65}$$

This situation is illustrated on the left in Figure A.1.

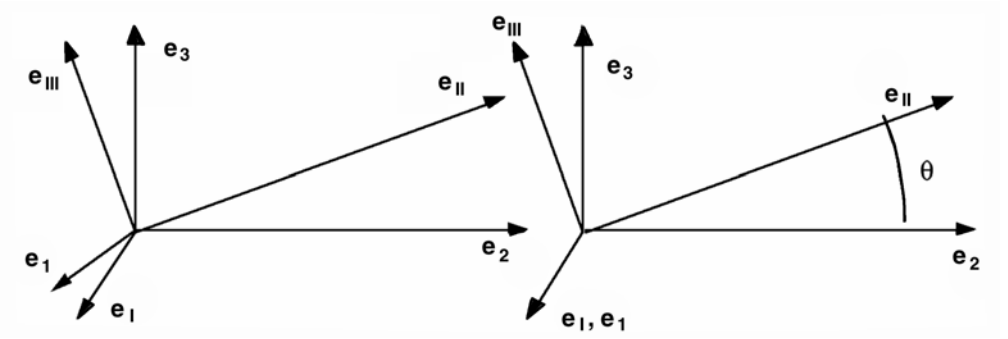



**Figure A.1**. The relative rotational orientation between coordinate systems.

Matrix $\mathbf{Q} = [Q_{i\alpha}]$ characterizing the change from Latin orthonormal basis $\mathbf{e}_i$ in an $N$-dimensional vector space to Greek basis $\mathbf{e}_\alpha$ (or vice versa) is a special type of linear transformation called an orthogonal transformation. Taking the scalar product of $\mathbf{e}_i$ with $\mathbf{e}_j$, where $\mathbf{e}_i$ and $\mathbf{e}_j$ both have representation (A62),

$$\mathbf{e}_i = \sum_{\alpha=1}^{\alpha=n} Q_{i\alpha}\mathbf{e}_\alpha \quad \text{and} \quad \mathbf{e}_j = \sum_{\beta=1}^{\beta=n} Q_{j\beta}\mathbf{e}_\beta\,, \tag{A66}$$

it follows that

$$\mathbf{e}_i \cdot \mathbf{e}_j = \delta_{ij} = \sum_{\alpha=1}^{\alpha=n}\sum_{\beta=1}^{\beta=n} Q_{i\alpha}Q_{j\beta}\mathbf{e}_\alpha \cdot \mathbf{e}_\beta = \sum_{\alpha=1}^{\alpha=n}\sum_{\beta=1}^{\beta=n} Q_{i\alpha}Q_{j\beta}\delta_{\alpha\beta} = \sum_{\alpha=1}^{\alpha=n} Q_{i\alpha}Q_{j\alpha}\,. \tag{A67}$$

There are a number of steps in calculation (A67) that should be considered carefully. First, the condition of orthonormality of the bases has been used twice, $\mathbf{e}_i \cdot \mathbf{e}_j = \delta_{ij}$ and $\mathbf{e}_\alpha \cdot \mathbf{e}_\beta = \delta_{\alpha\beta}$. Second, the transition from the term before the last equal sign to the term after that sign is characterized by a change from a double sum to a single sum over $n$ and the loss of Kronecker delta $\delta_{\alpha\beta}$. This occurs because the sum over $\beta$ in the double sum is always zero except in the special case when $\alpha = \beta$ due to the presence of Kronecker delta $\delta_{\alpha\beta}$. Third, a comparison of the last term in (A67) with the definition of matrix product (A20) suggests that it is a matrix product of $\mathbf{Q}$ with itself. However, a careful comparison of the last term in (A67) with the definition of matrix product (A20) shows that the summation is over a different index in the second element of the product. In order for the last term in (A67) to represent a matrix product, index $\alpha$ should appear as the first subscripted index rather than the second. However, this $\alpha$ index may be relocated in the second matrix by using the transposition operation. Thus, the last term in eq. (A67) is the matrix product of $\mathbf{Q}$ with $\mathbf{Q}^T$, as may be seen from the first of eqs. (A18). Thus, since the matrix of Kronecker delta components is unit matrix $\mathbf{1}$, it has been shown that

$$\mathbf{1} = \mathbf{Q}\cdot\mathbf{Q}^T. \tag{A68}$$

If we repeat the calculation of the scalar product, this time using $\mathbf{e}_\alpha$ and $\mathbf{e}_\beta$ rather than $\mathbf{e}_i$ and $\mathbf{e}_j$, then it is found that $\mathbf{1} = \mathbf{Q}^T\cdot\mathbf{Q}$ and, combined with the previous result,

$$\mathbf{1} = \mathbf{Q}\cdot\mathbf{Q}^T = \mathbf{Q}^T\cdot\mathbf{Q}. \tag{A69}$$

Using the fact that Det **1** = 1, and two results that are proved in §A.8, Det **A**·**B** = Det **A** Det **B**, and Det **A** = Det $\mathbf{A}^{\mathrm{T}}$, it follows from $\mathbf{1} = \mathbf{Q}\mathbf{Q}^{\mathrm{T}}$ or $\mathbf{1} = \mathbf{Q}^{\mathrm{T}}\mathbf{Q}$ that **Q** is nonsingular and Det **Q** = ±1. Comparing matrix equations $\mathbf{1} = \mathbf{Q}\cdot\mathbf{Q}^{\mathrm{T}}$ and $\mathbf{1} = \mathbf{Q}^{\mathrm{T}}\cdot\mathbf{Q}$ with the equations defining the inverse of **Q**, $\mathbf{1} = \mathbf{Q}\cdot\mathbf{Q}^{-1} = \mathbf{Q}^{-1}\cdot\mathbf{Q}$, it follows that

$$\mathbf{Q}^{-1} = \mathbf{Q}^{\mathrm{T}}, \tag{A70}$$

since the inverse exists (Det **Q** is not singular) and is unique. Any matrix that satisfies eq. (A69) is called an orthogonal matrix. Any change of orthonormal bases is characterized by an orthogonal matrix and is called an orthogonal transformation. Finally, since $\mathbf{Q}^{-1} = \mathbf{Q}^{\mathrm{T}}$ the representations of the transformation of bases (A62) may be rewritten as

$$\mathbf{e}_i = \sum_{\alpha=1}^{\alpha=n} Q_{i\alpha}\mathbf{e}_\alpha \quad \text{and} \quad \mathbf{e}_\alpha = \sum_{i=1}^{i=n} Q_{i\alpha}\mathbf{e}_i \,. \tag{A71}$$

Orthogonal matrices are very interesting, useful, and easy to handle; their determinant is always plus or minus one and their inverse is obtained simply by computing their transpose. Furthermore, the multiplication of orthogonal matrices has the closure property. To see that the product of two *n*-by-*n* orthogonal matrices is another *n*-by-*n* orthogonal matrix, let **R** and **Q** be orthogonal matrices and consider their product denoted by $\mathbf{W} = \mathbf{R}\cdot\mathbf{Q}$. The inverse of **W** is given by $\mathbf{W}^{-1} = \mathbf{Q}^{-1}\cdot\mathbf{R}^{-1}$ and its transpose by $\mathbf{W}^{\mathrm{T}} = \mathbf{Q}^{\mathrm{T}}\cdot\mathbf{R}^{\mathrm{T}}$. Since **R** and **Q** are orthogonal matrices, $\mathbf{Q}^{-1}\cdot\mathbf{R}^{-1} = \mathbf{Q}^{\mathrm{T}}\cdot\mathbf{R}^{\mathrm{T}}$, it follows that $\mathbf{W}^{-1} = \mathbf{W}^{\mathrm{T}}$, and therefore **W** is orthogonal. It follows then that the set of all orthogonal matrices has the closure property as well as the associative property with respect to the multiplication operation, an identity element (the unit matrix **1** is orthogonal), and an inverse for each member of the set.

Here we shall consider changing the basis to which a given vector is referred. While vector **v** itself is invariant with respect to a change of basis, the components of **v** will change when the basis to which they are referred is changed. The components of vector **v** referred to a Latin basis are then $v_i$, $i$ = 1, 2, 3, ..., $n$, while the components of the same vector referred to a Greek basis are $v_\alpha$, α = I, II, III, ..., $n$. Since vector **v** is unique,

$$\mathbf{v} = \sum_{i=1}^{i=n} v_i\mathbf{e}_i = \sum_{\alpha=1}^{\alpha=n} v_\alpha\mathbf{e}_\alpha \,. \tag{A72}$$

Substituting the second of (A71) into the second equality of (A72), one obtains

$$\sum_{i=1}^{i=n} v_i\mathbf{e}_i = \sum_{\alpha=1}^{\alpha=n}\sum_{i=1}^{i=n} Q_{i\alpha}v_\alpha\mathbf{e}_i \,, \tag{A73}$$

which may be rewritten as

$$\sum_{i=1}^{i=n}\left(v_i - \sum_{\alpha=1}^{\alpha=n} Q_{i\alpha}v_\alpha\right)\mathbf{e}_i = 0 \,. \tag{A74}$$

Taking the dot product of (A74) with $\mathbf{e}_j$, it follows that the sum over $i$ is only nonzero when $i = j$, and thus

$$v_j = \sum_{\alpha=1}^{\alpha=n} Q_{j\alpha}v_\alpha \,. \tag{A75}$$

If the first, rather than the second, of (A71) is substituted into the second equality of (A72), and similar algebraic manipulations accomplished, one obtains

$$v_\beta = \sum_{i=1}^{i=n} Q_{i\beta} v_i \ . \tag{A76}$$

Results (A75) and (A76) are written in matrix notation using superscripted ($L$) and ($G$) to distinguish between components referred to the Latin or Greek bases:

$$\mathbf{v}^{(L)} = \mathbf{Q} \cdot \mathbf{v}^{(G)}, \quad \mathbf{v}^{(G)} = \mathbf{Q}^T \cdot \mathbf{v}^{(L)} . \tag{A77}$$

**Problems**

A.6.1. Is matrix

$$\frac{1}{3}\begin{bmatrix} 2 & 1 & 2 \\ -1 & -2 & 2 \\ 2 & -2 & -1 \end{bmatrix}$$

an orthogonal matrix?.

A.6.2. Are matrices **A**, **B**, **C**, and **Q**, where **Q** = **C**·**B**·**A**, and where

$$\mathbf{A} = \begin{bmatrix} \cos\phi & \sin\phi & 0 \\ -\sin\phi & \cos\phi & 0 \\ 0 & 0 & 1 \end{bmatrix}, \quad \mathbf{B} = \begin{bmatrix} 1 & 0 & 0 \\ 0 & \cos\theta & \sin\theta \\ 0 & -\sin\theta & \cos\theta \end{bmatrix},$$

$$\mathbf{C} = \begin{bmatrix} \cos\psi & 0 & -\sin\psi \\ 0 & 1 & 0 \\ \sin\psi & 0 & \cos\psi \end{bmatrix}$$

all orthogonal matrices?

A.6.3. Does an inverse of the compositional transformation constructed in Problem A.5.7 exist?

A.6.4. Is it possible for an open product of vectors to be an orthogonal matrix?

A.6.5. Transform the components of vector $\mathbf{v}^{(L)} = [1, 2, 3]$ to a new (Greek) coordinate system using transformation

$$\mathbf{Q} = \frac{1}{2}\begin{bmatrix} 1 & \sqrt{\frac{3}{2}} & \sqrt{\frac{3}{2}} \\ -\sqrt{3} & \frac{1}{\sqrt{2}} & \frac{1}{\sqrt{2}} \\ 0 & -\sqrt{2} & \sqrt{2} \end{bmatrix}.$$

## A.7. SECOND-ORDER TENSORS

Scalars are tensors of order zero; vectors are tensors of order one. Tensors of order two will be defined using vectors. For brevity, we shall refer to "tensors of order two" simply as "tensors" throughout most of this section. The notion of a tensor, like the notion of a vector, was generated by physicists for application in physical theories. In classical dynamics the essential concepts of force, velocity, and acceleration are all vectors; hence, the mathematical language of classical dynamics is that of vectors. In the mechanics of deformable media the essential concepts of stress, strain, rate of deformation, etc., are all second-order tensors; thus, by analogy, one can expect to deal quite frequently with second-order tensors in this branch of mechanics. The reason for this widespread use of tensors is that they enjoy, like vectors, the property of being invariant with respect to the basis, or frame of reference, chosen.

The definition of a tensor is motivated by a consideration of the open or dyadic product of vectors **r** and **t**. Recall that the square matrix formed from **r** and **t** is called the open product of the *n*-tuples **r** and **t**; it is denoted by **r** ⊗ **t** and defined by (A30) for *n*-tuples. We employ this same formula to define the open product of vectors **r** and **t**. Both of these vectors have representations relative to all bases in the vector space, in particular the Latin and the Greek bases, and thus from (A72)

$$\mathbf{r} = \sum_{i=1}^{i=n} r_i \mathbf{e}_i = \sum_{\alpha=1}^{\alpha=n} r_\alpha \mathbf{e}_\alpha \ , \quad \mathbf{t} = \sum_{j=1}^{j=n} t_j \mathbf{e}_j = \sum_{\beta=1}^{\beta=n} t_\beta \mathbf{e}_\beta \ . \tag{A78}$$

The open product of vectors **r** and **t**, **r** ⊗ **t**, then has representation

$$\mathbf{r} \otimes \mathbf{t} = \sum_{j=1}^{j=n} \sum_{i=1}^{i=n} r_i t_j \mathbf{e}_i \otimes \mathbf{e}_j = \sum_{\beta=1}^{\beta=n} \sum_{\alpha=1}^{\alpha=n} r_\alpha t_\beta \mathbf{e}_\alpha \otimes \mathbf{e}_\beta \ . \tag{A79}$$

This is a special type of tensor, but it is referred to the general second-order tensor basis, $\mathbf{e}_i \otimes \mathbf{e}_j$, or $\mathbf{e}_\alpha \otimes \mathbf{e}_\beta$. A general second-order tensor is quantity **T**, defined by the formula relative to bases $\mathbf{e}_i \otimes \mathbf{e}_j$, $\mathbf{e}_\alpha \otimes \mathbf{e}_\beta$ and, by implication, any basis in the vector space:

$$\mathbf{T} = \sum_{j=1}^{j=n} \sum_{i=1}^{i=n} T_{ij} \mathbf{e}_i \otimes \mathbf{e}_j = \sum_{\beta=1}^{\beta=n} \sum_{\alpha=1}^{\alpha=n} T_{\alpha\beta} \mathbf{e}_\alpha \otimes \mathbf{e}_\beta \ . \tag{A80}$$

Formulas (A78) and (A80) have similar content in that vectors **r** and **t** and tensor **T** are quantities independent of a base or coordinate system while the components of **r**, **t**, and **T** may be expressed relative to any basis. In formulas (A78) and (A80), **r**, **t**, and **T** are expressed as components relative to two different bases. The vectors are expressed as components relative to bases $\mathbf{e}_i$ and $\mathbf{e}_\alpha$, while tensor **T** is expressed relative to bases $\mathbf{e}_i \otimes \mathbf{e}_j$ and $\mathbf{e}_\alpha \otimes \mathbf{e}_\beta$. Tensor bases $\mathbf{e}_i \otimes \mathbf{e}_j$ and $\mathbf{e}_\alpha \otimes \mathbf{e}_\beta$ are constructed from vector bases $\mathbf{e}_i$ and $\mathbf{e}_\alpha$.

**Example A.7.1**

If base vectors $\mathbf{e}_1$, $\mathbf{e}_2$, and $\mathbf{e}_3$ are expressed as $\mathbf{e}_1 = [1, 0, 0]^T$, $\mathbf{e}_2 = [0, 1, 0]^T$, and $\mathbf{e}_3 = [0, 0, 1]^T$, then it follows from (A77) that

$$\mathbf{v} = \sum_{i=1}^{i=3} v_i \mathbf{e}_i \ ,$$

and we can express **v** in this form:

$$\mathbf{v} = v_1 \begin{bmatrix} 1 \\ 0 \\ 0 \end{bmatrix} + v_2 \begin{bmatrix} 0 \\ 1 \\ 0 \end{bmatrix} + v_3 \begin{bmatrix} 0 \\ 0 \\ 1 \end{bmatrix}. \tag{A81}$$

Create a similar representation for **T** given by (A80) for $n = 3$.

**Solution**: The representation for **T** given by (A80),

$$\mathbf{T} = \sum_{j=1}^{j=3} \sum_{i=1}^{i=3} T_{ij} \mathbf{e}_i \otimes \mathbf{e}_j ,$$

involves base vectors $\mathbf{e}_1 \otimes \mathbf{e}_1$, $\mathbf{e}_1 \otimes \mathbf{e}_2$ etc. These "base vectors" are expressed as matrices of tensor components by

$$\mathbf{e}_1 \otimes \mathbf{e}_1 = \begin{bmatrix} 1 & 0 & 0 \\ 0 & 0 & 0 \\ 0 & 0 & 0 \end{bmatrix}, \ \mathbf{e}_1 \otimes \mathbf{e}_2 = \begin{bmatrix} 0 & 1 & 0 \\ 0 & 0 & 0 \\ 0 & 0 & 0 \end{bmatrix}, \ \mathbf{e}_2 \otimes \mathbf{e}_1 = \begin{bmatrix} 0 & 0 & 0 \\ 1 & 0 & 0 \\ 0 & 0 & 0 \end{bmatrix}, \text{ etc.} \tag{A82}$$

The representation for **T**,

$$\mathbf{T} = \sum_{j=1}^{j=3} \sum_{i=1}^{i=3} T_{ij} \mathbf{e}_i \otimes \mathbf{e}_j ,$$

then can be written in analogy to (A81) as

$$\mathbf{T} = T_{11} \begin{bmatrix} 1 & 0 & 0 \\ 0 & 0 & 0 \\ 0 & 0 & 0 \end{bmatrix} + T_{21} \begin{bmatrix} 0 & 0 & 0 \\ 1 & 0 & 0 \\ 0 & 0 & 0 \end{bmatrix} + T_{12} \begin{bmatrix} 0 & 1 & 0 \\ 0 & 0 & 0 \\ 0 & 0 & 0 \end{bmatrix} + T_{13} \begin{bmatrix} 0 & 0 & 1 \\ 0 & 0 & 0 \\ 0 & 0 & 0 \end{bmatrix} +$$

$$T_{31} \begin{bmatrix} 0 & 0 & 0 \\ 0 & 0 & 0 \\ 1 & 0 & 0 \end{bmatrix} + T_{22} \begin{bmatrix} 0 & 0 & 0 \\ 0 & 1 & 0 \\ 0 & 0 & 0 \end{bmatrix} + T_{23} \begin{bmatrix} 0 & 0 & 0 \\ 0 & 0 & 1 \\ 0 & 0 & 0 \end{bmatrix} + T_{32} \begin{bmatrix} 0 & 0 & 0 \\ 0 & 0 & 0 \\ 0 & 1 & 0 \end{bmatrix} + T_{33} \begin{bmatrix} 0 & 0 & 0 \\ 0 & 0 & 0 \\ 0 & 0 & 1 \end{bmatrix}.$$

The components of tensor **T** relative to the Latin basis, $\mathbf{T}^{(L)} = [T_{ij}]$, are related to the components relative to the Greek basis, $\mathbf{T}^{(G)} = [T_{\alpha\beta}]$, by

$$\mathbf{T}^{(L)} = \mathbf{Q} \cdot \mathbf{T}^{(G)} \cdot \mathbf{Q}^T \quad \text{and} \quad \mathbf{T}^{(G)} = \mathbf{Q}^T \cdot \mathbf{T}^{(L)} \cdot \mathbf{Q} . \tag{A83}$$

These formulas relating the components are the tensorial equivalent of vectorial formulas $\mathbf{v}^{(L)} = \mathbf{Q} \cdot \mathbf{v}^{(G)}$ and $\mathbf{v}^{(G)} = \mathbf{Q}^T \cdot \mathbf{v}^{(L)}$ given by (A77), and their derivation is similar. First, substitute the second of (A66) into (A80) twice, once for each base vector:

$$\mathbf{T} = \sum_{j=1}^{j=n} \sum_{i=1}^{i=n} T_{ij} \mathbf{e}_i \otimes \mathbf{e}_j = \sum_{j=1}^{j=n} \sum_{i=1}^{i=n} \sum_{\beta=1}^{\beta=n} \sum_{\alpha=1}^{\alpha=n} T_{\alpha\beta} Q_{i\alpha} Q_{j\beta} \mathbf{e}_i \otimes \mathbf{e}_j . \tag{A84}$$

Then gather together the terms referred to basis $\mathbf{e}_i \otimes \mathbf{e}_j$, and thus

$$\sum_{j=1}^{j=n} \sum_{i=1}^{i=n} \left( T_{ij} - \sum_{\beta=1}^{\beta=n} \sum_{\alpha=1}^{\alpha=n} T_{\alpha\beta} Q_{i\alpha} Q_{j\beta} \right) \mathbf{e}_i \otimes \mathbf{e}_j = 0 . \tag{A85}$$

Next, take the scalar product of (A85), first with respect to $\mathbf{e}_k$, and then with respect to $\mathbf{e}_m$. One finds that the only nonzero terms that remain are

$$T_{km} = \sum_{\beta=1}^{\beta=n} \sum_{\alpha=1}^{\alpha=n} Q_{k\alpha} T_{\alpha\beta} Q_{m\beta} \ . \tag{A86}$$

A comparison of the last term in (A86) with the definition of matrix product (A20) suggests that it is a triple matrix product involving $\mathbf{Q}$ twice and $\mathbf{T}^{(G)}$ once. Careful comparison of the last term in (A86) with the definition of matrix product (A20) shows that the summation is over a different index in the third element of the product. In order for the last term in (A86) to represent a triple matrix product, the $\beta$ index should appear as the first subscripted index rather than the second. However, this $\beta$ index may be relocated in the second matrix by using the transposition operation, as shown in the first equation of (A21). Thus, the last term in eq. (A86) is the matrix product of $\mathbf{Q}\cdot\mathbf{T}$ with $\mathbf{Q}^{\mathrm{T}}$. The result is the first equation of (A83). If the first, rather than the second, of (A67) is substituted into the second equality of (A80), and similar algebraic manipulations accomplished, one obtains the second equation of (A83).

The word *tensor* is used to refer to quantity $\mathbf{T}$ defined by (A80), a quantity independent of any basis. It is also used to refer to the matrix of tensor components relative to a particular basis, for example, $\mathbf{T}^{(L)} = [\mathrm{T}_{ij}]$ or $\mathbf{T}^{(G)} = [\mathrm{T}_{\alpha\beta}]$. In both cases "tensor" should be "tensor of order two," but the order of the tensor is generally clear from the context. A tensor of order $N$ in a space of $n$ dimensions is defined by

$$\mathbf{B} = \sum_{k=1}^{k=n} \cdots \sum_{j=1}^{j=n} \sum_{i=1}^{i=n} B_{ij\ldots k} \mathbf{e}_i \otimes \mathbf{e}_j \otimes \cdots \otimes \mathbf{e}_k = \sum_{\gamma=1}^{\gamma=n} \cdots \sum_{\beta=1}^{\beta=n} \sum_{\alpha=1}^{\alpha=n} B_{\alpha\beta\ldots\gamma} \mathbf{e}_\alpha \otimes \mathbf{e}_\beta \otimes \cdots \otimes \mathbf{e}_\gamma \ . \tag{A87}$$

The number of base vectors in the basis is the order $N$ of the tensor. It is easy to see that this definition specializes to that of second-order tensor (A80). The definition of a vector as a tensor of order one is easy to see, and the definition of a scalar as a tensor of order 0 is trivial.

In the section before last, §A.5 on Linear Transformations, the eigenvalue problem for a linear transformation, $\mathbf{r} = \mathbf{A}\mathbf{t}$, was considered. Here we extend those results by considering $\mathbf{r}$ and $\mathbf{t}$ to be vectors and $\mathbf{A}$ to be a symmetric second-order tensor, $\mathbf{A} = \mathbf{A}^{\mathrm{T}}$. The problem is actually little changed until its conclusion. The eigenvalues are still given by (A52) or, for $n = 3$, by (A54). The values of three quantities — $I_{\mathbf{A}}$, $II_{\mathbf{A}}$, $III_{\mathbf{A}}$ — defined by (A55), (A56), and (A57) are the same except that $A_{12} = A_{21}$, $A_{13} = A_{31}$, and $A_{32} = A_{23}$ due to the assumed symmetry of $\mathbf{A}$, $\mathbf{A} = \mathbf{A}^{\mathrm{T}}$. These quantities may now be called the invariants of tensor $\mathbf{A}$ since their value is the same independent of the coordinate system chosen for their determination. As an example of the invariance with respect to basis, this property will be derived for $I_{\mathbf{A}} = \mathrm{tr}\ \mathbf{A}$. Let $\mathbf{T} = \mathbf{A}$ in (A86), and then set indices $k = m$ and sum from 1 to $n$ over index $k$; thus,

$$\sum_{k=1}^{k=n} A_{kk} = \sum_{k=1}^{k=n} \sum_{\beta=1}^{\beta=n} \sum_{\alpha=1}^{\alpha=n} Q_{k\alpha} A_{\alpha\beta} Q_{k\beta} = \sum_{\beta=1}^{\beta=n} \sum_{\alpha=1}^{\alpha=n} A_{\alpha\beta} \sum_{k=1}^{k=n} Q_{k\alpha} Q_{k\beta} = \sum_{\beta=1}^{\beta=n} \sum_{\alpha=1}^{\alpha=n} A_{\alpha\beta} \delta_{\alpha\beta} = \sum_{\alpha=1}^{\alpha=n} A_{\alpha\alpha} \ . \tag{A88}$$

The transition across the second equal sign is a simple rearrangement of terms. The transition across the third equal sign is based on condition

$$\delta_{\alpha\beta} = \sum_{k=1}^{k=n} Q_{k\alpha} Q_{k\beta} \tag{A89}$$

which is an alternate form of (A67), a form equivalent to $\mathbf{1} = \mathbf{Q}^{\mathrm{T}}\cdot\mathbf{Q}$. The transition across the fourth equal sign employs the definition of the Kronecker delta and summation over $\beta$. The

result is that the trace of the matrix of second-order tensor components relative to any basis is the same number:

$$\sum_{k=1}^{k=n} A_{kk} = \sum_{\alpha=1}^{\alpha=n} A_{\alpha\alpha} \,. \tag{A90}$$

It may also be shown that $II_{\mathbf{A}}$ and $III_{\mathbf{A}}$ are invariants of tensor **A**.

**Example A.7.2 (extension of Example A.5.5)**

Consider the matrix given by (A58) in Example A.5.5 to be the components of a tensor. Construct the eigenvectors of that tensor and use those eigenvectors to construct an eigenbasis:

$$\mathbf{A} = \begin{bmatrix} 18 & 6 & 6 \\ 6 & 15 & 0 \\ 6 & 0 & 21 \end{bmatrix}. \tag{A58) repeated}$$

**Solution**: The eigenvalues were shown to be 27, 18, and 9. It can be shown that the eigenvalues must always be real numbers if **A** is symmetric. Eigen *n*-tuples were constructed using these eigenvalues. The first eigen *n*-tuple was obtained by substitution of (A58) and λ = 27 into (A49), and thus

$$-9t_1 + 6t_2 + 6t_3 = 0, 6t_1 - 12t_2 = 0, 6t_1 - 6t_3 = 0. \tag{A60) repeated}$$

These three conditions, only two of which are independent, gave $t_1 = t_3$ and $t_1 = 2t_2$, leaving an undetermined parameter in eigen *n*-tuple **t**. Now that **t** is a vector, we can specify the length of a vector. Another consequence of the symmetry of **A** is that these eigenvectors are orthogonal if the eigenvalues are distinct. Hence, if we set the length of the eigenvectors to be one to remove the undetermined parameter, we will generate an orthonormal basis from the set of three eigenvectors, since the eigenvalues are distinct. If we use normality condition $t_1^2 + t_2^2 + t_3^2 = 1$ and the results that follow from (A56), $t_1 = t_3$ and $t_1 = 2t_2$, we find that

$$\mathbf{t} = \pm\left(\frac{1}{3}\right)(2\mathbf{e}_1 + \mathbf{e}_2 + 2\mathbf{e}_3) \tag{A91}$$

which shows that both **t** and –**t** are eigenvectors. This will be true for any eigenvector because they are really eigen-directions. For the second and third eigenvalues, 18 and 9, we find that

$$\mathbf{t} = \pm\left(\frac{1}{3}\right)(-\mathbf{e}_1 - 2\mathbf{e}_2 + 2\mathbf{e}_3) \quad \text{and} \quad \mathbf{t} = \pm\left(\frac{1}{3}\right)(2\mathbf{e}_1 - 2\mathbf{e}_2 - \mathbf{e}_3)\,, \tag{A92}$$

respectively. It is easy to see that these three eigenvectors are mutually orthogonal.

It was noted above that, since the eigenvectors constitute a set of three mutually perpendicular unit vectors in a three-dimensional space, they can be used to form a basis or a coordinate reference frame. Let the three orthogonal eigenvectors be base vectors $\mathbf{e}_{\mathrm{I}}$, $\mathbf{e}_{\mathrm{II}}$, and $\mathbf{e}_{\mathrm{III}}$ of a Greek reference frame. From (A91) and (A92) we form a new reference basis for the example eigenvalue problem, and thus

$$\mathbf{e}_{\mathrm{I}} = \left(\frac{1}{3}\right)(2\mathbf{e}_1 + \mathbf{e}_2 + 2\mathbf{e}_3)\,, \quad \mathbf{e}_{\mathrm{II}} = \left(\frac{1}{3}\right)(-\mathbf{e}_1 - 2\mathbf{e}_2 + 2\mathbf{e}_3)\,,$$

$$\mathbf{e}_{\mathrm{III}} = \left(\frac{1}{3}\right)(2\mathbf{e}_1 - 2\mathbf{e}_2 - \mathbf{e}_3)\,. \tag{A93}$$

It is easy to verify that both the Greek and Latin base vectors form right-handed orthonormal systems. Orthogonal matrix **Q** for transformation from the Latin to the Greek system is given by (A64) and (A93) as

$$\mathbf{Q} = [Q_{i\alpha}] = \left(\frac{1}{3}\right)\begin{bmatrix} 2 & -1 & 2 \\ 1 & -2 & -2 \\ 2 & 2 & -1 \end{bmatrix}. \tag{A94}$$

Substituting **Q** of (A94) and the **A** specified by (A58) into the second of (A83), with **T** = **A**,

$$\mathbf{A}^{(G)} = \mathbf{Q}^T \cdot \mathbf{A}^{(L)} \cdot \mathbf{Q}\,, \tag{A95}$$

the following result is determined:

$$\mathbf{A}^{(G)} = \left(\frac{1}{9}\right)\begin{bmatrix} 2 & 1 & 2 \\ -1 & -2 & 2 \\ 2 & -2 & -1 \end{bmatrix}\begin{bmatrix} 18 & 6 & 6 \\ 6 & 15 & 0 \\ 6 & 0 & 21 \end{bmatrix}\begin{bmatrix} 2 & -1 & 2 \\ 1 & -2 & -2 \\ 2 & 2 & -1 \end{bmatrix} = \begin{bmatrix} 27 & 0 & 0 \\ 0 & 18 & 0 \\ 0 & 0 & 9 \end{bmatrix}. \tag{A96}$$

Thus, relative to the basis formed of its eigenvectors, a symmetric matrix takes on a diagonal form, the diagonal elements being its eigenvalues. This result, which was demonstrated for a particular case, is true in general in a space of any dimension *n* as long as the matrix is symmetric.

There are two points in the above example that are always true if the matrix is symmetric. The first is that the eigenvalues are always real numbers and the second is that the eigenvectors are always mutually perpendicular. These points will now be proved in the order stated. To prove that $\lambda$ is always real we shall assume that it could be complex; then we show that the imaginary part is zero. This proves that $\lambda$ is real. If $\lambda$ is complex, say $\lambda + i\mu$, then associated eigenvector **t** may also be complex and we denote it by **t** = **n** + *i***m**. With these notations (A48) can be written

$$(\mathbf{A} - \{\lambda + i\mu\}\mathbf{1}) \cdot (\mathbf{n} + i\mathbf{m}) = 0\,. \tag{A97}$$

Equating the real and imaginary parts, we obtain two equations,

$$\mathbf{A} \cdot \mathbf{n} = \lambda\mathbf{n} - \mu\mathbf{m}\,, \quad \mathbf{A} \cdot \mathbf{m} = \lambda\mathbf{m} + \mu\mathbf{n}\,. \tag{A98}$$

The symmetry of matrix **A** means that, for any vectors **n** and **m**,

$$\mathbf{m} \cdot \mathbf{A} \cdot \mathbf{n} = \mathbf{m} \cdot \mathbf{A}^T \cdot \mathbf{n} = \mathbf{n} \cdot \mathbf{A} \cdot \mathbf{m}\,, \tag{A99}$$

a result that can be verified in many ways. Substituting the two equations of (A98) into the first and last equalities of (A99), we find that $\mu = -\mu$, which means that $\mu$ must be zero and $\lambda$ real. This result also shows that **n** must be real.

We will now show that any two eigenvectors are orthogonal if the two associated eigenvalues are distinct. Let $\lambda_1$ and $\lambda_2$ be the eigenvalues associated with eigenvectors **n** and **m**, respectively; then

$$\mathbf{A}\cdot\mathbf{n}=\lambda_1\mathbf{n} \quad \text{and} \quad \mathbf{A}\cdot\mathbf{m}=\lambda_2\mathbf{m}\,. \tag{A100}$$

Substituting the two equations of (A100) into the first and last equalities of (A99), we find that

$$(\lambda_1-\lambda_2)\mathbf{n}\cdot\mathbf{m}=0\,. \tag{A101}$$

Thus, if $\lambda_1 \neq \lambda_2$, then **n** and **m** are perpendicular. If the two eigenvalues are not distinct, then any vector in a plane is an eigenvector, so that one can always construct a mutually orthogonal set of eigenvectors for a symmetric matrix.

Generalizing Example A.7.2 above from 3 to *n*, it may be concluded that any *n*-by-*n* matrix **A** of symmetric tensor components has a representation in which the eigenvalues lie along the diagonal of the matrix and the off-diagonal elements are all zero. The last expression in (A96) is a particular example of this when $n = 3$. If symmetric tensor **A** has *n* eigenvalues $\lambda_i$, then quadratic form $\psi$ may be formed from **A** and vector n-tuple **x**, and thus

$$\psi=\mathbf{x}\cdot\mathbf{A}\cdot\mathbf{x}=\sum_{i=1}^{i=n}\lambda_i x_i^2\,. \tag{A102}$$

If all the eigenvalues of **A** are positive, this quadratic form is said to be *positive definite* and

$$\mathbf{x}\cdot\mathbf{A}\cdot\mathbf{x}=\sum_{i=1}^{i=n}\lambda_i x_i^2 \triangleright 0 \quad \text{for all } \mathbf{x}\neq\mathbf{0}. \tag{A103}$$

(If all the eigenvalues of **A** are negative, the quadratic form is said to be *negative definite*.) Transforming tensor **A** into an arbitrary coordinate system, eq. (A102) takes the form

$$\mathbf{x}\cdot\mathbf{A}\cdot\mathbf{x}=\sum_{i=1}^{i=n}A_{ij}x_i x_j \triangleright 0 \quad \text{for all } \mathbf{x}\neq\mathbf{0}. \tag{A104}$$

Tensor **A** with property (A104), when used as the coefficients of a quadratic form, is said to be positive definite. In the mechanics of materials there are a number of tensors that are positive definite due to the physics they represent. The moment of inertia tensor is an example. Others will be encountered as material coefficients in constitutive equations in Chapter 5.

**Problems**

A.7.1. Consider two three-dimensional coordinate systems. One coordinate system is a right-handed coordinate system. The second coordinate system is obtained from the first by reversing the direction of the first ordered base vector and leaving the other two base vectors to be identical with those in the first coordinate system. Show that the orthogonal transformation relating these systems is given by

$$\mathbf{Q}=\begin{bmatrix}-1 & 0 & 0\\ 0 & 1 & 0\\ 0 & 0 & 1\end{bmatrix}$$

and that its determinant is –1.

A.7.2. Construct the eigenvalues and the eigenvectors of matrix **T** of tensor components where

$$\mathbf{T} = \frac{1}{2}\begin{bmatrix} 13 & 3\sqrt{3} & \sqrt{3} \\ 3\sqrt{3} & 7 & 1 \\ \sqrt{3} & 1 & 8 \end{bmatrix}.$$

A.7.3. Construct the eigenvalues and the eigenvectors of matrix **A** of tensor components where

$$\mathbf{A} = \frac{1}{4}\begin{bmatrix} 17 & 3\sqrt{3} \\ 3\sqrt{3} & 11 \end{bmatrix}.$$

A.7.4. Show that the eigenvalues of matrix **H**,

$$\mathbf{H} = \begin{bmatrix} 1 & 2 & 3 & 4 & 5 & 6 \\ 2 & 7 & 8 & 9 & 10 & 11 \\ 3 & 8 & 12 & 13 & 14 & 15 \\ 4 & 9 & 13 & 16 & 17 & 18 \\ 5 & 10 & 14 & 17 & 19 & 20 \\ 6 & 11 & 15 & 18 & 20 & 21 \end{bmatrix},$$

are 73.227, 2.018. 1.284, 0.602, 0.162, and –1.294.

A.7.5. Consider the components of tensor **T** given in Problem A.7.2 to be relative to a (Latin) coordinate system and denote them by $\mathbf{T}^{(L)}$. Transform these components to a new coordinate system (Greek) using transformation

$$\mathbf{Q} = \frac{1}{2}\begin{bmatrix} 1 & \sqrt{\frac{3}{2}} & \sqrt{\frac{3}{2}} \\ -\sqrt{3} & \frac{1}{\sqrt{2}} & \frac{1}{\sqrt{2}} \\ 0 & -\sqrt{2} & \sqrt{2} \end{bmatrix}.$$

A.7.6. Show that if a tensor is symmetric (skew-symmetric) in one coordinate system, then it is symmetric (skew-symmetric) in all coordinate systems. Specifically, show that if $\mathbf{A}^{(L)} = (\mathbf{A}^{(L)})^{\mathrm{T}}$, then $\mathbf{A}^{(G)} = (\mathbf{A}^{(G)})^{\mathrm{T}}$.

## A.8. THE MOMENT OF INERTIA TENSOR

The mass moment of inertia tensor illustrates many features of the previous sections such as the tensor concept and definition, the open product of vectors, the use of unit vectors, and the significance of eigenvalues and eigenvectors. The mass moment of inertia is the second moment of mass with respect to an axis. The first and zeroth moment of mass with respect to an axis is associated with the concepts of the center of mass of the object and the mass of the object, respectively. Let $dv$ represent the differential volume of object $O$. The volume of that object $V_O$ is then given by

$$V_O = \int_0 dv\,, \tag{A105}$$

and, if $\rho(x_1, x_2, x_3, t) = \rho(\mathbf{x}, t)$ is the density of object $O$, then mass $M_O$ of $O$ is given by

$$M_O = \int_0 \rho(\mathbf{x},t)dv\,. \tag{A106}$$

Centroid $\mathbf{x}_{\text{centroid}}$ and center of mass $\mathbf{x}_{\text{cm}}$ of object $O$ are defined by

$$\mathbf{x}_{centroid} = \frac{1}{V_O}\int_0 \mathbf{x}dv\,,\quad \mathbf{x}_{cm} = \frac{1}{M_O}\int_0 \mathbf{x}\rho(\mathbf{x},t)dv \tag{A107}$$

where $\mathbf{x}$ is a position vector locating the differential element of volume or mass with respect to the origin. The power of $\mathbf{x}$ occurring in the integrand indicates the order of the moment of mass — it is to the zero power in the definition of the mass of the object itself — and it is to the first order in the definition of the mass center. The second moments of area and mass with respect to the origin of coordinates are called the area and mass moments of inertia, respectively. Let $\mathbf{e}$ represent the unit vector passing through the origin of coordinates; then $\mathbf{x} - (\mathbf{x}\cdot\mathbf{e})\mathbf{e}$ is the perpendicular distance from the $\mathbf{e}$ axis to the differential element of volume or mass at $\mathbf{x}$ (Figure A.2). The second or mass moment of inertia of object $O$ about axis $\mathbf{e}$, a scalar, is denoted by $I_{ee}$ and given by

$$I_{ee} = \int_O (\mathbf{x}-(\mathbf{x}\cdot\mathbf{e})\mathbf{e})\cdot(\mathbf{x}-(\mathbf{x}\cdot\mathbf{e})\mathbf{e})\rho(\mathbf{x},t)dv\,. \tag{A108}$$

This expression for $I_{ee}$ may be changed in algebraic form by noting first that

$$(\mathbf{x}-(\mathbf{x}\cdot\mathbf{e})\mathbf{e})\cdot(\mathbf{x}-(\mathbf{x}\cdot\mathbf{e})\mathbf{e}) = \mathbf{x}\cdot\mathbf{x}-(\mathbf{x}\cdot\mathbf{e})^2 \quad \text{and}$$

$$\mathbf{x}\cdot\mathbf{x}-(\mathbf{x}\cdot\mathbf{e})^2 = \mathbf{e}\cdot\{(\mathbf{x}\cdot\mathbf{x})\mathbf{1}-(\mathbf{x}\otimes\mathbf{x})\}\cdot\mathbf{e}\,;$$

thus, from A(108),

$$I_{ee} = \mathbf{e}\cdot\left[\int_0 \{(\mathbf{x}\cdot\mathbf{x})\mathbf{1}-(\mathbf{x}\otimes\mathbf{x})\}\rho(\mathbf{x},t)dv\right]\cdot\mathbf{e}\,. \tag{A109}$$

If the notation for the mass moment of inertia tensor $\mathbf{I}$ is introduced,

$$\mathbf{I} = \int_0 \{(\mathbf{x}\cdot\mathbf{x})\mathbf{1}-(\mathbf{x}\otimes\mathbf{x})\}\rho(\mathbf{x},t)dv\,, \tag{A110}$$

then (A109) and (A108) simplify to

$$I_{ee} = \mathbf{e}\cdot\mathbf{I}\cdot\mathbf{e}\,. \tag{A111}$$

In this section mass moment of inertia $\mathbf{I}$ has been referred to as a tensor. A short calculation will demonstrate that the terminology is correct. From (A110) is easy to see that $\mathbf{I}$ may be written relative to the Latin and Greek coordinate systems as

$$\mathbf{I}^{(L)} = \int_0 \left\{(\mathbf{x}^{(L)}\cdot\mathbf{x}^{(L)})\mathbf{1}-(\mathbf{x}^{(L)}\otimes\mathbf{x}^{(L)})\right\}\rho(\mathbf{x}^{(L)},t)dv\,, \tag{A112}$$

and

$$\mathbf{I}^{(G)} = \int_0 \{(\mathbf{x}^{(G)}\cdot\mathbf{x}^{(G)})\mathbf{1}-(\mathbf{x}^{(G)}\otimes\mathbf{x}^{(G)})\}\rho(\mathbf{x}^{(G)},t)dv\,, \tag{A113}$$

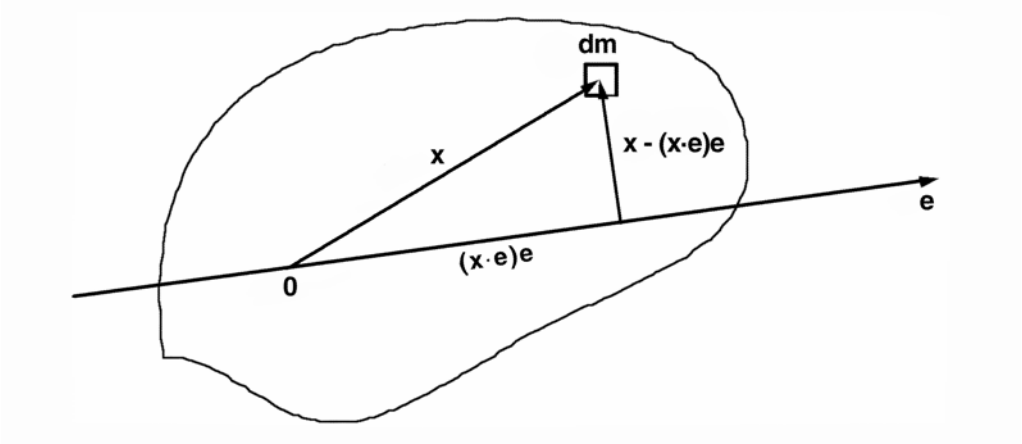



**Figure A.2**. A diagram for the calculation of the mass moment of inertia of an object about the axis characterized by the unit vector **e**. **x** is the vector from the origin O of coordinates to the element of mass dm; **x** – (**x**·**e**)**e** is the perpendicular distance from the axis **e** to the element of mass *dm*.

respectively. The transformation law for the open product of **x** with itself can be calculated by twice using the transformation law for vectors (A77) applied to **x**, and thus

$$\mathbf{x}^{(L)} \otimes \mathbf{x}^{(L)} = \mathbf{Q} \cdot \mathbf{x}^{(G)} \otimes \mathbf{Q} \cdot \mathbf{x}^{(G)} = \mathbf{Q} \cdot (\mathbf{x}^{(G)} \otimes \mathbf{x}^{(G)}) \cdot \mathbf{Q}^T . \tag{A114}$$

The occurrence of the transpose in the last equality of the last equation may be more easily perceived by recasting the expression in indicial notation:

$$\mathbf{x}_i^{(L)} \mathbf{x}_j^{(L)} = Q_{i\alpha} \mathbf{x}_\alpha^{(G)} Q_{j\beta} \mathbf{x}_\beta^{(G)} = Q_{i\alpha} \mathbf{x}_\alpha^{(G)} \mathbf{x}_\beta^{(G)} Q_{j\beta} . \tag{A115}$$

Now, contracting the open product of vectors in (A114) above to the scalar product, it follows that since $\mathbf{Q} \cdot \mathbf{Q}^T = \mathbf{Q}^T \cdot \mathbf{Q} = \mathbf{1}$ ($Q_{i\alpha} Q_{i\beta} = \delta_{\alpha\beta}$),

$$\mathbf{x}^{(L)} \cdot \mathbf{x}^{(L)} = \mathbf{x}^{(G)} \cdot \mathbf{x}^{(G)} . \tag{A116}$$

Combining results (A114) and (A116), it follows that the non-scalar portions of the integrands in (A112) and (A113) are related by

$$\{(\mathbf{x}^{(L)} \cdot \mathbf{x}^{(L)})\mathbf{1} - (\mathbf{x}^{(L)} \otimes \mathbf{x}^{(L)})\} = \mathbf{Q} \cdot \{(\mathbf{x}^{(G)} \cdot \mathbf{x}^{(G)})\mathbf{1} - (\mathbf{x}^{(G)} \otimes \mathbf{x}^{(G)})\} \cdot \mathbf{Q}^T .$$

Thus, from this result and (A112) and (A113), the transformation law for second-order tensors is obtained:

$$\mathbf{I}^{(L)} = \mathbf{Q} \cdot \mathbf{I}^{(G)} \cdot \mathbf{Q}^T , \tag{A117}$$

and it follows that tensor terminology is correct in describing the mass moment of inertia.

The matrix of tensor components of moment of inertia tensor **I** in a three-dimensional space is given by

$$\mathbf{I} = \begin{bmatrix} I_{11} & I_{12} & I_{13} \\ I_{12} & I_{22} & I_{23} \\ I_{13} & I_{23} & I_{33} \end{bmatrix}, \tag{A118}$$

where the components are given by

$$I_{11} = \int_0 (x_2^2 + x_3^2)\rho(\mathbf{x},t)dv\,, \quad I_{22} = \int_0 (x_1^2 + x_3^2)\rho(\mathbf{x},t)dv\,,$$

$$I_{33} = \int_0 (x_2^2 + x_1^2)\rho(\mathbf{x},t)dv\,, \quad I_{12} = -\int_0 (x_1x_2)\rho(\mathbf{x},t)dv \tag{A119}$$

$$I_{13} = -\int_0 (x_1x_3)\rho(\mathbf{x},t)dv\,, \quad I_{23} = -\int_0 (x_2x_3)\rho(\mathbf{x},t)dv\,.$$

**Example A.8.1**

Determine the mass moment of inertia of a rectangular prism of homogeneous material of density ρ and side lengths $a$, $b$, and $c$ about one corner. Select the coordinate system so that its origin is at one corner and let $a$, $b$, and $c$ represent the distances along the $x_1$, $x_2$, $x_3$ axes, respectively. Construct the matrix of tensor components referred to this coordinate system.

**Solution**: Integrations (A119) yield the following results:

$$I_{11} = \int_0 (x_2^2 + x_3^2)\rho(\mathbf{x},t)dv = \rho\int_0 (x_2^2 + x_3^2)dx_1dx_2dx_3$$

$$= a\rho\int_{0,0}^{b,c} (x_2^2 + x_3^2)dx_2dx_3 = \frac{\rho abc}{3}(b^2 + c^2)\,,$$

$$I_{22} = \frac{\rho abc}{3}(a^2 + c^2)\,, \quad I_{33} = \frac{\rho abc}{3}(a^2 + b^2)\,,$$

$$I_{12} = -\int_0 (x_1x_2)\rho(\mathbf{x},t)dv = -\rho c\int_{0,0}^{a,b} (x_1x_2)dx_1dx_2 = \frac{-\rho abc}{4}(ab)$$

$$I_{13} = \frac{-\rho abc}{4}(ac)\,, \quad I_{23} = \frac{-\rho abc}{4}(bc)\,,$$

and thus

$$I = \frac{\rho abc}{12}\begin{bmatrix} 4(b^2 + c^2) & -3ab & -3ac \\ -3ab & 4(a^2 + c^2) & -3bc \\ -3ac & -3bc & 4(a^2 + b^2) \end{bmatrix}.$$

**Example A.8.2**

In the special case when the rectangular prism in Example A.8.1 is a cube, that is to say, $a = b = c$, find the eigenvalues and eigenvectors of the matrix of tensor components referred to the coordinate system of the example. Then find the matrix of tensor components referred to the principal, or eigenvector, coordinate system.

**Solution**: The matrix of tensor components referred to this coordinate system is

$$I = \frac{\rho a^5}{12}\begin{bmatrix} 8 & -3 & -3 \\ -3 & 8 & -3 \\ -3 & -3 & 8 \end{bmatrix}.$$

The eigenvalues of **I** are $\rho a^5/6$, $11\rho a^5/12$, and $11\rho a^5/12$. Eigenvector $(1/\sqrt{3})[1, 1, 1]$ is associated with eigenvalue $\rho a^5/6$. Due the multiplicity of the eigenvalue $11\rho a^5/12$, any vector perpendicular to the first eigenvector, $(1/\sqrt{3})[1, 1, 1]$, is an eigenvector associated with the multiple eigenvalue $11\rho a^5/12$. Thus, any mutually perpendicular unit vectors in the plane perpendicular to the first eigenvector may be selected as the base vectors for the principal coordinate system. The choice is arbitrary. In this example the two perpendicular unit vectors, $(1/\sqrt{2})[-1, 0, 1]$ and $(1/\sqrt{6})[1, -2, 1]$, are the eigenvectors associated with multiple eigenvalue $11\rho a^5/12$, but any perpendicular pair of vectors in the plane may be selected. The orthogonal transformation that will transform the matrix of tensor components referred to this coordinate system to the matrix of tensor components referred to the principal, or eigenvector, coordinate system is then given by

$$\mathbf{Q} = \begin{bmatrix} 1/\sqrt{3} & 1/\sqrt{3} & 1/\sqrt{3} \\ -1/\sqrt{2} & 0 & 1/\sqrt{2} \\ 1/\sqrt{6} & -2/\sqrt{6} & 1/\sqrt{6} \end{bmatrix}.$$

Applying this transformation produced the matrix of tensor components referred to the principal, or eigenvector, coordinate system:

$$\mathbf{Q}\cdot\mathbf{I}\cdot\mathbf{Q}^T = \frac{\rho a^5}{12}\begin{bmatrix} 2 & 0 & 0 \\ 0 & 11 & 0 \\ 0 & 0 & 11 \end{bmatrix}.$$

Formulas for the mass moment of inertia of a thin plate of thickness $t$ and a homogeneous material of density $\rho$ are obtained by specializing these results. Let the plate be thin in the $x_3$ direction and consider the plate to be so thin that terms of order $t^2$ are negligible relative to the others; then formulas (A119) for the components of the mass moment of inertia tensor are given by

$$I_{11} = \rho t \int_0 x_2^2 dx_1 dx_2\,, \quad I_{22} = \rho t \int_0 x_1^2 dx_1 dx_2\,,$$

$$I_{33} = \rho t \int_0 (x_1^2 + x_2^2) dx_1 dx_2\,. \tag{A120}$$

$$I_{12} = -\rho t \int_0 (x_1 x_2) dx_1 dx_2\,, \quad I_{13} = 0\,, \quad I_{23} = 0\,.$$

When divided by $\rho t$, these components of the mass moment of inertia of a thin plate of thickness $t$ are called the components of the area moment of inertia matrix:

$$I_{11}^{\text{Area}} = \frac{I_{11}}{\rho t} = \int_O x_2^2 dx_1 dx_2\,,\quad I_{22}^{\text{Area}} = \frac{I_{22}}{\rho t} = \int_O x_1^2 dx_1 dx_2\,,\quad I_{33}^{\text{Area}} = \frac{I_{33}}{\rho t} = \int_O (x_1^2 + x_2^2) dx_1 dx_2\,,$$

$$I_{12}^{\text{Area}} = \frac{I_{12}}{\rho t} = -\int_O (x_1 x_2) dx_1 dx_2\,,\quad I_{13}^{\text{Area}} = 0\,,\ I_{23}^{\text{Area}} = 0\,. \tag{A121}$$

**Example A.8.3**

Determine the area moment of inertia of a thin rectangular plate of thickness $t$, height $h$, and width of base $b$. Specify precisely where the origin of the coordinate system that you are using is located and how the base vectors of that coordinate system are located relative to the sides of the rectangular plate.

**Solution**: The coordinate system that makes this problem easy is one that passes through the centroid of the rectangle and has axes parallel to the sides of the rectangle. If base $b$ is parallel to the $x_1$ axis and height $h$ is parallel to the $x_2$ axis, then integrations (A121) yield the following results:

$$I_{11}^{\text{Area}} = \frac{bh^3}{12}\,,\quad I_{22}^{\text{Area}} = \frac{hb^3}{12}\,,\quad I_{33}^{\text{Area}} = \frac{bh}{12}(b^2 + h^2)\,,$$

$$I_{12}^{\text{Area}} = 0\,,\quad I_{13}^{\text{Area}} = 0\,,\quad I_{23}^{\text{Area}} = 0\,.$$

**Example A.8.4**

Determine the area moments and product of inertia of a thin right-triangular plate of thickness $t$, height $h$, and width of base $b$. Let base $b$ be along the $x_1$ axis and height $h$ be along the $x_2$, axis and the sloping face of the triangle have endpoints at $(b, 0)$ and $(0, h)$. Determine the area moments and product of inertia of the right-triangular plate relative to this coordinate system. Construct the matrix of tensor components referred to this coordinate system.

**Solution**: Integrations (A121) yield the following results:

$$I_{11}^{\text{Area}} = \int_O x_2^2 dx_1 dx_2 = \int_0^h b(1 - x_2/h) x_2^2 dx_2 = bh^3/12\,,\quad I_{22}^{\text{Area}} = hb^3/12$$

$$I_{12}^{\text{Area}} = -\int_O (x_1 x_2) dx_1 dx_2 = -(1/2)\int_0^h b^2 (1 - x_2/h)^2 x_2 dx_2 = -(b^2 h^2/24)\,;$$

thus, the matrix of tensor components referred to this coordinate system is

$$\mathbf{I}^{\text{Area}} = \frac{bh}{24}\begin{bmatrix} 2h^2 & -bh \\ -hb & 2b^2 \end{bmatrix}.$$

**Example A.8.5**

In the special case when the triangle in Example A.8.4 is isosceles, that is to say, $b = h$, find the eigenvalues and eigenvectors of the matrix of tensor components referred to the coordinate

system of the example. Then find the matrix of tensor components referred to the principal, or eigenvector, coordinate system.

**Solution**: The matrix of tensor components referred to this coordinate system is

$$\mathbf{I}^{\text{Area}} = \frac{bh}{24}\begin{bmatrix} 2h^2 & -bh \\ -hb & 2b^2 \end{bmatrix}.$$

The eigenvalues of $\mathbf{I}$ are $h^4/8$ and $h^4/24$. Eigenvector $(1/\sqrt{2})[1, 1,1],\{-1,1\}-1]$ is associated with eigenvalue $h^4/8$ and eigenvector $(1/\sqrt{2})[1, 1]$ is associated with eigenvalue $h^4/24$. The orthogonal transformation that will transform the matrix of tensor components referred to this coordinate system to the matrix of tensor components referred to the principal, or eigenvector, coordinate system is then given by

$$\mathbf{Q} = \frac{1}{\sqrt{2}}\begin{bmatrix} 1 & 1 \\ -1 & 1 \end{bmatrix}.$$

Applying this transformation produced the matrix of tensor components referred to the principal, or eigenvector, coordinate system:

$$\mathbf{Q}\cdot\mathbf{I}^{\text{Area}}\cdot\mathbf{Q}^T = \frac{h^4}{24}\begin{bmatrix} 1 & 0 \\ 0 & 3 \end{bmatrix}.$$

The parallel axis theorem for moment of inertia matrix $\mathbf{I}$ is derived by considering the mass moment of inertia of object $O$ about two parallel axes, $I_{ee}$ about $\mathbf{e}$ and $I_{e'e'}$ about $\mathbf{e}'$. $I_{e'e'}$ is given by

$$I_{e'e'} = \mathbf{e}'\cdot\mathbf{I}'\cdot\mathbf{e}', \tag{A122}$$

where moment of inertia matrix **I'** is given by

$$\mathbf{I}' = \int_0 \{(\mathbf{x}'\cdot\mathbf{x}')\mathbf{1} - (\mathbf{x}'\otimes\mathbf{x}')\}\rho(\mathbf{x}',t)dv'. \tag{A123}$$

Let $\mathbf{d}$ be a vector perpendicular to both $\mathbf{e}$ and $\mathbf{e}'$ and equal in magnitude to the perpendicular distance between $\mathbf{e}$ and $\mathbf{e}'$, thus $\mathbf{x}' = \mathbf{x} + \mathbf{d}$, $\mathbf{e}\cdot\mathbf{d} = 0$, and $\mathbf{e}'\cdot\mathbf{d} = 0$. Substituting $\mathbf{x}' = \mathbf{x} + \mathbf{d}$ in **I'**, it follows that

$$\mathbf{I}' = \int_0 \{(\mathbf{x}\cdot\mathbf{x} + \mathbf{d}\cdot\mathbf{d} + 2\mathbf{x}\cdot\mathbf{d})\mathbf{1}\}\rho(\mathbf{x},t)dv$$

$$-\int_0 \{(\mathbf{x}\otimes\mathbf{x} + \mathbf{d}\otimes\mathbf{d} + \mathbf{d}\otimes\mathbf{x} + \mathbf{x}\otimes\mathbf{d})\}\rho(\mathbf{x},t)dv, \tag{A124}$$

or if (A124) is rewritten so that constant vector $\mathbf{d}$ is outside the integral signs,

$$\mathbf{I}' = \mathbf{1}\int_0 \{(\mathbf{x}\cdot\mathbf{x})\rho(\mathbf{x},t)dv + \mathbf{1}(\mathbf{d}\cdot\mathbf{d})\int_0 \rho(\mathbf{x},t)dv + \mathbf{1}(2\mathbf{d}\cdot\int_0 \mathbf{x})\rho(\mathbf{x},t)dv -$$

$$\int_0 \{(\mathbf{x}\otimes\mathbf{x})\rho(\mathbf{x},t)dv - (\mathbf{d}\otimes\mathbf{d})\int_0 \rho(\mathbf{x},t)dv -$$

$$\mathbf{d}\otimes\int_0 \mathbf{x}\rho(\mathbf{x},t)dv - \left(\int_0 \mathbf{x}\rho(\mathbf{x},t)dv\right)\otimes\mathbf{d};$$

then recalling definitions (A106) of mass $M_O$ of $O$ and (A107) of center of mass $\mathbf{x}_{cm}$ of object $O$, this result simplifies to

$$\mathbf{I}' = \mathbf{I} + \{(\mathbf{d}\cdot\mathbf{d})\mathbf{1} - (\mathbf{d}\otimes\mathbf{d})\}M_O +$$
$$2M_O\mathbf{1}(\mathbf{x}_{cm}\cdot\mathbf{d}) - M_O(\mathbf{d}\otimes\mathbf{x}_{cm} + \mathbf{x}_{cm}\otimes\mathbf{d}). \quad \text{(A125)}$$

Thus, when the origin of coordinates is taken at the center of the mass, it follows that $\mathbf{x}_{cm} = 0$ and

$$\mathbf{I}' = \mathbf{I}_{cm} + \{(\mathbf{d}\cdot\mathbf{d})\mathbf{1} - (\mathbf{d}\otimes\mathbf{d})\}M_O. \quad \text{(A126)}$$

In the special case of the area moment of inertia this formula becomes

$$\mathbf{I}' = \mathbf{I}_{\text{centroid}} + \{(\mathbf{d}\cdot\mathbf{d})\mathbf{1} - (\mathbf{d}\otimes\mathbf{d})\}A, \quad \text{(A127)}$$

where $\mathbf{I}$ are now the area moments of inertia and the mass of the object, $M_o$, has been replaced by the area of thin plate $A$.

**Example A.8.6**

Consider again the rectangular prism of Example A.8.1. Determine the mass moment of inertia tensor of that prism about its centroid or center of mass.

**Solution**: The desired result, the mass moment of inertia about the centroidal axes, is $\mathbf{I}_{cm}$ in (A126), and the moment of inertia about the corner, **I'**, is the result calculated in Example A.8.1:

$$\mathbf{I}' = \frac{\rho abc}{12}\begin{bmatrix} 4(b^2+c^2) & -3ab & -3ac \\ -3ab & 4(a^2+c^2) & -3bc \\ -3ac & -3bc & 4(a^2+b^2) \end{bmatrix}.$$

Formula (A126) is then written in the form

$$\mathbf{I}_{cm} = \mathbf{I}' - \{(\mathbf{d}\cdot\mathbf{d})\mathbf{1} - (\mathbf{d}\otimes\mathbf{d})\}M_O,$$

where $M_o = \rho abs$. Vector $\mathbf{d}$ is a vector from the centroid to the corner:

$$\mathbf{d} = -\left(\frac{1}{2}\right)(a\mathbf{e}_1 + b\mathbf{e}_2 + c\mathbf{e}_3).$$

Substituting **I'** and the formula for $\mathbf{d}$ into the equation for $\mathbf{I}$ above, it follows that the mass moment of inertia of the rectangular prism relative to its centroid is given by

$$\mathbf{I}_{cm} = \frac{\rho abc}{12}\begin{bmatrix} (b^2+c^2) & 0 & 0 \\ 0 & (a^2+c^2) & 0 \\ 0 & 0 & (a^2+b^2) \end{bmatrix}.$$

**Example A.8.7**

Consider again the thin right-triangular plate of Example A.8.4. Determine the area moment of inertia tensor of that right-triangular plate about its centroid.

**Solution**: The desired result, the area moment of inertia about the centroidal axes is the $\mathbf{I}^{\text{Area}}_{\text{centroid}}$ in (A127) and moment of inertia $\mathbf{I}'_{\text{Area}}$ about the corner is the result calculated in Example A.8.4:

$$\mathbf{I}'_{\text{Area}} = \frac{bh}{24}\begin{bmatrix} 2h^2 & -bh \\ -hb & 2b^2 \end{bmatrix}.$$

Formula (A126) is then written in the form

$$\mathbf{I}^{\text{Area}}_{\text{centroid}} = \mathbf{I}'_{\text{Area}} - \{(\mathbf{d}\cdot\mathbf{d})\mathbf{1} - (\mathbf{d}\otimes\mathbf{d})\}A\,,$$

where $A = bh$. Vector $\mathbf{d}$ is a vector from the centroid to the corner:

$$\mathbf{d} = -(1/3)(b\mathbf{e}_1 + h\mathbf{e}_2)\,.$$

Substituting $\mathbf{I}'$ and the formula for $\mathbf{d}$ into the equation for $\mathbf{I}_{\text{centroid}}$ above, it follows that the mass moment of inertia of the rectangular prism relative to its centroid is given by

$$\mathbf{I}^{\text{Area}}_{\text{centroid}} == \frac{bh}{72}\begin{bmatrix} 2h^2 & bh \\ hb & 2b^2 \end{bmatrix}.$$

**Problems**

A.8.1. Find the center of mass of a set of four masses. The form masses and their locations are mass 1 (2 kg) at (3, –1), mass 2 (4 kg) at (4, 4), mass 3 (5 kg) at (-4, 4), and mass 4 (1 kg) at (–3, –1).

A.8.2. Under what conditions does the center of mass of an object coincide with the centroid?

A.8.3. Find the centroid of a cylinder of length $L$ with a semicircular cross-section of radius $R$.

A.8.4. Find the center of mass of a cylinder of length $L$ with a semicircular cross-section of radius $R$ ($R < 2L$) if the density varies according to rule $\rho = \rho_o(1 + c(x_2)^2)$. The coordinate system for the cylinder has been selected so that $x_3$ is along its length $L$, $x_2$ is across its smallest dimension ($0 \le x_2 \le R$), and $x_1$ is along its intermediate dimension ($-R \le x_1 \le R$).

A.8.5. Show that moment of inertia matrix $\mathbf{I}$ is symmetric.

A.8.6. Develop the formulas for the mass moment of inertia of a thin plate of thickness $t$ and a homogeneous material of density $\rho$. Illustrate these specialized formulas by determining the mass moment of inertia of a thin rectangular plate of thickness $t$, height $h$, and width of base $b$, and a homogeneous material of density $\rho$. Specify precisely where the origin of the coordinate system that you are using is located and how the base vectors of that coordinate system are located relative to the sides of the rectangular plate.

A.8.7. In Example A.8.2 the occurrence of a multiple eigenvalue ($11\rho a^5/12$) made any vector perpendicular to the first eigenvector, $\mathbf{e}_1 = (1/\sqrt{3})[1, 1, 1]$, an eigenvector associated with multiple eigenvalue $11\rho a^5/12$. In Example A.8.2 the two perpendicular unit vectors, $\mathbf{e}_2 = (1/\sqrt{2})$ [–1, 0, 1] and $\mathbf{e}_3 = (1/\sqrt{6})[1, -2, 1]$, were selected as the eigenvectors associated with multiple eigenvalue $11\rho a^5/12$, but any two perpendicular vectors in the plane could have been selected. Select two other eigenvectors in the plane and show that these two eigenvectors are given by $\mathbf{e}_{\text{II}} = \cos\gamma\,\mathbf{e}_2 + \sin\gamma\,\mathbf{e}_3$ and $\mathbf{e}_{\text{III}} = -\sin\gamma\,\mathbf{e}_2 + \cos\gamma\,\mathbf{e}_3$. Let $\mathbf{R}$ be the orthogonal transformation between these Latin and Greek systems:

$$\mathbf{R} = \begin{bmatrix} 1 & 0 & 0 \\ 0 & \cos\gamma & \sin\gamma \\ 0 & -\sin\gamma & \cos\gamma \end{bmatrix}.$$

Show that when the Greek coordinate system is used rather than the Latin one, the coordinate transformation that diagonalizes matrix **I** is **Q**·**R** rather than **Q**. Show that both **R**·**Q** and **Q** transform matrix **I** into the coordinate system in which it is diagonal:

$$\mathbf{Q}\cdot\mathbf{I}\cdot\mathbf{Q}^T = \mathbf{R}\cdot\mathbf{Q}\cdot\mathbf{I}\cdot\mathbf{Q}^T\cdot\mathbf{R}^T = \frac{\rho a^5}{12}\begin{bmatrix} 2 & 0 & 0 \\ 0 & 11 & 0 \\ 0 & 0 & 11 \end{bmatrix}.$$

## A.9. THE ALTERNATOR AND VECTOR CROSS-PRODUCTS

There is a strong emphasis on the indicial notation in this section. It is advised that the definitions (in §A.3) of free indices and summation indices be reviewed carefully if one is not altogether comfortable with indicial notation. It would also be beneficial to redo some indicial notation problems.

The alternator in three dimensions is a three-index numerical symbol that encodes the permutations that one is taught to use expanding a determinant. Recall the process of evaluating the determinant of 3-by-3 matrix **A**:

$$\mathrm{Det}\mathbf{A} = \mathrm{Det}\begin{bmatrix} A_{11} & A_{12} & A_{13} \\ A_{21} & A_{22} & A_{23} \\ A_{31} & A_{32} & A_{33} \end{bmatrix} = \begin{vmatrix} A_{11} & A_{12} & A_{13} \\ A_{21} & A_{22} & A_{23} \\ A_{31} & A_{32} & A_{33} \end{vmatrix} = \tag{A128}$$

$$A_{11}A_{22}A_{33} - A_{11}A_{32}A_{23} - A_{12}A_{21}A_{33} + A_{12}A_{31}A_{23} + A_{13}A_{21}A_{32} - A_{13}A_{31}A_{22}\,.$$

The permutations that one is taught to use expanding a determinant are permutations of a set of three objects. The alternator is denoted by $e_{ijk}$ and defined so that it takes on values +1, 0, or –1 according to rule

$$e_{ijk} \equiv \begin{Bmatrix} +1 \text{ if } P \text{ is an even permutation} \\ 0 \quad \text{otherwise} \\ -1 \text{ if } P \text{ is an odd permutation} \end{Bmatrix}, \quad \mathrm{P} \equiv \begin{Bmatrix} 1 & 2 & 3 \\ i & j & k \end{Bmatrix}, \tag{A129}$$

where $P$ is the permutation symbol on a set of three objects. The only +1 values of $e_{ijk}$ are $e_{123}$, $e_{231}$ , and $e_{312}$. It is easy to verify that 123, 231, and 312 are even permutations of 123. The only –1 values of $e_{ijk}$ are $e_{132}$, $e_{321}$ , and $e_{213}$. It is easy to verify that 132, 321, and 213 are odd permutations of 123. The other 21 components of $e_{ijk}$ are all zero because they are neither even nor odd permutations of 123 due to the fact that one number (either 1, 2, or 3) occurs more than once in the indices (for example, $e_{122}$ = 0 since 122 is not a permutation of 123). One mnemonic device for the even permutations of 123 is to write 123123, then read the first set of three digits, 123, the second set, 231, and the third set, 312. The odd permutations may be read off 123123 also by reading from right to left rather than from left to right; reading from the right (but recording them then from the left, as usual) the first set of three digits, 321, the second set, 213, and the third set, 132.

The alternator may now be employed to shorten formula (A128) for calculating the determinant:

$$e_{mnp}\mathrm{Det}\mathbf{A} = \sum_{k=1}^{k=3}\sum_{j=1}^{j=3}\sum_{i=1}^{i=3} e_{ijk}A_{im}A_{jn}A_{kp} = \sum_{k=1}^{k=3}\sum_{j=1}^{j=3}\sum_{i=1}^{i=3} e_{ijk}A_{mi}A_{nj}A_{pk}\ . \tag{A130}$$

This result may be verified by selecting the values of *mnp* to be 123, 231, 312, 132, 321, or 213, then performing summation over three indices *i*, *j*, and *k* over 1, 2, and 3, as indicated on the right-hand side of (A130). In each case the result is the right-hand side of (A128). It should be noted that (A130) may be used to show $\mathrm{Det}\mathbf{A} = \mathrm{Det}\mathbf{A}^{\mathrm{T}}$.

The alternator may be used to express the fact that interchanging two rows or two columns of a determinant changes the sign of the determinant:

$$e_{mnp}\mathrm{Det}\mathbf{A} = \begin{vmatrix} A_{1m} & A_{1n} & A_{1p} \\ A_{2m} & A_{2n} & A_{2p} \\ A_{3m} & A_{3n} & A_{3p} \end{vmatrix} = \begin{vmatrix} A_{m1} & A_{m2} & A_{m3} \\ A_{n1} & A_{n2} & A_{n3} \\ A_{p1} & A_{p2} & A_{p3} \end{vmatrix}. \tag{A131}$$

Using the alternator again may combine these two representations:

$$e_{ijk}e_{mnp}\mathrm{Det}\mathbf{A} = \begin{vmatrix} A_{im} & A_{in} & A_{ip} \\ A_{jm} & A_{jn} & A_{jp} \\ A_{km} & A_{kn} & A_{kp} \end{vmatrix}. \tag{A132}$$

In the special case when $\mathbf{A} = \mathbf{1}$ ($A_{ij} = \delta_{ij}$), an important identity relating the alternator to the Kronecker delta is obtained:

$$e_{ijk}e_{mnp} = \begin{vmatrix} \delta_{im} & \delta_{in} & \delta_{ip} \\ \delta_{jm} & \delta_{jn} & \delta_{jp} \\ \delta_{km} & \delta_{kn} & \delta_{kp} \end{vmatrix}. \tag{A133}$$

The following special cases of (A133) provide three more very useful relations between the alternator and the Kronecker delta:

$$\sum_{k=1}^{k=3} e_{ijk}e_{mnk} = \delta_{im}\delta_{jn} - \delta_{in}\delta_{jm}\,,\ \sum_{k=1}^{k=3}\sum_{j=1}^{j=3} e_{ijk}e_{mjk} = 2\delta_{im}\,,\ \sum_{k=1}^{k=3}\sum_{j=1}^{j=3}\sum_{i=1}^{i=3} e_{ijk}e_{ijk} = 6\,. \tag{A134}$$

The first of these relations is obtained by setting indices *p* and *k* equal in (A133) and then expanding the determinant. The second is obtained from the first by setting indices *n* and *j* equal in the first. The third is obtained from the second by setting indices *i* and *m* equal in the second.

**Example A.9.1**

Derive the first of (A134) from (A133).

**Solution**: The first of (A134) is obtained from (A133) by setting indices *p* and *k* equal in (A133) and then expanding the determinant:

$$\sum_{k=1}^{3} e_{ijk}e_{mnk} = \begin{vmatrix} \delta_{im} & \delta_{in} & \delta_{ik} \\ \delta_{jm} & \delta_{jn} & \delta_{jk} \\ \delta_{km} & \delta_{kn} & 3 \end{vmatrix};$$

one finds that

$$\sum_{k=1}^{3} e_{ijk}e_{mnk} =$$

$$\sum_{k=1}^{3} (3\delta_{im}\delta_{jn} - \delta_{im}\delta_{jk}\delta_{kn} - 3\delta_{in}\delta_{jm} + \delta_{in}\delta_{km}\delta_{jk} + \delta_{ik}\delta_{jm}\delta_{kn} - \delta_{ik}\delta_{km}\delta_{jn}) .$$

Carrying out the indicated summation over index $k$ in the expression above,

$$\sum_{k=1}^{3} e_{ijk}e_{mnk} =$$

$$3\delta_{im}\delta_{jn} - \delta_{im}\delta_{jn} - 3\delta_{in}\delta_{jm} + \delta_{in}\delta_{jm} + \delta_{jm}\delta_{in} - \delta_{im}\delta_{jn} =$$

$$\delta_{im}\delta_{jn} - \delta_{in}\delta_{jm} .$$

This is the desired result, the first of (A134).

**Example A.9.2**

Prove that Det(**A**·**B**) = Det**A**Det**B**.

**Solution**: Replacing **A** in (A130) by **C** and selecting the values of *mnp* to be 123, then (A130) becomes

$$\mathrm{Det}\mathbf{C} = \sum_{k=1}^{k=3}\sum_{j=1}^{j=3}\sum_{i=1}^{i=3} e_{ijk}C_{i1}C_{j2}C_{k3} .$$

Now **C** is replaced by product **A**·**B** (with

$$C_{i1} = \sum_{m=1}^{m=3} A_{im}B_{m1} , \; C_{j2} = \sum_{n=1}^{n=3} A_{jn}B_{n2} , \text{ and } C_{k3} = \sum_{p=1}^{p=3} A_{kp}B_{p3} ,$$

and thus

$$\mathrm{Det}\mathbf{A}\cdot\mathbf{B} = \sum_{k=1}^{k=3}\sum_{j=1}^{j=3}\sum_{i=1}^{i=3} e_{ijk}\sum_{m=1}^{m=3} A_{im}B_{m1}\sum_{n=1}^{n=3} A_{jn}B_{n2}\sum_{p=1}^{p=3} A_{kp}B_{p3} ,$$

or

$$\mathrm{Det}\mathbf{A}\cdot\mathbf{B} = \sum_{m=1}^{m=3}\sum_{n=1}^{n=3}\sum_{p=1}^{p=3}\left(\sum_{k=1}^{k=3}\sum_{j=1}^{j=3}\sum_{i=1}^{i=3} e_{ijk}A_{im}A_{jn}A_{kp}\right)B_{m1}B_{n2}B_{p3} ,$$

where the order of the terms in the second sum has been rearranged from the first. Comparison of the first four rearranged terms from the second sum with the right-hand side of (A130) shows that the first four terms in the sum on the right may be replaced by $e_{mnp}$Det**A**; thus, applying the first equation of this solution again with **C** replaced by **B**, the desired result is obtained:

$$\mathrm{Det}\mathbf{A}\cdot\mathbf{B} = \mathrm{Det}\mathbf{A}\sum_{k=1}^{k=3}\sum_{j=1}^{j=3}\sum_{i=1}^{i=3} e_{mnp}B_{m1}B_{n2}B_{p3} = \mathrm{Det}\mathbf{A}\ \mathrm{Det}\mathbf{B} .$$

Consider now the question of the tensorial character of the alternator. Vectors were shown to be characterized by symbols with one subscript, (second rank) tensors were shown to be characterized by symbols with two subscripts. What is the tensorial character of a symbol with three subscripts; is it a third-order tensor? Almost. Tensors are identified on the basis of their tensor transformation law. Recall tensor transformation laws (A75) and (A76) for a vector, (A86) for a second-order tensor, and (A87) for a tensor of order $n$. An equation that contains a transformation law for the alternator is obtained from (A130) by replacing $\mathbf{A}$ by the orthogonal transformation $\mathbf{Q}$ given by (A64) and changing the indices as follows: $m \to \alpha$, $n \to \beta$, $p \to \gamma$, and thus

$$e_{\alpha\beta\gamma}\mathrm{Det}\mathbf{Q} = \sum_{k=1}^{k=3}\sum_{j=1}^{j=3}\sum_{i=1}^{i=3} e_{ijk}Q_{i\alpha}Q_{j\beta}Q_{k\gamma} \; . \tag{A135}$$

This is an unusual transformation law because the determinant of orthogonal transformation $\mathbf{Q}$ is either +1 or –1. The expected transformation law, on the basis of tensor transformation laws (A75) and (A76) for a vector, (A86) for a second-order tensor, and (A87) for a tensor of order $n$, is that $\mathrm{Det}\mathbf{Q} = +1$. $\mathrm{Det}\mathbf{Q} = +1$ occurs when the transformation is between coordinate systems of the same handedness (right- to right-handed or left- to left-handed). Recall that a right(left)-hand coordinate system or orthonormal basis is one that obeys the right(left)-hand rule, that is to say, if the curl of your fingers in your right (left) hand fist is in the direction of rotation from the first ordered positive base vector into the second ordered positive base vector, your extended thumb will point in the third ordered positive base vector direction. $\mathrm{Det}\mathbf{Q} = -1$ occurs when the transformation is between coordinate systems of the opposite handedness (left to right or right to left). Since handedness does not play a role in the transformation law for even order tensors, this dependence on the sign of $\mathrm{Det}\mathbf{Q}$ and therefore the relative handedness of the coordinate systems for the alternator transformation law is unexpected.

The title to this section mentioned both the alternator and the vector cross-product. How are they connected? If you recall the definition of vector cross-product **a** x **b** in terms of a determinant, the connection between the two is made:

$$\mathbf{a}\times\mathbf{b} = \begin{vmatrix} \mathbf{e}_1 & \mathbf{e}_2 & \mathbf{e}_3 \\ a_1 & a_2 & a_3 \\ b_1 & b_2 & b_3 \end{vmatrix} = \tag{A136}$$

$$(a_2b_3 - b_2a_3)\mathbf{e}_1 + (a_3b_1 - b_3a_1)\mathbf{e}_2 + (a_1b_2 - b_1a_2)\mathbf{e}_3 \, .$$

In indicial notation, vector cross-product **a** x **b** is written in terms of an alternator as

$$\mathbf{a}\times\mathbf{b} = \sum_{k=1}^{k=3}\sum_{j=1}^{j=3}\sum_{i=1}^{i=3} e_{ijk}a_ib_j\mathbf{e}_k \; , \tag{A137}$$

a result that may be verified by expanding it to show that it coincides with (A136). If $\mathbf{c} = \mathbf{a}$ x $\mathbf{b}$ denotes the result of the vector cross-product, then from (A137),

$$c_k = \sum_{j=1}^{j=3}\sum_{i=1}^{i=3} e_{ijk}a_ib_j \; . \tag{A138}$$

Is vector cross-product $\mathbf{c} = \mathbf{a}$ x $\mathbf{b}$ a vector or a tensor? It is called a vector, but a second-order tensorial character is suggested by the fact that the components of **a** x **b** coincide with the components of the skew-symmetric part of $2(\mathbf{a}\otimes\mathbf{b})$ (see eq. A32). The answer is that vector

cross-product **c** = **a** x **b** is unusual. Although it is, basically, a second-order tensor, it can be treated as a vector as long as the transformations are between coordinate systems of the same handedness. In that case eq. (A136) shows that the alternator transforms as a proper tensor of order three, and thus there is no ambiguity in representation (A137) for **a** x **b**. When students first learn about the vector cross-product they are admonished (generally without explanation) to always use right-handed coordinate systems. This handedness problem is the reason for that admonishment. The "vector" that is the result of the cross-product of two vectors has names like "axial vector" or "pseudo vector" to indicate its special character. Typical axial vectors are moments in mechanics and the vector curl operator (§A.11).

**Example A.9.3**

Prove that **a** x **b** = **–b** x **a**.

**Solution**: In formula (A137), let $i \to j$ and $j \to i$; thus,

$$\mathbf{a}\times\mathbf{b} = \sum_{k=1}^{k=3}\sum_{j=1}^{j=3}\sum_{i=1}^{i=3} e_{jik}\,a_j b_i \mathbf{e}_k \ .$$

Next, change $e_{jik}$ to $-e_{iik}$ and rearrange the order of $a_j$ and $b_i$, then the result is proved:

$$\mathbf{a}\times\mathbf{b} = -\sum_{k=1}^{k=3}\sum_{j=1}^{j=3}\sum_{i=1}^{i=3} e_{ijk}\,b_i a_j \mathbf{e}_k = -\,\mathbf{b}\times\mathbf{a} \ .$$

The scalar triple product of three vectors is a scalar formed from three vectors, $\mathbf{a}\cdot(\mathbf{b}\times\mathbf{c})$, and the triple-vector-product is a vector formed from three vectors, (**r** x (**p** x **q**)). An expression for the scalar-triple-product is obtained by taking the dot product of vector **c** with the cross-product in representation (A137) for **a** x **b**, and thus

$$\mathbf{c}\cdot(\mathbf{a}\times\mathbf{b}) = \sum_{k=1}^{k=3}\sum_{j=1}^{j=3}\sum_{i=1}^{i=3} e_{ijk}\,a_i b_j c_k \ . \tag{A139}$$

From the properties of the alternator it follows that

$$\mathbf{c}\cdot(\mathbf{a}\times\mathbf{b}) = \mathbf{a}\cdot(\mathbf{b}\times\mathbf{c}) = \mathbf{b}\cdot(\mathbf{c}\times\mathbf{a}) = \tag{A140}$$

$$-\,\mathbf{a}\cdot(\mathbf{c}\times\mathbf{b}) = -\,\mathbf{b}\cdot(\mathbf{a}\times\mathbf{c}) = -\,\mathbf{c}\cdot(\mathbf{b}\times\mathbf{a}) \ .$$

If three vectors **a**, **b**, and **c** coincide with the three non-parallel edges of a parallelepiped, scalar triple product $\mathbf{a}\cdot(\mathbf{b}\times\mathbf{c})$ is equal to the volume of the parallelepiped. In the following example a useful vector identity for triple vector product (**r** x (**p** x **q**)) is derived.

**Example A.9.4**

Prove that (**r** x (**p** x **q**)) = (**r**·**q**)**p** – (**r**·**p**)**q**.

**Solution**: First rewrite (A137) with change **a** → **r**, and again with changes **a** → **p** and **b** → **q**, where **b** = (**p** x **q**):

$$\mathbf{r}\times\mathbf{b} = \sum_{k=1}^{k=3}\sum_{j=1}^{j=3}\sum_{i=1}^{i=3} e_{ijk}\,r_i b_j \mathbf{e}_k \ , \quad \mathbf{b} = \mathbf{p}\times\mathbf{q} = \sum_{m=1}^{m=3}\sum_{n=1}^{n=3}\sum_{j=1}^{j=3} e_{mnj}\,p_m q_n \mathbf{e}_j \ .$$

Note that the second of these formulas gives the components of **b** as

$$b_j = \sum_{m=1}^{m=3}\sum_{n=1}^{n=3} e_{mnj} p_m q_n \,.$$

This formula for the components of **b** is then substituted into the expression for (**r** x **b**) = (**r** x (**p** x **q**) above, and thus

$$\mathbf{r}\times(\mathbf{p}\times\mathbf{q}) = \sum_{k=1}^{k=3}\sum_{j=1}^{j=3}\sum_{i=1}^{i=3}\sum_{m=1}^{m=3}\sum_{n=1}^{n=3} e_{ijk} e_{mnj} r_i p_m q_n \mathbf{e}_k \,.$$

On the right-hand side of this expression for $\mathbf{r}\times(\mathbf{p}\times\mathbf{q})$, $e_{iik}$ is now changed to $-e_{iki}$ and the first of (A134) is then employed:

$$\mathbf{r}\times(\mathbf{p}\times\mathbf{q}) = -\sum_{k=1}^{k=3i}\sum_{m=1}^{i=3m}\sum_{n=1}^{n=3} (\delta_{im}\delta_{kn} - \delta_{in}\delta_{km}) r_i p_m q_n \mathbf{e}_k \,;$$

then summing over *k* and *i,*

$$\mathbf{r}\times(\mathbf{p}\times\mathbf{q}) = -\sum_{m=1}^{m=3}\sum_{n=1}^{n=3} r_m p_m q_n \mathbf{e}_n - r_n p_m q_n \mathbf{e}_m = (\mathbf{r}\cdot\mathbf{q})\mathbf{p} - (\mathbf{r}\cdot\mathbf{p})\mathbf{q} \,.$$

In the process of calculating area changes on surfaces of objects undergoing large deformations, like rubber or soft tissue, certain identities that involve both vectors and matrices are useful. Two of these identities are derived in the following two examples.

**Example A.9.5**

Prove that **A**·**a**·(**A**·**b** × **A**·**c**) = **a**·(**b** × **c**)Det**A**, where **A** is a 3-by-3 matrix, and **a**, **b**, and **c** are vectors.

**Solution**: Noting the formula for the scalar triple product as a determinant,

$$\mathbf{a}\cdot(\mathbf{b}\times\mathbf{c}) = \begin{vmatrix} a_1 & a_2 & a_3 \\ b_1 & b_2 & b_3 \\ c_1 & c_2 & c_3 \end{vmatrix}$$

and the representation for multiplication of **A** times **a**,

$$A\mathbf{a} = \begin{bmatrix} A_{11} & A_{12} & A_{13} \\ A_{21} & A_{22} & A_{23} \\ A_{31} & A_{32} & A_{33} \end{bmatrix}\begin{bmatrix} a_1 \\ a_2 \\ a_3 \end{bmatrix} = \begin{bmatrix} A_{11}a_1 + A_{12}a_2 + A_{13}a_3 \\ A_{21}a_1 + A_{22}a_2 + A_{23}a_3 \\ A_{31}a_1 + A_{32}a_2 + A_{33}a_3 \end{bmatrix},$$

then

$$\mathbf{A}\mathbf{a}\cdot(\mathbf{A}\cdot\mathbf{b}\times\mathbf{A}\cdot\mathbf{c}) = \mathrm{Det}\begin{bmatrix} A_{11}a_1 + A_{12}a_2 + A_{13}a_3 & A_{21}a_1 + A_{22}a_2 + A_{23}a_3 & A_{31}a_1 + A_{32}a_2 + A_{33}a_3 \\ A_{11}b_1 + A_{12}b_2 + A_{13}b_3 & A_{21}b_1 + A_{22}b_2 + A_{23}b_3 & A_{31}b_1 + A_{32}b_2 + A_{33}b_3 \\ A_{11}c_1 + A_{12}c_2 + A_{13}c_3 & A_{21}c_1 + A_{22}c_2 + A_{23}c_3 & A_{31}c_1 + A_{32}c_2 + A_{33}c_3 \end{bmatrix}.$$

Recalling from Example A.9.2 that Det(**A**·**B**) = Det**A** Det**B**, it follows that the previous determinant may be written as a product of determinants:

$$\mathrm{Det}\begin{bmatrix} A_{11} & A_{12} & A_{13} \\ A_{21} & A_{22} & A_{23} \\ A_{31} & A_{32} & A_{33} \end{bmatrix} \mathrm{Det}\begin{bmatrix} a_1 & b_1 & c_1 \\ a_2 & b_2 & c_2 \\ a_3 & b_3 & c_3 \end{bmatrix} = \mathbf{a}\cdot(\mathbf{b}\times\mathbf{c})\,\mathbf{Det}\mathbf{A},$$

which is the desired result. In the last step the fact that the determinant of the transpose of a matrix is equal to the determinant of the matrix, Det**A** = Det**A**$^{\mathrm{T}}$, was employed.

**Example A.9.6**

Prove vector identity **(A·b** × **A·c)·A** = **(b** × **c)** Det**A**, where **A** is a 3-by-3 matrix, and **b** and **c** are vectors.

**Solution**: Recall the result of Example A.9.5, namely, that **A·a·(A·b** × **A·c)** = **a·(b** × **c)** Det**A**, and let **a** = **e**$_1$, then **e**$_2$ and then **e**$_3$, to obtain the following three scalar equations:

$$A_{11}w_1 + A_{21}w_2 + A_{31}w_3 = \mathrm{q}_1\,\mathrm{Det}\mathbf{A}$$

$$A_{12}w_1 + A_{22}w_2 + A_{32}w_3 = \mathrm{q}_2\,\mathrm{Det}\mathbf{A}$$

$$A_{13}w_1 + A_{23}w_2 + A_{33}w_3 = \mathrm{q}_3\,\mathrm{Det}\mathbf{A}$$

where **w** = (**A·b** × **A·c**), **q** = (**b** × **c**)**.** These three equations may be recast in matrix notation:

$$\begin{bmatrix} A_{11} & A_{21} & A_{31} \\ A_{12} & A_{22} & A_{32} \\ A_{13} & A_{23} & A_{33} \end{bmatrix}\begin{bmatrix} w_1 \\ w_2 \\ w_3 \end{bmatrix} = \begin{bmatrix} q_1 \\ q_2 \\ q_3 \end{bmatrix}\mathrm{Det}\mathbf{A},$$

or **A**$^{\mathrm{T}}$·**w** = **q** Det**A**, and since **w** = (**A·b** × **A·c**), **q** = (**b** × **c**),

$$\mathbf{A}^{\mathrm{T}}(\mathbf{A}\cdot\mathbf{b}\times\mathbf{A}\cdot\mathbf{c}) = (\mathbf{b}\times\mathbf{c})\,\mathrm{Det}\mathbf{A},\ \text{or}$$

$$(\mathbf{A}\cdot\mathbf{b}\times\mathbf{A}\cdot\mathbf{c})\cdot\mathbf{A} = (\mathbf{b}\times\mathbf{c})\,\mathrm{Det}\mathbf{A},$$

which is the desired result. In the last step, relation **a·F**$^{\mathrm{T}}$ = **F·a** (Problem 5.8) was employed.

**Problems**

A.9.1. Find cross-products **a x b** and **b x a** of two vectors **a** = [1, 2, 3] and **b** = [4, 5, 6]. What is the relationship between **a x b** and **b x a**?

A.9.2. Show that if **A** is a skew-symmetric 3-by-3 matrix, **A** = –**A**$^{\mathrm{T}}$, then Det**A** = 0.

A.9.3. Evaluate Det(**a**⊗**b**).

A.9.4. Show Det**A** = Det**A**$^{\mathrm{T}}$.

A.9.5. Show Det**Q** = ±1 if **Q**$^{\mathrm{T}}$·**Q** = **Q**·**Q**$^{\mathrm{T}}$ = **1**.

A.9.6. Find the volume of the parallelepiped if the three non-parallel edges of a parallelepiped coincide with three vectors **a**, **b**, and **c**, where **a** = [1, 2, 3] meters, **b** = [1, –4, 6] meters, and **c** = [1, 1, 1] meters.

A.9.7. If **v** = **a** x **x** and **a** is a constant vector, using indicial notation, evaluate div **v** and curl **v**.

## A.10. CONNECTION TO MOHR'S CIRCLES

The material in the section before last, namely, transformation law (A83) for tensorial components and the eigenvalue problem for linear transformations, is presented in standard textbooks on the mechanics of materials in a more elementary fashion. In those presentations the second-order tensor is taken to be the stress tensor and a geometric analog calculator is used for transformation law (A83) for tensorial components in two dimensions, and for the solution of the eigenvalue problem in two dimensions. The geometric analog calculator is called a Mohr circle. A discussion of the connection is included to aid in placing the material just presented in perspective.

The special case of the first transformation law from (A83), $\mathbf{T}^{(L)} = \mathbf{Q} \cdot \mathbf{T}^{(G)} \cdot \mathbf{Q}^T$, is rewritten in two dimensions ($n = 2$) in form $\boldsymbol{\sigma}' = \mathbf{Q} \cdot \boldsymbol{\sigma} \cdot \mathbf{Q}^{\mathrm{T}}$; thus, $\mathbf{T}^{(L)} = \boldsymbol{\sigma}'$ and $\mathbf{T}^{(G)} = \boldsymbol{\sigma}$, where matrix of stress tensor components $\boldsymbol{\sigma}$, matrix of transformed stress tensor components $\boldsymbol{\sigma}'$, and orthogonal transformation $\mathbf{Q}$ representing rotation of the Cartesian axes are given by

$$\boldsymbol{\sigma} = \begin{bmatrix} \sigma_x & \tau_{xy} \\ \tau_{xy} & \sigma_y \end{bmatrix}, \quad \boldsymbol{\sigma}' = \begin{bmatrix} \sigma_{x'} & \tau_{x'y'} \\ \tau_{x'y'} & \sigma_{y'} \end{bmatrix}, \quad \mathbf{Q} = \begin{bmatrix} \cos\theta & -\sin\theta \\ \sin\theta & \cos\theta \end{bmatrix}. \tag{A141}$$

Expansion of matrix equation $\boldsymbol{\sigma}' = \mathbf{Q} \cdot \boldsymbol{\sigma} \cdot \mathbf{Q}^{\mathrm{T}}$,

$$\boldsymbol{\sigma}' = \begin{bmatrix} \sigma_{x'} & \tau_{x'y'} \\ \tau_{x'y'} & \sigma_{y'} \end{bmatrix} = \begin{bmatrix} \cos\theta & -\sin\theta \\ \sin\theta & \cos\theta \end{bmatrix} \begin{bmatrix} \sigma_x & \tau_{xy} \\ \tau_{xy} & \sigma_y \end{bmatrix} \begin{bmatrix} \cos\theta & \sin\theta \\ -\sin\theta & \cos\theta \end{bmatrix}, \tag{A142}$$

and subsequent use of double-angle trigonometric formulas $\sin 2\theta = 2\sin\theta \cos\theta$ and $\cos 2\theta = \cos^2\theta - \sin^2\theta$ yield the following:

$$\begin{aligned} \sigma_{x'} &= (1/2)(\sigma_x + \sigma_y) + (1/2)(\sigma_x - \sigma_y)\cos 2\theta + \tau_{xy} \sin 2\theta \\ \sigma_{y'} &= (1/2)(\sigma_x + \sigma_y) - (1/2)(\sigma_x - \sigma_y)\cos 2\theta - \tau_{xy} \sin 2\theta, \\ \tau_{x'y'} &= -(1/2)(\sigma_x - \sigma_y)\sin 2\theta + \tau_{xy} \cos 2\theta. \end{aligned} \tag{A143}$$

These are formulas for stresses $\sigma_{x'}$, $\sigma_{y'}$, and $\tau_{x'y}$, as functions of stresses $\sigma_x$, $\sigma_y$, and $\tau_{xy}$ and angle $2\theta$. Note that the sum of the first two equations in (A98) yields the following expression, which is defined as $2C$:

$$2C \equiv \sigma_{x'} + \sigma_{y'} = \sigma_x + \sigma_y. \tag{A144}$$

The fact that $\sigma_{x'} + \sigma_{y'} = \sigma_x + \sigma_y$ is a repetition of result (A90) concerning the invariance of the trace of a tensor, the first invariant of a tensor, under change of basis. Next consider the following set of equations in which the first is the first of (A143), incorporating definition (A144) and transposing the term involving $C$ to the other side of the equal sign, and the second equation is the third of (A143):

$$\begin{aligned} \sigma_{x'} - C &= (1/2)(\sigma_x - \sigma_y)\cos 2\theta + \tau_{xy} \sin 2\theta, \\ \tau_{x'y'} &= -(1/2)(\sigma_x - \sigma_y)\sin 2\theta + \tau_{xy} \cos 2\theta. \end{aligned}$$

If these equations are now squared and added we find that

$$(\sigma_{x'} - C)^2 + (\tau_{x'y'})^2 = R^2 \tag{A145}$$

where

$$R^2 \equiv (1/4)(\sigma_x - \sigma_y)^2 + (\tau_{xy})^2 \quad . \tag{A146}$$

Equation (A145) is the equation for a circle of radius $R$ centered at point $\sigma_{x'} = C$, $\tau_{x'y'} = 0$. The circle is illustrated in Figure A.3.

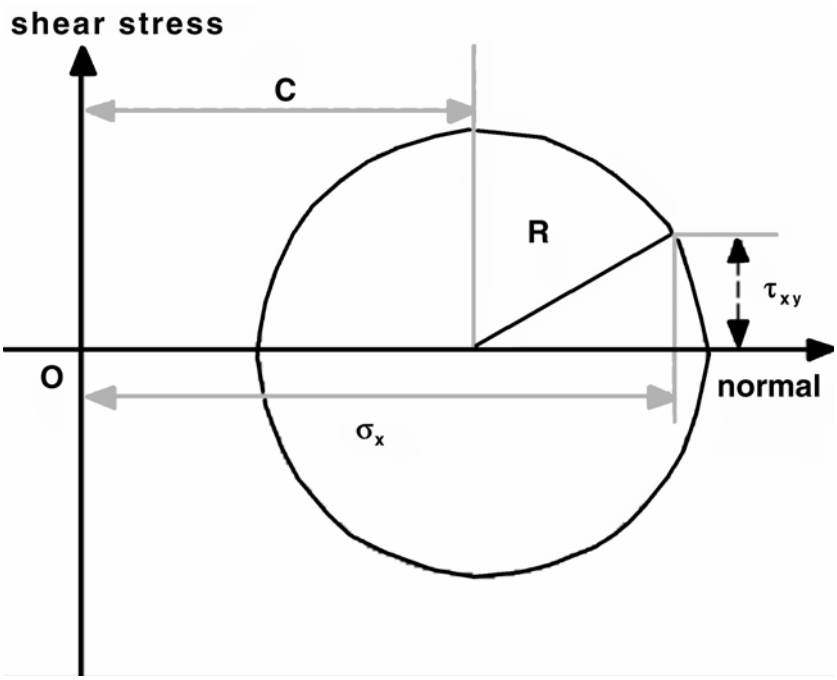



**Figure A.3**. An illustration of Mohr's circle for a state of stress.

The points on the circle represent all possible values of $\sigma_{x'}$, $\sigma_{y'}$, and $\tau_{x'y'}$; they are determined by the values of $C$ and $R$, which are, in turn, determined by $\sigma_x$, $\sigma_y$, and $\tau_{xy}$. The eigenvalues of matrix $\boldsymbol{\sigma}$ are the values of normal stress $\sigma_{x'}$ when the circle crosses the $\sigma_{x'}$ axis. These are given by numbers $C + R$ and $C - R$, as may be seen from Figure A.3. Thus, Mohr's circle is a graphical analog calculator for the eigenvalues of two-dimensional second-order tensor $\boldsymbol{\sigma}$, as well as a graphical analog calculator for equation $\boldsymbol{\sigma}' = \mathbf{Q}\cdot\boldsymbol{\sigma}\cdot\mathbf{Q}^{\mathrm{T}}$ representing transformation of components. The maximum shear stress is simply the radius of circle $R$, an important graphical result that is readable from Figure A.3.

As a graphical calculation device, Mohr's circles may be extended to three dimensions, but the graphical calculation is much more difficult than doing the calculation on a computer, so it is no longer done. An illustration of three-dimensional Mohr's circles is shown in Figure A.4. The shaded region represents the set of points that are possible stress values. The three points where the circles intersect the axis correspond to the three eigenvalues of the three-dimensional stress tensor and the radius of the largest circle is the magnitude of the largest shear stress.

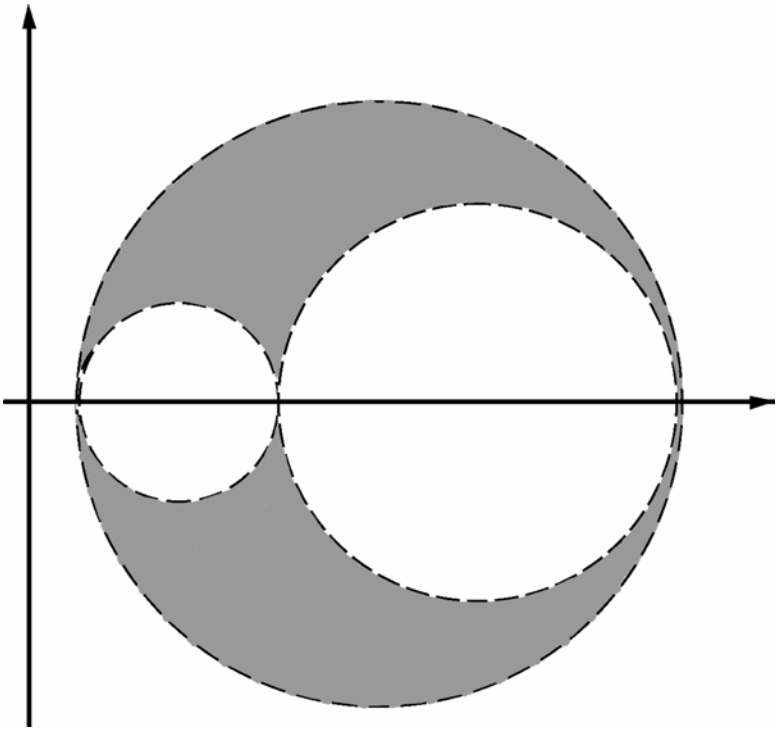


**Figure A.4**. Mohr's circles in three dimensions.

**Problems**

A.10.1. Construct the two-dimensional Mohr's circle for matrix **A** given in Problem A.7.3.

A.10.2. Construct the three-dimensional Mohr's circles for matrix **T** given in Problem A.7.2.

## A.11. SPECIAL VECTORS AND TENSORS IN SIX DIMENSIONS

The fact that the components of a second-order tensor in $n$ dimensions can be represented as an $n$-by-$n$ square matrix allows the powerful algebra of matrices to be used in the analysis of second-order tensor components. In general this use of the powerful algebra of matrices is not possible for tensors of other orders. For example, in the case of the third-order tensor with components $A_{ijk}$ one could imagine a generalization of a matrix from an array with rows and columns to one with rows, columns, and a depth dimension to handle the information of the third index. This would be like an $n$-by-$n$-by-$n$ cube sub-partitioned into $n^3$ cells that would each contain an entry like the entry at a row/column position in a matrix. Modern symbolic algebra programs might be extended to handle these $n$-by-$n$-by-$n$ cubes and to represent them graphically. By extension of this idea, fourth-order tensors would require an $n$-by-$n$-by-$n$-by-$n$ hypercube with no possibility of graphical representation. Fortunately, for certain fourth-order tensors (a case of special interest in continuum mechanics) there is a way to again employ the

matrix algebra of $n$-by-$n$ square matrices in representation of tensor components. The purpose of this section it to explain how this is done.

The developments in this text will frequently concern the relationship between symmetric second-order tensors in three dimensions. The symmetric second-order tensors of interest will include stress and stress rate and strain and strain rate, among others. The most general form of a linear relationship between second-order tensors in three dimensions involves a three-dimensional fourth-order tensor. In general the introduction of tensors of order higher than two involves considerable additional notation. However, since the interest here is only in three-dimensional fourth-order tensors that relate three-dimensional symmetric second-order tensors, a simple notational scheme can be introduced. The basis of the scheme is to consider a three-dimensional symmetric second-order tensor also as a six-dimensional vector, and then three-dimensional fourth-order tensors may be associated with second-order tensors in a space of six dimensions. When this association is made, all of the algebraic machinery associated with the linear transformations and second-order tensors is available for the three-dimensional fourth-order tensors.

The first point to be made is that symmetric second-order tensors in three dimensions may also be considered as vectors in a six-dimensional space. The one-to-one connection between the components of symmetric second-order tensors $\mathbf{T}$ and six-dimensional vector $\hat{\mathbf{T}}$ is described as follows. The definition of second-order tensor in a space of three dimensions $\mathbf{T}$ is a special case of (A80) written in the form

$$\mathbf{T} = \sum_{j=1}^{j=3} \sum_{i=1}^{i=3} T_{ij} \mathbf{e}_i \otimes \mathbf{e}_j = \sum_{\beta=1}^{\beta=3} \sum_{\alpha=1}^{\alpha=3} T_{\alpha\beta} \mathbf{e}_\alpha \otimes \mathbf{e}_\beta \tag{A147}$$

or, executing summation in the Latin system,

$$\mathbf{T} = T_{11}\mathbf{e}_1 \otimes \mathbf{e}_1 + T_{22}\mathbf{e}_2 \otimes \mathbf{e}_2 + T_{33}\mathbf{e}_3 \otimes \mathbf{e}_3 + T_{23}(\mathbf{e}_2 \otimes \mathbf{e}_3 + \mathbf{e}_3 \otimes \mathbf{e}_2) +$$

$$T_{13}(\mathbf{e}_1 \otimes \mathbf{e}_3 + \mathbf{e}_3 \otimes \mathbf{e}_1) + T_{12}(\mathbf{e}_1 \otimes \mathbf{e}_2 + \mathbf{e}_2 \otimes \mathbf{e}_1) . \tag{A148}$$

If a new set of base vectors defined by

$$\hat{\mathbf{e}}_1 = \mathbf{e}_1 \otimes \mathbf{e}_1, \quad \hat{\mathbf{e}}_2 = \mathbf{e}_2 \otimes \mathbf{e}_2, \quad \hat{\mathbf{e}}_3 = \mathbf{e}_3 \otimes \mathbf{e}_3 ,$$

$$\hat{\mathbf{e}}_4 = \frac{1}{\sqrt{2}}(\mathbf{e}_2 \otimes \mathbf{e}_3 + \mathbf{e}_3 \otimes \mathbf{e}_2), \quad \hat{\mathbf{e}}_5 = \frac{1}{\sqrt{2}}(\mathbf{e}_1 \otimes \mathbf{e}_3 + \mathbf{e}_3 \otimes \mathbf{e}_1) , \tag{A149}$$

$$\hat{\mathbf{e}}_6 = \frac{1}{\sqrt{2}}(\mathbf{e}_1 \otimes \mathbf{e}_2 + \mathbf{e}_2 \otimes \mathbf{e}_1)$$

is introduced as well as a new set of tensor components defined by

$$\hat{T}_1 = T_{11}, \quad \hat{T}_2 = T_{22}, \quad \hat{T}_3 = T_{33}, \quad \hat{T}_4 = \sqrt{2}T_{23}, \quad \hat{T}_5 = \sqrt{2}T_{13}, \quad \hat{T}_6 = \sqrt{2}T_{12} , \tag{A150}$$

then (A148) may be rewritten as

$$\hat{\mathbf{T}} = \hat{T}_1\hat{\mathbf{e}}_1 + \hat{T}_2\hat{\mathbf{e}}_2 + \hat{T}_3\hat{\mathbf{e}}_3 + \hat{T}_4\hat{\mathbf{e}}_4 + \hat{T}_5\hat{\mathbf{e}}_5 + \hat{T}_6\hat{\mathbf{e}}_6 , \tag{A151}$$

or

$$\hat{\mathbf{T}} = \sum_{i=1}^{i=6} \hat{T}_i \hat{\mathbf{e}}_i = \sum_{\alpha=1}^{\alpha=6} \hat{T}_\alpha \hat{\mathbf{e}}_\alpha , \tag{A152}$$

which is the definition of a vector in six dimensions. This establishes the one-to-one connection between the components of symmetric second-order tensors $\mathbf{T}$ and the six-dimensional vector, $\hat{\mathbf{T}}$.

The second point to be made is that fourth-order tensors in three dimensions, with certain symmetries, may also be considered as second-order tensors in a six-dimensional space. The one-to-one connection between the components of fourth-order tensors in three dimensions $\mathbf{C}$ and second-order tensors in six dimensions vector $\hat{\mathbf{C}}$ is described as follows. Consider next fourth-order tensor $\mathbf{c}$ in three dimensions defined by

$$\mathbf{C} = \sum_{m=1}^{m=3}\sum_{k=1}^{k=3}\sum_{j=1}^{j=3}\sum_{i=1}^{i=3} C_{ijkm}\,\mathbf{e}_i \otimes \mathbf{e}_j \otimes \mathbf{e}_k \otimes \mathbf{e}_m = \sum_{\delta=I}^{\delta=III}\sum_{\gamma=I}^{\gamma=III}\sum_{\beta=I}^{\beta=III}\sum_{\alpha=I}^{\alpha=III} C_{\alpha\beta\gamma\delta}\,\mathbf{e}_\alpha \otimes \mathbf{e}_\beta \otimes \mathbf{e}_\gamma \otimes \mathbf{e}_\delta\,, \quad \text{(A153)}$$

and having symmetry in its first and second pair of indices, $C_{ijkm} = C_{jikm}$ and $C_{ijkm} = C_{ijmk}$, but not another symmetry in its indices; in particular, $C_{ijkm}$ is not equal to $C_{kmij}$, in general. The results of interest are for fourth-order tensors in three dimensions with these particular symmetries because it is these fourth-order tensors that linearly relate two symmetric second-order tensors in three dimensions. Due to the special indicial symmetries just described, change of basis (A149) may be introduced in (A153) and may be rewritten as

$$\hat{\mathbf{c}} = \sum_{j=1}^{j=6}\sum_{i=1}^{i=6} \hat{\mathbf{C}}_{ij}\hat{\mathbf{e}}_i \otimes \hat{\mathbf{e}}_j = \sum_{\beta=I}^{\beta=VI}\sum_{\alpha=I}^{\alpha i=VI} \hat{\mathbf{C}}_{\alpha\beta}\hat{\mathbf{e}}_\alpha \otimes \hat{\mathbf{e}}_\beta\,, \quad \text{(A154)}$$

where the 36 components of $C_{ijkm}$, the fourth-order tensor in three dimensions (with symmetries $C_{ijkm} = C_{jikm}$ and $C_{ijkm} = C_{ijmk}$) are related to the 36 components of $\hat{C}_{ij}$, the second-order tensor in six dimensions by

$$\begin{gathered}
\hat{\mathbf{C}}_{11} = C_{1111},\ \hat{\mathbf{C}}_{22} = C_{2222},\ \hat{\mathbf{C}}_{33} = C_{3333},\ \hat{\mathbf{C}}_{23} = C_{2233},\ \hat{\mathbf{C}}_{32} = C_{3322},\\
\hat{\mathbf{C}}_{13} = C_{1133},\ \hat{\mathbf{C}}_{31} = C_{3311},\ \hat{\mathbf{C}}_{12} = C_{1122},\ \hat{\mathbf{C}}_{21} = C_{2211},\\
\hat{\mathbf{C}}_{44} = 2C_{2323},\ \hat{\mathbf{C}}_{55} = 2C_{1313},\ \hat{\mathbf{C}}_{66} = 2C_{1212},\ \hat{\mathbf{C}}_{45} = 2C_{2313},\ \hat{\mathbf{C}}_{54} = 2C_{1323},\\
\hat{\mathbf{C}}_{46} = 2C_{2312},\ \hat{\mathbf{C}}_{64} = 2C_{1223},\ \hat{\mathbf{C}}_{56} = 2C_{1312},\ \hat{\mathbf{C}}_{65} = 2C_{1213},\\
\hat{\mathbf{C}}_{41} = \sqrt{2}C_{2311},\ \hat{\mathbf{C}}_{14} = \sqrt{2}C_{1123},\ \hat{\mathbf{C}}_{51} = \sqrt{2}C_{1311},\ \hat{\mathbf{C}}_{15} = \sqrt{2}C_{1113},\\
\hat{\mathbf{C}}_{61} = \sqrt{2}C_{1211},\ \hat{\mathbf{C}}_{16} = \sqrt{2}C_{1112},\ \hat{\mathbf{C}}_{42} = \sqrt{2}C_{2322},\ \hat{\mathbf{C}}_{24} = \sqrt{2}C_{2223},\\
\hat{\mathbf{C}}_{52} = \sqrt{2}C_{1322},\ \hat{\mathbf{C}}_{25} = \sqrt{2}C_{2213},\ \hat{\mathbf{C}}_{62} = \sqrt{2}C_{1222},\ \hat{\mathbf{C}}_{26} = \sqrt{2}C_{2212},\\
\hat{\mathbf{C}}_{43} = \sqrt{2}C_{2333},\ \hat{\mathbf{C}}_{34} = \sqrt{2}C_{3323},\ \hat{\mathbf{C}}_{53} = \sqrt{2}C_{1333},\ \hat{\mathbf{C}}_{35} = \sqrt{2}C_{3313},.\\
\hat{\mathbf{C}}_{63} = \sqrt{2}C_{1233},\ \hat{\mathbf{C}}_{36} = \sqrt{2}C_{3312}\,.
\end{gathered} \quad \text{(A155)}$$

Using the symmetry of second-order tensors, $\mathbf{T} = \mathbf{T}^{\mathrm{T}}$ and $\mathbf{J} = \mathbf{J}^{\mathrm{T}}$, as well as the two indicial symmetries of $C_{ijkm}$, the linear relationship between $\mathbf{T}$ and $\mathbf{J}$,

$$T_{ij} = \sum_{k=1}^{j=3} \sum_{m=1}^{i=3} C_{ijkm} J_{km} , \tag{A156}$$

may be expanded to read

$$\begin{aligned}
T_{11} &= C_{1111} J_{11} + C_{1122} J_{22} + C_{1133} J_{33} + 2C_{1123} J_{23} + 2C_{1113} J_{13} + 2C_{1112} J_{12} , \\
T_{22} &= C_{2211} J_{11} + C_{2222} J_{22} + C_{2233} J_{33} + 2C_{2223} J_{23} + 2C_{2213} J_{13} + 2C_{2212} J_{12} , \\
T_{33} &= C_{3311} J_{11} + C_{3322} J_{22} + C_{3333} J_{33} + 2C_{3323} J_{23} + 2C_{3313} J_{13} + 2C_{3312} J_{12} , \\
T_{23} &= C_{2311} J_{11} + C_{2322} J_{22} + C_{2333} J_{33} + 2C_{2323} J_{23} + 2C_{2313} J_{13} + 2C_{2312} J_{12} \\
T_{13} &= C_{1311} J_{11} + C_{1322} J_{22} + C_{1333} J_{33} + 2C_{1323} J_{23} + 2C_{1313} J_{13} + 2C_{1312} J_{12} , \\
T_{12} &= C_{1211} J_{11} + C_{1222} J_{22} + C_{1233} J_{33} + 2C_{1223} J_{23} + 2C_{1213} J_{13} + 2C_{1212} J_{12} .
\end{aligned} \tag{A157}$$

The corresponding linear relationship between $\hat{\mathbf{T}}$ and $\hat{\mathbf{J}}$,

$$\hat{T}_i = \sum_{j=1}^{j=6} \hat{C}_{ij} \hat{J}_j , \tag{A158}$$

may be expanded to read

$$\begin{aligned}
\hat{T}_1 &= \hat{C}_{11} \hat{J}_1 + \hat{C}_{12} \hat{J}_2 + \hat{C}_{13} \hat{J}_3 + \hat{C}_{14} \hat{J}_4 + \hat{C}_{15} \hat{J}_5 + \hat{C}_{16} \hat{J}_6 , \\
\hat{T}_2 &= \hat{C}_{21} \hat{J}_1 + \hat{C}_{22} \hat{J}_2 + \hat{C}_{23} \hat{J}_3 + \hat{C}_{24} \hat{J}_4 + \hat{C}_{25} \hat{J}_5 + \hat{C}_{26} \hat{J}_6 , \\
\hat{T}_3 &= \hat{C}_{31} \hat{J}_1 + \hat{C}_{32} \hat{J}_2 + \hat{C}_{33} \hat{J}_3 + \hat{C}_{34} \hat{J}_4 + \hat{C}_{35} \hat{J}_5 + \hat{C}_{36} \hat{J}_6 , \\
\hat{T}_4 &= \hat{C}_{41} \hat{J}_1 + \hat{C}_{42} \hat{J}_2 + \hat{C}_{43} \hat{J}_3 + \hat{C}_{44} \hat{J}_4 + \hat{C}_{45} \hat{J}_5 + \hat{C}_{46} \hat{J}_6 , \\
\hat{T}_5 &= \hat{C}_{51} \hat{J}_1 + \hat{C}_{52} \hat{J}_2 + \hat{C}_{53} \hat{J}_3 + \hat{C}_{54} \hat{J}_4 + \hat{C}_{55} \hat{J}_5 + \hat{C}_{56} \hat{J}_6 , \\
\hat{T}_6 &= \hat{C}_{61} \hat{J}_1 + \hat{C}_{62} \hat{J}_2 + \hat{C}_{63} \hat{J}_3 + \hat{C}_{64} \hat{J}_4 + \hat{C}_{65} \hat{J}_5 + \hat{C}_{66} \hat{J}_6 .
\end{aligned} \tag{A159}$$

The advantage to notation (A158) or (A159) as opposed to notation (A156) or (A157) is that there is no matrix representation of (A156) or (A157) that retains the tensorial character while there is a simple, direct, and familiar tensorial representation of (A158) or (A159). Equations (A158) or (A159) may be written in matrix notation as linear transformation

$$\hat{\mathbf{T}} = \hat{\mathbf{C}} \cdot \hat{\mathbf{J}} . \tag{A160}$$

Recalling the rule for the transformation of the components of vectors in a coordinate transformation, (A73), the transformation rule for $\hat{\mathbf{T}}$ or $\hat{\mathbf{J}}$ may be written down by inspection:

$$\hat{\mathbf{J}}^{(L)} = \hat{\mathbf{Q}} \cdot \hat{\mathbf{J}}^{(G)} \quad \text{and} \quad \hat{\mathbf{J}}^{(G)} = \hat{\mathbf{Q}}^T \cdot \hat{\mathbf{J}}^{(L)} . \tag{A161}$$

Furthermore, using result (A77), second-order tensor $\hat{\mathbf{C}}$ in the space of six dimensions transforms according to rule

$$\hat{\mathbf{C}}^{(L)} = \hat{\mathbf{Q}} \cdot \hat{\mathbf{C}}^{(G)} \cdot \hat{\mathbf{Q}}^T \quad \text{and} \quad \hat{\mathbf{C}}^{(G)} = \hat{\mathbf{Q}}^T \cdot \hat{\mathbf{C}}^{(L)} \cdot \hat{\mathbf{Q}} . \tag{A162}$$

In short, second-order tensor $\hat{\mathbf{C}}$ in the space of six dimensions may be treated exactly like a second-order tensor in the space of three dimensions as far as the usual tensorial operations are concerned.

The relationship between components of the second-order tensor in three dimensions and the vector in six dimensions contained in (A150) may be written in *n*-tuple notation for $\mathbf{T}$ and $\mathbf{J}$ ($\hat{\mathbf{T}}$ and $\hat{\mathbf{J}}$):

$$\hat{\mathbf{T}} = [\hat{T}_1, \hat{T}_2, \hat{T}_3, \hat{T}_4, \hat{T}_5, \hat{T}_6]^T = [T_{11}, T_{22}, T_{33}, \sqrt{2}T_{23}, \sqrt{2}T_{13}, \sqrt{2}T_{12}]^T ,$$

$$\hat{\mathbf{J}} = [\hat{J}_1, \hat{J}_2, \hat{J}_3, \hat{J}_4, \hat{J}_5, \hat{J}_6]^T = [J_{11}, J_{22}, J_{33}, \sqrt{2}J_{23}, \sqrt{2}J_{13}, \sqrt{2}J_{12}]^T . \tag{A163}$$

These formulas permit conversion of three-dimensional second-order tensor components directly to six-dimensional vector components and vice versa. The $\sqrt{2}$ factor that multiplies the last three components of the definition of the six-dimensional vector representation of the three-dimensional second order tensor, (A150), assures that the scalar product of the two six-dimensional vectors is equal to the trace of the product of the corresponding second-order tensors, that is,

$$\hat{\mathbf{T}} \cdot \hat{\mathbf{J}} = \mathbf{T} : \mathbf{J} . \tag{A164}$$

The colon or double dot notation between the two second-order tensors illustrated in (A164) is an extension of the single dot notation between matrices $\mathbf{A}\cdot\mathbf{B}$, and indicates that one index from $\mathbf{A}$ and one index from $\mathbf{B}$ are to be summed over; the double dot notation between matrices $\mathbf{A}:\mathbf{B}$ indicates that both indices of $\mathbf{A}$ are to be summed with different indices from $\mathbf{B}$. As the notation above indicates, the effect is the same as the trace of the product, $\mathbf{A}:\mathbf{B} = \text{tr}(\mathbf{A}\cdot\mathbf{B})$. Note that $\mathbf{A}:\mathbf{B} = \mathbf{A}^{\mathrm{T}}:\mathbf{B}^{\mathrm{T}}$ and $\mathbf{A}^{\mathrm{T}}:\mathbf{B} = \mathbf{A}:\mathbf{B}^{\mathrm{T}}$, but that $\mathbf{A}:\mathbf{B} \neq \mathbf{A}^{\mathrm{T}}:\mathbf{B}$ in general. This notation is applicable for square matrices in any dimensional space.

Vector $\hat{\mathbf{U}} = [1, 1, 1, 0, 0, 0]^{\mathrm{T}}$ is introduced to be the six-dimensional vector representation of three-dimensional unit tensor $\mathbf{1}$. It is important to note that symbol $\hat{\mathbf{U}}$ is distinct from the unit tensor in six dimensions that is denoted by $\hat{\mathbf{1}}$. Note that $\hat{\mathbf{U}} \cdot \hat{\mathbf{U}} = 3$, $\hat{\mathbf{U}} \cdot \hat{\mathbf{T}} = \text{tr}\mathbf{T}$, and, using (A164), it is easy to verify that $\hat{\mathbf{T}} \cdot \hat{\mathbf{U}} = \mathbf{T} : \mathbf{1} = \text{tr}\mathbf{T}$. Matrix $\hat{\mathbf{C}}$ dotted with $\hat{\mathbf{U}}$ yields a vector in six-dimensions:

$$\hat{\mathbf{C}} \cdot \hat{\mathbf{U}} = \begin{bmatrix} \hat{\mathbf{C}}_{11} + \hat{\mathbf{C}}_{12} + \hat{\mathbf{C}}_{13} \\ \hat{\mathbf{C}}_{21} + \hat{\mathbf{C}}_{22} + \hat{\mathbf{C}}_{23} \\ \hat{\mathbf{C}}_{31} + \hat{\mathbf{C}}_{32} + \hat{\mathbf{C}}_{33} \\ \hat{\mathbf{C}}_{41} + \hat{\mathbf{C}}_{42} + \hat{\mathbf{C}}_{43} \\ \hat{\mathbf{C}}_{51} + \hat{\mathbf{C}}_{52} + \hat{\mathbf{C}}_{53} \\ \hat{\mathbf{C}}_{61} + \hat{\mathbf{C}}_{62} + \hat{\mathbf{C}}_{63} \end{bmatrix} , \tag{A165}$$

and, dotting again with $\hat{\mathbf{U}}$, a scalar is obtained:

$$\hat{\mathbf{U}} \cdot \hat{\mathbf{C}} \cdot \hat{\mathbf{U}} = \hat{\mathbf{C}}_{11} + \hat{\mathbf{C}}_{12} + \hat{\mathbf{C}}_{13} + \hat{\mathbf{C}}_{21} + \hat{\mathbf{C}}_{22} + \hat{\mathbf{C}}_{23} + \hat{\mathbf{C}}_{31} + \hat{\mathbf{C}}_{32} + \hat{\mathbf{C}}_{33} . \tag{A166}$$

Transformation rules (A161) and (A162) for the vector and second-order tensors in six dimensions involve six-dimensional orthogonal tensor transformation $\hat{\mathbf{Q}}$. The tensor components of $\hat{\mathbf{Q}}$ are given in terms of $\mathbf{Q}$ by

$$\hat{\mathbf{Q}} = \begin{matrix} \hat{Q}_{1\mathrm{I}} & \hat{Q}_{1\mathrm{II}} & \hat{Q}_{1\mathrm{III}} & \hat{Q}_{1\mathrm{IV}} & \hat{Q}_{1\mathrm{V}} & \hat{Q}_{1\mathrm{VI}} \\ \hat{Q}_{2\mathrm{I}} & \hat{Q}_{2\mathrm{II}} & \hat{Q}_{2\mathrm{III}} & \hat{Q}_{2\mathrm{IV}} & \hat{Q}_{2\mathrm{V}} & \hat{Q}_{2\mathrm{VI}} \\ \hat{Q}_{3\mathrm{I}} & \hat{Q}_{3\mathrm{II}} & \hat{Q}_{3\mathrm{III}} & \hat{Q}_{3\mathrm{IV}} & \hat{Q}_{3\mathrm{V}} & \hat{Q}_{3\mathrm{VI}} \\ \hat{Q}_{4\mathrm{I}} & \hat{Q}_{4\mathrm{II}} & \hat{Q}_{4\mathrm{III}} & \hat{Q}_{4\mathrm{IV}} & \hat{Q}_{4\mathrm{V}} & \hat{Q}_{4\mathrm{VI}} \\ \hat{Q}_{5\mathrm{I}} & \hat{Q}_{5\mathrm{II}} & \hat{Q}_{5\mathrm{III}} & \hat{Q}_{5\mathrm{IV}} & \hat{Q}_{5\mathrm{V}} & \hat{Q}_{5\mathrm{VI}} \\ \hat{Q}_{6\mathrm{I}} & \hat{Q}_{6\mathrm{II}} & \hat{Q}_{6\mathrm{III}} & \hat{Q}_{6\mathrm{IV}} & \hat{Q}_{6\mathrm{V}} & \hat{Q}_{6\mathrm{VI}} \end{matrix} = \tag{A167}$$

$$\begin{matrix} Q_{1\mathrm{I}}^2 & Q_{1\mathrm{II}}^2 & Q_{1\mathrm{III}}^2 & \sqrt{2}Q_{1\mathrm{II}}Q_{1\mathrm{III}} & \sqrt{2}Q_{1\mathrm{I}}Q_{1\mathrm{III}} & \sqrt{2}Q_{1\mathrm{I}}Q_{1\mathrm{II}} \\ Q_{2\mathrm{I}}^2 & Q_{2\mathrm{II}}^2 & Q_{2\mathrm{III}}^2 & \sqrt{2}Q_{2\mathrm{II}}Q_{2\mathrm{III}} & \sqrt{2}Q_{2\mathrm{I}}Q_{2\mathrm{III}} & \sqrt{2}Q_{2\mathrm{I}}Q_{2\mathrm{II}} \\ Q_{3\mathrm{I}}^2 & Q_{3\mathrm{II}}^2 & Q_{3\mathrm{III}}^2 & \sqrt{2}Q_{3\mathrm{II}}Q_{3\mathrm{III}} & \sqrt{2}Q_{3\mathrm{I}}Q_{3\mathrm{III}} & \sqrt{2}Q_{3\mathrm{I}}Q_{3\mathrm{II}} \\ \sqrt{2}Q_{2\mathrm{I}}Q_{3\mathrm{I}} & \sqrt{2}Q_{2\mathrm{II}}Q_{3\mathrm{II}} & \sqrt{2}Q_{2\mathrm{III}}Q_{3\mathrm{III}} & Q_{2\mathrm{II}}Q_{3\mathrm{III}}+Q_{3\mathrm{II}}Q_{2\mathrm{III}} & Q_{2\mathrm{I}}Q_{3\mathrm{III}}+Q_{3\mathrm{I}}Q_{2\mathrm{III}} & Q_{2\mathrm{I}}Q_{3\mathrm{II}}+Q_{3\mathrm{I}}Q_{2\mathrm{II}} \\ \sqrt{2}Q_{1\mathrm{I}}Q_{3\mathrm{I}} & \sqrt{2}Q_{1\mathrm{II}}Q_{3\mathrm{II}} & \sqrt{2}Q_{1\mathrm{III}}Q_{3\mathrm{III}} & Q_{1\mathrm{II}}Q_{3\mathrm{III}}+Q_{3\mathrm{II}}Q_{1\mathrm{III}} & Q_{1\mathrm{I}}Q_{3\mathrm{III}}+Q_{3\mathrm{I}}Q_{1\mathrm{III}} & Q_{1\mathrm{I}}Q_{3\mathrm{II}}+Q_{3\mathrm{I}}Q_{1\mathrm{II}} \\ \sqrt{2}Q_{1\mathrm{I}}Q_{2\mathrm{I}} & \sqrt{2}Q_{1\mathrm{II}}Q_{2\mathrm{II}} & \sqrt{2}Q_{1\mathrm{III}}Q_{2\mathrm{III}} & Q_{1\mathrm{II}}Q_{2\mathrm{III}}+Q_{2\mathrm{II}}Q_{1\mathrm{III}} & Q_{1\mathrm{I}}Q_{2\mathrm{III}}+Q_{2\mathrm{I}}Q_{1\mathrm{III}} & Q_{1\mathrm{I}}Q_{2\mathrm{II}}+Q_{1\mathrm{II}}Q_{2\mathrm{I}} \end{matrix}$$

To see that $\hat{\mathbf{Q}}$ is an orthogonal matrix in six dimensions requires some algebraic manipulation. The proof rests on the orthogonality of three-dimensional $\mathbf{Q}$:

$$\mathbf{Q}\cdot\mathbf{Q}^T = \mathbf{Q}^T\cdot\mathbf{Q} = \mathbf{1} \Rightarrow \hat{\mathbf{Q}}\cdot\hat{\mathbf{Q}}^T = \hat{\mathbf{Q}}^T\cdot\hat{\mathbf{Q}} = \hat{\mathbf{1}}\,. \tag{A168}$$

In the special case when $\mathbf{Q}$ is given by

$$\mathbf{Q} = \begin{bmatrix} \cos\alpha & -\sin\alpha & 0 \\ \sin\alpha & \cos\alpha & 0 \\ 0 & 0 & 1 \end{bmatrix}, \tag{A169}$$

$\hat{\mathbf{Q}}$ has representation

$$\hat{\mathbf{Q}} = \begin{bmatrix} \cos^2\alpha & \sin^2\alpha & 0 & 0 & 0 & -\sqrt{2}\cos\alpha\sin\alpha \\ \sin^2\alpha & \cos^2\alpha & 0 & 0 & 0 & \sqrt{2}\cos\alpha\sin\alpha \\ 0 & 0 & 1 & 0 & 0 & 0 \\ 0 & 0 & 0 & \cos\alpha & \sin\alpha & 0 \\ 0 & 0 & 0 & -\sin\alpha & \cos\alpha & 0 \\ \sqrt{2}\cos\alpha\sin\alpha & -\sqrt{2}\cos\alpha\sin\alpha & 0 & 0 & 0 & \cos^2\alpha-\sin^2\alpha \end{bmatrix}. \tag{A170}$$

It should be noted that while it is always possible to find $\hat{\mathbf{Q}}$ given $\mathbf{Q}$ by use of (A167), it is not possible to determine $\mathbf{Q}$ unambiguously given $\hat{\mathbf{Q}}$. Although $\hat{\mathbf{Q}}$ is uniquely determined by $\mathbf{Q}$, the reverse process of finding a $\mathbf{Q}$ given $\hat{\mathbf{Q}}$ is not unique in that there will be a choice of sign necessary in the reverse process. To see this non-uniqueness note that both $\mathbf{Q} = \mathbf{1}$ and $\mathbf{Q} = -\mathbf{1}$ correspond to $\hat{\mathbf{Q}} = \hat{1}$. There are 9 components of $\mathbf{Q}$ that satisfy 6 conditions given by $(\mathrm{A168})_1$. There are therefore only three independent components of $\mathbf{Q}$. However, there are 36 components of $\hat{\mathbf{Q}}$ that satisfy the 21 conditions given by $(\mathrm{A168})_2$ and hence 15 independent components of $\hat{\mathbf{Q}}$. Thus, while (A167) uniquely determines $\hat{\mathbf{Q}}$ given $\mathbf{Q}$, the components of $\hat{\mathbf{Q}}$

must be considerably restricted in order to determine $\mathbf{Q}$ given $\hat{\mathbf{Q}}$, and selection of signs must be made.

**Problems**

A.11.1. Construct six-dimensional vector $\hat{\mathbf{T}}$ that corresponds to three-dimensional tensor $\mathbf{T}$ given by

$$\mathbf{T} = \frac{1}{2}\begin{bmatrix} 13 & 3\sqrt{3} & \sqrt{3} \\ 3\sqrt{3} & 7 & 1 \\ \sqrt{3} & 1 & 8 \end{bmatrix}.$$

A.11.2. Prove that relationship $\hat{\mathbf{T}} \cdot \hat{\mathbf{J}} = \mathbf{T} : \mathbf{J}$ (A164) is correct by substitution of components.

A.11.3. Construct six-dimensional orthogonal transformation $\hat{\mathbf{Q}}$ that corresponds to three-dimensional orthogonal transformation $\mathbf{Q}$, where

$$\mathbf{Q} = \begin{bmatrix} \cos\psi & 0 & -\sin\psi \\ 0 & 1 & 0 \\ \sin\psi & 0 & \cos\psi \end{bmatrix}.$$

A.11.4. Construct six-dimensional orthogonal transformation $\hat{\mathbf{Q}}$ that corresponds to three-dimensional orthogonal transformation $\mathbf{Q}$, where

$$\mathbf{Q} = \frac{1}{2}\begin{bmatrix} 1 & \sqrt{\frac{3}{2}} & \sqrt{\frac{3}{2}} \\ -\sqrt{3} & \frac{1}{\sqrt{2}} & \frac{1}{\sqrt{2}} \\ 0 & -\sqrt{2} & \sqrt{2} \end{bmatrix}.$$

## A.12. THE GRADIENT OPERATOR AND THE DIVERGENCE THEOREM

The vectors and tensors introduced are all considered as functions of coordinate positions $x_1$, $x_2$, $x_3$, and time $t$. In the case of a vector or tensor this dependence is written $\mathbf{r}(x_1, x_2, x_3, t)$ or $\mathbf{T}(x_1, x_2, x_3, t)$, which means that each element of vector $\mathbf{r}$ or tensor $\mathbf{T}$ is a function of $x_1$, $x_2$, $x_3$, and $t$. The gradient operator is denoted by $\nabla$ and defined, in three dimensions, by

$$\nabla = \frac{\partial}{\partial x_1}\mathbf{e}_1 + \frac{\partial}{\partial x_2}\mathbf{e}_2 + \frac{\partial}{\partial x_3}\mathbf{e}_3 . \tag{A171}$$

This operator is called a vector operator because it increases the tensorial order of the quantity operated upon by one. For example, the gradient of a scalar function $f(x_1, x_2, x_3, t)$ is a vector given by

$$\nabla f(x_1, x_2, x_3, t) = \frac{\partial f}{\partial x_1}\mathbf{e}_1 + \frac{\partial f}{\partial x_2}\mathbf{e}_2 + \frac{\partial f}{\partial x_3}\mathbf{e}_3 . \tag{A172}$$

To verify that the gradient operator transforms as a vector, consider the operator in both the Latin and Greek coordinate systems:

$$\nabla^{(L)} f(\mathbf{x}^{(L)},t) = \sum_{i=1}^{i=3} \frac{\partial f}{\partial x_i}\mathbf{e}_i \quad \text{and} \quad \nabla^{(G)} f(\mathbf{x}^{(G)},t) = \sum_{\alpha=I}^{\alpha=III} \frac{\partial f}{\partial x_\alpha}\mathbf{e}_\alpha \,, \tag{A173}$$

respectively, and note that, by the chain rule of partial differentiation,

$$\frac{\partial f}{\partial x_i} = \sum_{i=1}^{i=3} \frac{\partial f}{\partial x_\alpha}\frac{\partial x_\alpha}{\partial x_i} \,. \tag{A174}$$

Now since, from (A77), $\mathbf{x}^{(G)} = \mathbf{Q}^{\mathbf{T}} \cdot \mathbf{x}^{(L)}$, or in index notation,

$$x_\alpha = \sum_{i=1}^{i=3} Q_{i\alpha} x_i \,,$$

it follows that $Q_{i\alpha} = \partial x_\alpha / \partial x_i$ and, from (A174),

$$\frac{\partial f}{\partial x_i} = \sum_{i=1}^{i=3} Q_{i\alpha} \frac{\partial f}{\partial x_\alpha}$$

or

$$\nabla^{(L)} f(\mathbf{x}^{(L)},t) = \mathbf{Q} \cdot \nabla^{(G)} f(\mathbf{x}^{(G)},t) \,. \tag{A175}$$

This shows that the gradient is a vector operator because it transforms like a vector under changes of coordinate systems.

The gradient of vector function $\mathbf{r}(x_1, x_2, x_3, t)$ is a second-order tensor given by

$$\nabla \otimes \mathbf{r}(x_1,x_2,x_3,t) = \sum_{i=1}^{3}\sum_{j=1}^{3} \frac{\partial r_j}{\partial x_i}\mathbf{e}_i \otimes \mathbf{e}_j \,, \tag{A176}$$

where

$$\left[\nabla \otimes \mathbf{r}\right]^T = \left[\frac{\partial r_i}{\partial x_j}\right] = \begin{bmatrix} \dfrac{\partial r_1}{\partial x_1} & \dfrac{\partial r_1}{\partial x_2} & \dfrac{\partial r_1}{\partial x_3} \\ \dfrac{\partial r_2}{\partial x_1} & \dfrac{\partial r_2}{\partial x_2} & \dfrac{\partial r_2}{\partial x_3} \\ \dfrac{\partial r_3}{\partial x_1} & \dfrac{\partial r_3}{\partial x_2} & \dfrac{\partial r_3}{\partial x_3} \end{bmatrix}. \tag{A177}$$

As this example suggests, when the gradient operator is applied, the tensorial order of the quantity operated upon it increases by one. The matrix that is the open product of the gradient and **r** is arranged in (A177) so that the derivative is in the first (or row) position and the vector **r** is in the second (or column) position. The divergence operator is a combination of the gradient operator and a contraction operation that results in reduction of the order of the quantity operated upon to one lower than it was before the operation. For example, the trace of the gradient of a vector function is a scalar called the divergence of the vector, tr[$\nabla\otimes\mathbf{r}$] = $\nabla\cdot\mathbf{r}$ = div **r**:

$$\nabla \cdot \mathbf{r} = \text{div}\ \mathbf{r} = \frac{\partial r_1}{\partial x_1} + \frac{\partial r_2}{\partial x_2} + \frac{\partial r_3}{\partial x_3}. \tag{A178}$$

The divergence operation is similar to the scalar product of two vectors in that the effect of the operation is to reduce the order of the quantity by two from the sum of the ranks of the combined quantities before the operation. The curl operation is the gradient operator cross-product with a vector function $\mathbf{r}(x_1, x_2, x_3, t)$; thus,

$$\nabla \times \mathbf{r} = \text{curl}\ \mathbf{r} = \begin{vmatrix} \mathbf{e}_1 & \mathbf{e}_2 & \mathbf{e}_3 \\ \dfrac{\partial}{\partial x_1} & \dfrac{\partial}{\partial x_2} & \dfrac{\partial}{\partial x_3} \\ r_1 & r_2 & r_3 \end{vmatrix}. \tag{A179}$$

A three-dimensional double gradient tensor defined by $\mathbf{O} = \nabla\otimes\nabla$ ($\text{tr}\mathbf{O} = \nabla^2$) and its six-dimensional vector counterpart $\hat{\mathbf{O}}$ ($\hat{\mathbf{O}} \cdot \hat{\mathbf{U}} = \text{tr}\mathbf{O} = \nabla^2$) are often convenient notations to employ. The components of $\hat{\mathbf{O}}$ are

$$\hat{\mathbf{O}} = \left[ \frac{\partial^2}{\partial x_1^2}, \frac{\partial^2}{\partial x_2^2}, \frac{\partial^2}{\partial x_3^2}, \sqrt{2}\frac{\partial^2}{\partial x_2 \partial x_3}, \sqrt{2}\frac{\partial^2}{\partial x_1 \partial x_3}, \sqrt{2}\frac{\partial^2}{\partial x_1 \partial x_2} \right]^T, \tag{A180}$$

and the operation of $\hat{\mathbf{O}}$ on a six-dimensional vector representation of a second-order tensor in three dimensions, $\hat{\mathbf{O}} \cdot \hat{\mathbf{T}} = \text{tr}\mathbf{O} \cdot \mathbf{T}$, is given by

$$\hat{\mathbf{O}} \cdot \hat{\mathbf{T}} = \frac{\partial^2 T_{11}}{\partial x_1^2} + \frac{\partial^2 T_{22}}{\partial x_2^2} + \frac{\partial^2 T_{33}}{\partial x_3^2} + 2\frac{\partial^2 T_{23}}{\partial x_2 \partial x_3} + 2\frac{\partial^2 T_{13}}{\partial x_1 \partial x_3} + 2\frac{\partial^2 T_{12}}{\partial x_1 \partial x_2}. \tag{A181}$$

The divergence of second-order tensor $\mathbf{T}$ is defined in a similar fashion to the divergence of a vector; it is a vector given by

$$\nabla \cdot \mathbf{T}(x_1, x_2, x_3, t) = \left( \frac{\partial T_{11}}{\partial x_1} + \frac{\partial T_{12}}{\partial x_2} + \frac{\partial T_{13}}{\partial x_3} \right) \mathbf{e}_1 +$$

$$\left( \frac{\partial T_{21}}{\partial x_1} + \frac{\partial T_{22}}{\partial x_2} + \frac{\partial T_{23}}{\partial x_3} \right) \mathbf{e}_2 + \left( \frac{\partial T_{31}}{\partial x_1} + \frac{\partial T_{32}}{\partial x_2} + \frac{\partial T_{33}}{\partial x_3} \right) \mathbf{e}_3. \tag{A182}$$

The divergence theorem (also called Gauss's theorem, Green's theorem, or Ostrogradsky's theorem, depending on the nationality) relates a volume integral to a surface integral over the volume. The divergence of vector field $\mathbf{r}(x_1, x_2, x_3, t)$ integrated over a volume of space is equal to the integral of the projection of the field, $\mathbf{r}(x_1, x_2, x_3, t)$, on the normal to the boundary of the region, evaluated on the boundary of the region, and integrated over the entire boundary:

$$\int_R \nabla \cdot \mathbf{r} dv = \int_{\partial R} \mathbf{r} \cdot \mathbf{n} dA, \tag{A183}$$

where $\mathbf{r}$ represents any vector field, $R$ is a region of three-dimensional space, and $\partial R$ is the entire boundary of that region (see Figure A.5). There are some mathematical restrictions on the validity of (A183). Vector field $\mathbf{r}(x_1, x_2, x_3, t)$ must be defined and continuously differentiable in the region $R$. Region $R$ is subject to mathematical restrictions, but any region of interest satisfies these restrictions. For the second-order tensor the divergence theorem takes the form

$$\int_R \nabla \cdot \mathbf{T} dv = \int_{\partial R} \mathbf{T} \cdot \mathbf{n} dA \,. \tag{A184}$$

To show that this version of the theorem is also true if (A183) is true, constant vector **c** is introduced and used with tensor field $\mathbf{T}(x_1, x_2, x_3, t)$ to form vector function field $\mathbf{r}(x_1, x_2, x_3, t)$, and thus

$$\mathbf{r} = \mathbf{c} \cdot \mathbf{T}(x_1, x_2, x_3, t) \,. \tag{A185}$$

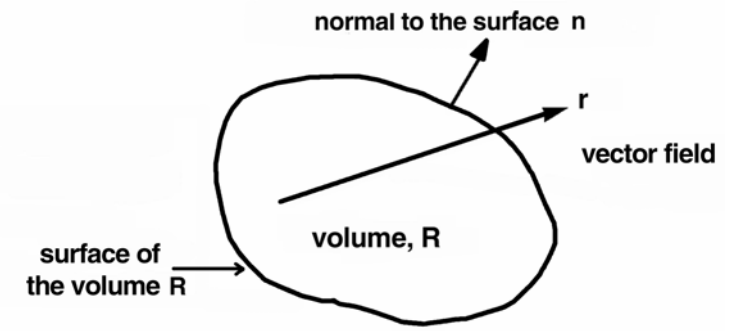



**Figure A.5**. An illustration of the geometric elements appearing in the divergence theorem.

Substitution of (A185) into (A183) for **r** yields

$$\int_R \nabla \cdot (\mathbf{c} \cdot \mathbf{T}) dv = \int_{\partial R} \mathbf{c} \cdot \mathbf{T} \cdot \mathbf{n} dA \,, \tag{A186}$$

and since **c** is a constant vector, (A186) may be rewritten as

$$\mathbf{c} \cdot \left\{ \int_R \nabla \cdot (\mathbf{T}) dv - \int_{\partial R} \mathbf{T} \cdot \mathbf{n} dA \right\} = 0 \,. \tag{A187}$$

This result must hold for all constant vectors **c**, and the divergence theorem for the second-order tensor, (A184), follows.

**Problems**

A.12.1. Calculate the gradient of function $f = (x_1)^2(x_2)^2(x_3)^3$ and evaluate the gradient at point (1, 2, 3).

A.12.2. Calculate the gradient of vector function $\mathbf{r}(x_1, x_2, x_3) = [(x_1)^2(x_2)^2, x_1x_2, (x_3)^2]$.

A.12.3. Calculate the divergence of vector function $\mathbf{r}(x_1, x_2, x_3) = [(x_1)^2(x_2)^2, x_1x_2, (x_3)^2]$.

A.12.4. Calculate the curl of vector function $\mathbf{r}(x_1, x_2, x_3) = [(x_1)^2(x_2)^2, x_1x_2, (x_3)^2]$.

A.12.5. Calculate the gradient of vector function $\mathbf{r}(x_1, x_2, x_3) = [(x_2)^2 + (x_3)^2, (x_1)^2 + (x_3)^2, (x_1)^2 + (x_2)^2]$.

A.12.6. Calculate the divergence of vector function $\mathbf{r}(x_1, x_2, x_3) = [(x_2)^2 + (x_3)^2, (x_1)^2 + (x_3)^2, (x_1)^2 + (x_2)^2]$.

A.12.7. Calculate the curl of vector function $\mathbf{r}(x_1, x_2, x_3) = [(x_2)^2 + (x_3)^2, (x_1)^2 + (x_3)^2, (x_1)^2 + (x_2)^2]$.

A.12.8. Calculate the divergence of vector function $\mathbf{r}(x_1, x_2, x_3) = \mathbf{a} \times \mathbf{x}$, where $\mathbf{a}$ is a constant vector.

A.12.9. Calculate the curl of vector function $\mathbf{r}(x_1, x_2, x_3) = \mathbf{a} \times \mathbf{x}$, where $\mathbf{a}$ is a constant vector.

A.12.10. Express the integral over a closed surface $S$, $\int \nabla(\mathbf{x}\cdot\mathbf{x})\cdot\mathbf{n}\, dS$, in terms of total volume $V$ enclosed by surface $S$.

## A.13. TENSOR COMPONENTS IN CYLINCRICAL COORDINATES

In several places use is made of cylindrical coordinates in the solutions to problems in this text. The base vectors in curvilinear coordinates are not generally unit vectors nor do they have the same dimensions. However, local Cartesian coordinates called physical components of the tensors may be constructed if the curvilinear coordinate system is orthogonal. Below, the standard formulas used in this text for cylindrical coordinates are recorded. In the case when cylindrical coordinates are employed, the vectors and tensors introduced are all considered as functions of the coordinate positions $r$, $\theta$, *and* $z$ in place of the Cartesian coordinates $x_1$, $x_2$, and $x_3$. In the case of a vector or tensor this dependence is written $\mathbf{v}(r,\theta,z,t)$ or $\mathbf{T}(r,\theta,z,t)$, which means that each element of the vector $\mathbf{v}$ or the tensor $\mathbf{T}$ is a function of $r$, $\theta$, $z$, and $t$. The gradient operator is denoted by $\nabla$ and defined, in three dimensions, by

$$\nabla = \frac{\partial}{\partial r}\mathbf{e}_r + \frac{1}{r}\frac{\partial}{\partial \theta}\mathbf{e}_\theta + \frac{\partial}{\partial z}\mathbf{e}_z, \tag{A188}$$

where $\mathbf{e}_r$, $\mathbf{e}_\theta$, and $\mathbf{e}_z$ are the unit base vectors in the cylindrical coordinate system. The gradient of a scalar function $f(x_1, x_2, x_3, t)$ is a vector given by

$$\nabla f = \frac{\partial f}{\partial r}\mathbf{e}_r + \frac{1}{r}\frac{\partial f}{\partial \theta}\mathbf{e}_\theta + \frac{\partial f}{\partial z}\mathbf{e}_z. \tag{A189}$$

The gradient of a vector function $\mathbf{v}(r,\theta,z,t)$ is given by

$$\left[\nabla \otimes \mathbf{v}\right]^T = \begin{bmatrix} \dfrac{\partial v_r}{\partial r} & \dfrac{1}{r}\dfrac{\partial v_r}{\partial \theta} & \dfrac{\partial v_r}{\partial z} \\ \dfrac{\partial v_\theta}{\partial r} & \dfrac{1}{r}\dfrac{\partial v_\theta}{\partial \theta} & \dfrac{\partial v_\theta}{\partial z} \\ \dfrac{\partial v_z}{\partial r} & \dfrac{1}{r}\dfrac{\partial v_z}{\partial \theta} & \dfrac{\partial v_z}{\partial z} \end{bmatrix}. \tag{A190}$$

The formula for the divergence of vector $\mathbf{v}$ in cylindrical coordinates is obtained by taking the trace of (A190), $\text{tr}[\nabla\otimes\mathbf{v}] = \nabla\cdot\mathbf{v} = \text{div}\ \mathbf{v}$. The curl is the gradient operator cross-product with a vector function $\mathbf{v}(r, \theta, z, t)$; thus,

$$\nabla \times \mathbf{v} = \text{curl}\ \mathbf{v} = \begin{bmatrix} \mathbf{e}_r & \mathbf{e}_\theta & \mathbf{e}_z \\ \dfrac{\partial}{\partial r} & \dfrac{\partial}{\partial \theta} & \dfrac{\partial}{\partial z} \\ v_r & r v_\theta & v_z \end{bmatrix}. \tag{A191}$$

The form of the double gradient three-dimensional second-order tensor defined by $\mathbf{O} = \nabla\otimes\nabla$ ($\mathrm{tr}\mathbf{O} = \nabla^2$) and its six-dimensional vector counterpart, $\hat{\mathbf{O}}$ ($\hat{\mathbf{O}}\cdot\hat{\mathbf{U}} = \mathrm{tr}\mathbf{O} = \nabla^2$) have the following cylindrical coordinate representations:

$$\mathbf{O} = [\nabla\otimes\nabla] = \begin{bmatrix} \frac{1}{r}\frac{\partial}{\partial r}(r\frac{\partial}{\partial r}) & \frac{1}{r}\frac{\partial^2}{\partial r\partial\theta} & \frac{\partial^2}{\partial r\partial z} \\ \frac{1}{r}\frac{\partial^2}{\partial r\partial\theta} & \frac{1}{r^2}\frac{\partial^2}{\partial\theta^2} & \frac{1}{r}\frac{\partial^2}{\partial z\partial\theta} \\ \frac{\partial^2}{\partial r\partial z} & \frac{1}{r}\frac{\partial^2}{\partial z\partial\theta} & \frac{\partial^2}{\partial z^2} \end{bmatrix}, \tag{A192}$$

and

$$\hat{\mathbf{O}} = \left[\frac{1}{r}\frac{\partial}{\partial r}(r\frac{\partial}{\partial r}), \frac{1}{r^2}\frac{\partial^2}{\partial\theta^2}, \frac{\partial^2}{\partial z^2}, \sqrt{2}\frac{1}{r}\frac{\partial^2}{\partial z\partial\theta}, \sqrt{2}\frac{\partial^2}{\partial r\partial z}, \sqrt{2}\frac{1}{r}\frac{\partial^2}{\partial r\partial\theta}\right]^T, \tag{A193}$$

and the operation of $\hat{\mathbf{O}}$ on a six-dimensional vector representation of a second-order tensor in three dimensions, $\hat{\mathbf{O}}\cdot\hat{\mathbf{T}} = \mathbf{O}:\mathbf{T} = \mathrm{tr}\,\mathbf{O}\cdot\mathbf{T}$, is given by

$$\hat{\mathbf{O}}\cdot\hat{\mathbf{T}} = \frac{\partial}{\partial r}\ r\frac{\partial T_{rr}}{\partial r} + \frac{1}{r^2}\frac{\partial^2 T_{\theta\theta}}{\partial\theta^2} + \frac{\partial^2 T_{zz}}{\partial z^2} + 2\frac{1}{r}\frac{\partial^2 T_{z\theta}}{\partial z\partial\theta} + 2\frac{\partial^2 T_{rz}}{\partial r\partial z} + 2\frac{1}{r}\frac{\partial^2 T_{r\theta}}{\partial r\partial\theta}. \tag{A194}$$

The divergence of a second-order tensor $\mathbf{T}$ is defined in a similar fashion to the divergence of a vector; it is a vector given by

$$\nabla\cdot\mathbf{T}(r,\theta,z,t) = \frac{\partial T_{rr}}{\partial r} + \frac{1}{r}\frac{\partial T_{r\theta}}{\partial\theta} + \frac{\partial T_{rz}}{\partial z}\ \mathbf{e}_r + \frac{\partial T_{r\theta}}{\partial r} + \frac{1}{r}\frac{\partial T_{\theta\theta}}{\partial\theta} + \frac{\partial T_{\theta z}}{\partial z}\ \mathbf{e}_\theta + \frac{\partial T_{zr}}{\partial r} + \frac{1}{r}\frac{\partial T_{z\theta}}{\partial\theta} + \frac{\partial T_{zz}}{\partial z}\ \mathbf{e}_z. \tag{A195}$$

The strain-displacement relations (3.52) are written in cylindrical coordinates as

$$E_{rr} = \frac{\partial u_r}{\partial r},\ E_{\theta\theta} = \frac{1}{r}\frac{\partial u_\theta}{\partial\theta} + \frac{u_r}{r},\ E_{r\theta} = \frac{1}{2}\ \frac{1}{r}\frac{\partial u_r}{\partial\theta} + \frac{\partial u_\theta}{\partial r} - \frac{u_\theta}{r}$$

$$E_{zz} = \frac{\partial u_z}{\partial z},\ E_{rz} = \frac{1}{2}\ \frac{\partial u_z}{\partial r} + \frac{\partial u_r}{\partial z}\ ,\ E_{\theta z} = \frac{1}{2}\ \frac{1}{r}\frac{\partial u_z}{\partial\theta} + \frac{\partial u_\theta}{\partial z}\ , \tag{A196}$$

and similar formulas apply for the rate of deformation-velocity tensor $\mathbf{D}$, (3.33) if the change of notation from $\mathbf{E}$ to $\mathbf{D}$ and $\mathbf{u}$ to $\mathbf{v}$ is accomplished. The stress equations of motion (4.37) in cylindrical coordinates are

$$\frac{\partial T_{rr}}{\partial r} + \frac{1}{r}\frac{\partial T_{r\theta}}{\partial\theta} + \frac{\partial T_{rz}}{\partial z} + \frac{T_{rr} - T_{\theta\theta}}{r} + \rho d_r = \rho u\ddot{x}_r,$$

$$\frac{\partial T_{r\theta}}{\partial r} + \frac{1}{r}\frac{\partial T_{\theta\theta}}{\partial\theta} + \frac{\partial T_{\theta z}}{\partial z} + \frac{T_{r\theta}}{r} + \rho d_\theta = \rho\ddot{x}_\theta,$$

$$\frac{\partial T_{rz}}{\partial r} + \frac{1}{r}\frac{\partial T_{\theta z}}{\partial\theta} + \frac{\partial T_{zz}}{\partial z} + \frac{T_{rz}}{r} + \rho d_z = \rho\ddot{x}_z. \tag{A197}$$

**Problem**

A.13.1. Calculate the components of the rate of deformation-velocity tensor **D** (3.33) in cylindical coordinates.

# CREDIT LINES

The quotation on page 1 is taken from RL Trelstad, FH Silver, 1981, Matrix Assembly, In *Cell biology of the extracellular matrix*, ed. ED Hay, pp. 179–216, New York: Plenum Press, with the kind permission of Springer Science and Business Media. Copyright © 1981, Springer.

Figure 1.1 is reprinted with permission from CR Anthony, N Kolthoff, 1975, *Textbook of anatomy and physiology*, 9th ed., St. Louis: Mosby. Copyright © 1975, Elsevier.

Figure 1.2 is reprinted with permission from BC Goodwin, 1989, Unicellular morphogenesis, In *Cell Shape*, ed. WD Stein, F Bronner, pp. 365–91, New York: Academic Press. Copyright © 1989, Elsevier.

Figure 1.3 is reprinted with permission from BC Goodwin, 1989, Unicellular morphogenesis, In *Cell Shape*, ed. WD Stein, F Bronner, pp. 365–91, New York: Academic Press. Copyright © 1989, Elsevier.

Figure 1.4 is reprinted with permission from CA de Duve, 1984, *A guided tour of the living cell*, New York: Scientific American. Copyright © 1984, Henry Holt.

Figure 1.5 is reprinted with permission from CA de Duve, 1984, *A guided tour of the living cell*, New York: Scientific American. Copyright © 1984, Henry Holt.

Figure 1.6 is reprinted with permission from J Darnell, H Lodish, D Baltimore, 1990, *Molecular cell biology*, New York: Scientific American. Copyright © 1990, W.H. Freeman and Company.

Figure 1.7 is reprinted from RB Gennis, 1989, *Biomembranes*, New York: Springer, with the kind permission of Springer Science and Business Media. Copyright © 1989 Springer.

Figure 1.8 is reprinted with permission from B Alberts, D Bray, J Lewis, M Raff, K Roberts, JD Watson, 1983, *Molecular Biology of the Cell*, New York: Garland. Copyright © 1983, Garland.

Figure 1.14a is courtesy of Art Winfree.

Figure 1.14b is reprinted from JD Murray, 1993, *Mathematical biology*, New York: Springer Verlag, with the kind permission of Springer Science and Business Media. Copyright © 1993, Springer.

Figure 1.15 is reprinted from JD Murray, 1993, *Mathematical biology*, New York: Springer Verlag, with the kind permission of Springer Science and Business Media. Copyright © 1993, Springer.

Figure 1.16 is reprinted with permission from SA Newman, HL Frisch, 1979, Dynamics of skeletal pattern formation in developing chick limb, *Science* **205**:662–668. Copyright © 1979, AAAS.

Figure 1.17 is reprinted with permission from SA Newman, HL Frisch, 1979, Dynamics of skeletal pattern formation in developing chick limb, *Science* **205**:662–668. Copyright © 1979, AAAS.

Figure 1.18 is reprinted from MS Alber, MA Kiskowski, JA Glazier, Y Jiang, 2002, On cellular automaton approaches to modeling biological cells, In *Mathematical systems theory in biology, communication, and finance, IMA*, Vol 142, ed. J Rosenthal, DS Gilliam, New York: Springer Verlag, with the kind permission of Springer Science and Business Media. Copyright © 2002, Springer.

Figure 1.20 is reprinted with permission from M Kuecken, 2004, *On the formation of fingerprints*, PhD thesis, University of Arizona.

Figure 1.21 is reprinted with permission from M Kuecken, 2004, *On the formation of fingerprints*, PhD thesis, University of Arizona.

Figure 1.22 is reprinted with permission from B Alberts, D Bray, J Lewis, M Raff, K Roberts, JD Watson, 1983, *Molecular Biology of the Cell*, New York: Garland. Copyright © 1983, Garland.

Figure 1.23 is reprinted with permission from JO Radler, I Koltover, 1997, Structure of DNA-cationic liposome complexes: DNA intercalation in multilamellar membranes in distin, *Science* **275**:810–814. Copyright © 1997, AAAS.

Figure 1.24 is reprinted from AK Harris, 1976, Is cell sorting caused by differences on the work of intercellular adhesion? A critique of the Steinberg hypothesis, *J Theor Biol* **61**:267–285, with the kind permission of Springer Science and Business Media. Copyright © 1976, Springer.

Figure 1.26 is reprinted from GM Odell, GF Oster, P Alberch, B Burnside, 1981, The mechanical basis of morphogenesis, I: epithelial folding and invagination, *Dev Biol* **85**:446–462, with the kind permission of Springer Science and Business Media. Copyright © 1981, Springer.

Figure 1.27 is reprinted from GM Odell, GF Oster, P Alberch, B Burnside, 1981, The mechanical basis of morphogenesis, I: epithelial folding and invagination, *Dev Biol* **85**:446–462, with the kind permission of Springer Science and Business Media. Copyright © 1981, Springer.

Figure 1.29 is reprinted with the kind permission of Jussi Koivunen. Permission granted by Kirsti Nurkkala, Publications Editor, University of Oulu.

Figure 1.30 is reprinted from JD Murray, 1993, *Mathematical biology*, New York: Springer Verlag, with the kind permission of Springer Science and Business Media. Copyright © 1993, Springer.

The first quotation on page 41 is taken from AK Harris, 1994, Multicellular mechanics in the creation of anatomical structures, In *Biomechanics of active movement and division of cells*, ed. N Akkas, pp. 87–129, New York: Springer Verlag, and is reprinted with the kind permission of Springer Science and Business Media. Copyright © 1994, Springer.

The second quotation on page 41 is taken from G Polya, 1945, *How to solve it*, Princeton: Princeton UP, and is reprinted with permission from Princeton University Press.

Figure 2.6 is reprinted with permission from AB Schultz, GBJ Andersson, 1981, Analysis of loads on the lumbar spine, *Spine* **6**:76–82. Copyright © 1981, Lippincott, Williams and Wilkins.

Figure 2.7 is reprinted with permission from AB Schultz, GBJ Andersson, R Örtengren, K Haderspeck, A Nachemson, 1982, Loads on the lumbar spine, *J Bone Joint Surg* **64A**:713–720. Copyright © 1982, the Journal of Bone and Joint Surgery.

Figure 2.8 is reprinted with permission from EJ Sprigings, JL Lanovaz, LG Watson, KW Russell, 1999, Removing swing from a handstand on rings using a properly timed backward giant circle: a simulation solution, *J Biomech* **32**:27–35. Copyright © 1999, Elsevier.

Figure 2.9 is reprinted with permission from DB Chaffin, GBJ Andersson, 1991, *Occupational biomechanics*, 2nd ed., New York: Wiley. Copyright © 1991, John Wiley & Sons Inc.

Figure 2.11 is reprinted with permission from L You, SC Cowin, M Schaffler, S Weinbaum, 2001, A model for strain amplification in the actin cytoskeleton of osteocytes due to fluid drag on pericellular matrix, *J Biomech* **34**:1375–1386. Copyright © 2001, Elsevier.

Figure 2.12 is reprinted with permission from R Furukawa, M Fechheimer, 1997, The structure, function, and assembly of actin filament bundles, *Int Rev Cytol* **175**:29–90. Copyright © 1997, Elsevier.

Figure 2.14 is reprinted with permission from TA McMahon, PR Greene, 1979, The influence of track compliance upon running, *J Biomech* **12**:893–904. Copyright © 1979, Elsevier.

Figure 2.15a is reprinted with permission from TA McMahon, PR Greene, 1978, Fast-running tracks, *Sci Am* **239**:148–163. Copyright © 1978, Elsevier.

Figure 2.16 is reprinted with permission from T Spägele, A Kistner, A Gollhofer, 1999, A multiphase optimal control technique for the simulation of a human vertical jump, *J Biomech* **32**:87–91. Copyright © 1999, Elsevier.

Figure 2.19 is reprinted with permission from R Skalak, K-LP Sung, G Schmid-Schönbein, S Chein, 1988, Passive deformation analysis of human leukocytes, *J Biomech Eng* **110**:27–36. Copyright © 1988, the American Society of Mechanical Engineers.

Figure 2.20 is reprinted with permission from M Nordin, VH Frankel, 1989, *Basic biomechanics of the musculoskeletal system*, 2nd ed., Philadelphia: Lea & Febiger. Copyright © 1989, Lippincott, Williams and Wilkins.

Figure 2.26 courtesy of Sinan Simsek, who drew the illustration.

Figure 2.28 is reprinted with permission from I Müller, 1985, *Thermodynamics*, Boston: Pitman. Copyright © 1985, Pitman.

Figure 2.29 is reprinted with permission from I Müller, 1985, *Thermodynamics*, Boston: Pitman. Copyright © 1985, Pitman.

Figure 2.30 is reprinted with permission from S Wolfram, 2002b, *A new kind of science explorer* [CD], Champaign, IL: Wolfram Media. Copyright © 2002, Wolfram Research.

Figure 2.31 is reprinted with permission from S Wolfram, 2002b, *A new kind of science explorer* [CD], Champaign, IL: Wolfram Media. Copyright © 2002, Wolfram Research.

Figure 2.32 is reprinted with permission from S Wolfram, 2002b, *A new kind of science explorer* [CD], Champaign, IL: Wolfram Media. Copyright © 2002, Wolfram Research.

Figure 2.33 is reprinted with permission from S Wolfram, 2002b, *A new kind of science explorer* [CD], Champaign, IL: Wolfram Media. Copyright © 2002, Wolfram Research.

Figure 2.34 is reprinted with permission from S Wolfram, 2002b, *A new kind of science explorer* [CD], Champaign, IL: Wolfram Media. Copyright © 2002, Wolfram Research.

Figure 2.35 is reprinted with permission from DH Rothman, S Zaleski, 1997, *Lattice–gas cellular automata*, Cambridge: Cambridge UP. Copyright © 1997, Cambridge University Press.

Figure 2.36 is reprinted with permission from M Krafczyk, M Cerrolaza, M Schulz, E Rank, 1998, Analysis of 3D transient blood flow passing through an artificial aortic valve by Lattice-Boltzmann methods, *J Biomech* **31**:453–462. Copyright © 1998, Elsevier.

Figure 2.37 is reprinted with permission from DH Rothman, S Zaleski, 1997, *Lattice–gas cellular automata*, Cambridge: Cambridge UP. Copyright © 1997, Cambridge University Press.

Figure 2.38 is reprinted with permission from DH Rothman, S Zaleski, 1997, *Lattice–gas cellular automata*, Cambridge: Cambridge UP. Copyright © 1997, Cambridge University Press.

Figure 2.39 is reprinted with permission from MS Alber, MA Kiskowski, JA Glazier, Y Jiang, 2002, On cellular automaton approaches to modeling biological cells, In *Mathematical systems theory in biology, communication, and finance*, ed. J Rosenthal, DS Gilliam, Institute for Mathematics and Its Applications, Vol. 142, pp. 1–39, New York: Springer Verlag. Copyright © 2002, Springer.

The quotation on page 95 is taken from http://www.johnvandrie.com, was translated by John H. Van Drie, and is reprinted here with his permission.

The quotation on page 119 is taken from HB Callen, 1960, *Thermodynamics*, New York: Wiley, and is reprinted here with permission from John Wiley & Sons Inc.

The quotation on page 139 is taken from AV Shubnikov, VA Koptsik, 1974, *Symmetry in science and art*, New York: Plenum, and is reprinted here with the kind permission of Springer Science and Business Media.

Figure 5.3 is reprinted with permission from SC Cowin, MM Mehrabadi, 1989, Identification of the elastic symmetry of bone and other materials, *J Biomech* **22**:503–515. Copyright © 1989, Elsevier.

Figure 5.6 is reprinted with permission from SA Wainwight, WD Biggs, JD Currey, JM Gosline, 1976, *Mechanical design in organisms*. London: Arnold, Copyright © 1976, Hodder Arnold Journals.

Figure 5.8 is reprinted with permission from D Hull, 1981, *An introduction to composite materials*, Cambridge: Cambridge UP. Copyright © 1981, Elsevier.

Figure 5.10 is reprinted with permission from P Chadwick, M Vianello, SC Cowin, 2001, A proof that the number of linear anisotropic elastic symmetries is eight, *J Mech Phys Solids* **49**:2471–2492. Copyright © 2001, Elsevier.

Figure 5.11 is reprinted with permission from M Rovati, A Taliercio, 2003, Stationarity of the strain energy density for some classes of anisotropic solids, *Int J Solids Struct* **40**:6043–6075. Copyright © 2003, Elsevier.

Figure 5.12 is reprinted with permission from M Rovati, A Taliercio, 2003, Stationarity of the strain energy density for some classes of anisotropic solids, *Int J Solids Struct* **40**:6043–6075. Copyright © 2003, Elsevier.

Figure 5.13 is reprinted from M Fraldi, SC Cowin, 2002, Chirality in the torsion of cylinders with trigonal material symmetry, *J Elast* **69**:121–148, with the kind permission of Springer Science and Business Media. Copyright © 2002, Springer.

Figure 5.14 M Fraldi, SC Cowin, 2002, Chirality in the torsion of cylinders with trigonal material symmetry, *J Elast* **69**:121–148, with the kind permission of Springer Science and Business Media. Copyright © 2002, Springer.

The quotation on page 169 is taken from CA Truesdell, W Noll, 1965, The non-linear field theories of mechanics. In *Handbuch der Physik*, ed. S Flugge, pp. 1–602, Berlin: Springer Verlag, and is reprinted here with the kind permission of Springer Science and Business Media.

The quotation on page 185 is taken from AEH Love, 1927, *Elasticity*, New York: Dover, and is reprinted here with the kind permission of Dover.

Figure 7.7 is reprinted with permission from FJ Lockett, 1972, *Nonlinear viscoelastic solids*. New York: Academic Press. Copyright © 1972, Elsevier.

The quotation on page 225 is taken from S Nemat-Nasser, M Hori, 1999, *Micromechanics: overall properties of heterogeneous materials*, Amsterdam: Elsevier, and is reprinted here with the kind of permission of Elsevier.

The quotation on page 247 is taken from MA Biot, 1941, General theory of three-dimensional consolidation, *J Appl Phys* **12**:155–164, and is reprinted here with the kind of permission of the American Institute of Physics.

Figure 9.6 is reprinted with permission from B Cohen,, WM Lai,, VC Mow, 1998, A transversely isotropic biphasic model for unconfined compression of growth plate and chondroepiphysis, *J Biomech Eng* **120**:491–496. Copyright © 1998, the American Society of Mechanical Engineers.

Figure 9.7 is reprinted with permission from B Cohen,, WM Lai,, VC Mow, 1998, A transversely isotropic biphasic model for unconfined compression of growth plate and chondroepiphysis, *J Biomech Eng* **120**:491–496. Copyright © 1998, the American Society of Mechanical Engineers.

Figure 9.8 is reprinted with permission from B Cohen,, WM Lai,, VC Mow, 1998, A transversely isotropic biphasic model for unconfined compression of growth plate and chondroepiphysis, *J Biomech Eng* **120**:491–496. Copyright © 1998, the American Society of Mechanical Engineers.

The quotation on page 289 is taken from J Woodhead-Galloway, 1980, *Collagen: the anatomy of a protein* (Studies in Biology, no. 117), London: Arnold, and is reprinted here with the kind of permission of John Woodhead-Galloway.

Figure 10.1 is reprinted with permission from V Mow, A Ratcliffe, AR Poole, 1992, Cartilage and diarthrodial joints as paradigms for hierarchical materials and structures, *Biomaterials* **13**:67–97. Copyright © 1992, Elsevier.

Figure 10.2 is reprinted with permission from V Mow, A Ratcliffe, AR Poole, 1992, Cartilage and diarthrodial joints as paradigms for hierarchical materials and structures, *Biomaterials* **13**:67–97. Copyright © 1992, Elsevier.

Figure 10.3 is reprinted with permission from http://www.kumc.edu/instruction/medicine/anatomy/histoweb/ct/Histoct.htm.

Figure 10.4 is reprinted with permission from http://www.kumc.edu/instruction/medicine/anatomy/histoweb/ct/Histoct.htm.

Figure 10.5 is reprinted with permission from B Alberts, D Bray, J Lewis, M Raff, K Roberts, JD Watson, 1983, *Molecular biology of the cell*, New York: Garland. Copyright © 1983, Garland.

Figure 10.6 is reprinted with permission from http://www.kumc.edu/instruction/medicine/anatomy/histoweb/ct/Histoct.htm.

Figure 10.7 is reprinted with permission from J Woodhead-Galloway, 1980, *Collagen: the anatomy of a protein* (Studies in Biology, no. 117), London: Arnold. Copyright © 1980, Arnold.

Figure 10.8 is reprinted with permission from http://bmbiris.bmb.uga.edu/wampler/tutorial/prot1.html. Copyright © 1996, J.E. Wampler.

Figure 10.9 is reprinted with permission from B Alberts, D Bray, J Lewis, M Raff, K Roberts, JD Watson, 1983, *Molecular biology of the cell*, New York: Garland. Copyright © 1983, Garland.

Figure 10.12 is reprinted with permission from FH Silver, JW Freeman, GP Seehra, 2003, Collagen self-assembly and the development of tendon mechanical properties, *J Biomech* **36**:1529–1554. Copyright © 2003, Elsevier.

Figure 10.14 is reprinted from RL Trelstad, FH Silver, 1981, Matrix assembly, In *Cell biology of the extracellular matrix*, ed. ED Hay, pp. 179–216, New York: Plenum Press, with the kind permission of Springer Science and Business Media. Copyright © 1981, Springer.

Figure 10.16 is reprinted with permission from B Alberts, D Bray, J Lewis, M Raff, K Roberts, JD Watson, 1983, *Molecular biology of the cell*, New York: Garland. Copyright © 1983, Garland.

Figure 10.17 is reprinted with permission from K Beck, B Brodsky, 1998, Supercoiled protein motifs: the collagen triple-helix and the α-helical coiled coil, *J Struct Biol* **122**:17–29. Copyright © 1998, Elsevier.

Figure 10.18 is reprinted with permission from C Cohen, 1998, Why fibrous proteins are romantic, *J Struct Biol* **122**:3–16. Copyright © 1998, Elsevier.

Figure 10.19 is reprinted with permission from FHC Crick, 1953, The packing of α-helices: simple coiled coils, *Acta Crystallogr* **6**:689–697. Copyright © 1953, Blackwell Publishing.

Figure 10.20 is reprinted with permission from FHC Crick, 1953, The packing of α-helices: simple coiled coils, *Acta Crystallogr* **6**:689–697. Copyright © 1953, Blackwell Publishing.

Figure 10.20 is reprinted courtesy of Davis S. Goodsell, of the Scripps Research Institute, who created the illustration.

Figure 10.21 is reprinted with permission from RL Trelstad, K Hayashi, 1979, Tendon fibrillogenesis: intracellular collagen subassemblies and cell surface charges associated with fibril growth, *Dev Biol* **7**:228–242. Copyright © 1979, Elsevier.

Figure 10.22 is reprinted from RL Trelstad, FH Silver, 1981, Matrix assembly, In *Cell biology of the extracellular matrix*, ed. ED Hay, pp. 179–216, New York: Plenum Press, with the kind permission of Springer Science and Business Media. Copyright © 1981, Springer.

Figure 10.23 is reprinted with permission from J Woodhead-Galloway, 1980, *Collagen: the anatomy of a protein* (Studies in Biology, no. 117), London: Arnold. Copyright © 1980, Arnold.

Figure 10.24 is reprinted with permission from J Woodhead-Galloway, 1980, *Collagen: the anatomy of a protein* (Studies in Biology, no. 117), London: Arnold. Copyright © 1980, Arnold.

Figure 10.26 is reprinted with permission from FH Silver, JW Freeman, GP Seehra, 2003, Collagen self-assembly and the development of tendon mechanical properties, *J Biomech* **36**:1529–1554. Copyright © 2003, Elsevier.

Figure 10.27 FH Silver, JW Freeman, GP Seehra, 2003, Collagen self-assembly and the development of tendon mechanical properties, *J Biomech* **36**:1529–1554. Copyright © 2003, Elsevier.

Figure 10.28 is reprinted with permission from FH Silver, JW Freeman, GP Seehra, 2003, Collagen self-assembly and the development of tendon mechanical properties, *J Biomech* **36**:1529–1554. Copyright © 2003, Elsevier.

Figure 10.29 is reprinted with permission from http://www.kumc.edu/instruction/medicine/anatomy/histoweb/ct/Histoct.htm.

Figure 10.30 is reprinted with permission from http://www.kumc.edu/instruction/medicine/anatomy/histoweb/ct/Histoct.htm.

Figure 10.32 is reprinted with permission from AC Neville, 1993, *Biology of fibrous composites*, Cambridge: Cambridge UP. Copyright © 1993, Cambridge University Press.

Figure 10.33 is reprinted with permission from MM Giraud-Guille, 1996, Twisted liquid crystalline supramolecular arrangements in morphogenesis, *Int Rev Cytol* **166**:59–101. Copyright © 1996, Elsevier.

Figure 10.34 is reprinted with permission from MM Giraud-Guille, 1996, Twisted liquid crystalline supramolecular arrangements in morphogenesis, *Int Rev Cytol* **166**:59–101. Copyright © 1996, Elsevier.

Figure 10.35 AC Neville, 1993, *Biology of fibrous composites*, Cambridge: Cambridge UP. Copyright © 1993, Cambridge University Press.

Figure 10.36 is reprinted with permission from FH Silver, JW Freeman, GP Seehra, 2003, Collagen self-assembly and the development of tendon mechanical properties, *J Biomech* **36**:1529–1554. Copyright © 2003, Elsevier.

Figure 10.37 is reprinted with permission from FH Silver, JW Freeman, GP Seehra, 2003, Collagen self-assembly and the development of tendon mechanical properties, *J Biomech* **36**:1529–1554. Copyright © 2003, Elsevier.

Figure 10.38 is reprinted with permission from http://www.msstate.edu/dept/poultry/avianemb.htm#stages with the permission of the Mississippi State Extension Service.

Figure 10.39 is reprinted with permission from FH Silver, JW Freeman, GP Seehra, 2003, Collagen self-assembly and the development of tendon mechanical properties, *J Biomech* **36**:1529–1554. Copyright © 2003, Elsevier.

Figure 10.40 is reprinted with permission from DE Birk, EJ Zycband, 1994, Assembly of the tendon extracellular matrix during development, *J Anat* **184**:457–463. Copyright © 1994, Blackwell Publishing.

Figure 10.41 is reprinted with permission from FH Silver, JW Freeman, GP Seehra, 2003, Collagen self-assembly and the development of tendon mechanical properties, *J Biomech* **36**:1529–1554. Copyright © 2003, Elsevier.

Figure 10.42 is reprinted with permission from FH Silver, JW Freeman, GP Seehra, 2003, Collagen self-assembly and the development of tendon mechanical properties, *J Biomech* **36**:1529–1554. Copyright © 2003, Elsevier.

Figure 10.43 is reprinted with permission from DE Birk, EJ Zycband, 1994, Assembly of the tendon extracellular matrix during development, *J Anat* **184**:457–463. Copyright © 1994, Blackwell Publishing.

Figure 10.44 is reprinted with permission from FH Silver, JW Freeman, GP Seehra, 2003, Collagen self-assembly and the development of tendon mechanical properties, *J Biomech* **36**:1529–1554. Copyright © 2003, Elsevier.

Figure 10.45 is reprinted with permission from FH Silver, JW Freeman, GP Seehra, 2003, Collagen self-assembly and the development of tendon mechanical properties, *J Biomech* **36**:1529–1554. Copyright © 2003, Elsevier.

Figure 10.46 is reprinted with permission from FH Silver, JW Freeman, GP Seehra, 2003, Collagen self-assembly and the development of tendon mechanical properties, *J Biomech* **36**:1529–1554. Copyright © 2003, Elsevier.

Figure 10.47 is reprinted with permission from FH Silver, JW Freeman, GP Seehra, 2003, Collagen self-assembly and the development of tendon mechanical properties, *J Biomech* **36**:1529–1554. Copyright © 2003, Elsevier.

Figure 10.48 is reprinted with permission from DE Birk, EJ Zycband, 1994, Assembly of the tendon extracellular matrix during development, *J Anat* **184**:457–463. Copyright © 1994, Blackwell Publishing.

Figure 10.49 is reprinted with permission from FH Silver, JW Freeman, GP Seehra, 2003, Collagen self-assembly and the development of tendon mechanical properties, *J Biomech* **36**:1529–1554. Copyright © 2003, Elsevier.

Figure 10.50 is reprinted with permission from FH Silver, JW Freeman, GP Seehra, 2003, Collagen self-assembly and the development of tendon mechanical properties, *J Biomech* **36**:1529–1554. Copyright © 2003, Elsevier.

Figure 10.51 is reprinted with permission from FH Silver, JW Freeman, GP Seehra, 2003, Collagen self-assembly and the development of tendon mechanical properties, *J Biomech* **36**:1529–1554. Copyright © 2003, Elsevier.

The quotation on page 841 is taken from FG Evans, 1973, *Mechanical properties of bone*, Springfield, IL: Charles C. Thomas, and is reprinted here with the kind of permission of Charles C. Thomas.

Figure 11.1 is reprinted with permission from SC Cowin, 1981, Mechanical properties of bones, In *Mechanics of structured media*, ed. APS Selvadurai, pp. 151–184, Philadelphia: Elsevier. Copyright © 1981, Elsevier.

Figure 11.2 is reprinted with permission from SC Cowin, 1981, Mechanical properties of bones, In *Mechanics of structured media*, ed. APS Selvadurai, pp. 151–184, Philadelphia: Elsevier. Copyright © 1981, Elsevier.

Figure 11.3 is reprinted with permission from SC Cowin, WC Buskirk Van, RB Ashman, 1987, The properties of bone, In *Handbook of bioengineering*, ed. R Skalak, S Chien, pp. 2.1–2.27, New York: McGraw-Hill. Copyright © 1987, the McGraw Hill Companies.

Figure 11.4 is reprinted with permission from LM Siperko, WJ Landis, 2001, Aspects of mineral structure in normally calcifying avian tendon, *J Struct Biol* **135**:313–320. Copyright © 2001, Elsevier.

Figure 11.5 is reprinted with permission from SC Cowin, MM Mehrabadi, 1989, Identification of the elastic symmetry of bone and other materials, *J Biomech* **22**:503–515. Copyright © 1989, Elsevier.

Figure 11.6 is reprinted with permission from SC Cowin, MM Mehrabadi, 1989, Identification of the elastic symmetry of bone and other materials, *J Biomech* **22**:503–515. Copyright © 1989, Elsevier.

Figure 11.7 is reprinted with permission from SC Cowin, 1999, Bone poroelasticity, *J Biomech* **32**:218–238. Copyright © 1999, Elsevier.

Figure 11.8 is reprinted with permission from EA Williams, RHJ Fitzgerald, PJ Kelly, 1984, Microcirculation in bone, In *The physiology and pharmacology of the microcirculation*, ed. NA Mortillaro, New York: Academic Press. Copyright © 1984, Elsevier.

Figure 11.9 is reprinted with permission from PJ Atkinson, AS Hallsworth, 1983, The changing structure of aging human mandibular bone, *Gerodontology* **2**:57–66. Copyright © 1983, Beech Hill Enterprises Inc.

Figure 11.12 is reprinted from SR Pollack, R Salzstein, D Pienkowski, 1984, The electric double layer in bone and its influence on stress-generated potentials, *Calcif Tissue Int* **36**:S77–S81, with the kind permission of Springer Science and Business Media. Copyright © 1984, Springer.

Figure 11.13 is reprinted with permission from L Wang, SP Fritton, SC Cowin, S Weinbaum, 1999, Fluid pressure relaxation depends upon osteonal microstructure: modeling of an oscillatory bending experiment, *J Biomech* **32**:663–672. Copyright © 1999, Elsevier.

Figure 11.14 is reprinted with permission from W Starkebaum, SR Pollack, E Korostoff, 1979, Microelectrode studies of stress-generated potentials in four-point bending of bone, *J Biomed Mater Res* **13**:729–751. Copyright © 1979, John Wiley & Sons Inc.

Figure 11.15 is reprinted with permission from L Wang, SP Fritton, SC Cowin, S Weinbaum, 1999, Fluid pressure relaxation depends upon osteonal microstructure: modeling of an oscillatory bending experiment, *J Biomech* **32**:663–672. Copyright © 1999, Elsevier.

Figure 11.16 is reprinted with permission from SC Cowin, 1999, Bone poroelasticity, *J Biomech* **32**:218–238. Copyright © 1999, Elsevier.

Figure 11.17 is reprinted from G Yang, J Kabel, B van Rietbergen, A Odgaard, R Huiskes, 1999, The anisotropic Hooke's law for cancellous bone and wood, *J Elast* **53**:125–146, with the kind permission of Springer Science and Business Media. Copyright © 1999, Springer.

Figure 11.18 is reprinted with permission from J Wolff, 1870, Uber der innere Architektur der Knochen und ihre Bedeutung fur die Frage vom Knochenwachstum, *Arch Path Anat Physiol Med, Virchovs Arch* **50**:389–453.

Figure 11.19 is reprinted with permission from G Yang, J Kabel, B van Rietbergen, A Odgaard, R Huiskes, 1999, The anisotropic Hooke's law for cancellous bone and wood, *J Elast* **53**:125–146, with the kind permission of Springer Science and Business Media. Copyright © 1999, Springer.

Figure 11.20 is reprinted with permission from G Yang, J Kabel, B van Rietbergen, A Odgaard, R Huiskes, 1999, The anisotropic Hooke's law for cancellous bone and wood, *J Elast* **53**:125–146, with the kind permission of Springer Science and Business Media. Copyright © 1999, Springer.

Figure 11.21 is reprinted with permission from G Yang, J Kabel, B van Rietbergen, A Odgaard, R Huiskes, 1999, The anisotropic Hooke's law for cancellous bone and wood, *J Elast* **53**:125–146, with the kind permission of Springer Science and Business Media. Copyright © 1999, Springer.

Figure 11.22 is reprinted with permission from G Yang, J Kabel, B van Rietbergen, A Odgaard, R Huiskes, 1999, The anisotropic Hooke's law for cancellous bone and wood, *J Elast* **53**:125–146, with the kind permission of Springer Science and Business Media. Copyright © 1999, Springer.

The quotation on page 385 is taken from HM Frost, 1964, *The laws of bone structure*, Springfield, IL: Charles C. Thomas, and is reprinted here with the kind of permission of Charles C. Thomas.

Figure 12.1 is reprinted with permission from SC Cowin, RT Hart, JR Balser, DH Kohn, 1985, Functional adaptation in long bones: establishing in vivo values for surface remodeling rate coefficients, *J Biomech* **18**:665–684. Copyright © 1985, Elsevier.

Figure 12.2 is reprinted with permission from SC Cowin, RT Hart, JR Balser, DH Kohn, 1985, Functional adaptation in long bones: establishing in vivo values for surface remodeling rate coefficients, *J Biomech* **18**:665–684. Copyright © 1985, Elsevier.

Figure 12.3 is reprinted with permission from SC Cowin, RT Hart, JR Balser, DH Kohn, 1985, Functional adaptation in long bones: establishing in vivo values for surface remodeling rate coefficients, *J Biomech* **18**:665–684. Copyright © 1985, Elsevier.

Figure 12.4 is reprinted with permission from SC Cowin, RT Hart, JR Balser, DH Kohn, 1985, Functional adaptation in long bones: establishing in vivo values for surface remodeling rate coefficients, *J Biomech* **18**:665–684. Copyright © 1985, Elsevier.

Figure 12.5 is reprinted with permission from SC Cowin, DH Hegedus, 1976, Bone remodeling, I: theory of adaptive elasticity, *J Biomech* **6**:313–326. Copyright © 1976, Elsevier.

Figure 12.7 is reprinted with permission from LE Lanyon, AE Goodship, CJ Pye, JH MacFie, 1982, Mechanically adaptive bone remodeling, *J Biomech* **15**:141–154. Copyright © 1982, Elsevier.

Figure 12.8 is reprinted with permission from SC Cowin, RT Hart, JR Balser, DH Kohn, 1985, Functional adaptation in long bones: establishing in vivo values for surface remodeling rate coefficients, *J Biomech* **18**:665–684. Copyright © 1985, Elsevier.

Figure 12.9 is reprinted with permission from SC Cowin, RT Hart, JR Balser, DH Kohn, 1985, Functional adaptation in long bones: establishing in vivo values for surface remodeling rate coefficients, *J Biomech* **18**:665–684. Copyright © 1985, Elsevier.

Figure 12.10 is reprinted with permission from SC Cowin, RT Hart, JR Balser, DH Kohn, 1985, Functional adaptation in long bones: establishing in vivo values for surface remodeling rate coefficients, *J Biomech* **18**:665–684. Copyright © 1985, Elsevier.

Figure 12.11 is reprinted with permission from SC Cowin, RT Hart, JR Balser, DH Kohn, 1985, Functional adaptation in long bones: establishing in vivo values for surface remodeling rate coefficients, *J Biomech* **18**:665–684. Copyright © 1985, Elsevier.

Figure 12.12 is reprinted with permission from SC Cowin, RT Hart, JR Balser, DH Kohn, 1985, Functional adaptation in long bones: establishing in vivo values for surface remodeling rate coefficients, *J Biomech* **18**:665–684. Copyright © 1985, Elsevier.

Figure 12.12 is reprinted with permission from SC Cowin, RT Hart, JR Balser, DH Kohn, 1985, Functional adaptation in long bones: establishing in vivo values for surface remodeling rate coefficients, *J Biomech* **18**:665–684. Copyright © 1985, Elsevier.

Figure 12.13 is reprinted with permission from SC Cowin, RT Hart, JR Balser, DH Kohn, 1985, Functional adaptation in long bones: establishing in vivo values for surface remodeling rate coefficients, *J Biomech* **18**:665–684. Copyright © 1985, Elsevier.

Figure 12.14 is reprinted with permission from SC Cowin, DH Hegedus, 1976, Bone remodeling, I: theory of adaptive elasticity, *J Biomech* **6**:313–326. Copyright © 1976, Elsevier.

Figure 12.15 is reprinted with permission from SC Cowin, DH Hegedus, 1976, Bone remodeling, I: theory of adaptive elasticity, *J Biomech* **6**:313–326. Copyright © 1976, Elsevier.

Figure 13.2 is reprinted with permission from JM Huyghe, PHM Bovendeerd, 2003, *Biological Mixtures*, Lecture notes for course 4A650, Technische Universiteit Eindhoven. Copyright © 2003, Jacques Huyghe.

Figure 13.4 is reprinted with permission from AJH Frijns, JM Huyghe, JD Janssen, 1997, A validation of the quadriphasic mixture theory for intervertebral disc tissue, *Int J Eng Sci* **35**:1419–1429. Copyright © 1997, Elsevier.

Figure 13.5 is reprinted with permission from AJH Frijns, JM Huyghe, JD Janssen, 1997, A validation of the quadriphasic mixture theory for intervertebral disc tissue, *Int J Eng Sci* **35**:1419–1429. Copyright © 1997, Elsevier.

Figure 13.6 is reprinted with permission from AJH Frijns, JM Huyghe, JD Janssen, 1997, A validation of the quadriphasic mixture theory for intervertebral disc tissue, *Int J Eng Sci* **35**:1419–1429. Copyright © 1997, Elsevier.

Figure 13.7 is reprinted with permission from AJH Frijns, JM Huyghe, JD Janssen, 1997, A validation of the quadriphasic mixture theory for intervertebral disc tissue, *Int J Eng Sci* **35**:1419–1429. Copyright © 1997, Elsevier.

Figure 13.8 is reprinted with permission from AJH Frijns, JM Huyghe, JD Janssen, 1997, A validation of the quadriphasic mixture theory for intervertebral disc tissue, *Int J Eng Sci* **35**:1419–1429. Copyright © 1997, Elsevier.

Figure 13.9 is reprinted with permission from AJH Frijns, JM Huyghe, JD Janssen, 1997, A validation of the quadriphasic mixture theory for intervertebral disc tissue, *Int J Eng Sci* **35**:1419–1429. Copyright © 1997, Elsevier.

The quotation on page 471 is taken from VC Mow, A Radcliffe, AR Poole, 1992, Cartilage and diarthroidal joints as paradigms for hierarchical materials, *Biomaterials* **13**:67–97, and is reprinted here with the kind of permission of Elsevier.

Figure 14.1 is reprinted with permission from http://www.medicinenet.com/osteoarthritis/page2.htm.

Figure 14.2 is reprinted with permission from http://www.kumc.edu/instruction/medicine/anatomy/histoweb/ct/Histoct.htm.

Figure 14.3 is reprinted with permission from http://www.kumc.edu/instruction/medicine/anatomy/histoweb/ct/Histoct.htm.

Figure 14.4 is reprinted with permission from http://www.kumc.edu/instruction/medicine/anatomy/histoweb/ct/Histoct.htm.

Figure 14.5 VC Mow, A Radcliffe, AR Poole, 1992, Cartilage and diarthroidal joints as paradigms for hierarchical materials, *Biomaterials* **13**:67–97, and is reprinted here with the kind of permission of Elsevier.

Figure 14.10 is reprinted with permission from VC Mow, A Radcliffe, AR Poole, 1992, Cartilage and diarthroidal joints as paradigms for hierarchical materials, *Biomaterials* **13**:67–97, and is reprinted here with the kind of permission of Elsevier.

Figure 14.11 is reprinted with permission from VC Mow, A Radcliffe, AR Poole, 1992, Cartilage and diarthroidal joints as paradigms for hierarchical materials, *Biomaterials* **13**:67–97, and is reprinted here with the kind of permission of Elsevier.

Figure 14.12 is reprinted with permission from J Hultkrantz, 1898, Ueber die spaltrichtungen der gelenkknorpel. *Verh Anat Ges* **12**:248–256.

Figure 14.13 is reprinted with permission from VC Mow, CS Proctor, MA Kelly, 1989, Biomechanics of articular cartilage, In *Basic biomechanics of the musculoskeletal system*, 2nd ed., ed. M Nordin, VH Frankel, pp. 31–58, Philadelphia: Lea & Febiger. Copyright © 1989, Lippincott, Williams and Wilkins.

Figure 14.14 is reprinted with permission from VC Mow, CS Proctor, MA Kelly, 1989, Biomechanics of articular cartilage, In *Basic biomechanics of the musculoskeletal system*, 2nd ed., ed. M Nordin, VH Frankel, pp. 31–58, Philadelphia: Lea & Febiger. Copyright © 1989, Lippincott, Williams and Wilkins.

Figure 14.15 is reprinted with permission from VC Mow, CS Proctor, MA Kelly, 1989, Biomechanics of articular cartilage, In *Basic biomechanics of the musculoskeletal system*, 2nd ed., ed. M Nordin, VH Frankel, pp. 31–58, Philadelphia: Lea & Febiger. Copyright © 1989, Lippincott, Williams and Wilkins.

Figure 14.16 is reprinted with permission from VC Mow, CS Proctor, MA Kelly, 1989, Biomechanics of articular cartilage, In *Basic biomechanics of the musculoskeletal system*, 2nd ed., ed. M Nordin, VH Frankel, pp. 31–58, Philadelphia: Lea & Febiger. Copyright © 1989, Lippincott, Williams and Wilkins.

Figure 14.17 is reprinted with permission from VC Mow, CS Proctor, MA Kelly, 1989, Biomechanics of articular cartilage, In *Basic biomechanics of the musculoskeletal system*, 2nd ed., ed. M Nordin, VH Frankel, pp. 31–58, Philadelphia: Lea & Febiger. Copyright © 1989, Lippincott, Williams and Wilkins.

Figure 14.18 is reprinted with permission from VC Mow, CS Proctor, MA Kelly, 1989, Biomechanics of articular cartilage, In *Basic biomechanics of the musculoskeletal system*, 2nd ed., ed. M Nordin, VH Frankel, pp. 31–58, Philadelphia: Lea & Febiger. Copyright © 1989, Lippincott, Williams and Wilkins.

Figure 14.19 is reprinted with permission from BP Conrad, 2001, The effects of glucosamine and chondroitin on the viscosity of synovial fluid in patients with osteoarthritis, Masters of Engineering Thesis, University of Florida. Copyright © 2001, Roger Tran-Son-Tay.

Figure 14.20 is reprinted with permission from F Balazs, D Gibbs, 1970, The rheological properties and biological function of hyaluronic acid, In *Chemistry and biology of the intercellular matrix*, ed. F Balazs, pp. 1241–1253, Academic Press. Copyright © 1970, Elsevier.

Figure 14.21 is reprinted with permission from VC Mow, CS Proctor, MA Kelly, 1989, Biomechanics of articular cartilage, In *Basic biomechanics of the musculoskeletal system*, 2nd ed., ed. M Nordin, VH Frankel, pp. 31–58, Philadelphia: Lea & Febiger. Copyright © 1989, Lippincott, Williams and Wilkins.

Figure 14.22 is reprinted with permission from VC Mow, A Radcliffe, KY Chern, MA Kelly, 1992b, Structure and function relationships of the menisci of the knee, In *Knee meniscus: basic and clinical foundations*, ed. VC Mow, SP Arnoczky, DW Jackson, pp. 37–57, New York: Raven Press. Copyright © 1992, Elsevier.

Figure 14.13 is reprinted with permission from NO Chahine, CC-B Wang, CT Hung, GA Ateshian, 2004, Anisotropic strain-dependent material properties of bovine articular cartilage in the transitional range from tension to compression, *J Biomech* **37**:1251–1261. Copyright © 2004, Elsevier.

Figure 14.24 is reprinted with permission from http://www.stoneclinic.com/menca.htm. Copyright © Kevin R. Stone MD.

Figure 14.25 is reprinted with permission from MA LeRoux, LA Setton, 2002, Experimental and biphasic FEM determinations of the material properties and hydraulic permeability of the meniscus in tension, *J Biomech Eng* **124**:315–321. Copyright © 2002, the American Society of Mechanical Engineers.

The quotation on page 507 is taken from YC Fung, 1967, Elasticity of soft tissues in simple elongation, *Am J Physiol* **213**:1532–1544. Copyright © 1967, the American Physiological Society.

Figure 15.7 is reprinted with permission from DA Danielson, 1973, Human skin as an elastic membrane, *J Biomech* **6**:539–546. Copyright © 1973, Elsevier.

Figure 15.16 is reprinted with permission from YC Fung, 1967, Elasticity of soft tissues in simple elongation, *Am J Physiol* **213**:1532–1544. Copyright © 1967, the American Physiological Society.

Figure 15.17 is reprinted with permission from YC Fung, 1967, Elasticity of soft tissues in simple elongation, *Am J Physiol* **213**:1532–1544. Copyright © 1967, the American Physiological Society.

Figure 15.18 is reprinted with permission from YC Fung, 1967, Elasticity of soft tissues in simple elongation, *Am J Physiol* **213**:1532–1544. Copyright © 1967, the American Physiological Society.

Figure 15.19 is reprinted with permission from YC Fung, 1967, Elasticity of soft tissues in simple elongation, *Am J Physiol* **213**:1532–1544. Copyright © 1967, the American Physiological Society.

Figure 15.20 is reprinted with permission from YC Fung, 1967, Elasticity of soft tissues in simple elongation, *Am J Physiol* **213**:1532–1544. Copyright © 1967, the American Physiological Society.

Figure 15.21 is reprinted with permission from YC Fung, 1967, Elasticity of soft tissues in simple elongation, *Am J Physiol* **213**:1532–1544. Copyright © 1967, the American Physiological Society.

Figure 15.22 is reprinted with permission from YC Fung, 1967, Elasticity of soft tissues in simple elongation, *Am J Physiol* **213**:1532–1544. Copyright © 1967, the American Physiological Society.

Figure 15.23 is reprinted with permission from Y Lanir, YC Fung. 1974, Two-dimensional mechanical properties of rabbit skin, I: experimental system, *J Biomech* **7**:29–34. Copyright © 1974, Elsevier.

Figure 15.24 is reprinted with permission from Y Lanir, YC Fung. 1974, Two-dimensional mechanical properties of rabbit skin, I: experimental system, *J Biomech* **7**:29–34. Copyright © 1974, Elsevier.

Figure 15.24 is reprinted with permission from Y Lanir, YC Fung. 1974, Two-dimensional mechanical properties of rabbit skin, I: experimental system, *J Biomech* **7**:29–34. Copyright © 1974, Elsevier.

Figure 15.25 is reprinted with permission from P Tong, YC Fung, 1976, The stress–strain relationship for the skin, *J Biomech* **9**:649–657. Copyright © 1976, Elsevier.

The quotation on page 559 is taken from CA Carlstedt, M Nordin, 1989, Biomechanics of tendons and ligaments, In *Basic biomechanics of the musculoskeletal system*, 2nd ed., ed. M Nordin, VH Frankel, Philadelphia: Lea & Febiger, and is reprinted here with the kind of permission of Lippincott, Williams and Wilkins.

Figure 16.1 is reprinted with permission from http://mywebpages.comcast.net/wnor/lesson5 mus&tendonsofhand.htm. Copyright © Wesley Norman.

Figure 16.2 is reprinted with permission from JA Weiss, JC Gardiner, 2001, Computational modeling of ligament mechanics, *Crit Rev Biomed Eng* **29**:1–70. Copyright © 2001, Begell House.

Figure 16.3 is reprinted with permission from M Nordin, VH Frankel, 1989, *Basic biomechanics of the musculoskeletal system*, 2nd ed., Philadelphia: Lea & Febiger. Copyright © 1989, Lippincott, Williams and Wilkins.

Figure 16.4 is reprinted with permission from P Kannus, 2000, Structure of the tendon connective tissue, *Scand J Med Sci Sports* **10**:312–320. Copyright © 2000, Blackwell Publishing.

Figure 16.5 is reprinted courtesy of Jeff Weiss.

Figure 16.6 is reprinted with permission from CA Carlstedt, M Nordin, 1989, Biomechanics of tendons and ligaments, In *Basic biomechanics of the musculoskeletal system*, 2nd ed., ed. M Nordin, VH Frankel, Philadelphia: Lea & Febiger. Copyright © 1989, Lippincott, Williams and Wilkins.

Figure 16.7 is reprinted with permission from FR Noyes, 1977, Functional properties of knee ligaments and alterations induced by immobilization, *Clin Orthop* **123**:210–222. Copyright © 1977, Lippincott, Williams and Wilkins.

Figure 16.8 is reprinted with permission from P Fratzl, K Misof, I Zizak, G Rapp, H Amenitsch, S Bernstorff, 1997, Fibrillar structure and mechanical properties of collagen, *J Struct Biol* **122**:119–22. Copyright © 1997, Elsevier.

Figure 16.9 is reprinted with permission from AL Nachemson, JH Evans, 1968, Some mechanical properties of the third human interlaminar ligament (ligamentum favum), *J Biomech* **1**:211–216. Copyright © 1968, Elsevier.

Figure 16.10 is reprinted with permission from KM Quapp, JA Weiss, 1998, Material characterization of human medial collateral ligament, *J Biomech Eng* **120**:757–763. Copyright © 1998, the American Society of Mechanical Engineers.

Figure 16.11 is reprinted with permission from JA Weiss, JC Gardiner, C Bonifasi-Lista, 2002, Ligament material behavior is nonlinear, viscoelastic and rate-independent under shear loading, *J Biomech* **35**:943–950. Copyright © 2002, Elsevier.

Figure 16.12 is reprinted with permission from JA Weiss, JC Gardiner, C Bonifasi-Lista, 2002, Ligament material behavior is nonlinear, viscoelastic and rate-independent under shear loading, *J Biomech* **35**:943–950. Copyright © 2002, Elsevier.

Figure 16.13 is reprinted from CK Untaroiu, J Darvish, J Crandall, B Deng, JT Wang, 2005, Characterization of the lower limb soft tissues in pedestrian finite element models, In *Proc. 19th International technical conference on the enhanced safety of vehicles conference*, Washington, DC: ESV, with the kind permission of Springer Science and Business Media. Copyright © 2005, Springer.

Figure 16.14 is reprinted with permission from CK Untaroiu, J Darvish, J Crandall, B Deng, JT Wang, 2005, Characterization of the lower limb soft tissues in pedestrian finite element models, In *Proc. 19th International technical conference on the enhanced safety of vehicles conference*, Washington, DC: ESV, with the kind permission of Springer Science and Business Media. Copyright © 2005, Springer.

Figure 16.15 is reprinted with permission from CK Untaroiu, J Darvish, J Crandall, B Deng, JT Wang, 2005, Characterization of the lower limb soft tissues in pedestrian finite element models, In *Proc. 19th International technical conference on the enhanced safety of vehicles conference*, Washington, DC: ESV, with the kind permission of Springer Science and Business Media. Copyright © 2005, Springer.

Figure 16.16 is reprinted with permission from CK Untaroiu, J Darvish, J Crandall, B Deng, JT Wang, 2005, Characterization of the lower limb soft tissues in pedestrian finite element models, In *Proc. 19th International technical conference on the enhanced safety of vehicles conference*, Washington, DC: ESV, with the kind permission of Springer Science and Business Media. Copyright © 2005, Springer.

Figure 16.17 is reprinted with permission from C Bonifasi-Lista, SP Lake, MS Small, JA Weiss, 2005, Viscoelastic properties of the human medial collateral ligament under longitudinal, transverse and shear loading, *J Orthop Res* **23**:67–76. Copyright © 2005, Elsevier.

Figure 16.18 is reprinted with permission from C Bonifasi-Lista, SP Lake, MS Small, JA Weiss, 2005, Viscoelastic properties of the human medial collateral ligament under longitudinal, transverse and shear loading, *J Orthop Res* **23**:67–76. Copyright © 2005, Elsevier.

Figure 16.19 is reprinted with permission from C Bonifasi-Lista, SP Lake, MS Small, JA Weiss, 2005, Viscoelastic properties of the human medial collateral ligament under longitudinal, transverse and shear loading, *J Orthop Res* **23**:67–76. Copyright © 2005, Elsevier.

Figure 16.20 is reprinted with permission from L Yin, DM Elliott, 2004, A biphasic and transversely isotropic mechanical model for tendon: application to mouse tail fascicles in uniaxial tension, *J Biomech* **37**:907–916. Copyright © 2004, Elsevier.

Figure 16.21 is reprinted with permission from L Yin, DM Elliott, 2004, A biphasic and transversely isotropic mechanical model for tendon: application to mouse tail fascicles in uniaxial tension, *J Biomech* **37**:907–916. Copyright © 2004, Elsevier.

# INDEX


**A**

Acceleration, 104–105
  and entropy inequality, 439–440
  in mixtures, 428
Achilles tendon, 562–563
Achiral symmetry, 147
Achondroplasia, 473
Actin, 35
Actin belt tightening, 31–33
Actin filaments, 18, 35–37, 56
Action-at-a-distance force, 129, 136, 198
Activator in chemical reaction, 21
Activator-inhibitor model, 28
Adenosine triphosphate (ATP), 15
Adhesion
  cell, 35–36, 48–50
  differential, 24–25
Amino acids
  composition sequence of, 295–297
  definition of, 295
  in the tendon, 325–326
  residues, 295, 297
Amino group, 295
Angular momentum, 50–52, 129–133
Angular velocity, 105
Anions in tissue equilibrium, 444
Anisotropic elasticity theory, 224
Anisotropic material properties, 139
Anisotropy, 145–146, 176–178
  and compression, 270–286
  of articular cartilage, 484
  of cancellous bone, 374, 377–380
  of cortical bone, 356–358
  of stress–strain relations, 573
Annular region, 56
Annulus fibrosus, 479–482
Anterior cruciate ligament (ACL), 559, 563
Apatite, 29, 342
Apical junctions, 31
Apical membrane, 8
Apico-basal polarity, 8
Apoptosis, definition of, 6
Applied strain, 497–498
Appositional growth, 476
Arthritis, 472–473
Arthroidal cartilage, 482
Articular cartilage, 293, 472, 477–478, 482–484, 490–491
  and consolidation model, 65–66
  compressive strain of, 493–495
  linear models for, 492–495
  mechanical modeling of, 492–499
  properties of, 476–478
Assembly
  by cellular activity, 35–37
  supramolecular, 38
Astbury, V.T., 305
ATP. *See* Adenosine triphosphate (ATP)
Axial compressive strain history, 281
Axial diffusion coefficients, 462–463
Axial loading
  and bone remodeling, 399–403
  and intervertebral disc, 480
  of medial collateral ligament, 575–579
Axial permeability, 588
Axon, 9

**B**

Balance of energy, 431–433
Balance of mass, 431–432
Balance of momentum, 431–432
Basement membrane, 310–311
Basolateral membrane, 8
Beam theory, 402
Bearing deformation, 487
Belousov-Zhabotinskii (BZ) reaction, 21–22
Bending moment, 199–200
Bernard, Claude, 349
Biaxial loading, 543
Biglycan, 562
Bilateral external symmetry, 2
Bilateria, 2
Biological structures
  epigenetic information of, 6
  genetic information of, 6–7
  mechanical modeling of, 41–85
Biomechanics
  definition of, 41
  models, 41, 46–47
  problem solving, 45
Biot effective stress coefficient tensor, 249–251, 256, 279

Biot model of poroelasticity, 426
Biot, Maurice Anthony, 248
Biphasic theory, 492
Birefringence pattern, 311–312
Blastula, 32, 34
  -to-gastrula transition, 32, 34
Blood
  as connective tissue, 8
  supply of, 351–352
Bone, 293, 313
  and representative volume element (RVE), 141–142
  cells, 353–356
  deposition, 387–389
  electrokinetic effects in, 362–368
  fluid, 352–353
  function of, 341
  grain direction, 356
  literature of mechanics, 381
  loading, 349, 386–387
  porosity of, 347–351
Bone-lining cells, 354
Bone marrow, 353
Bone matrix, 389–390
  and mechanical loading, 391–392
Bone remodeling, 386–387, 389–392
  and surface adaptation, 399–404
  estimating parameters, 395–399
  stimulus for, 419–421
Bone strain adaptation theories, three-dimensional, 415–418
Bone tissue, 341–384
  adaptation of, 385–422
  cellular mechanisms for, 418–421
  literature of, 421–422
  types of, 342–347
  cancellous, 343–344
  lamellar, 345
  osteonal, 345–347
  woven, 347
Boosted lubrication, 489–490
Border cell, 56
Boundary
  lubrication, 486–492
  movement of, 492–493
  pressure, 188
Boundary conditions
  in bone adaptation, 416
  in bone remodeling, 394
  in intervertebral disc, 460, 462
Boundary-value problems, 186, 196–198
Bright line, 345
Brillouin scattering of collagen, 309
Brush border cell, 56–57
Buckling, 25–28
Bulk and shear moduli, 231–235
Bulk density of mixtures, 429
Bulk modulus, 252–253, 278, 360–361
  and undrained elastic coefficients, 258
Bulk modulus $k$, 194
Bulk stiffness, 425–426
Buoyancy force, 48

## C

C-propetide, 326–327
Cable model in bone remodeling, 420
*Caenorhabditis elegans*, 6
Calcium carbonates, 29
Calcium transport in bone, 349
Callen, Herbert, 119
Canaliculus, 55–56, 347–350, 355–356
Cancellous bone, 342–344, 351
  and fabric tensor, 241
  architecture of, 372–374
  elastic properties of, 374–381
  porosity of, 347
Carboxyl group, 295
Cardiac muscle, 8
Cartesian coordinate system, 44
Cartilage, 313, 471–504
  arthroidal, 482
  articular, 472, 477–478, 482–484, 490–491
  compressive strain of, 493–495
  and intervertebral disc, 480
  linear models, 492–495
  mechanical modeling of, 492–499
  diathroidal, 482
  diseases of, 472–473
  elastic, 471, 474–475
  fibrocartilage, 471–472, 474–476, 482
  hyaline, 471–474, 482
  incompressibility of, 492
  investing, 482
  temporary, 473–474
  types of, 471–472
  white, 474
  yellow, 474
Cartilaginous joints, 471–472
Cations in tissue equilibrium, 444
Cauchy stress, 528, 530–531, 533, 578
Cauchy-Green deformation tensor, 523–524, 534–535
Cayley Hamilton theorem, 535
Cell adhesion, 35, 48–50
Cell chemotaxis, 35
Cell contact guidance, 35, 37
Cell locomotion, 35, 37
Cell membrane, 10–12
  and fibril development, 328–329, 333–334
Cell muscle, 35
Cell process, 55–56
Cell sensors, 35
Cell sorting, 82
Cell surface receptors, 12
Cell-to-cell adhesion, 36
Cell-to-extracellular matrix ratio, 564

Cell-to-matrix adhesion, 36
Cells
  and tissue assembly, 35–37
  definition of, 5–6
  structure and function of, 9–19
Cellular automata, 42, 77–84
  model, 47
Cellular interface (IC), 348–349, 353, 355
Cellular packing, 33
Cement line, 347–349
Centric axial load, 399–400
Centric loading and bone remodeling, 395–396
Centriole, 15
Centroid and bending of bone, 402–403
Chemical potential, 443
Chemical reaction, 21
Chemotaxis, 35
Chick embryogenesis, 326–329, 334
Chiral constant, 163
Chiral symmetry, 147
Chirality, 163–166
Cholesteric liquid crystals, 321, 323–324
Chondral entheses, 589–590
Chondrification, 474
Chondroblasts, 474
Chondrocytes, 472–473, 476, 482–483, 488, 564
Chondrodystrophies, 472
Chondron, 483
Ciliate protozoa and locomotion, 3–4
Cisternae, 17, 29
Class 1 collagens, 310
Class 2 collagens, 310
Class 3 collagens, 310
Class 4 collagens, 310–311
Class 6 collagens, 311
Clausius Duhem inequality, 437
Closed loading cycle, 179–182
Coefficient of friction, 485
Collagen, 289–338
  amino acid content of, 297
  axial Young's modulus of, 307–310
  and bone mineralization, 344
  coiled-coil structure of, 301, 306
  collagen interactions, 478
  extracellular matrix, 291–295
  fibrous, 471
  hierarchical structure of, 19
  in ligaments, 564–566
  in menisci, 501–502
  in tendons, 560, 564–566
  production of, 28–29
  proteoglycans, 479
  stress–strain curve, 567–575
  structure of, 305–307, 312–321
  supramolecular assembly of, 321–324
  types of, 310–312
Collagen triple helix, 297, 299–304, 306–307
Collagen-apatite porosity (PCA), 347–348, 351
  and fluid pressure, 358
Compact bone, 342
Complex modulus, 219
Composite materials, 143–145, 225–226
Compressibility and undrained elastic coefficients, 257–258
Compression
  of anisotropic disk, 270–286
  of intervertebral disc, 459–466
Compressive strain, 498–499
  of articular cartilage, 493–495
Concentration gradient in intervertebral disc, 460
Conditioning period, 459–461
Conditions of compatibility, 196
Condyle, 500
Confined compression, 496
Congruence, 147
Connected cellular network (CCN), 354–356, 419, 564
Connective tissue, 8, 293, 295
  development of, 33
Connexin 43, 564
Conservation laws for mixtures, 430–433
Conservation of angular momentum, 120
Conservation of energy, 119–120, 134–138, 430
Conservation of mass, 120–122, 259, 430
Conservation of momentum, 120, 430
Conservation principles of mechanics, 41–42
Consolidation model, 64–66
Consolidation period, 459–461
Constant second-rank tensor, 511
Constitutive equations
  for continuum model for charged porous medium, 448–453
  formulation of, 169–184
  and material symmetry, 176–178
  for tendons and ligaments, 575
Constitutive ideas, 170–172
Constitutive linearity, 492
Constitutive models, 176
Constitutive properties, 58
Contact guidance, cell, 35, 37
Contactive element, 66
Continuum formulation
  of conservation of energy, 134–138
  of conservation of mass, 120–122
Continuum kinematics, 95–117
Continuum mixture model, 426
  of charged porous medium, 448–453
Continuum model, 76–77
Continuum properties and material microstructure, 226
Continuum theories, formation of, 185–186
*Continuum, The* (Weyl), 43
Contractile element model, 60
Control period, 459–460
Control volumes, 42
Convective flux, 457
Coordinate invariance, 175–176
Coronal plane, 2

Cortical bone, 342, 346
elastic symmetry of, 356–358
poroelastic model for, 358–362
porosity of, 347
strength of, 368–372
Costochondritis, 473
Coulomb, Charles Augustin de, 58
Coulomb friction, 58
Cranial-caudal direction, 2
Creep, 58–59, 571–572
and stress relaxation, 58–59
Creep function, 59, 69–70
stress level-dependent, 580, 582–584
Crick, Francis Harry Compton, 306
Crimp pattern in collagen fibers, 330–331, 565–567
Cross-fluxes, 456
Cross-sectional area in deformation, 508
Crosslinking of tendons, 570
Crystalline materials, 142–146
Crystalline symmetry, 142
Crystals
in bone mineralization, 344
symmetry of, 143
Cubic symmetry, 152–153, 161
Culmann and Meyer drawings (Culmann), 421
Culmann, C., 421
Curl grad, 116
Curvilinear anisotropy, 162
Curvilinear orthotropy, 162
Curvilinear transverse isotropy, 162
Cusp, 365, 367
Cylindrical cavities and elastic constants, 233–236
Cylindrical twist, 323–324
Cytoplasmic channel, 332
Cytoskeletal proteins, 12
Cytoskeleton, 18, 35
Cytosol, 12

**D**

Darcy element, 60–63
Darcy, Henri Philibert Gaspard, 61
Darcy's law for mass transport in a porous medium, 170–172, 175, 186, 236, 249, 254, 256, 260, 456
Dashpot, 58, 63, 65, 220
model of electrical circuit, 91–93
da Vinci, Leonardo, 565
Decorin, 330, 562
Deep zone of collagen, 484
Deflection, 68–71
Deflection curve, 204
Deformable continuum model, 42, 46, 55–57
Deformable material model, 95–104
Deformation, 171, 515–517, 549, 551
of articular cartilage, 493
large, 507–555
large homogeneous, 508–515
of object to indicate motion, 97, 101
of porous medium, 247
pure homogeneous, 524
small, 507–508
tissue, 512–513
volume and surface changes in, 526–528
Deformation elasticity, finite, 531
Deformation gradient, 102, 513–514, 519, 526–527, 531, 536
in mixtures, 427
Deformation gradient tensor, 101, 102–104, 111, 515
Deformation hyperelasticity, finite, 534–535
Deformational motion, 46, 102, 112
Dendrites, 9
Density of mixtures, 429
Deoxyribonucleic acid. *See* DNA
Dermatosparaxis, 308
Dermis, inner, 26
Determinism, 97, 174
Detruser, 7
Developmental embryology, 30–34
Diaphysial region of bone, 342
Diarthroidal cartilage, 482
Diarthroidal joints, 472, 490
Differential adhesion hypothesis, 24–25, 82–83
Diffusion
in charged gradients, 456
in porous media, 186–191
Diffusion constant, 279
Diffusion equations, 80, 260–261
Diffusion velocity, 453–454
in mixtures, 431–433
Diffusive flux, 457
Digital model, 47
Dimensionless pressure, 265
Direct analog, 91, 93
Direct integration of first-order differential equations, 90–91
Direct tendon, 559, 564, 588
Displacement, 116, 266
in infinitesimal motion, 110
Displacement boundary, 197
Displacement gradient, 521–522
Displacement vector, 102–103
DNA, 17
double helix, 30, 31
Donnan equilibrium, 440–448
Donnan osmosis, 460, 464
Dorsal-ventral direction, 2
Drained elastic compliance tensor, 253
Drained elastic constants, 248–250, 358
in cancellous bone, 374
Drained technical constants for cortical bone, 356–357
Dwarfism, 473
Dynamic stiffness, 586

**E**

Eccentric axial load, 399–400
Effective elastic constants, 231–236

Effective material parameters, 228–231
Effective permeability, 236–237
Effective Skempton parameter, 426
Effective stress, 452
Eigenbases, 374, 376–377
Eigenvalues, 376–377, 532–533
Eigenvectors, 376–377
Elastic cartilage, 471, 474–475
Elastic compliance tensor, 250
Elastic constants, 77, 194–195, 248
  effective, 231–236
  for cortical bone, 356–357
Elastic lamellae, 294
Elastic ligaments, 562
Elastic material coefficients, 178–179
Elastic modulus, 495
Elastic orthotropic symmetry, 241–242
Elastic shells, 26
Elastic solids, theory of, 191–207
Elastic strain energy function, 549
Elastic stress response, 552–553
Elastic symmetry
  of cancellous bone, 374–375
  of cortical bone, 356–358
Elastic tension deflection curve, 541
Elasticity
  incompressible, 536–537
  theory, 224
Elastin, 292, 294, 474, 562
Elastodynamic boundary value problems, 196
Elastohydrodynamic lubrication, 487
Elastoquasi-static boundary value problems, 196
Elastostatic boundary value problems, 196
Electrical circuit, models of, 91–93
Electrical potential and fluid flow, 463–464
Electric charges and swelling, 426
Electrokinetic effects in bone, 362–368
Electromagnetic forces, 129–130
Electron microscope, 13
Electroneutrality in continuum model for charged porous medium, 449
Ellipsoids, deformation of, 511–513
Elliptic partial differential equation, 185
Embryology, developmental, 30–34
Endochondral ossification, 474
Endocytosis, 12, 14
Endoplasmic reticulum, 19
Endosome, 14
Endosteal vessel, 352
Endosteum, 342, 349
Endotenon, 566, 584
Energy
  conservation of, 119, 134–138
  supply in mixtures, 431
Enthesis, 588–589
Entropy, 434–437, 450–452
  inequality in continuum model for charged porous medium, 449–453
  in mixtures, 438–440
Epidermis, 26
Epigenetic information of biological structures, 6
Epiligament, 566
Epiphysial region of bone, 342
Epitenon, 37, 566, 584
Epithelia, 8
  morphogenetic folding of, 30–32
Equilibrium, definition of, 1
Euclidean space, 95–96
  model, 43–44
Eukaryotes, 10
Eulerian strain tensor, 520–524
Euler, Léonard, 50
Euler's equations, 50
Exercise experiments in bone strain, 387, 389, 396
Exocytosis, 12, 14–15
Exponential index, 538
Extension ratio, 537
External force systems, 142
External symmetry in animals, 4
Extracellular matrix (ECM), 7, 291–295
  synthesis of, 297

**F**

Fabric tensor, 239–244
Fading memory hypothesis, 216
Fascia, 566
Fascicles, 320–321, 588
Fat in bone, 353
Fiber, 7, 320–321
  diffraction, 306–307
Fiber family strain energy, 549
Fibrillogenesis, 326–330
Fibrils, 314–316
  and birefringence pattern, 312
  formation of, 326–330
  segments, 329–330, 336
Fibroblasts, 35, 328–330, 476, 563–564
Fibrocartilage, 471–472, 474–476, 482
Fibrocartilaninous entheses, 589–590
Fibrochondrocytes, 502
Fibrocytes, 564
Fibrous collagen, 471
Fibrous entheses, 589–590
Fibrous joints, 471
Fick's law for diffusion of a solute in a solvent, 171, 456
Fimbrin, 56–57
Fingerprints as buckling example, 26–28
Finite deformation elasticity, 75–76, 531
Finite deformation hyperelasticity, 534–535
Finite-element (FE) method, 375
First Piola-Kirchhoff stress tensor, 529–531, 534, 536

First-order differential equations, 90–91
Flexo-digitorum superficialis tendons, 559
Flow instabilities, 81
Fluid content, 257, 274–275
  in poroelasticity, 252, 260
Fluid content-stress-pore pressure, 256
  constitutive relation, 252–253
Fluid film lubrication, 485–486, 490
Fluid flow, 61–63
  and porosity, 170–171
  interstitial, 587–588
  through rigid porous media theory, 186–191
Fluid mass flow rate, 254
Fluid mosaic model, 12
Fluid movement in bone channels, 362–363
Fluid pressure, 248
Fluid shear stress and bone remodeling, 420
Fluids in bone, 347–348, 351–353
Fluid theory, 224
Fluid volume flux, 186
Fluxes and gradients of chemical potentials, 456–457
Force generator, 60
Force-current analog, 93
Force-deformation-time behavior, 68–69
Forced steady-state oscillations, 217
Forces on body, 54
Force-voltage analog, 91
Formulas of Nanson, 527
Fourier's law of heat conduction, 171
Free energy, 450–451
Free object diagrams, 42
Free-swelling, 497–498
Friction, 58
Frictional resistance between cations and anions, 453
Functional, 171–172
Functional adaptation, 385–389
Fung's exponential strain energy function, 537–547
Fung's quasi-linear viscoelasticity (QLV), 552–555, 579
Fung, Y.C., 537

## G

Galileo, 369
Gap junctions, 12, 419, 564
Gas
  modeled as spheres, 74–75
  model of, 79–81
Gastrula, 32, 34
Genetic information of biological structures, 6–7
Geometrical linearity, 492
Geometrical nonlinearity, 522
Global coordinate system, 402–403
Glycine, 297, 335
  in collagen, 301
Glycocalyx, 351
Glycoproteins, 474
Glycosaminoglycans, 458, 477
Glycosylation, 298
Golgi apparatus, 16–17
Golgi saccules, 15, 16, 298, 301
Grain coordinate system, 356
Gravity, 129–130
  effect on locomotion, 2–3
Green, George, 77
Guthrie, Woody, 6

## H

Harris, Albert, 41
Havers, Clopton, 345
Haversian canal, 347–348
Haversian systems, 345
Heat flux vector, 135, 450–451
Helical spirals, 163–164
Helical structure
  and chirality, 165
  of collagen, 297–307
Helicoidal pattern, 166, 324
Helmholz free energy, 437
Hexagonal symmetry, 152, 163
Hill, Archibald Vivian, 66
Hill model, 66
Homeostasis, definition of, 1
Homogeneity and material symmetry, 177–178
Homogeneous constitutive models, 176
Homogeneous deformations, 508–515
Hooke, Robert, 5, 58
Hooke's law for elastic materials, 170, 175, 191–192, 231, 233, 255, 409, 446
Hookian model, 58
*How to Solve It* (Polya), 45
Huntingdon's disease, 6
Hyaline cartilage, 471–474, 482
Hyaluronan, 330, 489–490
Hydrodynamic lubrication, 486–487
Hydroxyapatite, 342
Hydroxylation, 297, 298
Hydroxyproline, 297
  in collagen, 301–302
Hyperbolic partial differential equation, 186
Hyperelastic material, 182, 534
Hyperelasticity, finite deformation, 534–535
Hypermineralization, 347
Hysteresis, 539–541, 571

## I

IC, and strain adaptation, 385, 393
Imino acids, 297
Immiscible lattice-gas model, 81–84
Immiscible mixtures, 426
Immobilization experiments in bone strain, 386–387, 395–396

Incompressibility, 209, 426
of cartilage, 492
in continuum model for charged porous medium, 449
and undrained elastic coefficients, 257–258
Incompressibility constraints, 254–257
Incompressible elasticity, 536–537
Incompressible poroelasticity
equations of, 261–262
Infinitesimal motion, 110–115
Infinitesimal rotation tensor, 112
Infinitesimal strain tensor, 112, 174
Inhomogeneous constitutive models, 176
Initial displacement, 266
Instantaneous time rate of change, 106
Interface friction, 487
Interfaces of bone, 347–348
Intermediate filaments, 18, 35–36
Internal bone strain adaptation, one-dimensional model of, 407–415
Internal energy, 134–135, 437
Internal force systems, 142–143
Internal strain adaptation, 385–386, 392–393
Internal strain adaptation rate coefficients, 416
Internal symmetry in animals, 4
Interstitial fluid flow, 247, 588
modeling of, 425
Interstitial growth, 476
Intervertebral disc, 479–482
properties of, 476–478
swelling and compression of, 458–466
Intramembrane ossification, 474
Intrinsic permeability tensor, 254
Inverse analog, 91, 93
Inverse deformation gradient tensor, 101–104
Investing cartilage, 482
Involuntary muscle, 8
Ion channels, 12
Irreversibility in mixture processes, 433–440
Irreversible thermodynamics, 453–458
Isochronal curve, 581–582
Isogenous groups, 476
Isotropy and stress–strain relation, 531–534
Isotropic effective stress coefficient, 250
Isotropic elastic compliance tensor, 253
Isotropic elastic constants, 194–195
Isotropic function, 549
Isotropic finite deformation stress–strain relation, 531–534
Isotropic material properties, 139
Isotropic poroelasticity, 262–270
Isotropic symmetry, 143, 152, 156–157, 159, 161, 188–189, 356
Isotropy, 145, 278–279, 282
and incompressible elasticity, 536

**J**

Jacobian of the deformation, 526
Joints, 471–472
cartilaginous, 471–472
diarthroidal, 472, 490
fibrous, 471
synovial, 472, 485–492

**K**

Kelvin, Lord, 509
Kepler, Johannes, 48
Keratin, 289
Kinetic theory of rubber, 75–76
Kirchhoff stress tensor, 529
Knee joint, 499–503

**L**

Lacunae, 347–349, 354–355
Lacunar-canalicular interface (ILC), 348–349, 361
Lacunar-canalicular porosity (PLC), 284–285, 347–348, 350–351, 353, 361
and fluid pressure, 358–359
Lagrange elasticity, 536–537
Lagrange multiplier, 208–209, 257, 449
Lagrangian strain tensor, 520–524, 545–546
Lagrangian stress tensor, 528–529, 543
Lamellae, 458
in intervertebral disc, 481–482
Lamellar bone, 345, 347, 369
Lamellar structure of cortical bone, 346
Laminae, 345, 347
Laplace's equation, 185–186
Laplace transforms, 86–90, 275–280
LaPlace, Marquis Pierre-Simon de, 95
Large deformations, 507–555
strain measures of, 519–526
volume and surface charges in, 526–528
Large homogeneous deformations, 508–515
Lateral collateral ligament (LCL), 559
Lathyrism, 308
Lattice, 143
Lattice-Boltzmann method, 81
Lattice-gas, 79–81
models of immiscible fluids, 81–84
Length scales, 20, 45
Leukocyte in Maxwell model, 64
Ligaments, 292, 313, 559–591
Ligamentum flavum, 562, 570
Limb development, 21, 23
Limbs, adaptation to gravity, 2
Lineal dimension porosity, 350–351
Linear continuum models, 492
Linear elasticity, 150–154
Linear elastic material, 181–182
Linear growth of fibrils, 335, 337
Linear irreversible thermodynamics, 453–458
Linear models for articular cartilage, 492–495
Linear momentum, 129–133
Linear transformations, 139–140

Linear viscoelasticity, 552–553
Linearization, 175
Lipids in plasma membrane, 11–12
Liquid crystals, 321
  biological analogs of, 321–322
Load deformation curve, 542
Load elongation curve, 568
Load history, 280
Loading of solid, 251
Local time rate, 105
Localization and constitutive equations, 172–173
Locomotion, 2–4
  cell, 35, 37
Loss modulus, 218–219, 490–491
Loss tangent, 219
Lubricant, 486–488
Lubrication in synovial joints, 485–492
Lubricin, 488–489, 567
Lumbar spine, force on, 51–52
Lumped parameter models, 47, 58–74
Lumped three-parameter models, 66–71
Lumped two-parameter models, 64–65
Lunge stretch, 72–73
Lymph as connective tissue, 8
Lysosome, 12–14

**M**

Macrodensity and representative volume element (RVE), 226–227
Marine creatures and gravity, 2–3
Marrow sinusoids, 351–352
Mass balance in mixtures, 430
Mass conservation, 120–122, 259
  equation, 259
  in continuum model for charged porous medium, 448
Mass flow rate, 230
Material coefficient tensors, 176–177
  restrictions of, 182–183
  symmetry of, 178–182
Material coordinate system, 101, 102
Material description of motion, 97, 427–429
Material filament, 519–521, 524, 526
Material functions, 217
Material gradient, 521
Material inhomogeneities, 573
Material microstructure
  modeling of, 225–244
Material mixture, 426
Material parameter fields, 227
Material strain tensor, 520–524
Material symmetry, 142, 145, 150–157
  and constitutive equations, 176–178
  modeling of, 139–166
Material time derivative, 104–105, 108, 120, 428–429
Material time rate, 105, 107
Material volume, 140
Mathematical theory of elasticity, 185
Matrix elastic constant, 248–250, 358
Matrix material
  incompressibility constraint, 254–257
Maxwell, James Clerk, 64
Maxwell model, 64, 92, 220–221
Mean intercept length (MIL) tensor, 240
Mechanical instability, 25
Mechanical loading
  and biological structure adaptation, 7
  in bone, 391–392, 395, 420
  in menisci, 503
  in synovial joints, 485
Mechanical modeling of biological structures, 41–85
Mechanical power, 135–137, 435
Mechanoreception, 419
Mechanosensation in bone, 422
Mechanosensory, 419
Mechanotransduction, 419
Medial collateral ligament (MCL), 559, 563
  and axial loading, 575–575
  and interstitial fluid flow, 587
  shear loading, 577–579
  viscoelasticity of, 579
Medial cruciate ligament, 570
Medullary canal, 342, 351–352
Membrane tension and locomotion, 3–4
Menisci, 499–503, 588
  literature of, 502–504
  properties of, 476–478
Mesenchymal cells, 36
Mesenchymal morphogenesis, 21, 24, 28
Mesenchyme, 293, 295, 474
Messenger ribonucleic acid. *See* mRNA
Metacarpal bone and strain adaptation, 386–387
Metaphysial regions, 342
Meyer, G.H., 421
Micelles, 11
Microfibril, 312–315
Microfilaments, 35
Microgravity, 7
Microstructure, tensorial representations of, 239–244
Microtubules, 18, 35
Microvilli, 12
Middle zone of collagen, 483, 484
Milieu intérieur, 349
Mineral transport in bone, 349
Mineralization of bone, 29, 342, 344
Mirror plane, 147
Mirror symmetry, 147–150
Mitochondrion, 15
Mixed boundary value problem, 198
Mixtures
  and linear irreversible thermodynamics, 453–458
  conservation laws for, 430–433
  irreversibility in processes, 433–440
  kinematics of, 427–430
  theory, 466–467

Models
and physical world, 43–44
biological tissues, 45
Modules of cartilage, 499
Molar fraction of fluid, 457–458
Molecular gliding, 569–570
Molecular self-assembly, 30–31
Molecular state and thermodynamics, 436–437
Moment of inertia, 52–53
Momentum conservation, 259
Momentum supply, 430, 433
Monoclinic symmetry, 151, 154, 158, 160
Monosaccharides, 291
Mooney-Rivlin strain energy, 537, 575–576, 579
Morphogen, 21, 24
Morphogenesis, 2, 21, 29–38
Morphosis state of tissue, 322
Motion
deformational, 95–104, 112
infinitesimal, 110–115
material description of, 427–429
planar, 97–98
planar homogenous, 99–100
rotational, 102, 112
spatial representation of, 104–110, 428
stress equations of, 129–133
translational, 102
translational rigid object, 97
types of, 46
mRNA, 17, 28, 297
Muscle behavior, 66–71
Muscle cells, 8
Muscle contractility, 60
Myosin, 35

**N**

NaCl. *See* Salt
Narwhal, 166
Navier equations of elasticity, 196
Navier-Stokes equations, 208, 236
Nematic liquid crystals, 321
Neo-Hookian material, 537
Nerve cells, 9
Neurons, 9
Neutrino, 119
Newton's second law, 120, 125
Newton, Isaac, 48
Newtonian law of viscosity, 171, 175, 177–178, 183, 207
Newtonian laws, 48
*Non-Linear Field Theories of Mechanics* (Truesdell & Noll), 169
Non-mechanical power, 435
Non-Newtonian fluid, 489
Nonlinear viscoelasticity, 552
Nonlinearity of articular cartilage, 493–498
Normal rates of deformation, 106
Normal strains, 113
Normal stress, 124
N-propetides, 326–327
Nuclear magnetic resonance (NMR) spectroscopy, 305
Nucleolus, 18
Nucleus, 17–18
Nucleus pulposus, 479–481
Nutrient arteries, 351

**O**

*On Growth and Form* (Thompson), 4–5
One-sided flatfish, 3
Onsager relation, 455
Optical microscope, 13
Organelles, 10
Orthogonal transformation, 147–150
Orthotropic elastic compliance tensor, 253
Orthotropic material symmetry, 356
Orthotropic symmetry, 151, 154–156, 158, 160, 178, 188, 356–358
of cancellous bone, 373, 376–377
Orthotropy, 145
Osmosis, 441
Osmotic pressure, 444–448, 478, 497
Osmotic swelling, 495
Ossification, 474
Osteoarthritis, 472–473
Osteoblasts, 353–355
Osteoclasts, 353
Osteocytes, 354–355
and bone remodeling, 419–420
and porosity, 351
Osteogenesis imperfecta, 310
Osteoid, 353
Osteonal bone, 345–347, 369
Osteonal canals, 347–348, 350, 352
Osteons, 344–348, 356, 365, 367
and strain adaptation, 386
strength of, 368–369
Osteoprogenitor cells, 353
Outer boundary, displacement of, 281–282
Ovine ulnar ostectomy in bone remodeling, 397–399

**P**

Parabolic partial differential equation, 186
Paratenon, 566
Partial differential equations, 185–186
Particle in reference coordinate system, 95–97
Particle model, 46, 47–50
Passive-active stress feedback, 32
Patellar tendon, 563
Pauling, Linus Carl, 305–306
pC-collagen, 337
Peptide bond, definition of, 295
Peptide, definition of, 295
Pericellular matrix, 483
Perichondrium, 476

Periosteal entheses, 589–590
Periosteal vessel, 352
Periosteum, 342, 348
Permeability
  effective, 236–237
  of articular cartilage, 493–494
Permeability coefficients, 230–231, 463
Permeability constant, 63
Permeability element, 60–63, 65
Permeability tensor, 182–183, 187
Peroxisome, 16
Persistence length of collagen, 309
Phagosome, 12
Phase plane plot, 412–413
Phospholipid bilayer, 11
Phospholipids in plasma membrane, 11
Phosphorus transport in bone, 349
Piola-Kirchhoff stress tensor, 528, 529
Planar homogeneous motion, 99–100
Planar motion, 97–98
Planar sinusoidal waviness, 565
Planar twist, 323–324
Plane of isotropy, 152, 156–157, 159, 163
Plane of mirror symmetry, 147–154
Plane of reflective symmetry, 147–150
Plane of symmetry, 150–154, 237–239
Plane waves propagation, 204–206
Plasma membrane, 10–12
Platens, 397
pN-collagen, 337
Poise, 211
Poiseuille flow, 210–211
Poiseuille, Jean-Louis-Marie, 211
Poisson-Boltzmann equation, 363
Poisson's ratio, 77, 186, 195, 250–251, 253, 356
  for cancellous bone, 379–380
Poisson, S.D., 77
Polar decomposition
  of deformation gradient, 515–519
  of tensor, 516–519
Polya, George, 45
Polycrystalline materials, 143
Polyisoprene, 75
Polysaccharides, 291, 458
Pore fluid, 186–188, 191, 247
  incompressibility constraint, 254–257
Pore fluid pressure, 247, 358–359
  gradient of, 254
Pore fluid pressure diffusion coefficient, 360
Pore pressure, 188, 251, 274–275, 493–495
  and undrained elastic coefficient, 257
  in poroelasticity, 252
Pore water, 476
Poroelastic constants, 360
Poroelastic materials, 247–249
Poroelastic model for bone, 358–362, 389–390
Poroelasticity, 247–287
  basic equations of, 260–261
Porosity
  and fluid flow, 170–171
  of bone, 347–351
  and cancellous bone, 374
  and fluid pressure, 358
  of the inter-trabecular space (PIT), 348, 351, 353
Porous matrix medium, 247
Porous media, 186–191
  continuum mixture model of, 448–453
Positional information, 24–26
Posterior-anterior direction, 2
Posterior cruciate ligament (PCL), 559, 563
Preosteoblasts, 353
Preosteoclasts, 353
Pressure
  and body fluids, 358–359
  and fluid flow, 62–63
  and localization, 172
  turgor, 4, 8
Pressure diffusion equation, 263–266, 269–270
Pressure gradient, 230, 236
Primary osteons, 346
Pro-collagen, 29
Problem solving, 45
Procollagen, 297–305, 326
Procollagen I molecule, 337
Proline, 297
  in collagen, 301, 302
Propeptides, 335
Prosthesis, 386
Proteins
  definition of, 7, 289, 295
  post-translational modification of, 16–17
  production of, 28–29
  self-assembly of, 30
  synthesis, 18, 297
Proteoglycan 4, 488
Proteoglycan monomer, 290
Proteoglycans, 291–292, 477–478, 483, 492
  collagen interactions, 478–479
  in fibrillogenesis, 330, 336
  in tendons and ligaments, 562
Protozoa and locomotion, 3
Pseudomorphoses, 321–322
Pure homogeneous deformation, 524

## Q

Quantitative stereology, 239
Quasi-linear viscoelasticity (QLV), 552–555, 579

## R

Radial external symmetry, 2
Radiata, 2
Ramachandran, G.N., 306
Ramp loading, 283–284
Rate-of-deformation tensor, 105–107, 109–110

Rate of work, 137
Rates of change, 104–110
Reaction-diffusion equation, 21–22
Reduced relaxation function, 552, 579, 585
Reductionism, limits of, 84–85
Reference coordinate system, 95–96
Reflective symmetry, 154
Relaxation curve, 541
Relaxation functions, 70–71, 220, 552, 554, 581–585
Relaxation time of pore fluid pressure, 359–360, 366
Remodeling equilibrium, 409
  stress, 404–405
Remodeling rate constants, 404–405
Renewal and remodeling of tissue, 2
Representative volume element (RVE), 139–142, 225–228, 393
  and chirality, 164–165
  for cortical bone, 358
  and effective material parameters, 228
  and material symmetry, 143
  for porous medium, 248–249
  and structural gradients, 237–239
Retarder in chemical reaction, 21
Retinacula, 560
Reynolds number, 209
Reynolds, Osborne, 209
Rheumatoid arthritis, 472–473
Ribosomal RNA. *See* rRNA
Ribosomes, 15, 19
Riccati differential equations, 409
Rigid object model, 42, 46, 50–55
Rigid object motions, 173–174
Rigid object rotation, 112
Rigid porous media, theory of, 224
Rotation, 515–517
Rotational motion, 46, 50, 102, 112
Rotation tensor, 115, 515
rRNA, 18, 28, 297
Rubber, kinetic theory of, 75–76
Rule 30, 79
Rule 90, 79
Rule 254, 77–78

**S**

Sagittal plane, 2
Salt and osmotic pressure, 444–446
Scanning electron microscope (SEM), 13
Sea urchin and gastrulation, 32, 34
Second-order tensors, 44
Second Piola-Kirchhoff stress tensor, 529, 531, 534, 536
Secondary osteons, 346
Secretion granules, 15
Self-assembly, 30–31
  of collagen, 332–338
Semi-inverse method, 199
Semipermeable membrane, 442
Sensor domain, 419
Sensors, cell, 35
Severity ratio, 404–405
Shear loading, 574, 577–579
Shear modulus, 232–235, 356, 577–578
Shear rates of deformation, 106
Shear strains, 113–115
Shear strength of bone tissue, 370
Shear stress, 50
Shear thinning, 489–491
Shearing, 107–108
Shearing strain, 221
Shearing stress, 124, 128
Simple extension, 524–525
Single-scalar-linear equation fluid content-stress-pore pressure constitutive relation, 249
Situs inversus, 4
Six-dimensional linear transformation C, 158–162
Skeletal muscle, 8
Skempton compliance difference tensor, 257–258
Skempton compressibility coefficient, 360–361
Ski jumper's trajectory, 48–49
Skin
  as connective tissue, 8
  human, 26
Slider lubrication, 486–487
Slip plane, 363
Small deformations, 507–508
Smectic liquid crystals, 321
Smooth muscle, 8
Solid matrix strain, 497
Solid volume fraction, 373, 376–377, 380
Spatial coordinate system, 101–102
Spatial description of motion, 104, 428
Spatial gradient, 521
Spatial representation of motion, 104–110
Spatial strain tensor, 520–524
Specific internal energy, 434–436
Sphere model for gases, 74–75
Spherical symmetry, 4–5
Spin tensor, 105, 110
Spinal loading, 51–52
Split lines, 484, 485
Spongy bone, 343
  porosity of, 347
Spring element, 65
Spring model of electrical circuit, 91–93
Squeeze film lubrication, 486–487
Standard linear solid (SLS), 66–71, 92
State of stress, 122–128
Statistical mechanics, 46
Statistical models, 47, 74–77
Steady stress, 410–413
Stiffness, 590
Stimulus and strain adaptation, 392–395
Storage modulus, 218–219, 490–491

Strain, 272
and bone deposition, 388
of bone tissue, 370
in creep and stress relaxation, 59
in internal bone strain adaptation, 408
of matrix material, 251
in ovine ulnar ostectomy, 397–399
in porous material, 251
in poroelasticity, 252
measures of large deformation, 519–526
rate on material properties, 572
ratio, 537
Strain adaptation, 385–386
Strain conditions of compatibility, 116–117
Strain displacement, 201–204
Strain energy, 181–182, 537
per unit volume, 542
Strain energy function, 452, 534–535, 545, 575
for tissues, 547–552
Strain tensor, 112–115, 230, 248
and compatibility, 116–117
in bone adaptation, 416–417
Strain variables in poroelasticity, 248–249
Strain-displacement relations, 196
Strain-generated potentials (SGPs), 362, 365–368, 420
Strain–stress relationship, 495–499
Strain–stress-pore pressure relation, 249
Streaming current vector, 363–364
Stress, 122–128, 171, 273
of bone tissue, 370
compressive, 27
effective, 256
and entropy inequality, 439–440
in internal bone strain adaptation, 408
and large deformation, 508
in poroelasticity, 252
in porous matrix medium, 247
under rigid object motions, 173–174
and viscoelastic materials, 212–222
Stress concentration factor, 226–227
Stress equations of motion, 120, 129–133, 208
Stress measure, 528–531
Stress-pore-pressure strain relation, 249
Stress relaxation, 59, 284–286, 571–572, 575
function, 59
test, 552
Stress–strain curves
for collagen, 308–309, 567–575, 583
for shear, 573–574
Stress–strain of articular cartilage, 493
Stress–strain-pore pressure, 256
constitutive relation, 248–252
Stress–strain relations, 192, 216–219, 495–499, 542, 578
Stress tensor, 123–128, 131–133, 228–229, 248, 529, 531
Stress variables in poroelasticity, 248–249
Stress vector, 122–128
Stretch, 524
Stretch-contraction model, 31–33
Stretch tensor, 515, 517
Striated muscle, 8
Structural gradients, 237–239
Superficial tangential zone, 484
Superficial zone protein, 488
Superhelix, 312
Superior-inferior direction, 2
Supramolecular assembly, 38
of collagen, 321–325, 331–338
Surface adaptation and bone remodeling, 399–404
Surface changes in large deformations, 526–528
Surface loading, 267–269
Surface settlement, 267–269
Surface strain adaptation, 385–386, 392–395
coefficients, 393–394
Surface tension, 25
Surface traction, 129, 136
Surface velocity in bone remodeling, 405
Surface zone of collagen, 484
Swelling
of intervertebral disc, 459–466
of tissue, 426
Swelling period, 459–461
Symmetry
in animals, 2–4
and chirality, 163–166
and incompressibility, 255
of material coefficient tensors, 178–182
restriction, 181
spherical, 4–5
*Symmetry* (Weyl), 166
Synovial cells, 584
Synovial fluid, 489–491
Synovial joints, 472, 485–492
Synpase, 9

**T**

Tait, P.G., 509
Telopeptides, 335
Temperature and free energy, 437
Template assembly, 30
Temporary cartilage, 473–474
Tendon, 289, 293, 559–591
anisotropy of stress–strain relations, 573
assembly of, 324–338
cells and cell systems of, 563–564
and collagen composition, 312
collagen fibers in, 564–566
constituents, 561–563
constitutive equations for, 575
crosslinking of, 570
formation, 33
hierarchical structure of, 19–20
insertions of, 588–590
and interstitial fluid flow, 587–588
and lubricating, 488–489
lubrication system in, 566–567

material inhomogeneities, 573
material properties, 572
mechanical properties of, 567
structural adaptation of, 590–591
structure of, 317–320
viscoelasticity of, 571–573, 579–586
and x-ray diffraction, 305
Tenoblasts, 584
Tenocytes, 564
Tensile properties in menisci, 502–503
Tensile strain, 498–499
Tensile strength of bone tissue, 370
Tension
field, 35–36
generated by contractile element, 60
in muscle, 67–68
Tension-compression bilinearity, 494–497
Tensor of creep function, 213–222
Tensor of deformation gradient, 428
Tensor of elastic coefficients, 183
Tensor of relaxation functions, 213, 215–222
Tensor of velocity gradient, 105, 109, 429
Tensors, 44, 176
constant second-rank, 511
in linear transformations, 139–140
polar decomposition of, 515–519
Territorial matrix, 483
Terzaghi consolidation method, 65–66
Terzaghi, Karl, 65
Tetragonal symmetry, 151–152, 161
Textured materials, 142–146
Theory of elastic solids, 191–207
*Theory of Elasticity* (Love), 185
Theory of rigid porous media, 224
Theory of viscoelastic materials, 212–222
Theory of viscous fluids, 207–212
Thermodynamics
of mixtures, 433–440
of the steady state, 453–458
Thermodynamic substrate, 434
Thompson, D'Arcy Wentworth, 4–5
Three-dimensional linear transformation A, 154
Tibia, 500
Tidemark zone of collagen, 483–484
Time, concept of, 43
Time-dependent coefficients, 99, 101
Time scale, 45
Tissues
adaptation of, 2–7
assembly of structure, 29–38
deformation, 512–513
electrical effects in soft, 425–427
electroneutrality of, 440–441, 443
hierarchical structure of, 19–20
plans for structure of, 21–28
strain energy function for, 547–552
structure of, 1–38
types of, 7–9, 293
Toe-off, 487
Total energy, 134–135
Total stress, 553
Trabeculae, 343
and strain adaptation, 386
Trabecular bone, 342–343
and representative volume element (RVE), 228
Trabecular grain, 372–373
Traction boundary, 197
value problem, 197–198
Transcription of proteins, 17, 28, 297
Transfer RNA. *See* tRNA
Transient displacement, 266
Translational motion, 46–48, 50, 102
Translational rigid object motion, 97
Translation of proteins, 18, 28–29, 298
Transmembrane communication, 12
Transmission electron microscope (TEM), 13
Transverse isotropy, 145, 152, 278–279, 282
Transverse plane, 2
Transversely isotropic symmetry, 156–157, 159, 161, 163, 272–273, 356–358
*Treatise on Natural Philosophy* (Kelvin and Tait), 509
Triclinic symmetry, 151, 154, 158, 160
Trigonal symmetry, 151, 160, 163, 239
Triphasic theory, 492
tRNA, 28, 297
True material density, 429
True stress, 528
Turgor pressure, 4, 8
Turing system, 21–24
Turing, Alan, 21
Twisted plywood model, 323–324
Two-porosity poroelastic model, 361, 365
Type I collagen, 297, 300, 310, 312, 314, 325, 476, 560
self-assembly of, 332–338
Type II collagen, 310, 473–474, 476, 483
Type II fibrils, 478
Type III collagen, 310
Type IV collagen, 310–311
Type V collagen, 310
Type VI collagen, 310
Type VII collagen, 311
Type VIII collagen, 310–311
Type IX collagen, 310, 476–477, 478
Type X collagen, 311
Type XI collagen, 310
Type XII collagen, 310
Type XIV collagen, 310
Type XVII collagen, 311

**U**

Ulnar ostectomy
and bone remodeling, 404–405
experiment in bone strain, 387–388, 390, 397
Ultimate strain, 569
Ultimate tensile strength, 569
Ultraviolet microscope, 13

Unconfined compression, 270–286, 496–497
Undrained elastic coefficients, 257–259
Undrained elastic constant, 248, 358
Uniform dilation, 524–525
Unit step function, 70
Unsaturated porous media, 425–426

**V**

van't Hoff relation for osmotic pressure, 444
Vascular cells, 584
Vascular porosity (PV), 347–348, 350, 361
  and fluid pressure, 358–359, 366
Vasculature in bone, 351
Vector, 44
  in reference coordinate system, 95–97, 102
Velocity, 104
  in mixtures, 428
  of surface during strain adaptation, 394
Veronda and Westmann strain energy, 577, 579
Vertebral endplate, 479, 482
Villin, 56–57
Viscoelastic materials, theory of, 212–222
Viscoelasticity, 59, 171
  of collagen, 309
  of tendons and ligaments, 571–573, 579–586
  theory, 224
Viscosity coefficients, 207
Viscosity for hyaluronan molecules, 490–491
Viscous fluids
  model, 58
  theory of, 207–212
Viscous stress power, 183
Voigt model, 64–65, 92, 221–222
Voigt, Wodemar, 64
Volar pads, 26–27
Volkmann, Alfred Wilhelm, 347
Volkmann canals, 346–347, 350, 352
Voltage distribution in bone, 365–367
Volume
  changes in large deformations, 526–528
  deformation, 526
Volume flow rate in rigid object motions, 173
Volume fraction, 429
  in bone adaptation, 415–416
Voluntary muscle, 8

**W**

Waddington, C.H., 30
Water in collagen, 477–478
Wave equation, 80
Weightlessness, 7
Wertheim, Guillaume, 77, 369–370
Weyl, Hermann, 43
White cartilage, 474
Whorl pattern of finger print, 27
Wolff, J., 422
Wolff's law of trabecular architecture, 421–422
Wolpet, Lewis, 24
Worm and genetic adaptation, 6
Woven bone, 347
Wraparound tendon, 559, 564
Wringing-out effect, 587

**X**

X-ray diffraction
  of collagen, 305, 308

**Y**

Yellow cartilage, 474
Young's modulus, 235, 253, 356, 374, 463, 503, 537
  of cancellous bone, 378–380
  of collagen, 307–310
Young, Thomas, 196

**Z**

Zeta potential, 363